Numerical and field investigation of dynamic soil-structure interaction at full-scale

A thesis submitted to Imperial College London in partial fulfilment of the requirements for the degree of Doctor of Philosophy and for the Diploma of Imperial College

by

Marios Koronides

Department of Civil and Environmental Engineering

Imperial College London

London SW7 2AZ

JUNE 2023

This PhD thesis is dedicated to my family, my wife Irini,, my parents Athinodoros and Dimitra, and my siblings Constantinos, Stephanie and Antonis

Declaration

The work presented in this thesis was carried out in the Geotechnics Section of the Department of Civil & Environmental Engineering at Imperial College London.

I hereby declare that this thesis is a result of my own work, within the timeframe of my PhD. Any quotation from, or description of the work of others is acknowledged herein by reference to the sources, whether published or unpublished. This thesis is not the same as any that I have submitted for any degree, diploma or other qualification at any other university. No part of this thesis has been or is being concurrently submitted for any such degree, diploma or other qualification.

The copyright of this thesis rests with the author. Unless otherwise indicated, its contents are licensed under a Creative Commons Attribution-Non Commercial 4.0 International Licence (CC BY-NC). Under this licence, you may copy and redistribute the material in any medium or format. You may also create and distribute modified versions of the work. This is on the condition that: you credit the author and do not use it, or any derivative works, for a commercial purpose. When reusing or sharing this work, ensure you make the licence terms clear to others by naming the licence and linking to the licence text. Where a work has been adapted, you should indicate that the work has been changed and describe those changes. Please seek permission from the copyright holder for uses of this work that are not included in this licence or permitted under UK Copyright Law.

Marios Koronides

London, June 2023

Abstract

This PhD thesis details the numerical and field investigation of Soil-Structure Interaction (SSI) and foundation rocking effects on the dynamic response of a steel-frame structure that was founded on a surface foundation. The main focus of the study is on the impact of nonlinearities associated with soil hysteresis and foundation detachment from the adjacent soil domain. For this purpose, an experimental campaign was specifically designed and carried out, consisting of real-scale free and forced vibration experiments on the prototype structure of EUROPROTEAS.

The local site conditions are investigated in the first part of the thesis, where both equivalent linear and fully nonlinear one-dimensional site response analyses are carried out. The calibration of the numerical model benefits from strong motion seismic data recorded by a permanently installed downhole array of accelerometers. The second part of the thesis involves a thorough investigation of the SSI effects and foundation rocking by interpreting the experimental data.

The third part of the thesis presents three-dimensional analyses that simulate the field experiments, explicitly modelling the soil domain and accounting for soil nonlinearity and foundation rocking. The numerical model is calibrated against experiments that induced various levels of SSI effects, soil strains and foundation uplift. A comprehensive discussion is conducted on the modelling of the soil-foundation interface. The study's major contribution relates to a novel approach proposed to simulate areas where the foundation and the soil are not in contact (gap areas). The proposed interface model enables the rigorous simulation of either permanent interface gaps or successions of gap opening and closure. An additional significant novelty is the suggested method to manipulate interface stresses under static conditions, which are crucial for the rocking behaviour of structures. The numerical results highlight the significant influence of interface gaps, interface static normal stresses and soil nonlinearity on the SSI response, under specific circumstances.

Acknowledgements

I am incredibly fortunate to have received the unwavering support of numerous individuals throughout my PhD journey. First and foremost, I would like to express my deepest gratitude to my two research supervisors and mentors, Dr Stavroula Kontoe and Professor Lidija Zdravković. I cannot express how grateful I am for their continuous guidance, unfailing support and encouragement for both academic and non-academic matters. I am profoundly indebted to them, for providing me the opportunity to become a member of the Geotechnics family at Imperial College London and to undertake high quality research. It has been an exceptional honour and privilege to collaborate with them.

This research project was funded by Skempton Scholarship, A.G. Leventis Foundation and Cyprus State Scholarship. Their support has been invaluable. I would also like to express my sincere appreciation to the Seismology and Earthquake Engineering Research Infrastructure Alliance for Europe (SERA) for funding the experiments, as well as to the Engineering Seismology and Earthquake Engineering (ITSAK-EPPO), Laboratory of Soil Dynamics and Geotechnical Earthquake Engineering (SDGEE) of Aristotle University of Thessaloniki (AUTH) for providing us with the necessary instrumentation.

My sincere gratitude to Dr Dimitris Pitilakis and Athanasios Vratsikidis for their exceptional organisation and execution of the experiments. Our collaboration and discussions were highly fruitful. I would also like to thank my PhD examiners, Dr David Taborda and Professor Ioannis Anastasopoulos for the insightful viva discussion, their valuable feedback and rigorous evaluation of this work.

My time at the college has been an enriching experience, thanks to the contributions of the academic and non-academic staff, as well as my fellow PhD students. Special thanks are made to Dr David Solans and Dr Katharina Möller for the constructive discussions and assistance, whenever I needed it.

Finally, there are no words to describe how thankful I am to my family. I am immensely grateful to my parents, Dimitra and Athinodoros for shaping the person I am today. I am grateful to my siblings, Constantinos, Stephanie, and Antonis, for their unconditional love and support. I am grateful to my little nephews, Raphael and Maximilianos, whose arrival brought us immeasurable light and joy. I would like to make special reference to my beloved wife, Irini, who was the person that gave me the motivation to pursue a doctoral degree, believed the most in my abilities, encouraged me throughout these years, demonstrated immense patience and recently showed me what is the true strength to people.

Table of Contents

Declaration **4**

Abstract **5**

Acknowledgements **6**

Table of Contents **7**

List of Figures **16**

List of Tables **47**

List of Symbols **52**

Chapter 1 Introduction **60**

1.1 Background 60

1.2 Scope of research 62

1.3 Thesis layout 63

Chapter 2 Overview of Soil-Structure-Interaction **66**

2.1 Introduction 66

2.2 Kinematic interaction 66

2.3 Inertial interaction 70

2.4 Impedance functions of rigid footings 72

2.5 Foundation Rocking 74

2.6 Factors that affect SSI effects 79

2.7 Importance of foundation soil 81

2.8 Simplified methods to account for SSI 82

2.8.1 Single-degree-of-freedom models 82

2.8.2 Winkler-based models 84

2.8.3 Macroelement soil-foundation model 85

2.8.4 Numerical procedures 85
2.9 Finite element fully nonlinear analyses 86
2.9.1 Advantages 87
2.9.2 Challenges and commonly adopted boundary conditions 87
2.10 Summary 90
Chapter 3 Existing real-scale experiments 92
3.1 Introduction 92
3.2 System Identification methods 92
3.2.1 Non-parametric identification technique 93
3.2.2 Parametric identification technique 94
3.3 Overview of essential experimental studies 94
3.3.1 Lotung nuclear containment models 94
3.3.2 Hualien nuclear containment model 97
3.3.3 Garner valley differential array and Wildlife liquefaction array 98
3.3.4 Edmonton large scale pier 103
3.3.5 EUROPROTEAS 105
3.4 Numerical modelling of real-scale experiments 107
3.5 Summary 108
Chapter 4 Euroseistest Site Description and Site Response Analyses 111
4.1 Introduction 111
4.2 Euroseistest wider site 119
4.3 TST site 121
4.3.1 Soil profile 121
4.3.2 Adopted soil profile 125
4.3.3 Adopted G-γ-D curves 127
4.3.4 Permanently installed downhole array of accelerometers 128
4.4 Site response analyses 129
4.4.1 Examined seismic events 129

4.4.2 Equivalent linear approach 129
4.4.3 Nonlinear approach 130
4.4.4 Nonlinear constitutive model 132
4.4.5 Nonlinear constitutive model calibration 134
4.4.6 V_s back-calculation procedure 135
4.4.7 Comparison between EQL and NLIN results 136
4.4.8 Bedrock depth investigation 137
4.4.9 Natural periods 139
4.4.10 Soil nonlinearity 141
4.5 Summary 143
Chapter 5 Experimental Campaign: Forced and Free Vibration Tests on a Structure Founded on a Surface Foundation 145
5.1 Introduction 145
5.2 EUROPROTEAS prototype structure 146
5.2.1 Conception of the structural design 147
5.2.2 Structural configurations examined 147
5.2.3 Foundation bearing capacity 149
5.2.4 Experimental imperfections 152
5.2.5 Fixed-base dynamic characteristics of the examined structural configurations . 156
5.3 Instrumentation 161
5.3.1 Vibrator characteristics 161
5.3.2 Pull-out system 163
5.3.3 Available monitoring instrumentation and installation 165
5.3.4 Data acquisition system 166
5.4 Raw data conversion 167
5.5 Conception of the test set-up and experimental procedures 167
5.5.1 Structure's instrument configuration 167
5.5.2 Soil instrument configuration 169

5.5.3 Forced vibration tests 172
5.5.4 Free vibration tests 172
5.6 Name convention for the experiments and instruments 173
5.7 Summary of tests carried out 173
5.7.1 Forced vibration experiments summary 174
5.7.2 Free vibration tests 175
5.8 Data reliability 175
5.8.1 Vibrator 176
5.8.2 Forced vibration tests repeatability 179
5.8.3 Free vibration tests repeatability 183
5.8.4 Monitoring instruments 185
5.8.5 Summary of unreliable data 193
5.9 Summary 194
Chapter 6 Experimental Data Interpretation and System Identification of SSI Response 196
6.1 Introduction 196
6.2 Free vibration tests 198
6.2.1 Identification of natural frequencies and modes of oscillation 198
6.2.2 Motion decomposition method 203
6.2.3 Natural frequencies of the swaying and torsional modes 205
6.2.4 SSI system's damping 209
6.2.5 Evaluation of nonlinear effects 216
6.2.6 Evidence of soil nonlinearity 220
6.2.7 Evidence of soil-foundation-structure interaction 223
6.2.8 Soil motion attenuation with distance 226
6.3 Forced Vibration tests 229
6.3.1 Strong motion data integration 229
6.3.2 Identification of modes of oscillations 237
6.3.3 Motion decomposition method 241

6.3.4 Identification of natural frequencies 242
6.3.5 Natural frequencies of the swaying and torsional modes 247
6.3.6 Evaluation of nonlinear effects 256
6.3.7 Evidence of soil nonlinearity 259
6.3.8 Evidence of Soil-Foundation-Structure Interaction 262
6.3.9 Soil motion attenuation with distance 269
6.4 Comparison between free and forced vibration experiments 278
6.5 Summary 280
Chapter 7 Soil-Structure-Interaction Numerical Model Calibration 283
7.1 Introduction 283
7.2 Modelled Experiments 288
7.3 Numerical challenges 290
7.4 Static and dynamic numerical analyses 292
7.5 3D half-geometry model 293
7.5.1 Problem geometry and boundary conditions 293
7.5.2 Input motion for free vibration tests 300
7.5.3 Input motion for forced vibration tests 300
7.6 Nonlinear soil constitutive model 301
7.7 Interface modelling and gaps simulation 304
7.7.1 Conventional interface model (Conv) 304
7.7.2 Interface elements formulation 305
7.7.3 Elastic and Elastoplastic interface model without gaps (ELint, EPint) 308
7.7.4 Gaps simulation with elastoplastic interface elements (EPint_*g*mm) 308
7.7.5 Gaps simulation with low stiffness elastic interface elements (LSELint) 310
7.7.6 Hybrid interface model with gaps (HYBint) 310
7.7.7 Gaps configurations 310
7.7.8 Static self-weight analyses: Interface stiffness and distribution of interface normal stresses 311

7.8 Calibration procedure 313
7.8.1 Advantages of forced vibration tests 313
7.8.2 Advantages of free vibration tests 314
7.8.3 Procedure 314
7.9 Calibration criteria and results interpretation 316
7.9.1 Free vibration 316
7.9.2 Forced vibration 317
7.9.3 Normalised response 317
7.10 Structural connections and structural damping 317
7.11 Linear elastic analyses without interface imperfections 321
7.11.1 Free vibration 321
7.11.2 Forced Vibration 323
7.11.3 Discussion and next calibration step 326
7.12 Calibration of interface gaps 327
7.12.1 Forced vibration simulations: Elastic interface elements 327
7.12.2 Forced vibration simulations: Elastoplastic interface elements 330
7.12.3 Free vibration tests 336
7.12.4 Discussion and next calibration step 341
7.13 Nonlinear model calibration against free vibration tests 342
7.13.1 Depth of nonlinear soil layers 342
7.13.2 G-γ-D curves calibration 343
7.13.3 Impact of G_{min} 357
7.13.4 Assessment of the calibrated nonlinear model against other free vibration experiments 361
7.13.5 Assessment of the calibrated nonlinear model against other forced vibration experiments 364
7.14 Calibration of the static interface normal stresses against free vibration tests 366
7.14.1 Free vibration simulations 367

7.14.2 Forced vibration simulations 373
7.14.3 Discussion 373
7.15 Initial opening investigation 376
7.15.1 Free Vibration simulations 377
7.16 Final model calibration 380
7.17 Interface modelling considerations in practical applications 382
7.18 Soil domain dimensions 383
7.18.1 Free Vibration simulations 384
7.18.2 Forced Vibration simulations 385
7.18.3 Discussion 387
7.19 Summary and discussion 387
7.19.1 Calibration procedure 387
7.19.2 Validation 388
7.19.3 Soil behaviour 389
7.19.4 Interface model 390
7.19.5 Applications of the interface model in practical scenarios 393
Chapter 8 Predictive Analyses: Impact of soil compliance, interface gaps and nonlinearities on the system response 394
8.1 Introduction 394
8.2 Free vibration tests 395
8.2.1 Natural frequencies and motion amplitude of the swaying mode 395
8.2.2 Period lengthening mechanisms 397
8.2.3 Damping mechanisms 398
8.2.4 Soil nonlinearity 400
8.2.5 Soil-foundation interface nonlinearity 402
8.2.6 Soil motion 404
8.3 Forced vibration tests 411
8.3.1 Natural frequencies and motion amplitude of the swaying mode 412

8.3.2 Soil nonlinearity 414
8.3.3 Soil-foundation interface nonlinearity 415
8.3.4 Soil motion 418
8.4 Summary 426
Chapter 9 Conclusions and Recommendations 430
9.1 Introduction 430
9.2 Free-field site response 431
9.3 Efficiency of the soil-structure interaction numerical model 432
9.4 Soil constitutive model 434
9.5 Interface model 435
9.6 Practical applications of the proposed methods for interface modelling 437
9.7 Importance of soil-structure interaction effects and foundation rocking 438
9.8 Field evidence of nonlinear response 439
9.9 Soil nonlinearity 440
9.10 Interface nonlinearity and gaps 440
9.11 Period lengthening and damping development mechanisms 443
9.12 Soil motion 443
9.13 Recommendations for future research 445
References 449
Appendix A Site response analyses input and results 469
Appendix A.1 Sample testing details in resonant column and cyclic triaxial apparatuses 469
Appendix A.2 Calibration of G-γ-D curves 470
Appendix A.3 G-γ-D curves input in the EQL site response models 472
Appendix A.4 Parameters and G-γ-D curves input in the Nonlinear site response analyses 473
Appendix A.5 EQL approach description 477
Appendix A.6 Imperial College Generalised Small Strain Stiffness (IC.G3S) Model 478
Appendix A.7 Comparison between experimental and numerical data 479
Appendix B Input excitation details 482

Appendix B.1 Forced vibration tests: applied frequencies 482

Appendix B.2 Free vibration tests: applied pull-out forces 487

Appendix C Reliability of the experiments 489

Appendix C.1 Vibrator reliability: Peak to Peak method 489

Appendix C.2 Vibrator reliability: Series of Fourier Spectra method 493

Appendix C.3 Repeatability of data recorded during the Fully Braced 2-Top Slab experiments 496

Appendix C.4 Repeatability of data recorded during the experiments on the Partly Braced structure loaded along its Weak plane 510

Appendix C.5 Repeatability of data recorded during the experiments on the Partly Braced structure loaded along its Strong plane 524

Appendix C.6 Error between repeated top slab response of repeated experiments 538

Appendix D Free Vibration tests 541

Appendix D.1 Top slab Fourier spectra 541

Appendix E Forced Vibration tests 545

Appendix E.1 Evaluation of the response of the Fully Braced 2-Top Slab structure 545

Appendix E.2 Evaluation of the response of the Pully Braced structure loaded along its Weak plane 547

Appendix E.3 Evaluation of the response of the Pully Braced structure loaded along its Strong plane 549

Appendix E.4 Evaluation of the response of the Fully Braced 1-Top slab structure 551

Appendix F Numerical Model 553

Appendix F.1 Modelled forced vibration experiments 553

Appendix F.2 Modelled free vibration experiments 553

Appendix F.3 2D analyses: Model dimensions investigation 554

Appendix F.4 Input parameters of the examined calibrations of the nonlinear model 557

Appendix F.5 Boundary effects using the final calibration 558

Appendix G Predictive Results 567

Appendix G.1 Free Vibration: Soil motion 567

List of Figures

Figure 2.1: Base slab averaging due to kinematic effects: (a) vertical deformations, (b) horizontal deformations, (c) horizontal high frequency deformations. 68

Figure 2.2: Translational and rotational transfer functions defined as the ratio of the input motion at the foundation level to the free-field motion, which resulted assuming vertical incident S waves. The analysis considers a rigid cylindrical foundation, of radius r, embedded at different depths (e) on elastic half-space (taken from Stewart et al. (1998), adapted from Day (1977)). 69

Figure 2.3: A single-degree-of-freedom structure with (a) fixed-base conditions and (b) flexible base considering soil compliance. (c) The impact of SSI effects on the design spectral accelerations is schematically illustrated (adapted from Mylonakis and Gazetas (2000)). 71

Figure 2.4: Illustrative numerical results from displacement-controlled analyses of a footing subjected to monotonic rotation: (a) moment-rotation curve, (b) rotational stiffness normalised by the elastic stiffness varied with monotonically applied foundation rotation (strip footing), (c) deformed shape and plastic strains contours (Gazetas et al., 2013). 76

Figure 2.5: Contours of plastic strains and normalised moment rotation curves of rigid structure-footing-soil system, characterised with different FSv, subjected to cyclic pushover test (Su: undrained shear strength, B: half width of footing, $\vartheta c, \infty$: angle to which systems topples when FSv=∞) (Gazetas, 2015). 77

Figure 2.6: Impact of soil-to-structure stiffness ratio (σ) and slenderness ratio (h/r) on period lengthening ratio (TT) and foundation damping (βf) (NIST, 2012). 80

Figure 2.7: Impact of structure-to-soil mass ratio (γm) on period lengthening ratio (TT) and damping ratio of the flexible-base system (ζ), as a function of soil-to-structure stiffness ratio (σ) (taken from Maravas et al. (2014), who assumed structural damping ζ=0.02 and $h/r = 1$). 81

Figure 3.1: Displacement components required for system identification in the case of (a) seismic event or (b) forced vibration (refer to Table 3.1 for notation) (Star et al., 2019). 93

Figure 3.2: Experimental set-up of the 1/4-scale nuclear containment structure: (a) vertical and (b) horizontal cross sections of the structural model, illustrating the positions of the structural accelerometers; location of soil instruments placed (c) downhole and (d) on the soil surface (Amorosi et al., 2017). 96

Figure 3.3: Experimental set-up of the permanent structure at the GVDA site (Tileylioglu et al., 2011). 99

Figure 3.4: Experimental set-up of the portable structure placed in WLA and GVDA sites (Star et al., 2015). 100

Figure 3.5: Experimental set-up of the large-scale soil-footing-structure system in Edmonton shown: (a) schematically, (b) in a photo (Sharma and Deng, 2020). 104

Figure 4.1: Mygdonian basin (a) in plan view and (b) looking towards the East. The blue pin shows the TST site; and the red line is a cross section line connecting the Profitis and Stivos villages while passing from the TST site (photos taken from Google Earth). 120

Figure 4.2: Profitis-Stivos (PS) cross section (PS line shown in Figure 4.1), illustrating the faults, offsets of soil formations and bedrock depth variations. The A to G formations are originally proposed by Pitilakis et al. (1999). 120

Figure 4.3: Satellite photo of the Mygdonian basin, illustrating with triangles the positions of the permanent strong motion stations (taken from EUROSEISTEST Strong Motion Network, 1993). 121

Figure 4.4: Plan view of Euroseistest facilities at the TST site, depicting the locations of boreholes (Pitilakis et al., 2018). 122

Figure 4.5: TST stratigraphy interpreted from data collated from (a) BH1-BH11 boreholes (Pitilakis et al., 1999), (b) the 30m deep BH-02 borehole and (c) the 15m deep BH-01 borehole (Pitilakis et al., 2012). The positions of downhole accelerometers are indicated with green dots. 124

Figure 4.6: TST stratigraphy as per Figure 4.5, focusing on the first 40m of soil. The positions of samples tested in resonant column and cyclic triaxial apparatus are shown. 125

Figure 4.7: Vs at the TST site, as interpreted by previous studies. Profiles of (a) 200m and (b) 30m soil columns are presented. 125

Figure 4.8: Soil stratigraphy and shear wave velocity profile adopted in numerical models. 126

Figure 4.9: Illustration of the two-step calibration procedure of G-γ-D curves. Data shown for layer 2. 128

Figure 4.10: FE model illustrating dimensions (not in scale), layering and boundary conditions. 132

Figure 4.11: Illustrative example of the consequences when the calibration prioritises the stiffness or the damping curves. 134

Figure 4.12: Acceleration response spectra at surface and all depths where records are available, that were resulted from the back-calculation procedure. The results were obtained by simulating the 2005 event, with the bedrock modelled at varying depths. 136

Figure 4.13: Site response results recorded and computed by EQL and NLIN analyses, that simulate the 2005 event. The results are presented as acceleration response spectra at the locations where records are available. 137

Figure 4.14: Acceleration time histories or recorded at the soil surface or computed by EQL analysis using the surface to 73m model. The input time history applied at 73m is also presented. 138

Figure 4.15: Acceleration response spectra of EQL (surface to 73m model) motion at surface, using the different durations of the output motion. The recorded and input motions are also presented. 139

Figure 4.16: Acceleration response spectra and transfer functions computed by EQL linear analyses, that simulate the 2005 event, compared with recorded ones. Some theoretical natural frequencies are superimposed to illustrate the origin of amplification. 140

Figure 4.17: Numerical (NLIN) and experimental transfer functions of three seismic events, superimposed by some theoretical natural frequencies. 140

Figure 4.18: Shear stress-shear strain curves computed at the centre of layer 1 by the simulations of the 2005, 2006 and 2016 seismic events. 141

Figure 4.19: G-γ-D curves input in ICFEP, superimposed by the corresponding values computed at integration points of Layers 1 to 3. The values were computed by the simulations of 2005, 2006 and 2016 events and correspond to the time increment when $Ed*$ was the maximum computed. 142

Figure 5.1: (a) Schematic EUROPROTEAS structural elements and dimensions, (b) EUROPROTEAS picture including some instrumentation. 146

Figure 5.2: Structural configuration and loading direction combinations examined under forced vibrations. 148

Figure 5.3: Structural configurations examined under free vibrations. 149

Figure 5.4: Failure envelope in the M-H plane estimated for the case of the EUROPROTEAS'S foundation that correspond to (a) FBr_2Ts and (b) FBr_1Ts structural configuration. 151

Figure 5.5: Impact of contact interface area on the failure envelope in the M-H plane estimated for the case of the EUROPROTEAS'S foundation that correspond to (a) FBr_2Ts and (b) FBr_1Ts structural configuration. 151

Figure 5.6: Experimental configuration of the single-column lab tests. (a) Steel column-foundation and steel column-steel brace connection in front view, (b) steel column-foundation connection in plan view, (c) detail of steel column-steel brace connection in front view. All dimensions are in mm units. (Pitilakis et al., 2012). 153

Figure 5.7: Force-Displacement curves resulted from the static lateral force tests when the force was applied along (a) X-diretion and (b) Y-direction (Pitilakis et al., 2012). 154

Figure 5.8: Displacement time histories and the corresponding Fourier Spectra recorded on the top of the column during the single column free vibration tests. Initial excitation was applied along the (a) X-direction and (b) Y-direction (Pitilakis et al., 2012)..... 154

Figure 5.9: Plan view of a structure subjected to torsional rotation of $1rad$ and the resultant forces produced by a column. 159

Figure 5.10: (a) Vibrator in plan view, (b) Toshiba VF-S9 adjustable speed drive. 161

Figure 5.11: Illustration of the vibrator's masses rotation and the resultant forces (NERA, 2014)... 162

Figure 5.12: Magnitudes of the applied sinusoidal force for each plate combination placed on the vibrator. 163

Figure 5.13: Pictures of (a) Pulling hoist connected to the counterweight and (b) "Sacrificed" wire ropes. 164

Figure 5.14: Schematic illustration of free vibration system. 165

Figure 5.15: Pictures of the instruments used during the experiments: (a) accelerometer clamped on the foundation slab, (b)seismometer buried into the ground, and (c) downhole accelerometer. 166

Figure 5.16: Plan views of the three structural instrument configurations 168

Figure 5.17: Plan views of the configurations of soil instruments placed on the soil surface. The depth of the downhole accelerometer, where available, is also shown in the cross sections. 171

Figure 5.18: Comparison between input frequencies read out from the vibrator's speed drive with frequencies calculated using the peak-to-peak method. (a) Frequency time history inferred from top slab instruments, (b) Mean frequency time history with the corresponding standard deviations, (c) Error between the in-situ and calculated input frequencies. Processed data (2.1n, 2.2n, 2.5n) were recorded during the FBr_2Ts(5)_mD experiment. 177

Figure 5.19: Comparison between frequency time history read out in-situ from the vibrator's speed drive with the time history calculated by employing the SoFS method. (a) Fourier spectra inferred from accelerations recorded by top slab instruments, (b) frequency time histories. (c) Error between in-situ frequencies and frequencies that were calculated by exploiting the 2.5n data. Processed data (2.1n, 2.2n, 2.1n) were recorded during the FBr_2Ts(5)_mD experiment. 178

Figure 5.20: Illustrative example of the acceleration time histories recorded along the North-South direction by the centre top slab instrument (2.5n) during the FBr_2Ts(5)_mD experiment. The response at six different frequencies is shown. 180

Figure 5.21: Peak accelerations recorded on the top slab by the 2.5n instrument during the three experiments on the fully braced two-top slab structure (FBr_2TS). Results are extracted from experiments where the plate mass placed on the vibrator was (a) mA, (b) mB, (c) mC and (d) mD (Table 5.9). 181

Figure 5.22: Peak accelerations recorded on the top slab by the 2.5n instrument during the three experiments on the partly braced two-top slab structure loaded along its weak axis (PBr_W). Results are extracted from experiments where the plate mass placed on the vibrator was (a) mB, (b) mC and (c) mD (Table 5.9). 182

Figure 5.23: Peak accelerations recorded on the top slab by the 2.5n instrument during the three experiments on the partly braced two-top slab structure loaded along its strong axis (PBr_S). Results are extracted from experiments where the plate mass placed on the vibrator was (a) mB, (b) mC and (c) mD (Table 5.9). 182

Figure 5.24: Repeatability investigation for the free vibration test on the FBr_2Ts structure which was loaded initially with pull-out forces of 10.10kN and 9.64kN. Investigation is made through: (a) Normalised acceleration time histories, (b) Variation of normalised peak acceleration with time and (c) Error between the two experiments. The exploited data were recorded by the 2.5n top slab instrument. 184

Figure 5.25: Repeatability investigation for the free vibration test on the FBr_2Ts structure which was loaded initially with pull-out forces of 2.94kN and 2.40kN. Investigation is made through: (a) Normalised acceleration time histories, (b) Variation of normalised peak acceleration with time and (c) Error between the two experiments. The exploited data were recorded by the 2.5n top slab instrument. 185

Figure 5.26: Faulty instrument synchronization example. Acceleration time histories recorded along the North-South direction by the top slab centre instrument (2.5n) during the FBr_2Ts(5)_mD experiment. The response at six different frequencies is shown. 186

Figure 5.27: Comparison of acceleration time histories recorded by an instrument (1.1n) which was poorly clamped on the foundation during FBr_2Ts(1)_mC (exp1) and properly clamped during FBr_2Ts(5)_mC (exp5) experiments. The applied frequency time history is also presented. 187

Figure 5.28: Velocity time histories recorded by the a soil instrument in the NS direction (0.1n) during the FBr_2Ts(1)_mD (exp1), FBr_2Ts(2)_mD (exp2) and FBr_2Ts(5)_mD (exp5) experiments. 188

Figure 5.29: Filtering of velocity time histories recorded by the 0.1n soil instrument in the NS direction during the free vibration PBr_W(11)_2.0kN experiment. (a) Velocity time histories after applying the original and new filters, (b) New-filtered velocity time histories (zoom). 189

Figure 5.30: Acceleration time histories recorded by the downhole accelerometer in the North-South direction (3.1n) during the FBr_2Ts(1)_mD (exp1) and FBr_2Ts(2)_mD (exp2) experiments. 190

Figure 5.31: Fourier spectra inferred from data recorded by the downhole accelerometer in the North-South direction (3.1n) during the FBr_2Ts(1)_mD (exp1) and FBr_2Ts(2)_mD (exp2) experiments. 191

Figure 5.32: Acceleration time histories recorded by the downhole accelerometer in the East-West direction (3.1e) during the FBr_2Ts(1)_mD (exp1) and FBr_2Ts(2)_mD (exp2) experiments. 191

Figure 5.33: Fourier spectra inferred from data recorded by the downhole accelerometer in the East-West direction (3.1e) during the FBr_2Ts(1)_mD (exp1) and FBr_2Ts(2)_mD (exp2) experiments. . 192

Figure 5.34: Acceleration time histories recorded by the downhole accelerometer in vertical direction (3.1z) during the FBr_2Ts(1)_mD (exp1) and FBr_2Ts(2)_mD (exp2) experiments. 192

Figure 5.35: Fourier spectra inferred from data recorded by the downhole accelerometer in the vertical direction (3.1z) during the FBr_2Ts(1)_mD (exp1) and FBr_2Ts(2)_mD (exp2) experiments. 193

Figure 6.1: Plan views of the top slabs displaced along the (a) conventional NS swaying mode, (b) conventional EW swaying mode and (c) torsional mode. 198

Figure 6.2: Acceleration time histories recorded on the top slab by the 2.1 and 2.5 instruments along the North-South (n) and East-West (e) directions during the free vibration experiments: (a) PBr_W(11)_13.90kN, (b) FBr_2Ts(3)_15.70kN. 199

Figure 6.3: Snapshots in plan of the displaced top slab and Fourier spectra of the motion at three locations, that result from a theoretical monochromatic (a) swaying and (b) torsional oscillation of the top slab. 201

Figure 6.4: Fourier Spectra inferred from acceleration time histories recorded on the top slab by the 2.1 and 2.5 instruments along the North-South (n) and East-West (e) directions during the free vibration experiments: (a) PBr_W(11)_13.90kN, (b) FBr_2Ts(3)_15.70kN. 202

Figure 6.5: Fourier Spectra inferred from acceleration time histories computed as the subtraction of the North-South motion recorded by the 2.1n and 2.5n instruments, exploiting data from the free vibration experiments: (a) PBr_W(11)_13.90kN, (b) FBr_2Ts(3)_15.70kN. 203

Figure 6.6: (a) motion decomposition of a simple SSI model, (b) cross section of the EUROPROTEAS structure (fully braced configuration indicatively) mapping the motion components (red arrows) and dimensions between the simplified SSI model with the real structure. The recorded components (blue arrows) that are used in the calculations are also shown. 205

Figure 6.7: Vibratory surface footing transmitting waves to (a) soil stratum over a stiffer half-space (Vs1<Vs2) or (b) homogeneous half-space. 210

Figure 6.8: Acceleration time histories and decay motion envelopes of the motions recorded at the centre of the top slab during the experiments: (a) PBr_W(11)_5.44kN, (b) FBr_2Ts(3)_15.70kN. ... 211

Figure 6.9: Damping ratio values produced during the PBr_W(11) experiments of various pull-out forces, which are computed using different pairs of i and j. Data recorded by the 2.5n instrument on the top slab centre in the NS direction, were processed. 213

Figure 6.10: Damping ratio values produced during the FBr_2Ts(3) experiments of various pull-out forces, which are computed using different pairs of i and j. Data recorded by the 2.5n instrument on the top slab centre in the NS direction, were processed. 213

Figure 6.11: Comparison between acceleration time histories recorded during the PBr_W and FBr_2Ts free vibration experiments, at the centre of the top slab. 214

Figure 6.12: Acceleration time histories and decay envelopes of the motion resulted from the subtraction of the 2.5n motion from the 2.1n one. Data from PBr_W and FBr_2Ts experiments of different pull-out forces are processed. 215

Figure 6.13: Impact of nonlinear effects during PBr_W(11) experiments on the natural frequency and damping of the SSI system. The effects are illustrated through: (a) Fourier spectra of the normalised response, (b) Peak-to-Peak frequencies, (c) Computed damping ratios. All data were produced by exploiting the motion recorded on the top slab by the 2.5n instrument. 219

Figure 6.14: Impact of nonlinear effects during FBr_2Ts(3) experiments on the natural frequency and damping of the SSI system. The effects are illustrated through: (a) Fourier spectra of the normalised response, (b) Peak-to-Peak frequencies, (c) Computed damping ratio. All data were produced by exploiting the motion recorded on the top slab by the 2.5n instrument. 220

Figure 6.15: Comparison of the soil response between the PBr_W and FBr_2Ts free vibration experiments of similar pull-out forces. The compared quantities are: (a, b) Soil NS motion recorded by the 0.1n instrument; and (c, d) Soil vertical motion recorded by the 0.1z instrument. 222

Figure 6.16: Calibrated G-γ-D curves and stiffness degradation and damping ratio values that correspond to “experimental” strains inferred from free vibration data recorded by the 0.1n instrument. 223

Figure 6.17: Comparison of the foundation response between the PBr_W and FBr_2Ts free vibration experiments of similar pull-out forces. The compared quantities are: (a, b) Foundation horizontal (NS) motion; and (c, d) Foundation rotation. 224

Figure 6.18: Motion decomposition of the total top slab accelerations recorded during the PBr_W and FBr_2Ts experiments of different pull-out forces. 225

Figure 6.19: Peak particle velocity (PPV) attenuation with distance recorded, during the PBr_W(11) experiment, by instruments located North and East to the foundation. The (a) vertical and (b) horizontal (North-South) motion components are presented, as well as their corresponding normalised values (c, d). 228

Figure 6.20: Peak particle velocity (PPV) attenuation with distance recorded, during the FBr_2Ts(4) experiment, by instruments located North and East to the foundation. The (a) vertical and (b) horizontal (North-South) motion components are presented, as well as their corresponding normalised values (c, d). 228

Figure 6.21: Unprocessed acceleration time history and corresponding velocity and displacement time histories through integration. The exploited data were recorded by the 2.5n instrument during the FBr_2Ts(5)_mD experiment). 230

Figure 6.22: Flow chart of the procedure to integrate strong motion acceleration time histories to velocity and displacement time histories. 231

Figure 6.23: Step 1. Filtered acceleration, velocity and displacement time histories. The exploited data used were recorded by the 2.5n instrument during the FBr_2Ts(5)_mD experiment. 232

Figure 6.24: Steps 2 and 3. Baseline correction of individual filtered velocity and displacement time histories integrated from a recorded acceleration time history segment of a constant 7.5Hz input

frequency. The exploited data were recorded by the 2.5n instrument during the FBr_2Ts(5)_mD experiment when the input frequency was 7.5Hz. 235

Figure 6.25: Velocity and displacement time histories integrated from the presented 10s-duration acceleration time history. The exploited data used were recorded by the 2.5n instrument during the FBr_2Ts(5)_mD experiment when the input frequency was 7.5Hz. 237

Figure 6.26: Snapshots in plan of the displaced slab taken during a fictitious (a) swaying motion, (b) torsional motion and (c) motion that results from the combination of the latter motions. (d) presents the displacement time histories of sinusoidal oscillations of the above modes. 238

Figure 6.27: Phase angle difference with applied frequency between data recorded along the in-plane (n) and out-of-plane (e) directions by the top slab 2.1 and 2.3 corner instruments during the FBr_1Ts(14)_mD experiment. 241

Figure 6.28: Variation of normalised peak accelerations with applied frequency, inferred from data recorded at the top slab centre by the 2.5 instrument along North-South, East-West and vertical directions, during (a) FBr_2Ts(5)_mD experiment, (b) PBr_W(7)_mD experiment 244

Figure 6.29: Variation of normalised peak accelerations with applied frequency, inferred from data recorded at the top slab by the 2.1 and 2.3 corner instruments along North-South and East-West directions, during FBr_1Ts(14)_mD experiment. 245

Figure 6.30: Variation of Fourier amplitude peaks with applied frequency, inferred from data recorded at the top slab centre by the 2.5 instrument along North-South, East-West and vertical directions, during (a) FBr_2Ts(5)_mD experiment, (b) PBr_W(7)_mD experiment. 246

Figure 6.31: Natural frequencies and deformation modes of the FBr_2Ts(5)_mD experiment, as illustrated by the plots: (a) Normalised peak accelerations with applied frequency, (b) Fourier amplitudes with applied frequency, (c) Difference of phase angle between data recorded by the 2.1 and 2.4 instruments, along the NS (n) and EW (e) directions. 249

Figure 6.32: Snapshots of the FBr_2Ts(5)_mD experiment, illustrating the deformed shapes of the top slab in plan at the identified resonant frequencies. The displacements are exaggerated by 250 times. The North and the direction of the applied force (F) are also shown. 250

Figure 6.33: Natural frequencies and deformation modes of the PBr_W(7)_mD experiment, as illustrated by the plots: (a) Normalised peak accelerations with applied frequency, (b) Fourier amplitudes with applied frequency, (c) Difference of phase angle between data recorded by the 2.1 and 2.4 instruments, along the NS (n) and EW (e) directions. 250

Figure 6.34: Snapshots of the PBr_W(7)_mD experiment, illustrating the deformed shapes of the top slab in plan at the resonant frequencies identified. The displacements are exaggerated by 215 times. The North and the direction of applied force are also shown. 251

Figure 6.35: Natural frequencies and deformation modes of the PBr_S(8)_mD experiment, as illustrated by the plots: (a) Normalised peak accelerations with applied frequency, (b) Fourier amplitudes with applied frequency, (c) Difference of phase angle between data recorded by the 2.1 and 2.4 instruments, along the NS (n) and EW (e) directions. 251

Figure 6.36: Snapshots of the PBr_S(8)_mD experiment, illustrating the deformed shapes of the top slab in plan at the resonant frequencies identified. The displacements are exaggerated by 250 times. The North and the direction of applied force (F) are also shown. 252

Figure 6.37: Natural frequencies and deformation modes of the FBr_1Ts(14)_mD experiment, as illustrated by the plots: (a) Normalised peak accelerations with applied frequency, (b) Fourier amplitudes with applied frequency, (c) Difference of phase angle between data recorded by the 2.1 and 2.4 instruments, along the NS (n) and EW (e) directions. 253

Figure 6.38: Snapshots of the FBr_1Ts(14)_mD experiment, illustrating the deformed shapes of the top slab in plan at the resonant frequencies identified. The displacements are exaggerated by 170 times. The North and the direction of applied force are also shown. 254

Figure 6.39: Comparison of the top slab normalised response of the FBr_2Ts structure as inferred from experiments with different mass of plates mounted on the vibrator. The (a) North-South and (b) East-West response, recorded by the 2.1, instrument is presented. 258

Figure 6.40: Comparison of the top slab normalised response of the FBr_1Ts structure as inferred from experiments with different mass of plates mounted on the vibrator. The (a) North-South and (b) East-West response, recorded by the 2.1 instrument, is presented. 258

Figure 6.41: Comparison of the top slab normalised response of the PBr_W structure as inferred from experiments with different mass of plates mounted on the vibrator. The (a) North-South and (b) East-West response, recorded by the 2.1 instrument, is presented. 259

Figure 6.42: Comparison of the top slab normalised response of the PBr_S structure as inferred from experiments with different mass of plates mounted on the vibrator. The (a) North-South and (b) East-West response, recorded by the 2.1 instrument, is presented. 259

Figure 6.43: Calibrated G-γ-D curves and stiffness degradation and damping ratio values that inferred from “experimental” strains, using forced vibration tests on the four different structural configurations. The strong motion data used were recorded by the instruments shown in Table 6.13

and located 3m from the foundation edge. Results from experiments of which the vibrator plate mass was (a) mC and (b) mD are presented. 262

Figure 6.44: Motion decomposition of the top slab displacements estimated from data recorded during the (a) FBr_2Ts_mD, (b) FBr_1Ts_mD, (c) PBr_W_mD and (d) PBr_S_mD experiments..... 263

Figure 6.45: Comparison of foundation (a, b) horizontal and (c, d) rotation as computed from forced vibration tests on the four different configurations. Results from experiments of which the vibrator plate mass was (a, c) mC and (b, d) mD are presented. 264

Figure 6.46: Comparison of the vibrator input demand and the top slab accelerations recorded during the (a) FBr_2Ts_mD, (b) FBr_1Ts_mC, (c) PBr_W_mD and (d) PBr_S_mD experiments. 266

Figure 6.47: Comparison of soil motion recorded by the 0.1/0.40 instruments along the (a, b) NS and (c, d) vertical directions during the experiments on different structural configurations. Results from experiments of which the vibrator plate mass was (a, c) mC and (b, d) mD are presented. 267

Figure 6.48: Fourier spectra inferred from normalised accelerations recorded by the downhole, 3.1, instrument during the (a) FBr_2Ts_mD, (b) PBr_W_mD and (c) PBr_S_mD experiments. 268

Figure 6.49: Peak particle velocity variation with applied frequency, as processed from data recorded by instruments located at different distance from the foundation edge. Processed data were recorded during the (a) FBr_2Ts(1)_mD, (b) PBr_S(13)_mD and (c) PBr_W(12)_mD experiments. Instruments of which data are used can be found in Table 6.14 271

Figure 6.50: Peak particle velocity attenuation with distance from the foundation edge, that corresponds to different applied frequencies. Processed data were recorded during the (a) FBr_2Ts(1)_mD, (b) PBr_S(13)_mD and (c) PBr_W(12)_mD experiments. Instruments of which data are used can be found in Table 6.14. 272

Figure 6.51: Peak foundation accelerations recorded at each applied frequency during the (a) FBr_2Ts(1)_mD and (b) PBr_S(13)_mD experiments. 274

Figure 6.52: Soil motion attenuation with distance from the foundation, computed during swaying (blue lines) and torsional (red lines) modes. The processed data were recorded during the (a) FBr_2Ts(1)_mD and (b) PBr_S(13)_mD experiments by instruments presented in Table 6.15, the records of which were dominated by the corresponding mode. 275

Figure 6.53: Transfer functions defined as the ratio of Fourier amplitude inferred from soil motion to the amplitude of foundation motion. The amplitudes correspond to a spectral frequency equal to the applied one. The processed data were recorded during the (a) FBr_2Ts(1)_mD and (b)

PBr_S(13)_mD experiments, by the instruments presented in Table 6.15, the records of which were dominated by one of the examined modes. 277

Figure 6.54: Impact of the force magnitude on peak particle velocity attenuation with distance from the foundation edge, assessed through (a,b) velocity units and (c,d) Transfer Functions defined as soil to foundation motion. Processed data correspond to the torsional resonant frequencies and were recorded during the (a, c) FBr_2Ts(1) and (b, d) PBr_S(13) . Instruments of which data are used can be found in Table 6.14. 278

Figure 7.1: Comparison of top slab in-plane and out-of-plane motions recorded during the forced vibration tests which were exploited in the calibration process. 289

Figure 7.2: Comparison of the top slab in-plane and out-of-plane motions recorded during the free vibration tests which were exploited in the calibration process. 290

Figure 7.3: FE mesh, dimensions and some boundary conditions of the (a) static self-weight and pull-out analyses, (b) dynamic analyses, (c) structural model of the fully braced 2-top slab configuration, (d) structural model of the partly braced configuration, (e) structural model of the fully braced 1-top slab configuration. 295

Figure 7.4: Application of the cone boundary on a 2D model (Kontoe, 2006). 296

Figure 7.5: (a) Experimental and (b) simulated pull-out force, prior to free vibration tests. 300

Figure 7.6: (a) p' profiles under free-field conditions and below the foundation, (b) Impact of p' dependency on the maximum shear modulus, by comparing shear modulus profiles of free-field and below the foundation defined with different pairs of G0 and mG that can be found in Table 7.7. .. 303

Figure 7.7: Mohr-Coulomb yield surface. 306

Figure 7.8: Illustration of the impact of Ks and Kn values on the response through snapshots of displaced mesh captured from forced vibration simulations of the PBr_W_2Hz experiment. The snapshots correspond to an increment where the magnitude of the applied force is maximised, while displacements were exaggerated by 1520 times. The deformed shape is due to the dynamic loading only, as any statically induced deformation have been subtracted. 307

Figure 7.9: Modelled contact conditions between the foundation and soil in plan. 311

Figure 7.10: Effective normal static stresses (σ'n) resulted from the StSW8 analysis assuming nonlinear soil. (a) contours of σ'n and (b) σ'n along cross sections cs1, cs2 and cs3 shown in (a). .. 312

Figure 7.11: Effective normal static stresses (σ'n) resulted from the StSW4 analysis assuming nonlinear soil. (a) contours of σ'n and (b) σ'n along cross sections cs1, cs2 and cs3 shown in (a). .. 312

Figure 7.12: Effective normal static stresses (σ'n) resulted from the StSW3 analysis assuming nonlinear soil. (a) contours of σ'n and (b) σ'n along cross sections cs1, cs2 and cs3 shown in (a). .. 313

Figure 7.13: Calibration of Young's modulus of beams extended into foundation (EF) and top slab (ETS), through modelling the PBr_W_2.03kN experiment. Fixed-base conditions are assumed. 318

Figure 7.14: Impact of soil compliance and the imposition of stiff elastic interface elements on the numerical results of the simulation of the PBr_W_2.03kN experiment. 319

Figure 7.15: Impact of gaps and soil nonlinearity on the numerical results of the simulation of the PBr_W_2.03kN experiment. 320

Figure 7.16: Simulations of free vibration tests on the PBr_W structure, demonstrating the impact of soil compliance and interface modelling without initial gaps on the horizontal top slab response, at the position of the 2.5 instrument. 322

Figure 7.17: Simulations of free vibration tests on the FBr_2Ts structure, demonstrating the impact of soil compliance and interface modelling without initial gaps on the horizontal top slab response, at the position of the 2.5 instrument. 322

Figure 7.18: Simulations of free vibration tests on the FBr_1Ts structure, demonstrating the impact of soil compliance and interface modelling without initial gaps on the horizontal top slab response, at the position of the 2.1 instrument. 323

Figure 7.19: Simulations of the PBr_W_mD_2Hz forced vibration test, demonstrating the impact of soil compliance and interface modelling without initial gaps on the SSI response. 324

Figure 7.20: Simulations of the FBr_2Ts_mD_5Hz forced vibration test, demonstrating the impact of soil compliance and interface modelling without initial gaps on the SSI response. 325

Figure 7.21: Simulations of the FBr_1Ts_mC_5Hz forced vibration test, demonstrating the impact of soil compliance and interface modelling without initial gaps on the SSI response. 326

Figure 7.22: Simulations of the PBr_W_mD_2Hz forced vibration test, investigating the impact of interface gaps on the SSI response. Analyses are linear elastic, while gaps are simulated through LSELint..... 328

Figure 7.23: Simulations of the FBr_2Ts_mD_5Hz forced vibration test, investigating the impact of interface gaps on the SSI response. Analyses are linear elastic, while gaps are simulated through LSELint..... 329

Figure 7.24: Simulations of the FBr_1Ts_mC_5Hz forced vibration test, investigating the impact of interface gaps on the SSI response. Analyses are linear elastic, while gaps are simulated through LSELint..... 330

Figure 7.25: Illustration of the existence of high frequency content in foundation (1.2) and soil (0.2) time history motions and the effectiveness of filtering. The results are produced by FBr_1Ts_mC_5Hz forced vibration simulations of g=0.1mm initial opening. 332

Figure 7.26: Illustration of the existence of high frequency content in Fourier amplitude spectra that are inferred from foundation (1.2) and soil (0.2) motions and the effectiveness of filtering. The results are produced by FBr_1Ts_mC_5Hz forced vibration simulations of g=0.1mm initial opening. 332

Figure 7.27: Impact of the initial opening, prescribed at the initially open interface elements, on the results of the FBr_2Ts_mD_5Hz forced vibration simulation, assuming linear elastic soil. 334

Figure 7.28: Impact of the initial opening, prescribed at the initially open interface elements, on the results of the FBr_1Ts_mC_5Hz forced vibration simulation, assuming linear elastic soil. 334

Figure 7.29: Contours of normal plastic strains (opening) of interface elements computed at an increment when the top slab displacement was the maximum towards the positive x-axis. Results from EPint_0.2mm forced vibration simulations of the (a) FBr_2Ts_mD_5Hz and (b) FBr_1Ts_mC_5Hz experiments are shown. Black contours indicate closed interface elements (εpl=0m)..... 335

Figure 7.30: Fourier spectra of the top slab horizontal motion (2.5n or 2.1n) computed by linear elastic free vibration analyses with and without interface gaps. Results are compared with experimental data, where available..... 336

Figure 7.31: Fourier spectra of the foundation horizontal and vertical motion components (1.1n, 1.1z) computed by linear elastic free vibration analyses with and without interface gaps. Results are compared with experimental data, where available. 337

Figure 7.32: Horizontal normalised acceleration time histories of the top slab (2.5n or 2.1n) computed by linear elastic free vibration analyses with and without interface gaps. Results are compared with experimental data, where available. 338

Figure 7.33: Damping ratio values computed for the motions between the second peak and the next j peaks. They are inferred from experimental and numerical top slab accelerations. The numerical results are based on linear elastic free vibration analyses with and without interface gaps. Results are compared with experimental data, where available. 339

Figure 7.34: Fourier spectra of horizontal and vertical soil motion components (0.1n, 0.1z) computed by linear elastic free vibration analyses with and without interface gaps. Results are compared with experimental data, where available..... 340

Figure 7.35: Comparison between analyses that prescribed the first 0.80m of soil or the whole soil domain as nonlinear. Comparisons are made for the horizontal top slab (2.5n), vertical foundation (1.1z) and vertical soil (0.1z) motions, computed by simulations of the FBr_2Ts_15.70kN free vibration test. 343

Figure 7.36: G-γ-D curves of which applicability is investigated. 344

Figure 7.37: Comparison of the top slab response predicted by the FBr_2Ts_2.94kN simulations that incorporate nonlinear soil model that is calibrated against Calibr2 or Calibr6 (Set A curves - Figure 7.36a). The response is examined in terms of: (a) acceleration time histories, (b) Fourier amplitude spectra, (c) peak-to-peak frequencies, (d) damping ratio. 346

Figure 7.38: Comparison of the top slab response predicted by the FBr_2Ts_15.70kN simulations that incorporate nonlinear soil model that is calibrated against Calibr2 or Calibr6 (Set A curves - Figure 7.36a). The response is examined in terms of: (a) acceleration time histories, (b) Fourier amplitude spectra, (c) peak-to-peak frequencies, (d) damping ratio. 347

Figure 7.39: Comparison of the top slab response predicted by linear and nonlinear analyses using the calibration Calibr0. 349

Figure 7.40: Comparison of the top slab response predicted by nonlinear analyses of the model calibrations included in Set B curves (Figure 7.36b): Calibr0, Calibr1 and Calibr3. 350

Figure 7.41: Comparison of the top slab response predicted by nonlinear analyses of model calibrations included in Set C curves (Figure 7.36c): Calibr4, Calibr5 and Calibr6. 351

Figure 7.42: Quantification of stiffness degradation and damping ratio values developed within the soil elements highlighted with solid colour in (a) at the times shown in (b) and (c). The values shown in (d) and (e) are extracted from simulations of the FBr_2Ts_2.94kN and FBr_2Ts_15.70kN experiments respectively. 353

Figure 7.43: Deviatoric stress (J) – deviatoric total strain (Ed,t) paths computed at the integration point shown in (a). (b) compares the J-Ed,t paths between the FBr_2Ts_2.94kN and FBr_2Ts_15.70kN simulations, while (c) and (d) isolate the paths of the former and latter simulations, respectively. 355

Figure 7.44: Monotonic and cyclic stiffness degradation curves prescribed by the calibrations Calibr2 and Calibr6. 356

Figure 7.45: Results of the simulation FBr_2Ts_15.70kN, when the Calibr2 is adopted. (a) Displacement time history, (b) G-γ-D curves and the corresponding values developed in the soil volume shown in Figure 7.42a, (c) deviatoric strain – stress path developed in the integration point shown in Figure 7.43a. 357

Figure 7.46: (a) Displacement time histories and (b) G-γ-D curves resulted from the simulation of the FBr_2Ts_15.70kN experiment, by adopting Calibr6 and incorporating Gmin=0.15Go. The presented stiffness and damping ratio values are developed at the times P0-P5, at the integration points enclosed within the soil volume shown in Figure 7.42a. 358

Figure 7.47: Impact of Gmin on the J-Ed,t paths developed at the integration point shown in Figure 7.43a. (a) stress paths start from the same initial stress-strain state highlighting the mobilisation of Gmin during monotonic loading, (b) manipulated stress paths so that they have a common stress-strain state at the beginning of the dynamic analysis, highlighting the mobilisation of Gmin during free vibration. 360

Figure 7.48: Impact of Gmin on the horizontal top slab response (2.5n) predicted by simulations of the FBr_2Ts_15.70kN experiment. The simulations incorporate the Calibr6 calibration in the nonlinear soil constitutive model. The response is examined in terms of: (a) acceleration time histories, (b) Fourier amplitude spectra, (c) peak-to-peak frequencies and (d) damping ratio 361

Figure 7.49: Horizontal top slab response (2.5n) computed by the simulations of the PBr_W_13.90kN experiment, assuming either linear or nonlinear soil 362

Figure 7.50: Horizontal top slab response (2.1n) computed by the simulations of the FBr_1Ts_15.70kN experiment, assuming either linear or nonlinear soil. 363

Figure 7.51: Fourier spectra of the horizontal (n) and vertical (z) motions of the top slab (2.1), foundation (1.2) and soil (0.2). Results of the FBr_1Ts_mC_5Hz forced vibration simulations that assume either linear or nonlinear soil are compared. 364

Figure 7.52: Fourier spectra of the horizontal (n) and vertical (z) motions of the top slab (2.5), foundation (1.1) and soil (0.1). Results of the FBr_2Ts_mD_5Hz forced vibration simulations that assume either linear or nonlinear soil are compared. 365

Figure 7.53: Fourier spectra of the horizontal (n) and vertical (z) motions of the top slab (2.5), foundation (1.1) and soil (0.1). Results of the PBr_W_mD_2Hz forced vibration simulations that assume either linear or nonlinear soil are compared. 365

Figure 7.54: Horizontal top slab (2.1n) response computed by simulations of the FBr_1Ts_15.70kN free vibration test. The analyses employ elastic or hybrid interface elements, while various interface conditions at the StSW analysis. 368

Figure 7.55: Variation of plastic normal strain with time computed at all integration points of the numbered interface elements shown in (a). The results are extracted from simulations of the FBr_1Ts_15.70kN free vibration experiment, using the initial stress distribution of (b) StSW8, (c) StSW4 and (d) StSW3. 370

Figure 7.56: Horizontal top slab response (2.5n) as computed by simulations of the FBr_2Ts_15.70kN free vibration test. The analyses use either elastic or hybrid interface elements. 371

Figure 7.57: Plastic normal strain variation with time computed at all integration points of the numbered interface elements shown in Figure 7.55a. The results are extracted from the HYBint_GC2_StSW3 analysis that simulates the FBr_2Ts_15.70kN free vibration experiment. 372

Figure 7.58: Horizontal top slab response (2.5n) as computed by simulations of the PBr_W_13.90kN free vibration test. The analyses employ either elastic or hybrid interface elements. 372

Figure 7.59: Fourier spectra of the horizontal (n) and vertical (z) motions of the top slab (2.1), foundation (1.2) and soil (0.2). The compared results are computed by the FBr_1Ts_mC_5Hz forced vibration simulations that assume nonlinear soil, while elastic or hybrid interface elements are used. 374

Figure 7.60: Fourier spectra of the horizontal (n) and vertical (z) motions of the top slab (2.5), foundation (1.1) and soil (0.1). The compared results are computed by the FBr_2Ts_mD_5Hz forced vibration simulations that assume nonlinear soil, while elastic or hybrid interface elements are used. 375

Figure 7.61: Fourier spectra of the horizontal (n) and vertical (z) motions of the top slab (2.5), foundation (1.1) and soil (0.1). The compared results are computed by the PBr_W_mD_2Hz forced vibration simulations that assume nonlinear soil, while elastic or hybrid interface elements are used. 375

Figure 7.62: Horizontal top slab response computed by simulations of the FBr_2Ts_15.70kN free vibration test. The analyses employ hybrid or elastoplastic of various magnitudes of initial opening. 377

Figure 7.63: Horizontal top slab response computed by simulations of the FBr_1Ts_15.70kN free vibration test. The analyses employ hybrid or elastoplastic of various magnitudes of initial opening. 378

Figure 7.64: Plastic normal strain variation with time computed at all integration points of the numbered interface element shown in (a). The results are extracted from simulations of the (b) FBr_2Ts_15.70kN and (c) FBr_1Ts_15.70kN free vibration experiments, using the initial stress StSW3 and prescribing various initial openings..... 380

Figure 7.65: Boundary effects on the structural response predicted by the FBr_2Ts_15.70kN free vibration simulation. 384

Figure 7.66: Boundary effects on the soil response at different locations predicted by the FBr_2Ts_15.70kN free vibration simulation. 385

Figure 7.67: Boundary effects on the structural response predicted by the FBr_2Ts_mD_5Hz forced vibration simulation. 386

Figure 7.68: Boundary effects on the soil response at different locations predicted by the FBr_2Ts_mD_5Hz forced vibration simulation. 386

Figure 8.1: Fourier spectra inferred from numerical and experimental top slab response, shown in the left plots. The right plots present the identified natural frequencies and the corresponding Fourier amplitude. The results are taken from free vibration experiments of different pull-out forces applied on (a) FBr_2Ts, (b) FBr_1Ts and (c) PBr_W structures. 396

Figure 8.2: Variation of period lengthening produced by different models and different pull-out forces. 398

Figure 8.3: Variation damping ratio values produced by different models that simulate free vibration experiments of different pull-out forces. 399

Figure 8.4: Mesh of the numerical model, shading the soil areas of which soil behaviour is investigated. 400

Figure 8.5: G-γ-D curves and the corresponding values computed by the analysis that simulates the FBr_2Ts_15.70KN free vibration experiment, incorporates soil nonlinearity and adopts the interface model HYBint_StSW3_GC2. The presented data are computed at integration points within the shaded soil volumes shown in Figure 8.4. They refer to the P1 time increment as shown in Figure 7.42c. 401

Figure 8.6: Variation of soil stiffness degradation and damping ratio values with applied pull-out force, as developed at the first displacement peak after load removal. The mean values and standard deviation of integration points enclosed in BCE area (Figure 8.4) are presented. 402

Figure 8.7: Normal plastic strain time series extracted from free vibration simulations of the FBr_1Ts structure, which was excited by (a) 6.38kN, (b) 10.10kN and (c) 15.70kN pull-out force. The strains correspond to integration points of various interface elements shown in Figure 7.55a. 403

Figure 8.8: Normal plastic strain time series extracted from free vibration simulations of the FBr_2Ts structure, which was excited by (a) 6.38kN, (b) 10.10kN and (c) 15.70kN pull-out force. The strains correspond to integration points of different interface elements shown in Figure 7.55a. 404

Figure 8.9: Variation of normalised vertical soil motion component predicted by different models that simulate free vibration experiments of different pull-out forces. The presented motions were taken at the position of 0.1 instrument which is 1.2m far from foundation edge. 405

Figure 8.10: Variation of normalised horizontal soil motion component predicted by the different models that simulate free vibration experiments of different pull-out forces. The presented motions were taken at the position of 0.1 instrument which is 1.2m far from foundation edge. 406

Figure 8.11: Variation of (a, b) vertical and (c, d) horizontal soil motion components with distance from foundation edge, as computed from FBr_2Ts simulations. 408

Figure 8.12: Comparison of (a, b) vertical and (c, d) horizontal motion dissipation with distance produced by the FBr_2Ts, FBr_1Ts and PBr simulations. 409

Figure 8.13: Comparison of variation of transfer functions with distance, that are computed from results of the FBr_2Ts, FBr_1Ts and PBr simulations. 410

Figure 8.14: Transfer function ratio values of horizontal to vertical foundation motion (1.2n/1.2z) computed from FBr_2Ts, FBr_1Ts and PBr simulations. 411

Figure 8.15: Variation of normalised top slab motion amplitudes with input frequencies, inferred from numerical and experimental data. Solid data points indicate simulations that exhibited resonant features. 413

Figure 8.16: Variation of soil stiffness degradation and damping ratio values with input frequencies, that were developed at an increment of maximum acceleration of the steady state part of the motion, where reached. The mean values and standard deviation of all integration points enclosed in BCE area, with reference to Figure 8.4, are presented. 414

Figure 8.17: Variation of normal plastic strains with input frequencies. Each data point corresponds to the mean strain value of the interface element 16, shown in Figure 7.55a. Data were computed at an increment of maximum acceleration of the steady state part of the motion, where reached. Results from simulations of forced vibration tests on the FBr_1Ts structural configuration are shown. 416

Figure 8.18: Comparison of the variation of foundation (a) vertical and (b) soil motions with applied frequency, that were produced by FBr_2Ts, FBr_1Ts and PBr_W simulations. 417

Figure 8.19: Variation of foundation transfer function (TF) ratio with applied frequencies. The TFs are computed as the foundation horizontal (1.2n) to vertical (1.2z) motion, which were produced by the FBr_2Ts, FBr_1Ts and PBr_W simulations..... 417

Figure 8.20: Variation of normalised vertical soil motion, in Fourier amplitude units, with applied frequency, comparing numerical with experimental data. The caption of each figure reflects to the experiment and instruments of which data are used. Solid data points indicate simulations that exhibited resonant features..... 419

Figure 8.21: Difference of soil motion produced by the mC and mD simulations. The difference is computed in terms of Fourier amplitude, which are presented in Figure 8.20..... 419

Figure 8.22: Variation of soil to foundation vertical motion transfer function ratios with applied frequency, comparing numerical with experimental data. The caption of each figure reflects to the experiment and instruments of which data are used. Solid data points indicate simulations that exhibited resonant features..... 421

Figure 8.23: Vertical soil motion attenuation with distance, that is inferred from mD simulations and experiments. Soil motions are evaluated as Fourier amplitudes of the main peak of the corresponding spectra. 423

Figure 8.24: Variation of soil to foundation motions transfer function with distance from the foundation edge. Data are inferred from mD simulations and experiments. 424

Figure 8.25: Impact of the vibrator force on the variation of soil to foundation motions transfer function with distance from the foundation edge. Data are inferred from simulations that imposed a 5Hz input excitation. 425

Figure 8.26: Comparison of soil motion attenuation between the FBr_2Ts, FBr_1Ts and PBr_W simulations. The soil motion is evaluated in terms of (a) maximum Fourier amplitudes and (b) soil to foundation motions transfer functions. 426

Figure A.1: Profitis-Stivos cross section illustrating the sites from where samples were retrieved, according to Table A.1 (Raptakis et al., 2000) 470

Figure A.2: Experimental and in-situ G-γ-D curves for each layer, compared against experimental data, where available. 473

Figure A.3: Reference and calibrated G-γ-D curves for all layers. 477

Figure A.4: Comparison of the recorded site response with results computed by EQL and NLIN analyses, that simulate the 2006 event. The results are presented in terms of acceleration response spectra at the locations where records are available. 480

Figure A.5: Comparison of the recorded site response with results computed by EQL and NLIN analyses, that simulate the 2013 event. The results are presented in terms of acceleration response spectra at the locations where records are available. 480

Figure A.6: Comparison of the recorded site response with results computed by EQL and NLIN analyses, that simulate the 2016 event. The results are presented in terms of acceleration response spectra at the locations where records are available. 481

Figure C.1: Comparison between in-situ input frequency time history with (a) frequency time history inferred from top slab instruments and (b) mean frequency time history with the corresponding standard deviations. (c) error between the in-situ and estimated input frequencies. Data taken from the FBr_2Ts(1)_mD experiment. 489

Figure C.2: Comparison between in-situ input frequency time history with (a) frequency time history inferred from top slab instruments and (b) mean frequency time history with the corresponding standard deviations. (c) error between the in-situ and estimated input frequencies. Data taken from the FBr_2Ts(2)_mD experiment. 490

Figure C.3: Comparison between in-situ input frequency time history with (a) frequency time history inferred from top slab instruments and (b) mean frequency time history with the corresponding standard deviations. (c) error between the in-situ and estimated input frequencies. Data taken from the FBr_2Ts(5)_mD experiment. 490

Figure C.4: Comparison between in-situ input frequency time history with (a) frequency time history inferred from top slab instruments and (b) mean frequency time history with the corresponding standard deviations. (c) error between the in-situ and estimated input frequencies. Data taken from the PBr_W(7)_mD experiment. 490

Figure C.5: Comparison between in-situ input frequency time history with (a) frequency time history inferred from top slab instruments and (b) mean frequency time history with the corresponding standard deviations. (c) error between the in-situ and estimated input frequencies. Data taken from the PBr_W(9)_mD experiment. 491

Figure C.6: Comparison between in-situ input frequency time history with (a) frequency time history inferred from top slab instruments and (b) mean frequency time history with the corresponding

standard deviations. (c) error between the in-situ and estimated input frequencies. Data taken from the PBr_W(12)_mD experiment. 491

Figure C.7: Comparison between in-situ input frequency time history with (a) frequency time history inferred from top slab instruments and (b) mean frequency time history with the corresponding standard deviations. (c) error between the in-situ and estimated input frequencies. Data taken from the PBr_S(8)_mD experiment. 491

Figure C.8: Comparison between in-situ input frequency time history with (a) frequency time history inferred from top slab instruments and (b) mean frequency time history with the corresponding standard deviations. (c) error between the in-situ and estimated input frequencies. Data taken from the PBr_S(10)_mD experiment. 492

Figure C.9: Comparison between in-situ input frequency time history with (a) frequency time history inferred from top slab instruments and (b) mean frequency time history with the corresponding standard deviations. (c) error between the in-situ and estimated input frequencies. Data taken from the PBr_S(13)_mD experiment. 492

Figure C.10: Comparison between in-situ input frequency time history with (a) frequency time history inferred from top slab instruments and (b) mean frequency time history with the corresponding standard deviations. (c) error between the in-situ and estimated input frequencies. Data taken from the FBr_1TS(14)_mD experiment. 492

Figure C.11: (a) Comparison between the frequency time history read out in-situ from the vibrator's speed drive with the one calculated by employing the SoFS method. (b) Error between in-situ frequencies and frequencies that were calculated by exploiting the 2.5n data. Data taken from the FBr_2Ts(1)_mD experiment 493

Figure C.12: (a) Comparison between the frequency time history read out in-situ from the vibrator's speed drive with the one calculated by employing the SoFS method. (b) Error between in-situ frequencies and frequencies that were calculated by exploiting the 2.5n data. Data taken from the FBr_2Ts(2)_mD experiment 493

Figure C.13: (a) Comparison between the frequency time history read out in-situ from the vibrator's speed drive with the one calculated by employing the SoFS method. (b) Error between in-situ frequencies and frequencies that were calculated by exploiting the 2.5n data. Data taken from the FBr_2Ts(5)_mD experiment 494

Figure C.14: (a) Comparison between the frequency time history read out in-situ from the vibrator's speed drive with the one calculated by employing the SoFS method. (b) Error between in-situ

frequencies and frequencies that were calculated by exploiting the 2.5n data. Data taken from the PBr_W(7)_mD experiment 494

Figure C.15: (a) Comparison between the frequency time history read out in-situ from the vibrator's speed drive with the one calculated by employing the SoFS method. (b) Error between in-situ frequencies and frequencies that were calculated by exploiting the 2.5n data. Data taken from the PBr_W(9)_mD experiment 494

Figure C.16: (a) Comparison between the frequency time history read out in-situ from the vibrator's speed drive with the one calculated by employing the SoFS method. (b) Error between in-situ frequencies and frequencies that were calculated by exploiting the 2.5n data. Data taken from the PBr_W(12)_mD experiment 495

Figure C.17: (a) Comparison between the frequency time history read out in-situ from the vibrator's speed drive with the one calculated by employing the SoFS method. (b) Error between in-situ frequencies and frequencies that were calculated by exploiting the 2.5n data. Data taken from the PBr_S(8)_mD experiment 495

Figure C.18: (a) Comparison between the frequency time history read out in-situ from the vibrator's speed drive with the one calculated by employing the SoFS method. (b) Error between in-situ frequencies and frequencies that were calculated by exploiting the 2.5n data. Data taken from the PBr_S(10)_mD experiment 495

Figure C.19: (a) Comparison between the frequency time history read out in-situ from the vibrator's speed drive with the one calculated by employing the SoFS method. (b) Error between in-situ frequencies and frequencies that were calculated by exploiting the 2.5n data. Data taken from the PBr_S(13)_mD experiment 496

Figure C.20: (a) Comparison between the frequency time history read out in-situ from the vibrator's speed drive with the one calculated by employing the SoFS method. (b) Error between in-situ frequencies and frequencies that were calculated by exploiting the 2.5n data. Data taken from the FBr_1Ts(14)_mD experiment 496

Figure C.21: Peak accelerations recorded along the North-South direction by the 2.5n instrument, at each applied frequency 497

Figure C.22: Peak accelerations recorded along the North-South direction by the 2.5e instrument, at each applied frequency 497

Figure C.23: Peak accelerations recorded along the North-South direction by the 2.5z instrument, at each applied frequency 498

Figure C.24: Peak accelerations recorded along the North-South direction by the 2.3n instrument, at each applied frequency..... 498

Figure C.25: Peak accelerations recorded along the North-South direction by the 2.3e instrument, at each applied frequency..... 499

Figure C.26: Peak accelerations recorded along the North-South direction by the 2.3z instrument, at each applied frequency..... 499

Figure C.27: Peak accelerations recorded along the North-South direction by the 2.2n instrument, at each applied frequency..... 500

Figure C.28: Peak accelerations recorded along the North-South direction by the 2.2e instrument, at each applied frequency..... 500

Figure C.29: Peak accelerations recorded along the North-South direction by the 2.2z instrument, at each applied frequency..... 501

Figure C.30: Peak accelerations recorded along the North-South direction by the 2.1n instrument, at each applied frequency..... 501

Figure C.31: Peak accelerations recorded along the North-South direction by the 2.1e instrument, at each applied frequency..... 502

Figure C.32: Peak accelerations recorded along the North-South direction by the 2.1z instrument, at each applied frequency..... 502

Figure C.33: Peak accelerations recorded along the North-South direction by the 1.7n instrument, at each applied frequency..... 503

Figure C.34: Peak accelerations recorded along the North-South direction by the 1.7e instrument, at each applied frequency..... 503

Figure C.35: Peak accelerations recorded along the North-South direction by the 1.7z instrument, at each applied frequency..... 504

Figure C.36: Peak accelerations recorded along the North-South direction by the 1.6n instrument, at each applied frequency..... 504

Figure C.37: Peak accelerations recorded along the North-South direction by the 1.6e instrument, at each applied frequency..... 505

Figure C.38: Peak accelerations recorded along the North-South direction by the 1.6z instrument, at each applied frequency..... 505

Figure C.39: Peak accelerations recorded along the North-South direction by the 1.5n instrument, at each applied frequency..... 506

Figure C.40: Peak accelerations recorded along the North-South direction by the 1.5e instrument, at each applied frequency..... 506

Figure C.41: Peak accelerations recorded along the North-South direction by the 1.5z instrument, at each applied frequency..... 507

Figure C.42: Peak accelerations recorded along the North-South direction by the 1.2n instrument, at each applied frequency..... 507

Figure C.43: Peak accelerations recorded along the North-South direction by the 1.2e instrument, at each applied frequency..... 508

Figure C.44: Peak accelerations recorded along the North-South direction by the 1.2z instrument, at each applied frequency..... 508

Figure C.45: Peak accelerations recorded along the North-South direction by the 1.1n instrument, at each applied frequency..... 509

Figure C.46: Peak accelerations recorded along the North-South direction by the 1.1e instrument, at each applied frequency..... 509

Figure C.47: Peak accelerations recorded along the North-South direction by the 1.1z instrument, at each applied frequency..... 510

Figure C.48: Peak accelerations recorded along the North-South direction by the 2.5n instrument, at each applied frequency..... 511

Figure C.49: Peak accelerations recorded along the North-South direction by the 2.5e instrument, at each applied frequency..... 511

Figure C.50: Peak accelerations recorded along the North-South direction by the 2.5z instrument, at each applied frequency..... 512

Figure C.51: Peak accelerations recorded along the North-South direction by the 2.4n instrument, at each applied frequency..... 512

Figure C.52: Peak accelerations recorded along the North-South direction by the 2.4e instrument, at each applied frequency..... 513

Figure C.53: Peak accelerations recorded along the North-South direction by the 2.4z instrument, at each applied frequency..... 513

Figure C.54: Peak accelerations recorded along the North-South direction by the 2.3n instrument, at each applied frequency..... 514

Figure C.55: Peak accelerations recorded along the North-South direction by the 2.3e instrument, at each applied frequency..... 514

Figure C.56: Peak accelerations recorded along the North-South direction by the 2.3z instrument, at each applied frequency..... 515

Figure C.57: Peak accelerations recorded along the North-South direction by the 2.2n instrument, at each applied frequency..... 515

Figure C.58: Peak accelerations recorded along the North-South direction by the 2.2e instrument, at each applied frequency..... 516

Figure C.59: Peak accelerations recorded along the North-South direction by the 2.2z instrument, at each applied frequency..... 516

Figure C.60: Peak accelerations recorded along the North-South direction by the 2.1n instrument, at each applied frequency..... 517

Figure C.61: Peak accelerations recorded along the North-South direction by the 2.1e instrument, at each applied frequency..... 517

Figure C.62: Peak accelerations recorded along the North-South direction by the 2.1z instrument, at each applied frequency..... 518

Figure C.63: Peak accelerations recorded along the North-South direction by the 1.6n instrument, at each applied frequency..... 518

Figure C.64: Peak accelerations recorded along the North-South direction by the 1.6e instrument, at each applied frequency..... 519

Figure C.65: Peak accelerations recorded along the North-South direction by the 1.6z instrument, at each applied frequency..... 519

Figure C.66: Peak accelerations recorded along the North-South direction by the 1.5n instrument, at each applied frequency..... 520

Figure C.67: Peak accelerations recorded along the North-South direction by the 1.5e instrument, at each applied frequency..... 520

Figure C.68: Peak accelerations recorded along the North-South direction by the 1.5z instrument, at each applied frequency..... 521

Figure C.69: Peak accelerations recorded along the North-South direction by the 1.2n instrument, at each applied frequency..... 521

Figure C.70: Peak accelerations recorded along the North-South direction by the 1.2e instrument, at each applied frequency..... 522

Figure C.71: Peak accelerations recorded along the North-South direction by the 1.2z instrument, at each applied frequency..... 522

Figure C.72: Peak accelerations recorded along the North-South direction by the 1.1n instrument, at each applied frequency..... 523

Figure C.73: Peak accelerations recorded along the North-South direction by the 1.1e instrument, at each applied frequency..... 523

Figure C.74: Peak accelerations recorded along the North-South direction by the 1.1z instrument, at each applied frequency..... 524

Figure C.75: Peak accelerations recorded along the North-South direction by the 2.5n instrument, at each applied frequency..... 525

Figure C.76: Peak accelerations recorded along the North-South direction by the 2.5e instrument, at each applied frequency..... 525

Figure C.77: Peak accelerations recorded along the North-South direction by the 2.5z instrument, at each applied frequency..... 526

Figure C.78: Peak accelerations recorded along the North-South direction by the 2.4n instrument, at each applied frequency..... 526

Figure C.79: Peak accelerations recorded along the North-South direction by the 2.4e instrument, at each applied frequency..... 527

Figure C.80: Peak accelerations recorded along the North-South direction by the 2.4z instrument, at each applied frequency..... 527

Figure C.81: Peak accelerations recorded along the North-South direction by the 2.3n instrument, at each applied frequency..... 528

Figure C.82: Peak accelerations recorded along the North-South direction by the 2.3e instrument, at each applied frequency..... 528

Figure C.83: Peak accelerations recorded along the North-South direction by the 2.3z instrument, at each applied frequency..... 529

Figure C.84: Peak accelerations recorded along the North-South direction by the 2.2n instrument, at each applied frequency..... 529

Figure C.85: Peak accelerations recorded along the North-South direction by the 2.2e instrument, at each applied frequency..... 530

Figure C.86: Peak accelerations recorded along the North-South direction by the 2.2z instrument, at each applied frequency..... 530

Figure C.87: Peak accelerations recorded along the North-South direction by the 2.1n instrument, at each applied frequency..... 531

Figure C.88: Peak accelerations recorded along the North-South direction by the 2.1e instrument, at each applied frequency..... 531

Figure C.89: Peak accelerations recorded along the North-South direction by the 2.1z instrument, at each applied frequency..... 532

Figure C.90: Peak accelerations recorded along the North-South direction by the 1.6n instrument, at each applied frequency..... 532

Figure C.91: Peak accelerations recorded along the North-South direction by the 1.6e instrument, at each applied frequency..... 533

Figure C.92: Peak accelerations recorded along the North-South direction by the 1.6z instrument, at each applied frequency..... 533

Figure C.93: Peak accelerations recorded along the North-South direction by the 1.5n instrument, at each applied frequency..... 534

Figure C.94: Peak accelerations recorded along the North-South direction by the 1.5e instrument, at each applied frequency..... 534

Figure C.95: Peak accelerations recorded along the North-South direction by the 1.5z instrument, at each applied frequency..... 535

Figure C.96: Peak accelerations recorded along the North-South direction by the 1.2n instrument, at each applied frequency..... 535

Figure C.97: Peak accelerations recorded along the North-South direction by the 1.2e instrument, at each applied frequency..... 536

Figure C.98: Peak accelerations recorded along the North-South direction by the 1.2z instrument, at each applied frequency..... 536

Figure C.99: Peak accelerations recorded along the North-South direction by the 1.1n instrument, at each applied frequency..... 537

Figure C.100: Peak accelerations recorded along the North-South direction by the 1.1e instrument, at each applied frequency 537

Figure C.101: Peak accelerations recorded along the North-South direction by the 1.1z instrument, at each applied frequency..... 538

Figure C.102: Errors between forced vibration tests repeated on FBr_2Ts structure. 539

Figure C.103: Errors between forced vibration tests repeated on PBr_W structure. 539

Figure C.104: Errors between forced vibration tests repeated on PBr_S structure. 540

Figure D.1: Fourier spectra inferred from top slab accelerations recorded by different instruments during the free vibration experiments on the fully braced structure with 2 top slabs (FBr_2Ts). 543

Figure D.2: Fourier spectra inferred from top slab accelerations recorded by different instruments during the free vibration experiments on the partly braced structure with 2 top slabs loaded along its weak axis (PBr_W). 544

Figure E.1: Top slab response during the FBr_2Ts(5), when the plates of mass mA were placed on the vibrator. Displacements are exaggerated by 900 times. 545

Figure E.2: Top slab response during the FBr_2Ts(2), when the plates of mass mB were placed on the vibrator. Displacements are exaggerated by 700 times. 546

Figure E.3: Top slab response during the FBr_2Ts(5), when the plates of mass mC were placed on the vibrator. Displacements are exaggerated by 370 times. 546

Figure E.4: Top slab response during the FBr_2Ts(5), when the plates of mass mD were placed on the vibrator. Displacements are exaggerated by 250 times. 547

Figure E.5: Top slab response during the PBr_W(7), when the plates of mass mB were placed on the vibrator. Displacements are exaggerated by 540 times. 548

Figure E.6: Top slab response during the PBr_W(9), when the plates of mass mC were placed on the vibrator. Displacements are exaggerated by 300 times. 548

Figure E.7: Top slab response during the PBr_W(7), when the plates of mass mD were placed on the vibrator. Displacements are exaggerated by 215 times. 549

Figure E.8: Top slab response during the PBr_S(10), when the plates of mass mB were placed on the vibrator. Displacements are exaggerated by 685 times. 550

Figure E.9: Top slab response during the Pros(10), when the plates of mass mC were placed on the vibrator. Displacements are exaggerated by 380 times. 550

Figure E.10: Top slab response during the PBr_S(8), when the plates of mass mD were placed on the vibrator. Displacements are exaggerated by 250 times. 551

Figure E.11: Top slab response during the FBr_1Ts(14), when the plates of mass mC were placed on the vibrator. Displacements are exaggerated by 360 times. 552

Figure E.12: Top slab response during the FBr_1Ts(14), when the plates of mass mD were placed on the vibrator. Displacements are exaggerated by 170 times. 552

Figure F.1: Examined meshes with different soil domain dimensions 555

Figure F.2: Comparison of the SSI response computed by the analyses with different mesh. The horizontal (n) and vertical (z) response of the top slab (2.5), foundation (1.1) and soil (0.1, 0.2) are assessed, when the applied frequency was 8Hz. 557

Figure F.3: Boundary effects on the structural response predicted by the FBr_2Ts_15.70kN free vibration simulation. 559

Figure F.4: Boundary effects on the structural response predicted by the PBr_W_13.90kN free vibration simulation. 560

Figure F.5: Boundary effects on the soil response at different locations predicted by the FBr_2Ts_15.70kN free vibration simulation. 561

Figure F.6: Boundary effects on the soil response at different locations predicted by the PBr_W_13.90kN free vibration simulation 562

Figure F.7: Boundary effects on the structural response predicted by the FBr_2Ts_mD_5Hz forced vibration simulation 563

Figure F.8: Boundary effects on the structural response predicted by the FBr_1Ts_mC_5Hz forced vibration simulation 563

Figure F.9: Boundary effects on the structural response predicted by the PBr_W_mD_2Hz forced vibration simulation 564

Figure F.10: Boundary effects on the soil response at different locations predicted by the FBr_2Ts_mD_5Hz forced vibration simulation 564

Figure F.11: Boundary effects on the soil response at different locations predicted by the PBr_W_mD_2Hz forced vibration simulation 565

Figure F.12: Boundary effects on the soil response at different locations predicted by the FBr_1Ts_mC_5Hz forced vibration simulation. 566

Figure G.1: Variation of (a, b) vertical and (c, d) horizontal soil motion components with distance from the foundation edge, as computed by FBr_2Ts simulations. The results are obtained from nodes and instrument of the North line. 568

Figure G.2: Variation of (a, b) vertical and (c, d) horizontal soil motion components with distance from the foundation edge, as computed by FBr_2Ts simulations. The results are obtained from nodes and instrument of the East line. 569

Figure G.3: Variation of (a, b) vertical and (c, d) horizontal soil motion components with distance from the foundation edge, as computed by PBr_W simulations. The results are obtained from nodes and instrument of the North line. 570

Figure G.4: Variation of (a, b) vertical and (c, d) horizontal soil motion components with distance from the foundation edge, as computed by PBr_W simulations. The results are obtained from nodes and instrument of the East line. 571

List of Tables

Table 3.1: Input and output pairs for system identification of various base fixity conditions (Star et al., 2019). 93

Table 4.1: Earthquake events for which numerical models were developed and used in the back-calculation process (taken from EUROSEISTEST Strong Motion Network, 1993). 130

Table 4.2: Elastic soil properties input in the numerical model. 132

Table 5.1: Names and description of structural configurations examined. 149

Table 5.2: Stiffness values of EUROPROTEA'S column, in kN/m units, assumed fixed at its base and as back-calculated from static lateral force and free vibration tests. 155

Table 5.3: Stiffness of the rotational spring at the base of the cantilever $K\theta$ (kNm/rad). 156

Table 5.4: Geometric quantities and nominal elastic properties of columns and braces according to Eurocode 3 (BS EN 1993-1-1:2005). 159

Table 5.5: Inertial components (mm) of the examined structural configurations. 160

Table 5.6: Stiffness of individual columns and braces. 160

Table 5.7: Total stiffness of the examined fixed-base EUROPROTEAS configurations 160

Table 5.8: Fixed-base natural frequencies of the four structural configurations computed either numerically or analytically based on SDOF assumption. 160

Table 5.9: Total vibrator eccentricity for each combination of plates that can be placed on each shaft. 162

Table 5.10: Summary of experiments carried out. 174

Table 5.11: Range of applied frequencies for each of the forced vibration experiment carried out. The total number of different frequencies is also shown in brackets. 175

Table 5.12: Magnitudes of the pull-out forces applied during the three free vibration experiments. 175

Table 5.13: Records that required additional filtering, while filtering input are also shown. 189

Table 5.14: Faulty forced vibration experiments. 193

Table 5.15: Faulty data recorded during forced vibration tests. 194

Table 5.16: Faulty data recorded during free vibration tests. 194

Table 6.1: Input data used for quantifying the motion components that comprise the overall top slab response. 205

Table 6.2: Resonant frequencies and the corresponding modes of oscillation identified by interpreting free vibration data. 208

Table 6.3: Period lengthening ratios of the two swaying modes and the torsional mode of the two structural configurations. 208

Table 6.4: “Average damping values of the torsional mode. 215

Table 6.5: Peak particle velocities recorded along the North-South direction by the 0.1n instrument, and the corresponding shear strains, stiffness degradation and damping ratio values. 223

Table 6.6: List of instruments used for the evaluation of soil motion attenuation, with cross-reference to Figure 5.17. 226

Table 6.7: Input data used for interpreting strong motion acceleration data to velocity and displacement time histories. 236

Table 6.8: Instrument pairs used for the calculation of phase difference. 240

Table 6.9: Input data used for the calculation of motion components that constitute the total top slab response of the examined experiments. 242

Table 6.10: Series of experiments of which data were processed to identify the natural frequencies and the corresponding mode of each structural configuration (name convention according to Table 5.10). 247

Table 6.11: Experimental natural frequencies and the corresponding modes of the examined SSI systems with different structural configurations. 255

Table 6.12: Period lengthening ratios of the two swaying modes and the torsional mode of three structural configurations. 256

Table 6.13: Peak particle velocities, strains and stiffness degradation levels computed at the identified natural frequencies of the experiments with vibrator mass mC and mD. The instruments of which records were used is also stated. 261

Table 6.14: Instruments and recording direction of which data were used to evaluate soil motion attenuation. 270

Table 6.15: Foundation soil motions dominated by the identified foundation modes. The presented soil motions were used to relate soil motion attenuation with the swaying and torsional modes. . 274

Table 6.16: Range of natural frequencies and lengthening ratios of the predominant periods for the corresponding modes inferred from strong motion free and forced vibration data. 279

Table 7.1: Forced vibration experiments for which numerical models were used in the calibration process..... 289

Table 7.2: Free vibration experiments for which numerical models were used in the calibration process..... 289

Table 7.3: Elastic properties of the structural elements. 298

Table 7.4: Elastic soil properties. 298

Table 7.5: Frequencies and angular frequencies used in the calculation of Rayleigh damping, for each structural configuration. 299

Table 7.6: Time steps used in the forced and free vibration numerical analyses..... 299

Table 7.7: Values of the mG and G0 parameters that define the Gmax profile. 303

Table 7.8: Adopted properties of interface elements. 308

Table 7.9: Initial gap openings prescribed prior to the StSW and StP/Dynamic analyses 309

Table 7.10: Values of interface stiffness selected for the static self-weight analyses..... 311

Table 7.11: Transfer function T(F) values computed as Fourier amplitude ratios of soil to foundation motion (0.1/1.1). The presented values correspond to a spectral frequency equal to the fundamental frequency of the SSI system. The results are inferred from numerical analyses, with or without interface gaps, that simulate the three free vibration tests. 341

Table 7.12: Examined sets of G-γ-D curves and their aim. 345

Table 7.13: Free vibration simulations carried out to investigate the impact of initial opening magnitude..... 376

Table 7.14: Elastic properties of the structural elements. 380

Table 7.15: Input parameters, of the calibration Calibr6, that are incorporated in the nonlinear IC.G3S model. 381

Table 7.16: Adopted Interface properties. 382

Table 7.17: Interface model adopted by each analysis. 382

Table A.1: Sample testing details in RC and CX apparatuses (Koronides, 2018). 469

Table A.2: Input parameters for Darendeli (2001) equations, when assuming experimental conditions. 470

Table A.3: Calibrated of φi's parameters of Darendeli (2001) equations. 471

Table A.4: Default φi's parameters of Darendeli (2001) equations 471

Table A.5: Input for Darendeli (2001) equations assuming in-situ conditions. 471

Table A.6: Layer 1: Calibrated parameters of the nonlinear model. 473

Table A.7: Layer 2: Calibrated parameters of the nonlinear model. 473

Table A.8: Layer 3: Calibrated parameters of the nonlinear model. 474

Table A.9: Layer 4: Calibrated parameters of the nonlinear model. 474

Table A.10: Layer 5: Calibrated parameters of the nonlinear model. 474

Table A.11: Layer 6: Calibrated parameters of the nonlinear model. 474

Table A.12: Layer 7: Calibrated parameters of the nonlinear model. 474

Table A.13: Layer 8: Calibrated parameters of the nonlinear model. 474

Table A.14: Layer 9: Calibrated parameters of the nonlinear model. 474

Table A.15: Layer 10: Calibrated parameters of the nonlinear model. 475

Table A.16: Layer 11: Calibrated parameters of the nonlinear model. 475

Table A.17: Layer 12: Calibrated parameters of the nonlinear model. 475

Table A.18: Layer 13: Calibrated parameters of the nonlinear model. 475

Table A.19: Layer 14: Calibrated parameters of the nonlinear model. 475

Table A.20: Layer 15: Calibrated parameters of the nonlinear model. 475

Table A.21: Layer 16: Calibrated parameters of the nonlinear model. 476

Table B.1: Applied frequencies and for vibrator masses during exp1 (03/04/2019) 482

Table B.2: Applied frequencies and for vibrator masses during exp2 (03/04/2019) 483

Table B.3: Applied frequencies and for vibrator masses during exp5 (03/04/2019) 483

Table B.4: Applied frequencies and for vibrator masses during exp7 (04/04/2019) 484

Table B.5: Applied frequencies and for vibrator masses during exp8 (04/04/2019) 484

Table B.6: Applied frequencies and for vibrator masses during exp9 (04/04/2019) 485

Table B.7: Applied frequencies and for vibrator masses during exp10 (04/04/2019) 485

Table B.8: Applied frequencies and for vibrator masses during exp12 (05/04/2019) 486

Table B.9: Applied frequencies and for vibrator masses during exp13 (04/04/2019) 486

Table B.10: Applied frequencies and for vibrator masses during exp14 (17/10/2019) 487

Table B.11: Magnitudes of the pull-out forces applied during the FBr_2Ts(3) experiment (exp3, 03/04/2019) 487

Table B.12: Magnitudes of the pull-out forces applied during the FBr_2Ts(4) experiment (exp4, 03/04/2019) 487

Table B.13: Magnitudes of the pull-out forces applied during the PBr_W(11) experiment (exp11, 04/04/2019) 488

Table F.1: Modelled forced vibration experiments. 553

Table F.2: Modelled free vibration experiments carried out on the fully braced 2-top slab structure. 554

Table F.3: Elastic properties of the structural elements. 556

Table F.4: Elastic soil properties. 556

Table F.5: Input parameters of the calibration Calibr0. 557

Table F.6: Input parameters of the calibration Calibr1. 558

Table F.7: Input parameters of the calibration Calibr2. 558

Table F.8: Input parameters of the calibration Calibr3 558

Table F.9: Input parameters of the calibration Calibr4 558

Table F.10: Input parameters of the calibration Calibr5 558

Table F.11: Input parameters of the calibration Calibr6 558

List of Symbols

Roman alphabet

A/Ac	Ratio defined as the interface contact area to the critical interface area at failure
a_0	Normalised frequency
A_f	Foundation area
B	Half width of footing
c_j	Damping coefficient of the j^{th} vibratory mode
$c_{j,rad}$	Radiation damping coefficient of the j^{th} vibratory mode
C_θ	Rocking damping coefficient
E	Young's modulus
E_F	Young's modulus of the beam elements extended from columns to the foundation
E_{TF}	Young's modulus of the beam elements extended from columns to the top slab
E_d^*	Deviatoric shear strain since the last reversal
f	Frequency loading
F_{centr}	Centrifugal force
f_{max}	Maximum frequency loading
f_{NL}	Site-specific frequency below which the response amplifies and above which it de-amplifies due to nonlinearities in relation to a linear response
F_p	Natural frequency associated with compressional waves
$F_{p,weak}$	Natural frequency at very small strains associated with compressional waves
F_s	Fundamental frequency of soil column
F_{sh}	Vibratory force

F_x	Force component in the x-direction
F_y	Force component in the y-direction
G	Shear stiffness
G_0	shear stiffness that corresponds to a reference confining reference pressure
G_{max}	Shear stiffness at very small strains
G_{min}	Minimum shear stiffness
G_{tan}	Tangential shear modulus
h	Height of the structure
H(iω)	Complex-valued transmissibility function
h/r	Slenderness ratio
h_f	Half thickness of foundation
H_s	Thickness of soil column
h_{ts}	Top slab thickness
I_f	Foundation moment of inertia
I_y	Strain index defined as the ratio of the peak velocity of the input motion to the time-averaged shear-wave velocity of the first 30m of soil profile
$\overline{K_{dyn,J}}$	Impedance function of the jth vibratory mode
$K_{dyn,x}$	Dynamic horizontal stiffness of foundation soil
$K_{dyn,\theta}$	Dynamic rotational stiffness of foundation soil
K_h	Stiffness in the horizontal direction
K_j	Static stiffness of soil of the jth vibratory mode
k_j	Stiffness dynamic coefficient of the jth vibratory mode
K_m	Stiffness component of the m mode
k_s	Structural stiffness
K_θ	Torsional stiffness
M	Constrain modulus
m_f	Foundation mass
m_m	inertial component of the m mode
M_{max}	Constrain modulus at very small strains
m_s	Superstructural mass
N	Number of cycles
n_G	Scaling factor

p'	Mean effective stress
p'_{ref}	Reference pressure
r	Foundation radius
$R_{G,min}$, α, b, m_G, $d^*_{1,G}$, $d_{2,G}$, $d_{3,G}$, $d_{4,G}$, α_0, α_1, α_2, b_0, $d'_{1,G}$, $d''_{1,G}$	Input parameters of the IC.G3S model
r_u	Effective radius for translational foundation motion
r_θ	Effective radius for rotational foundation motion
S_u	Undrained shear strength
T	Predominant period of the equivalent-fixed-base system
$\tilde{T}$	Predominant period of the flexible-base system
T_x	Horizontal predominant frequency of a rigid structure
T_θ	Rotational predominant frequency of a rigid structure
$\tilde{T}/T$	Period elongation
$u_{f,r}$	Recorded horizontal foundation displacements
$\ddot{u}_f$ / u_f	Top of foundation acceleration / displacement
$\ddot{u}_g$	Free-field acceleration
$\ddot{u}_s$ / u_s	Relative structural acceleration / displacement
u_{ts}	Top slab displacements
$u_{ts,r}$	Recorded top slab displacements
$v_{f,r}$	Recorded vertical motion
V_p	P-wave velocity
$V_{p,weak}$	P-wave velocity at very small strains
V_s	Shear wave velocity of soil
$V_{s,aver}$	Average shear wave velocity
$V_{s,eff}$	Effective shear wave velocity
$V_{s,min}$	Minimum shear wave velocity
$V_{s,weak}$	Shear wave velocity at very small strains
V_{s0}	Free-field shear wave velocity
z_p	Effective depth

Greek alphabet

β	Damping value of the fixed-base system

$\tilde{\beta}$	Damping value of the flexible-base system
β_0	Soil hysteretic damping value
γ_{exp}	Shear strain inferred from experimental data
γ_m	Structure-to-soil mass ratio
γ_{max}	Maximum shear strain
$\Delta\sigma_v$	Overburden pressure
ζ	Damping ratio of the equivalent-fixed-base system
$\tilde{\zeta}$	Damping ratio of the flexible-base system
$\widetilde{\zeta_0}$	Foundation damping
ζ_h	Soil hysteretic damping
ζ_x	Radiation damping ratio from the translational mode
ζ_θ	Radiation damping ratio from the rotational mode
$\ddot{\theta}_f$ / θ_f	Foundation rotation derived from accelerations / displacements
λ_{min}	Minimum wavelength
ν	Poisson's ratio
ρ	Soil density
σ	Soil-to-Structure stiffness ratio
σ'_{v0}	Free-field overburden pressure
ϕ'	Effective angle of shearing resistance
ϕ_i's (ϕ_1 - ϕ_{12})	Input parameters of Darendeli equations
ω	Angular frequency

Abbreviations

Acc	Recorded acceleration signal
Acc_f	Filtered acceleration time histories
ASA	Annealing simulation approach
BCE	Below contact area's edge
BFC	Below foundation centre
BL_times	Number of times that the baseline correction is applied
Calibr1 Calibr6	Name of various calibrations of the nonlinear model
CC	Stress-strain analysis

CH	Cross-hole test
CONV	Conventional technique
Conv	Conventional soil-foundation interface model
CTX	Cyclic triaxial
DH	Down-hole test
Disp_f	Filtered velocity time histories
Disp_f_segm	Segments of velocity time histories
Disp_final	Filtered and baseline corrected displacement time histories
Dispin	Displacement-controlled analyses (displacements as input excitation)
DRM	Domain reduction method
ELint	Elastic interface elements without gaps
EPint	Elastoplastic interface elements without gaps
EPint_*g*mm	Elastoplastic interface elements with gaps of *g* mm opening
EQL	Equivalent linear
ETF	Empirical Transfer function
EW	East-West
exp1-exp12	Unique number for each experiment
FBr_1Ts	Fully braced structure with one top slab
FBr_2Ts	Fully braced structure with two top slabs
FD	Finite difference
FE	Finite element
FEA	Finite element analysis
FIM	Foundation input motion
Fin	Force-controlled analyses (force as input excitation)
Fs	Sampling frequency

FS_v	Factor of safety of the vertical loads
FxB	Fixed-base analysis
GVDA	Garner valley differential array
G-γ-D	Stiffness degradation and damping ratio curves
HighCutF	Higher cut-off frequencies
HYBint	Hybrid interface model
HYBint_GC2_StSw8 HYBint_GC2_StSw4 HYBint_GC2_StSw3	An analysis that employs the hybrid interface model, simulates the gap configuration GC2 and initiates with static stresses computed by the StSw8/StSw4/StSw3 analysis
IC.G3S	Imperial College Generalised Small Strain Stiffness model
ICFEP	Imperial College finite element program
LINs_Conv	Analysis with linear soil and conventional interface model
LINs_ELint_GC2	An analysis that assumes linear soil and incorporates an interface model with elastic interface elements and gaps modelled according to the GC2 configuration
LowCutF	Lower cut-off frequencies
LSELint	Elastic interface elements with gaps
LVDT	Linear variable differential transformers
mA	Forced vibration experiments during which mass A was placed on each of the two axes of the vibrator
mA_Disp_f	Displacement moving average time histories
mA_Disp_f_segm	Segment of displacement moving average time histories
mA_Vel_f	Velocity moving average time histories
mA_Vel_f_segm	Segment of velocity moving average time histories
mB	Forced vibration experiments during which masses A and B were placed on each of the two axes of the vibrator
mC	Forced vibration experiments during which masses A, B and C were placed on each of the two axes of the vibrator

mD	Forced vibration experiments during which masses A, B, C and D were placed on each of the two axes of the vibrator
n	Order of the filter
NEES@UCSB	Network for Earthquake Engineering Simulations of the University of California, Santa Barbara
NLIN	Nonlinear analyses
NLINs_ELint_StSw3_GC2	An analysis that assumes nonlinear soil, initiated with static stresses computed by the StSW3 analysis. It incorporates an interface model with elastic interface elements and gaps modelled according to the GC2 configuration
NLINs_HYBint_StSw3_GC2	An analysis that assumes nonlinear soil, initiated with static stresses computed by the StSW3 analysis. The hybrid interface model is used, while gaps of the GC2 configuration are modelled
NS	North-South
OCR	Overconsolidation rate
PBr	Fully braced structure with two top slabs
PBr_S	Fully braced structure with two top slabs loaded along its strong axis
PBr_W	Fully braced structure with two top slabs loaded along its weak axis
PI	Plasticity index
PPV	Peak particle velocity
QC	Quality control
RC	Resonant column
REF	Refraction test
SA	Spectral acceleration
SPAC	Spatial Auto-Correlation coefficient
SS1.2	Soil surface, 1.2m far from foundation
StP	Static pull-out analysis
StSw	Static self-weight analysis

StSw3	Static self-weight analysis that uses $K_s=K_n=1E3kN/m^3$ for the interface elements at the contact area
StSw4	Static self-weight analysis that uses $K_s=K_n=1E4kN/m^3$ for the interface elements at the contact area
StSw8	Static self-weight analysis that uses $K_s=K_n=1E8kN/m^3$ for the interface elements at the contact area
SWI	Surface wave inversion test
Taper_perc	Percentage of the recorded motion which is replaced by tapers
TF	Transfer function
UCS	Unified soil classification system
Vel_f	Filtered displacement time histories
Vel_f_segm	Segments of velocity time histories
Vel_final	Filtered and baseline corrected velocity time histories
WLA	Wildlife liquefaction array
ZeroPadTime	Time duration or the zero padding

Chapter 1

Introduction

1.1 Background

Experience from earthquake events (e.g. Mexico City 1985, Northridge 1994, Kobe 1995) have shown that Soil-Structure-Interaction (SSI) and foundation rocking can affect the structural response either beneficially (Gazetas, 2001; Sakellariadis *et al.*, 2020) or detrimentally (Mylonakis and Gazetas, 2000; Gazetas, 2001; Mylonakis *et al.*, 2006). Despite the demonstrated significance of SSI phenomena, modern provisions permit practitioners to neglect the effects, recognising only their beneficial role. Guidelines for incorporating SSI effects in the design process are inadequate to capture the complexity of the effects. To simplify the phenomena, these can be distinguished into kinematic and inertial interaction mechanisms, which are typically studied separately.

The kinematic effects can alter the soil response in the vicinity of the foundation and hence are important for the estimation of the input motion at the foundation level. The effects can be perceived when comparing the free-field response with the response of the same site when a massless foundation is present. The difference between the two can be attributed to the inability of the foundation to conform with the free-field motion. Analytical (Day, 1977; Elsabee *et al.*, 1997) and experimental (Kim and Stewart, 2003; Givens *et al.*, 2012) studies have shown that kinematic effects can decrease horizontal motion and increase rotational motion components at the foundation level. This impact is particularly pronounced for embedded structures and when input motions are incoherent and of high frequency.

The present study focusses on inertial interaction, which arises from the compliance of foundation soil. It refers to the development of inertial forces in a vibrating structure and the transmission of motion from the structure to the soil, which would not occur for fixed-base structures. Inertial interaction effects can be associated with the reduction of the fundamental frequency and increase

of damping of an SSI system, in relation to an equivalent fixed-base structure (e.g. Veletsos and Meek, 1974; Veletsos and Nair, 1975). The fundamental frequency and the damping of an SSI system can be further affected when nonlinear effects take place during a seismic event. Soil nonlinearity and plasticity, that are manifested through soil stiffness degradation and damping development, can further promote the decrease of a system's fundamental frequency and the increase of damping. For structures founded on shallow foundations that are prone to rotate, foundation geometric nonlinearity, commonly referred to as rocking, can decrease the fundamental frequency as well. Rocking dominated systems were also found to develop less damping compared to identical systems that exhibit less rocking and more foundation translation (Gajan and Kutter, 2008; Gazetas, 2015; Sharma and Deng, 2020). This is associated with the fact that the rotational modes of foundation oscillation can radiate less energy to the soil medium than the translational modes (e.g. Gazetas, 1983, 1991; Amorosi *et al.*, 2017).

The significance of inertial interaction SSI effects and foundation rocking depends on various parameters. These include structural characteristics, such as stiffness, mass and slenderness, as well as soil stiffness, frequency content and intensity of the input motion. SSI effects are more pronounced on SSI systems with lower soil-to-structure stiffness ratio, i.e. structures with high fixed-base natural frequency founded on soft soil, as indicated by analytical (e.g. Veletsos and Nair, 1975), numerical (Amorosi *et al.*, 2017) and real-scale experimental (e.g Star *et al.*, 2015) studies. Veletsos and Nair (1975) and Amorosi *et al.* (2017) have shown that slender structures are expected to exhibit more foundation rotation than squatty structures, which can affect the system's natural frequency and damping as described previously. According to the same studies, for seismic problems, the impact of structural mass on the significance of SSI effects cannot be directly described, as it depends on the soil-to-stiffness ratio. However, in the case of a system excited by a load applied on the structure (i.e. free or forced vibration tests), a lighter structure is anticipated to exhibit stronger response and potentially stronger foundation rocking than an identical but heavier structure. As a result of the increased foundation rocking, the lighter structure is expected to have a more pronounced decrease of the system's fundamental frequency and damping.

A rigorous way to observe and analyses SSI effects is by the means of real-scale experiments, which, however, are scarce due to the high operational costs. Such experiments were carried out in the Garner Valley, Wildlife liquefaction array (California, USA), Lotung, Hualien (Taiwan), Edmonton (Canada) and Euroseistest site (Greece). The purpose of most of the tests was to compare experimental outcomes with analytical solutions and establish impedance functions (Barros and Luco, 1995; Tileylioglu *et al.*, 2008, 2011; Givens, 2013; Star *et al.*, 2019). To the best of the author's knowledge, there has been only one study (Sharma and Deng, 2020) that has specifically examined

the soil-foundation interface behaviour under static loading conditions. However, there have been no studies that have exploited strong motion data to investigate the interface behaviour under dynamic conditions. Furthermore, only one study exists in the literature (Amorosi *et al.*, 2017) that use data from real-scale experiments to calibrate a numerical finite element (FE) model.

Finite element analysis (FEA) is the most rigorous approach to study dynamic SSI phenomena. FEA, which is commonly referred to as the direct method, simulates SSI problems in a single step in the time domain, considering the continuous interaction between the structure and the soil. It enables comprehensive soil modelling, considering soil nonlinearity, soil plasticity, pore water pressure generation, soil stiffness dependence on the mean effective stress and other facets of soil behaviour, depending on the soil type and on the adopted constitutive model. It also allows for a rigorous modelling of the soil-foundation interface, enabling foundation uplift and sliding. These are the main advantages of FEA over other methods that exist in the literature, such as Winkler models (Raychowdhury and Hutchinson, 2009; Pelekis *et al.*, 2021), lumped models (Stewart *et al.*, 1999a; Maravas *et al.*, 2014) and the substructure method (Bode *et al.*, 2002; Pitilakis *et al.*, 2008). The disadvantages of FEA are the high computational cost and the lack of a rigorous numerical procedure for SSI related problems. Numerical challenges in FEA are associated with modelling the structural elements, the soil-foundation interface and soil constitutive behaviour appropriately. These uncertainties can be mitigated when an FE model is validated against real-scale experiments, which can allow a thorough calibration of the entire SSI system.

1.2 Scope of research

The aim of the present research is to contribute to the advancement of knowledge regarding the modelling of SSI related problems and propose modelling approaches to simulate numerical aspects that require consideration. The discussion in Section 1.1 highlighted the scarcity of rigorously calibrated FE SSI studies and the significance of strong motion data obtained from field experiments to address this research gap. Within this context, this study presents three-dimensional FE analyses that simulate SSI real-scale experiments, whose data are used for calibration purposes. The analyses are characterised by a rigorous calibration of the soil behaviour, soil-foundation interface behaviour and structural elements. The experiments consist of free and forced vibration experiments on the prototype structure of EUROPROTEAS which is located at the centre of the Euroseistest site, within a valley in Northern Greece (Pitilakis *et al.*, 2018).

This study sets several objectives to contribute to the accomplishment of the above aim, that constitutes the general scope of the research. The first objective is the deployment of a procedure to calibrate the numerical model effectively. The second objective is the numerical investigation of the

importance of adopting a suitable constitutive behaviour for the soil and appropriately modelling the soil-foundation interface. The thesis proposes a novel approach to model interface gaps and to manipulate the static stresses at the interface. Another objective is to establish quantitatively the impact of both soil nonlinearity and interface gaps on the SSI response and justify relative qualitative conclusions drawn by interpreting field data.

The field data collected from the forced and free vibration tests are interpreted, aiming to investigate experimentally the importance of SSI effects, soil nonlinearity and foundation rocking on the response of the system. Additionally, field data interpretation aims to investigate the significance of SSI effects with respect to some of the parameters mentioned in Section 1.1, including structural mass, structural stiffness, frequency content and intensity of the input motion. It also seeks to examine the importance of SSI effects on period elongation and damping development for the different modes of oscillation. To ensure the reliability of the experiments, the field observations are compared with outcomes of previous studies.

Finally, an initial part of the thesis is devoted to one-dimensional site response analyses that aim to calibrate the free-field soil profile, investigate the impact of bedrock depth on the response of the site and to identify the origin of the observed resonances.

1.3 Thesis layout

The work presented in the thesis is organised into nine chapters as described herein.

Chapter 2 provides an overview of the literature on SSI effects giving more emphasis on the inertial interaction and foundation rocking. The impact of the structural and soil characteristics on the significance of SSI response is discussed by synthetising results of previous studies. Analytical solutions are provided, while the simplified procedures that are commonly used are described. The advantages and challenges of fully nonlinear finite element analyses are also discussed.

Chapter 3 presents a comprehensive examination of the existing real-scale experiments and a description of the main outcomes of past studies that exploited strong motion data. An extensive reference is made on the use of strong motion data for system identification purposes and for establishing impedance functions. This chapter aims to demonstrate the worth of strong motion data and highlight the limited utilisation of such data in rigorously calibrated numerical studies.

Chapter 4 starts with a literature review on site response analyses, before presenting results from one-dimensional site response analyses that were carried out for the purpose of the present study. The study benefits from strong motion data that were recorded by a downhole array of accelerometers that is permanently installed at the site of interest. A calibration procedure is

proposed aiming to calibrate the free-field soil profile that can be incorporated in the subsequent numerical SSI analyses. Fully nonlinear analyses are compared against equivalent linear analyses to validate the applicability of the latter simplified method for small strain problems. Furthermore, a series of analyses are conducted to model the soil to different depths, aiming to explore the influence of bedrock depth on the site response and identify the origin of the observed resonances.

Chapter 5 describes the field experiments, presenting the EUROPROTEAS protype structure, the soil characterisation based on previous studies and the instrumentation employed. The chapter further outlines the conception of the experimental set-up and examines thoroughly the reliability of the data. Ensuring the instruments' reliability and overall experimental reliability was crucial prior to interpreting the recorded data.

Chapter 6 presents the interpretation of experimental data obtained from both free and forced vibration tests. For each type of test, a system identification technique is proposed, aiming to identify the natural frequencies, damping and modal shapes that were distinct during the experiments. The chapter further explores the impact of structural mass, structural stiffness, frequency and amplitude of the input motion on the response. It also evaluates nonlinear phenomena, making a qualitative distinction between soil and interface nonlinearities, before examining the attenuation of soil motion with distance from the foundation. In the final section of the chapter, results obtained from free and forced vibration tests are compared, aiming to examine their agreement and corroborate the efficacy of the suggested system identification techniques.

Chapter 7 presents results from the three-dimensional numerical analyses, that simulate the field experiments. It proposes a rigorous calibration procedure that involves several steps, each of which focuses on calibrating a specific feature of the model. The calibration procedure makes use of meticulously selected strong motion data. These data are recorded during both free and forced vibration tests, and the advantages of each type of test are exploited during the calibration procedure. The procedure begins with calibrating the structural model, followed by the calibration of the soil-foundation interface and soil models. Regarding the interface model, a novel approach to model interface gaps and manipulate interface static stresses is proposed. The chapter discusses extensively the impact of interface gaps on the response, especially on the system’s natural frequency and damping. It also presents a parametric analysis with adopting various calibrations of the soil constitutive model, demonstrating the significance of adopting an appropriate soil model for SSI problems. An additional aim of the chapter is to employ quantitative numerical results to validate qualitative conclusions drawn from data interpretation in Chapter 6.

Chapter 8 presents results from the calibrated numerical model that simulates free and forced vibration tests, additional to the tests that were used in the calibration process. The numerical results are compared with the experimental ones to further validate the numerical model. The chapter also presents results from numerical analyses that assume fixed-base conditions or linear or nonlinear soil and consider or neglect interface gaps. These analyses aim to provide quantitative evidence of how the system's natural frequency and damping are affected by the following mechanisms: soil compliance, interface gaps, interface nonlinearity and soil nonlinearity. The overall impact of nonlinear effects on system's natural frequency and damping is evaluated by comparing the associated values inferred from analyses that simulate experiments of various excitations. Regarding the interface nonlinearity, the time variation of opening and closure of areas at the soil-foundation interface is presented in relation to the excitation levels. Soil nonlinearity is quantitatively assessed by presenting computed values of stiffness degradation and damping ratio of soil. The impact of interface gaps, interface nonlinearity and soil nonlinearity on the soil motion resulting from structural oscillation is also discussed. Lastly, the chapter aims to validate the experimental outcomes of Chapter 6 with numerical results.

Chapter 9 presents a summary of the main conclusions drawn from the present work. It compares the conclusions with relative results of existing studies and makes recommendations for future research.

Chapter 2

Overview of Soil-Structure-Interaction

2.1 Introduction

Numerous studies have demonstrated the significant impact of Soil-Structure-Interaction (SSI) effects on structural response due to seismic or dynamic loading. These investigations include analytical studies (e.g. Veletsos and Meek, 1974; Veletsos and Nair, 1975; Stewart *et al.*, 1999), lab studies (e.g. Drosos *et al.*, 2012; Anastasopoulos *et al.*, 2013; Park and Kim, 2013), field tests (e.g. Kim and Stewart, 2003; Tileylioglu *et al.*, 2011; Star *et al.*, 2015; Pitilakis *et al.*, 2018) and numerical studies (e.g. Anastasopoulos and Kontoroupi, 2014; Gazetas, 2015; Amorosi *et al.*, 2018; Pelekis *et al.*, 2021; Zhang and Far, 2022). The above studies rely on various assumptions which simplify the complexity of the SSI phenomena. SSI phenomena are typically distinguished into kinematic and inertial interaction phenomena. Kinematic interaction stems for the inability of a stiff foundation to conform to the free-field deformation pattern induced by a particular ground motion. As a result, the motion at the foundation level deviates from the free-field motion. The inertial interaction refers to the development of inertial forces in the vibrating structure associated with a compliant base, which would not occur for a fixed-base structure. The structural response induces, in return, stresses in the foundation soil, while it may cause the foundation to displace (slide) or rotate (foundation rocking).

This chapter aims to describe the principles of SSI focusing on the inertial interaction effects, which are of interest for the present study. The most widely methods for studying SSI phenomena are presented, along with a discussion of their assumptions and limitations.

2.2 Kinematic interaction

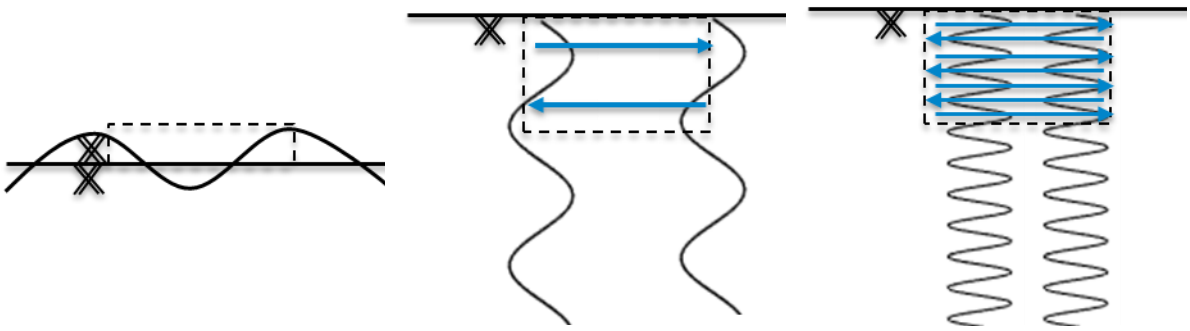
Kinematic interaction effects, which are more important for embedded structures, result from the contribution of three mechanisms (Stewart *et al.*, 1998): (a) Base-Slab Averaging, (b) Embedment effects and (c) Wave scattering.

(a) Base slab averaging is schematically illustrated in Figure 2.1. Foundations are stiffer than the surrounding soil applying kinematic constraints that result in averaging of inclined and incoherent wave fields near the foundation. Figure 2.1a shows that a rigid foundation cannot comply with the free-field vertical deformations and therefore the surface deformations should be altered to satisfy the kinematic constraints of the soil-foundation system. Figure 2.1b shows that the coherent horizontal free-field deformations tend to move the upper part of the foundation to the right and the lower part to the left, which will result in increasing the rotational component of the input motion at the foundation level and decreasing the horizontal one. Kinematic interaction effects decrease further the horizontal motion at the foundation level when the input deformations are of higher frequency. Figure 2.1c shows that the high frequency free-field deformations tend to displace some parts of the foundations to the right and some others to the left, which in return results in averaging of the incoming waves and to a considerable decrease of the horizontal motion. Finally, the averaging is even more pronounced when the incoming and the reflected waves are incoherent and inclined as these cancel out with each other.

(b) Embedment effects reduce the translational motion relative to the corresponding free-field motion of embedded foundations subjected to seismic waves. They also develop shear strains, that would have not occurred in the free-field, along the sides of the excavation, that may result to rocking motion.

(c) Wave scattering refers to the scattering of seismic waves at foundations corners and is related to the base slab averaging and embedment effects and cannot be studied alone.

Veletsos and Prasad (1989) and Veletsos *et al.* (1997) studied analytically the effect of base slab averaging assuming rigid, massless footings of both circular and rectangular shapes (considering different aspect ratios) resting on the surface of a homogeneous elastic half-space. They assumed coherent or incoherent, vertically or inclined propagating SH waves. The latter features of wave propagation were considered through the angle of wave incident in relation to the vertical axis and an incoherence function. These were incorporated in a cross spectra density function that expresses the special variability of the soil motion at the foundation level. The above studies produced transfer functions that relate the horizontal and torsional foundation motion to the free-field ones. Results of these studies show that the translational motion is insensitive to the inclination of the incident waves and to the aspect ratio of the footing. In contrast, torsional motion becomes more pronounced for lower aspect ratio footings and non-vertically incident wave fields.



(a) (b) (c)

Figure 2.1: Base slab averaging due to kinematic effects: (a) vertical deformations, (b) horizontal deformations, (c) horizontal high frequency deformations.

Embedment effects were studied by Day (1977) and Elsabee and Murray (1977). Day (1977) assumed a rigid cylindrical foundation embedded in a homogeneous elastic half-space, while Elsabee and Murray (1977) assumed a viscoelastic soil layer of finite depth over bedrock. Both studies conducted finite element analyses and applied vertically propagating coherent SH waves producing transfer functions (TF) that relate the translational and rocking motions of the foundation to free-field motions. The TF values are presented as a function of normalised frequeny a_0, calculated as $\omega r/V_s$ (where ω is the angular frequeny, r is foundation radius and V_s the shear wave velocity of soil). The results of these studies show that, for the case of half-space, the amplitude of the TF of the translational motion decreases with applied frequency, while the rotational TF increases at relatively small frequencies (a_0<1.5) before starting reducing (Figure 2.2). The studies also reveal that the increase of embedment decreases the horizontal motion and increases the rocking motion especially at relatively low frequencies (a_0<2). A similar trend was observed for the case of a finite soil layer over rigid bedrock, with the difference being the flactuations in TF values for a_0>1.5. Overall, the embedment effects were found to decrease the translational motion component at the foundation level for a_0<1.5 and to introduce significant rocking component for a_0>1.

Ulinke analytical studies that are based on idealised conditions, e.g. vertical wave propagation, studies that are based on field data provided a more realistic investigation of the kinematic interaction effects. Field data can consist of seismic soil motions recorded near or farther from the structure of interest. Kinematic interaction effects are assessed through transfer function ratios of foundation level motion to soil motion far from the structures. Chao (1996) and Borja *et al.* (1999) used experimental data (Lotung area) and produced 3D nonlinear SSI models to show that kinematic interaction effects were more significant in the translational than the vertical motion and in areas where soil nonlinearity and plasticity took place. Kim and Stewart (2003) compared results from field data with analytical models and attributed their difference in the simplified assumptions underpinning the models. Earthquakes

produce complex wave fields containing inclined waves that further contribute to base slab averaging. Also, noise that exists in earthquake records contributes to the scatter seen in the field data, posing challenges in their processing. Similarly, Givens *et al.* (2012) used data from an area in Japan to assess the embedment effects by comparing field TFs with semi-empirical solutions given in NIST (2012). They have shown that the semi-empirical solutions are conservative, as they suggest larger input motion at the foundation level than the experimental data.

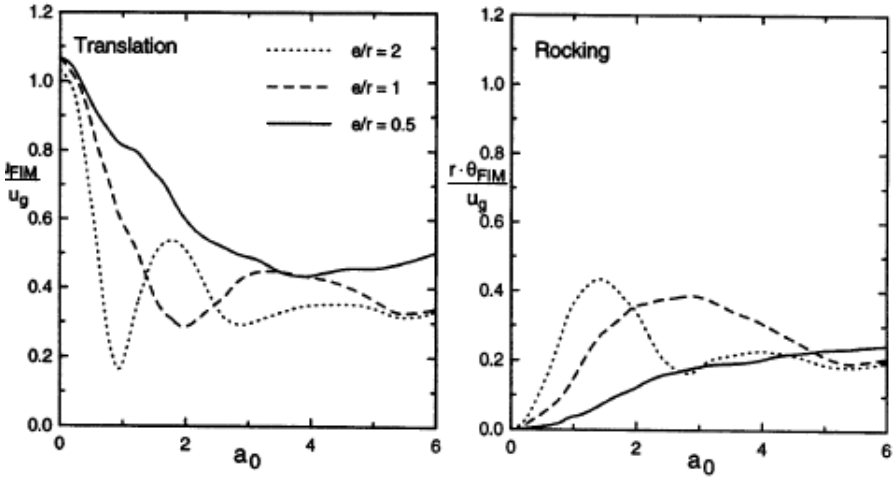


Figure 2.2: Translational and rotational transfer functions defined as the ratio of the input motion at the foundation level to the free-field motion, which resulted assuming vertical incident S waves. The analysis considers a rigid cylindrical foundation, of radius r, embedded at different depths (e) on elastic half-space (taken from Stewart *et al.* (1998), adapted from Day (1977)).

There are many studies that investigate kinematic interaction effects, but they are not going to be analysed here, as this goes beyond the scope of the current research which concentrates more around inertial interaction effects. In general, these effects were found to reduce the foundation horizontal input motion at high frequencies with respect the free-field motion, especially for short and wide structures. However, the effects can be detrimental when they develop rotational motion for slender structures which are prone to rotate (Roesset, 2013). Also, Stewart *et al.* (1999b) exploited strong motion data to demonstrate that even though kinematic interaction decreased the foundation motion relative to the free-field motions, they did not significantly affect spectra accelerations. Spectral accelerations at the natural frequency of an SSI system were found not to differ significantly when computed from response spectra inferred from either free-field input motion or foundation input motion that accounted for kinematic effects. The different impact of kinematic interaction effects on the foundation motion and spectral accelerations can be attributed to inertial interaction effects, highlighting the importance of considering both effects concurrently.

2.3 Inertial interaction

Inertial interaction, which arises from the compliance of foundation soil, leads to the development of inertial forces in a vibrating structure impacting the structural response, in relation to a corresponding fixed-base structure. The fixed-base approach (Figure 2.3a) is sufficient for cases of stiff foundation soil, whereas soil compliance should be considered when a stiff structure is founded on soft soil. Soil compliance can be simplistically illustrated through springs at the foundation level (Figure 2.3b), that allow the foundation to translate or rotate. As it can be easily understood from Figure 2.3a and b, a compliant-base structure is more flexible than a fixed-base structure (e.g. Veletsos and Meek, 1974). Additionally, soil compliance increases the system's damping by radiating structural energy to the half-space (e.g. Veletsos and Meek, 1974; Veletsos and Nair, 1975). This damping mechanism, commonly referred to as radiation damping, can be simplistically modelled as translational and rotational dashpots at the foundation level (not depicted in Figure 2.3b).

Veletsos and Meek (1974) and Veletsos and Nair (1975) derived analytically the predominant period lengthening ratio ($\tilde{T}/T$) of an SSI system depicted in Figure 2.3b:

$$\tilde{T}/T = \sqrt{1 + \frac{k_s}{K_{dyn,x}} + \frac{k_s h^2}{K_{dyn,\theta}}} \qquad 2.1$$

where, $\tilde{T}$ is the natural frequency of the flexible-base system, T is the natural frequency of the equivalent fixed-base system, k_s is the structural stiffness and h is the height of the structure. $K_{dyn,x}$ and $K_{dyn,\theta}$ correspond to the dynamic horizontal and rotational stiffness of foundation soil, respectively. The same studies approximate the damping ratio of the flexible-base system ($\tilde{\zeta}$) as:

$$\tilde{\zeta} = \widetilde{\zeta_0} + \frac{\zeta}{\left(\tilde{T}/T\right)^n} \qquad 2.2$$

where, ζ is the hysteretic damping of the fixed-base system (structural damping) and $\widetilde{\zeta_0}$ is the foundation damping. The n exponent takes a value equal to 3 when assuming viscous structural damping (Veletsos and Meek, 1974; Veletsos and Nair, 1975), while it should be taken as 2 when hysteretic structural damping is assumed (Wolf and Song, 2002; Givens *et al.*, 2016). Foundation damping is an aggregation of both hysteretic material damping and radiation damping. Many formulations of $\widetilde{\zeta_0}$ have been proposed by previous studies (Veletsos and Meek, 1974; Veletsos and Nair, 1975; Wolf and Song, 2002; Maravas *et al.*, 2014; Givens *et al.*, 2016); indicatively the one proposed by Wolf and Song (2002) and which is suggested by NIST (2012) is presented:

$$\widetilde{\zeta_0} = \left[1 - \frac{1}{\left(\tilde{T}/T\right)^2}\right]\zeta_h + \frac{\zeta_x}{\left(\tilde{T}/T_x\right)^2} + \frac{\zeta_\theta}{\left(\tilde{T}/T_\theta\right)^2} \qquad 2.3$$

where, ζ_h is the soil hysteretic damping; ζ_x and ζ_θ are the radiation damping ratios from the translational and rotational modes; T_x and T_θ are the horizontal and rotational predominant frequencies of a rigid structure.

$$T_x = 2\pi\sqrt{\frac{m}{K_{dyn,x}}} \quad , \quad T_\theta = 2\pi\sqrt{\frac{mh^2}{K_{dyn,\theta}}} \qquad 2.4$$

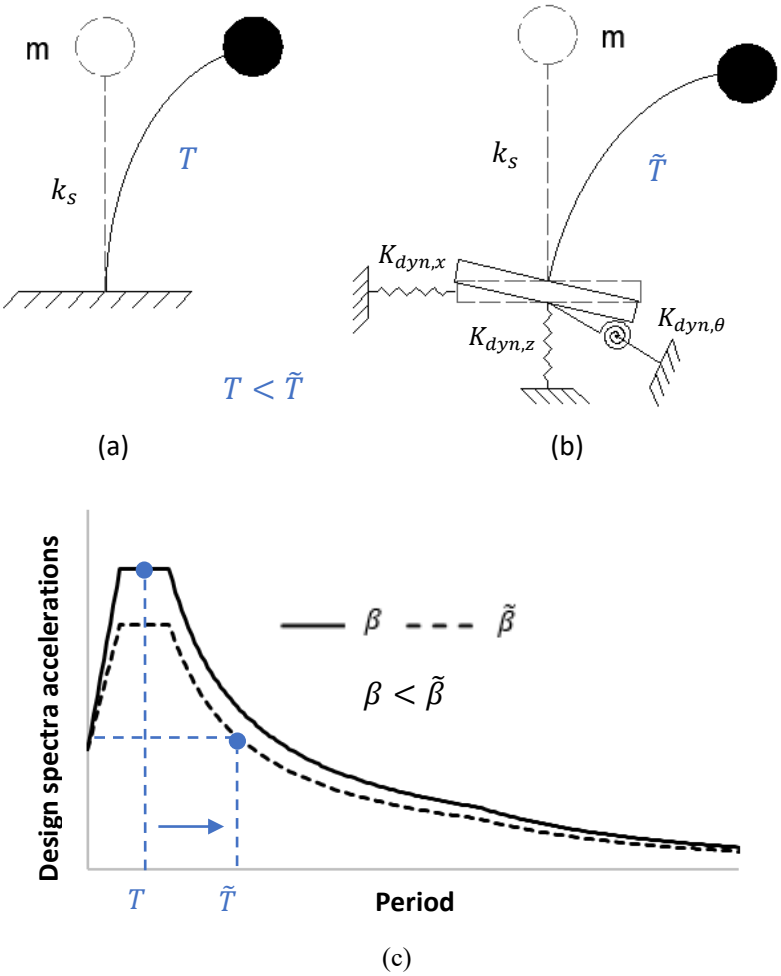


Figure 2.3: A single-degree-of-freedom structure with (a) fixed-base conditions and (b) flexible base considering soil compliance. (c) The impact of SSI effects on the design spectral accelerations is schematically illustrated (adapted from Mylonakis and Gazetas (2000)).

Figure 2.3c presents schematically the design spectra of Eurocode 8 (British Standards Institution, 2004c) computed for damping values that correspond to fixed (β) or flexible ($\tilde{\beta}$) base systems, with the spectral accelerations at the periods of fixed-base (T) and flexible-base ($\tilde{T}$) systems. It illustrates that the SSI effects, period and damping increase, can result in smaller design spectral accelerations than those that result assuming fixed-base conditions. It is noted that the significance of the impact of inertial interaction SSI effects on the structural response depends on several factors that are

incorporated in Eqs. 2.1-2.4, e.g. structural stiffness, structural mass, structural slenderness, that are subsequently discussed in Section 2.6. Also, it varies with site conditions (e.g. soil stiffness, layering, bedrock depth) and input frequency, as the dynamic stiffness ($K_{dyn,x}$, $K_{dyn,\theta}$) and radiation damping (ζ_x, ζ_θ) are dependent on the above parameters (Gazetas, 1983, 1991).

The energy transmitted from a vibrating structure to the half-space is manifested as induced soil strains that are spread out with distance from the foundation (geometrical spreading). The induced strains promote soil nonlinearity, while, under strong foundation motion, they can cause soil plasticity in the vicinity of the foundation where they accumulate (e.g. Anastasopoulos *et al.*, 2010; Anastasopoulos and Kontoroupi, 2014; Gazetas, 2015). Both soil nonlinearity and plasticity can further increase both the damping and the natural period of the SSI system. Strong foundation motion can also produce foundation sliding and uplift (rocking) relative to the soil beneath which impacts further the response of an SSI system (e.g. Anastasopoulos *et al.*, 2013; Gazetas, 2015; Sharma and Deng, 2020; Pelekis *et al.*, 2021).

2.4 Impedance functions of rigid footings

The dynamic stiffness and damping that represents the foundation stiffness and damping of a soil-foundation system subjected to dynamic loading is commonly referred to as impedance functions ($\overline{K_{dyn,j}}$). These frequency dependent functions can be written in a complex-valued form to account for the fact that dynamic force and displacement are out of phase. The real and imaginary components reflect the stiffness and damping of soil, respectively, as illustrated by the equation proposed by Veletsos and Verbic (1973):

$$\overline{K_{dyn,J}} = K_{dyn,j}\,(\alpha_0, \mu) + i\omega c_j(\alpha_0, \nu) \qquad 2.5$$

where, α_0 is the normalised frequency defined earlier, ν is the Poisson's ratio, $K_{dyn,\mathrm{j}}$ is the dynamic stiffness of the vibratory mode j (translational, vertical, rotational or torsional) and c_j is the damping coefficient of the vibratory mode j (translational, vertical, rotational or torsional). $K_{dyn,\mathrm{j}}$ can be determined as the product of the static stiffness (computed from the theory of elasticity), K_j, and a frequency dependent dynamic coefficient, k_j, as per Eq. 2.6. The damping coefficient is an aggregation of radiation damping coefficient, $c_{j,rad}$, and soil hysteretic damping coefficient (which is a function of soil hysteretic damping β_0), as per Eq. 2.7.

$$K_{dyn,j} = K_j k_j(\alpha_0, \nu) \qquad 2.6$$

$$c_j = c_{j,rad} + 2K_{dyn,j}\beta_0/\omega \qquad 2.7$$

The dynamic spring stiffness and dashpot coefficients can be estimated from Gazetas (1983, 1991), which summarise impedance functions proposed in various studies. The collated impedance functions

are based on both numerical and analytical approaches, assuming a massless rigid foundation that was subjected to machine-type loading to mobilise either translational, vertical, rocking or torsional vibration mode of the system. Dynamic stiffness and damping coefficients are calculated for surface or embedded foundations of different shapes (strip, circular, rectangular, arbitrary) resting on different soil conditions: homogeneous half-space, soil stratum underlying bedrock, soil stratum underlying a half-space. Gazetas (1983, 1991) investigated, also, the influence of soil inhomogeneity (stiffness increasing with depth), anisotropy and non-linearity as well as the type of vibratory mode.

The above parametric studies suggest that, for the homogeneous half-space case, the dynamic stiffness of all vibratory modes decreases with increasing input frequency, except for the stiffness of the horizontal mode. The horizontal dynamic stiffness is relatively constant with frequency and almost equal to the static one for the frequency range relevant to engineering problems, i.e. up to 10Hz (Luco and Westmann, 1971; Veletsos and Wei, 1971; Gazetas, 1991). The radiation damping coefficients of the translational (horizontal and vertical) modes were also found to be frequency independent, in contrast with the rotational modes which showed a significance dependence. The rotational damping coefficients are zero at zero input frequency, while they increase for larger frequencies. In general, they are smaller than the damping produced by the translational modes, which radiate more energy to the half-space (Gazetas, 1983, 1991). The damping increase with the input frequency has been verified by Tileylioglu *et al.* (2011) using strong motion data from forced vibration tests applied on a real scale structure. The same study also showed that radiation damping dominated the overall damping of the SSI system, demonstrating its significance on the structural response. The latter observation aligns with a claim made by Gazetas, (1991), that the generated radiation damping can be much larger than the small strain material damping in most cases. Exceptions to this are rotational oscillations at low frequencies, for the reason explained above, and low frequency translational oscillations on a thin soil layer above bedrock as explained below.

The described relation between impedance functions and input frequency becomes more complicated by the existence of a rigid bedrock or a strong impedance contrast of soil stiffness at a shallow depth. As Gazetas (1983, 1991) shows, the values of the impedance functions fluctuate with increasing frequency, due to resonance features within the softer stratum (i.e. dynamic stiffness coefficient minimises at resonance). For frequencies lower than the first resonance one, rigid bedrock leads to wave trapping within the soil layer and hence radiation damping of all modes is negligible. Impedance functions' fluctuations are also observed, to a smaller level, for the case of inhomogeneous soil conditions, with these conditions concurrently decreasing the dynamic stiffness and damping coefficients due to wave reflection. The discrepancy between the dynamic coefficients of homogeneous and inhomogeneous media becomes negligible at high frequencies. This occurs

because the emitted waves have such short wavelengths that any changes in the media's profile (e.g. linearly increasing stiffness) are undetectable. Finally, foundation embedment was found to increase significantly radiation damping and the rate of stiffness reduction with frequency for all modes.

2.5 Foundation Rocking

A complex wavefield that may exist below a shallow foundation can increase the rotational component of the input motion at the foundation level and promote foundation rocking (Stewart *et al.*, 1998). More importantly, foundation rocking can be a result of the inertial structural forces that are transferred at the foundation level as forces and moments, as discussed by Gazetas and Stokoe (1991). These authors carried out lab free vibration tests on a rigid block founded on soft soil to show that a lateral force applied on the top of the block results in a coupled swaying-rocking motion, with the latter component being the dominant one.

For a rigid structure based on stiff soil, Gazetas *et al.* (2013) calculated analytically the variation of the natural frequency of the SSI system with the foundation's angle of rotation. By neglecting foundation translation and accounting for P-Δ effects, they showed that the system becomes more flexible for stronger rocking. Based on the same system and assumptions, Gazetas (2015) verified the above conclusion through 2D numerical simulations. Anastasopoulos *et al.* (2013) carried out shaking table tests on two pier models; one pier was founded on a conventionally designed foundation and the other on a rocking foundation with smaller dimensions. In the context of a conventionally designed system, the foundation's moment capacity surpasses that of the pier, which directs the plastic hinge formation at the base of the pier. Conversely, in the case of the rocking isolated system, the moment capacity was approximately 40% less than that of the pier, leading to plastic deformation occurring at the interface between the soil and the foundation. The latter approach is usually referred to as "inverse capacity design". The mentioned study demonstrated that the rocking-isolated pier exhibited a much more flexible response than the other model, attributing the difference to the smaller stiffness of the rocking model. This demonstrate that a low rotational foundation stiffness, imposed by a foundation that is designed to exhibit rocking, can affect the stiffness and hence the response of the entire SSI system.

A second impact of foundation rocking is the decrease of system's damping in relation to a system that includes a foundation that does not rotate. A foundation-soil system develops damping through radiation damping, hysteretic damping (i.e. soil nonlinearity and plasticity) and damping caused by the reattachment of the foundation to the soil after impact (Anastasopoulos and Kontoroupi, 2014). Among the above mechanisms, foundation rocking decreases radiation damping. Gajan and Kutter (2008) carried out centrifuge tests on a stiff and slender structure founded on a surface footing (shear

wall-footing system), with the foundation being loaded at different levels of the initial vertical loads. They applied lateral cyclic loading and dynamic base shaking on the structure. Sharma and Deng (2020) carried out large scale tests on a cyclic laterally loaded pier that was founded on a surface footing. Gazetas (2015) studied numerically the response of a rigid, slender and elastic SDOF structure that was subjected to the same type of loading. All three studies produced base moment-rotation (M-θ) loops and observed that the lightly loaded foundations exhibited stronger foundation rocking. They also observed that the response of the structure with the lightly loaded foundation produced narrower M-θ loops, concluding that rocking decreased system's damping.

The decrease of both the natural frequency and the damping of an SSI system due to foundation rocking can be attributed to the smaller contact area between the foundation and the soil. Sharma and Deng (2020) monitored the contact interface area of the cyclically loaded large-scale pier-footing and observed that a considerable percentage of the foundation base was detached from the soil. A decrease of the contact interface area makes the foundation soil system and hence the entire SSI system more flexible. Also, the decrease of contact interface area decreases the ability of the foundation to transmit energy to the half-space, limiting radiation damping and justifying the observed reduced damping for rocking dominated systems.

Wolf and Song (2002) studied analytically the impact of foundation uplift on the response of a SDOF model, that was founded on circular rigid foundations over an elastic half-space and excited by an artificial seismic loading. According to the authors, an uplifted foundation can be approximated as a smaller circular foundation of the same properties, i.e. centre of gravity, contact interface area and moment of inertia for rocking. By carrying out a parametric study of different soil types, the analytical solutions have shown that uplift initiates with a smaller earthquake acceleration when the soil is stiff than when it is soft. As expected, uplift was found to reduce the overturning moments and increase the structural displacements (as expected for more flexible systems). Other studies mentioned below, by assuming constant soil conditions, investigated the impact of foundation dimensions and foundation's factor of safety against vertical bearing capacity (FS_v) on the significance of foundation rocking. The studies are mainly divided into three types of SSI models: footing-soil model, rigid elastic structure-footing-soil model and compliant elastoplastic structure-footing-soil model.

The performance of an isolated surface footing-soil system subjected to static or dynamic moment loads was studied by Gazetas *et al.* (2013) and Gazetas (2015), among others. These studies carried out 2D and 3D numerical analyses that simulate a rigid surface footing over nonlinear soil coupled with the Von Mises failure criterion (i.e. total stress undrained analysis). By applying displacement-controlled moment loading on footings that were initially subjected to different levels of vertical loads and hence different FS_v values, they constructed M-θ loops. They found that the heavier loaded

foundation (e.g. FS_v=2) can exhibit higher ultimate moment capacity than lightly loaded foundations (e.g. FS_v=20) (Figure 2.4a). The authors attributed this to the ductile rotational behaviour of the heavily loaded footing and to the rapid degradation of the stiffness of the lightly loaded footing (Figure 2.4b). The stiffness of the soil-footing system with high FS_v drops very rapidly due to uplift of the footing (geometric nonlinearity) which controlled the moment capacity of the system, as illustrated in Figure 2.4c. On the contrary, as the same figure illustrates, footings with lower FS_v do not exhibit significant uplift, allowing the plastic strains to develop in the soil. This condition promotes the mobilisation of the ultimate capacity of a larger area in the soil, thus, increasing the ultimate capacity of the system. It should be noted, though, that the decrease of FS_v can lead to a decrease of the ultimate moment capacity, when the factor of safety is too low (e.g. FS_v=1.25), as shown in Figure 2.4a.

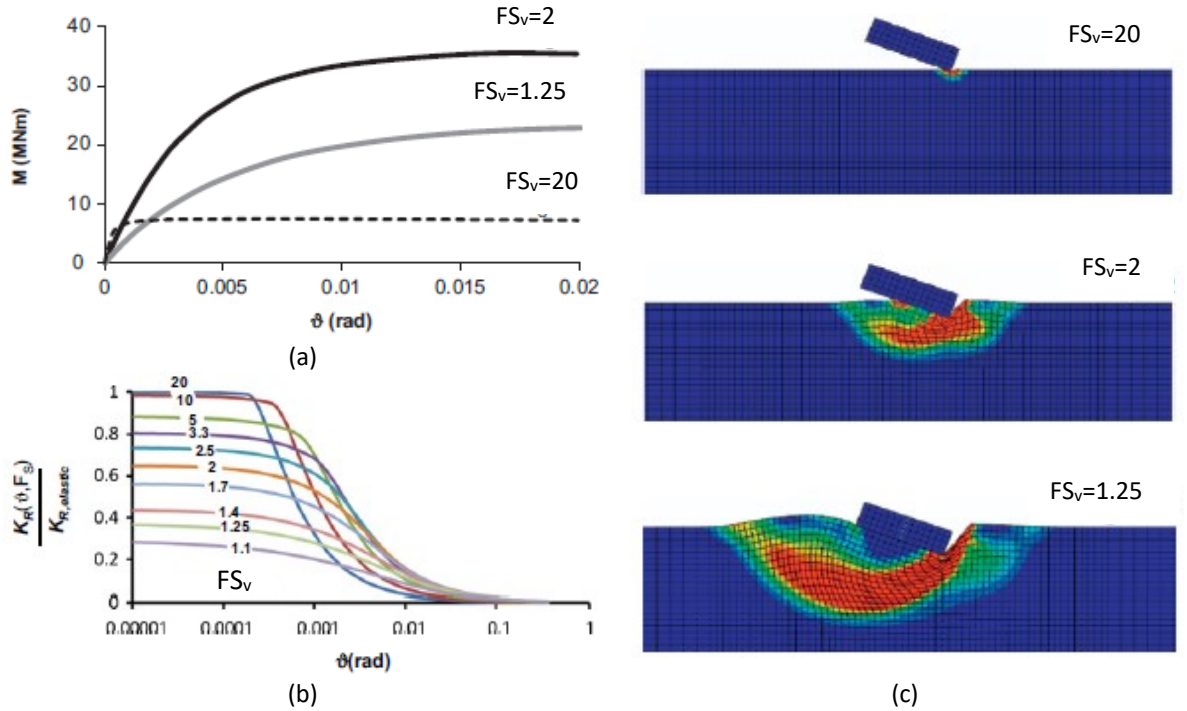


Figure 2.4: Illustrative numerical results from displacement-controlled analyses of a footing subjected to monotonic rotation: (a) moment-rotation curve, (b) rotational stiffness normalised by the elastic stiffness varied with monotonically applied foundation rotation (strip footing), (c) deformed shape and plastic strains contours (Gazetas *et al.*, 2013).

It was therefore concluded geometric that nonlinearity of the interface and soil plasticity are the controlling parameters for systems with footings that are prone or not to rotate, respectively. Aiming to incorporate on the above results the P-Δ effects and the role of re-centring, other studies carried out laboratory and numerical tests of an SSI system that consists of a rigid slender structure on a surface footing, subjected to static or cyclic lateral loads. Anastasopoulos and Kontoroupi (2014) and Gazetas (2015) carried out 3D and 2D numerical analyses, respectively, on such problem accounting for interface geometric nonlinearity, soil nonlinearity and plasticity (by employing a kinematic

hardening model coupled with the Von Mises plasticity model). Due to the P-Δ effects, the M-θ curves produced by pushover analyses were different to those produced from the tests on a footing-soil system, described above. At relatively large angles of rotation, P-Δ effects induced an additional aggravating moment on the base leading to a more rapid stiffness degradation with θ, before collapse. Following this analysis, the same author carried out cyclic pushover analyses on systems with various FS_v values. As per the footing-soil system, the rigid structure-footing-soil system with higher FS_v exhibited more degradation due to higher levels of rocking than the system with lower FS_v that exhibited higher levels of soil plasticity (Figure 2.5).

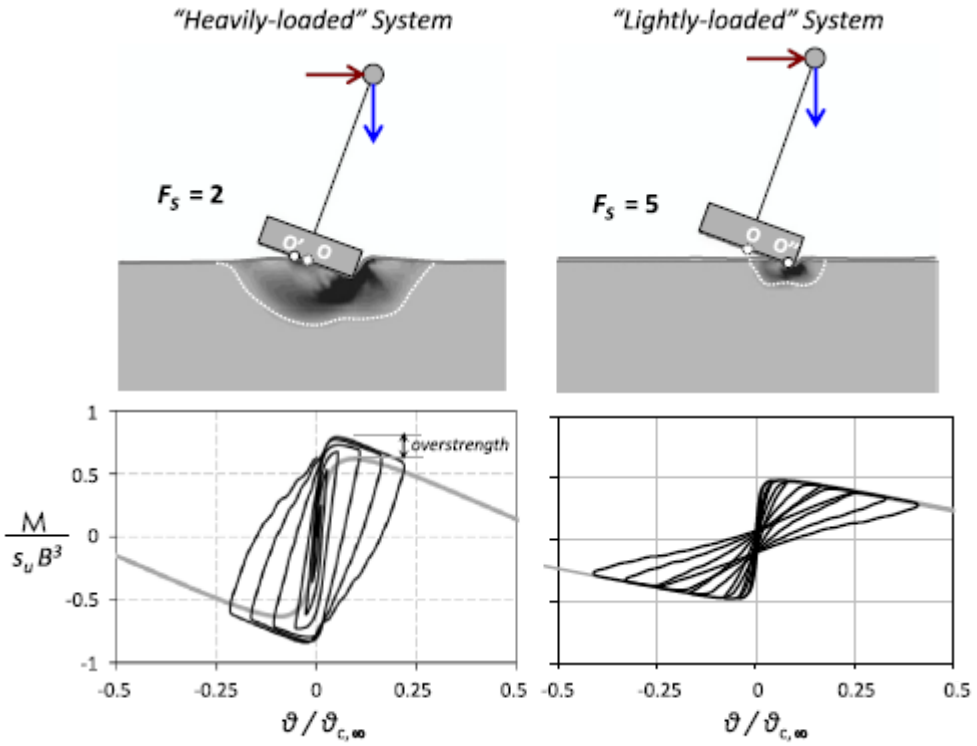


Figure 2.5: Contours of plastic strains and normalised moment rotation curves of rigid structure-footing-soil system, characterised with different FS_v, subjected to cyclic pushover test (Su: undrained shear strength, B: half width of footing, $\vartheta_{c,\infty}$: angle to which systems topples when $FS_v=\infty$) (Gazetas, 2015).

Anastasopoulos *et al.* (2013) and Anastasopoulos and Kontoroupi (2014) carried out shaking table tests and numerical tests, respectively, on seismically loaded SSI systems where the structure was rigid and elastic. They verified that a lightly loaded (higher FS_v) footing exhibited strong uplift, while they also observed that a heavier loaded footing exhibited more vertical settlement due to soil plasticity (lower FS_v). A system with low FS_v footing, though, was found to decrease the inertial forces that are transmitted to the structure, as the capacity of the system was restricted by the soil plasticity. The beneficial effect of reducing inertial forces on the structural integrity was illustrated by Anastasopoulos *et al.* (2013), Anastasopoulos and Kontoroupi (2014) and Gazetas (2015) who carried

out numerical analyses similar to the above described, but with the assumption of an elastoplastic structure. The authors observed that a smaller footing with a low FS_v can save the structure from damage, i.e. yielding at its base, that would have happened when the footing was conventionally designed to have a large FS_v. A smaller footing was also found to decrease the permanent drift of a conventionally designed structure, demonstrating the beneficial effect of the self-centring ability of a smaller footing (Gajan and Kutter, 2008; Anastasopoulos *et al.*, 2013; Anastasopoulos and Kontoroupi, 2014; Gazetas, 2015; Sharma and Deng, 2020).

The structural displacements of a conventionally designed SSI is mostly a result of structural deformability (Gazetas, 2015). Conversely, many studies have showed that for SSI systems designed to promote foundation rocking, e.g. tall and slender structures founded on small foundations, the structural displacements were primarily dominated by foundation rotation with minimal structural distortion (e.g. Tabatabaiefar *et al.*, 2014; Gazetas, 2015; Zhang and Far, 2022a). The nonlinear behaviour of such systems is controlled by P-Δ effects, interface nonlinearity and soil nonlinearity. In favour of the ductility demands of modern provisions, these mechanisms can provide an increased ductility to structures, in relation to conventionally designed structures of which nonlinear behaviour is controlled by plastic hinging of the structural elements.

It should be noted that, despite the above benefits, a footing with a low FS_v can exhibit larger residual settlements and rotation than a conventionally designed footing. The settlements and rotation can be deemed tolerable considering that the structure is saved from damages. However, for low intensity seismic events which do not produce any damages on structures founded on conventionally designed footings, smaller footings would increase residual settlement rotation without providing any significant benefit (Anastasopoulos *et al.*, 2013).

The rate of foundation settlement per loading cycle may change during a seismic event. In fact, centrifuge (Anastasopoulos *et al.*, 2011) and shaking table tests (Drosos *et al.*, 2012; Anastasopoulos *et al.*, 2013) have shown that the rate can decrease with the number of cycles, due to soil densification. Soil densification increases soil vertical stiffness, increasing foundation moment capacity and promoting uplift. Also, due to densification, an initially surface footing may become partially embedded providing extra strength to the system (Anastasopoulos *et al.*, 2013; Sharma and Deng, 2020). Sharma and Deng (2020) exploited field data of a pier subjected to cyclic lateral loading to show that foundation rocking increased the unit weight and strength of the soil below the footing edges as well as the moment capacity of the foundation. The above observations indicate a potential beneficial impact of preceded seismic events on the seismic response of a structure. However, shaking table tests of Anastasopoulos *et al.* (2013) have shown that a system may accumulate foundation rotation and structural tilt at the end of each seismic event. Foundation rotation and structural tilt are further

promoted when an initial tilted structure is subjected to seismic loading, due to the aggravated impact of P-Δ effects.

2.6 Factors that affect SSI effects

The significance of SSI effects depends on several factors, which are a function of structural, foundation and soil properties. Herein, only the factors that affect the inertial interaction effects are discussed. For a SDOF oscillator of equivalent fixed-base natural frequency f_0, height h and mass m, that rests on a circular footing of radius r over homogeneous soil of shear wave velocity V_s, these factors are (Veletsos and Meek, 1974; Veletsos and Nair, 1975; Stewart *et al.*, 1999a; NIST, 2012; Maravas *et al.*, 2014; Amorosi *et al.*, 2017):

(i) Soil-to-Structure stiffness ratio (σ):

$$\sigma = \frac{V_s}{hf_0} \tag{2.8}$$

(ii) Slenderness ratio (h/r)

(iii) Structure-to-soil mass ratio (γ_m):

$$\gamma_m = \frac{m}{\pi\rho hr^2} \tag{2.9}$$

As it can be easily understood from Eqs. 2.1-2.4, the period lengthening and damping increase due to SSI effects are more pronounced for stiffer structures. They are also promoted by soft soil conditions, which is a condition that results in low dynamic stiffness ($K_{dyn,x}$, $K_{dyn,\theta}$) and high radiation damping (ζ_x, ζ_θ) (Gazetas, 1983, 1991). The above was verified by analytical (Veletsos and Meek, 1974; Veletsos and Nair, 1975; Maravas *et al.*, 2014; Givens *et al.*, 2016) and numerical studies (Amorosi *et al.*, 2017). Amorosi et al. (2017) carried out parametric FE analyses on SDOF structures, of various properties, founded on a soil domain, on the base of which a seismic signal (recorded at Tarcento site during the 1976 Friuli event in Italy) was input. The above study showed that for lower σ values the period lengthening ratio and system's damping increase (see Figure 2.6). This was further verified by field large scale experiments (Star et al., 2019) that showed that a stiffer structure (e.g. braced) exhibited stronger SSI effects than an identical but more flexible structure (e.g. without braces).

The same analytical and numerical studies showed that the period lengthening ratio is more pronounced on slender structures, i.e. higher h/r, due to increased foundation rotation caused by the increased overturning moment around the foundation level. The studies also observed that slender structures produced less damping than squatty structures whose foundation is dominated by the translational motions (see Figure 2.6). This is justified by the smaller energy that is radiated by the rotational than translational foundation motion (Gazetas, 1983, 1991). Structural slenderness also

affects the significance of the impact of σ on the SSI effects. In fact, for more slender structures, small changes of σ have more pronounced impact on both period lengthening and foundation damping, as illustrated in Figure 2.6. The combined impact of σ and h/r on the SSI effects was further verified experimentally by Stewart *et al.* (1999b). The authors exploited strong motion data recorded during seismic events on instrumented structures, showing a greater influence of σ than h/r.

The above study, however, did not include in its database very stiff and slender structures, i.e. large $1/\sigma$ and h/r, because such structures are not very common. For such structures, the slenderness dominates over the relative stiffness factor, as it decreases massively the foundation damping. Also, when such structures are subjected to seismic loading, they develop large base shear and moment, which in combination with a small foundation damping can lead to motion amplification (Stewart *et al.*, 1998) in relation to the equivalent fixed-base structure. This may be further aggravated by the fact that tall structures may develop P-Δ effects, which further promote displacements, as already discussed in Section 2.5. The seismic response of very slender and stiff structures was studied numerically by Zhang and Far (2022a, 2022b), who verified that the SSI effects of such structures can detrimentally affect their response. Therefore, it comes to no surprise that, despite the fact that Eurocode 8 (British Standards Institution, 2004c) does not give specific guidelines towards the consideration of SSI phenomena, it requires for their consideration in structures that are prone to P-Δ effects.

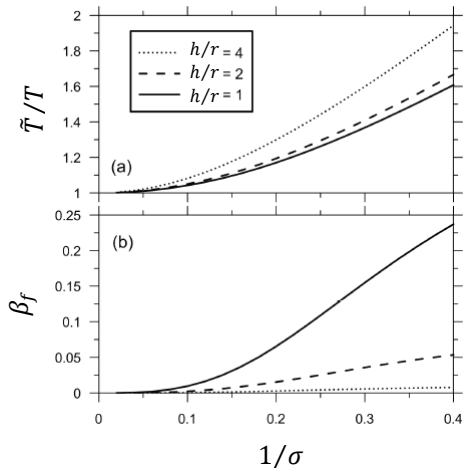


Figure 2.6: Impact of soil-to-structure stiffness ratio (σ) and slenderness ratio (h/r) on period lengthening ratio ($\tilde{T}/T$) and foundation damping (β_f) (NIST, 2012).

The impact of structure-to-soil mass ratio on the importance of SSI effects was studied analytically by Maravas *et al.* (2014) and numerically by Amorosi *et al.* (2017). Both studies have shown that the increase of γ_m exhibit stronger period lengthening and increase of damping. For a squatty structure ($h/r = 1$), this is illustrated by Figure 2.7 produced by Maravas *et al.* (2014), that plots the variation

of $\tilde{T}/T$ and flexible-base system damping ($\tilde{\zeta}$) with $1/\sigma$. The figure also shows that for low σ values, i.e. stiff structures on soft soil, SSI systems that consist of heavy structures can produce less damping than systems of lighter structures. This is explained by the fact that heavier structures can develop higher inertial forces, which can cause stronger foundation rotation and therefore less radiation damping (Amorosi *et al.*, 2017).

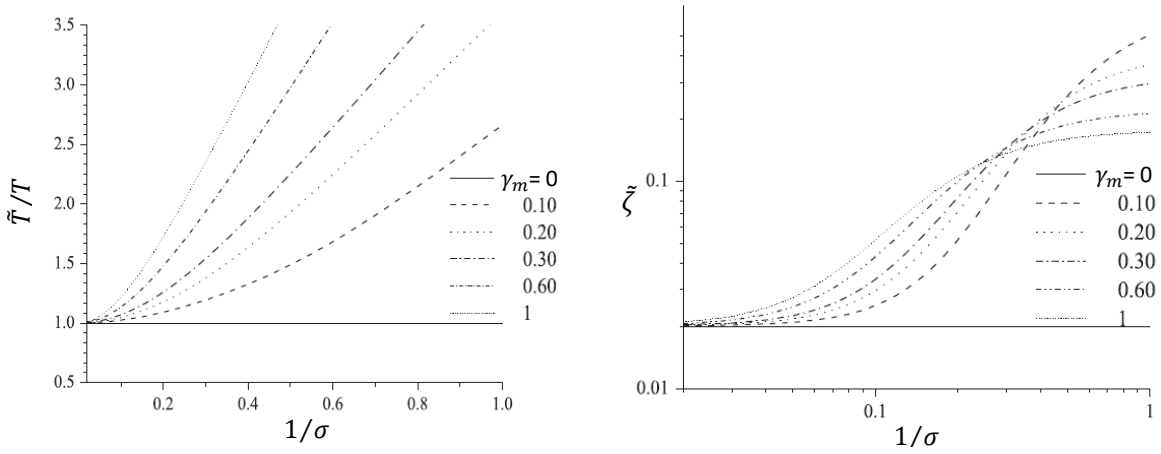


Figure 2.7: Impact of structure-to-soil mass ratio (γ_m) on period lengthening ratio ($\tilde{T}/T$) and damping ratio of the flexible-base system ($\tilde{\zeta}$), as a function of soil-to-structure stiffness ratio (σ) (taken from Maravas *et al.* (2014), who assumed structural damping ζ=0.02 and $h/r = 1$).

2.7 Importance of foundation soil

It can be seen from Eqs. 2.1 to 2.4, that the estimation of the natural frequency and damping of an SSI system requires the shear wave velocity of the soil. The derivation of these equations was based on the assumption of homogeneous half-space, which is not common in reality. As Stewart *et al.* (1999a) mention, it is common to assume a nonuniform soil profile, e.g. V_s increases with depth, as a uniform profile of equivalent properties. The equivalent V_s can be estimated as the time average of the V_s values of layers within an effective depth below the foundation. The depth depends on the oscillation mode of the foundation, which affects the effective depth of pressure bulbs, i.e. bulbs from the translational mode extend deeper than those of the rocking mode (Gazetas and Stokoe, 1991). It also depends on the foundation geometry, that affect the effective radius, r_u and r_θ for translational and rocking foundation motion, respectively. Considering the above, the effective depth can be estimated as (Stewart *et al.*, 2003; Tileylioglu *et al.*, 2011):

$$\text{Foundation translational motion: } z_p = 0.75 r_u = 0.75\sqrt{A_f/\pi} \qquad 2.10a$$

$$\text{Foundation rocking motion: } z_p = 0.75 r_\theta = 0.75\sqrt[4]{4I_f/\pi} \qquad 2.10b$$

where, A_f is foundation area and I_f is foundation moment of inertia.

Gazetas and Stokoe (1991) and Tileylioglu *et al.* (2011) compared lab and field data, respectively, with analytical results to appreciate the importance of the stiffness of the shallow soil layers. They observed that the adoption of an appropriate z_p is essential for the estimation of both natural frequency and damping of an SSI system. The damping was found to decrease when a reduction of soil stiffness exists near the ground surface. They also observed that the effective shear wave velocity, that represents the equivalent half-space and is incorporated in the analytical solutions (e.g. Eqs. 2.1 to 2.4), should account for a stiffness increase due to the self-weight of structures. Within this context, many SSI studies (Gazetas and Stokoe, 1991; Tileylioglu *et al.*, 2011; Star *et al.*, 2015) account for the impact of overburden pressure on the soil stiffness through the following:

$$V_{s,eff}(z) \approx V_{s0}\left(\frac{\sigma_{v0}^{'}(z)+\Delta\sigma_v(z)}{\sigma_{v0}^{'}(z)}\right)^{n/2} \quad 2.11$$

where, $V_{s,eff}$ is the effective shear wave velocity, at depth z, corrected to account for the overburden pressure due to self-weight ($\Delta\sigma_v$); V_{s0} is the free-field shear wave velocity; $\sigma'_{v0}(z)$ is the free-field overburden pressure; n varies from 0.5 for granular soil to 1 for cohesive soil.

In addition to the self-weight, the soil stiffness in the vicinity of the foundation can change due to the dynamic oscillation of the structure. For the case of granular soil, the impact of soil densification below the foundation edges due to rocking on the response was already discussed in Section 2.5. Likewise, for the case of partly saturated cohesive soil with degree of saturation 85% to 98%, Sharma and Deng (2020) investigated the impact of foundation rocking on the soil unit weight and undrained shear strength. Soil samples were retrieved from the soil in the vicinity of the foundation before and after the tests. The samples were subjected to unconfined compression tests to estimate the undrained shear strength of the soil. It was found that both the soil unit weight and undrained shear strength increased significantly due to the structural oscillation. This increase was considerable up to a depth that corresponded to half of the foundation width.

2.8 Simplified methods to account for SSI

2.8.1 Single-degree-of-freedom models

SSI inertial interaction effects are commonly studied with simplified models, that consist of a SDOF structure founded on springs and dashpots (lumped models), as shown in Figure 2.3b (Veletsos and Nair, 1975; Stewart *et al.*, 1999a; Wolf and Song, 2002; Maravas *et al.*, 2014; Star *et al.*, 2019). For 2D problems, the soil is represented by two translational and one rotational springs and dashpots, while for three translational and three rotational springs and dashpots are required for 3D problems. A SDOF

structure-springs-dashpots model can be equivalently assumed as a fixed-base SDOF structure with adjusted properties. The structural stiffness and damping are adjusted so that the fixed-base SDOF structure has the same natural period and damping capacity with the compliant SSI system. The equivalent natural periods and damping can be calculated as per Eqs. 2.1 to 2.4. SDOF models are applicable for structures whose response is dominated by their fundamental mode (Stewart *et al.*, 1998), considering also that higher modes are not affected by SSI (Jennings and Bielak, 1973).

For design purposes, the equivalent fixed-base model can be used in the equivalent lateral force or response spectrum procedures to determine the seismic base shear (Stewart *et al.*, 2003). For investigation purposes, a flexible base SDOF model can be used to evaluate the impact of SSI effects analytically (Stewart *et al.*, 1999a; Tileylioglu *et al.*, 2011; Givens *et al.*, 2016; Star *et al.*, 2019).

The properties of springs and dashpots, commonly referred to as impedance functions, can be estimated as briefly described in Section 2.4. For linear systems, these can be adopted from (Gazetas, 1983, 1991), while solutions are also available for nonlinear systems. Gazetas *et al.* (2013) and Anastasopoulos and Kontoroupi (2014) proposed nonlinear relationships of rocking stiffness of a surface foundation with foundation rotation. The proposed solutions, that are a function of the factor of safety against vertical loads, account for foundation uplift and soil nonlinearity. They were retrieved from 3D FE analyses of a stiff and slender SDOF structure founded on nonlinear soil domain. The interface model allowed foundation uplift but restricted sliding, with the modelled structural motion being deliberately dominated by the rocking component (due to high slenderness). For this reason, the translational stiffness and dashpots were assumed as linear.

Anastasopoulos and Kontoroupi (2014) computed the moment-rotation relations through monotonic 3D FE analyses. The same study carried out cyclic push over analyses to produce the variation of rocking dashpot coefficient (C_θ) with foundation rotation. Despite the highly nonlinear relationship, authors suggest the use of a linear dashpot in lumped models, with a coefficient being equal to the maximum of the C_θ-θ curve. By comparing FE results against results produced with using the simplified SDOF structure-spring-dashpot model, it was shown satisfactory agreement, highlighting the need of adopting a nonlinear rotational spring and appropriate rotational damping coefficient.

However, it is important to recognize that the proposed simplified model comes with several limitations that necessitate careful consideration. Firstly, the use of nonlinear springs whose stiffness was derived from monotonic loading, neglects the fact that the soil stiffness varies differently with strains during monotonic and cyclic loadings. Secondly, the model is unable to predict foundation uplifting, which was observed for the case of a foundation with large factor of safety against vertical loads (e.g. a value of 5 was examined). More importantly, a linear dashpot was found to result in

overestimation of the developed moment for the case of foundations with low factors of safety combined with very strong seismic excitations. For the same conditions, where soil plasticity was prominent, the simplified model also fell short in reproducing the residual foundation rotation as predicted by a more rigorous FE analysis. Nevertheless, the combination of foundations of very low factor of safety (e.g. a value of 2 was considered in the study) along with very strong seismic events was deemed unreasonable by the abovementioned authors. Therefore, the above limitation cannot prohibit the use of the simplified model for the preliminary design of the foundation process.

2.8.2 Winkler-based models

Winkler-based models simulate soil with closely spaced independent springs that are distributed below foundations. In dynamic analyses, springs are accompanied with dampers aiming to simulate radiation and material damping. Several variations of Winkler-based models exist in the literature, some of them designed to capture soil nonlinearity, as well as foundation uplift. Raychowdhury and Hutchinson (2009) propose a model with vertical nonlinear springs, coupled with a dashpot and gap-elements, to capture foundation uplift and settlement. The model consists, also, of horizontal springs placed at the footing sides to represent resistance to sliding and passive pressure. The springs are characterised by elastic stiffness, a backbone curve that can be calibrated against single-footing experiments to model soil nonlinearity. They are also characterised by a tension capacity to allow simulation of foundation uplifting. The rotational stiffness of the footing is captured by an appropriate selection of the springs' stiffness below the footing, i.e. stiffer springs are placed near the edges of the footing to represent the stress concentration. The authors validated the model against centrifuge tests, showing that the model reproduced well base loads (moment and shear), settlements and hysteresis loops (moment-rotation and shear).

According to Pelekis *et al.* (2021) the above described model has a limitation associated with friction that is not a function of the contact area, as it should be. Also, friction is always present, which is not the case when the footing loses contact from soil completely. Aiming to address the above limitations, the authors proposed a modified version of the nonlinear Winkler-based model. They replaced the horizontal spring that accounts for friction with a series of horizontal springs distributed below the footing. Their stiffness is a function of the vertical force and can be coupled with Mohr-Coulomb failure criterion, hence, sliding can be modelled while the horizontal stiffness switches to zero when uplifting occurs. This modification ensured that only the contact interface area contributes to friction, while the total friction vanishes when full detachment takes place. Also, aiming to account for radiation damping due to lateral motion, the authors proposed the use of dampers distributed below the footing, whose viscosity becomes zero when sliding occurs.

2.8.3 Macroelement soil-foundation model

An alternative method to model rocking dominated SSI systems, without springs and dashpots, was proposed by Gajan and Kutter (2009). This method represents the rigid footing-soil system with a macro-element model. This model allows nonlinear relations between load and displacements of the footing-soil system, when the foundation is subjected to combined vertical, shear and moment loading. It accounts for both soil yielding and foundation uplift, which are facilitated by tracking the contact interface area and the shape of soil surface beneath the footing. Interface tracking also allows modelling the moment-rotation-settlement behaviour of the foundation. The coupling effect between moment (M), vertical (V) and horizontal loading (H) is achieved by utilising a M-V-H interaction diagram. The performance of the macro-element was validated against centrifuge results, showing sufficient capability in capturing stiffness degradation, deformations and energy dissipation. The model accounts for energy dissipation through hysteresis while neglecting radiation damping, which the authors deem insignificant for rocking systems. For this reason, this model is not suitable for sliding-dominated foundations, whose primary damping mechanism is radiation damping. Another possible limitation of this method is the assumption made by the authors regarding a uniform initial stress distribution beneath the footing, which may not always be the case.

2.8.4 Numerical procedures

The above simplified approaches can investigate the impact of inertial interaction effects while neglecting kinematic effects. Numerical procedures are employed to incorporate the combined effect of the two mechanisms. These procedures are typically distinguished into the direct method and the substructure method (Stewart *et al.*, 1998; NIST, 2012).

The direct method requires modelling both the structure and the soil domain with finite elements or finite differences and analyses in the time-domain both the structural and soil response in a single step. Soil nonlinearity can either be accounted for through equivalent linear approach or through fully nonlinear analyses (Fatahi and Tabatabaiefar, 2014; Tabatabaiefar *et al.*, 2015). Equivalent nonlinear analyses comprise several linear analyses performed in an iterative manner, each one using an updated stiffness and damping coefficient for the soil layers based on the characteristic shear strains obtained from the previous iteration. This process is carried out until the stiffness and damping coefficients of two consecutive iterations converge. The converged stiffness and damping values are expected to deviate from the ones at very small strains (linear), accounting indirectly for soil nonlinearity. Full nonlinear analyses account more realistically for the nonlinear behaviour of soil through an appropriate selection of constitutive models. As it is subsequently discussed in Section 2.9, despite that this method is the most rigorous approach to study dynamic SSI phenomena, it is

characterised by a high level of complexity mostly associated with the adopted modelling approaches, constitutive laws and input parameters.

The substructure method simplifies SSI problems by breaking them down into subdomains, which are analysed independently. The responses obtained from each subdomain are then combined using superposition to produce the final response. The method usually consists of three distinct steps, which are detailed by Stewart *et al.* (1998) and NIST (2012) and briefly stated here. At the first step the input motion at the foundation level (FIM) is computed. This step requires the evaluation of free-field motion, which is related to FIM through transfer functions that account for kinematic interaction effects (see Section 2.2). The second step of the process involves characterising the soil-foundation interaction through springs and dashpots. NIST (2012) suggests the use of impedance functions (see Section 2.8.1) for rigid footings, while for flexible footings they suggest Winkler models (see Section 2.8.2). At the final step, the superstructure is modelled along with the foundation model determined in the previous step. Then, the FIM computed in step one is applied at the base of the model and the dynamic structural response is computed. Due to frequency dependence of the transfer and impedance functions in step 1 and 2, respectively, the response is usually computed in the frequency domain (e.g. Pitilakis *et al.*, 2008; Pitilakis and Clouteau, 2010).

The advantage of this method over the direct method lies in its simplicity i.e. less input parameters and lower computational costs, while simultaneously offering insights into the physical mechanisms of SSI. However, by breaking the phenomenon into three steps and employing the simplified foundation-soil interface model, the method does not consider the interaction rigorously and cannot represent a realistic constitutive behaviour. Also, the superposition of the responses of the independent subdomains implies linear solution, rendering the method limited to linear systems. To mitigate this limitation and account for soil nonlinearity, an equivalent linear substructure method was derived by Pitilakis and Clouteau (2010). It comprises an iteration of linear analyses solved in the frequency domain, which converges in a similar manner as for the equivalent linear analyses solved in the time domain, described earlier. A detailed description of this method, which is beyond the scope of the current study, can be found in the mentioned study.

2.9 Finite element fully nonlinear analyses

The Finite element (FE) direct integration method is a time domain method that is based on the principle of discretising the problem geometry into several finite elements and the loading (or prescribed displacements) into increments. For each increment, the equation of motion is solved and the incremental displacements, acceleration (etc.) are computed. Fully nonlinear FE analyses can account for all types of nonlinearities that can take place in an SSI problem: soil nonlinearity, structural

nonlinearity, P-Δ effects, interface inelasticity (foundation sliding) and interface geometric nonlinearity (foundation uplift). Such analyses are considered the most rigorous way to study SSI related problems as they offer a number of advantages over the simplified methods (see Section 2.9.1), however their practical use is constrained by a number of challenges (see Section 2.9.2).

2.9.1 Advantages

Unlike the substructure method, the direct FE method solves the SSI response in a single step, without the need of superpositioning independent solutions, and concurrently rigorously accounts for the abovementioned nonlinearities. With appropriate selection of a soil constitutive model and corresponding calibration, soil nonlinearity, soil plasticity and pore water pressure generation can be rigorously considered. In dynamic problems, this method can consider efficiently wave propagation (i.e. wave reflection, wave trapping, motion amplification), resulting in a sensible assessment of energy radiation (or radiation damping). It also allows for a realistic assessment of the soil response and provides insights into the time variation of various aspects (e.g. strains, displacements, stiffness degradation, hysteretic damping) of soil elements. The FE method can also offer a rigorous modelling of the soil-foundation interface, allowing the simulation of sliding and detachment between the two materials at different increments of the motion.

2.9.2 Challenges and commonly adopted boundary conditions

The challenges that need to be addressed are mostly associated with the selection of boundary conditions, soil constitutive modelling and soil-foundation interface modelling.

The dimensions of the soil domain, mesh discretisation and the boundary conditions at the boundary nodes of the soil domain should be carefully selected for modelling wave propagation appropriately. The mesh size should be carefully selected, as it significantly affects the computational cost, which is one of the main concerns in FE analyses. In dynamic problems and especially when the input excitation is applied at the base of the model, the depth of the soil domain is dependent on the bedrock depth or the depth where a downhole motion is available. In such problems the mesh is wider than in static problems to allow for waves to propagate far from the structure of interest, without them returning back to the structure after reflection at the boundaries. Within this context, when the excitation is applied at the ground surface, springs and dashpots (referred to as cone boundary conditions) are commonly employed at the lateral boundaries of the soil domain to absorb the energy of the impinged waves and simulate radiation damping (Kellezi, 2000; Kontoe, 2006; Kontoe *et al.*, 2009). If the bedrock is not simulated, these boundary conditions should also be applied at the base of the soil domain. More about the cone boundary conditions can be found in Section 7.5.1. However, for seismic

motions applied on the bedrock, tied-degrees-of-freedom are preferred to be imposed at the lateral boundaries.

The dimensions of the elements are decided so that the frequencies in the range of interest can be captured by the numerical model. Kuhlemeyer and Lysmer (1973) suggested that the dimension of 8-noded isoparametric elements should be four to five times smaller than the minimum wavelength. This rule has been adopted by many studies in the past and implemented in other types of elements as well (e.g. Kontoe *et al.*, 2007, 2008; Pelecanos, 2013; Han, 2014; Taborda *et al.*, 2016).

The discretization of the soil-foundation interface and the soil domain is usually refined at the foundation edges to accurately capture stress localisation that can result from foundation rotation. For the case of shear bands formation in sand, Gudehus and Nübel (2004) suggested the use of an element size of 3 times the mean grain size. However, this is not adopted in practice, as it necessitates computational resources that are prohibitively high. The element width of the interface and the soil below foundation edges can be equal to the width of the anticipated shear band, which in sand is typically taken as 16 times the grain size (Agalianos *et al.*, 2023). A preliminary sensitivity analysis on the element size was carried out by Anastasopoulos *et al.* (2011), for the case of a surface foundation on either clay or sand. The study suggests that the interface should be discretised to an element size smaller than one-tenth of the width of the foundation to ensure realistic reproduction of both the bearing capacity failure to vertical loads and the rocking behaviour. Nevertheless, the selection of the element size beneath the foundation edges should be tailored to the specific conditions of each problem, as it may vary depending on the frequency and intensity of the applied motions, among other factors.

An additional challenge in SSI FE analyses is associated with the selection of an appropriate constitutive model for the soil domain and a rigorous calibration of the model. To model soil's ultimate strength, a plasticity model (e.g. Mohr-Coulomb or Von Mises failure surfaces) can be used. This can be coupled with a cyclic nonlinear model to capture the hysteretic behaviour of soil through stress-strain relationships; some principles of which can be found in Section 4.4.4. The model can be calibrated against experimental data, while when these are not available, empirical relations can be adopted (e.g. Darendeli, 2001). The model calibration is primarily important for the shallow soil layers, which are crucial in SSI problems, as discussed in Section 2.7. A challenge arises from accounting for the strain-dependent elastic stiffness and the effects of densification in numerical analyses.

Cyclic nonlinear models can simulate well either the stiffness degradation (G-γ) or the damping evolution (D-γ) with cyclic shear strain. Previous studies (Phillips and Hashash, 2009; Papaspiliou *et al.*, 2012; Taborda and Zdravkovic, 2012; Han, 2014; Han *et al.*, 2016) have shown that when the

calibration prioritises a better match of the stiffness degradation curve, this class of models underestimate damping at small strains and overestimate the damping at medium to large strains. In contrast, when the models reproduce the damping ratio curve satisfactorily, the accurate prediction of stiffness is sacrificed. Previous site response studies (Papaspiliou *et al.*, 2012; Han *et al.*, 2017) suggest the prioritization of the accurate representation of damping, while to the author's knowledge, little, if any, discussion has been made regarding SSI analyses.

Anastasopoulos *et al.* (2011) proposed the use of a simplified cyclic kinematic hardening constitutive model coupled with the Von Mises failure criterion in SSI analyses. The authors calibrated the cyclic model to capture the target stiffness curves, recognising the overestimation of damping at the medium strain range (i.e. around 0.1-1%). Amorosi *et al.* (2017) presented 3D SSI analyses, where they employed for the soil the HSS model (Schanz *et al.*, 1999), extended by Benz (2007). The authors prioritised the calibration of the stiffness curve as well. Recognising the underestimation of damping at very small strains, they added a small amount of Rayleigh damping (e.g. 1-3%). The HSS model incorporates in its formulation a stiffness limit (G_{min}) beyond which soil stiffness does not degrade, maintaining a constant value. When this constraint is mobilised, the stress-strain loops become narrow resulting in decrease of damping with increasing strains. Despite that this is not realistic, authors, claimed that this limitation is insignificant, as at the strain level where the G_{min} is mobilised, the soil develops plasticity which dominates both the stiffness and damping. With a following response to the previous paper, Amorosi *et al.* (2018) discusses about another drawback of the HSS model, which can be extended to the general use of cyclic models. They observed overshooting of the stress-strain reloading curve with respect to the monotonic curve when large strains are induced monotonically prior to the application of dynamic loading. This condition leads to a significant stiffness regain after the first unloading, causing a significantly different stress-strain behaviour between the monotonic and dynamic loadings. While this circumstance may produce unrealistically accumulated displacements, the authors consider them to have an insignificant impact on the predicted response. However, the impact might have been significant if the authors accounted for interface nonlinearity, rather than full bonding between the foundation and the soil. Further discussion on this follows in Chapter 7.

Soil-foundation interface modelling is another challenging aspect of SSI analyses, as it may require allowing foundation to slide or uplift in relation to the supporting soil in a seismic event. Many SSI numerical studies ignored this possibility, simply considering full bonding between the two materials (Chao, 1996; Borja *et al.*, 1999b; Pitilakis *et al.*, 2015; Amorosi *et al.*, 2017; Zangeneh *et al.*, 2018). Other studies employed special interface elements (sometimes referred to as contact or joint or gaps or surface-to-surface elements) to allow relative displacements between the two materials

(Anastasopoulos *et al.*, 2010, 2011; Gazetas *et al.*, 2013; Anastasopoulos and Kontoroupi, 2014; Tabatabaiefar *et al.*, 2014, 2015; Zhang and Far, 2022b). These elements are usually coupled with a Mohr-Coulomb failure criterion of zero tensile strength. Once the stress state of an element reaches the failure envelope, sliding occurs, while reaching the prescribed tensile strength causes the element to open and permit foundation uplift. In any other stress states, the foundation and soil are in contact and the interface stiffness is controlled by their elastic behaviour. A more comprehensive discussion about the constitutive behaviour and input parameters of interface elements follows in Chapter 7.

2.10 Summary

This chapter provides an overview of the impact of inertial interaction SSI effects, giving a brief description of the methods that can be used to account for these effects. Inertial interaction effects were found to increase the natural period and damping of a structure, in relation to an equivalent fixed-base structure. The predominant damping mechanism in linear elastic systems is radiation damping, i.e. energy is spread geometrically away from structures, which would have not existed in a fixed-base assumption. In a nonlinear system, both predominant period lengthening and damping development are further promoted by soil hysteresis and plasticity, which decreases the stiffness of the soil and increases soil damping.

Inertial interaction effects can promote, under certain circumstances, foundation rocking, which was found to significantly alter the system's response. Foundation rocking increases displacements of structures but decreases bending moments acting on structural elements, with the foundation flexibility controlling the flexibility of the overall system. It can also promote plasticity of soil in the vicinity of foundation, promoting further the development of damping and constraining large inertial forces to develop on the structure. Therefore, foundation rocking can be assumed beneficial preventing structural damage. However, care should be taken in rocking structures where P-Δ effects can play a significant role on the response. These effects promote further development of displacements and reduce the damping of a system; it is well known that the rotational foundation motion produces less radiation damping than the translational motion.

Inertial SSI effects can be considered through simplified procedures, where the foundation-soi system can be modelled through impedance functions, or Winkler models (series of springs and dashpots) or macro-element models. Past studies have advanced these models to allow for soil nonlinearity, foundation rocking and foundation sliding. However, they can capture neither the constitutive behaviour of soil realistically nor kinematic effects. Numerical analyses, substructure and direct approaches, can overcome these limitations of the simplified models. The substructure method divides the SSI problem into subdomains, which are solved separately. This method, though, cannot

realistically capture the interaction between the structure and the soil, while it is not reliable to nonlinear systems. Full nonlinear FE analyses is the most rigorous method to investigate SSI phenomena, as it allows for a realistic simulation of the soil behaviour, wave propagation and soil-foundation interface. Several challenges, though, are required to be addressed, including the selection and calibration of constitutive model for soil and modelling soil-foundation interface.

Chapter 3

Existing real-scale experiments

3.1 Introduction

Strong motion data collected by real-scale experiments can provide useful insights into SSI effects and be used for calibration and validation of analytical solutions or numerical procedures. Such data incorporate the combined effect of kinematic and inertial interaction mechanisms, including local site effects (i.e. wave propagation/reflection/refraction), wave reflection at the foundation, downward waves induced by the foundation etc. However, the availability of such experiments in the literature is limited due to their high operational costs. A review of full-scale tests carried out in the 20th century can be found in Trifunac *et al.* (2001) and Todorovska (2002). This chapter briefly describes more recent experimental studies, that were carried out in the Garner Valley, Wildlife liquefaction array, Lotung, Hualien, Edmonton and Euroseistest site. It also presents some results of related research conducted on these experiments, including system identification and numerical studies.

3.2 System Identification methods

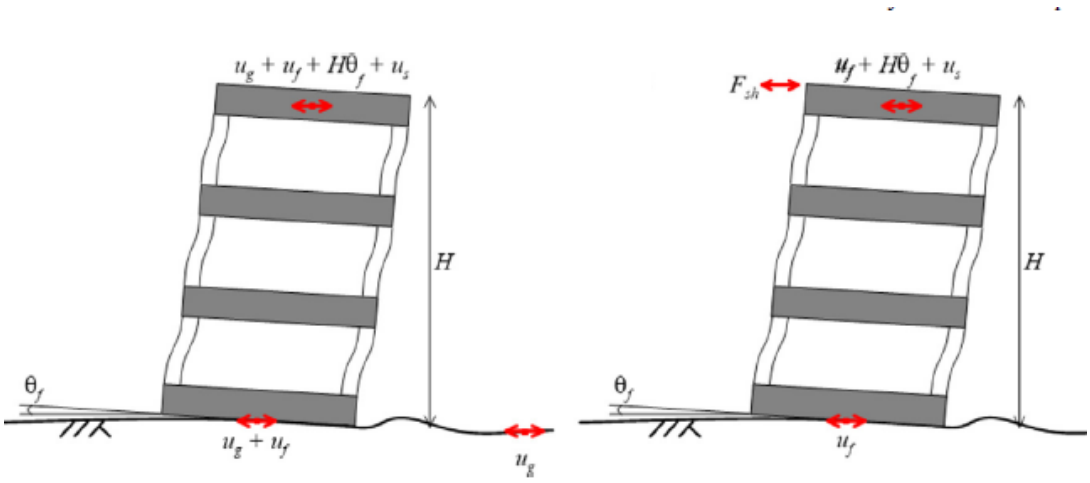
System identification aims to establish the modal properties of a structure, such as natural frequencies, modal shapes and damping. There are two main system identification techniques for evaluating SSI effects from strong motion recordings available in the literature, parametric and non-parametric techniques, which are described in Stewart et al. (1998). These methods employ transfer or transmissibility functions of different output to input ratios, depending on the input motion (earthquake motion or forced vibration) and the intended output modal parameters. These can be either fixed-base, pseudo-flexible-base or flexible-base. Pseudo-flexible conditions accounts for foundation rocking only, while neglecting the ability of the foundation to translate horizontally. Table 3.1 presents the output/input pairs for seismic input motion proposed by Stewart *et al.* (1998), and the corresponding pairs for forced vibration tests proposed by Star *et al.* (2019). The notation of the motion components presented in the table are illustrated in Figure 3.1.

Table 3.1: Input and output pairs for system identification of various base fixity conditions (Star *et al.*, 2019).

	Seismic excitation		Force vibration	
Base fixity condition	**Input**	**Output**	**Input**	**Output**
Flexible-base	$\ddot{u}_g$	$\ddot{u}_g + \ddot{u}_f + H\ddot{\theta}_f + \ddot{u}_s$	$\frac{-F_{sh}}{m_s}$	$\frac{-F_{sh}}{m_s} + \ddot{u}_f + H\ddot{\theta}_f + \ddot{u}_s$
Pseudo flexible-base	$\ddot{u}_g + \ddot{u}_f$	$\ddot{u}_g + \ddot{u}_f + H\ddot{\theta}_f + \ddot{u}_s$	$\frac{-F_{sh}}{m_s} + \ddot{u}_f$	$\frac{-F_{sh}}{m_s} + \ddot{u}_f + H\ddot{\theta}_f + \ddot{u}_s$
Fixed-base	$\ddot{u}_g + \ddot{u}_f + H\ddot{\theta}_f$	$\ddot{u}_g + \ddot{u}_f + H\ddot{\theta}_f + \ddot{u}_s$	$\frac{-F_{sh}}{m_s} + \ddot{u}_f + H\ddot{\theta}_f$	$\frac{-F_{sh}}{m_s} + \ddot{u}_f + H\ddot{\theta}_f + \ddot{u}_s$

$\ddot{u}_g$ = free-field acceleration, $\ddot{u}_f$ = top of foundation acceleration, $\ddot{u}_s$ = Relative structural acceleration

$\ddot{\theta}_f$= foundation rotation, F_{sh} = Vibratory force



(a) (b)

Figure 3.1: Displacement components required for system identification in the case of (a) seismic event or (b) forced vibration (refer to Table 3.1 for notation) (Star *et al.*, 2019).

3.2.1 Non-parametric identification technique

The non-parametric system identification technique evaluates a system's response in the frequency domain by employing complex-valued transmissibility functions H(iω). These functions can be defined as the Fourier amplitude ratio of the output to input motions of Table 3.1. However, this ratio may result to undefined values, hence the function is conveniently computed from power spectral density functions and cross spectral density functions of the input and output motions. All values at all frequencies of these functions always exist, but their quality relies on a high level of coherence between the density functions used and low levels of signal noise (Stewart *et al.*, 1998).

The main peaks of the transmissibility functions indicate the modal frequencies of a system, while their width indicate damping levels. As discussed in Stewart *et al.* (1998), the accuracy of the non-parametric technique in estimating modal parameters is limited to the fist mode, while higher modes of weak energy cannot be captured. Also, a second limitation of the technique is the dependence of the transmissibility functions on parameters associated with the computation of the density functions (e.g. number of frequency points and smoothing technique). These parameters can impact the output modal frequencies but more significantly the damping ratios (Stewart *et al.*, 1999a).

3.2.2 Parametric identification technique

The parametric system identification technique, derived for linear structures by Safak (1991), requires the computation of transfer functions in the Laplace domain of the output to input pairs presented in Table 3.1. Unlike the non-parametric technique, the computed transfer functions are fitted by an underlying model, whose parameters are calibrated to minimise the error between model output and recorded output. Advantages of this method over the non-parametric method are that it requires only two input parameters, time delay and number of modes, and it can provide a more robust solution by following a procedure described in Stewart *et al.* (1998). Since the transfer function can be expressed analytically, the modal properties of a structure can be estimated analytically as well. The analytical expression of transfer function creates a 3D surface, with the horizontal axes being the imaginary and real parts, that are associated with frequency and damping, respectively. The intersection of the 3D surface with the imaginary part, gives a 2D surface equivalent to the transmissibility functions of the non-parametric technique. Peaks of this surface occur at natural frequencies of the structures.

It should be noted that this method is based on the assumptions of linear systems and proportional damping, i.e. damping varies linearly with stiffness and mass matrices. The validity of these assumptions becomes questionable when structural or soil nonlinearity is prominent, rendering the method inapplicable in such cases. Nonlinear systems can be modelled by employing recursive analyses, that comprises linear analyses whose parameters are time dependent. Essentially, linear systems of different parameters are computed for each time-step to investigate the variation of system's properties with time.

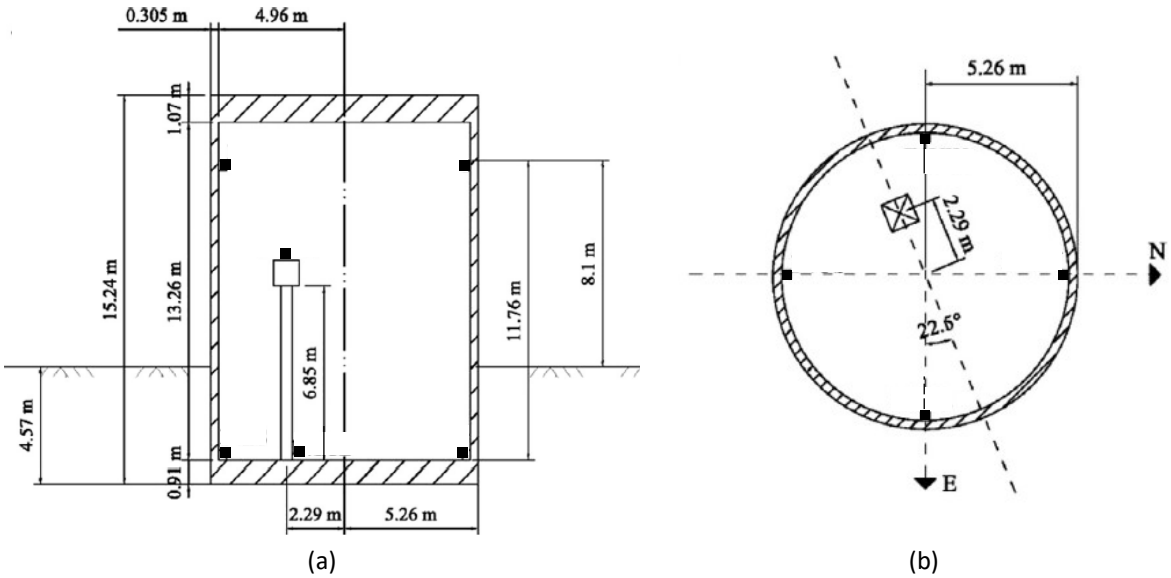
3.3 Overview of essential experimental studies

3.3.1 Lotung nuclear containment models

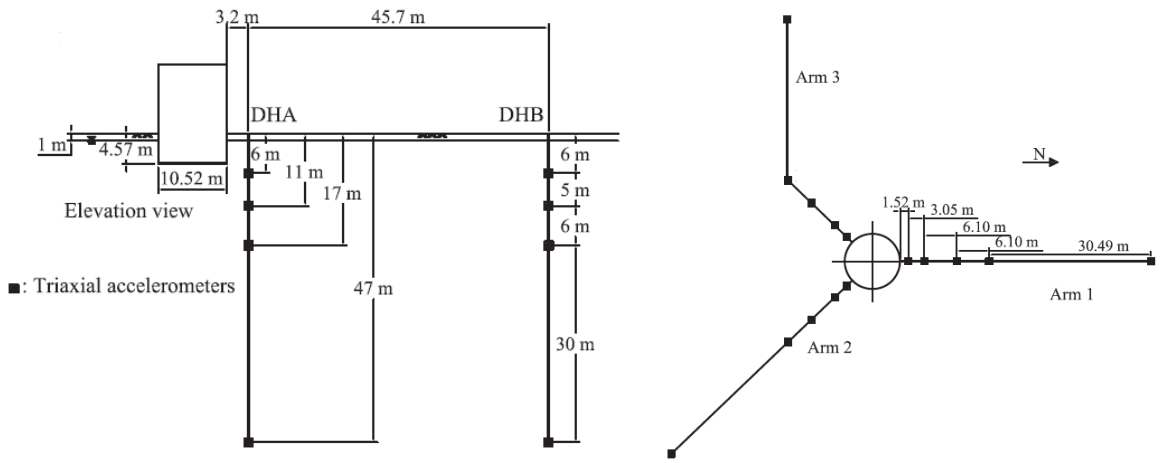
Two large scale (1/4 and 1/12 scales) nuclear containment models were built in Lotung, North-East of Taiwan, which is a highly seismic region with small recurrence interval of strong earthquakes (Tang *et al.*, 1990; Amorosi *et al.*, 2017). SSI effects were found to be prominent on the examined model

structures, owing to the large stiffness of the structure and the soft soil foundation soil (see explanation in Section 2.6). The 1/4-scale model was a reinforced-concrete cylindrical shape structure with a radius of 5.26m, a total height of 15.24m and embedment of 4.57m (Figure 3.2a, b). The model was designed to have a natural frequency within the range of the anticipated dominant frequencies of the seismic events in Lotung (3-8Hz) (Tang *et al.*, 1990). The foundation slab was thick (0.91m) and deliberately designed to move as a rigid body under dynamic excitation. Under free-field conditions, cross-hole tests indicated a shear wave velocity of 100m/s near the ground, which increased linearly to 300m/s at a depth of 47m.

As shown in Figure 3.2, several triaxial accelerometers were placed at various positions at the interior of the structure, downhole in the soil and on the soil surface. The structure was monitored by 10 accelerometers, of which 4 were placed at the basement, 4 on the roof and 2 on an equipment of nuclear plants called steam generator prototype. Two downhole arrays of accelerometers were installed in the soil; one placed near the structure (DHA) and the other one (DHB) far to measure the free-field soil response (Figure 3.2c). The surface instruments were placed along three arms that extend radially away from the structure (Figure 3.2d). Finally, aiming to capture the contact conditions between structure and supporting soil, pressure cells were placed at the horizontal interface between the foundation slab and the soil, and between the embedded vertical wall and soil. The instruments recorded low-level forced vibration tests, that were used to define the characteristics of the SSI system, as well as several seismic events of various intensities.



(a) (b)



(c) (d)

Figure 3.2: Experimental set-up of the 1/4-scale nuclear containment structure: (a) vertical and (b) horizontal cross sections of the structural model, illustrating the positions of the structural accelerometers; location of soil instruments placed (c) downhole and (d) on the soil surface (Amorosi *et al.*, 2017).

Tang et al. (1990) employed a blind prediction technique (a round-robin approach but no more details were given) to replicate experimental data. The SSI model used in the blind prediction analysis was calibrated against forced vibration data. The calibrated model was used to predict the SSI response under seismic events, when the input motion was free-field motions recorded at the soil surface far from the structure. Within the blind prediction analysis, vertically propagating shear waves were assumed, while the soil properties (shear modulus and damping) were selected from G-γ-D curves according to the strain levels induced by the examined seismic events. The results of the analyses were in a fairly good agreement with the experimental data with respect both the frequency content and amplitude of the response. They concluded that the softness of soil controlled the flexibility of the entire system, causing the structure to respond as a rigid body and the rocking motion to dominate. However, rocking motion was underestimated by the analyses, which according to the authors implies that more significant stiffness degradation took place during the experiments than the computed one, especially at the shallow soil layer. It can also imply that foundation detachment or pore water pressure build-up may have taken place during the seismic events. Also, authors attributed the discrepancies between results of analyses and experimental data to the simplified assumptions of the method and input uncertainties such as soil layer boundaries and soil properties.

Amorosi *et al.* (2017) exploited strong motion data recorded on the same model structure during seismic events. They decomposed the structural motion to structural deformation, foundation horizontal motion and the contribution of foundation rocking. The results agreed with Tang et al. (1990) that the structural response was dominated by the rocking motion of the foundation, attributing this to the high stiffness of the structure and the soft soil conditions. Amorosi *et al.* (2017) also compared strong motion data recorded near the structure's basement and free-field data

recorded far from the structure at the same depth. They observed different recordings providing evidence of SSI effects. They highlighted more the impact of SSI effects on the structural response by employing transfer functions. These were defined as ratio of the power spectral density function of the signal recorded at the top of the structure to the cross spectral density function of the same signal and the free-field motion. They compared transfer functions (TFs) computed from the strong motion data with predicted TFs assuming fixed-base conditions to demonstrate the significant decrease of both the natural frequency and amplitude of the response due to SSI effects.

3.3.2 Hualien nuclear containment model

Similar to the Lotung site, at the Hualien site in Taiwan an 1/4-scale containment model of a nuclear power plant was constructed and equipped with accelerometers that recorded the structural and soil motions during forced vibration tests (Barros and Luco, 1995). The structure was of reinforced concrete with similar dimensions shown in Figure 3.2a and b; total height of 16.13m, diameter of 10.82m and embedment of 5.15m. It was founded on soft soil deposits, with cross-hole and downhole tests revealing a significant variation in free-field shear wave velocities: 100-300m/s near the surface and 400-480m/s at a depth of 12m. After the construction of the structure, the V_s of the soil below the structure was also found to vary between 200-475m/s. The structure was subjected to four forced vibration tests using a shaker, which applied harmonic horizontal loads along the NS or EW direction on the top of the structure or on its foundation. A fifth test consisted of a vertical force applied at the foundation of the model.

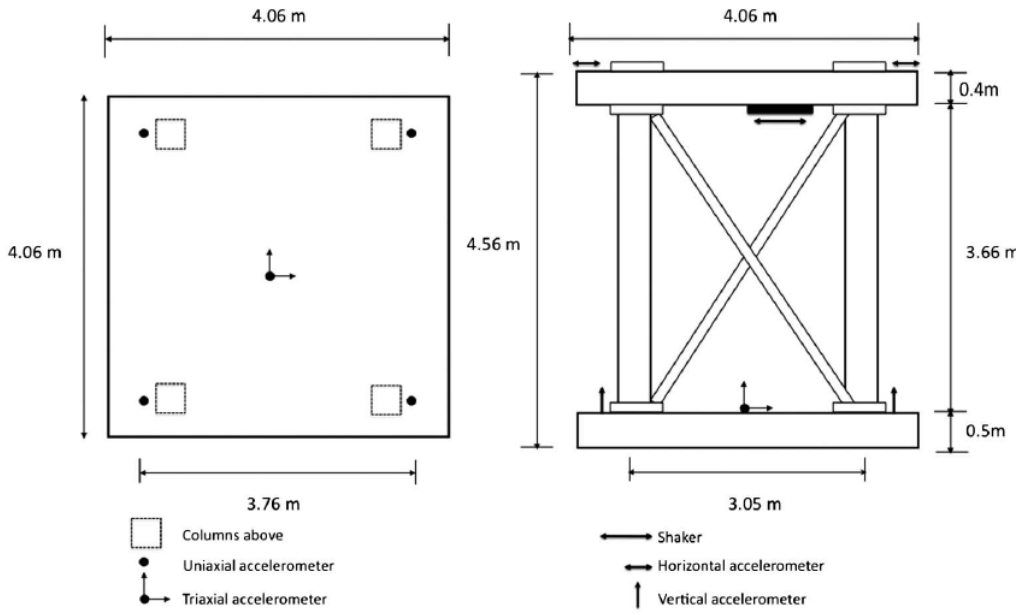
Barros and Luco (1995) exploited the strong motion data and computed the experimental impedance functions by following a procedure derived based on the assumption of a lumped-mass model with distributed masses and impedance functions at its base. Data recorded on both the base and the top of the structure were used in the calculations, while the soil was assumed as linear elastic. The description of the procedure is beyond the scope of the present research, but it can be found in the mentioned study. The results showed that the impedance functions differed when considering the experiments that applied horizontal loads along the NS or the EW directions. This suggested an anisotropic behaviour of soil, lateral variation of soil properties or non-uniform contact conditions between the foundation and soil. Barros and Luco (1995) also compared the experimental impedance functions with the theoretical ones (Luco and Wong, 1992), observing discrepancies possibly due to the uncertainty regarding the V_s of soil. The authors exploited the strong motion data to alleviate this uncertainty. Assuming full contact interface conditions and that the experimental impedance functions are the correct ones, the authors back-calculated the V_s so that the experimental and theoretical impedance functions matched.

Having established the impedance functions, Barros and Luco (1995) computed the theoretical response of the SSI system (i.e. using the lumped-mass model), showing sufficiently good agreement with the experimental data. The slight discrepancies were attributed by the authors to the linear assumption for the soil domain. They suggested the use of a larger soil damping for the experiments where the excitation was applied on the top of the structure, that induced larger strains in the soil than when the excitation was at the base.

3.3.3 Garner valley differential array and Wildlife liquefaction array

SSI experiments were carried out by the Network for Earthquake Engineering Simulations of the University of California, Santa Barbara (NEES@UCSB) at two sites (Star *et al.*, 2015). These are the Garner valley differential array (GVDA) and Wildlife liquefaction array (WLA) sites, both located in regions of high seismicity in California. Prior to the SSI experiments, the sites had been well characterised by previous geotechnical and geophysical studies mentioned by Star *et al.* (2015). The shallow soil layers of the WLA site primarily consisted of silty clay and clayey silt of shear wave velocity 95m/s which increased to 108m/s after the construction of the structure. The surface soil of the GVDA site (silts and clays) is of higher shear wave velocities, which was estimated to be 176m/s and 196m/s prior to and after the construction of the structure, respectively.

At the GVDA site, a permanent structure of dimensions 4 x 4m in plan and 4.5m tall was constructed on the ground surface, as illustrated in Figure 3.3 (Tileylioglu *et al.*, 2011). The structure consists of two reinforced concrete slabs of masses 20.5 and 16.4Mgr used as foundation and superstructural mass, respectively. The two slabs are connected via steel columns on which braces can be configured. The experiments examined the response of a fully braced structural configuration, where braces were placed at all four sides, and the response of an unbraced configuration. Both the foundation and the top slab were instrumented with accelerometers at the positions shown in Figure 3.3, which recorded the structural response during weak intensity earthquakes and forced vibration tests (Tileylioglu *et al.*, 2011). These tests were carried out by the means of a shaker that was placed at the bottom of the top slab and applied unidirectional forces. The braced and unbraced structures were examined under two types of loadings: fast sweep tests were the input frequency imposed by the shaker decreased gradually from 15Hz to 5Hz; and harmonic tests where the structures were subjected to various forces of constant frequencies (i.e. each frequency was held constant for 30s before the next frequency was applied).

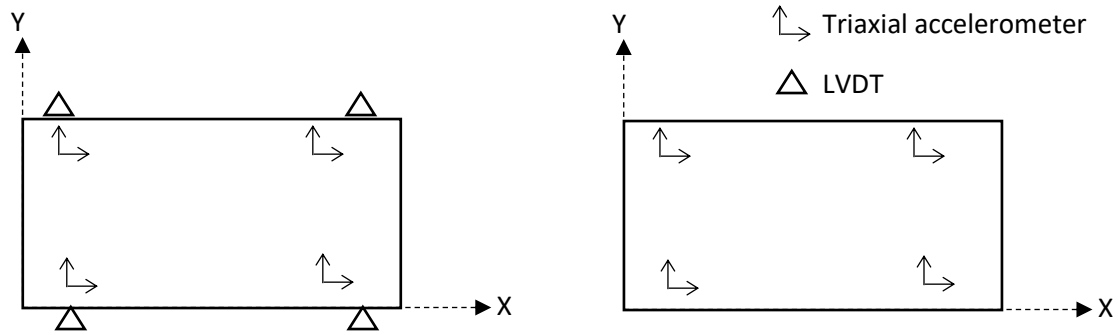


(a) Foundation in plan (b) Elevation

Figure 3.3: Experimental set-up of the permanent structure at the GVDA site (Tileylioglu *et al.*, 2011).

In addition to the permanent structure, a second portable structure was tested in both WLA and GVDA sites. The portable structure was constructed with the same concept as the permanent one, but of smaller dimensions: 2 x 4m in plan and 3m height. As mentioned by Star *et al.* (2015), the structure was designed with a high fixed-based fundamental frequency (11Hz and 35Hz for the unbraced and braced configurations, respectively) to promote strong SSI effects. Also, the structural mass was large to facilitate soil nonlinearity during oscillation, while the foundation was nearly rigid to ensure compatibility between the analytical models (e.g. see Section 2.4). A shaker that was placed either on the top of the roof or the foundation applied loads of various frequencies and amplitudes, allowing the assessment of the nonlinear frequency-dependent response. The vibrations were applied on the portable structure with the same manner as they were applied on the permanent structure, described above. An additional test consisted of a large triaxial Vibroseis vehicle that applied vibrations on the ground surface at a distance of 20m from the structure at the WLA site, imposing ground motions at the foundation level as large as 0.15g.

During the experiments, the foundation and top slab response was monitored through eight accelerometers, shown in Figure 3.4. The foundation was also instrumented with four LVDTs (linear variable differential transformers) to measure relative displacements between the foundation and soil. Below the foundation, eight pressure cells were installed to measure the pressure at different positions of the soil-foundation interface. The ground surface motion was also instrumented via accelerometers that were placed at a distance 1.5-4.3m from the structure along both the positive x and y-directions, with reference to the coordinate system of Figure 3.4.



(a) Foundation in plan (b) Top slab in plan

Figure 3.4: Experimental set-up of the portable structure placed in WLA and GVDA sites (Star et al., 2015).

Tileylioglu (2008), Tileylioglu *et al.* (2011) and Givens (2013) exploited strong motion data collected from the forced vibration tests on the permanent structure of the GVDA site to back-calculate the foundation impedances, stiffness and damping. This was achieved by assuming the problem as a simplified to a SDOF structure founded on springs and dashpots (Figure 2.3b), whose response is governed by the equation of motion that is defined as:

$$M\ddot{U} + C\dot{U} + KU = F \tag{3.1a}$$

$$U = [u_f\ \theta_f\ u_s]^T \tag{3.1b}$$

$$M = \begin{pmatrix} m_f + m_s & m_f h_f + m_s h & m_s \\ m_f h_f + m_s h & I_f + m_f {h_f}^2 + m_s h^2 & m_s h \\ m_s & m_s h & m_s \end{pmatrix} \tag{3.1c}$$

$$K = \begin{pmatrix} k_x & k_{yx} & 0 \\ k_{xy} & k_{yy} & 0 \\ 0 & 0 & k_s \end{pmatrix} \tag{3.1d}$$

$$C = \begin{pmatrix} c_x & c_{yx} & 0 \\ c_{xy} & c_{yy} & 0 \\ 0 & 0 & c_s \end{pmatrix} \tag{3.1e}$$

$$F = [F_s\ hF_s\ F_s]^T \tag{3.1f}$$

where, the displacement components of vector U are defined as in Section 3.2; m_f and m_s refer to foundation and superstructural mass, respectively; I_f is the moment of inertia of the foundation; h and h_f is the vertical distance from the bottom of the foundation to the centre of mass of the top and foundation slabs, respectively; k_s and c_s are the structural stiffness and viscous damping; k_x and k_{yy} are the horizontal and rotational foundation stiffnesses, while k_{yx} and k_{xy} are the coupling stiffnesses; c_x and c_{yy} are the horizontal and rotational foundation damping coefficients, with the c_{yx} and c_{xy} being the coupling damping coefficients; and F_s denotes the horizontal vibrator's force.

The above equations imply negligible torsional and translational out-of-plane (i.e. perpendicular to the loading direction) motions, while the use of strain-invariant stiffness assume elastic response. Tileylioglu (2008), Tileylioglu *et al.* (2011) and Givens (2013) also assumed zero coupled foundation stiffness and damping terms, which can be deemed reasonable as the foundation does not have any embedment (Gazetas, 1983, 1991). By combining the above equations and applying Fourier transforms, authors have shown that the impedance functions can be estimated from forced vibration data as per Eqs. 3.2 and 3.3. The overbar denotes variables in the frequency domain obtained from the Fourier transform of the measured quantities.

$$\bar{\mathrm{k}}_{\mathrm{f}} = \mathrm{k}_x + i\omega c_x = \frac{\bar{\mathrm{F}}_{\mathrm{s}} + \omega^2 m_s(\bar{\mathrm{u}}_{\mathrm{s}} + h\bar{\theta}_{\mathrm{f}} + \bar{\mathrm{u}}_{\mathrm{f}}) + \omega^2 m_f(\bar{\mathrm{u}}_{\mathrm{f}} + h_f\bar{\theta}_{\mathrm{f}})}{\bar{\mathrm{u}}_{\mathrm{f}}} \qquad 3.2$$

$$\bar{\mathrm{k}}_{\theta} = \mathrm{k}_{yy} + i\omega c_{yy} = \frac{h\bar{\mathrm{F}}_{\mathrm{s}} + \omega^2 m_s h(\bar{\mathrm{u}}_{\mathrm{s}} + h\bar{\theta}_{\mathrm{f}} + \bar{\mathrm{u}}_{\mathrm{f}}) + \omega^2 I_f\bar{\mathrm{u}}_{\mathrm{f}} + \omega^2 m_f h_f(\bar{\mathrm{u}}_{\mathrm{f}} + h_f\bar{\theta}_{\mathrm{f}})}{\bar{\theta}_{\mathrm{f}}} \qquad 3.3$$

By following the above procedure, Tileylioglu *et al.* (2011) and Givens (2013) have verified experimentally some of the claims presented in Section 2.4, that were concluded from theoretical models. They have shown that the horizontal foundation stiffness was constant with frequency, while k_{yy} was found to decrease with increasing frequency. Tileylioglu *et al.* (2011) have shown that the damping terms, c_x and c_{yy}, increased linearly with frequency, with the increase being more pronounced on the rotational term. These authors have also shown that the foundation's horizontal motion produced stronger damping than the rotational motion, demonstrating the foundation's ability to dissipate energy far from the structure during the former motion. These observations were verified by fast sweep and harmonic tests on both braced and unbraced structures. Similar foundation stiffness and damping were obtained from the braced and unbraced experiments, with the latter however being contaminated by noise. This rendered the data obtained from the unbraced experiments unreliable above a certain frequency (e.g. 9Hz).

Finally, Tileylioglu *et al.* (2011) compared the experimental impedance function with the theoretical solutions provided by Pais and Kausel (1988), which assume homogeneous half-space. The authors showed that in order to achieve good agreement, it was essential to consider an appropriate shear wave velocity value in the theoretical solutions. This should be increased relative to the free-field V_s, accounting for the strength gain provided by the structural weight. The structural weight affect the average V_s values of layers within a reasonable effective depth below the foundation, i.e. the depth suggested by Stewart *et al.* (2003) (Eq. 2.10). Likewise, Givens (2013) followed the same procedure to find that the theoretical model captured well the translational damping but underestimated the rotational damping. The author attributed this discrepancy to the friction at the soil-foundation interface, the potential existence of a thin and soft layer below the foundation and soil nonlinearity.

The same study investigated further the impact of nonlinearity on the impedance functions by comparing results from experiments of different intensities. The authors have shown, through shear force-translation and moment-rotation loops computed at the foundation level, that stronger excitation can decrease the stiffness of the soil-foundation system and hence decrease the natural frequency of the entire SSI system. Givens (2013) compared the stiffnesses inferred from experiments of various input frequencies and force amplitudes, observing a decrease of the system's stiffness with increasing input frequency. Considering that vibratory force increases with increasing frequency, the author attributed this to system's nonlinearity. This trend, however, was observed until the input frequency coincided with the resonant one. Beyond this, the soil-foundation system regained some stiffness indicating smaller nonlinear effects. The structural response was weaker when the input frequency was far from resonance compared to the response at resonance, inducing smaller strains in the soil, justifying the previous observation. In general, Givens (2013) verified that the increase of the levels of structural oscillation resulted in a smaller stiffness for the soil-foundation system, through soil stiffness degradation, and increase of damping.

Tileylioglu (2008), Tileylioglu *et al.* (2011), Givens (2013) and Star *et al.* (2019) employed the parametric system identification technique (see Section 3.2.2) to identify the modal frequencies and damping of the examined SSI systems. Similarly to the process followed by Tileylioglu *et al.* (2011) to estimate foundation impedances, the former studies assumed the same simplified SDOF model governed by Eq. 3.1. To further simplify the calculations, they assumed that the impact of the $m_f {h_f}^2$ and $m_f h_f$ terms was negligibly small.

Tileylioglu *et al.* (2008) exploited earthquake motions recorded on the permanent structure in the GVDA site to calculate the modal parameters of the SSI system. They estimated the fixed-base and pseudo flexible-base modal natural frequencies and damping of the system, whereas flexible-base parameters were unable to be calculated due to the lack of free-field data. They found that the SSI effects significantly increased the natural period and the damping of the braced structure, with the impact being less pronounced on the unbraced structure. They compared the experimental results with theoretical solutions (see Section 2.3), showing that the latter solutions underestimated the period lengthening ratios and overestimated foundation damping. It should be noted that the earthquake motions considered in the above study were of small intensity, limiting the above conclusions to small-strain conditions.

Similar results were obtained by Tileylioglu (2008) that exploited data recorded during two seismic events (of different intensity) on the unbraced structure, while having free-field data available. The analysis showed that although the period lengthening ratio was the same for both events, the damping

of the system was much higher for the stronger event. Tileylioglu (2008) exploited, also, forced vibration data on the same structure, producing slightly smaller period lengthening ratios and damping values than the ones produced from earthquake data. The authors attribute the difference to the weaker strain levels induced in the soil by the forced vibration experiments.

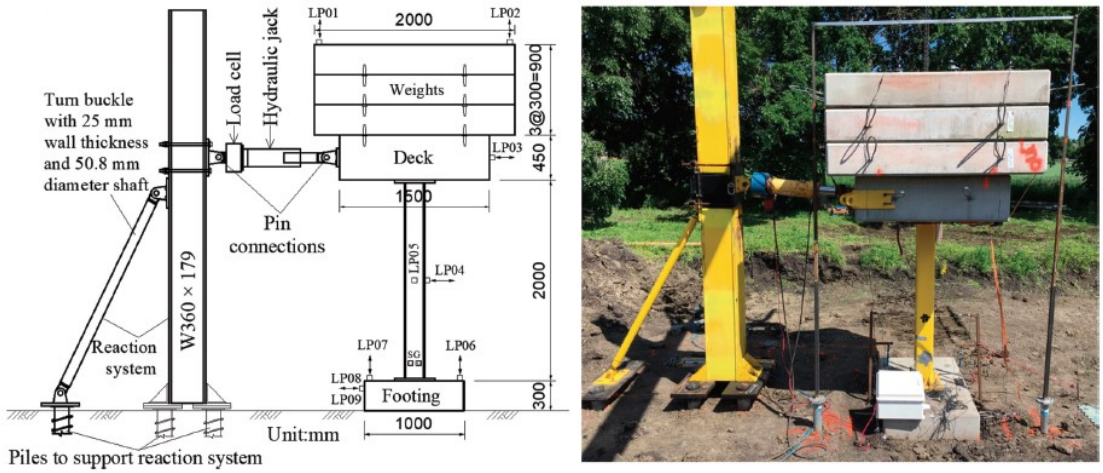
Star *et al.* (2019) exploited forced vibration data recorded on the permanent structure founded in GVDA site as well as the portable structure founded on both GVDA and WLA sites. The authors verified that systems with lower soil-to-structure stiffness ratio (see Eq. 2.8) experience stronger SSI effects. In this context, it was observed that the braced structure and the structure founded on the softer WLA site exhibited stronger period lengthening and foundation damping than the unbraced structure and the structure founded on the stiffer GVDA site, respectively. The effects were found also to be more pronounced for stronger external loads, which induced higher strains in the soil, promoting nonlinear phenomena, i.e. stiffness degradation and hysteretic damping increase, which in-turn increased both the natural period and damping of the system.

Star *et al.* (2019) compared also the experimental period lengthening and damping of the system with the theoretical models of Veletsos and Meek (1974) and Givens *et al.* (2016) (see Section 2.3). In the models, they accounted for soil nonlinearity, by estimating the induced shear strains (γ_{eff}=PGV/V_s, PGV=peak ground velocity that was recorded) and extracting a reduced soil stiffness and increased damping from the Darendeli (2001) curves. It was also found necessary to include interface nonlinearity in the theoretical models, as in some experiments the authors observed gapping between the foundation and the soil. When gapping is incorporated in the calculations by reducing the dimensions of the foundation, the theoretical models predicted stronger period lengthening and smaller damping than when full contact was assumed. Such adjustment brought the theoretical solutions closer to the observed results, for the experiments where gapping took place. In general, the theoretical models underpredicted the period lengthening ratios, with the difference being more pronounced for systems with smaller soil-to-structure stiffness ratio. Regarding the damping, it was observed that theoretical models tend to underpredict damping for larger ratio values, while overpredicting it for smaller ratios.

3.3.4 Edmonton large scale pier

A field SSI test was carried out in Edmonton, Canada, at the premises of the University of Alberta. The tests consisted of a large-scale soil-footing-structure system (Figure 3.5) that was designed to simulate a bridge pier and exhibit pronounced rocking motion. The shallow footing was 1.5m long and 1.0m wide, and the structure's steel column was 2m tall. The superstructural mass, consisting of concrete slabs, varied to achieve different levels of initial factor of safety under vertical loads (FS_v). The structure

was founded on cohesive lake deposits of which properties were characterised by field and lab tests, as described in Sharma and Deng (2020). Using a hydraulic jack shown in Figure 3.5a, it was subjected to slow cyclic loading of a large period (140s) to avoid the generation of inertia force. During the tests, the vertical and horizontal motion of the footing and deck were monitored through nine linear potentiometers and strain-gauges were attached at the base of the column to measure the bending moments and shear forces. Strain-gauges were also attached on the reinforcement bars of the footing to allow tracking the contact area at the interface of the foundation and soil. The contact area was also manually measured using a tape measure.



(a) (b)

Figure 3.5: Experimental set-up of the large-scale soil-footing-structure system in Edmonton shown: (a) schematically, (b) in a photo (Sharma and Deng, 2020).

The aim of the above experiment was to investigate the impact of the interface nonlinearity, foundation rocking, on the response of the examined system. Some of the results of this experiment, presented by Sharma and Deng (2020), have already been discussed in Section 2.5. Experimental data have shown that both foundation sliding and rocking took place, with their behaviour being coupled. Foundation sliding was found to increase with foundation rotation and the number of cycles. Foundation rocking contributed to the nonlinear behaviour of the system, as rotational stiffness of the foundation was found to decrease with increasing foundation rotation. Experimental data have shown that the stiffness degradation was more pronounced for large A/Ac ratios, that are defined as the interface contact area to the critical interface area at failure. Likewise, the equivalent damping ratio of the examined SSI system decreased with increasing foundation rotation especially for large A/Ac ratios. These experimental observations align with previous lab and numerical studies presented in Section 2.5. It was explained in that section that footings subjected to light loads (i.e. large A/Ac) may demonstrate more noticeable stiffness degradation with an increase in foundation rotation and may

not effectively engage the soil motion. For the same reason, the experimental results of Sharma and Deng (2020) have shown significant residual settlements for the systems with a low A/Ac ratio.

3.3.5 EUROPROTEAS

Real scale tests were carried out on EUROPROTEAS prototype structure that was founded in the Euroseistest of Mygdonian basin in Northern Greece. The current thesis focuses on experiments on the same structure, hence, a detailed description of both the structure and the soil conditions can be found in Chapter 5. Pitilakis *et al.* (2018) describes the field tests were carried out in 2012 on the prototype structure (3 x 3m in plan and 5m tall), that consisted of free and forced vibrations as well as ambient noise experiments. The structure can be either braced or unbraced, with fixed-base natural frequencies of the translational mode around to 13Hz and 1.78Hz, respectively (Pitilakis *et al.*, 2018).

Identification of modal properties

Pitilakis *et al. (*2014, 2018) identified the natural frequencies and equivalent damping ratios of the examined SSI system at very small strains by exploiting ambient noise data. This was achieved by employing output-only or stochastic parametric and non-parametric system identification techniques, that are described in the referred studies. The above studies highlighted the significant impact of SSI effects on decreasing the natural frequency of the SSI system, with respect to the fixed-base system. The impact was found to be more prominent on the swaying than the torsional mode, with the predominant period lengthening ratios estimated about 2.3 and 1.2, respectively.

Pitilakis *et al.* (2013), Pitilakis and Vratsikidis (2017), Vratsikidis and Pitilakis (2018) and Amendola *et al.* (2021) exploited free vibration data to estimate natural frequencies of the SSI systems. These were identified from the main peak of Fourier spectra inferred from motions recorded on the top slab. Natural frequencies were also extracted from forced vibration data, by identifying the frequency which maximised the structural response, as described by Pitilakis *et al.* (2018) and Vratsikidis and Pitilakis (2018). The above studies identified a decrease of these frequencies with increasing magnitude of the excitation due to nonlinear phenomena. In fact, Pitilakis *et al.* (2018) have shown that the forced vibration experiment with the weakest excitation exhibited a natural frequency closed to the one at very small strains identified from ambient noise data. This frequency was found to decrease by 25% when the excitation was the strongest applied. Amendola *et al.* (2021) further investigated the impact of nonlinearity on the natural frequency of a freely vibrated system using Fourier spectra of smaller motion durations. They have shown an increase of natural frequency with time, indicating strain weakening and stiffness regain while the motion dissipates.

Pitilakis and Vratsikidis (2017, 2018), Pitilakis *et al.* (2018), Vratsikidis and Pitilakis (2018) and Amendola *et al.* (2021) estimated damping from free vibration data using the logarithmic decrement

and dissipated energy methods (Chopra, 2011). The former method estimates the equivalent damping ratio through the motion amplitude decay within a prescribed number of cycles, as described in Section 6.2.4. The dissipated energy method estimates an average damping of a system with rotational natural frequency ω_n, that oscillates at a rotational frequency ω as per Eq. 3.4. The studies showed that the computed damping ratios (ζ) increased for larger excitations; i.e. ζ varied between 3% and 9%. Especially for the experiments with large pull-out forces (e.g. 15kN) exerted on the structure prior to free vibration, the damping was calculated to be larger at the first cycles (i.e. 13%). For the next cycles, the motion dissipated, with the computed energy being similar to the one at very small strains (i.e. 2%), as inferred from ambient noise (Pitilakis and Vratsikidis, 2017, 2018). The variation of damping ratio with time was illustrated by Amendola *et al.* (2021), who estimated several values of damping for various time-windows of the motion. They have shown a significant decrease of damping with time, associated with decay of the significance of soil nonlinearity.

$$\zeta = \frac{1}{4\pi\omega/\omega_n} \cdot \frac{E_D}{E_{tot}} \quad 3.4a$$

$$E_{tot} = 0.5 \times mass \times velocity^2 + 0.5 \times stiffenss \times dispalcement^2 \quad 3.4b$$

$$E_D = energy\ at\ the\ beginning\ of\ the\ cycle - energy\ at\ the\ end\ of\ the\ cycle \quad 3.4c$$

Back-calculation of impedance functions

Pitilakis and Vratsikidis (2018), Vratsikidis and Pitilakis (2018) and Amendola *et al.* (2021) employed the procedure proposed of Tileylioglu *et al.* (2011), that was earlier described in Section 3.3.3, to back-calculate impedance functions from forced vibration data. These include foundation stiffness and damping of the swaying and rotational modes. The horizontal foundation stiffness computed by Pitilakis and Vratsikidis (2018) and Vratsikidis and Pitilakis (2018) was found to be in a satisfied accord with the theoretical solutions of Pais and Kausel (1988), for frequencies with low levels of noise (5Hz). However, the theoretical solutions were found to undrestimate the rotational stiffness of the foundation-soil system. The experimentally computed foundation damping, which includes both hysteretic and radiation damping, exhibited significant scatter, but was generally higher than the theoretical values assuming a hysteretic soil damping of approximately 5%.

A similar procedure was followed by Amendola *et al.* (2021), who expressed the real component of the impedance functions, reflecting the foundation stiffness, and the imaginary component that is an indicative measure of damping. They computed the above quantities from forced vibration experimetns with different excitation magnitudes. They showed that, due to nonlinearities, both swaying and rotational foundation stiffnesses decreased with the increase of the excitation. The rotational stiffness was more impacted by the level of excitation, as the excitation resulted in stronger rocking-induced than swaying-induced strains. The authors compared the experimental impedance

functions, obtained from experiments with the weakest excitation force, with theoretical models of Veletsos and Verbic (1973), Pais and Kausel (1988) and Gazetas, 1991). They showed good agreement for the swaying and rotational stiffness; and for the imaginary component at low input frequencies (a_0=0.5). For higher frequencies, the experimental imaginary component was larger than the theoretical values. This can be attributed to amplified soil nonlinearity, considering that the excitation force increases with input frequency.

Soil motion decay with distance from the foudnation

Pitilakis *et al.* (2018) exploited strong motion data recorded on the soil surface during both free and forced vibration tests. They showed that the rate of soil motion dissipation with distance from the foundation increased with increasing excitation force, which is an additional evidence of the existence of soil nonlinearity. Pitilakis *et al.* (2013) utilised downhole soil recordings obtained from forced vibration tests and demonstrated that motion dissipation occurred primarily within a depth equivalent to the foundation width. The above observations can highlight more the important role, in SSI problems, of the soil conditions in the vicinity of foundations, where the soil nonlinearity is more prominent.

3.4 Numerical modelling of real-scale experiments

Numerical models that are calibrated against real-scale experiments are scarce in the literature. To the author's knowledge, the existing studies simulated the Lotung's and EUROPROTEAS's experiments that have been earlier described in Sections 3.3.1 and 3.3.5, respectively. Chao (1996), Borja *et al.* (1999) and Amorosi *et al.* (2017) studied numerically the response of the Lotung's SSI system, and Pitilakis *et al.* (2015), Abate *et al.* (2017) and Massimino *et al.* (2019) developed SSI numerical models for the EUROPROTEAS's tests. The model calibration, assumptions and limitations of the above numerical studies are detailed in the introduction of Chapter 7. Herein, some results of these studies are briefly presented.

Chao (1996) and Borja *et al.* (1999) developed a 3D numerical model using a simplified nonlinear constitutive model for soil to simulate a seismic event recorded by Lotung's experimental facilities. Chao (1996) have shown good agreement between the numerical and experimental results regarding the soil surface motion in all three directions (two horizontal and the vertical). Borja *et al.* (1999) mentioned (but did not give evidence) that the structural response was also well captured, with the analysis, though, underpredicting the rocking component. The same study compared the downhole soil responses computed numerically under two different conditions: free-field conditions and below the structure affected by SSI phenomena. They found that SSI effects reduced the computed peak

ground surface accelerations in the horizontal directions by 40%, with the impact being more pronounced near the surface. Apart from the horizontal peak soil motion, the remaining horizontal motion as well as the entire vertical soil motions at any depth were mostly unaffected by the SSI effects.

Amorosi *et al.* (2017) developed 3D models to simulate more seismic events recorded in the Lotung site, presenting comprehensively the calibration of the nonlinear soil profile. The calibrated model reproduced fairly well the free-field motion at the ground surface, i.e. the motion far from the structure. However, it was found to overestimate the natural frequency of the SSI system and underestimate the foundation rocking motion, with the discrepancy increasing with the intensity of the modelled seismic event. As claimed in the study, the discrepancy can be attributed to the non-rigorous calibration of the structural properties, which was due to the lack of experimental data. This is only valid, though, for low-intensity seismic events that exhibit a linear response. The increasing discrepancies observed with the motion intensity can be attributed to a non-appropriate simulation of the nonlinear response, which is associated with soil and interface nonlinearity.

Pitilakis *et al.* (2015) developed 3D models to simulate forced vibration tests on the EUROPROTEAS structure by assuming linear elastic soil, with adjusting the soil damping according to the motion intensity. In a similar manner, Abate *et al.* (2017) and Massimino *et al.* (2019) carried out linear elastic 2D FE analyses to simulate similar experiments. This study acounted for soil nonlinearity indirectly by adopting equivalent reduced shear stiffness and damping ratio values, with respect to the ones at very small strains. These values were inferred from the lab-obtained G-γ-D curves for the strain levels estimated from the recorded soil motions (i.e. $\gamma=PPV/V_s$). Despite the simplified soil models, Pitilakis *et al.* (2015) and Abate *et al.* (2017) showed numerical results that captured sufficiently well the structural and soil response. This may indicate that a rigorous simulation of soil may not be necessary in forced vibration simulations, however, further investigation is required.

3.5 Summary

This chapter summarises some important real-scale SSI experiments and their main outcomes. Most of the studies aimed to study experimentally the response of the examined soil-structure system. They investigated the significance of the SSI effects under various conditions, such as different structural stiffness (Tileylioglu *et al.*, 2011), structural mass (or equivalently FS_v) (Sharma and Deng, 2020) and soil properties (Star *et al.*, 2015). The significance of the effects were mainly assesed through period lengthening ratios and equivalent damping of the examined systems (Tileylioglu *et al.*, 2008; Pitilakis *et al.*, 2018; Star *et al.*, 2019). The contribution of foundation rocking to the nonlinear response of a

system has also been investigated experimetnally (Sharma and Deng, 2020). Impedance functions were computed from strong motion data and have been used to validate existing theoretical models (Barros and Luco, 1995; Tileylioglu *et al.*, 2011; Givens, 2013; Pitilakis and Vratsikidis, 2018; Vratsikidis and Pitilakis, 2018; Amendola *et al.*, 2021). Finally, a limited number of studies carried out FE numerical simulations of real-scale experiments in the time domain (Chao, 1996; Borja *et al.*, 1999b; Pitilakis *et al.*, 2015; Abate *et al.*, 2017; Amorosi *et al.*, 2017; Massimino *et al.*, 2019).

Some of the outcomes of the referred studies are listed below, with a few of them verifying insights gained from theoretical solutions:

- SSI effets were found to signficantly decrease the natural frequencies and increase the damping of an SSI system with respect to the fixed-base system
- The above impact was found to be more pronounced on the swaying (fundamental) mode of oscillation than the torsional mode
- The observed differences in soil motions recorded below foundations with respect to free-field motions at the same depth, demonstrated the impact of SSI effects on the foundation input motion
- SSI effects were found to be more prominent on stiffer structures
- SSI effects were found to be more prominent on a structure that was founded on softer soil conditions, than on the same structure founded on stiffer soil
- For the case of a stiff structure and soft soil conditions, the structure responded as a rigid body and foundation rocking dominated
- The natural frequencies and damping of an SSI system were found to vary under different levels of excitation. This observation is attributed to nonlinear effects, soil and interface (foundation rocking) nonlinearities
- Soil nonlinearity decreased the natrual frequency and increased the damping of the examined systems
- Foundation rocking contributed to the nonlinear behaviour of the system, with the system's rotational stiffness and damping decreasing with increasing foundation rotation
- Rotational stiffness degradation and damping reduction due to rocking were found to be more pronounced on systems with large A/Ac ratios
- Some studies have shown that theroterical models, that assume homogenous linear elastic soil, could capture the experimental response only if soil nonlinearity was taken into account indirectly

- One study have also claimed that theoretical models should indirectly incorporate gapping effects to replicate the experimental natural period. These effects were found to increase period lengthening ratios and decrease damping of the system
- Theoretical models require also an input V_s that accounts for strength gain provided by the structural weight. Also, the input Vs should reflect to the average V_s values of layers within a reasonable depth below the foundation. The necessity of V_s correction demonstrates the important role of the shallow soil layers in the vicinity of the foundation
- The experimentally derived impedance functions and their variation with input frequencies were found to agree with those derived from theoretical models
- The computation of foundation damping was found more challenging than the computation of foundation stiffness from strong motion data
- The damping produced by the translational mode was found experimentally to produce stronger damping than the rotational mode, which agrees with theoretical mode

Chapter 4

Euroseistest Site Description and Site Response Analyses

4.1 Introduction

It is well established that seismic waves can be considerably modified as they propagate through a ground profile, in terms of their amplitude, frequency and direction. This modification of the seismic motion due to the local site conditions can be detrimental to the integrity of structures, as it was evidenced in previous events such as the Mexico City, 1985, (Seed *et al.*, 1991) and Loma Prieta, 1989, (Seed *et al.*, 1991) earthquakes and many more. Local site conditions should be taken into consideration, as they can significantly modify the site response in relation with the bedrock motion, under certain circumstances. Site response analyses are useful in predicting motion amplification, modification of the frequency content and modification of the wavefield at a location. These analyses can be conducted in either the frequency domain using simplified procedures or the time domain. The frequency domain method is carried out through theoretical (TTF) or empirical (ETF) transfer functions, while the time domain method is carried out usually by the means of finite element of finite difference analyses.

TTFs are based on closed form solutions that result from one-dimensional wave propagation theory. Their calculation requires as an input the detailed soil stratigraphy and associated dynamic properties based on the assumption that the soil behaves as a linear-viscoelastic material overlying bedrock (Kramer, 1996). The bedrock can be assumed as either perfectly rigid or as linear viscoelastic material of finite stiffness. Unlike TTFs that are based on simplified assumptions, ETFs do not rely on any simplifications and can reflect to the observed amplification between the in-depth reference site and the surface. They require soil motions recorded at the surface and at different depths, which are provided by downhole accelerometers.

There are many downhole arrays of accelerometers operating in several seismic areas in the world; many of them are summarised in Elgamal et al. (2001). The downhole arrays that attracted the highest interest by other researchers, according to the author's knowledge, are the Garner Valley in California, Lotung in Taiwan and KiK-net in Japan. Past studies exploited downhole data to evaluate the applicability of TTFs by comparing them with ETFs (e.g. Baise, 2000; Thompson et al., 2009); while other studies aimed to identify the origin of soil motion amplifications or de-amplifications (e.g. Dikmen et al., 2016; Elgamal et al., 1995; Elia et al., 2017; Verdugo, 2002) and investigate site effects (e.g. Cadet *et al.*, 2012, 2012; Kawase, 2019). Downhole data are particularly important in investigating soil nonlinearity (e.g. Assimaki et al., 2008; Han et al., 2015, 2018; Huang et al., 2001; Kokusho, 2004; Régnier et al., 2013, 2017; Wen et al., 1995; Zeghal et al., 1995), which is inherently associated with the variation of dynamic properties with induced strains. When small strains are induced in the soil, which is the case for weak seismic events, data can be interpreted to provide the small strain soil stiffness profile (e.g. Elgamal et al., 1995; Glaser and Baise, 2000; Harichane et al., 2005; Teague et al., 2018). Where downhole arrays of instruments are available, the recorded data can be used to establish stiffness degradation and damping ratio curves (e.g. Han et al., 2015; Tsai and Hashash, 2009; Zeghal et al., 1995). Downhole data were also exploited to associate nonlinear phenomena with pore water pressure development (e.g Groholski and Hashash, 2013; Han et al., 2018; Verdugo, 2002; Zeghal et al., 1995) and to provide evidence of liquefaction (Baise, 2000; Baise *et al.*, 2001). Other studies used downhole data to calibrate numerical models aiming to replicate field data, by assuming either 1D (Kaklamanos *et al.*, 2015; Régnier *et al.*, 2016, 2018; Foti *et al.*, 2019) or 3D wave propagation (Amorosi *et al.*, 2016). Finally, downhole data were used to develop and calibrate constitutive models at the site of interest (Tsai and Hashash, 2008; Groholski and Hashash, 2013; Groholski *et al.*, 2016).

Downhole data interpretation can provide a rigorous characterisation of a site, including natural frequencies and small strain stiffness profile. Elgamal et al. (1995, 1996) employed a correlation technique to estimate the average shear wave velocity between two stations. The technique employs a cross-correlation function to correlate acceleration time histories recorded by two downhole stations. The function maximises at time t_d that is the time required for a propagating wave to cover the distance d between the two downhole stations. Once t_d is determined, the average velocity between the two stations can be calculated as d/t_d. The same studies identified natural frequencies from downhole data, using surface and downhole records, by combining cross-spectrum energy functions, phase angle spectra and coherence functions. Natural frequency is identified at the frequency where the cross-spectrum energy function is maximised, provided that the two examined motions are in 0^o or 180^o phase and the coherence function approaches unity. They also used the same spectra to establish the modal shapes of the identified natural frequencies.

Despite the rigour of the method that employs cross-spectrum energy functions, natural frequencies and small strain stiffness profiles are commonly established in the literature using the borehole spectra ratio method (e.g. Thompson *et al.*, 2009; Régnier *et al.*, 2013, 2017; Teague *et al.*, 2018). This method is simpler as it makes use of either Fourier or response spectra, that are commonly employed in engineering practice. Natural frequencies can be inferred from the peaks of ETF defined as surface to downhole spectra. Once the fundamental frequency (F_s) is identified, the average wave velocity (V) is defined as:

$$V = 4H_s \cdot F_s \qquad 4.1$$

where H_s is the thickness of soil column for which the frequency is exerted. Commonly, a horizontal motion component is used in the calculations, producing the shear wave velocity (V_s). Han *et al.* (2015) proposes the same formulation for estimating P-wave velocity (V_p) by exploiting the vertical motion component, however in this case, H_s should not be larger than the water table depth, below which V_p becomes very large. A limitation of this approach, though, is that Eq. 4.1 is based on the assumption of homogeneous soil, which may not be the case when the associated downhole instruments are distant from each other.

As Kokusho and Sato (2008) mention, a correct estimation of V_S requires a careful estimation of the soil thickness H_s, as more than one peak, that correspond to different resonances, may appear in ETFs. Some peaks may correspond to fundamental modes of different soil columns, while others may be explained by higher modes. Similarly, Baise and Glaser (2000) and Verdugo (2002) showed that an identified fundamental frequency can be correlated with the response of a shallow soil column, especially when an impedance contrast exists within the soil profile. However, not every peak in ETFs can be assigned to a natural frequency, as according to Steidl *et al.* (1996) and Cadet *et al.* (2012) peaks in ETFs can be a result of constructing interference of waves at a given depth. Downhole instruments record a motion that consists of both upward and downward propagating waves, that result from wave reflections at the surface or interfaces between soil layers. Destructive interference between these waves create gaps in the frequency spectrum of the downhole motion at some frequencies (Shearer and Orcutt, 1987; Elgamal *et al.*, 1996; Steidl *et al.*, 1996; Thompson *et al.*, 2009). At these frequencies, the ETF, which is defined as surface to downhole spectra ratio, exhibit maxima related to downhole destructive interference and not to amplification due to resonance. Steidl *et al.* (1996) mention that the first mode of destructive interference occurs at the frequency $F^*=V_s^*/4H^*$, where H^* is the thickness and V_s^* the average shear wave velocity of soil layers between the two examined locations. It should be noted that constructing interference is important to be taken into consideration when a deep downhole motion is used to produce ETF, whereas its impact diminishes

when a shallow recorded soil motion is used. This is explained by the fact that shallow layers are usually highly dissipative, reducing the amplitude of the reflected motions.

By following the above spectra ratio method and exploiting data from weak seismic events, the velocity profiles at very small strains can be obtained. Stronger seismic events, though, may produce profiles of variable V_s, due to soil nonlinearity. ETFs, computed as spectral ratios of surface to downhole recorded motions, have been widely used in the literature to study nonlinear phenomena (e.g. Wen *et al.*, 1995; Kokusho, 2004; Kokusho and Sato, 2008; Régnier *et al.*, 2013, 2017). The peaks that appear in ETFs are assigned to natural frequencies, while the amplitude represents the motion amplification at the surface relative to the downhole site. Nonlinear phenomena are associated with degradation of soil stiffness and increase of damping with increasing strains, under cyclic loading. The impact of these phenomena on the site response is the decrease of the site's predominant frequency and the motion's amplitude around this frequency. Wen *et al.* (1995), Zeghal *et al.* (1995) and Régnier *et al.* (2013, 2017) exploited downhole data to evaluate the impact of nonlinearities over a wide frequency range, proving that the impact is frequency dependent. They have shown that nonlinearity is negligible at relatively low frequencies (e.g. lower than 1Hz for the sites of the Kik-net database examined by Régnier *et al.* (2013, 2017)) because the wavelength is too large to detect changes of the dynamic properties of soil. Nonlinearities become more important when excess pore water pressure, liquefaction, or cyclic mobility are present. Pore water pressure, water table level and soil permeability are particularly important when considering the compressional site response (Han *et al.*, 2018; Kontoe *et al.*, 2018). However, compressional response is beyond the scope of the present study, hence it is not further discussed.

Régnier *et al.* (2013) introduced the site-specific frequency, f_{NL}, below which the response amplifies and above which it de-amplifies due to nonlinearities in relation to a linear response. Nonlinear phenomena do not exert any influence on the response at this frequency. Régnier *et al.* (2013, 2017) showed that f_{NL} lies between the fundamental and predominant frequencies. The fundamental frequency corresponds to the first peak of ETFs and is associated with the resonance of surface to bedrock column, while the predominant frequency corresponds to the most amplified peak associated with the resonance of shallower layers. The earlier observation indicates the shallower layers can be more affected by nonlinearity; a feature that is more pronounced on sites with stronger impedance contrast near the surface. This explained the stronger modification of the peaks above the fundamental frequency, complying with the same observation made by Kokusho (2004). As it can be inferred from Régnier *et al.* (2017), the fundamental peak can also be affected at stronger events that excite the nonlinear response of deeper layers. The latter was the reason of the observation made by Régnier *et al.* (2017) that f_{NL} can decrease with the intensity of a seismic event.

Aiming to infer the nonlinear soil properties, some studies exploited downhole data to estimate stiffness degradation and damping ratio (G-γ-D) curves of the examined soil layers. Zeghal et al. (1995) calculated shear stresses from recorded accelerations by assuming a one-dimensional shear beam and estimated shear strains using displacements numerically integrated from recorded data. Both calculations were based on linear interpolation between downhole sensors. Authors converted the estimated shear stress and strain time histories into stress-strain cycles, from where they computed the G-γ-D curves, that correspond to the soil between the sensors considered. However, this approach is reliable only when the sensors are very closely spaced. Alternatively, Glaser and Baise (2000) computed time dependent stiffness and equivalent viscous damping values between two sensors by employing a lumped mass-dashpot system. The system consisted of a mass equivalent to the half layer, while the other half is assigned to the base of the system. The values of the springs and dampers were found through system identification. Shear soil stiffness (G) can be estimated in a simpler way by combining Eq. 4.1 and 4.2, as already applied by Kokusho (2004). Normalised degradation curves can be computed by normalising the stiffness by the stiffness calculated using data of a very weak event (G_{max}), that are representative of a linear response, as shown in Eq. 4.3. The same equation demonstrates that the shear stiffness degradation can be directly associated with identified natural frequencies. As proposed by Han *et al.* (2015) and shown in Eq. 4.4, the constrained modulus degradation (M) can be equivalently estimated when using the compressional velocities (V_p) or natural frequencies (F_p).

$$G = \rho \cdot V_s^2 \qquad 4.2$$

$$G/G_{max} = (V_s/V_{s,weak})^2 = (F_s/F_{s,weak})^2 \qquad 4.3$$

$$M/M_{max} = (V_p/V_{p,weak})^2 = (F_p/F_{p,weak})^2 \qquad 4.4$$

where, ρ is soil density; G_{max}, M_{max}, $F_{s,weak}$ and $F_{p,weak}$ are calculated from data recorded during weak events, where linear response is anticipated.

The linear response of soil is limited to a very narrow strain range, especially for low plasticity materials and under low mean effective stress (e.g. Vucetic and Dobry, 1991; Ishibashi and Zhang, 1993; Darendeli, 2001). Although there is extensive laboratory evidence to support the latter claim, field data are limited and can be provided by downhole data only. Kaklamanos *et al.* (2015) made use of KiK-net's downhole data to show that nonlinearity should be considered in site response numerical analyses for strains within the range of 0.01%-0.1%. Régnier *et al.* (2013) carried out a statistical analysis exploiting downhole strong motion data and showed that for the KiK-net area, the nonlinear phenomena are expected to significantly affect the response with a probability of 20%, for downhole PGAs larger than 30cm/s^2. They suggest that this probability is three times larger for sites with

important site effects, such as soil layering and basin effects, while it also increases for sites where velocity contrast exists, especially near the surface. This study provided evidence that nonlinear phenomena can significantly affect the response even under weak seismic excitations. Therefore, it is indispensable for site response studies to consider realistically nonlinear behaviour of soil under both small and large induced strains.

Nonlinear site response studies are usually carried out by employing either frequency domain equivalent linear (EQL) analyses or time domain nonlinear (NLIN) analyses. The EQL procedure, introduced by Seed and Idriss (1970), establishes the 1D transfer function method which provides a closed-form solution based on the viscoelastic soil and is applicable for a multi-layered stratigraphy. The procedure considers non-linearity indirectly, in that it uses reduced time-invariant shear moduli and increased damping ratio values in relation to the ones for very small strains. Unlike the EQL analysis, time domain NLIN analyses consider the variation of soil stiffness and damping with time. NLIN analyses require the use of a finite element (FE) or a finite difference (FD) program, that employs the direct integration method. They are based on the principle of dividing the external excitation into increments, while for each increment the equation of the motion is solved to compute incrementally site response. Despite the rigour of NLIN method, its main shortcoming is associated with the lack of expertise of users to make decisions regarding boundary conditions and the soil constitutive model calibration.

The assumptions of the EQL method make the use of the method limited to relatively weak events. It is generally accepted that EQL should be avoided when high strains are expected and for soft soils with pronounced nonlinear behaviour (e.g. Assimaki *et al.*, 2008; Kaklamanos *et al.*, 2015; Kim *et al.*, 2016; Foti *et al.*, 2019). Different studies in the past proposed strain thresholds beyond which the reliability of the EQL method becomes questionable. Assimaki *et al.* (2008) suggest that EQL approach yields satisfactory results for relative stiff sites subjected to strain levels approximately below 0.1%. They also mention that for stronger events this approach overestimates the peak ground acceleration. Kaklamanos *et al.* (2015) carried out site response analyses of various input motions recorded by downhole arrays installed in six sites in KiK-net. They showed that, for these sites, site response studies benefit from NLIN analyses when the maximum shear strain (γ_{max}) exceeds a value around 0.05%. Régnier *et al.* (2018) suggest that for two examined sites in KiK-net and PARI strong-motion stations, the EQL method is applicable for induced strains smaller than 0.2%.

Kim *et al.* (2016) introduced a strain index (I_γ), defined as the ratio of the peak velocity of the input motion to the time-averaged shear-wave velocity of the first 30m of soil profile. They suggest that EQL results become not reliable for I_γ larger than 0.03% when considering frequencies larger than 5Hz. For moderate frequencies, i.e. 1Hz to 3Hz, EQL and NLIN analyses were found to deviate for I_γ larger than

0.1%, while this value can be larger than 0.2% for smaller frequencies. The same study also suggests that the reliability of EQL results is further questioned for frequencies near the soil column's resonance. This is explained by the higher strains that are induced in the soil at resonance, which raises doubts regarding the applicability of time invariant soil stiffness and damping, that are adopted by EQL analyses. The authors showed that, at resonant frequencies, EQL models underpredicted stiffness degradation and damping, which resulted in overprediction of the site response. On the contrary, at high frequencies, EQL models were found to overpredict the latter dynamic properties and hence underpredict the response. The latter conclusions were made by Kim *et al.* (2016) by comparing the EQL results with the ones from NLIN analyses, which were assumed as the benchmark by the authors. A similar observation was earlier made by Assimaki *et al.* (2008), who also highlighted that high frequency suppression became more pronounced when analysing deep sites.

For both equivalent linear and nonlinear analyses, many researchers have raised considerations regarding the input motion, in relation to the conditions of the reference site. The input motion can either be a motion recorded near the site of interest either at an outcrop rock or recorded downhole in depth. Due to lack of downhole data, it is very common in engineering practice that the input motion is recorded at a bedrock outcrop which might be very far from the site of interest. The large distance between the site of interest and reference site might lead to input motion of spurious components, which are a result of wave propagation and radiation (Wen *et al.*, 1995; Cadet *et al.*, 2012). A limitation of outcrop input motions is associated with rock compliance, especially when the near surface rock is weathered, which is a condition that affects the high frequency range of the motion. As stated by Steidl *et al.* (1996), if a reference site is an outcrop rock that has a site response of its own, the soil surface motion might be underestimated at some frequencies. Care should also be taken to the "free surface effect". Upward propagated waves are constructively interfered with downward ones that are reflected at the free surface; a process that increases the surface motion by a factor of 2.

The above limitations of outcrop rock reference sites can be overcome when using bedrock motion, recorded by downhole arrays, as input motion. However, as mentioned by many authors (e.g. Kokusho and Sato, 2008; Cadet *et al.*, 2012; Régnier *et al.*, 2016, 2018) care should paid in this case as well, because recorded downhole motions can be contaminated by downward propagated waves that resulted from reflection. The upward and downward propagating waves are destructively interfered at particular frequencies, mentioned earlier, that are dependent on the depth of the downhole instrument and the shear wave profile. Consequently, at these frequencies, the recorded downhole motion is weaker than the actual motion. When this record is used as input motion in a numerical analysis, then the analysis is expected to underestimate the response at the mentioned frequencies.

It is therefore apparent that in both outcrop and within assumptions for input motion in a numerical model, care should be paid in interpreting the numerical results.

For 1D site response software, e.g. STRATA (Kottke and Rathje, 2009), the input motion is either applied as “outcrop” or “within”, which imply compliant and rigid base respectively. The “outcrop” input motion corresponds to a motion recorded at an outcrop rock, while the “within” input motion corresponds to a motion recorded by a downhole instrument at the bedrock. It should be mentioned that the outcrop option can also be used when the input motion was recorded at in-depth compliant soil, if an appropriate adjustment is made (Anthi, 2021).

For time-domain numerical site response studies that use input motion recorded on an outcrop rock, the simulation of a compliant base is suggested (e.g. Kwok *et al.*, 2007; Régnier *et al.*, 2016, 2018), allowing downward waves to radiate into the half-space. Compliant base is also appropriate to be modelled when the input motion is recorded by a downhole instrument at a compliant soil. On the contrary, a rigid base is employed for the case of input motion recorded on a stiff bedrock by a downhole instrument. As suggested by Kwok *et al.* (2007), for both cases where motion is available from outcrop or downhole recordings, the recorded motions are applied unchanged as input at the base of the numerical model. This is in disagreement with Régnier *et al.* (2016, 2018) that propose the division of the outcrop records by 2 to account for the free-surface effect. The above boundary conditions for the outcrop motion neglect that the near surface rocks may have a site response of their own, as already discussed. Also, the abovementioned boundary conditions for the downhole input motion neglect the interference between upward and downward propagating waves that exist in the record. Nevertheless, the deconvolution of the above components is very challenging to be achieved, and hence this limitation should be mitigated by considering the input motion uncertainty when interpreting site response results.

The present study makes use of downhole data recorded in the Euroseistest experimental facility located in the Mygdonian Valley in Northern Greece. The geotechnical and geological characteristics of the site are well documented by previous studies (Pitilakis *et al.*, 1999, 2018; Raptakis *et al.*, 2000; Raptakis and Makra, 2015). A downhole array of accelerometers is permanently installed at the centre of the valley, having recorded several seismic events of low to medium intensity. The downhole strong motion data are exploited through ETs and are used as input motion at the rigid bedrock (within assumption) of the numerical model. The numerical results were produced by both EQL and nonlinear site response analyses, assuming in both cases 1D conditions. The STRATA software (Kottke and Rathje, 2009) is employed for the EQL site response analyses, while the Imperial College Finite Element program (ICFEP) (Potts and Zdravković, 1999) is used for the nonlinear analyses. EQL and nonlinear results are compared to examine the applicability of the former method for the examined cases.

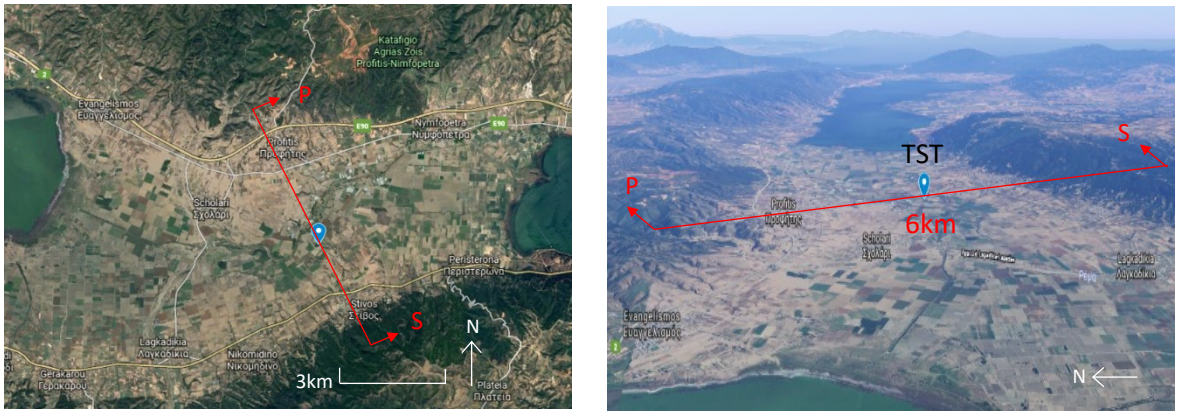
The results from site response analyses are compared against strong motion data aiming to calibrate and validate the numerical model. The calibrated model will then be used in the numerical Soil-Structure-Interaction analyses, in the way discussed in Chapter 7. Both strong motion and numerical data are exploited to investigate the impact of the bedrock depth on the response. Finally, this study identifies the natural periods of the site, determines the origin of these periods and investigates the impact of soil nonlinearity on the response.

4.2 Euroseistest wider site

Euroseistest site is located in Volvi valley which is part of the Mygdonian basin in northern Greece. Figure 4.1 presents the valley showing the geomorphology and the location of the site of interest, TST, that is discussed in Section 4.3. The Euroseistest site is located at a very seismically active area which accommodates two major tectonic phenomena; the extension of Aegean Sea across the N-S and the Western termination of the north Anatolian strike-slip fault (Papazachos et al., 1979; Raptakis et al., 2000). This activity formed the valley with four normal faults perpendicular to the extension giving features such as grabens, variation of the thickness of deep strata, disappearance of some formations and most importantly variation of the bedrock depth. Figure 4.2 illustrates these features of the valley through the cross section of the PS line shown in Figure 4.1, that connects the Profitis and Stivos villages while passing from the TST site. The figure shows the different classified formations of soil layers (A to G*) and bedrock (G) proposed by Pitilakis *et al.* (1999). The lateral heterogeneity, shown in Figure 4.2, led many authors (Chávez-García et al., 1998, 2017; Pitilakis et al., 1999; Chávez-García and Faccioli, 2000; Raptakis et al., 2000, 2005; Makra et al., 2005; Manakou et al., 2010; Maufroy et al., 2015; Makra and Chávez-García, 2016) to suggest and verify through numerical analysis that site effects play an important role in the site response throughout the valley. Site effects were found to affect the response even at the centre of the valley, 3km far from the edges, where the bedding is horizontal and the bedrock is found to be at 196m depth.

The site geology and soil properties were determined through site investigation campaigns that were part of a major study that lasted 25 years collecting exceptional amount of information. These campaigns were launched by the Laboratory of Soil Dynamics and Geotechnical Earthquake Engineering (SDGEE) of Aristotle University of Thessaloniki (AUTH). Initially, the site of interest was confined between the Profitis and Stivos villages, producing the cross section shown in Figure 4.2. In 2003, the survey extended and covered the region between the two lakes, Lagada and Volvi (Figure 4.1), which is the current form of the Euroseistest site. The studies were launched to fulfil the site characterization of the basin, covering an area of 100km^2 (Manakou et al., 2010). A geophysical study comprising electrical, magnetic and gravimetric methods, as well as electric resistivity surveys was

carried out to define the geology, tectonics of the site, locations of the faults and the sediments-bedrock interface (Raptakis et al., 2000). Three underground explosion experiments were carried out and provided more information about the wave field of the valley. The geotechnical survey, consisted of CPT, SPT, cyclic triaxial, resonant column, oedometer and unconfined compression tests, was conducted to define the geometry, the stratigraphy of the site and the soil properties. Additionally, borehole drilling, surface wave inversion (SWI), P and SH refraction (REF), cross-hole (CH) and down-hole (DH) tests were carried out at the location of the boreholes, while electrical and magnetic soundings were also performed. The shear wave profiles were established mainly through the SWI method, while at the center of the valley CH, DH and REF data were exploited. Data from P-wave refraction tests were exploited to determine P-wave velocity profiles above the water table, and the water table depth. The water table depth was found by Pitilakis *et al.* (1999) to vary between 4m to about 34m below the ground surface.



(a) (b)

Figure 4.1: Mygdonian basin (a) in plan view and (b) looking towards the East. The blue pin shows the TST site; and the red line is a cross section line connecting the Profitis and Stivos villages while passing from the TST site (photos taken from Google Earth).

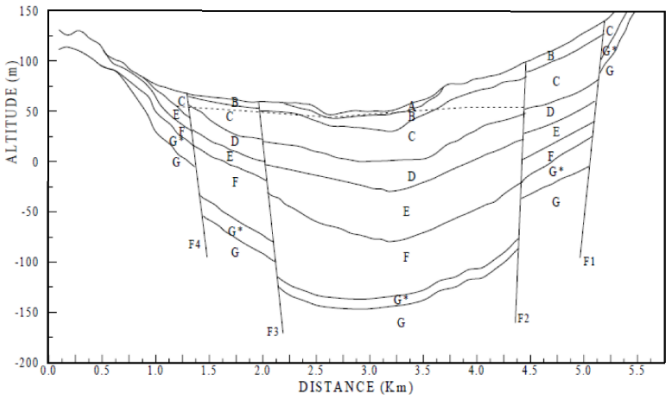


Figure 4.2: Profitis-Stivos (PS) cross section (PS line shown in Figure 4.1), illustrating the faults, offsets of soil formations and bedrock depth variations. The A to G formations are originally proposed by Pitilakis *et al.* (1999).

A great asset for the EUROSEISTEST site is the permanent strong motion network of stations that has recorded several earthquake events. Their locations are indicated with triangles in Figure 4.3; at the sites where more than one triangle is shown, a downhole array exists. There are in total 21 high resolution triaxial accelerographs, 15 of those rest on the surface, while the remaining 6 are installed in boreholes. The surface instruments form two longitudinal arrays that are perpendicular to each other. The borehole instruments create two downhole arrays; the first one is located near Profitis village and the second at the centre of the valley, which is subsequently detailed in Section 4.3.4. In total, 17 out of 21 accelerographs are mounted on alluvial deposits and the remaining four rest on rock outcrops or on bedrock within boreholes.



Figure 4.3: Satellite photo of the Mygdonian basin, illustrating with triangles the positions of the permanent strong motion stations (taken from EUROSEISTEST Strong Motion Network, 1993).

4.3 TST site

The site of interest, TST, is located at the centre of the valley, as depicted in Figure 4.1. EUROPROTEAS structure, for which Soil-Structure-Interaction studies are performed in the ensuing chapters, is founded on the TST site. Prior to these studies, site response analyses are performed herein for this site, exploiting the available geotechnical characterisation and strong motion data. The site characterisation benefited from the field and lab data collated by the earlier mentioned investigations carried out by SDGEE-AUTH.

4.3.1 Soil profile

Pitilakis *et al.* (1999) interpreted the available field and lab data to provide the soil stratigraphy of the TST site, characterising an 196m soil column, below which bedrock is met. A more recent study, that

is detailed in Pitilakis *et al.* (2012) and summarised in Pitilakis *et al.* (2018), was conducted to focus more on the characterisation of the shallow soil layers. Figure 4.4 shows a plan view of the Euroseistest facilities at the TST site, illustrating also the positions of the boreholes (BH). As part of the older studies, 11 boreholes were drilled South to the EUROPROTEAS structure (BH1-BH11). The more recent investigation consisted of drilling two boreholes; a 30m deep borehole below the geometrical centre of the structure's foundation (BH-02) and a 15m deep borehole at 0.5m distance from the foundation edge (BH-01).

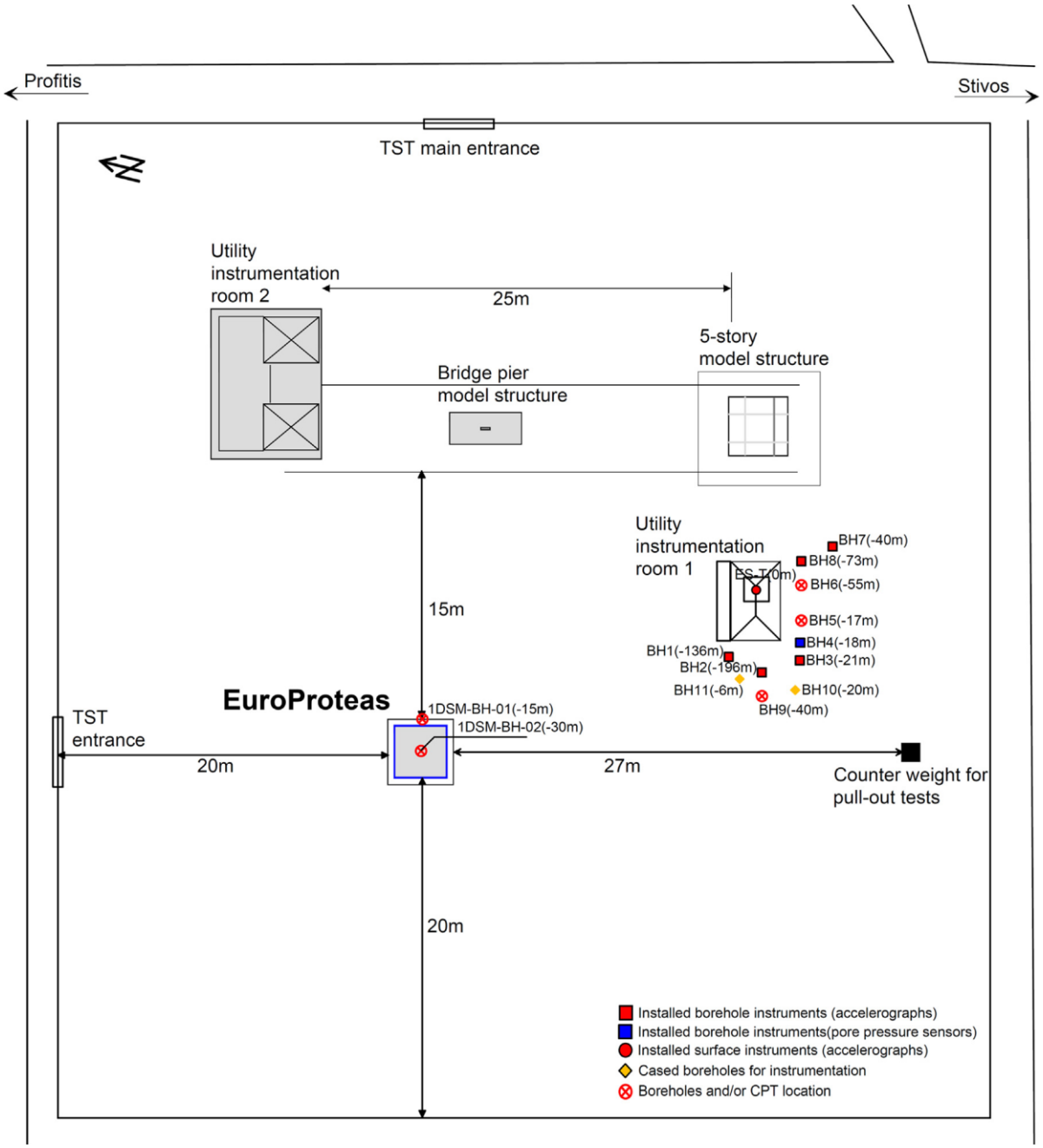


Figure 4.4: Plan view of Euroseistest facilities at the TST site, depicting the locations of boreholes (Pitilakis *et al.*, 2018).

Figure 4.5 presents the soil stratigraphy interpreted by Pitilakis *et al.* (1999) from the data collated from BH1-BH11 boreholes. It also presents the stratigraphy interpreted from characterisation of samples taken from the BH-01 and BH-02 boreholes, as given in Pitilakis *et al.* (2012). Figure 4.6 presents the same soil stratigraphies focusing on the first 40m of soil. The shallow soil layers consist mostly of silty sand and low plasticity clay with some inclusions of gravel. At a depth of 70m, a 9m-thick high plasticity clay layer is encountered, while 12.5m of weathered schist is met above gneiss bedrock. Figures 4.5 and 4.6 also present the positions of permanently installed downhole accelerometers and the positions of samples tested in resonant column and cyclic triaxial apparatus, for which more details are given in Sections 4.3.4 and 4.3.3, respectively.

Figure 4.7 presents the shear wave velocity profiles at the TST site which resulted from the interpretation of data collected from the two site investigation campaigns. Pitilakis et al. (1999) and Raptakis et al. (2000) proposed surface to bedrock V_s profiles after synthesising results from SWI, REF, CH and DH tests, that were carried out during the first campaign. Although the V_s profiles provided by the two studies were generally similar, they proposed different V_s values for certain layers, revealing the inherent subjectivity in interpreting field data. More recently, Raptakis and Makra (2015) used the same data as well as additional more recent data acquired through the same techniques, referred to as conventional (CONV) techniques. They also used seismic data recorded in vertical arrays, that were interpreted through techniques namely seismic interferometry (CC), stress-strain analysis (SS) and annealing simulation approach (ASA). Finally, they exploited ambient noise measurements, which were interpreted through Spatial Auto-Correlation coefficient (SPAC) analysis. The description of the above techniques can be found in the mentioned study, while it is beyond the scope of the present research. The study collected from the above techniques produced 62 V_s profiles, which were synthesised to provide the "mean" profile shown with yellow in Figure 4.7. Raptakis and Makra (2015) and Pitilakis *et al.* (2018) developed V_s profiles focusing on the shallow soil layers. The former study used data from SWI, CH and DH tests, while the latter study used data from downhole tests in the BH-02 borehole.

As Figure 4.7 shows, the shallow soil layers consist of very soft sediments, while sediments become stiffer with depth relatively linearly up to 100m depth. Beyond this depth, V_s increases exponentially, while a relatively strong impedance contrast is met at 135m. Stronger impedance contrasts are met at the interfaces between sediment-weathered schist (184m) and weathered schist-gneiss bedrock (196m). The soft soil deposits and the existence of strong impedance contrasts are expected to promote soil motion amplification, as investigated herein.

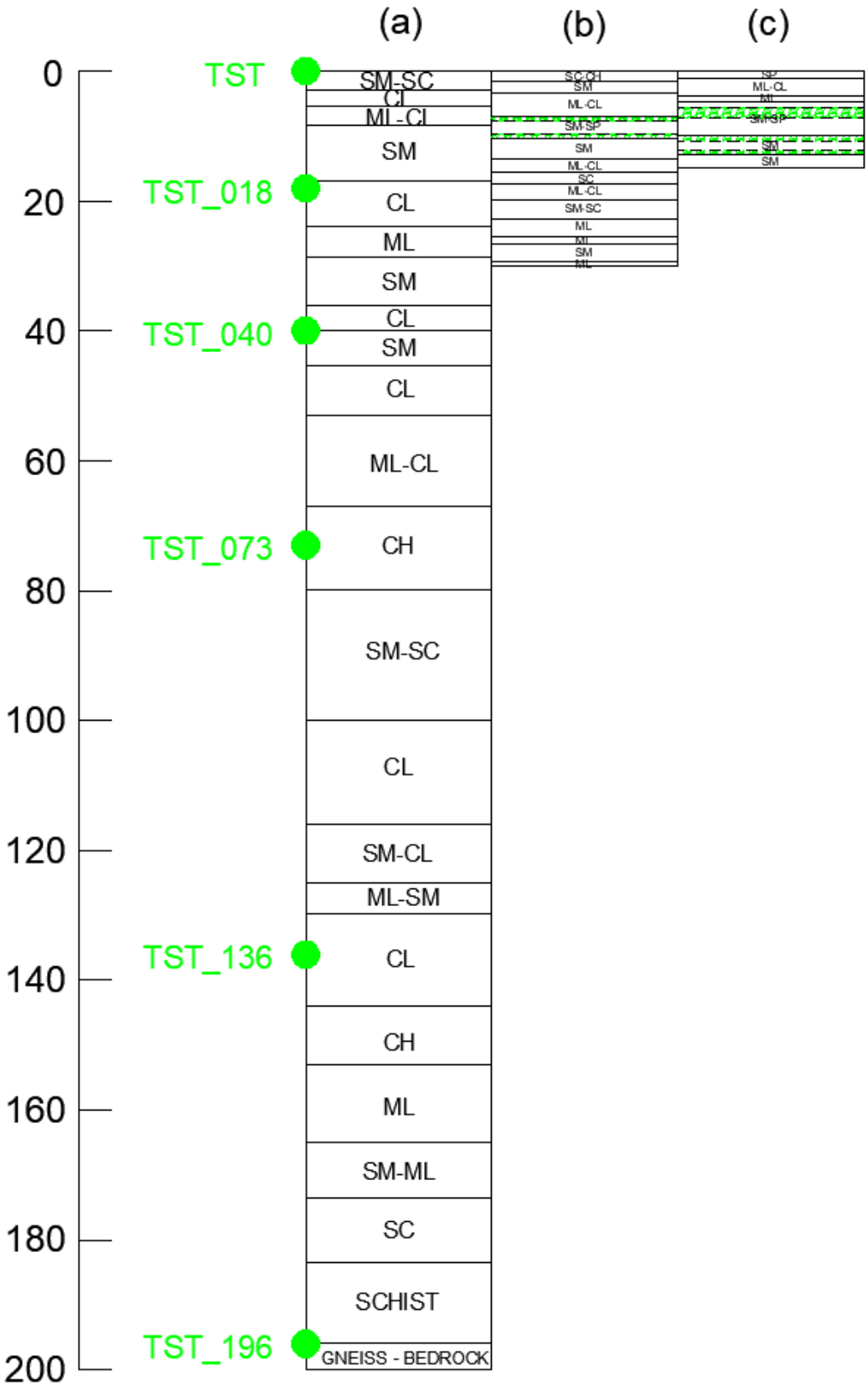


Figure 4.5: TST stratigraphy interpreted from data collated from (a) BH1-BH11 boreholes (Pitilakis *et al.*, 1999), (b) the 30m deep BH-02 borehole and (c) the 15m deep BH-01 borehole (Pitilakis *et al.*, 2012). The positions of downhole accelerometers are indicated with green dots.

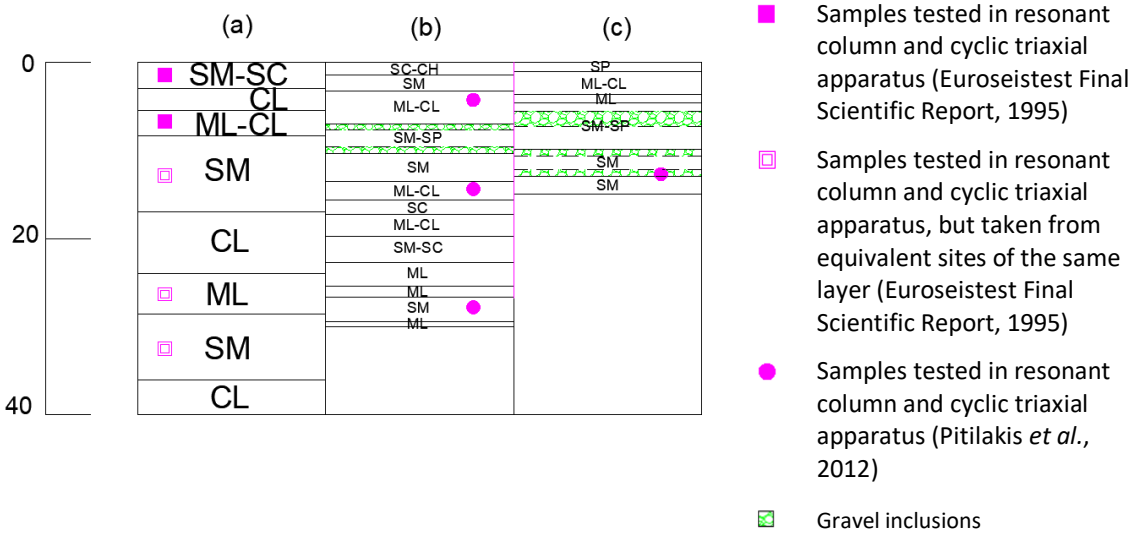
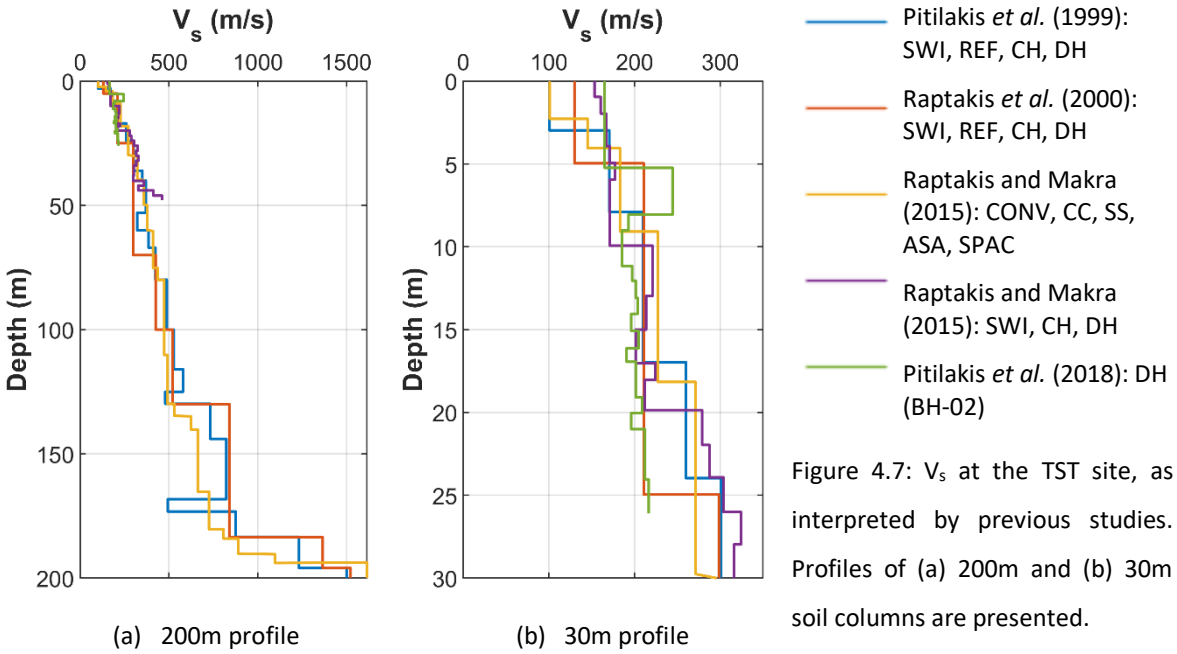


Figure 4.6: TST stratigraphy as per Figure 4.5, focusing on the first 40m of soil. The positions of samples tested in resonant column and cyclic triaxial apparatus are shown.



(a) 200m profile (b) 30m profile

Figure 4.7: V_s at the TST site, as interpreted by previous studies. Profiles of (a) 200m and (b) 30m soil columns are presented.

The water table depth was found by Pitilakis *et al.* (1999) to be at 4m below the ground surface, while a few years later it was found by Pitilakis *et al.* (2018) at 1.7m depth, indicating a difference that can be presumably attributed to seasonal variation.

4.3.2 Adopted soil profile

The V_s profiles and soil layer classification, derived from the aforementioned field and lab tests, were dependent on the type of test and the data interpretation process. The different studies gave various profiles that spread over a relatively wide range of V_s values, where a unique soil for numerical analyses cannot be established. For this reason, a simplified, yet representative soil profile is inferred

from the available field and lab data. This profile, shown in Figure 4.8, is adopted in the numerical models. The adopted soil stratigraphy consists of 16 soil layers, merging together one or more layers identified by previous studies. The merging process was made on three criteria. The grouped layers should have a similar classification according to the unified soil classification system (USCS), similar G-γ-D curves and similar shear wave velocity. The latter ensured that the analyses incorporate every significant impedance contrast identified from the field tests. The proposed V_s profile is back-calculated from field data, following an iterative procedure based on numerical site response analyses, that is described in Section 4.4.

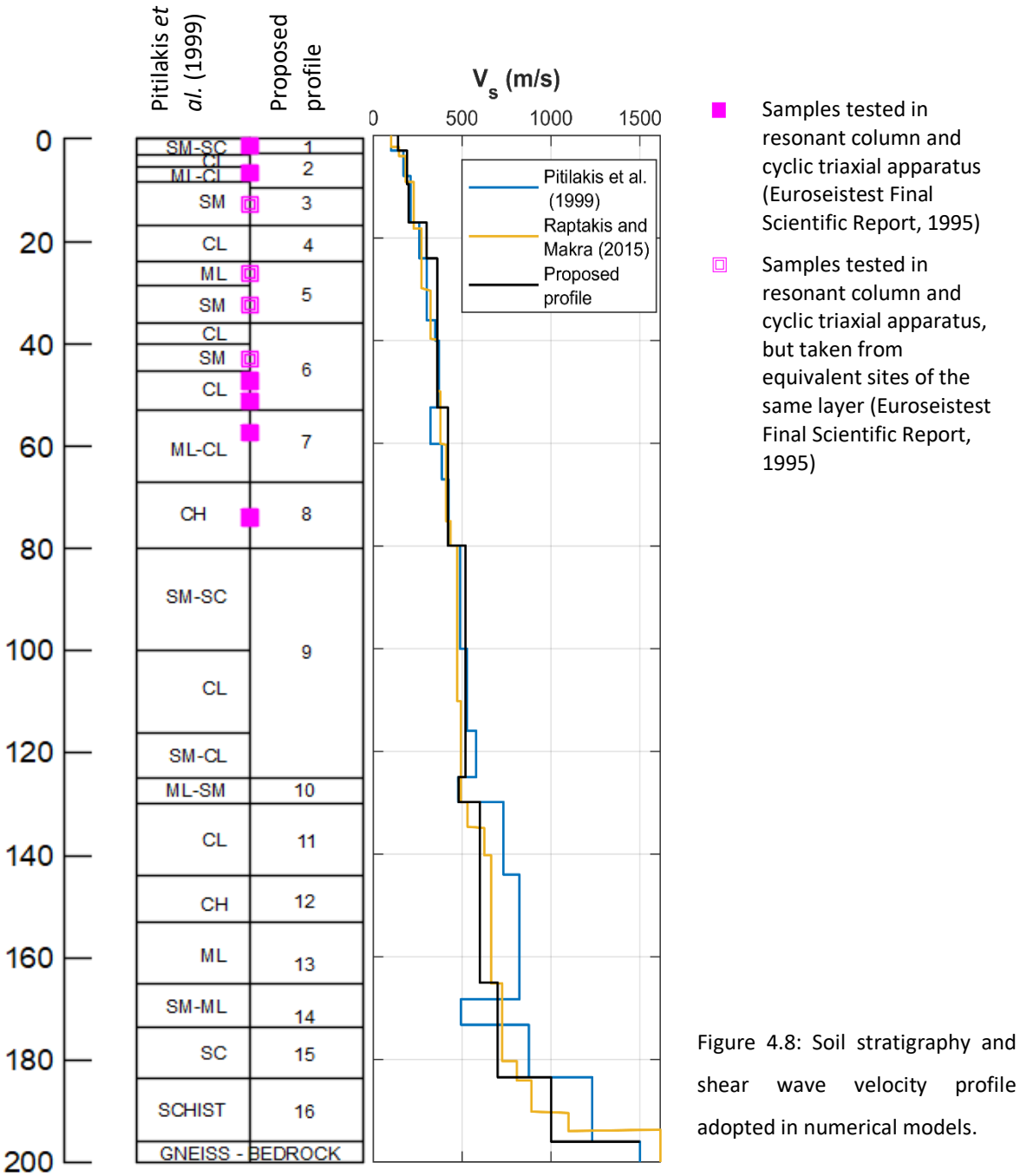


Figure 4.8: Soil stratigraphy and shear wave velocity profile adopted in numerical models.

4.3.3 Adopted G-γ-D curves

As part of the two site investigation campaigns, samples were retrieved from various locations throughout the valley. Some of these were tested on resonant column (RC) and cyclic triaxial (CTX) apparatus to provide the variation of stiffness and damping ratio with strains under cyclic loading (details about the interpretation can be found in Euroseistest Final Scientific Report (1995) and Pitilakis et al. (2012, 2018)). The locations of samples for which G-γ-D curves are computed are depicted in Figures 4.6 and 4.8, which indicate that some samples were retrieved far from the TST site. As Figure 4.2 illustrates, deep soil layers at the TST site can be found in shallower depths near the basin edges. Aiming to facilitate sampling, near surface samples at other locations were considered representative of deep layers at the TST site. This decision assumes that layers of the same material within the valley preserve the same behaviour. The present study also assumes that the nonlinear behaviour of some shallow layers for which G-γ-D curves are not available, is equivalent to the behaviour of another layer of the same USCS. Details about tested samples and resonant column tests can be found in Appendix A.

The G-γ-D curves output from lab tests were further calibrated to account for the different laboratory and in-situ conditions. The calibration procedure aims to firstly deal with the fact that samples prior to being subjected to torsion were not consolidated to the in-situ stress state. Secondly, RC tests impose to the samples high frequency loading (f) and multiple number of cycles (N), much larger than the ones that take place during earthquakes. Although the latter two parameters do not significantly affect the degradation of the stiffness, they affect the variation of damping with shear strain. Therefore, the effect of the two parameters should be calibrated.

The first step of the calibration process involved fitting the Darendeli (2001) G-γ-D curves to the curves obtained from laboratory tests. At this stage, the lab conditions were considered; p' was set equal to the mean effective stress imposed in the lab, while f and N were given representable values for RC and CTX tests. Other input parameters such as PI and OCR were available from lab data (Euroseistest Final Scientific Report, 1995). The remaining input parameters of Darendeli's (2001) formulation, named as ϕ_i's (ϕ_1 to ϕ_{12}), required calibration. The original curves proposed by the referred author incorporate mean ϕ_i's values, that resulted from a statistical analysis. The present study calibrates ϕ_i's to amend the original G-γ-D curves aiming to capture the lab data. To ensure reasonable calibration, the calibrated values of ϕ_i's are selected to be within the $\mu \pm \sigma$ range of the corresponding soil type. The parameters μ and σ are the mean and standard deviation values of a ϕ_i, given by Darendeli (2001). This first step of the calibration is illustrated in Figure 4.9a, which compares the lab data with the original and calibrated G-γ-D curves.

The second step of the calibration involves the computation of the G-γ-D curves using the Darendeli equations with the adjusted statistical parameters (ϕ_i's) of the first stage, considering the in-situ conditions (p′, f, N). The mean effective stress of each layer was computed assuming the overburden pressure at the centre of the layer and K_0 conditions ($K_0 = (1 - \sin\varphi') \cdot OCR^{\sin\varphi'}$). The loading frequency was set equal to 1 and number of cycles equal to 10, as these values are commonly used in geotechnical earthquake engineering (Taborda, 2011). The second step of the calibration is illustrated in Figure 4.9b, which compares the lab data with the calibrated curves that assume lab or in-situ conditions.

The calibrated Darendeli (2001) curves calculated based on the in-situ conditions are input or used as target curves in the ensuing numerical models. The above calibration procedure is followed for all layers for which lab data are available. As shown in Figure 4.8, G-γ-D curves are available for layers 1 to 8, above 80m depth. This study assumes that the nonlinear behaviour of deeper layers comply with the original G-γ-D curves proposed by Darendeli (2001), while considering appropriate mean effective stress (p'), overconsolidation ratio (OCR), effective frictional angle (ϕ') and plasticity index (PI). All input parameters and the resulting curves for all layers can be found in Appendix A.

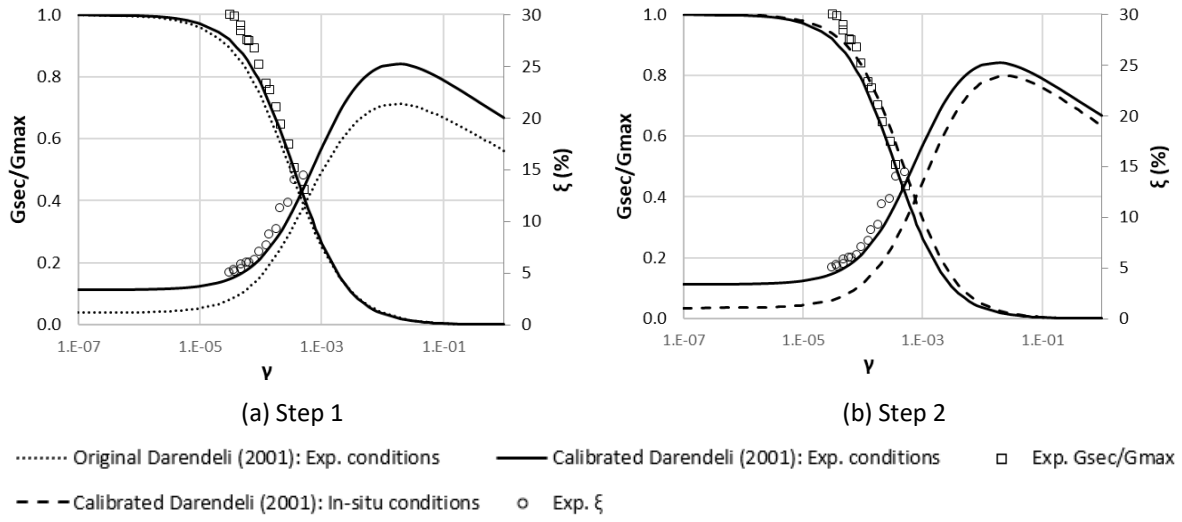


Figure 4.9: Illustration of the two-step calibration procedure of G-γ-D curves. Data shown for layer 2.

4.3.4 Permanently installed downhole array of accelerometers

A great asset of the TST site is the permanently installed downhole strong motion network of stations that has recorded several earthquake events in the past. The downhole array consists of 6 high resolution triaxial accelerometers installed at depths of 0, 18, 40, 73, 136 and 196m, as shown in Figure 4.5. Conventionally, the names of these accelerometers are TST, TST_018, TST_040, TST_073, TST_136 and TST_196. At 196m, the bedrock is met; hence the records of the TST_196 can be considered the most appropriate input motion, when rigid base (within) is assumed in the numerical models.

4.4 Site response analyses

The natural frequency of a uniform soil column can be calculated analytically by employing Eq. 4.1, which was derived based on wave propagation within an 1D domain bounded by a rigid base and a free surface. The average shear wave velocity is calculated as per Eq. 4.5 which expresses the weighted velocity of the column, with reference the thickness (t_i) of each layer (i).

$$V_{s,aver} = \frac{\sum t_i \cdot V_{s,i}}{\sum t_i} \quad 4.5$$

Numerical 1D site response analyses are carried out by employing both equivalent linear (EQL) and nonlinear (NLIN) approaches. Acceleration response spectra (5% damping is assumed) and transfer functions (TF) are employed herein to interpret site response, identify natural periods and determine the origin of these periods. Transfer functions are calculated as the surface to downhole spectral ratios. The abscissa of a peak in a TF corresponds to a natural period of the site. When an identified natural period coincides with a natural period estimated analytically, then this period is assigned to the resonance of the soil column considered in the analytical calculation.

The one-dimensional approach that is adopted for both EQL and NLIN analyses is based on the assumptions of 1D SH-waves propagating vertically, horizontal bedding and that lateral boundaries do not affect the motion. The approach also neglects multi-directionality of wave propagation and the possible existence of other body, Rayleigh or Love waves in the wavefield.

4.4.1 Examined seismic events

The numerical model is validated against data recorded during four earthquake events, the characteristics of which are summarised in Table 4.1. This study considers only the EW component of the motion. According to the table, all three events are of low intensity producing weak peak accelerations. In particular, the largest PGA recorded since the stations commenced operation is 100cm/s^2 (0.1g). The implication of this is that the present study can achieve calibration of the model by back-calculation the soil properties at small strains only.

4.4.2 Equivalent linear approach

The EQL approach, introduced by Seed and Idriss (1970) and subsequently implemented into computer codes (Schnabel et al., 1972), is the most widely used approach for 1D site response analysis. The procedure has gained popularity due to its simplicity, as the required input are limited to soil stratigraphy, V_s profile, density and G-γ-D curves for each layer. The EQL approach assumes viscoelastic soil; this assumption is reasonable for small induced strains, which is expected to be the case for the weak seismic events examined herein (Table 4.1).

Table 4.1: Earthquake events for which numerical models were developed and used in the back-calculation process (taken from EUROSEISTEST Strong Motion Network, 1993).

Date	Time	Epicentre distance (km)	Depth (km)	Local Magnitude	Maximum acceleration (cm/s^2)					
					Surface	18m	40m	73m	136m	196m
12/09/2005	19:08	7.9	9.7	4.4	100.6	37.7	34.3	32.5	26.2	15.4
10/05/2006	07:01	19.4	2.0	4.2	16.8	6.6	5.7	3.9	5.0	3.1
11/10/2013	05:15	10.5	4.0	4.4	45.4	16.0	13.1	15.2	13.2	-
2016/12/13	23:18	17.7	6.3	3.3	12.8	-	3.1	4.0	4.9	3.7

The EQL approach provides a closed-form solution in the frequency domain by establishing the 1D transfer function method. The procedure considers non-linearity indirectly, in that it uses time-invariant decreased shear moduli and increased damping ratio values in relation to the ones at very small strains. The converged values correspond to the so-called ''effective shear strain'', that is calculated as a percentage of the maximum strain (e.g. $0.6\gamma_{max}$). The principles of the EQL approach and transfer functions derivations can be found in Kramer (1996), while the approach is briefly described in a stepwise manner in Appendix A. The most important limitation of this approach is its inability to consider variations of soil stiffness and damping with time, which might be important for strong seismic events. Also, it does not consider the plastic response of the soil and the associated volumetric changes, positive or negative pore water pressure generation for sands and overconsolidated clay, respectively, and liquefaction. This method uses superposition of Fourier series, implying linear analysis, which violates in an extent the nonlinear nature of soil. The extent that the above limitations affect the results depend on the motion intensity. It has been shown that for weak events, the EQL method is considered reliable (Assimaki *et al.*, 2008; Kaklamanos *et al.*, 2015; Kim *et al.*, 2016).

The present study employs the STRATA software (Kottke and Rathje, 2009) to carry out EQL site response analyses. The input G-γ-D curves are those resulted from the procure described in Section 4.3.3, while various Vs profiles were examined. Following the procedure described subsequently in Section 4.4.6, it was found that the back-calculated profile shown in Figure 4.8 reproduces field data satisfactorily.

4.4.3 Nonlinear approach

Fully nonlinear analyses can be carried out using of FE programs, that employ the direct integration method to solve the site response in the time domain. This approach considers the time variation of shear strains, soil stiffness and damping, that is neglected by the EQL approach. This is achieved by the adoption of a cyclic nonlinear elastic model. Due to the expected low levels of induced strains, this

study neglects the generation of excess pore water pressure and the ensuing decrease of strength, i.e. analyses are not coupled with any plasticity model.

The present study uses the Imperial College Finite Element Program (ICFEP) (Potts and Zdravković, 1999), within which the implemented dynamic finite element formulation, boundary conditions and time integration schemes can be found in Kontoe (2006). In all numerical analyses presented, the generalised α-integration scheme (Chung and Hulbert, 1993) is used. The scheme is capable to dissipate numerically high frequency modes without significantly affecting lower modes, by modifying the *spectral radius at infinity* (ρ_∞). Algorithmic dissipation increases with decreasing ρ_∞, taking values between 0 and 1, with the current study using a value of 0.818 (9/11). Also, a 2nd order Gaussian integration and a time step of 0.01s are adopted.

Figure 4.10 presents the FE model used for the NLIN site response analyses, illustrating the dimensions, layering and boundary conditions. The entire surface to bedrock soil column, 196m depth, is modelled. At the deepest level the input motion is applied as horizontal motion, while the vertical displacement of all nodes is restricted. This boundary condition models a rigid bedrock, while it is consistent with the "within" option incorporated in the STRATA software. Tied degrees of freedom (Zienkiewicz *et al.*, 1989), the formulation of which can be found in Kontoe (2006), have been applied between the nodes of the lateral boundaries that have the same elevation. This boundary condition ensures equal displacements between lateral nodes of the same depth, representing free-field conditions (Kontoe *et al.*, 2007).

The width of the model is 2m, which is divided into two columns of 8-noded isoparametric solid elements. The vertical dimension of the elements was decided to ensure that the frequencies within the range of interest can be captured by the model. According to Kuhlemeyer and Lysmer (1973), this dimension should be four to five times smaller than the minimum wavelength (λ_{min}), as shown in Eq. 4.6. λ_{min} is calculated as the ratio of the minimum shear wave velocity ($V_{s,min}$) in the model and the maximum input frequency (f_{max}), as per Eq. 4.7. Using these equations and assuming $V_{s,min}$=140m/s and f_{max}=20Hz, the elements dimension should be smaller than 1.4m. Complying with this estimation, the model is discretised with 1m-thick elements. Table 4.2 presents the input elastic properties of each layer, including Young's modulus (E), Poisson's ratio (ν) and density (ρ). Finally, all presented analyses assume undrained conditions below the water table, which was set at 4m depth.

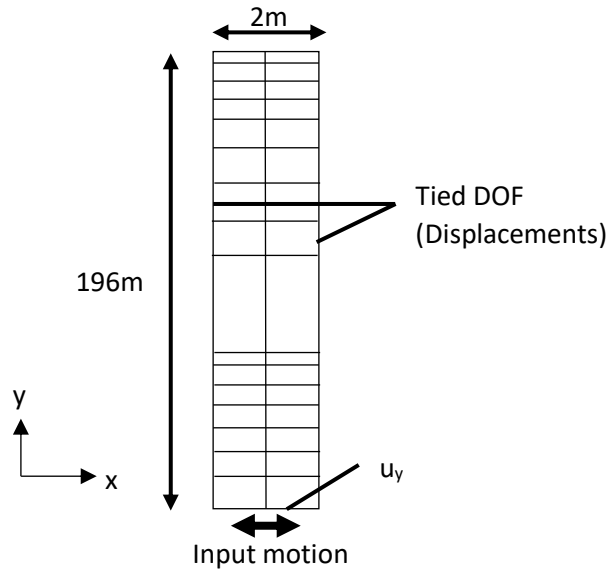


Figure 4.10: FE model illustrating dimensions (not in scale), layering and boundary conditions.

$$\Delta l = \frac{\lambda_{min}}{5} \sim \frac{\lambda_{min}}{4} \quad 4.6$$

$$\lambda_{min} = \frac{V_{s,min}}{f_{max}} \quad 4.7$$

Table 4.2: Elastic soil properties input in the numerical model.

	E (MPa)	**ν**	**ρ (Mgr/m^3)**		**E (MPa)**	**ν**	**ρ (Mgr/m^3)**
Layer 1	100	0.25	2.05	*Layer 9*	1453	0.25	2.15
Layer 2	186	0.2	2.15	*Layer 10*	1288	0.3	2.15
Layer 3	215	0.25	2.15	*Layer 11*	2217	0.4	2.20
Layer 4	457	0.25	2.15	*Layer 12*	2297	0.45	2.20
Layer 5	648	0.25	2.15	*Layer 13*	2059	0.3	2.20
Layer 6	648	0.25	2.15	*Layer 14*	2803	0.3	2.20
Layer 7	1074	0.3	2.10	*Layer 15*	2695	0.25	2.20
Layer 8	1053	0.45	2.10	*Layer 16*	5749	0.15	2.50

4.4.4 Nonlinear constitutive model

The present study employs the Imperial College Generalised Small Strain Stiffness (IC.G3S) model proposed by Taborda *et al.* (2016), which is a cyclic nonlinear elastic model. The model is formulated

in the 3D stress-strain space to simulate both monotonic and cyclic behaviour of soil under multi-directional loading. The complete set of equations of the IC.G3S model can be found in Taborda *et al.* (2016), while they are also presented in Appendix A. The nonlinear elastic behaviour of soil is governed by the variation of tangent shear modulus with the accumulated deviatoric shear strain since the last reversal (E_d^*), as shown in Eq. 4.8.

$$G_{tan} = G_{max} \cdot \left(R_{G,min} + \frac{(1 - R_{G,min})}{1 + \left(\frac{E_d^*}{n_G \cdot \alpha} \right)^b} \right) \geq G_{min} \qquad 4.8$$

where, $R_{G,min}$ is a parameter introduced to limit the degradation of shear stiffness, parameter *a* controls the horizontal position of the degradation curve and parameter *b* controls the degradation rate (Measham *et al.*, 2014). Parameter *a* is dependent on the stress state, while both *a* and *b* depend on the loading direction, which is neglected herein. G_{min} is the minimum shear stiffness beyond which the stiffness does not degrade. G_{max} is the shear modulus at very small strains, which is determined as:

$$G_{max} = G_0 \cdot f(e) \cdot \left(\frac{p'}{p'_{ref}} \right)^{m_G} \qquad 4.9$$

where, G_0 is the shear stiffness that corresponds to a reference confining pressure p'_{ref}, while m_G controls the dependency of G_{max} on the mean effective stress p'. The function $f(e)$ accounts for the influence of void ratio on stiffness, which however is neglected herein (i.e. $f(e)$=1).

The scaling factor n_G, that is incorporated in Eq. 4.8, controls the degradation of shear stiffness. For monotonic loading, a constant value of one is set for n_G, with the equation defining the "backbone curve". During cycling loading,, n_G adopts different values, with a constant value of 2 being proposed by the well-known Masing rules (Masing, 1926; Kramer, 1996). However, as stated by many researchers, this value leads the model to underestimate damping ratios at small strains and overestimate them at medium to large strains, in comparison with lab data (Phillips and Hashash, 2009; Papaspiliou *et al.*, 2012; Taborda and Zdravkovic, 2012; Kaklamanos *et al.*, 2015; Amorosi *et al.*, 2016; Taborda *et al.*, 2016). Taborda and Zdravkovic (2012) and Taborda *et al.* (2016) have proposed the use of a strain dependent scaling factor, as per Eq. 4.10.

$$n_G = \left(d_{1,G}^* + 2 \right)^{E_d^{*d_{2,G}}} \cdot \left(\frac{\left(d_{3,G} + 1 \right) \cdot E_d^*}{1 + \left(d_{3,G} + 1 \right) \cdot E_d^*} \right)^{d_{4,G}} \qquad 4.10$$

where, $d_{1,G}^*$, $d_{2,G}$, $d_{3,G}$ and $d_{4,G}$ are parameters of the model. The overestimation of damping at larger strains is also mitigated by adopting an appropriate value for $R_{G,min}$, in the calculation of G_{tan} (see Eq. 4.8) (Han, 2014; Korma, 2014).

The IC.G3S model allows the calibration of the bulk modulus degradation in a similar manner as shear modulus (see equations in Appendix A). However, the calibration of the bulk modulus degradation and the corresponding damping component is not possible due to the lack of relevant data. Hence, the bulk modulus is inferred from the shear modulus through a constant Poisson's ratio for each layer (Table 4.2), assuming identical degradation between the two moduli.

4.4.5 Nonlinear constitutive model calibration

The calibration of the IC.G3S model aims to select the appropriate model parameters so that the computed G-γ-D curves match the target curves presented in Section 4.3.3 and used in the EQL analyses. As the model cannot fit perfectly both the stiffness and damping curves, the first aspect of the calibration is to decide whether the stiffness or damping curves are more accurately captured. As observed by other studies (Phillips and Hashash, 2009; Papaspiliou *et al.*, 2012; Taborda and Zdravkovic, 2012; Han, 2014; Han *et al.*, 2016), when the calibration prioritises to better match the stiffness degradation curve, the model underestimates the damping at small strains and overestimate the damping at medium to large strains (Figure 4.11). On the contrary, when the model reproduces the damping ratio curve satisfactorily, the accurate prediction of stiffness is sacrificed, as illustrated by Figure 4.11.The figure also shows that the model predicts damping ratio values that decrease with increasing strains at the medium to large strain range. This is a consequence of the $R_{G,min}$ parameter that limits the stiffness degradation with accumulating E_d^*. The impact of $R_{G,min}$ becomes more significant with increasing E_d^*, while at the medium strain range (e.g. 1%) the stiffness reduction becomes weak. At this strain range, the stress-strain cycles become narrower with increasing strains and hence damping ratio starts to reduce. This study prioritises the accurate simulation of damping ratio curves in the small to medium strain range, as the soil damping is expected to be the dominant factor in the site response (Papaspiliou *et al.*, 2012; Han *et al.*, 2017).

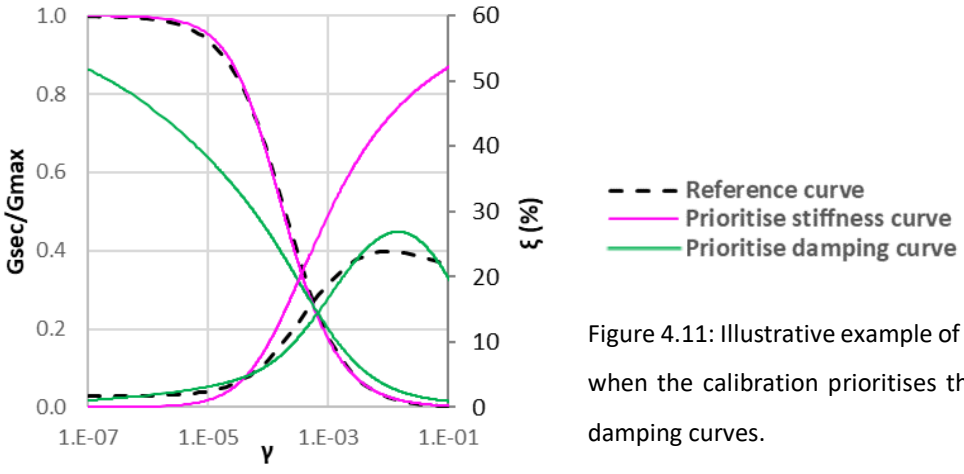


Figure 4.11: Illustrative example of the consequences when the calibration prioritises the stiffness or the damping curves.

To accurately reproduce the target damping curves and approximate the target stiffness curves using the cyclic model, a number of the model's parameters ($R_{G,min}$, α_0, α_1, α_2, b_0, $d'_{1,G}$, $d''_{1,G}$, $d_{2,G}$, $d_{3,G}$, $d_{4,G}$) required calibration. The parameters α_1, α_2 and $d''_{1,G}$, that account for the impact of p' on the curves, are set to zero, because their impact is already considered in the target curves through Darendeli (2001) equations. The remaining parameters incorporated in Eq. 4.8 and 4.10 for the calculation of G_{tan} and n_G are calibrated. Aiming to ensure compatibility between G_{max} incorporated in EQL and NLIN analyses m_G was set equal to zero to neglect the G_{max} dependence on the stress state. Consequently, G_{max} values are directly associated with G_0 of each layer. G_0 values were inferred from the V_s values input in EQL analyses, through Eq. 4.2. Despite that in reality G_{max} increases with p', the assumption of constant stiffness within a layer is reasonable because layers thicknesses are very small in relation with the height of the examined soil column (196m). It is considered that a sufficient resolution of the stiffness profile is provided, without the need of refining the profile based on p' dependence. All parameters input in the nonlinear model and the resulting curves can be found in Appendix A.

4.4.6 V_s back-calculation procedure

The Vs profile was back-calculated by following an iterative procedure which consisted of several EQL analyses. The procedure exploited also all available strong motion data recorded, during the earthquake events mentioned in Table 4.1, by the downhole instruments installed at surface, 18m, 40m, 73, 136m and 196 depths (Figure 4.5). The procedure consists of five steps; each one simulated a soil column of different depth and different input motion. At the first step, analyses investigated the site response of a soil column consisting of soil layers from the surface to 18m depth, where the first instrument was installed. The records of this instrument were used as input motion at the bottom of the soil column, where rigid bedrock was simulated through the "within" option. The V_s of each modelled layer was adjusted iteratively, so that the EQL analyses reproduce the motion at the surface. At the second step, the surface to 40m depth soil column was modelled. The input motion recorded by the instrument installed at the latter depth was applied at the bottom of the column, where rigid bedrock was assumed. By keeping constant the already back-calculated layers, iterative EQL analyses were carried out to calibrate the layers between 18m and 40m, so that the analysis reproduces the motion recorded both at the surface and at 18m depth. Equivalently the next three steps simulated the surface to 73m, surface to 136m and surface to 196m (bedrock) depths to calibrate the layers between 40m and 73m, 73m and 136m, and 136m and 196m, respectively.

Figure 4.12 illustrates the back-calculation procedure, by presenting numerical and recorded data of the 2005 event. It presents acceleration response spectra at the locations of the downhole

instruments, computed by analyses at the end of each of the five steps. The figure demonstrates that at the end of each step, the simulated soil response reproduces the recorded response.

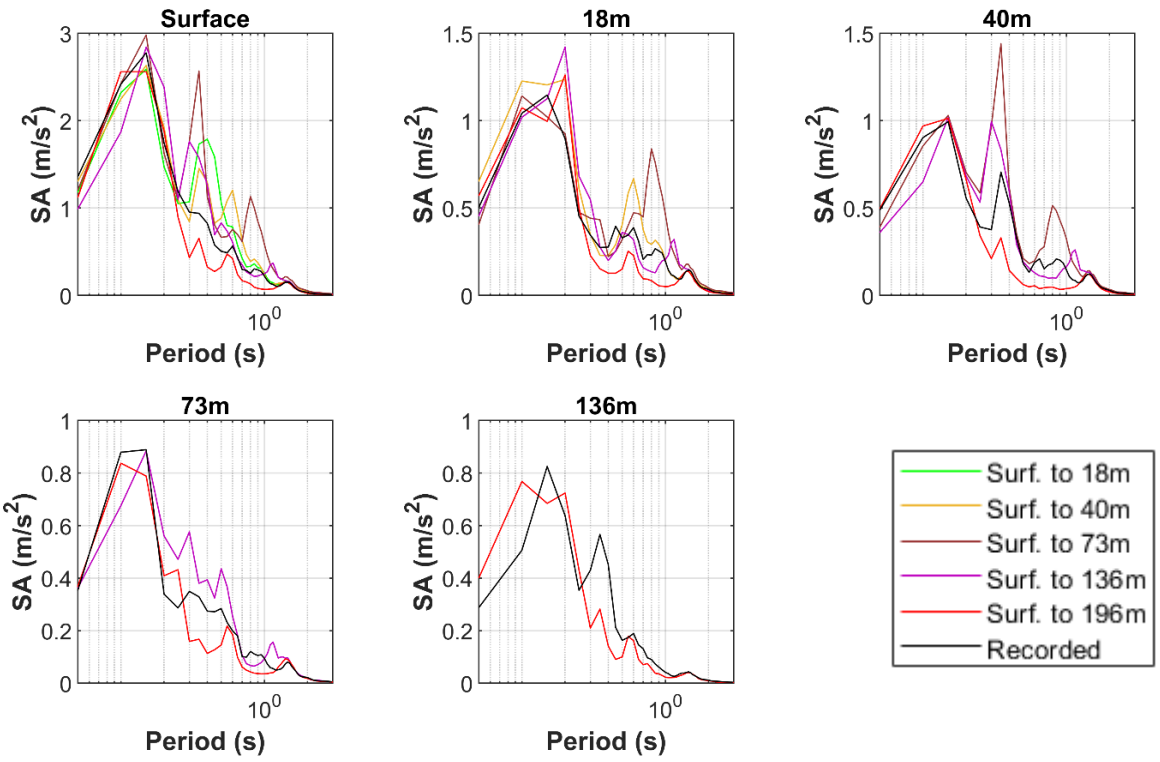


Figure 4.12: Acceleration response spectra at surface and all depths where records are available, that were resulted from the back-calculation procedure. The results were obtained by simulating the 2005 event, with the bedrock modelled at varying depths.

The above procedure was followed using the data recorded during the 2005 earthquake event, which was the strongest event available. The same procedure was followed for the remaining events mentioned in Table 4.1 and the V_s profile was adjusted, where needed. It is important to highlight that the back-calculation process took into consideration the V_s profiles proposed in previous studies (as described in Section 4.3.1), ensuring that the resulting back-calculated V_s profile was reasonably consistent with these prior findings. The calibrated numerical model, that incorporates the back-calculated V_s profile, the assumed soil layering (see Section 4.3.2) and the calibrated G-γ-D curves (see Section 4.3.3), is found suitable for reproducing the soil response of the four examined seismic events. Therefore, it is believed that the calibrated numerical analyses can reproduce events of similar intensities.

4.4.7 Comparison between EQL and NLIN results

Figure 4.13 compares experimental downhole data recorded during the 2005 event (Table 4.1) with EQL and NLIN results produced by simulations of the corresponding event. In both numerical models, the input motion was applied at the real bedrock depth (196m), while the comparison is made in terms

of acceleration response spectra. Comparison of results between the two methods, that simulate the 2006, 2013 and 2016 events can be found in Appendix A. The comparisons demonstrate that NLIN analyses predict very similar site response with EQL analyses, at all examined depths. This validates the applicability of the EQL method for the simulation of these low intensity seismic events.

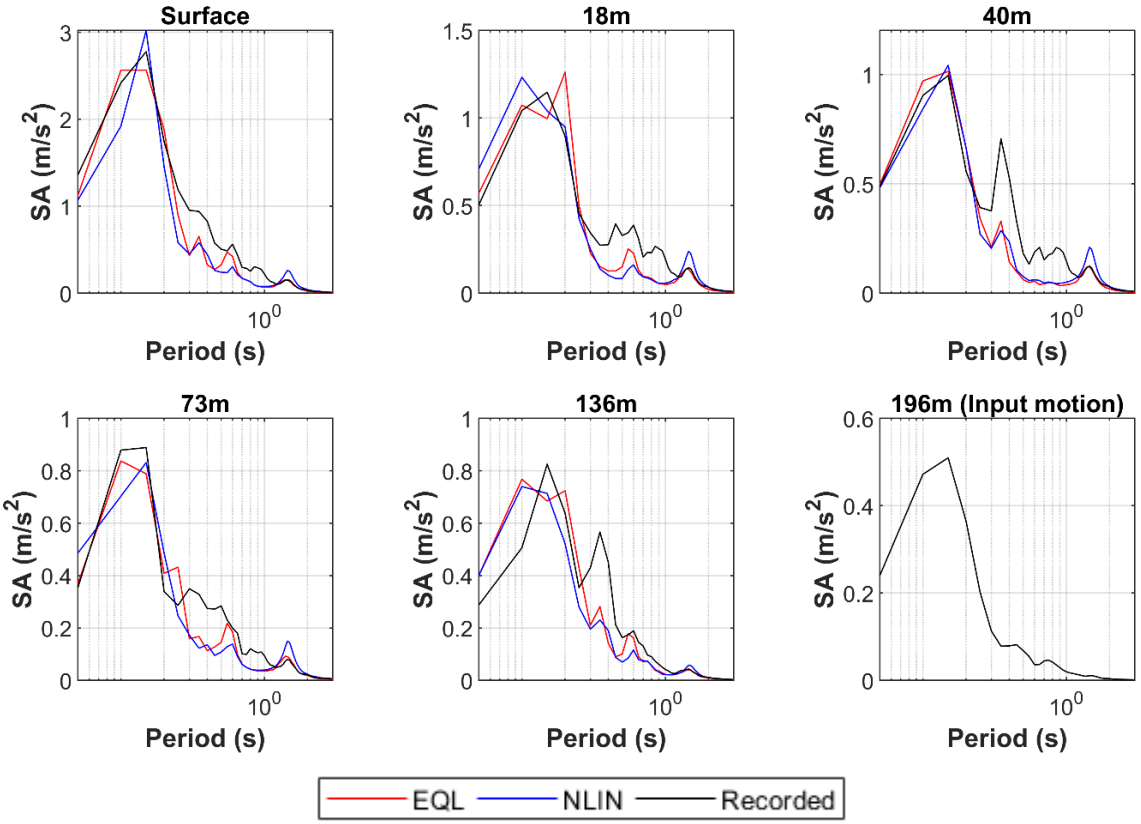


Figure 4.13: Site response results recorded and computed by EQL and NLIN analyses, that simulate the 2005 event. The results are presented as acceleration response spectra at the locations where records are available.

4.4.8 Bedrock depth investigation

The bedrock depth effect is investigated using experimental data and EQL results. Figure 4.12 shows that some spurious spectra acceleration (SA) peaks were present when simulating the bedrock at shallow depths. The peaks disappeared, though, when simulating the entire surface to bedrock (196m) site and applying the recorded bedrock motion as input motion. This can be explained by comparing spectra computed from different durations of a soil motion produced by EQL analyses. Indicatively, the surface motion produced by the surface to 73m depth model is presented in Figure 4.14. The figure presents the acceleration time history produced by the surface to 73m-EQL model, and the time histories recorded in-situ at the surface and at 73m depth. The latter time history was used as input motion in the model. By observing the figure, it is evident that the EQL time history can be distinguished into three parts. For the first 3s, which is the time interval of the most intense motion, EQL analyses reproduce well the recorded data. Between 3s and 10s, the numerical results overpredict

the response. At 10s, the input motion showed a sudden increase before being completely damped. At the same time (10s), the recorded surface motion was completely damped and was not affected by the sudden momentary increase observed in the input motion. On the contrary, this increase significantly affected the numerical results, as indicated by the substantial increase of the numerical motion at 10s. Starting from this time instant, the response followed a free vibration until rest (20s). The disagreement between the numerical and experimental results over the 3 to 20s motion can be attributed to the multiple reflections of waves on the surface and the shallow bedrock. The reflections are consequence of placing the bedrock at shallow depth, 73m, instead at the real bedrock depth, 196m. The motion overprediction can also be attributed to the 1D conditions assumed by the numerical analyses, that may restrict the development of radiation damping.

Figure 4.15 presents the acceleration response spectra computed from the same EQL data considering the motion intervals: 0-3s, 0-10s, 0-20s. The figure demonstrates that the spurious peaks appear on the 0-20s spectra are due to the motion overprediction between 3s and 20s. In particular, the spurious peak observed at a period of 0.8s is associated with the motion predicted after 10s. Also, the spurious peak observed at a period of 0.35s is associated with the motion between 3s and 10s. Considering the first 3s of the motion, the resulting spectra can sufficiently reproduce the experimental spectra.

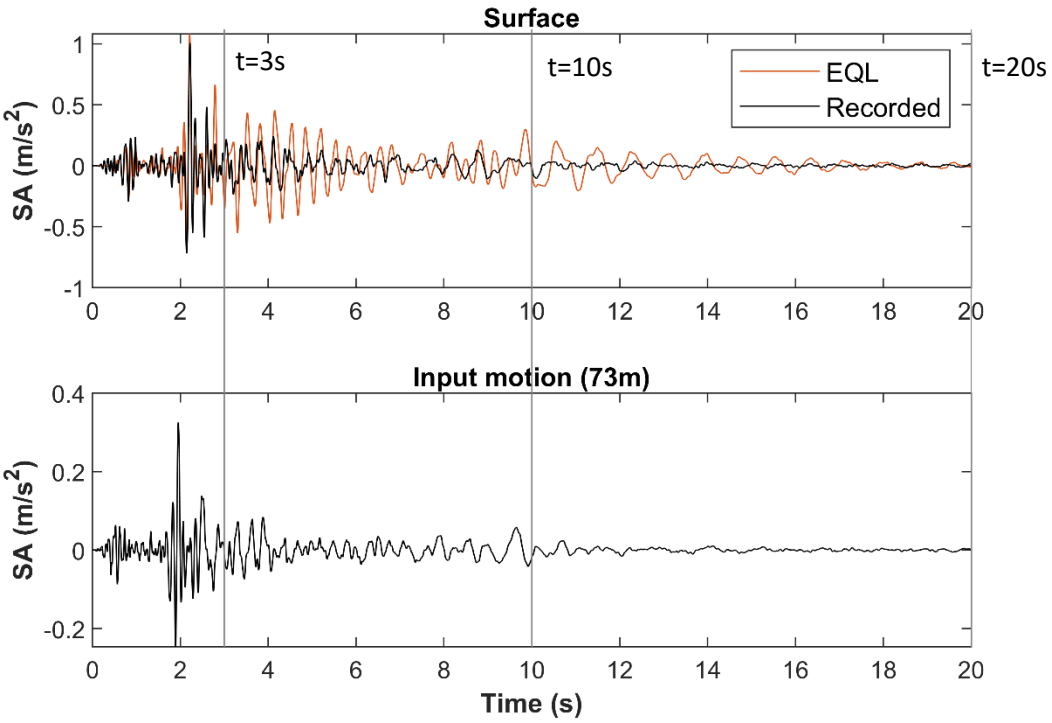


Figure 4.14: Acceleration time histories or recorded at the soil surface or computed by EQL analysis using the surface to 73m model. The input time history applied at 73m is also presented.

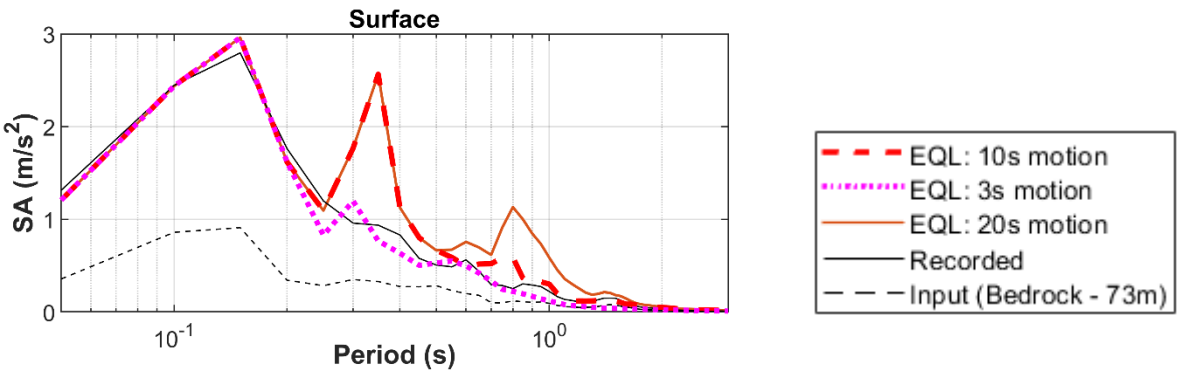


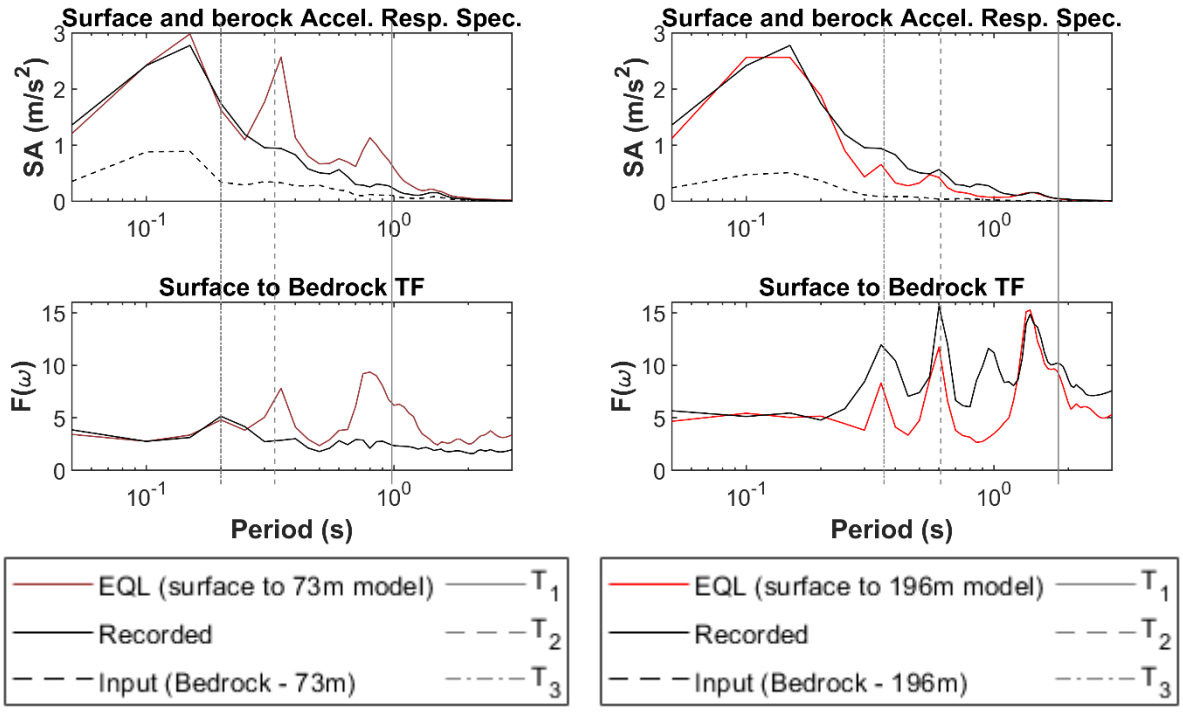
Figure 4.15: Acceleration response spectra of EQL (surface to 73m model) motion at surface, using the different durations of the output motion. The recorded and input motions are also presented.

Figure 4.16 presents the surface and bedrock response spectra, computed by EQL simulations of the 2005 event, and the corresponding transfer functions. Indicatively, the presented results refer to analyses that simulate the first 73m of soil (Figure 4.16a) and the entire surface to bedrock soil column (Figure 4.16b). The response spectra and transfer functions are superimposed by the first three natural periods (T1, T2 and T3) of the modelled soil column, that were calculated as per Eq. 4.1 and 4.5 based on the assumption of 1D propagation of waves that emit from a rigid bedrock. The figure indicates that the spurious peaks, that appear when simulating the bedrock at shallow depth, are associated with resonant features at the natural frequencies of the modelled soil column. In particular, as Figure 4.16a demonstrates, the two spurious SA peaks predicted by the 73m deep model are associated with the first and second natural periods of the model. Another important outcome form both Figure 4.16a and b is that some peaks in the TFs are not associated with the surface to bedrock natural periods.

4.4.9 Natural periods

Following the latter conclusions, the origins of the natural periods are further investigated through transfer functions computed using experimental and NLIN data, shown in Figure 4.17. The numerical data were produced by NLIN analyses, that simulate the 2005, 2006 and 2016 events, while imposing the bedrock at 196m depth. All transfer functions were computed as the ratio of surface to bedrock acceleration response spectra, considering 25s-duration motions starting from the time when the input excitations were triggered.

The figure verifies that some peaks that appear on all transfer functions are associated with the soil-to bedrock natural frequencies. More importantly, the main peak of the TFs is associated with the resonance of surface to 130m depth column. This observation agrees with the observation made by Baise and Glaser (2000), Verdugo (2002) and Kokusho and Sato (2008) who provided evidence that an identified fundamental frequency can be correlated with the response of a soil column above the rigid bedrock.



(a) Surface to 73m model (b) Surface to 196m model

Figure 4.16: Acceleration response spectra and transfer functions computed by EQL linear analyses, that simulate the 2005 event, compared with recorded ones. Some theoretical natural frequencies are superimposed to illustrate the origin of amplification.

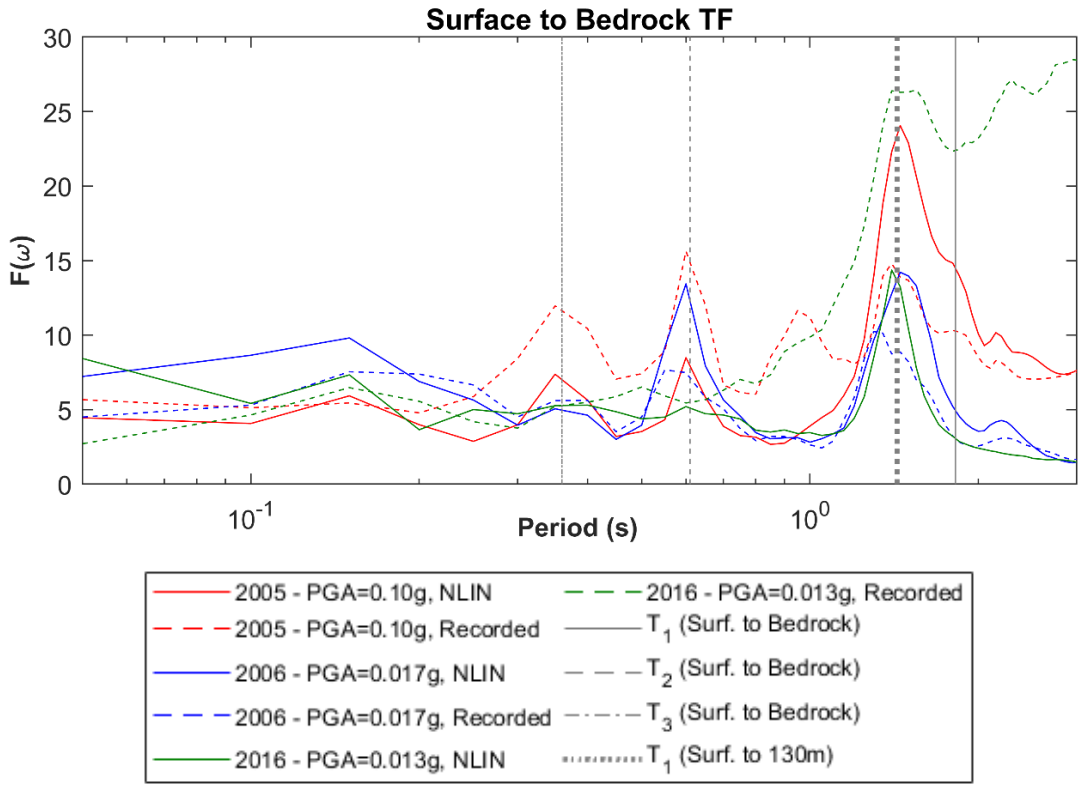
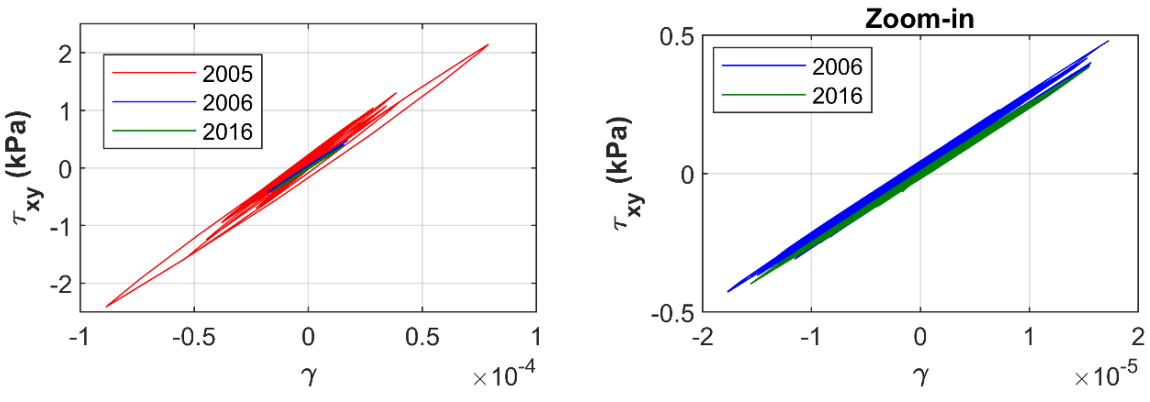


Figure 4.17: Numerical (NLIN) and experimental transfer functions of three seismic events, superimposed by some theoretical natural frequencies.

4.4.10 Soil nonlinearity

Soil nonlinearity is investigated by exploiting both experimental data and numerical NLIN results. The amplitudes of the TFs shown in Figure 4.17 are not distinctly related with the earthquake intensity, indicating a not clear impact of the nonlinear damping on the response. The same figure shows that the peaks appear on the same periods for all events, indicating equal natural periods of the site for the three examined events. This is an evidence of weak stiffness degradation and soil nonlinearity. Weak nonlinearity is further invigorated by Figures 4.18 and 4.19. Figure 4.18 presents the shear stress-shear strain paths computed by the simulations of 2005, 2006 and 2016 events at the centre of the first layer. This layer, being the softest, is expected to exhibit the most pronounced motion amplification and hence the strongest nonlinearity. Figure 4.19 displays the G-γ-D curves input in ICFEP, with a superposition of the stiffness and damping values that have been computed at the integration points of Layers 1 to 3. The values were computed by the simulations of the 2005, 2006 and 2016 events and correspond to the time increment when E_d^* was the maximum computed. Consequently, the presented normalised shear stiffness values are the most degraded ones, while the presented damping ratio values are the most amplified ones computed by the analyses.

Figure 4.18 shows that the simulation of the 2005 event, which is the strongest event examined, computed the largest stresses and strains, in comparison with the 2006 and 2016 simulations. It also shows that the 2005 simulation predicted a decrease of the slope in the stress-strain plane, which indicates degradation of stiffness, for one cycle only, while for the remaining cycles the slope was relatively constant. Almost constant slope and hence weak stiffness degradation is observed for both 2006 and 2016 simulations. Likewise, the stress-strain loops of the 2005 event are the widest, followed by the 2006 event, while the 2016 simulation produced the narrowest cycles. As expected, the width of the cycles and hence the development of hysteretic damping in the soil increase with the event's intensity (see Table 4.1 for events' intensity).



(a) (b)

Figure 4.18: Shear stress-shear strain curves computed at the centre of layer 1 by the simulations of the 2005, 2006 and 2016 seismic events.

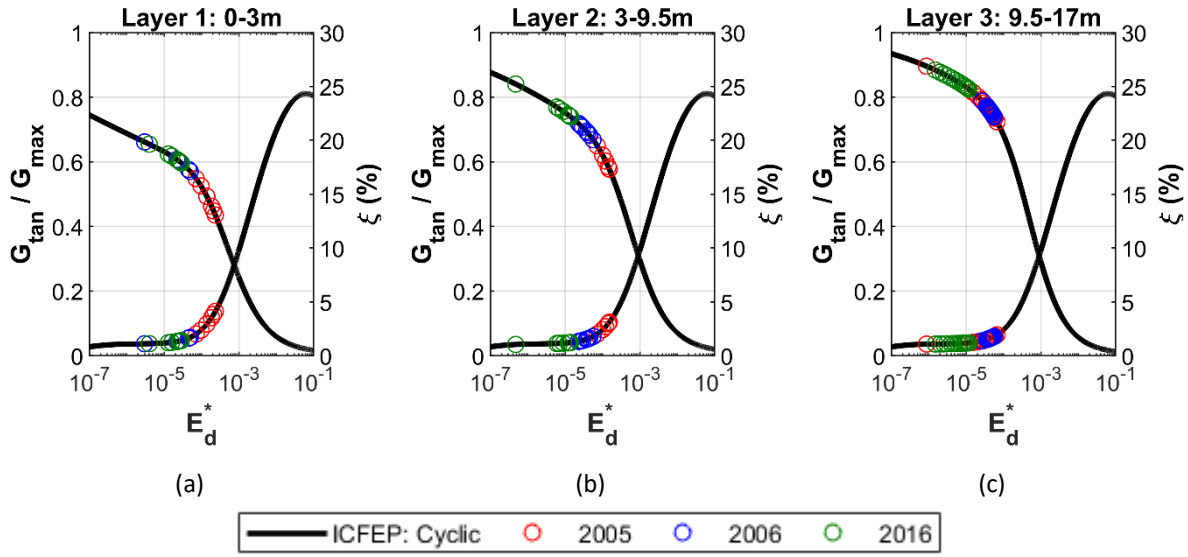


Figure 4.19: G-γ-D curves input in ICFEP, superimposed by the corresponding values computed at integration points of Layers 1 to 3. The values were computed by the simulations of 2005, 2006 and 2016 events and correspond to the time increment when E_d^* was the maximum computed.

The above observations regarding stiffness degradation and damping are reflected in Figure 4.19. The simulation of the 2005 event, which was the strongest event examined, produced the strongest stiffness degradation and damping development. On the contrary, the weakest event, 2016, produced the weakest degradation and damping. The figure also demonstrates that the level of soil nonlinearity decreases substantially with depth, where strains are much smaller. As Figure 4.19c shows, both shear modulus reduction and damping ratio were significantly smaller for layer 3 (i.e. depth of 13.25m) than for layers 1 and 2 (i.e. depths of 1.5m and 6.25m) shown in Figure 4.19a.

The significantly larger shear modulus reduction produced by the 2005 simulation for layers 1 and 2 in comparison the other two events is not reflected on the response depicted in Figure 4.17. As already mentioned, the three simulations produced very similar natural periods of the site, as indicated by the abscissas of the peaks in Figure 4.17. This can be explained by the fact that stiffness degradation was important only for the first 2 layers which cover a depth of 9.5m out of 196m of soil. Therefore, the stiffness degradation of such a short soil column in relation to the surface to bedrock column cannot alter the overall natural frequency of the site. Additionally, the normalised shear stiffness values presented in Figure 4.19 are the smallest calculated by the analyses. The latter implies that the average stiffness of each layer will be closer to the one at very small strains than the one presented in Figure 4.19.

4.5 Summary

This chapter presents the wider Euroseistest site, as well as the TST site, which is the site of interest. The Euroseistest site covers an area of 100km^2 and it is located at a seismically active area of Northern Greece. Its geotechnical and geophysical properties have been well documented by previous studies, while it is permanently monitored at different locations. More detailed site characterisation studies have been carried out at the TST site, which is located in the centre of the Euroseistest valley. Also, at this site a downhole array of accelerometers is permanently installed, monitoring the seismic response of soil at the surface, 18m, 40m, 73m and 136m and 196m depths. The strong motion data recorded by the latter instruments were used herein to assess the site response and calibrate numerical model. The numerical analyses simulate the response of the site during four different seismic events of weak intensity.

This study presents both equivalent linear (EQL) and nonlinear site (NLIN) response analyses, which were carried out based on the assumption of 1D wave propagation. The input properties of the numerical analyses were taken from the available site characterisation data. The experimental G-γ-D curves required further calibration to account for the different boundary conditions (p', input frequency and number of cycles) that were imposed during the experiments and those exist in-situ. The V_s profile was back-calculated by following an iterative procedure that consisted of multiple EQL analyses.

The present study proposes a back-calculation procedure that exploits the available downhole data. The procedure consists of a number of steps equal to the number of downhole instruments. Each step simulates a soil column extending from surface to a depth where strong motion data exists, starting from the shallowest and progressing to increasingly deeper depths. Strong motion data recorded at the corresponding depths are used as input motions at the base of the model. At the end of each step, the shear wave velocities of the modelled soil layers are back-calculated. At the next step, the already back-calculated layers are maintained, while the V_s of newly added layers in the updated model are back-calculated.

Using the back-calculated V_s profile, NLIN analyses were carried out. For these analyses, a cyclic nonlinear elastic constitutive model was adopted, whose properties required calibration. The calibration prioritised the accurate simulation of damping ratio curves, which was expected to have a more significant effect on the response than the simulation of the stiffness curves, for which accuracy was sacrificed. According to the results of the NLIN analyses, the examined events induced very small to small strains in the soil. The analyses produced results very similar to the EQL analyses, verifying

previous claims made in the literature that EQL method is applicable for small strain problems (e.g. Assimaki *et al.*, 2008; Kaklamanos *et al.*, 2015; Kim *et al.*, 2016; Foti *et al.*, 2019).

EQL results were also used to investigate the effect of the bedrock depth, where the input motion was applied. It was found that when the bedrock was imposed at depths shallower than the real bedrock depths, spurious peaks were produced in acceleration response spectra inferred from the surface motion. These peaks were associated with a part of the surface acceleration time histories that was affected by the multiple reflections of waves on the surface and the shallow rigid base. In fact, the peaks were found to be associated with the natural periods of the modelled soil column. For this reason, the spurious peaks disappear when simulating the entire soil column from surface to the real bedrock.

Surface to bedrock transfer functions (TFs) were used to identify natural periods of the site, by exploiting strong motion data and NLIN results. It was verified that some natural periods were associated to the first or higher modes of resonance of the surface to bedrock soil column. It was also shown that a natural period was associated with the resonance of the surface to 130m soil column. This observation agrees with the claims made in the literature (Baise and Glaser, 2000; Verdugo, 2002; Kokusho and Sato, 2008) that fundamental periods can be associated with the resonance of soil well above the bedrock. The identified natural periods were the same for the examined events, despite their different intensity. This implied that soil nonlinearity was not important during any of the examined events, which was also verified by stiffness degradation and damping ratio values produced by the analyses.

Chapter 5

Experimental Campaign: Forced and Free Vibration Tests on a Structure Founded on a Surface Foundation

5.1 Introduction

Soil-Structure-Interaction (SSI) phenomena can be rigorously studied by interpreting field data collected from real-scale experiments. The interpretation of field data can be very challenging when both kinematic and inertial interaction mechanisms, which constitute the SSI phenomena, co-exist during the experiments. This can happen when the input motion is not directly imposed on the examined structure, such as the case of a seismic event, or when a vibrating source is located close to the examined structure.

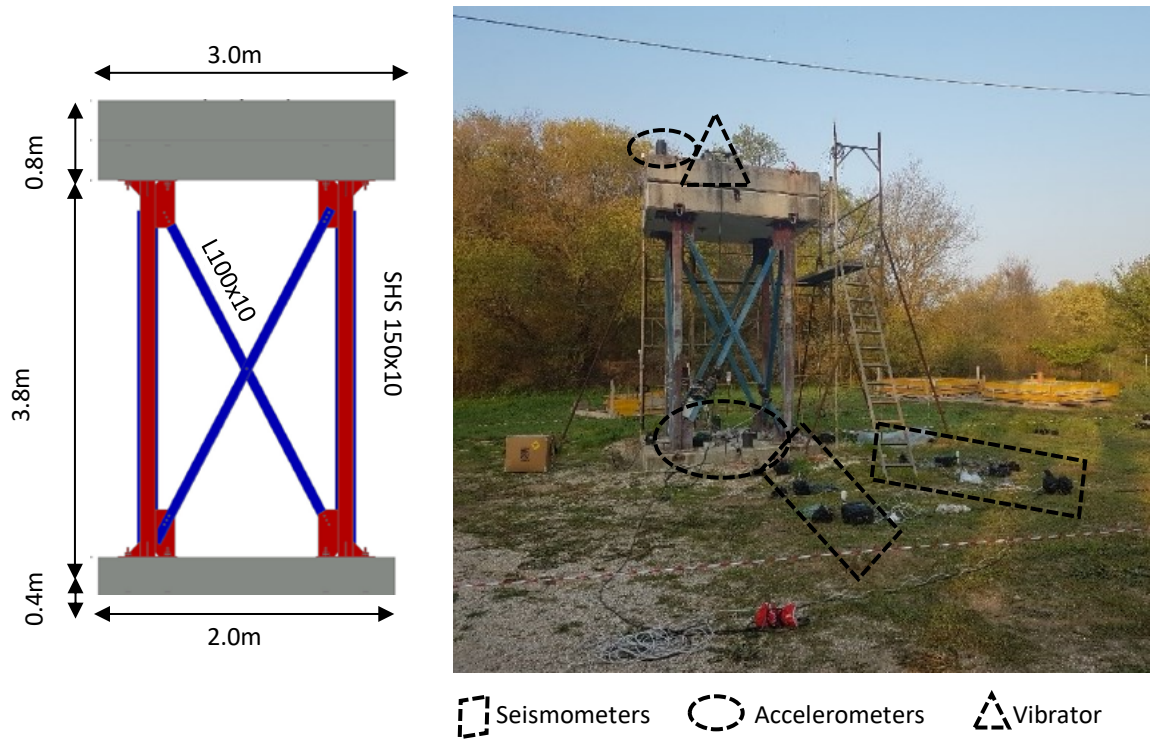
As already mentioned in Section 2.2, the kinematic interaction mechanism is responsible for the alteration of motion at the foundation level relative to the free-field case. Therefore, the kinematic part of the SSI can be neglected when the experimental input motion is a pre-defined excitation that is applied on the examined structure directly. This is a fundamental underlying assumption for the experiments conducted as part of this PhD research.

This research benefits from the field-testing programme of the research project "Dynamic Soil Structure Interaction: Three-dimensional Time-domain Analysis of Field Model Scale Experiments", which was carried out by Imperial College London (ICL) in collaboration with the Aristotle University of Thessaloniki (AUTH). The field testing involved real scale tests of a prototype structure (EUROPROTEAS) that were carried out by the AUTH research team in collaboration with ICL under a Transnational Access User Agreement funded by SERA (Seismology and Earthquake Engineering Research Infrastructure Alliance for Europe). The experiments consisted of two suites; the first suite of experiments was carried out in April 2019, while the second one in October 2019.

5.2 EUROPROTEAS prototype structure

EUROPROTEAS prototype structure was built in 2012 as part of the SERIES (Seismic Engineering Research Infrastructures for European Synergies) research programme, and it has been re-used for the purpose of the current research. It was designed to promote SSI effects involving foundation rocking, as it is described in Pitilakis et al. (2012). EUROPROTEAS is placed at the centre of the Euroseistest site in Northern Greece (Figure 4.1), TST, the geotechnical and geological properties of which are well documented by previous studies, as described in Section 4.3. The shallow soil layers consist mostly of silty sand and low plasticity clay of very low stiffness, a condition that accentuates the SSI effects.

EUROPROTEAS (Figure 5.1) is a 5m tall symmetric frame structure with steel columns (SHS 150 x 150 x 10mm) and removable cross-bracing system (L-shape 100 x 100 x 10mm), founded on a shallow foundation. The foundation consists of one (9Mgr) reinforced concrete slab. The superstructural mass consists of one or two (9Mgr or 18Mgr) identical slabs, with dimensions 3m x 3m x 0.4m each. The structure was subjected to free and forced vibration tests, during which the structural and soil motions were monitored by a comprehensive instrumentation (Figure 5.1b). The conceptualization of the structural design and experimental set-up are described herein.



(a) (b)

Figure 5.1: (a) Schematic EUROPROTEAS structural elements and dimensions, (b) EUROPROTEAS picture including some instrumentation.

5.2.1 Conception of the structural design

EUROPROTEAS prototype structure's design was dedicated to study SSI phenomena as well as foundation rocking. It is well known and discussed in Section 2.6 that two of the parameters that affect the significance of the SSI phenomena are the structure-to-soil stiffness ratio (σ) and the structure-to-soil mass (γ_m) (Amorosi *et al.*, 2017). These two parameters are a function of structural stiffness, structural mass, structural geometry and soil properties, as shown in Eqs. 2.8 and 2.9. Although structural geometry and soil properties remain unchanged during the experiments, the structural design allows the adjustment of the structural stiffness and mass. Aiming to investigate the impact of the SSI effects under different values of σ and γ_m, the structure was designed to have removable bracing system and adjustable superstructural mass. The bracing system can be placed on all four sides of the structure, on any combination of sides or be completely removed. The superstructural mass can consist of one or two reinforced concrete slabs, which accumulates to 9Mgr and 18Mgr respectively.

The structural design conformed to the provisions of modern codes and regulations. The steel members and connections were designed according to the Eurocode 3 (BS EN 1993-1-1:2005). The connections between the steel columns and the concrete slabs, as well as the steel columns and the braces (Figure 5.6) were assumed rigid. The reinforced concrete slabs were designed according to the Greek code for Reinforced Concrete (EKOS2000), while the bearing capacity of the foundation soil was estimated according to the Greek Aseismic code (EAK2000). More about the foundation design can be found in Section 5.2.3. The structure was designed to be very stiff with minimal flexural deformability to allow foundation rocking. More details regarding the structural design can be found in Pitilakis et al. (2012).

5.2.2 Structural configurations examined

The structural design allows the reconfiguration of the structural stiffness and mass, as already mentioned. Two structural configurations were subjected to forced or free vibration tests. Although for the free vibration tests the loading direction was constant (conventional South), the vibrator used for the forced vibration tests could apply unidirectional forces along two perpendicular directions (conventional North-South and East-West). Figure 5.2 and Figure 5.3 present the combinations of the structural configurations and loading directions that were examined under forced and free vibration tests respectively, as part of the current research.

Three experimental configurations, which include different combinations of structural configuration and/or loading direction, were subjected to forced vibration tests. The first experimental configuration comprises a symmetric fully braced structure with cross-bracing system at all four sides and two top slabs (FBr_2Ts) of around 18Mgr mass, shown in Figure 5.2a. The second is a symmetric

fully braced structure with one 9Mgr top slab (FBr_1Ts), shown in Figure 5.2b. The force applied on each of the FBr_2Ts and FBr_1Ts structures by the vibrator was acting along the conventional North-South (NS) direction. The third structural configuration is a partly braced structure with two top slabs (PBr), where the cross-bracing system was placed in the North-South planes only. Exploiting the asymmetric stiffness of the structure, the response of the PBr structure was examined under two different loading directions. The PBr structure was subjected to forced vibrations that were acting along either the structure's weak axis (PBr_W), or the structure's strong axis (PBr_S), as shown in Figure 5.2 c and d, respectively. The strong axis of the structure is determined as the East-West axis where the cross-bracing system was acting, while the North-South axis is considered the weak one.

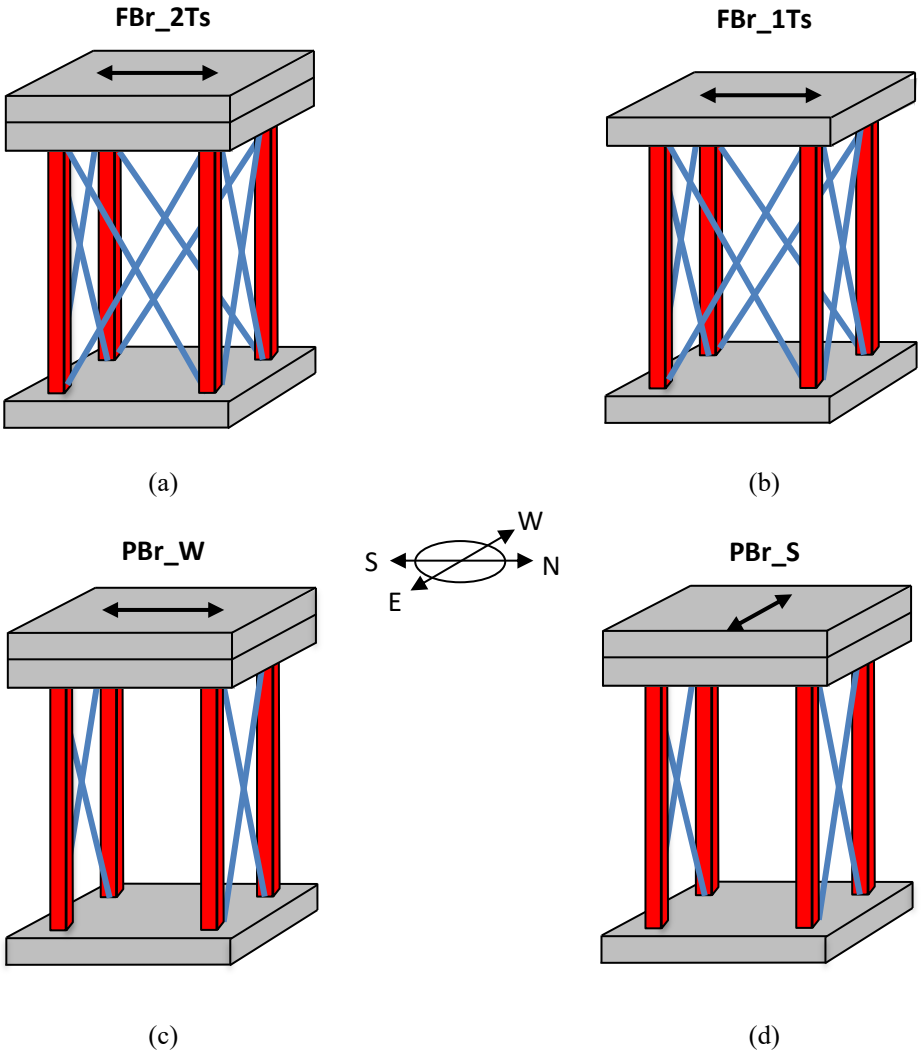


Figure 5.2: Structural configuration and loading direction combinations examined under forced vibrations.

Figure 5.3 presents the two structural configurations subjected to free vibrations. The first is a symmetric fully braced structure (FBr_2Ts), while the second is partly braced (PBr_W). Both structures have two reinforced concrete slabs on the top (18Mgr) on which the pull-out force (F) was applied at

an angle of 9°. The force was acting along the North-South direction, which is the weak axis of the PBr structure. Table 5.1 summarises the structural configurations examined.

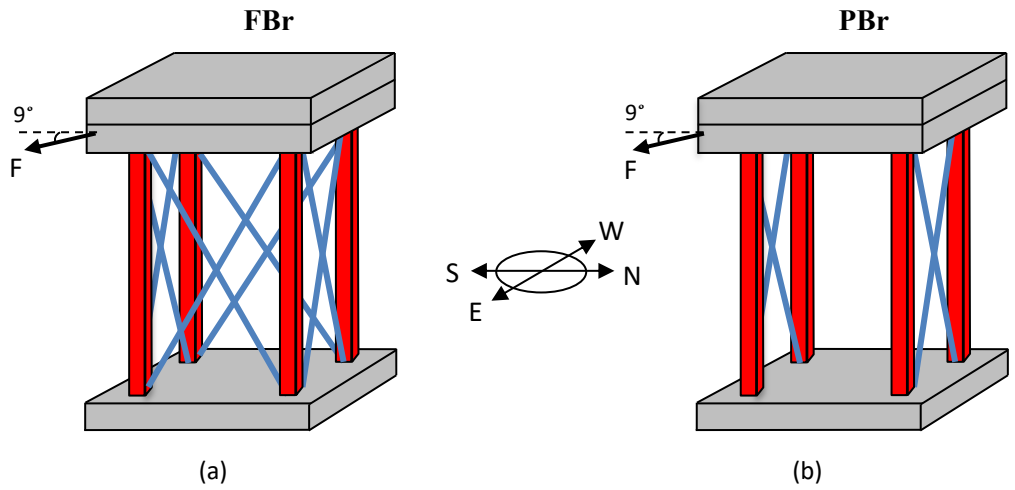


Figure 5.3: Structural configurations examined under free vibrations.

Table 5.1: Names and description of structural configurations examined.

Configuration name	Bracing system	Mass (Mgr)	Loading direction
FBr_2Ts	Full – All four sides were braced	18	NS
FBr_1Ts	Full – All four sides were braced	9	NS
PBr_W	Partly – The North and South sides were braced	18	NS (Weak axis)
PBr_S	Partly – The North and South sides were braced	18	EW (Strong axis)

It should be noted that the experiments on the two-top-slab structures (FBr_2Ts and PBr) were carried out during the first suite of experiments in April 2019, while the experiments on the one top slab structure (FBr_1Ts) during the second suite (October 2019). In between the two suites, site conditions might have changed, as subsequently discussed in Section 5.2.4. This raises a potential uncertainty on whether consistent comparisons can be made between the FBr_1Ts experiments and the remaining experiments.

5.2.3 Foundation bearing capacity

The bearing capacity of the foundation to vertical loads is estimated according to the guidelines provided by Eurocode 7 (British Standards Institution, 2004b). In this estimation, the presence of moment and horizontal forces was disregarded, while the soil is assumed to have an effective angle of shearing resistance of 30°, cohesion of 10kPa, and an effective unit weight of 20kN/m3. Based on these assumptions, the drained bearing capacity of the foundation soil is calculated to be 973kPa. For a 3m x 3m foundation, the ultimate vertical force is N_u=8758kN. The applied vertical load (N) is estimated around 265kN and 177kN for the structural configurations with two (2Ts) and one top slab

(1Ts), respectively. This estimation takes into account the mass of both the superstructure (1 or 2 slabs) and the foundation slab, with each slab weighing approximately 9Mgr.

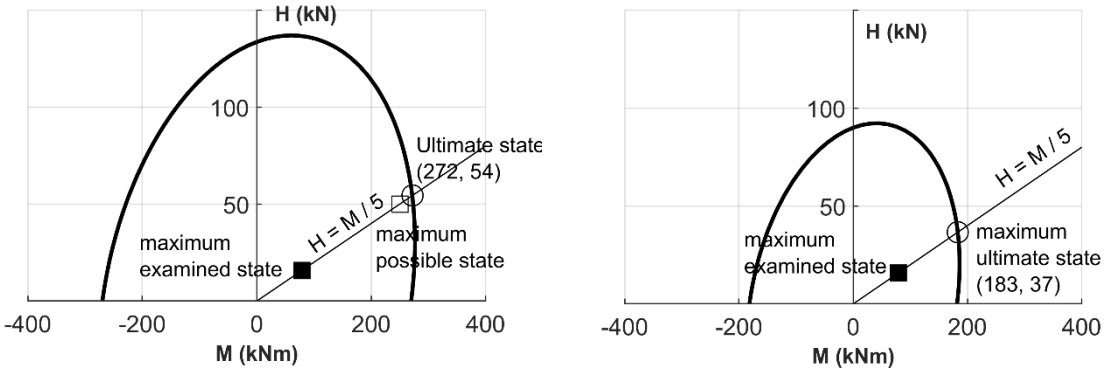
The moment (M) and shear (H) capacity of the foundation is determined using the empirically derived $N-H-$M interaction diagram, proposed by Butterfield and Gottardi (1994):

$$\left(\frac{H}{t_h}\right)^2+\left(\frac{M}{B\cdot t_m}\right)^2+\frac{2\cdot C\cdot M\cdot H}{B\cdot t_h\cdot t_m}=\left[\frac{N}{N_u}\cdot(N_u-N)\right]^2 \qquad 5.1$$

where $B=3$m is the width of the foundation, and t_h=0.52, t_m=0.35 and C=0.22 are parameters whose values correspond to the interaction diagram that provides the best fit to the experimental data. These data were obtained from laboratory experiments conducted on roughened and rigid surface footings placed on dense sand. Naturally the examined configuration does not fully comply with the experimental set up of Butterfield and Gottardi (1994), however, Eq. 5.1 is sufficient to approximate the load on the foundation with respect to the proposed interaction diagram.

Using the above expression and assuming a constant vertical load (as computed above), the $M-H$ failure envelopes for the foundation of EUROPROTEAS for the 2Ts and 1Ts structural configurations are illustrated in Figure 5.4. In the examined experiments, the foundation shear and moment forces are related by the equation $M=H\cdot h$, where $h=5$m, representing the vertical distance between the load application point and the foundation base. Exploiting this constraint as shown in Figure 5.4, the ultimate moment (M_u) and shear (H_u) forces of the foundation are estimated. These are found to be 272kNm and 54kN for the 2Ts configuration and 183kNm and 37kN for the 1Ts configuration.

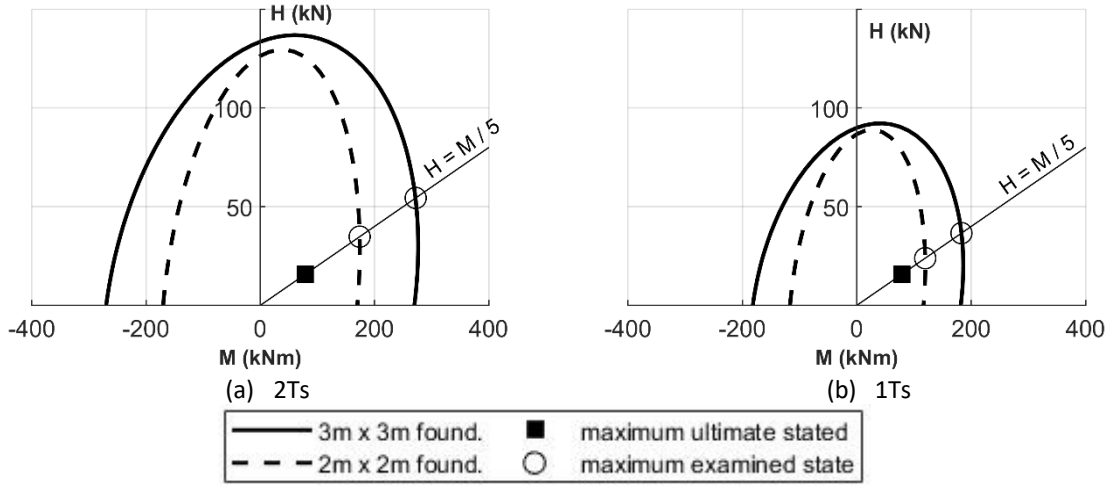
The foundation was designed considering the 2Ts configuration only and the maximum horizontal force that can be applied by the vibrator, which is 50kN (Euroseistest Final Scientific Report, 1995). For this excitation, the ultimate possible state, shown in Figure 5.4a, lies close but below the failure envelope. The maximum horizontal force applied during the experiments was 15.7kN, which resulted in base moment 78.5kNm. As also illustrated in Figure 5.4 a and b, this maximum examined state lies well below the failure envelope, hence, the foundation was expected to exhibit elastic response without uplifting or sliding.



(a) 2Ts (b) 1Ts

Figure 5.4: Failure envelope in the M-H plane estimated for the case of the EUROPROTEAS'S foundation that correspond to (a) FBr_2Ts and (b) FBr_1Ts structural configuration.

It should be noted that the above calculations assume that the foundation and the soil are in full contact prior to the excitation load. However, as explained in the subsequent section, the foundation was not in full contact with the soil. To consider this imperfection in the calculations, a contact area 2m x 2m, which will be adopted for the majority of numerical analyses presented in Chapter 7, is assumed. Following the above procedure, the M-H interaction diagrams are constructed for this assumed case. Figure 5.5 presents the diagrams for the case of full and reduced interface contact area, for the configurations with two and one top slabs. As expected, the decrease of the contact area results in reduction of the foundation capacity, yet the maximum examined M-H state still lies below the yield surface. This observation indicates that even for the case of assumed interface conditions with significant gap areas and reduced contact areas, the foundation is expected to behave elastically without uplifting.



(a) 2Ts (b) 1Ts

Figure 5.5: Impact of contact interface area on the failure envelope in the M-H plane estimated for the case of the EUROPROTEAS'S foundation that correspond to (a) FBr_2Ts and (b) FBr_1Ts structural configuration.

5.2.4 Experimental imperfections

Experimental imperfections are inevitable, as geometry cannot be perfect and therefore symmetry is lost. Additional to the geometry imperfections, imperfections associated with the soil-foundation interface and column-slab connections existed during the experiments. All types of imperfections might have affected the experimental results, thus posing challenges for their interpretation.

Prior to the experiments, the foundation soil was prepared to allow good contact conditions between the foundation base and the soil beneath. The first 0.20m of the superficial soil was removed and the ground surface was levelled before the structure was placed in its final position. There was no instrumentation available to indicate the contact interface conditions, and therefore the perfect contact between the foundation and the soil was not ensured. The latter creates an uncertainty regarding the soil-foundation interface conditions. The interface conditions might not be the same for all experiments. Between the first (April 2019) and the second (October 2019) suite of experiments the structure was moved for the purpose of other experiments and then returned to its initial position. This fact raised the concern that the interface conditions were different between the experiments on the one top slab structure (FBr_1Ts), which were carried out in October 2019, and the remaining experiments which were carried out in April 2019.

The soil-foundation interface uncertainty increases when considering that the base of the reinforced concrete foundation might have not been flat. The foundation was pre-cast with a timber formwork which was supported at two edges only. This casting procedure might have resulted in a foundation which has a base shape close to a parabola, as a result of the compliance of the unsupported formwork. The uncertain shape of the foundation base and the crude preparation of the foundation soil, prior to the foundation placement, are expected to form contact imperfections at the soil-foundation interface. These imperfections are envisaged to affect the response of the SSI system as well as its natural frequencies.

The natural frequencies of the examined SSI systems as well as the corresponding fixed-base systems are affected by structural connections, in addition to the impact of the already mentioned interface conditions. The natural frequencies are expected to be more sensitive to the column-slab connections which carry a substantial proportion of the moment loading during structural oscillation, than the axially loaded column-brace connections. The column-slab connection behaviour can be inferred from single column, cantilever, lab tests (Pitilakis et al., 2012) that were carried out prior to the construction of the structure. These tests, which include static lateral force and free vibration tests, aimed to establish the stiffness, natural frequency and damping of the cantilever.

The lab test configuration, which Is depicted in Figure 5.6a, comprised a column identical to the EUROPROTEA'S columns. The column was fixed at its lower end via the bolted connection shown in Figure 5.6b, while the top of the column was free, forming a cantilever. For the static lateral force tests, a horizontal force was incrementally applied either along the X or Y directions on the top of the column. During these tests, the force and the displacement of the top of the column were monitored producing the force-displacement curves shown in Figure 5.7. Once the lateral static applied force reached the value of 6kN, the force was instantaneously released allowing the cantilever column to vibrate freely. The displacement time histories recorded at the top of the column and the Fourier Spectra inferred from the free vibration tests are shown in Figure 5.8.

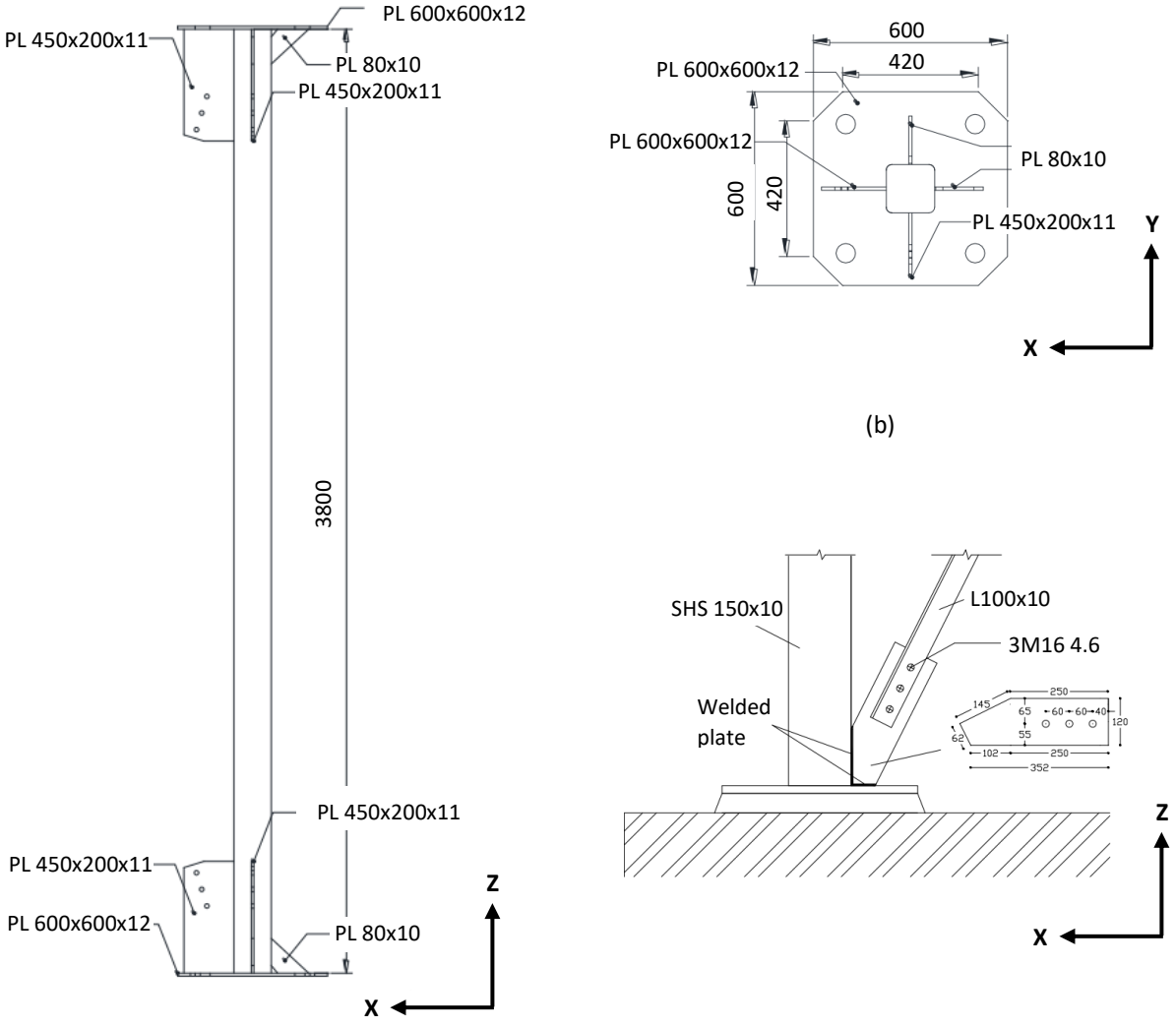


Figure 5.6: Experimental configuration of the single-column lab tests. (a) Steel column-foundation and steel column-steel brace connection in front view, (b) steel column-foundation connection in plan view, (c) detail of steel column-steel brace connection in front view. All dimensions are in mm units. (Pitilakis et al., 2012).

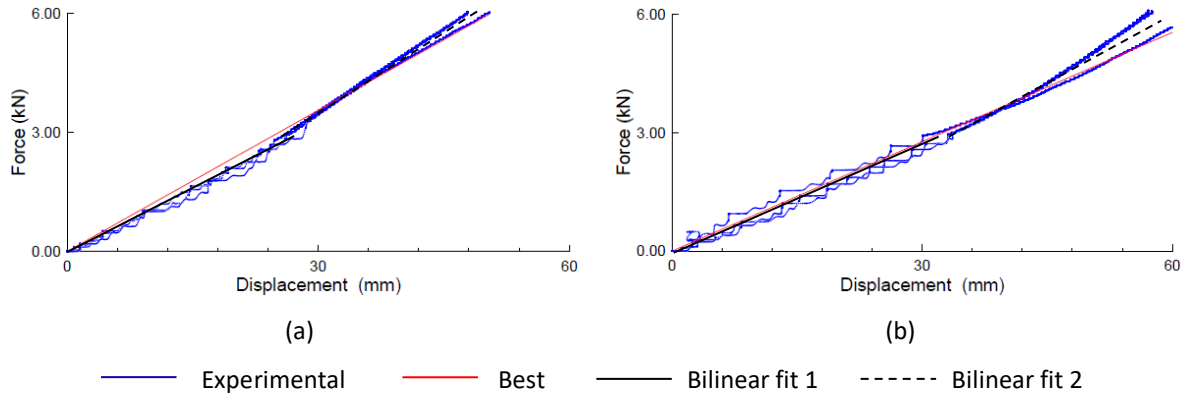


Figure 5.7: Force-Displacement curves resulted from the static lateral force tests when the force was applied along (a) X-diretion and (b) Y-direction (Pitilakis et al., 2012).

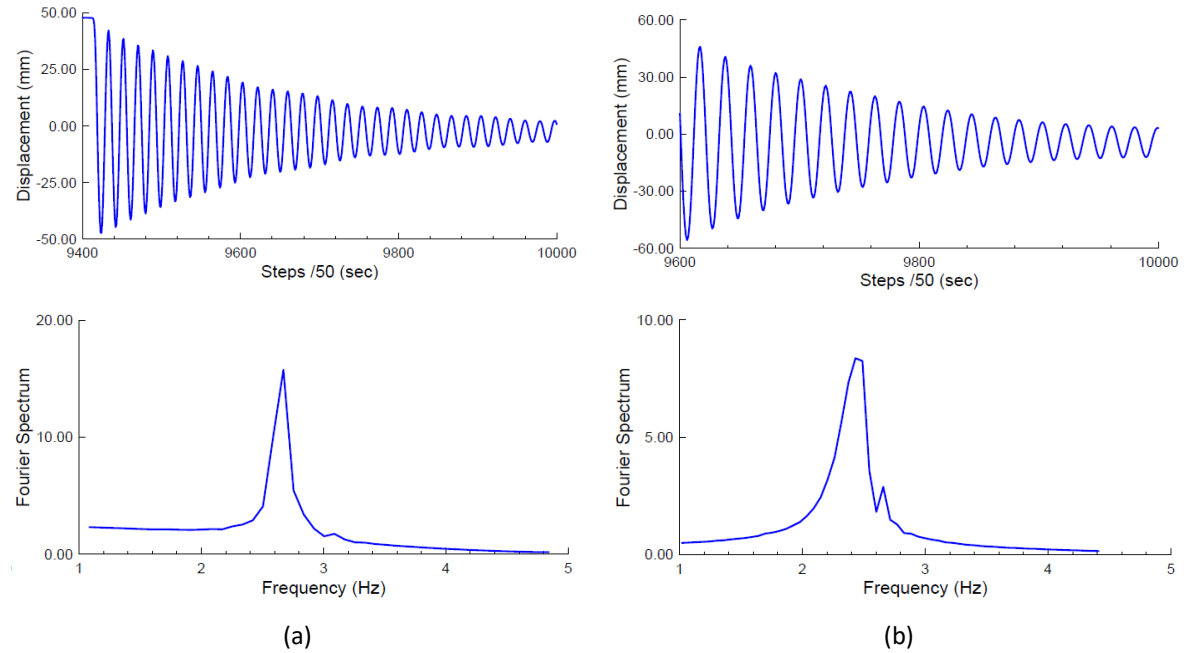


Figure 5.8: Displacement time histories and the corresponding Fourier Spectra recorded on the top of the column during the single column free vibration tests. Initial excitation was applied along the (a) X-direction and (b) Y-direction (Pitilakis et al., 2012).

The force-displacement curves resulted from the static lateral force tests, shown in Figure 5.7, did not produce a constant force to displacement ratio, indicated by the slope of the curve. A bilinear fit matches the experimental data better than the best fit which has a constant slope, as shown in Figure 5.7. The stiffness of the cantilever, which is equivalent to the force to displacement ratio, was not constant, instead, it increased when the applied force approached 3kN. This increase of stiffness can be attributed to the compliance of the connection between the column's lower end and the base. The connection, possibly, was softer at the beginning of the experiment, but it hardened for larger applied

lateral force. The two stiffness values estimated from the slope of the bilinear fit differ between the experiments during which the force is applied along the X and Y directions. This stems from the fact that the connection designed at the ends of the column is not completely symmetric.

The stiffness of the column can also be estimated from the free vibration tests carried out. The cantilever stiffness can be back calculated using the experimental natural frequency inferred from the Fourier spectra (Figure 5.8) and by employing the Eqs. 5.2 and 5.3. Eq. 5.2 defines the natural frequency (F_1) of a fixed-base cantilever with distributed mass m, density ρ, cross sectional area A, length L, Young's modulus E and bending moment of inertia I (Chopra, 2011). The stiffness of the same fixed-base cantilever is defined as per Eq. 5.3.

$$F_1 = 1/2\pi \times 3.516 \times \sqrt{\frac{EI}{mL^4}} \ , \ m = \rho_{steel} \times A \qquad 5.2$$

$$K_{c,fixed} = \frac{3EI}{L^3} \qquad 5.3$$

where, L=3.8m and the remaining properties were assumed according to the Eurocode 3 (British Standards Institution, 2005) as follows: E=200Gpa, ρ=7.85Mgr/m^3, A=54.9cm^2 and I=1770cm^4.

The Fourier spectra (Figure 5.8) which resulted from the free vibration tests indicate F_1 equals to 2.7Hz and 2.4Hz for initial excitations acting along the X and Y directions, respectively. By employing the Eq. 5.2, EI can be back-calculated (209kNm^2 and 165kNm^2 for the two tests) and then substituted to the Eq. 5.3 to estimate the stiffness of the cantilever, under free vibration.

The present study computes the stiffness of the cantilever based on different assumptions, as shown in Table 5.2 Assuming a perfectly symmetric fixed-base cantilever, the stiffness is estimated by employing the Eq. 5.3. The stiffness of the cantilever is also back-calculated from the static lateral force tests, inferred from the slope of the force-displacement curves (Figure 5.7). Three stiffness values are presented for each test, the stiffness of the cantilever at the beginning of the tests (Bilinear Fit 1), the stiffness at the mid to end stages of the tests (Bilinear Fit 2) and the stiffness inferred from the best fit curve. Finally, the stiffness of the cantilever is also back-calculated from the free vibration tests by following the procedure described above.

Table 5.2: Stiffness values of EUROPROTEA'S column, in kN/m units, assumed fixed at its base and as back-calculated from static lateral force and free vibration tests.

	Fixed-base cantilever	Static lateral force test			Free Vibration test
		Bilinear Fit 1	Bilinear Fit 2	Best Fit	
Loaded along the X-direction	193.5	106.2	134.7	118.6	11.4
Loaded along the Y-direction	193.5	90.7	116.4	92.2	9.0

It is evident from Table 5.2 that the back-calculated stiffness of the cantilever is much lower than the stiffness of the equivalent fixed-base cantilever. Assuming that the Young's modulus and the bending moment of inertia of the column do not deviate substantially from the nominal values presented earlier, this difference stems from the compliance of the column-base connection. The column cannot be considered fixed at the base, instead, it should be considered as a cantilever founded on a rotational spring. The horizontal stiffness of a rigid cantilever ($K_{c,spr,rigid}$) founded on a rotational spring of stiffness K_θ can be estimated as per Eq. 5.4a (Chopra, 2011). For a compliant beam over a rotational spring, the beam's stiffness ($K_{c,spr}$) and the stiffness contributed by the spring ($K_{c,spr,rigid}$) act in a row. Therefore, the stiffness $K_{c,spr}$ of a compliant cantilever founded on a rotational spring of stiffness K_θ can be estimated by employing Eq. 5.4b. Table 5.3 presents the K_θ values that are back calculated from the static lateral force and free vibration tests. The K_θ inferred from the different experiments cover a very wide range of values, making the conclusion of a single stiffness value impossible.

$$K_{c,spr,rigid} = \frac{K_\theta}{L^2} \quad 5.4a$$

$$\frac{1}{K_{c,spr}} = \frac{1}{K_{c,fixed}} + \frac{1}{K_{c,spr,rigid}} = \frac{1}{K_{c,fixed}} + \frac{L^2}{K_\theta} \quad 5.4b$$

Table 5.3: Stiffness of the rotational spring at the base of the cantilever K_θ (kNm/rad).

	Static lateral force test			Free Vibration test
	Bilinear Fit 1	Bilinear Fit 2	Best Fit	
Loaded along the X-direction	3400	6400	4424	175
Loaded along the Y-direction	2465	4218	2543	136

The above-described cantilever lab tests were not conclusive regarding the stiffness of the cantilever column, as well as the stiffness of the connection between the column and the base that existed in the lab. Therefore, the exact stiffness of the connections between EUROPROTEA'S columns and reinforced concrete slabs remains unknown. This also creates uncertainty about the fixed-base natural frequencies of the different EUROPROTEAS structural configurations that were examined for the purpose of this study.

5.2.5 Fixed-base dynamic characteristics of the examined structural configurations

The structural configurations, described in Section 5.2.2, have different fixed-base natural frequencies as a consequence of their different dynamic characteristics, structural stiffness and/or superstructural mass. The calculation of the fixed-base natural frequencies requires assumptions regarding the uncertainties about the compliance of the column-slab connections and the imperfect symmetry of the structural geometry, which were discussed in Section 5.2.4. For simplicity, it is assumed that the

structures are perfectly symmetric and the connections are rigid, acknowledging that these assumptions may result in larger fixed-base frequencies than the actual ones.

Based on the above assumptions, Pitilakis et al. (2018) carried out 3D FE modal analyses on fixed-base models to estimate the uncoupled swaying natural frequencies of the FBr_2Ts, FBr_1Ts and fully unbraced structures (the latter is not examined herein). These frequencies ranged from 1.78Hz to 13.06Hz for the different structural configurations. The largest swaying natural frequency, 13.06Hz, corresponds to the FBr_1Ts structure, while the natural frequency of the FBr_2Ts structure was computed at 9.13Hz. The fully unbraced structure is the most flexible one, hence its swaying natural frequency is the smallest, 1.78Hz. Similar analyses were carried out by Pitilakis et al. (2014) which estimated the torsional natural frequency of the FBr_2Ts structure to be around 11.87Hz.

It is noted that the swaying natural frequencies of the fully braced and fully unbraced structures, correspond to both swaying modes, due to their symmetry. However, symmetry was not the case for the partly braced (PBr) structural configuration, as the structural stiffness was very different between two perpendicular planes. Braces existed at the North (N) and South (S) sides of the structure only, acting along the East-West (EW) structural motion (orientation is compatible with Figure 5.2). Although the natural frequencies of the PBr configuration were not numerically computed, they can be estimated using the modal frequencies computed for the fully braced and fully unbraced structures with two top slabs. Assuming a perfectly symmetric structure and uncoupled swaying modes, it is inferred that, during a swaying mode, the braces acting perpendicular to the motion do not contribute to the stiffness of the structure. The implication of this is that the NS swaying mode, which is parallel to the unbraced side of the structure, engage the same structural stiffness as the swaying (NS or EW) oscillation of the fully unbraced structure. Similarly, the EW swaying mode of the PBr structure, which is along the planes were braces act, engage the same structural stiffness as the swaying mode of the FBr_2Ts structure. Provided that the structural mass is the same between the compared structures, the NS swaying natural frequency of the PBr structure should be equal to the swaying natural frequency of the fully unbraced structure. Likewise, the natural frequency of the EW mode equals to the swaying frequency of the FBr_2Ts structure.

In this study the natural frequencies of the swaying and torsional modes are estimated by simplifying the structures to single-degree-of-freedom (SDOF) models. The natural frequency that corresponds to the m mode of a SDOF model with stiffness $\mathrm{K_m}$ and inertial component m_m is estimated as Eq. 5.5

$$F_m = \frac{1}{2\pi} \times \sqrt{\frac{K_m}{m_m}} \qquad 5.5$$

The calculation of the natural frequencies of the swaying and torsional modes requires more assumptions, additional to the perfect symmetry and rigid column-slab connections. For the swaying mode, it is assumed that the mass (inertial component) of the SDOF model is equal to the mass of the superstructural mass ($\mathrm{m_s}$). For the estimation of the mass, the unit weight of the reinforced concrete slabs is assumed to be $25\mathrm{kN/m^3}$. The stiffness of the structure is estimated as the sum of the horizontal stiffness of the four columns and the horizontal stiffness provided by the braces. It is assumed that only the in-plane braces, which act in the direction of the deformation mode (either North-South or East-West), provide stiffness to the structure, while the stiffness of the out-of-plane braces are neglected. The horizontal stiffness of each column having both ends clamped ($\mathrm{K_{h,column}}$), Young's modulus E, bending moment of inertia I and heigh h is estimated by the Eq. 5.6. Eq. 5.7 is used for the estimation of the horizontal stiffness of each brace ($\mathrm{K_{h,brace}}$), where a is the angle between the brace and the horizontal axis (Chopra, 2011). The total stiffness of the structure under the swaying mode of oscillation ($\mathrm{K_{swaying}}$), for the fully and partly braced structural configurations, is calculated by employing Eq. 5.8

$$\mathrm{K_{h,column}} = \frac{12\mathrm{EI}}{\mathrm{h^3}} \tag{5.6}$$

$$\mathrm{K_{h,brace}} = \frac{\mathrm{EA}}{\mathrm{L}} \cdot \cos^2(\mathrm{a}) \tag{5.7}$$

$$\begin{aligned} \mathrm{K_{swaying,FBr}} &= 4 \times (\mathrm{K_{h,column}} + \mathrm{K_{h,brace}}) \\ \mathrm{K_{swaying,PBr_W}} &= 4 \times (\mathrm{K_{h,column}}) \\ \mathrm{K_{swaying,FBr_S}} &= 4 \times (\mathrm{K_{h,column}} + \mathrm{K_{h,brace}}) \end{aligned} \tag{5.8}$$

For the calculation of the torsional natural frequency of the fixed-base structural configuration of EUROPROTEAS, the inertial component is assigned to the top slab moment of inertia ($\mathrm{I_0}$) about the axis that is normal to the slab and passes through the centre of mass. The moment of inertia of a slab with distributed mass $\mathrm{m_s}$ and dimensions a x b, in plan, is defined in Eq. 5.9. The torsional stiffness of the structure ($\mathrm{K_\theta}$) is defined as the stiffness that resists the torsional response of the top slab produced by each column ($\mathrm{K_{\theta,column}}$) and brace ($\mathrm{K_{\theta,brace}}$). $\mathrm{K_{\theta,column}}$ and $\mathrm{K_{\theta,brace}}$ are equivalent to the resulting forces of a column or brace when the top slab is excited by a rotation of 1^{rad}. The latter deformed shape of a slab is depicted in Figure 5.9, that also illustrates the origin of the coordinate system (Oxy) placed at the centre of the slab. For a column and a brace with symmetric cross-sectional area and coordinates (x, y), $\mathrm{K_{\theta,column}}$ and $\mathrm{K_{\theta,brace}}$ can be estimated by employing the Eqs. 5.10 and 5.11, respectively. For a structure with symmetric stiffness, which is the case for EUROPROTEAS, the centre of rotation coincides with the centre of mass of the top slab. The total torsional stiffness of the structure ($\mathrm{K_\theta}$) equals to the sum of all stiffness components that are produced by all columns and

braces. It is noted that only the half of the braces (4) contribute to the torsional stiffness of the structures, as the forces produced by the remaining braces, during top slab rotation, cancel out. Following the above assumptions, Eq. 5.12 defines $\mathrm{K_\theta}$ for the examined fully and partly braced configurations of EUROPROTEAS.

$$I_0 = \mathrm{m_s} \times \frac{a^2 + b^2}{12} \tag{5.9}$$

$$\mathrm{K_{\theta,column}} = x^2 K_{x,column} + y^2 K_{y,column} = K_{h,column} \times (x^2 + y^2) \tag{5.10}$$

$$\mathrm{K_{\theta,brace}} = x^2 K_{x,brace} + y^2 K_{y,brace} = K_{h,brace} \times (x^2 + y^2) \tag{5.11}$$

$$\begin{aligned} \mathrm{K_{\theta,FBr}} &= 4 \times K_{\theta,column} + 4 \times \mathrm{K_{\theta,brace}} \\ \mathrm{K_{\theta,PBr}} &= 4 \times K_{\theta,column} + 2 \times \mathrm{K_{\theta,brace}} \end{aligned} \tag{5.12}$$

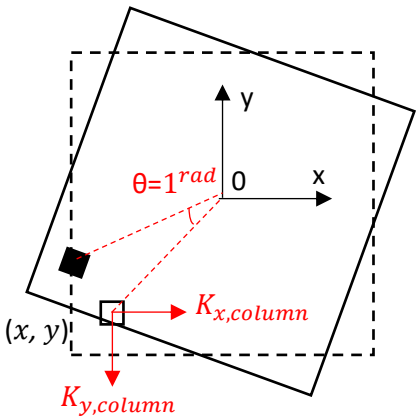


Figure 5.9: Plan view of a structure subjected to torsional rotation of 1^{rad} and the resultant forces produced by a column.

Table 5.4 presents the geometric quantities of the structural components of EUROPROTEAS as well as their nominal elastic properties according to Eurocode 3 (BS EN 1993-1-1:2005). These properties are substituted into Eqs. 5.6 to 5.12 to calculate the inertial (m_m) and stiffness (K_m) components of the equivalent SDOF models. The inertial components, the individual stiffness of columns and braces, as well as the total stiffness of the fixed-base EUROPROTEAS configurations, are shown in Tables 5.5, 5.6 and 5.7 respectively.

Table 5.4: Geometric quantities and nominal elastic properties of columns and braces according to Eurocode 3 (BS EN 1993-1-1:2005).

			Column			Brace			Slab
$\mathbf{E_{steel}}$ $(\mathbf{GPa})$	$\boldsymbol{\rho_{steel}}$ $(\mathbf{Mgr/m^3})$	$\boldsymbol{\rho_{concrete}}$ $(\mathbf{Mgr/m^3})$	**h** $(\mathbf{m})$	**I** $(\mathbf{cm^4})$	**A** $(\mathbf{cm^2})$	**L** $(\mathbf{m})$	**θ** $(\mathbf{rad})$	**x, y** $(\mathbf{m})$	**a, b** $(\mathbf{m})$
200	7.85	2.5	3.8	1770	19.2	4.23	1.12	1	3

Table 5.5: Inertial components (m_m) of the examined structural configurations.

Structural configuration	Swaying mode $\mathbf{m_s}$ $\mathbf{(Mgr)}$	Torsional mode $\mathbf{I_0}$ $\mathbf{(Mgr \cdot m^2)}$
FBr_2Ts	18	27
FBr_1Ts	9	13.5
PBr_W	18	27
PBr_S	18	27

Table 5.6: Stiffness of individual columns and braces.

Column		Brace	
$\mathbf{K_{h,column}}$ $\mathbf{(kN/m)}$	$\mathbf{K_{\theta,column}}$ $\mathbf{(kNm)}$	$\mathbf{K_{h,brace}}$ $\mathbf{(kN/m)}$	$\mathbf{K_{\theta,brace}}$ $\mathbf{(kNm)}$
774	1548	17408	34817

Table 5.7: Total stiffness of the examined fixed-base EUROPROTEAS configurations

Structural configuration	Swaying mode $\mathbf{K_{swaying}}$ $\mathbf{(kN/m)}$	Torsional mode $\mathbf{K_\theta}$ $\mathbf{(kNm)}$
FBr_2Ts	72731	284730
FBr_1Ts	72731	284730
PBr_W	3097	145461
PBr_S	72731	145461

Table 5.8: Fixed-base natural frequencies of the four structural configurations computed either numerically or analytically based on SDOF assumption.

Structural configuration	Swaying mode				Torsional mode	
	Numerically estimated by Pitilakis et al. (2018)		SDOF assumption		Numerically estimated by Pitilakis et al. (2014)	SDOF assumption
	NS	EW	NS	EW		
FBr_2Ts	9.13	9.13	10.12	10.12	11.87	11.68
FBr_1Ts	13.06	13.06	14.31	14.31	n/a	16.52
PBr	1.78*	9.13**	2.09	10.12	n/a	8.43

* This value was numerically estimated by Pitilakis et al. (2018) for a fully unbraced structure and assumed to be equal for the NS mode of the PBr structure. For simplicity, it is assumed that the braces acting perpendicular to the motion, in a case of a purely unidirectional swaying mode, do not contribute to the stiffness of the structure.

** Considering the above assumption, the PBr structure is envisaged to have the same fixed-base natural frequency with the FBr_2Ts, considering the EW swaying mode of oscillation.

Table 5.8 presents the swaying and torsional natural frequencies of the three fixed-base structural configurations that were subjected to free and/or forced vibration tests, for the purpose of this research. For the case of fully symmetric structures (FBr_2Ts and FBr_1Ts), the natural frequencies of the NS and EW modes are assumed to coincide. As already mentioned, these were estimated numerically (Pitilakis et al., 2014, 2018) and analytically by simplifying the structures to SDOF models (Eq. 5.4). The two methods give very similar swaying and torsional natural frequencies, which validates the results. It is noted that the natural frequencies presented in Table 5.8 are upper bound values, as the rigid column-slab connection and perfect structural symmetry assumptions indicate stiffer structures than the actual ones.

5.3 Instrumentation

5.3.1 Vibrator characteristics

Forced vibration tests were carried out by means of an MK-500U (ANCO Engineers Inc) eccentric mass vibrator system (Figure 5.10a), provided by the Institute of Engineering Seismology and Earthquake Engineering (ITSAK-EPPO) (Salonikos *et al.*, 2005). The vibrator can apply horizontal unidirectional sinusoidal forces. The frequency of the sinusoidal force can be manually controlled, using a Toshiba VF-S9 adjustable speed drive (Figure 5.10b). The vibrator generates the forces by rotating two shafts, one clockwise and one anticlockwise. The shafts carry plates of which centre of mass is eccentrically placed from the centre of rotation of the shaft (NERA, 2014). The rotating masses produce centrifugal forces (F_{centr}), the x-components (F_x) of which cancel out, while the sum of the y-components (F_y) gives the total applied force. The magnitude of the applied force is a function of the masses that are carried by the rotating shafts, the eccentricity of the masses relative to the centre of rotation and the input frequency. Figure 5.11 illustrates the resultant forces for a vibrator system of which plates of mass, m, rotate at an eccentric distance, e, from the centre with an angular frequency, ω.



(a)



(b)

Figure 5.10: (a) Vibrator in plan view, (b) Toshiba VF-S9 adjustable speed drive.

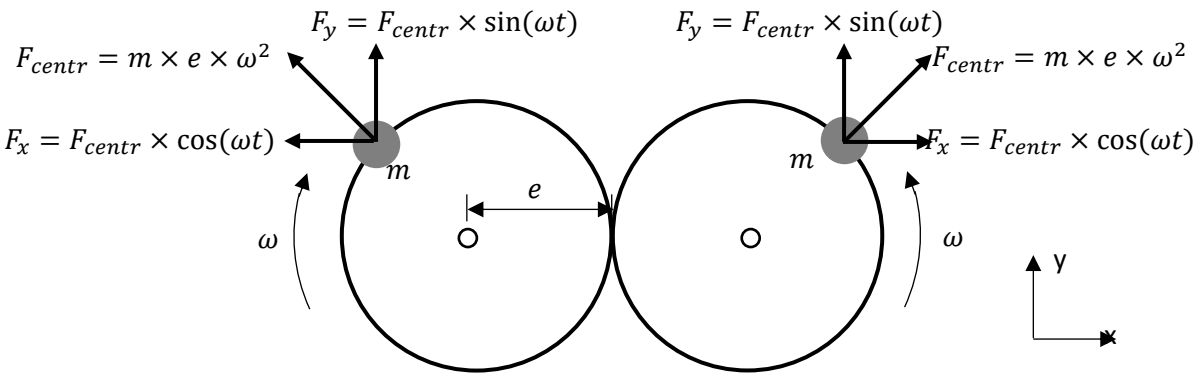


Figure 5.11: Illustration of the vibrator's masses rotation and the resultant forces (NERA, 2014).

The total unidirectional force, as a function of time (t), is given by:

$$F(t) = 2 \times m \times e \times \omega^2 \times sin(\omega t) \quad 5.13$$

The amplitude of the sinusoidal force is therefore calculated using the following equation (Pitilakis *et al.*, 2013):

$$F = E \times (2\pi f^2) \quad 5.14$$

where, F is the amplitude in N, f in Hz is the input frequency to which masses rotate and E is the total eccentricity of the vibrator in Kg·m. E is a function of the vibrator geometry and the mass of the rotating plates.

The MK-500U eccentric mass vibrator, that was used during the forced vibration experiments of the current study, is equipped with 4 pairs of plates of different masses (A, B, C, D) that can adjust the vibrator's total eccentricity. Each shaft can carry either plate A only (mA); A and B (mB); A, B and C (mC); or all four plates (mD). Table 5.9 presents the total eccentricities for the four combinations of plates that can be placed on each shaft. The vibrator can operate between 0.1 and 20Hz and can apply a maximum force of 50kN (Pitilakis et al., 2018). The maximum frequency that can be applied for mA experiments is 20Hz, while it is 10.5Hz for mD experiments. Figure 5.12 presents the magnitudes of the sinusoidal forces that can be produced by the vibrator for each plate combination.

Table 5.9: Total vibrator eccentricity for each combination of plates that can be placed on each shaft.

Vibrator mass name	**Plates on each shaft**	**Total eccentricity E (Kg·m)**
mA	A	1.85
mB	A+B	3.93
mC	A+B+C	6.93
mD	A+B+C+D	11.31

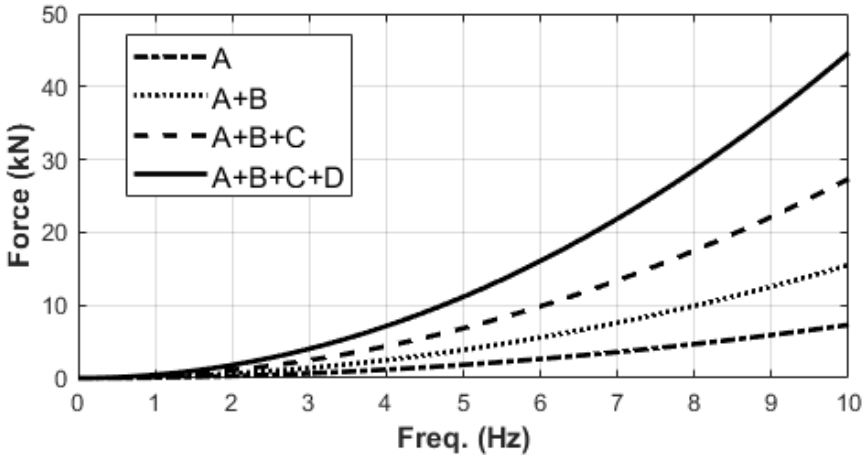


Figure 5.12: Magnitudes of the applied sinusoidal force for each plate combination placed on the vibrator.

For the current experimental campaign, all four combinations of plates that can be adjusted on the vibrator were employed. This allowed the examination of the soil-structure response under the same frequency but different load magnitude and the investigation of non-linear behaviour of the system with increasing load. The vibrator was mounted at the centre of the top slab, so that the force is applied at the centre of mass and rotation, acting along one of the two axes of symmetry of the structures (Figure 5.2). The vibrator applied sinusoidal unidirectional forces along either of two perpendicular directions, which were manipulated to coincide with the two axes of symmetry of the structure. The loading direction was selected by the appropriate adjustments to the orientation of the rotating shafts, without the need of rotating the vibrator itself. This study made use of this flexibility of the vibrator for the specific experiments in which the stiffness of the examined structural configuration was not the same along its two main axes. Such a case were the experiments on the partly braced structure, during which the soil-structure system response was examined under vibratory loads that were acting either along the weak or strong axis of the structure, as shown in Figure 5.2.

5.3.2 Pull-out system

Prior to the free vibration of the structures, a static pull-out force was applied incrementally on the top slab along the South direction, as shown in Figure 5.3. The force was applied by a wire rope-pulling hoist-counterweight system. The wire rope connected the top slab with the pulling hoist, while the latter was connected to a buried mass of concrete which acted as a counterweight to resist sliding of the hoist (Figure 5.13a). The pulling hoist, which has a working limit of 32kN (Pitilakis et al., 2018), applied tension forces to the wire rope, which are transferred as pull-out forces on the top slab. The forces were measured in-situ by a Z-beam tension load cell of 50kN working limit (Pitilakis et al., 2018). The load cell was attached between the wire rope and the top slab, while the wire rope was linked to

the pulling hoist via a weaker “sacrificed” wire rope (Figure 5.13b). The maximum applied force was 16kN, as it was determined by the nominal strength of the “sacrificed” wire ropes.

When the magnitude of the pull-out force reached a desired value, then the “sacrificed” wire rope was cut manually instantaneously (as much as practically possible), and the structure was free to oscillate until rest. The Z-beam tension load cell enabled real-time monitoring of the applied load variations. Observing the output of the instrument, it became possible to discern whether the wire cut resulted in an immediate load release. In instances where the load release was not deemed instantaneous, the experiment was excluded and subsequently repeated. In other cases, the tensioned force measured by the load cell was fluctuating because of the oscillation of the wire, stress relaxation, sliding of the wire or progressive yielding of the wire. Aiming to increase the reliability of the tension force measurement, it was important to allow the measurement to converge to a constant value before cutting the wire. Likewise, in some cases during the experiments, the “sacrificed” wire rope failed in tension without being cut due to its low strength. These cases were also disregarded.

Figure 5.14 illustrates the geometry of the pull-out system. The counterweight and the pull-out mechanical tool were located 27m South from the structure. The pull-out forces were imposed on the middle of the lower top slab, at a height of 4.4m from the ground surface. They were applied towards the South direction at an angle of 9° and were acting along the plane of symmetry of the structure.



(a) (b)

Figure 5.13: Pictures of (a) Pulling hoist connected to the counterweight and (b) “Sacrificed” wire ropes.

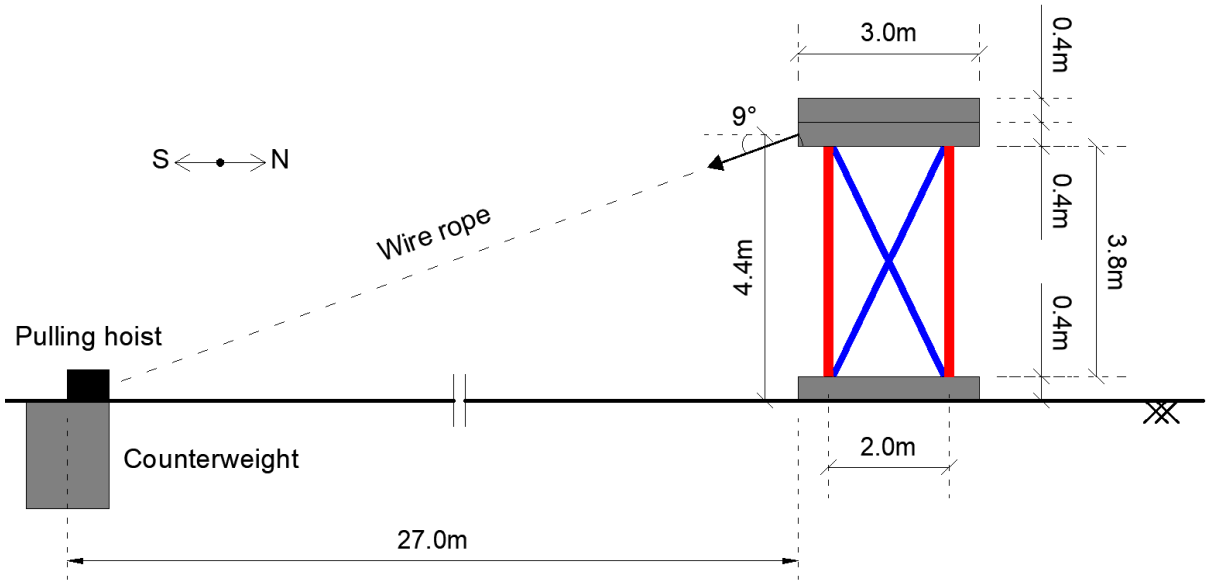


Figure 5.14: Schematic illustration of free vibration system.

5.3.3 Available monitoring instrumentation and installation

During the free and forced vibration experiments, the response of the soil-structure system was monitored by a comprehensive instrumentation placed on the structure and the soil surface. In total, during the first suite of experiments (April 2019), there were 9 triaxial accelerometers (4 CMG-5TCDE and 5 CMG-5T type) that were mounted on the structure, 13 seismometers (7 CMG-6T and 6 CMG-10 type) that monitored the soil surface motion and one downhole accelerometer (CMG-5TB). During the second suite of experiments (October 2019), 9 accelerometers (3 CMG-5TCDE and 5 ETNA2 type) and 6 seismometers (CMG-40 type) were used to record the structural and soil surface motions respectively. All instruments were manufactured by Guralp systems Ltd, with the exception the ETNA2 accelerometers which were manufactured by Kinemetrics. The CMG-5TCDE type accelerometers and CMG-40 type of seismometers were made available by the Research Unit of Soil Dynamics and Geotechnical Earthquake Engineering of Aristotle University of Thessaloniki (SDGEE-AUTH). The CMG-5T type of accelerometer, CMG-6T type of seismometer, CMG-5TB type of borehole accelerometer were provided by ITSAK.

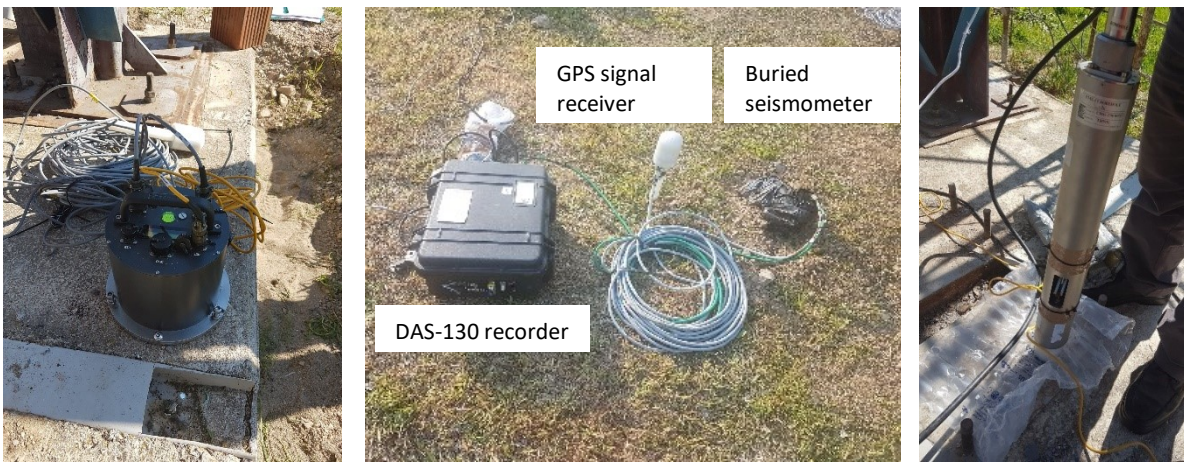
The accelerometers were clamped on the reinforced concrete slabs (Figure 5.15a) to ensure zero compliance of the instrument itself, while the seismometers, CMG-40 type, were buried into the ground (Figure 5.15b). For each seismometer, a 30cm deep hole was excavated, where the instrument was placed. Then, the cavity around the instrument was filled with the excavated soil, which was densified manually by applying a pressure on the top. This installation process aimed to retrieve the in-situ soil conditions around the seismometer and achieve a good adhesion between the instrument and surrounding soil. Both the seismometers and accelerometers were oriented towards the North

and it was ensured that they were placed vertically. Also, all instruments were operating at a sampling frequency of 200Hz and connected to a common global positioning system (GPS) antenna to ensure time consistency and synchronization between each other.

In addition to the soil seismometers and structural accelerometers, a triaxial sensor downhole accelerometer (Figure 5.15c) was placed in a cased borehole below the foundation centre. Once the sensor, which was located within the first 40cm from the top of the metal cube of the instrument, reached the desired depth, then the instrument was clamped on the wall of the borehole via a single-jaw hole lock unit. The single-jaw hole lock unit existed between the brown colour tapes shown in the Figure 5.15c. The borehole was also used to determine the water table depth, which was measured to be 0.80m below the ground surface during the experiments.

5.3.4 Data acquisition system

Data recorded by the accelerometers (CMG—5TCDE and CMG-5T) and the MG-6T seismometers were monitored in-situ in real time during the experiments, as they were connected to a computer. Their recordings were also stored in an internal digitizer. This feature of the instruments was particularly important as it enabled the inspection of the records and identification of faulty instruments during the experiments. The data recorded by the CMG-40 seismometers, though, could be only interpreted after the completion of the experiments. Their records were saved in external hard-disc, DAS-130 recorder (Pitilakis et al., 2018), shown in the Figure 5.15b, from where they could be retrieved.



(a) (b) (c)

Figure 5.15: Pictures of the instruments used during the experiments: (a) accelerometer clamped on the foundation slab, (b)seismometer buried into the ground, and (c) downhole accelerometer.

5.4 Raw data conversion

Raw data, recorded by the instruments during the experiments were retrieved by the means of the data acquisition system as described in 5.3.4. The data conversion process includes the conversion of the *Raw* data to *Converted* and *Synchronised* data through a process that was carried out by SDGEE-AUTH, as described in Pitilakis et al. (2018). The *Raw* data retrieved from the accelerometers and seismometers were in counts and volts units respectively. These data were baseline corrected and by following a calibration procedure given by the manufacturer were converted to data with engineering units (m/s^2, m/s). A 4th order Butterworth bandpass filter with 0.02Hz and 50Hz lower and higher cut-off frequencies was then applied to the data, forming the *Converted* data. The *Converted* data inferred from the CMG-40 type seismometers had a different starting time, conventional "time zero", to the rest of the instrumentation which had a common GPS time. Within this context, the *Converted* data inferred from the different types of instruments were synchronised to a common GPS time, so that the "time zero" of all instruments was identical.

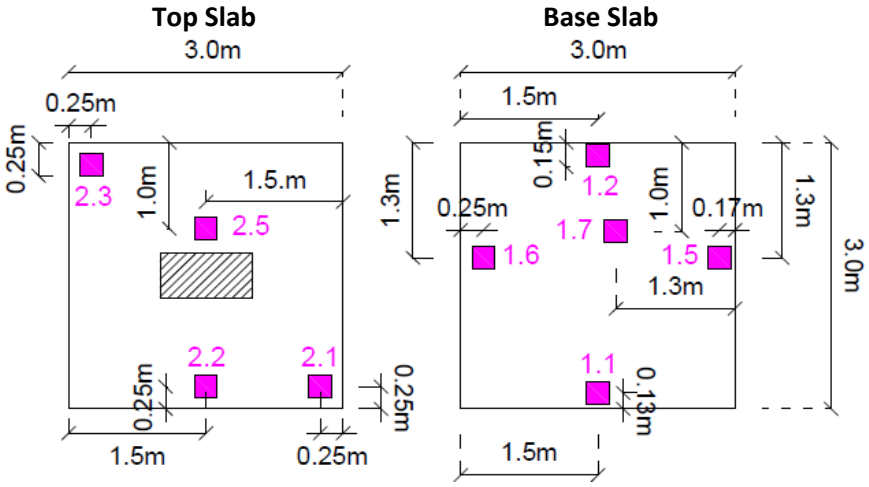
5.5 Conception of the test set-up and experimental procedures

The forced and free vibration experiments were designed so that the Dynamic Soil-Structure-Interaction (DSSI) effects can be studied comprehensively. The study includes the identification of the natural frequencies of each of the examined soil-structure configurations (Figures 5.2 and 5.3), their corresponding deformation mode and damping of the system. The experiments also aim to study the transmission of the motion from the foundation to the soil at different applied load magnitudes and frequencies, as well as the attenuation of the soil motion with distance from the foundation. Within this context, the instrument configurations and the experimental procedures, including the magnitude and frequencies of the excitation force, were designed, as discussed in the subsequent sub-sections. The locations of some instruments were also selected to facilitate the use of the recorded data in the numerical model. The design of the instrument configurations and the experimental procedures complied with the availability of the monitoring instruments and the capacity of the excitation instruments, which have been described in Sections 5.2 and 5.3.

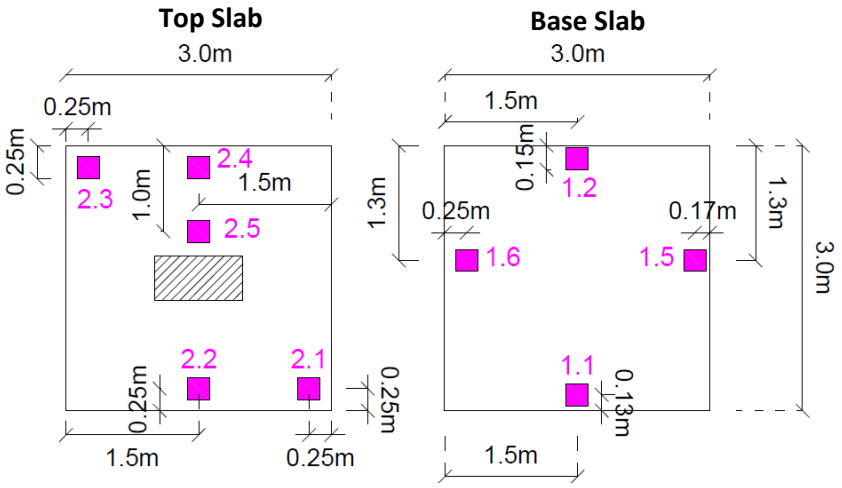
5.5.1 Structure's instrument configuration

Figure 5.16 shows the top slab and foundation slab plan views of each of the three structure's instrument configurations (I, II and III) selected during the experiments. The configuration I and II were placed during the first suite of experiments (April 2019), while the configuration III during the second suite (October 2019). Figure 5.16 also shows each instrument's distance from the slab edge and its

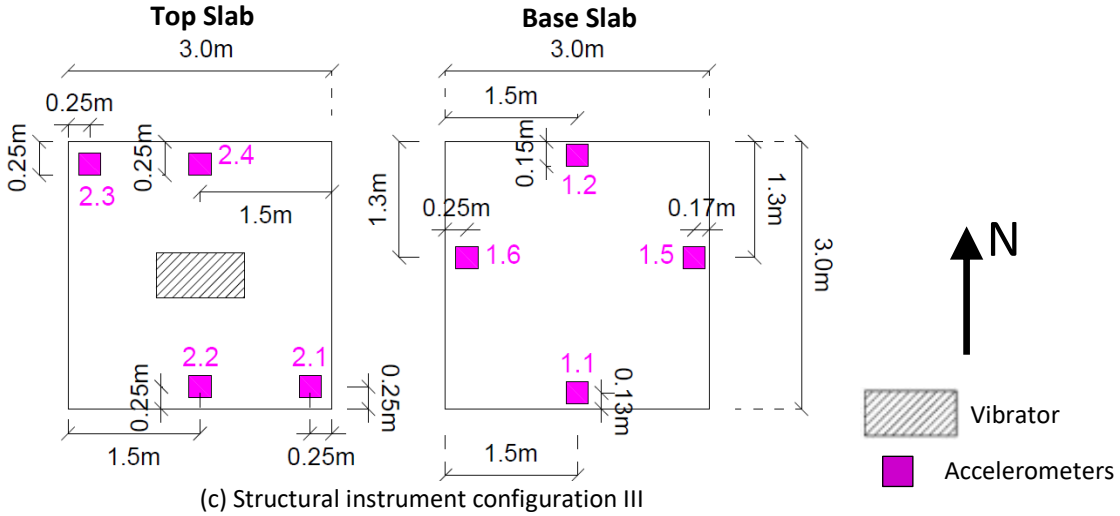
number, which is unique per instrument. For simplicity, the numbers of the top slab instruments start with "2." And foundation instruments with "1."



(a) Structural instrument configuration I



(b) Structural instrument configuration II



(c) Structural instrument configuration III

Figure 5.16: Plan views of the three structural instrument configurations

Aiming to acquire a representative motion for the two slabs, the 2.5 top slab and 1.7 base slab instruments were placed at the centre of the corresponding slabs. As discussed later in Chapter 6, these instruments were close to the centre of rotation, hence are expected to record the weakest torsional motion component, which is a consequence of experimental imperfections. Based on this, they can be considered the least prone to imperfections experimental data and hence the most comparable data with results produced by finite element and analytical computations, which are unable to model imperfections. The records of the 2.5 top slab instrument can also be used as input motion in the numerical models, facilitating the calibration of the numerical model, as it is discussed in Chapter 7.

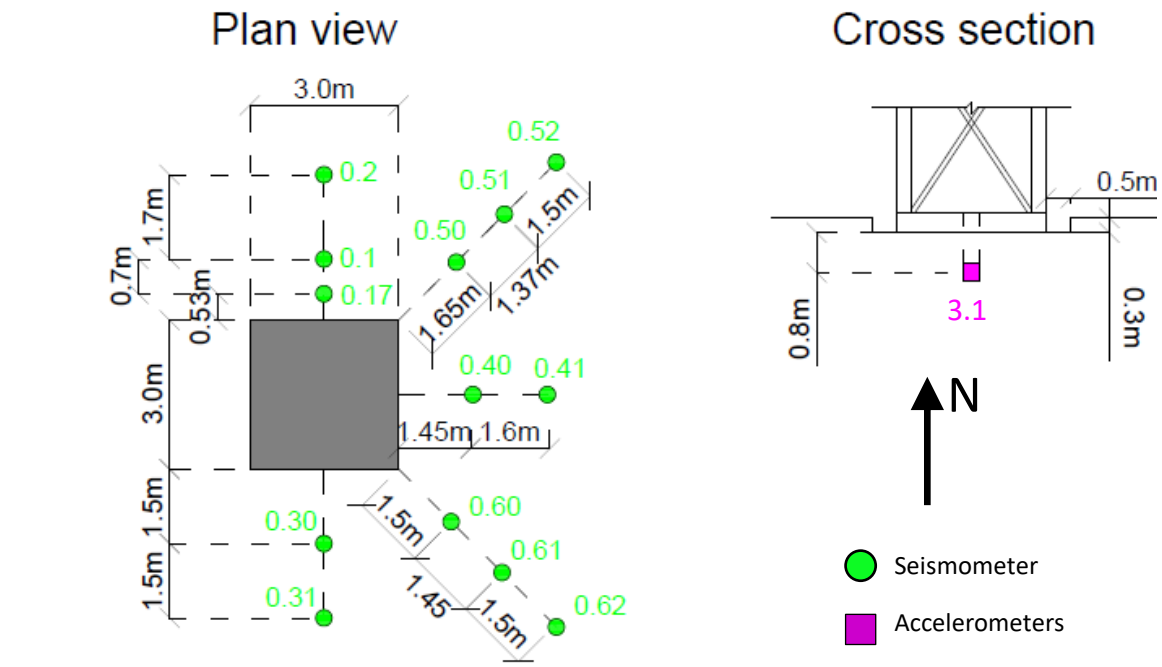
The positions of the remaining structural instruments were selected so that the deformation shape can be captured. The edge foundation instruments (1.1, 1.2, 1.5 and 1.6) aimed to capture the in-plane (North-South), out-of-plane (East-West), torsional and rocking motion of the foundation. The top slab rocking motion can be captured by exploiting the records of the edge instruments (2.1, 2.2, 2.3, 2.4, 2.5), while the 2.1 and 2.3 instruments are particularly important in capturing the torsional motion of the slab.

5.5.2 Soil instrument configuration

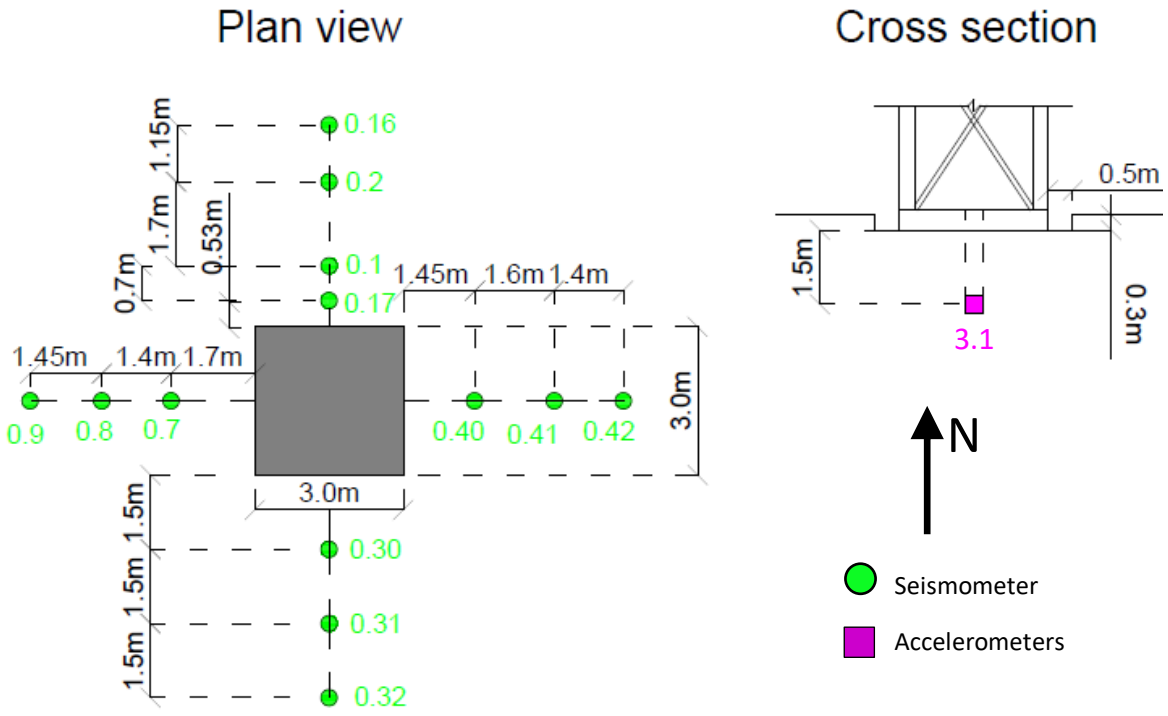
Figure 5.17 shows the four soil instrument configurations (A, B, C and D) placed during the experiments. This figure also shows each instrument's distance from the foundation edge as well as its number. The number of each soil instrument starts with "0.", while 3.1 is the number of the downhole accelerometer that is placed below the foundation edge.

Soil instrument configuration A (Figure 5.17a) aimed to record the soil surface motion near the corners of the foundation. There, the motion was anticipated to be stronger and the induced strains larger than for locations farther away from the vibrating foundation. Soil instrument configuration B (Figure 5.17b) aimed to investigate the validity of the plane strain approximation and the evaluation the potential applicability of the axis of symmetry for the numerical model. Soil instrument configuration C (Figure 5.17c) aimed to allow the assessment of the energy attenuation and soil motion decay with distance from the vibrating foundation. This configuration allowed the assessment of motion attenuation in the in-plane, out-of-plane and diagonal directions, by exploiting data recorded by instruments located North, East and North-East to the foundation, respectively. The above three soil instrument configurations were placed during the first suite of experiments (April 2019). During the second suite of experiments (October 2019), 6 seismometers were available to record the soil motion. Figure 5.17d shows the soil instrument configuration D that was placed during the second suite of experiments. This configuration aimed to capture the in and out-of-plane soil motion in the vicinity of

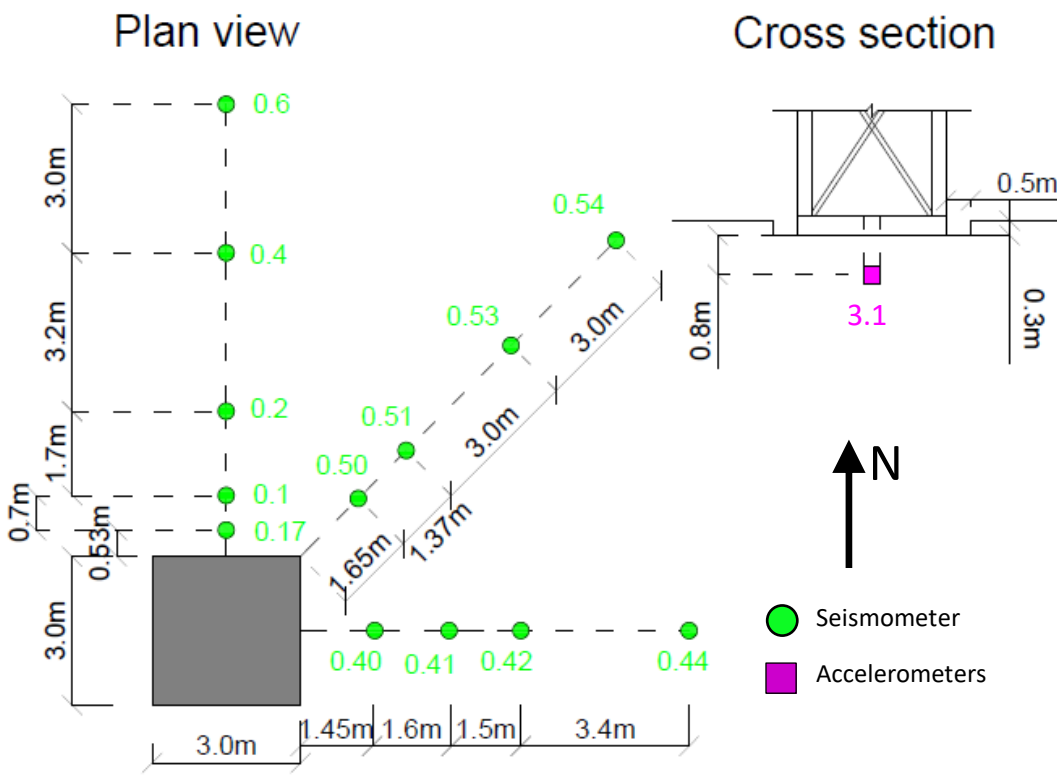
the structure, as well as to assess the in-plane (North-South) soil motion attenuation with distance from the foundation.



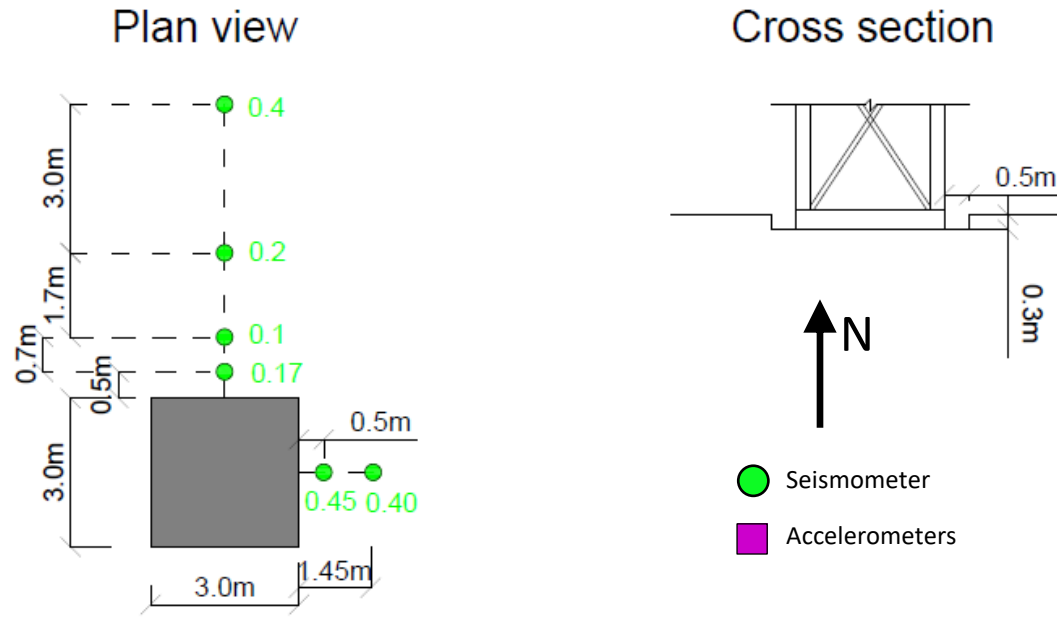
(a) Soil instrument configuration A



(b) Soil instrument configuration B



(c) Soil instrument configuration C



(d) Soil instrument configuration D

Figure 5.17: Plan views of the configurations of soil instruments placed on the soil surface. The depth of the downhole accelerometer, where available, is also shown in the cross sections.

5.5.3 Forced vibration tests

In addition to the structural and instrument configurations, the applied frequencies and the mass of plates placed on the vibrator had to be specified for the forced vibration tests. The whole range of the available applied frequencies, 1Hz to 10Hz, was covered, choosing a frequency step of 1Hz. The frequency step was refined around the anticipated resonant frequencies of the soil-structure systems. The resonances were visually identified in-situ by conducting a trial experiment prior to the recorded experiments. Similarly, all available plate mass configurations (Table 5.9) were exploited, where possible due to time and budget restrictions. This allowed the examination of each structure under the same applied frequency, but different applied load magnitude (Figure 5.12). This examination aimed to reveal the non-linear behaviour of the SSI system with increasing load magnitude, as already mentioned.

5.5.4 Free vibration tests

As discussed in Section 5.2.2, the fully braced structure with the two top slabs (FBr_2Ts) and the partly braced structure with two top slabs (PBr_W) were examined under free vibration. Both structures were initially excited along their North-South axis of symmetry (Figure 5.3), exciting statically the NS swaying mode of the structures. Exciting the structure at one of its natural modes, then the structure is free to oscillate at this mode, provided that the structure-loading system is fully symmetric (Chopra, 2011).

In addition to the selection of the structural configurations and instrument configurations, the design of the free vibration tests includes the decision about the magnitudes of the pull-out forces. The SSI response, including the resonant frequency and damping of the system, was envisaged to be different under different applied forces due to non-linear effects. As mentioned earlier, the non-linear effects that were anticipated to take place during the experiments are mainly associated with soil stiffness degradation, soil damping and foundation detachment. The influence of all these three factors was envisaged to increase with the applied force. The strains induced in the soil were expected to increase with increasing applied force, which results in higher stiffness degradation and damping development. Also, increasing the magnitude of the applied force, the rotational moment at the foundation level increases promoting foundation detachment.

Aiming to study the impact of the applied force magnitude on the resonant frequencies and damping of the SSI systems, a wide range of forces were imposed on the structure. The largest forces applied were of 16kN magnitude, complying with the limit set by the pulling hoist (see Section 5.3.2). Given this limit, the FBr_2Ts and PBr_W structural configurations were subjected to several pull-out forces within the range of 2kN to 16kN. The range of magnitudes of the forces applied were anticipated to

induce a wide range of strains in the soil, to produce different levels of foundation detachment, and therefore promote different levels of nonlinearity.

5.6 Name convention for the experiments and instruments

The name convention of an experiment includes the structural configuration according to Figure 5.3 and a superscript with the number of the experiment according to Table 5.10, which distinguishes between experiments with the same structural configuration. The structural configuration name includes the bracing system (FBr or PBr), while when referring to the fully braced structures the number of slabs is also included. The partly braced structures examined had always two top slabs, hence the number of slabs is omitted from the name of a partly braced experiment. Similarly, the direction of the loads applied on the FBr structures is not needed to be clarified, as they were always applied towards the North-South direction. When referring to the PBr structure, though, it is important to state the loading direction, which is either along the strong axis (S) or the weak axis (W) of the structure (Figure 5.3). For the forced vibration tests, the plates' mass that was placed on the vibrator is also stated in the name of the experiment, according to Table 5.9. Likewise, the name convention of a free vibration experiment includes the amplitude of the pull-out force.

For example the forced vibration FBr_2Ts$^{(5)}$_mD experiment corresponds to the experiment number 5 on the fully braced structure with two top slabs, when the A, B, C and D plates were clamped on the vibrator (mD mass combination). Likewise, the free vibration PBr_W$^{(11)}$_2.03kN experiment corresponds to the experiment number 11 during which the partly braced structure was subjected to a pull-out force of 2.03kN that was applied along the weak axis of the structure.

The names of the accelerometers and seismometers are shown in the Figure 5.16 and Figure 5.17 respectively. The name of the instruments starts with "0." For soil instruments, "1." For foundation instruments, "2." For top slab instruments, while the downhole accelerometer is named as 3.1. Every instrument has 3 sensors which record the motion along the conventional North-South (n), East-West I and vertical directions (z). For brevity, the previous directions are noted as n, e and z respectively. For example, the 2.5n data were recorded by the 2.5 top slab instrument along the North-South direction.

5.7 Summary of tests carried out

Following the above conceptualization and restriction imposed by the instrumentation and time availability, the following forced and free vibration tests were carried out. Table 5.10 lists all the experiments in the order that were carried out. The table gives details about the date, time started,

time finished and type of each experiment. The soil and structure's instrument configurations (refer to Figure 5.16 and Figure 5.17), the structural configurations and the loading directions (refer to Figure 5.2 and Figure 5.3) of each experiments are also stated.

In total, 14 sets of experiments were carried out, including 10 sets of forced vibration tests, 3 sets of free vibration tests and one ambient noise experiment which is not discussed herein. Each set of forced and free vibration experiments comprises individual experiments of different magnitude of applied force, as discussed subsequently in Sections 5.7.1 and 5.7.2 respectively.

Table 5.10: Summary of experiments carried out.

No	Experiment name	Date	Time started	Time finished	Type	Loading direction	Number of slabs	Soil instrument configuration (Figure 5.17)	Structure's instrument configuration (Figure 5.16)	Structural configuration (Figure 5.2, Figure 5.3)
exp1	FBr_2Ts[(1)]	02/04/2019	12:42:00	15:19:00	Forced Vibration	NS	2	C	I	FBr_2Ts
exp2	FBr_2Ts[(2)]	02/04/2019	16:09:00	18:00:00	Forced Vibration	NS	2	A	I	FBr_2Ts
exp3	FBr_2Ts[(3)]	03/04/2019	11:24:00	11:49:56	Free Vibration	NS	2	A	I	FBr_2Ts
exp4	FBr_2Ts[(4)]	03/04/2019	12:55:13	13:18:15	Free Vibration	NS	2	B	I	FBr_2Ts
exp5	FBr_2Ts[(5)]	03/04/2019	13:37:00	16:01:00	Forced Vibration	NS	2	B	I	FBr_2Ts
exp6	n/a	04/04/2019	10:43:00	11:00:00	Ambient noise	NS	2	B	II	FBr_2Ts
exp7	PBr_W[(7)]	04/04/2019	11:03:00	13:41:40	Forced Vibration	NS	2	B	II	PBr_W
exp8	PBr_S[(8)]	04/04/2019	11:27:00	13:24:00	Forced Vibration	EW	2	B	II	PBr_S
exp9	PBr_W[(9)]	04/04/2019	15:08:00	16:27:40	Forced Vibration	NS	2	A	II	PBr_W
exp10	PBr_S[(10)]	04/04/2019	15:21:00	16:42:40	Forced Vibration	EW	2	A	II	PBr_S
exp11	PBr_W[(11)]	04/04/2019	13:58:00	14:19:31	Free Vibration	NS	2	B	II	PBr_W
exp12	PBr_W[(12)]	05/04/2019	10:00:00	10:10:40	Forced Vibration	NS	2	C	II	PBr_W
exp13	PBr_S[(13)]	05/04/2019	10:12:00	11:25:20	Forced Vibration	EW	2	C	II	PBr_S
exp14	FBr_1Ts[(14)]	17/10/2019	-	-	Forced Vibration	NS	1	D	III	FBr_1Ts

5.7.1 Forced vibration experiments summary

Ten sets of forced vibration tests were carried out. Each set of forced vibration experiment consists of individual sub-experiments during which different mass of plates (mA, mB, mC and mD) was clamped on the vibrator (refer to Table 5.9 and Eq. 4.1) and therefore different force output was produced. During each sub-experiment, the structure was subjected to sinusoidal forces of a number of different input frequencies. Table 5.11 shows the range of applied frequencies and the total number of different applied frequencies (in brackets), for each of the forced vibration experiments carried out. All applied frequencies of all experiments as well as their duration can be found in detail in Appendix B. Each frequency was kept constant for about 30 to 60 seconds, so that the steady state motion is achieved for each frequency.

5.7.2 Free vibration tests

Three sets of free vibration experiments were carried out. Each set of experiment consists of individual sub-experiments during which forces of different magnitudes were applied on the structure. Table 5.12 lists the magnitudes of all applied forces, while date and local time of the experiments can be found in Appendix B.

Table 5.11: Range of applied frequencies for each of the forced vibration experiment carried out. The total number of different frequencies is also shown in brackets.

Exp. No	Exp. Name (Table 5.10)	mA	mB	mC	mD
exp1	FBr_2Ts(1)	1Hz-11Hz (16)	1Hz-11Hz (16)	1Hz-8Hz (15)	1Hz-8Hz (15)
exp2	FBr_2Ts(2)	1Hz-10Hz (15)	1Hz-11Hz (16)	1Hz-8Hz (15)	1Hz-8Hz (15)
exp5	FBr_2Ts(5)	1Hz-11Hz (16)	1Hz-11Hz (16)	1Hz-8Hz (15)	1Hz-8Hz (15)
exp7	PBr_W(7)	n/a	0.7Hz-7Hz (13)	0.3Hz-7Hz (14)	0.3Hz-7Hz (14)
exp8	PBr_S(8)	n/a	1Hz-8Hz (17)	1Hz-8Hz (17)	1Hz-8Hz (15)
exp9	PBr_W(9)	n/a	0.7Hz-7Hz (13)	0.7Hz-7Hz (13)	0.7Hz-7Hz (13)
exp10	PBr_S(10)	n/a	1Hz-8Hz (17)	1Hz-8Hz (17)	1Hz-8Hz (16)
exp12	PBr_W(12)	n/a	0.6Hz-7Hz (13)	0.7Hz-7Hz (13)	0.7Hz-7Hz (13)
exp13	PBr_S(13)	n/a	1Hz-8Hz (17)	1Hz-8Hz (17)	1Hz-8Hz (17)
exp14	FBr_1Ts(14)	n/a	n/a	1Hz-8Hz (15)	1Hz-8Hz (15)

Table 5.12: Magnitudes of the pull-out forces applied during the three free vibration experiments.

(a) FBr_2Ts(3)

No	Applied Force (KN)
1	2.94
2	6.38
3	10.10
4	15.70

(b) FBr_2Ts(4)

No	Applied Force (KN)
1	1.96
2	2.40
3	5.03
4	9.64
5	12.53

(c) PBr_W(11)

No	Applied Force (KN)
1	1.96
2	2.40
3	5.03
4	9.64
5	12.53

5.8 Data reliability

It was essential to ensure the reliability of the instruments and the overall reliability of the experiments, prior to the interpretation of the recorded data. This investigation is facilitated by comparing results between experiments that were repeated more than once.

5.8.1 Vibrator

The overall reliability of a forced vibration experiment was mainly controlled by the reliability of the vibrator. The input frequency and the magnitude of the loads that were applied by the vibrator could not be measured in-situ, and therefore the applied sinusoidal force cannot be accurately determined. The input frequency was read out from the vibrator's speed drive (Figure 5.10), while the magnitude of the sinusoidal force can only be estimated by employing Eq. 4.1. Although the experimental data interpretation cannot verify the latter, it can verify the input frequencies. This study proposes two methods for the estimation of the input frequencies applied during forced vibration tests. These are the *Peak-to-peak (Peak2Peak)* method and the *Series of Fourier Spectra (SoFS)* method*,* both based on the assumption that the structure oscillates at the input frequency.

The *Peak2Peak* method is based on the idea that the frequency (in Hz) of a single vibration cycle can be estimated by inverting the time difference between the two successive peaks of the cycle. Repeating this process for every two successive peaks of a time history recorded during an experiment, a frequency time history can be obtained. An illustrative example is presented in Figure 5.18. Figure 5.18a compares the frequency time history, inferred from the FBr_2Ts$^{(5)}$_mD experiment, with the in-situ frequencies which were read out from the vibrator's speed drive during the experiment (all frequencies can be found in Appendix B). The data recorded by the top slab's instruments 2.1, 2.2 and 2.5 (Figure 5.16) were used. Each dot in this figure corresponds to the inverted time difference between two successive peaks. Figure 5.18b compares the in-situ input frequencies with the mean lines and the corresponding plus or minus standard deviation of the dotted data are shown in Figure 5.18a. Figure 5.18c plots for each applied frequency (F) the error between the in-situ and calculated input-frequencies, which is calculated as $(F_{in\text{-}situ}\text{-}F_{mean}/F_{in\text{-}situ})*100$. All three figures verify the reliability of the vibrator regarding the input frequencies, as the calculated and in-situ frequencies match very well. For the accuracy required, the error between the in-situ read out and the calculated frequencies lies within a satisfactory range, as it is consistently lower than 5%. For the presented experiment, the error maximised at around 3Hz, which, as it will be discussed in Sections 6.2.3 and 6.3.5, corresponds to a natural frequency of the system. Figure 5.18 also verifies that the oscillation frequency of the structure was dominated by the input force. The above observations are consistent with observation made by processing data from other experiments, which can be found in Appendix C.

The *SoFS* approach, which is an alternative of *Peak2Peak*, computes a Fourier spectrum for every frequency applied during an experiment. Every spectrum is inferred from a frequency-constant time history sector recorded by top slab instruments. The frequency where the peak of the spectrum appears corresponds to the dominant frequency of the recorded motion. Assuming that the vibrator

dominated the motion, the above frequency is assigned to the vibrator's input frequency. The accuracy of the identified frequency is dependent on the discretization of the frequency axis of the Fourier spectrum. Herein, this axis is chosen to be very finely discretised to increase the accuracy of the captured frequency. However, a fine discretization results in non-meaningful series of smaller peaks, hence Fourier spectra of fine frequency discretization should be avoided for purposes other than identifying the main frequency of a motion.

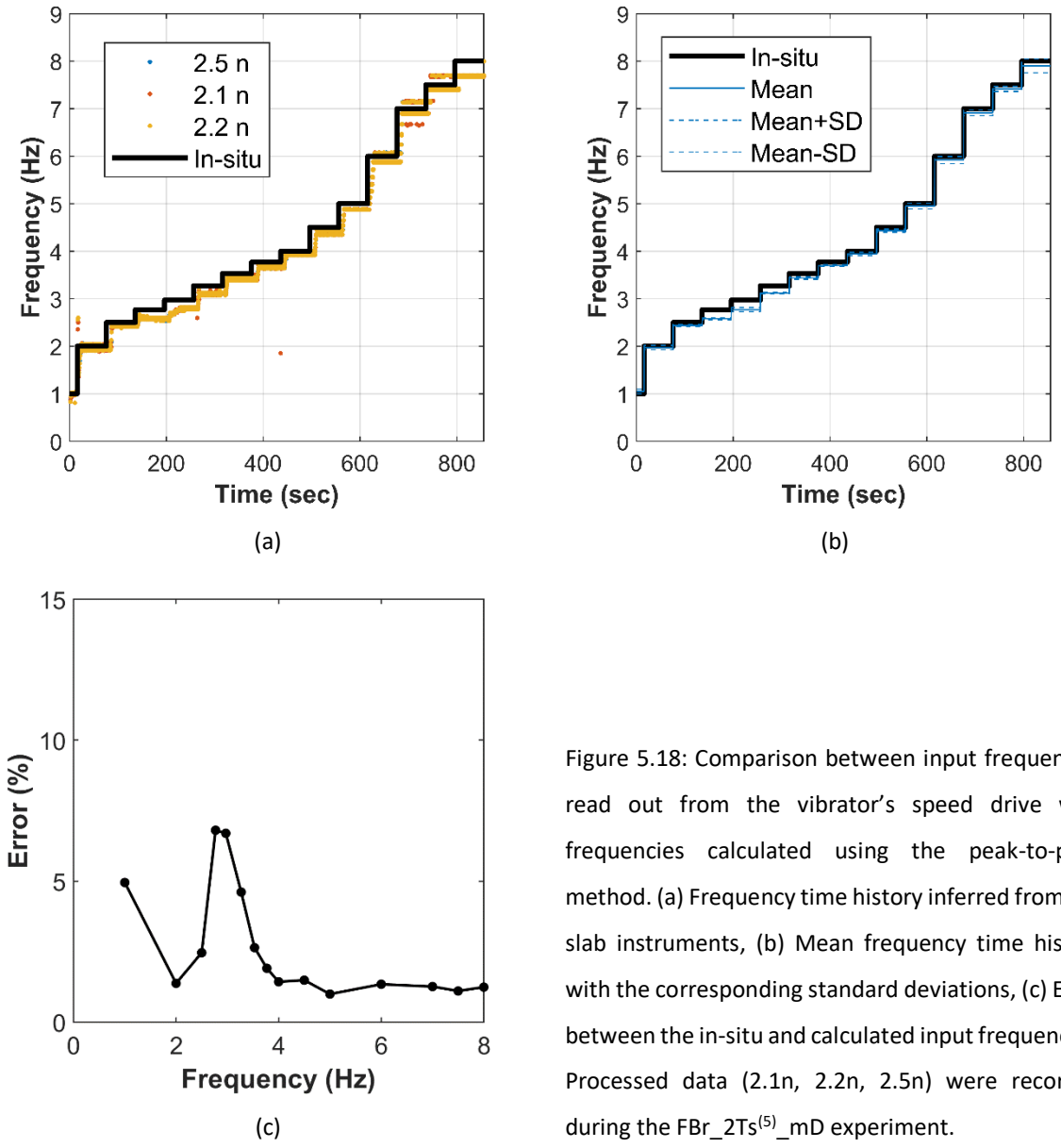


Figure 5.18: Comparison between input frequencies read out from the vibrator's speed drive with frequencies calculated using the peak-to-peak method. (a) Frequency time history inferred from top slab instruments, (b) Mean frequency time history with the corresponding standard deviations, (c) Error between the in-situ and calculated input frequencies. Processed data (2.1n, 2.2n, 2.5n) were recorded during the FBr_2Ts$^{(5)}$_mD experiment.

Repeating this process for every applied frequency, a frequency time history is produced. An illustrative example of this method is presented for the FBr_2Ts$^{(5)}$_mD experiment in Figure 5.19. Figure 5.19a presents the Fourier spectra inferred from accelerations recorded in the North-South direction by three top slab instruments (2.1, 2.2 and 2.5). During the experiment, 15 different

frequencies were applied, hence, 15 individual spectra are plotted for each instrument. By identifying the frequency where the main peak of each instrument appears in each spectrum, the computed applied frequency time history is produced (Figure 5.19b). The computed time history compares very well with the in-situ input frequencies, as the error between the in-situ frequencies and the computed ones is lower than 7% (Figure 5.19c). This verifies the reliability of the vibrator as far as the produced input frequencies are concerned, as also concluded by employing the Peak2Peak method. More applications of the SoFS method are presented in Appendix C

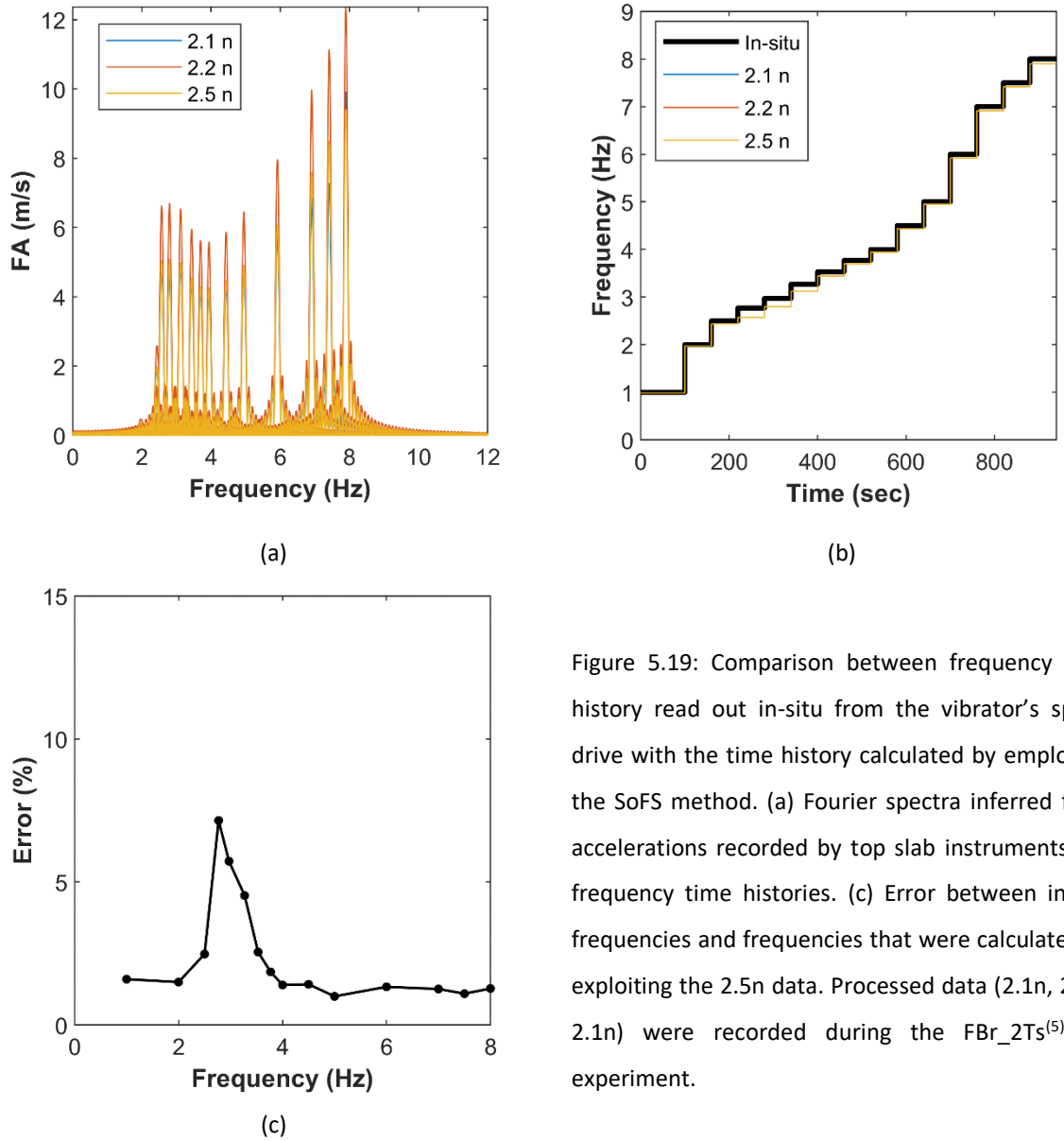


Figure 5.19: Comparison between frequency time history read out in-situ from the vibrator's speed drive with the time history calculated by employing the SoFS method. (a) Fourier spectra inferred from accelerations recorded by top slab instruments, (b) frequency time histories. (c) Error between in-situ frequencies and frequencies that were calculated by exploiting the 2.5n data. Processed data (2.1n, 2.2n, 2.1n) were recorded during the FBr_2Ts$^{(5)}$_mD experiment.

Both the Peak2Peak and SoFS methods verify the reliability of the vibrator concerning the input frequency that is applied to the structure. It is therefore concluded that the input frequencies that were read out from the vibrator's speed drive, which are presented in Appendix B, are of sufficient accuracy to be used for the purpose of this study. At some input frequencies, the structure oscillated

at a slightly smaller frequency (e.g. 3Hz for the FBr_2Ts$^{(5)}$_mD), which is associated with resonance phenomena.

5.8.2 Forced vibration tests repeatability

As mentioned above, the reliability of the forced vibration experiments is affected by the reliability of the vibrator's output force. The latter could neither be measured nor inferred from the recorded data. The overall reliability of the experiments can be examined by conducting a repeatability investigation, where possible. The reliability of an experiment can be confirmed when experimental data recorded from different experiments on the same structural and loading configuration are comparable. The reliability criteria used herein is a combination of qualitative and quantitative judgment. The qualitative criterion is a visual judgment of the comparability between the maximum motion amplitudes recorded at each frequency. The quantitative is the deviation, in percentage units, between the motion amplitudes (a) recorded for each applied frequency during repeated experiments. The deviation, referred to as *error*, between experiments i and j at a certain applied frequency is calculated as:

$$error\ (\%) = (a_i - a_j)/a_i * 100 \qquad 5.15$$

It is challenging to define a unique limit to distinguish whether data are repeatable or not, as this might require adjustment on a case-by-case basis. The structural response was unstable at resonance, hence, for frequencies close to the resonant ones the limit should be more tolerable than for other frequencies. For very small input frequencies, where the motion amplitude was very weak, the limit should also increase to account for the sensitivity of the instruments and the dominance of noise at such weak motions. The same applies for soil instruments, where the recorded motion was weak as well. Finally, the limit should be higher for experiments where response was affected significantly by the impact of imperfections, in that imperfections might have changed with time.

Despite the difficulty to set a limit to define reliability, when experimental results are of difference below 5-10% approximately, these are considered reliable. A more tolerable limit is adopted, 15-20%, for frequencies below 2Hz and for frequencies near the SSI system's resonant ones. The upper bound of the limits is adopted for mA and mB experiments which produced weaker response than mC and mD experiments, for which the lower bound is adopted. The above limit values are approximate due to the variability of the experiments; hence, the qualitative criterion is used in combination of the qualitative one mentioned earlier.

The forced vibration experiment on the fully braced structure with two top slabs (Fbr_2Ts) was repeated three times (exp1, exp2 and exp5 with reference to the Table 5.10). Although each of the three experiments used a different soil instrument configuration, most of the instruments were at the

same place and therefore the experiment repeatability could be investigated. The same applies for the experiments on the partly braced structure loaded along the structure's weak (exp7, exp9 and exp12, with reference to the Table 5.10), or the strong plane (exp8, exp10 and exp13, with reference to the Table 5.10).

The structural response under a forced vibration with a constant frequency was a sinusoidal motion of a constant amplitude and frequency, in most cases, as shown by an illustrative example in Figure 5.20. Figures 5.21, 5.22 and 5.23 compare the amplitudes (peak accelerations) that were recorded along the North-South loading direction by the centre top slab instrument (2.5n) during three different forced vibration experiments. Figure 5.21 compares the recorded peak accelerations against applied frequency for the FBr_2Ts structure as extracted from the experiments exp1, exp2 and exp5, with reference Table 5.10. Figure 5.22 compares the peak accelerations recorded on the PBr_W structure during the experiments exp7, exp9 and exp13, while Figure 5.23 presents the same data inferred from the exp8, exp10 and exp13 experiments on the PBr_S structure. It is observed that the experiments during which larger mass plates are placed on the vibrator produced more consistent results than experiments of smaller masses. The experiments characterized by the imposition of the mA or mB masses on the vibrator, which produced weaker excitation forces, yielded a different top slab response upon repetition (Figures 5.21 a, b; 5.22 a, b; and 5.23 a, b). In contrast, the structural response was very consistent when the applied force was larger, which was the case when the mC or mD masses were placed on the vibrator.

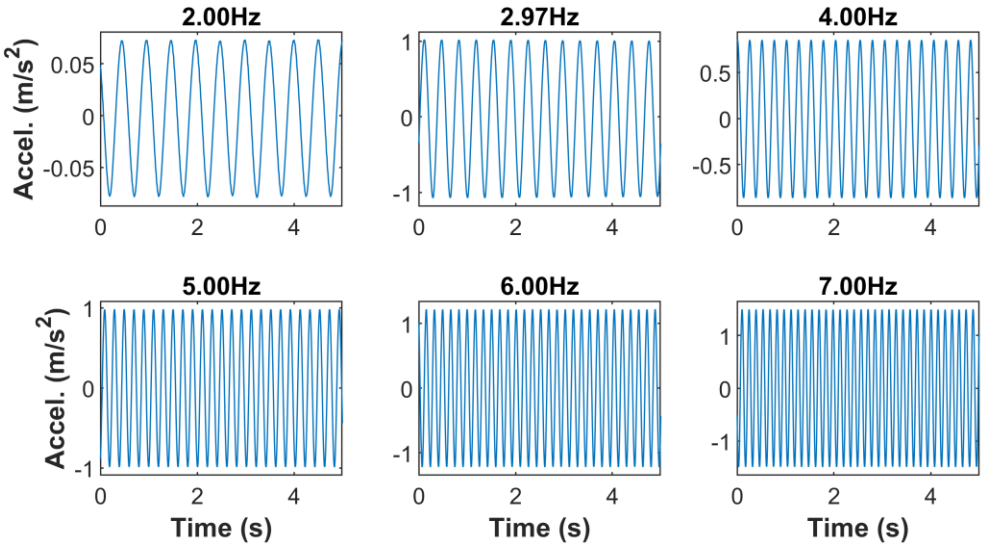


Figure 5.20: Illustrative example of the acceleration time histories recorded along the North-South direction by the centre top slab instrument (2.5n) during the FBr_2Ts$^{(5)}$_mD experiment. The response at six different frequencies is shown.

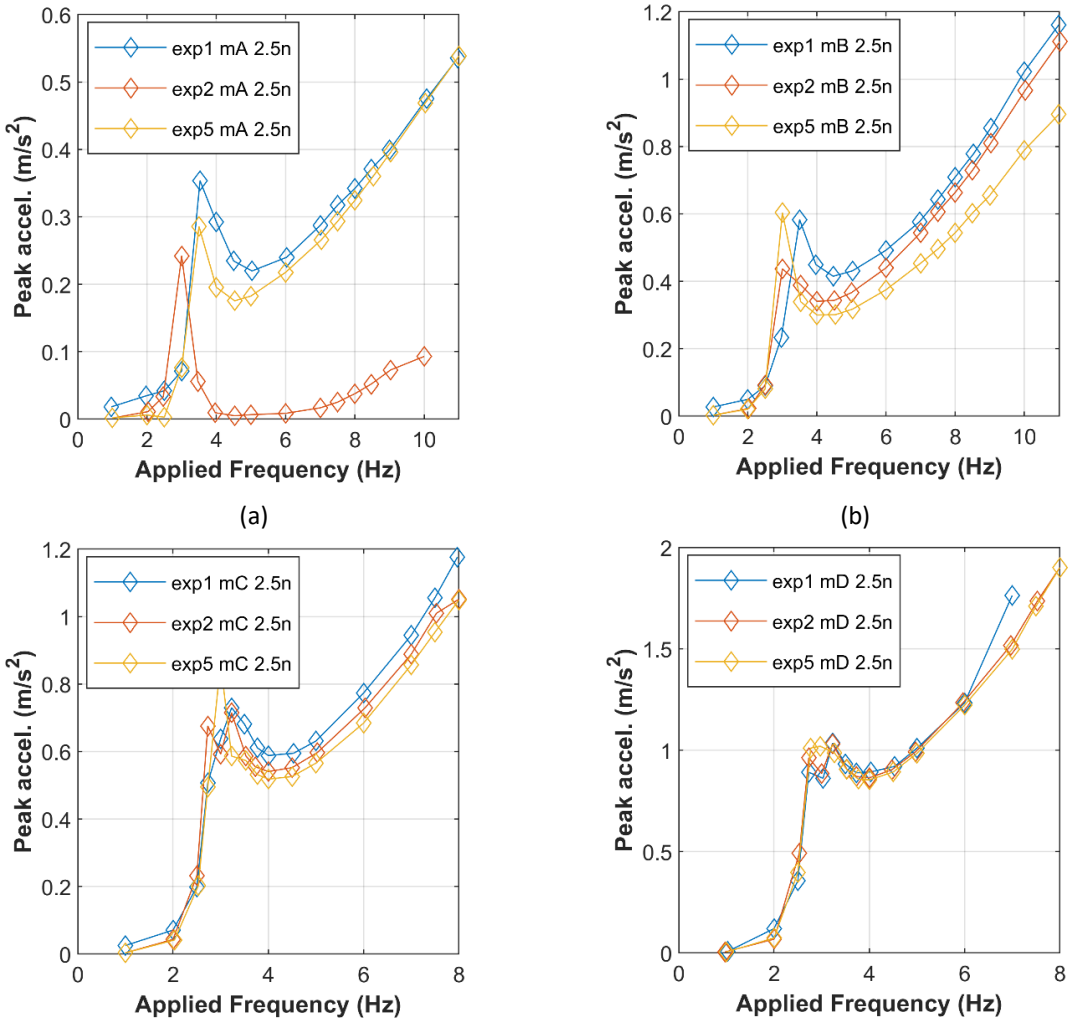
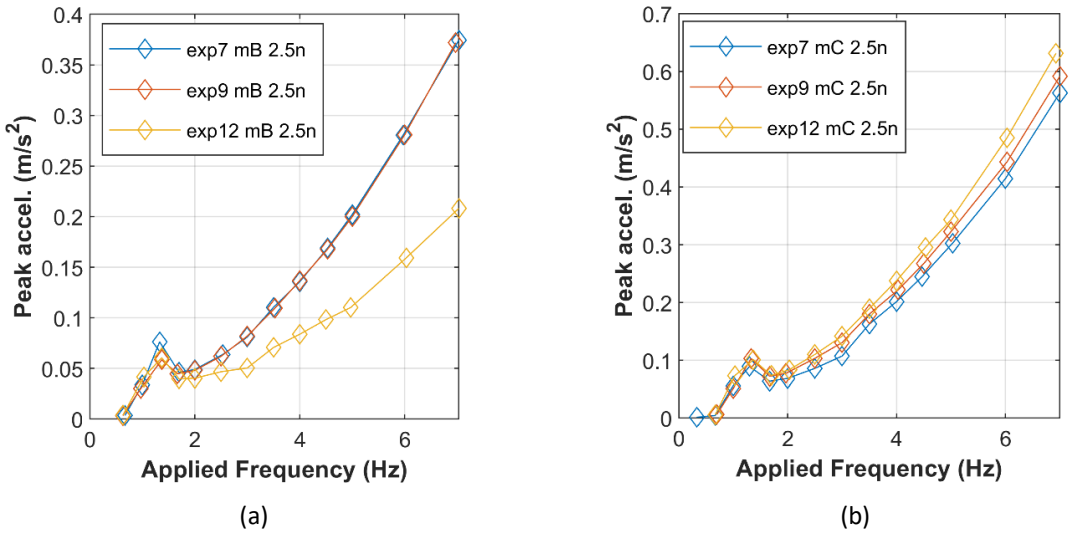
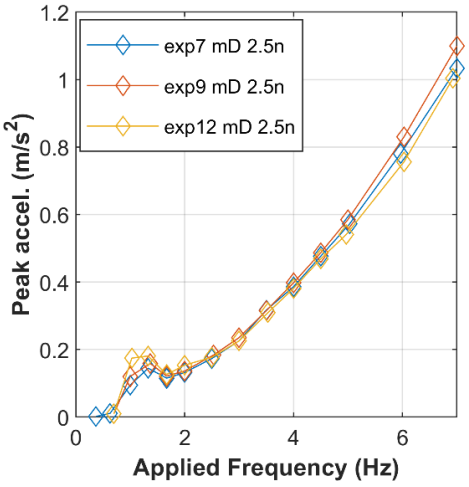


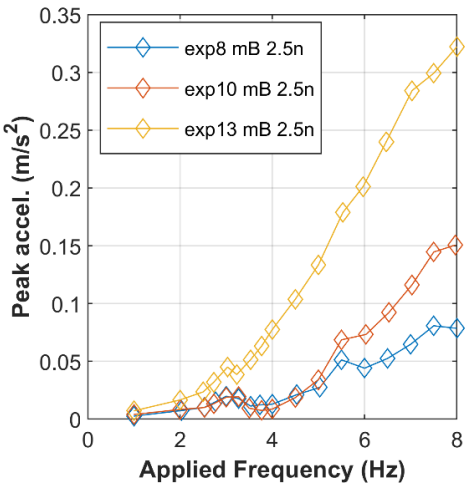
Figure 5.21: Peak accelerations recorded on the top slab by the 2.5n instrument during the three experiments on the fully braced two-top slab structure (FBr_2TS). Results are extracted from experiments where the plate mass placed on the vibrator was (a) mA, (b) mB, (c) mC and (d) mD (Table 5.9).



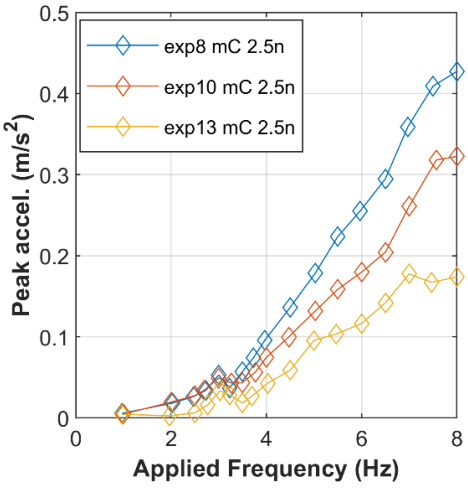


(c)

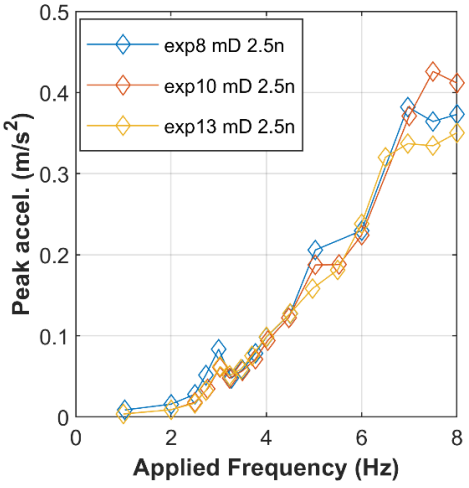
Figure 5.22: Peak accelerations recorded on the top slab by the 2.5n instrument during the three experiments on the partly braced two-top slab structure loaded along its weak axis (PBr_W). Results are extracted from experiments where the plate mass placed on the vibrator was (a) mB, (b) mC and (c) mD (Table 5.9).



(a)



(b)



(c)

Figure 5.23: Peak accelerations recorded on the top slab by the 2.5n instrument during the three experiments on the partly braced two-top slab structure loaded along its strong axis (PBr_S). Results are extracted from experiments where the plate mass placed on the vibrator was (a) mB, (b) mC and (c) mD (Table 5.9).

The poor repeatability performance observed in experiments with weaker excitation intensity can potentially be attributed to the influence of experimental imperfections on their response. A vibrating

system that is highly sensitive to experimental imperfections is anticipated to exhibit limited repeatability, as the imperfections might have changed between the experiments. Such changes can be associated with the potential occurrence of softening/hardening of the structural connections. They can also be linked with variations of the interface contact conditions, that could have been influenced by intervening experiments between the ones being compared. Furthermore, the vibrator performance could be sensitive to small excitation loads, potentially resulting in inconsistent input motions between the compared experiments.

More evidence of the reliability of the records can be found in Appendix C, where the repeatability of all structural instruments is assessed, where possible. Overall, the following experiments are not considered reliable: FBr_2Ts$^{(2)}$_mA, FBr_2Ts$^{(2)}$_mB, FBr_2Ts$^{(5)}$_mB, PBr_W$^{(12)}$_mB, PBr_S$^{(13)}$_mB and PBr_W$^{(13)}$_mC. Care should also be taken when interpreting the data of the FBr_1Ts$^{(14)}$ experiment as it was the only experiment that was not repeated more than once. Therefore, repeatability investigation could not be carried out and experiment's reliability cannot be ensured. The above claims regarding the reliability of the experiments are supported qualitatively by the errors, calculated as per Eq. 5.15, that are presented in Appendix C.

5.8.3 Free vibration tests repeatability

As for the forced vibration tests, the reliability of the free vibration tests is affected, amongst others, by the accuracy of the pull-out force. Although, the pull-out force could be measured by the load cell in-situ, the measurement cannot be verified against experimental data. Repeatability analysis is carried out, where possible, to indicate the reliability of some of the free vibration tests. Free vibration tests on the FBr_2Ts structure were repeated when comparable pull-out forces were applied. Figure 5.24 compares the top slab response between experiments with pull-out force 10.10kN and 9.64kN, while Figure 5.25 between 2.94kN and 2.40kN. Aiming to minimise the force difference between the compared experiments, the recorded accelerations are normalised by the applied force of each experiment. Comparisons between experiments are made in terms of (a) top slab normalised acceleration time histories, (b) variation of normalised peak accelerations with time, and (c) error between the compared experiments. The error (%) is calculated as $(a_{exp3}-a_{exp4})/a_{exp3}$, where a_{exp3} and a_{exp4} correspond to the absolute values of normalised peak accelerations recorded during the experiments exp3 and exp4 respectively.

Figures 5.24 a and b illustrate that during the experiments where the pull-out forces were 10.10kN and 9.64kN, the frequency content and the motion amplitude of the recorded structural response were very similar. The error is lower than 10% (Figure 5.24c) with the exception of one frequency, which is within a satisfactory range; hence, the two compared experiments are considered reliable.

This is not the case for the experiments where the pull-out forces were 2.94kN and 2.40kN. Although the frequency content of the response recorded during the two experiments is very similar (Figure 5.25a), the motion amplitude is substantially different (Figure 5.25b). The difference is as high as 40% in some frequencies, which rises doubts regarding the reliability either of the two experiments. The difference can be attributed to unavoidable experimental imperfections, sensitivity of the instruments to record such low accelerations and the accuracy of the measured applied forces. It is reasonable that the impact of the instrument sensitivity is more pronounced when the recorded quantities are smaller. The latter can justify why the repeatability of the free vibration experiments of smaller pull-out force was not as good as the repeatability of the experiments of larger force. The latter observation is consistent with the one made previously for the forced vibration tests. As discussed earlier in Section 5.8.2, forced vibration experiments which imposed stronger excitation (mC, mD) show better repeatability than the ones imposed weaker excitation (mA, mB).

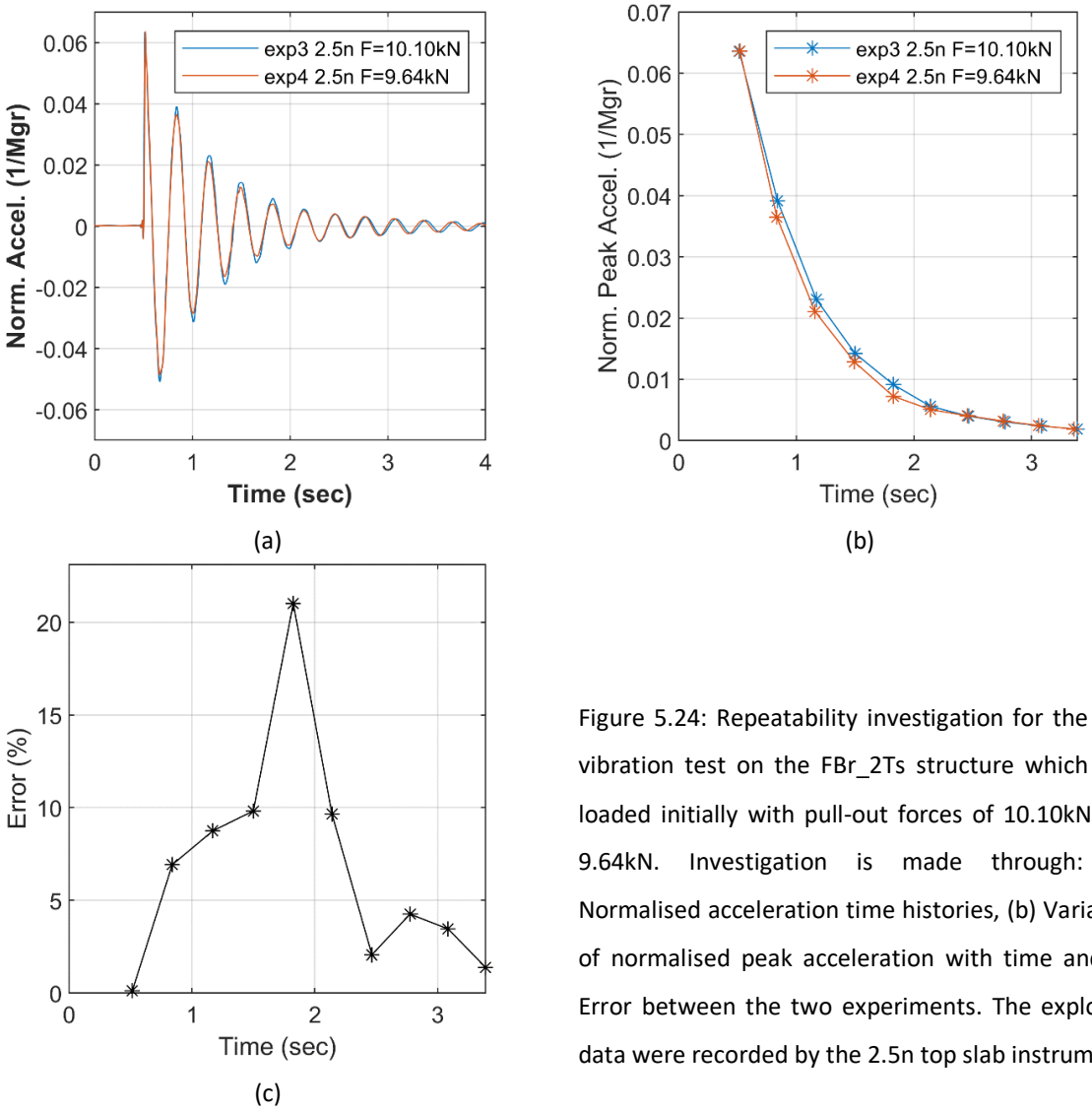


Figure 5.24: Repeatability investigation for the free vibration test on the FBr_2Ts structure which was loaded initially with pull-out forces of 10.10kN and 9.64kN. Investigation is made through: (a) Normalised acceleration time histories, (b) Variation of normalised peak acceleration with time and (c) Error between the two experiments. The exploited data were recorded by the 2.5n top slab instrument.

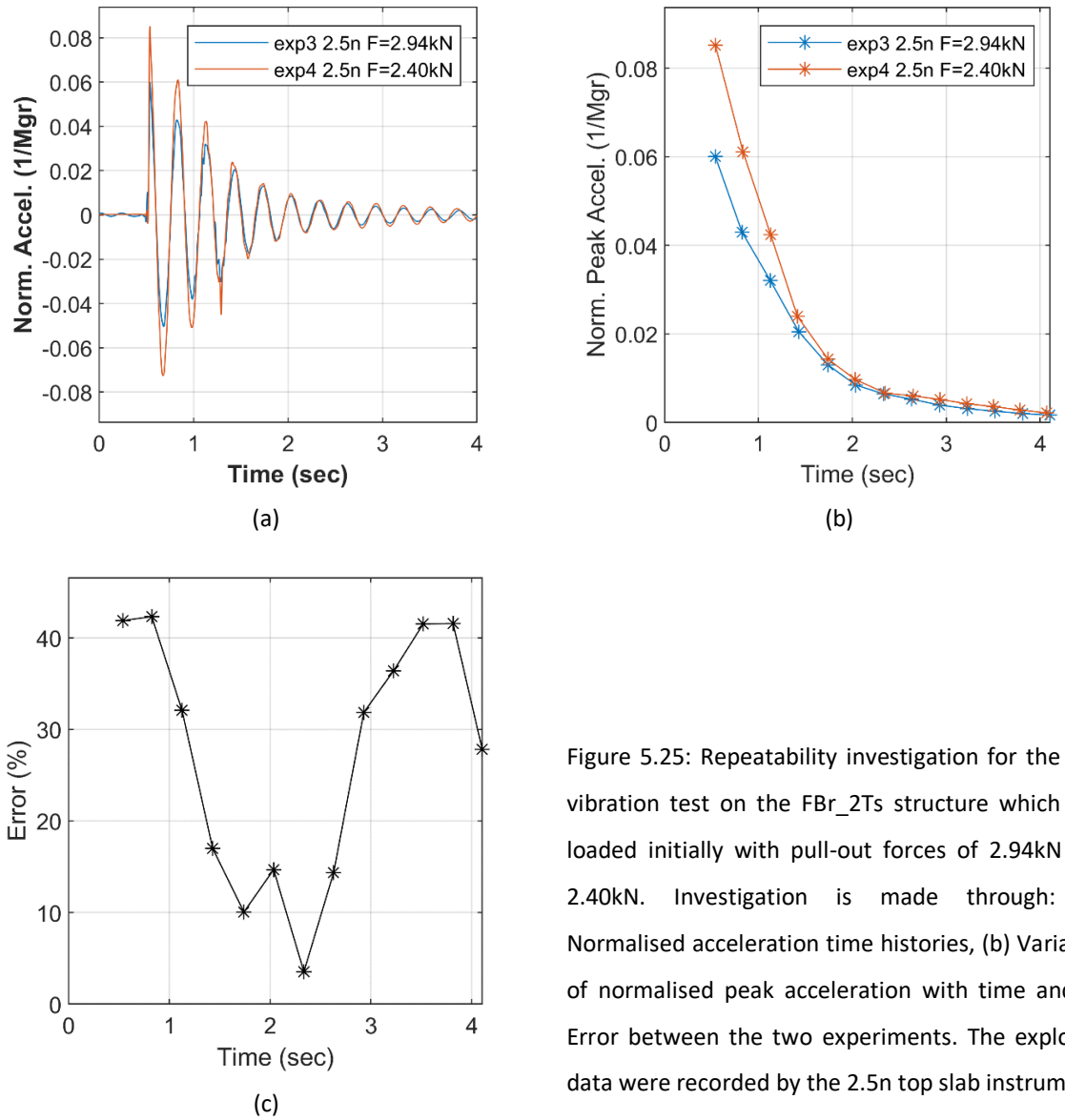


Figure 5.25: Repeatability investigation for the free vibration test on the FBr_2Ts structure which was loaded initially with pull-out forces of 2.94kN and 2.40kN. Investigation is made through: (a) Normalised acceleration time histories, (b) Variation of normalised peak acceleration with time and (c) Error between the two experiments. The exploited data were recorded by the 2.5n top slab instrument.

It is also noted that the foundation-soil interface conditions might have not been consistent between experiments. It was observed that during the application of the static pull-out force on the fully braced structure, the foundation detached from the soil beneath at some areas. When the force was released, the ensuing inertial forces tended to return the foundation to a resting position. The inertial forces also caused the foundation to slide relative to the soil, shearing the soil-foundation interface. This uplifting and sliding process of the foundation that took place during some of the free vibration experiments, may had changed the interface conditions and can justify some differences observed between the experiments results of similar pull-out force.

5.8.4 Monitoring instruments

The reliability of the individual monitoring instruments, accelerometers and seismometers, can be investigated by inspecting the data visually. It can also be investigated by comparing data recorded from identical experiments that were repeated more than once, similarly to the procedure followed

for the investigation of the overall reliability of the forced and free vibration tests (Sections 5.8.2 and 5.8.3). It was found that one or more sensors of some instruments did not work or produced erroneous amplitudes of accelerations/velocities during entire experiments. Also, some other instruments were not synchronised with the remaining ones, despite that the recorded amplitudes and frequency content were reasonable. Such a case is presented in Figure 5.26 which plots the North-South top slab accelerations recorded by four instruments during the forced vibration FBr_2Ts$^{(5)}$_mD experiment of six different applied frequencies. It is illustrated that there is a time lag between the accelerations recorded by the 2.3n instrument in comparison with the ones recorded by the 2.1n and 2.5n instruments.

Care should have been taken during the installation of the structural instruments on the slabs. During the FBr_2Ts$^{(1)}$_mD experiment all foundation instruments were poorly clamped on the concrete slab. Indicatively, Figure 5.27 compares acceleration time histories recorded by the 1.1n instrument during the FBr_2Ts$^{(1)}$_mD (exp1) and FBr_2Ts$^{(5)}$_mD (exp5) experiments. It is observed that the FBr_2Ts$^{(1)}$_mD experiment, during which the instrument was poorly clamped on the foundation, the recorded motion contained high frequency content. The high frequency motion disappeared when the instrument was properly clamped during the FBr_2Ts$^{(5)}$_mD experiment.

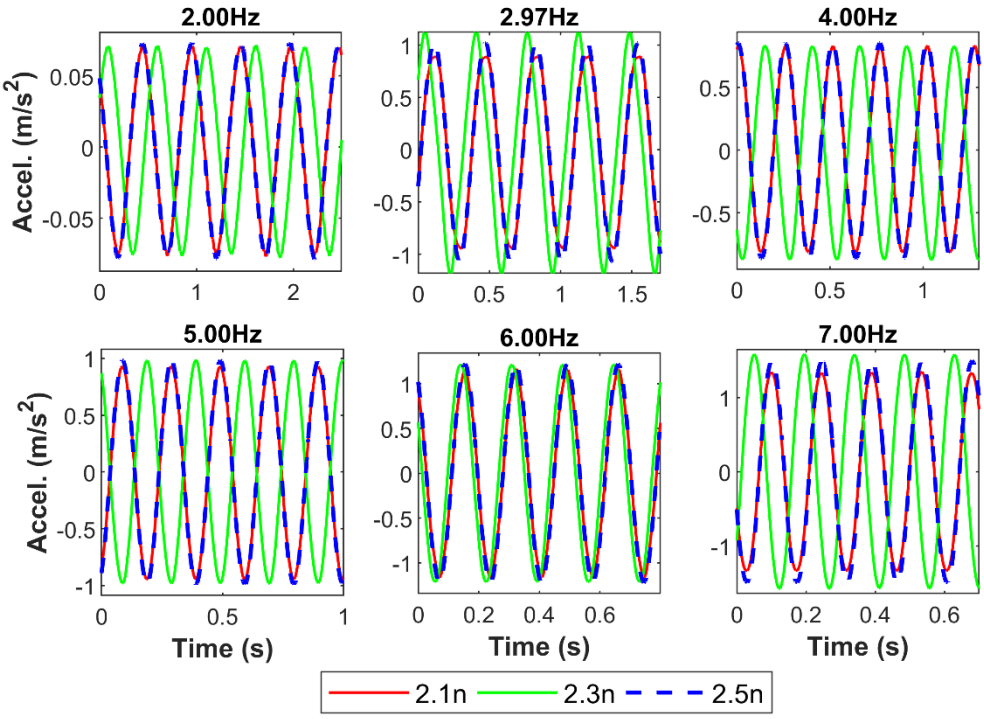


Figure 5.26: Faulty instrument synchronization example. Acceleration time histories recorded along the North-South direction by the top slab centre instrument (2.5n) during the FBr_2Ts$^{(5)}$_mD experiment. The response at six different frequencies is shown.

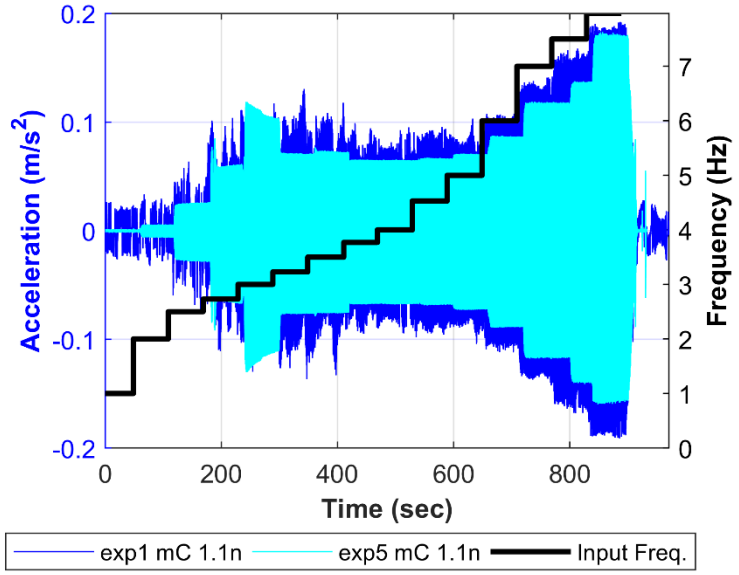


Figure 5.27: Comparison of acceleration time histories recorded by an instrument (1.1n) which was poorly clamped on the foundation during FBr_2Ts$^{(1)}$_mC (exp1) and properly clamped during FBr_2Ts$^{(5)}$_mC (exp5) experiments. The applied frequency time history is also presented.

Uncertainty arises in relation to the calibration of both structural and soil instruments, as there is a possibility that they were not appropriately calibrated either before or during the experiments. Additionally, the installation of the soil instruments on the ground surface was a manual process (see Section 5.3.3) which may had resulted in variable conditions around the instruments. If the soil was not well compacted around the instrument, then the records could be faulty. However, the above uncertainties cannot be investigated by comparing records of repeated experiments. The calibration process of the structural and soil instruments, as well as the soil conditions around the soil instruments were the same during the experiments, hence the error, if any, was consistent. These uncertainties should be considered when interpreting both the structural and soil motion from the recorded data.

In general, the soil motion recorded during identical experiments, that were carried out more than once, was found to be repeatable, although it was less consistent than the structure's instruments due to the variability of the soil conditions. Indicatively, Figure 5.28 compares velocity time histories recorded during the FBr_2Ts_mD forced vibration experiments that were repeated three times (exp1, exp2 and exp5). The comparison between the soil motion recorded during the different experiments is satisfactory for most of the applied frequencies. It is less accurate, though, for low applied frequencies, e.g. 2-3Hz, during which the input excitation was very weak. As it has already been mentioned, during weak excitations the response is more sensitive to experimental imperfections and the impact of any inaccuracies in measurements, due to instruments' sensitivity, is more pronounced. The above can explain the degraded consistency of recorded soil motions observed when the applied

frequency was small, given that according to Eq. 5.14 the input excitation decreases with input frequency.

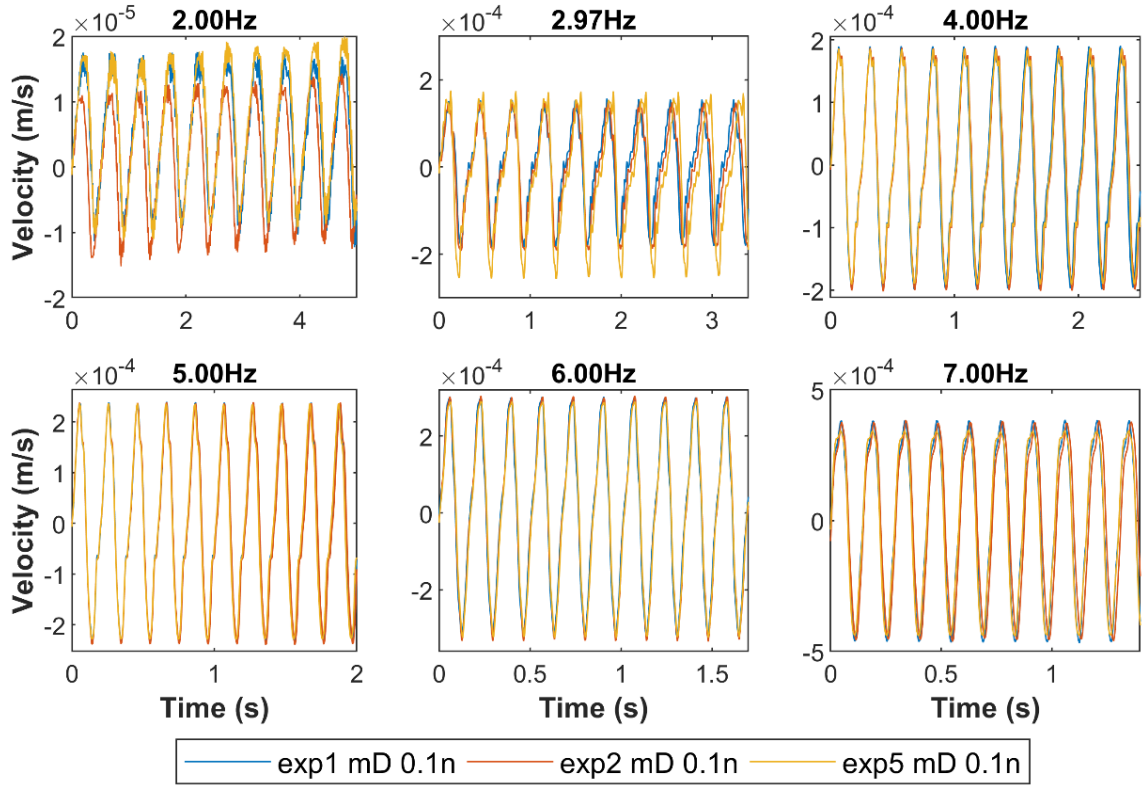
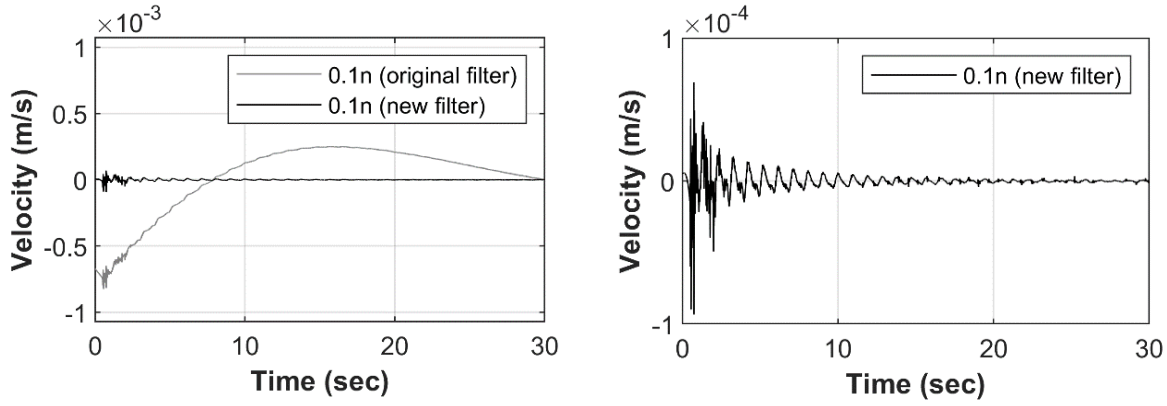


Figure 5.28: Velocity time histories recorded by the a soil instrument in the NS direction (0.1n) during the FBr_2Ts$^{(1)}$_mD (exp1), FBr_2Ts$^{(2)}$_mD (exp2) and FBr_2Ts$^{(5)}$_mD (exp5) experiments.

Figure 5.28 shows that for the applied frequency of 2Hz, the recorded motion contains a low frequency content which resulted in an upward trendline. This issue appeared to be more pronounced in the records of the free vibration tests. Figure 5.29 shows the velocity time histories recorded by the 0.1n soil instrument in the North-South direction during the free vibration PBr_W$^{(11)}$_2.0kN experiment. Figure 5.29a shows that a low frequency content dominates the presented motion, implying that the Butterworth bandpass filter that was originally applied on recorded motions, as described in 5.4, was not sufficient. This low frequency content disappears when a new filter, with an increased lower cut-off frequency (e.g. 0.5Hz instead of the original 0.2Hz), is applied to the motion. The new filter is sufficient to provide reasonable data, as it is shown in Figure 5.29b. Records that required a new filtering with increased low cut-off frequency are summarised in Table 5.13. The table gives the inputs of the Butterworth bandpass filter, including the order (n), and lower and higher cut-off frequencies. The remaining records not included in the table were filtered by a 4th order Butterworth bandpass filter of 0.02Hz and 50Hz lower and higher cut-off frequencies (see Section 5.4).



(a) (b)

Figure 5.29: Filtering of velocity time histories recorded by the 0.1n soil instrument in the NS direction during the free vibration PBr_W$^{(11)}$_2.0kN experiment. (a) Velocity time histories after applying the original and new filters, (b) New-filtered velocity time histories (zoom).

Table 5.13: Records that required additional filtering, while filtering input are also shown.

Exp. No	Pull-out force (kN)	Instrument No	Order n	Cut-off frequencies	
				Lower (Hz)	Higher (Hz)
PBr_W$^{(11)}$	2.03	0.1n	4	0.3	50
PBr_W$^{(11)}$	2.03	0.1e	4	0.3	50
PBr_W$^{(11)}$	2.03	0.32n	4	0.3	50
PBr_W$^{(11)}$	2.03	0.41n	4	0.3	50
PBr_W$^{(11)}$	2.03	0.41e	4	0.3	50
PBr_W$^{(11)}$	5.44	0.1n	4	0.5	50
PBr_W$^{(11)}$	5.44	0.1e	4	0.5	50
PBr_W$^{(11)}$	7.31	0.1n	4	0.6	50
PBr_W$^{(11)}$	7.31	0.1e	4	0.6	50
PBr_W$^{(11)}$	10.03	0.1n	4	0.7	50
PBr_W$^{(11)}$	10.03	0.1e	4	0.7	50
PBr_W$^{(11)}$	10.03	0.32e	4	0.2	50
PBr_W$^{(11)}$	10.03	0.40e	4	0.2	50
PBr_W$^{(11)}$	10.03	0.41e	4	0.2	50
PBr_W$^{(11)}$	13.90	0.1n	4	0.6	50
PBr_W$^{(11)}$	13.90	0.1e	4	0.6	50
PBr_W$^{(11)}$	13.90	0.2e	4	0.6	50
PBr_W$^{(11)}$	13.90	0.31n	4	0.6	50
PBr_W$^{(11)}$	13.90	0.40e	4	0.6	50

Unlike the soil surface motion, the in-depth soil motion recorded by the 3.1 downhole accelerometer was not consistent, especially in the horizontal directions. Figures 5.30, 5.32 and 5.34 present respectively the NS, EW and vertical downhole acceleration time histories recorded during the FBr_2Ts$^{(1)}$_mD and FBr_2Ts$^{(2)}$_mD experiments. The presented data were recorded by the 3.1 instrument in 0.8m depth from the ground surface. The time histories are of 5-cycles duration and correspond to six different input frequencies. Figures 5.31, 5.33 and 5.35 present the corresponding Fourier spectra inferred from the above acceleration time histories. Figure 5.30 and Figure 5.32 show that the repeatability of the North-South and East-West downhole accelerations is not satisfactory, especially at low input frequencies. The input frequencies are not easily distinguishable neither from the time histories nor the Fourier spectra (Figures 5.31, 5.33), as high frequency content dominated the motion, which was not the case for the ground surface motion. The high frequency content was not apparent in the vertical downhole acceleration time histories (Figure 5.34), which are of much larger amplitude than the horizontal downhole counterpart. The vertical downhole acceleration time histories are found to satisfy the repeatability criterion set earlier (10% difference between the motion amplitudes of the repeated experiments). In return, the input frequency can be easily inferred from both time histories (Figure 5.34) and Fourier spectra (Figure 5.35). Overall, the downhole accelerations recorded in the vertical direction can be considered as reliable, whereas care should be taken when interpreting the horizontal accelerations.

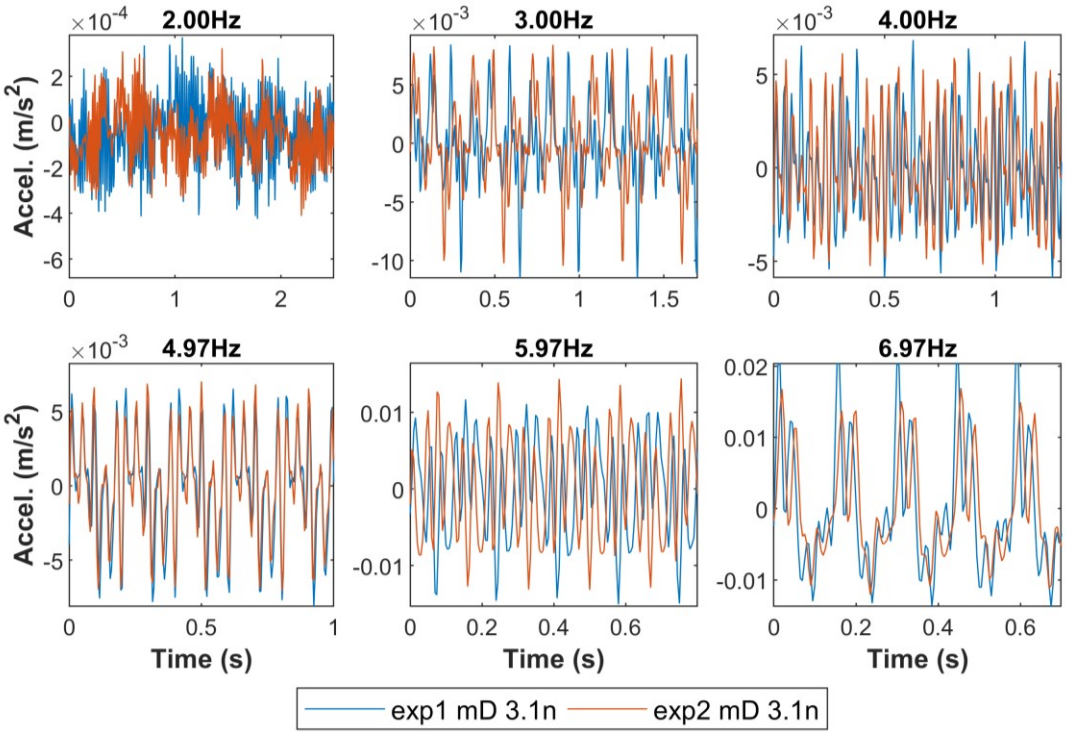


Figure 5.30: Acceleration time histories recorded by the downhole accelerometer in the North-South direction (3.1n) during the FBr_2Ts$^{(1)}$_mD (exp1) and FBr_2Ts$^{(2)}$_mD (exp2) experiments.

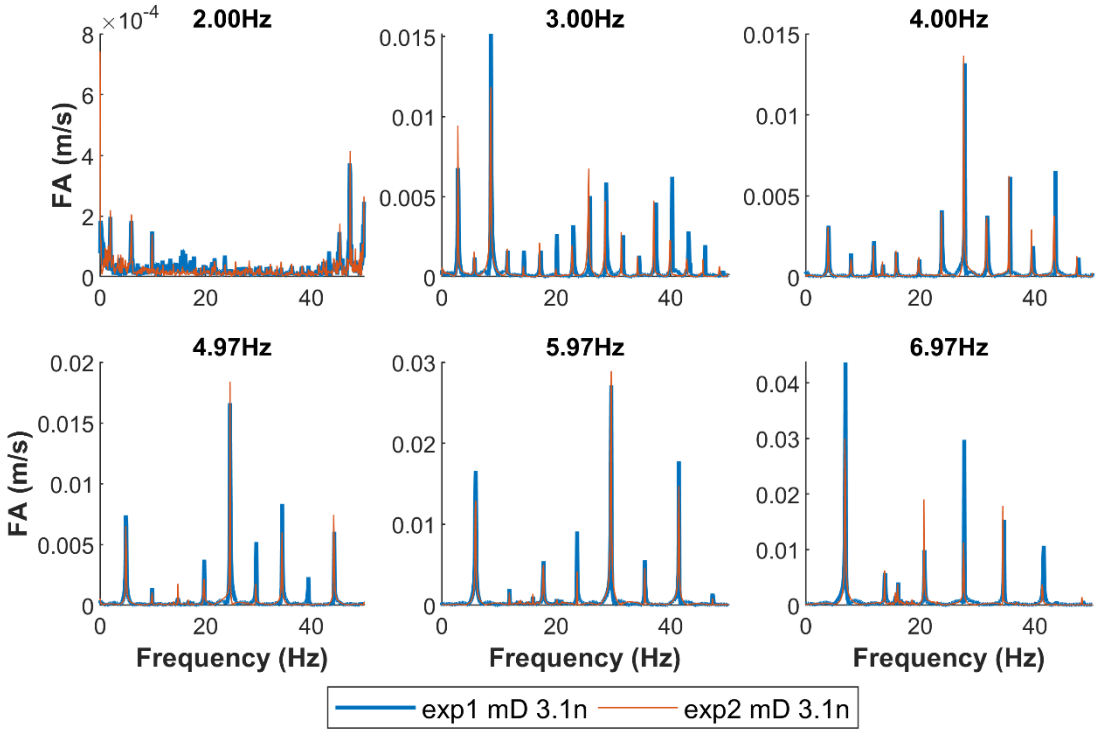


Figure 5.31: Fourier spectra inferred from data recorded by the downhole accelerometer in the North-South direction (3.1n) during the FBr_2Ts$^{(1)}$_mD (exp1) and FBr_2Ts$^{(2)}$_mD (exp2) experiments.

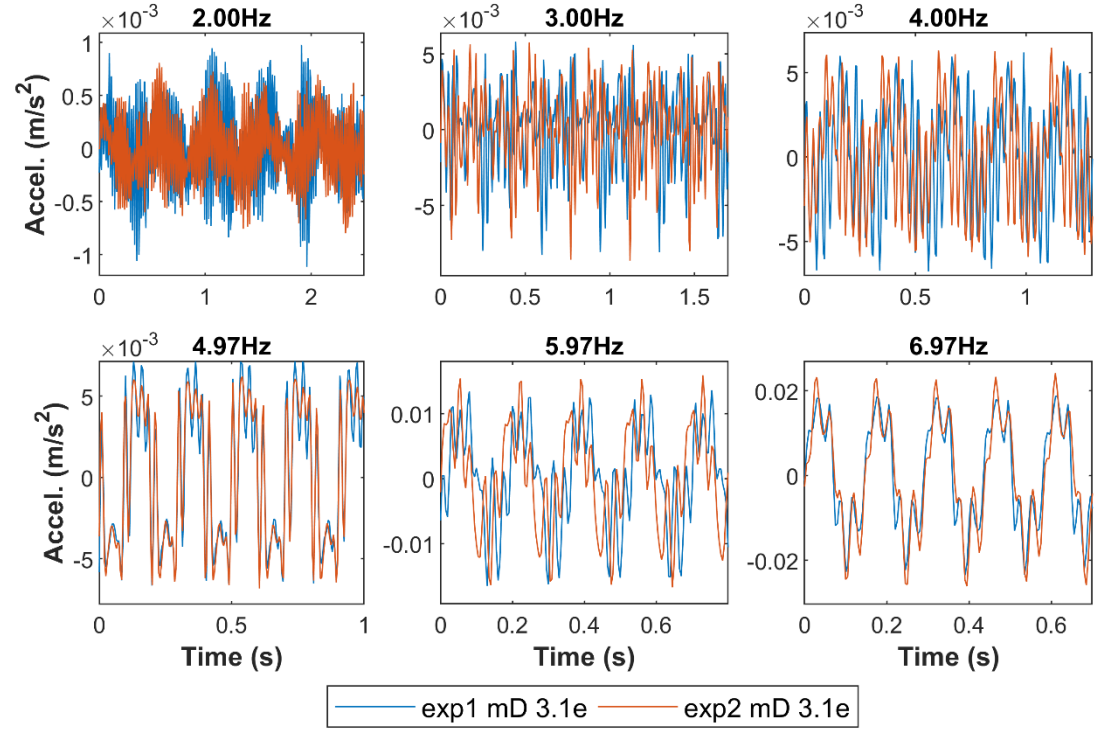


Figure 5.32: Acceleration time histories recorded by the downhole accelerometer in the East-West direction (3.1e) during the FBr_2Ts$^{(1)}$_mD (exp1) and FBr_2Ts$^{(2)}$_mD (exp2) experiments.

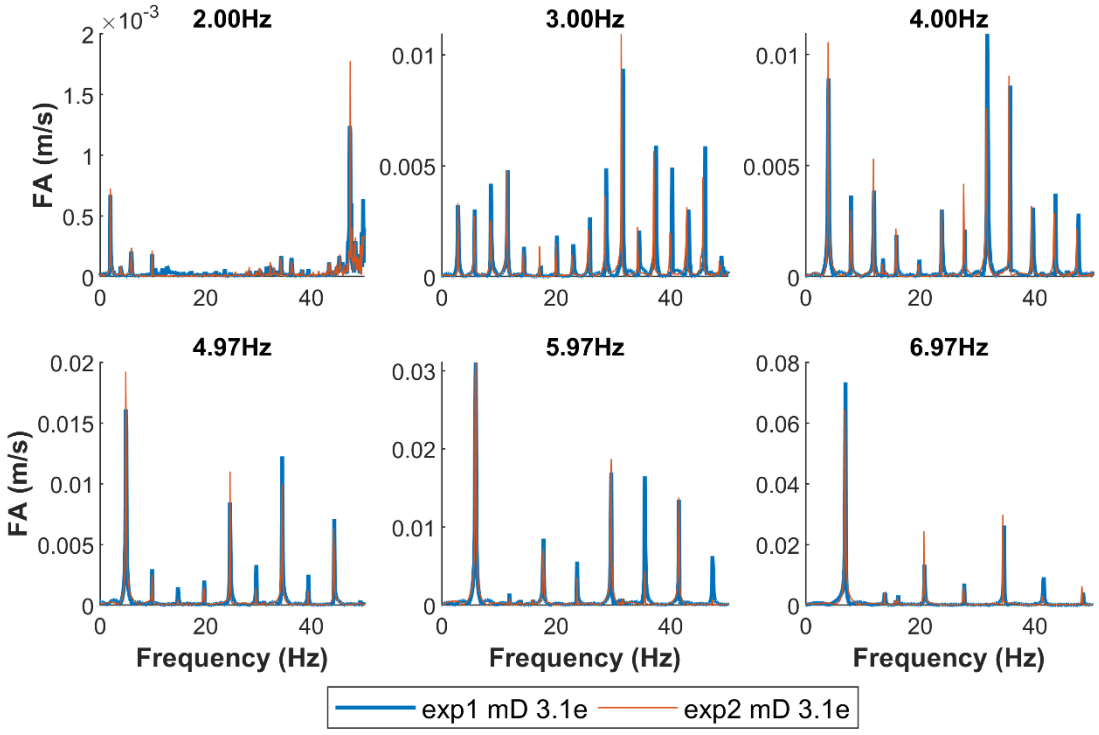


Figure 5.33: Fourier spectra inferred from data recorded by the downhole accelerometer in the East-West direction (3.1e) during the FBr_2Ts$^{(1)}$_mD (exp1) and FBr_2Ts$^{(2)}$_mD (exp2) experiments.

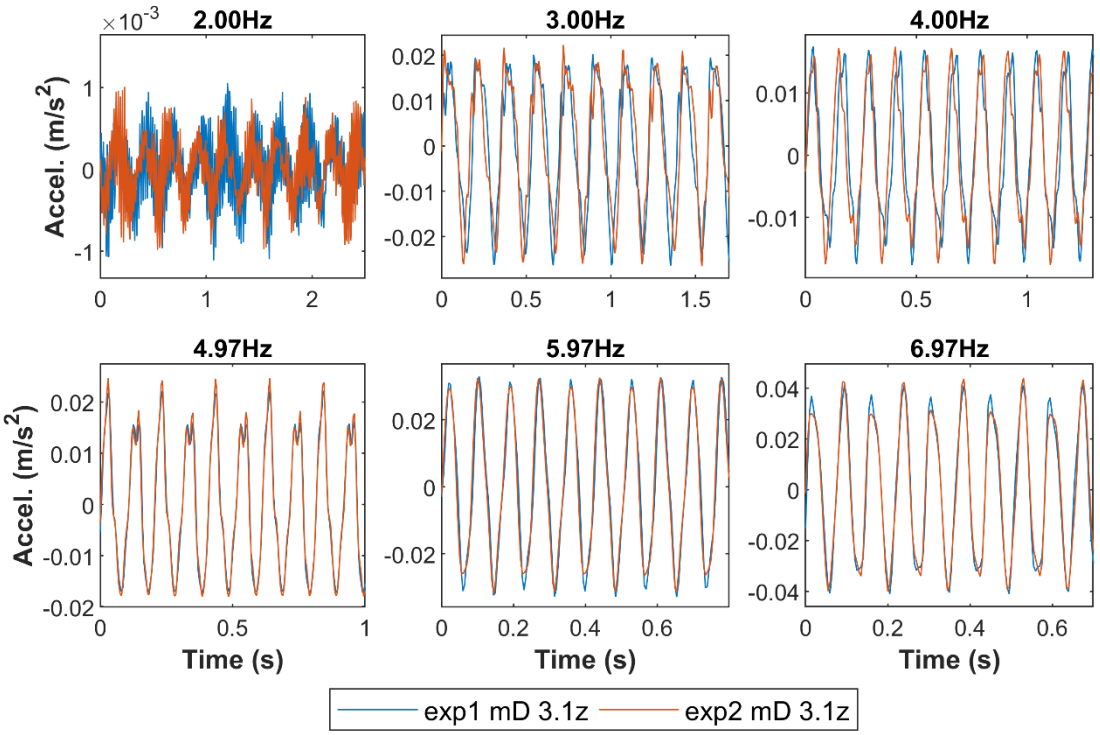


Figure 5.34: Acceleration time histories recorded by the downhole accelerometer in vertical direction (3.1z) during the FBr_2Ts$^{(1)}$_mD (exp1) and FBr_2Ts$^{(2)}$_mD (exp2) experiments.

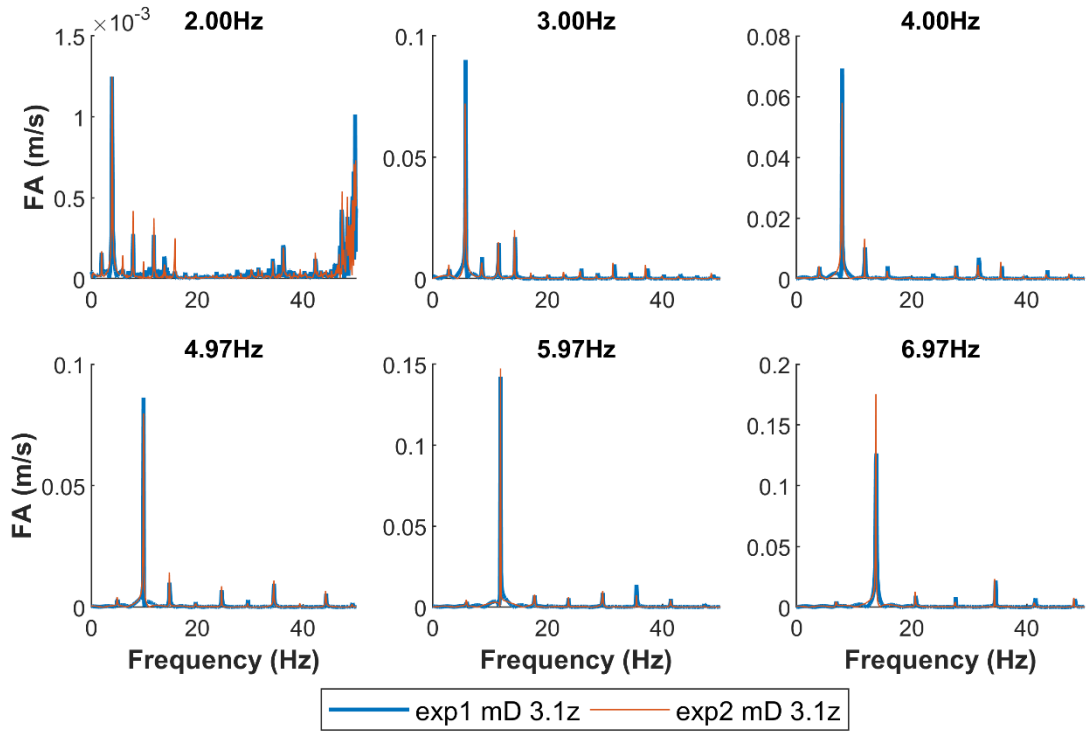


Figure 5.35: Fourier spectra inferred from data recorded by the downhole accelerometer in the vertical direction (3.1z) during the FBr_2Ts$^{(1)}$_mD (exp1) and FBr_2Ts$^{(2)}$_mD (exp2) experiments.

5.8.5 Summary of unreliable data

Table 5.14 presents the forced vibration experiments which were judged to be faulty, while Tables 5.15 and 5.16 summarise the unreliable data recorded during forced and free vibration tests respectively. The latter tables include the experiment's name, instrument number and recording direction (n for North-South, e for East-West and z for vertical) of each faulty record.

Table 5.14: Faulty forced vibration experiments.

Exp. No	Experiment Name
exp2	FBr_2Ts$^{(2)}$_mA
exp2	FBr_2Ts$^{(2)}$_mB
exp5	FBr_2Ts$^{(5)}$_mB
exp12	PBr_W$^{(12)}$_mB
exp13	PBr_S$^{(13)}$_mB
exp13	PBr_W$^{(13)}$_mC

Table 5.15: Faulty data recorded during forced vibration tests.

Exp. No	Experiment Name	Vibrator masses	Instruments	Direction
exp1-exp13	FBr_2Ts$^{(1-13)}$, PBr$^{(1-13)}$	mA, mB, mC, mD	2.3, 1.6 (both not synchronised)	n, e, z
exp1	FBr_2Ts$^{(1)}$	mA, mB, mC, mD	0.17, 1.1, 1.2, 1.5, 1.6, 1.7, 2.3	n, e, z
		mA, mB, mC, mD	2.5	z
exp2	FBr_2Ts$^{(2)}$	mA, mB, mC, mD	0.17	e
		mA, mB, mC, mD	1.5, 2.3	n, e, z
exp5	FBr_2Ts$^{(5)}$	mA, mB, mC, mD	0.17	e
		mA, mB, mC, mD	2.3	n, e, z
exp7-exp13	PBr$^{(7-13)}$	mB, mC, mD	0.17	e, z
exp7	PBr$^{(7)}$_W	mB	0.17, 0.2, 0.40, 0.41, 0.42	n, e, z
		mD	0.40, 0.41, 0.42	n, e
exp9	PBr$^{(9)}$_W	mB	0.2, 0.41, 0.62	n, e, z
		mC	0.2, 0.40, 0.41, 0.51, 0.62	n, e, z
		mD	0.2, 0.41, 0.62	n, e, z
exp12	PBr$^{(12)}$_W	mB, mC, mD	0.42	n, e, z
exp8	PBr$^{(8)}$_S	mB	0.1, 0.2, 0.31, 0.40, 0.41, 0.42, 0.31, 0.7	n, e, z
		mC	0.2, 0.42, 0.9, 2.1	n, e, z
		mD	0.2, 0.42, 0.7	n, e, z
exp10	PBr$^{(10)}$_S	mB, mC, mD	0.2, 0.5	n, e, z
exp13	PBr$^{(13)}$_S	mB	0.1, 0.42	n, e, z
		mC	0.12, 0.42, 0.44, 2.1	n, e, z
		mD	0.42, 0.5	n, e, z
exp14	FBr_1Ts$^{(14)}$	mC, mD	0.17, 1.1, 1.5 (not synchronised)	n, e, z
			0.1	n

Table 5.16: Faulty data recorded during free vibration tests.

Exp. No	Experiment Name	Pull-out force (kN)	Instruments	Direction
exp3, exp4	FBr_2Ts$^{(3,4)}$	all	0.17	e
		all	2.3	n, e, z
exp11	PBr$^{(11)}$_W	all	0.42, 0.7	n, e, z
		13.9	0.32	n, e, z

5.9 Summary

This chapter describes the experimental campaign, carried out as part of the present research. The experimental campaign comprised forced and free vibration tests on the EUROPROTEAS structure, which have been designed with an adjustable bracing system and superstructural mass. Three

different structural configurations were tested so that the SSI effects could be examined for structures of a wide range of fixed-base natural frequencies. The fixed-base natural frequencies of the examined structures varied between 2Hz and 13Hz, for the swaying mode, and between 11Hz to 23Hz, for the torsional mode (Table 5.8). These values are considered to be upper bound natural frequencies, as they were calculated assuming a fully symmetric structure and full moment connection between the columns and the slabs. As mentioned in Section 5.2.4, none of these assumptions reflect to the real experimental conditions. Full symmetry cannot be achieved in experimental studies as imperfections are inevitable. Also, evidence from a previous lab work has indicated that the column-slab connections cannot be considered as full moment connections. The softer connections are anticipated to shift the fixed-base natural frequencies of the examined structural configurations to lower values, relative to the frequencies computed assuming rigid connections.

Additional experimental uncertainties were also associated with the instrumentation employed during the experiments. The vibrator's output forces and frequencies could not be measured in-situ, therefore, the accuracy of vibrator's output was not ensured. Vibrator's output frequencies could be read-out by the vibrator's speed drive in-situ. The readings were found to be reliable after exploiting the experimental data (Section 5.8.1). The vibrator's force could be estimated through Eq. 4.1, but its reliability and accuracy could not be verified. The vibrator, though, was found to produce consistent output during the experiments, as identical experiments which were repeated more than once gave very comparable results (Section 5.8.2). Similarly, the repeatability of the free vibration tests was found to be satisfactory by comparing tests during which similar pull-out forces were applied on the same structural configuration (5.8.3). A repeatability investigation was also carried out for the identification of unreliable experiments or faulty instruments, which are summarised in Section 5.8.5. It was found that the repeatability degraded for experiments of weak excitations. Weak excitation was a condition that amplified the impact of experimental uncertainties on the output data. The uncertainties include geometrical imperfections, interface imperfections, uncertainty regarding the excitation force and instrument sensitivity to weak measurements.

Overall, 10 sets of forced vibration tests and 3 sets of free vibration tests were carried out. Each set of forced vibration experiment comprised individual sub-experiments during which different masses were placed on the vibrator. During each sub-experiment, 12 to 15 different input frequencies, ranging from 1Hz to 12Hz, and different forces, of 50kN maximum, were applied on the structure. Each set of free vibration test consisted of sub-experiments of different pull-out forces. The magnitudes of the pull-out forces ranged between 2kN and 16kN. The application of different magnitude forces on the structure aimed to evaluate the nonlinear behaviour of the SSI system with increasing load.

Chapter 6

Experimental Data Interpretation and System Identification of SSI Response

6.1 Introduction

Experimental data collected from real-scale experiments can be exploited to investigate dynamic Soil-Structure-Interaction (SSI) phenomena rigorously. The investigation is more effective when controllable site conditions exist during the experiments and the input excitation is prescribed. Within this context, real-scale experiments, which are already described in Chapter 5, were carried out for the purpose of this study. The experiments consisted of a frame structure founded on a shallow footing at a well-documented site, while the structure was subjected to free and forced vibration excitations. One of the aims of the experiments was to advance the understanding of SSI phenomena by interpreting the collected data.

The interpretation of experimental data poses challenges mainly arising from experimental imperfections (see Section 5.2.4) and instruments' limitations (see Section 5.8). Star et al. (2019) proposed a procedure to evaluate the dynamic properties of a soil-structure system by interpreting data obtained from forced vibration tests. As described in Section 3.2.2, the latter study modified the parametric system identification method developed by Stewart and Fenves (1998) which is applicable only for seismic events, provided that the free-field motion is available. The method is based on the assumption of a linear system with proportional damping, while nonlinear systems can be investigated by recursive parametric identification that calculates time dependent first-mode parameters. The modified parametric system identification technique employs transfer functions, defined as ratios of output to input motions, to evaluate modal vibration periods and damping ratios. The proposed input-output pair is a function of the recorded roof and foundation motions, as well as the input excitation. However, the input excitation was not measured during the forced vibration tests carried out for the

present research (see Section 5.3.1), therefore, the above method is not applicable herein. Output only system identification methods, which do not require the input excitation, are also available in the literature. Blind system identification is an example of such a method that has been adopted and modified by Ghahari et al. (2012, 2013) to extract modal properties of SSI systems from ambient noise data and data recorded during seismic events. It is based, though, on complex mathematical expressions which are cumbersome to employ in practice, hence, the blind system identification technique is not adopted either.

This study employs a simple system identification technique which exploits the simplicity of the free and forced vibration tests, without the need of adopting any of the assumptions of the aforementioned approaches. The advantages of the free and forced vibration tests over earthquake and ambient noise tests are that the recorded structural motions are periodical of known frequencies and contain very limited high frequency content or noise. This makes the interpretation of experimental data easier and more direct. The aim of the system identification in this study is to evaluate the SSI system's natural frequencies and damping ratios of the corresponding modes that were triggered during the experiments, as well as to evaluate the importance of SSI effects. These modal properties and the importance of the SSI effects, including foundation rocking, are anticipated to vary between experiments on the same structural configuration but of different applied load magnitude. Any differences observed between experiments with different applied load can be attributed to non-linear effects, which are discussed in this chapter. The modal SSI properties and the impact of SSI effects are also anticipated to be different between the examined structural configurations with different stiffness and/or superstructural mass (Figures 5.2 and 5.3), which is also discussed in this chapter. The latter two properties affect the natural frequencies of structures. It is well established in the literature that more flexible structures exhibit lower interaction with the foundation soil than the stiffer ones. Within this context, the significance of the impact of the SSI effects on the response, with relation to structural stiffness and mass, is investigated through the experimental data interpretation. The recorded soil motions can give an indication of the importance of SSI effects with larger soil motions indicating a more pronounced impact. The soil motion attenuation is also investigated. A comparison between attenuation observed from different experiments is carried out, aiming to establish a relationship between attenuation rate, mode of oscillation and load intensity.

This chapter exploits experimental data to demonstrate fundamental aspects of SSI effects, including lengthening of the predominant period and increase of damping relative to a fixed-base structure. Evidence of SSI phenomena, foundation rocking and nonlinear effects is also discussed. The dependence of these phenomena on structural stiffness, superstructural mass, input frequency and

load magnitude is also evidenced. The first part of this chapter presents results obtained from free vibration tests, while the second one interprets the forced vibration data.

6.2 Free vibration tests

6.2.1 Identification of natural frequencies and modes of oscillation

A structure exhibits free vibration when it is initially displaced from its static equilibrium position and is then allowed to oscillate freely without been subjected to any external loads. If the initial displaced shape of a structure reflects to a mode of the structure, or equivalently to a mode of the SSI system, then the SSI system oscillates at its natural frequency that corresponds to this mode. The oscillation maintains the shape of this mode throughout the motion, while the contribution of other modes is negligible (Chopra, 2011). During the free vibration tests conducted for the purpose of this study, the top slab of the structure was initially displaced horizontally towards the South. This was achieved by applying a load that was designed to pass through the mass centre of the top slab and act parallel to the plane of symmetry of the SSI system (see Section 5.3.2). Assuming these loading conditions, a perfectly symmetric structure and homogeneous soil conditions, the initial displacement of the structure is expected to trigger the conventional North-South (NS) swaying mode (Figure 6.1a) of the SSI system. Hence, the free vibration tests are expected to reveal the NS swaying natural frequency and the corresponding damping of the SSI system, while the contribution of the EW swaying and torsional modes (Figure 6.1 b and c, respectively) can be considered minimal.

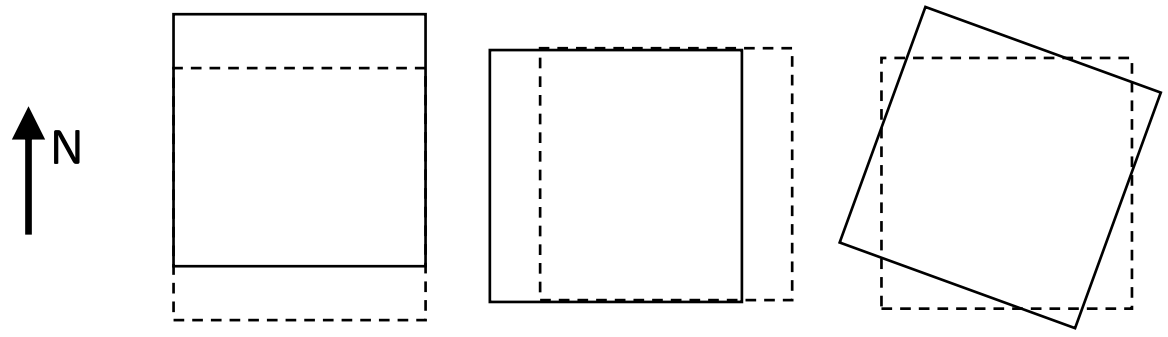


Figure 6.1: Plan views of the top slabs displaced along the (a) conventional NS swaying mode, (b) conventional EW swaying mode and (c) torsional mode.

Although the conducted experiments had imperfections, the above assumptions can be considered reasonable for the case of free vibration tests on the partly braced structure (PBr), which was initially excited along its weak axis. The imperfections, during these experiments, did not appear to have an important effect on the deformation of the structure. This is because the PBr structure has a plane (NS) which is much weaker than the other orthogonal plane (EW), thus, the modal frequencies of the

two swaying modes differ significantly. The implication of this is that by exciting the NS mode of the structure, which in the presented experiments corresponds to a displaced shape where the top slab is displaced parallel to the weak plane of the structure (Figure 5.3b), the resulted free oscillation was dominated by the NS mode. On the contrary, the EW swaying mode, which is triggered by the existence of imperfections, had a very weak contribution to the motion. This is demonstrated in Figure 6.2a which shows that during the PBr_W_13.90kN experiment the top slab motion recorded by the 2.1 and 2.5 instruments was much stronger in the NS direction (denoted by n) than in the EW direction (denoted by e). This feature was consistent for all free vibration experiments on the PBr structure that were carried out, while more evidence can be found in Appendix D.

Unlike the partly braced structure, the fully braced with the two top slab structure (FBr_2Ts) is symmetric and its two swaying modes (Figure 6.1 a and b) are of very similar modal frequencies. The implication of this is that if the initial top slab displacement does not perfectly match the shape of one of the swaying modes, the other swaying mode will contribute significantly to the motion. It is therefore expected that experimental imperfections played an important role on the free vibration tests of the FBr_2Ts structure. Figure 6.2b compares the NS (n) and EW (e) top slab accelerations recorded by the 2.1 and 2.5 instruments during the FBr_15.70kN experiment. The figure shows that the EW motion was of a similar order of magnitude to the In-plane motion after the first cycles of the motion. The similar contribution of the NS and EW deformation modes resulted in a structure oscillating translationally along a diagonal horizontal axis.

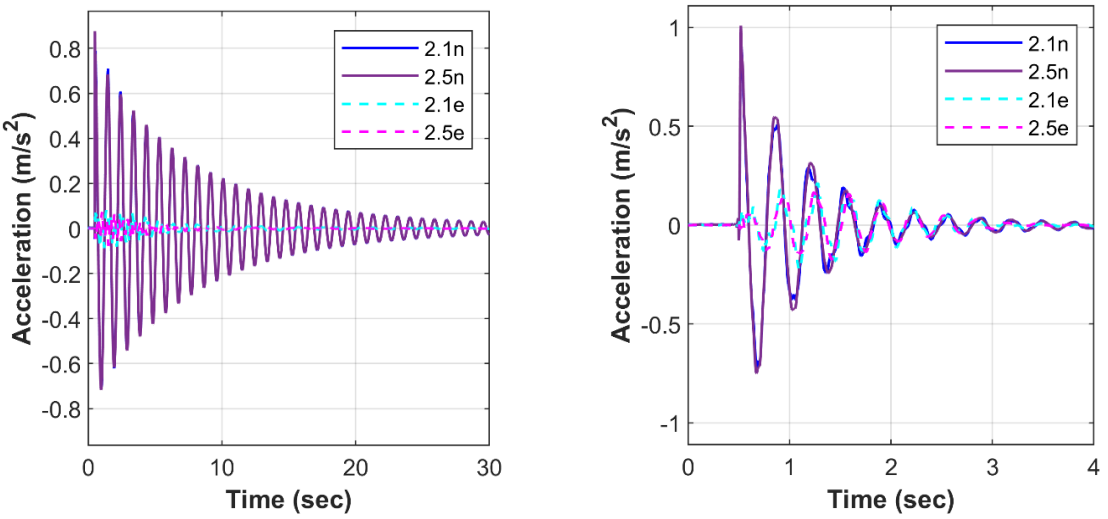


Figure 6.2: Acceleration time histories recorded on the top slab by the 2.1 and 2.5 instruments along the North-South (n) and East-West (e) directions during the free vibration experiments: (a) PBr_W$^{(11)}$_13.90kN, (b) FBr_2Ts$^{(3)}$_15.70kN.

Free vibration tests allow the direct estimation of the fundamental frequency of SSI systems (Chopra, 2011). The tests on the PBr structure can reveal the natural frequency of the NS swaying mode, while the tests on the FBr_2Ts structure can be used for the estimation of both NS and EW modal frequencies, which coincide. The natural frequencies can be identified form the ordinates that correspond to peaks of Fourier spectra which are inferred from the top slab recorded accelerations (Pitilakis *et al.*, 2013; Pitilakis and Vratsikidis, 2017; Vratsikidis and Pitilakis, 2018). If more than one peaks are present, then other modes participate in the motion. The contribution (contribution factor) of each mode can be qualitatively inferred from the amplitude of the corresponding peak relative to the fundamental one. These modes are associated either with higher modes of the fundamental swaying mode or with a different deformation mode (e.g. torsional). The modes can be distinguished between swaying and torsional by comparing the Fourier spectra of the top slab's motion recorded by different instruments at different locations. When a peak appears at the same frequency with the same amplitude in all Fourier spectra inferred from records of different instruments, then the slab exhibits a swaying mode without rotation, as shown in Figure 6.3a. The figure illustrates that all points on the top slab are displaced by the same amount, hence, the spectra at different locations are identical. This is not the case when the slab rotates. Edge points of the top slab exhibit stronger motion resulting in larger Fourier amplitude than inner points, while the point at the centre of rotation exhibits zero motion (Figure 6.3b). This procedure is followed herein to qualitatively characterise the modes that contribute to the motion, while a more detailed modal analysis and estimation of the contribution factors are beyond the scope of this research.

Figure 6.4 illustrates how the above theoretical approach is implemented in the current study to identify the natural frequencies and the associated modes of the SSI system. The figure presents the Fourier spectra inferred from the acceleration time histories recorded at the top slab by the 2.1 and 2.5 instruments along the NS (n), and EW (e) directions. The presented data correspond to the free vibration experiments on the partly braced structure which was subjected to a pull-out force of 13.90kN (PBr_W$^{(11)}$_13.90kN) and the fully braced 2-top slab structure loaded by a 15.70kN force (FBr_2Ts$^{(3)}$_15.70kN). The main peak of the spectra clearly reveals the fundamental frequencies of both SSI experiments. The peak observed at 1Hz in the spectra of the PBr structure is assigned to the NS mode, as the peak is much more pronounced in the NS motion (2.1n, 2.5n) than the EW motion (2.1e, 2.5e). Similarly, the peak observed at 3Hz in the FBr_2Ts spectra is assigned to both NS and EW modes, as the peak is pronounced for both top slab motion components. As expected, the free vibration of the soil-PBr structure system was dominated by the NS swaying mode, as it can be concluded from the almost monochromatic Fourier spectra. Figure 6.4a plots the results at a different scale, to allow the identification of other peaks. These peaks are associated with the contribution of

other modes, which, though, are very small, as the amplitudes of these peaks are very small relative to the fundamental peak. These peaks can be associated with higher swaying modes or with a different mode. The peak observed at around 3Hz is more pronounced for the EW motion (e) than the NS motion. Therefore, according to Figure 6.3a, it can be claimed that this peak can be assigned the EW mode (Figure 6.1b) of the structure. A second peak is also observed at 8Hz in the Fourier spectra inferred from the FBr_2TS free vibration tests (Figure 6.4b). At this frequency, the edge instrument (2.1) recorded a motion with a richer content than the centre instrument (2.5). The Fourier spectra of the recorded top slab motions at 8Hz resembles the Fourier spectra shown in Figure 6.3b which corresponds to a perfectly torsional response. This indicates that the 8Hz peak is associated with the torsional mode. For the same reasons, although not very clear, the peak observed at around 6Hz in Figure 6.3a indicates the torsional frequency of the PBr structure.

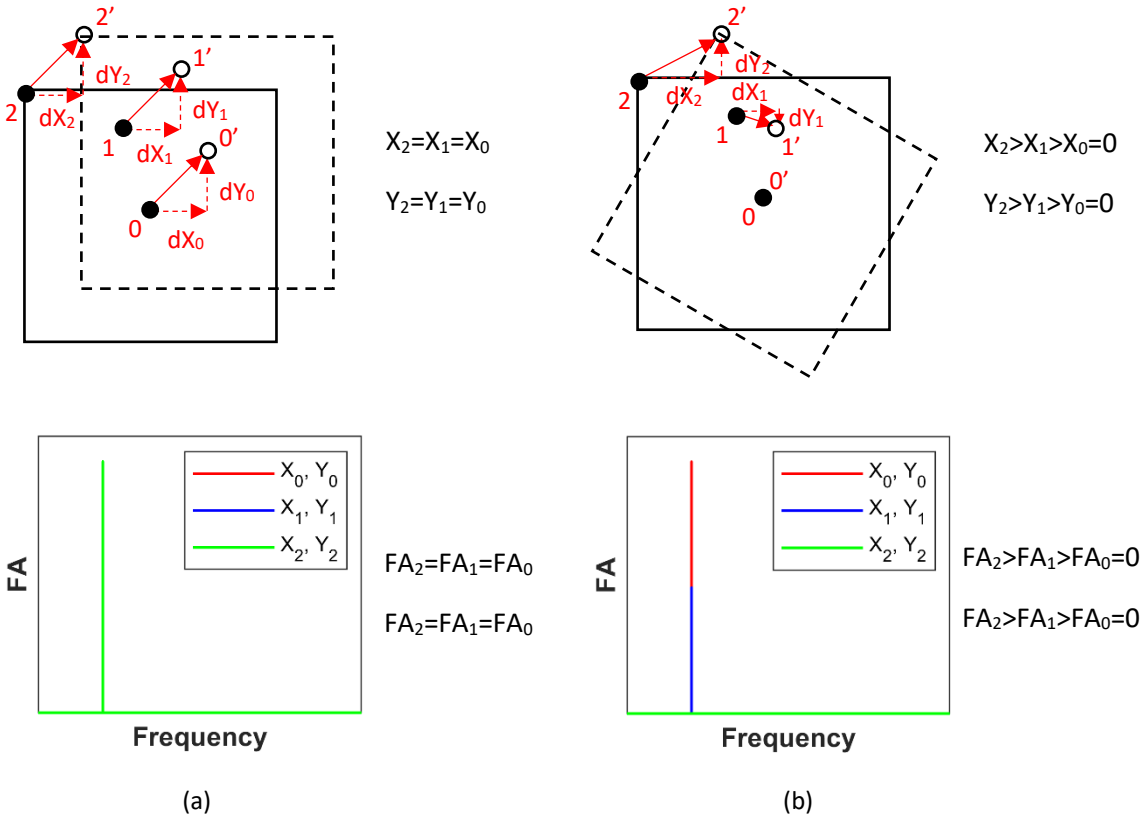
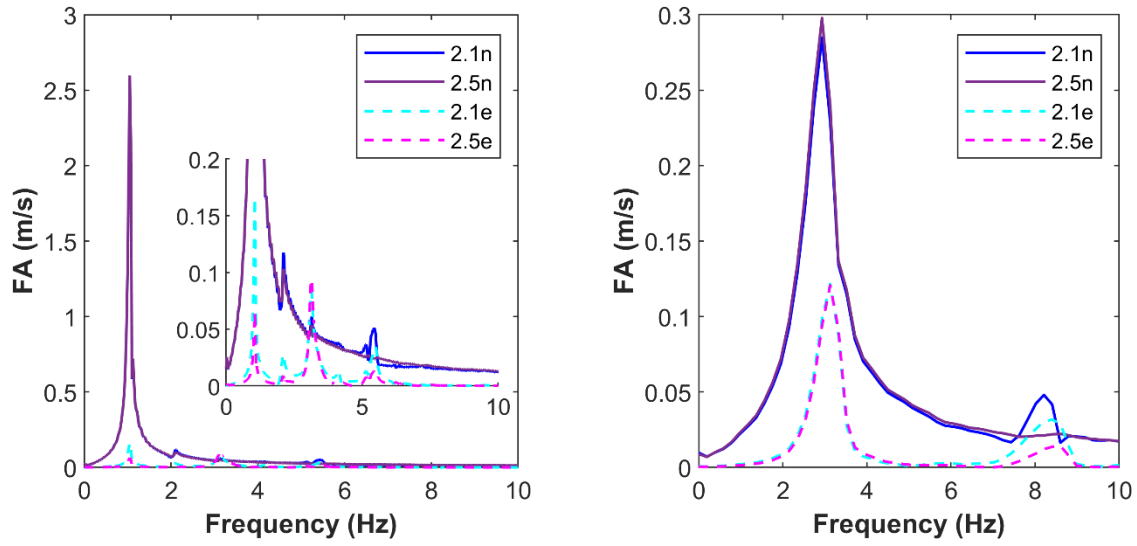


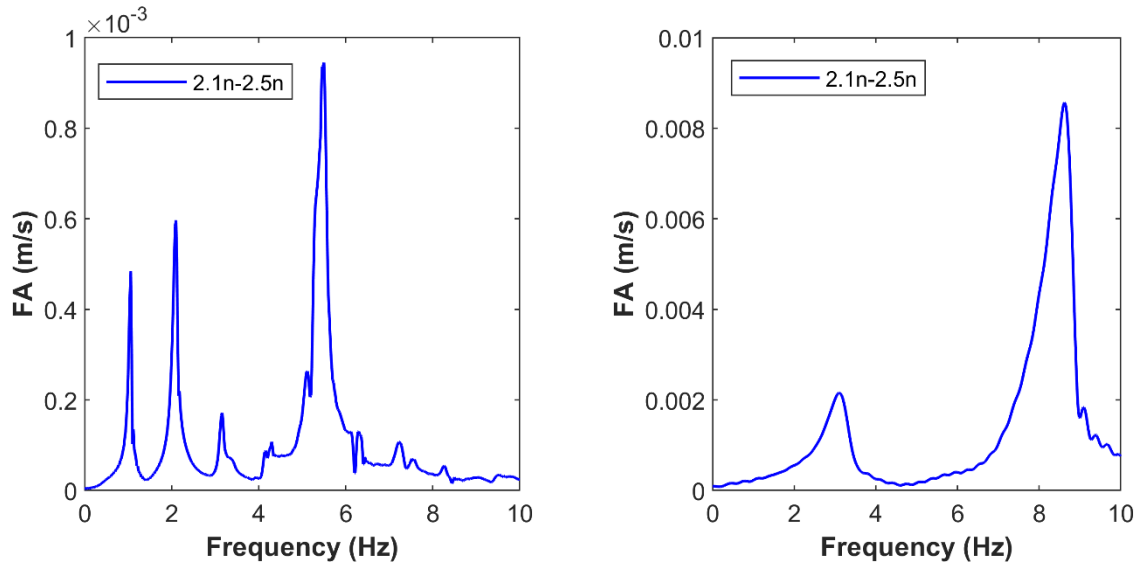
Figure 6.3: Snapshots in plan of the displaced top slab and Fourier spectra of the motion at three locations, that result from a theoretical monochromatic (a) swaying and (b) torsional oscillation of the top slab.



(a) PBr_W$^{(11)}$_13.90kN (b) FBr_2Ts$^{(3)}$_15.70kN

Figure 6.4: Fourier Spectra inferred from acceleration time histories recorded on the top slab by the 2.1 and 2.5 instruments along the North-South (n) and East-West (e) directions during the free vibration experiments: (a) PBr_W$^{(11)}$_13.90kN, (b) FBr_2Ts$^{(3)}$_15.70kN.

As it can be seen in Figure 6.4a, peaks associated with torsional natural frequencies may not be easily identified from the Fourier spectra. The identification of the peaks is facilitated when the torsional component is isolated by removing the translational component from the time histories. Assuming that the centre of the slab coincides to the centre of rotation, the top slab centre exhibits translational motion only, while the motions at any other point contain both torsional and translational components. By subtracting the translational component from a time history recorded at the top slab, the remaining motion can be considered as the motion component associated with torsion alone. During the current experiments, the 2.5 instrument was the one closest to the top slab centre, hence it is considered that it recorded the translational motion only. As already mentioned, data recorded by the corner instruments (i.e. 2.1 and 2.3) contained the most pronounced torsional components. Hence, the acceleration time histories of isolated torsional components are computed as the subtraction of the NS horizontal motion recorded by the 2.5 instrument from the corresponding records of the 2.1 instrument (2.1n-2.5n). A Fourier Amplitude spectrum computed from the latter motion, can clearly reveal the torsional natural frequency of the examined systems. Spectra resulted from such a procedure, by processing data recorded during the (a) PBr_W$^{(11)}$_13.90kN and (b) FBr_2Ts$^{(3)}$_15.70kN experiments, are demonstrated in Figure 6.5. The highest peak observed in each of the spectra corresponds to the torsional natural frequency of the two SSI systems. The identified torsional frequencies agree with the ones shown in Figure 6.4, validating the assumptions made for this procedure.



(a) PBr_W$^{(11)}$_13.90kN (b) FBr_2Ts$^{(3)}$_15.70kN

Figure 6.5: Fourier Spectra inferred from acceleration time histories computed as the subtraction of the North-South motion recorded by the 2.1n and 2.5n instruments, exploiting data from the free vibration experiments: (a) PBr_W$^{(11)}$_13.90kN, (b) FBr_2Ts$^{(3)}$_15.70kN.

6.2.2 Motion decomposition method

The method described in Section 6.2.1 allows the assessment of the deformed shape of the slabs in plan, distinguishing between translational, torsional, or a combination of the two deformations. Herein, the deformed shape of the structure is evaluated in elevation view, aiming to assess the contribution of structural deformability, foundation translation and foundation rocking to the total structural motion. Assuming zero torsional contribution, rigid foundation and rigid top slab, Stewart and Fenves (1998) proposed a motion decomposition method dealing with seismic data, while the method was extended to forced vibration data by Star et al. (2019). A similar procedure is used in the current study, having as input experimental accelerations recorded by several instruments mentioned below. The method, though, is described in terms of displacements, for better visualisation.

The total top slab displacements (u_{ts}) are decomposed into structural flexural deformation (u_s), foundation translation (u_f) and the contribution of foundation rotation (rocking) (u_θ), as defined in Eq. 6.1. Assuming rigid body rotation and small displacements, u_θ is calculated as the product of the foundation rotation (θ) and the height of the structure (h), as shown in Eq. 6.2.

$$u_{ts} = u_s + u_f + u_\theta \quad (6.1)$$

$$u_\theta = h \cdot \theta \quad (6.2)$$

Figure 6.6a illustrates the motion decomposition of a simplified SSI model consisting of a single-degree-of-freedom (SDOF) structure founded on translational and rotational springs that simulate soil compliance. Figure 6.6b shows a cross section of the EUROPROTEAS structure (a fully braced

configuration is shown indicatively). The figure maps the equivalent motion components, u_{ts} and u_f (red arrows) and dimensions of the simplified model to the corresponding quantities of the EUROPROTEAS structure, as well as it presents the recorded data used in the calculations (blue arrows). Similar to Star et al. (2019), the foundation translation component (u_f) corresponds to the displacement of the base of the foundation, while the total top slab response (u_{ts}) corresponds to the displacement of the centre of mass of the top slab. Since none of u_f and u_{ts} were measured in situ, they are inferred by modifying the closest horizontal motion recorded at the foundation ($u_{f,r}$) and top slab ($u_{ts,r}$) respectively. The recorded motions, $u_{f,r}$ and $u_{ts,r}$, differ from u_f and u_{ts} by a component that results from the foundation and top slab rotation respectively, as defined by Eq. 6.3 and 6.4.

$$u_f = u_{f,r} - \theta \cdot h_f \quad 6.3$$

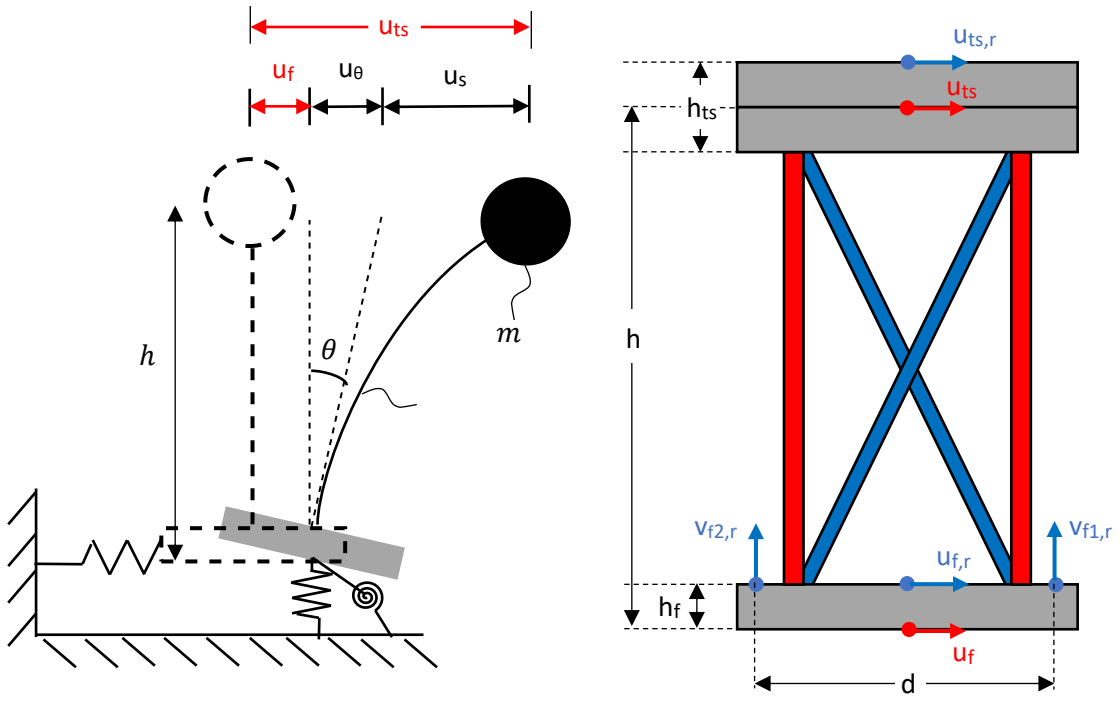
$$u_{ts} = u_{ts,r} - \theta \cdot h_{ts}/2 \quad 6.4$$

where, h_f and h_{ts} are the thickness of foundation and top slab respectively (Figure 6.6b)

The foundation rotation θ is also inferred from the recorded data. It is estimated as the difference of vertical motion recorded by two foundation instruments, $v_{f1,r}$ and $v_{f2,r}$, divided by the distance between them (d), as defined in Eq. 6.5. As shown in Figure 6.6b, the instruments used in the calculations should be located on the foundation diametrically, while a straight line that connects the two instruments should be parallel to the loading direction.

$$\Theta = (v_{f1,r} - v_{f2,r})/d \quad 6.5$$

A limitation of the method is that it is applicable to oscillations where the contribution of torsion is small. The impact of the latter limitation is expected to be small when it is used for the presented free vibration data. The torsional component was very weak during all experiments (see Section 6.2.3 and Appendix D), hence the method is applicable. Aiming to further increase the reliability of the method by minimising the torsional component, $u_{f,r}$ and $u_{ts,r}$ were chosen to correspond to records of instruments closest to the foundation centre and top slab centre respectively. These instruments were the closest to the centre of rotation, hence they recorded the weakest torsional component. Care should also be taken when choosing the remaining instruments records of which are used in the calculations. The motion component $v_{f1,r}$ should be chosen, so that it is in phase with $u_{f,r}$ and $u_{ts,r}$, whereas the $v_{f2,r}$ should be in 180˚ phase difference. Finally, it is fundamental that all instruments are synchronised, while a small time lag can produce unreasonable results. Table 6.1 summarises the instruments of which records are used in the calculations to decompose the total free vibration structural response.



(a) (b)

Figure 6.6: (a) motion decomposition of a simple SSI model, (b) cross section of the EUROPROTEAS structure (fully braced configuration indicatively) mapping the motion components (red arrows) and dimensions between the simplified SSI model with the real structure. The recorded components (blue arrows) that are used in the calculations are also shown.

Table 6.1: Input data used for quantifying the motion components that comprise the overall top slab response.

Experiment	Instrument				d (m)	h (m)
	$u_{ts,r}$	$u_{f,r}$	$v_{f1,r}$	$v_{f2,r}$		
FBr_2Ts(3)	2.5n	1.7n	1.1z	1.2z	2.72	4.4
FBr_2Ts(4)	2.5n	1.1n (+)	1.1z	1.2z	2.72	4.4
PBr_W(11)	2.5e (*)	1.1e (*, +)	1.6z (**)	1.5z (**)	2.58	4.4

(*) The load was applied along the East-West direction, hence, the East-West component was used in the calculations.
(**) The load was applied along the East-West direction, hence the instruments placed on the East and West sides of the foundation were used in the calculation of the angle θ.
(+) The centre 1.7 instrument was not available.

6.2.3 Natural frequencies of the swaying and torsional modes

Following the above procedure, the natural frequencies and the corresponding modes have been identified for all free vibration experiments, which are tabulated in Table 6.2. The Fourier spectra from which the above quantities are inferred can be found in Appendix D. The spectra were computed by considering the first 3.5s and 29.5s of the motion after the load removal, for the FBr_2Ts and PBr_W experiments respectively. Exceptions are the *Low Strain* spectra which are computed by taking into

account only a part of the records that contains motion that is dissipated by 90% to 99%. This ensures the computation of spectra based on very low strain responses, during which any nonlinearities were negligible. Therefore, the identified *Low Strain* natural frequency can be considered to represent a linear elastic SSI system.

Table 6.2 presents the NS and EW swaying, and torsional natural frequencies ($F_{swaying}$, $F_{torsional}$) of the FBr_2Ts and PBr structures that are identified from the free vibration tests. The two swaying natural frequencies of the FBr_2Ts structure, due to the symmetry of the structure, were assumed to coincide. The $F_{swaying}$ varies between 3.50Hz for very low strains to 2.93Hz for the experiment with the largest applied pull-out force, while the $F_{torsional}$ takes values between 8.6Hz to 9Hz. Unlike the FBr_2Ts structure, the PBr structure has asymmetric stiffness, hence the NS and EW swaying modes correspond to different resonant frequencies. The NS swaying mode, which corresponds to the mode of oscillation along the weak axis of the structure, varies between 1.17Hz at very low strains to 1.05 at the largest applied force. The resonant frequency of the EW swaying mode, which corresponds to structural oscillation along its stiff plane, varies between 3.14Hz to 3.80Hz. Finally, the torsional natural frequency of the PBr structure-soil system varies between 5.50Hz to 5.80Hz. It is noted that the second and third modes of this structural configuration can be misunderstood as higher order of the NS swaying modes, as coincidentally they are three and five times larger than the NS $F_{swaying}$. However, looking carefully at the Fourier spectra and considering the mode identification procedure described in Section 6.2.1, the second and third modes can be identified as separate deformation modes.

Comparing the natural frequencies between the fully and partly braced structural configurations, it can be seen that the former structure has a much stiffer response. This was expected as the fully braced structure has two additional pairs of braces which provide a substantial stiffness in the NS direction, compared to the partly braced configuration. It is noted, though, that the natural frequency of the EW swaying mode of the partly braced structure is very similar to the swaying modes (NS or EW) of the fully braced structure. This is attributed to the fact that these modes engaged almost the same structural stiffness during the oscillation of both structural configurations, given that the two structures have the same mass.

The fact that the natural frequencies are characterised by a range instead of a single value is a consequence of nonlinearities that took place during the experiments. The sources of nonlinearities are discussed subsequently in Section 6.2.5. By comparing the assumed linear elastic natural frequencies (inferred from the *Low strain spectra*) of an SSI system, with the ones of the corresponding fixed-base system, the impact of soil compliance on the natural frequencies can be investigated.

Clearly, the comparison of the natural frequencies of a nonlinear SSI system with the fixed-base ones reveals the impact of both soil compliance and nonlinearities. Typically, in the literature, this combined impact is referred to as *lengthening of the predominant period* and is quantified as the ratio of natural periods of an SSI system to the natural period of the corresponding fixed-base system. Equivalently, the impact can be expressed as the ratio of the natural frequency of the fixed-base system to the natural frequency of the SSI system. The fixed-base natural frequencies are calculated as described in Section 5.2.5 and are summarised in Table 5.8. The calculations are based on the assumption of a perfectly symmetric structure and rigid structural connections. However, as mentioned in Section 5.2.4, the connections were not rigid and hence the fixed-base natural frequencies are overestimated.

Table 6.3 summarises the period lengthening ratios, which are calculated as described above. The *Low Strain* ratios that are calculated using the low strain natural frequencies of the SSI systems, aim to investigate the impact of soil compliance. The soil compliance decreased the natural frequency of the swaying modes of the FBr_2Ts fixed-base structure substantially, by 2.6 times. This illustrates the significant impact of the soil compliance on the natural frequency of the SSI system, as well as the high levels of interaction between the structure and soil during oscillation. The interaction was weaker during the NS swaying oscillation of the partly braced structure, as the period lengthening was much lower (1.5). The NS plane is the weak plane of the PBr structure; hence, this oscillation engaged much lower structural stiffness to resist the motion than the NS oscillation of the FBr_2Ts structure, leading to a more flexible response. This is in agreement with the literature (e.g. Stewart *et al.*, 1998; Star *et al.*, 2015; Amorosi *et al.*, 2017), where it is well established that a stiffer response leads to stronger SSI effects, including lengthening of the predominant period, than a more flexible response.

The EW swaying response of the PBr structure was stiffer than the NS, therefore, the SSI phenomena were more pronounced for the corresponding mode which justifies the higher value of the lengthening, 2.40. This value is comparable with the one calculated for the FBr_2Ts structure's swaying modes. As mentioned earlier, the similar values of the two ratios are attributed to the fact that the two modes of the two structural configurations engage a similar amount of structural stiffness to participate in the motion. The SSI phenomena had a weaker impact on the torsional natural frequency of the fully and partly braced structural configurations. Interestingly, the lengthening of the torsional natural period was very similar between the two structural configurations, 1.30 and 1.45 for the assumed linear elastic FBr_2Ts and PBr systems, respectively.

Table 6.3 also presents the period lengthening ratios of the experiments which triggered the highest nonlinearity for the two examined configurations. These experiments were the FBr_2Ts_15.70kN and PBr_W_13.90kN experiments during which the largest pull-out forces were applied. Nonlinearity

increased further the lengthening ratios, while its significance depends on the structural configuration and mode of oscillation considered. Nonlinear phenomena increased the lengthening ratios of the NS and EW swaying modes of the FBr_2Ts structure and the EW swaying mode of the PBr structure by 20%. The lower interaction between the structure and the soil observed during the NS swaying mode of the PBr system led to a weaker impact of nonlinearities on the corresponding ratio, which increased by 11% only. The impact of the nonlinear phenomena on the torsional frequencies was even weaker, as they decreased the low stain torsional period lengthening ratios marginally by 5%. SSI system's nonlinearity is further discussed in Section 6.2.5.

Table 6.2: Resonant frequencies and the corresponding modes of oscillation identified by interpreting free vibration data.

Experiment	Force (kN)	$F_{swaying}$ (Hz)		$F_{torsional}$ (Hz)
		NS	EW	
FBr_2Ts	Low Strain	3.50	3.50	9.0
FBr_2Ts[(4)]	1.96	3.32	3.32	9.0
FBr_2Ts[(4)]	2.40	3.32	3.32	9.0
FBr_2Ts[(3)]	2.94	3.32	3.32	8.8
FBr_2Ts[(4)]	5.03	3.32	3.32	8.8
FBr_2Ts[(3)]	6.38	3.13	3.13	8.8
FBr_2Ts[(4)]	9.64	3.13	3.13	8.8
FBr_2Ts[(3)]	10.10	3.13	3.13	8.6
FBr_2Ts[(4)]	12.53	3.13	3.13	8.6
FBr_2Ts[(3)]	15.70	2.93	2.93	8.6
PBr_W	Low Strain	1.17	3.80	5.80
PBr_W[(11)]	2.03	1.15	3.42	5.69
PBr_W[(11)]	5.44	1.12	3.32	5.62
PBr_W[(11)]	7.31	1.10	3.27	5.57
PBr_W[(11)]	10.03	1.07	3.22	5.54
PBr_W[(11)]	13.90	1.05	3.14	5.50

Table 6.3: Period lengthening ratios of the two swaying modes and the torsional mode of the two structural configurations.

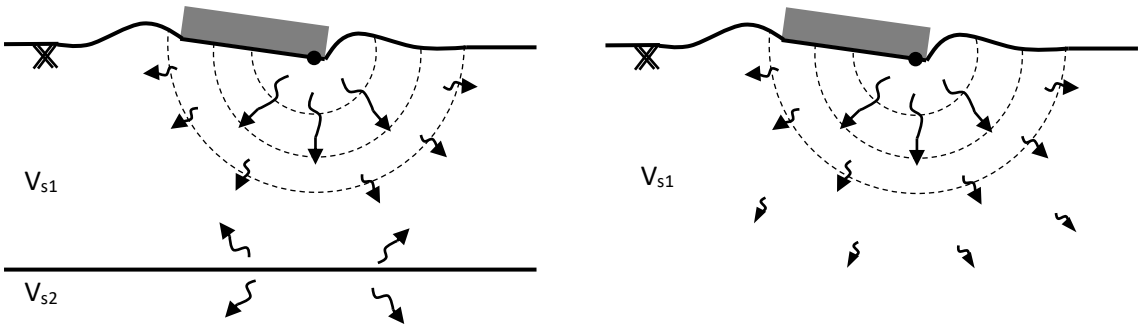
Structural configuration	Low Strain			Highest experimental Nonlinearity		
	Swaying		Torsional	Swaying		Torsional
	NS	EW		NS	EW	
FBr_2Ts	2.61	2.61	1.30	3.12	3.12	1.36
PBr	1.52	2.40	1.45	1.70	2.91	1.53

6.2.4 SSI system's damping

The dissipation mechanisms stem from the material (hysteretic) damping of both structural and soil elements, as well as from the system's radiation damping. Material damping results from energy dissipation during friction, heat generation, hysteresis and plastic yielding; and it is strain dependent. Radiation damping commonly consists of impedance effect and geometrical spreading (Kramer, 1996). Impedance effect results in energy loss when incoming waves impinge on an interface between materials of different properties, and it can be effective in reducing upward propagating (e.g. seismic) waves. This effect, though, can prohibit energy radiation for the case of a vibrating foundation, which emits energy in the soil domain in the form of downward propagating waves (e.g. Gazetas, 1983). The existence of a strong stiffness contrast between layers at a shallow depth can reflect the downward propagating waves back to the footing resulting in wave trapping in the upper layer (Figure 6.7a).

Conversely, the entire amount of energy that is transmitted to the soil medium is radiated when a foundation vibrates over a homogeneous half-space (Figure 6.7b). These conditions can closely prescribe the conditions of the examined experiments, as there is not any strong stiffness contrast between the shallow soil layers (Figure 4.7). Assuming the foundation as a dimensionless point which emitted a total of energy I in linear elastic soil, then the energy per unit area of a point located at distance r from the source was E/Area of a hemisphere. The area is a function of r^2, hence it is apparent that the motion attenuated exponentially with distance, as a consequence of geometrical spreading. It is therefore expected that impedance effect to be negligible, while geometrical spreading is expected to be dominant in producing damping for those experiments that engaged the soil participation in the motion of the SSI system. SSI system's damping is expected to be higher in experiments which transferred larger motion to the soil medium, as more energy is radiated away from the structure. Larger soil motion also resulted in higher soil strains, which increases material damping through hysteresis.

The damping of a structure or of an SSI system can be estimated from free vibration data by employing the logarithmic decrement method (Chopra, 2011). The damping corresponds to the predominant mode of the oscillation, which in both FBr_2Ts and PBr_W structures was the swaying mode. The contribution of the torsional modes in the motion was very weak in all experiments, hence the damping that is produced by this mode is considered negligible.



(a) (b)

Figure 6.7: Vibratory surface footing transmitting waves to (a) soil stratum over a stiffer half-space ($V_{s1}<V_{s2}$) or (b) homogeneous half-space.

The logarithmic decrement method is based on that the ratio of peak displacements (u), that correspond to two successive cycles (i, i+1) of a free vibration motion with constant damping (ζ), can be estimated from Eq. 6.6. Assuming small values and damping, the value of $\sqrt{1-\zeta^2}$ can be considered as unity, which simplifies the ratio, as shown in Eq. 6.7.

$$\frac{u_i}{u_{i+1}} = e^{\frac{2\pi\zeta}{\sqrt{1-\zeta^2}}} \quad 6.6$$

$$\frac{u_i}{u_{i+1}} = e^{2\pi\zeta} \quad 6.7$$

The above expression is generalised for the peak displacements ratio between j cycles starting from the i^{th} displacement peak, as given by Eq. 6.8. Solving the latter equation, the damping of a lightly damped (i.e. ζ<20%) system can be estimated according to Eq. 6.9, which can also be expressed in terms of accelerations (Eq. 6.10). The latter equation is the one that is used herein to calculate the experimental SSI damping, using free vibration data recorded on the top slab.

$$\frac{u_i}{u_{i+j}} = e^{2\pi\zeta\cdot j} \quad 6.8$$

$$\zeta = \frac{1}{2\pi j} ln \frac{u_i}{u_{i+j}} \quad 6.9$$

$$\zeta = \frac{1}{2\pi j} ln \frac{\ddot{u}_i}{\ddot{u}_{i+j}} \quad 6.10$$

Once the damping of the recorded motion is determined, the motion envelope (Figure 6.8) that illustrates the decay of the motion can be determined by Eq. 6.11, where ρ is a constant, in acceleration units, and ω_n is the undamped angular natural frequency of the SSI system (Chopra, 2011). The undamped natural period (T_n) is related to the damped natural period (T_D) as shown in Eq. 6.12. As previously mentioned, assuming low damping ratio values, the denominator is close to unity.

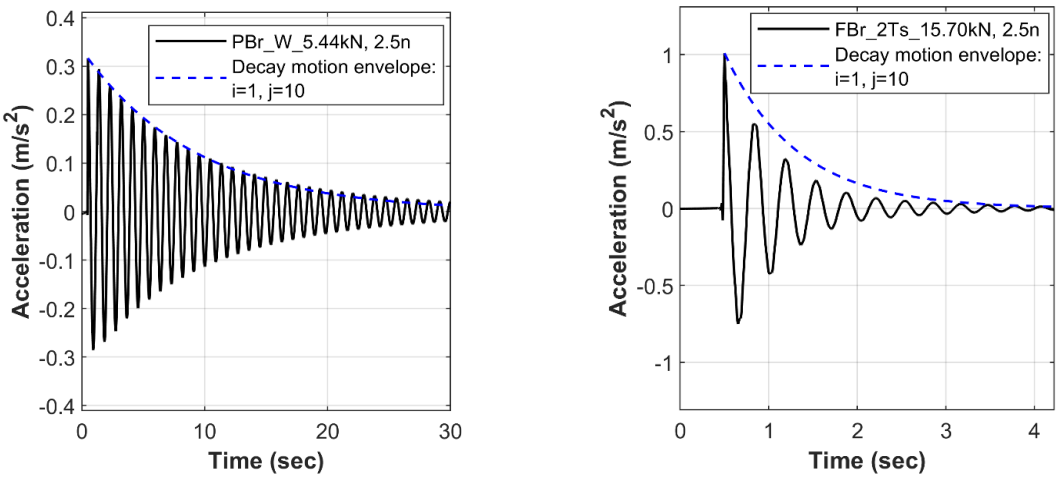
Hence, it is reasonable for the purpose of this study to assume that the undamped and damped natural periods coincide. For the calculation of the decay motion envelope, ω_n assumed to be equal to the angular natural frequency of the SSI system, which was computed from the experimental data discussed in Section 6.2.3. To ensure that the motion envelope equation replicates both the i^{th} and j^{th} cycles, ρ is taken equal to the first peak acceleration ($\ddot{u}_i$) that was considered in the calculations. The decay motion envelope equation that is used in this study is given by Eq. 6.13.

$$\ddot{u}(t)_{envelope} = \rho e^{\zeta \omega_n t} \tag{6.11}$$

$$T_D = \frac{T_n}{\sqrt{1-\zeta^2}} \tag{6.12}$$

$$\ddot{u}(t)_{envelope} = \ddot{u}_i \cdot e^{\zeta \omega_n t} \tag{6.13}$$

The above definition of the acceleration envelope predicts accurately the accelerations of i^{th} and $(i+j)^{th}$ cycles, while it approximates the remaining ones. The accuracy of the approximation decreases when nonlinear phenomena become more pronounced. Figure 6.8 shows the acceleration time histories and the decay envelopes of the motions that were recorded at the top slab centre, by the 2.5n instrument, during the PBr_W_5.44kN and FBr_2Ts_15.70kN experiments. The damping of both experiments was calculated by considering the first peak (i=1) and the next 10 cycles (j=10) in the calculations. It can be seen that the envelope calculated by Eq. 6.13 is accurate for the PBr_W_5.44kN free vibration experiment, which was expected to exhibit very weak nonlinearities. For the FBr_2Ts_15.70kN experiment, during which nonlinear phenomena were more pronounced, Eq. 6.13 cannot sufficiently produce an envelope of maximum accelerations. This is attributed to the fact that when nonlinear phenomena are pronounced, the damping is not constant, whereas Eq. 6.13 assumes a constant damping, ζ, for the entire time history. It is therefore apparent that, for nonlinear free vibration motions, the computed damping ratio value can vary for different pairs of i and j.



(a) (b)

Figure 6.8: Acceleration time histories and decay motion envelopes of the motions recorded at the centre of the top slab during the experiments: (a) PBr_W$^{(11)}$_5.44kN, (b) FBr_2Ts$^{(3)}$_15.70kN.

Figure 6.9 and Figure 6.10 present the variation of damping ratio of the PBr_W and FBr_2Ts SSI systems respectively, computed using different pairs of the i and j variables. The damping ratio values are calculated using strong motion data recorded by the 2.5n instrument along the NS (in-plane) direction at the centre of the top slab. Comparing the two figures, it is apparent that the soil-FBr_2Ts structure system produced larger damping overall than the soil-PBr_W structure system. The implication of this on the response, is shown in Figure 6.11. The figure compares acceleration time histories recorded on the top slab during free vibration tests of the two configurations, which were excited by a similar magnitude of pull-out force. The figure shows that motion duration of the FBr_2Ts structure was much shorter than the one of the PBr_W structure, despite that the peak accelerations at the first cycle were very similar. The large difference in the duration of the motion is a result of the much larger damping developed during the experiment on the FBr_2Ts than the PBr_W structure.

The next important feature that can be revealed from Figure 6.9 and Figure 6.10, is the dependence of computed damping on the selection of the cycles (i, j parameters) that are used in the calculation. As Figure 6.9a and b show, the damping ratio, produced by the PBr_W system when the pull-out force was 2.03kN or 5.44kN, was almost constant and independent from the selection of i and j. The latter implies a relatively linear behaviour of the SSI system during these experiments. For larger applied forces, though, such as the PBr_W_10.03kN and PBr_W_13.90kN experiments, nonlinearity was more pronounced leading to damping ratio values that are dependent on the selection of i and j. As mentioned earlier, nonlinear phenomena were much more pronounced during the FBr_2Ts free vibration tests, which explains the large range of the computed damping ratio values, shown in Figure 6.10. The damping ratio takes values between 4% and 10%, depending on the magnitude of the pull-out forces as well as by the selection of i-j pair.

As observed in both PBr_W and FBr_2Ts free vibration experiments (Figure 6.9 and Figure 6.10), the damping ratio is larger when it is computed by considering the first acceleration peak in the calculations (i=1) than by taking any subsequent peak. This implies that the experimental damping was larger at the first cycles of the motion, while it decreased with time. This can be explained by the fact at the first cycles of the motion, where the motion amplitude was the largest, larger strains were induced in the soil producing stronger nonlinearity and hence higher soil damping. When motion intensity reduced at a subsequent time, though, the strains and nonlinear phenomena became weaker producing smaller soil damping. However, Figure 6.10 shows that damping can increase with j, which according to the above argument was not expected. This can be attributed to interface nonlinear phenomena which are subsequently discussed in Section 6.2.5.

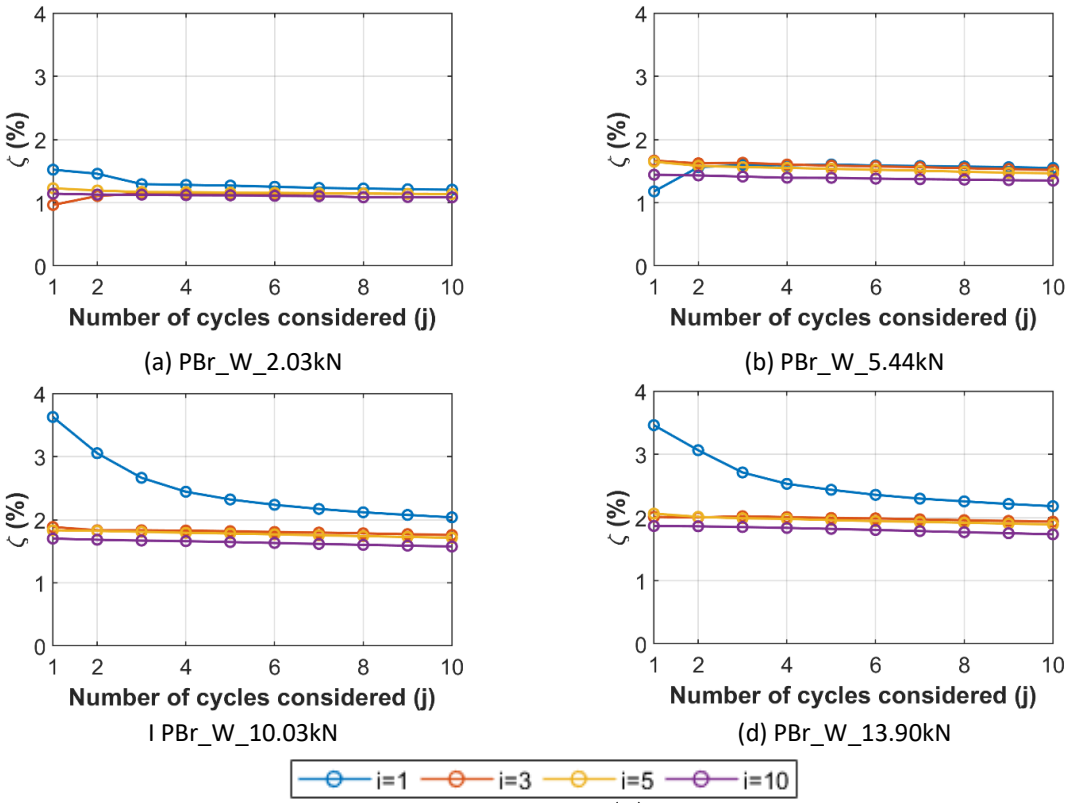


Figure 6.9: Damping ratio values produced during the PBr_W(11) experiments of various pull-out forces, which are computed using different pairs of i and j. Data recorded by the 2.5n instrument on the top slab centre in the NS direction, were processed.

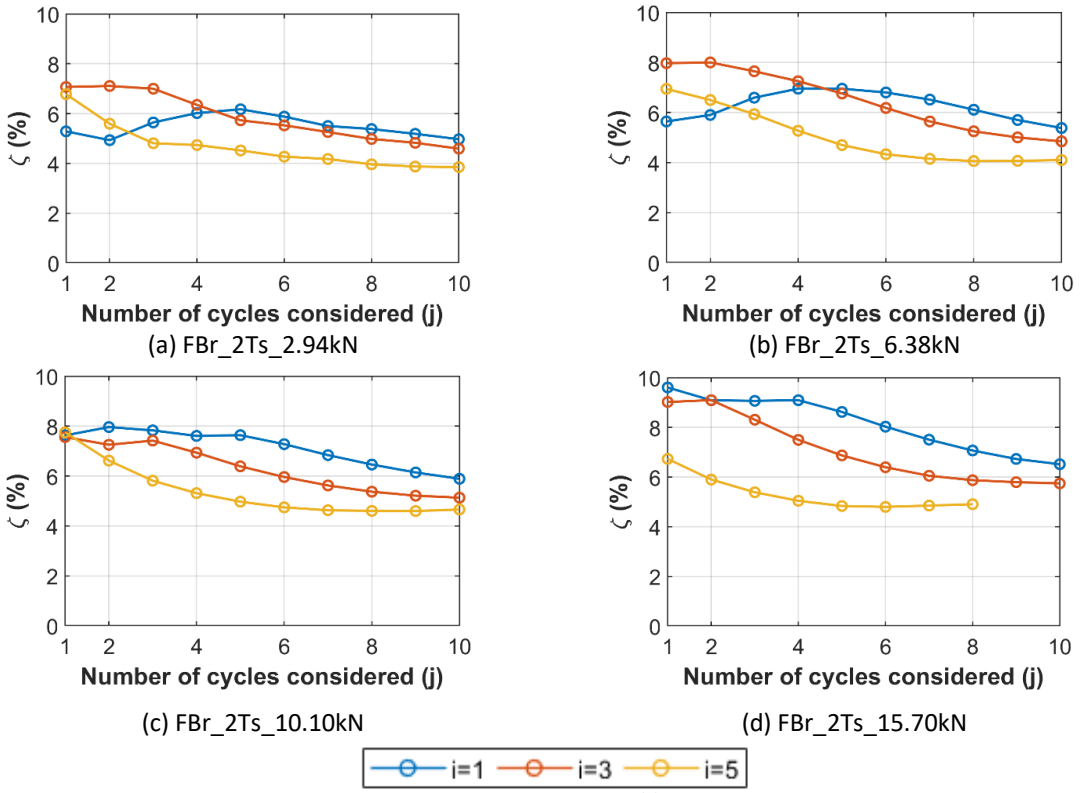
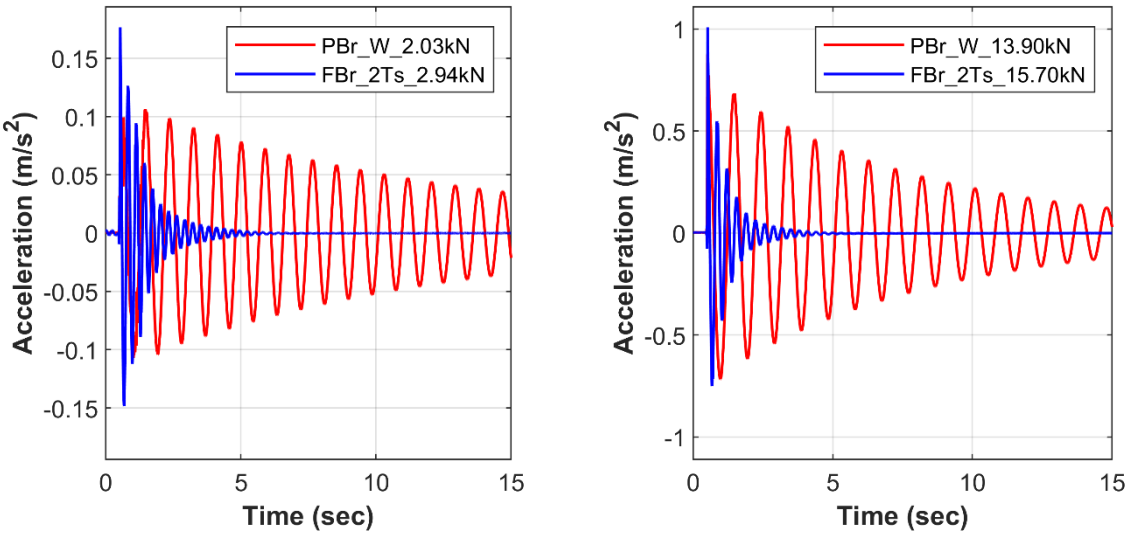


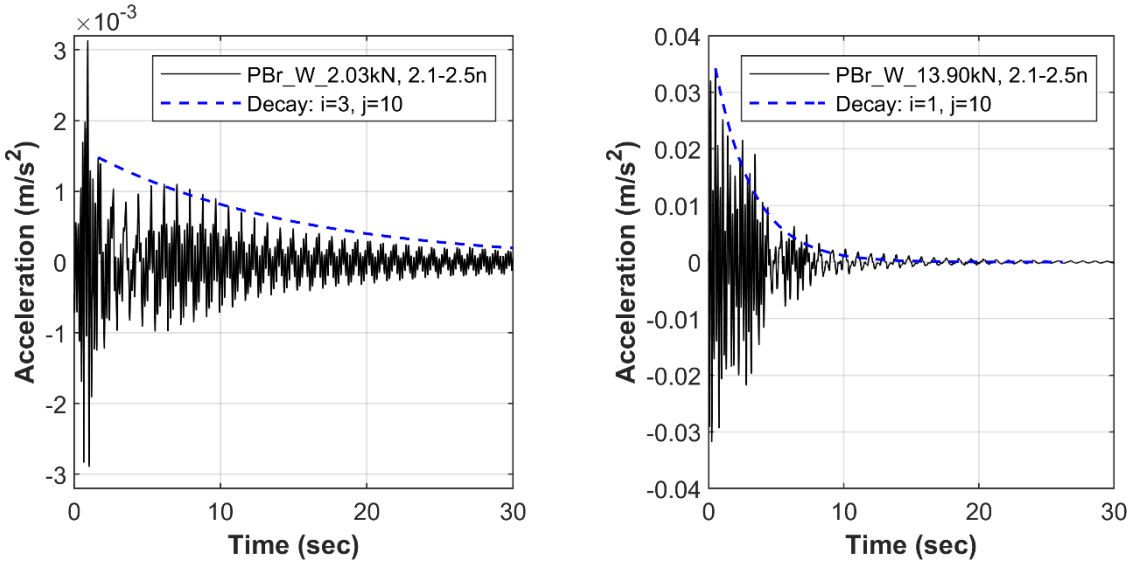
Figure 6.10: Damping ratio values produced during the FBr_2Ts(3) experiments of various pull-out forces, which are computed using different pairs of i and j. Data recorded by the 2.5n instrument on the top slab centre in the NS direction, were processed.



(a) (b)

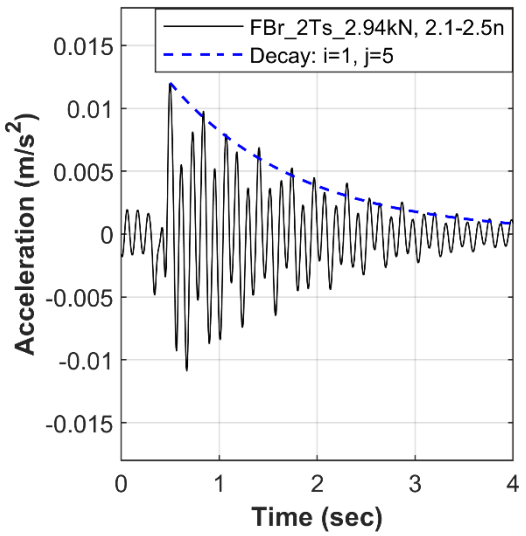
Figure 6.11: Comparison between acceleration time histories recorded during the PBr_W and FBr_2Ts free vibration experiments, at the centre of the top slab.

The above-mentioned damping values refer to the NS swaying mode of the PBr_W and both NS and EW modes of the FBr_2Ts SSI systems. The damping of the torsional mode is challenging to be estimated through the free vibration tests, as the contribution of torsion in the motion was very weak. The torsional motion, though, can be decomposed by subtracting the motion recorded at the centre of the top slab from the one recorded at the corner, as explained in Section 6.2.1. The *torsional acceleration time history* that results from the subtraction is usually dominated by high-frequency noise and does not allow the calculation of torsional damping at different times, as calculated earlier for the swaying mode. An "average" torsional damping can be estimated, though, in a way that the decay envelope, computed as per Eq. 6.13, approaches the maximum response. Figure 6.12 presents the decay envelops of the torsional acceleration time histories processed from data recorded during the PBr_W (a,b) and FBr_2Ts (c,d) experiments of different pull-out forces. Although the envelopes do not follow exactly the peak accelerations, the variation of torsional damping with time is not as pronounced as observed for the swaying damping. Hence, the average damping values, for which the envelopes are computed, can be considered as a reliable indication of the torsional damping ratio. The damping ratios used in the computation of the envelopes are listed in Table 6.4. As observed for the swaying mode, the torsional damping ratios were larger for the stiffer, FBr_2Ts structure, while they increase with the magnitude of pull-out force. As previously, the latter is attributed to nonlinear phenomena, the source of which is discussed in Section 6.2.5.

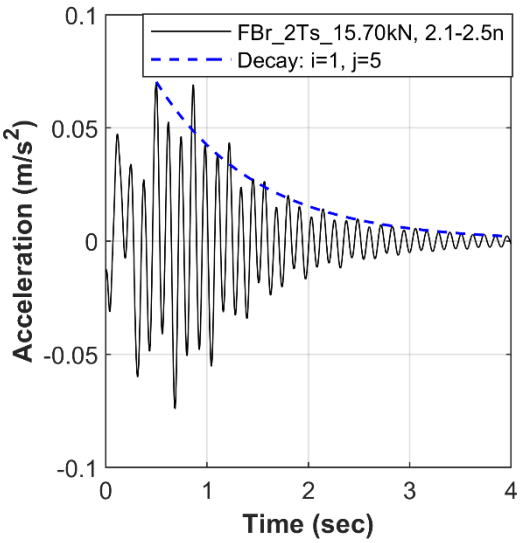


(a) PBr_W_2.03kN

(b) PBr_W_13.90kN



(c) FBr_2Ts_2.94kN



(d) FBr_2Ts_15.70kN

Figure 6.12: Acceleration time histories and decay envelopes of the motion resulted from the subtraction of the 2.5n motion from the 2.1n one. Data from PBr_W and FBr_2Ts experiments of different pull-out forces are processed.

Table 6.4: "Average damping values of the torsional mode.

	PBr_W		FBr_2Ts	
	F=2.03kN	F=13.90kN	F=2.94kN	F=15.70kN
ζ (%)	0.99	1.03	1.30	1.90

6.2.5 Evaluation of nonlinear effects

Nonlinear response of an SSI system with increasing intensity of input excitation can be attributed to different sources of nonlinearity. Structural material yielding and geometric nonlinearity (P-δ effects) are two of the sources. However, it is expected that these did not take place or were negligibly small during the conducted experiments, as the motion intensity was not strong enough to trigger such nonlinearities. For the same reason, soil yielding, which is also a source of nonlinearity, is expected to have negligible effects. Soil nonlinearity, though, is envisaged to play a significant role during the experiments, as the linear strain region of soils is very limited (Jardine *et al.*, 1986; Darendeli, 2001; Taborda *et al.*, 2016). The higher intensity of the motion results in stronger soil nonlinearity, leading to more inclined and wider hysteresis loops in the stress-strain domain. Therefore, soil nonlinearity is expected to be more pronounced in the vicinity of the foundation, where the strongest response is expected, and to diminish as the distance from the foundation increases. Similarly, the overall soil nonlinearity produced by an experiment is expected to increase with the magnitude of the input excitation, as stronger input excitation develops larger strains in the soil. Nonlinear phenomena degrade the stiffness of the soil and increase the damping produced through hysteresis, which in return reduces the natural frequency and increases the overall damping of an SSI system.

Additional sources of nonlinearity that can be dominant in soil-shallow foundation-structure systems is the soil-foundation interface inelasticity and interface geometric nonlinearity (Drosos *et al.*, 2012). Interface inelasticity refers to the relative sliding between a shallow foundation and the adjacent soil. Sliding develops permanent horizontal displacements and dissipates energy through friction that is generated at the interface. Interface geometric nonlinearity is evident through foundation uplift, which is the nonlinear mechanism that prevails in stiff and slender structures (Amorosi *et al.*, 2017), while it is accentuated for smaller or heavier loaded foundations (Gazetas *et al.*, 2013; Gazetas, 2015). Dynamic foundation uplift, which is commonly referred to as rocking, results in a decreased contact area between the foundation and soil, making the system more flexible. Also, rocking significantly affects the damping of the system through two counteracting effects. When a footing is heavily loaded, foundation rocking increases damping through hysteresis that is generated from soil yielding and plastic deformations below the foundation corners. The second effect of foundation rocking is that it transfers weaker motion to the soil and hence produces smaller radiation damping than the translational foundation mode (Gazetas, 1983, 1991; Amorosi *et al.*, 2017). Finally, foundation rocking densifies the soil below the foundation corners (Drosos *et al.*, 2012), which increases the mean effective stress locally resulting in an increase of the soil stiffness and decrease of soil damping (Darendeli, 2001; Taborda, 2011).

Overall, nonlinear phenomena decrease the natural frequency of an SSI system, increase damping which can also decrease when foundation rocking is prominent. This expectation is verified in Figure 6.13 and Figure 6.14 which quantify the impacts of nonlinear phenomena on the natural frequency and damping ratio, as inferred from free vibration data recorded during the PBr_W$^{(11)}$ and FBr_2Ts$^{(3)}$ experiments respectively. In both cases, the exploited data were recorded on the top slab centre by the 2.5n instrument. Nonlinear phenomena are investigated by comparing the free vibration response of the top slab, under different magnitudes of pull-out force. The response, in terms of the predominant frequency, is assessed by the means of Fourier spectra and *Peak-to-Peak frequency* time series. The Fourier spectra (Figures 6.13a and 6.14a) are inferred from the top slab acceleration time histories that are normalised to the amplitude of the pull-out force. Under different pull-out forces, a linear elastic SSI system develops identical normalised free vibration response, while any difference is attributed to nonlinear phenomena. Although Fourier spectra that are inferred from free vibration data can provide the predominant frequency, they cannot be used to detect the variation of response frequency with time. *Peak-to-peak frequency* time series (Figure 6.13b, Figure 6.14b) aim to address the latter consideration. These time series comprise frequency points which are calculated as the inverse of time difference between two successive peaks, as described in Section 5.8.1. The level of variation of frequency with time can be an indication of the significance of the nonlinearity that took place during an experiment. Nonlinearity can also be qualitatively assessed through the variation of damping ratio of an SSI system with time. Figure 6.13c and Figure 6.14c present damping time series, which consist of damping ratio data points computed between every two successive peaks (j=1), by employing the logarithmic decrement method described in Section 6.2.4. The overall damping of a free vibration experiment can also be qualitatively evaluated through the width of the main peak of Fourier spectra, as a wider peak can indicate more damping than a narrower one (due to additional low frequency content through stiffness degradation).

Figure 6.13a shows that the predominant frequency of the soil-partly braced structure system is not sensitive to the magnitude of loading, as the predominant frequency varies only between 1.07Hz and 1.15Hz (see also Table 6.2). This is also validated by the peak-to-peak frequencies (Figure 6.13b) which take values within a similar range, indicating weak nonlinear phenomena. As expected, the impact of nonlinear phenomena was more pronounced on the stiffer, FBr_2Ts, structural configuration than the PBr_W, although the trends were the same. Figure 6.14a shows that the experiments of various pull-out force amplitudes (2.94kN, 6.38kN, 10.10kN and 15.70kN) infer natural frequencies of the FBr_2Ts configuration between 2.93Hz and 3.32Hz (see also Table 6.2). This is a relatively wide range, demonstrating that the significance of nonlinearities on the response of the FBr_2TS structure. The nonlinear response is also apparent in the peak-to-peak frequency time series, which deviate for the

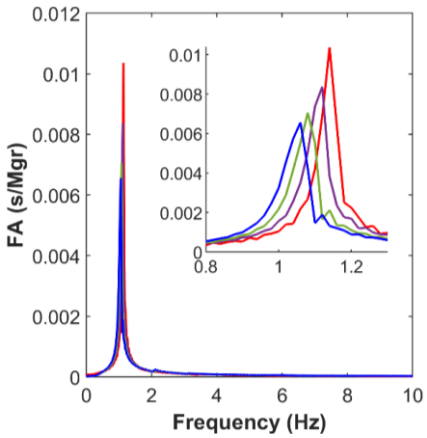
compared experiments, as shown in Figure 6.14b. Nonlinear phenomena affected the amplitude of the structural response of both structural configurations, as indicated by the amplitude of the Fourier spectra that decrease with applied force (Figures 6.13a, 6.14a). The latter is an indication that larger damping was produced during the heavier loaded experiments. The correlation between damping and pull-out force is also verified by the width of the spectra (Figures 6.13a, 6.14a) and the computed damping ratios (Figures 6.13c, 6.14c), which both increase with the magnitude of pull-out force.

It Is therefore well evidenced that the nonlinear phenomena were more pronounced during the experiments with larger pull-out force. Larger excitation resulted in higher strains induced in the soil and more pronounced foundation uplift and sliding. Higher soil strains resulted in stronger soil nonlinearities, such as soil stiffness degradation and soil damping generation. The soil stiffness degradation as well as the foundation uplift and sliding made the SSI system more flexible under higher intensity motion, justifying the tendency of the natural frequency to decrease with increasing pull-out force. Similarly, the higher levels of soil damping explain the observed higher damping ratio values produced by the entire SSI systems during the experiments of larger pull-out force. More importantly, the latter observation demonstrates that soil damping was the dominant source of damping.

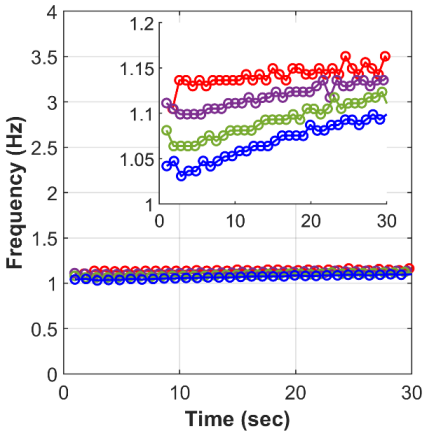
Soil and interface nonlinearities were more pronounced during the first cycles of the oscillations, when the motion was the strongest. As the motion progressed, both motion intensity and nonlinearities decayed, explaining the increase of natural frequency and decrease of damping ratio with time, observed in Figure 6.13a,b and Figure 6.14a,b. After a certain number of cycles when a significant amount of energy was dissipated, the peak-to-peak frequencies of all experiments tended to converge to a common value. The converged value of frequency corresponds to the predominant frequency of the linear elastic systems, as strains became very low and nonlinearity negligible. This converged frequency value is around 3.5Hz for the FBr_2Ts structural configuration and 1.15Hz for the PBr_W structure. Both values agree with the low strain swaying natural periods inferred from Fourier spectra of free vibration records dissipated by 90-99%, as presented in Section 6.2.3 and shown in Table 6.2. Similarly, the damping ratios of the compared experiments tended to converge to a damping of the equivalent linear elastic system. These values, though, cannot be accurately determined due to numerical instabilities in the calculation of damping ratio. The damping values of the linear elastic PBr_W and FBr_2Ts systems are estimated around 1% and 3% respectively. A factor that can justify the difference between them is the damping contribution of the braces that were removed from the partly braced structure. More importantly, the difference can be assigned to radiation damping which was triggered more pronouncedly during the FBr_2Ts experiments. For the case of the PBr_W structure, the converged value can be assigned to the structural damping as the foundation motion

and hence the SSI effects were very weak. The converged damping value of the FBr_2Ts experiment is an aggregation of material damping of structural and soil elements, as well as radiation damping.

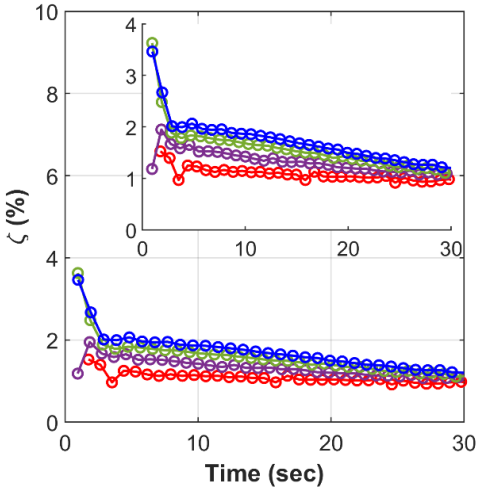
Despite that the peak-to-peak frequencies were expected to increase with time for the reasons explained above, in some experiments, a decrease is observed between the first and the second cycles (Figure 6.13b and Figure 6.14b). This observation implies that the response of the SSI systems was stiffer at the first cycle of motion than at the subsequent ones. During the first cycle, the system gained stiffness, which, according to the author's opinion, can be associated with the change of contact conditions between the foundation and the adjacent soil. It is presumed that, under static conditions, the foundation was not in full contact with the soil beneath, as some gaps at the interface could be visually inspected during the experiments. Some of the gaps might had closed during the application of the pull-out force and during the first cycle of the motion. The ensuing increased interface contact conditions provided additional stiffness to the system, increasing temporarily the natural frequency of the SSI system. Beyond the first cycle, the gaps opened again and stayed opened throughout the motion, making the system more flexible, which can explain the decrease of the peak-to-peak frequencies between the first and second cycles. This claim is numerically verified in Section 7.15.



(a)



(b)



(c)

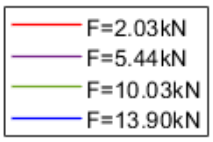


Figure 6.13: Impact of nonlinear effects during PBr_W[(11)] experiments on the natural frequency and damping of the SSI system. The effects are illustrated through: (a) Fourier spectra of the normalised response, (b) Peak-to-Peak frequencies, (c) Computed damping ratios. All data were produced by exploiting the motion recorded on the top slab by the 2.5n instrument.

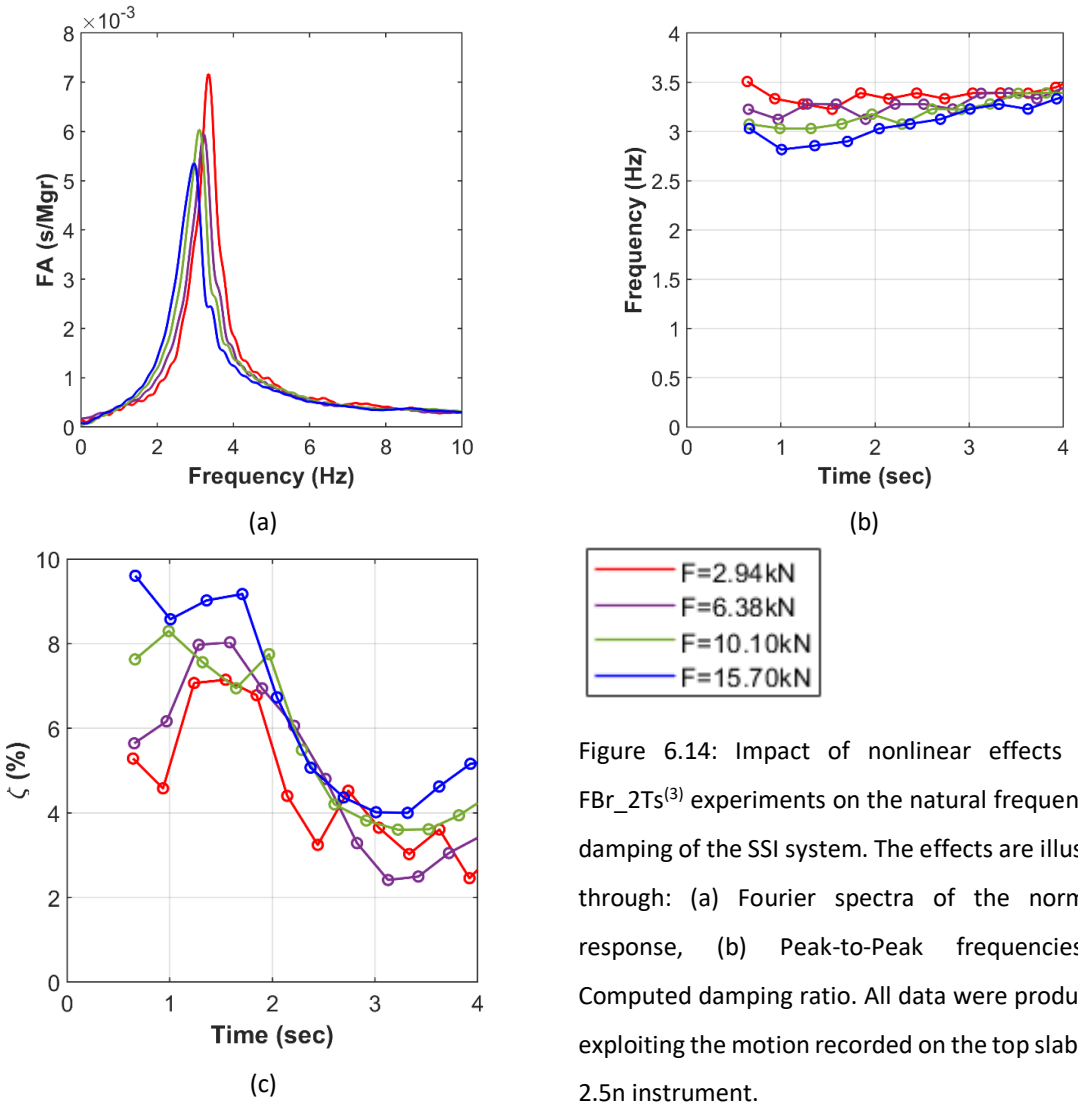


Figure 6.14: Impact of nonlinear effects during FBr_2Ts[3] experiments on the natural frequency and damping of the SSI system. The effects are illustrated through: (a) Fourier spectra of the normalised response, (b) Peak-to-Peak frequencies, (c) Computed damping ratio. All data were produced by exploiting the motion recorded on the top slab by the 2.5n instrument.

6.2.6 Evidence of soil nonlinearity

In the previous section, the impact of nonlinearity on the SSI response was discussed. Herein, an attempt to provide evidence of soil nonlinearity is made. The level of soil nonlinearity is proportional to the strain levels induced in the soil. Despite that these were not measured in-situ, they can be indirectly assessed through the amplitudes of the recorded soil motions. Figure 6.15 compares the soil response recorded during the experiments on the PBr_W and FBr_2Ts structures that were subjected to similar the pull-out forces (i.e. PBr_W _2.03kN Vs FBr_2Ts_2.94kN, PBr_W_13.90kN Vs FBr_2Ts_15.70kN). The presented data correspond to the NS (Figure 6.15a, b) and vertical (Figure 6.15c, d) soil motion components, recorded by the 0.1 instrument which was located at 1.2m to the North of the foundation edge (Figure 5.17).

The figure demonstrates that stronger soil motion was recorded on the soil surface during experiments on the FBr_2Ts structure than the PBr_W one. This can be considered as evidence of the

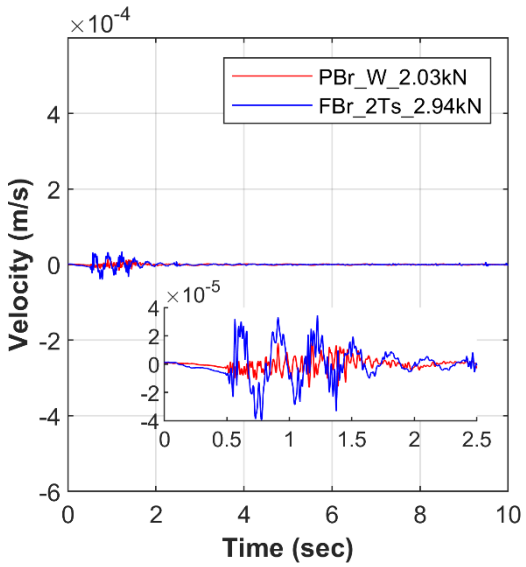
claim made earlier in Section 6.2.5, that nonlinear effects were more important during the former experiments. The stronger soil response exhibited during the FBr_2Ts experiment indicates that larger strains were induced in the soil, resulting in higher stiffness degradation (G/G_{max}) and damping ratio (ζ). Figure 6.16 maps the "experimental" secant stiffness degradation (G_{sec}/G_{max}) and ζ, to stiffness degradation and damping ratio (G-γ-D) curves that correspond to the superficial layer. The G-γ-D curves are produced according to Darendeli (2001), the parameters of which were calibrated as discussed in Chapter 4. The "experimental" G_{sec}/G_{max} and ζ values are inferred from the G-γ-D curves using "experimental" shear strains (γ_{exp}) which were estimated as defined in Eq. 6.14 (Newmark, 1967; Kramer, 1996).

$$\gamma_{\exp} = \mathrm{PPV}/V_s \qquad 6.14$$

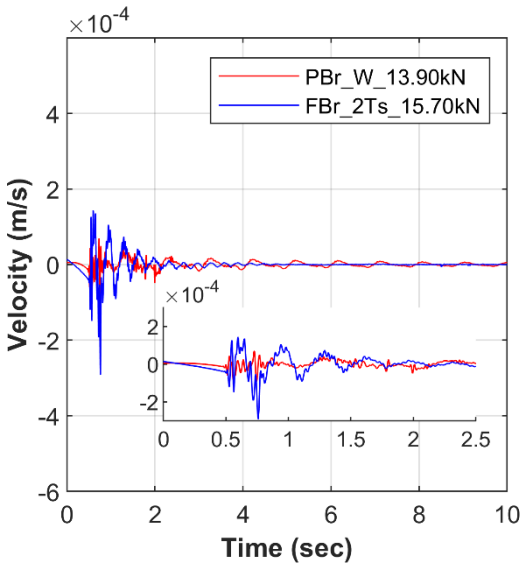
where, V_s is the shear wave velocity of the superficial layer taken equal to 140m/s, which is a value resulted from the calibration of the soil properties, as shown in Section 4.3.2. PPV refers to peak particle velocity recorded in the NS (in-plane) direction by the 0.1n instrument on the soil surface.

The above equation gives a very rough estimate of the experimental strains. Its derivation is based on one-dimensional conditions, where a shear wave propagates in an infinitely long, linear elastic rod which constrains the lateral radiation. The "experimental" G/G_{max} and ζ values indicate the stiffness degradation and damping ratio of the soil locally in the vicinity of instrument 0.1. G/G_{max} and ζ are time dependent, as shear strains change with time. The experimental PPV values, incorporated in the calculations, correspond to the maximum values recorded during each experiment. Therefore, the G/G_{max} and ζ values can be assumed as the lowest and highest values that took place around the location of 0.1 instrument during the examined experiment. With reference Figure 6.16, Table 6.5 presents the values of the experimental secant stiffness degradation (G_{sec}/G_{max}) and ζ.

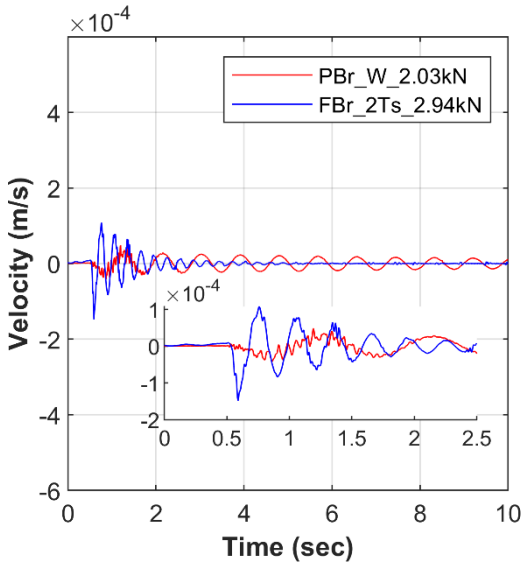
Figure 6.16 verifies that the FBr_2Ts experiments produced smaller G_{sec}/G_{max} and larger ζ than the PBr_W experiments. However, the difference is not large enough to justify the difference of the impact of nonlinear effects on period lengthening and damping, shown in Figures 6.13 and 6.14. The latter indicates that the soil surface motion at the location of 0.1 instrument had already dissipated substantially before reaching the instrument. It is presumed that the interface nonlinearity and soil nonlinearity in the vicinity of the foundation controlled the overall nonlinearity developed during the examined experiments. It is expected that, during the experiments, much higher strains, than the ones shown in Figure 6.16, were induced in the soil below the foundation edges. This area of soil controlled the degradation of soil stiffness affecting the natural frequencies, as well as the production of damping. Although there is no experimental evidence of accumulation of strains in the vicinity of the foundation, it is subsequently verified numerically in Section 7.13 and in Section 8.2.4.



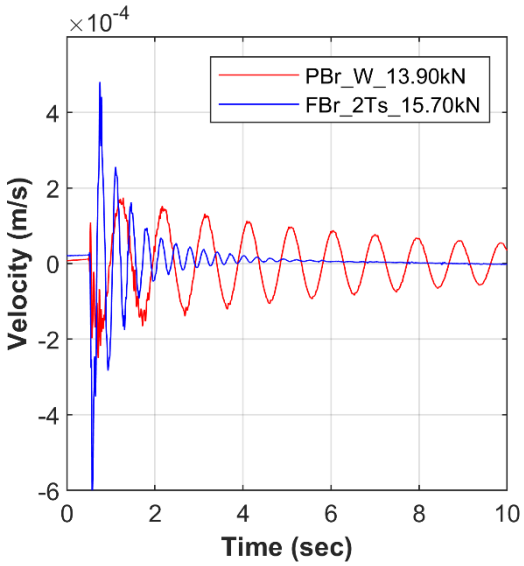
(a) Soil NS motion, F=2.03-2.94kN



(b) Soil NS motion, F=13.90-15.70kN



(c) Soil vertical motion, F=2.03-2.94kN



(d) Soil vertical motion, F=13.09-15.70kN

Figure 6.15: Comparison of the soil response between the PBr_W and FBr_2Ts free vibration experiments of similar pull-out forces. The compared quantities are: (a, b) Soil NS motion recorded by the 0.1n instrument; and (c, d) Soil vertical motion recorded by the 0.1z instrument.

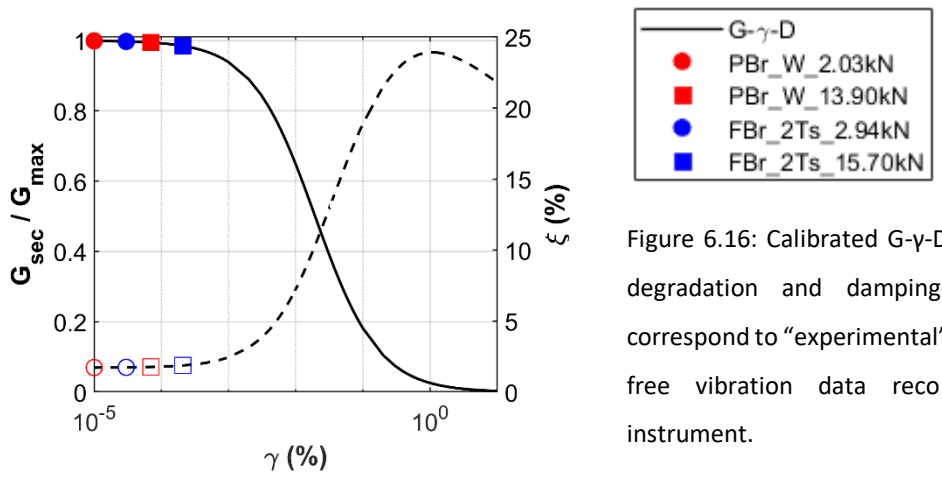


Figure 6.16: Calibrated G-γ-D curves and stiffness degradation and damping ratio values that correspond to "experimental" strains inferred from free vibration data recorded by the 0.1n instrument.

Table 6.5: Peak particle velocities recorded along the North-South direction by the 0.1n instrument, and the corresponding shear strains, stiffness degradation and damping ratio values.

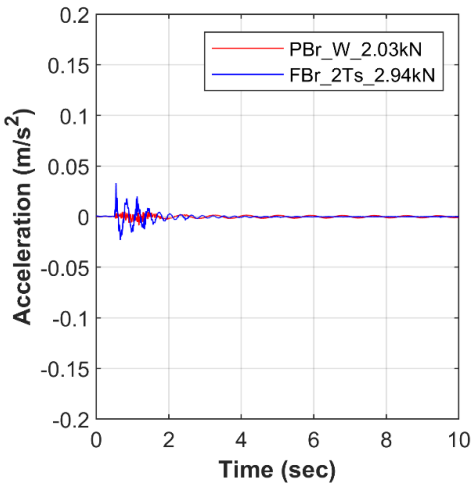
	PBr_W		FBr_2Ts	
	2.03kN	**13.90kN**	**2.94kN**	**15.70kN**
NS PPV (m/s)	1.93E-05	9.30E-05	3.90E-05	2.90E-04
γ (%)	1.38E-07	6.64E-07	2.79E-07	2.07E-06
G/G_{max}	0.999	0.994	0.997	0.985
ζ (%)	1.73	1.78	1.74	1.88

6.2.7 Evidence of soil-foundation-structure interaction

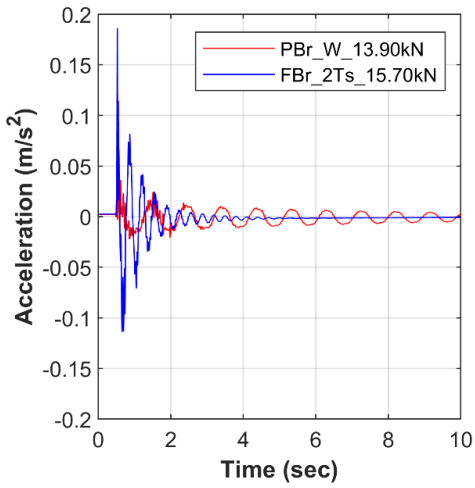
The co-existence of SSI effects and foundation motion is commonly referred to as Soil-Foundation-Structure Interaction (SFSI) effects, which are evaluated herein, aiming to provide evidence of the above sources of nonlinearities. The foundation motion can be evaluated through the horizontal and the rotational motion of the foundation. Figure 6.17 compares the foundation response recorded during the experiments on the PBr_W and FBr_2Ts structures that were subjected to similar pull-out forces (i.e. PBr_W _2.03kN Vs FBr_2Ts_2.94kN, PBr_W_13.90kN Vs FBr_2Ts_15.70kN). The presented North-South (NS) horizontal foundation motion (Figure 6.17a, b) was recorded by the 1.1n and 1.7n instruments (Figure 5.16) during the PBr_W and FBr_2Ts experiments, respectively. The foundation rotation (θ) (Figure 6.17c, d), is calculated using Eq. 6.5, exploiting data recorded by the instruments mentioned in Table 6.1. It is noted that the rotation is presented in terms of rad/s units, as it was calculated from accelerations data in lieu of displacement data.

Figure 6.17 shows that the foundation horizontal motion and rotation were much stronger during the experiment on the fully braced structure than the corresponding partly braced one. Stronger foundation motion engaged stronger SSI effects, increasing the impact of soil compliance on the predominant frequency of the system. This explains why a linear elastic soil-FBr_2Ts structure system exhibited higher elongation of the predominant period, with reference to a fixed-base system, than

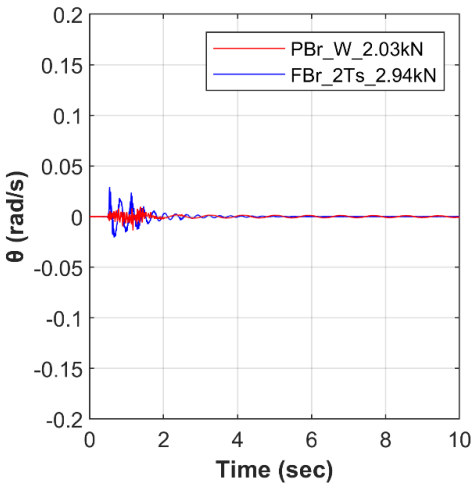
the soil-PBr_W structure system (refer to the "Low Strain" column of Table 6.3). Although it is not evidenced from experimental data, foundation uplift was visually observed during some of the experiments. The larger foundation rotation recorded during the FBr_2Ts than PBr_W free vibration experiment (Figure 6.17c, d) indicates possibly more pronounced foundation uplift during the former experiment. Considering that foundation uplift increases further the predominant periods of a nonlinear SSI system, the latter observation can partly explain the larger impact of nonlinearities observed during the FBr_2Ts experiments.



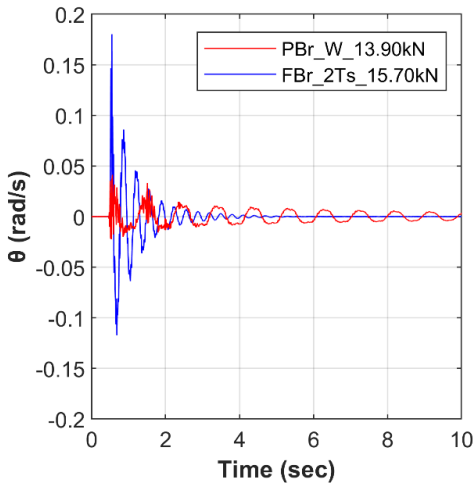
(a) Foundation Horizontal, F=2.03-2.94kN



(b) Foundation Horizontal, F=13.09-15.70kN



(c) Foundation rotation, F=2.03-2.94kN



(d) Foundation rotation, F=13.90-15.70kN

Figure 6.17: Comparison of the foundation response between the PBr_W and FBr_2Ts free vibration experiments of similar pull-out forces. The compared quantities are: (a, b) Foundation horizontal (NS) motion; and (c, d) Foundation rotation.

It is noted that foundation uplift was not expected to take place, as explained in Section 5.2.3. The observation of foundation uplift can be as a result of the occurrence of interface gaps prior to the application of the excitation load as well the peculiar shape of the foundation base (see Section 5.2.4).

The importance of foundation motion on the SSI response is depicted in Figure 6.18. The figure shows the contribution of the foundation rotation (hθ), foundation translation (u_f) and structural deformability (u_s) to the total top slab accelerations (u_{total}). The different motion components are computed as described in Section 6.2.2. Figure 6.18a and b demonstrate that, during the partly braced free vibration experiments, the top slab accelerations were dominated by the flexural deformability of the structure. Independently of the magnitude of the applied load, the hθ component was very small relative to the u_{total}, indicating negligible interface nonlinearity during the PBr_W experiments. Conversely, the hθ motion component dominated the motion during the fully braced experiments, while the u_f and u_s components were less important, as illustrated in Figure 6.18c and d. The contribution of the foundation rotation became even more important when the pull-out force increased. In particular, when the force was 15.70kN, the total hθ component was almost equal to the u_{total} one, while the flexural deformability was negligible. During this experiment, the foundation rotation controlled the flexibility of the entire SSI system. The structure was very stiff relative to the foundation-soil system, hence, the structure-foundation system deformed like a rigid body.

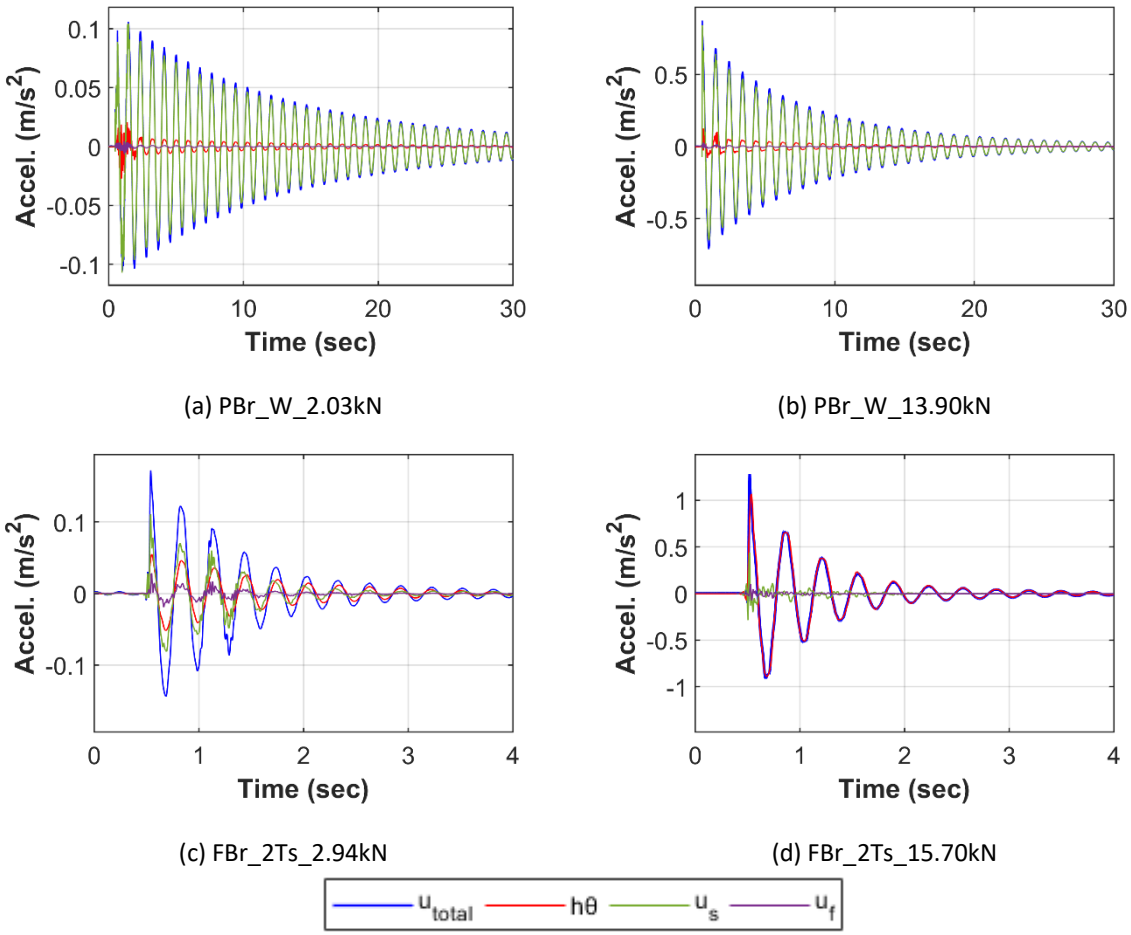


Figure 6.18: Motion decomposition of the total top slab accelerations recorded during the PBr_W and FBr_2Ts experiments of different pull-out forces.

6.2.8 Soil motion attenuation with distance

The attenuation of soil motion with distance is evaluated through the change of the peak particle velocities (PPV) that were recorded by instruments located at different distances from the foundation edge. Table 6.6 presents the instruments that were used for the assessment of attenuation of soil motion with distance. The distance of each instrument from the foundation edge is also stated, with reference to Figure 5.17. Both the vertical and horizontal (North-South) PPV values, as well as their normalised values are assessed. The normalisation is achieved by dividing the PPV values by the magnitude of the applied force (F), so that the impact of nonlinearities on the attenuation can be investigated. Comparison between PPV attenuation is made between instruments aligned to two different directions, perpendicular to each other. The attenuation processed by the instrument array located at the ground surface North to the foundation, which is aligned with the loading direction (North-South), is compared with the attenuation of PPV recorded by an array of instruments located East to the foundation.

Table 6.6: List of instruments used for the evaluation of soil motion attenuation, with cross-reference to Figure 5.17.

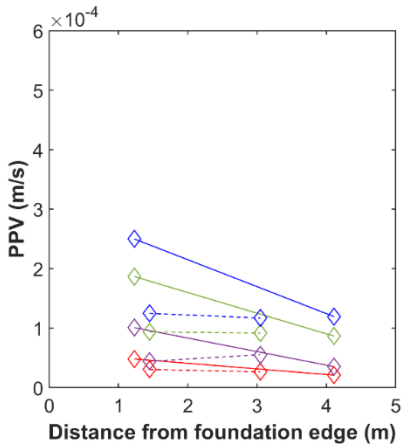
Experiment	Instruments' location relative to the foundation	Instrument Name	Dist. from foundation (m)
PBr_W(11)	North	0.1	1.20
		0.16	4.05
	East	0.40	1.45
		0.41	3.05
FBr_2Ts(4)	North	0.1	1.20
		0.2	2.90
		0.16	4.05
	East	0.40	1.45
		0.41	3.05
		0.42	4.45

Figure 6.19 and Figure 6.20 present the variation of PPV with distance as recorded during the PBr_W(11) and FBr_2Ts(4) experiments, respectively. In both experiments, the vertical component of soil motion recorded North to the foundation was stronger (solid lines of Figure 6.19a and Figure 6.20a) than the vertical motion recorded by the instruments located East to the foundation (dashed lines of Figure 6.19a and Figure 6.20a). The difference between the PPV values recorded North and East to the structure was much more pronounced during the FBr_2Ts(4) experiment, which exhibited stronger foundation motion (see Section 6.2.7). This difference is almost negligible in the horizontal soil motion (Figure 6.19b and Figure 6.20b), as the PPVs recorded along the two perpendicular arrays of instruments were of very similar amplitudes. These observations illustrate the important role of the

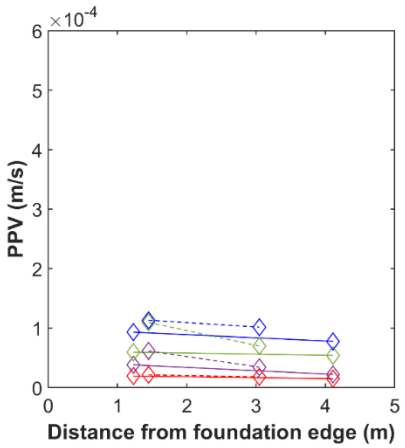
foundation rocking along the loading direction (in-plane), North-South. The in-plane foundation rocking, which was more pronounced than the out-of-plane one, transmitted waves in the soil of stronger vertical component, relative to the horizontal one. The vertical soil motion component dominated the soil motion and perhaps the nonlinearity, which increased with the soil motion intensity.

The PPV variation with distance, computed for experiments conducted with varying pull-out force amplitudes, suggests that the soil motion attenuated non-proportionally with increasing excitation (Figures 6.19a, b and 6.20a, b). The slope is much larger when the motion intensity was stronger, a feature that was more evident from the FBr_2Ts experiment (Figure 6.20a). It is noted that the non-proportional relation between excitation magnitude and soil motion attenuation was controlled by the radiation damping. The experiments with stronger excitation transmitted more energy to the soil, resulting in a greater amount of energy being radiated. This justifies the steeper slope of PPV values computed for these experiments.

Figures 6.19a, b and 6.20a, b show that most of motion dissipation took place in the vicinity of the structure. More than 50% of the motion amplitude attenuated between the instruments located 1.2m and 3m far from the foundation, while the rate of attenuation decreased significantly between farther instruments. Wave radiation was the primary reason of the exponential decrease of soil motion with distance, while soil nonlinearity, which was stronger near the foundation, might have also contributed. The impact of soil nonlinearity on the soil motion can be qualitatively seen in Figures 6.19c, d and 6.20c, d. The figures present the normalised PPV values against distance, illustrating that the experiments with the smallest applied forces produced the largest normalised soil velocities. This observation can be an indication of larger soil hysteresis developed in the vicinity of the foundation for the experiments with stronger excitation, which resulted in more pronounced soil dissipation. Soil motion attenuation with distance cannot be assessed for the PBr_W[(11)] experiment, as only two instruments were available in each of the two examined arrays of instruments.



(a) Vertical soil motion



(b) Horizontal soil motion

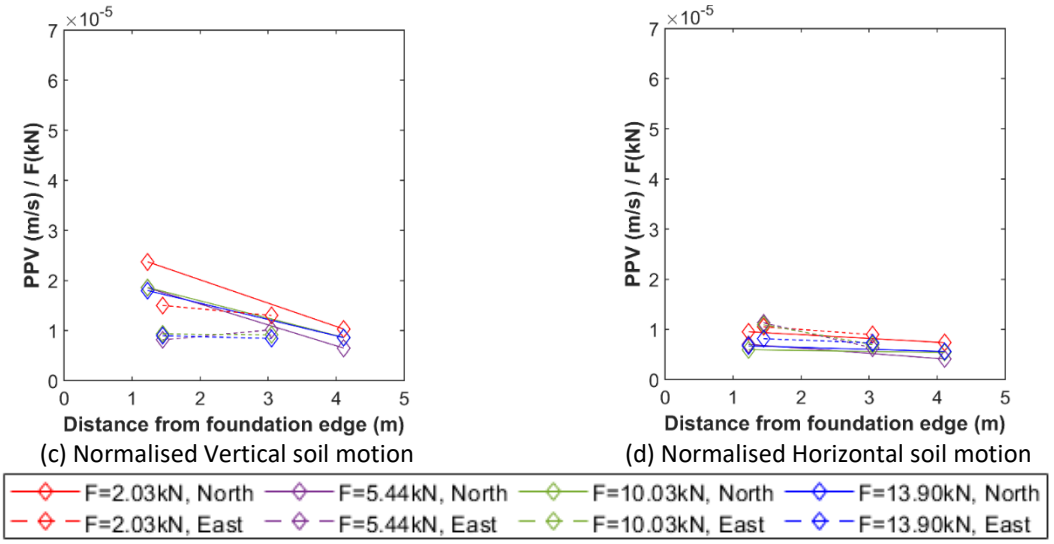


Figure 6.19: Peak particle velocity (PPV) attenuation with distance recorded, during the PBr_W(11) experiment, by instruments located North and East to the foundation. The (a) vertical and (b) horizontal (North-South) motion components are presented, as well as their corresponding normalised values (c, d).

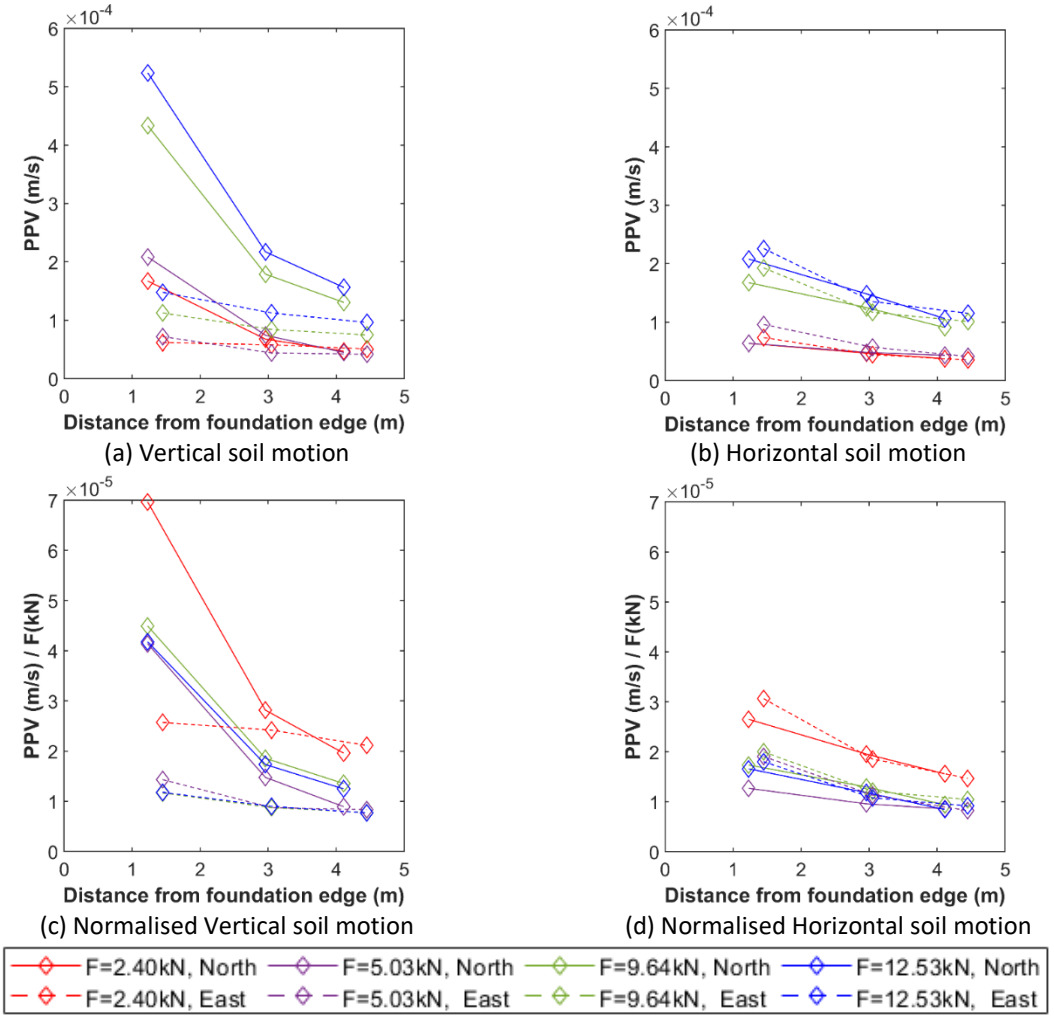


Figure 6.20: Peak particle velocity (PPV) attenuation with distance recorded, during the FBr_2Ts(4) experiment, by instruments located North and East to the foundation. The (a) vertical and (b) horizontal (North-South) motion components are presented, as well as their corresponding normalised values (c, d).

6.3 Forced Vibration tests

As described in Section 5.7.1, 15 different frequencies, ranging from 1Hz to 10Hz, were applied to the structure by the vibrator during each experiment, while each frequency was kept constant so that the steady-state structural response is recorded. The steady-state response of each applied frequency is the meaningful part of the response, which is interpreted herein, while the transient part between frequency adjustments is not discussed. Unlike the free vibration experiments where a structure oscillates at its fundamental frequency (see Section 6.2.1), during the forced vibration tests, the structure oscillates at the frequency imposed by the vibrator (see Section 5.8.1). When an applied frequency coincides or is close to a natural frequency of the SSI system, then the response of the system maximises owing to resonant features. Therefore, the natural frequencies and the associate deformation modes can be identified. Based on this, a system identification procedure is employed to interpret the forced vibration data.

6.3.1 Strong motion data integration

It is well established in the literature that the integration of acceleration strong motion data to velocities or displacements can result in non-physical values (Trifunac *et al.*, 1973; Iwan *et al.*, 1985; Boore and Bommer, 2005; Tan *et al.*, 2008; Jones *et al.*, 2017). This is illustrated in Figure 6.21 which shows the velocity and displacement time histories integrated from recorded acceleration time histories without any processing (apart from the process described in Section 5.4). The accelerations were recorded on the top slab by the 2.5n instrument during the FBr_2Ts$^{(5)}$_mD experiment. The outer shape of the velocity time history indicates realistic velocity values with the exception of the applied frequency at 8Hz (time between 800s and 880s), where unreasonable low frequency content exists. The low-frequency content is much more prominent in the unprocessed displacements, which increases with time to unrealistically large values.

The non-physical values is a consequence of the unknown boundary conditions, including initial acceleration, velocity and displacement (Boore and Bommer, 2005). These are assumed to be zero when integrating accelerations to velocities and displacements. However, zero initial conditions are not the case in strong motion data, as the data include the motion of interest only, while the motion prior to this motion is lost. Additional reasons that result in unrealistic velocities and displacements integrated from strong motion accelerations are the unknown baseline and the low-frequency noise that comes from various sources including ambient processes and instrument imperfections (Trifunac *et al.*, 1973; Boore and Bommer, 2005). The low-frequency noise is normally reduced by applying a baseline correction and a low-cut filter (e.g. Butterworth), which can be either *causal* or *acausal*

(Boore and Bommer, 2005). Causal filters produce phase shifts of the signal, while the acausal ones achieve zero phase shift. The low cut-off frequency is selected as the frequency below which the recorded data are not reliable and frequencies that are out of interest. Similarly, high cut-off filters can also be used to reduce the high frequency noise in the signal.

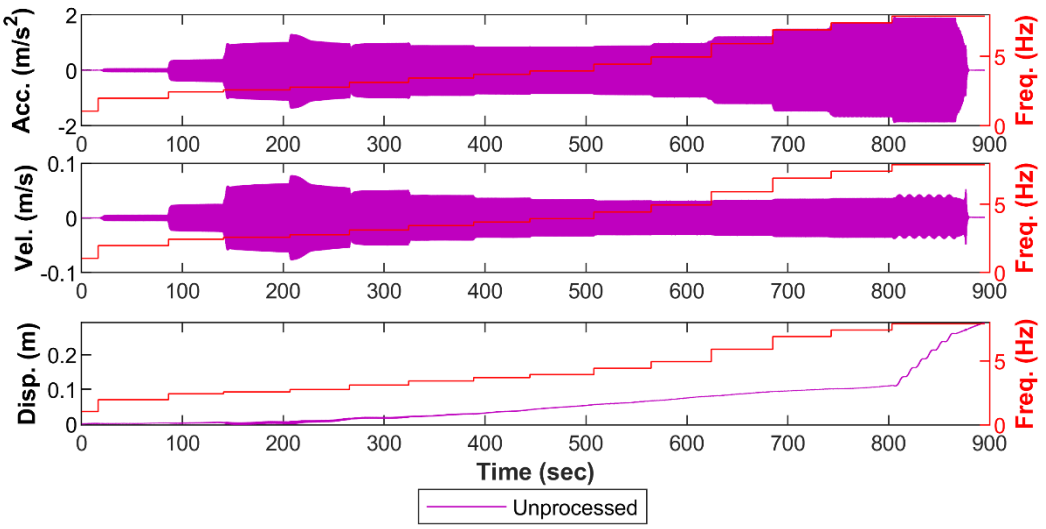


Figure 6.21: Unprocessed acceleration time history and corresponding velocity and displacement time histories through integration. The exploited data were recorded by the 2.5n instrument during the FBr_2Ts$^{(5)}$_mD experiment).

Jones et al. (2017) propose a procedure to integrate and calibrate recorded acceleration time histories to meaningful velocity and displacement time histories. The calibration is an iterative process that includes a series of acausal filtering and base line corrections. The process was developed to calibrate seismic data of the U.S. Geological Survey database. A similar but simplified calibration procedure is developed for the purpose of this study. It makes use of the Butterworth bandpass acausal filter and a newly developed baseline correction procedure. The baseline correction procedure exploits the advantages of the forced vibration data, which are the low signal noise and the known dominant frequencies of the recorded motions. The procedure takes as input recorded data acceleration time histories and produces the final acceleration, velocity and displacement time histories.

Figure 6.22 shows the flow chart of the calibration procedure for the integration of the acceleration time histories to meaningful velocities and displacements. The procedure requires as input the recorded acceleration signal (Acc), the sampling frequency (Fs) and Butterworth bandpass filter inputs, which are lower and higher cut-off frequencies (LowCutF, HighCutF) as well as the order (n) of the filter. It also requires the percentage of the recorded motion which is replaced by tapers (Taper_perc) at the front and end of the motion, the time duration or the zero padding (ZeroPadTime) that is added

at both ends as well. The last input parameter is the number of times that the baseline correction (BL_times) is applied on the recorded motion.

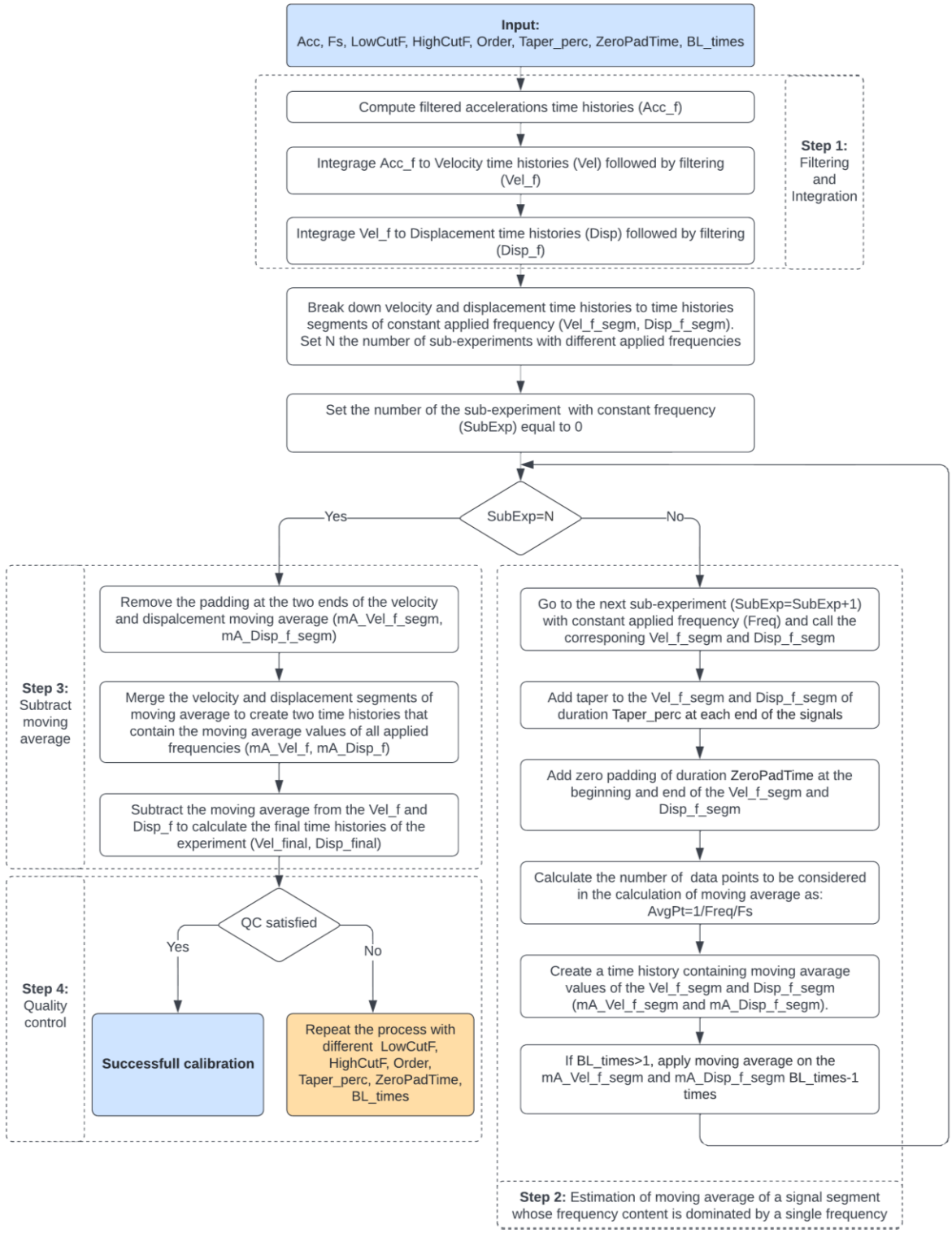


Figure 6.22: Flow chart of the procedure to integrate strong motion acceleration time histories to velocity and displacement time histories.

The procedure is divided into four main steps, which are summarised below:

- *Step 1:* Filtered accelerations are integrated to velocities and displacements, which are broken down into segments of constant frequency
- *Step 2:* Tapering and zero-padding is applied at the front and end of each segment time history. For each resulting segment, the baseline is computed following the procedure described below
- *Step 3:* Remove the baseline from velocities and displacements
- *Step 4:* Quality control

The above four steps are further elaborated below:

Step 1: the recorded acceleration time histories are filtered, producing Acc_f, which are then integrated to velocity time histories (Vel). Vel are filtered to produce Vel_f, while the latter is integrated to displacement time histories (Disp) which are also filtered (Disp_f). As mentioned above, filtering is effective in reducing both the low and high frequency noise with the appropriate selection of LowCutF and HighCutF. Illustrative example of step 1 is presented in Figure 6.23 which shows the filtered time histories of the example previously shown in Figure 6.22. The figure demonstrates that the filter selected for the example (LowCutF=0.4Hz, HighCutF=50Hz, n=4) was very effective in decreasing the low frequency content observed in the unprocessed velocities and displacements (shown earlier in Figure 6.22). However, the zoom-in figures show that there is a low frequency content remaining, which is removed via a baseline correction in steps 2 and 3.

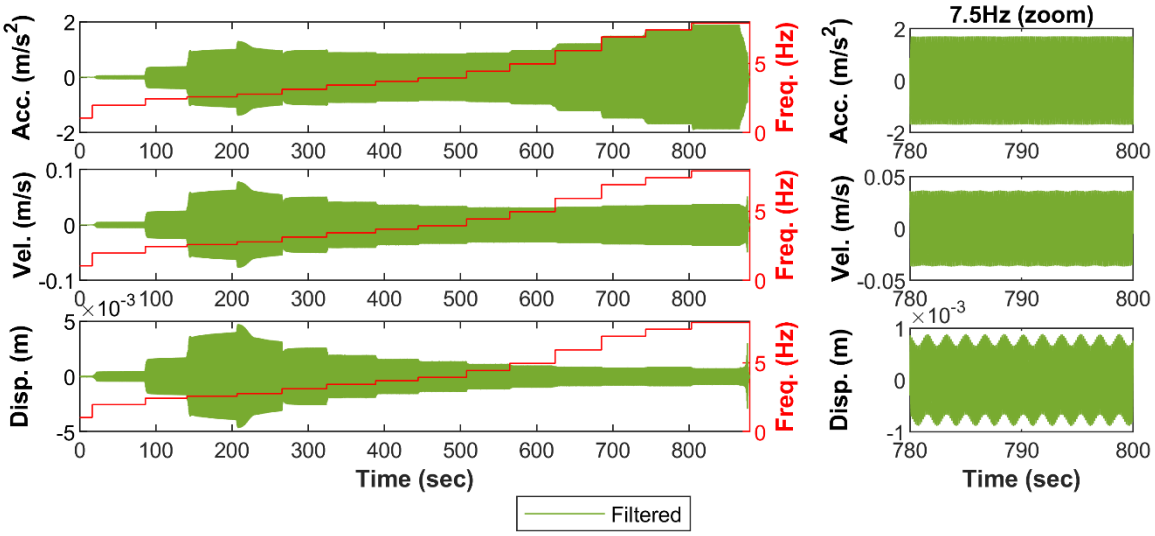


Figure 6.23: Step 1. Filtered acceleration, velocity and displacement time histories. The exploited data used were recorded by the 2.5n instrument during the FBr_2Ts$^{(5)}$_mD experiment.

The filtered time histories, Vel_f and Disp_f, are broken down to smaller segments of time histories (Vel_f_segm, Disp_f_segm), so that each segment corresponds to a certain sub-experiment of constant applied frequency.

Step 2: tapering is applied at the front and end of each time history segment sacrificing a certain percentage of the recorded motion (equal to Taper_perc). Herein, Taper_perc was selected to be 0.5% of the motion duration at each end. Also, zero-padding of a prescribed duration (ZeroPadTime), which was selected to be 40s herein, is added at the two ends of each time history segment. The tapering and padding are illustrated in Figure 6.24 which shows the processed velocity and displacement time history segments of the FBr_2Ts$^{(5)}$_mD experiment, when the applied frequency was 7.5Hz.

Subsequently at the same step, the baseline of each filtered, tapered and padded velocity and displacement time history segment is estimated. The baseline is approached as a time history that contains moving average values of the Vel_f_segm or Disp_f_segm. The velocity and displacement moving average time histories (mA_Vel_f_segm, mA_Disp_f_segm) have the same number of data points with the Vel_f_segm and Disp_f_segm respectively. Each moving average point is calculated as the average value of a certain number (AvgPt) of velocity or displacement data points contained in a sliding window. Then, the window slides forward one velocity or displacement data point enclosing the same numbers of data points. The average value of this sub-dataset gives the next moving average point, while the repetition of this procedure for every displacement and velocity data point produces the mA_Vel_f_segm and mA_Disp_f_segm. The appropriate selection of the AvgPt value is crucial for the calculation of the moving average time history. Assuming zero experimental permanent displacements, and that velocity and displacement time histories were symmetric around the time axis, the area of a full cycle across the time axis should be zero. Equivalently, provided that the sampling frequency is constant, the average value of data points contained within a single full cycle should be zero as well. If the average value is not zero, then the average value should be subtracted from the corresponding velocity or displacement data point to ensure zero symmetric velocities and displacements. Based on the above, the AvgPt should be equal to the number of data points that constitute a full cycle. Therefore, the AvgPt can be calculated as:

$$\mathrm{AvgPt} = 1/(\mathrm{Freq} \cdot \mathrm{Fs}) \qquad 6.15$$

where, Freq is the applied frequency and Fs is the sampling frequency.

The AvgPt is dependent on the input frequencies that were applied during the forced vibration tests. However, applied frequencies varied during a single experiment, which justifies the need of dividing the experiments into smaller sub-experiments (Vel_f_segm, Disp_f_segm) with constant applied frequency.

The moving average procedure for each time history segment is carried out BL_times times. According to author's experience, a single application of moving average (BL_times=1) was enough for the majority of the examined time histories. In some exceptions, the moving average time histories

contained useful data that should not be removed from the original data. Aiming to correct this situation, moving average is applied on the moving average time histories (BL_times-1) times. Cases where BL_times was set equal to 2 was at sub-experiments during which steady-state conditions were not achieved because of resonant features (PBr_W when the input frequency was 1.33Hz).

Step 3: the padding is removed from the two ends of mA_Vel_f_segm and mA_Disp_f_segm. Subsequently, all velocity and displacement moving average segments are merged together to produce two moving average time histories that contain all applied frequencies (mA_Vel_f, mA_Disp_f). At the final stage of baseline correction procedure, the merged velocity and displacement moving average time histories are subtracted from the filtered velocities (Vel_f) and displacements (Disp_f) respectively, producing the filtered and baseline corrected velocity and displacement time histories (Vel_final, Disp_final).

Step 4: quality control (QC) is carried out to ensure that the Vel_final and Disp_final time histories are reasonable. When the quality control is not satisfied, then the integration procedure is repeated with revised filtering input (LowCutF, HighCutF, Order), while less likely is the need of revising the tapering input (Taper_perc), padding input (ZeroPadTime) or the number times of applying baseline correction (BL_times).

Figure 6.24 illustrates the baseline correction procedure (Steps 2 and 3) by using data from FBr_2Ts$^{(5)}$_mD experiment when the applied frequency was 7.5Hz (same experiment presented in Figure 6.22 and Figure 6.23). The data shown are processed from the 7.5Hz frequency segment shown in Figure 6.23. As Figure 6.24 shows, a non-physical low frequency content exists in the filtered displacements and velocities (less pronouncedly). The moving average time history approaches this content and baseline correction is achieved after subtracting the moving average from the filtered data. The final filtered and baseline corrected velocity and displacement time histories have reasonable values, while the non-physical motion that resulted from integration is removed.

Herein, the recorded forced vibration strong motion data (structural accelerations) are interpreted to velocity and displacement time histories following the procedure described above (Figures 6.21 to 6.25). The input parameters required are summarised in Table 6.7. For simplicity, common filtering, tapering and padding inputs were used for all the experiments, while the number of baseline correction application (BL_times) was either 1 or 2. A value of the latter parameter equal to 1 was sufficient for the majority of the experiments. However, some applied frequencies of the experiments mentioned in Table 6.7 required further calibration of the baseline. Setting BL_times equal to 2, the baseline was better predicted for the certain applied frequencies, while the remaining applied frequencies of the experiments were almost unaffected.

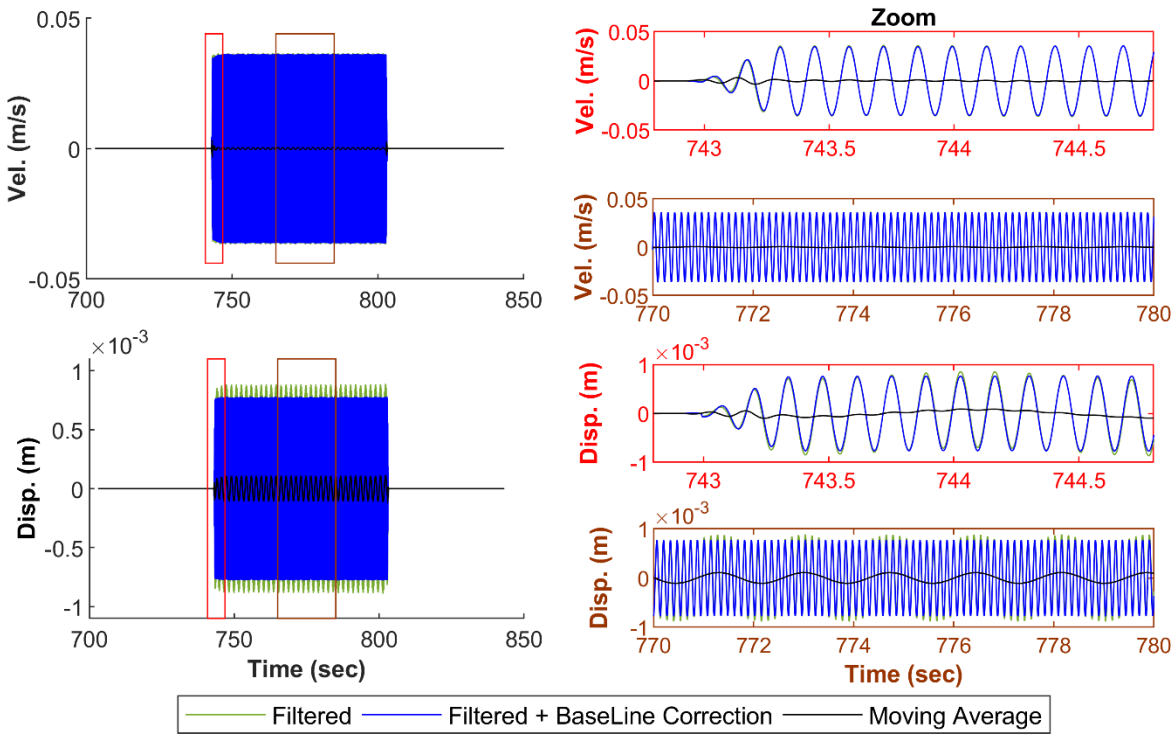


Figure 6.24: Steps 2 and 3. Baseline correction of individual filtered velocity and displacement time histories integrated from a recorded acceleration time history segment of a constant 7.5Hz input frequency. The exploited data were recorded by the 2.5n instrument during the FBr_2Ts$^{(5)}$_mD experiment when the input frequency was 7.5Hz.

The proposed integration algorithm did not work well for forced vibration experiments during which the applied frequency was 0.6Hz. This stems from the fact that the certain applied frequency is close to the low cut-off frequency selected (0.4Hz), which results in filtering out useful data from the input signal. However, experiments of such low applied frequencies are less important than the remaining ones, hence, this limitation can be neglected. Also, the assumption made about perfectly symmetric response around the time-axis neglects any permanent displacements that might have existed. Although these were not measured, it is estimated that they were extremely small and can be ignored. It is believed that the proposed integration procedure is accurate enough to meet the purpose of the current study. The reliability of the algorithm has been validated numerically. Numerical simulations of the experiments (presented in Chapters 7 and 8), which use as input motion displacements interpreted from strong motion accelerations, reproduce the experimental structural accelerations. The latter validates that the input motion was appropriate as well as the reliability of the proposed integration procedure. The procedure also works well for interpreting accelerations and displacements from forced vibration strong motion velocities (instead of accelerations as it has already discussed) with the appropriate adjustments, which are not discussed herein.

Table 6.7: Input data used for interpreting strong motion acceleration data to velocity and displacement time histories.

Experiments	LowCutF	HighCutF	Order	Taper_perc	ZeroPadTime	BL_times
All experiments with the exceptions below	0.4Hz	50Hz	4	0.5%	40s	1
PBr_S$^{(8)}$_mD PBr_W$^{(9)}$_mB,mC,mD PBr_S$^{(10)}$_mB,mC,mD PBr_W$^{(12)}$_mB,mC,mD	0.4Hz	50Hz	4	0.5%	40s	2

The procedure that calibrates velocities and displacements integrated from strong motion accelerations was illustrated via an example where accelerations of an entire experiment (15 different applied frequencies and duration 900s) were integrated (see Figures 6.22, 6.23, 6.24). The calibration procedure can also be applied to a time history of shorter duration (e.g. 10s), provided that the applied frequency of the examined forced vibration data is constant. Figure 6.25 presents unprocessed, filtered, and filtered and baseline corrected velocity and displacement time histories integrated from a 10s acceleration history, which is also presented. The accelerations were recorded during the FBr_2Ts$^{(5)}$_mD experiment which was presented previously, when the input frequency was 7.5Hz. Comparing Figure 6.22 with Figure 6.25, it can be observed that the unprocessed velocities and displacements require more correction when these are integrated from a shorter acceleration time history than from a longer one. The impact of the eliminated initial signal is more pronounced when the integrated duration is shorter. In this example, the unprocessed velocity is shifted vertically towards negative velocity values, while when the velocities are integrated, the resulting displacements have a linear trend. Although filtering corrects the time histories significantly, the baseline correction should also be applied to correct the two ends of the filtered signal. It should be noted that, in this example, baseline correction is sufficient to correct the velocity and displacement time histories, without the need of filtering. This is because the examined velocities and displacements have a clear trend that can be removed through baseline correction alone, while low or high frequency content, which could be removed through filtering, does not exist.

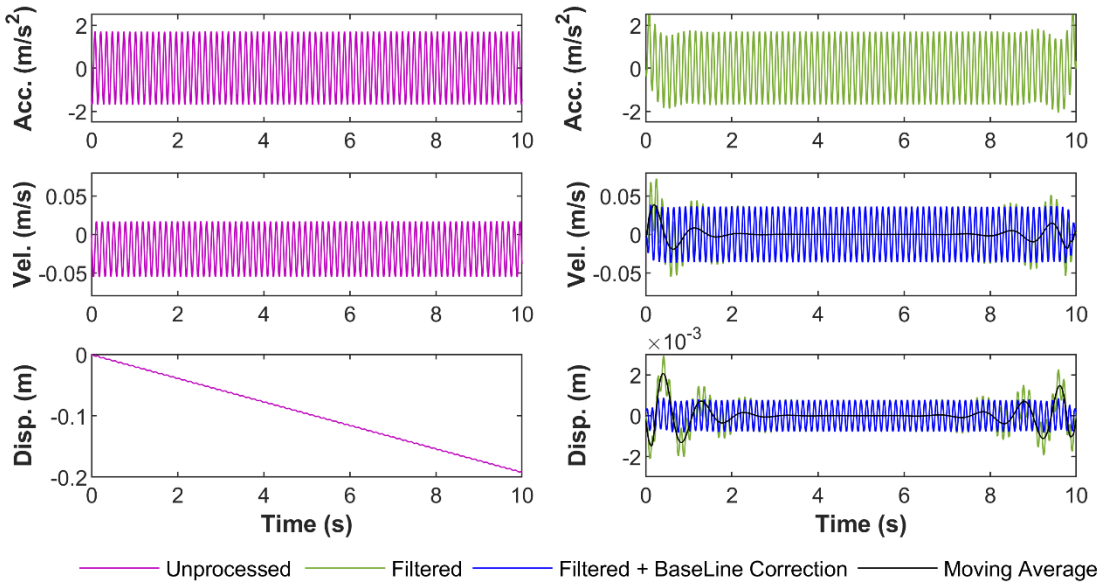


Figure 6.25: Velocity and displacement time histories integrated from the presented 10s-duration acceleration time history. The exploited data used were recorded by the 2.5n instrument during the FBr_2Ts$^{(5)}$_mD experiment when the input frequency was 7.5Hz.

6.3.2 Identification of modes of oscillations

A procedure to identify the modes of oscillations from forced vibration data is deployed to enable comprehensive assessment of the structural response. Identifying the modes of oscillations allows consistent comparisons of resonant frequency values that correspond to the same mode for different experimental configurations (e.g. the translational mode appeared in all experiments).

Two procedures of defining the displaced shape of the top and base slabs during oscillations are deployed and described herein. The first approach determines qualitatively the shape of the slab oscillation by exploiting the acceleration time histories only, without the need of making any assumptions. The second procedure involves drawing snapshots of the shape of the displaced slabs based on assumptions that are discussed subsequently. Both methods were employed to verify and validate each other.

Acceleration time histories

The procedure to infer modes of oscillation of an SSI system from forced vibration time histories is similar to the one followed for the free vibration data (6.2.1). Figure 6.26 presents snapshots of an assumed rigid slab during (a) swaying oscillation, (b) torsional oscillation and (c) oscillation that results from the sum of the latter two. The snapshots of the displaced slab (dashed lines) are compared with the slab position at rest (solid lines), while the displacements of two distinct points (1 and 2 which move to 1’ and 2’) are illustrated by the arrows. The displacements along the conventional X-axis is

denoted by $dX_{i,S}$, $dX_{i,T}$ and $dX_{i,S+T}$ for the cases of swaying, torsional and a combination of the two motions, respectively. Similarly, the displacements along the Y-axis are denoted by $dY_{i,S}$, $dY_{i,T}$ and $dY_{,S+T}$, where i is the position considered on the slab for which displacements are plotted.

As it was already mentioned in Section 6.2.1, when a swaying mode takes place, all slab's positions move by the same amount (Figure 6.26a), while the displacements differ from point to point during torsional oscillation (Figure 6.26b). This is better shown in Figure 6.26d which shows fictitious displacement time histories of the two points on the slab, when the slab sways (dashed lines) or rotates (dotted lines) around its centre. For the former case, the X-displacements of the two examined points are equal ($dX_{1,S}$= $dX_{2,S}$), while they differ for the torsional mode ($dX_{1,T}$> $dX_{2,T}$). The phase difference between the swaying (dashed) and torsional (dotted) time histories is 180° for the two examined points. Hence, when both swaying and torsional exist in the motion, the sum of the above displacements results in X-displacements that are smaller than the swaying ones ($dX_{1,S+T}$ <$dX_{1,s}$, $dX_{2,S+T}$ <$dX_{2,s}$).

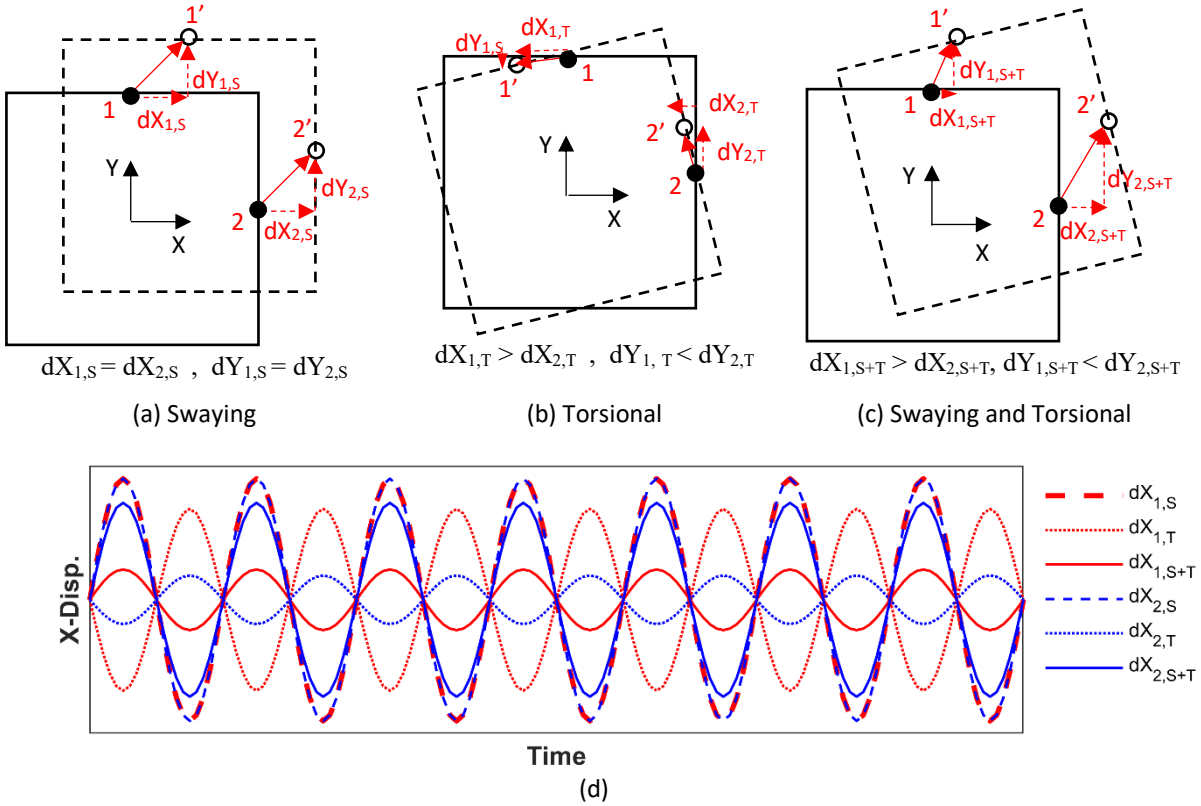


Figure 6.26: Snapshots in plan of the displaced slab taken during a fictitious (a) swaying motion, (b) torsional motion and (c) motion that results from the combination of the latter motions. (d) presents the displacement time histories of sinusoidal oscillations of the above modes.

The above approach neglects the contribution of the vertical motion of the slab to the horizontal displacements, which is anticipated to be minimal. Also, it assumes a perfectly swaying mode (Figure 6.26a) and a slab rotating perfectly around the centre of mass of the slab (Figure 6.26b). However,

experimental imperfections (see Section 5.2.4) existed, which prohibited perfect swaying or torsional modes to take place. It is possible that the centre of rotation did not perfectly coincide with the centre of mass of the top slab, or that the excitation load was not applied perfectly at the centre of mass. Both imperfections led to the development of an inherently torsional component. As it is shown subsequently, the structure oscillation consisted of both swaying and torsional motions (Figure 6.26c). The dominance of the two motions can be inferred by comparing the motion amplitudes recorded on the top slab at different locations. When there is a pronounced difference in the amplitude of motions recorded by different instruments, then the torsional mode was achieved, otherwise, the swaying motion dominated.

When the torsional mode dominated the motion, data recorded at different locations on the top slab were not in-phase, as the torsion produced out-of-phase torsional components, illustrated in Figure 6.26d (e.g. $dX_{1,T}$ Vs $dX_{2,T}$). It is noted that phase difference between motions at different locations on the top slab existed throughout the experiments, due to the abovementioned inherently torsional component of the structure. Based on this, the torsional resonant mode can be identified when the phase difference between data recorded on the top slab maximised. The phase angles are calculated as follows:

a. Computation of the Discrete Fourier Transform (DFT) of all time histories of constant applied frequency, $X_{i,j}$, where, i and j are the instrument and applied frequency respectively. The time histories should include a representative steady-state response recorded during sub-experiments when the applied frequency was constant (10s duration time histories were used for the purpose of this study).
b. Computation of a Fourier amplitude spectrum ($|X_{i,j}|$) for each of the above results.
c. Identification of the frequency that corresponds to the maximum amplitude. This frequency should be very close to the applied one.
d. For the above frequency the phase angle is estimated as the inverse tangent (arctangent) of the ratio of the imaginary part over the real part of the Fourier transform.

Once phase angles are inferred from data recorded by two top slab instruments, then the difference between the angles, that correspond to the same applied frequency, provides the phase difference. The two instruments for which phase angles are compared should be located on two diagonal top slab corners where the impact of torsion maximises. Based on this, instruments 2.1 and 2.3 is the ideal pair to be used. However, in some experiments, 2.3 was not synchronised with the remaining instruments and it was substituted by instrument 2.4 (where available) or 2.5 instrument (see instrument locations in Figure 5.16). The pairs of instruments used for the evaluation of phase angle differences for the various experiments are presented in Table 6.8.

Table 6.8: Instrument pairs used for the calculation of phase difference.

Experiment	Instrument Pair	
	Instr. 1	Instr. 2
FBr_2Ts$^{(5)}$_mD	2.5 $^{(*)}$	2.1
PBr_W$^{(7)}$_mD	2.4 $^{(*)}$	2.1
PBr_S$^{(8)}$_mD	2.4 $^{(*)}$	2.1
FBr_1Ts$^{(14)}$_mC	2.3	2.1

(*) instrument 2.3 was not synchronised with the remaining instruments

The phase angle difference is evaluated for the motions parallel and perpendicular to the loading direction, which herein are referred to as in-plane and out-of-plane motions respectively. Figure 6.27 presents the absolute phase difference values between data recorded along the in-plane (NS, n) and out-of-plane (EW, e) directions by the 2.1 and 2.3 top slab instruments, during the FBr_1Ts$^{(14)}$_mC experiment. It is illustrated that the phase angle difference is maximised at 8Hz, which is a frequency close to the torsional resonant one. It is also observed that the difference is more pronounced when it is inferred from the out-of-plane (e) motion component. This can be explained by the fact that the translational motion component of the in-plane motion was much stronger than the motion component produced by torsion. The consequence of this is that torsion did not change the phase angle significantly. Conversely, the translational and torsional motion components of the top slab's out-of-plane motion were of similar order of magnitude. Hence, the existence of torsion produced a very pronounced difference between phase angles of motions at different locations on the top slab.

The computation of the phase difference is very sensitive to data synchronization, while it might be not very accurate when the motion amplitude is very weak or when a high frequency content is prominent in the motion. Although the computation of phase difference might need further calibration to address the above limitations, which is beyond the scope of this research, the results can qualitatively be used to describe the mode of oscillation.

Using the above-described procedure and data interpretation, the modes of oscillation of the SSI system can be qualitatively identified. The data used for interpretation are primarily top slab acceleration time histories (equivalent to displacements shown in Figure 6.26d) recorded along both in-plane (parallel to load) and out-of-plane (perpendicular to load) directions. It is essential that both NS and EW directions are examined as a mode can be associated with the one plane only or with a combination of the two. As already justified, the out-of-plane swaying and torsional modes cannot be identified when observing the in-plane motion component only.

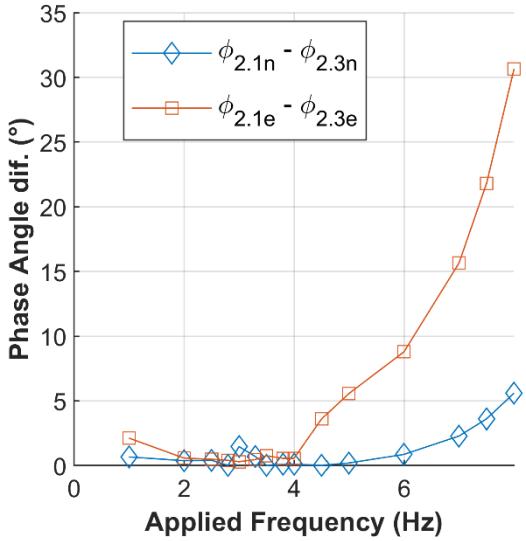


Figure 6.27: Phase angle difference with applied frequency between data recorded along the in-plane (n) and out-of-plane (e) directions by the top slab 2.1 and 2.3 corner instruments during the FBr_1Ts$^{(14)}$_mD experiment.

Drawing snapshots of displaced slabs in plan

The second procedure to identify the modes of oscillation that correspond to resonance requires drawing the displaced top slab in plan. For a certain frequency applied by the vibrator on the structure that led to resonance of the examined SSI system, displaced slab snapshots are drawn at different times to represent a full cycle. A full cycle can be representative of the forced vibration response, provided that steady-state conditions are achieved, which was the case for most of the applied frequencies. The resulting sets of drawn snapshots of the displaced top slab are interpreted to indicate the mode of oscillation of the SSI systems during the examined applied frequency and magnitude.

The snapshot drawings are achieved using displacement time histories inferred from the acceleration time histories by following the integration procedure described in Section 6.3.1. The data used were recorded by different instruments that were placed on the top slab at different locations. Prescribing horizontal displacements at two or more different locations on the top slab, the displaced shape of the slab can be captured through geometrical rules. The rules are based on the assumptions that the slab moved as a rigid body and the vertical motion of the slab resulted in negligible horizontal displacements.

Once the displaced shape in plan of the top slab is drawn, it is interpreted to identify the mode of oscillation. The mode can be NS swaying, EW swaying and torsional, or a combination of the three.

6.3.3 Motion decomposition method

Section 6.3.2 presents a method to assess the deformed shape of the slabs in plan, allowing the characterisation of the shape as either translational, torsional, or a combination of the two. In the

current section, the deformed shape of the structure is examined in elevation view aiming to assess the contribution of the different motion mechanisms on the top slab displacement. The total structure top slab displacement (u_{ts}) is decomposed into structural flexural deformation (u_s), foundation translation (u_f) and the contribution of foundation rotation (rocking) (u_θ). The motion decomposition method employed to interpret the forced vibration data is the same to the one used for the interpretation of free vibration data, described in Section 6.2.2. Herein, though, "recorded" displacements were processed instead of recorded accelerations. The displacements were interpreted from recorded accelerations as described in Section 6.3.1.

As mentioned in Section 6.2.2, a limitation of the method is that it is applicable to oscillations where the contribution of torsion is small. As it is subsequently discussed in Section 6.3.5, the forced vibration applied on the structure excited the torsional mode of the SSI system. The contribution of the torsional mode to the structural oscillation was significant for some applied frequencies, and for those cases the applicability of the method is questionable. In order to maximise its applicability, $u_{f,r}$, $u_{ts,r}$, $v_{f1,r}$ and $v_{f2,r}$, with reference the Figure 6.6, were carefully selected to meet the criteria presented earlier in Section 6.2.2. All instruments should be synchronised, while a small time lag can produce unreasonable results. Table 6.9 summarises the instruments of which records are used in the calculations to decompose the total structural forced vibration response.

Table 6.9: Input data used for the calculation of motion components that constitute the total top slab response of the examined experiments.

Experiment	Instrument				d (m)	h (m)
	$u_{ts,r}$	$u_{f,r}$	$v_{f1,r}$	$v_{f2,r}$		
FBr_2Ts$^{(5)}$_mD	2.5n	1.7n	1.1z	1.2z	2.72	4.4
PBr_W$^{(7)}$_mD	2.5n	1.1n (++)	1.1z	1.2z	2.72	4.4
PBr_S$^{(8)}$_mD	2.5e (*)	1.1e (*,++)	1.6z (**)	1.5z (**)	2.58	4.4
FBr_1Ts$^{(14)}$_mC	2.2n (+)	1.2n	n/a (-)	1.2z	1.35 (-)	4.2

(*) The load was applied along the East-West direction, hence the East-West component was used in the calculations.

(**) The load was applied along the East-West direction, hence the foundation instruments placed along the East-West direction were used in the calculation of the angle θ.

(+) The centre 2.5 instrument was not available.

(++) The centre 1.7 instrument was not available.

(-) Instrument diametrically opposite to $v_{f2,r}$ did not exist, as 1.1z did not work. In this case, $v_{f1,r}$ was assumed to be equal to zero, reflecting to the centre of the foundation, with the appropriate adjustment to the distance d.

6.3.4 Identification of natural frequencies

As already mentioned in Section 6.1, the identification of SSI systems' characteristics from forced vibration data that was adopted herein does not require assumptions or advanced mathematical

tools. The system identification procedure employed is simple and exploits the advantages of forced vibration tests, which are the absence of high frequency noise from the recorded signals and the prescribed applied frequencies. When an applied frequency was close to a natural frequency of the SSI system, the response maximised allowing the identification of the natural frequency. The response is examined in terms of structural accelerations that were recorded on the top slab. Although base slab records can also be used, they produce less pronounced maximisation of the motion. The identification procedure requires processing of top slab data recorded in the directions both parallel (in-plane) and perpendicular (out-of-plane) to the loading.

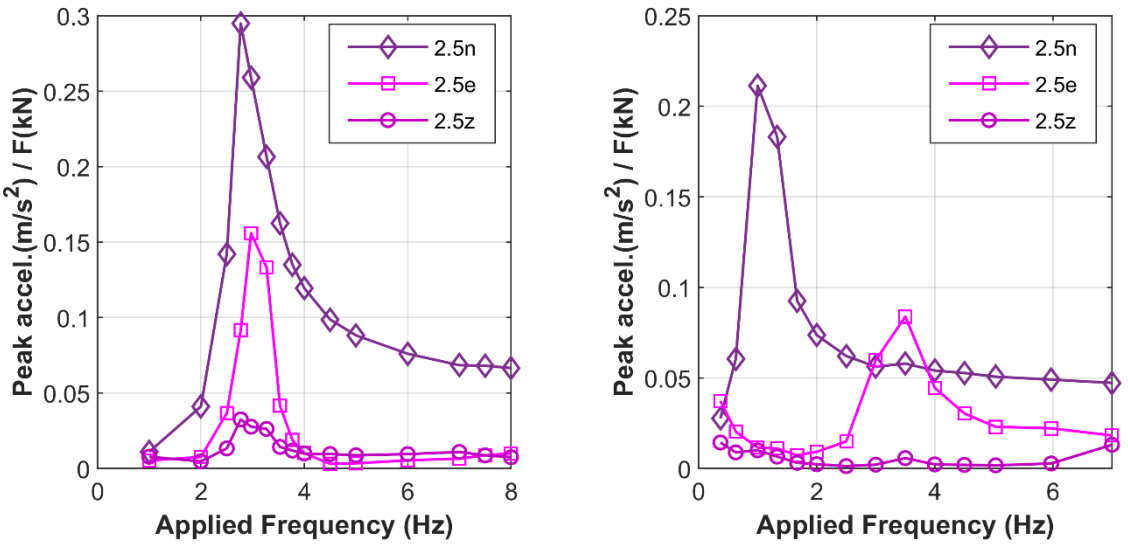
The force applied by the vibrator increased with input frequency according to Eq. 5.14. Aiming to isolate the impact of the applied frequency on the structural response, the recorded response is normalised by the magnitude of the sinusoidal applied force. Two equivalent procedures to identify the resonant frequencies are employed; the *Peak Normalised Accelerations* and the *Peak Fourier Amplitudes*. They both produce similar results and validate each other.

Peak Normalised Accelerations

For each applied frequency, the peak normalised acceleration is inferred from the corresponding steady-state part of the motion. Any peaks in the plot of normalised peak acceleration versus applied frequency indicate maximisation of the structural response and therefore natural frequencies. Figure 6.28a illustrates the above procedure by processing data from the FBr_2Ts$^{(5)}$_mD experiment that were recorded by the centre top slab instrument (2.5) along the North-South (n), East-West (e) and vertical (z) directions. The normalised response is maximised at 2.77Hz indicating the smallest natural frequency of the system. It is important that the response is assessed along both North-South and East-West components, as a natural frequency can produce maximisation of any of the two structural motion components. As discussed in Section 6.3.2, the natural frequency can correspond to in-plane, out-of-plane and diagonal translational modes, as well as to a torsional mode or a combination of the above (see Figure 6.1 and Figure 6.26). Hence, assessing only the in-plane motion component, the out-of-plane natural mode can be missed. Such an example is illustrated in Figure 6.28b which assesses the top slab response recorded by the centre instrument (2.5) during PBr_W$^{(7)}$_mD experiment. A natural frequency associated with the EW, out-of-plane, direction is observed at 3.5Hz, which can only be identified by assessing the EW (e) motion of the top slab, while it is not apparent from the NS, in-plane, (n) top slab motion.

The above procedure can be used to estimate the natural frequencies associated with the in-plane, out-of-plane and diagonal translational oscillation of the SSI system through assessing data recorded by a single instrument. However, as mentioned in Section 6.3.2, the identification of the torsional

natural frequency requires the comparison of data recorded by more than one instrument. It is noted that a torsional natural frequency is identified when the torsional motion component maximises, while the translational component which is driven by the vibrator's input also exists. As it has already been discussed in Section 6.3.2, torsion tends to increase the motion components at some locations on the slab, while it decreases the motion at some other (see Figure 6.26). Figure 6.29 processes data recorded along the in-plane (n) and out-of-plane (e) directions by two instruments (2.1 and 2.3) located at two diagonal corners of the top slab (Figure 5.16), illustrating a torsional case at 8Hz. It is observed that the out-of-plane motion component increases at the location of the 2.1 instrument, while it decreases at the location of the 2.3 instrument. Conversely, the in-plane top slab motion component decreases at the location of 2.1, while it increases at the location of 2.3. The combination of the above figures demonstrates that the 8Hz frequency was close to the torsional resonant frequency of the SSI system, where the contribution of the torsional response on the total recorded motion maximised.



(a) (b)

Figure 6.28: Variation of normalised peak accelerations with applied frequency, inferred from data recorded at the top slab centre by the 2.5 instrument along North-South, East-West and vertical directions, during (a) FBr_2Ts$^{(5)}$_mD experiment, (b) PBr_W$^{(7)}$_mD experiment

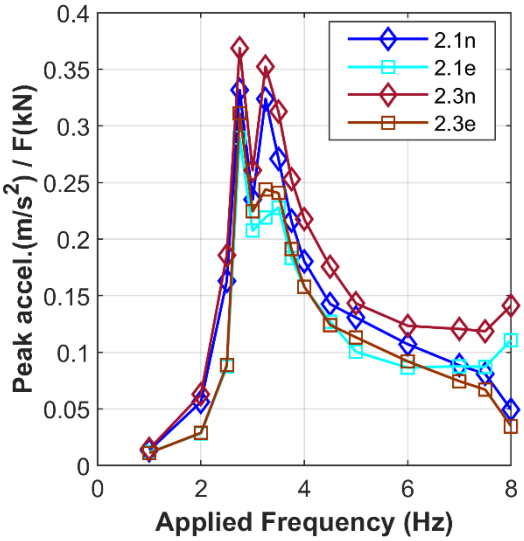


Figure 6.29: Variation of normalised peak accelerations with applied frequency, inferred from data recorded at the top slab by the 2.1 and 2.3 corner instruments along North-South and East-West directions, during FBr_1Ts$^{(14)}$_mD experiment.

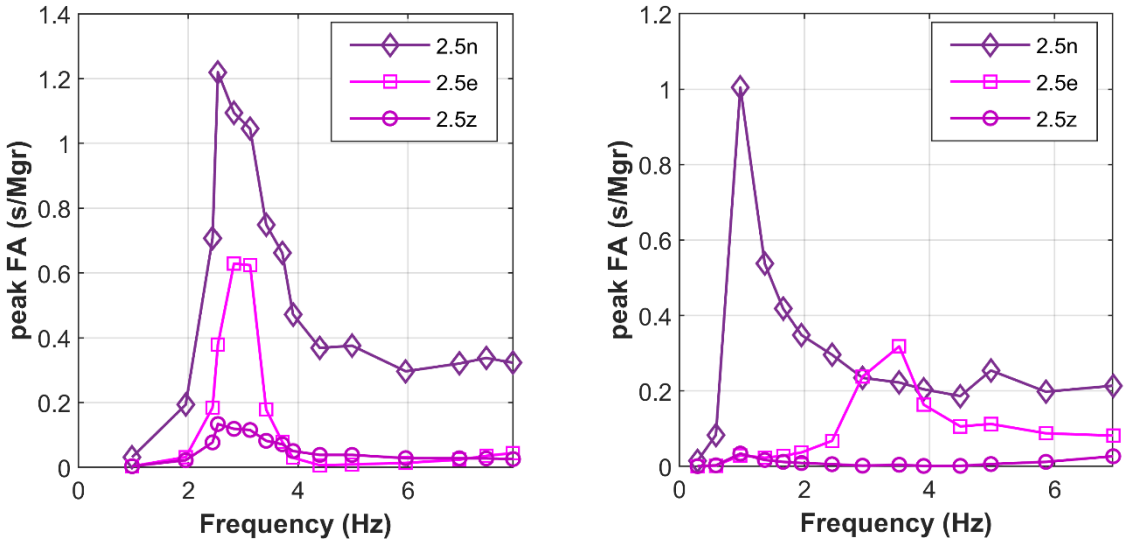
Peak Fourier Amplitudes

This procedure is equivalent to the *Peak Normalised Accelerations*, but it employs Fourier Amplitude spectra instead of evaluating the normalised accelerations directly. It evaluates the amplitude of the response at the applied frequency only, while it neglects the contribution of other frequencies. This procedure can be more effective than the *Peak Normalised Accelerations* when forced vibration data include high frequency peaks which can be misunderstood as the maximum response.

For each sub-experiment of constant applied frequency, a Fourier Amplitude (FA) spectrum is computed. Equivalent to the *Peak Normalised Accelerations* method, the spectrum is inferred from forced vibration normalised accelerations, which include a part of the steady-state motion of the sub-experiment (10s motion duration was used herein). The peak FA observed at the applied frequency is a quantitative measure of the amplitude of the response. The maximisation of the response indicates resonance, as previously discussed. The instruments and the motion components that are exploited are the same with the ones used in the *Peak Normalised Accelerations* method.

Figure 6.30 presents the variation of the Fourier amplitude peaks with applied frequencies, which resulted from the application of the *Peak Fourier Amplitudes* method. The presented application of this method refers to the same experiment as the example application of the *Peak Normalised Accelerations*, shown in Figure 6.28. The two methods produce very similar results, as far as the outline of the peaks is concerned, validating each other. A small difference is observed at peaks of 2.5e data recorded during the PBr_W$^{(7)}$_mD experiment. At frequencies lower than 2Hz, the *Peak Normalised*

Accelerations method produces peaks that increase with decreasing frequency, while the opposite is produced by the *Peak Fourier Amplitudes* method. This stems from the fact that at such low frequencies, the 2.5e motion, which is the out-of-plane component, was very weak and dominated by high frequency noise rather than by the vibrator's input. This high frequency content increased the maximum response of the structure and hence the peak normalised accelerations. However, it is more reasonable to assess the amplitude of the response around the applied frequency only, which is expected to give more representative results about the impact of the applied frequency on the response. This conception is adopted by the *Peak Fourier Amplitudes* method, hence producing more reasonable results, when high frequency content is prominent in the motions.



(a) FBr_2Ts$^{(5)}$_mD (b) PBr_W$^{(7)}$_mD

Figure 6.30: Variation of Fourier amplitude peaks with applied frequency, inferred from data recorded at the top slab centre by the 2.5 instrument along North-South, East-West and vertical directions, during (a) FBr_2Ts$^{(5)}$_mD experiment, (b) PBr_W$^{(7)}$_mD experiment.

The accuracy of the two procedures, *Peak Normalised Accelerations* and *Peak Fourier Amplitudes*, is dependent on the frequency step used during the experiments. The frequency step was approximately 1Hz, while it was refined around the anticipated natural frequencies, as described in Section 5.5.3. The chosen frequency steps allow the identification of the natural frequencies accurately enough for the purpose of this study. The number of the natural frequencies that can be identified by the current procedure is dependent on the range of the applied frequencies, which was approximately between 1Hz and 10Hz (see Section 5.5.3).

6.3.5 Natural frequencies of the swaying and torsional modes

As mentioned in Chapter 5, the same experiments were repeated more than once to ensure the reliability of the experiments. The reliability was found to be very satisfactory in Section 5.8.2, although, some experiments were found more reliable over others. Following the latter investigation, Table 6.10 presents the series of experiments of which data were processed to identify the natural frequencies and corresponding modes of the different SSI systems. Each series of experiments contained 2-4 sub-experiments of forced vibration tests, during which different masses of plates (mA, mB, mC and mD) were applied on the vibrator. The plate mass determines the force magnitude imposed by the vibrator (see Section 5.3.1), triggering different levels of nonlinearity. Hence, the natural frequencies will be computed for each sub-experiment separately. The procedure to identify natural frequencies and their deformation modes from forced vibration data described in Sections 6.3.4 and 6.3.2 is employed herein.

Table 6.10: Series of experiments of which data were processed to identify the natural frequencies and the corresponding mode of each structural configuration (name convention according to Table 5.10).

Experiment	**mA**	**mB**	**mC**	**mD**
FBr_2Ts	exp5	exp2	exp5	exp5
PBr_W	n/a	exp7	exp9	exp7
PBr_S	n/a	exp10	exp10	exp8
FBr_1Ts	n/a	n/a	exp14	exp14

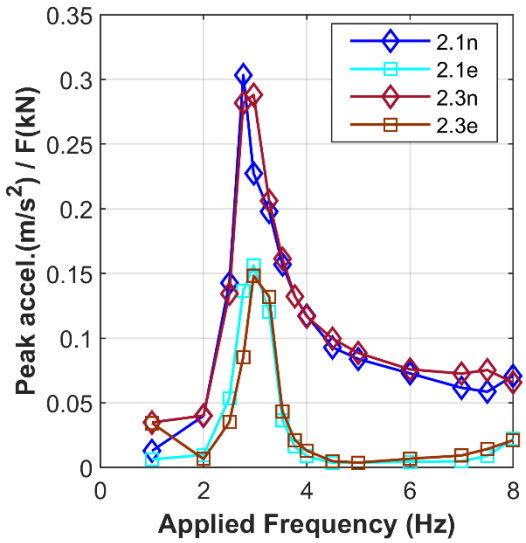
Figures 6.31 to 6.37 aim to identify the natural frequencies and modes of the different examined SSI systems, FBr_2Ts, PBr_W, PBr_S and FBr_1Ts. Figures 6.31, 6.33, 6.35 and 6.37 present the variation of (a) normalised peak accelerations, (b) Fourier Amplitude (FA) peaks and (c) phase angle difference, with applied frequency. The data exploited are North-South (n) and East-West (e) top slab acceleration time histories recorded during the experiments. Figures 6.32, 6.34, 6.36 and 6.38 present snapshots of the displaced top slab in-plan. For visualisation reasons, the displacements are exaggerated by a factor, which is reported on the figures' caption. Each figure compares top slab shapes drawn for four different snapshots, that correspond to maximum, minimum and zero displacement, as well as to the position at rest. An oscillation that was predominantly parallel to the loading direction is referred to as in-plane, while out-of-plane oscillation describes a motion perpendicular to the loading direction. All figures presented herein are processed from data recorded during experiments where the mD plates' mass (with reference to Section5.8.1) was placed on the vibrator. More figures developed for experiments with other vibrator masses can be found in Appendix E.

As Figure 6.31 illustrates, the predominant frequency of the FBr_2Ts structure was around 2.77Hz where the normalised peak accelerations maximised. This frequency is verified by both normalised

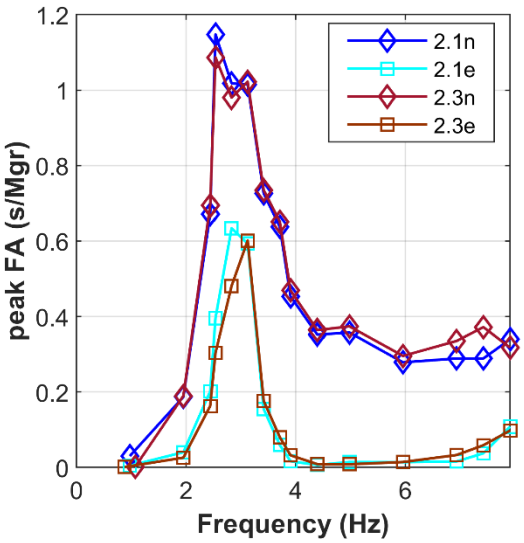
peak acceleration (Figure 6.31a) and peak FA (Figure 6.31b) variations with applied frequency. Both Figure 6.31 a and b demonstrate that this mode corresponds to the swaying mode, as the two examined instruments recorded almost identical accelerations. The in-plane (NS) swaying mode at 2.77Hz is depicted in Figure 6.32. At this frequency the top slab oscillated predominantly in-plane, although weaker out-of-plane motion also existed as a result of experimental imperfections. The torsional natural frequency has been approached, but not reached, at 8Hz of applied frequency which is the largest applied one. This is shown by the increase of the out-of-plane motions at instruments 2.1e and 2.3e and the in-plane 2.1n motions, while the in-plane 2.3n motion tends to decrease. The latter feature is an indication of the torsional response, as explained in Section 6.3.2. This presumption is validated by Figure 6.31c which shows that the phase angle difference between the 2.1 and 2.3 records tend to maximise at the same, 8Hz, frequency. Further validation is given by Figure 6.32, which illustrates that at 8Hz, the oscillation of the top slab was predominantly torsional. Therefore, it is expected that the torsional natural frequency of the FBr_2Ts SSI system was close to 8Hz (e.g. 9Hz). It has not been triggered experimentally, though, as it was beyond the maximum frequency applied during the presented experiment. During the experiments where the mA or mB mass of plates were placed on the vibrator and the maximum applied frequency was 11Hz, the torsional mode was more clearly trigger at 8.4Hz, as evidenced in Appendix E.

The modal properties of the partly braced structure, of which only the North and South sides were braced, can be studied by the PBr_W and PBr_S forced vibration experiments. During the PBr_W experiment, the vibrator applied a load in the direction of the weak plane (NS) of the structure, while the load was applied along the strong plane (EW) during the PBr_S experiment. The two load configurations triggered some common modes of the SSI system, along with one that appeared during the PBr_W experiments only, as shown in Figures 6.33 and 6.35. Figure 6.33a and b present the peak response in terms of normalised accelerations and FA, that are processed from the PBr_W experiments. They show that the North-South, in-plane, natural swaying mode was excited at 1Hz, while the East-West, out-of-plane, swaying mode was excited at 3.5Hz. For applied frequencies lower than 5Hz, the two examined instruments, 2.1 and 2.3, recorded very similar accelerations, implying swaying mode. Beyond this frequency, some records showed a slight increase (i.e. 2.1n, 2.1e and 2.3n), while some others decrease (i.e. 2.3e) in the normalised response. This feature is maximised between 5Hz and 6Hz of applied frequency. The natural torsional frequency lies within this range, for the reasons explained earlier. The latter is in agreement with the outcome of Figure 6.33c, which demonstrates that the phase angle difference between the 2.1 and 2.3 motions maximised at around the same frequency. The natural frequencies of the East-West swaying and the torsional modes are validated against the PBr_S experiments. Figure 6.35 a and b present the normalised acceleration and

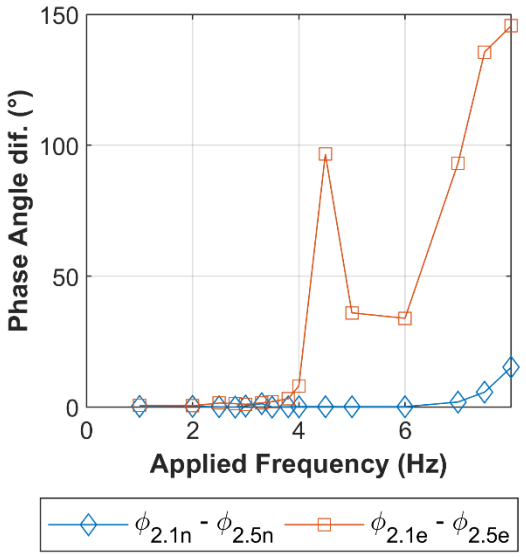
FA response processed from the PBr_S data set, showing an EW swaying natural frequency of around 3Hz. It also illustrates a torsional natural frequency at around 5Hz, which also agrees with the phase angle difference presented in Figure 6.35c. The above two modal natural frequencies are slightly different when estimated from the PBr_W or PBr_S experiments. The difference can be attributed to the different levels of nonlinearity that were engaged in the motion during the two experiments, as subsequently discussed in Section 6.3.6.



(a)



(b)



(c)

Figure 6.31: Natural frequencies and deformation modes of the FBr_2Ts$^{(5)}$_mD experiment, as illustrated by the plots: (a) Normalised peak accelerations with applied frequency, (b) Fourier amplitudes with applied frequency, (c) Difference of phase angle between data recorded by the 2.1 and 2.4 instruments, along the NS (n) and EW (e) directions.

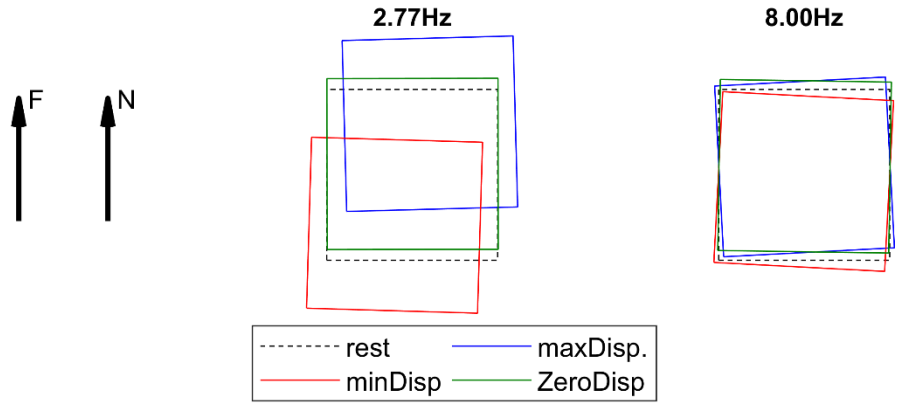


Figure 6.32: Snapshots of the FBr_2Ts[(5)]_mD experiment, illustrating the deformed shapes of the top slab in plan at the identified resonant frequencies. The displacements are exaggerated by 250 times. The North and the direction of the applied force (F) are also shown.

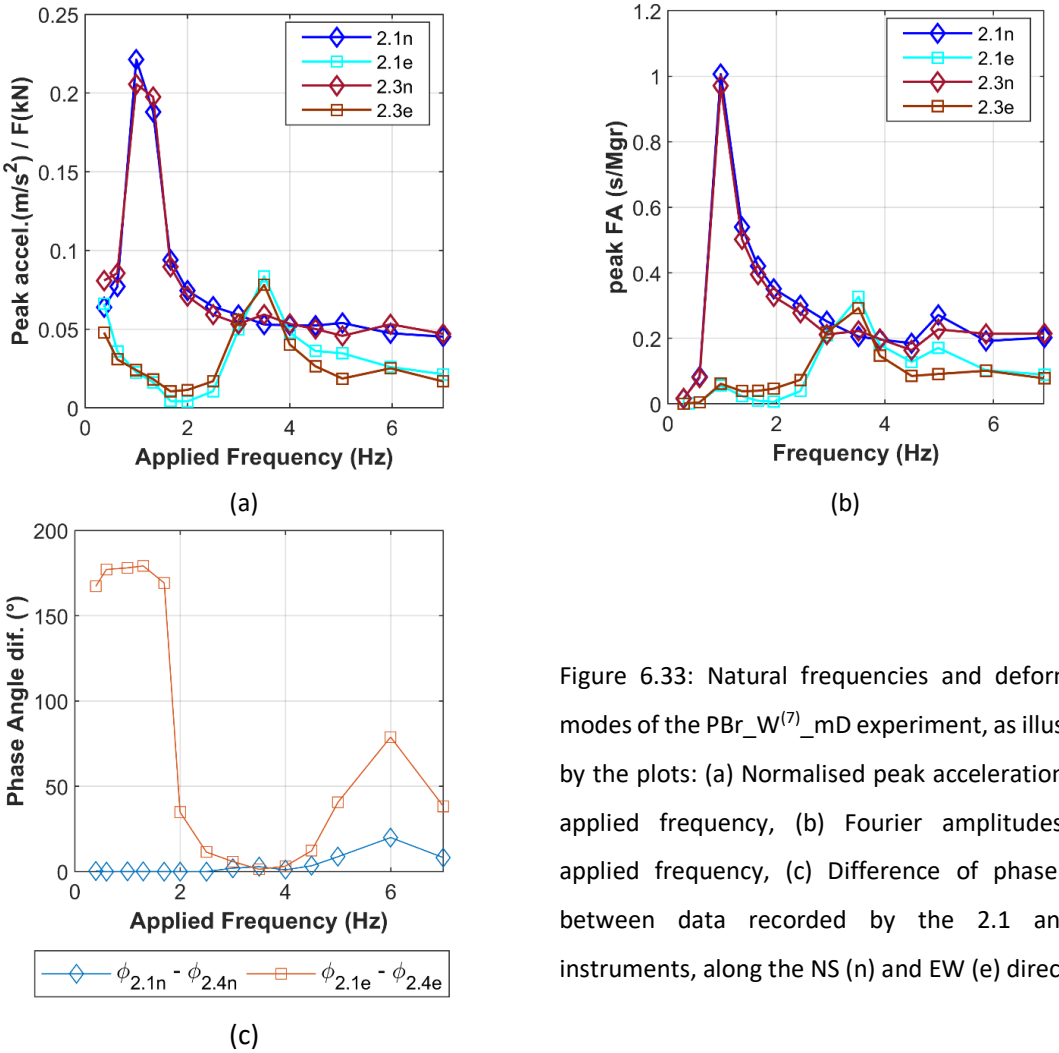


Figure 6.33: Natural frequencies and deformation modes of the PBr_W[(7)]_mD experiment, as illustrated by the plots: (a) Normalised peak accelerations with applied frequency, (b) Fourier amplitudes with applied frequency, (c) Difference of phase angle between data recorded by the 2.1 and 2.4 instruments, along the NS (n) and EW (e) directions.

The deformation modes, discussed above, are verified by the Figures 6.34 and 6.36 which present snapshots of the displaced top slab during the PBr_W and PBr_S experiments respectively. They both reveal the EW swaying mode between 3Hz and 3.5Hz as mentioned earlier, as well as the torsional mode at 5Hz.

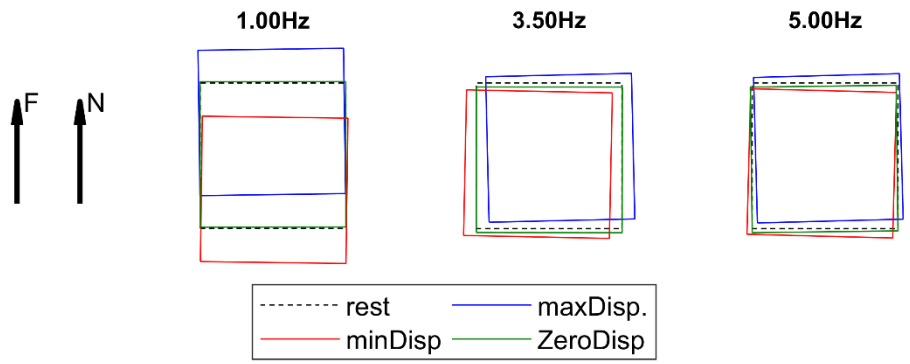
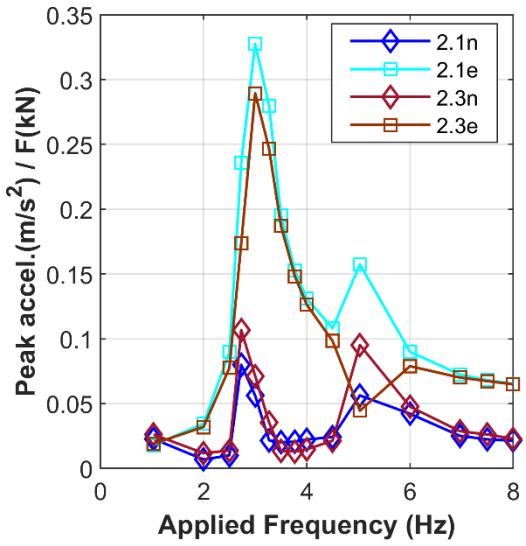
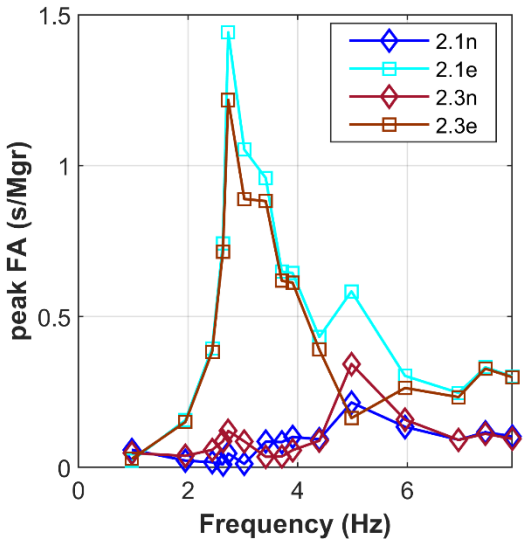


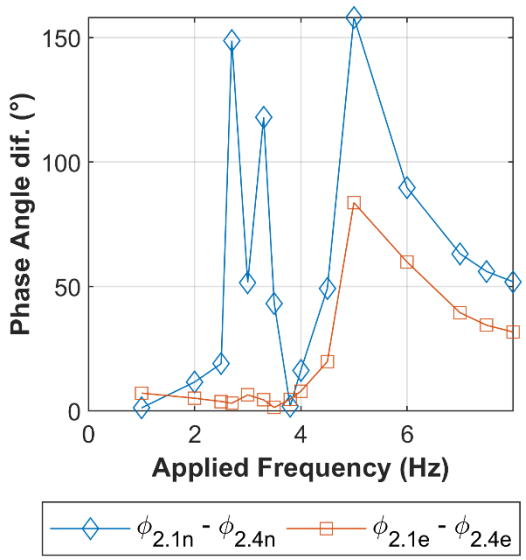
Figure 6.34: Snapshots of the PBr_W[(7)]_mD experiment, illustrating the deformed shapes of the top slab in plan at the resonant frequencies identified. The displacements are exaggerated by 215 times. The North and the direction of applied force are also shown.



(a)



(b)



(c)

Figure 6.35: Natural frequencies and deformation modes of the PBr_S[(8)]_mD experiment, as illustrated by the plots: (a) Normalised peak accelerations with applied frequency, (b) Fourier amplitudes with applied frequency, (c) Difference of phase angle between data recorded by the 2.1 and 2.4 instruments, along the NS (n) and EW (e) directions.

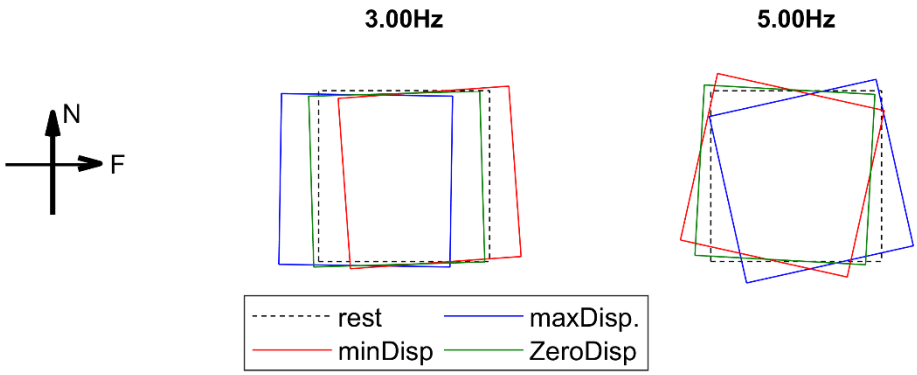
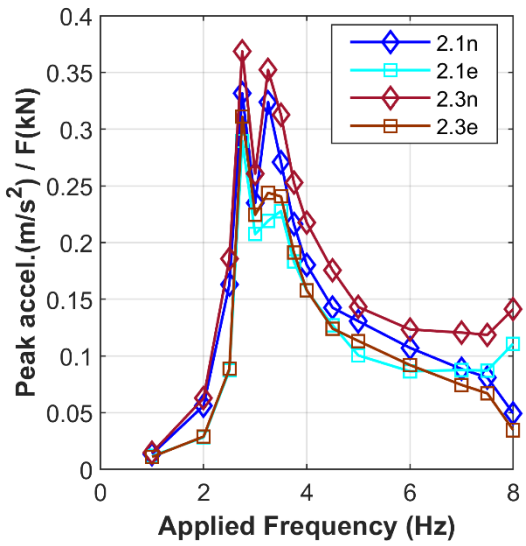


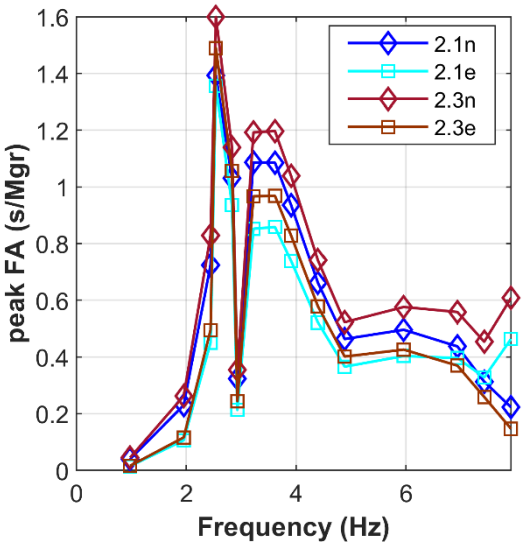
Figure 6.36: Snapshots of the PBr_S$^{(8)}$_mD experiment, illustrating the deformed shapes of the top slab in plan at the resonant frequencies identified. The displacements are exaggerated by 250 times. The North and the direction of applied force (F) are also shown.

Unlike the previous experiments, the experiments on the fully braced structure with 1 top slab (FBr_1Ts) did not clearly reveal the modal NS and EW swaying modes. As Figure 6.37 a and b show, two natural frequencies are identified at 2.75Hz and 3.25Hz. At these frequencies, the amplitudes of the NS (n) and EW (e) motion components are very similar, implying that the experimental conditions did not promote structural oscillation that was dominated by a single mode (i.e. any of the theoretical modes shown in Figure 6.1). Instead, the structure oscillated along the diagonal axis, showing a similar contribution by the NS and EW swaying modal frequencies. The two top slab oscillations are depicted in Figure 6.38, which shows snapshots of the displaced slab at 2.75Hz and 3.25Hz. The diagonal axis was different between the two natural frequencies, as at 2.75Hz the structure oscillated along the NW-SE direction, while at 3.25Hz it oscillated along the NE-SW. The mode of oscillation, resulted from the contribution of the two swaying modes, was controlled by experimental imperfections. The impact of imperfections was more pronounced on the FBr_1Ts experiments than on any other experiment carried out. Assuming that the experimental imperfections were the same for the FBr_2Ts and FBr_1Ts experiments, it can be concluded that lighter structures are more sensitive to imperfections. Under the same vibratory load, the lighter FBr_1Ts structure developed larger displacements than the heavier FBr_2Ts one. The larger displacements might have accentuated the impact of geometric imperfections promoting out-of-plane structural motion. Also, the larger structural displacements developed during the FBr_1Ts experiment, promoted foundation uplift and sliding, as shown subsequently. The larger foundation motion accentuated the impact of existing imperfections at the soil-foundation interface on the SSI response. The latter imperfections, according to the author's opinion, were the dominant imperfections which promoted further the out-of-plane and torsional motion. Another reason that can justify the diagonal deformed shape could be associated with the vibrator load, as accidentally the orientation of the load might have been deviated from the NS direction.

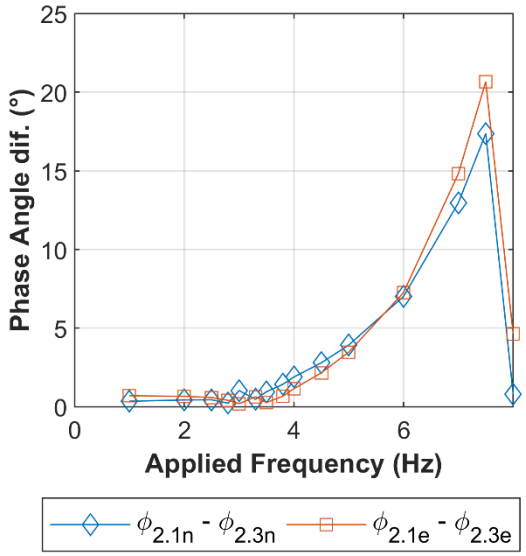
Torsion existed throughout the duration of the FBr_1Ts experiments. This is shown by the different motion amplitudes recorded by two different top slab instruments along the same direction. For applied frequencies smaller than 4Hz, though, the torsional component was weak in comparison with the translational one. Within this range of frequencies, very small differences were observed between the phase angle of the two top slab instruments (Figure 6.37c). The difference maximised at 8Hz of applied frequency, which is considered the torsional natural frequency, as it is also verified by the snapshot presented in Figure 6.38.



(a)



(b)



(c)

Figure 6.37: Natural frequencies and deformation modes of the FBr_1Ts$^{(14)}$_mD experiment, as illustrated by the plots: (a) Normalised peak accelerations with applied frequency, (b) Fourier amplitudes with applied frequency, (c) Difference of phase angle between data recorded by the 2.1 and 2.4 instruments, along the NS (n) and EW (e) directions.

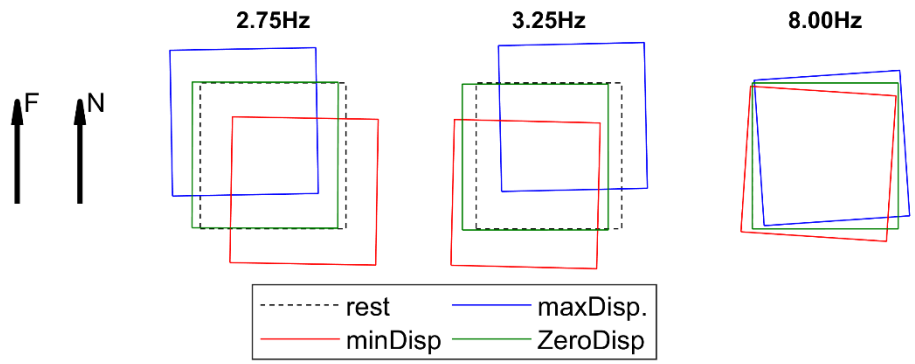


Figure 6.38: Snapshots of the FBr_1Ts$^{(14)}$_mD experiment, illustrating the deformed shapes of the top slab in plan at the resonant frequencies identified. The displacements are exaggerated by 170 times. The North and the direction of applied force are also shown.

Table 6.11 summarises the natural frequencies and the corresponding modes of the examined structural configurations, that could be identified through the forced vibration data. The variation of the natural frequencies with the mass of plates mounted on the vibrator is also demonstrated. As the table shows, the natural frequency of the FBr_2Ts SSI system's swaying (NS or EW) mode was around 3Hz. The NS mode of the PBr structure (excited during the PBr_W experiment) was around 1Hz, much smaller than the one's of the FBr_2Ts structure. The latter is a consequence of the partly braced structure's smaller structural stiffness acting along the NS plane, which made the NS response more flexible. On the contrary, the EW response of the PBr structure was much stiffer, 3Hz, as the braces were acting along this plane. It is observed that the natural frequency of the NS and EW modes of FBr_2Ts and EW mode of the PBr SSI systems were very similar. This is attributed to the fact that during the previous modes and experiments, the structural stiffnesses that were engaged in the motions were very similar. The torsional natural frequency of the PBr system was much lower than the one of the FBr_2Ts system, 5.5Hz and 8.5Hz respectively. Similarly, the difference is a result of the lower structural stiffness that constrained the torsional response of the partly braced structure during the experiments.

According to Table 5.8, the theoretical swaying and torsional natural frequencies of the fixed-base FBr_1Ts structure are larger than the ones of the fixed-base FBr_2Ts structure. However, the experimental natural frequencies of the FBr_1Ts SSI system were similar to the one of the FBr_2Ts SSI system. The latter is evidence of stronger soil-foundation-structure interaction (SFSI) effects and soil nonlinearity that took place during the experiments on the structure with one top slab than the structure with two top slabs. The SFSI effects and soil nonlinearity are also the reasons of the variation of the natural frequencies with the mass of plates mounted on the vibrator, as it is discussed subsequently in Section 6.3.6.

Table 6.11: Experimental natural frequencies and the corresponding modes of the examined SSI systems with different structural configurations.

Experiment	Vibrator mass	$F_{swaying}$ (Hz)		$F_{torsional}$ (Hz)
		NS	EW	
FBr_2Ts[5]	mA	3.50	3.50	8.50
FBr_2Ts[2]	mB	3.00	3.00	8.50
FBr_2Ts[5]	mC	3.00	3.00	>8.00*
FBr_2Ts[5]	mD	2.77	2.77	>8.00*
PBr_W[7]	mB	1.33	3.50	5.00-6.00
PBr_W[9]	mC	1.33	3.50	5.00-6.00
PBr_W[7]	mD	1.00	3.50	5.00-6.00
PBr_S[10]	mB	n/a	3.27	5.50
PBr_S[10]	mC	n/a	3.27	5.50
PBr_S[8]	mD	n/a	3.00	5.00
FBr_1Ts[14]	mC	3.50	2.75**	n/a
FBr_1Ts[14]	mD	3.25**	2.75**	8.00

* Approached but not reached

** Oscillations that had almost equal NS and EW components

The impact of the SFSI effects on the natural frequencies can be evaluated through the lengthening of the predominant periods of the SSI system, relative to the corresponding fixed-base one. The lengthening ratio is calculated as the ratio of the theoretical fixed-base natural frequency, given by Table 5.8, over the experimental SSI natural frequency presented in Table 6.11. Table 6.12 presents the period lengthening ratios of the swaying and torsional natural periods of each experimental configuration. Two values are given for each configuration, which are computed from data of experiments which triggered the lowest and highest nonlinearity. The lowest nonlinearity was triggered during the experiments where the applied force was the smallest, or equivalently when the smallest mass of plates was placed on the vibrator (i.e. mA). Similarly, the highest nonlinearity is expected that took place during the mD experiments, during which the applied sinusoidal force was the largest.

A higher period lengthening ratio value indicates stronger SFSI effects. Table 6.12 indicates that SFSI effects had the smallest impact on the NS mode of the PBr structure, which was the most flexible mode. The period lengthening ratio value of the EW mode of the same structure was almost identical to the lengthening of the swaying modes of the FBr_2Ts structure. This indicates that the level of impact of the SFSI effects was similar on both structures at the corresponding modes. The most

pronounced lengthening of the predominant period was observed on the swaying mode of the FBr_1Ts structure. The lengthening ratio value of this structure varied between 3.7 and 4.75, in comparison to the values 2.6-3.3 computed for the FBr_2Ts experiments. The above observations align with the literature, where it is well established that stiffer structures exhibit stronger SSI effects (e.g. Amorosi *et al.*, 2017).

The lengthening ratios of the torsional natural periods were much smaller than the ratios of the swaying modes, which is in agreement with the observation made by Pitilakis *et al.* (2014). This can be attributed to the more pronounced impact of soil compliance, nonlinearities and foundation rocking on the swaying mode. As it is subsequently evidenced in Section 6.3.8, foundation nonlinearity, rocking, was stronger during the swaying mode than during the torsional one, which increased more the lengthening ratio of the former mode.

Table 6.12: Period lengthening ratios of the two swaying modes and the torsional mode of three structural configurations.

Structural configuration	Lowest experimental Nonlinearity			Highest experimental Nonlinearity		
	Swaying		Torsional	Swaying		Torsional
	NS	EW		NS	EW	
FBr_2Ts	2.61	2.61	1.37	3.30	3.30	1.37
PBr	1.34	2.61	1.53	1.78	3.04	1.69
FBr_1Ts	3.73	4.75	n/a	4.02	4.75	2.07

6.3.6 Evaluation of nonlinear effects

The sources of nonlinearity that can develop during SSI experiments, as it has already been discussed in Section 6.2.5, are structural yielding, P-δ effects, soil nonlinearity, interface geometric nonlinearity and interface yielding. Among the aforementioned sources, only soil nonlinearity and soil-foundation interface nonlinearity are discussed herein. These two types are envisaged to have the most pronounced impact on the forced vibration response of the SSI system, while the remaining nonlinearities were negligible. The impact of the nonlinear effects on the natural frequencies are evaluated through the top slab response normalised by the magnitude of the applied sinusoidal force (F). The magnitude of the sinusoidal force is a function of the mass of the plates that were placed on the vibrator. According to Section 5.3.1, four different pairs of plates could be used, mA, mB, mC and mD. When the mA mass was used, the vibrator imposed a sinusoidal force of the smallest magnitude, while the mD mass produced the maximum magnitude (Figure 5.12). Any deviation in the normalised response between experiments, of which the magnitude of the load was the only difference, can be attributed to nonlinear effects. The level of the induced nonlinearity is dependent on the intensity of the foundation and soil motion. The intensity of these motions was affected by both the magnitude

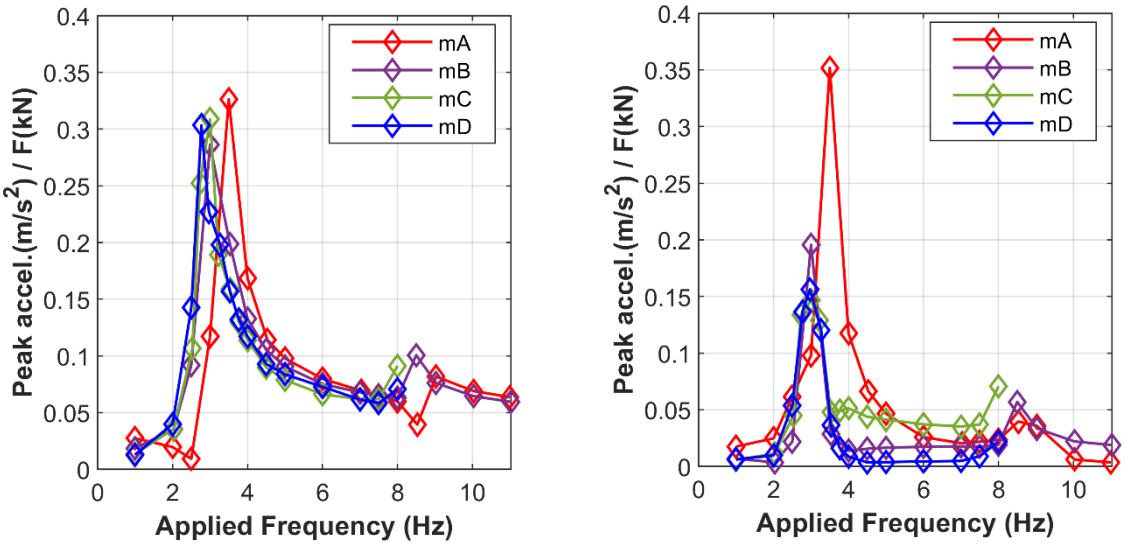
of the load and the structural configuration. Comparisons of natural frequencies between the different experimental configurations give evidence of the latter claim.

Figures 6.39 to 6.42 present the North-South and East-West top slab normalised peak accelerations against applied frequency, inferred from the FBr_2Ts, PBr_W, PBr_S and FBr_1Ts experiments. Each figure contains data processed from experiments in which different mass of plates was placed on the vibrator (mA, mB, mC or mD). The figures demonstrate that the experiments with larger mass, which produced larger magnitude sinusoidal forces, produced smaller normalised response and natural frequencies. This feature is a result of the higher level of nonlinearity that took place during the experiments of larger force (e.g mD). Larger applied forces might have resulted in more pronounced foundation uplift, hence, more pronounced geometric nonlinearities at the soil-foundation interface. The stronger soil motion developed more pronounced soil nonlinearity, including higher stiffness degradation of the foundation soil. Both interface and soil nonlinearities decreased the natural frequencies, justifying the smaller natural frequencies observed at larger applied forces.

The frequency shift of the same structural configuration due to nonlinearities is more pronounced on the swaying modes of the FBr_2Ts system (Figure 6.39) during which, as already mentioned, strong soil-foundation-interaction phenomena took place. The impact of the nonlinearities on the FBr_1Ts system (Figure 6.40), which is also a system which exhibited strong SFSI, cannot be evaluated due to the lack of experiments with smaller applied load (i.e. mA or mB). As expected and inferred from the PBr_W experiment (Figure 6.41a), the NS natural frequency of the PBr system, which has the most flexible response (1Hz), was the least affected by nonlinearities. On the same experiment, the natural frequency of the EW mode was also unaffected by the magnitude of the applied load, despite that this was a relatively stiff (3.5Hz) response (Figure 6.41a). This stems from the fact, that during all PBr_W experiments, the EW (out-of-plane) motion, was very weak followed by weak nonlinearity. Additional reason is that the shift, if any, is expected to be very small around 3.5Hz (e.g. 3.25Hz, 3.75Hz), which would require further refinement of the input (i.e. application of smaller frequency steps). The same mode of the same structure (EW mode of the partly braced structure), though, showed very prominent frequency shift during the PBr_S experiments, as inferred from the normalised acceleration amplitudes in Figure 6.42b. During this experiment, the vibratory load was applied along the EW direction, triggering predominantly the EW mode. Therefore, the nonlinearities impacted the corresponding natural frequency, which varied between 3.27Hz to 3Hz depending on the load magnitude.

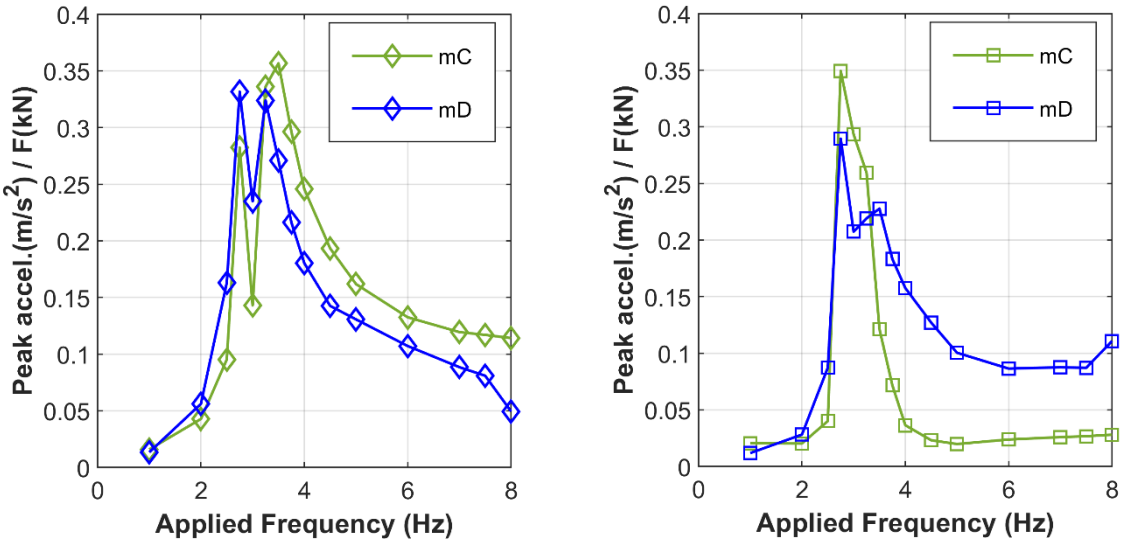
Apart from the natural frequency, nonlinearities affected the amplitude of the motion through the development of damping. Experiments of larger applied force (e.g. mD) promoted soil nonlinearity producing more damping than experiments with smaller applied force (e.g. mA). This is reflected on

the smallest amplitude of normalised motion observed in mD experiments, during which the force was the largest. Likewise, the amplitude increased from mC to mA experiments, during which the forced decreased (Figures 6.39 to 6.42). This stems from the fact that stronger excitation generated wider stress-strain loops in the soil, producing larger damping. More evidence of damping and its dependence on soil motion intensity and magnitude of the excitation force is presented subsequently in Sections 6.3.8 and 6.3.9.



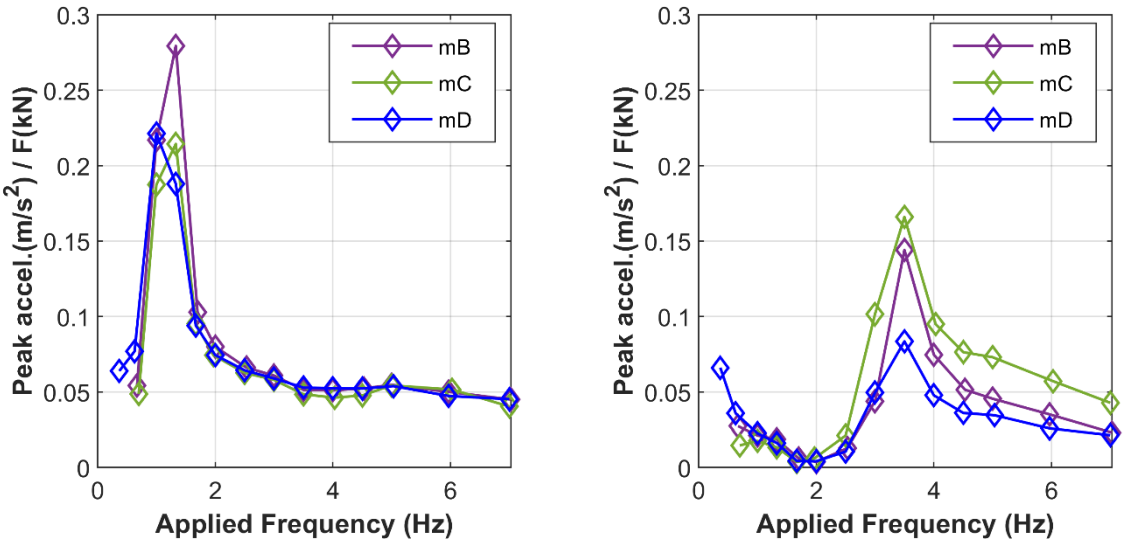
(a) NS (in-plane) (b) EW (out-of-plane)

Figure 6.39: Comparison of the top slab normalised response of the FBr_2Ts structure as inferred from experiments with different mass of plates mounted on the vibrator. The (a) North-South and (b) East-West response, recorded by the 2.1, instrument is presented.



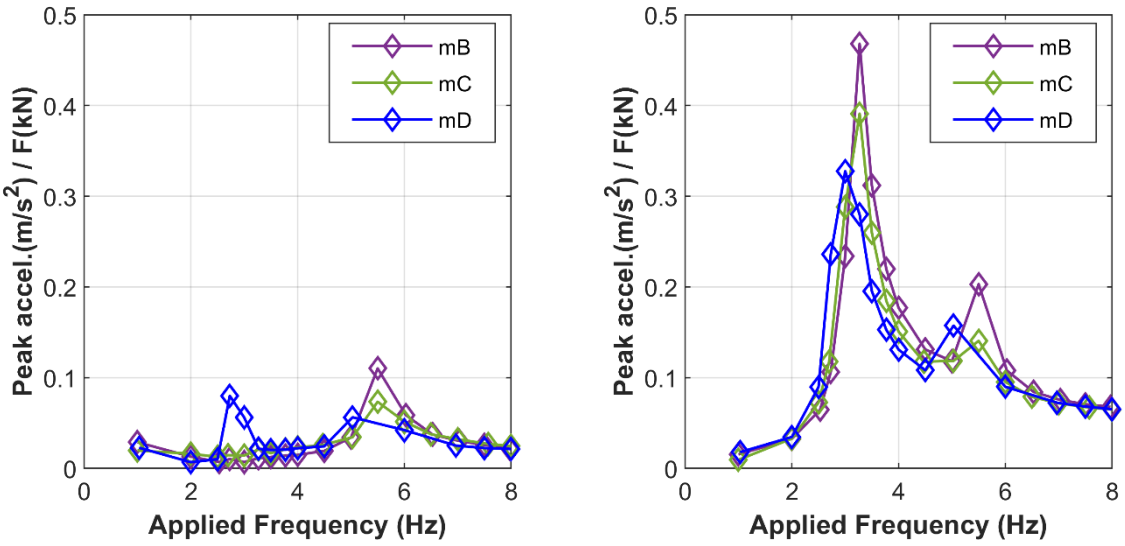
(a) NS (in-plane) (b) EW (out-of-plane)

Figure 6.40: Comparison of the top slab normalised response of the FBr_1Ts structure as inferred from experiments with different mass of plates mounted on the vibrator. The (a) North-South and (b) East-West response, recorded by the 2.1 instrument, is presented.



(a) NS (in-plane) (b) EW (out-of-plane)

Figure 6.41: Comparison of the top slab normalised response of the PBr_W structure as inferred from experiments with different mass of plates mounted on the vibrator. The (a) North-South and (b) East-West response, recorded by the 2.1 instrument, is presented.



(a) NS (out-of-plane) (b) EW (in-plane)

Figure 6.42: Comparison of the top slab normalised response of the PBr_S structure as inferred from experiments with different mass of plates mounted on the vibrator. The (a) North-South and (b) East-West response, recorded by the 2.1 instrument, is presented.

6.3.7 Evidence of soil nonlinearity

Quantitative evidence of soil nonlinearity is presented, aiming to partly justify the deviation between the normalised responses of the structures subjected to different applied forces (i.e. different mass of vibrator plates), discussed in Section 6.3.6. Table 6.13 presents, for a selection of experiments, the

peak particle velocities (PPV) recorded by the instruments referred in the table. It also presents the estimated "experimental" strains (γ) and degradation of the secant stiffness (G_{sec}/G_{max}). The "experimental" strains, degradation of the secant stiffness and damping ratio values are computed as discussed in Section 6.2.6. For compatibility reasons, the instruments, of which data are used, are selected according to the loading direction. When the load was applied along the NS, the strong motion data used were recorded by the NS sensor of the 0.2 instrument. Equivalently, for EW loading excitation, data from the EW sensor of the 0.41 are exploited, while both 0.2 and 0.41 were located at a distance of 3m from the foundation. The presented γ and G_{sec}/G_{max} values are inferred from PPVs which were recorded during the swaying and torsional resonant oscillations.

Table 6.13 shows that even for the largest recorded PPV values, the soil stiffness degradation is very weak. This is better illustrated in Figure 6.43, which maps the "experimental" G_{sec}/G_{max} and damping ratio (ζ) on the G-γ-D curves. The figure shows that the FBr_2Ts, Fbr_1Ts and PBr_S experiments produced lower levels of G_{sec}/G_{max} and higher ζ than the ones produced during the PBr_W experiment. This observation is justified from the stronger foundation and soil motions developed during the former experiments, evidence of which is subsequently presented in Section 6.3.8. The stronger soil motion resulted in higher induced strain levels, hence more hysteresis in the stress-strain domain increasing the levels of stiffness degradation and damping. For the same reason, the mD experiments, during which the response was stronger, produced larger stiffness degradation and damping ratio than the mC experiments.

However, the variation of the level of G_{sec}/G_{max} degradation and ζ development estimated from the compared experiments is weak, with the actual levels of the above quantities being small. This is attributed to the fact that the processed data were recorded by an instrument 3m away from the foundation. The variation is envisaged that was important at the vicinity of the foundation, where data are not available. As already mentioned in Section 6.2.6, the area around the foundation controlled the overall nonlinearity of the SSI system. There, nonlinearities mechanisms that dominated the SSI response occurred, including soil stiffness degradation and damping development as well as foundation uplift and sliding.

Table 6.13: Peak particle velocities, strains and stiffness degradation levels computed at the identified natural frequencies of the experiments with vibrator mass mC and mD. The instruments of which records were used is also stated.

Experiment	Loading dir.	Freq. (Hz)	Mode of oscillation	Instrument	PPV	γ (%)	G_{sec}/G_{max}
FBr_2Ts$^{(5)}$_mC	NS	3.00	NS swaying	0.2n	1.27E-04	9.07E-05	0.993
FBr_2Ts$^{(5)}$_mC	NS	8.00	Torsional	0.2n	1.85E-04	1.32E-04	0.990
FBr_2Ts$^{(5)}$_mD	NS	2.77	NS swaying	0.2n	1.57E-04	1.12E-04	0.991
FBr_2Ts$^{(5)}$_mD	NS	8.00	Torsional	0.2n	3.72E-04	2.66E-04	0.981
FBr_1Ts$^{(14)}$_mC	NS	2.75	Swaying diagonal	0.2n	5.18E-05	3.70E-05	0.997
FBr_1Ts$^{(14)}$_mC	NS	3.50	NS swaying	0.2n	1.05E-04	7.49E-05	0.994
FBr_1Ts$^{(14)}$_mD	NS	2.75	Swaying diagonal	0.2n	1.04E-04	7.45E-05	0.994
FBr_1Ts$^{(14)}$_mD	NS	3.25	Swaying diagonal	0.2n	1.31E-04	9.39E-05	0.993
FBr_1Ts$^{(14)}$_mD	NS	8.00	Torsional	0.2n	3.18E-04	2.27E-04	0.984
PBr_W$^{(12)}$_mC	NS	1.33	NS swaying	0.2n	5.57E-06	3.98E-06	1.000
PBr_W$^{(12)}$_mC	NS	3.50	EW swaying	0.2n	7.72E-06	5.51E-06	0.999
PBr_W$^{(12)}$_mC	NS	6.00	Torsional	0.2n	2.87E-05	2.05E-05	0.998
PBr_W$^{(12)}$_mD	NS	1.00	NS swaying	0.2n	6.43E-06	4.59E-06	1.000
PBr_W$^{(12)}$_mD	NS	3.50	EW swaying	0.2n	1.72E-05	1.23E-05	0.999
PBr_W$^{(12)}$_mD	NS	6.00	Torsional	0.2n	6.27E-05	4.48E-05	0.996
PBr_S$^{(13)}$_mC	EW	3.27	EW swaying	0.41e	1.28E-04	9.16E-05	0.993
PBr_S$^{(13)}$_mC	EW	5.50	Torsional	0.41e	1.10E-04	7.85E-05	0.994
PBr_S$^{(13)}$_mD	EW	3.00	EW swaying	0.41e	1.67E-04	1.20E-04	0.991
PBr_S$^{(13)}$_mD	EW	5.00	Torsional	0.41e	1.91E-04	1.36E-04	0.990

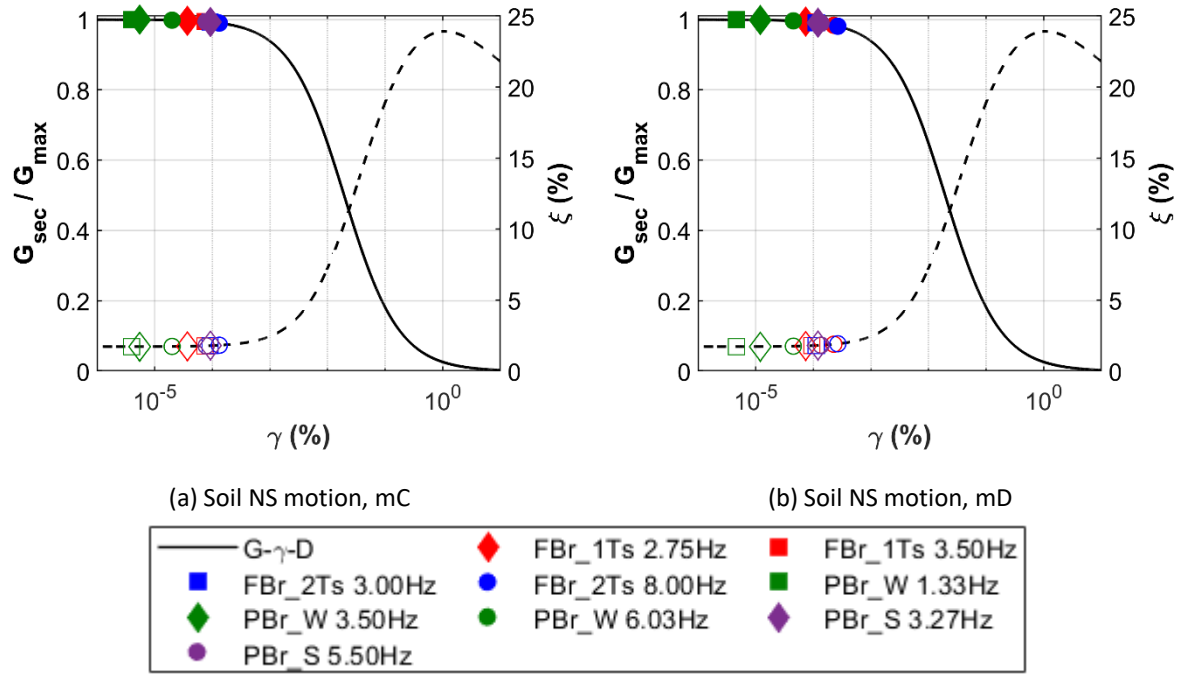


Figure 6.43: Calibrated G-γ-D curves and stiffness degradation and damping ratio values that inferred from "experimental" strains, using forced vibration tests on the four different structural configurations. The strong motion data used were recorded by the instruments shown in Table 6.13 and located 3m from the foundation edge. Results from experiments of which the vibrator plate mass was (a) mC and (b) mD are presented.

6.3.8 Evidence of Soil-Foundation-Structure Interaction

Soil-Foundation-Structure Interaction (SFSI) effects are an aggregation of the impacts of both soil compliance and foundation motion on the SSI response. The impact of soil compliance has already been evidenced in Section 6.3.6, by comparing the period elongation of a linear elastic SSI system relative to the equivalent fixed-base linear elastic system. Herein, evidence of the impact of foundation motion on the structural response is provided.

The intensity of the foundation and soil motion can give an indication about the significance of the SFSI effects. For weak foundation motions, which can be the case of a system consisting of a foundation much stiffer than the superstructure, the superstructure will behave similar to the equivalent fixed-base structure. Conversely, for stiff superstructures relative to foundation stiffness, the foundation motion will be more significant promoting SFSI effects and affecting the deformability of the structure (e.g. Amorosi *et al.*, 2017). Following the latter consideration, the experimental top slab response (u_{ts}) is decomposed into structural flexural deformation (u_s), foundation translation (u_f) and the contribution of foundation rotation (rocking) ($u_\theta=h\theta$). The motion decomposition method followed is described in Section 6.3.3, while the strong motion data used are shown in Table 6.9.

Figure 6.44 presents the maximum displacements of each of the above motion components against applied frequency. The motion components of all four experimental configurations are examined by exploiting data recorded during the experiments where the plate mass mD was adjusted on the vibrator. The figure demonstrates that the total response of the FBr structures (Figure 6.44a and b) was dominated by the foundation rotation (hθ), while the structural flexural deformation and foundation horizontal motion were weak. A similar but less pronounced feature was observed during the oscillation of the PBr structure when it was loaded along its strong axis (Figure 6.44c). The structure oscillated along its stiff axis, producing a stiff response promoting foundation rotation (Figure 6.44d). On the contrary, when the same structure oscillated along its weak (NS) axis (i.e. PBr_W experiments), the foundation motion was negligible and the flexural deformation dominated (Figure 6.44d).

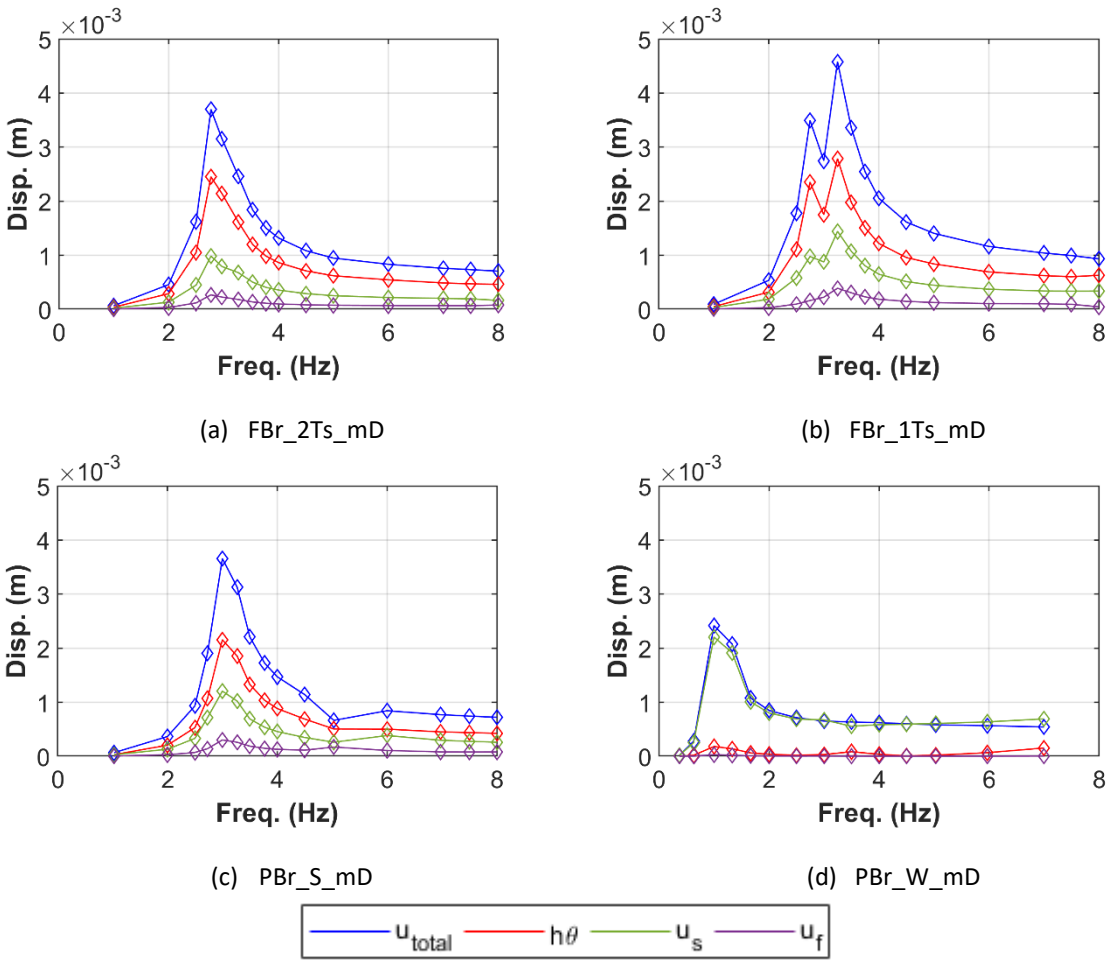
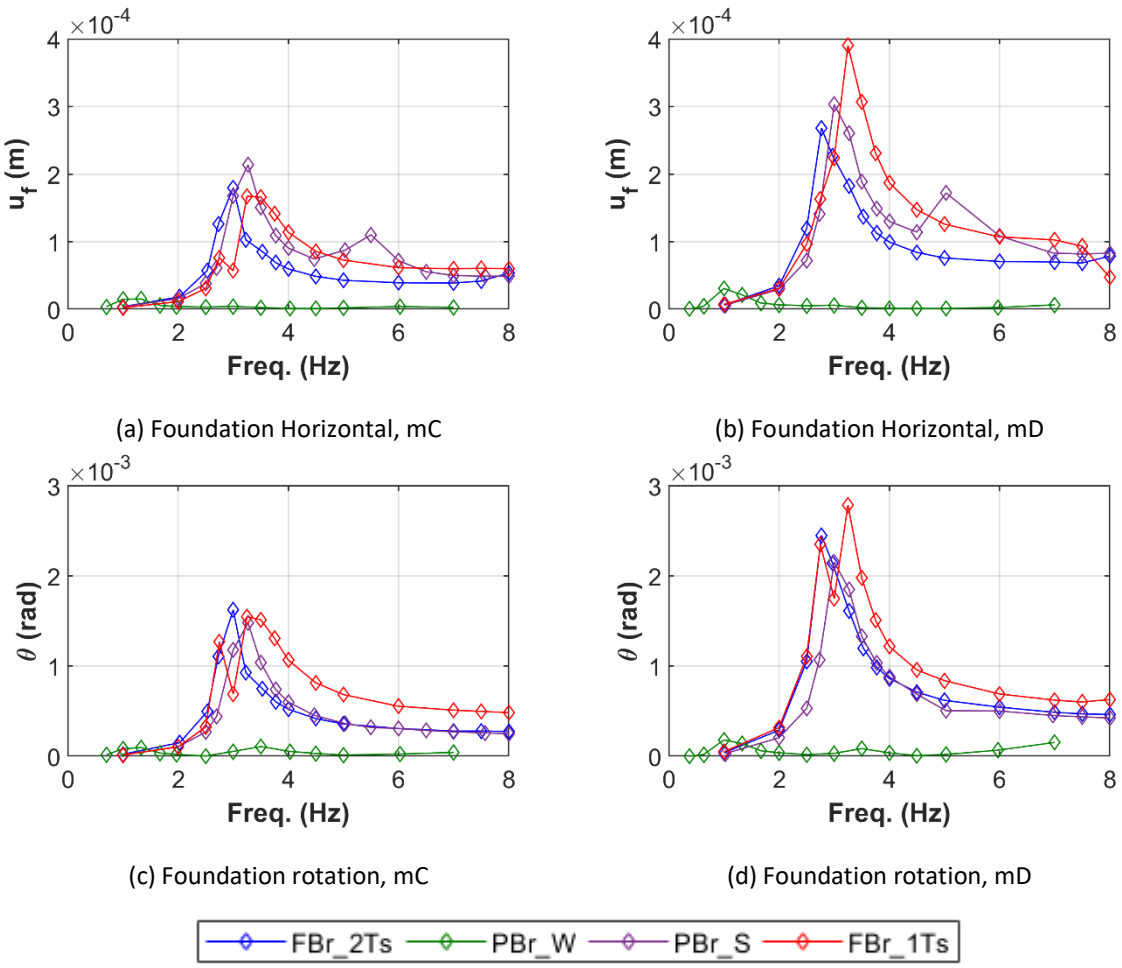


Figure 6.44: Motion decomposition of the top slab displacements estimated from data recorded during the (a) FBr_2Ts_mD, (b) FBr_1Ts_mD, (c) PBr_W_mD and (d) PBr_S_mD experiments.

The foundation translation (u_f) and rotation (θ) developed during the forced vibration tests on the four configurations are compared in Figure 6.45. The presented results refer to experiments during which the mC (a, c) or mD (b, d) mass of plates were placed on the vibrator. It is verified that the

foundation motion was negligible during the PBr_W experiment as it excited the most flexible response of the system. Conversely, when the response was stiff, which was the case for the FBr_2Ts, FBr_1Ts and PBr_S experiments, both foundation components were significant. Both foundation horizontal motion (Figure 6.45a, b) and rocking (Figure 6.45c, d) increased with increasing external load.

The comparison between systems with the same bracing system, but different superstructural mass, reveals that the lighter structure (FBr_1Ts) exhibited stronger foundation motion than the heavier one (FBr_2Ts). This is reasonable, as, under the same applied load, the lighter structure exhibited larger top slab hence foundation displacements. Also, the fixed-base FBr_1Ts was stiffer than the FBr_2Ts structural configuration (Table 5.8), which is a condition that promoted further foundation rocking. The stronger foundation motion exhibited during the FBr_1Ts experiment can justify the stronger impact of SFSI effects on the lengthening of the predominant period observed on the FBr_1Ts than the FBr_2Ts configuration (Table 6.12).



(a) Foundation Horizontal, mC

(b) Foundation Horizontal, mD

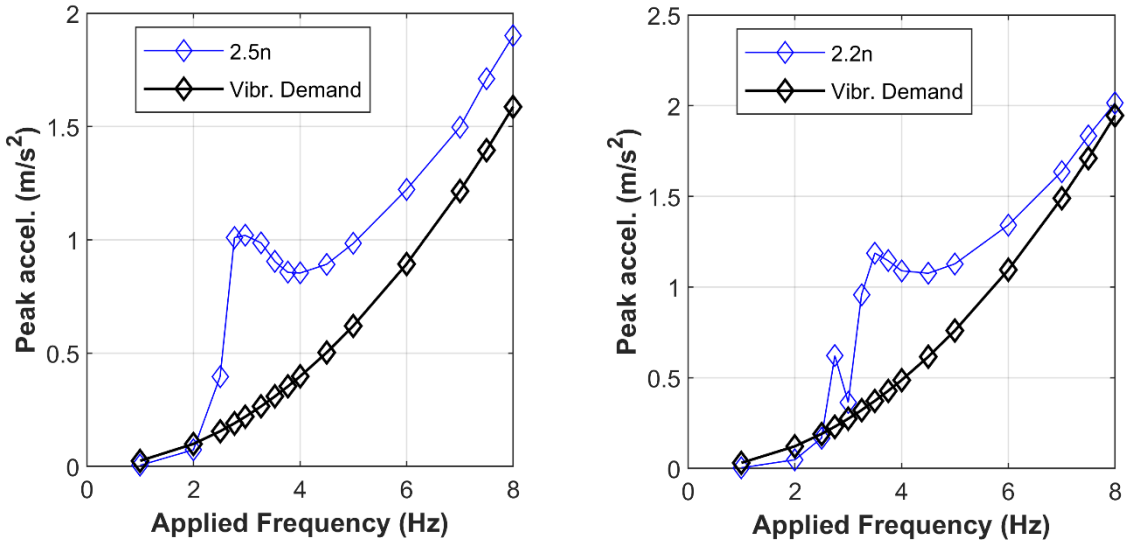
(c) Foundation rotation, mC

(d) Foundation rotation, mD

Figure 6.45: Comparison of foundation (a, b) horizontal and (c, d) rotation as computed from forced vibration tests on the four different configurations. Results from experiments of which the vibrator plate mass was (a, c) mC and (b, d) mD are presented.

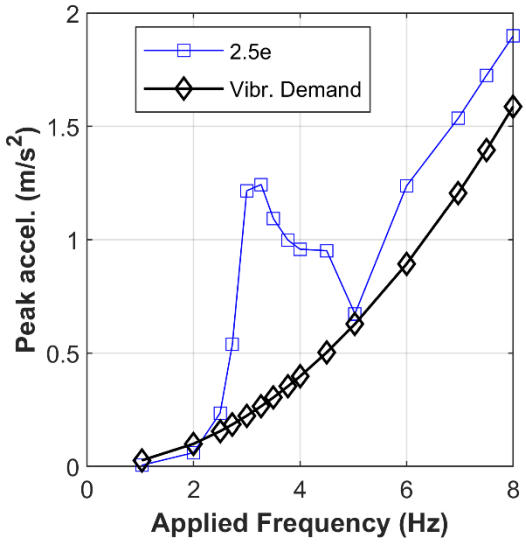
The foundation motion can also be evaluated by comparing the recorded top slab accelerations with the vibrator input demand. Any difference between the two can be attributed to the generation of inertial forces resulting due to resonant features or foundation rocking. The vibrator demand is calculated as the vibrator magnitude of the sinusoidal load, as per Eq. 5.14, divided by the top slab mass, assuming SDOF conditions and zero participation of the foundation mass in the motion. The latter assumptions are considered reasonable when the foundation motion and the torsional response were very weak during the experiments. Figure 6.46 compares the vibrator demand with the maximum top slab accelerations recorded during mD forced vibration experiments on the four different configurations. It is observed that at resonance, the demand was exceeded, as the SSI response was dominated by inertial forces. When the FBr_2Ts, FBr_1Ts, and PBr_S configurations oscillated far from resonance, their structural response exceeded the input demand as well. This can be attributed to foundation rocking, which, as illustrated by Figure 6.44, dominated the structural response of the above configurations. The response approaches the demand at frequencies larger than 6Hz, for which foundation rotation becomes weak (see Figure 6.44). Unlike FBr_2Ts, FBr_1Ts, and PBr_S experiments, during the PBr_W experiment, where the foundation motion was negligible, the top slab motion closely matched the vibrator demand. Therefore, it can be claimed that foundation rocking increased the structural response, as compared to a system with negligible rocking.

Figure 6.47 presents the peak particle horizontal and vertical soil velocities recorded during each applied frequency on the soil surface by an instrument located around 1.3m far from the foundation. For consistency, the compared soil motions were selected according to the loading direction. For the FBr_2Ts, FBr_1T and PBr_W experiments, where the load was applied in the NS direction, the exploited motion was the NS motion component recorded by the 0.1 instrument, which was located North to the foundation. Equivalently, for the PBr_S experiment, where the force was applied in the EW direction, the exploited motion is the EW motion component recorded by the 0.40 instrument, located East of the foundation. Figure 6.47 illustrates that the recorded soil velocities follow the trend of the foundation accelerations presented above. The horizontal (Figure 6.47a, b) and vertical (Figure 6.47c, d) soil motion components were larger during the FBr_1Ts, FBr_2Ts and PBr_S experiments, where the foundation motion was the strongest. Equivalently, the PBr_W experiment produced weak soil motion, as a consequence of the weak foundation motion. The relation between the intensities of the foundation and soil motions can also explain the stronger soil response produced by the mD than the mC experiments.

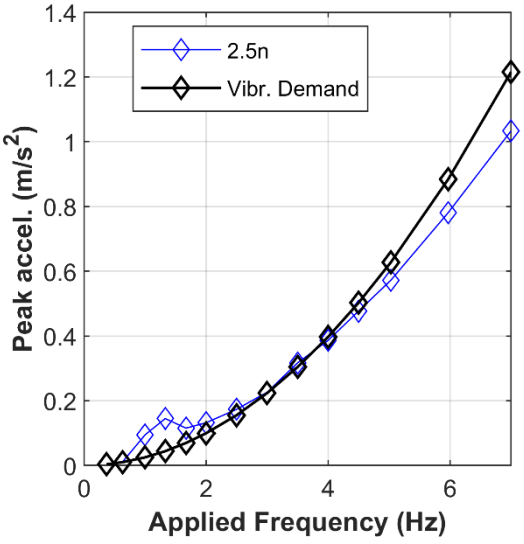


(a) FBr_2Ts_mD

(b) FBr_1Ts_mC*



(c) PBr_S_mD



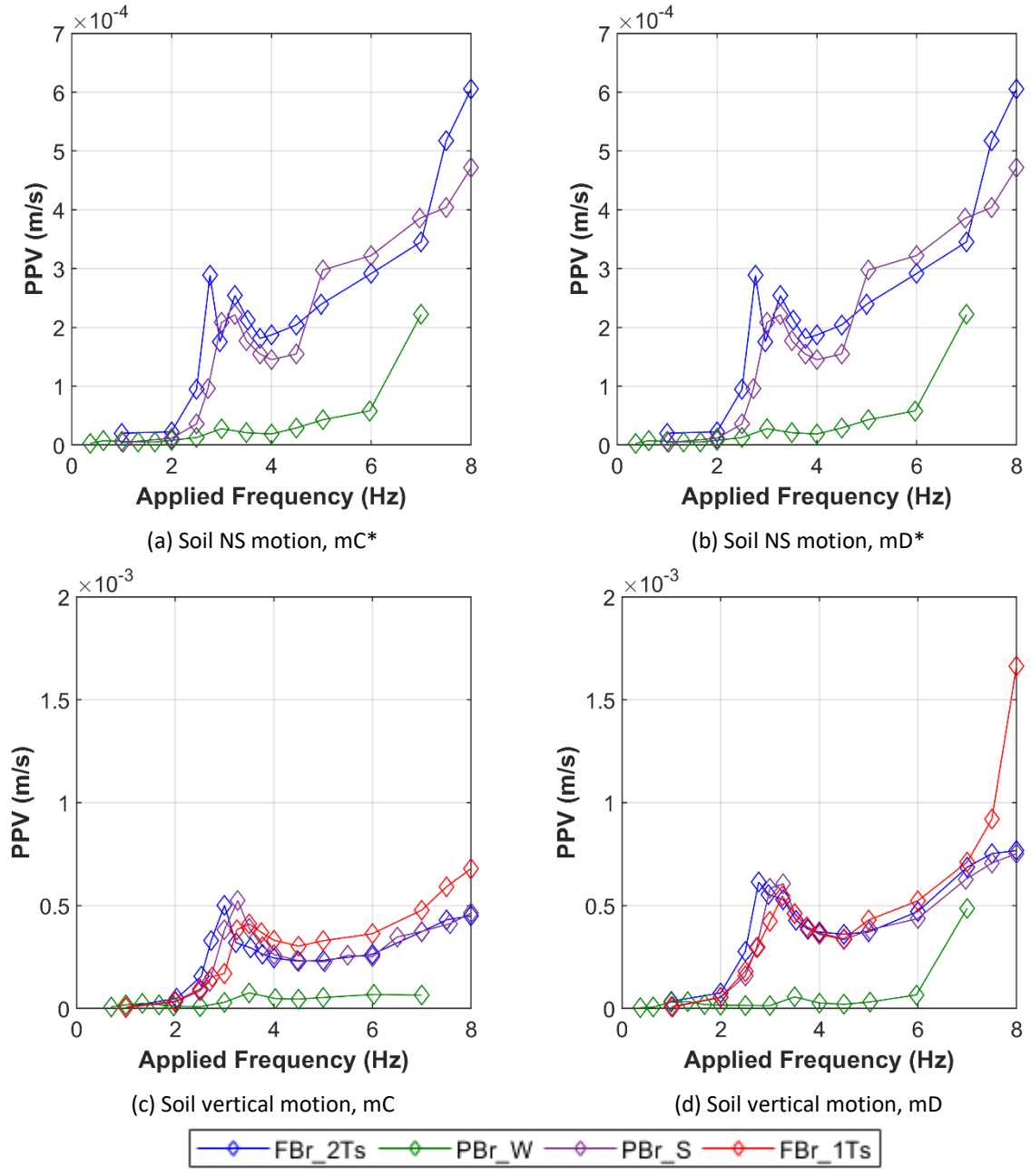
(d) PBr_W_mD

* FBr_1Ts_mC was used over FBr_1Ts_mD, as the latter produced very pronounced out-of-plane motion, which makes the calculation of vibrator demand not applicable. Also, centre instrument (i.e. 2.5) was not available, substituted recorded by data of 2.2 instrument.

Figure 6.46: Comparison of the vibrator input demand and the top slab accelerations recorded during the (a) FBr_2Ts_mD, (b) FBr_1Ts_mC, (c) PBr_W_mD and (d) PBr_S_mD experiments.

Another outcome that can be drawn by Figure 6.47 is that the natural frequencies of the SSI system can be identified through the soil motion, provided that the foundation participates in the oscillation. Peaks in soil velocities are observed around the predominant (swaying) frequencies presented in Table 6.11. Also, an increase in the soil horizontal motion is observed at the resonance of the torsional mode. During the presented experiments, the torsional mode was achieved at 8Hz during the FBr_2Ts_mD and FBr_1Ts_mD experiments; at 5.5Hz during the PBr_S_mC and at 5Hz during the PBr_S_mD; and at 5.5-6Hz during the PBr_W_mC and PBr_W_mD experiments. At these frequencies of the

corresponding experiments, with the exception of the PBr_W ones, an increase in the soil motion is observed more pronouncedly in the horizontal motion component than the vertical component. The latter demonstrates that the soil motion depended, apart from the amplitude of the foundation motion, on the foundation mode of oscillation as well. It is noted that the torsional mode of oscillation of the PBr_W experimental configuration was not indicated in soil data, because the foundation motion was very weak.



(a) Soil NS motion, mC*

(b) Soil NS motion, mD*

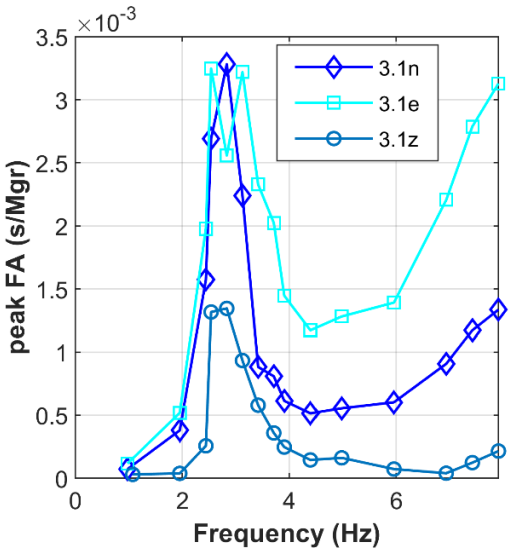
(c) Soil vertical motion, mC

(d) Soil vertical motion, mD

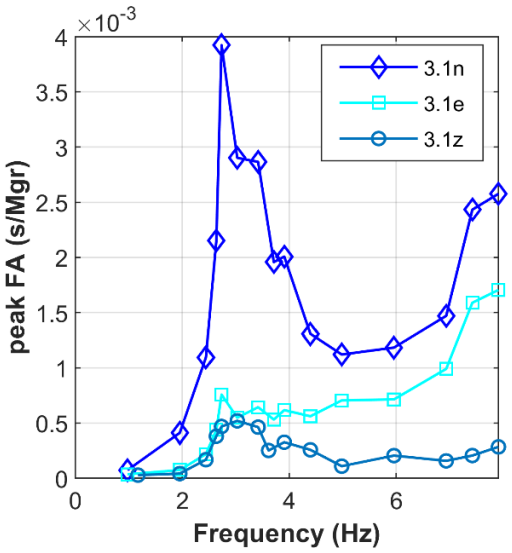
*the NS sensor of the 0.1 instrument did not work during the FBr_1Ts experiments, the data of which are not plotted.

Figure 6.47: Comparison of soil motion recorded by the 0.1/0.40 instruments along the (a, b) NS and (c, d) vertical directions during the experiments on different structural configurations. Results from experiments of which the vibrator plate mass was (a, c) mC and (b, d) mD are presented.

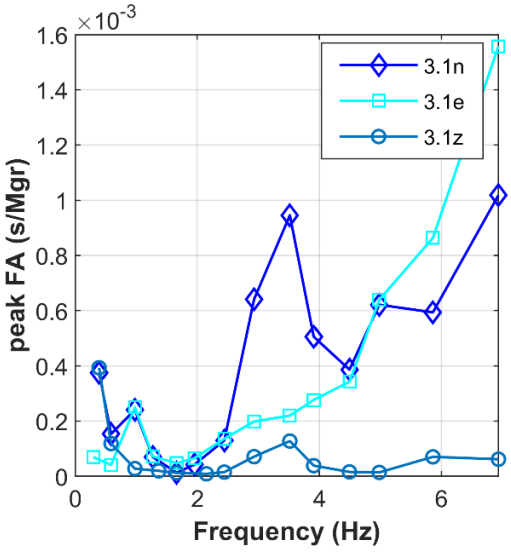
The impact of the foundation response on the soil response can also be observed through the downhole soil motion recorded by the instrument 3.1. The downhole accelerometer recorded high frequency content; hence its records can be better evaluated through Fourier spectra than PPV values. The spectra can distinguish the amplitude of the motion at the applied frequency which is of the main interest. Figure 6.48 presents the Fourier amplitude spectra which are inferred from accelerations time histories normalised by the applied force (F). The exploited accelerations were recorded by the downhole instrument along the NS (n), EW (e) and vertical directions (z). Results for the FBr_2Ts, PBr_W and PBr_S experimental configurations are presented. The figure demonstrates that all three components maximised around the swaying modes (of which frequencies can be found at Table 6.11), when the foundation motion was the most prominent. Also, the horizontal soil motions increased at the torsional frequencies, which agrees to what have been previously observed from strong motion data recorded on the ground surface (Figure 6.47).



(a) FBr_2Ts_mD



(b) PBr_S_mD



(c) PBr_W_mD

Figure 6.48: Fourier spectra inferred from normalised accelerations recorded by the downhole, 3.1, instrument during the (a) FBr_2Ts_mD, (b) PBr_W_mD and (c) PBr_S_mD experiments.

Overall, it has been shown that the impact of SFSI on the structural response is inherently associated with the capacity of the foundation to participate in the motion. Stronger foundation motion increases the importance of soil compliance, soil nonlinearity and interface nonlinearity on the structural response. All three aspects promote SFSI effects. The stiff response of the Fbr_2Ts, FBr_1Ts and PBr_S SSI systems significantly engaged foundation motion. This justifies the observation made in Section 6.3.5 about the more pronounced period elongation estimated for the mentioned systems than the PBr_W one, which exhibited a more flexible response. Period elongation, which is quantified for each experiment in Table 6.12, was more pronounced on swaying than the torsional modes. Also, as shown by the same table, the period elongation of the swaying mode was more significantly impacted by (both soil and interface) nonlinearities. Despite the higher PPV values in the torsional mode (Figure 6.47), the swaying mode exhibited stronger foundation rocking (Figure 6.45c, d), explaining the previous observation. It is thus demonstrated the dominant impact of foundation rocking and SFSI phenomena on the natural periods of the examined SSI systems.

6.3.9 Soil motion attenuation with distance

In the previous sections, soil response was evaluated through data recorded by an instrument close to the foundation (i.e. 0.1). Herein, data from more instruments are compared aiming to investigate the motion attenuation with distance from the foundation. The attenuation is evaluated along the directions North, East and North-East of the structure. As described in Section 5.5.2, soil motion attenuation can be evaluated through data recorded during the experiments where the instrument configuration C was placed. At this configuration the soil instruments were located along the above three directions up to 9m far from the foundation. According to Table 5.10, the experiments during which this configuration was in place are FBr_2Ts$^{(1)}$_mD, PBr_S$^{(13)}$_mD and PBr_W$^{(12)}$_mD. The soil configuration placed during the FBr_1Ts experiments does not allow the study of soil motion attenuation, as only 2 reliable instruments are available per direction.

Table 6.14 presents the instruments and recording directions of which data were used to evaluate soil motion attenuation for the different experimental configurations, along different directions relative to the foundation. To maintain compatible comparisons between experiments, the instruments and the sensor orientations are carefully selected considering the loading direction. Aiming to study the soil motion attenuation along the loading direction, which herein is referred to as in-plane attenuation, the following instruments are selected. For the FBr_2Ts$^{(1)}$_mD and PBr_W$^{(12)}$_mD experiments during which the loading was applied along the NS, the instruments located North and their NS sensor are used. Similarly, the PBr_S$^{(13)}$_mD experiment where the load was applied along the EW direction, the instruments at the East of the foundation and their EW records are opted.

Table 6.14: Instruments and recording direction of which data were used to evaluate soil motion attenuation.

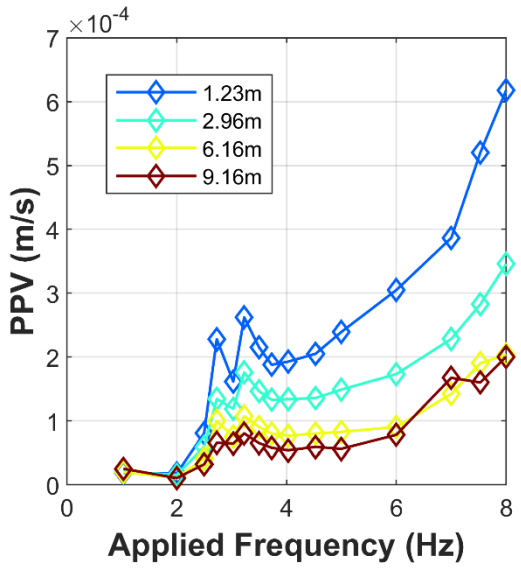
Exp.	Instruments' location relative to the foundation			Rec. direction
	North	East	North-East	
FBr_2Ts	(in-plane) 0.1, 0.2, 0.4, 0.6	0.40, 0.41, 0.42, 0.44	0.50, 0.51, 0.53, 0.55	NS
PBr_S	0.17, 0.1, 0.2, 0.4, 0.6	(in-plane) 0.40, 0.41, 0.42, 0.44	0.50, 0.51, 0.53, 0.55	EW
PBr_W	(in-plane) 0.17, 0.1, 0.2, 0.4, 0.6	0.40, 0.41, 0.42, 0.44	0.50, 0.51, 0.53, 0.55	NS

Figure 6.49 presents PPV recorded at each applied frequency by different instruments located in the loading (in-plane) direction. The figure evaluates the in-plane soil motion recorded during the FBr_2Ts$^{(1)}$_mD (Figure 6.49a), PBr_S$^{(13)}$_mD (Figure 6.49b), and PBr_W$^{(12)}$_mD (Figure 6.49c) experiments. Figures show that the natural frequencies can be identified from the soil motion recorded even relatively far from the foundation, through peaks that indicate response maximisation. These peaks become less pronounced with distance from the foundation, as the motion dissipated with distance. Therefore, the resonance can be missed when interpreting soil data recorded far from the source, with the torsional resonance (torsional frequencies can be found in Table 6.11) be more susceptible to this. It should be noted though that through soil data interpretation is not possible to identify natural frequencies related solely to a structural oscillation (e.g. negligible foundation and soil motion). This is the case of the NS swaying natural frequency of the PBr_W structure, that took place at 1Hz (refer to Table 6.11). During this resonance, as already discussed in Section 6.3.8, the foundation and soil motion were negligible, hence maximisation of soil motion, which indicates resonance, could not be identified from soil data (Figure 6.49c).

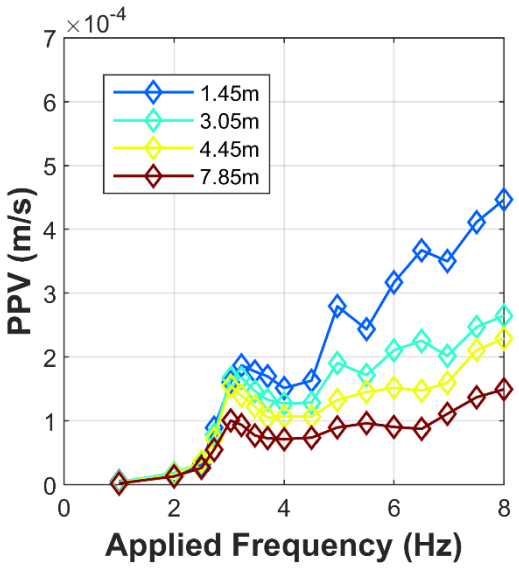
Figure 6.49 also shows that soil motion decayed rapidly within a close distance from the foundation edge, while the rate of attenuation decreased with distance. The soil motion attenuation with distance is better illustrated in Figure 6.50, which plots the PPV with distance, inferred from the FBr_2Ts$^{(1)}$_mD (Figure 6.50a), PBr_S$^{(13)}$_mD (Figure 6.50b), and PBr_W$^{(12)}$_mD (Figure 6.50c) experiments. The inclination of the curves, which indicates the rate of attenuation, is more pronounced close to the foundation, while the curves flatten with increasing distance. This observation implies exponential attenuation of the soil motion with distance, which complies with the observation made from free vibration data (Section 6.2.8). As mentioned in Section 6.2.8, this stems from radiation damping which spreads the energy of emitted waves on the surface of an expanding hemisphere, whose area is a function of the distance squared.

The data shown in Figure 6.50 can also be interpreted to identify the natural frequencies. The maximisation of the response is manifested as an abrupt increase of PPV relative to other frequencies

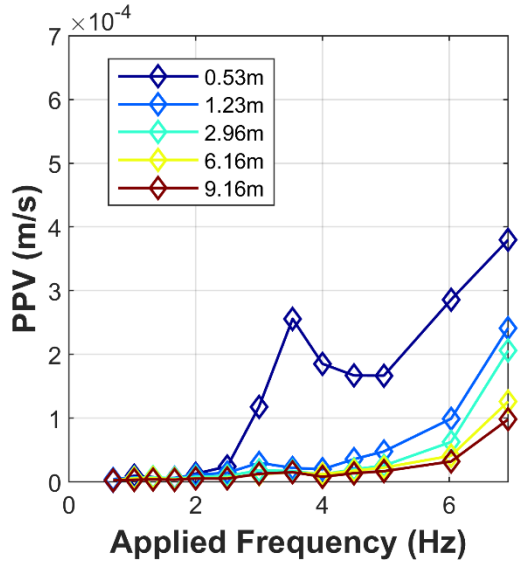
of close values. Although, the abrupt increase is very clear for the swaying resonance, it might not be clear for the torsional one, as the identification of maximised torsional response requires the interpretation of more than one different records, as discussed in Section 6.3.4. The natural frequencies, which are indicated with thicker lines in the Figure 6.50, are verified against the ones observed in Figure 6.49 and the ones observed from the interpretation of structural response (Section 6.3.5).



(a) FBr_2Ts$^{(1)}$_mD

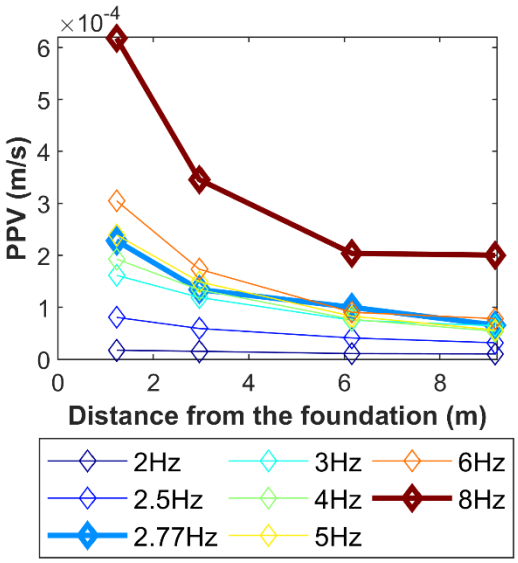


(b) PBr_S$^{(13)}$_mD

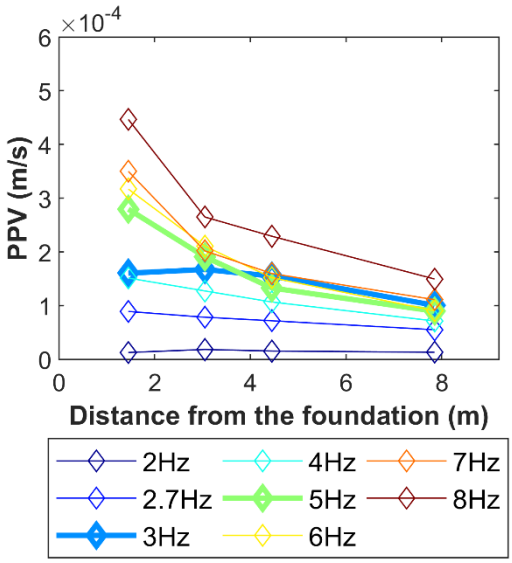


(c) PBr_W$^{(12)}$_mD

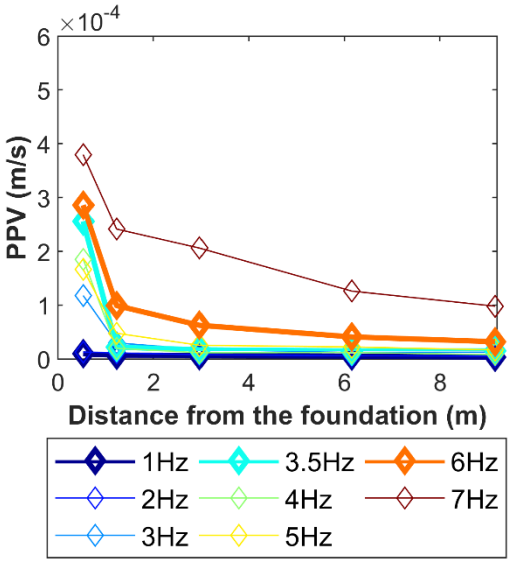
Figure 6.49: Peak particle velocity variation with applied frequency, as processed from data recorded by instruments located at different distance from the foundation edge. Processed data were recorded during the (a) FBr_2Ts$^{(1)}$_mD, (b) PBr_S$^{(13)}$_mD and (c) PBr_W$^{(12)}$_mD experiments. Instruments of which data are used can be found in Table 6.14



(a) FBr_2Ts$^{(1)}$_mD



(b) PBr_S$^{(13)}$_mD



(c) PBr_W$^{(12)}$_mD

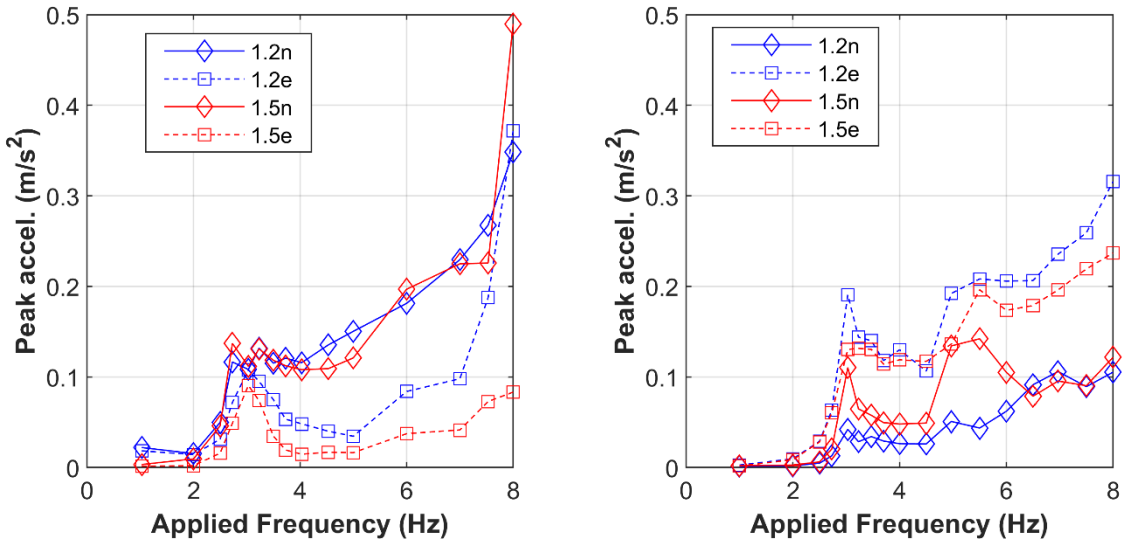
Figure 6.50: Peak particle velocity attenuation with distance from the foundation edge, that corresponds to different applied frequencies. Processed data were recorded during the (a) FBr_2Ts$^{(1)}$_mD, (b) PBr_S$^{(13)}$_mD and (c) PBr_W$^{(12)}$_mD experiments. Instruments of which data are used can be found in Table 6.14.

The comparisons of soil motion attenuation of experiments with different applied frequencies, presented in Figures 6.49 and 6.50, may not be fully consistent, as the foundation mode differed for the compared frequencies. The foundation mode of oscillation determines the motion intensity that it is transferred to the soil and the types of waves of the wavefield. According to Gazetas (1983), foundation rocking produces primarily P-waves, foundation horizontal motion produces both P and S-waves, while SH waves dominate the wavefield during foundation torsion. Also, according to the same author, rocking and torsional oscillations of foundation produce smaller radiation damping than swaying oscillations. This is attributed to the fact that rocking and torsional oscillations induce shallower stress and strain pressure bulbs than the swaying oscillation. Waves emitted from the former rotational oscillations decay rapidly away from the vibrated foundation due to constructive

interference, limiting the extent of the waves. The effect of the constructive interference become more pronounced in layered and inhomogeneous soil where the induced wave field is complex. These soil conditions existed during the real scale experiments that were carried out for the purpose of the present study. The latter in combination with the fact that more than one mode participated in the foundation oscillation made the wave field complex. The existence of a complex wave field and soil layering might have resulted in multiple wave reflections during the experiments, producing Rayleigh waves, additional to the body waves. Rayleigh dissipate much slower through radiation than body waves (i.e. P, SV and SH waves), as the energy of the surface waves is spread over a smaller area. Rayleigh waves propagate near the surface within a cylindrical surface of height approximately one Rayleigh wavelength (λ_R) and radius the distance d from the foundation, hence the energy (E) per unit area is calculated as $E/(2\pi \lambda_R d)$. The latter quantity decreases linearly with distance, in contrast with the body waves that are radiated exponentially with distance, demonstrating that the radiation damping is more effective on body waves (Meek and Wolf, 1993). The following soil motion interpretation aims to verify the validity of the above claims.

Aiming to relate the mode with the attenuation rate, herein, motion attenuation is compared between the swaying and torsional foundation modes, both co-existed with rocking. The soil motions that are exploited for this purpose are associated with the foundation motions that were significantly affected by the examined mode. These foundation motions, recorded either along the NS or EW directions, are the ones that increased abruptly at resonant frequencies, with respect to smaller frequencies. Concurrently, the other motion component recorded by the same instrument should not be significantly affected by resonance. The selected soil motion should be recorded in the same direction by soil instruments located near the edge of the foundation where the selected foundation motion was recorded. The above procedure ensures that the selected soil motions were dominated by the examined foundation mode.

The foundation motions are extracted from interpretation of data shown in Figure 6.51. The figure presents the peak foundation accelerations recorded by the 1.2 and 1.5 instruments along the NS (n) and EW (e) directions during the FBr_2Ts$^{(1)}$_mD and PBr_S$^{(13)}$_mD experiments. With reference to Figure 5.16, the 1.2 instrument is located at the North edge of the foundation, while the 1.5 at the East edge. The selected foundation motions as well as the soil motions, exploited to investigate the impact of foundation mode with the soil motion attenuation, are summarised in Table 6.15.



(a) FBr_2Ts$^{(1)}$_mD (b) PBr_S$^{(13)}$_mD

Figure 6.51: Peak foundation accelerations recorded at each applied frequency during the (a) FBr_2Ts$^{(1)}$_mD and (b) PBr_S$^{(13)}$_mD experiments.

Table 6.15: Foundation soil motions dominated by the identified foundation modes. The presented soil motions were used to relate soil motion attenuation with the swaying and torsional modes.

Exp.	Applied Freq. (Hz)	Mode	Foundation motion dominated by the referred mode	Soil motion dominated by the referred mode
FBr_2Ts	2.77	NS swaying	1.5n	0.40, 0.41, 0.42, 0.44
FBr_2Ts	8	Torsional	1.2n	0.1, 0.2, 0.4, 0.6
PBr_S	3	EW swaying	1.2e	0.1, 0.2, 0.4, 0.6
PBr_S	5	Torsional	1.5e	0.40, 0.41, 0.42, 0.44

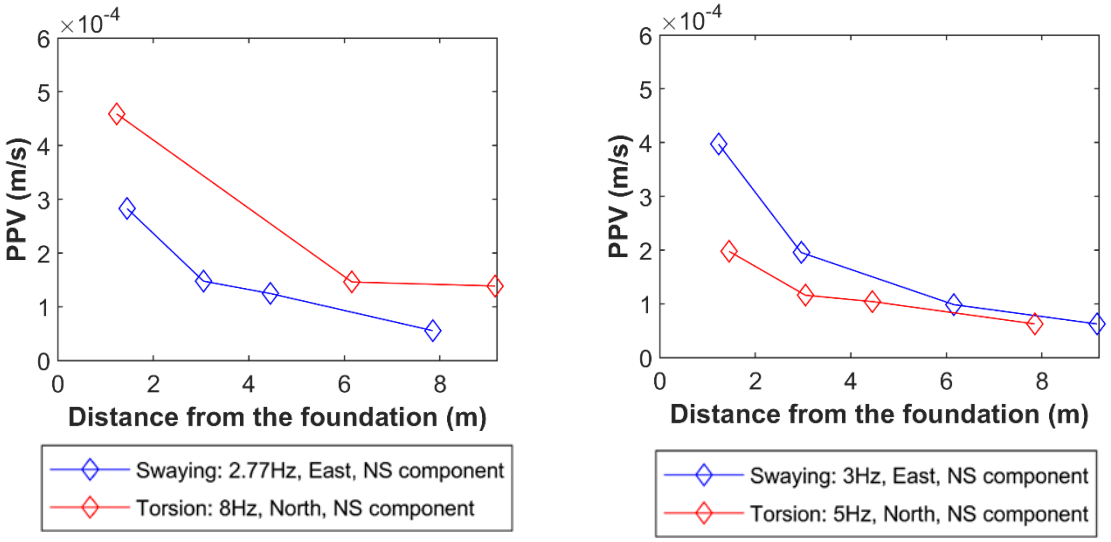
*The notation for foundation motion is with reference to Figure 5.16, while the notation for soil motion is with reference to Figure 5.17.

Exploiting the above data sets, Figure 6.52 compares the soil motion attenuation observed during the swaying (blue lines) and torsional (red lines) foundation modes. Figure 6.52a presents the attenuation of PPV with distance of the FBr_2Ts$^{(1)}$_mD experiment. It is shown that the soil motion was stronger during the torsional than swaying mode, as a result of the stronger foundation motion that took place during the former mode (Figure 6.51a). During the PBr_S$^{(13)}$_mD experiment, the foundation motion was stronger at the swaying mode of the structure (Figure 6.51d), justifying the larger soil motions recorded during the latter mode than the torsional one shown in Figure 6.52b. In both cases, the attenuation was more pronounced on stronger soil and foundation motions, independently of the mode of foundation oscillation. A better comparison of the attenuation motion between the two different modes can be achieved when excluding the effect of the intensity of the source, which is the foundation motion. The soil response normalised to the foundation motion can be expressed through

Transfer Functions (TF). Herein, TF are calculated as the Fourier Amplitude (FA) spectra of the soil motion divided by the spectra of the foundation motion. Aiming to avoid divisions by very small numbers, the normalised response of each soil component is expressed as the ratio between soil to foundation Fourier Amplitudes computed at the applied frequency only, as per Eq. 6.16. The FA observed at the applied frequency is usually the largest value, hence, the ratio can give an indication of the maximum normalised soil response. It is noted that in order to achieve dimensionless TF, the recorded foundation accelerations were converted to velocity units, which is the unit of soil motion, by following the procedure described in Section 6.3.1.

$$(TF)_{f,i} = \frac{(FA)_{f,i}^{soil}}{(FA)_{f,j}^{found.}} \qquad 6.16$$

where, f is the applied frequency, i and j are the instrument number placed on soil and foundation respectively, which are chosen according to Table 6.15.



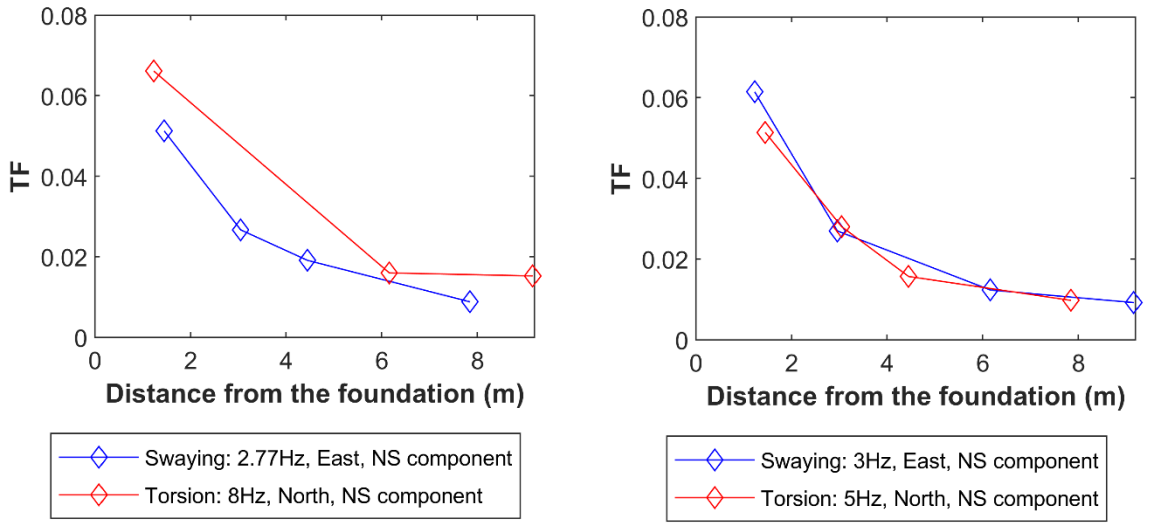
(a) FBr_2Ts$^{(1)}$_mD (b) PBr_S$^{(13)}$_mD

Figure 6.52: Soil motion attenuation with distance from the foundation, computed during swaying (blue lines) and torsional (red lines) modes. The processed data were recorded during the (a) FBr_2Ts$^{(1)}$_mD and (b) PBr_S$^{(13)}$_mD experiments by instruments presented in Table 6.15, the records of which were dominated by the corresponding mode.

As stated in Section 6.3.7, the recorded soil motions indicated almost linear soil response, as the stiffness degradation G_{sec}/G_{max} was estimated to be larger than 0.99 (see Table 6.13 and Figure 6.43). Therefore, by reasonably assuming linear elastic soil response, the attenuation of soil motion normalised by the foundation motion can isolate the impact of radiation damping, as it is the only damping mechanism remained. The comparison of the TF between two modes can give an indication

of the effectiveness of radiation damping during each mode. A TF value larger for one mode than the other, implies that this foundation mode is capable to emit more wave energy in the soil, rendering more efficient radiation damping. When the attenuation of TF is slower with distance, then this can be partly explained through the generation of Rayleigh waves. As mentioned earlier, Rayleigh waves dissipate much slower through radiation than body waves (i.e. P, SV and SH waves), as the energy of the surface waves is spread over a smaller area.

Figure 6.53 compares the transfer functions of the soil to foundation motion computed from data recorded when the applied frequencies coincided with the "swaying" (blue lines) and "torsional" (red lines) resonant frequencies. It is noted that both foundation oscillations co-existed with foundation rocking, while for simplicity they are referred to as "swaying" and "torsional". Figure 6.53b shows that during both FBr_2Ts$^{(1)}$_mD (Figure 6.53a) and PBr_W$^{(13)}$_mD experiments, the amplitudes of the transfer functions of the two modes are very similar, implying similar level of radiation damping. Also, the attenuation rate of the TF is very similar between the two modes, which implies similar wavefield existed in the soil during the compared modes. The experimental data presented is not in agreement with Gazetas (1983), according to which the swaying foundation mode was expected to produce larger radiation damping than the torsional one. Two possible reasons of the disagreement can be the existence of rocking and soil nonlinearity, as explained below. The foundation rocking was the most prominent motion component of the foundation at all applied frequencies. Rocking was even more pronounced during the swaying than torsional motion (Figure 6.45), fact that affected the types of waves existed in the wavefield and radiation damping during the two modes. As mentioned earlier, radiation damping decreases with the increasing rocking motion component of the foundation. Therefore, the rocking foundation component produced smaller radiation damping during the "swaying" mode than "torsional" mode of foundation. This compensated the larger radiation damping produced by the swaying oscillation of the foundation than the torsional one. The latter counteracting effects can explain why the two foundation oscillations produced similar levels of radiation damping. The second possible reason is associated with the assumption made about soil linearity, which might not be applicable for the soil in the vicinity of the foundation, where the induced strains were the largest. The lack of strong motion data in this area does not allow the evaluation of the energy attenuation from the source to the first available instrument. It is likely that the normalised soil motion produced during the "swaying" was larger near the foundation, while it dissipated by the time the propagating waves reached the first instrument. The above consideration though, requires further investigation which is beyond the scope of the current research.

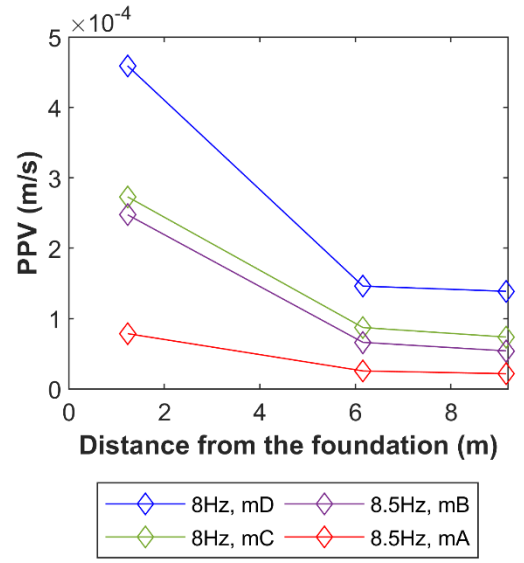


(a) FBr_2Ts$^{(1)}$_mD, Transfer function

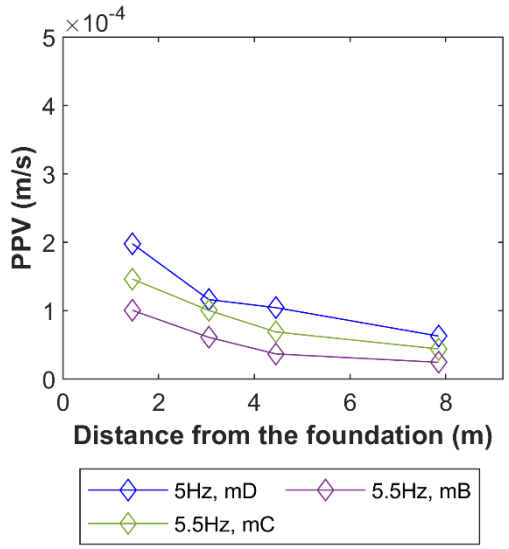
(b) PBr_S$^{(13)}$_mD, Transfer function

Figure 6.53: Transfer functions defined as the ratio of Fourier amplitude inferred from soil motion to the amplitude of foundation motion. The amplitudes correspond to a spectral frequency equal to the applied one. The processed data were recorded during the (a) FBr_2Ts$^{(1)}$_mD and (b) PBr_S$^{(13)}$_mD experiments, by the instruments presented in Table 6.15, the records of which were dominated by one of the examined modes.

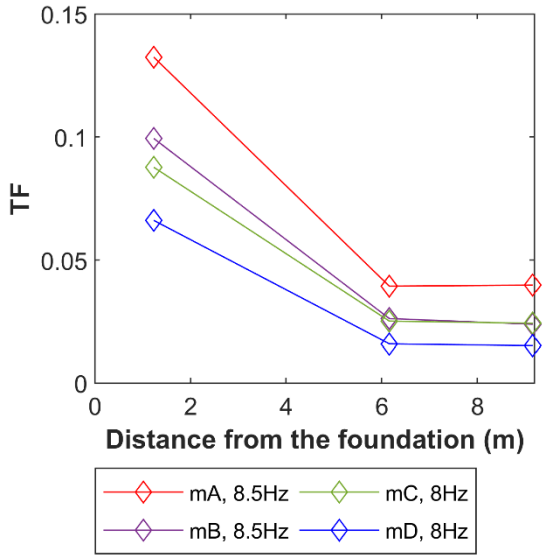
Figure 6.54 investigates the impact of nonlinear phenomena on the attenuation of the soil motion away from the vibrating foundation. The figure illustrates the impact of the excitation magnitude on soil motion attenuation with distance, using velocity units (Figure 6.54a, b) and transfer functions (Figure 6.54c, d). The processed data were recorded during the FBr_2Ts$^{(1)}$_mD and PBr_S$^{(13)}$_mD experiments, when the applied frequency coincided with the torsional resonant one (around 8Hz and 5Hz respectively). Figure 6.54a and b verify that the soil motion, in velocity units, increased with increasing input excitation (i.e. mD produced the largest excitation and mA the smallest). It is interesting to notice that the difference between the soil motion (in velocity values) produced by experiments of different level of excitation decreases with distance. This is a consequence of radiation damping, which, as already mentioned, is more effective (considering the decrease of soil velocities in absolute values) when the soil motion was stronger. The stronger attenuation of the mD experiments can also be justified by the stronger nonlinearity existed. The impact of nonlinearity on the attenuation can be isolated by normalising the soil velocities to the foundation excitation, by the means of transfer functions as described earlier. Figure 6.54c, d present the transfer function inferred from the same experiments and frequencies as the a and b figures. The figures show that the TFs decrease when the excitation level increases (i.e. mD), while the largest difference between the compared TFs is observed at the location of the instrument closest to the foundation. These observations can serve as evidence of the existence of soil nonlinearity, while the latter observation verifies that nonlinearity was more important for the soil near the foundation.



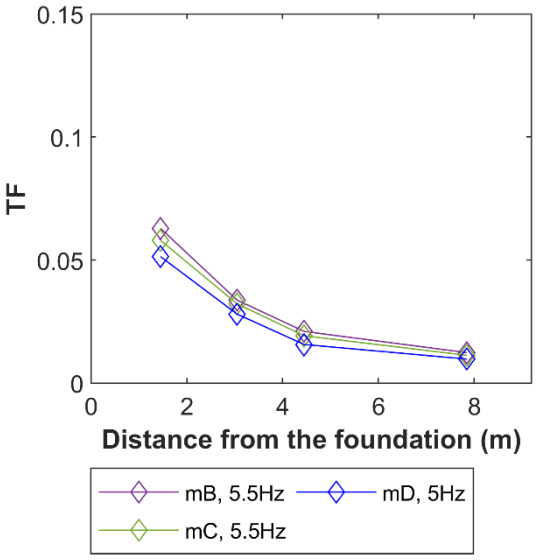
(a) FBr_2Ts$^{(1)}$_mD, Soil motion velocity values



(b) PBr_S$^{(13)}$_mD, Soil motion in velocity values



(c) FBr_2Ts$^{(1)}$_mD, Transfer function



(d) PBr_S$^{(13)}$_mD, Transfer function

Figure 6.54: Impact of the force magnitude on peak particle velocity attenuation with distance from the foundation edge, assessed through (a,b) velocity units and (c,d) Transfer Functions defined as soil to foundation motion. Processed data correspond to the torsional resonant frequencies and were recorded during the (a, c) FBr_2Ts$^{(1)}$ and (b, d) PBr_S$^{(13)}$. Instruments of which data are used can be found in Table 6.14.

6.4 Comparison between free and forced vibration experiments

The structural configurations subjected to both free and forced vibration loading were the fully braced structure with two top slabs, and the partly braced structure. New methods to identify the natural frequencies from free and forced vibration strong motion data were derived. All methods worked effectively as they exploited the advantages of each test. Table 6.16 presents the natural frequencies,

lengthening of the predominant periods in relation to the equivalent fixed-base systems and the corresponding modes, inferred from the free and forced vibration data. The table shows that the interpretation of both free and forced vibration data produced similar values of natural frequencies and lengthening ratios, validating further the methods and experiments. The slightly different natural frequencies inferred from the two types of tests can be attributed to different levels of nonlinearity and different interface conditions as discussed below. Nonlinearities can also explain why the natural frequencies are characterised by a range, instead of a single value. The nonlinearity that took place during the forced vibration experiments was slightly more important, as indicated by the smaller estimated natural frequencies and the wider range, with the exception of the EW swaying mode of the PBr structure.

Table 6.16: Range of natural frequencies and lengthening ratios of the predominant periods for the corresponding modes inferred from strong motion free and forced vibration data.

Experimental config.		**Natural Freq. (Hz)**		**Period lengthening ratio**	
		FBr_2Ts	**PBr**	**FBr_2Ts**	**PBr_W**
NS $F_{swaying}$ (Hz)	Free Vibr.	2.93-3.50	1.05-1.17	2.61-3.12	1.52-1.70
	Forced Vibr.	2.77-3.50	1.00-1.33	2.61-3.30	1.34-1.78
EW $F_{swaying}$ (Hz)	Free Vibr.	2.93-3.50	3.14-3.80	2.61-3.12	2.40-2.91
	Forced Vibr.	2.77-3.50	3.50	2.61-3.30	2.61-3.04
$F_{torsion}$ (Hz)	Free Vibr.	8.60-9.00	5.50-5.80	1.30-1.36	1.45-1.53
	Forced Vibr.	8.50	5.00-6.00	1.37	1.53-1.69

Stronger interface nonlinearity and soil nonlinearity are indicated by larger foundation rotation and soil recorded velocities, respectively. The foundation rotation during the first cycles of the free vibration data (Figure 6.17b) was approximately 5-10 times stronger than the rotation during the steady-state motion of the forced vibration tests (Figure 6.45d). The instrument closest to the foundation edge (1.20m far) recorded surface velocities of the same order of magnitude during the two types of tests (refer to Figure 6.15d and Figure 6.47d), implying similar soil nonlinearity at the area of the instrument. This might not be case in the vicinity of the foundation, where the majority of soil nonlinearity took place, as concluded in Section 6.2.6, but not verified due to the lack of instrumentation in this area. It is believed that the impact of the foundation on the ground surface, at the time that the load removed prior to free vibration, induced high strains in the soil. Therefore, it is likely that the soil nonlinearity was more pronounced during the first cycles of the free vibration, in the vicinity of the foundation, than during forced vibration tests. The larger foundation rotation and soil nonlinearity that took place during the first cycles of the free vibration tests should have resulted to a more flexible response, than the response observed during the forced vibration tests. However, this is not verified by the experimental data, tabulated in Table 6.16, which indicate that the forced

vibration tests produced a slightly more flexible response. This can possibly be attributed to different interface conditions existed during the two types of experiments. After multiple repetitions of forced vibration tests, the foundation rotation compacted the soil below the foundation's edges, forming gaps at the interface between the foundation and the soil. Fewer gaps were in place during the free vibration tests, as foundation sliding, that occurred at the impact of the foundation on the soil, might had produced a better adhesion at the interface. According to the above considerations, more gaps between the foundation and the soil existed during the forced than free vibration tests, decreasing the contact area at the interface. The smaller contact interface area made the SSI system more flexible, while its impact overcame the impact of lower nonlinearities existed during the forced vibration tests. The latter can justify the lower natural frequencies observed during the forced vibration in comparison with the free vibration tests.

6.5 Summary

Soil-Foundation-Structure-Interaction (SFSI), which combine the effect of soil compliance, soil nonlinearity and foundation rocking and sliding, under certain circumstances, can have a significant impact on the structural response. Within this context, this chapter provides insights into SFSI effects as interpreted from strong motion data collected during the free and forced vibration tests carried out. The advantage of this study is the simplicity of the input excitation, comprehensive instrumentation and known ground conditions, which allowed the extraction of useful outcomes. However, it is important to recognize that the interpretation of the SSI response encountered challenges due to uncertainties stemming from the experimental conception and structural construction. These uncertainties, including the structural connections, soil-foundation contact conditions, peculiarities in the shape of the foundation base and instrument calibration, were carefully considered in the system identification procedure.

The Importance of SFSI was evaluated against different structural configurations with different superstructural mass and/or structural stiffness, as well as against excitations of different magnitude and frequency. Evidence of SFSI effects and associated nonlinearities were presented, while the impact of these effects on the natural frequencies and damping of the SSI system are quantified.

The natural frequencies and the corresponding modes were derived by following the proposed methods which are simple and effectively exploited the advantages of free and forced vibration tests. For each test, different methods were employed validating the results of each other. The natural frequencies output from the free and forced vibration data were very similar enhancing further the reliability of the employed methods. Slight differences can be attributed to different levels of

nonlinearity, as well as to possibly different interface conditions existed during the two types of experiments. The natural frequencies of the NS swaying, EW swaying and torsional modes of the SSI system were established. Additionally, the free vibration data were used to calculate the damping of the SSI system, by the means of the Logarithmic Decrement method (Chopra, 2011). Both natural frequencies and damping were found to vary with excitation levels, providing insights about the nonlinear behaviour of the SSI systems. The two properties of the equivalent linear elastic system were established by interpreting part of the motion which was significantly dissipated.

Both forced and free vibration tests showed that stiffer structural response exhibited stronger SFSI effects, a fact that is already well established in the literature (e.g. Amorosi *et al.*, 2017). It was shown that the stiff structural oscillations were dominated by foundation rotation, while the flexural deformability of the structures was small. The susceptibility of the foundation to rotate promoted further SFSI effects. Stronger SFSI effects were evidenced by stronger lengthening of natural periods relative to an equivalent fixed-base structure, larger damping, stronger foundation motion and stronger soil motion. Period lengthening was more pronounced on the swaying modes of the SSI systems than the torsional one, which is in agreement with the observation made by Pitilakis *et al.* (2014).

This chapter also demonstrates that the SFSI effects accentuated with increasing magnitude of the applied force. The latter observation is attributed to systems' nonlinearities, the impact of which was quantified through period elongation. The natural frequencies of the swaying modes were strongly affected by nonlinearities, as a 20% deviation was observed between frequencies inferred from motions of the lowest and highest intensity. Conversely, the torsional resonant frequencies were marginally affected by nonlinearities, as the smallest and largest computed frequencies differ by 5% only. Additional evidence of nonlinearity was the variation of natural frequencies and damping developed during free vibration experiments of different pull-out forces. As the excitation force increased, the free vibration experiments exhibited smaller natural periods and larger damping at the initial cycles. However, as the motion was dissipated, after a number of cycles, the natural period and damping values of the different experiments converged to a common value each. The converged natural period and damping corresponded to those properties of a linear elastic SSI system.

Nonlinear phenomena can be associated with different sources, with the most prominent during the experiments being the geometric nonlinearity at the soil-foundation interface and soil nonlinearity. Both nonlinearities increased with applied force and became more pronounced for higher structural to foundation stiffness ratio. The interface nonlinearity, which was manifested through foundation uplift, decreased the contact area between the foundation and the adjacent soil, which in-return made the SSI system more flexible. Soil nonlinearity increased further the flexibility of the system as a result

of stiffness degradation of soil, which is always accompanied with damping development. It was indirectly inferred from both free and forced vibration data that soil nonlinearity was dominated by the nonlinearity developed in the soil in the vicinity of the foundation.

The soil motion, which was recorded by instruments at multiple locations on the soil surface, decayed exponentially with distance from the foundation. This is a consequence of radiation damping, which dissipates the energy of propagated waves proportionally to the square of distance from the source (Meek and Wolf, 1993). Radiation damping is more pronounced for heavier loaded structures, as the vibration of these structures transfers more energy to the soil, resulting in a greater energy loss due to wave spreading. This was verified by comparing soil motions, at various locations, recorded during experiments with different magnitude of applied force. This comparison has shown that stronger initial excitation resulted in stronger soil motion and attenuation, in absolute velocity units, hence more energy was lost through wave spreading. However, when the soil motion is normalised by the foundation motion, so that the compared soil motion corresponds to the same “input”, it is observed that experiments with stronger foundation motion produced weaker normalised response. This is additional evidence of the nonlinear behaviour of the examined SSI systems. Finally, an attempted was made to distinguish between the significance of radiation damping during swaying and torsional foundation oscillations, which were co-existent with foundation rocking. Although it was expected that swaying motion would produce more radiation damping (Gazetas, 1983), it was found that the two modes produced similar levels of damping. This can possibly imply that the rocking foundation component controlled the development of radiation damping during the experiments.

Chapter 7

Soil-Structure-Interaction Numerical Model Calibration

7.1 Introduction

Finite element analyses (FEA) are the most rigorous approach to consider dynamic Soil-Structure-Interaction (SSI) phenomena. FEA, which is commonly referred to as direct method, simulates SSI problems in a single step in the time domain, considering the continuing interaction between the structure and the soil. Also, it allows rigorous soil modelling, considering nonlinearity, soil plasticity, pore water pressure generation, soil stiffness dependence on mean effective stress, appropriate wave propagation and other. These are the main advantages over other methods that exist in the literature, such as the Winkler model, lumped model and the substructure method, which are discussed in Chapter 2. The disadvantage of FEA is the high computational time, while the appropriate selection of input parameters is one of the main challenges. The uncertainty regarding the input parameters is mitigated when a FE model is validated against real scale experiments, which allow a rigorous calibration of the structural, soil and soil-foundation interface properties. However, such numerical SSI studies are scarce in the literature, due to the cost of real scale experiments as well as the lack of a rigorous numerical procedure for SSI related problems.

Pitilakis *et al.* (2015) simulated experiments very similar to the forced vibration tests presented in Chapter 5. However, their model was based on simplified assumptions such as linear soil and full bond between the foundation and the adjacent soil. Chao (1996), Borja *et al.* (1999b) and Amorosi *et al.* (2017) developed three-dimensional (3D) FE models to assess SSI phenomena observed during seismic events at the Large-Scale Seismic Test (LSST) site located in Lotung, Taiwan. The site consisted of a 1/4-scale nuclear plant containment structure and a number of structural and soil instruments, as described in Section 3.3.1 and depicted in Figure 3.2. As the figure shows, the experimental set-up consisted, among other instruments, of two downhole arrays of triaxial accelerometers which reached a depth of 47m. The first array (DHA) was located 3m far from the structure's edge, while the second

array (DHB) was located 49m away. The records of the DHA array were affected by the existence of the structure, while the DHB array represented free-field conditions. Chao (1996) and Borja *et al.* (1999b) simulated both the structure and the soil in three dimensions, which were assumed to behave elastically and elastoplastically, respectively. For the soil, a total stress-based bounding surface plasticity model proposed by Borja and Amies (1994) was adopted which was calibrated based on the free-field downhole data, as described in Borja *et al.* (1999a). By comparing numerical data computed at different depths at the positions of the DHA and DHB downhole stations, Borja *et al.* (1999b) showed that SSI effects decreased significantly the horizontal peak accelerations near the ground surface only. Conversely, SSI effects had a negligible impact on the horizontal motion of deeper layers (i.e. deeper than 11m), and the vertical motion remained unaffected at any depth. A limitation of these studies is the incapability of the adopted soil constitutive model to simulate accurately the soil behaviour at small strains. Additional limitation is the fact that the nonlinear model was validated against one event only, raising doubts about its validity on other events. Finally, the above two studies concentrated more on the soil response, while they did not make use of the structural recordings, implying that the numerical model might not be fully validated against the whole SSI system.

Amorosi *et al.* (2017) developed a 3D SSI model to simulate the same experiments, addressing some of the above limitations of the aforementioned studies. They modelled the structure as a linear elastic material, while they employed an isotropic hardening elastoplastic model for the soil. This model is the Hardening soil model (Schanz *et al.*, 1999), extended by Benz (2007) to predict nonlinear behaviour of soil even at very small strains, named as the HSS model. Within this context, the HSS model makes use of a modified version of Masing's rules (Masing, 1926) coupled to a hardening plasticity model and takes into account the soil non-linearity through the stiffness degradation and damping ratio curves. The tangential shear stiffness is a function of the deviatoric strain history, which is achieved by employing a scalar strain history-dependent variable that accounts for the incremental strain variations. The parameters associated with soil stiffness at very low strains were selected according to the shear wave velocity profile of the site, based on cross-hole tests. Some of the model's parameters were calibrated to reproduce the same normalised stiffness degradation and damping ratio curves used by Chao (1996) and Borja *et al.* (1999b), mentioned above. The HSS model underestimates the damping at very small strains, hence, the authors added Rayleigh damping, the value of which differed between the different events examined. The 3D model was calibrated against a single event and was validated against three events of different motion intensities and frequency contents. This model validation enhances the reliability Amorosi *et al.* (2017) study compared to the studies conducted by Chao (1996) and Borja *et al.* (1999b), who did not validate their models.

In all of the above studies, the nonlinear model was calibrated against free-field site response data, recorded by the DHB downhole array of accelerometers, while the stiffness degradation and damping ratio curves reflected to relatively thick layers of soil. A possible limitation of these studies is that they did not refine the calibration of the soil in the vicinity of the foundation. According to the author's experience, SSI effects are primarily dominated by the soil conditions in the vicinity of the structure, while deeper layers are not as important. Also, the overburden stress due to the existence of the structure changes the elastic stiffness of the soil close to the structure, relative to the free-field conditions (Tileylioglu *et al.*, 2011; NIST, 2012; Star *et al.*, 2015; Taborda *et al.*, 2016). The soil stiffness dependence on the mean effective stress was not considered by the abovementioned studies.

The studies of Chao (1996), Borja *et al.* (1999b) and Amorosi *et al.* (2017) considered as input motions acceleration time histories recorded by a downhole instrument during seismic events. Although this instrument was located in compliant soil, the numerical models assumed rigid bedrock at the level where the input motion was applied; a fact that created an additional uncertainty. The calibration of SSI numerical models, that use seismic strong motion data as input excitation, can be very challenging due to the continuous interaction of kinematic and inertial mechanisms. The uncertainty regarding the input and the complexity of the calibration are mitigated when the input motion is applied on the structure, which isolates the inertial interaction effects and simplifies the response. Experiments with dynamic loads imposed on the structure facilitate the interpretation of the response and hence the calibration of the model.

A final limitation of Chao (1996), Borja *et al.* (1999b) and Amorosi *et al.* (2017) studies is the lack of an appropriate model for the interface between the soil and the foundation. They all assumed full adhesion and bonding between the foundation and the adjacent soil. Such an assumption for the soil-foundation interface model does not allow relative displacements between the two, as well as it promotes unreasonably high effective stresses at the interface. In the literature, there are various interface models, that can be incorporated in SSI FE models where both the structure and the soil are modelled. Herrmann (1979) proposed the use of "bond elements" that can be used to link the two materials in contact. Bond elements are essentially normal and shear springs, which can have nonlinear stiffness or can be coupled with an elastoplastic Mohr-Coulomb failure criterion to allow sliding and separation of the two linked materials. These elements cannot predict the constitutive behaviour of the interface, as stresses and strains cannot be evaluated.

The constitutive behaviour of the interface can be investigated when finite elements are placed between the two materials. An approach is to use thin conventional finite elements of which the behaviour is based on standard constitutive laws (Pande and Sharma, 1979; Griffiths, 1985). As Griffiths (1985) mentions though, when the aspect ratio of these elements is very large, convergence

issues may arise, while the elements are not appropriate when sliding between the two materials is prominent. With respect to the latter, interface or joint elements of either finite or zero thickness, the formulation of which is different to the conventional elements, have been widely used for SSI related problems. Many authors in the past (e.g. Ghaboussi, Wilson and Isenberg, 1973; Desai *et al.*, 1984; Zaman, Desai and Drumm, 1984) have proposed different formulations for finite-thickness interface elements. The thickness is one of the parameters that should be determined, as it affects the shear stiffness, while in dynamic analyses, it will also affect the mass and damping of the element (Desai *et al.*, 1984; Zaman *et al.*, 1984). A choice of very small thickness may lead to computational issues, whereas when the thickness is of a similar order of magnitude to the other dimension of the interface element, the element will behave as a conventional element. The uncertainty regarding the thickness of the interface element vanishes by adopting zero-thickness interface or joint elements (e.g. Goodman, Taylor and Brekke, 1968; Day and Potts, 1994).

The elastic properties of the interface elements are the normal (K_n) and shear (K_s) stiffnesses, which control the elastic relative displacements between two adjacent materials. Experimental data for K_n and K_s are usually not available, hence many studies considered arbitrary high values for both properties (e.g. Gazetas *et al.*, 2013; Gazetas, 2015). High values of the above properties essentially restrict elastic relative displacements between the two materials. For the case of a shallow foundation, that is prone to uplift or slide, relative displacements between the foundation and the soil can take place, which results in plastic displacements in numerical terms. Interface model can achieve plastic displacements by using an appropriate elastoplastic model for the interface elements, as it has been proposed by other studies (e.g. Gazetas *et al.*, 2013; Gazetas, 2015). Although some numerical studies (e.g. Gazetas *et al.*, 2013; Gazetas, 2015) developed FE models with a foundation that was allowed to detach and slide relative to the soil beneath, their main focus was not on the interface model. They did not evaluate the dependency of the SSI response on the input parameters of the selected interface constitutive model, as well as they did not investigate the impact of interface imperfections.

This chapter proposes a rigorous calibration procedure of 3D numerical models which simulate the real-scale experiments presented in Chapter 5. The experiments consisted of free and forced vibration tests on the EUROPROTEAS structure, during which a comprehensive instrumentation recorded both the structural and the soil response. EUROPROTEAS is a frame structure which is designed to have reconfigurable bracing system and superstructural mass. Three structural configurations of different structural stiffness and/or mass were subjected to various loads, aiming to assess the impact of the above parameters on the structural and soil response, as well as on the soil-foundation interface response. The structure rests on the ground surface at the Mygdonian Valley in Northern Greece. The geotechnical and geological properties of this site have been well documented by previous studies

(Pitilakis *et al.*, 1999, 2014, 2018; Raptakis *et al.*, 2000), as described in Chapter 4. The same chapter presents the calibration of the nonlinear constitutive model of soil layers from the ground surface to the bedrock (196m depth). In this chapter, this calibration is better refined for the soil in the vicinity of the foundation, which is crucial for the calibration of the overall SSI numerical model.

The calibration procedure makes use of both free and forced vibration tests that were carried out, by exploiting the advantages of each experiment. It exploits strong motion data recorded at both the structure and the soil, aiming to develop a numerical model that can replicate the structural, foundation and soil response. During the experiments, a wide range of frequencies and magnitudes were applied on the structure, allowing the calibration of the model over a relatively wide range of induced strains. Data recorded from experiments of various excitation intensities were used to calibrate the properties of the nonlinear model employed for the soil, focusing more on the soil in the vicinity of the foundation. This study, also, places particular emphasis on the modelling of the soil-foundation interface. This is one of the major challenges of modelling dynamic SSI problems of which the foundation is prone to slide or rotate relative to the adjacent soil. A novel approach to model potential interface imperfections is proposed, that takes into account areas where the foundation and the soil are not in contact. Results from FEA of different non-contact area configurations are compared, demonstrating their impact on the structural and soil response. The interface stress conditions prior to the application of the dynamic loading are also a matter of discussion in the chapter.

The presented numerical analyses were undertaken with the Imperial College Finite Element Program (ICFEP) (Potts and Zdravković, 1999), which includes state-of-the-art features for the modelling of geotechnical problems. Details of the dynamic finite element formulation, appropriate boundary conditions and time integration schemes implemented in ICFEP can be found in Kontoe (2006). The calibrated model produces results which are in a very good agreement with strong motion data. The results provide evidence of strong dynamic SSI effects, in terms of period elongation and increased damping of the SSI system. They highlight the importance of nonlinear phenomena and the need of prescribing the soil in the vicinity of the foundation with an appropriate nonlinear constitutive law. This chapter also demonstrates the significant impact of interface imperfections (gaps) and foundation rocking on the predicted response. It emphasises the important role, in SSI problems, of the distribution of static stresses present at the interface prior to the application of the excitation force. The stress distribution was found to be particularly important for the experiments which produced pronounced foundation detachment and re-attachment to the soil, during structural oscillation.

7.2 Modelled Experiments

A large number of the experiments were modelled, which can be found in Appendix F. For the forced vibration tests, one analysis was carried out per experiment of constant applied frequency. The duration of each analysis was between 10-15 full cycles ensuring that steady state conditions were reached. Similarly, each free vibration numerical analysis modelled an experiment of a certain pull-out force, computing the SSI response between the time of the pull-out force removal until a time instant for which the structural motion had decayed more than 90%.

Experiments that have been predominantly used for the calibration of the numerical model were carefully selected. The forced and free vibration experiments for which numerical models were developed and used in the calibration process, are presented in Table 7.1 and Table 7.2, respectively. The selection of the forced vibration tests was based on three criteria. The first one was the selection of reliable experiments according to the data reliability investigation presented in Section 5.8. Secondly, the applied frequency of the selected forced vibration experiments should be far from any natural frequency, as at resonance the experimental results are very difficult to be predicted. Finally, the structural response of the selected experiments should have exhibited weak motion in the direction perpendicular to the loading one (out-of-plane direction), relative to the motion recorded in the loading direction (in-plane). Experiments which produced a motion predominantly along one of the two main directions, allowed the use of 3D models that simulate half the geometry of the physical problem. The use of 3D half-geometry models significantly decreases the computational time in comparison with a full geometry 3D model.

Based on the above three criteria, one forced vibration experiment per structural configuration was selected, as shown in Table 7.1. Figure 7.1 demonstrates that the selected experiments, indeed, exhibited weak out-of-plane motion in comparison with the in-plane one. It is noted that the forced vibration experiment during which the load was applied along the strong axis of the structure (PBr_S), is not modelled in the present thesis. Also, the calibration procedure exploited data from free vibration tests of the two structural configurations (FBr_2Ts and PBr_W), as shown in Table 7.2. It makes use of the experiments during which the smallest and largest applied forces were applied on the structures. This allowed the calibration of the model over the entire range of strains that were induced in the soil during the experiments. Also, the different examined configurations triggered different levels of structural, foundation and soil motions, allowing a better and more systematic calibration of the SSI system, as it is subsequently discussed in this chapter. Figure 7.2 compares the in and out-of-plane top slab motions recorded during the free vibration tests of which data were used in the calibration process. It is evident that the requirement of weak out-of-plane motion is mostly met. When the

motion dissipated significantly though, the in and out-of-plane motions became of a similar amplitude making the use of the half geometry model not appropriate. However, at the time instant when the two motions become of similar amplitude, the in-plane motion has already dissipated by more than 70%, making the consequences rising from the limitation of the half geometry model not important.

The free vibration numerical analyses were particularly important for investigating the agreement between the experimentally and numerically computed predominant frequencies of the SSI systems. This investigation was more difficult to be conducted from the forced vibration numerical analyses, as explained later in this chapter. This is the reason why the calibration process included free vibration numerical analyses on the fully braced 1-top slab structure, although these experiments were not physically carried out (see Table 7.2).

Table 7.1: Forced vibration experiments for which numerical models were used in the calibration process.

Exp. Name	Bracing system	Top slab masses No.	Vibr. mass	Freq. (Hz)
FBr_2Ts_mD_5Hz	Fully braced	2	mD	5
FBr_1Ts_mC_5Hz	Fully braced	1	mC	5
PBr_W_mD_2Hz	Partly braced	2	mD	2

Table 7.2: Free vibration experiments for which numerical models were used in the calibration process.

Exp. Name	Bracing system	Top slab masses No.	Force (kN)
FBr_2Ts_2.94kN	Fully braced	2	2.94
FBr_2Ts_15.70kN	Fully braced	2	15.7
FBr_1Ts_15.70kN*	Fully braced	1	15.7
PBr_W_2.94kN	Partly braced	2	2.03
PBr_W_13.90kN	Partly braced	2	13.9

*Numerical analyses for which the physical experiment was not available.

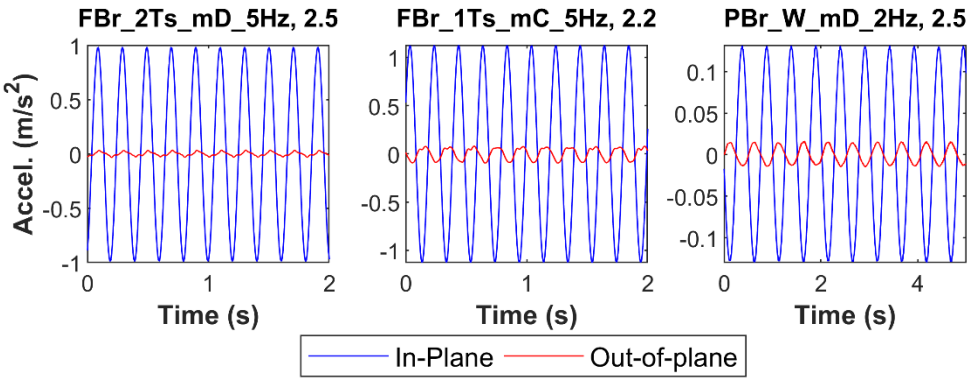


Figure 7.1: Comparison of top slab in-plane and out-of-plane motions recorded during the forced vibration tests which were exploited in the calibration process.

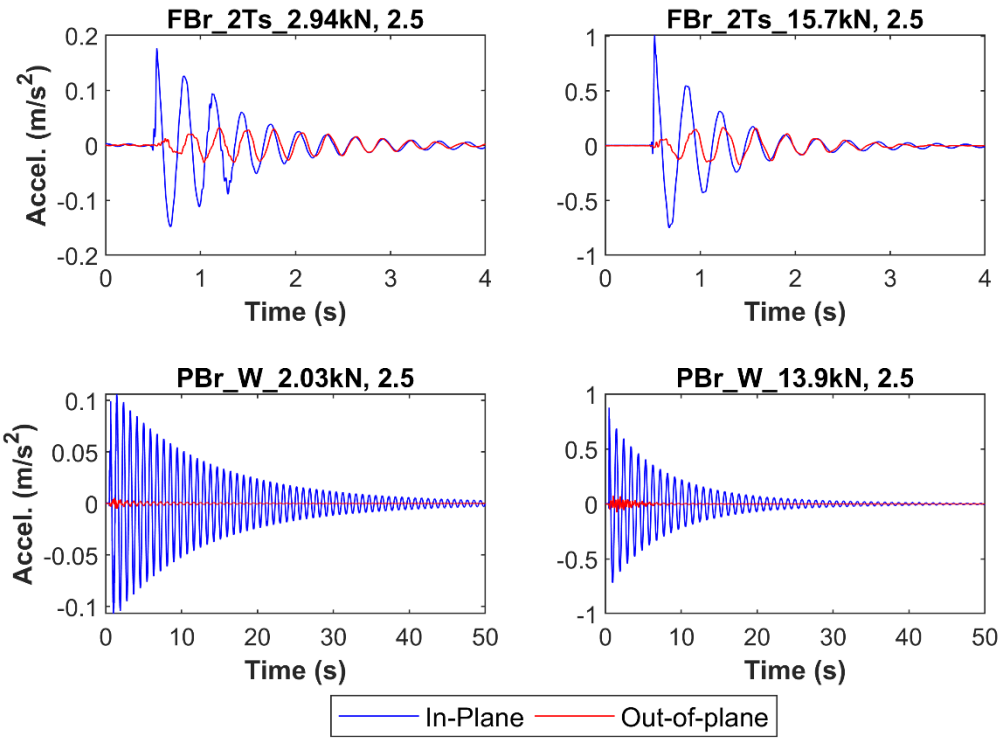


Figure 7.2: Comparison of the top slab in-plane and out-of-plane motions recorded during the free vibration tests which were exploited in the calibration process.

7.3 Numerical challenges

Simulations of SSI numerical problems pose many challenges which further increase when the simulations aim to reproduce experimental data. A very common challenge in earthquake geotechnical engineering is the computational time, which is normally long, as a consequence of the demand of modelling large soil domains. This demand increases more when the input excitation is applied far from the structure of interest, such as the case when the input motion is a seismic motion applied on the bedrock. Aiming to decrease the dimensions of the soil domain, Bielak et al. (2003) and Yoshimura et al. (2003) developed the *Domain Reduction Method* (DRM), which was extended by Kontoe *et al.* (2008) to deal with dynamic couple consolidation problems. The DRM is effective in reducing the soil domain when the input excitation is far from the examined structure. However, during the presented experiments, the input excitation was applied on the structure, hence the DRM is not applicable. Alternatively, the soil domain can be truncated by imposing dashpots at the boundaries to ensure a realistic wave propagation over the frequency range of interest. Kontoe *et al.* (2009) showed that when dashpots are close to the excitation, the structural and soil response can be underestimated due to overdamping. It is therefore imperative to select appropriate soil domain dimensions and boundary conditions in order to ensure that the produced boundary effects are

negligible and the computational time is reasonable. More details about the soil domain model can be found in Section 7.5.1.

The second challenge of the numerical simulation is the calibration of linear and nonlinear properties of soil. Although the soil properties are documented by previous studies (see Chapter 4), a refinement of the properties of the very shallow soil layer (e.g. top 0.80m) is likely to be needed. Herein, it is assumed that the elastic properties of all soil layers are those concluded from site response analyses presented in Chapter 4. The same applies for the nonlinear properties of all layers, with the exception of the very shallow soil layer. The nonlinear soil constitutive model of the very shallow soil layer is further calibrated, as this layer controls the stiffness and the dissipative capacity of the entire SSI system.

When numerical SSI models aim to replicate experimental results, the existence of experimental imperfections adds a significant challenge to the calibration of the model. Geometric imperfections arose from the non-perfectly symmetric structure, as well as from the input force whose direction did not perfectly match with one of the structure's axes of symmetry. Geometric imperfections played a significant role in the SSI response as shown in Chapter 6, as evidenced by the recorded out-of-plane and torsional SSI response. Although imperfections are impossible to be modelled rigorously, at the calibration stage, the impact of geometric imperfections is mitigated by simulating experiments during which the in-plane motion dominated the response. These experiments, which have already been mentioned in Section 7.2, were insensitive to imperfections. Modelling these experiments requires an input excitation to be appropriately prescribed, which is one more challenge for model calibration. As already discussed in Sections 5.8.1 and 5.8.2, during the forced vibration tests, the magnitude and the frequency content of the imposed vibratory load were not measured in-situ, while the loading direction was not ensured. An approach that copes with the uncertainties related to the input excitation of forced vibration simulations is described in Section 7.5.3.

An additional challenge of this study is the simulation of the column-slab connections, which cannot be considered as full-moment while their moment capacity remains unknown, as evidenced in Section 5.2.4. It is crucial to calibrate this property, as it affects the dynamic characteristics of the equivalent fixed-base structure and hence the SSI response.

The numerical SSI response is also significantly affected by the soil-foundation interface model, which is one the main challenges of this study. The interface model should allow foundation uplift and sliding, while it should also facilitate the simulation of interface imperfections. The interface imperfections discussed herein are non-contact areas (gaps) between the foundation and the soil beneath, that existed when the structure was at rest. Such areas were visually observed during the experiments

below the foundation edge, while their spatial distribution in other areas is unknown. The static stresses at the soil-foundation interface are also unknown. Theoretically, the static stresses below a rigid foundation that is in perfect adhesion with the soil are concentrated below the foundation edges, while they decrease closer to the centre. The stress concentration is more pronounced when linear elastic soil is assumed, whereas it is alleviated by soil nonlinearity which results to a smoother stress distribution. However, the above postulations might had not taken place during the experiments, irrespective of the high rigidity of the foundation relative to the soil stiffness. It is likely that the foundation developed a base shape similar to a parabola, resulting from the foundation casting procedure described in Section 5.2.4. This foundation shape might have led to a more uniform stress distribution at the interface than the one described above. The static interface stress distribution is one more parameter that is investigated in this Chapter.

Finally, the large number of parameters that required calibration, considering that some parameters may impact the response in the same way, poses an additional challenge to the study. To ensure accurate calibration, it is crucial to isolate the effect of each parameter to be calibrated. Failure to do so would result in biased calibration. The devised calibration procedure, described in Section 7.8, aims to tackle the latter challenge, where possible.

7.4 Static and dynamic numerical analyses

Prior to the dynamic analyses, a Static Self-Weight (StSW) analysis was carried out, wherein the structure was constructed on the soil surface within one increment. The aim of this analysis is to create the static conditions in the structure and in the soil after construction. For the case of free vibration numerical simulations, the StSW analysis was followed by a second static analysis step, during which the pull-out force was applied on the structure within 25 increments (StP). Subsequently, dynamic analyses were undertaken, where the force was removed instantaneously in a single increment, while beyond this increment the numerical model computed the free oscillation of the SSI system. For the simulation of forced vibration experiments, dynamic analyses were carried out after the StSW analysis. These analyses applied the vibratory load incrementally at the top of the slab, while computing the SSI response.

For the static (StSW and StP) analyses drained conditions were assumed, implying no change in pore water pressure in the ground (i.e. instantaneous drainage) due to the building self-weight and the pull-out stage. In the subsequent dynamic analyses, the soil below the ground water table was assumed to behave in an undrained manner.

7.5 3D half-geometry model

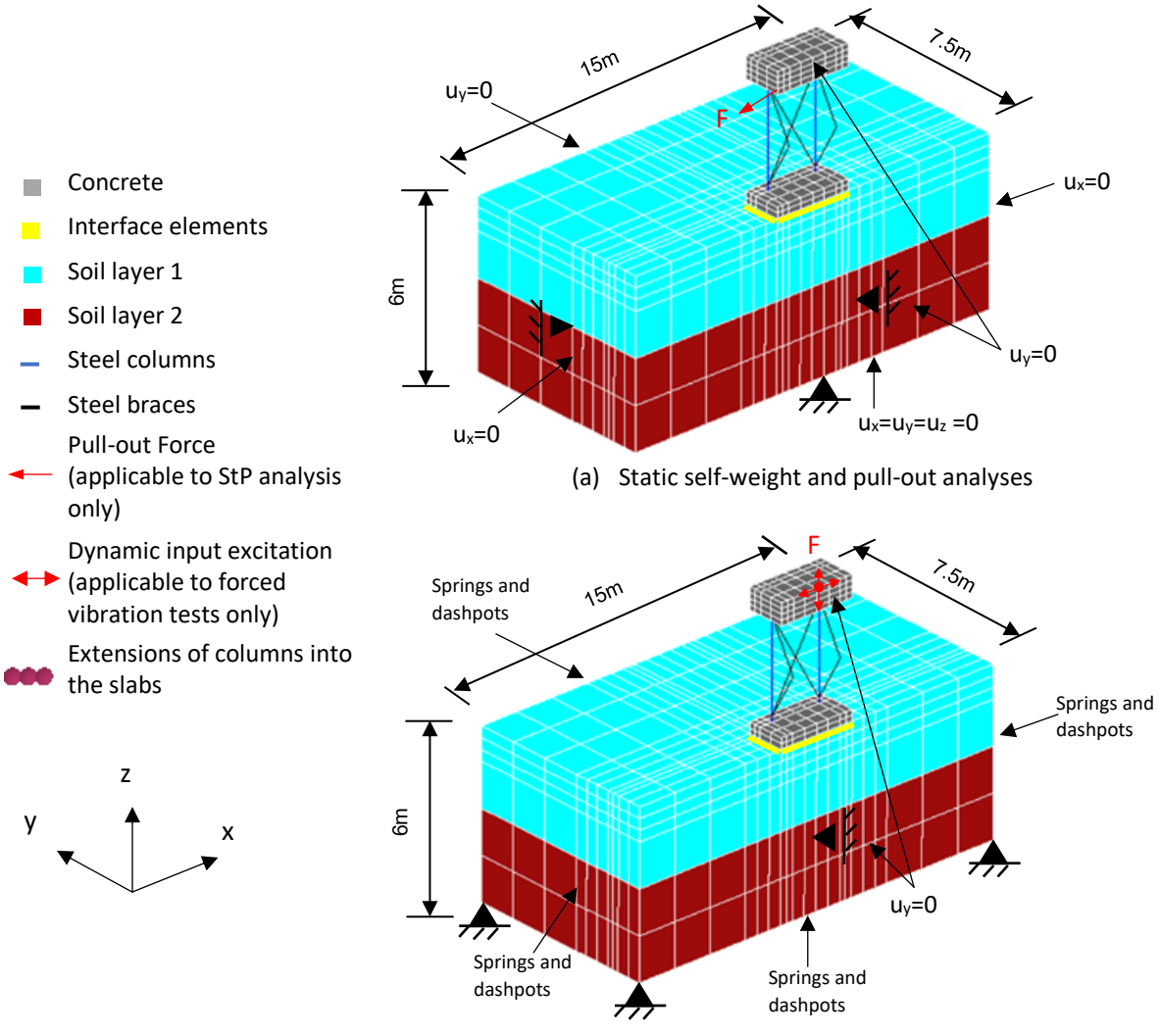
The calibration of the numerical model was based on the development of 3D numerical models which simulate only half of the geometry of the real conditions, exploiting the symmetry of the problem. The latter assumption neglects the geometric imperfections mentioned earlier. To ensure the applicability of the 3D half-geometry numerical model, the modelled experiments exhibited weak out-of-plane motion relative to the in-plane one, as it has already been discussed in Section 7.2.

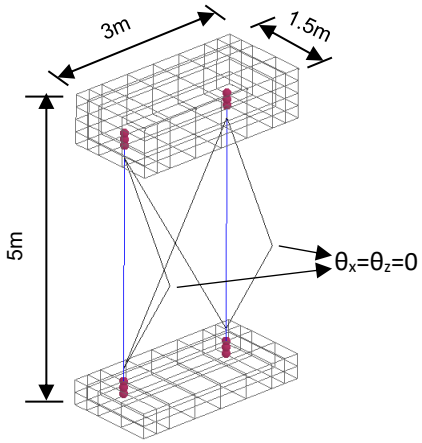
7.5.1 Problem geometry and boundary conditions

The finite element mesh, dimensions and some boundary conditions used in the numerical model calibration process are depicted in Figure 7.3. The simulated soil domain has dimensions 15m x 7.5m x 6m, which were found to produce negligible boundary effects on the structural response and tolerable effects on the soil response. A sensitivity analysis regarding the adequacy of the soil domain dimensions is presented in Appendix F. Also, as Figure 6.20 and Figure 6.50 show, the experimental soil motion decreased by approximately 70% between the instrument closest to the structure (1.5m) and the instrument placed 6m from the foundation edge. It is anticipated that the soil motion recorded on the soil surface at 6m from the foundation edge was dissipated by more than 90% in comparison with the motion in vicinity of the foundation, where instrumentation was not available. The latter presumption is based on the conclusion made in Chapter 6, according to which the largest soil dissipation took place in the vicinity of the foundation. Therefore, the lateral boundaries, which are placed 6m from the foundation edge, are expected to have weak effects on the SSI response. The adequacy of a small soil domain is facilitated by the input excitation. In fact, dynamic SSI analyses, where the input excitation is applied on structures, require much smaller mesh than analyses which use seismic data as input.

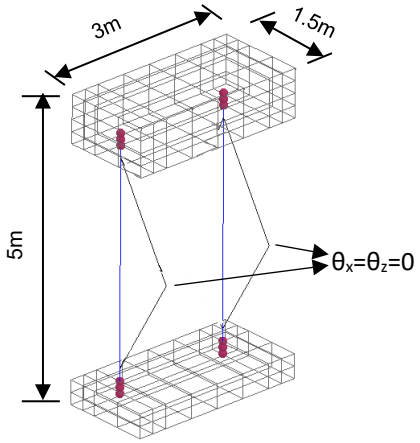
The water table is placed at 0.80m depth reflecting the in-situ water table depth (Section 5.3.3). Hydrostatic pore water pressures were prescribed below the water table, while above the water table, hydrostatic suction was prescribed, to ensure that non-zero effective stresses and hence a non-zero soil stiffness are simulated at the soil surface. The simulated soil domain is modelled with 20-noded brick elements and is divided into two layers, according to the soil stratigraphy of the site presented in Figure 4.8. The dimensions of the brick elements are decided so that the frequencies in the range of interest can be captured by the numerical model. Kuhlemeyer and Lysmer (1973) suggested that the dimension of 8-noded isoparametric elements should be four to five times smaller than the minimum wavelength. The present study implements this rule on the adopted brick elements.

Given that only half of the geometry of the experiments is modelled, the displacements perpendicular to the plane of symmetry, u_y according to the coordinate system shown in Figure 7.3, are restricted in all analyses. During both StSW and StP static analyses, the three displacement components of all nodes at the bottom boundary of the soil domain were constrained. The nodes that lie on the lateral boundaries were restricted in the direction perpendicular to the plane of each boundary, as shown in Figure 7.3a. The conditions on the boundary nodes change for the dynamic analyses, with the exception of the conditions of the nodes at the plane of symmetry which remain unchanged (Figure 7.3b). The corner nodes of the bottom boundary of the soil domain are fully fixed, while a normal and two tangential springs and viscous dashpots are applied on the remaining soil boundary nodes, but the ground surface and plane of symmetry. The formulation of springs and dashpots boundary conditions, which are commonly referred to as cone boundary conditions, can be found in Kontoe (2006).

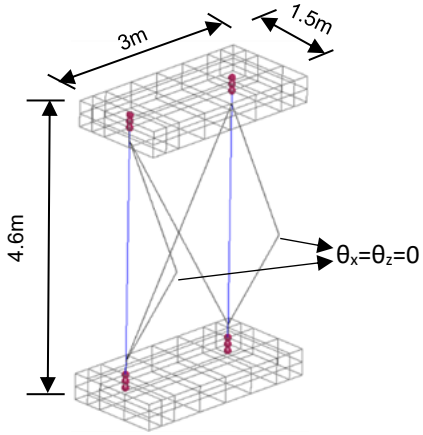




(c) Structural model of the fully braced 2-top slab configuration



(d) Structural model of the partly braced configuration



(e) Structural model of the fully braced 1-top slab configuration

Figure 7.3: FE mesh, dimensions and some boundary conditions of the (a) static self-weight and pull-out analyses, (b) dynamic analyses, (c) structural model of the fully braced 2-top slab configuration, (d) structural model of the partly braced configuration, (e) structural model of the fully braced 1-top slab configuration.

The dashpots aim to model the geometric spreading of the energy away from the structure, while the springs aim to model the stiffness of the unbounded soil domain. According to Kontoe (2006) and Kontoe *et al.* (2009), the imposition of springs reduces the rigid body movements of the soil domain, which would have occurred at low input frequencies if only the dashpots were imposed. The derivation of the cone boundary conditions was based on the assumption of a vibratory load applied on the free surface of a half-space, which leads to downward propagating waves whose energy is spread within an area that increases with depth (Kellezi, 2000). Figure 7.4 shows an application of the cone boundary on a 2D model, illustrating a cone created between the source and the boundary at a radial distance r. The horizontal and vertical stiffness (K_H, K_V) and dashpots (C_H, C_V) at the boundary of a cone with boundary surface area A(r) can be calculated as per Eq. 7.1.

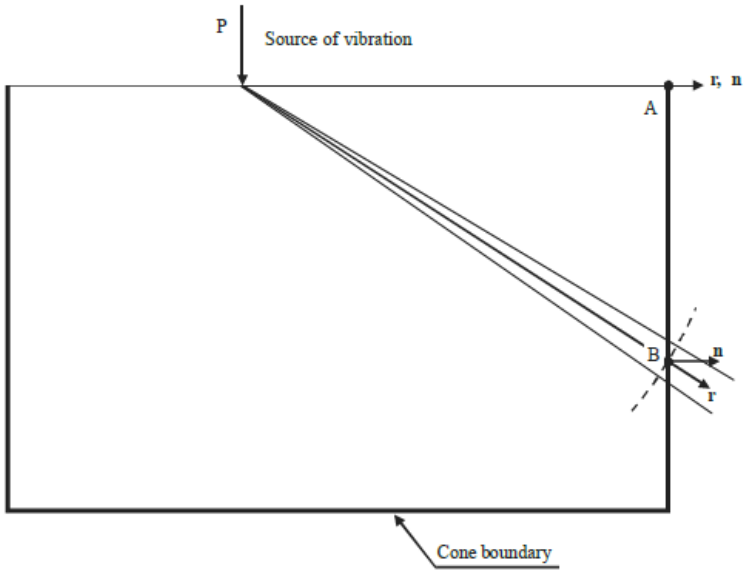


Figure 7.4: Application of the cone boundary on a 2D model (Kontoe, 2006).

$$K_H = A(r)\rho {V_s}^2/r \quad 7.1a$$

$$K_V = A(r)\rho {V_p}^2/r \quad 7.1b$$

$$C_H = A(r)\rho V_s \quad 7.1c$$

$$C_V = A(r)\rho V_p \quad 7.1d$$

Therefore, the properties of springs are a function of the distance between the input source and each node where a spring is applied. The latter can be considered as a limitation of the cone boundary conditions for applications of seismic input motion where this distance is mostly unknown. However, these boundary conditions are fully applicable in the presented numerical models where the position of the input source is known, which herein is assumed at the centre of the foundation base. Both dashpots and springs values are a function of the density and the shear or compressional wave velocity of the unbounded soil, depending on the direction of the propagated waves aimed to be absorbed. Kontoe (2006) suggests that appropriate boundary conditions should be employed to absorb Rayleigh waves, which play a significant role in SSI related problems. This was not considered in the present study; however, its impact is expected to be small as the overall impact of the springs was found to be negligible.

At the interface of foundation and ground surface, zero thickness interface elements (Day and Potts, 1994) were employed, as shown in Figure 7.3a and b. The elastic and plastic properties of these elements are calibrated as discussed subsequently in Section 7.7.

The structural model explicitly simulates the dimensions of the real structural configurations. Figure 7.3c, d and e present the structural models of the fully braced 2-top slab, partly braced and fully braced 1-top slab configurations, respectively. The reinforced concrete slabs, which have dimensions 3m x

1.5m in plan, are modelled with 20-noded brick elements, while the steel columns and braces with 3-noded beam elements. Full moment was prescribed for the connections between the braces, while simple connections were selected for the column-brace connections. Simple connections were achieved by tying the three displacement degrees of freedom (dof) between the connected nodes of the columns and braces, while their rotational dofs remain separated. This boundary condition allows common displacements between the corresponding nodes, while zero moment is transferred, which is a condition that reflects to the real experimental conditions. The concept of tied degrees of freedom can be found in Zienkiewicz *et al.* (1989), Potts and Zdravković (1999).

Unlike the brace-to-brace and brace-to-column connections, the column to slab connections are more complicated. As it was explained in Section 5.2.4, the configuration of the connection, shown in Figure 5.6, was probably not a full moment connection and allowed relative rotation between columns and slabs. Due to the lack of rotational degrees of freedom of the brick elements, the beam elements of the columns are extended into the brick elements of the slab to achieve moment connection between the columns and slabs (see Figure 7.3c, d and e). The extension has a length of one element (0.20m) and has common nodes with the edge of the adjacent four brick elements. The common displacement degrees of freedom between the extended beam and brick elements essentially can produce a moment at the column-slab connections resisting the relative rotation between the two components. The stiffness of the connection is determined by the stiffness of the extended beam, a property that requires calibration, as discussed herein. It is noted that the end node of each of the extended elements, the one that is not attached to the column's end node, has the twisting degree of freedom fixed. Otherwise, the extended beam-column-extended beam system is free to rotate torsionally, producing local instability that affects analysis convergence.

All structural elements and in some analyses soil elements were considered as linear elastic. All structural properties are selected according to modern regulations (i.e. British Standards Institution, 2004, 2005). Table 7.3 summarises the elastic properties of the structural elements, including Young's modulus (E), Poisson's ratio (ν), density (ρ), cross sectional area (A), moment of inertia (I) and torsional constant (J). The target Rayleigh damping (ξ) of the structural elements and the stiffnesses of the extended beams are the two structural properties which are calibrated subsequently. Soil properties regarding the nonlinear model are also calibrated herein. The small strain stiffness soil profile was inferred from previous site characterisation and site-response studies mentioned in Section 4.3 and shown in Figure 4.7. Table 7.4 presents the Young's modulus, Poisson's ratio and density of the two soil layers modelled. A target Rayleigh damping (ξ) of 5% was selected for linear elastic soil, while when nonlinear soil is prescribed, damping is controlled by the nonlinear model.

Table 7.3: Elastic properties of the structural elements.

	E (GPa)	**ν**	**ρ (Mgr/m^3)**	**A (cm^2)**	**I (cm^4)**	**J (cm^4)**	**ξ (%)**
Concrete	31	0.2	2.5	-	-	-	tbc
Braces	200	0.25	7.85	19.2	177	6.97	tbc
Columns	200	0.25	7.85	54.9	1770	2830	tbc
Beam elements extended into the foundation and top slab	tbc	0.25	0.05	54.9	1770	2830	-

Table 7.4: Elastic soil properties.

	E (MPa)	**ν**	**ρ (Mgr/m^3)**	**ξ (%)**
Layer 1	100	0.25	2.0	5%
Layer 2	186	0.2	2.1	5%

The dissipative capacity of both linear elastic structural and soil materials, but the extended beam elements, have been introduced in the analyses by imposing viscous damping on the materials. The damping matrix [C] is defined as a linear combination of the stiffness [K] and mass [M] matrices, as shown in Eq. 5.2, while damping of the vibration mode i is calculated as Eq. 7.3.

$$[\mathrm{C}] = \alpha[\mathrm{M}] + \beta[\mathrm{K}] \quad 7.2$$

$$\xi = \frac{a}{2\omega_i} + \frac{\beta\omega_i}{2} \quad 7.3$$

where, α and β are Rayleigh coefficients and ω is the angular frequency. Herein, the Rayleigh coefficients are calculated based on the formulation proposed by Woodward and Griffiths (1996). These coefficients are a function of the target Rayleigh damping ratio and two angular frequencies (ω_1, ω_2). At the two angular frequencies the target damping is perfectly acquired, while for frequency values between the two angular frequencies damping is underpredicted and it is overestimated for the remaining ranges. The values of these frequencies were selected so that the resulting damping is reasonably close to the target damping for a desired range of frequencies. The first angular frequency is chosen to be equal to the angular frequency related to the smallest resonance of each SSI system. The second angular frequency is chosen equal to the largest resonant frequency excited during the experiments. Table 7.5 presents the frequencies and angular frequencies used for the calculation of Rayleigh damping in each structural configuration.

In all numerical analyses presented, the generalised α-integration scheme (Chung and Hulbert, 1993) is used. According to Kontoe (2006), this scheme is capable of dissipating high frequency modes without significantly affecting the lower modes through an appropriate selection of the *spectral radius*

at infinity (ρ_∞). ρ_∞ can take values between 0 and 1, while algorithmic dissipation increases with decreasing ρ_∞. In the current study, unless otherwise stated, ρ_∞ is taken equal to 0.818 (9/11) which provides stability to the scheme. All conditions that are required for stability of the single-phase formulation can be found in Kontoe *et al.* (2008). All analyses employ Gaussian integration for the evaluation of, among others, stresses and body forces. The Gaussian integration order determines the number of integration points, commonly referred to as Gauss points, per element. In all analyses, unless otherwise stated, 3rd order Gaussian integration (referred to as full integration) was employed, which led to 27 (3x3x3) integration points for the 3-dimensional brick elements and 9 (3x3) integration points for the 2-dimensional interface elements. The 2nd order integration, which is generally sufficient for geotechnical problems (e.g. Potts and Zdravković, 1999) and is more computationally efficient, was found to lead to some stress oscillations within the interface elements, in particular when their plasticity was introduced. These oscillations were eliminated with the use of the 3rd order integration.

Table 7.5: Frequencies and angular frequencies used in the calculation of Rayleigh damping, for each structural configuration.

Structural Configuration	**F_1 (Hz)**	**ω_1 (Hz)**	**F_2 (Hz)**	**ω_2 (Hz)**
FBr_2Ts	3	18.8	8	50.3
FBr_1Ts	3	18.8	8	50.3
PBr_W	1	6.3	7	44.0

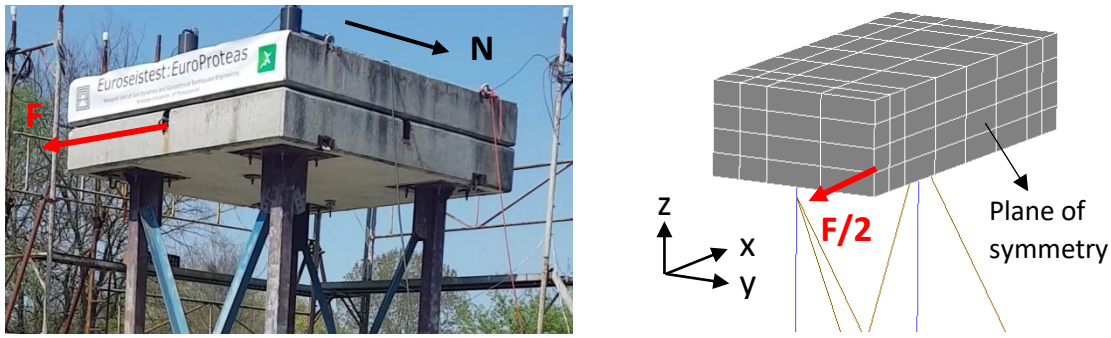
Another numerical parameter that should be selected is the time step. For the presented numerical analyses, it was found that sufficiently accurate results are produced when a full motion cycle is divided into 20 or more increments. This leads to the criterion that the time step should be larger than T/20, where T is the period of the output numerical motion. In forced vibration simulations, T is calculated as 1/F, where F is the applied frequency. In free vibration numerical simulations T equals to the inverse of the predominant frequency of the structure. Table 7.6 summarises the time steps used in the numerical analyses which meet the above criterion.

Table 7.6: Time steps used in the forced and free vibration numerical analyses.

Forced Vibration		**Free Vibration tests**	
Applied frequencies (Hz)	**Time step (s)**	**Structural configuration**	**Time step (s)**
1-2	0.02	FBr_2Ts	0.01
2-5	0.01	PBr_W	0.01, 0.02
5-8	0.005		

7.5.2 Input motion for free vibration tests

Prior to the free vibration tests, the pull-out force was applied at the centre of the South side of the lower top-slab (Figure 7.5a). The force was applied along the South direction at an angle of 9° to the horizontal plane. These boundary conditions were considered explicitly in the numerical model. As only half of the geometry was simulated, the force was applied at the corresponding node of the plane of symmetry, while the magnitude of the applied force was half the one measured in-situ (Figure 7.5b).



(a) (b)

Figure 7.5: (a) Experimental and (b) simulated pull-out force, prior to free vibration tests.

7.5.3 Input motion for forced vibration tests

Unlike the free vibration tests, during the forced vibration tests the input force was not measured, and it can only be estimated through Eq. 5.14 that is given by the vibrator's manual. As already mentioned in Sections 5.8.1 and 5.8.2, the input force is an important experimental uncertainty, which is expected to impact the numerical results. For calibration purposes, the uncertainty regarding the input motion can be addressed by applying recorded motions as input excitation, instead of applying an estimated force. However, as discussed in Section 6.3.1, the recorded strong motion acceleration data are integrated to unphysical velocities and displacements, hence they cannot be used directly in the numerical model. To address this issue, displacements, interpreted from recorded accelerations following the procedure described in Section 6.3.1, are used as input in the numerical models, at the calibration stage.

An input excitation prescribed with "recorded" displacements incorporates the magnitude, frequency content and direction of the experimental force. Displacement-controlled analyses (Dispin) address the uncertainties regarding the above quantities, which would have existed in force-controlled analyses (Fin). An additional advantage of the displacement-controlled forced vibration simulations is that the response of the structure is primarily dominated by the input motion, whereas it is not significantly affected by the dynamic characteristics of the system. This reduces the relative significance of the adopted structural stiffness and soil properties for this type of tests and allows the

rigorous calibration of the interface conditions. The above advantage plays a significant role in the proposed calibration procedure, described subsequently in Section 7.8.

It is acknowledged by the author that the above procedure would not be suitable for applications other than model calibration, due to the fact that the excitation input in the numerical model incorporates the experimental output response. It is also acknowledged that Dispin analyses cannot predict resonant features as the top slab motion is prescribed. Such features are examined in Section 8.3.1 of Chapter 8, where forces are applied as input excitation. Nevertheless, this chapter primarily aims to calibrate the numerical model against the field data, hence, in the author's opinion, the merits of prescribing "recorded" displacements as input motion outweigh the disadvantages. Furthermore, to ensure limited impact of the disadvantages, any conclusions drawn from Dispin forced vibration analyses are verified through independent free vibration analyses presented herein, as well as through Fin forced vibration analyses outlined in Chapter 8.

The input excitation was chosen to be top slab displacements "recorded" by the instrument nearest to the vibrator and top slab geometrical centre. The motion components recorded along the North-South (NS) and vertical directions were imposed at the node in the numerical model with coordinates of the position of this instrument. The NS recorded motion was applied along the x-direction while the vertical motion was applied along the z-direction, with reference to the coordinate system presented in Figure 7.5b. The input motions were tapered at the front (for about 0.5s duration) to achieve a smoother SSI response. Also, the duration of the motions was selected to ensure that they accommodate 10-15 motion cycles. This number of cycles was found to be sufficient to allow the development of steady state response for 7-12 cycles.

7.6 Nonlinear soil constitutive model

For the nonlinear analyses, the Imperial College Generalised Small Strain Stiffness (IC.G3S) model developed by Taborda *et al.* (2016) was used. The description of this nonlinear model was detailed in Section 4.4.4, while the calibration of the parameters of the model are presented in Section 4.4.5. The input parameters of the model, which determine the G-γ-D curves, were calibrated against G-γ-D curves interpreted from the lab data considering the in-situ conditions. The calibration of the model allows the accurate simulation of either the stiffness degradation or damping ratio curves, while the other curve is not prescribed accurately. Taborda and Zdravkovic (2012) have shown that when the calibration prioritises the accurate simulation of shear modulus degradation curves, the soil damping is highly underestimated and highly overestimated at the very low and medium strain range respectively. When, though, the calibration prioritises damping ratio curves, the stiffness is

underestimated at low strains and overestimated at medium strains, while the stiffness degrades more linearly at low strains. As mentioned in Section 4.4.5, the calibration strategy prioritised the accurate simulation of the damping ratio in the small and medium strain range, as soil damping is expected to be more dominant than soil stiffness in site response problems (Papaspiliou *et al.*, 2012; Han *et al.*, 2017). This is also shown herein for SSI problems, as it is subsequently evidenced in Section 7.13.

The curves that correspond to the shallow soil layer are further refined, as this layer is crucial for the examined SSI problem. Apart from the G-γ-D curves, attention is also paid on the variation of the elastic soil stiffness with depth of this layer. In the site response analyses presented in Section 4.4, soil stiffness was reasonably assumed as constant within a layer for the sake of simplicity. Unlike site response analyses, in SSI analyses the input excitation is applied on the structure, and consequently the precise simulation of the stiffness of shallow layers is very important. A smaller precision is required for deeper layers, as the analyses are insensitive to small changes of the stiffness of these layers. Aiming to model soil stiffness more realistically, the maximum shear modulus (G_{max}) is calculated by the model as a function of mean effective stress (p') as shown in Eq. 7.4.

$$G_{max} = G_0 \cdot f_G(e) \cdot \left(\frac{p'}{p'_{ref}}\right)^{m_G} \qquad 7.4$$

where, G_0 is the magnitude of maximum shear modulus for p' equal to the reference mean effective stress, i.e. atmospheric pressure (p'_{ref}=101.3kPa), $f_G(e)$ is a function that incorporates the influence of void ratio on the shear modulus and m_G is a parameter that defines the nonlinearity of the dependence of G_{max} on p'.

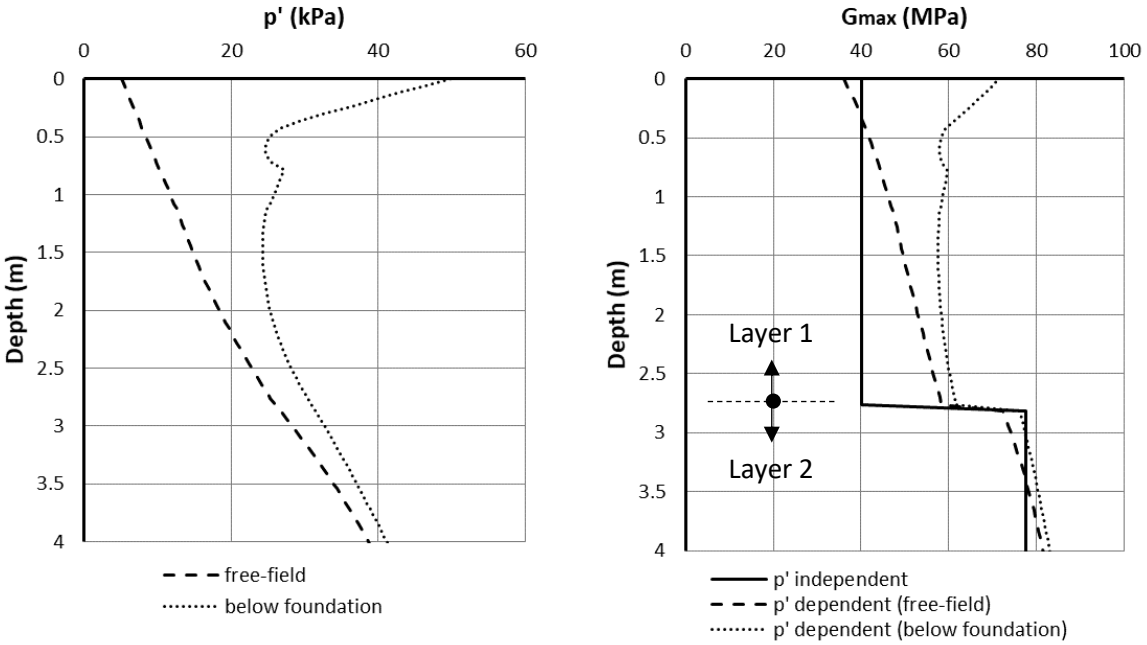
This study neglects the influence of the void ratio on G_{max}. The values of m_G and G_0 are selected so that, under free-field conditions, G_{max} increases with depth, while it does not deviate much from the G_{max} profile concluded in Section 4.3.2 (i.e. m_G=0 and G_0=40MPa). Table 7.7 presents the m_G and G_0 values of the p' independent stiffness profile and the calibrated values for the p' dependent profile. The impact of modelling the maximum shear stiffness of soil to be p' dependent is more pronounced on the stiffness profile below the foundation, as evidenced in Figure 7.6. Figure 7.6a compares the free-field p' profile with the one below the foundation. The p' profiles were extracted from a vertical line, the starting node of which belongs to the element that developed the largest increase of p', due to the existence of the structure. The free-field profile was computed along the same line, without the presence of the structure. The p' profiles are a result of the stress interpolation at the adjacent elements. It is observed that the overburden pressure applied by the self-weight of the structure increases p' considerably in the vicinity of the foundation (i.e. the first 2m). According to Eq. 7.4, the

increase of p' is expected to affect the stiffness of soil within this area. Figure 7.6b compares the stiffness profile which is independent of p' (m_G=0 and G_0=40MPa) with the p' dependent profile under free-field conditions (m_G=0.3, G_0=88MPa and p' is taken from free-field conditions) and the p' dependent profile (m_G=0.3, G_0=88MPa and p' is affected by the existence of structure). All profiles refer to the same line below the foundation, that was mentioned above. The figure illustrates a significant increase of soil stiffness at the first 2m below the foundation due to the existence of the structure, while it reduces to values close to the free-field stiffness profile for larger depths.

Figure 7.6 also demonstrates the importance of suction in the free-field conditions. The suction prescribed above the water table, according to Section 7.5.1, results in non-zero p' on the soil surface under free-field conditions. Hence, suction allows the development of non-zero stiffness at the soil surface, while the omission of suction would have resulted to unreasonably low, zero values of soil stiffness.

Table 7.7: Values of the m_G and G_0 parameters that define the G_{max} profile.

	p' independent stiffness (MPa)		**p' dependent stiffness (MPa)**	
	m_G	**G_0**	**m_G**	**G_0**
Layer 1	0	40.2	0.3	88.4
Layer 2	0	77.6	0.3	108.6



(a) (b)

Figure 7.6: (a) p' profiles under free-field conditions and below the foundation, (b) Impact of p' dependency on the maximum shear modulus, by comparing shear modulus profiles of free-field and below the foundation defined with different pairs of G_0 and m_G that can be found in Table 7.7.

Mean effective stresses can also affect the G-γ-D curves, as it is well established that the increase of p' decreases the soil stiffness degradation and damping (e.g. Darendeli, 2001; Taborda, 2011). As detailed in Section 4.4.5, the nonlinear model was calibrated against G-γ-D curves that have been established using the in-situ mean effective stress, implying that the impact of p' on the curves is incorporated in the calibration. The above calibration is sufficient for site response analyses (i.e. free-field conditions) where the variation of p' within a layer is small, hence a single G-γ-D curve can be used to describe the model behaviour of the entire layer. However, as shown in Figure 7.6a, in the first 2m of soil, p' varies significantly, implying that a single set of curves may not be representative. The above p' profile refers to static conditions, while it is anticipated to change during oscillation. The implication of this is that the G_{max} profile and hence the G-γ-D curves are also anticipated to change during structural oscillation. Despite that the latter claims demonstrate the need of prescribing p' dependent G-γ-D curves, the lack of experimental data prohibits the calibration of this feature of the model. The adopted nonlinear model employs a single pair of curves for each layer.

An additional parameter of the nonlinear model which requires calibration for the SSI analyses, and was not considered in the site response analyses of Chapter 4, is the minimum shear modulus (G_{min}). G_{min} affects the G-γ-D curves at the medium to large strain range. This parameter is particularly important when high strains develop leading to unreasonably high stiffness degradation. This was not the case for the site response analyses as the soil strains induced in the soil lied within the very small to small strain range. However, as it is subsequently discussed, G_{min} is an important parameter in the presented SSI analyses, where the induced strains were larger. In particular, high strains took place during the monotonic loading applied in the static pull-out analyses, as well as at the first cycles of free vibration. A limitation of this study is the lack of lab G-γ data of soil under monotonic loading, meaning that this soil behaviour could not be rigorously calibrated.

7.7 Interface modelling and gaps simulation

The calibration procedure requires investigation of the impact of different soil-foundation interface models on the SSI response. The investigation aims to highlight the significance of modelling the interface appropriately and to demonstrate the impact of the constitutive behaviour of the interface model. Also, a novel approach to model potential contact imperfections at the interface is proposed.

7.7.1 Conventional interface model (Conv)

The conventional interface model (Conv) assumes that the foundation is fixed on top of the adjacent soil. In numerical terms, the foundation and the soil beneath share the same nodes at the interface, hence there is compatibility of displacements between the soil and foundation at the interface. As a

consequence of this the foundation is not allowed to uplift or slide relative to the soil, which is a condition that does not reflect the experimental interface behaviour.

7.7.2 Interface elements formulation

Aiming to allow relative displacements between the foundation and the soil, zero thickness interface elements were placed at the interface. The formulation of the employed interface elements can be found in Day and Potts (1994) or Potts and Zdravković (1999). The elastic properties of the interface elements are the normal (K_n) and shear (K_s) stiffnesses, which relate the elastic normal (ε) and tangential (γ) interface strains with the normal (σ) and shear (τ) stress. Due to lack of element thickness, the stiffnesses are in kN/m^3 units, while the strains are in length units. The shear strain (γ) refers to the relative horizontal displacement between the "top" (u^{top}) and the "bottom" (u^{bot}) of the interface boundaries, while the normal strain (ε) is defined as the relative vertical displacement (v), as shown in Eq. 7.5.

$$\gamma = u^{bot} - u^{top} \quad \text{7.5a}$$

$$\varepsilon = v^{bot} - v^{top} \quad \text{7.5b}$$

The above constitutive behaviour can estimate relative displacements between the foundation and the soil, within the elastic region. It is unable though to simulate foundation uplift, which is a plastic deformation component. With respect to the latter, an elastoplastic Mohr-Coulomb failure surface (Figure 7.7), of maximum angle of shearing resistance ϕ', cohesion c' and angle of dilation ν, is used for the interface elements. For stress states below the failure surface, the interface behaviour is governed by the elastic constitutive matrix [D], while when on the yield surface it is governed by an elastoplastic stiffness matrix [D_{ep}]. More about the elastic constitutive law, yield function (F) and plastic potential can be found in Day and Potts (1994).

More importantly these interface elements are capable of opening when a mobilised tensile normal stress exceeds the tensile strength set as c'/tanϕ. While an interface element remains open, both shear and normal stiffness reduce to zero, while the normal and shear stresses remain $c'/\tan\phi'$ and zero respectively. At the same time, normal strains corresponding to the amount of interface opening are accumulated in the plastic hardening parameter (representing the plastic part of normal strains ε_{pl}). The value of ε_{pl}, which is in length units, equals to the opening between the elements at the two sides of the interface elements, which herein corresponds to the detachment between the foundation and the soil. When the loading conditions change in a way that forces the opening to reduce and eventually close, the plastic hardening parameter reduces and becomes zero upon full closure of the interface opening. At that stage the normal and shear stress start to change again and interface regains its elastic stiffness. During free and forced vibration simulations, some interface elements may

open and close at different increments, a feature which is enabled by a complex contact-tracing algorithm in ICFEP (Potts and Zdravković, 1999).

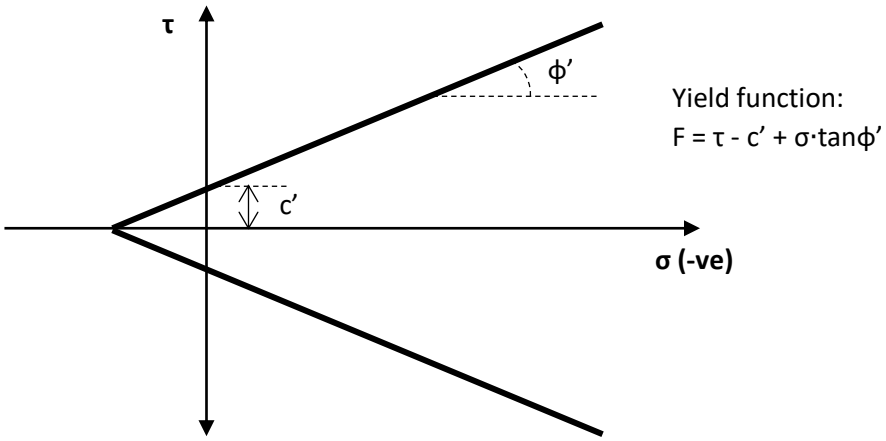
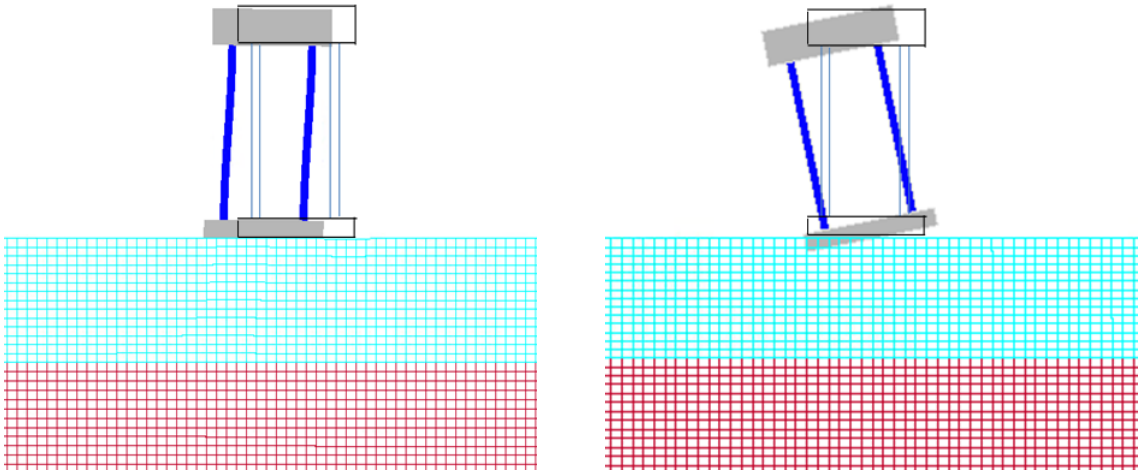


Figure 7.7: Mohr-Coulomb yield surface.

Appropriate values of the above elastic and plastic properties should be selected. As already mentioned, K_s and K_n control the elastic interface stiffness affecting the structural response. Qualitatively when the interface stiffness is very low relative to the structural stiffness, then the response of the SSI system is controlled by the flexibility of the interface. Figure 7.8 presents snapshots of the deformed mesh obtained from 2D simulations of the PBr_W_2Hz forced vibration experiment; the analyses details can be found in Appendix F. Figure 7.8a demonstrates that when the shear stiffness is very low and normal stiffness high (i.e. K_s=1E2kN/m^3, K_n=1E8kN/m^3), the low shear stiffness controls the oscillation mode resulting in significant foundation sliding and weak flexural deformation of the structure. Similarly, when the normal interface stiffness is very small, while shear stiffness is high, (i.e. K_s=1E8kN/m^3, K_n=1E2kN/m^3), the foundation rotation is the dominant motion mechanism while the structural bending is negligible. In both cases, the soil motion appears to be nearly zero since the significant relative motion between the foundation and soil results in minimal strain transfer to the soil medium. The above examples demonstrate the significant impact of the interface stiffness on the structural response, and the necessity of selecting reasonable values for K_s and K_n.

In the dynamic and static pull-out analyses presented herein, for interface areas where the foundation and soil are in full contact prior to the application of loading, high values for K_n and K_s are adopted. High interface stiffness values essentially restrict elastic relative displacements between the two materials. This assumption is deemed reasonable as elastic differential normal displacements are expected to be zero due to the interface's zero strength in tension, while differential elastic shear displacements are expected to be negligibly small. According to López *et al.* (2022) that used the same interface elements in 3D analyses, K_n and K_s should be high enough to minimise penetration between

the contacting bodies, while very high values should be avoided as they cause numerical instabilities. Day and Potts (1994) showed, through 2D analyses, that numerical instabilities arise when either of the two interface stiffnesses is larger than 100E, where E is the Young's modulus of the stiffer contacting material. This is an empirical rule, as direct comparison between interface and solid element stiffnesses cannot be made since they have different units (kN/m^3 for interface elements and kN/m^2 for solid elements).



(a) K_s=1E2kN/m^3, K_n=1E8kN/m^3 (b) K_s=1E8kN/m^3, K_n=1E2kN/m^3

Figure 7.8: Illustration of the impact of K_s and K_n values on the response through snapshots of displaced mesh captured from forced vibration simulations of the PBr_W_2Hz experiment. The snapshots correspond to an increment where the magnitude of the applied force is maximised, while displacements were exaggerated by 1520 times. The deformed shape is due to the dynamic loading only, as any statically induced deformation have been subtracted.

Following the empirical rule and considering that the largest Young's modulus between the contacting materials is 31GPa for the foundation, a value of 1E8kN/m^3 is adopted for both K_n and K_s. This value is adopted for interface elements which model full contact conditions between the foundation and soil prior to the application of loading. It is adopted for dynamic and static pull-out analyses, as well as in some static self-weight (StSW) analyses. It is subsequently shown in Section 7.14 that K_n and K_s can affect the distribution of interface stresses at the interface due to the self-weight, which in turn can affect the dynamic SSI response, under specific circumstances. Within this context, a calibration of the interface stiffness is presented herein for the StSW analysis. Additionally, for interface elements, which simulate non-contact areas, other values may be adopted, as it is discussed subsequently.

The elastoplastic Mohr-Coulomb failure surface, which controls the plastic deformations of interface elements, adopts cohesion c'=0, angle of shearing resistance ϕ'=30° and angle of dilation v=0. Zero cohesion was selected to simulate the zero interface tensile strength (c'/tanϕ=0), enabling opening when the normal effective stress of an integration point becomes zero. The angle of shearing

resistance was selected to be equal to the corresponding value of the soil. It was found that the analyses are insensitive to changes of ϕ' and ν, hence these properties are not discussed herein. The latter implies that the failure surface is not reached due to shearing by many integration points and shearing is not important, therefore, more attention is paid on the opening and closure of interface elements. The latter aligns with Gazetas *et al.* (2013) claim that foundation uplift is more prominent than foundation sliding in slender structures, which is the case for the fully braced structural configurations examined herein.

Table 7.8 summarises the elastic and plastic interface properties adopted for each of the analyses carried out. The table also shows the properties that are calibrated at a later stage (denoted with tbc).

Table 7.8: Adopted properties of interface elements.

Analyses	**Contact areas**		**Non-contact areas**		**c'(kPa)**	**ϕ'(°)**	**ν'(°)**
	K_s (kN/m^3)	**K_n (kN/m^3)**	**K_s (kN/m^3)**	**K_n (kN/m^3)**			
StSW	tbc	tbc	tbc	tbc	0	30	0
StP	1E8	1E8	tbc	tbc	0	30	0
Dynamic	1E8	1E8	tbc	tbc	0	30	0

7.7.3 Elastic and Elastoplastic interface model without gaps (ELint, EPint)

Two of the interface models of which impact on the SSI response is investigated are the elastic interface (ELint) and the elastoplastic interface models (EPint), both without the simulation of interface gaps. The ELint analyses investigate the impact of the imposition of elastic interface elements which allow only elastic differential displacements, as described in Section 7.7.2. The EPint analyses aim to show the impact of plastic interface deformations, placing more attention on foundation detachment from the soil beneath.

7.7.4 Gaps simulation with elastoplastic interface elements (EPint_*g*mm)

During the experiments, under static loads, gaps between the foundation and the soil beneath were visually inspected at the foundation edges. Given that the distribution and the magnitude of the gaps are not known, these parameters are calibrated through a parametric investigation. The aim of this task is to initiate gaps between the foundation and the soil at a pre-defined area, after the StSW and prior to the StP analyses. The prescribed amount of the gap opening represents the experimental gaps that existed under rest conditions prior to the forced and free vibration experiments.

Herein, a novel approach to initiate gaps between the foundation and the soil is proposed, using the above MC model formulation for interface elements. The proposed formulation initiates a detachment (gap) of the surface foundation from the soil by initiating the analysis with a non-zero value for the previously mentioned hardening parameter of the model. The magnitude of the

hardening parameter reflects to the magnitude of the opening, while when it is not equal to zero at an integration point, the stiffness at this integration point vanishes, modelling essentially a gap. The gap is initiated at the start of an analysis (e.g. StSW or StP), while during the analysis the values of the hardening parameter can change, enlarging or decreasing the gap.

The procedure that is proposed to model gaps consists of three main steps. In the first step, the non-contact areas and the magnitude of opening (*g*) are chosen (both parameters require calibration). The second step requires the initiation of gaps for the StSW analysis by prescribing a relatively large value of hardening parameter for the integration points of the elements where gaps are intended. It is noted that at this stage, the magnitude of opening is larger than *g*, while it should be large enough to ensure that at the end of the StSW analysis, the initially open gaps will not close due to the self-weight by the end of the StSW analysis. The magnitude of the required gap is dependent on the normal stiffness of the selected interface elements, as lower stiffness results in larger vertical displacements, hence larger gaps are required. The target interface condition at the end of the StSW analysis is zero stresses at the interface elements that are intended to be initially open. In the final step of the process, in the analysis that follows the StSW analysis, the magnitude of the open integration points is re-defined to be equal to *g*. At the end of this 3-step procedure, gaps of magnitude *g* are prescribed at a pre-defined area, where zero interface stresses are ensured. At this stage of the analysis, the StP analysis is carried out for free vibration simulations, or the dynamic analysis is carried out for forced vibration simulations.

The adopted name conversion for analyses which employ elastoplastic interface elements with defined initial gaps at the interface is EPint_*g*mm, where *g* is the magnitude of gap in mm units. Table 7.9 summarises the analyses that are presented herein, also showing the initial gap magnitudes prescribed prior to the StSW and StP/Dynamic analyses. Prior to the StSW analyses, during which K_n was equal to 1E8kN/m^3, an initial opening of 2mm was found to ensure that the elements do not close. Analyses with gap magnitudes ranging from 0.05mm to 0.5mm prior to the StP/Dynamic were carried out, to investigate the impact of this parameter on the SSI response.

Table 7.9: Initial gap openings prescribed prior to the StSW and StP/Dynamic analyses

Structural configuration	**Analysis name**	**Gap magnitude (mm)**	
		StSW	**StP (for free vibr.) or Dynamic (for forced vibr.)**
FBr_2Ts	EPint_0.05mm	2	0.05
	EPint_0.1mm	2	0.1
	EPint_0.2mm	2	0.2
	EPint_0.3mm	2	0.3
FBr_1Ts	EPint_0.1mm	2	0.1
	EPint_0.2mm	2	0.2
	EPint_0.5mm	2	0.5

7.7.5 Gaps simulation with low stiffness elastic interface elements (LSELint)

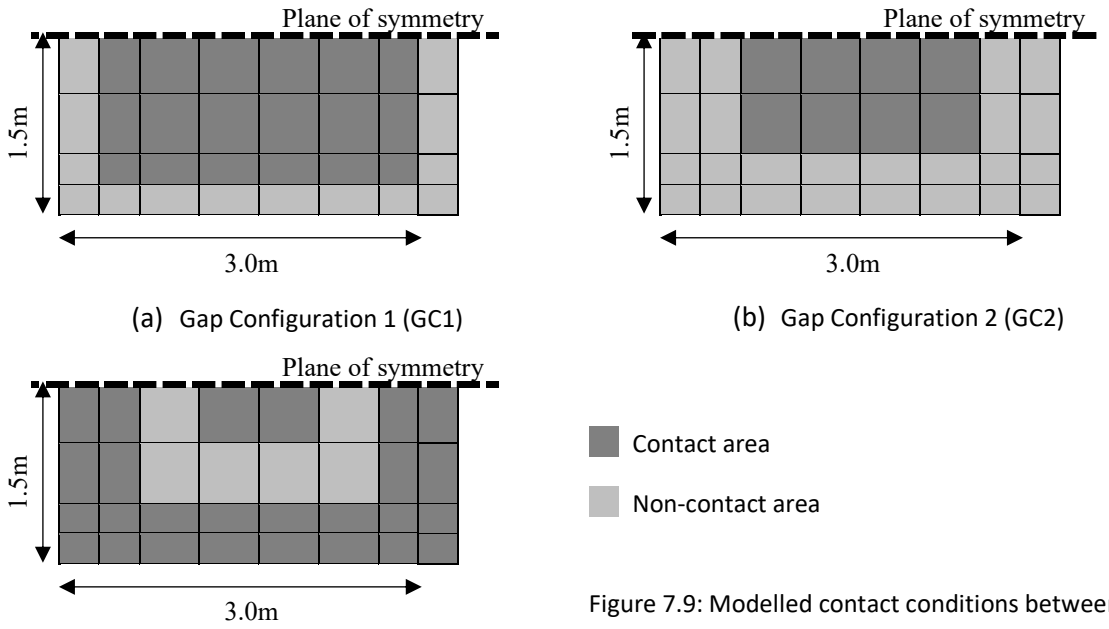
As mentioned in Section 7.7.2, when a gap is formed at an interface element through the formulation of an elastoplastic interface model, the stiffness of this element is set to zero. If the gap does not close at any increment during an analysis, then the corresponding interface element retains zero stiffness during the entire analysis. With respect to the latter, it is attempted here to model the gaps that never close by adopting a very low stiffness (i.e. Ks= Kn=1e2kN /m^3) of elastic interface elements (LSELint). The interface elements which intend to model non-contact interface areas should maintain stiffness that is much lower than the stiffness of the elements in full-contact areas. Herein, the non-contact interface elements are prescribed with stiffness $K_s=K_n$=1E2kN/m^3, which is much lower than the stiffness of contact elements (1E8kN/m^3). The advantage of the LSEint analyses is that it is less computational expensive than the EPint_*g*mm analyses, as the plasticity model is not necessary to be incorporated in the model.

7.7.6 Hybrid interface model with gaps (HYBint)

In some analyses, it was deemed necessary to incorporate in the same numerical model interface elements that remain always open and elements that, although initially closed, open and close at different increments during the excitation. The most effective interface simulation comprises both elastic and elastoplastic interface elements, referred to as hybrid interface model (HYBint). In HYBint analyses, the permanently open interface elements are modelled as LSEint, while the remaining elements are initially close and prescribed with an elastic perfectly plastic behaviour (EPint).

7.7.7 Gaps configurations

This study compares the impact of three different gap configurations, which are prescribed prior to the application of external loading. Figure 7.9 presents, in plan, the three contact conditions between the foundation and the soil that are incorporated in the numerical models. The figure also shows the discretization of the interface elements. The gap configuration 1 and 2 (GC1, GC2), shown in Figure 7.9a and b, simulate gaps at the edges of the foundation; however, they differ in terms of the total area of gaps. The non-contact area of GC3 was prescribed along an internal line of interface elements, as shown in Figure 7.9c.



(a) Gap Configuration 1 (GC1)

(b) Gap Configuration 2 (GC2)

(c) Gap Configuration 3 (GC3)

Figure 7.9: Modelled contact conditions between the foundation and soil in plan.

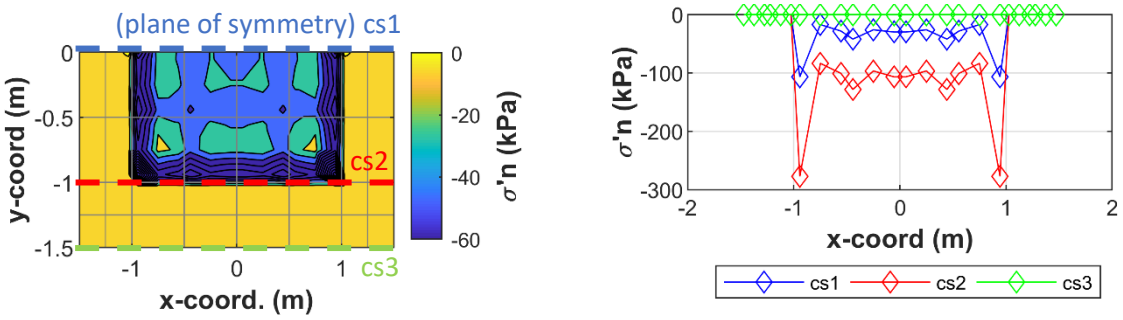
7.7.8 Static self-weight analyses: Interface stiffness and distribution of interface normal stresses

The stiffness of interface elements has been established for the StP and dynamic analyses based on the reasoning described in Sections 7.7.2, 7.7.4 and 7.7.5, while an investigation is required for the static self-weight analysis. The interface stiffness, predominantly the normal (K_n) one, affects the normal stresses at the soil-foundation interface, while as it is subsequently shown in Section 7.14, the interface normal stresses affect the foundation uplift. With respect to the latter, during the static self-weight analyses, different K_s and K_n pairs are used for the interface elements. The investigation of the impact of the interface elements stiffness on the static stresses and hence on the SSI response is carried out by employing the hybrid interface model (Section 7.7.6) and the gap configuration CG2 (Figure 7.9b). As described in Section 7.7.5, the interface elements stiffness of the non-contacts areas is prescribed as K_s= K_n=1e2kN /m^3, while the stiffness of the remaining interface elements is subjected to investigation. The values chosen for investigation are tabulated in Table 7.10. The StSW8 is used for the majority of the analyses, unless otherwise specified.

Table 7.10: Values of interface stiffness selected for the static self-weight analyses.

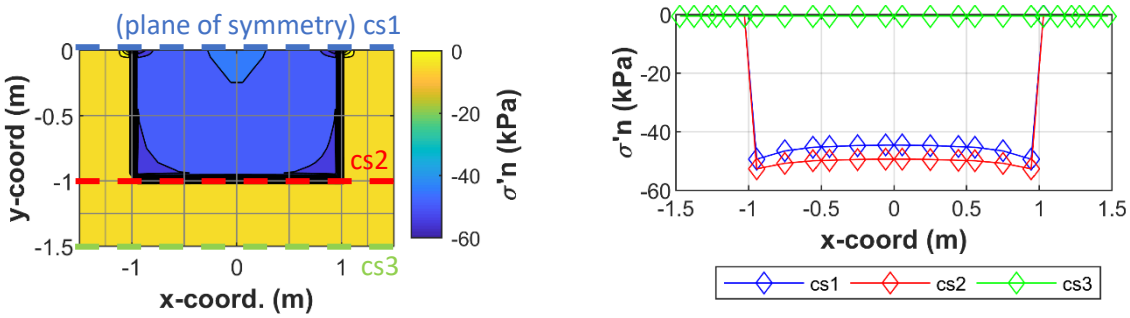
Analysis name	**Contact areas**		**Non-contact areas**	
	K_s (kN/m^3)	**K_n (kN/m^3)**	**K_s (kN/m^3)**	**K_n (kN/m^3)**
StSW3	1E3	1E3	1E2	1E2
StSW4	1E4	1E4	1E2	1E2
StSW8	1E8	1E8	1E2	1E2

The impact of the interface stiffness at the contact areas on the static interface effective normal stresses (σ'_n) is illustrated in Figures 7.10, 7.11 and 7.12. The figures plot (a) the σ'_n contours over the entire interface area, and (b) the σ'_n variation along three cross sectional lines (cs1, cs2 and cs3) that are shown in (a). Each discrete point presented in figures (b) corresponds to σ'_n of a certain integration point, while all results are extracted from nonlinear analyses, as they are described subsequently. Figure 7.10 plots the stress distribution resulted from the StSW8 analysis, demonstrating than when the contact interface area is assigned to a very large stiffness (i.e. 1E8kN/m^3), the contact area behaves as a rigid foundation. This is manifested through the large concentration of stresses at the edges and especially at the corners of contact area (with respect Figure 7.9b). This feature vanished for a smaller interface stiffness, such as is the case of StSW4 and StSW3 analyses. Figure 7.11, that plots results from the StSW4 analysis, shows that the variation σ'_n at the contact area was much smoother with a small stress concentration at interface between contact and non-contact areas. This stress concentration disappeared completely for the StSW3 analysis, as the distribution of normal effective stresses over the contact area was almost uniform (Figure 7.12). In all analyses, the effective normal stresses that developed at the areas considered as non-contact areas (with respect to Figure 7.9b) were much smaller than the stresses at the contact areas. This is an indication that indeed the imposition of low stiffness interface elements worked essentially as gaps.



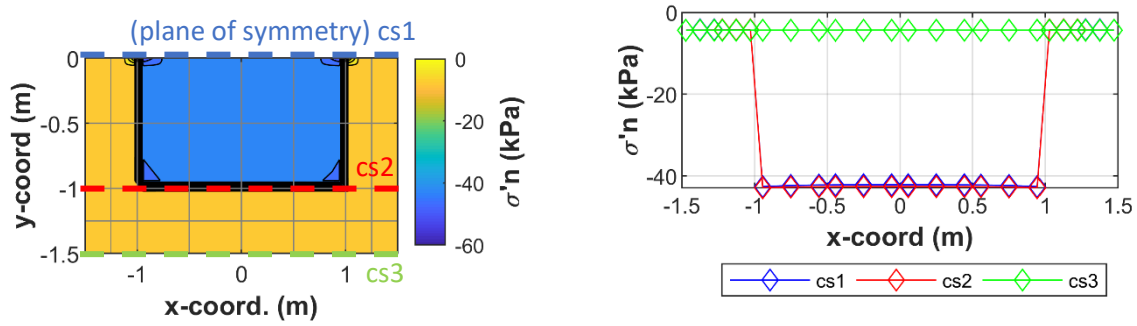
(a) (b)

Figure 7.10: Effective normal static stresses (σ'_n) resulted from the StSW8 analysis assuming nonlinear soil. (a) contours of σ'_n and (b) σ'_n along cross sections cs1, cs2 and cs3 shown in (a).



(a) (b)

Figure 7.11: Effective normal static stresses (σ'_n) resulted from the StSW4 analysis assuming nonlinear soil. (a) contours of σ'_n and (b) σ'_n along cross sections cs1, cs2 and cs3 shown in (a).



(a) (b)

Figure 7.12: Effective normal static stresses (σ'$_n$) resulted from the StSW3 analysis assuming nonlinear soil. (a) contours of σ'$_n$ and (b) σ'$_n$ along cross sections cs1, cs2 and cs3 shown in (a).

7.8 Calibration procedure

7.8.1 Advantages of forced vibration tests

The first advantage of forced vibration analyses is that they reduce the impact of Rayleigh damping on the response, hence damping calibration is not necessary. The latter can be explained by considering a single-degree of freedom (SDOF) structure, of viscous damping ξ, subjected to a forced vibration force =$p(t) = p_0 sin\omega t$, where p_0 is the amplitude of the load, ω is the input frequency and $t$is time. Solving the differential equation governing such a system, the forced vibration response in terms of displacements (u) is given by Eq. 7.6 (Chopra, 2011).

$$\mathrm{u(t)} = \underbrace{e^{-\xi\omega_n t}(A\cos\omega_D t + B\sin\omega_D t)}_{\text{transient}} + \underbrace{C\sin\omega t + D\cos\omega t}_{\text{Steady state}} \qquad 7.6$$

where $\omega_D = \omega_n\sqrt{1-\xi^2}$, while A and B are constants which are determined from the initial conditions u(0) and $\dot{u}$(0). C and D are defined as a function of the system's natural frequency ω_n, stiffness k, p_0, ξ and ω, as follows:

$$C = \frac{p_0}{k}\cdot\frac{1-(\omega/\omega_n)^2}{[1-(\omega/\omega_n)^2]^2+[2\xi(\omega/\omega_n)]^2} \qquad 7.7a$$

$$D = \frac{p_0}{k}\cdot\frac{-2\xi\omega/\omega_n}{[1-(\omega/\omega_n)^2]^2+[2\xi(\omega/\omega_n)]^2} \qquad 7.7b$$

As the above equations show, the response of the SDOF structure subjected to forced vibration consists of a transient and a steady state part. The damping term plays a dominant role on the transient motion, while the steady state part is less significantly affected by damping. Consequently, the transient part decays exponentially with time becoming eventually negligible, while the steady state part dominates. This study considers only the steady state part of the forced vibration response.

Therefore, according to the above, the forced vibration simulations do not require the calibration of damping.

The second advantage is that the displacement-controlled forced vibration analyses do not require precise calibration of the structural stiffness. As mentioned in Section 7.5.3, in the presented forced vibration analyses, the input excitation is defined as prescribed displacements integrated from the top slab experimental accelerations. Consequently, the structural response is prescribed, rendering it less susceptible to variations in structural stiffness. Hence, displacement-controlled analyses decrease the aspects that require calibration, allowing a more targeted calibration of the interface model.

7.8.2 Advantages of free vibration tests

The free vibration tests are particularly useful for investigating the fundamental frequency of the numerical models. These tests allow the calibration of all properties of the models, while they are useful to validate the parameters calibrated by the forced vibration tests. The calibration procedure benefits from free vibration experimental data collected from tests which triggered different levels of foundation and soil motion. Free vibration tests which triggered low levels of foundation motion can be considered as fixed-base vibrations, hence, they allow the calibration of structural properties alone. Also, experiments which trigger weak soil motion can be used for the calibration of the nonlinear model at low strains, while experiments which induced higher strains in the soil can be used for the model calibration in the corresponding strain range.

7.8.3 Procedure

The numerical parameters that require calibration are column-slab connections, damping of structural elements, interface model and input parameters of the nonlinear constitutive model for the soil. As detailed in Section 7.5, the remaining structural properties are selected according to code provisions (i.e. British Standards Institution, 2004, 2005), the small strain stiffness soil profile was inferred from previous site characterisation and site-response studies (detailed in Section 4.3), while a 5% value was considered for the viscous damping ratio (ξ) in the case of linear elastic soil.

The first step of the calibration process involves the determination of the stiffness of the connections and the structural damping. These properties are calibrated against strong motion data collected during experiments which trigger very weak foundation motion. Such experiments exhibited structural response which can be approximated with fixed-base conditions (i.e. soil is not modelled and fixity conditions are applied below the foundation), and therefore any impact of the soil and interface conditions can be reasonably neglected. The experiment that meets the above criteria is the free vibration test on the partly braced structure for a 2kN pull-out force (PBr_2.0kN). As evidenced by Figures 6.15 and 6.17, during this experiment the soil and foundation motions were very weak in

comparison with other experiments, while the contribution of the foundation motion on the structural response was negligibly small (Figure 6.18). Based on the PBr_2.0kN experiment, the Young's moduli of the extensions are calibrated to replicate the natural frequency of the SSI system, while the damping values of all structural elements are calibrated to replicate the amplitude of the response.

At the second step, the interface conditions, including gap configuration and initial opening of gaps, are calibrated, employing a forced vibration experiment that engaged strong foundation uplift for the fully braced structure at an input frequency of 5Hz (FBr_5Hz). An advantage of the displacement-controlled forced vibration simulations is that the response of the structure is primarily dominated by the input motion, in contrast with the free vibration response which is strongly affected by the dynamic characteristics of the system. This reduces the relative significance of the adopted soil properties for this type of tests and allows the calibration of the interface model using a linear elastic soil. Additional benefit of forced vibration simulations is that they eliminate the impact of material damping on the response, as explained in Section 7.8.1.

Subsequently, the soil nonlinear constitutive model is calibrated against free vibration tests, which are found to be strongly affected by soil behaviour. The chosen experiments are the free vibration tests of pull-out force equal to 2.9kN and 15.7kN on the fully braced structure (FBr_2.9kN, FBr_15.7kN). More experiments which triggered intermediate levels of strain are also used to validate the calibration. These experiments triggered a relatively wide range of strains in the soil, allowing model's calibration over this strain range. At first, the calibration aimed to replicate the G-γ-D curves concluded from the site response analyses described in Chapter 4, with further refinement where needed to adjust the numerical results to the experimental ones.

At the final stage of the calibration process, the static stresses at the soil-foundation interface are calibrated. As it is subsequently shown, these stresses affected both the natural frequency of the SSI system and the soil motion, while the impact was more pronounced on the experiments which exhibited the strongest foundation uplift. These were forced vibration experiments on the fully braced 1-top slab (FBr_1Ts) structure, while other experiments were found to be less sensitive to changes of the static interface stresses. However, the simulation of the FBr_1Ts forced vibration experiment cannot be used alone to calibrate the static interface stresses, as it is unable to examine the impact of these stresses on the natural frequency of the numerical model. This stems from the fact that in Dispin forced vibration simulations, the response is prescribed, implying that any change on the interface model will not affect the frequency content of the response. The natural frequency of the numerical model can be examined through free vibration simulations. Although free vibration field data are not available for the FBr_1Ts experiment, free vibration simulations of this experiment are carried out. The aim of these simulations is to calibrate the static interface stresses so that the natural frequency

of the FBr_1Ts numerical model agrees with the experimental natural frequency. The experimental in-plane (North-South) natural frequency of the FBr_1Ts was inferred from strong motion forced vibration data, as detailed in Section 6.3.5.

It should be noted that each calibration stage is validated against the subsequent stages with further refinements, where needed. The final calibrated SSI model is validated against an independent set of experiments which were not involved in the calibration process.

7.9 Calibration criteria and results interpretation

The criteria used in the calibration process differ between the free and forced vibration simulations, as each type of test can produce different outcomes. The criteria selected align with the procedure followed in Sections 6.2.1 and 6.3.4 to identify the natural frequencies of the examined systems through free and forced vibration data, respectively.

7.9.1 Free vibration

Criteria:

- Capture natural frequency
- Capture variation of natural frequency with time
- Capture motion amplitude
- Capture the variation of computed damping with time

Results interpretation:

The free vibration tests revealed the natural frequency, which coincided with the in-plane modal one of each SSI system examined, while the contribution of the other modes was mostly weak (see Section 6.2.3). The free vibration simulations aim to capture the natural frequency of the modelled SSI systems. This can be achieved by comparing Fourier amplitude spectra inferred from the experimental and numerical top slab response. When the frequencies that correspond to the main peak of the two spectra coincide, then the “average” natural frequency and hence the dynamic characteristics of the examined system are captured. Herein, a closer comparison of the experimentally and numerically produced frequency content is carried out. As shown in Section 6.2.5, during free vibration motions, the response frequency increased with time, as a consequence of decreasing nonlinear effects. The comparison of experimental and numerical variation of response frequency with time is achieved by the means of peak-to-peak frequency time series, that are derived according to Section 6.2.1.

In addition to the frequency content, the numerical models aim to replicate the amplitude of the experimental motion. The experimental and numerical motion amplitudes are compared by

examining the amplitudes of either the corresponding Fourier spectra or acceleration time histories. The motion amplitude is inherently connected with the damping developed by the SSI systems, hence damping time series produced through experimental and numerical data are also a criterion of the calibration process. Damping values are calculated by employing the logarithmic decrement method (Chopra, 2011), as described in Section 6.2.4.

7.9.2 Forced vibration

Criterion:

- Capture the amplitude soil and foundation motions (top slab motion and motion frequency are prescribed)

Results interpretation:

For the calibration of forced vibration tests, the numerical and experimental results are compared by the means of response (acceleration or velocity) time series and Fourier amplitude spectra.

7.9.3 Normalised response

In many of the results presented herein, the response of the free and forced vibration numerical response is normalised by the amplitude of the input force. This force is the pull-out force for free vibration experiments and the maximum amplitude of the sinusoidal force applied during forced vibration experiments. The normalised response is defined as a/F (1/Mgr) and v/F (s/Mgr) for the structural and soil response respectively, where a is acceleration, v is velocity and F is the amplitude of the input force. The normalisation facilitates the comparison of experiments with different magnitude of input excitation, as well as the investigation of numerical nonlinearities. Any difference between normalised results of experiments with identical structural configuration but different magnitude of input force can be attributed to the nonlinear behaviour of the numerical SSI system. Also, results from a linear elastic analysis with input force of unity magnitude, can be compared with normalised field data recorded during the modelled experiments of any force magnitude.

7.10 Structural connections and structural damping

The procedure commences by calibrating the Young's moduli of the beam elements extended from columns to the foundation (E_F) and to the top slab (E_{TS}). To simplify the calibration, column-foundation connections are assumed to be rigid, i.e. E_F=200E4GPa, considering that the bolts were regularly tightened during the experiments. On the contrary, the bolts of the column-top slab connections were not inspected frequently, hence E_{TS} is calibrated to account for the compliance of those connections. As earlier explained, the structural properties are calibrated against PBr_2.0kN free vibration

experiment, while assuming fixed-base conditions in the numerical model. Figure 7.13 investigates parametrically the impact of E_{TS} on the horizontal top slab motion (2.5n). It demonstrates that the stiffness of the connections affects significantly the natural frequency of the SSI system, as it is clearly indicated by the main peak of the spectra. Assuming a full moment connection, i.e. E_{TS}=200E4GPa, the numerical model predicts a natural frequency that is double the experimental one. The figure demonstrates that E_{TS}=3GPa is an appropriate value to consider in the subsequent analyses.

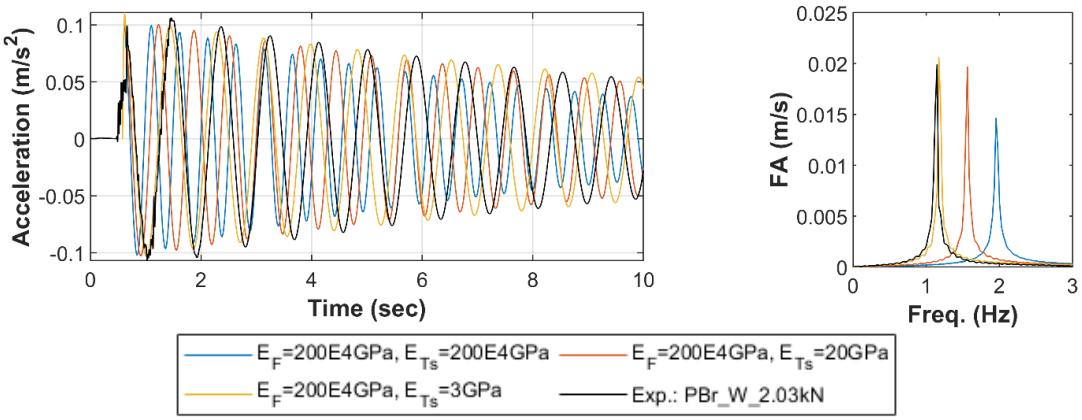


Figure 7.13: Calibration of Young's modulus of beams extended into foundation (E_F) and top slab (E_{TS}), through modelling the PBr_W_2.03kN experiment. Fixed-base conditions are assumed.

In the above analyses, the steel braces and columns were prescribed a 2% target Rayleigh damping ratio, which is typically used for steel structures. A lower value of 1% target damping was assigned to the concrete slabs, as the slabs essentially moved like rigid bodies with negligible bending. The above damping values are deemed suitable, as the motion amplitude produced by the numerical model is in a good agreement with the experimental data.

The claim about the applicability of the fixed-base approximations is verified by comparing results of numerical models where the soil is explicitly modelled. Figure 7.14 compares the top slab response produced by the fixed-base analysis with results produced by two analyses that simulate the soil, according to Figure 7.3, as linear elastic. The two analyses incorporate the above calibrated column-slab connections and structural damping, while they apply different interface models. LINs_Conv conventionally bonds the foundation nodes to the soil nodes, while LINs_ELint analysis imposes elastic interface elements of K_s=K_n=1E8 at the soil foundation interface.

Figure 7.14 shows that the fixed-base analysis produces very similar results to the ones where the soil was modelled, demonstrating the weak impact of soil compliance and hence of SSI effects on the response of the SSI system. The simulation of soil makes the response slightly more flexible, while the two interface models produce identical results. The latter is attributed to the fact that the interface elements of the ELint interface model are very stiff, restricting the relative displacement between foundation and soil, which is also the case for the Conv model.

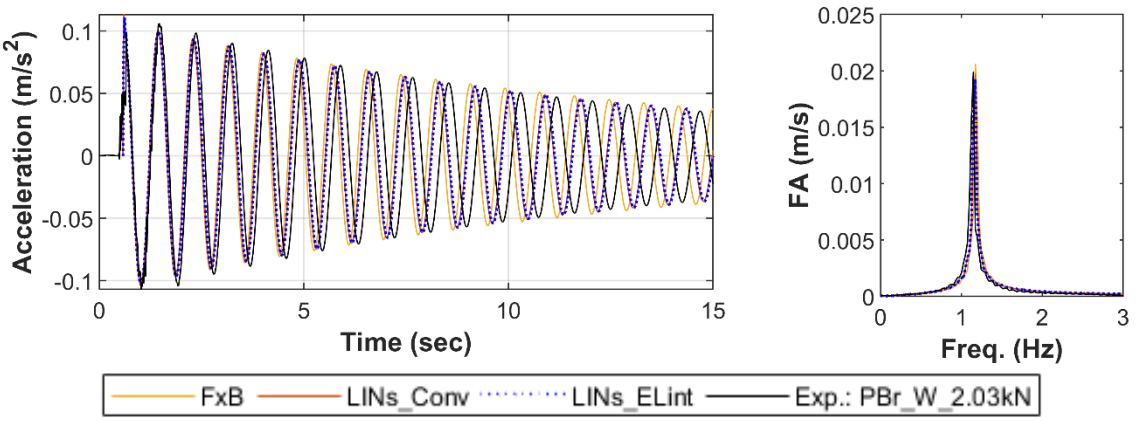
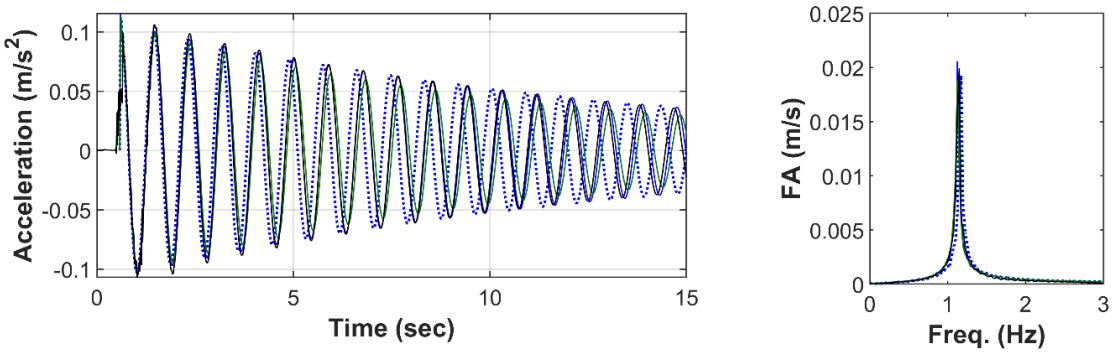


Figure 7.14: Impact of soil compliance and the imposition of stiff elastic interface elements on the numerical results of the simulation of the PBr_W_2.03kN experiment.

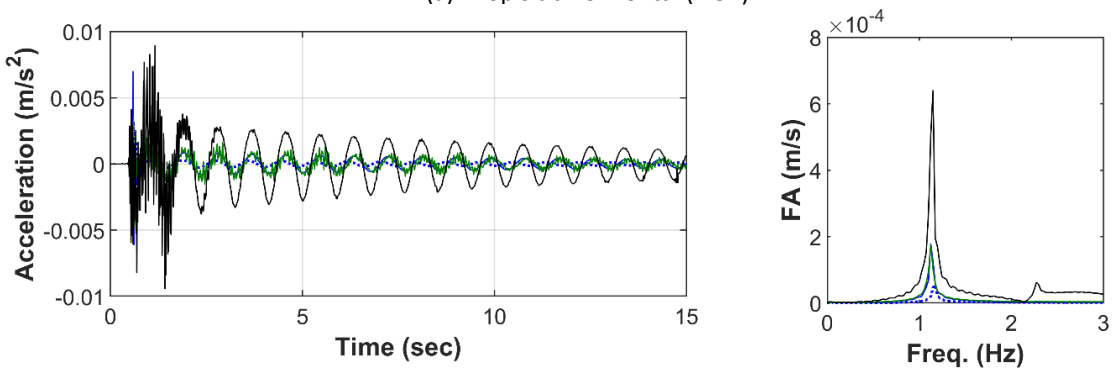
The other two aspects that are subsequently discussed in the calibration process are the gaps at the interface and soil nonlinearity. The impact of these aspects on the PBr_W_2.03kN simulations is illustrated in Figure 7.15, aiming to fully validate the calibration of the structural parameters. The figure presents the horizontal (n) and vertical (z) response of the top slab (2.5) and foundation (1.1) as computed from linear elastic analyses without and with interface gaps (LINs_ELint, LINs_ELint_GC2) as well as from nonlinear analyses with gaps (NLINs_ELint_GC2). For the analyses with interface gaps, low stiffness interface elements were used to simulate the gap configuration GC2 shown in Figure 7.9b, while the input of the nonlinear model is subsequently discussed.

Figure 7.15a shows that the existence of gaps decreases slightly the predominant frequency (horizontal swaying mode) of the SSI systems, capturing better the experimental predominant frequency. However, the impact is very small and hence it could be neglected, while soil nonlinearity does not change the frequency content or amplitude of the predicted motion. The weak impact of the interface conditions and negligible impact of soil nonlinearity on the predominant frequency and damping of the SSI system aligns with corresponding conclusions drawn from the interpretation of the field data, discussed in Section 6.2. The impact of gaps, though, is considerable on the vertical top slab response (Figure 7.15b), as well as on both the horizontal and vertical foundation response (Figure 7.15c, d). The latter motions increase with the existence of interface gaps, capturing better the experimental response. The impact of soil nonlinearity on the latter motion components is negligible due to the low intensity motion.

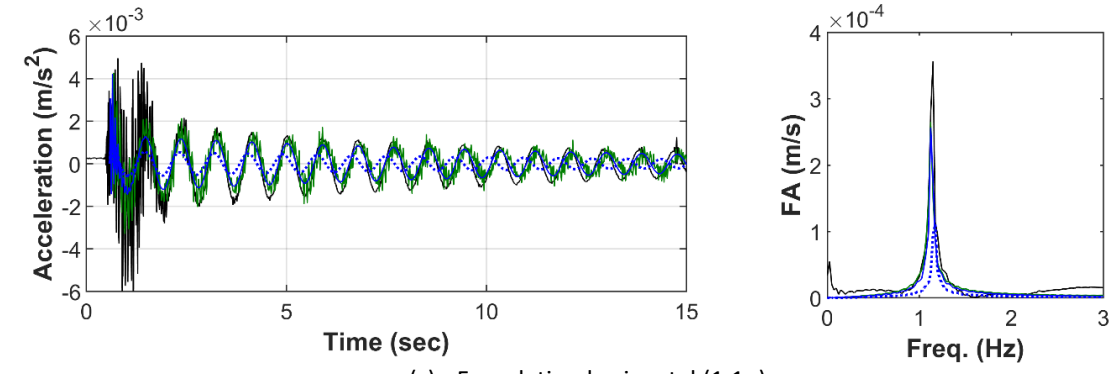
Overall, the calibrated structural properties work well for the PBr_W_2.03kN experiment, which are used for the remaining analyses. For simplification, this study assumes that the damping generated from the structural elements was constant, i.e. any strain dependence of damping is neglected.



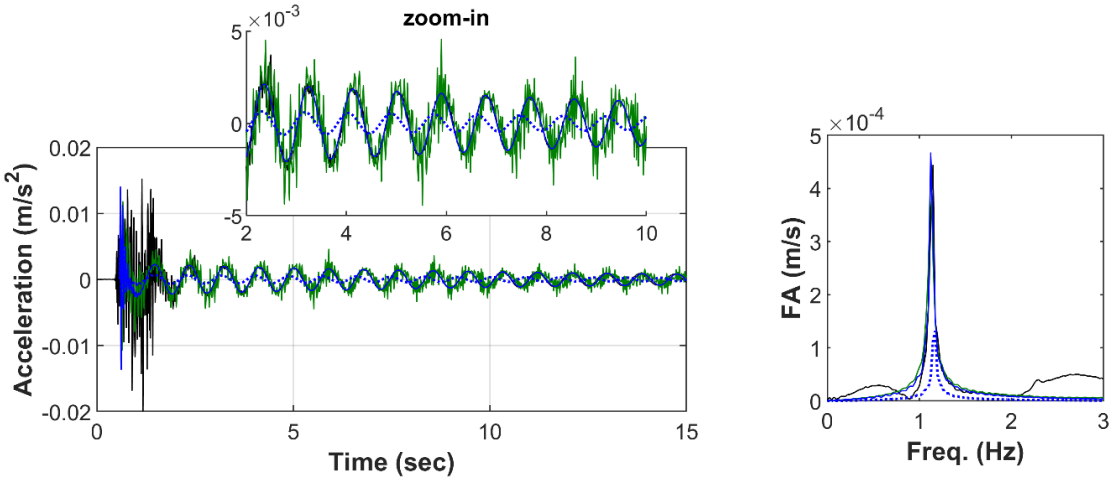
(a) Top slab horizontal (2.5n)



(b) Top slab vertical (2.5z)



(c) Foundation horizontal (1.1n)



(d) Foundation vertical (1.1z)

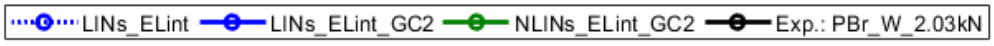


Figure 7.15: Impact of gaps and soil nonlinearity on the numerical results of the simulation of the PBr_W_2.03kN experiment.

7.11 Linear elastic analyses without interface imperfections

This section presents numerical SSI analyses of experiments which exhibited both weak and strong SSI effects. The presented numerical models simulate explicitly the soil, which is assumed as linear elastic (LINs), or they completely omit the soil domain assuming fixed-base conditions (FxB). For the former case, interface elements are placed between the foundation and soil. The interface elements are assumed to be either elastic (LINs_ELint) or elastoplastic (LINs_EPint) with the properties mentioned in Table 7.8. In both simulations, the foundation and soil are considered to be in full contact initially, as imperfections are not simulated at the interface.

7.11.1 Free vibration

Figures 7.16, 7.17 and 7.18 present the horizontal top slab (2.5n or 2.1n) response computed from free vibration simulations of the PBr_W, FBr_2Ts and FBr_1Ts structural configurations, respectively. The figures compare results of the FxB, LINs_ELint and LINs_EPint analyses described above. The numerical results are also compared with field data, where available, recorded during two experiments where the pull-out force was the smallest and the largest applied. The experimental and numerical responses presented are in acceleration units (a) normalised by the pull-out force (F) of each experiment. Due to the adopted normalisation, the presented linear elastic analyses (FxB and LINs_ELint) can represent any experiment irrespective of the magnitude of the pull-out force. On the contrary, when plasticity is incorporated (LINs_EPint), separate analyses with the corresponding pull-out force should be carried out to achieve compatible comparison with the field data. Any difference between LINs_EPint simulations of different pull-out force is attributed to the engagement of plasticity in the interface elements, implying either sliding or uplift of the foundation relative to the soil.

Figure 7.16 illustrates that, unlike the PBr_W free vibration experiments of small pull-out force (PBr_W_2.03kN), the PBr_W_13.90kN experiment cannot be represented by the fixed-base approximation. As discussed in Sections 6.2.5and 6.2.7, nonlinear effects, associated with interface and soil nonlinearity, had a more pronounced impact on the response during the PBr_W_13.90kN experiment than the PBr_W_2.03kN one. Soil nonlinearity and soil compliance were more significant during the free vibration experiments on the FBr_2Ts structure (Figure 7.17), which justifies the inability of the FxB model to approach the experimental results. The same applies to the free vibration experiments of the FBr_1Ts structure, which were not physically carried out. Figure 7.18 illustrates that, for this structural configuration, the predominant frequency predicted by the FxB approximation (12Hz) is far from the target in-plane (North-South) natural frequency of system, which was found to be between 3.25Hz to 3.50Hz (see Table 6.11).

The FxB analyses are compared with LINs_ELint and LINs_EPint analyses, aiming to evaluate the impact of soil compliance numerically. The impact of soil compliance can be demonstrated by the shift of the natural period predicted by the LINs in comparison with FxB analyses. As already discussed, the impact of soil compliance is weak on the PBr_W free vibration simulations (Figure 7.16), while it is very significant on the response of the FBr_2Ts (Figure 7.17) and FBr_1Ts (Figure 7.18) simulations. When elastic interface elements are used, relative displacements between the foundation and the soil are essentially restricted due to the high stiffness of interface elements (K_s=K_n=1E8kN/m^3). Relative displacements can take place when elastoplastic interface elements of the same elastic stiffness are used, under the stress conditions described in Section 7.7.2. The figures, though, illustrate that the results of LINs_ELint and LINs_EPint analyses coincide, irrespective of the amplitude of the pull-out force. This observation indicates that the plasticity of the interface elements was not triggered during any of the simulations, hence not gapping or sliding took place.

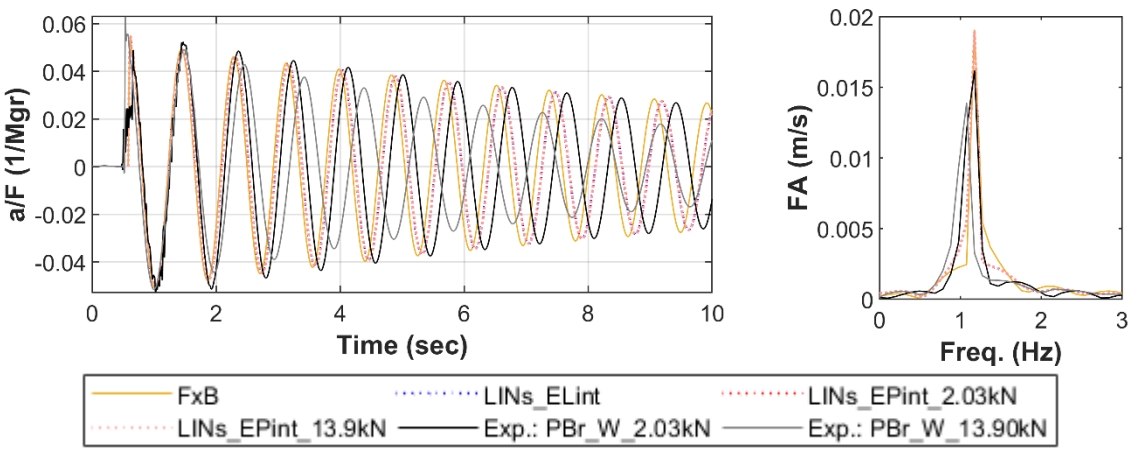


Figure 7.16: Simulations of free vibration tests on the PBr_W structure, demonstrating the impact of soil compliance and interface modelling without initial gaps on the horizontal top slab response, at the position of the 2.5 instrument.

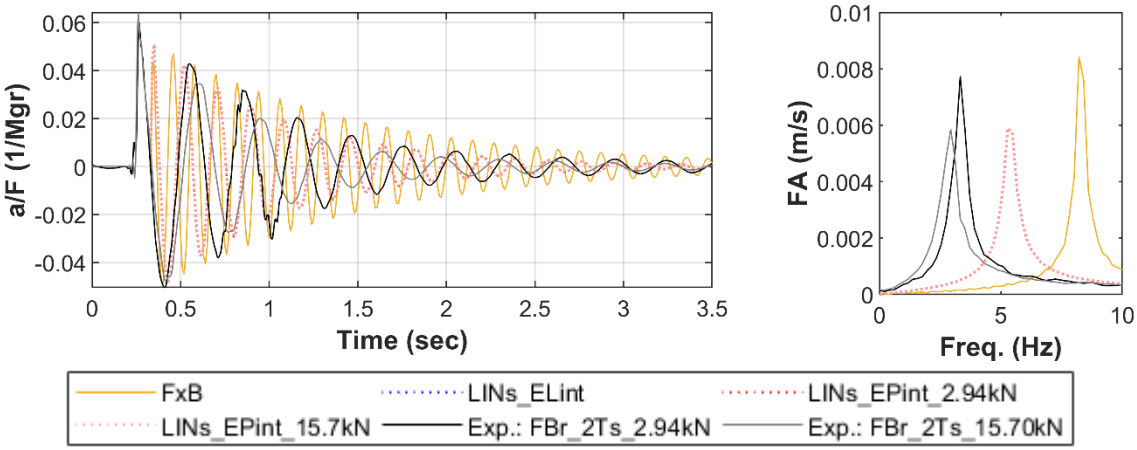


Figure 7.17: Simulations of free vibration tests on the FBr_2Ts structure, demonstrating the impact of soil compliance and interface modelling without initial gaps on the horizontal top slab response, at the position of the 2.5 instrument.

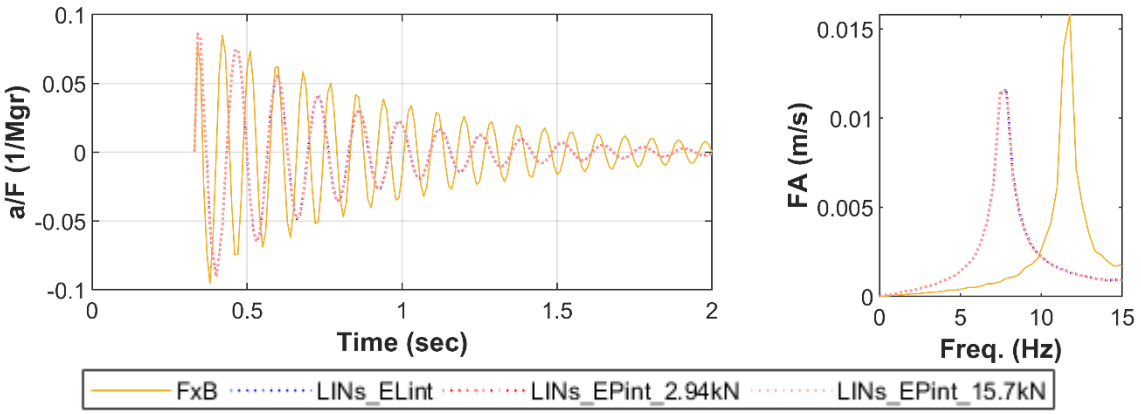


Figure 7.18: Simulations of free vibration tests on the FBr_1Ts structure, demonstrating the impact of soil compliance and interface modelling without initial gaps on the horizontal top slab response, at the position of the 2.1 instrument.

The above analyses demonstrate the need of simulating the soil domain in the majority of the free vibration tests. They also demonstrate that the elastoplastic interface model adopted is not sufficient to model gapping and sliding of the foundation, which can partly justify why the numerical simulations do not replicate the experimental data.

7.11.2 Forced Vibration

The same numerical models (FxB, LINs_ELint, LINs_EPint) are used to simulate forced vibration experiments. The response of the SSI system is examined in terms of time histories and Fourier spectra. Given that the response frequency is prescribed by the input excitation, the above plots are used to compare the motion amplitudes between numerical and experimental results. The top slab response is represented through the motion of a centre node at the position of the 2.5 instrument, while the foundation motion is expressed through the 1.1 foundation edge instrument. The soil motion is represented through the 0.1 instrument which is located 1.2m far from the foundation edge. When the above instruments were not available during an examined experiment, which was the case for the FBr_1Ts experiments, the 2.1, 1.2 and 0.2 (2.9m far from the foundation edge) instruments were used. The configuration of the instruments can be found in Figures 5.16 and 5.17.

Figures 7.19, 7.20 and 7.21 present the SSI response predicted by simulations of the PBr_W_mD_2Hz, FBr_2Ts_mD_5Hz and FBr_1Ts_mC_5Hz forced vibration experiments (Table 7.1), respectively. In all simulations the top slab response is very well predicted by the numerical models, as this response was prescribed by the input excitation. The simulations underpredict the foundation motion, especially the vertical component (z), while they highly overestimate the soil response. The latter observations are more pronounced on the simulations of FBr_2Ts_mD_5Hz (Figure 7.20Figure 7.21) and FBr_1Ts_mC_5Hz (Figure 7.21) experiments, which exhibited stronger SSI effects and foundation

motion. Also, similar to free vibration analyses, forced vibration analyses did not trigger plasticity of the interface elements (neither sliding nor uplifting), as indicated by the same results produced by LINs_EPint and LINs_ELint analyses.

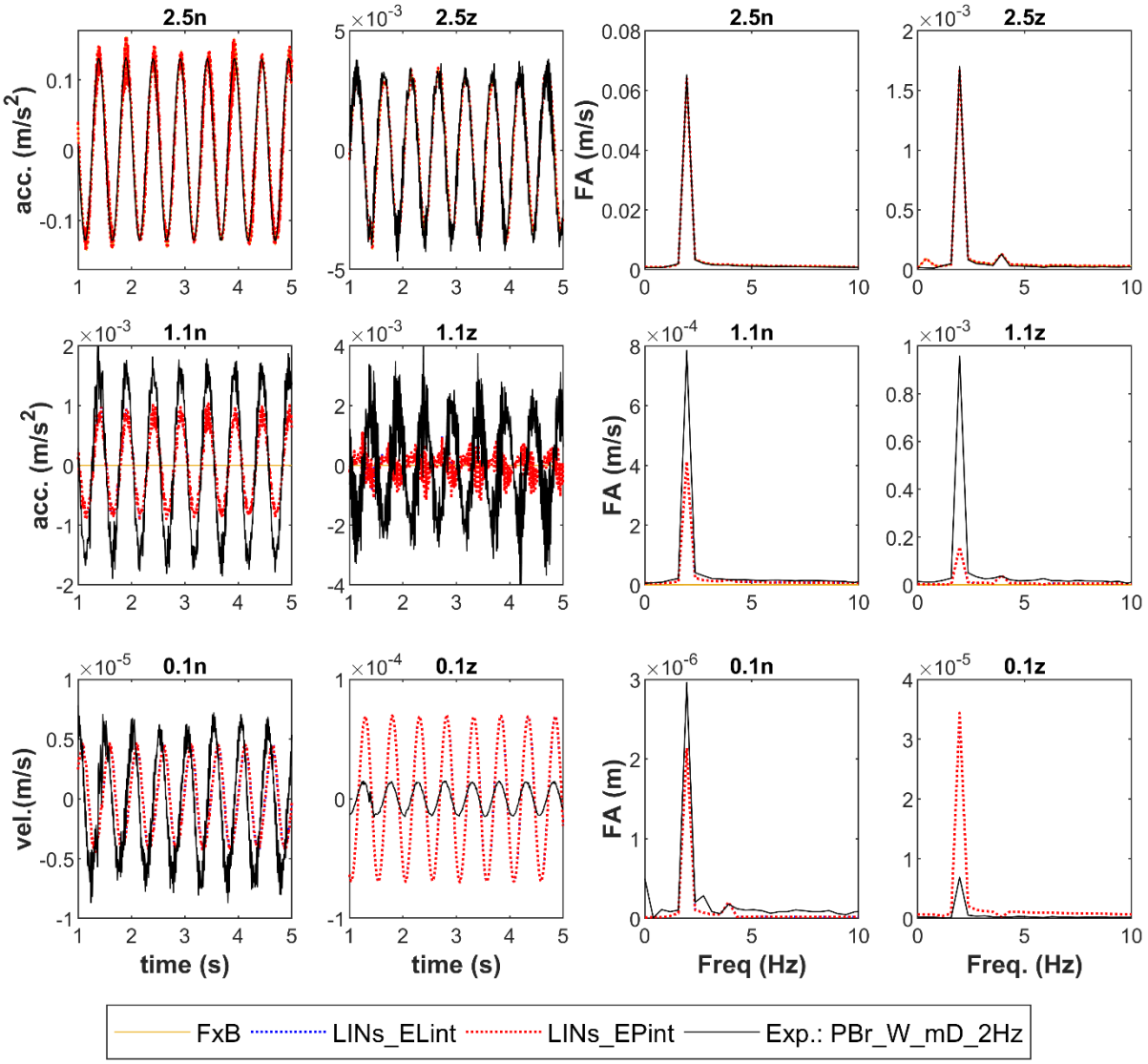


Figure 7.19: Simulations of the PBr_W_mD_2Hz forced vibration test, demonstrating the impact of soil compliance and interface modelling without initial gaps on the SSI response.

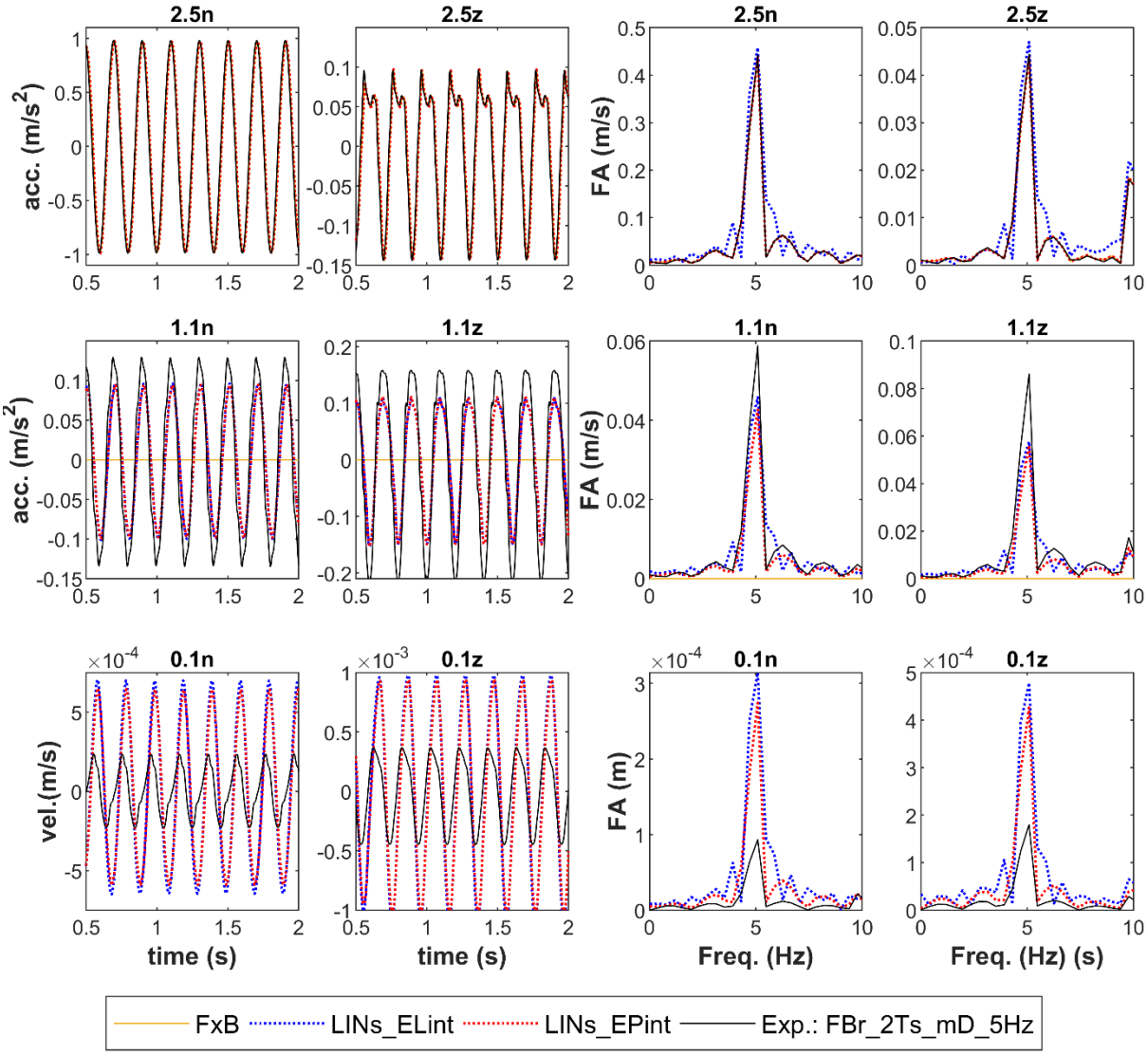


Figure 7.20: Simulations of the FBr_2Ts_mD_5Hz forced vibration test, demonstrating the impact of soil compliance and interface modelling without initial gaps on the SSI response.

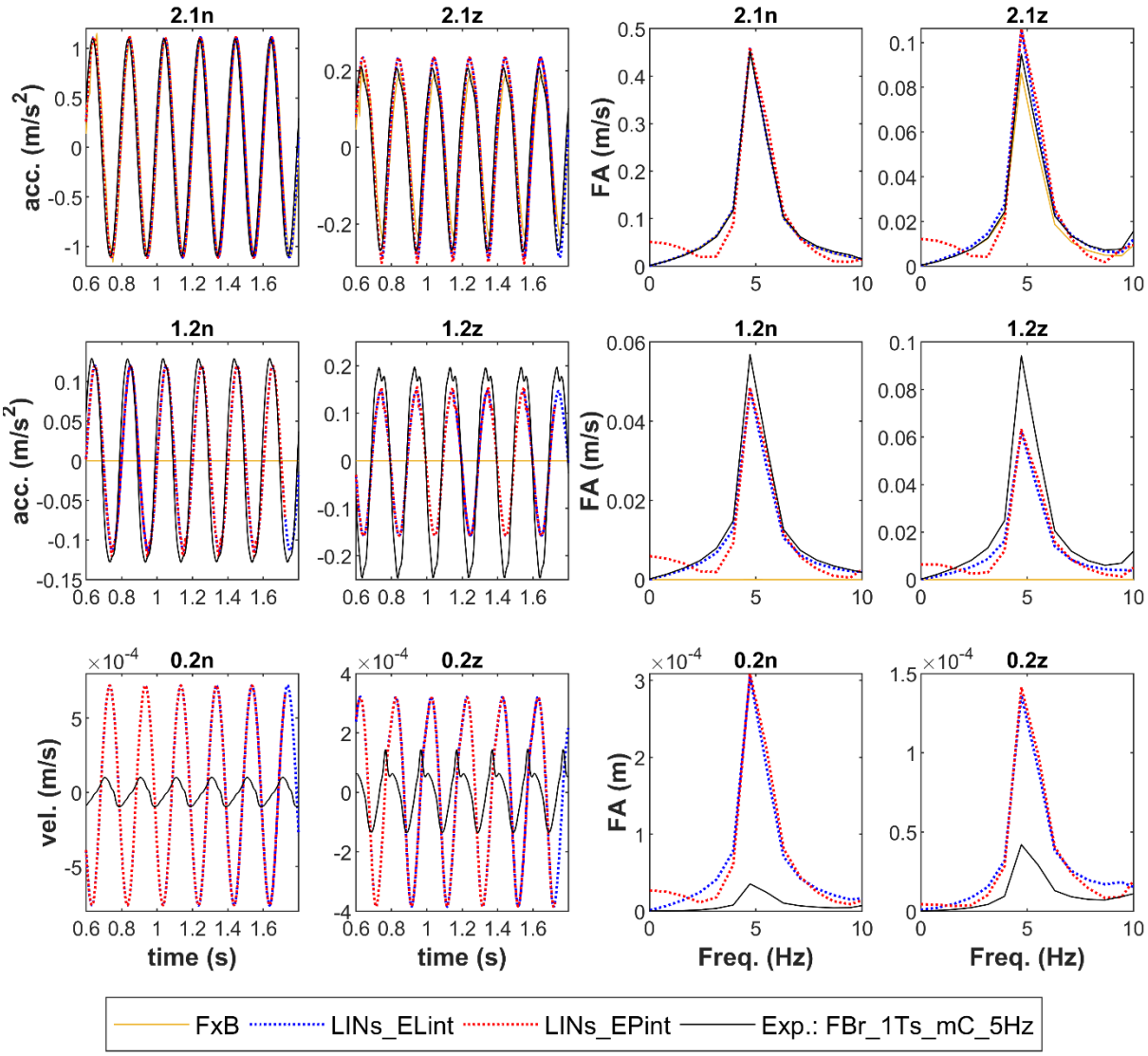


Figure 7.21: Simulations of the FBr_1Ts_mC_5Hz forced vibration test, demonstrating the impact of soil compliance and interface modelling without initial gaps on the SSI response.

7.11.3 Discussion and next calibration step

The interface models that were discussed above consisted of stiff interface elements (K_s=K_n=1E8kN/m^3) that either behave elastically or elastoplastically. These models simulate full contact conditions between the foundation and the soil, under static conditions. The elastoplasticity was incorporated to allow foundation uplift and sliding relative to the soil, however, none of these were engaged during the analyses. The inability of the interface model to simulate such conditions, that existed during the experiments, can partly explain the difference between numerical and experimental results. The second reason is the nonlinear behaviour of soil, which was neglected in the above analyses.

Free vibration results are expected to be equally affected by soil nonlinearity and the interface model, as both affect the stiffness and hence the natural frequency of the SSI system. For the reasons explained in Section 7.8.1, the forced vibration response is not very sensitive to soil nonlinearity. This can justify that, despite the simplified assumptions made, the models can sufficiently replicate the forced vibration structural response (Figures 7.19, 7.20 and 7.21). The soil response is not well captured due to the inadequacy of the interface model to represent the experimental conditions. Following the above reasoning, the soil foundation interface model is subsequently calibrated against forced vibration tests, aiming to capture better the soil response.

7.12 Calibration of interface gaps

During the experiments and prior to the application of the excitation force, gaps between the foundation and the soil were visually inspected. These gaps are modelled either through the formulation of elastoplastic model (EPint_*g*mm) or by the means of low stiffness elastic interface elements (LSELint), as described in Sections 7.7.4 and 7.7.5 respectively. Herein, the initial opening, *g*, which are modelled in EPint_*g*mm analyses, as well as the gap configuration are calibrated. The impact of the three gap configurations, presented in Figure 7.9, is investigated. The interface model is calibrated against forced vibration tests, while it is subsequently verified against free vibration tests. Aiming to isolate the impact of interface imperfections, the soil is assumed as linear elastic.

7.12.1 Forced vibration simulations: Elastic interface elements

The forced vibration simulations presented herein incorporate elastic interface elements at the soil-foundation interface, while gaps are modelled by the means of low stiffness interface elements (LSELint), as described in Section 7.7.5. LSELint analyses are less computationally expensive than EPint_*g*mm analyses, facilitating parametric investigations. A parametric investigation is carried out to investigate the applicability of the three examined gap configurations (GC1, GC2 and Gc3) shown in Figure 7.9.

Figures 7.22, 7.23 and 7.24 present the top slab (2.5/2.1), foundation (1.1/1.2) and soil (0.1/0.2) response as predicted by analyses that simulate the PBr_W_mD_2Hz, FBr_2Ts_mD_5Hz and FBr_1Ts_mC_5Hz forced vibration experiments, respectively. Each figure compares results from analyses in which different initial contact conditions were incorporated. The figures demonstrate that the vertical foundation motion (rocking) and the soil response are significantly affected by the initial contact conditions. As it can be seen, the existence of gaps at the foundation edge (i.e. GC1, GC2) accentuate foundation rocking and the decrease of both the NS and EW soil motion components. These features are more pronounced when the non-contact area is larger below the foundation edge

(e.g. GC2). On the contrary, when the gap area is modelled at an inner part of the interface, which is the case for the GC3, the gaps do not affect the response. This is illustrated by the fact that in simulated experiments, the analyses with the GC3 gap configuration produce the same results as the analyses without gaps. The impacts of interface gaps are more significant on simulations where the structure is stiff and the foundation is prone to rotate. These are the FBr_2Ts and FBr_1Ts forced vibration simulations of which results were more affected by the existence of gaps (Figure 7.23, Figure 7.24), relative to the PBr_W simulations (Figure 7.22).

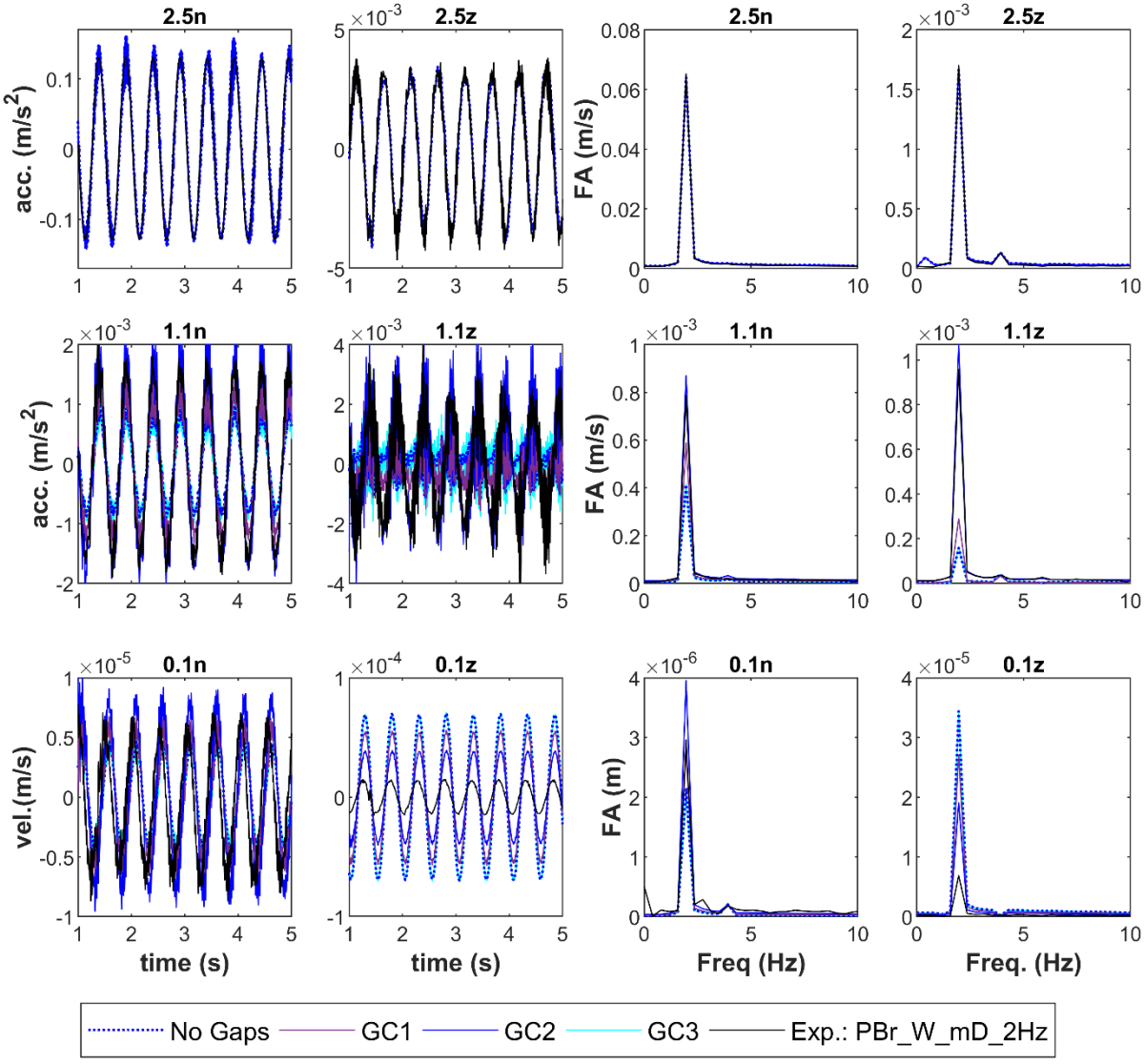


Figure 7.22: Simulations of the PBr_W_mD_2Hz forced vibration test, investigating the impact of interface gaps on the SSI response. Analyses are linear elastic, while gaps are simulated through LSELint.

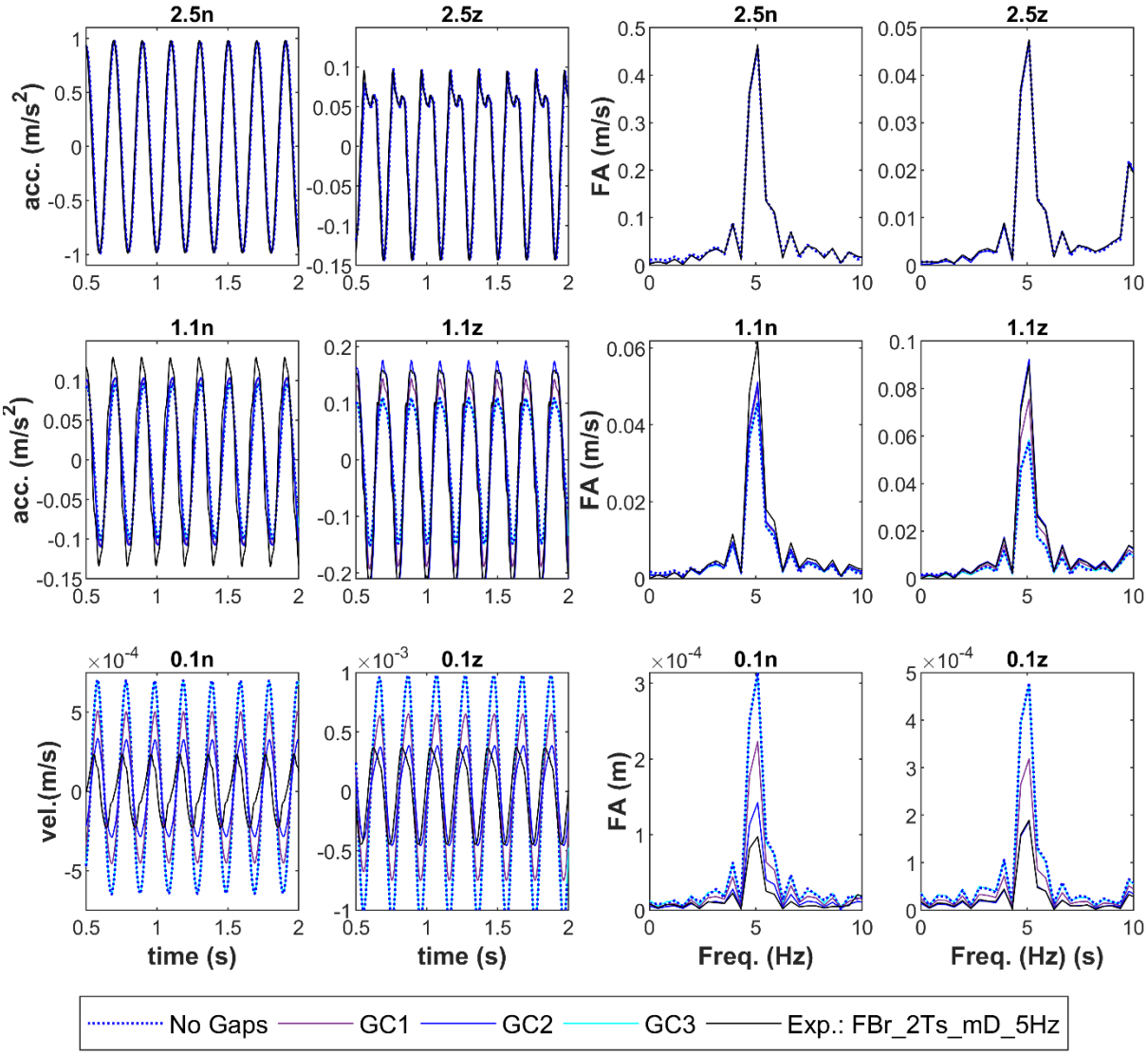


Figure 7.23: Simulations of the FBr_2Ts_mD_5Hz forced vibration test, investigating the impact of interface gaps on the SSI response. Analyses are linear elastic, while gaps are simulated through LSELint.

All simulated forced vibration experiments are better replicated by the numerical models that incorporate the gap configuration GC2. Figure 7.24 shows that the soil motion of the fully braced 1-top slab experiment is overestimated by the GC2 numerical model. The latter observation implies that this simulation should allow more gapping between the foundation and the soil than the modelled one. This aligns with the conclusions made in Section 6.3.8, that the FBr_1Ts structure exhibited stronger foundation uplift than the FBr_2Ts and PBr structures. However, these interface conditions could not be modelled by the adopted LSELint interface model, which restricts opening and closure of interface elements in addition to the permanently open ones. This limitation of the interface model as well as the omission of the nonlinear soil behaviour can justify the overestimation of the soil motion by the simulations of the FBr_1Ts experiments.

Having isolated the effect of gaps, the GC2 gap configuration was found to be the most appropriate among the examined configurations. The applicability of the GC2 is subsequently examined against forced and free vibration tests where soil nonlinearity is incorporated.

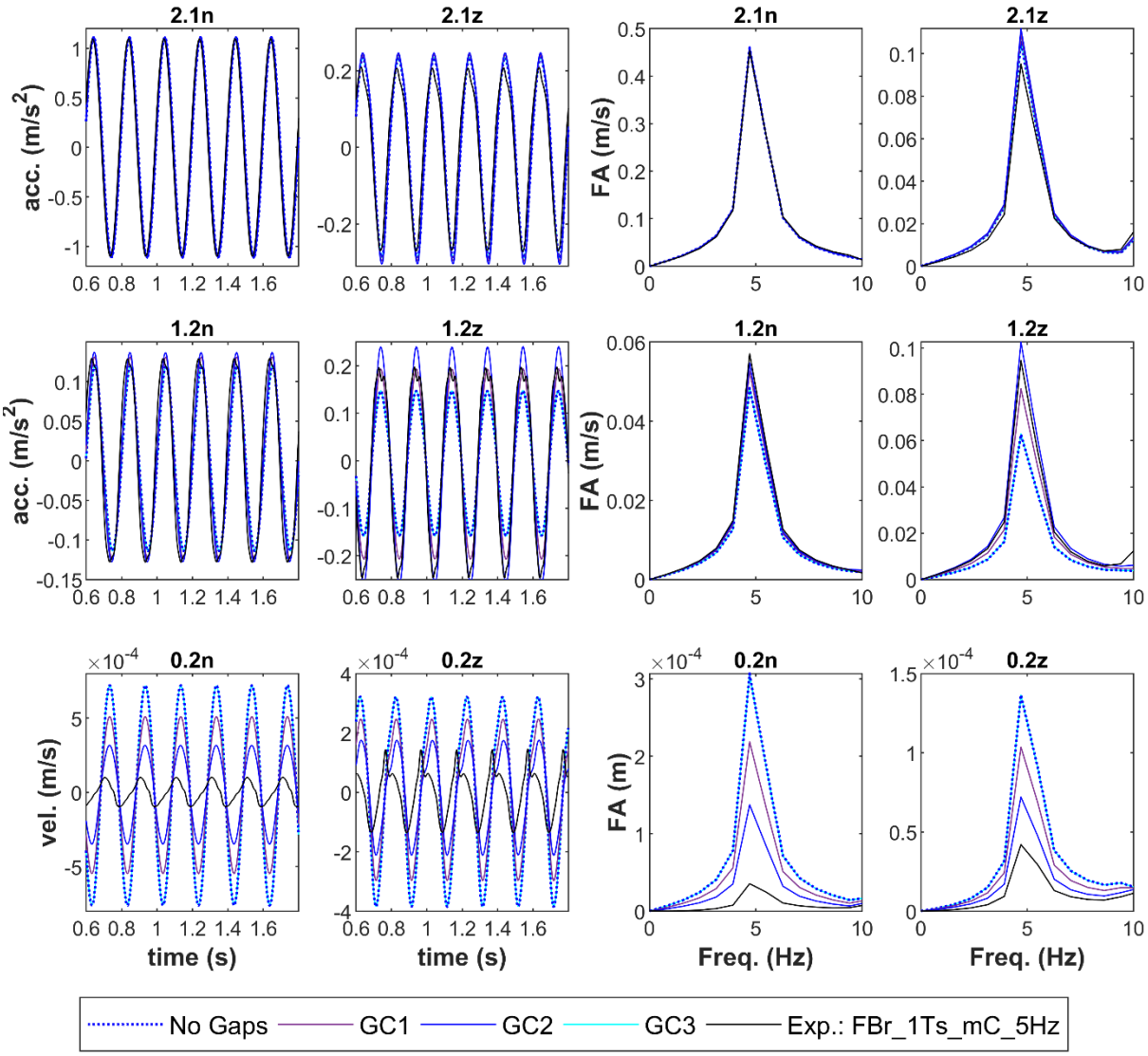


Figure 7.24: Simulations of the FBr_1Ts_mC_5Hz forced vibration test, investigating the impact of interface gaps on the SSI response. Analyses are linear elastic, while gaps are simulated through LSELint.

7.12.2 Forced vibration simulations: Elastoplastic interface elements

The forced vibration simulations presented herein incorporate elastoplastic interface elements at the soil-foundation interface. Interface gaps are modelled through the formulation of the plasticity model as described in Section 7.7.4. Herein, these analyses are referred to as EPint_*g*mm, where *g* is the amount of opening. Unlike the LSELint analyses presented earlier, which simulate permanently open elements, EPint_*g*mm analyses can simulate opening and closure of the elements rigorously. A second advantage of these analyses is that they allow the opening of more elements in addition to those that are prescribed as initially opened. This interface model, though, requires the calibration of the initial

opening value. As explained in Section 7.7.4, this is equivalent to the initial value prescribed for the hardening parameter of the adopted plasticity model that correspond to the normal plastic strain (ε_{pl}).

The aim of the presented analyses is to calibrate the initial opening, as well as to examine the applicability of this interface model. The analyses model the gap configuration GC2 (Figure 7.9), which was earlier found to be the one, amongst the examined configurations, that produces numerical results closer to the experimental ones. All initially open interface elements are prescribed prior to the forced vibration with an initial opening of ε_{pl}=*g*mm, while the examined values of *g* are defined in Table 7.9.

A limitation of this approach is that the opening and closure of the interface elements can produce high frequency noise in the numerical results. This is illustrated in Figure 7.25 which plots foundation and soil motions, at the positions of 1.2 and 0.2 instruments, produced by an analysis that simulates the Fbr_1Ts_mC_5Hz forced vibration experiment. The analysis incorporates elastoplastic interface elements, with the initially open ones being prescribed with an initial gap of *g*=0.1mm (EPint_0.1mm). As Figure 7.25 shows, the high frequency noise is more prominent in the foundation horizontal and vertical motions (1.2n, 1.2z), while it is also apparent in the foundation horizontal and soil motions (0.2n and 0.2z). The high frequency content can be also identified through Figure 7.26 that presents the Fourier spectra inferred from the time histories presented in Figure 7.25. The figure illustrates motion amplification at large frequencies, while reasonable motion is predicted at low frequencies, as shown by the zoom-in figures. The high frequency noise, that results from EPint_*g*mm analyses, does not exist in experimental data and cannot be physically explained. Although not shown here, the corresponding displacement time histories do not include high frequency noise.

As it is well established in the literature (Kontoe *et al.*, 2008; Bo Han *et al.*, 2015; Tsaparli *et al.*, 2017) the spurious high frequency content is a result of poor spatial discretization that does not allow the accurate representation of high frequency modes. As shown in the above studies and discussed in Section 7.5.1, numerical damping is able to dissipate high frequency modes without affecting low to medium frequency modes by prescribing a lower value to the spectral radius at infinity (ρ_∞). Although this method could rigorously reduce high frequency noise in the motions, a common ρ_∞ is preferred for all analyses for compatibility reasons. An alternative way to eliminate spurious high frequency noise is by applying a filter to the output motion. Provided that filtering does not affect the frequency range of interest, filtering is considered applicable. Herein, the high frequencies are eliminated by applying to the motion time series a 4^{th} order Butterworth bandpass filter of 0.2Hz and 30Hz lower and higher cut-off frequencies, respectively. As Figure 7.25 and Figure 7.26 show, this filter is effective in eliminating the high frequency peaks from raw numerical data. The same filter is applied to all presented results produced by EPint_*g*mm analyses.

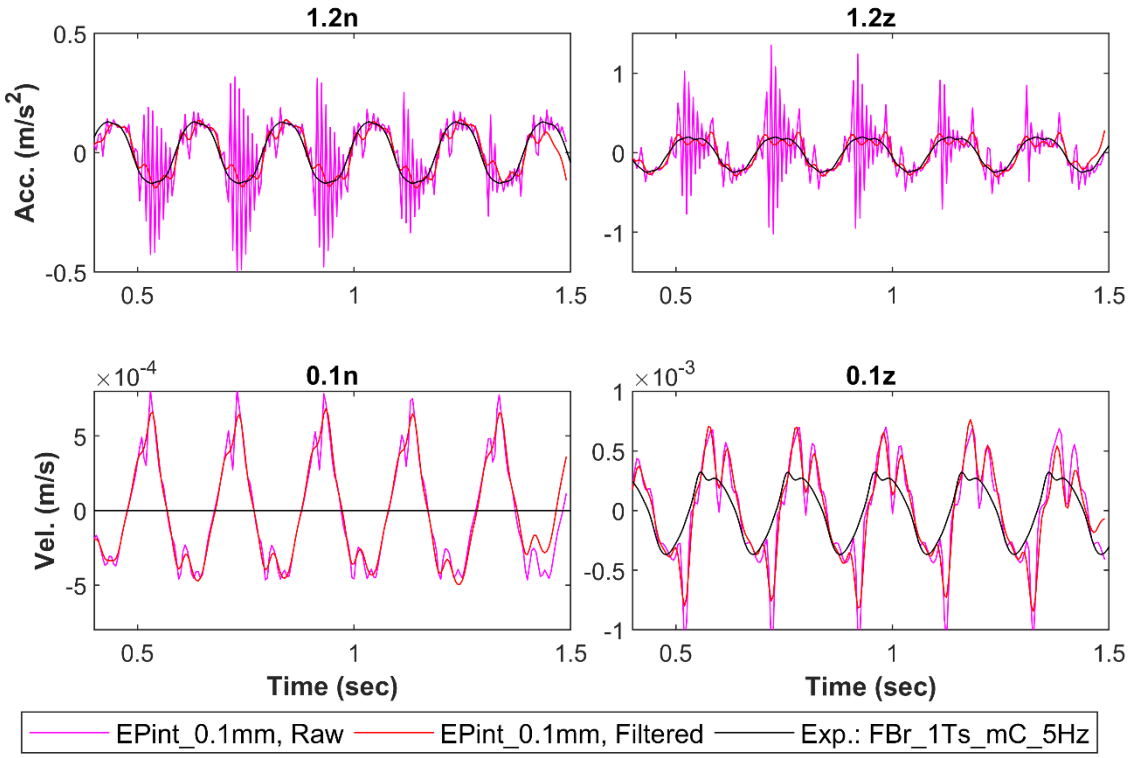


Figure 7.25: Illustration of the existence of high frequency content in foundation (1.2) and soil (0.2) time history motions and the effectiveness of filtering. The results are produced by FBr_1Ts_mC_5Hz forced vibration simulations of *g*=0.1mm initial opening.

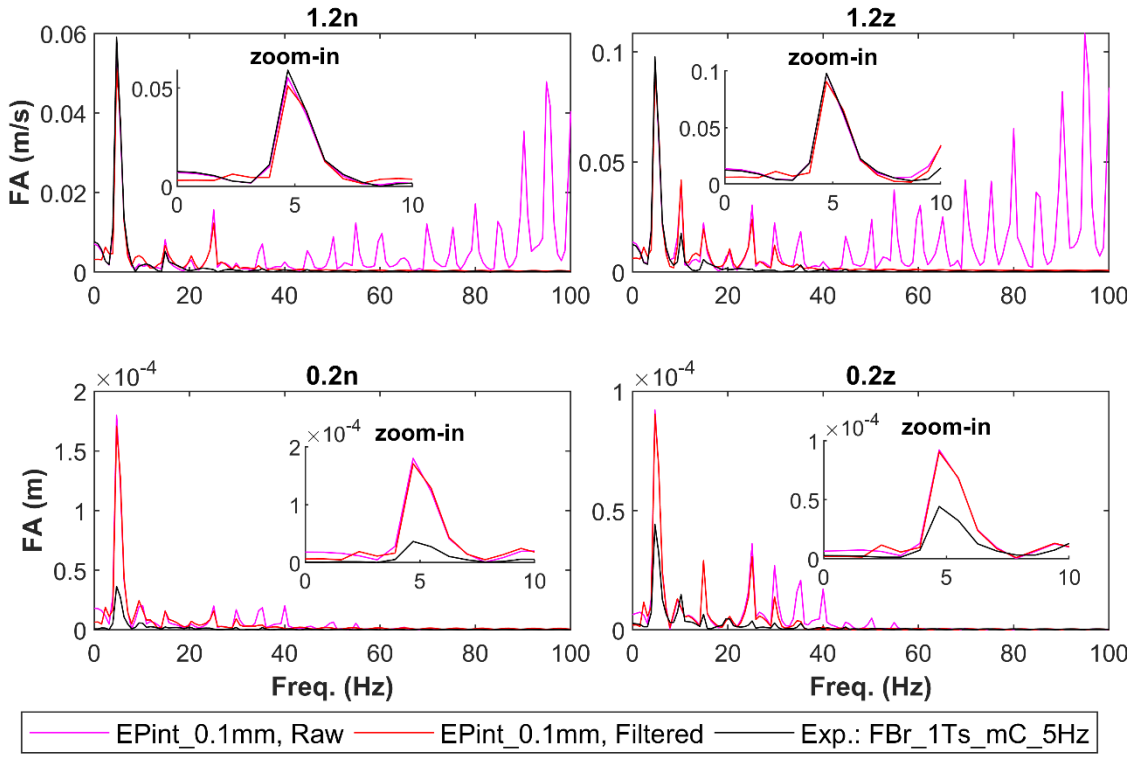


Figure 7.26: Illustration of the existence of high frequency content in Fourier amplitude spectra that are inferred from foundation (1.2) and soil (0.2) motions and the effectiveness of filtering. The results are produced by FBr_1Ts_mC_5Hz forced vibration simulations of *g*=0.1mm initial opening.

Due to the existence of high frequency noise, the response of the SSI systems computed by analyses, that simulate gaps through the plasticity model (EPint_*g*mm), is investigated by the means of Fourier spectra. Figure 7.27 and Figure 7.28 illustrate the impact of the opening values prescribed at the initially open interface elements on the results produced by the simulations of the FBr_2Ts_mD_5Hz and FBr_1Ts_mC_5Hz forced vibration experiments, respectively.

The existence of an initial opening at the interface has the same impacts as when the gaps are simulated via low stiffness interface elements, as presented in Section 7.12.1. These impacts, also referred to as gapping effects, are the increase of foundation and decrease of soil motions relative to the analysis where gaps are not simulated. The latter features are observed in Figure 7.27 and Figure 7.28 even for the smallest initial opening examined. This observation demonstrates that even a very small initial opening can produce opening and closure of interface elements during an excitation. Smaller prescribed initial opening results to a smaller permanently open interface area, while it leads to a larger area of interface elements that close and open at different increments during the excitation. The smaller non-contact interface area, that is predicted by analyses with small initial opening, e.g. EPint_0.1mm, weakens the effects of gapping. When the non-contact area increases, the gapping effects become more pronounced, as it is demonstrated by analyses that prescribe larger initial opening. The increase of the initial opening results in numerical response that approaches the one produced by the ELint_GC2 analysis. This is attributed to the fact that when initially open interface elements are prescribed with a large magnitude of gap, the elements never close, which is the case modelled by ELint_GC2 analysis.

The analyses with elastoplastic interface elements that produce results similar to the corresponding ELint_GC2 analysis are the EPint_0.2mm (Figure 7.27) and EPint_0.5mm (Figure 7.28) for the two and one top slab simulations respectively. The simulations of the 1-top slab forced vibration tests require larger amount of initial opening than the 2-top slab simulations to achieve zero closure of the initially open interface elements. This can be explained by the fact that, under the same loading, the lighter structure exhibits larger displacements and stronger foundation rocking than the heavier one, evidenced also by experimental data presented in Figure 6.45. Further numerical evidence of the latter is given by Figure 7.29. The figure plots the contours of normal plastic strains ε_{pl} (opening) of interface elements as computed by EPint_0.2mm analyses which simulate forced vibration experiments on the two structural configurations. The black contours indicate close interface elements (ε_{pl}=0m). The contours presented correspond to the increment when the top slab displacement was maximum towards the positive x-axis, with reference to the coordinate system shown in the figure. At this increment, the opening is expected to be the smallest at the positive x-axis and the largest at the negative x-axis of the foundation edge.

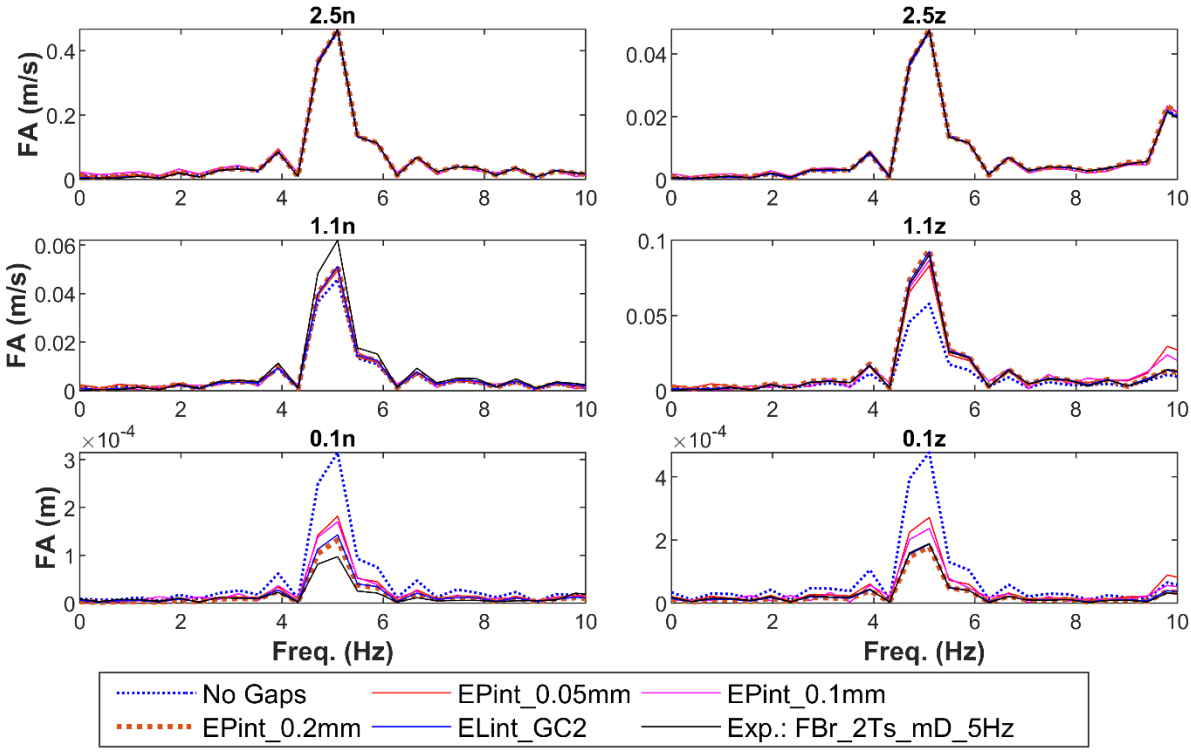


Figure 7.27: Impact of the initial opening, prescribed at the initially open interface elements, on the results of the FBr_2Ts_mD_5Hz forced vibration simulation, assuming linear elastic soil.

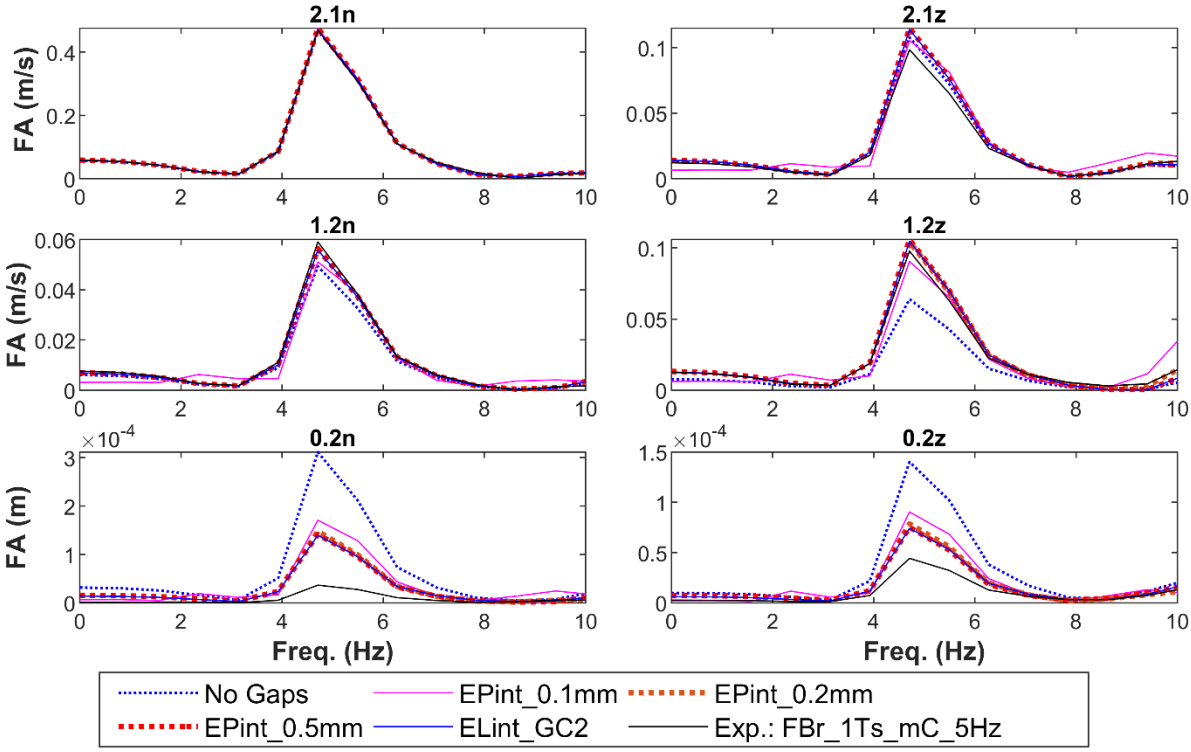
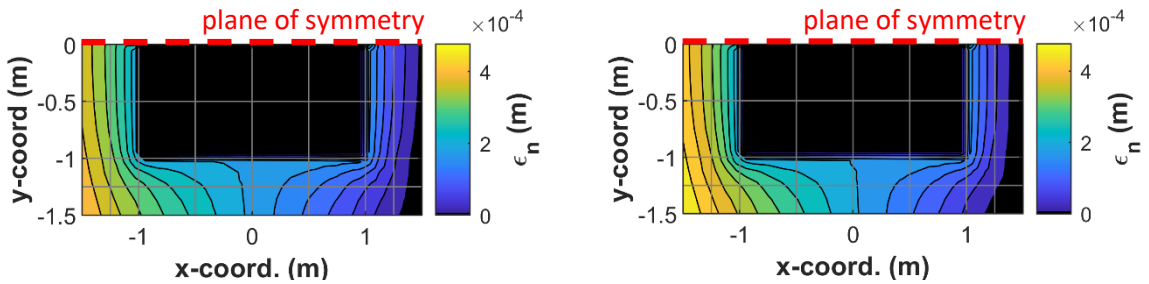


Figure 7.28: Impact of the initial opening, prescribed at the initially open interface elements, on the results of the FBr_1Ts_mC_5Hz forced vibration simulation, assuming linear elastic soil.

Figure 7.29a shows that the simulation of experiment on the 2-top slab structure exhibited almost zero closure of the interface elements that were initially prescribed as open. On the contrary, the FBr_1Ts simulation predicted closure of interface elements over a significant area of the foundation edge at the positive x-axis (Figure 7.29b). Likewise, the detachment between the soil and the foundation edge at the negative x-axis was larger for the FBr_1Ts simulation than the FBr_2Ts. These observations imply that during the FBr_1Ts simulation, the interface elements at the foundation edges, at x=-1.5m and x=1.5m, exhibited stronger opening and closure at different increments. This is a consequence of larger foundation rocking that took place during the former FBr_1Ts simulation than the FBr_2Ts one. It is noted that the magnitude of the load applied on the structure during the FBr_1T_mC_5Hz simulation is much smaller than the one applied during the FBr_2T_mD_5Hz simulations. The two simulations applied forces that correspond to the mC and mD vibratory loads, respectively, according to Figure 5.12. It becomes apparent, that the difference in the contact conditions between the vibrations of the FBr_2Ts and FBr_1Ts structures would be much more pronounced when a compatible load was applied. It is therefore verified that the lighter structure is more prone to rotate at the foundation level than the heavier structure.

Figure 7.29 also demonstrates that in both simulations, the initially close interface elements, which can be seen in Figure 7.9b, did not open at the certain increment. Although not shown here, they did not open at any increment during the analysis, disclosing a possible limitation of the current interface model, which is addressed subsequently in Section 7.14. Among the presented numerical analyses that employ the EPint_*g*mm interface model, the ones which simulate the largest opening between the foundation and the soil produced results the closest to experimental data. These analyses give very similar results with the ones that simulate gaps through elastic interface elements (ELint_GC2). ELint_GC2 interface model is more time effective than EPint_*g*mm, hence it is adopted for the majority of the following analyses presented. Its applicability on free vibration simulations is subsequently investigated.



(a) FBr_2Ts_mD_5Hz (b) FBr_1Ts_mC_5Hz

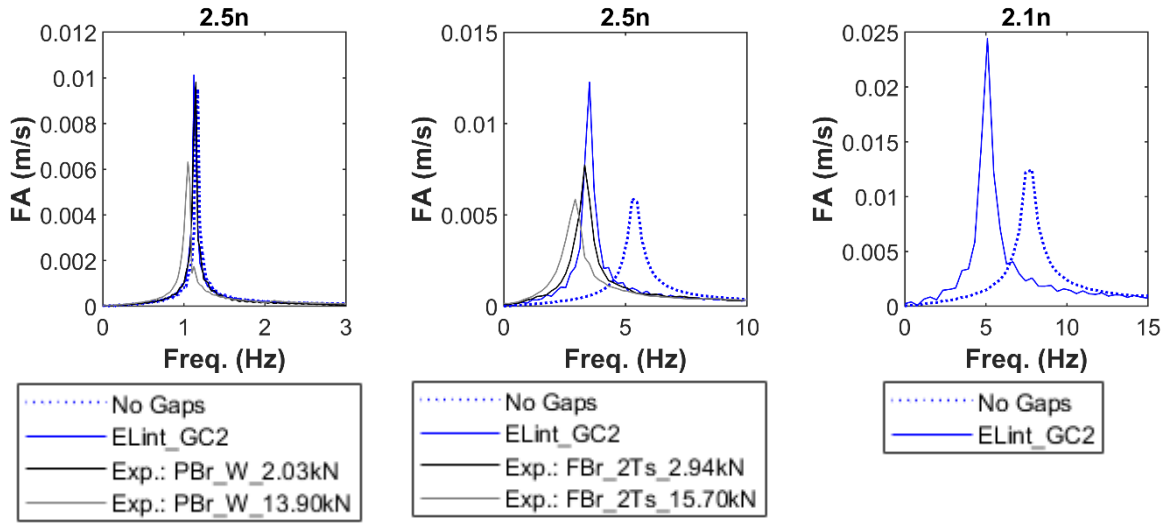
Figure 7.29: Contours of normal plastic strains (opening) of interface elements computed at an increment when the top slab displacement was the maximum towards the positive x-axis. Results from EPint_0.2mm forced vibration simulations of the (a) FBr_2Ts_mD_5Hz and (b) FBr_1Ts_mC_5Hz experiments are shown. Black contours indicate closed interface elements (ε_{pl}=0m).

7.12.3 Free vibration tests

Free vibration analyses which simulate the soil as linear elastic are presented. The first aim of the analyses is to assess the applicability of the linear soil assumption. The second aim is to establish the impact of gaps at the interface between the foundation and soil on the free vibration response of the PBr_W, FBr_2TS and PBr_1Ts structural configurations. The gap configuration GC2 (Figure 7.9b) is modelled, which, among the examined configurations, was earlier found to be the most appropriate for the forced vibration tests (7.12.1). The interface gaps are simulated through the more computationally effective low stiffness elastic interface elements, described in Section 7.7.5.

Figures 7.30, 7.31 and 7.34 present Fourier spectra inferred from the top slab, foundation and soil response, respectively. The response of the SSI system is computed by free vibration simulations on the (a) PBr_W, (b) FBr_2Ts and (c) Fbr_1Ts structural configurations. The figures compare field data, where available, with numerical results of models with and without interface gaps. The presented field data were recorded during the experiments when the structure was excited by the smallest or largest applied pull-out forces.

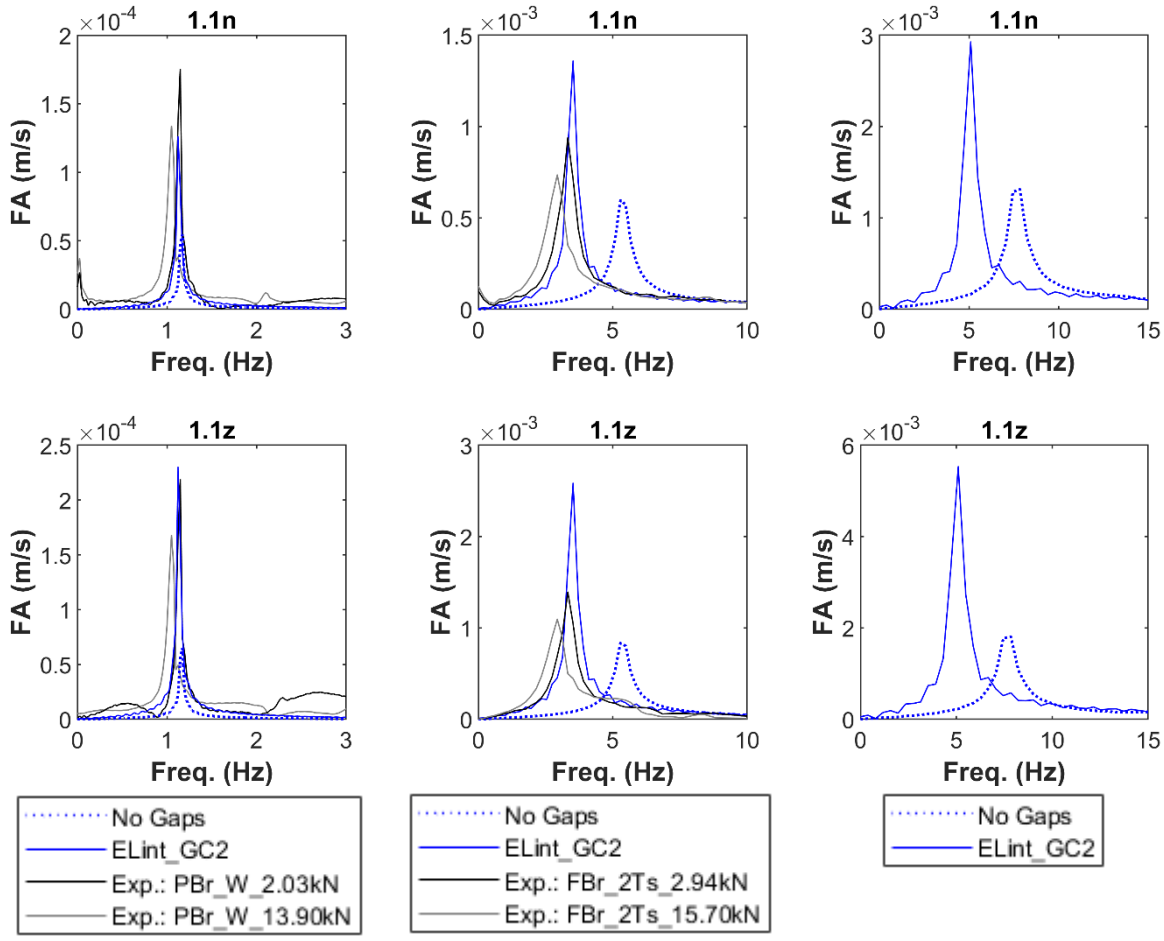
Figure 7.30a verifies that gaps do not play a significant role on the response of the partly braced experiment. Conversely, the existence of interface gaps significantly affects the natural frequency of the fully braced experiments, as demonstrated by the main peak of Figure 7.30b and c. In particular, the natural frequencies of both one and two top slab systems decrease by 35% due to the existence of interface gaps, relative to the frequency predicted by analyses that simulate perfect bonding between foundation and soil.



(a) PBr_W (b) FBr_2Ts (c) FBr_1Ts

Figure 7.30: Fourier spectra of the top slab horizontal motion (2.5n or 2.1n) computed by linear elastic free vibration analyses with and without interface gaps. Results are compared with experimental data, where available.

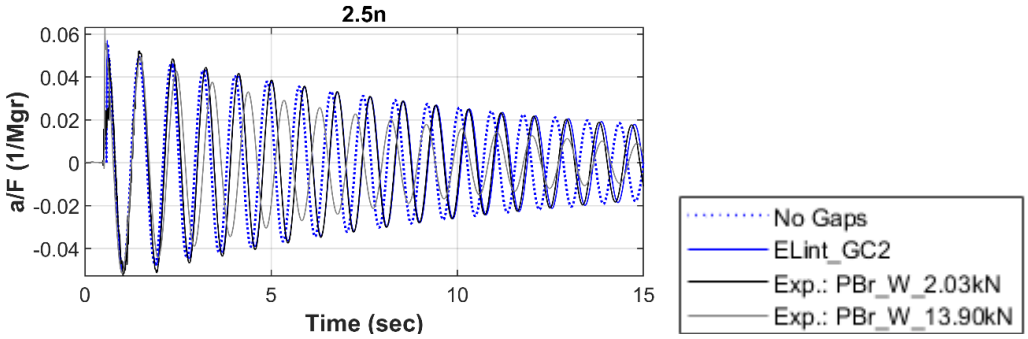
The decrease of numerical natural frequencies due to the existence of gaps can be attributed to the lower contact area at the interface. The SSI system with interface gaps below foundation edges can be equivalently simulated as an identical model with smaller foundation. This assumed foundation would be of smaller inertia, a fact that for simplicity is neglected aiming to facilitate qualitative comparisons between the present study and other studies in literature. According to Amorosi *et al.* (2017), a smaller foundation amplifies the structural motion and decreases the natural frequency of the system. This is in agreement with the current observations made from the analyses that model interface gaps. Also, Gazetas (2015) attributes the natural frequency decrease to the increase of foundation rocking that take place for smaller foundations. The latter claim is also verified by the numerical studies presented herein. Figure 7.31 demonstrates that the existence of gaps increases significantly both foundation motion components. The increase of the two components is as high as 2.5 to 4 times the motion predicted by analyses that model perfect bonding between soil and foundation.



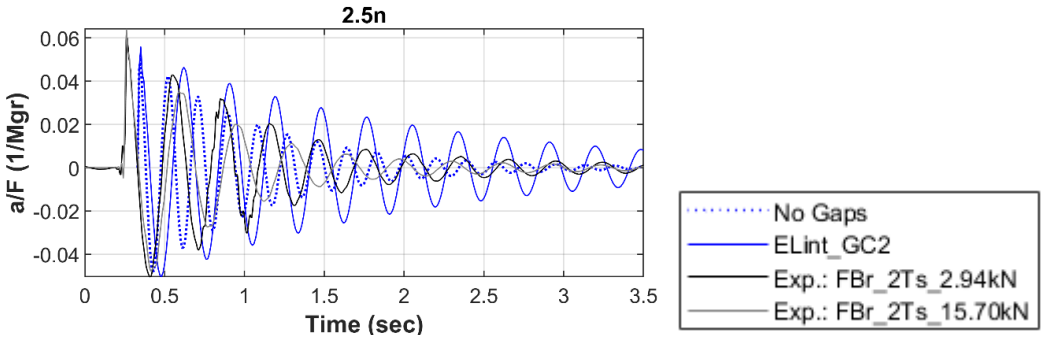
(a) PBr_W (b) FBr_2Ts (c) FBr_1Ts

Figure 7.31: Fourier spectra of the foundation horizontal and vertical motion components (1.1n, 1.1z) computed by linear elastic free vibration analyses with and without interface gaps. Results are compared with experimental data, where available.

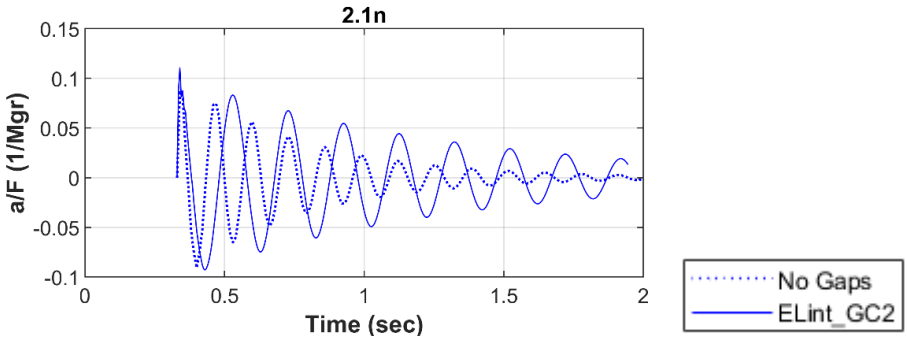
The second impact of the existence of gaps, that is demonstrated in Figures 7.30 and 7.31, is the increase of the amplitude of both top slab and foundation motions. The variation of motion amplitude with time is better depicted through time histories. Figure 7.32 presents the normalised top slab acceleration time histories resulted from the simulations of free vibration tests on (a) PBr_W, (b) FBr_2Ts and (c) FBr_1Ts structural configurations. The figure compares experimental data with numerical ones predicted by two analyses, the one of which incorporates interface gaps while the other does not. The figure shows that, for all simulated experiments, the two numerical analyses predicted the same peak top slab acceleration after the load removal. After the main peak, the results of the two analyses with different interface conditions differ both in terms of frequency content and motion amplitude, as also evidenced in Figure 7.30.



(a) PBr_W



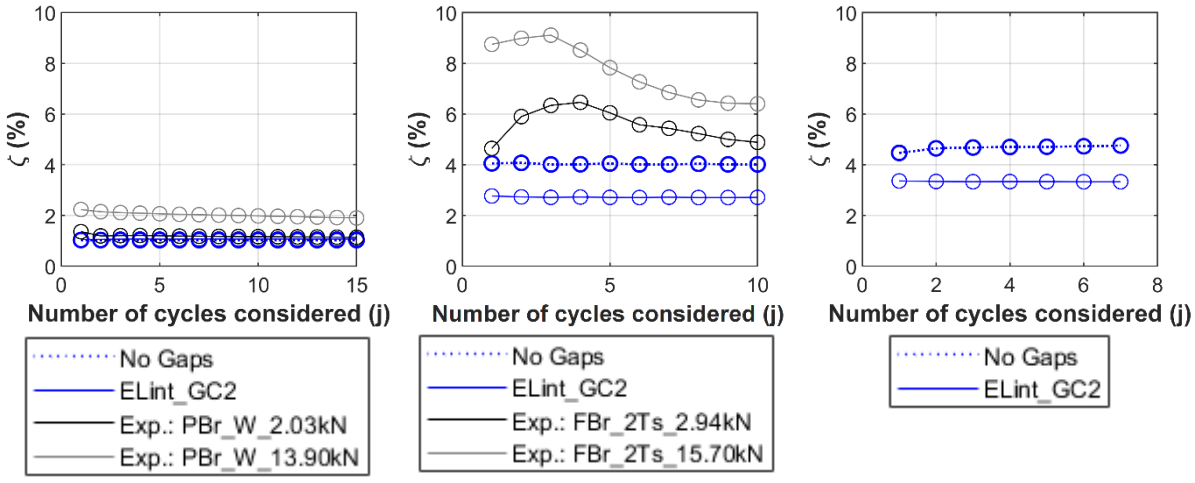
(b) FBr_2Ts



(c) FBr_1Ts

Figure 7.32: Horizontal normalised acceleration time histories of the top slab (2.5n or 2.1n) computed by linear elastic free vibration analyses with and without interface gaps. Results are compared with experimental data, where available.

Figure 7.32a shows that gaps do not affect the motion amplitude of the free vibration of the partly braced structure, which is also the case for the natural frequency, as mentioned above. Conversely, Figure 7.32b and c demonstrate that for the fully braced simulated experiments, the existence of gaps significantly declines the motion decay with time. This difference is attributed to the smaller damping developed in the analyses that do not simulate gaps, as it is evidenced in Figure 7.33. The figure presents damping values that are computed using Eq. 6.10 of the logarithmic decrement method (Chopra, 2011), that is described in Section 6.2.4. The method computes the damping ratio developed between j cycles starting from the i^{th} peak of a free vibration motion. The presented damping ratios were inferred from the time histories presented in Figure 7.32, while they were calculated for several j values and assuming i=2. Due to the linearity and elasticity of the numerical model, the decay rate is found to be constant leading to a constant damping value, irrespective of the number of cycles (j) considered in the calculations. Figure 7.33 demonstrates that the existence of interface gaps decreases the damping produced by the oscillation of the SSI system. The decrease is significant in experiments where the SSI effects and foundation motion were more pronounced, i.e. fully braced experiments, while it is negligible when the SSI effects were weak, i.e. partly braced experiments.

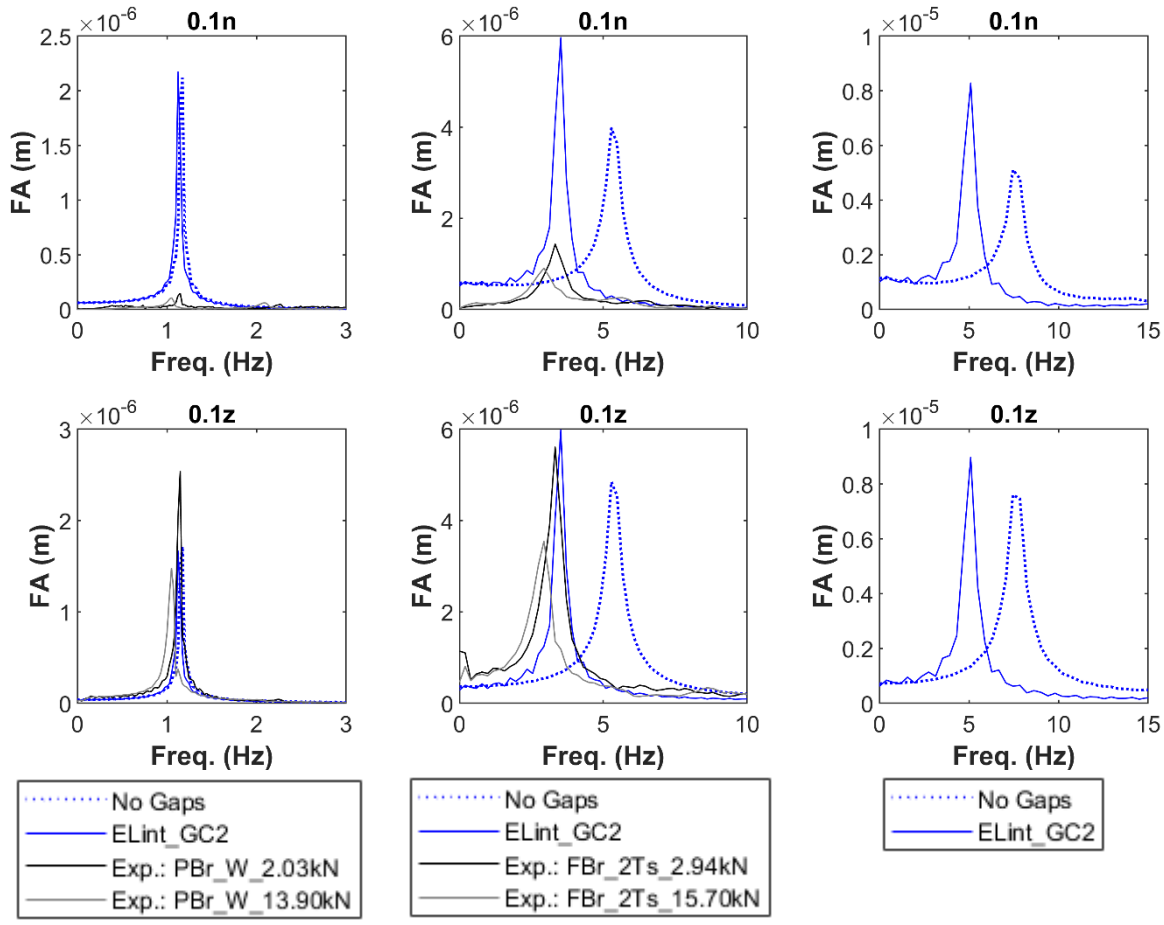


(a) PBr_W (b) FBr_2Ts (c) FBr_1Ts

Figure 7.33: Damping ratio values computed for the motions between the second peak and the next j peaks. They are inferred from experimental and numerical top slab accelerations. The numerical results are based on linear elastic free vibration analyses with and without interface gaps. Results are compared with experimental data, where available.

The observation made about the smaller damping predicted by the numerical models that simulate interface gaps is attributed to the accentuated foundation rotation. It is well established in the literature (e.g. Gazetas, 1983, 1991) that the rotational mode of foundation oscillation produces less radiation damping than the translational one. This was also verified by numerical studies carried out by Amorosi *et al.* (2017) which also suggest that foundations that are more prone to rotate, i.e. of smaller dimensions, can produce less damping than foundations of larger dimensions.

The smaller radiation damping produced by the numerical analyses that incorporate interface gaps is indicated by the weaker soil response. Figure 7.34 shows that the soil motion predicted by analyses with interface gaps is larger than the motion predicted by analyses without gaps. This should not be interpreted as soil motion amplification due to gaps, instead it is a consequence of the larger foundation motion shown in Figure 7.31. The impact of gaps on the soil response can be isolated by looking the transfer functions (TF) of the soil to foundation motion ratio, as defined in Eq. 6.16. The TF is defined as the amplitude of the main peak of the Fourier spectrum inferred from soil velocities to the corresponding amplitude of the spectrum inferred from foundation velocities. Each TF value essentially corresponds to the motion de/amplification from foundation to soil at the fundamental frequency. Table 7.11 presents transfer function values of the examined experiments, showing smaller TF values for analyses that simulate interface gaps. The latter implies that the existence of gaps decreases the percentage of motion that is transferred from the foundation to the soil. This is in agreement with the observation made from forced vibration analyses, which also showed that gaps decreases the soil motion (see Figures 7.22, 7.23 and 7.24).



(a) PBr_W (b) FBr_2Ts (c) FBr_1Ts

Figure 7.34: Fourier spectra of horizontal and vertical soil motion components (0.1n, 0.1z) computed by linear elastic free vibration analyses with and without interface gaps. Results are compared with experimental data, where available.

Table 7.11: Transfer function T(F) values computed as Fourier amplitude ratios of soil to foundation motion (0.1/1.1). The presented values correspond to a spectral frequency equal to the fundamental frequency of the SSI system. The results are inferred from numerical analyses, with or without interface gaps, that simulate the three free vibration tests.

TF	PBr_W		FBr_2Ts		FBr_1Ts	
Ratio	No Gaps	ELint_GC2	No Gaps	ELint_GC2	No Gaps	ELint_GC2
0.1n/1.1n	0. 29	0. 12	0.22	0.10	0. 18	0. 09
0.1z/1.1z	0. 19	0. 05	0.19	0.05	0. 20	0. 05

7.12.4 Discussion and next calibration step

It was shown that the forced vibration analyses, that simulate the GC2 gap configuration (Figure 7.9b) at the soil-foundation interface, predict SSI motions close to the experimental one, when linear elastic soil is assumed. The applicability of this gap configuration should also be investigated when soil nonlinearity is incorporated in the model.

The overall stiffness of the SSI model depends on the structural properties, interface model, soil properties and constitutive model. Given that displacement-controlled forced vibration analyses prescribe the structural response, the response is not dependent on the structural stiffness. Hence, these analyses are not appropriate to investigate the correctness of the modelled stiffness of the SSI model. As the stiffness controls the fundamental frequency of the model, it was investigated by the means of free vibration simulations which reveal this frequency.

Figure 7.30 shows that the simulation of gaps decreases the stiffness of the SSI model. This is demonstrated through the decrease of the fundamental frequency relative to the one predicted by analyses that omit gaps simulation. The presented analyses that assume linear soil and simulates the GC2 gap configuration at the soil-foundation interface (ELint_GC2) are sufficient to predict the fundamental frequency of the PBr_W experiments. They are also sufficient to predict the frequency content of the FBr_2Ts structural configuration when the pull-out force was the smallest (i.e. 2.94kN). However, this model fails to predict the fundamental frequency of the same structural configuration when the pull-out force is larger. ELint_GC2 analysis also overpredicts the fundamental frequency of the FBr_1Ts structural configuration. In addition to the frequency content which is not always captured by the ELint_GC2 analyses, the numerical analyses overestimate the structural (Figure 7.30, Figure 7.32), foundation (Figure 7.31) and soil (Figure 7.34) motions. The latter shortcoming of the models is a consequence of the underestimation of the damping produced by the presented numerical analyses in comparison with the ones produced during the experiments (Figure 7.33).

The above observations regarding the overestimation of the fundamental frequency and motion amplitude by the analyses are more pronounced for the simulations of larger pull-out force. This is an indication that soil nonlinearity should be incorporated in the model. Soil nonlinearity is expected to decrease the soil stiffness and hence the fundamental frequency. It will also increase the produced damping and hence decrease the predicted motion amplitude. The following steps in the calibration process consider the nonlinear behaviour of the soil aiming to capture better the experimental data.

7.13 Nonlinear model calibration against free vibration tests

For the nonlinear analyses the Imperial College Generalised Small Strain Stiffness (IC.G3S) model (Taborda *et al.*, 2016), that was described in Section 4.4.4, was used. The calibrated nonlinear model that was used in the site response analyses, presented in Section 4.4.5, is used as a reference model for the soil-structure-interaction simulations. The nonlinear behaviour of the shallow soil layer required further calibration, as it was found that the examined SSI simulations are sensitive to even small changes in the properties of this layer. The calibration of the nonlinear model includes the calibration of the stiffness degradation and damping ratio curves (G-γ-D), as well as the minimum shear modulus (G_{min}). The remaining properties of the IC.G3S model are taken to be the same as those used for the site response analyses.

7.13.1 Depth of nonlinear soil layers

The employment of the nonlinear model in analyses significantly increases the computational cost of the analyses relative to linear ones. Aiming to minimise the computational time, the minimum depth of soil beyond which soil nonlinearity is unimportant is investigated. The investigation is carried out for the experiment of the FBr_2Ts structure under the maximum applied pull-out force, 15.70kN. This free vibration experiment, FBr_2Ts_15.70kN, is the one that triggered the highest levels of soil nonlinearity among the other tests, for the reasons explained in Section 6.2.5 and evidenced in Figure 6.14.

Figure 7.35 presents the horizontal top slab (2.5n), vertical foundation (1.1z) and vertical soil (0.1z) motions computed by the simulation of the FBr_2Ts_15.70kN free vibration experiment. The figure compares the response predicted by analyses that prescribed either the first 0.80m of the soil domain or the entire soil domain as nonlinear. The analyses incorporate the nonlinear behaviour of the soil layers that were calibrated through site response analyses in Chapter 4. Figure 7.35 demonstrates that prescribing the entire soil domain as nonlinear led to a slightly more flexible and damped motion compared to the analysis where only the first 0.80m was prescribed as nonlinear. The difference

between the two motions, though, can be considered negligible, considering the computational gain of the analysis that prescribed only the first 0.80m as nonlinear. Therefore, for the nonlinear analyses presented herein, only a superficial thin soil layer of 0.80m is prescribed to behave nonlinearly. The remaining soil domain and structural elements behaves linearly.

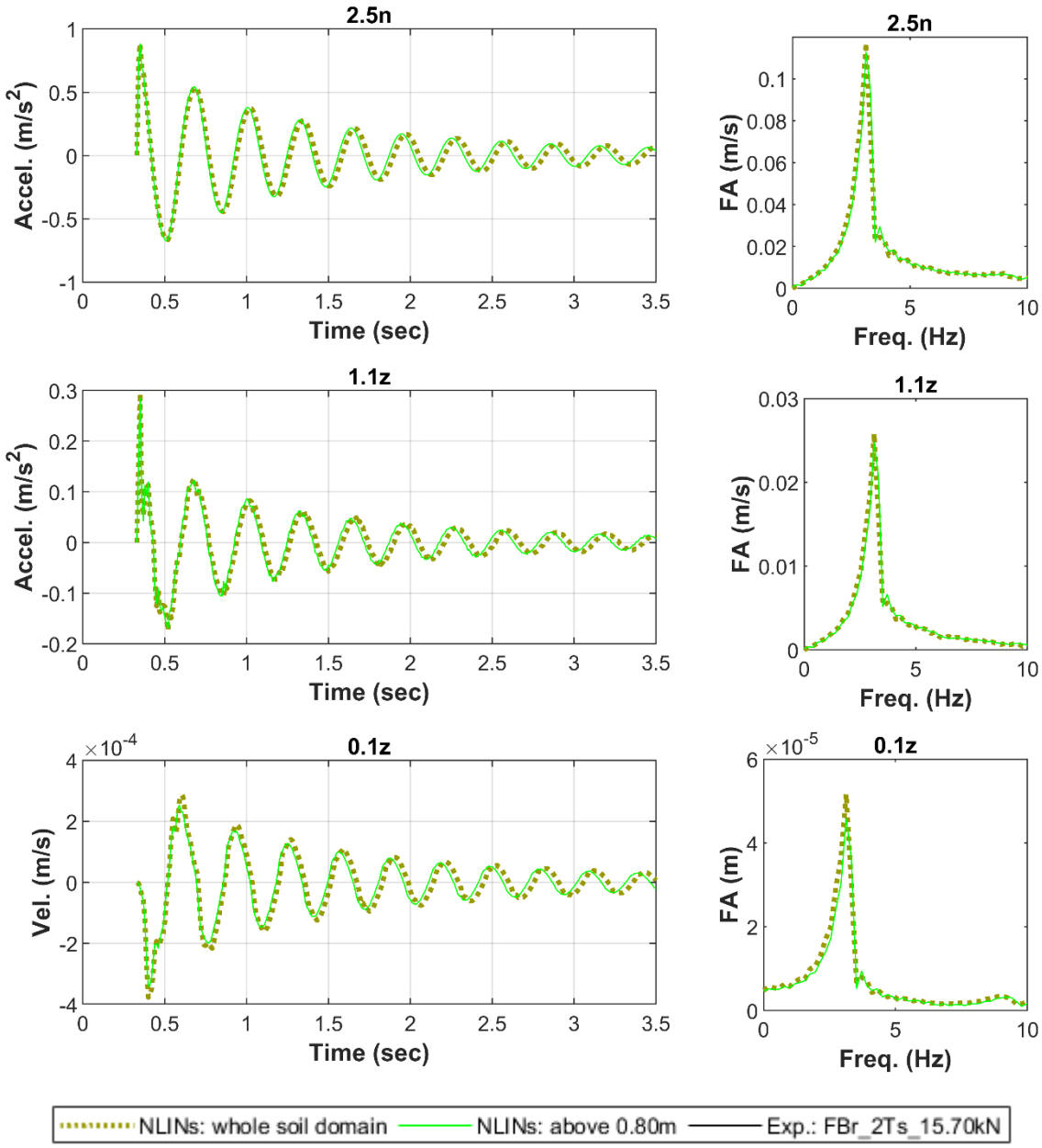


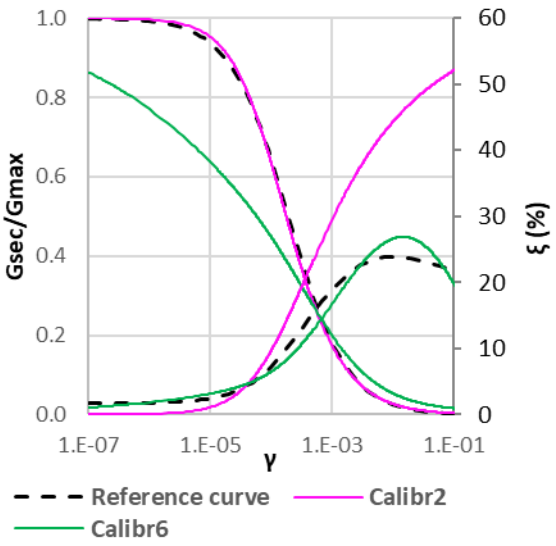
Figure 7.35: Comparison between analyses that prescribed the first 0.80m of soil or the whole soil domain as nonlinear. Comparisons are made for the horizontal top slab (2.5n), vertical foundation (1.1z) and vertical soil (0.1z) motions, computed by simulations of the FBr_2Ts_15.70kN free vibration test.

7.13.2 G-γ-D curves calibration

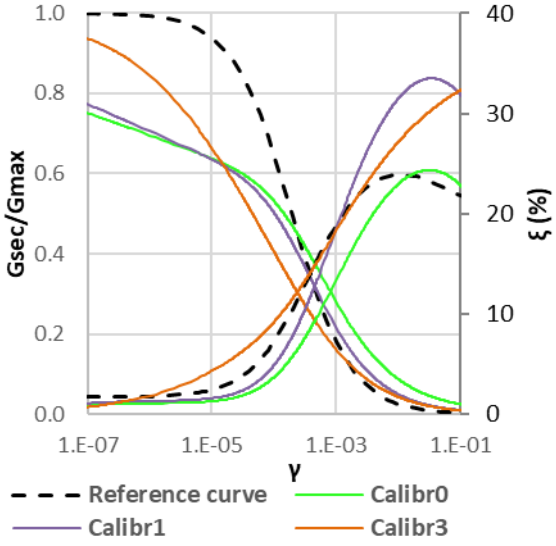
The G-γ-D curves of the first 0.80m of soil are calibrated against the FBr_2Ts_2.94kN and FBr_2Ts_15.70kN free vibration tests. These experiments allow the calibration of the nonlinear model

over a strain range between the small to medium strains. The calibration is subsequently validated against the PBr_W_13.90kN and FBr_1Ts_15.70kN experiments. Herein, conventionally, deviatoric strains (E_d) below 0.001% are considered very small, strains below 0.03% are considered small, while strains beyond this value are considered medium. It is also considered that large strains are not imposed in the soil by the modelled experiments, as the intensity of the motion is small. The latter convention agrees with the one suggested by Vucetic (1993) for soils with plasticity index of 10%, that are subjected to simple shearing, i.e. deviatoric strains are equal to shear strains.

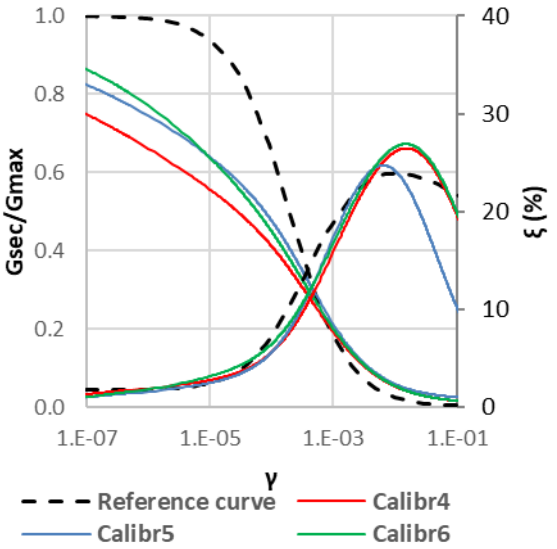
Figure 7.36 presents the examined G-γ-D curves, which are divided into three sets of curves. The aims of each set and the curves contained in the set are summarised in Table 7.12. The input parameters of the examined calibrations of the nonlinear model are presented in the Appendix F.



(a) Set A



(b) Set B



(c) Set C

Figure 7.36: G-γ-D curves of which applicability is investigated.

Table 7.12: Examined sets of G-γ-D curves and their aim.

Set	G-γ-D curves included	Aim
A	Calibr2, Calibr6	Investigate the consequence of calibrating the curves against either stiffness degradation (Calibr2) or damping ratio curves (Calibr6).
B	Calibr0, Calibr1, Calibr3	Investigate the impact of the change of damping at small (Calibr3) and large (Calibr0, Calibr1) strains.
C	Calibr4, Calibr5, Calibr6	Aiming to produce the final model calibration, G-γ-D curves are refined around the optimum curve obtained from sets A and B

Figures 7.37 and 7.38 present results from nonlinear analyses that adopt the G-γ-D curves of Set A (Figure 7.36a). The aim of this investigation is to examine the impact of prioritising the calibration of the G-γ-D curves against stiffness (Calibr2) or damping (Calibr6). As Figure 7.36a illustrates, when the calibration prioritises the stiffness, the damping at very small strains is underestimated, while it is highly overestimated at medium strains. When the calibration of damping is prioritised, the stiffness is underestimated at very small to small strain range. Figures 7.37 and 7.38 present results from the simulation of the FBr_2Ts_2.94kN and FBr_2Ts_15.70kN experiments, respectively. The response is examined in terms of (a) top slab accelerations, (b) the corresponding Fourier spectra, (c) peak to peak frequencies and (d) damping ratio. Each damping ratio value is calculated using the logarithmic decrement method (Eq. 6.10) to express the damped motion between the first peak and the $(j+1)^{th}$ peak of the motion.

Figure 7.37a, b and c demonstrate that when the calibration prioritises damping (Calibr6), the analysis predicts a more flexible system than the analysis which prioritises the stiffness (Calibr2). This is a result of the underestimation of stiffness by the Calibr6 analysis at very small to small strains, which is the strain range of our interest for the presented simulation. Within this strain range, Calibr2 underestimates the damping ratio, while Calibr6 prescribes damping values very close to the reference ones. The underestimation of damping by Calibr2 is reflected by the smaller damping ratio values predicted by this analysis than Calibr6, as shown in Figure 7.37d. It is noted though, that for the very small to small strain range the damping produced by the soil in both analyses is very small, around 1% for Calibr6 and 0% for Calibr2. These values are very small in comparison with the damping produced by radiation damping, which is the damping mechanism that dominates. The latter claims justify the small difference in the damping produced by the Calibr2 and Calibr6 analyses that is shown in Figure 7.37d.

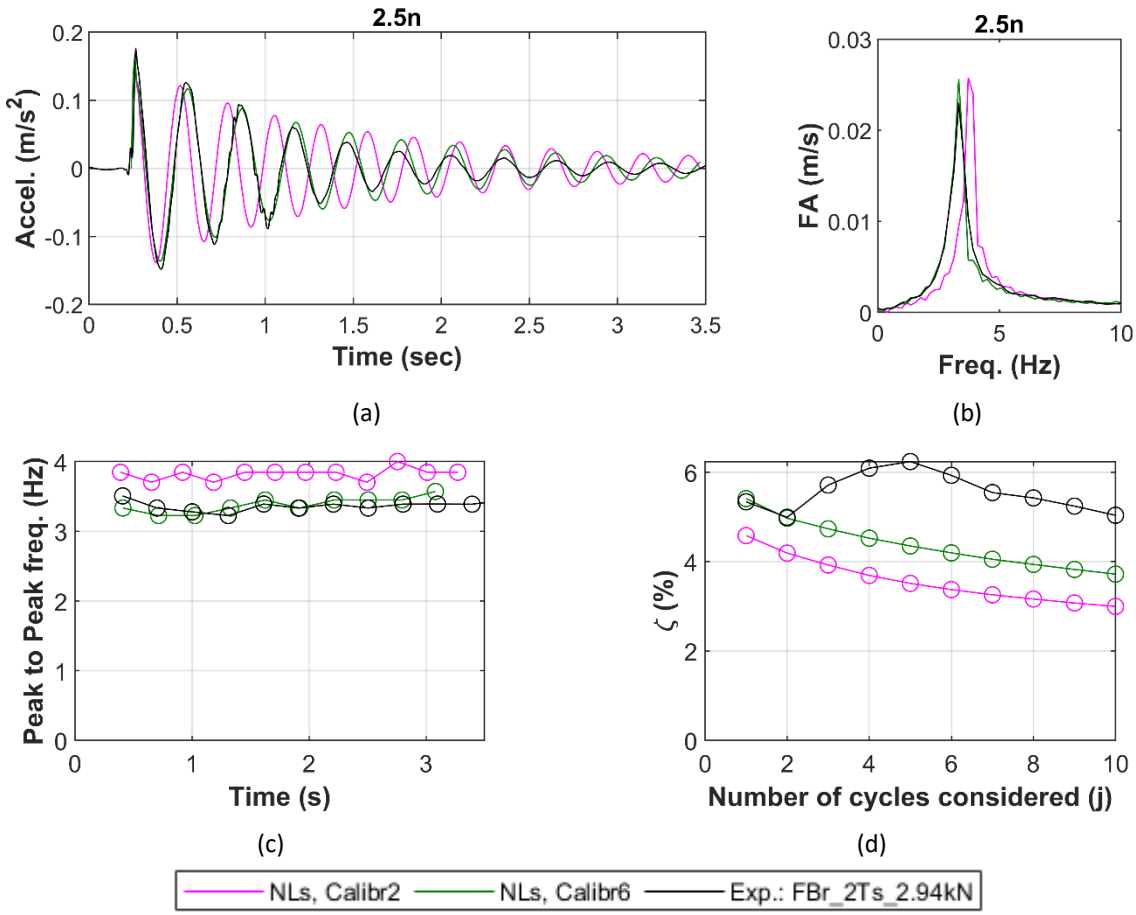


Figure 7.37: Comparison of the top slab response predicted by the FBr_2Ts_2.94kN simulations that incorporate nonlinear soil model that is calibrated against Calibr2 or Calibr6 (Set A curves - Figure 7.36a). The response is examined in terms of: (a) acceleration time histories, (b) Fourier amplitude spectra, (c) peak-to-peak frequencies, (d) damping ratio.

Figure 7.38 shows that the difference between the analyses increases when the pull-out force increases to 15.70kN. Figure 7.38a, b and c demonstrate that the Calibr2 analysis, which prioritise the calibration of stiffness, predicts a much stiffer response than the analysis that prioritises the calibration of damping (Calibr6). Figure 7.38c shows that at the first half cycle, the response frequency was very similar between the two analyses, while the difference increases with time. This is attributed to the fact that at the beginning of the motion, the soil stiffness predicted by the two analyses was similar. Strains of medium range were induced in the soil, while according to Figure 7.36a, within this range, the soil stiffness prescribed by the two calibrations was very close to each other.

However, at the same strain levels, the two calibrations differ significantly as far as the damping ratio is concerned. In particular, the Calibr2 calibration highly overestimates the damping ratio, while the Calibr6 one prescribes damping values close to the reference values (Figure 7.36a). The implication of this is reflected to the smaller amplitude of the motion, shown in Figure 7.38a and b, as well as to the larger damping values produced at the first cycles by the Calibr2 analysis (Figure 7.38d). The very large

damping that is generated in the first cycles of Calibr2 analysis resulted in an abrupt decrease of the motion and hence of the strains induced in the soil. This increased the soil stiffness, as indicated by the increase of the peak-to-peak natural frequencies after the first cycle. The large variation of peak-to-peak natural frequencies predicted by the Calibr2 analysis justify the wider spectra inferred from this analysis.

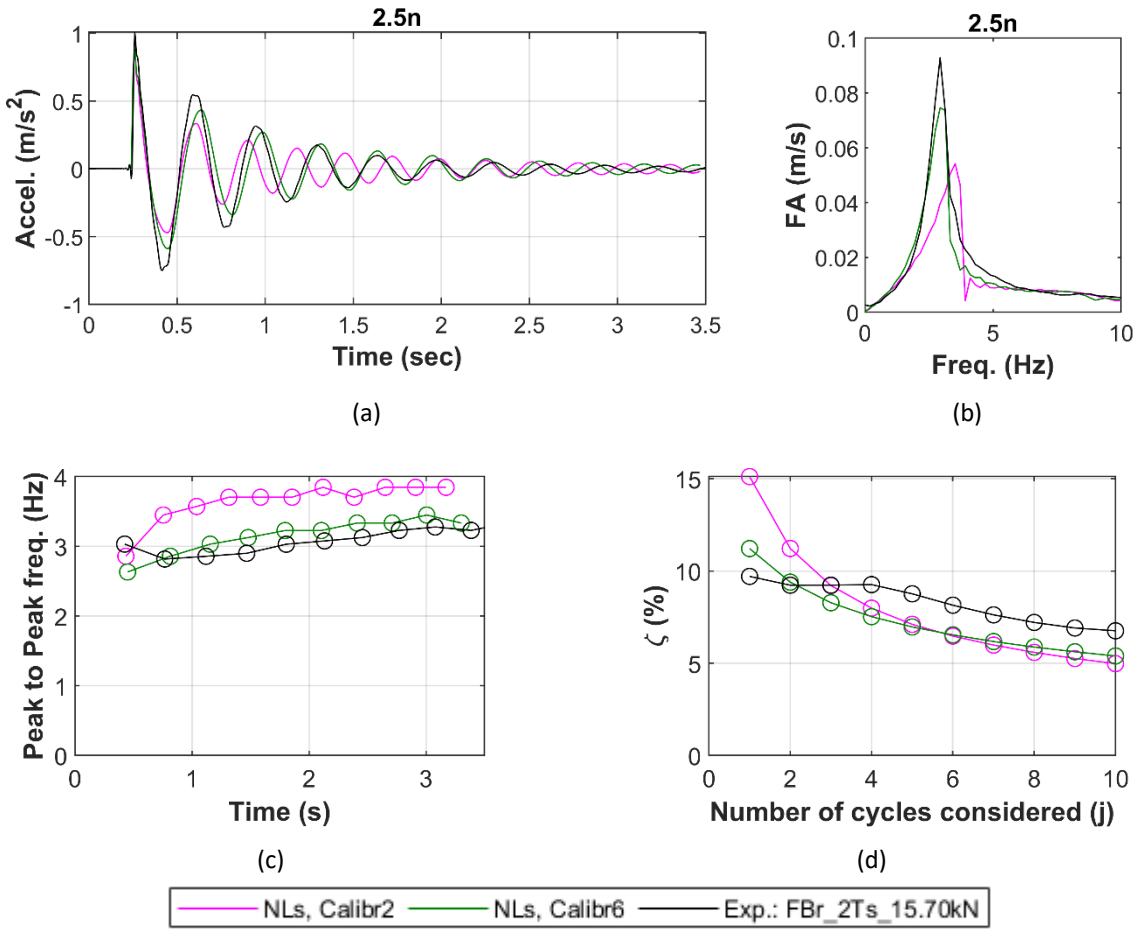


Figure 7.38: Comparison of the top slab response predicted by the FBr_2Ts_15.70kN simulations that incorporate nonlinear soil model that is calibrated against Calibr2 or Calibr6 (Set A curves - Figure 7.36a). The response is examined in terms of: (a) acceleration time histories, (b) Fourier amplitude spectra, (c) peak-to-peak frequencies, (d) damping ratio.

It is therefore illustrated that an appropriate calibration of damping variation with strains is very important when nonlinear phenomena become more pronounced, which is the case for the FBr_2Ts_15.70kN experiment. When the simulation of the latter experiment incorporates G-γ-D curves that prioritise stiffness, the overestimation of damping at the medium strain range results in a significantly overdamped motion that cannot replicate the experimental results. In SSI related problems, soil stiffness is also important as it controls the natural frequency of the system, as shown in Figure 7.37b and Figure 7.38b. The underestimation of stiffness at very small to small strains, that

happens when the calibration of the nonlinear model prioritises the damping (Calibr6), can be compensated by prescribing a larger soil stiffness at very small strains, i.e. G_{max}. The IC.G3S nonlinear model, used in the presented studies, accounts for the G_{max} dependency on p' (Eq. 7.4). Hence, as illustrated in Figure 7.6b, it predicts an increased stiffness for the soil below the foundation, relative to the free-field stiffness and the one used in the linear elastic analyses. This stiffness increase can compensate the underestimation of stiffness at small strains that results from model calibration.

The above investigation shows that, for SSI simulations, the nonlinear model should prioritise the calibration of damping. This calibration strategy was also adopted by the site response analyses, allowing the use of the G-γ-D curves calibrated through these analyses (Calibr0), presented in Section 4.4.5, in the nonlinear SSI analyses, as a first attempt. Figure 7.39 compares the top slab response, in terms of acceleration time histories and Fourier spectra, as computed by two free vibration simulations of pull-out force (a) 2.94kN and (b) 15.70kN. The first simulation assumes the soil as linear using a Rayleigh damping of 5%, while the second one accounts for soil nonlinearity using the calibration Calibr0.

Figure 7.39b illustrates that the nonlinear analysis predicted a much weaker motion amplitude, implying that the damping ratio values produced in the vicinity of the structure was much larger than 5% that was prescribed in the linear analysis. Soil nonlinearity also shifted the natural frequency of the system to a lower value in comparison with the linear analyses, which is a result of soil stiffness degradation. The impact of soil nonlinearity is less significant on the free vibration response of the structure that is excited by the smallest force 2.94kN (Figure 7.39a), implying weak nonlinear phenomena.

Comparing the numerical results computed by the nonlinear analyses with the experimental data, the numerical model overestimates the motion. Assuming that the FBr_2Ts_2.94kN and FBr_2Ts_15.70kN experiments induce strains in the small and medium strain range respectively, the next calibration attempt should target the following changes with respect the Calibr0:

- considerably larger damping at small strains to capture the amplitude of the FBr_2Ts_2.94kN experiment
- slightly larger damping at the medium strain range strains to capture the amplitude of the FBr_2Ts_15.70kN experiment
- stronger soil stiffness degradation at the medium strain range to compensate the stiffer response the Calibr0 analysis predicts for the FBr_2Ts_15.70kN experiment (Figure 7.39b)

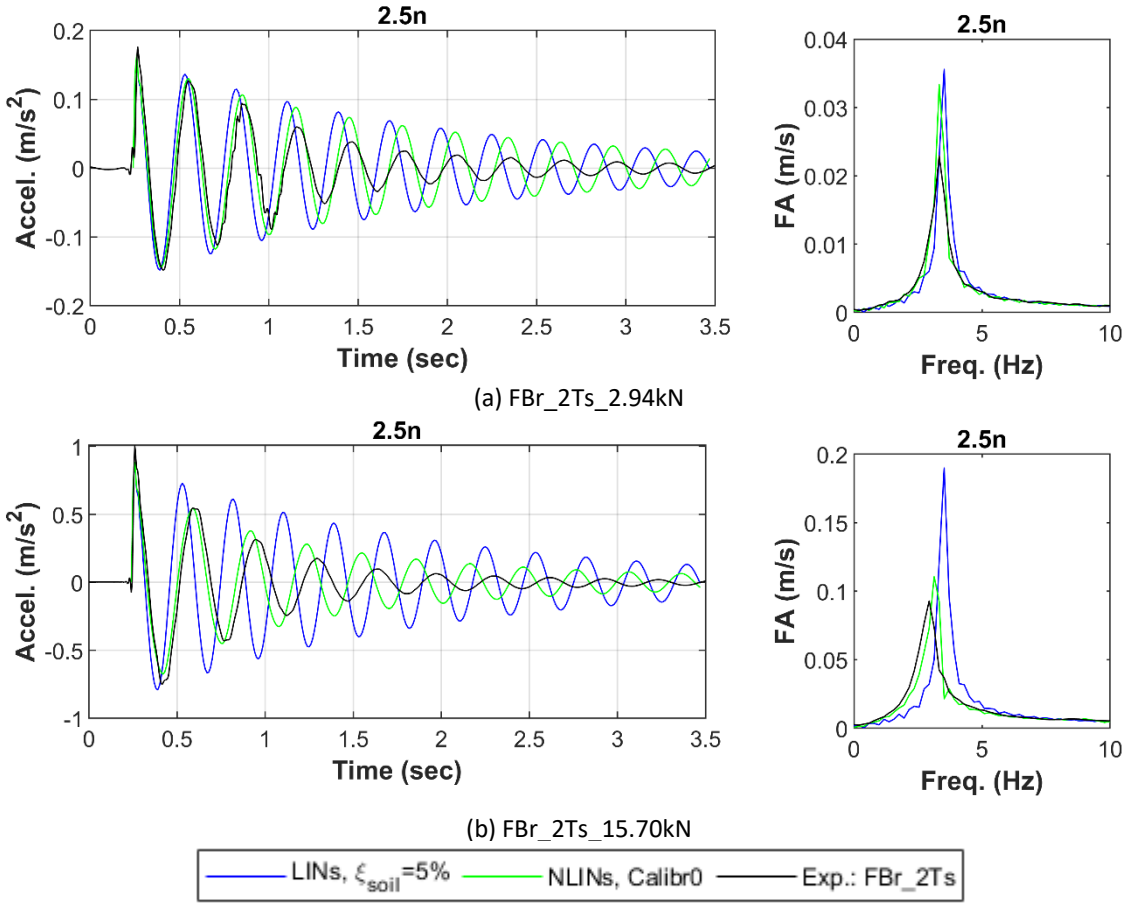


Figure 7.39: Comparison of the top slab response predicted by linear and nonlinear analyses using the calibration Calibr0.

The impact of each of the above targeted features of G-γ-D curves is investigated separately, by carried out nonlinear analyses that incorporate the G-γ-D curves of Set B (Figure 7.36b). The comparison of results between Calibr0 and Calibr1 analyses will give an indication about the impact of damping increase at the medium strain range, while Calibr3 will give an indication of the impact of the increase of damping at the small strain range. Figure 7.40 presents the top slab response of the above analyses when simulating the (a) FBr_2Ts_2.94kN and (b) FBr_2Ts_15.70kN experiments.

Figure 7.40a demonstrates that the Calibr0 and Calibr1 analyses predict almost the same top slab free vibration response when the pull-out force is 2.94kN, due to the small induces soil strains, i.e. smaller than 5e-5. However, the two analyses predict different results when the analyses simulate the free vibration experiment of the largest pull-out force. This indicates that this experiment induces strains in the soil that reach the medium range, where the two calibrations diverge. Figure 7.40b shows that the Calibr1 analysis, which employs the calibration with larger damping at medium strains, produces a more damped motion. The same analysis also produces a slightly more flexible response, as the incorporated stiffness curves prescribe larger degradation at the same strain range than the curves incorporated in the Calibr0 analysis.

As Figure 7.40b shows, the Calibr1 analysis predicts well the motion of the FBr_2Ts_15.70kN experiment at the first cycles. However, for subsequent cycles when the motion and hence the induced soil strains dissipate, the analysis overpredicts the motion. Similarly, Calibr1 analysis overestimates the top slab accelerations relative to the strong motion data, for the experiment that induces small strains only, FBr_2Ts_2.94kN (Figure 7.40a). The above can imply that the Calibr1 is suitable for medium strains but underestimates the damping at small strains. Within this context, Calibr3 prescribes an increased damping at the small strain range and similar damping for medium strains relative to Calibr1.

Figure 7.40a shows that the Calibr3 analysis replicates sufficiently well the strong motion data recorded during the experiment with the smallest pull-out force. However, it predicts a very flexible response and highly overdamps the first cycles of the experiment with the strongest pull-out force (Figure 7.40b). Therefore, it is apparent that Calibr3 prescribes suitable calibration at small strains, while it is overestimates both stiffness degradation and damping at higher strains.

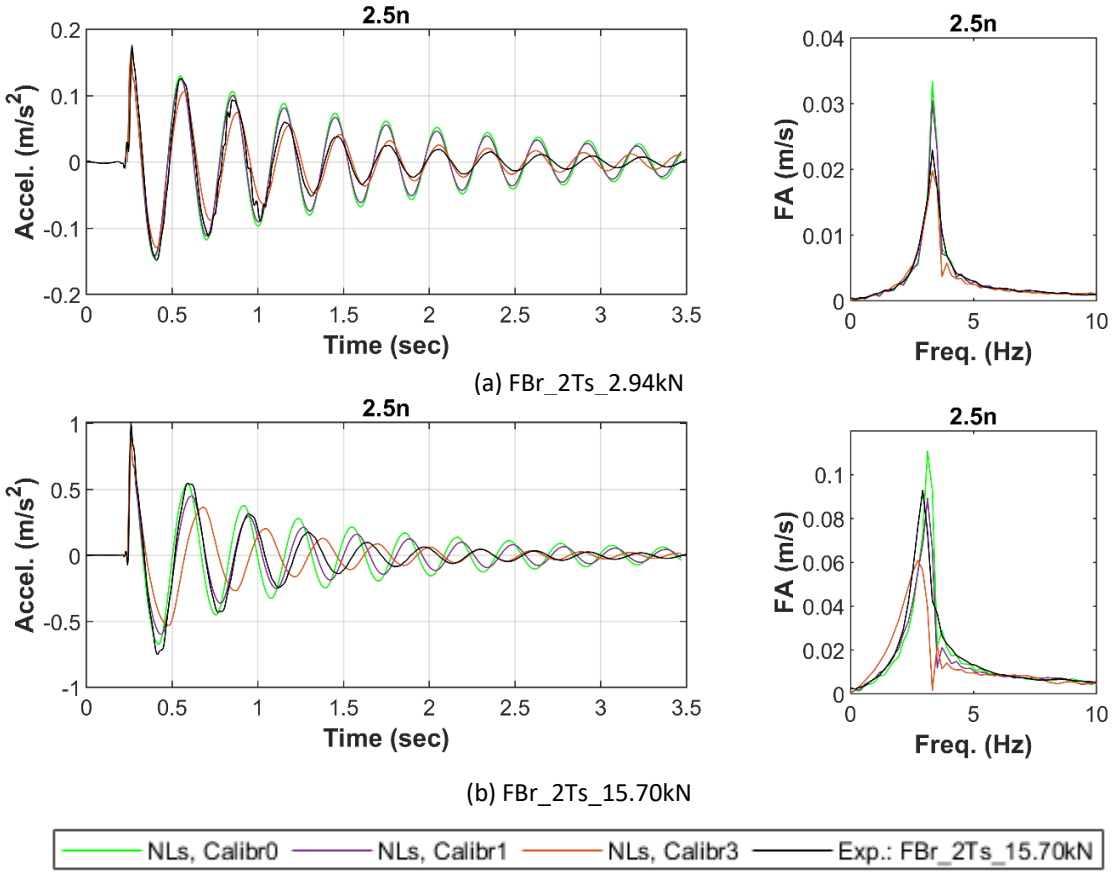
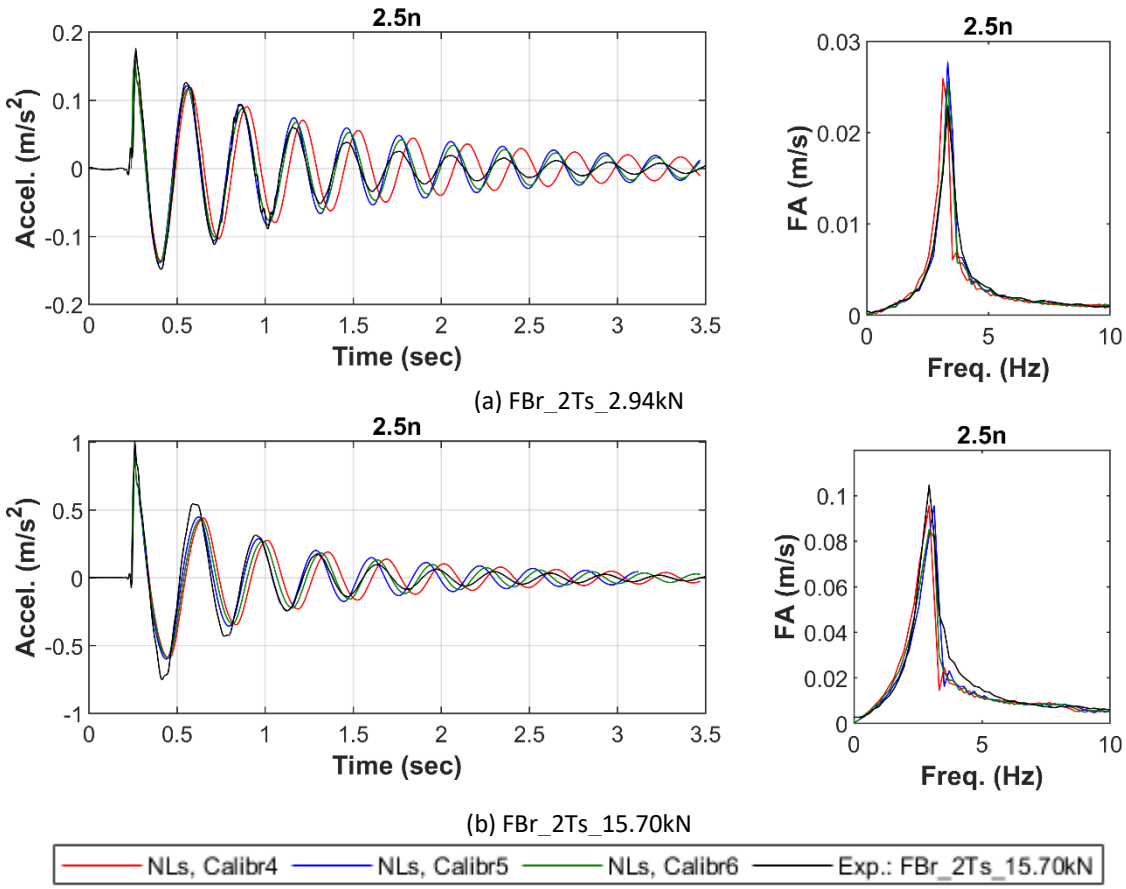


Figure 7.40: Comparison of the top slab response predicted by nonlinear analyses of the model calibrations included in Set B curves (Figure 7.36b): Calibr0, Calibr1 and Calibr3.

The G-γ-D curves of Set C (Figure 7.36c) refine further the calibration of the nonlinear model, according to the latter conclusion. All three examined curves included in Set C (Calibr4, Calibr5 and Calibr6) have

similar damping ratio curves, prescribing smaller damping values at small to medium strain range with respect to Calibr3 curve. The three curves, though, have different stiffness degradation, with Calibr4 to prescribe the smallest soil stiffness. Figure 7.41 presents the top slab response, as computed by the same free vibration analyses that incorporate the three calibrations of Set C.

Figure 7.41 demonstrates that the three calibrations replicate sufficiently well the motion amplitude of the field data, indicating the suitability of the calibrated damping ratio curves. The three analyses, though, predict different stiffness for the SSI system. The Calibr4 predicts an SSI system more flexible than the experimental one, which is attributed to the low soil stiffness predicted by the calibration. This is attempted to be corrected by Calibr5 that prescribes a weaker degradation of soil stiffness. Calibr5 analysis predicts well the frequency content of the experiment with the smallest pull-out force (Figure 7.41a), while it predicts a slightly stiffer response of the experiment with the largest pull-out force (Figure 7.41b). Following this observation, Calibr6 prescribes slightly stronger soil stiffness degradation at medium strains, while, maintaining a similar stiffness degradation at small strains. As Figure 7.41 shows, nonlinear analyses that incorporate the G-γ-D curves of Calibr6 replicate sufficiently well the experimental frequency content and motion amplitude of both tests.



(a) FBr_2Ts_2.94kN

(b) FBr_2Ts_15.70kN

Figure 7.41: Comparison of the top slab response predicted by nonlinear analyses of model calibrations included in Set C curves (Figure 7.36c): Calibr4, Calibr5 and Calibr6.

Despite that Calibr6 analysis replicates the motion sufficiently well overall, as Figure 7.41b shows, it underestimates the motion of the experiment with the largest pull-out force at the first cycles. This feature is not observed in the results of the simulation of the experiment with the smallest pull-out force (Figure 7.41a). The structural oscillation during the first cycles of the motion of the FBr_2Ts_15.70kN experiment was the strongest examined among all free vibration tests carried out; hence it induced the strongest strains in the soil. The underestimation of the motion in the first cycles of this experiment can be attributed to overestimation of damping within range of the induced strains.

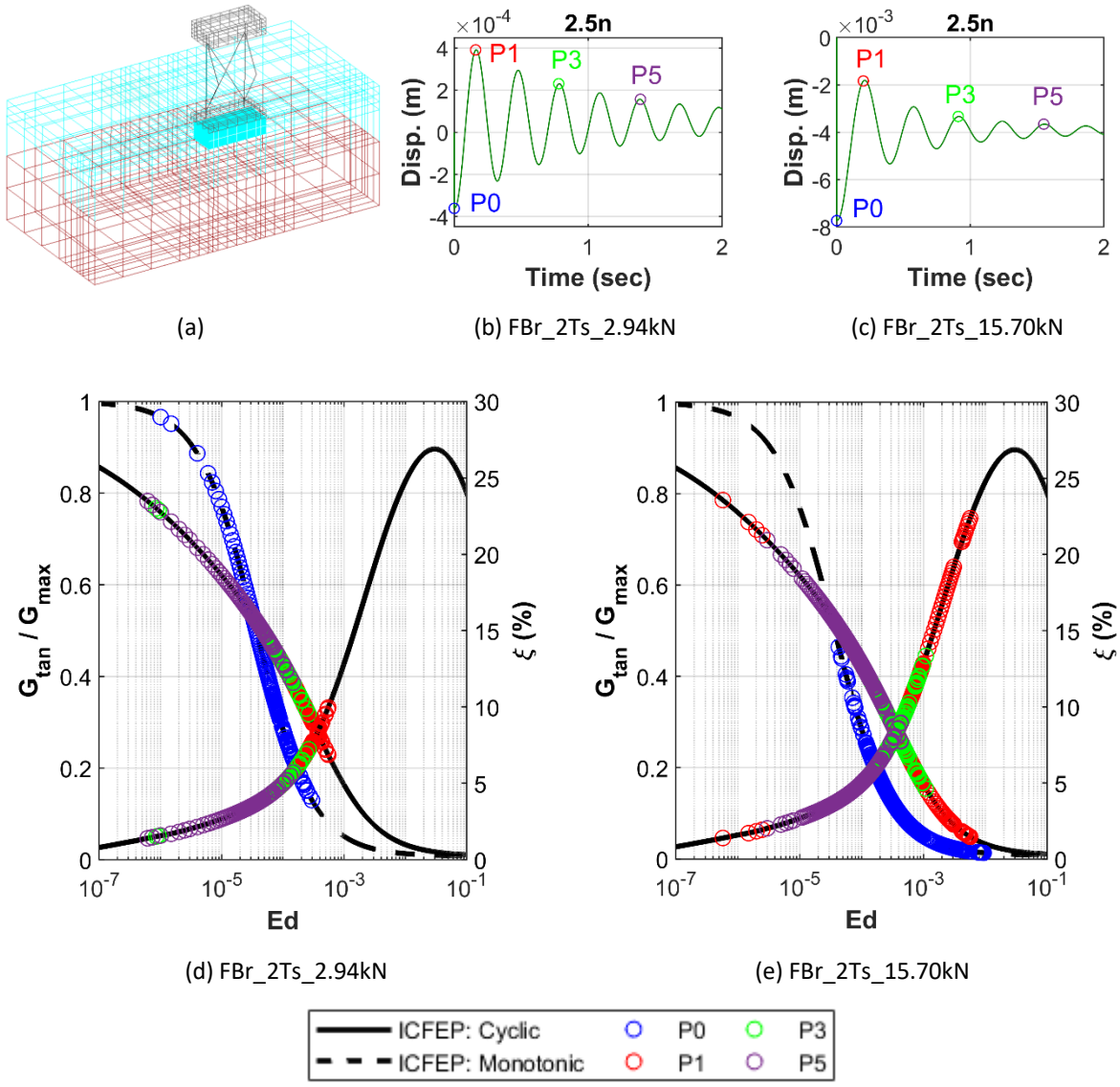
Aiming to assess this claim, Figure 7.42 quantifies the induced strains, stiffness degradation and damping ratio values developed below the foundation at integration points within the volume of soil shaded with solid colour in Figure 7.42a. Figure 7.42b and c present the displacement time history produced by the numerical simulations of the FBr_2Ts_2.94kN and FBr_2Ts_15.70kN experiments respectively. The stiffness degradation and damping ratio values are estimated at the time following times, which are indicated with bullets on the time histories:

- P0: time zero prior to load removal, when the load was still static
- P1: time of the first positive displacement peak after load removal
- P3: time of the third positive displacement peak after load removal
- P5: time after the fifth positive displacement peak after time removal

Figure 7.42d and e present the stiffness degradation curves for monotonic and cyclic conditions and the damping ratio curve for the latter condition. They also present the corresponding stiffness degradation and damping ratio values of all integration points mentioned earlier. It should be noted that the x-axis of the figures refers to the accumulation of deviatoric shear strain (E_d) since the last reversal, which is the strain used for the calculation of stiffness and damping. E_d is different to the total deviatoric strain in cyclic loading, while they coincide in monotonic loading. The monotonic curve is computed by assuming scaling factor equal to unity, while a strain-dependent scaling factor is adopted for the curves under cyclic conditions (Taborda *et al.*, 2016).

Figure 7.42d and e present results for the FBr_2Ts_2.94kN and FBr_2Ts_15.70kN simulations respectively. The figures verify that the simulations of 2.94kN pull-out force triggered much smaller deviatoric strains in the soil than the simulation of the 15.70kN force. Noticeably, at the first cycle of the motion after the load removal (P1), the latter simulation developed very high damping values, up to 23%. Such high values of damping overdamped the motion at the first cycles, as highlighted earlier and observed in Figure 7.41b. At subsequent cycles (i.e. third and fifth cycles), the strains and hence the damping values decrease significantly shifting the induced strains from the medium to small range.

Strains are small throughout the motion predicted by the FBr_2Ts_2.94kN simulation, hence this simulation does not overdamp the top slab motion (Figure 7.41a).



(a) (b) FBr_2Ts_2.94kN (c) FBr_2Ts_15.70kN

(d) FBr_2Ts_2.94kN (e) FBr_2Ts_15.70kN

Figure 7.42: Quantification of stiffness degradation and damping ratio values developed within the soil elements highlighted with solid colour in (a) at the times shown in (b) and (c). The values shown in (d) and (e) are extracted from simulations of the FBr_2Ts_2.94kN and FBr_2Ts_15.70kN experiments respectively.

An additional observation made from Figure 7.42b and c is the unrecoverable displacements predicted by the two simulations. The unrecoverable displacements are very significant when the pull-out force is large (Figure 7.42c), while they are small for smaller pull-out forces (Figure 7.42b). Generally, unrecoverable displacements that result from nonlinear elastic analyses can be attributed to stress-strain loading cycles that do not close during the excitation. Figure 7.43 presents the deviatoric stress (J) – deviatoric total strain ($E_{d,t}$) loops exported from the (a) FBr_2Ts_2.94kN and (b) FBr_2Ts_15.70kN

simulations. The stresses and strains correspond to an integration point of a soil element below the foundation, at the plane of symmetry and at a position where the foundation is in contact with the soil. The exact position of the integration point is shown in Figure 7.43a. Figure 7.43b shows that the FBr_2Ts_2.94kN simulation predicts almost closed J-$E_{d,t}$ loops, justifying the small unrecoverable displacements shown in Figure 7.42b. However, the FBr_2Ts_15.70kN simulation predicts a stress-strain curve, the first loop of which does not close after the application of the 15.70kN pull-out force (Figure 7.43c). The opened stress-strain loop is manifested as large unrecoverable displacements at the end of the oscillation, shown in Figure 7.42c.

The fact that the first stress-strain loop does not close can be attributed to the very pronounced degradation of soil stiffness during the application of the static pull-out force, which was applied incrementally over 25 increments. During the application of the static force, the stiffness degrades according to the monotonic curve. The strong degradation of stiffness during the static pull-out analysis is reflected in the significant decrease of inclination of the stress strain curve. At the end of the static pull-out analysis, the curve tends to become horizontal, which agrees to the very low stiffness values shown in Figure 7.42e. After the pull-out force removal, when the dynamic analysis begins, the response of the system depends on the cyclic, instead of the monotonic, stiffness degradation curve. According to Figure 7.42e, in the medium strain range, the cyclic curve prescribes a much higher soil stiffness than the monotonic. Hence, at the first positive peak (P1) the soil stiffness is much stiffer than the one predicted at the last increment of the application of pull-out force (P0). Consequently, the stress-strain curve at different integration points in the soil do not close, producing unrecoverable displacements to the structure, agreeing with a similar observation made by Amorosi *et al.* (2018).

The pronounced degradation of stiffness shown with blue circles in Figure 7.42e resulted to large top slab horizontal displacements at time zero, shown in Figure 7.42c. These displacements are unrealistically high and cannot be eliminated during the dynamic analysis, for the reasons explained above. The same features are also evident, but much less pronouncedly in the results of the experiment with the smaller pull-out force. Figure 7.42d and Figure 7.43b shows that the soil stiffness degradation under monotonic loading was also significant, but did not reach almost zero stiffness, leading to smaller unrecoverable displacements that are shown in Figure 7.42b.

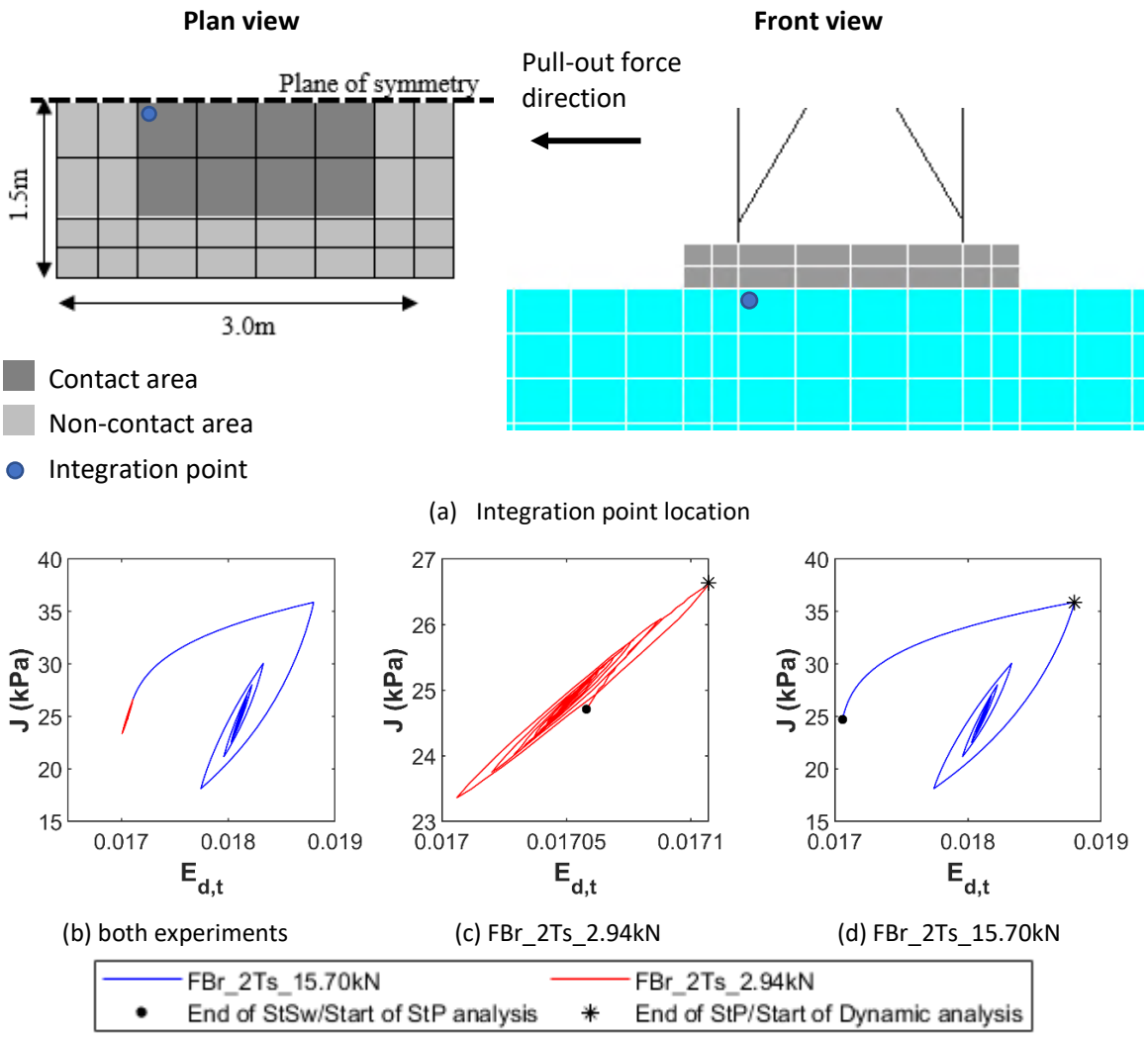


Figure 7.43: Deviatoric stress (J) – deviatoric total strain ($E_{d,t}$) paths computed at the integration point shown in (a). (b) compares the J-$E_{d,t}$ paths between the FBr_2Ts_2.94kN and FBr_2Ts_15.70kN simulations, while (c) and (d) isolate the paths of the former and latter simulations, respectively.

Following the above discussion, the unrecoverable displacements can be attributed to the different stiffness degradation curves that dominate the motion under monotonic and cyclic conditions. Especially, the chosen calibration (Calibr6), which prioritises damping, prescribes a stiffness behaviour which highly degrades with strains in comparison with the curve that is predicted by Calibr2 model, that prioritises stiffness, as shown in Figure 7.44. The figure shows that the Calibr2, which captures the stiffness better, prescribes a much stiffer behaviour under both monotonic and cyclic loading than Calibr6. Calibr2 prescribes a monotonic behaviour with a larger linear range and higher degradation with strains than the cyclic behaviour. The latter relation between monotonic and cyclic behaviours is the one expected according to the knowledge obtained for past lab studies (Tatsuoka *et al.*, 1995). However, this is not the case for the Calibr6 which prescribes lower stiffness for the cyclic behaviour.

As already discussed earlier, the underestimation of stiffness by Calibr6 is a consequence of capturing the damping well.

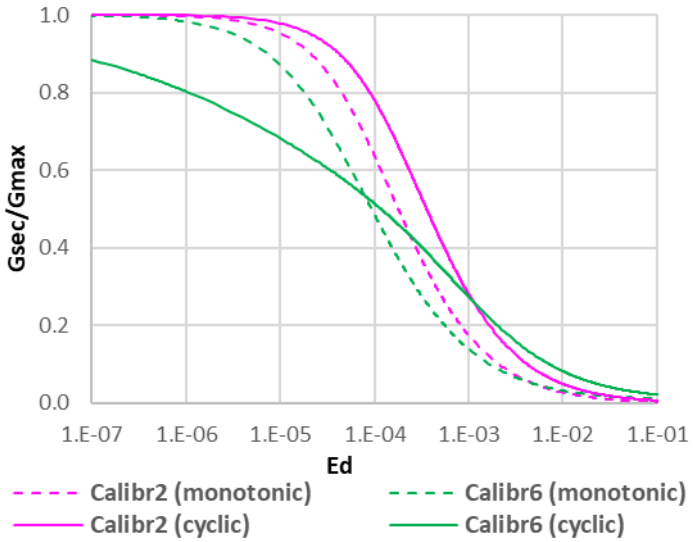


Figure 7.44: Monotonic and cyclic stiffness degradation curves prescribed by the calibrations Calibr2 and Calibr6.

Calibr2 produced much smaller horizontal top slab displacements than Calibr6 during the monotonic pull-out loading, due to the larger stiffness predicted by the former analysis. With reference the P0, Figure 7.45a shows that the horizontal displacement of the top slab at the end of the pull-out analysis is around 5mm when the Calibr2 is used, while the corresponding value for the Calibr6 analysis is 8mm (Figure 7.42c). In both analyses, the stiffness of the examined integration point degraded up to very low values (see Figure 7.42e and, Figure 7.45b) during pull-out (P0) and at the end of the first cycle (P1). The difference between the two analyses, though, stems from the significantly lower monotonic stiffness predicted by Calibr6. This led the latter analysis to produce larger initial displacement of the top slab. The second difference is that the stiffnesses of soil during the monotonic pull-out and the first cycle of dynamic free vibration were similar for the Calibr2 analysis, while they were very different for the Calib6 analysis. The similar stiffness predicted by Calibr2 resulted in a stress strain loop, created by the first loading-unloading cycle, that tends to close, as shown in Figure 7.45c. The implication of this is the small unrecoverable displacements predicted by the Calibr2 nonlinear elastic analyses, which is depicted in Figure 7.45a. This is in vast contrast with results of Calibr6, which showed significantly open stress-strain loops (Figure 7.42e) and hence large unrecoverable displacements (Figure 7.42c). Following the above observations, the unrecoverable displacements can be attributed to the significant difference of stiffness at medium strains, between the monotonic and cyclic loading.

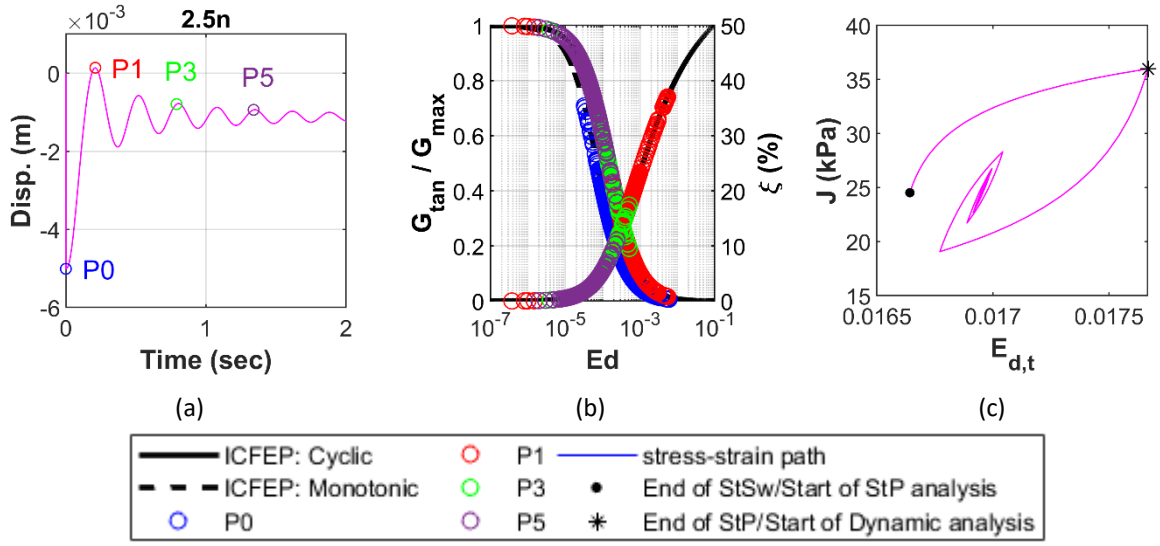


Figure 7.45: Results of the simulation FBr_2Ts_15.70kN, when the Calibr2 is adopted. (a) Displacement time history, (b) G-γ-D curves and the corresponding values developed in the soil volume shown in Figure 7.42a, (c) deviatoric strain – stress path developed in the integration point shown in Figure 7.43a.

The above presented calibration of the soil nonlinear model concludes that the calibration Calibr6 can be the best choice, among the compared calibrations, to be incorporated in the numerical model. However, results of Calibr6 analyses discloses two drawbacks. The analyses overestimate the damping at the first cycles of the motion predicting a weaker response, as well as they produce unrecoverable displacements. These observations were found to become more pronounced for simulations of larger pull-out force. Unrecoverable displacements cannot be explained physically as they result from an elastic analysis. They are produced from the stress-strain loops developed by the nonlinear model that do not close during loading-unloading cycles. It should be noted that the unrecoverable displacements do not affect the output acceleration and velocities, when the analyses are linear. However, when plasticity is incorporated in the analyses, such as the case when elastoplastic interface elements are adopted, the unrecoverable displacements can significantly modify the results. For this reason, the next step of the calibration process involves a process to mitigate the unrecoverable displacements.

7.13.3 Impact of G_{min}

The above drawback of Calibr6, related to unrecoverable displacements, can be mitigated by incorporating a threshold below which the stiffness does not degrade (G_{min}). This will prohibit the development of unreasonably high soil stiffness degradation and horizontal top slab displacements during pull-out, hence decreasing the unrecoverable displacements. Also, higher value of G_{min} will prohibit the development of very low stiffness values and hence very high damping ratio values during the first cycle of the motion. Therefore, a higher G_{min} is anticipated to correct the overestimation of

damping and underestimation of the response at the first cycles of the response of the FBr_2Ts_15.70kN simulation, that was earlier observed through Figure 7.41b.

All previous nonlinear analyses presented adopted a G_{min} value equal to 0.8MPa, which is approximated as $0.01G_o$ (G_o=88MPa). After iterations, a G_{min} value equal to 13.2MPa, which is equal to $0.15G_o$, was found to be suitable. When this value of G_{min} is incorporated in the IC.G3S nonlinear model, the analyses produce negligible unrecoverable horizontal top slab displacements, as shown in Figure 7.46a. The impact of G_{min} on the permanent displacements can be explained through interpretation of Figure 7.46b. The figure presents the monotonic and cyclic G-γ-D curves as well as the numerical data points, that developed at times P0-P5 shown in Figure 7.46a, at the integration points enclosed within the soil volume shaded in Figure 7.42a. As Figure 7.46b shows, G_{min} limits the degradation of soil stiffness under both monotonic and cyclic loading. The implication of this is that during the monotonic pull-out force (P0), the stiffness does not degrade to very small values that were observed earlier when G_{min} was set equal to 0.01Go (Figure 7.42e). The computed lateral top slab displacement 3.2mm (Figure 7.46a), developed under the pull-out force (P0), is more reasonable than the 8mm displacement predicted by the earlier analysis (Figure 7.42c).

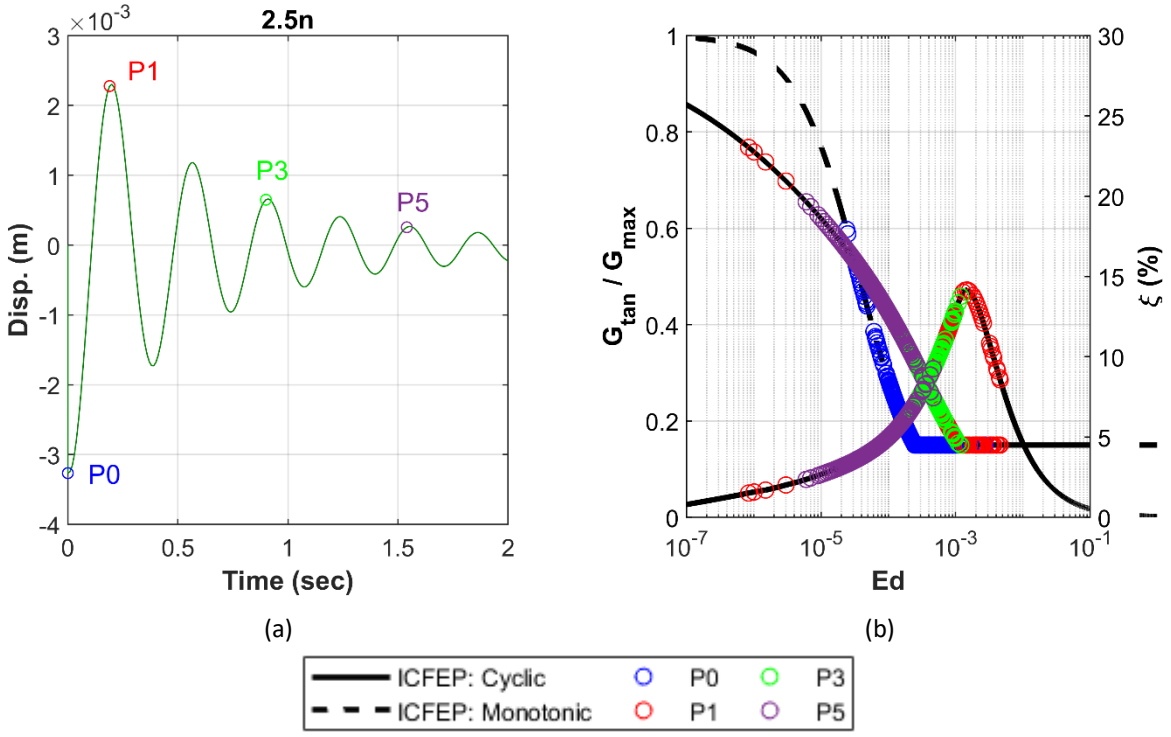


Figure 7.46: (a) Displacement time histories and (b) G-γ-D curves resulted from the simulation of the FBr_2Ts_15.70kN experiment, by adopting Calibr6 and incorporating G_{min}=$0.15G_o$. The presented stiffness and damping ratio values are developed at the times P0-P5, at the integration points enclosed within the soil volume shown in Figure 7.42a.

Also, the soil stiffness during the first cycle of the motion (P1), that follows the cyclic curve, is similar to the one developed during pull-out (P0). It is therefore apparent that the imposition of a higher G_{min} value addresses the issue related to different stiffness behaviour between P0 and P1 and permanent displacements, observed in the analyses that use G_{min} =0.01G_o. The similar monotonic and cyclic stiffness values predicted by the analysis that uses G_{min}=0.15G_o, results in more closed stress-strain loops, as shown in Figure 7.47. The figure compares the J-E_d paths as computed, at the integration point shown in Figure 7.43a, by the nonlinear analyses that use G_{min} values equal to 0.01G_o and 0.15G_o. Figure 7.47a presents the stress strain paths that start from the same initial stress-strain state. The monotonic loading corresponds to the stress-strain path between the dot and star markers, while beyond the star maker the free vibration initiates. Unlike the analysis that uses a small G_{min} value, the analysis that uses G_{min}=0.15G_o produces a closed first stress-strain loop. Overall, this analysis produces a stress-strain path that consists of almost closed loops, justifying the very small unrecoverable displacements shown in Figure 7.46a.

From the monotonic loading path (between the dot and star markers) shown in Figure 7.47a, it is apparent the imposition of a higher G_{min} value significantly increases the stiffness of the response, as indicated by the larger inclination of the path. At the point where the two stress-strain paths start to deviate, G_{min} is mobilised on the monotonic curve (see P0 points in Figure 7.46b), hence the stiffness and the inclination of the path become constant. G_{min} can also be mobilised during cyclic loading. As Figure 7.46b shows, G_{min} can be mobilised around the first peak (P1) only. Figure 7.47b aims to quantify the impact of G_{min} mobilisation on the free vibration (dynamic response), that initiates after the star marker. The presented paths are manipulated so that the two analyses, with different G_{min}, have common stress-strain state at the beginning of the dynamic analysis. As previously, the state where the G_{min} is mobilised is indicated by the deviation between the two analyses. The impact of G_{min} on the stress-strain path, though, is much weaker than previously, implying weaker impact of G_{min} on the dynamic response than the static one.

The impact of G_{min} on the dynamic response is associated with the narrower stress-strain loops observed when larger G_{min} is incorporated in the analysis (Figure 7.47b). Figure 7.46 shows that when the degradation of stiffness reaches G_{min}, the damping ratio starts decreasing. Taborda (2011) has already established that the decrease of damping is a consequence of forcing constant tangential stiffness with increasing strains. In this case, the secant stiffness decreases with strains, while the hysteresis loops become narrower (Amorosi *et al.*, 2016). This justifies the observation made in Figure 7.46b about the decrease of damping ratio beyond the strain level where the tangential stiffness becomes constant.

The decrease of damping after this strain level can essentially affect the motion of the current simulations at the first cycle only, during which the strains induced in the soil can mobilise G_{min}. The impact of the response is illustrated in Figure 7.48, that compares results produced by analyses that use G_{min} equal to $0.01G_o$ and $0.15G_o$. The figure presents the top slab horizontal response at the position of the 2.5 instrument, in terms of (a) acceleration time histories and (b) the corresponding Fourier spectra. It also presents (c) peak-to-peak frequencies (inverted time between successive peaks) and (d) damping ratio values computed by employing the logarithmic decrement method (Chopra, 2011), as described in Section 6.2.4, by taking the first peak into account (i=1).

Figure 7.48b and c show that G_{min} does not have any significant effect on the response frequency of the SSI system, while it affects the motion amplitude. The analysis that uses larger G_{min} value predicts a stronger acceleration response (Figure 7.48a) at the first two cycles of the motion. The stronger response is a manifestation of the smaller damping developed during the first cycle of the motion by the analysis with higher G_{min}, as it is illustrated in Figure 7.48d. The difference in the system's damping produced by the two analyses is attributed to the larger soil damping developed by the analysis with smaller G_{min} than the one with higher G_{min}, as shown in Figure 7.42b and Figure 7.46b respectively.

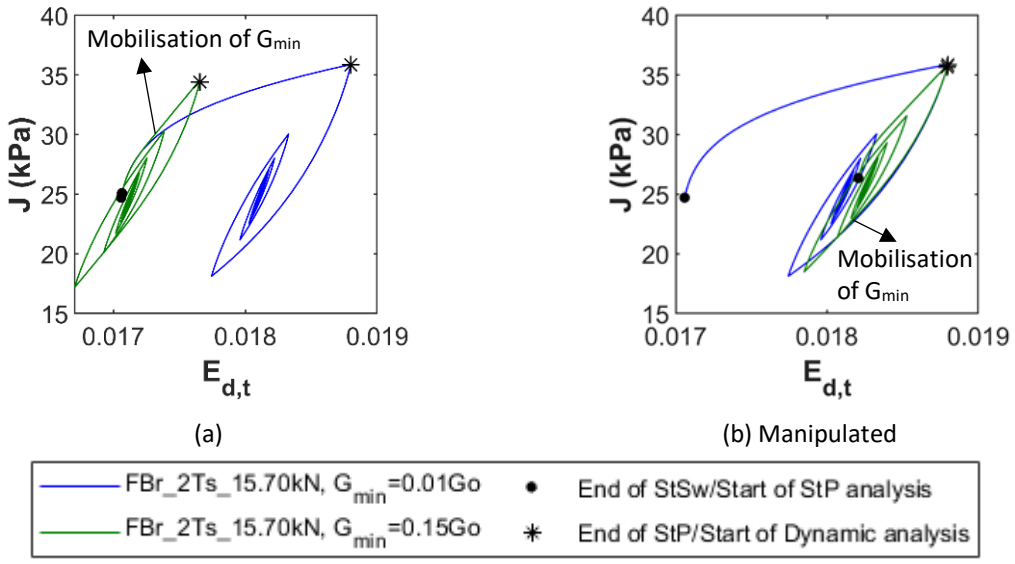


Figure 7.47: Impact of G_{min} on the J-$E_{d,t}$ paths developed at the integration point shown in Figure 7.43a. (a) stress paths start from the same initial stress-strain state highlighting the mobilisation of G_{min} during monotonic loading, (b) manipulated stress paths so that they have a common stress-strain state at the beginning of the dynamic analysis, highlighting the mobilisation of G_{min} during free vibration.

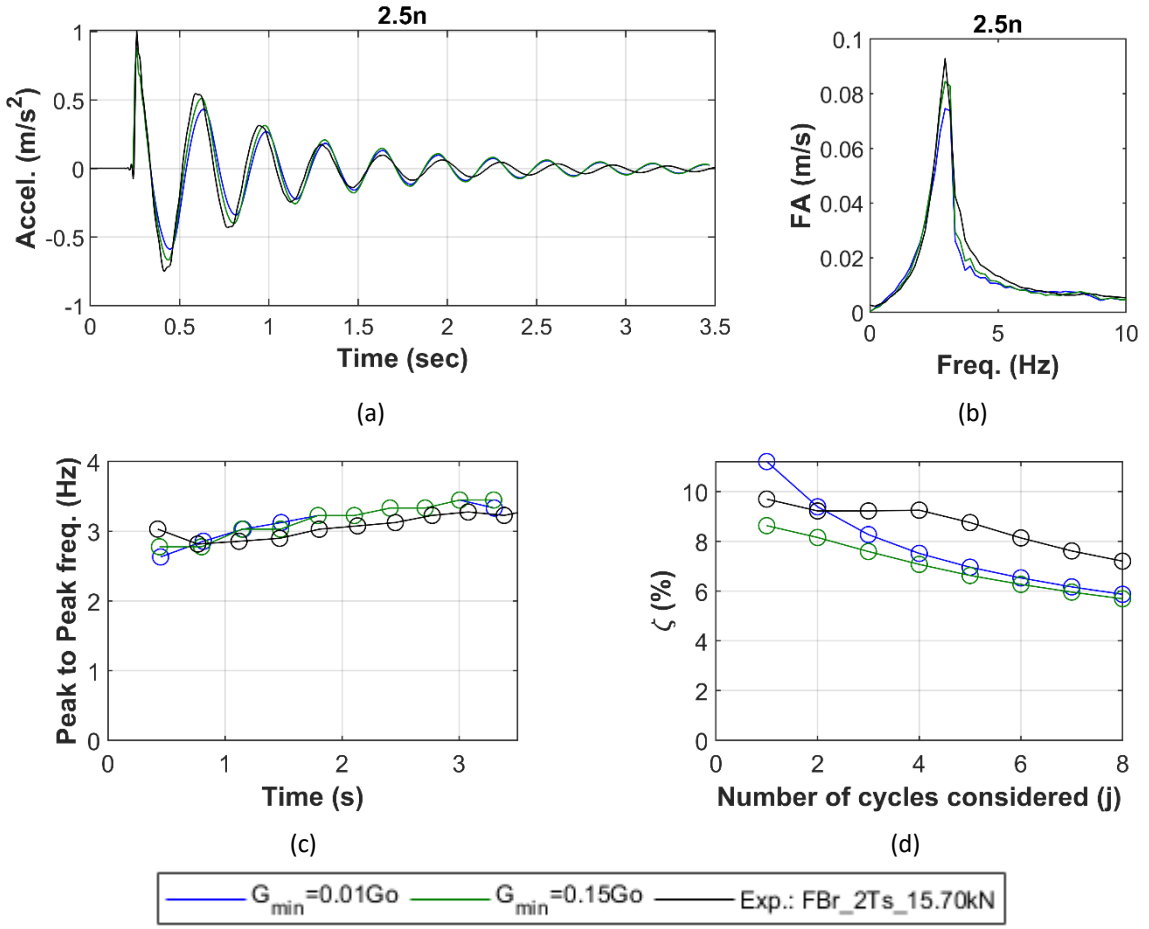


Figure 7.48: Impact of G_{min} on the horizontal top slab response (2.5n) predicted by simulations of the FBr_2Ts_15.70kN experiment. The simulations incorporate the Calibr6 calibration in the nonlinear soil constitutive model. The response is examined in terms of: (a) acceleration time histories, (b) Fourier amplitude spectra, (c) peak-to-peak frequencies and (d) damping ratio.

The above investigation regarding the impact of G_{min}, concludes that the calibrated value of G_{min} addresses the two issues that were observed in the analyses that use G_{min}=0.01G_o. These issues were the unrecoverable displacements and underestimation of the motion (overdamping) at the first cycles. A higher G_{min}, also, compensates the unreasonably highly degraded monotonic curve and prevents the development of very large displacements under monotonic pull-out loading. In the remaining nonlinear analyses presented herein, a G_{min} value equal to 13.2MPa, that corresponds to 0.15G_o, is used. The model calibration is subsequently validated against other free and forced vibration simulations of different structural configurations (FBr_2Ts, PBr_W, FBr_1Ts).

7.13.4 Assessment of the calibrated nonlinear model against other free vibration experiments

The nonlinear model was calibrated against the FBr_2Ts_2.94kN and FBr_2Ts_15.70kN experiments, which as discussed earlier induced a relatively wide range of strains in the soil. Herein, the calibration is validated against field data recorded during the free vibration test on the partly braced structure

that was excited by the largest applied force 13.90kN (PBr_W_13.90kN). It is also validated against free vibration tests on the fully braced structure with one top slab (FBr_1Ts). Despite that these experiments were not physically conducted; numerical simulations of these tests are carried out to investigate the natural frequency of the numerical model.

Figure 7.49 presents the horizontal top slab (2.5n) response computed by the simulation of the PBr_W_13.90kN experiment assuming linear (LINs) and nonlinear (NLINs) soil. The response is presented in terms of acceleration time histories and the corresponding Fourier spectra. The figure demonstrates that the calibration of the nonlinear model decreases considerably the frequency of the response and the amplitude of the motion, relative to the linear analysis. The nonlinear analysis predicts a response very close to the experimental one; a fact that validates the applicability of the calibration on the examined experiment.

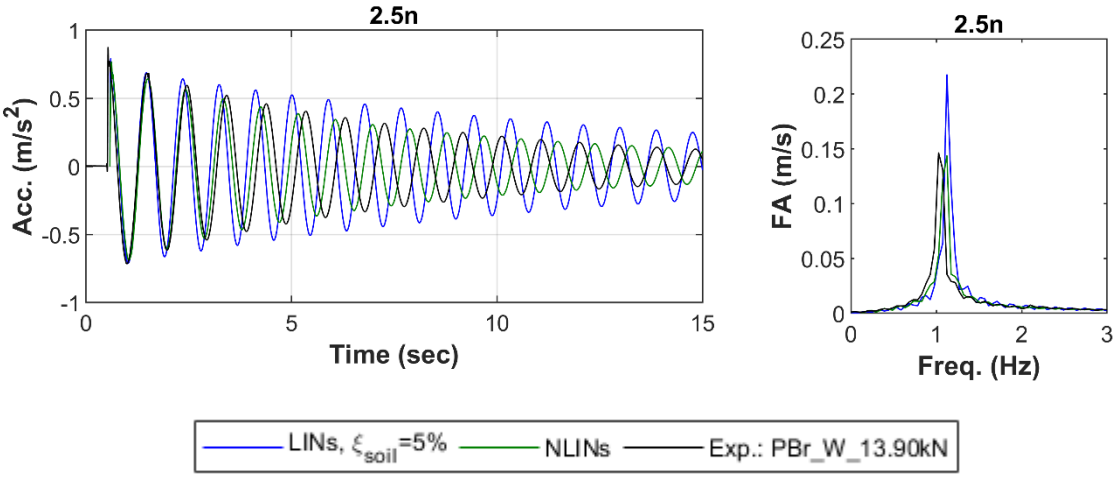


Figure 7.49: Horizontal top slab response (2.5n) computed by the simulations of the PBr_W_13.90kN experiment, assuming either linear or nonlinear soil

Figure 7.50 compares numerical results of the simulation of the FBr_1Ts_15.70kN free vibration tests which are based on the assumptions of linear and nonlinear soil. As previously, soil nonlinearity significantly decreases the fundamental frequency of the system and the amplitude of the motion. Given that field data are not available for this simulation, the amplitude of the motion cannot be validated. The fundamental frequency predicted by the numerical analysis, though, can be verified against the one interpreted from the forced vibration tests. With reference to the main peaks of the spectra, the linear and nonlinear analyses estimated the fundamental frequency of the model equal 5.1Hz and 3.9Hz, respectively. The nonlinear analysis predicted fundamental frequency that is far from the target one, which is around 3.25Hz to 3.50Hz (see Table 6.11).

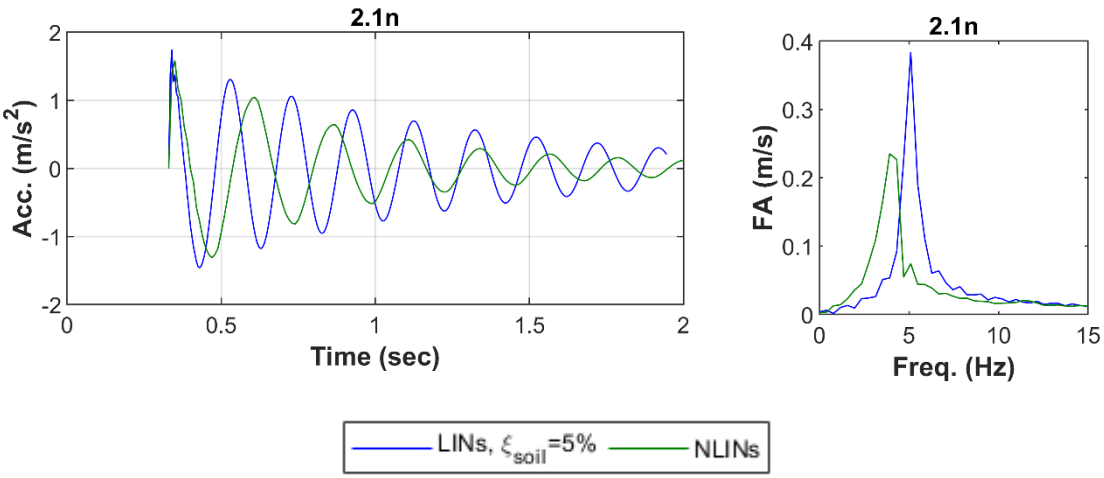


Figure 7.50: Horizontal top slab response (2.1n) computed by the simulations of the FBr_1Ts_15.70kN experiment, assuming either linear or nonlinear soil.

It is therefore apparent that the numerical model fails to predict the dynamic characteristics of the fully braced 1-top slab structure. This could raise doubts about the applicability of the nonlinear model calibration on the presented experiment. However, the calibration is less likely to explain the disagreement mentioned above, as this model is applicable on the remaining experiments examined. A possible reason that can explain the overestimation of the fundamental frequency of the numerical model can be the soil-foundation interface model. The interface model used in the above analyses is the ELint_GC2 model that employs elastic interface elements and simulates the GC2 gap configuration (Figure 7.9b) using low stiffness interface elements. As mentioned above, the limitation of this model is that it does not allow opening of interface elements in addition to the initially opened ones. Although, this interface model was found to be applicable for modelling forced and free vibration tests on the fully braced 2-top slab and partly braced structural configurations, it might not be applicable for the fully braced 1-top slab configuration. As evidenced in Section 6.3.8 by interpreting forced vibration field data, the 1-top slab structure exhibited stronger foundation motion and hence stronger foundation uplift than the 2-top slab structures. The larger foundation uplift was manifested as more pronounced lengthening of natural periods (shortening of the natural frequencies), as discussed in Section 6.3.6 and quantified in Table 6.12.

To simulate the experiments on the FBr_1Ts structure, it is necessary to modify the interface model. Specifically, the modification should allow more interface elements to open, under the same excitation, during the simulations of the experiments on the FBr_1Ts structure compared to the FBr_2Ts structure. The subsequent section, Section 7.14, further investigates the soil-foundation interface model aiming to produce a unique model that is applicable to all experiments.

7.13.5 Assessment of the calibrated nonlinear model against other forced vibration experiments

Figures 7.51, 7.52 and 7.53 investigate the applicability of the calibrated nonlinear model on the forced vibration response of the FBr_1Ts, FBr_2Ts and PBr_W structural configurations, respectively. As expected, the top slab response is unaffected by soil nonlinearity, as its response is determined by the input excitation which is applied as prescribed displacements. Although the impact is very small, the nonlinear analysis tends to increase both foundation components, relative to the results of the linear analysis. The impact is more significant on the soil motion, which for simplicity is represented by the motion at a single point where field data are available. As expected, soil motion was found to decrease by the effect of nonlinear phenomena in the soil. The above observations are more pronounced on the response of the SSI systems that consist of the fully braced structures (FBr_1Ts and FBr_2Ts). The forced vibration of these structures exhibited stronger interaction with the soil than the vibration of the partly braced structure, hence, they are more sensitive to soil nonlinearity.

The nonlinear analyses predict SSI responses sufficiently close to the experimental responses. The calibration of the nonlinear model is considered applicable on the forced vibration simulations; hence, it is validated.

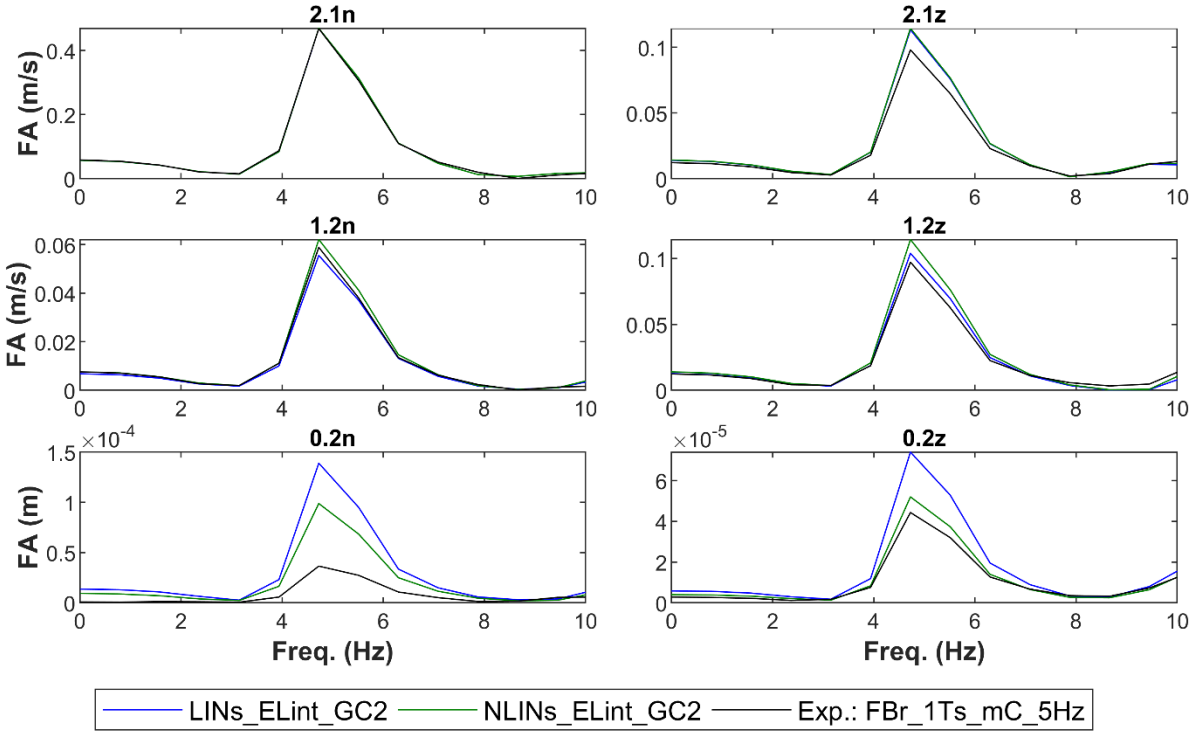


Figure 7.51: Fourier spectra of the horizontal (n) and vertical (z) motions of the top slab (2.1), foundation (1.2) and soil (0.2). Results of the FBr_1Ts_mC_5Hz forced vibration simulations that assume either linear or nonlinear soil are compared.

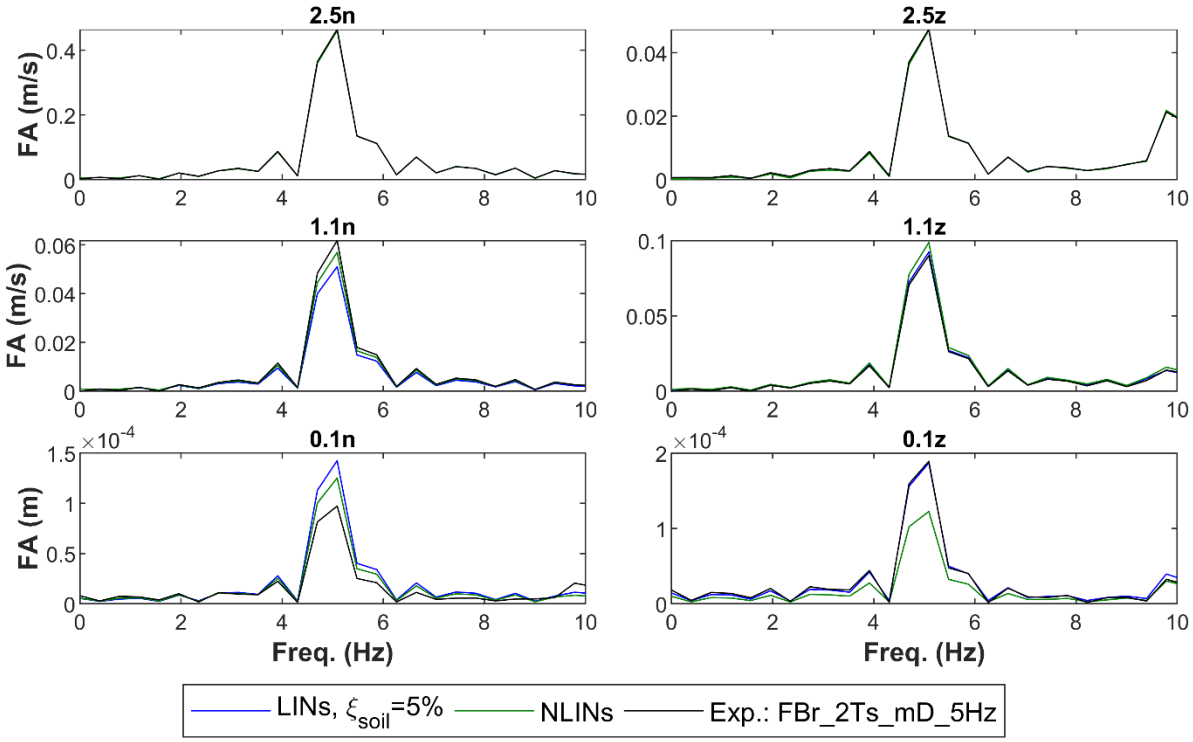


Figure 7.52: Fourier spectra of the horizontal (n) and vertical (z) motions of the top slab (2.5), foundation (1.1) and soil (0.1). Results of the FBr_2Ts_mD_5Hz forced vibration simulations that assume either linear or nonlinear soil are compared.

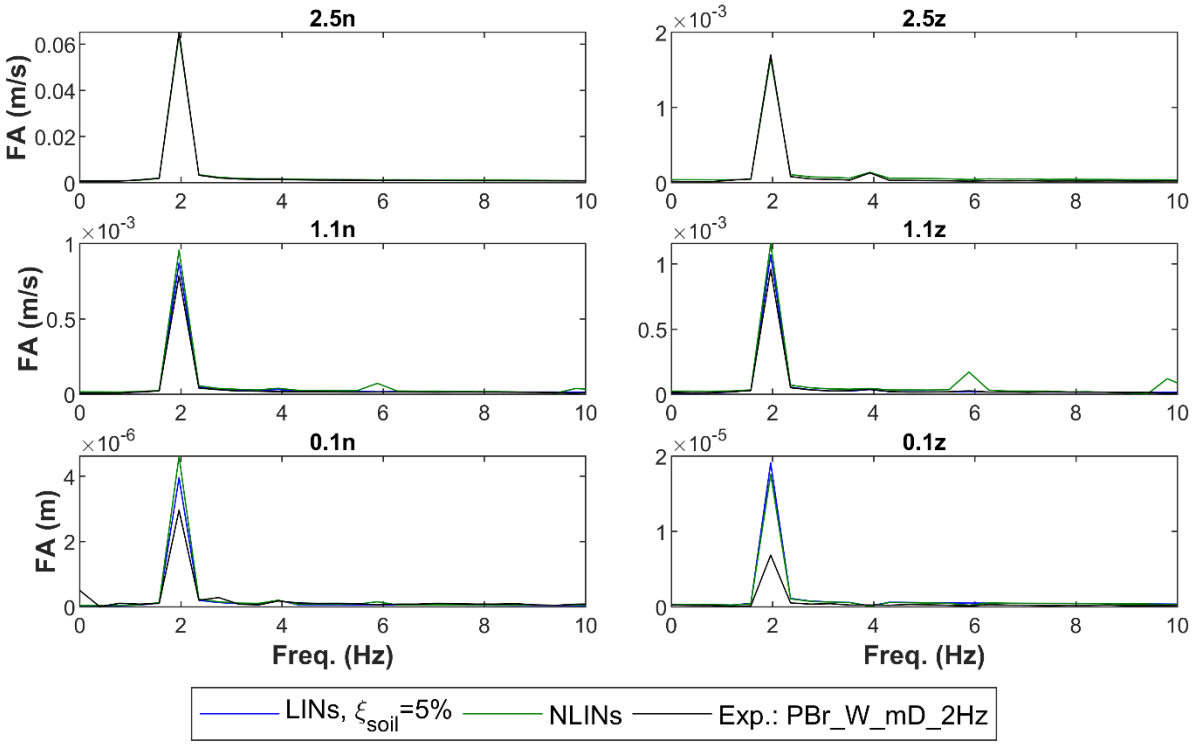


Figure 7.53: Fourier spectra of the horizontal (n) and vertical (z) motions of the top slab (2.5), foundation (1.1) and soil (0.1). Results of the PBr_W_mD_2Hz forced vibration simulations that assume either linear or nonlinear soil are compared.

7.14 Calibration of the static interface normal stresses against free vibration tests

It was earlier justified that the simulations of the 1-top slab experiments should allow opening of more interface elements in addition to the ones prescribed as always opened. This makes the use of elastic interface elements inappropriate, while implying the need of using elastoplastic interface elements. As evidenced in Section 7.12.2, the imposition of elastoplastic interface elements at the soil-foundation interface, without the prescription of initial detachment, does not allow the interface elements to open. The reason of this is the high accumulation of normal stresses at the interface elements below the edges of the contact area. Figure 7.10a plots contours of static effective normal stresses (σ'_n) of the interface elements when the gap configuration GC2 (Figure 7.9b) is adopted and when K_s and K_n are set equal to 1E8kN/m^3. The large stiffness of interface elements simulates conventionally a foundation that is much stiffer than the soil beneath. This results in accumulation of interface stresses at the edges of the contact area, while the stresses are particularly high at the corners of contact area. At the inner part of the contact area the normal stresses are much lower, while zero static stresses are maintained at the non-contact area.

This distribution of the static effective normal stresses that corresponds to a stiff foundation might have not been the case during the experiments that were carried out as part of the present study. Due to the casting procedure of the foundation, that is described in Section 5.2.4, it is likely that the foundation had a base shape similar to a parabola. This foundation shape might have contributed to a more uniform interface stress distribution, under self-weight, than the one described above. A more uniform distribution of the normal stresses at the interface is expected to facilitate the opening and closure of interface elements, however its applicability requires investigation.

The stress distribution of the interface elements under static self-weight loads can be controlled by the stiffness K_s and K_n of these elements. In particular, K_n controls the normal stress distribution, which is the stress component at the interface that affects the opening and closure of interface elements (gaps formation). High K_n (e.g. 1E8kN/m^3) values result in the above described stress distribution, where stresses are accumulated under the edges of the interface contact area. When, though, a very low value (e.g. 1E2kN/m^3) is assigned to K_n, then a uniform stress distribution can be achieved. In fact, very low values of K_n can model an interface stress distribution that corresponds to a flexible foundation.

Aiming to model permanently open interface elements, while concurrently allowing the opening of those that are initially closed, the hybrid interface model is employed. As described in Section 7.7.6,

this model employs elastic interface elements of low stiffness for the permanently non-contact area, while elastoplastic interface elements are employed for the remaining (initially in contact) area. The stiffness of the interface elements during the application of the static self-weight, StSW analysis, is different for the contact and non-contact areas. The stiffness also differs between the StSW analysis and static pull-out analysis (for free vibration simulations) and dynamic analysis (Table 7.8, Table 7.10).

The examined interface stiffness values selected for the static self-weight analysis are presented in Table 7.10. For simplicity, K_s and K_n are assumed to be equal. Three different static self-weight analyses are run, StSW3, StSW4, StSW8, with the values of K_s and K_n for the contact area set at 1E3, 1E4 and 1E8kN/m3, respectively. The effective normal static stresses (σ'_n) resulted at the interface elements from the three analyses, assuming nonlinear soil, are presented in Figures 7.10, 7.11 and 7.12, which are discussed in Section 7.7.8. These interface stresses existed prior to the static pull-out and dynamic analyses, for the case of free and forced vibration simulations, respectively. For the static pull-out and dynamic analyses, K_s and K_n are set equal to 1E8kN/m^3 at the contact interface area. For all analyses, for the non-contact area, a value of 1E2kN/m^3 is assigned to these properties (Table 7.8).

The impact of the different static σ'_n distribution on the free vibration response is examined. The distribution of the interface normal stress under the self-weight of the structure is calibrated against free vibration simulations of the fully braced 1-top slab structure. This structure is anticipated to be the most sensitive to changes of the interface stresses, as it is the lightest and hence the one that exhibits the stronger foundation uplift. The calibrated interface stresses, which are associated with the selection of K_s and K_n, are validated against free vibration tests of the FBr_2Ts and PBr_W structural configurations, while they are also validated against the forced vibration response of all three structural configurations.

7.14.1 Free vibration simulations

The aim of the free vibration simulations of the FBr_1Ts structural configuration is to calibrate the distribution of σ'_n that exists at the interface elements prior to the static pull-out analysis. The calibrated model should predict a fundamental frequency around 3.25Hz to 3.50Hz. The amplitude of the output motion cannot be investigated, due to the lack of free vibration field data.

Figure 7.54 compares the horizontal top slab response (2.1n) as computed by nonlinear analyses that employ either elastic (ELint_GC2) or hybrid (HYBint_GC2) interface elements at the soil-foundation interface. Results from three different analyses that use the HYBint_GC2 interface model are compared, while all interface models simulate the GC2 gap configuration. All three analyses have identical inputs for the StP and dynamic free vibration analyses, while they are initiated with different interface stress distribution. The HYBint_GC2_StSW8, HYBint_GC2_StSW4 and HYBint_GC2_StSW3

analyses use, prior to the StP and dynamic analyses, the stress conditions produced by the StSW8, StSW4 and StSW3 analyses, respectively.

Figure 7.54a shows that HYBint_GC2_StSW8 and ELint_GC2 analyses produce identical top slab response, in terms of Fourier spectra. The same observation is made looking the peak-to-peak frequencies (Figure 7.54b) and damping ratio (Figure 7.54c) that is computed using the logarithmic decrement method (assuming i=1 according to Section 6.2.4). The same response predicted by the HYBint_GC2_StSW8 and ELint_GC2 analyses implies similar foundation detachment between the two analyses and that interface plasticity was not mobilised during the former analysis. This happens due to the due to the stress concentration that exists at the edges of the contact area, shown in Figure 7.10. The above conditions led to the generation of identical contact areas during both analyses, which justifies the similarity of their results.

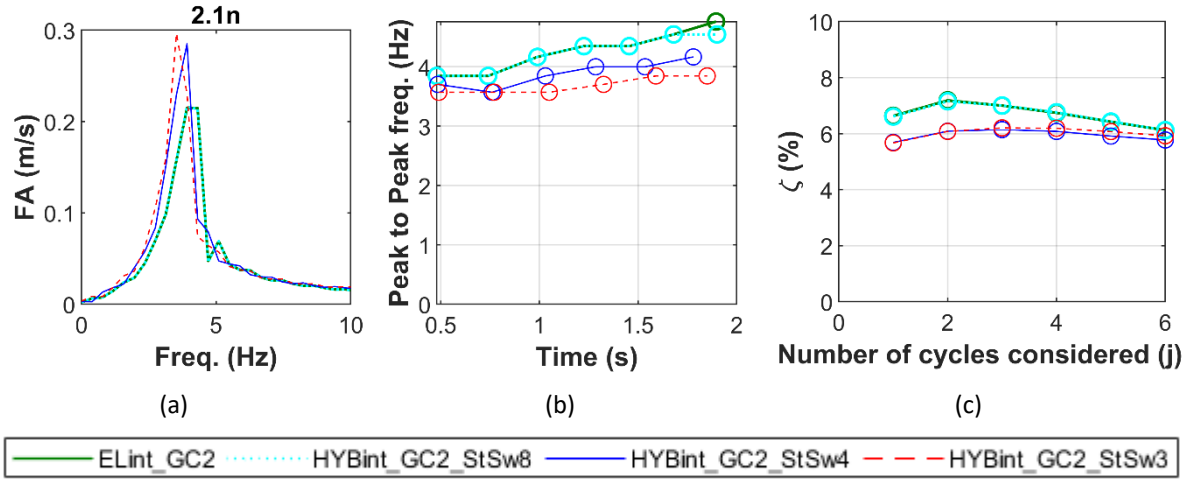


Figure 7.54: Horizontal top slab (2.1n) response computed by simulations of the FBr_1Ts_15.70kN free vibration test. The analyses employ elastic or hybrid interface elements, while various interface conditions at the StSW analysis.

The HYBint_GC2_StSW4 and HYBint_GC2_StSW3 analyses produce different results relative to the other two. This indicates different interface contact conditions between the compared analyses during excitation. The HYBint_GC2_StSW4 and HYBint_GC2_StSW3 free vibration analyses started with a more uniform interface normal stress distribution than the HYBint_GC2_StSW8. These interface conditions facilitated the opening and closure of the interface elements that were initially close. The analyses predicted a smaller foundation area that was in contact with the soil, making the system more flexible, as illustrated by the main peaks of the Fourier amplitude in Figure 7.54a. The more flexible response predicted by the HYBint_GC2_StSW4 and HYBint_GC2_StSW3 analyses is also illustrated in Figure 7.54b, that shows smaller peak-to-peak frequency values for these analyses.

Figure 7.54c demonstrates that the analyses, that produced larger foundation detachment, produced smaller values of damping and hence larger motion amplitude that is shown in Figure 7.54a. As already shown through forced vibration simulations in Section 7.12.1, this is because when larger foundation detachment exists, the foundation motion cannot transmit as much motion to the soil, reducing radiation damping.

Figure 7.55 invigorates the above claims about the opening and closure of the interface elements that were initial closed. It presents the variation of normal plastic strains (ε_{pl}) with time, which are in meters units and reflect to the actual opening of the elements. Zero ε_{pl} represents a close element indicating that the foundation is in contact with the soil, while a non-zero value indicates detachment. The presented strains are computed at the nine integration points of the four numbered interface elements shown in Figure 7.55a. The figure shows the initial interface conditions of the gap configuration GC2 and the loading direction. In accordance with the loading direction, the elements of which ε_{pl} values are presented are those which anticipate opening during the application of the pull-out force. Figure 7.55b, c and d present the plastic normal strains as computed by HYBint_GC2_StSW8, HYBint_GC2_StSW4 and HYBint_GC2_StSW3 analyses that simulate the FBr_1Ts_15.70kN free vibration experiment.

Figure 7.55b verifies that, when prior to the StP analysis, the normal stress distribution at the interface is initiated according to the StSW8 analysis, the initially close interface elements do not open at any time during free vibration. Figure 7.55c and d demonstrate that when under self-weight loads the normal stress distribution is more uniform, which is the case for the StSW4 and StSW3, the initially close interface elements open and close at different times during the excitation. In fact, the magnitude of opening, ε_{pl}, is found to be highly sensitive to the static interface stresses and the choice of interface stiffness. The StSW3 analysis produced significantly stronger ε_{pl} than the StSW4 analysis, despite the relatively small difference in their input properties (i.e. K_s and K_n for the StSW analyses). This observation justifies why the HYBint_GC2_StSW3 free vibration analysis produces a more flexible response than the HYBint_GC2_StSW4, as observed in Figure 7.54a. The opening magnitude of interface elements depends also on the position of the elements in relation with the gap area. The interface elements 16 and 26, that are close to the boundary between initially contact and non-contact areas, exhibited much stronger opening than the inner elements 15 and 25. The latter elements exhibit very limited to zero opening during the free vibration.

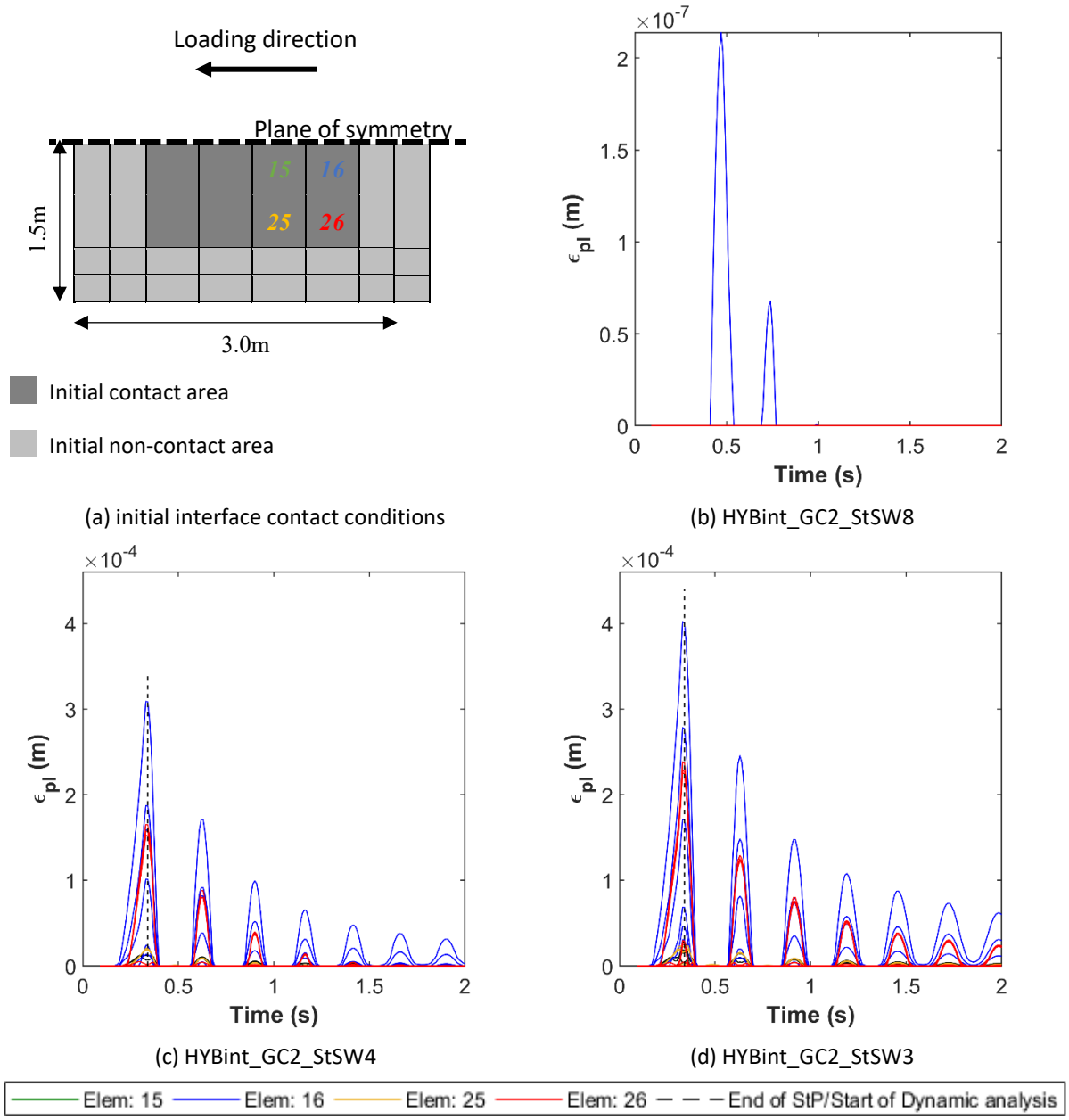


Figure 7.55: Variation of plastic normal strain with time computed at all integration points of the numbered interface elements shown in (a). The results are extracted from simulations of the FBr_1Ts_15.70kN free vibration experiment, using the initial stress distribution of (b) StSW8, (c) StSW4 and (d) StSW3.

Figure 7.54a and b show that the HYBint_GC2_StSW3 free vibration analysis predicts a fundamental frequency of the SSI system close to the target one, which is between 3.25Hz to 3.50Hz. Therefore, the use of K_s=K_n=1E3kN/m^3 for the StSW analysis and the adoption of the resulted stress distribution (Figure 7.12) are the most applicable among the investigated ones. Aiming to provide a single calibration for all experiments, the applicability of these interface conditions on the free vibration response of the FBr_2Ts and PBr_W structures is investigated.

Figure 7.56 compares the horizontal top slab response (2.5n) computed by the FBr_2Ts_15.70kN simulations that use either the ELint_GC2 interface model, suggested earlier in the thesis, or the newly proposed HYBint_GC2_StSW3 model. Figure 7.56a and b show that the latter analysis reproduces well both the frequency content and the amplitude of the motion. Figure 7.56a and c show that despite the HYBint_GC2_StSW3 predicts a slightly more flexible motion at the first cycles, it predicts a better frequency response of the subsequent cycles than the ELint_GC2 analysis. Finally, Figure 7.56d shows that the analysis with the hybrid interface elements produces less damping at the first cycles of the motion, which is attributed to the opening of initially closed interface elements. The opening of these elements is evidenced in Figure 7.57 that plots the variation of ε_{pl} with time. The figure shows that a significant number of integration points of the initially closed interface elements open at the first cycle of the motion, while thereafter the majority of these points stay closed until the end of the motion. This justifies the more flexible response predicted by the HYBint_GC2_StSW3 than the ELint_GC2 analysis.

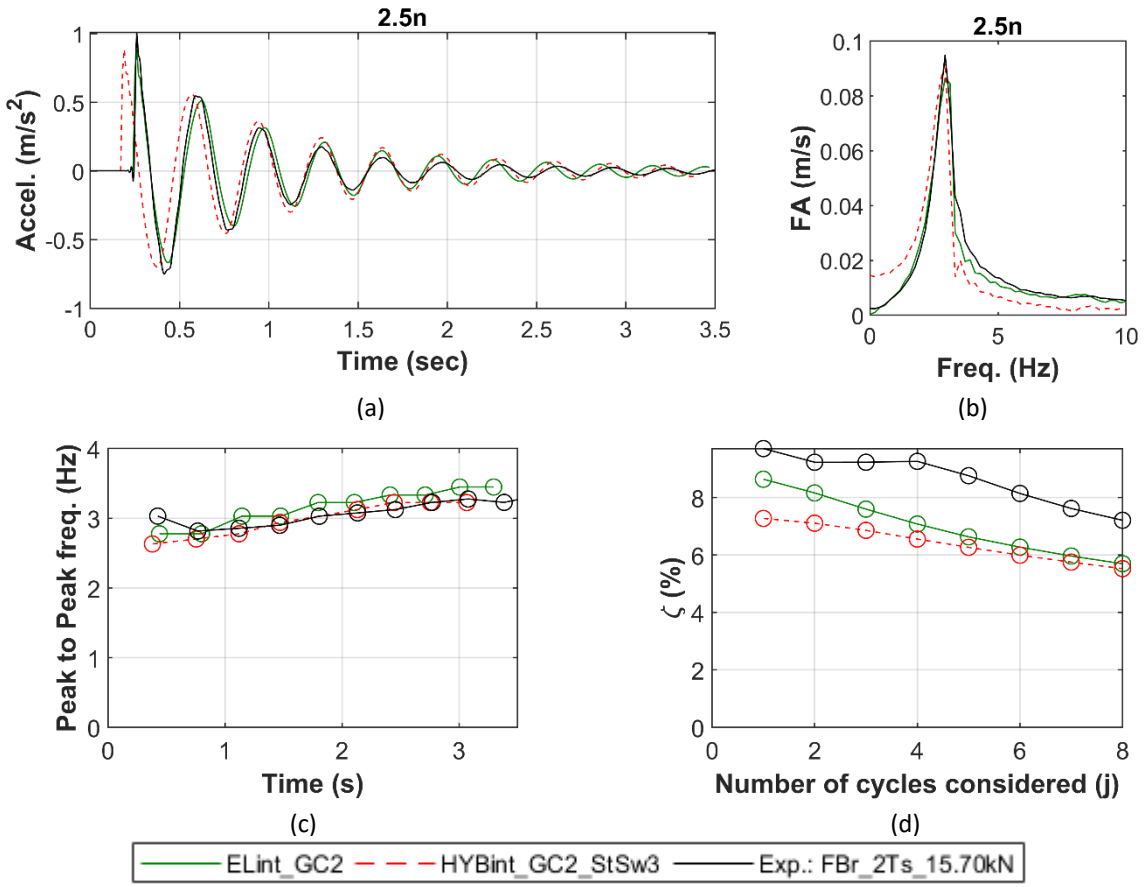


Figure 7.56: Horizontal top slab response (2.5n) as computed by simulations of the FBr_2Ts_15.70kN free vibration test. The analyses use either elastic or hybrid interface elements.

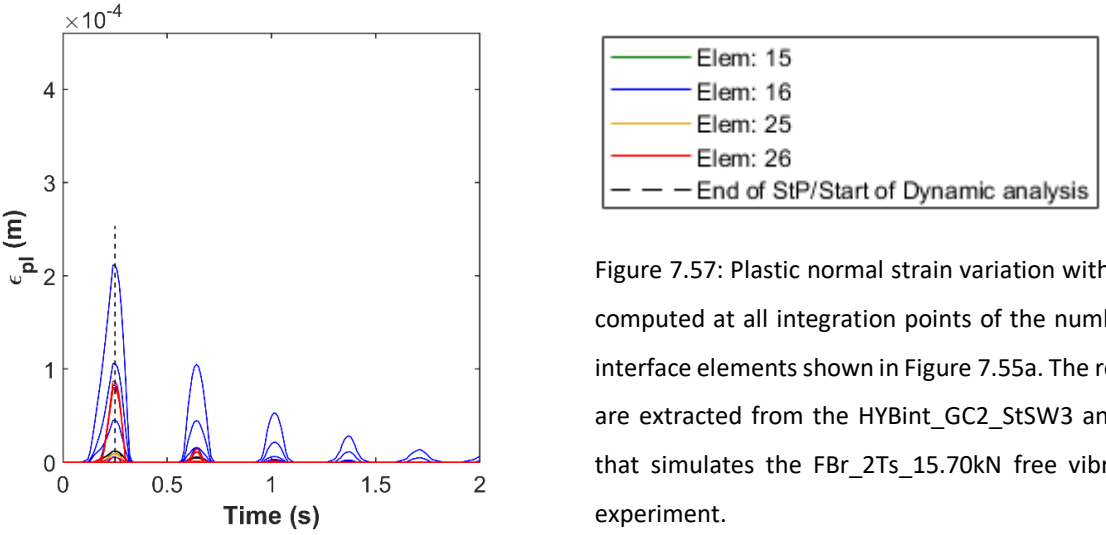


Figure 7.57: Plastic normal strain variation with time computed at all integration points of the numbered interface elements shown in Figure 7.55a. The results are extracted from the HYBint_GC2_StSW3 analysis that simulates the FBr_2Ts_15.70kN free vibration experiment.

Figure 7.58 illustrates that the new HYBint_GC2_StSW3 and ELint_GC2 analyses predict very similar horizontal top slab response when the PBr_W_13.90kN experiment is simulated. The free vibration of the partly braced structure engages weaker foundation motion than the experiments on the fully braced structures, hence, mobilising weak opening of the initially close interface elements. The latter implies that the two compared analyses predict similar contact conditions throughout the motion, justifying their similar results.

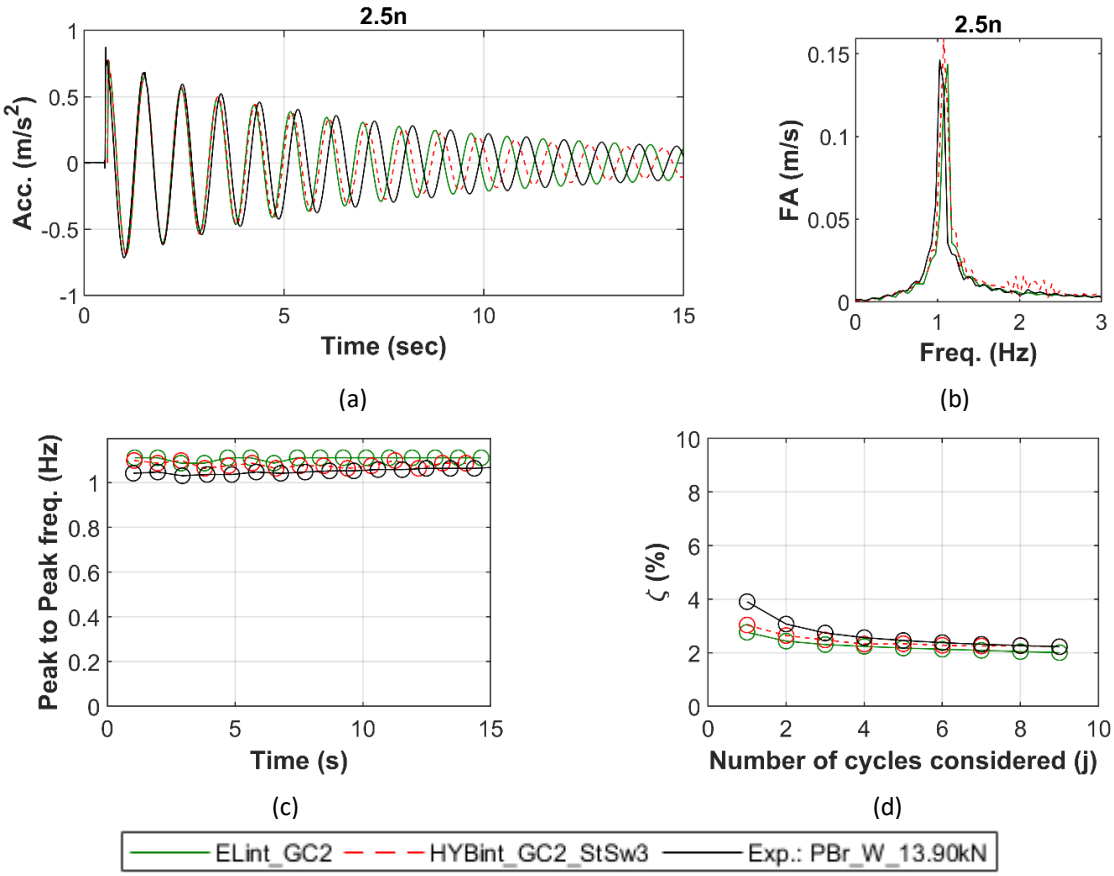


Figure 7.58: Horizontal top slab response (2.5n) as computed by simulations of the PBr_W_13.90kN free vibration test. The analyses employ either elastic or hybrid interface elements.

The applicability of the hybrid interface model HYBint_GC2_StSW3 has been validated against free vibration tests on all structural configurations, FBr_1Ts, FBr_2Ts and PBr_W. The calibrated interface model and the initial interface conditions, produce satisfactory results replicating the physical experiments. The new model is necessary for the simulation of free vibration experiments on the FBr_1Ts structure, while both the HYBint_GC2_StSW3 and ELint_GC2 models can be used for the simulation of the FBr_2Ts and PBr_W free vibration experiments.

7.14.2 Forced vibration simulations

Figures 7.59, 7.60 and 7.61 present the SSI response computed by the FBr_1Ts_mC_5Hz, FBr_2Ts_mD_5Hz and PBr_W_mD_2Hz simulations, respectively, aiming to investigate the applicability of the interface HYBint_GC2_StSW3 model. The results computed using this model are compared with the ones produced by employing the ELint_GC2 model. Any difference between them is attributed to the different contact conditions at the soil-foundation interface. In both analyses, the soil is assumed to behave nonlinearly (NLINs).

The figures demonstrate that the hybrid interface model tends to increase the foundation and decrease the soil motion, in relation to the ELint_GC2 model. The impact on the response though is very small, hence, for the presented experiments, the latter model is preferred to as it is more computationally efficient. However, care should be taken when simulating forced vibration tests of a larger applied force. Larger applied forces accentuate foundation uplift, imposing the necessity of employing hybrid interface elements. Considering the susceptibility of the FBr_1Ts structure to foundation uplift, the subsequent simulations of forced vibration tests on this structure will incorporate the HYBint_GC2_StSW3 model, unless stated otherwise.

7.14.3 Discussion

This investigation shows that the initial normal interface stresses, that result from the impact of self-weight, can affect the response of both the structure and the soil. The significance of the impact depends on the structural configuration, magnitude of the excitation and type of experiment. The calibration of the interface stresses is important when modelling the free vibration response of the FBr_1Ts structure, which is prone to rotate around the foundation level. This structure is less sensitive to changes of the initial interface stresses when it is subjected to forced vibration tests, however, it can become sensitive under large forced vibratory loads.

The above investigation proposes a calibrated distribution of the self-weight normal stresses at the soil-foundation interface. The calibrated interface stresses, which are presented in Figure 7.12, are relatively uniformly distributed along the area where the foundation is in contact with the soil. A small stress concentration appears along the line that defines the boundaries between contact and non-

contact interface area. This stress distribution was achieved by incorporating in the self-weight static analysis $K_s=K_n=1E3kN/m^3$ for the interface elements below the contact interface area (StSW3 according to Table 7.10).

The calibrated static interface stress distribution (StSW3) and the hybrid interface model (HYBint_GC2) are validated against free and forced vibration tests on all three structural configurations, FBr_1Ts, FBr_2Ts and PBr_W. The above investigation shows that this interface model (HYBint_GC2_StSW3) facilitates a good comparison of the computed response with the field data. Unless otherwise stated, for the analyses that are presented thereafter, the HYBint_GC2_StSW3 interface model is used for the simulation of experiments on the FBr_1Ts structure. The same model is used for the majority of free vibration analyses of the FBr_2Ts and PBr_W configuration, while the ELint_GC2 interface model is preferred for the computationally expensive free vibration simulations. The ELint_GC2 interface model is also preferred for the simulation of forced vibration experiments on the FBr_2Ts and PBr_W structures. This preference stems from the observation that these experiments exhibit a reduced tendency towards nonlinear foundation responses.

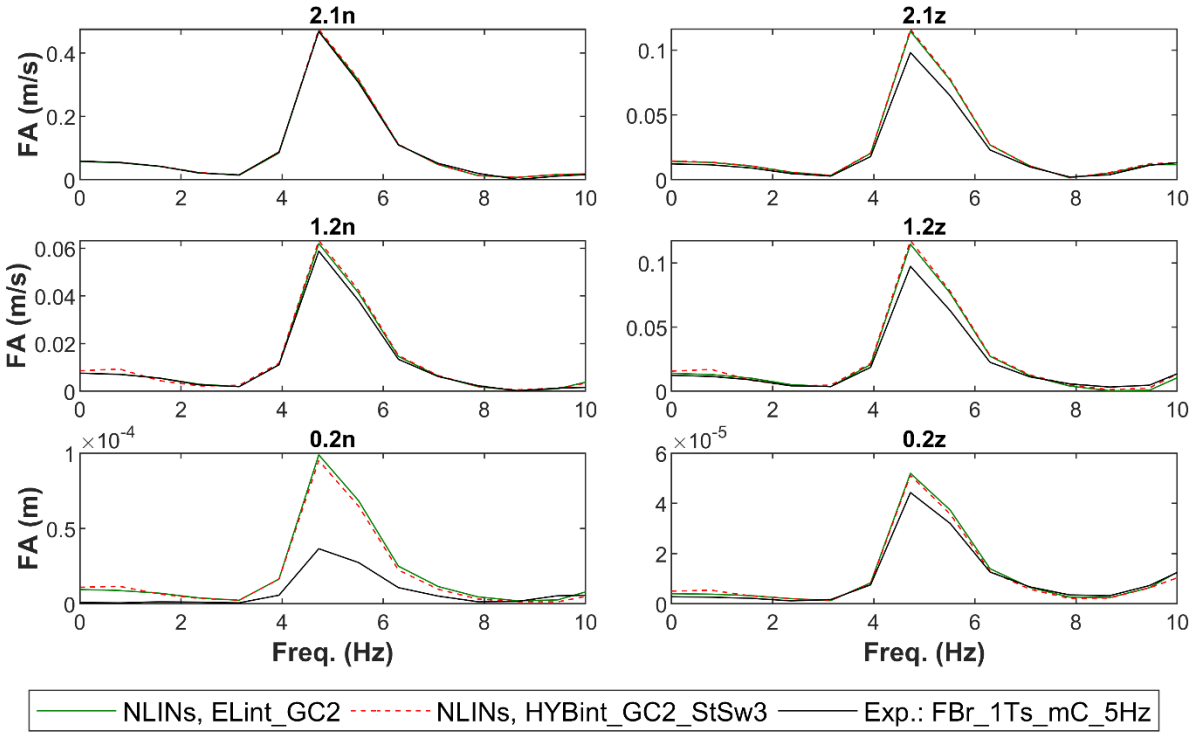


Figure 7.59: Fourier spectra of the horizontal (n) and vertical (z) motions of the top slab (2.1), foundation (1.2) and soil (0.2). The compared results are computed by the FBr_1Ts_mC_5Hz forced vibration simulations that assume nonlinear soil, while elastic or hybrid interface elements are used.

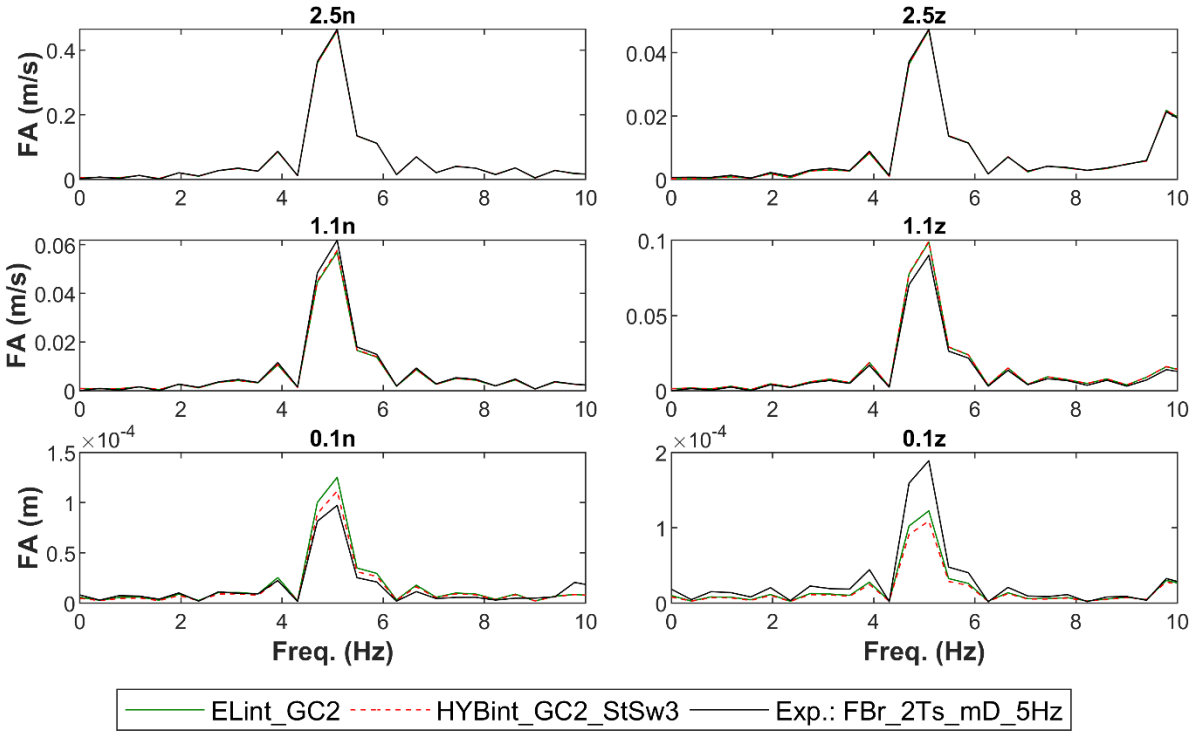


Figure 7.60: Fourier spectra of the horizontal (n) and vertical (z) motions of the top slab (2.5), foundation (1.1) and soil (0.1). The compared results are computed by the FBr_2Ts_mD_5Hz forced vibration simulations that assume nonlinear soil, while elastic or hybrid interface elements are used.

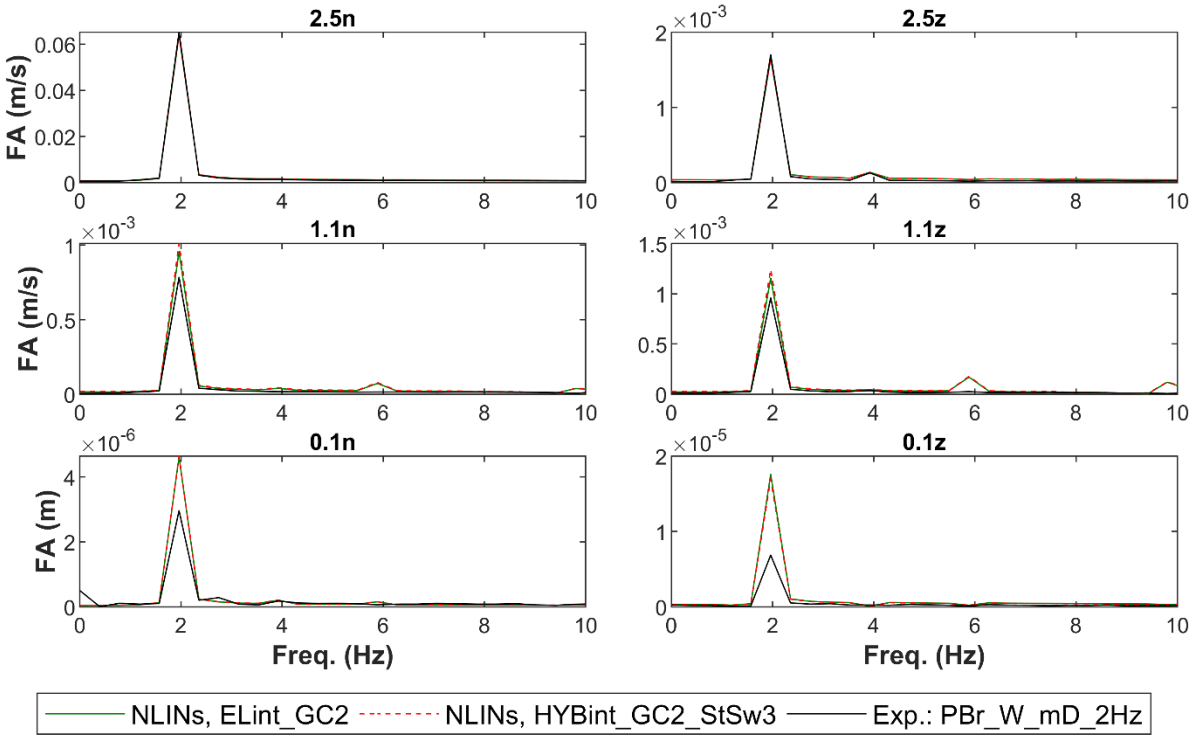


Figure 7.61: Fourier spectra of the horizontal (n) and vertical (z) motions of the top slab (2.5), foundation (1.1) and soil (0.1). The compared results are computed by the PBr_W_mD_2Hz forced vibration simulations that assume nonlinear soil, while elastic or hybrid interface elements are used.

7.15 Initial opening investigation

Although the HYBint_GC2_StSW3 model is found in Section 7.14 to be suitable for the simulations of the experiments, it poses a limitation. It simulates permanently detachment between the foundation edge and the soil. This contact condition may be representative for weak foundation vertical displacements, while may not be applicable for stronger. Under large pull-out forces or at the first cycles of the free vibration, where the strongest foundation rocking takes place, some gaps below the foundation edge may temporarily close. When the motion is dissipated after the first cycles of the response, the gaps below the foundation edges open, which is the condition that remains until rest. This closure and opening of the gaps below foundation edges creates a stiffer response at the first cycles than the subsequent ones.

Such a feature was earlier observed in Section 6.2.5 in the field data. Figures 6.13 and 6.14, that plot the peak-to-peak frequencies of the PBr_W and FBr_2Ts free vibration response, show that the response was stiffer at the first cycles of the motion than the subsequent ones. At the first cycles, the peak-to-peak frequencies decrease, while at subsequent cycles they increase with time. The latter feature is expected as the strains and hence nonlinear phenomena dissipate with time. The unexpected decrease of the frequencies was earlier attributed to possible closures of gaps at the first cycles, before the gaps become permanently opened at the subsequent cycles of the motion. This claim is numerically investigated in this section.

The investigation is carried out by imposing elastoplastic interface elements (EPint) at the entire soil-foundation interface. The presented analyses retain the calibrated self-weight normal effective stress distribution (StSW3) (see Section 7.14). The GC2 gap configuration (Figure 7.9b) is rigorously simulated through the initiation of non-zero values for the hardening parameter of the model that corresponds to the normal plastic strains, as described in Section7.7.4. The new interface model is referred to as EPint_*g*mm_StSW3, where *g* is the magnitude of initial opening of the gaps below the foundation edge. The current investigation adopts the initial gap openings that are presented in Table 7.13. As the table shows, the investigation is carried out through simulating the FBr_2Ts_15.70kN and FBr_1Ts_15.70kN free vibration tests.

Table 7.13: Free vibration simulations carried out to investigate the impact of initial opening magnitude.

Experiment	Analysis code	Initial opening *g* (mm)
FBr_2Ts_15.70kN	EPint_0.1mm_StSW3	0.1mm
	EPint_0.3mm_StSW3	0.3mm
	HYBint_GC2_StSW3	n/a
FBr_1Ts_15.70kN	EPint_0.2mm_StSW3	0.2mm
	EPint_0.5mm_StSW3	0.5mm
	HYBint_GC2_StSW3	n/a

7.15.1 Free Vibration simulations

Figure 7.62 presents the horizontal top slab response (2.5n) computed by the simulations of the FBr_2Ts_15.70kN free vibration experiments. The compared simulations employ either the hybrid or elastoplastic interface model of initial opening of 0.1mm and 0.2mm. Figure 7.62a presents the Fourier spectra inferred from top slab motions, illustrating that the different simulations produced a similar response, including the natural frequency of the SSI system. However, differences can be observed by inspecting the peak-to-peak frequencies, which are presented in Figure 7.62b. The figure shows the analyses with elastoplastic interface elements produce a stiffer response frequency at the first cycles of the motion than the analysis with hybrid elements. In fact, the predicted response at the first cycles become stiffer when smaller initial gaps are prescribed, i.e. EPint_0.1mm_StSW3. The EPint_0.3mm_StSW3 analysis, which prescribes three times larger initial gaps than the former one, produces a response closer to the one predicted by the HYBint_GC2_StSW3 one.

The magnitude of gap opening also affects the produced damping. Figure 7.62c presents the damping developed by the SSI system computed using the logarithmic decrement method, described in Section 6.2.4. The presented damping values express the motion dissipation between the second and the next j peaks, i.e. i=2, according to Eq. 6.10. The figure shows that larger damping develops when smaller magnitude of initial gaps is prescribed. The EPint_0.1mm_StSW3 analysis produces an interface contact area which is larger at the first cycles than the EPint_0.2mm_StSW3 and HYBint_GC2_StSW3 analyses. It is therefore verified that the increase of non-contact interface area decreases the damping produced by the SSI system. This aligns with the observation made in Section 7.12 according to which gaps formation decreases the transmission of motion in the soil domain and hence decreasing the radiation and soil material damping.

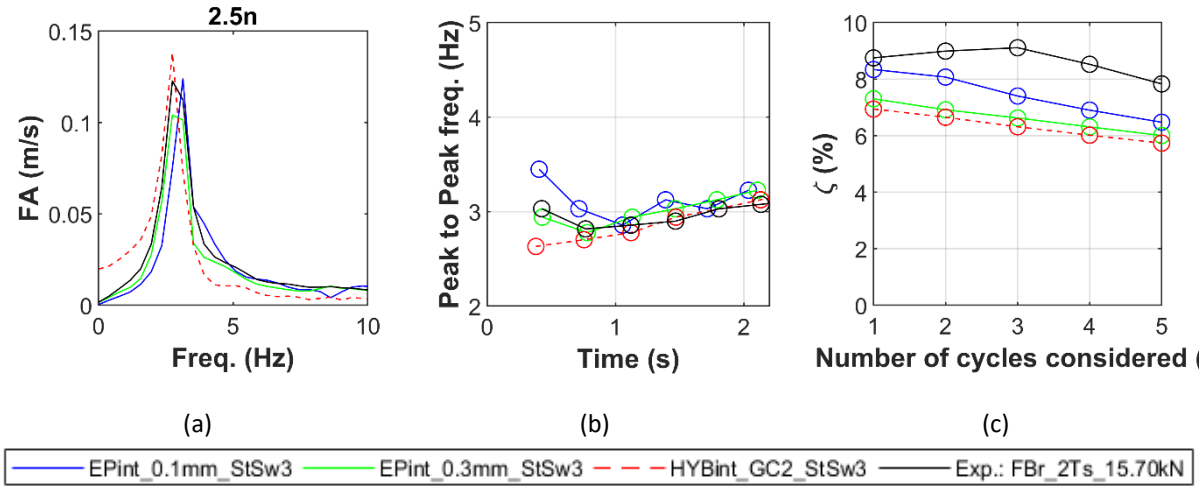


Figure 7.62: Horizontal top slab response computed by simulations of the FBr_2Ts_15.70kN free vibration test. The analyses employ hybrid or elastoplastic of various magnitudes of initial opening.

Figure 7.63 investigates the impact of initial gap opening on the response of the FBr_1Ts structure when the structure is subjected to the same pull-out force (FBr_1Ts_15.70kN). The compared simulations employ either the hybrid or elastoplastic interface model of initial openings of 0.2mm and 0.5mm. The elastoplastic interface model and magnitude of gaps impact the response of the FBr_1Ts structure in the same way they impact the FBr_2Ts one, but more pronouncedly. The difference of response frequency between the first and second cycle is more pronounced on the response of the lighter (Figure 7.63b) than the heavier one (Figure 7.62b). Also, the increase of damping produced by EPint analyses relative to the one produced by HYBint analysis is more significant on the FBr_1Ts_15.70kN (Figure 7.63c) than FBr_2Ts_15.70kN simulation (Figure 7.62c). This stems from the fact that the lighter structure is more prone to rotate around the foundation level, creating larger foundation vertical displacements. Hence, it promotes the temporary closure of more interface elements that were initially open, which they become permanently open in subsequent cycles. This condition creates a significant difference of the interface contact area between the first and the second cycles, resulting in a large variation of the response frequency. Also, the larger contact area produced by the FBr_1Ts simulations can justify the stronger sensitivity of system's damping to the choice of hybrid or elastoplastic interface elements.

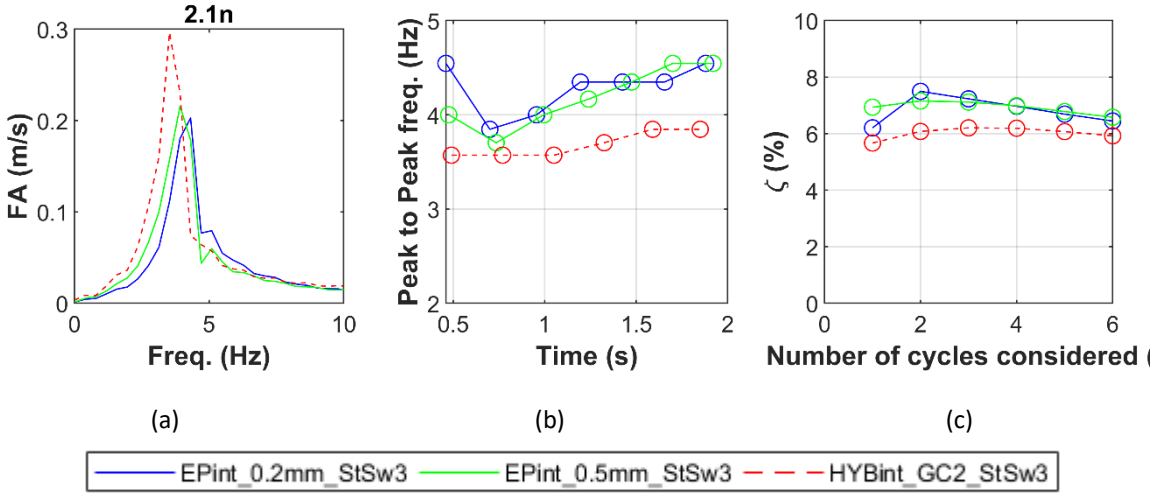


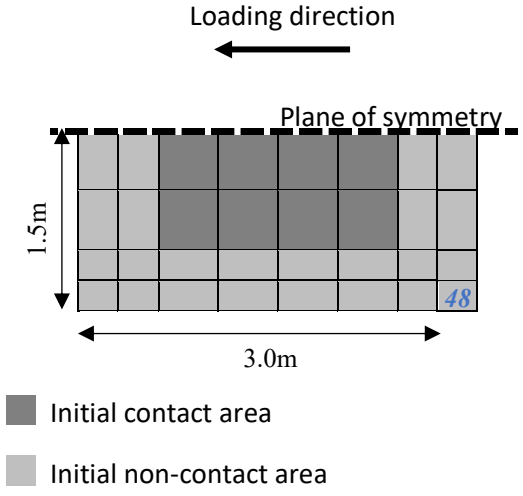
Figure 7.63: Horizontal top slab response computed by simulations of the FBr_1Ts_15.70kN free vibration test. The analyses employ hybrid or elastoplastic of various magnitudes of initial opening.

The above observations demonstrate that when elastoplastic interface elements are used for the entire soil-foundation interface, the initially open interface elements can close at the first stages of the analyses. The extent of the initially open interface area that closes during the analysis depends on the opening value that is assigned at the beginning of the analysis, as indicated by Figure 7.64. The figure plots the normal plastic strains (ε_{pl}), which reflect the opening of gaps, of all nine integration points of the element 48 that is indicated in Figure 7.64a. According to the figure, this element is at

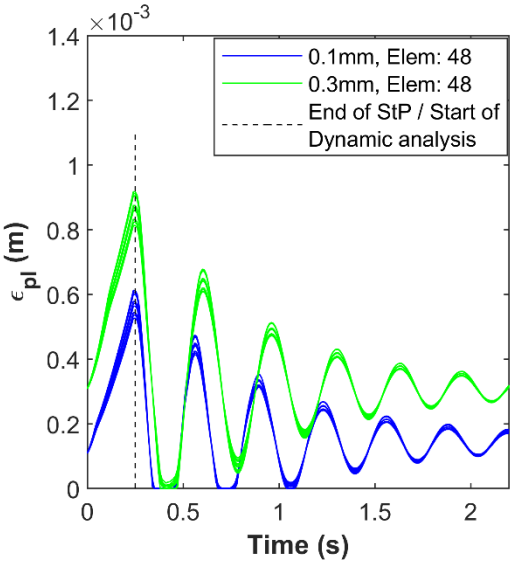
the foundation corner and, in relation to the loading direction, is expected to exhibit the strongest opening during the application of the pull-out force than the remaining interface elements.

Figure 7.64b and c present the ε_{pl} values computed by the simulations of the FBr_2Ts_15.70kN and FBr_1Ts_15.70kN experiments, respectively. The figures show that the elements open during the application of the pull-out force, which is completed at the time instant indicated by black dashed line. This line also indicates the load removal and the initiation of free vibration. Beyond this line, the structure tends to move to its initial position and consequently the gaps below of this element tends to close. At the foundation impact on the soil, the interface element closes completely and opens again at the next cycle of the motion. When the motion dissipates, the element remains open for the remaining vibration. The number of cycles, during which the alternating opening and closing of the element takes place, increases with decreasing initial opening. In particular, for the simulation of the FBr_2Ts_15.70kN experiment, the element opens and close for one cycle when the initial opening is prescribed with 0.2mm (Figure 7.64b). When initial gaps of 0.1mm opening are chosen, though, the element opens and closes for 3 cycles, demonstrating the important impact of the magnitude of the initial gap.

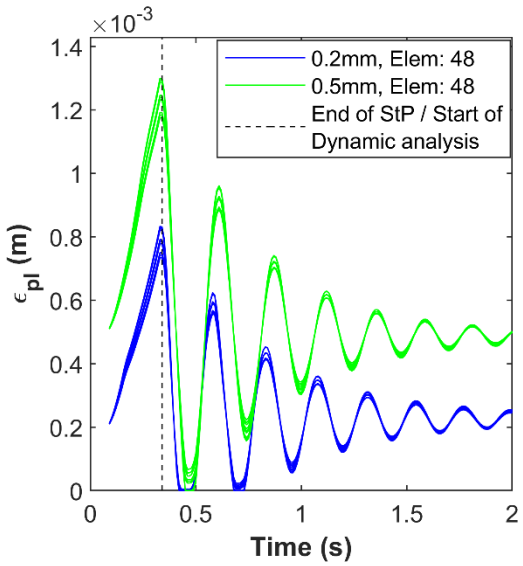
The comparison between experimental and numerical results, shown in Figure 7.62, discloses that an initial opening of 0.3mm is sufficient for modelling the free vibration tests on the FBr_2Ts structure. However, it is more computationally expensive than the ELint_GC2 and HYBint_GC2_StSW3 interface models which were also shown to produce satisfactory results. For this reason, for the subsequently presented analyses, interface gaps are simulated through elastic low stiffness interface elements, considering that this simulation does not allow closure of these elements.



(a) initial interface contact conditions



(b) FBr_2Ts_15.70kN



(c) FBr_1Ts_15.70kN

Figure 7.64: Plastic normal strain variation with time computed at all integration points of the numbered interface element shown in (a). The results are extracted from simulations of the (b) FBr_2Ts_15.70kN and (c) FBr_1Ts_15.70kN free vibration experiments, using the initial stress StSW3 and prescribing various initial openings.

7.16 Final model calibration

The following model calibration is used for all modelled experiments, free and forced vibration tests on the FBr_2Ts, FBr_1Ts and PBr_W structural configurations. The proposed calibration was earlier found to replicate sufficiently well the physical experiments, validating its applicability.

Table 7.14 presents the elastic properties of the structural elements that are incorporated in the calibrated model. The name convention of the properties is already discussed in Section 7.5.1. The structural properties that were subjected to calibration are indicated with darker colour, while the remaining properties were selected according to modern regulations (i.e. British Standards Institution, 2004, 2005). The elastic soil, presented in Table 7.4, properties were not subjected to calibration, as they were inferred from previous site characterisation and site-response studies mentioned in Section 4.3 and shown in Figure 4.8.

Table 7.14: Elastic properties of the structural elements.

	E (GPa)	ν	ρ (Mgr/m^3)	A (cm^2)	I (cm^4)	J (cm^4)	ξ (%)
Concrete	31	0.2	2.5	-	-	-	1
Braces	200	0.25	7.85	19.2	177	6.97	2
Columns	200	0.25	7.85	54.9	1770	2830	2
Beam elements extended into the foundation	200E4	0.25	0.05	54.9	1770	2830	-
Beam elements extended into the top slab	3.0	0.25	0.05	54.9	1770	2830	-

Unlike the elastic soil properties, the nonlinear soil behaviour was thoroughly investigated. The investigation included the calibration of the stiffness degradation and damping ratio curves, as well as the calibration of the limit of the minimum degraded shear stiffness (G_{min}). The calibration Calibr6 and a G_{min} value equal to $0.15G_o$ are chosen. Table 7.15 presents the calibrated input parameters incorporated in the nonlinear IC.G3S model.

Table 7.15: Input parameters, of the calibration Calibr6, that are incorporated in the nonlinear IC.G3S model.

G_0 (MPa)	88	b_0	0.932	a_2	0.0	$d_{2,G}$	0.001
m_G	0.3	a_0	3.619E-05	$d'_{1,G}$	3.6	$d_{3,G}$	3000.0
$R_{G,min}$	0.008	a_1	0.0	$d''_{1,G}$	0.0	$d_{4,G}$	0.7
G_{min} (MPa)	13.2						

The soil-foundation interface model required calibration of the initial interface contact conditions, elastic shear (K_s) and normal (K_n) stiffness of the interface elements, as well as calibration of the constitutive behaviour of these elements. Different properties and constitutive behaviour are required at the interface elements which intend to model interface gaps in relation to the elements that model contact conditions. Also, the interface elements properties differ between the static self-weight (StSW), static pull-out (StP) and dynamic free vibration analyses. Although, more than one interface models were found to be suitable, the final interface model is chosen to be the most computationally effective.

Under static conditions, the GC2 gap configuration, shown in Figure 7.9b, is chosen. The GC2 prescribes the foundation to be detached from the soil at its edges, while it is initially in contact at the inner area. The calibrated model simulates permanent gaps at the edges using low stiffness (i.e. 1E2kN/m^3) elastic interface elements. For simulations of forced vibration experiments on the FBr_2Ts and PBr_W structural configurations, the ELint_GC2 interface model is adopted, which uses stiff elements for the contact interface area. The same model is also used for simulating computationally expensive free vibration tests on the above structural configurations. The ELint_GC2 model is deemed not applicable for the simulation of FBr_1Ts experiments, due to its inability to model gaps at the interface area that was initially modelled as contact area. These experiments as well as free vibration tests on the FBr_2Ts and PBr_W structural configurations adopt the HYBint interface model. The model use both elastic and elastoplastic interface elements for modelling the initial gap and contact areas, respectively. For the contact area, the interface elements are coupled with elastoplastic Mohr-Coulomb failure surface (Figure 7.7), of maximum angle of shearing resistance ϕ', cohesion c' and angle of dilation v. When a zero normal stress takes place at an element, then the element opens representing non-contact area.

When aiming to simulate gaps at an area where the foundation and soil are initially in full contact, the calibration of the static normal stresses at the soil-foundation interface has been found to be crucial, particularly when the HYBint model is used. The normal stresses were controlled by adjusting the K_s and K_n values of the interface elements at the contact area. The calibrated K_s and K_n values for the initially close interface elements at the StSW analysis are set equal to 1E3kN/m^3. This analysis is denoted as StSW3. When elastic interface elements are used, then 1E8kN/m^3 are assigned to the interface stiffness. The same value is assigned to the initially close interface elements for the StP and dynamic analyses, irrespective of the type of interface model (HYBint or ELint). Table 7.16 summarises the calibrated stiffness values of the interface elements, for the three types of analyses.

Table 7.16: Adopted Interface properties.

Analyses	**Initially contact areas**		**Initially non-contact areas**		**c'(kPa)**	**ϕ'(°)**	**ν'(°)**
	K_s (kN/m^3)	**K_n (kN/m^3)**	**K_s (kN/m^3)**	**K_n (kN/m^3)**			
StSW	1E3 / 1E8*	1E3 / 1E8*	1E2	1E2	0	30	0
StP	1E8	1E8	1E2	1E2	0	30	0
Dynamic	1E8	1E8	1E2	1E2	0	30	0

*1E3kN/m^3 is used when the hybrid interface model is employed, while 1E8kN/m^3 is chosen for the elastic interface model

Following the above considerations, Table 7.17 summarises the interface model that is employed for each experiment. It is noted that the aim of the calibration process is to propose a common model for all experiments; the HYBint_GC2_StSW3 model was found suitable for all examined experiments. Despite that this model can produce sufficient results, the ELint_GC2 model is adopted, where it is applicable, as it is less computationally expensive.

Table 7.17: Interface model adopted by each analysis.

Structural configuration	**Forced vibration simulations**	**Free vibration simulations**
FBr_1Ts	HYBint_GC2_StSW3	HYBint_GC2_StSW3
FBr_2Ts	ELint_GC2	ELint_GC2 / HYBint_GC2_StSW3
PBr_W	ELint_GC2	ELint_GC2 / HYBint_GC2_StSW3

7.17 Interface modelling considerations in practical applications

The final interface model described in the previous section was back-analysed from numerous field experiments. Despite that the real interface conditions were impossible to be modelled due to the lack of relative data, the calibration aimed to simulate the impact of these conditions. The adopted initial interface contact area and the distribution of static normal stresses exhibited distinct

characteristics not commonly encountered in practical applications. These features were a result of the specific conditions present at the soil-foundation interface, primarily as a consequence of the foundation's casting procedure (see Section 5.2.4). Unlike the examined experiments, practical foundation applications typically involve in-situ casting, ensuring a very good contact condition with the soil. In such cases, initial interface gaps are not expected to pose significant concerns, while foundation rocking and the associated impacts (i.e. period lengthening and radiation damping reduction) are anticipated to be less pronounced.

However, interface gaps may still form due to foundation motion following strong earthquake motions. These gaps should be accounted for in analyses for future earthquake events, where the interface modelling procedure proposed by the current study finds a useful application. Additionally, this procedure can be applied effectively in offshore foundation projects or any other endeavours where in-situ casting is not feasible, necessitating the use of precast foundations. Another evident application is the interaction between a railway track and the soil, where the contact area between rail sleepers and subgrade constantly changes as trains pass over. Similarly, the proposed procedure for manipulating the distribution of static normal stresses at the interface can find utility in projects where the stresses are believed for any reason to differ from the norm.

7.18 Soil domain dimensions

The simulation of SSI problems with input excitation applied on the structure requires smaller mesh than problems of which the input excitation is applied deep in the soil domain (e.g. bedrock). In SSI simulations, an appropriate simulation of the soil in the vicinity of foundations is crucial to the structural response, while the accurate simulation of soil behaviour in the far field is less significant (see Section 7.13.1). It is important though for a model to prescribe boundary conditions that represent the propagation of seismic waves to the half-space, aiming to simulate radiation damping which is of fundamental importance in dynamic problems. This can be achieved either by modelling a very large soil domain or through the imposition of absorbing boundary conditions on the boundaries of a smaller domain. The present study employs the cone boundary condition, which consist of one normal and two tangential sets of springs and dashpots, that are applied on the boundary nodes, with exception the nodes on the plane of symmetry (Figure 7.3b).

The imposition of cone boundary aims to mitigate boundary effects. As it has already been discussed in Section 7.5.1, the soil domain dimensions have been selected after carrying out a sensitivity analysis on 2D models, that is presented in Appendix F. Herein, using the calibrated model, the boundary effects of the model used so far are quantified. The results of the already used model (M15x7.5x6),

the soil domain of which has dimensions 15 x 7.5 x 6m, are compared with those produced by a larger model that simulates soil of dimensions 39 x 19.5 x 20.4m (M39x19.5x20.4). The larger model is assumed to have negligible boundary effects is thus considered as the benchmark model. Any difference between the results produced by the two models is attributed to boundary effects.

7.18.1 Free Vibration simulations

The free vibration response of the SSI systems is evaluated through Fourier spectra that were inferred from numerical and experimental time series. Figure 7.65 presents the top slab (2.5) and foundation (1.1) motion produced by the FBr_2Ts_15.70kN simulations that adopt the M15x7.5x6 and M39x19.5x20.4 meshes. The figure demonstrates that the smaller soil domain produced negligibly small boundary effects on the structural response. Boundary effects are pronounced, though, on the soil response as illustrated by Figure 7.66 that plots the predicted soil motions at various locations. With reference to Figure 5.17, the presented data correspond to locations of instruments that were placed at the North side of the structure, which reflects to the positive x-axis according to Figure 7.3. The instruments were on the soil surface at 0.50m (0.17), 1.20m (0.1) and 2.90m (0.2) distances from the foundation edge. The figure shows that the smaller soil domain overamplified the soil motion. For locations near the foundation and far from the lateral boundaries of the mesh (i.e. 0.1), the motion amplification was pronounced for the horizontal motion component, while it was negligible for the vertical component. Boundary effects were more significant for soil motions near the boundaries (i.e. 0.2), where both horizontal and vertical motion components were affected. Similar results were observed from the simulation of the PBr_W free vibration experiments, with the investigation of boundary effects presented in Appendix F.

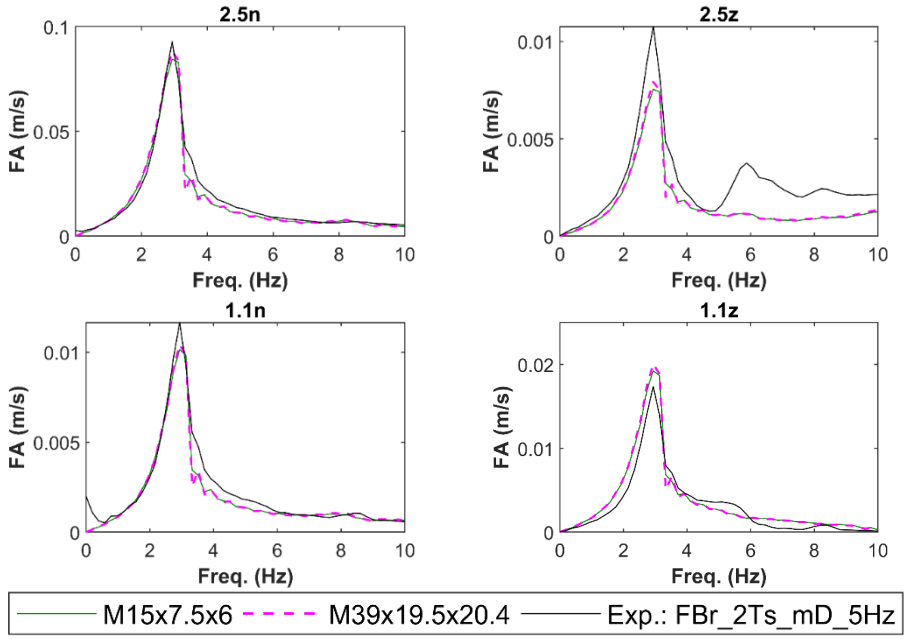


Figure 7.65: Boundary effects on the structural response predicted by the FBr_2Ts_15.70kN free vibration simulation.

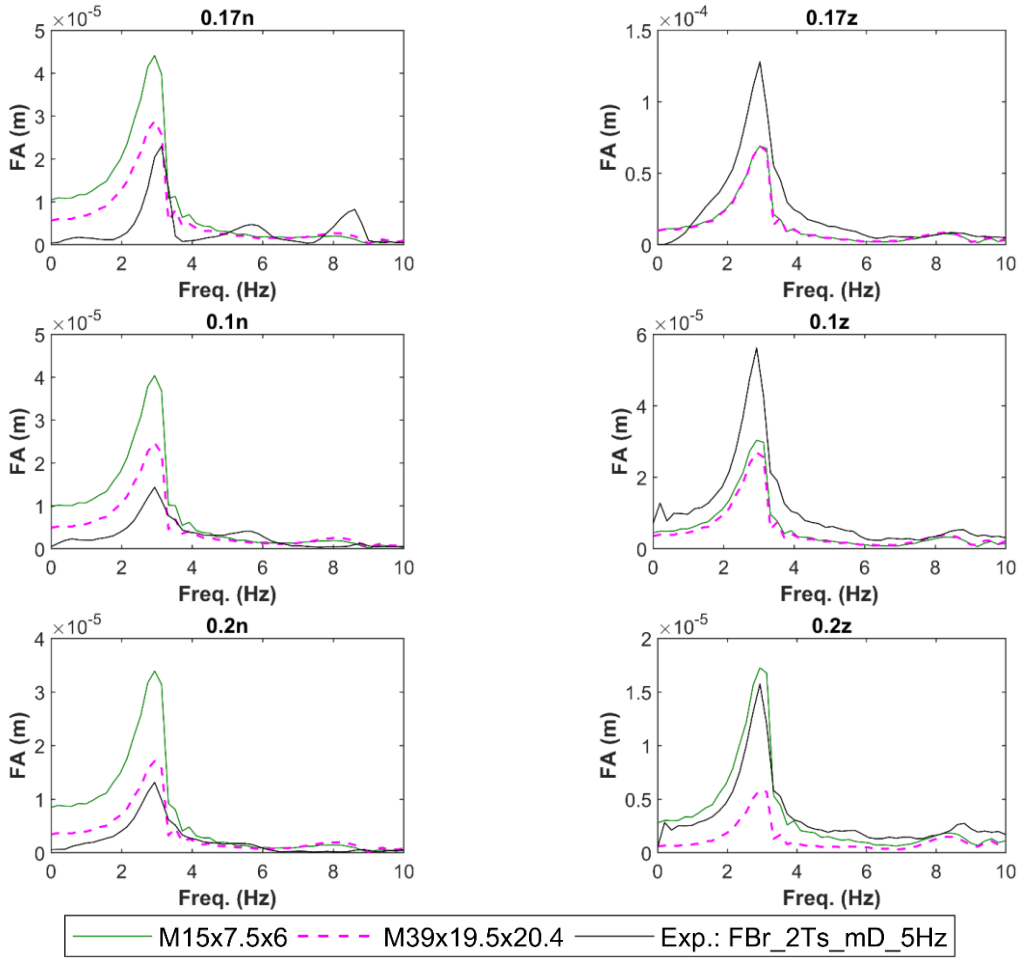


Figure 7.66: Boundary effects on the soil response at different locations predicted by the FBr_2Ts_15.70kN free vibration simulation.

7.18.2 Forced Vibration simulations

Figure 7.67 compares the horizontal (n) and vertical (z) top slab (2.5) and foundation (1.1) forced vibration response as computed by the M15x7.5x6 and M39x19.5x20.4 models, that simulate the FBr_2Ts_mD_5Hz experiment. The figures show that the two models produce identical structural response, demonstrating the weak impact of the boundary effects. The impact of the boundary effects is apparent on the soil response. Figure 7.68 compares the soil response computed by the two models at three different locations. The presented data were retrieved from the 0.17, 0.1 and 0.2 positions, whose locations were earlier mentioned. As observed from free vibration data, forced vibration data show that the horizontal soil motion component is more sensitive to boundary effects than the vertical component. The impact of the boundary effects on the soil motion increases at locations closer to the boundaries of the domain (i.e. 0.2), where both horizontal and vertical components are significantly impacted. The investigation of the impact of boundary effects on the FBr_1Ts_mC_5Hz and PBr_W_mD_2Hz experiments, that can be found in Appendix F, showed similar observations.

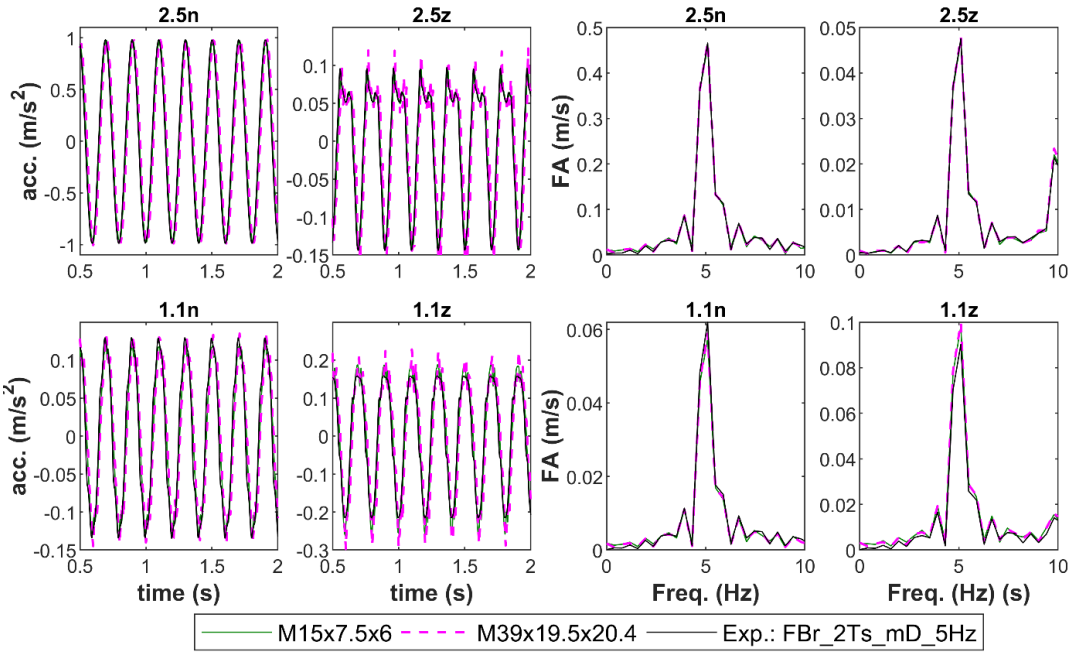


Figure 7.67: Boundary effects on the structural response predicted by the FBr_2Ts_mD_5Hz forced vibration simulation.

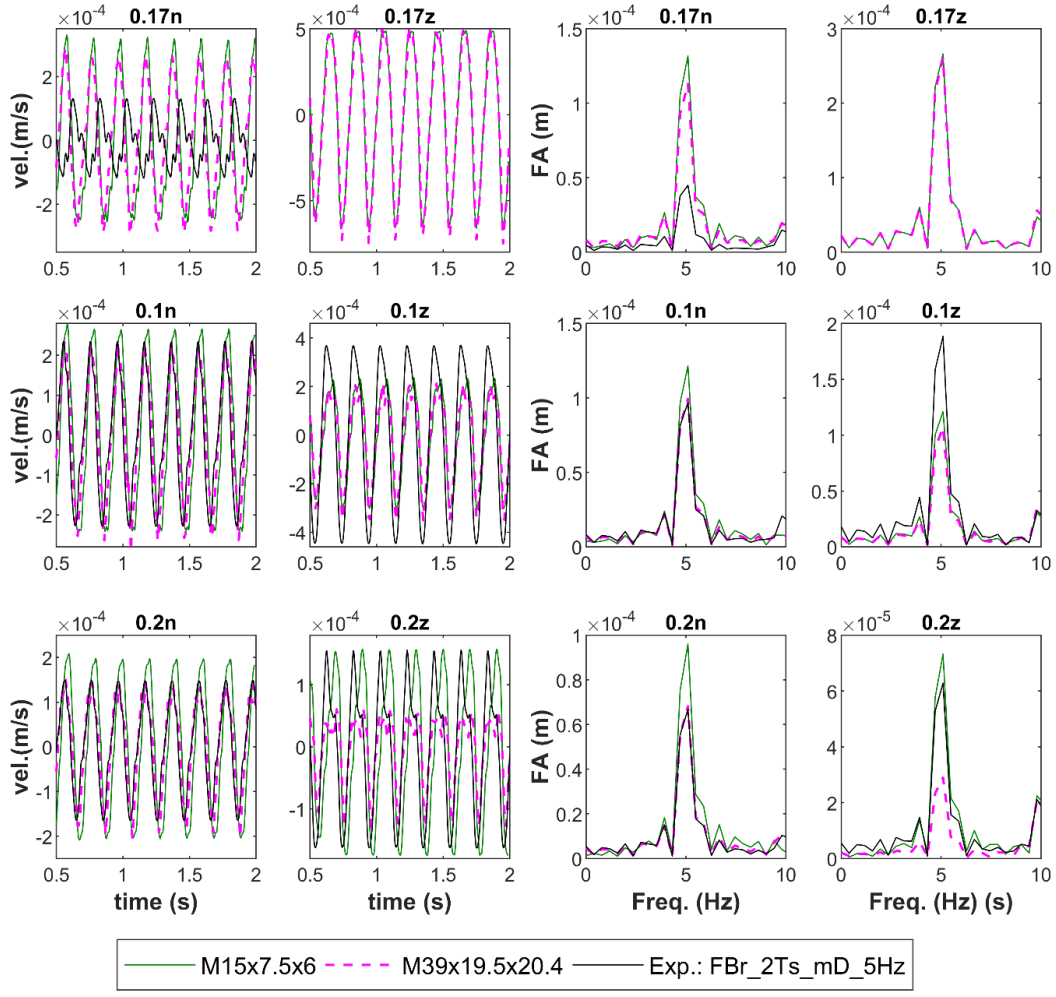


Figure 7.68: Boundary effects on the soil response at different locations predicted by the FBr_2Ts_mD_5Hz forced vibration simulation.

7.18.3 Discussion

Both free and forced vibration simulations showed that the adoption of the smaller soil domain results in overestimation of the soil motion, especially near the boundaries of the domain. This is a strong indication that the absorbing boundary conditions are unable to fully represent the propagation of induced waves to the half-space. Instead, the use of these conditions in the smaller mesh results in motion amplification, which is mitigated by the use of a larger mesh. The larger mesh, in most of the cases, predicts a soil motion closer to the experimental data, validating further the numerical calibration. Given that the structural motion is unaffected by the boundary effects, it is concluded that the impact of the boundary effects is tolerable, while the computational gain of using the smaller model outweighs it. Therefore, the analyses presented thereafter employ the smaller M15x7.5x6 model, sacrificing a tolerable accuracy on the soil response.

7.19 Summary and discussion

This chapter presents three-dimensional soil-structure-interaction analyses which simulate some of the real scale forced and free vibration experiments presented in Chapter 5. For the examined experiments, the numerical results showed a good agreement with the field data. A rigorous calibration procedure has been proposed, placing particular emphasis on the calibration of nonlinear behaviour of soil as well as on the modelling of the interface between soil and foundation. Structural connections and structural damping were also parameters that required calibration. This study demonstrates the significant impact of soil compliance, soil nonlinearity and interface imperfections on the response of both the structure and the soil. It shows the necessity, under circumstances, of modelling the soil domain explicitly, accounting for soil nonlinearity and modelling the soil-foundation interface appropriately.

7.19.1 Calibration procedure

A rigorous calibration procedure has been proposed. The calibration procedure benefits from free and forced vibration experiments that were carried out on different structural configurations. The field data collated from free vibration tests were exploited for the calibration of the natural frequencies and the produced damping of the examined SSI systems. The structural properties, structural connections and damping, were calibrated against the free vibration experiment during which the interaction of the structural response with the soil was negligible. The soil behaviour was calibrated against free vibration tests of different levels of excitation that induced very small to medium range of strains in the soil. The nonlinear soil constitutive model was able to be calibrated within this range.

Finally, the soil-foundation interface model was calibrated against forced vibration data, which for the reasons explained in Section 7.8.1, isolate the impact of the interface conditions. The model was refined against free vibration experiments that mobilised the strongest foundation uplift.

The calibration was achieved by using a numerical model that simulates half of the geometry, exploiting the symmetry of the problem. This can be considered a limitation of the study, as the model is unable to predict out-of-plane motion. However, the model was calibrated against experiments that exhibited weak out-of-plane motion, hence the assumption of unidirectional oscillation is considered reasonable. Also, the recorded experimental out-of-plane motion was a result of geometrical imperfections that were impossible to be modelled. Additional limitation of the study is the assumption that the structural stiffness and damping is linear, while their variation with strains is neglected. The study also neglects any softening and hardening of the connections that may have taken place during the experiments. While the structural properties were not thoroughly investigated in this research, it is expected that small changes in these properties would have minimal impact on the SSI response, which was found to be dominated by rocking in most of the experiments. Overall, the experimental imperfections and calibration challenges were important, which is a fact that makes the above limitations insignificant.

7.19.2 Validation

A common calibration was validated against all examined experiments, free vibration and forced vibration tests on the FBr_1Ts, FBr_2Ts and PBr_W configurations. The numerical results verify features that were observed through strong motion data in Chapter 6 and are well established in the literature, enhancing the reliability of the model. The current study verified that the SSI phenomena are more significant on stiffer structures. The period elongation and damping production, relative to a fixed-base system, are shown to be more pronounced on the FBr_2Ts (stiffer) structure than on the PBr_W one. The period elongation, but not damping, is more pronounced on the FBr_1Ts than the FBr_2Ts structure. The lighter structure has a larger fixed-base natural frequency, justifying the larger period elongation than the heavier one. The period elongation, though, was not a result of soil compliance alone but was also affected by foundation nonlinearity. Given that the excitation was applied on the top of the structure, the lighter structure, under the same excitation, exhibited stronger displacements and therefore stronger foundation uplift than the heavier structure. This interface nonlinearity promoted stronger period elongation for the FBr_1Ts than the FBr_2Ts structure, as well as smaller development of damping. As it is well established in the literature, the rotational foundation mode transmits lower motion to the soil and therefore it produces lower radiation damping, in relation to the translational mode. Therefore, the stronger foundation rotation of the FBr_1Ts

structure in comparison with the FBr_2Ts one justifies the weaker damping produced by the oscillation of the former structure.

7.19.3 Soil behaviour

The study showed that, for the modelled experiments, an accurate calibration of the soil behaviour is essential only for the soil in the vicinity of the foundation. Herein, it was sufficient to calibrate the nonlinear behaviour of the first 0.80m of soil (see Section 7.13.1), while the remaining soil layers were assumed as linear. The nonlinear behaviour of this soil layer significantly affects the natural frequency of the SSI system in relation to the one predicted by linear analyses, as shown through the simulations of free vibration tests. In particular, nonlinear analyses decrease the natural frequency, as they simulate soil of lower stiffness due to stiffness degradation. The impact increases for stronger excitation, i.e. pull-out force, which produces a foundation response that induces larger strains in the soil and hence stronger stiffness degradation. Soil nonlinearities, including both stiffness degradation and development of hysteresis damping, are more important on stiffer structures which mobilise stronger soil motion.

This study aimed to calibrate both the stiffness degradation and damping ratio curves, with reference interpreted field data that were available. As Figure 7.36a shows, when the calibration of a cyclic nonlinear model prioritises the stiffness curve, the damping is underestimated at low strains and highly overestimated at medium strains. On the other hand, the prioritization of damping results in underestimation of the soil stiffness under cyclic conditions at the very small and small strain range. It also underestimates the stiffness under monotonic conditions for the entire small strain range (Figure 7.44). The study showed that the calibration should prioritise the damping curve over the stiffness curve, otherwise the motion will be highly overdamped when the soil strains reach the medium range. This was the case of free vibration simulations of the FBr_2Ts structures when the pull-our force was strong (i.e. FBr_2Ts_15.70kN). When the motion intensity is low and the induced soil strains are small, the dominant damping mechanism is the radiation damping, whereas damping produced from soil hysteresis is not important. Given that, prioritising the model calibration against stiffness would be preferred for small strain simulations. However, a common simulation was aimed to be adopted for all experiments, hence modelling damping reasonably is prioritised, without significantly affecting the low strain problems. The underestimation of stiffness at low strains can be compensated by prescribing a p' dependent G_{max} (Figure 7.6b) and hence increasing the stiffness of the soil below the foundation.

As output from the FBr_2Ts_15.70kN free vibration simulation, during the application of the static pull-out force and at the first cycle of the free vibration, the strains induced in the soil beneath the

foundation were up to 1% (Figure 7.42e). The first consequence of this is the development of large soil damping at the first cycle, up to 25%, that led to motion overdamping. The second consequence of this is the huge soil degradation under pull-out loading, which resulted in unreasonable large horizontal static displacements. These horizontal displacements were not recovered after the load removal, as the loading and unloading stiffness behaviours were controlled by the monotonic and cyclic curves respectively, which were considerably different. The large difference in soil stiffness between the first loading and the subsequent unloading loop, results in an open stress-strain loop which is manifested as unrecoverable displacements at the end of the oscillation.

Both motion overdamping and unrecoverable displacements were addressed by the imposition of a higher value of minimum shear stiffness (G_{min}). The calibrated G_{min} is mobilised only by high intensity experiments (e.g FBr_2Ts_15.70kN), while it has a marginal impact on low intensity experiments (e.g. FBr_2Ts_2.94kN). The implication of a higher G_{min} value on the damping curve is the decrease of damping values with strains beyond the strain at which G_{min} is mobilised. Hence, high intensity experiments that use a high G_{min} produced much lower soil damping than the one produced by the analysis of lower G_{min}. Also, a higher G_{min} compensates the unreasonably highly degraded monotonic curve and prevents the development of very large displacements during pull-out loading. The smaller static horizontal displacements are recovered after the load removal, leading to negligible unrecoverable displacements at the end of the motion. A limitation of the calibration of the nonlinear model is the non-rigorous calibration of the monotonic curve due to the lack of related experimental data. The static pull-out analysis that incorporates the calibrated G-γ-D curves and G_{min}, though, resulted in reasonable horizontal displacements, enhancing the reliability of the incorporated monotonic curve.

7.19.4 Interface model

Zero thickness of interface elements have been placed at the soil-foundation interface, aiming to allow detachment and sliding of the foundation relative to the soil. The elastic deformations are controlled by the elastic normal (K_n) and shear (K_s) stiffness of the interface elements, while the plastic ones are controlled by the plastic behaviour of the elements. In many of the presented analyses, the interface elements were coupled with an elastoplastic Mohr-Coulomb failure surface of zero cohesion. Foundation detachment is modelled when zero normal stress takes place, which is a condition that allows the interface elements to open. An opened interface element retains zero normal and shear stiffnesses, while it develops normal plastic strains (ε_{pl}), which correspond to the magnitude of the formed gap. This study proposed a novel approach to model initial gaps at the interface prior to the application of the excitation, representing interface contact imperfections. The aspects required

calibration related to the interface model are the initial gaps configuration, the modelling approach of gaps, the constitutive behaviour of interface elements and the initial interface stresses under static conditions.

The gaps are rigorously simulated through the formulation of the elastoplastic model employed for the interface elements. They are initiated by prescribing a non-zero hardening parameter of the Mohr-Coulomb interface model, that corresponds to the plastic normal strain (ε_{pl}). The magnitude of ε_{pl} reflects to the magnitude of initial opening, which is a parameter that required calibration. When a small ε_{pl} is prescribed to a gap, then the gap is able to close and re-open during the structural oscillation. On the contrary, when the initial gap is of a larger magnitude, the gap remains open throughout the motion. For the latter case, the study showed that the gaps can also be simulated through low stiffness of elastic interface elements, which are more computationally effective.

This study showed also that the existence of gaps between the foundation and the soil can affect both the structural and soil response, under circumstances. They can decrease the natural frequency and accentuate foundation motion and especially the rocking component. The increase of the rocking component decreases the motion that is transferred from the structure to the soil. This implies that gaps decrease the radiation damping, which is a crucial damping mechanism in SSI problems, and hence decreasing the damping of the entire SSI system. The impact of gaps is more pronounced when these are modelled below foundation edges, while it is negligible when gaps are formed below an inner area of the foundation. Also, free vibration simulations have demonstrated that the impact of gaps on the natural frequency and damping of the examined SSI systems was more pronounced on the response of the stiff structures (FBr_2Ts and FBr_1Ts). These structures exhibited very limited structural bending, while the whole deformability was dominated by foundation rotation, which was intensified by the existence of gaps. Conversely, for the experiments on the PBr_W structure, the foundation motion was weak, even with the existence of gaps, in relation to the flexural deformability; hence, the gaps did not impact the structural response significantly.

A sensitivity analysis has demonstrated that the impact of gaps increases with increasing non-contact area. A gap configuration that consists of two rows of permanently open interface elements below the foundation edges, was found to be sufficient for the simulation of experiments on the FBr_2Ts and PBr_W structures. However, this interface contact condition was not applicable for the FBr_1Ts structure, which required more interface element to open during a simulation than the former structures. As claimed in Section 6.3.8 and numerically verified herein, the lighter structure exhibited stronger foundation rocking and detachment than the heavier ones. It was found that the simulations could not allow opening of the initially close interface elements, when a large K_n value is used, as it is commonly chosen in the literature. This is attributed to the normal stress concertation at the interface

elements near the edges of the contact area, under static self-weight loads. These stresses were too high and could not be reduced to zero during the dynamic analysis, thereby preventing the initially close interface elements from opening This stress distribution is reasonable for stiff foundations, however, for the reasons explained in Section 7.14, it is considered not applicable on the current experiments.

The interface normal stress distribution, resulting due to self-weight, was calibrated by an appropriate selection of a K_n value that is assigned to the initially close interface elements for the self-weight static analysis. This investigation has shown that the distribution of self-weight normal stresses at the interface can significantly affect the SSI response. It has demonstrated that a smoother distribution facilitates the opening of initially close interface elements, increasing the gap area and hence accentuating the gapping effects described above. The significance of the impact of the static stress distribution on the dynamic response increases with the magnitude of the excitation, while it depends on the structural configuration and type of experiment. The impact is more pronounced on the response of a structure that is prone to rotate around foundation level, which was the case of the FBr_1Ts structure. It is also more important on the free vibration than the forced vibration response.

Finally, this study investigates the impact of the magnitude of gaps when the gaps are prescribed through the plasticity model. The study has demonstrated that even a very small initial opening can promote successive opening and closure of interface elements during an excitation. For a small initial opening, the area of initially open interface elements that close during an excitation increases, weakening the effects of gaps, in relation to larger gaps. For larger initial openings, the non-contact area is larger and hence gapping effects become more pronounced. The opening and closure of initially open interface elements with time was quantified through normal plastic strain time histories extracted from free vibration simulations of the FBr_1Ts and FBr_2Ts structures. These time histories showed that the initially open elements closed and subsequently re-opened for one to three cycles before they remained permanently open. At the first cycles of the motion, the contact interface area was larger than at subsequent cycles. The consequence of this is that the response of the SSI system was stiffer at the first cycles than the following ones. At the time that the interface elements became permanently open, the contact conditions became constant with time and the response frequency started decreasing with time. This decrease is attributed to the decay of motion intensity and consequently the decay of nonlinear phenomena with time. The observed variation of response frequency with time is validated against field data that were presented in Section 6.2.5, enhancing the reliability of the model.

7.19.5 Applications of the interface model in practical scenarios

In most practical scenarios, in-situ casting for foundations ensures good contact conditions and negligible gaps at the interface. However, the proposed method to simulate initial gaps between a foundation and the soil can find application in real case problems where in-situ casting of foundations is not feasible. Such a case is offshore foundation projects where precast foundations are placed on a not well prepared subgrade soil layer, therefore, any potential gaps at the interface should be considered in the design. Another evident application is the interaction between a railway track and the soil, where the contact area between rail sleepers and subgrade constantly changes as trains pass over. Also, interface gaps may be formed due to foundation motion during strong earthquake motions. The existence of these gaps should be accounted for in analyses for future earthquake events. Similarly, the proposed procedure for manipulating the distribution of static normal stresses at the interface can find utility in projects where the stresses are anticipated to deviate from the norm for various reasons.

Chapter 8

Predictive Analyses: Impact of soil compliance, interface gaps and nonlinearities on the system response

8.1 Introduction

The numerical model of the SSI system was validated against selected free and forced vibration experiments, presented in Chapter 7. Herein, the model calibration is further validated against independent available field experiments that were described in Chapter 5. During these experiments, the structure was subjected to different excitation intensities than during the experiments that were used for calibration purposes. An additional aim of this chapter is to validate experimental outcomes, presented in Chapter 6, associated with the importance of Soil-Structure Interaction (SSI) effects and foundation motion. The validated SSI model is also used beyond the available experimental datasets to investigate the mechanisms of period lengthening and damping. These mechanisms include soil compliance, soil-foundation imperfections and nonlinear phenomena. The latter phenomena consist of structural nonlinearity, soil nonlinearity, soil plasticity, interface nonlinearity (rocking) and interface plasticity (sliding). Insights about soil and foundation nonlinearities are discussed herein, while the remaining nonlinearities are neglected.

These investigations are made possible through the simulations of both free and forced vibration tests. Aiming to consider the interface nonlinearity appropriately, the HYBint_StSW3_GC2 interface model is adopted for the simulations of experiments during which foundation rocking is more prominent. This interface model is adopted for all free vibration simulations and for the simulation of the forced vibration experiment on the FBr_1Ts structure. For the remaining forced vibration simulations, the ELint_GC2 interface model is employed.

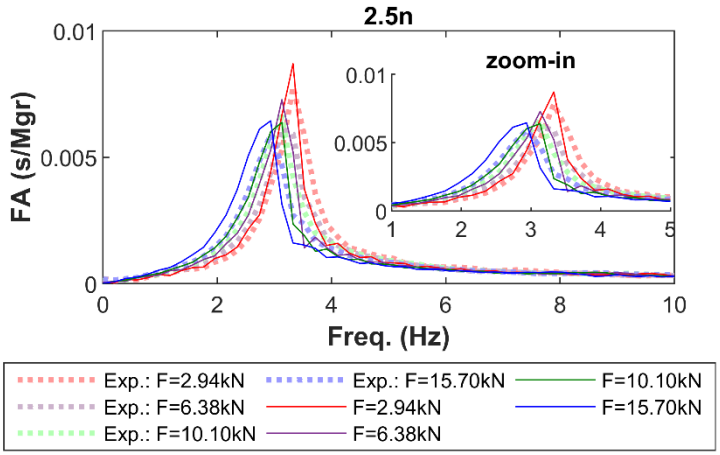
8.2 Free vibration tests

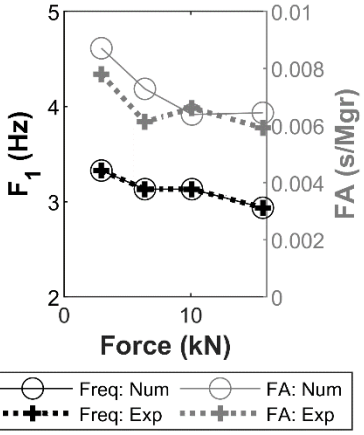
8.2.1 Natural frequencies and motion amplitude of the swaying mode

The computed natural frequencies of the swaying model and top slab motion amplitude of the free vibration response are compared with the experimental ones. The natural frequency of an SSI system can be inferred from the frequency coordinate of the main peak of the Fourier spectrum that is computed from top slab accelerations. Similarly, the amplitude of the same peak is a qualitative measure of the amplitude of the top slab motion. Figure 8.1 compares the computed Fourier spectra for the horizontal top slab response normalised by the applied pull-out force (F) with the corresponding experimental one. The response was computed/recorded from experiments of different pull-out forces that were applied on (a) FBr_2Ts, (b) FBr_1Ts and (c) PBr_W structures. As already mentioned, free vibration tests on the FBr_1Ts experiments were not available, hence experimental data are not presented in the corresponding figure (Figure 8.1b).

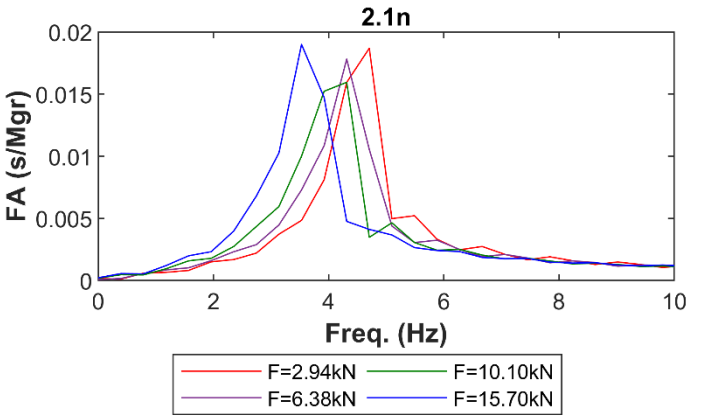
Figure 8.1a and c demonstrate that the numerical model can sufficiently reproduce field data for all the free vibration tests that were carried out on the FBr_2Ts and PBr structural configurations. The two figures illustrate that the numerical model reproduces the decrease of both natural frequency and motion amplitude with increasing pull-out force, that has been observed in the field data in Section 6.2.3. The decrease of natural frequency with increasing pull-out force is more pronounced on the response of the FBr_1Ts structure, as shown in Figure 8.1b. The inclination of the frequency line shown in the right plot of Figure 8.1b, indicates that the increase of the force from 10.10kN to 15.70kN resulted in the most pronounced decrease of natural frequency. The normalised response of the FBr_1Ts structure, though, was much stronger when the force was 15.70kN than 10.10kN. The latter observation demonstrates that the increase of the force may result in increase of the response, which cannot be verified due to the lack of associated experimental data.

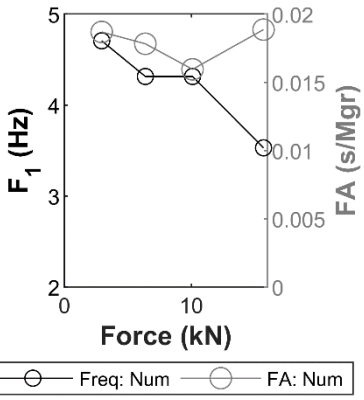
As discussed in Section 6.2.5, the above observations can be attributed to nonlinear effects and are further investigated in the following Sections (Sections 8.2.2, 8.2.3 and 8.2.4) aiming to quantify the triggering mechanisms of nonlinearity. The subsequent investigations can also explain the increase of motion amplitude with applied force that was observed for the FBr_1Ts simulation, which was not observed in other free vibration experiments.



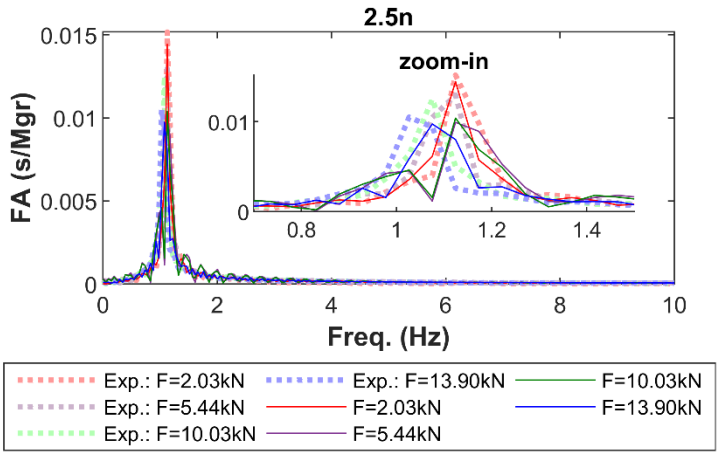


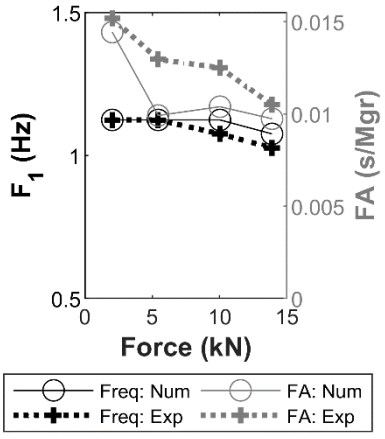
(a) FBr_2Ts





(b) FBr_1Ts





(c) PBr_W

Figure 8.1: Fourier spectra inferred from numerical and experimental top slab response, shown in the left plots. The right plots present the identified natural frequencies and the corresponding Fourier amplitude. The results are taken from free vibration experiments of different pull-out forces applied on (a) FBr_2Ts, (b) FBr_1Ts and (c) PBr_W structures.

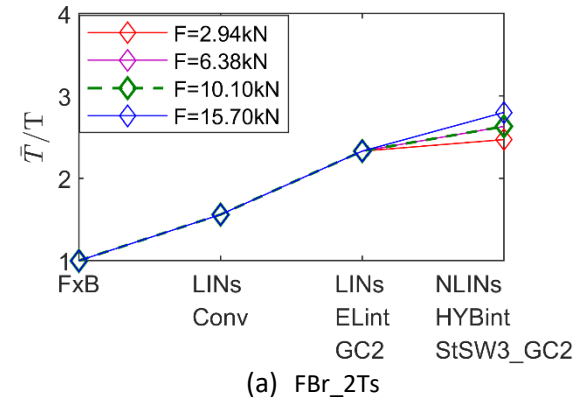
8.2.2 Period lengthening mechanisms

The period elongation ($\tilde{T}/T$) is defined as the ratio between the natural period of an SSI system to the one of an equivalent fixed-base system. Relative to an equivalent fixed-base system, the period elongation of an SSI system can be attributed to soil compliance, soil-foundation interface imperfections (e.g. gaps) and soil nonlinearity. Aiming to evaluate the impact of the above mechanisms on the natural frequency of the examined SSI systems, the period lengthening between SSI analyses with fixed-base (FxB) analyses are compared. The period lengthening, predicted by an SSI analysis adopting linear elastic soil domain and conventional full bonding between the foundation and the adjacent soil medium (LINs_Conv), is attributed to soil compliance only. The impact of interface gaps on period lengthening can be evaluated by comparing the lengthening ratios produced by the latter analysis and an identical analysis which simulates permanently open gaps (LINs_ELint_GC2). The comparison between lengthening ratios produced by the latter analysis and a nonlinear analysis with interface gaps (NLINs_HYBint_StSW3_GC2) can give an indication of the impact of soil nonlinearity. When initially closed interface elements open, a feature enabled by the utilisation of elastoplastic interface elements, the interface nonlinearity can be assessed.

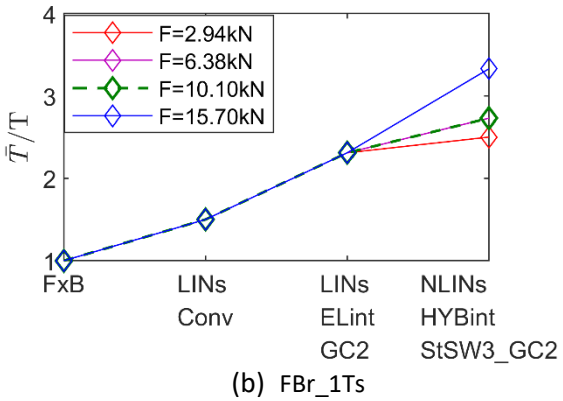
Figure 8.2 presents the computed period elongation ratios for the different adopted models. The ratios presented correspond to experiments on (a) FBr_2Ts, (b) FBr_1Ts and (c) PBr_W structures, which were subjected to different pull-out forces. The ratios of the same structural configuration but of different pull-out force deviate when nonlinearities are incorporated in the model. Larger $\tilde{T}/T$ values indicate stronger impact of the different mechanisms. The inclination of the lines presented in Figure 8.2 indicates the importance of the impact of each mechanism on period lengthening, with relation to the other mechanisms.

Figure 8.2a and b illustrate the important impact of soil compliance on the natural frequencies of the FBr_2Ts and FBr_1Ts systems ($\tilde{T}/T = 1.5$). They also demonstrate that the existence of gaps imposes an even more significant impact, as it increases the $\tilde{T}/T$ from 1.5 to 2.3. The stronger impact of gaps in relation to soil compliance is indicated by the larger line inclination that connects the LINs_Conv and LINs_ELint_GC2 analyses, than the line inclination between the FxB and LINs_Conv analyses. Figure 8.2c shows that similar features under a much smaller scale are observed for the PBr_W free vibration experiments. The response of the partly braced structure was only marginally affected by both soil compliance ($\tilde{T}/T = 1.02$) and the existence of interface gaps ($\tilde{T}/T = 1.05$). Figure 8.2a, b and c also quantify the increase of predominant period due to nonlinearities (NLINs). The magnitude of the lengthening ratio depends on the magnitude of the pull-out force which determines the excitation level. As expected, larger applied forces result in higher lengthening ratios due to the larger

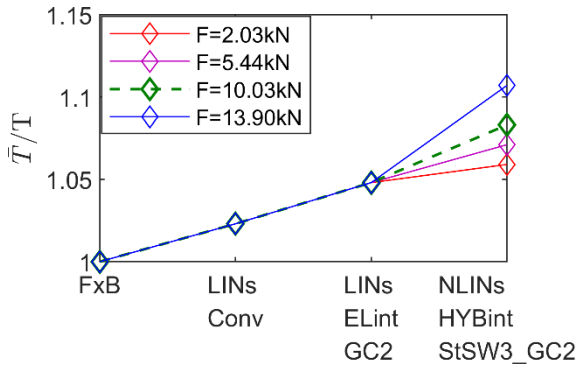
strains induced in the soil and hence stronger soil stiffness degradation, while lengthening can also be attributed to stronger interface nonlinearity.



(a) FBr_2Ts



(b) FBr_1Ts



(c) PBr_W

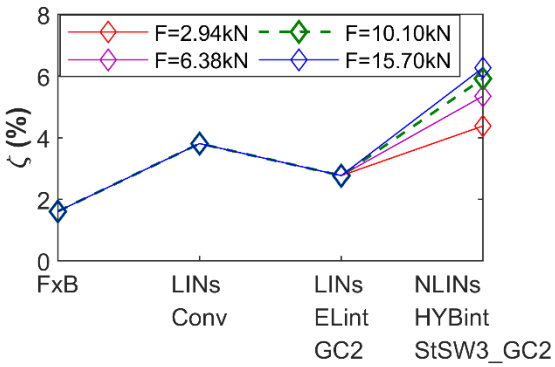
Figure 8.2: Variation of period lengthening produced by different models and different pull-out forces.

8.2.3 Damping mechanisms

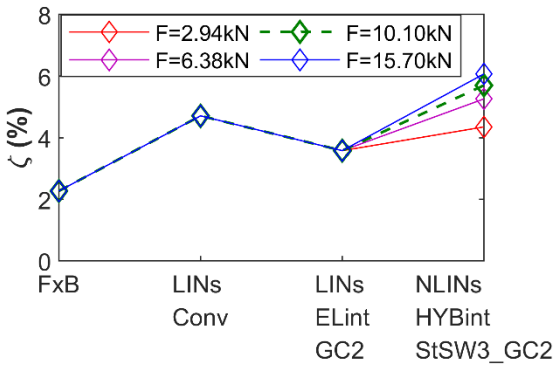
The damping ratio is calculated with the logarithmic decrement method (Chopra, 2011), as described in Section 6.2.4. This method requires a selection of two peaks (i, j+i) of the free vibration motion between which the damped motion is quantified. Herein, the first peak (i=1) of each acceleration time history, after load removal, is considered in the calculations. As a second peak the 6th peak (j=5) for the FBr_2Ts and FBr_1Ts experiments is considered, and the 16th peak (j=15) for the PBr_W experiments. As for the period elongation, the mechanisms that contribute to alterations of damping relative to a fixed-base system are soil compliance, interface gaps, soil and interface nonlinearities. The evaluation of the contribution of each mechanism to damping development is achieved by comparing results of different analyses that isolate each mechanism. The approach employed here is the same to the one used for evaluation of the impact of these mechanisms on period lengthening, described earlier in Section 8.2.2.

Figure 8.3 presents the variation of damping ratio produced by different numerical models. The comparison of damping produced by the FxB and LINs_Conv analyses establishes the very effective role of modelling the soil domain in producing damping. The difference between damping produced by the two analyses is attributed to the radiation damping that develops by the means of energy

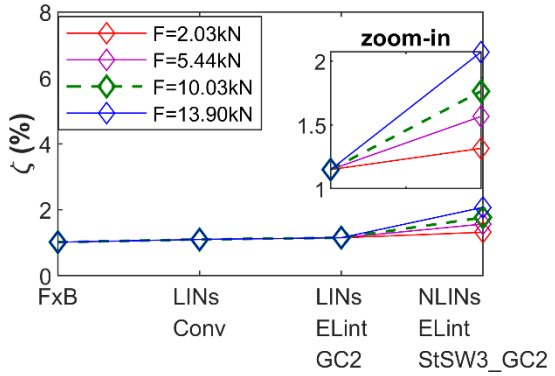
geometric spreading away from the structure, when the soil is modelled. In particular, the analysis which models the soil domain explicitly produces more than twice the damping values seen for the fixed-base analysis. As expected, the existence of interface gaps decreases significantly the damping produced by the SSI systems. The impact of gaps is evaluated by comparing the damping produced by LINs_Conv and LINs_ELint_GC2 analyses. The smaller contact area between the foundation and adjacent soil prevents the full transmission downwards propagating waves to the soil domain and hence leads to smaller radiation damping. The most important damping mechanism is the soil nonlinearity, as indicated by the largest inclination of the line that connects the results produced by the LINs_ELint_GC2 and NLINs_HYBint_StSW3_GC2 analyses. This damping mechanism becomes the dominant one when strong excitation takes place (i.e. large pull-out force). It is still important for the weak pull-out force cases, establishing the important role of soil hysteretic damping on the overall response of an SSI system, under different levels of excitation. In addition, having in mind that only the first 0.8m of the soil is modelled as nonlinear material, this observation highlights the dominant role of the very shallow soil layers, in SSI problems, in producing hysteretic damping.



(a) FBr_2Ts (i=1, j=5)



(b) FBr_1Ts (i=1, j=5)



(c) PBr_W (i=1, j=15)

Figure 8.3: Variation damping ratio values produced by different models that simulate free vibration experiments of different pull-out forces.

It is observed that the NLINs_HYBint_StSW3_GC2 analysis, which incorporates both soil and interface nonlinearities, produced a stronger increase of damping, relative to the LINs_ELint_GC2 analysis, for the FBr_2Ts than the FBr_1Ts SSI system. This is opposite to the observation drawn in Section 8.2.3, where soil nonlinearity increased more the period of the FBr_1Ts SSI system than the FBr_2Ts one.

The contradictory impact of soil nonlinearity on the period and damping of the SSI system is attributed to interface nonlinearity, as it is subsequently discussed in Section 8.2.5.

The damping mechanisms, associated with soil compliance and soil nonlinearity, are very effective on the response of the FBr_2Ts (Figure 8.3a) and FBr_1Ts (Figure 8.3b) structures, while they have a very weak impact on the response of the PBr structure (Figure 8.3c). This aligns with the observations made earlier for period lengthening. This is additional evidence that the PBr-Soil system behaved closely to a fixed-base system.

8.2.4 Soil nonlinearity

It was earlier shown that soil nonlinearity can be very important on the response of the SSI system, under certain circumstances. It can significantly decrease the natural frequencies (Section 8.2.2) and be the dominant damping mechanism (Section 8.2.3) of an SSI system. Also, it has been shown in Section 7.13.1 that soil nonlinearity is important only in the vicinity of the foundation. This justifies the choice of prescribing only the first 0.80m of soil to behave nonlinearly, while linear behaviour is assumed for the remaining domain. Herein, quantitative evidence is given to invigorate the dominant role of the soil in the vicinity of the foundation in relation to the overall soil nonlinearity. Figure 8.4 presents the mesh of the numerical model shading soil areas of which soil behaviour is investigated. The soil behaviour is evaluated at integration points enclosed within an area below the foundation centre (BFC), below the corner of the contact area's edge (BCE) and near the soil surface at a distance of 1.2m from the foundation edge (SS1.2), which is below the location of the 0.1 instrument.

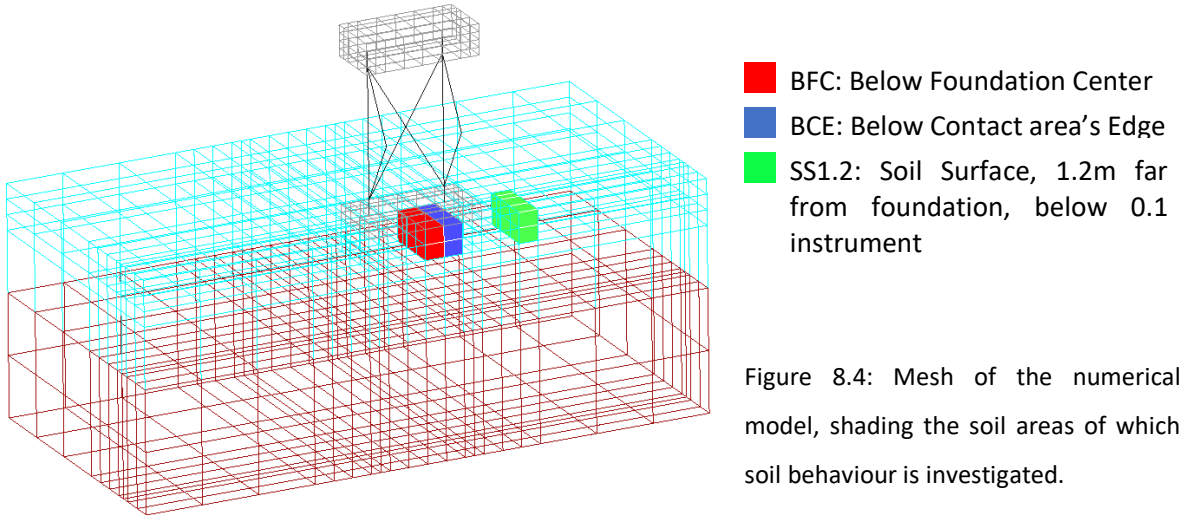


Figure 8.4: Mesh of the numerical model, shading the soil areas of which soil behaviour is investigated.

Figure 8.5 presents the stiffness degradation and damping ratio curves (G-γ-D) that were used for the calibration of the constitutive model. It also presents the stiffness and damping ratio values computed by the simulation of the FBr_2Ts_15.70KN free vibration analysis, that incorporates soil nonlinearity

and the interface model HYBint_StSW3_GC2. The presented data were computed for all integration points that are enclosed in the soil volumes mentioned earlier. They refer to the increment where the maximum strains are anticipated to be induced in the soil. This is the first peak after load removal, which corresponds to P1 with reference to Figure 7.42c.

The figure demonstrates that the soil below the edge of the interface contact area exhibited the strongest nonlinear phenomena, including stiffness degradation and damping development. This is reasonable as the foundation rotation, which is the predominant mode of the foundation, imposes the largest strains at this area. The soil elements enclosed within the BFC area were induced to much lower strains, as this area is very close to the centre of rotation of the foundation. The smaller strains in the BFC area are indicated through smaller stiffness degradation and damping ratios than those developed in BCE. Finally, Figure 8.5 shows that very weak stiffness degradation and damping ratios took place around the SS1.2 soil area which is 1.2m far from the foundation edge. It indicates that the soil motion and hence strains were strongly dissipated by this distance from the foundation. This observation verifies that indeed the nonlinear behaviour of the SSI system, associated with the soil, is dominated by the soil area in the vicinity of the foundation.

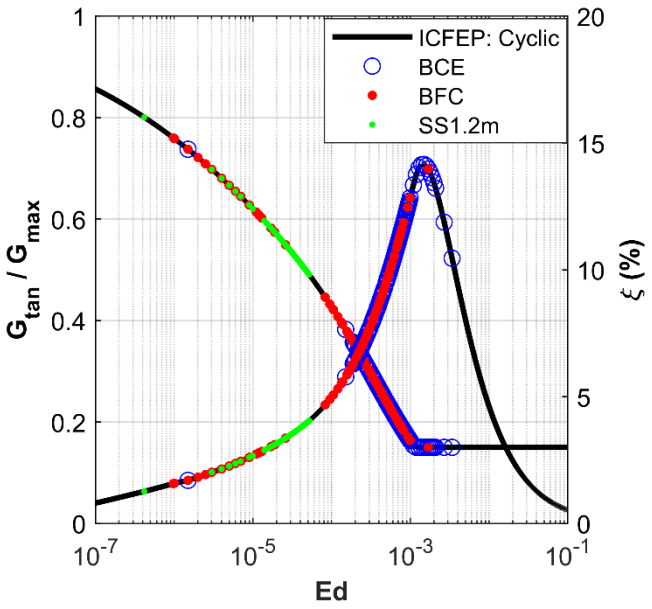
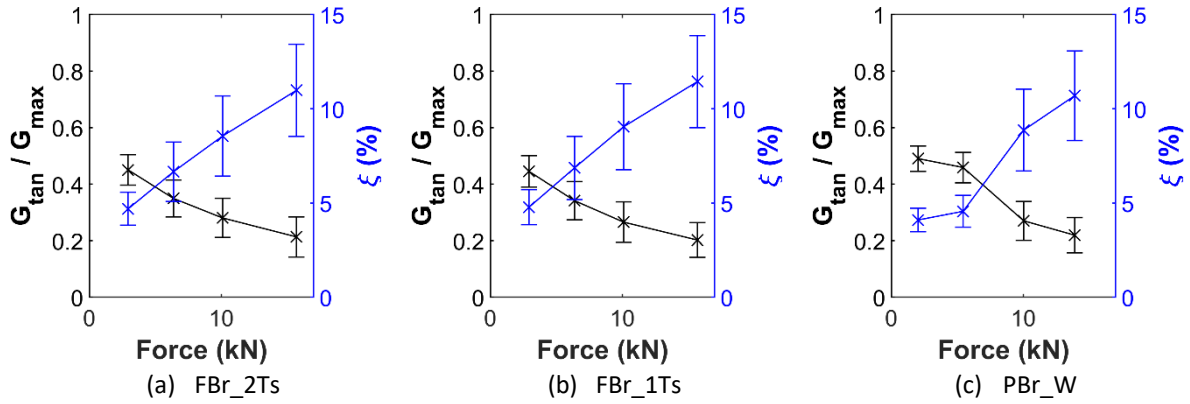


Figure 8.5: G-γ-D curves and the corresponding values computed by the analysis that simulates the FBr_2Ts_15.70KN free vibration experiment, incorporates soil nonlinearity and adopts the interface model HYBint_StSW3_GC2. The presented data are computed at integration points within the shaded soil volumes shown in Figure 8.4. They refer to the P1 time increment as shown in Figure 7.42c.

Following the latter claim, the highly nonlinear response of soil below the foundation can be deemed as a dominant factor influencing the dependency of the response on soil nonlinearity, that was evidenced in Figures 8.2 and 8.3. Figure 8.6 presents the variation of soil stiffness degradation and damping ratios with applied pull-out force, as developed at the increment when the first displacement peak took place after load removal. The figure presents the mean values and standard deviation of all integration points enclosed within the BCE (Figure 8.4) area, which is the area where nonlinearities were more pronounced. Figure 8.6a, b and c present the variation of the above quantities as produced

by analyses that simulate the free vibration response of the FBr_2Ts, FBr_1Ts and PBr_W structural configurations, respectively.

For all three experiments, damping ratio increases significantly with pull-out force, explaining the increase of systems damping produced by nonlinear analyses, that was earlier presented in Figure 8.3. Similarly, significant stiffness degradation is observed, which increased with pull-out force. This observation can justify the increase of period lengthening ratio observed in Figure 8.2, when soil nonlinearity was incorporated in the model. The variation of the stiffness degradation computed by the FBr_1Ts simulations (Figure 8.6b) does not verify the abrupt increase of the system's period when the pull-out force increased from 10.10kN to 15.70kN, shown in Figure 8.2b. The analysis of the latter force produced relatively larger soil stiffness degradation than the analysis of the smaller force. However, the difference is not large enough to justify the difference in period produced by the two analyses. This implies that the period lengthening cannot be attributed to soil nonlinearity alone, instead, it can also be attributed to interface nonlinearity, as it is subsequently shown in Section 8.2.5.



(a) FBr_2Ts (b) FBr_1Ts (c) PBr_W

Figure 8.6: Variation of soil stiffness degradation and damping ratio values with applied pull-out force, as developed at the first displacement peak after load removal. The mean values and standard deviation of integration points enclosed in BCE area (Figure 8.4) are presented.

8.2.5 Soil-foundation interface nonlinearity

Aiming to investigate the impact of interface nonlinearity (gapping) on the response, the normal plastic strain time series of the FBr_1Ts free vibration simulations are presented in Figure 8.7. The strains correspond to integration points of four initially closed interface elements, that are shown in Figure 7.55a. Although not presented here, when a 2.94kN pull-out force was applied on the structure, the initially closed interface elements did not open at any time of the response. As Figure 8.7a shows, this was also the case for the 6.38kN force, whereas some integration points opened when the force was 10.10kN (Figure 8.7b). Figure 8.7c illustrates that when a 15.70kN pull-out force was applied on the structure, then a very significant part of the initially closed interface area opened and closed at

various times during the response. This led to a significantly smaller contact interface area during the FBr_1Ts_15.70kN simulation than the FBr_1Ts_10.10kN one. This explains the important difference between the lengthening ratios produced by the two experiments, as shown in Figure 8.2b.

Regarding the system's damping produced by the FBr_1Ts_15.70kN and FBr_1Ts_10.10kN simulations, the increase of pull-out force, which was the only difference between the simulations, led to two counteracting effects. The first effect is associated with the increase of hysteretic soil damping, as indicated by Figure 8.6. The smaller contact interface area that took place during the FBr_1Ts_15.70kN simulation, though, decreased the transmission of energy from the structural oscillation to the soil domain. The combination of the two effects can explain the small difference in system's damping that was produced by the two simulations, when soil nonlinearity and the hybrid interface model are adopted (Figure 8.3b).

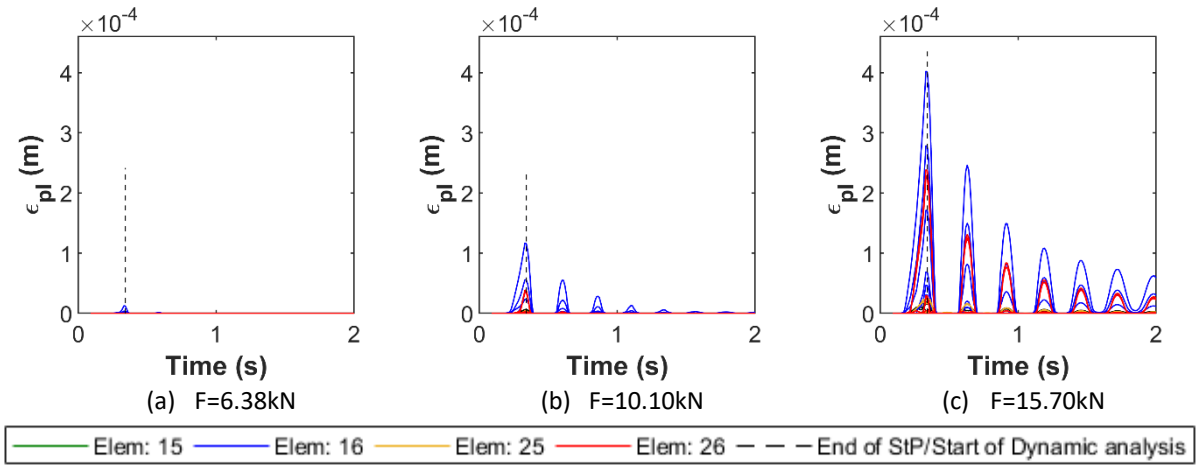


Figure 8.7: Normal plastic strain time series extracted from free vibration simulations of the FBr_1Ts structure, which was excited by (a) 6.38kN, (b) 10.10kN and (c) 15.70kN pull-out force. The strains correspond to integration points of various interface elements shown in Figure 7.55a.

During the FBr_1Ts simulations the foundation exhibited the strongest detachment from the soil beneath (interface nonlinearity), in relation to the other simulations. This is corroborated by Figure 8.8 that presents the plastic normal strain time series of the same integration points, computed by the FBr_2Ts free vibration simulations. It is apparent from Figure 8.7 and Figure 8.8 that when the two structures were excited by the same pull-out force, the foundation of the FBr_2Ts structure exhibited much smaller detachment. The largest difference in plastic strains amplitudes between the FBr_1Ts and FBr_2Ts simulations is observed when the pull-out force was the largest, 15.70kN. The FBr_1Ts_15.70kN analysis predicted a smaller contact interface than the FBr_2Ts_15.70kN one. This justifies the stronger period lengthening computed by the former than the latter analyses, shown in Figure 8.2a and b.

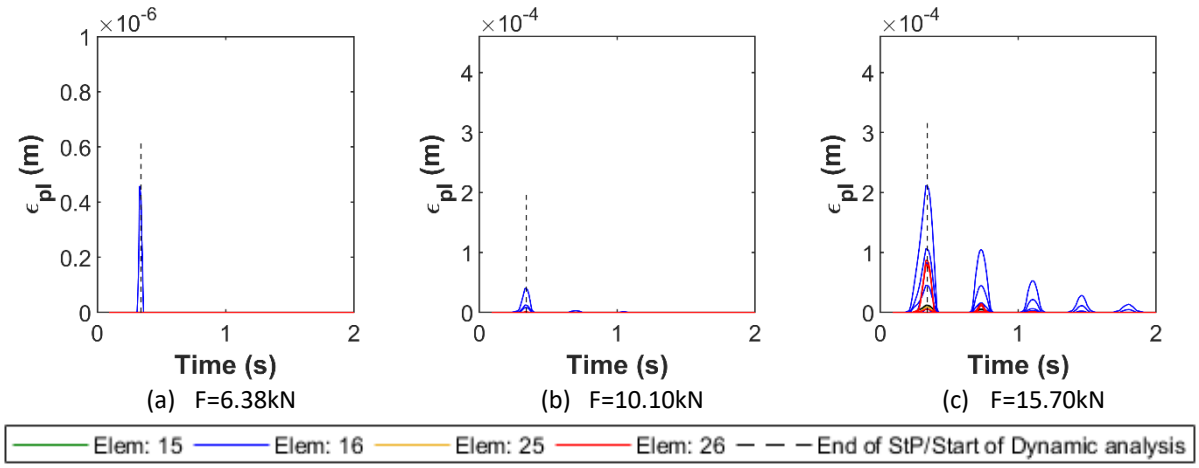


Figure 8.8: Normal plastic strain time series extracted from free vibration simulations of the FBr_2Ts structure, which was excited by (a) 6.38kN, (b) 10.10kN and (c) 15.70kN pull-out force. The strains correspond to integration points of different interface elements shown in Figure 7.55a.

8.2.6 Soil motion

The soil motion, that is a consequence of the structural response, is dependent on the soil-foundation interface model and soil nonlinearity. Figure 8.9 and Figure 8.10 present the variation of the horizontal and vertical soil motion components, respectively, predicted by different numerical models that simulate free vibration experiments of different pull-out forces. The variation of the soil motion is presented in terms of the maximum Fourier amplitude (FA) taken from the main peak of the corresponding spectrum. The spectra are inferred from velocities time histories predicted by the models at the position of the 0.1 instrument, which is 1.2m far from the foundation edge. The velocities are normalised by the applied pull-out force, allowing the comparison of experiments of various forces. For compatibility reasons, all time histories consist of 5 cycles of the motion and are divided to the same number of data points (500).

Figure 8.9a and b show that, for the FBr_2Ts and FBr_1Ts simulations, the largest vertical soil motion is predicted by the LINs_Conv model. This model prescribes linear soil and full bond between the foundation and the soil beneath. The simulation of gaps at the interface (LINs_ELint_GC2) decreases the soil motion, supporting the earlier finding (in Sections 6.3.8, 7.12.3 and 8.2.3) that interface gaps limit the development of radiation damping through geometrical spreading. It also agrees with Gazetas (1983), according to which foundation rotation leads to lower radiation damping than the swaying mode. The existence of gaps indeed promotes foundation rocking and decreases the horizontal motion of the foundation, reducing the energy that is transmitted from the structure to the soil medium.

The existence of gaps also decreases the difference of stiffness between the structure and foundation-soil system. The ratio of soil-foundation stiffness to structural stiffness is crucial in SSI problems, as lower ratios promote SSI effects. When the foundation-soil system is much stiffer than the structure, then the deformability of the SSI system is controlled by the deformability of the structure, while SSI effects are insignificant. Interface gaps essentially reduce the flexural deformability of the structure and increases foundation displacements. The impact of this on the soil motion is evident from the simulation of the PBr structure, which was not prone to rotation without interface gaps. Figure 8.9c shows that the LINs_Conv model produces weak soil motion as the foundation did not participate significantly in the motion. The simulation of gaps, LINs_ELint_GC2, promotes foundation motion and hence leads to an increase of the soil motion. Considering this observation and the one made earlier form the FBr_2Ts and FBr_1Ts experiments, it can be concluded that existence of gaps can decrease or increase the soil motion depending on the ratio of foundation-soil system to structural stiffness. For low ratios, gaps can decrease the soil motion, while for high ratios they can the increase it.

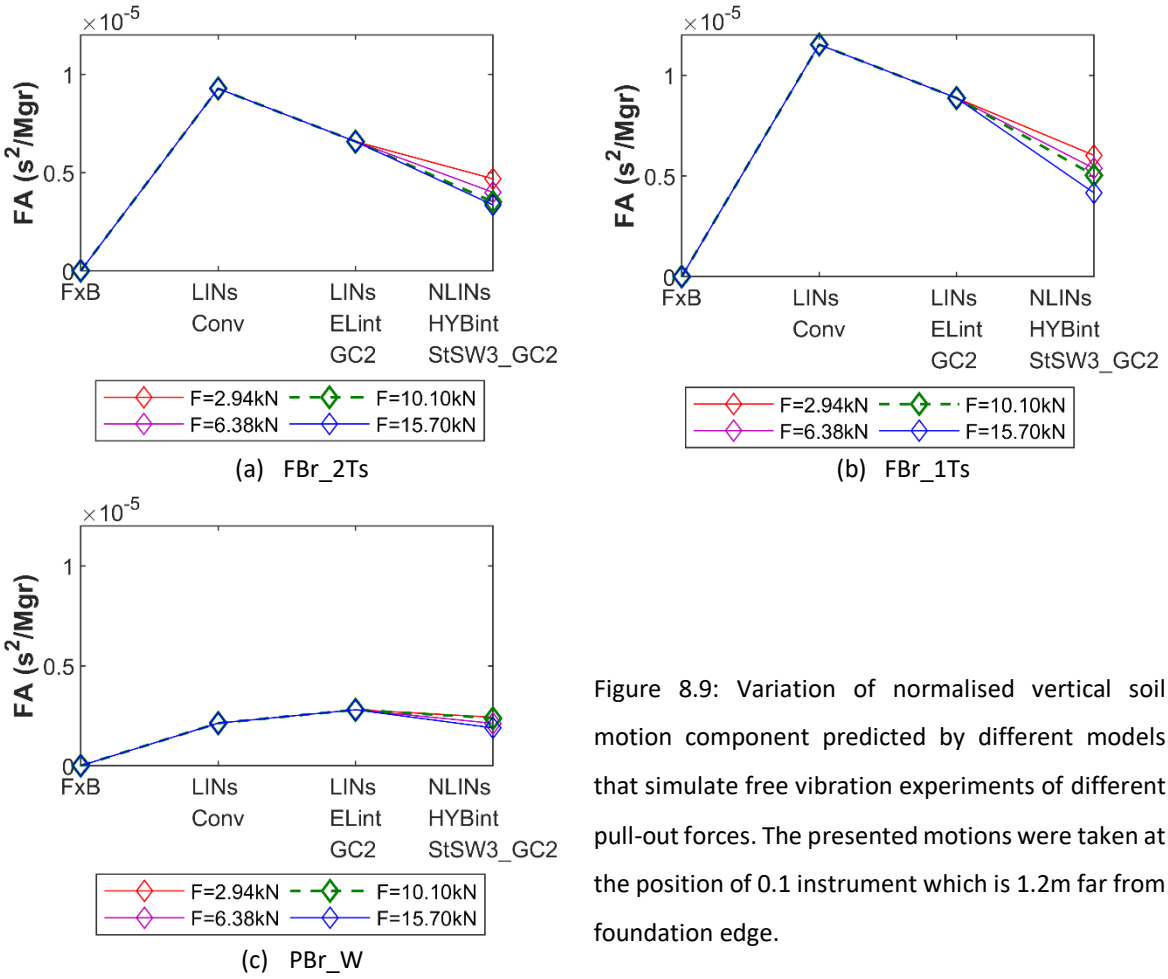
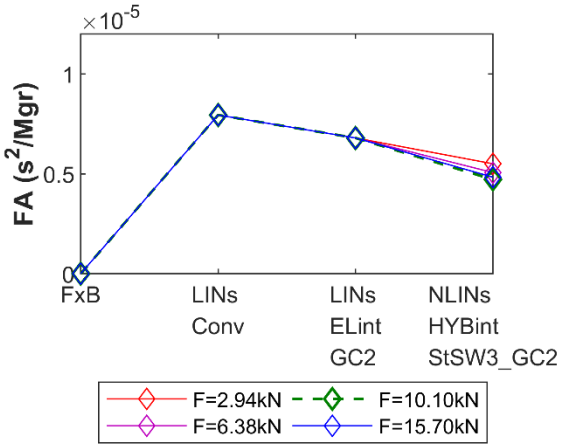


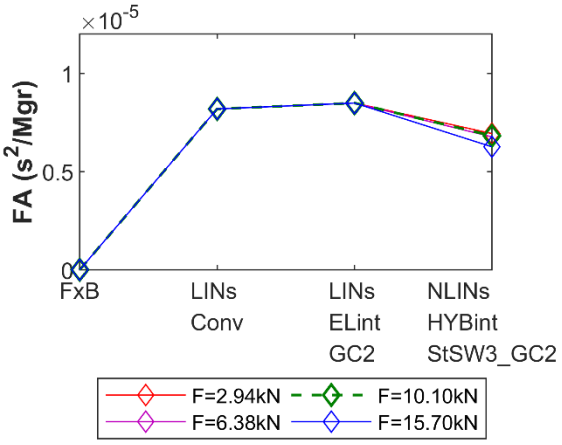
Figure 8.9: Variation of normalised vertical soil motion component predicted by different models that simulate free vibration experiments of different pull-out forces. The presented motions were taken at the position of 0.1 instrument which is 1.2m far from foundation edge.

Figure 8.10 demonstrates that the gaps have a similar, but less pronounced, impact on the horizontal soil motion, which is apparent when comparing results from the LINs_Conv and LINs_ELint_GC2

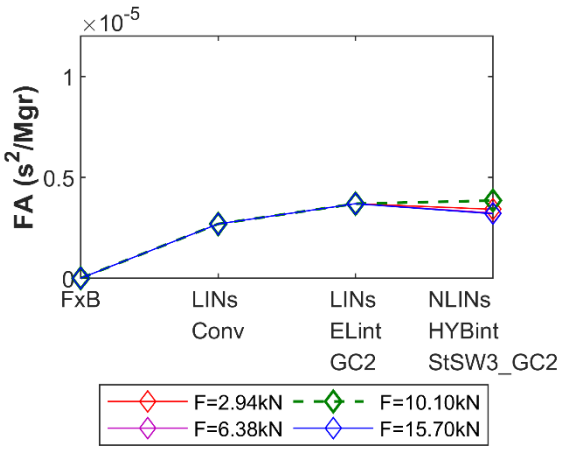
models. Figure 8.9 and Figure 8.10 also demonstrate that soil nonlinearity decreases both horizontal and vertical soil motion components, as indicated by the smaller normalised soil motion predicted by NLINs_HYBint_StSW3_GC2 analyses. The impact becomes more pronounced for the simulations of larger pull-out force, where the soil material damping is much larger in the vicinity of the foundation as evidenced in Section 8.2.4.



(a) FBr_2Ts



(b) FBr_1Ts



(c) PBr_W

Figure 8.10: Variation of normalised horizontal soil motion component predicted by the different models that simulate free vibration experiments of different pull-out forces. The presented motions were taken at the position of 0.1 instrument which is 1.2m far from foundation edge.

The above figures provided the amplitude of the soil motion at a certain location on the soil surface. The following figures present the variation of soil motion amplitude with distance from the foundation edge, as interpreted from strong motion data or computed by numerical analyses. The numerical results are extracted from the NLINs_HYBint_StSW3_GC2 analyses along a line on the soil surface that lies in the plane of symmetry. The line is placed North to the foundation, which coincides with the positive x-axis of the numerical model, with reference to the coordinate system shown in Figure 7.3. Figure 8.11 presents the variation of (a, b) vertical and (c, d) horizontal soil motions, as computed from the FBr_2Ts simulations. As previously, the soil motion is evaluated as the maximum amplitude of Fourier spectra that are inferred from velocity time series (a, c), while results normalised by the pull-out force are also presented (b, d). The comparison between numerical and experimental vertical soil

motion is considered satisfactory. However, the model highly overestimates the horizontal soil motion, which can be attributed to the experimental uncertainties associated with the installation of the soil instruments, as described in Section 5.3.3. According to Section 5.8.4, the installation procedure may had resulted in variable conditions around the instruments. If poorly compacted soil existed around an instrument, then the instrument is likely to record smaller horizontal soil motion than the real one. Furthermore, the disparity could potentially be linked to boundary effects, which as shown in Section 7.18 primarily impact the horizontal soil motion.

Figure 8.11 also illustrates that the numerical model predicts a weaker dissipation of motion with distance from the foundation edge than the dissipation existed during the experiments. This can stem from the fact that the numerical model simulates the half geometry of the problem, and consequently it may not simulate accurately the wave propagation. This is aggravated by the small soil domain, which as shown in Section 7.18, it cannot perfectly simulate the propagation of waves to the half-space. The boundary effects on the soil response are evident through the increase of soil motion with distance at the nodes near to the lateral boundary, which is at 6m from the foundation.

As expected, the amplitudes of the soil motion are larger for the larger pull-out force (Figure 8.11a, c). However, the normalised soil response decreases with increasing force (Figure 8.11b, d), which can be attributed to stronger soil nonlinearity that existed under stronger excitation. Soil nonlinearity can also explain the stronger soil motion dissipation with distance for experiments of larger pull-out force, as indicated by the larger inclination of lines in the normalised plots. Figure 8.11a and b provide evidence that the vertical soil motion is mostly dissipated within the first meter from the foundation. This agrees with the outcome drawn from Section 8.2.4, that soil nonlinearity is more important in the vicinity of the foundation.

The partly braced simulations yield similar founding in terms of the comparison between numerical and experimental data, as well as the soil motion dissipation. Results of these simulations can be found in Appendix G. Exploiting results from the FBr_2Ts and PBr_W simulations, the Appendix also presents the variation of soil motion taken from nodes that lay on the soil surface on a line perpendicular to the loading direction.

Figure 8.12 compares the variation of vertical and horizontal soil motion components with distance, that are produced by the FBr_2Ts, FBr_1Ts and PBr simulations. The soil motion is evaluated by the means of Fourier amplitude as above. For compatibility reasons, only the first 5 cycles of the motions were considered in the computation of the spectra, while an equal number of data points (500) was ensured. It is observed that under the same pull-out force, the FBr_1Ts simulations produced much stronger soil motion than the FBr_2Ts simulations. The lighter structure allowed stronger foundation

motion and hence transmission of stronger motion to the soil. Due to the larger amplitude of motion, the dissipation of the motion with distance was more pronounced for the FBr_1Ts simulations than the FBr_2Ts and PBr simulations.

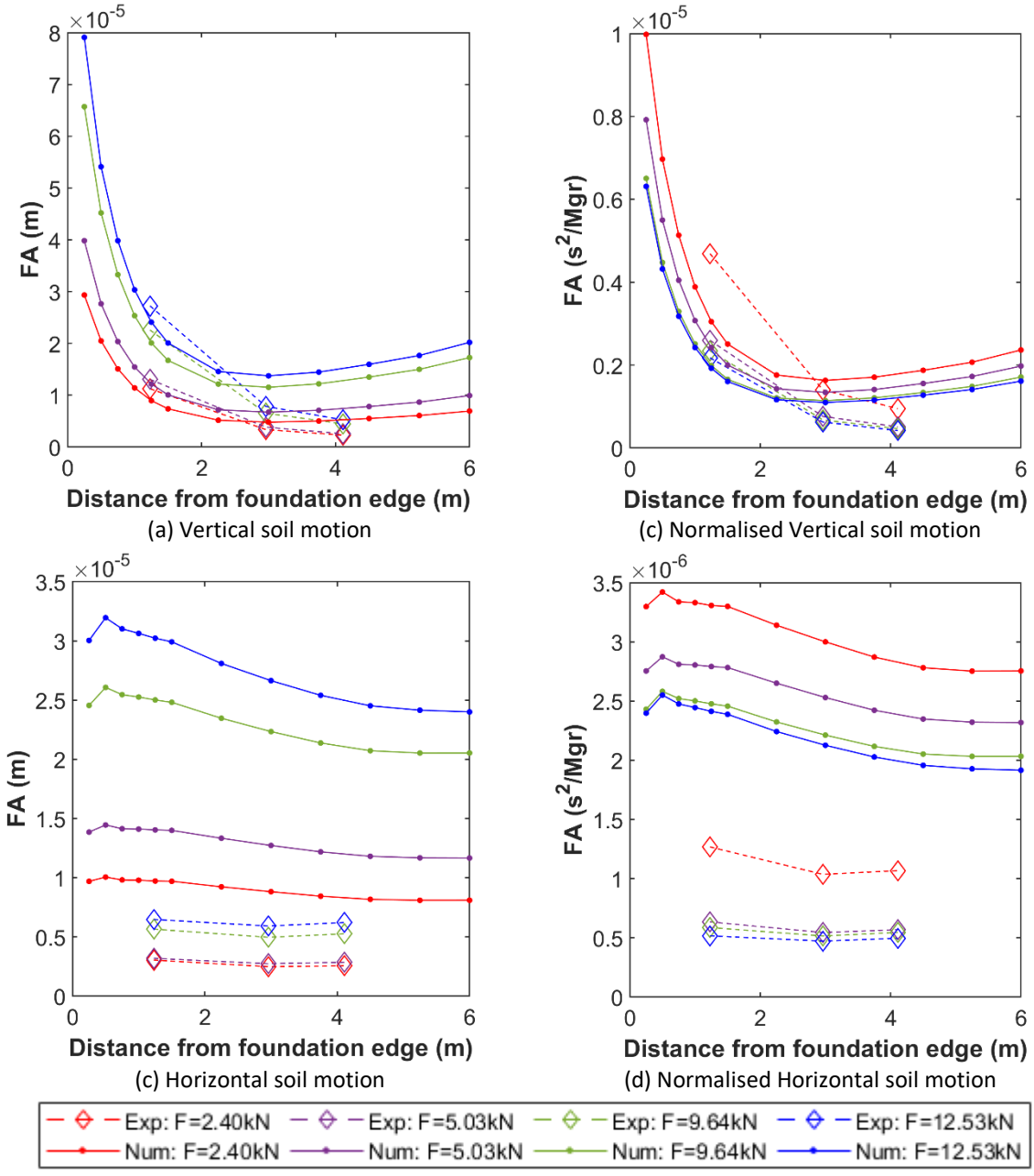


Figure 8.11: Variation of (a, b) vertical and (c, d) horizontal soil motion components with distance from foundation edge, as computed from FBr_2Ts simulations.

The above investigation demonstrated that the motion transferred to the soil is inherently associated with the foundation motion, as previously discussed in Section 6.2.8 by interpreting field data. The relation between the foundation motion amplitude and soil motion can be better seen when normalising the soil motion by the foundation motion. This normalisation is achieved through a transfer function (TF) which is computed as the ratio between Fourier amplitude of the main peak of

the spectrum inferred from soil motion to the corresponding amplitude of the spectrum inferred from foundation motion (see Eq. 6.16). This ratio expresses the motion de/amplification at the natural frequency of the system from the source (foundation) to a specific location of the soil.

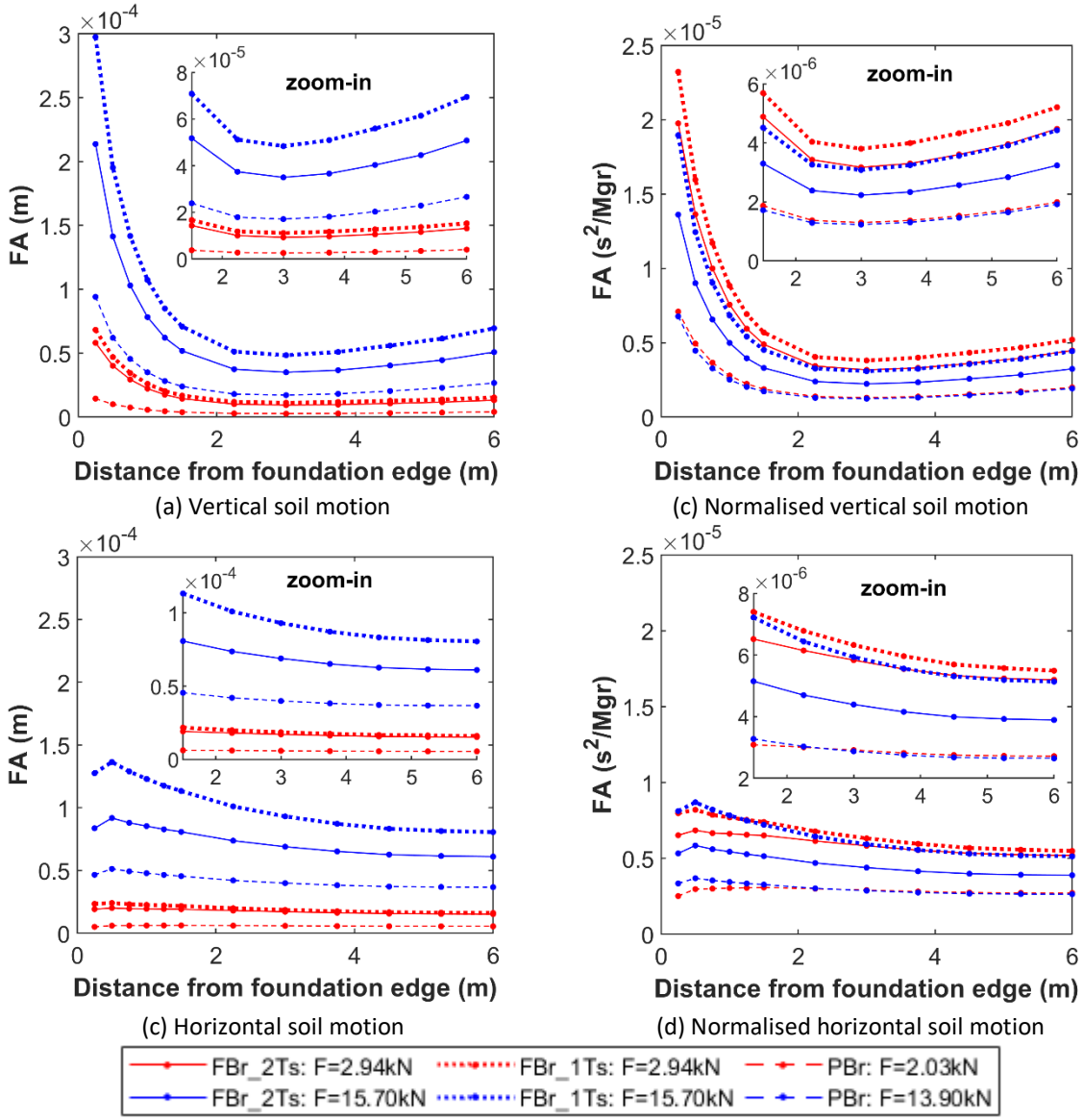


Figure 8.12: Comparison of (a, b) vertical and (c, d) horizontal motion dissipation with distance produced by the FBr_2Ts, FBr_1Ts and PBr simulations.

Figure 8.13 presents the variation of transfer function values with distance from the foundation edge, that are interpreted from the results of the FBr_2Ts, FBr_1Ts and PBr simulations. The figure shows that larger TF values were computed for the horizontal (Figure 8.13b) than the vertical soil motion component (Figure 8.13a), with the exception of the first meter of the foundation. This observation indicates that the horizontal foundation motion can transfer larger motion to the soil, which agrees with similar claims made in the literature (e.g. Gazetas, 1983, 1991). For the same reason, the largest TF values were produced by PBr_W analyses, for which foundation rocking was the smallest. Likewise,

the simulations of experiments which exhibited stronger foundation rocking developed smaller TF values. This was the case for the FBr_1Ts_15.70kN experiment, which according to Figure 8.7c exhibited the strongest foundation rocking and the smallest TF ratios. Similarly, smaller TFs were produced by simulations of larger pull-out force (i.e. 15.70kN, 13.90kN), as larger forces promoted rocking.

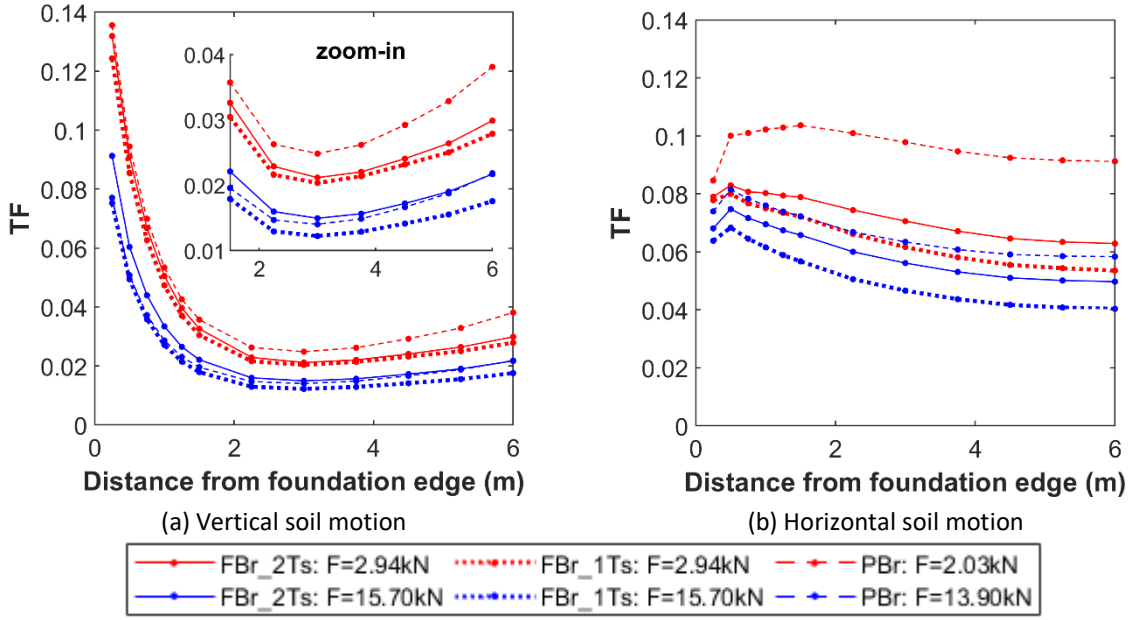


Figure 8.13: Comparison of variation of transfer functions with distance, that are computed from results of the FBr_2Ts, FBr_1Ts and PBr simulations.

Figure 8.14 presents the transfer function values computed as the ratio of the Fourier amplitude of the horizontal foundation motion to the Fourier amplitude of the vertical foundation motion (1.2n/1.2z). Each amplitude was taken from the main peak of the corresponding spectrum. Larger TF values indicate larger foundation horizontal motion, while smaller values indicate a foundation that is more prone to rotation. The figure demonstrates that the horizontal foundation motion component was more important for smaller pull-out forces, while for larger forces the foundation rotation was more prominent. Considering that the translational foundation motion transfers stronger motion to the soil than the rotational one, the above observation can partly justify the larger normalised soil motion produced by experiments with smaller pull-out force. For the smallest pull-out force, the PBr simulation produced the highest foundation TF (Figure 8.14) which explains the largest normalised horizontal and vertical soil motions produced by this simulation in Figure 8.13. The response of the FBr_1Ts structure exhibited the lowest horizontal to vertical foundation motion, indicating strong foundation rocking, and hence justifying the smallest soil motion when this is normalised by the foundation motion (Figure 8.13).

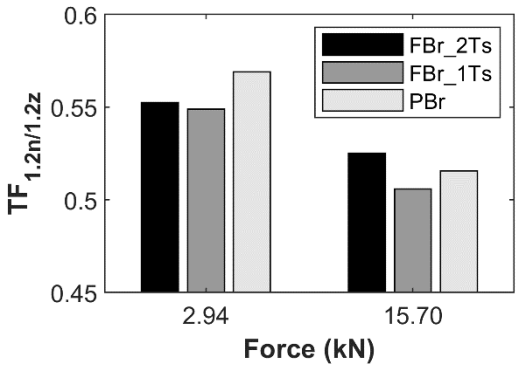


Figure 8.14: Transfer function ratio values of horizontal to vertical foundation motion (1.2n/1.2z) computed from FBr_2Ts, FBr_1Ts and PBr simulations.

The above investigation verified that foundations, whose predominant motion is the rotational, transfer less motion to the soil than foundations which are able to exhibit stronger translational motion. This is inherently associated with the capability of the foundation-soil system to produce radiation damping, which as it has already mentioned decreases with foundation rotation.

8.3 Forced vibration tests

As mentioned in Section 6.3, the structural motion perpendicular to the loading direction (out-of-plane motion) was important during the forced vibration tests. The out-of-plane motion was not important during the FBr_2Ts_5Hz, FBr_1Ts_5Hz and PBr_W_2Hz experiments (of any vibrator's mass), based on which the half-geometry numerical model was calibrated in Chapter 7. For the majority of the remaining experiments, the out-of-plane motion was important, which make the application of the half-geometry model inapplicable. Nevertheless, this model is employed to simulate these forced vibration experiments, aiming to establish numerical natural frequencies and provide evidence regarding the importance of nonlinear phenomena. Although the experimental forced vibration tests revealed more than one natural frequencies of different modes of oscillation (see Table 6.11), the boundary conditions of the half-geometry numerical model can predict only the fundamental frequency. This frequency corresponds to the North-South swaying mode of the physical model, which is referred to, herein, as the in-plane mode.

Displacement-controlled analyses, that were employed in the calibration process, cannot reveal the natural frequency of the model, for the reasons explained in Section 7.5.3. Therefore, the presented analyses impose the vibratory excitation as a force that is applied parallel to the plane of symmetry on the centre of the top slab. Given that the model simulates half of the problem geometry, the magnitude of the applied force is half the experimental one. The experimental force is a sinusoidal force of which amplitude can be estimated via Eq. 5.14. According to this equation and as

demonstrated in Figure 5.12, the force amplitude depends on the mass of plates (mA, mB, mC and mD) that were placed on the vibrator. The force was the smallest when the mA mass was placed on the vibrator, while it was the largest when the mD mass was used.

8.3.1 Natural frequencies and motion amplitude of the swaying mode

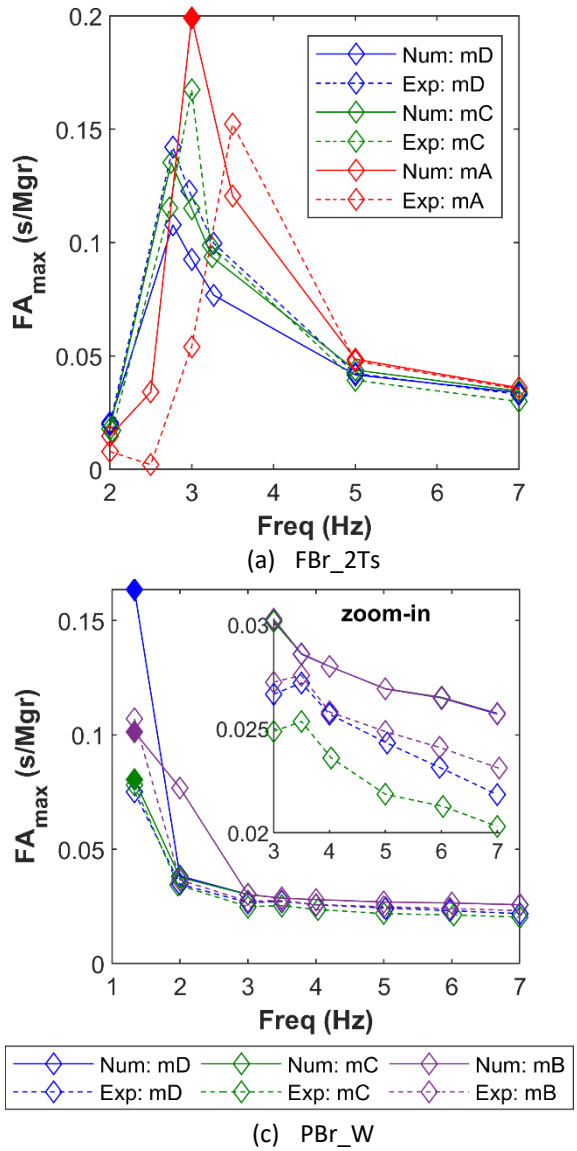
Figure 8.15 presents the variation of top slab motion with applied frequencies, predicted by (a) FBr_2Ts, (b) FBr_1Ts and (c) PBr_W simulations. The top slab motion is evaluated by the means of Fourier amplitude of the main peak of spectrum inferred from acceleration time histories recorded at the top slab. For compatibility reasons, the time histories that are used for the computation of spectra consist of 6 full cycles, while each cycle consist of 100 data points. The top slab response is normalised by the maximum magnitude of the applied sinusoidal force, allowing the comparison of normalised top slab response under various vibratory loads. The numerical results are also compared with the experimental ones. The solid data points indicate simulations that produced resonant features resulting in time histories that do not reach steady state conditions. Although these points may not correspond to a representative FA amplitude, they clearly reveal the swaying in-plane natural frequency of the model. For simulations which did not produce resonant features, the numerical natural frequency is indicated by the maximum normalised top slab response observed in the figures.

Due to the model's boundary conditions, the captured natural frequencies correspond to the swaying North-South (in-plane) experimental natural frequency, which can be found in Table 6.11. Figure 8.15 demonstrates that the numerical model can capture sufficiently well the swaying natural frequency of the three SSI systems. The difference between experimental and numerical motion amplitudes maximises around resonance. This is reasonable as the numerical response at resonance, i.e. the input frequency coincided or was very close to the fundamental frequency of the model, is generally unstable and of very high amplitude. Unstable response was not observed in the experimental data, as the experimental response reached always steady state conditions, with the exception of the PBr_W_1.33Hz experiment.

Far from resonance, the difference between the numerical and experimental results can be attributed to uncertainties regarding the loading direction and magnitude of the input excitation, as well as to geometric imperfections. These imperfections, which cannot be modelled, can be the reason of the existence of the experimental out-plane motion. The out-of-plane motion was completely restricted by the boundary conditions of the numerical model and hence could not be reproduced. The imperfections were not important for the FBr_2Ts and FBr_1Ts experiments when the applied frequency was 5Hz as well as for the PBr_W experiment of 2Hz frequency, as demonstrated in Section

7.2. For this reason, the simulations of these experiments predict results close to the experimental ones.

As mentioned in Chapter 6, the differences observed between normalised responses of experiments with different excitation magnitude (i.e. different vibrator's plates mass), can be attributed to nonlinear phenomena. Figure 8.15 shows that larger vibratory force (e.g. mD) leads to smaller normalised response, verifying the observations made by interpreting experimental data in Section 6.3.6. Experimental results also showed decrease of natural frequencies with increasing force, which numerically was reproduced by the FBr_2Ts and FBr_1Ts simulations. As Figure 8.15a shows, the mD simulation produced a smaller fundamental frequency than the mA simulation, which is a consequence of the larger force applied during the former simulation. The nonlinear response is attributed to soil and foundation nonlinearity, for which numerical evidence is subsequently provided.



(a) FBr_2Ts

(b) FBr_1Ts

(c) PBr_W

Figure 8.15: Variation of normalised top slab motion amplitudes with input frequencies, inferred from numerical and experimental data. Solid data points indicate simulations that exhibited resonant features.

8.3.2 Soil nonlinearity

Figure 8.16 presents evidence of soil nonlinearity that took place during the simulated forced vibration experiments on the (a, b, c) FBr_2Ts and (d, e) FBr_1Ts structures. It presents the variation of stiffness degradation and damping ratio values, that developed at an increment when the acceleration of the steady state part of the motion maximised. Where steady state motion was not reached, which was the case of the simulations that are indicated with solid colours in Figure 8.15, a representative increment was selected. The figure presents the mean values and standard deviation of all integration points enclosed in the BCE area (Figure 8.4), where the strongest nonlinearities are anticipated to take place, as evidenced in Section 8.2.4.

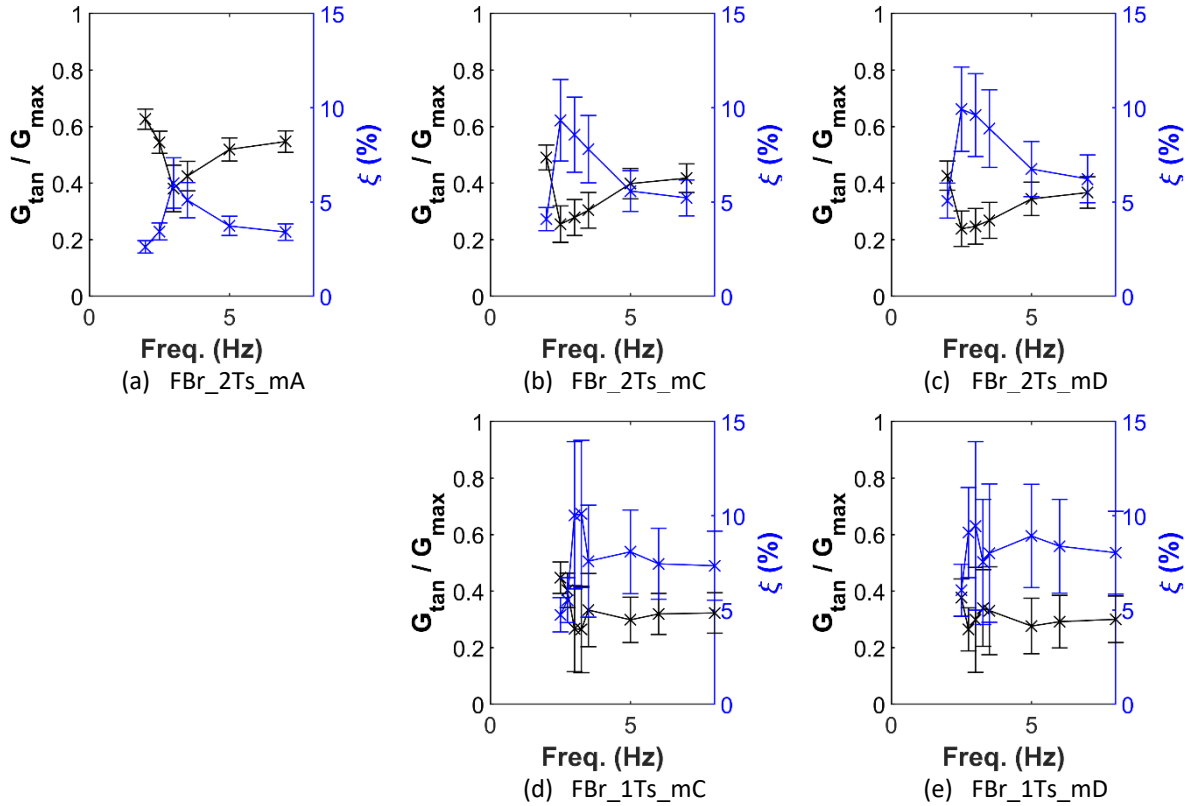


Figure 8.16: Variation of soil stiffness degradation and damping ratio values with input frequencies, that were developed at an increment of maximum acceleration of the steady state part of the motion, where reached. The mean values and standard deviation of all integration points enclosed in BCE area, with reference to Figure 8.4, are presented.

Figure 8.16 demonstrates that soil nonlinearities, associated with stiffness degradation and damping, were considerable, although less pronounced than the ones developed by the free vibration simulations (Figure 8.6). The figure also shows that nonlinearities maximised at the natural frequencies of the systems that were identified from Figure 8.15, indicating soil motion maximisation at resonance. Soil nonlinearities were more important on the forced vibration response of the FBr_1Ts

structure (Figure 8.16d and e), which exhibited stronger foundation motion and hence soil response than the FBr_2Ts structure (Figure 8.16a, b and c). Also, as expected, nonlinearities were stronger for larger vibratory forces, which is the case of the mD experiments (Figure 8.16c, e).

8.3.3 Soil-foundation interface nonlinearity

Soil-foundation interface nonlinearity can be evaluated when the interface model allows opening and closure of interface elements. The ELint_GC2 interface model simulates permanent gaps, but it does not allow further opening of interface element; therefore, ensuring constant contact interface conditions during the excitation. For this reason, results produced by FBr_2Ts and PBr_W forced vibration analyses, that employ the ELint_GC2 model, are not suitable for investigating interface nonlinearity and hence are not discussed. The presented results were produced by analyses that employ the HYBint_GC2_StSW3 interface model and simulate the FBr_1Ts_mC and FBr_1Ts_mD forced vibration experiments. This interface model allows the initially closed interface elements to open and close multiple times during the excitation.

Soil-foundation interface nonlinearity is evaluated in Figure 8.17, that presents the variation of normal plastic strains with input frequencies. For compatibility, the strains and the earlier presented soil stiffness degradation and damping ratio values (Figure 8.16) were computed at the same increments. Each selected increment corresponds to a maximum acceleration of the steady state part of the motion, where reached. Each data point is calculated as the mean value of normal plastic strains of the interface element 16, the location of which is shown in Figure 7.55a. The location of this element and the selection of increments ensure that the presented normal plastic strains are the largest existed at any element of the interface and at any time of the excitation.

Figure 8.17 shows that for a given input frequency, foundation detachment increases with the magnitude of the vibratory load. As expected, the mD analysis, the input load of which was larger, produced stronger foundation detachment than the mC one. More importantly, the figure demonstrates that the magnitude of interface gaps maximised around resonance (i.e. 3Hz). Although the force increases with increasing input frequency (see Figure 5.12), the gaps tend to decrease for frequencies larger than the resonant one. The large opening of the examined interface element at resonance, with respect to other frequencies, indicates that the identified fundamental frequency is associated with the rotational mode of oscillation. Foundation rotation tends to create a strong interface nonlinearity. Although not shown herein, when the HYBint interface model is used in the FBr_2Ts and PBr_W simulations, the initially close interface elements did not open during the excitation. The strong interface nonlinearity that exists during the excitation of the FBr_1Ts structure,

which is negligible for the other structures, can justify the larger lengthening of predominant period observed for the former structure (see Section 8.2.2).

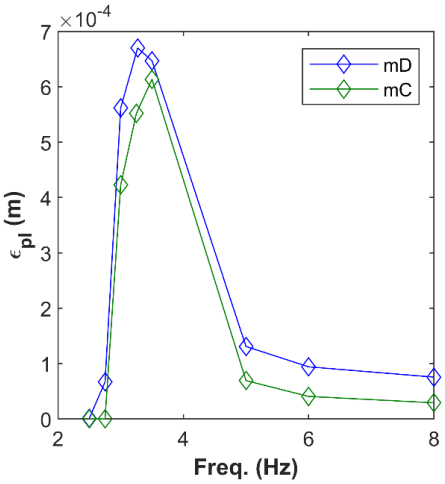
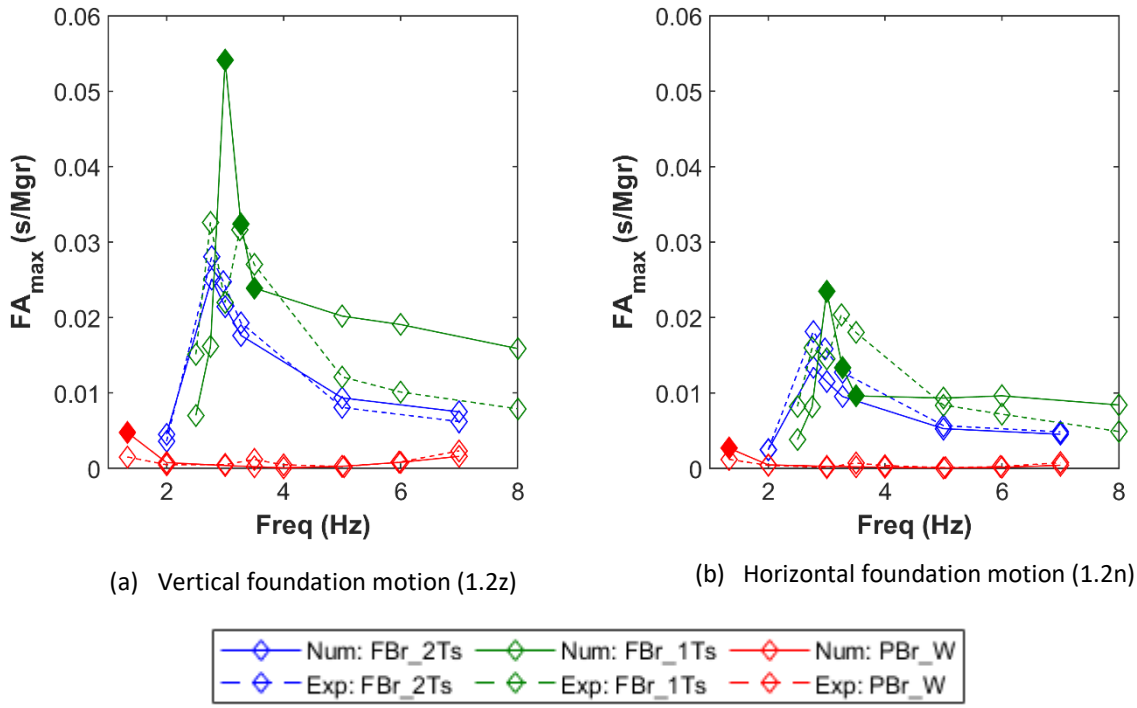


Figure 8.17: Variation of normal plastic strains with input frequencies. Each data point corresponds to the mean strain value of the interface element 16, shown in Figure 7.55a. Data were computed at an increment of maximum acceleration of the steady state part of the motion, where reached. Results from simulations of forced vibration tests on the FBr_1Ts structural configuration are shown.

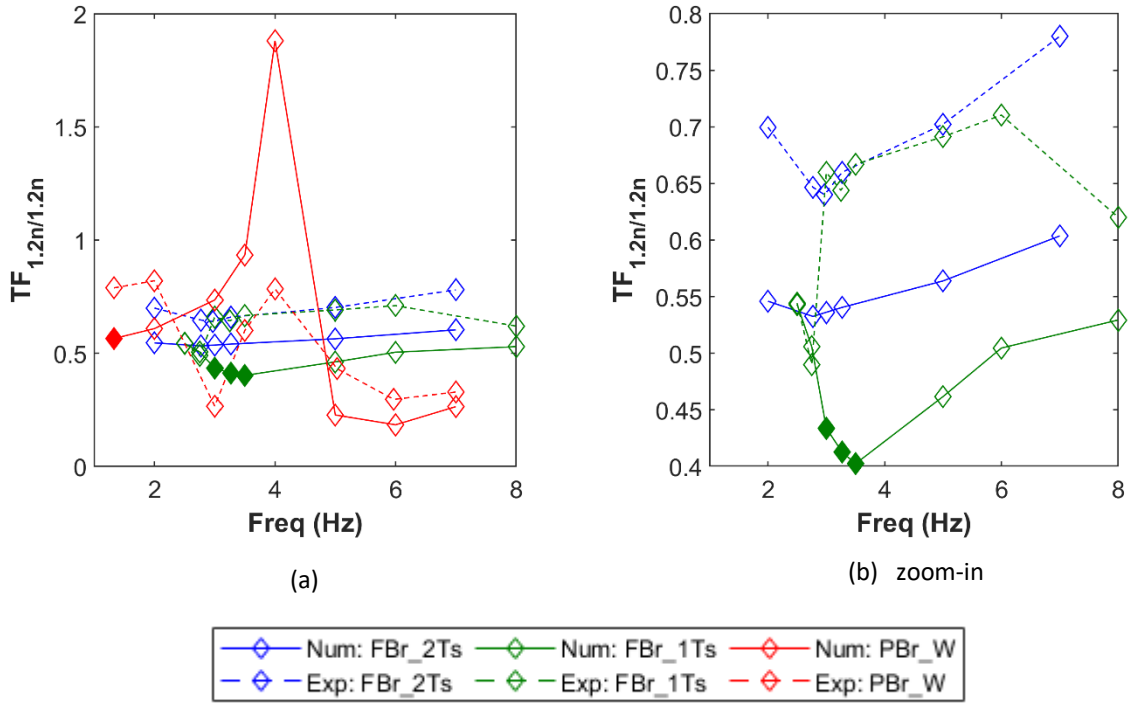
The stronger interface nonlinearity that took place during the FBr_1Ts simulation, in relation to the FBr_2Ts and PBr_W simulations, is manifested as stronger foundation motion. Figure 8.20 presents the variation of FA of the normalised (a) vertical and (b) horizontal motions, recorded at the foundation edge (1.2), with input frequency. It shows that the FBr_1Ts simulations produced the strongest foundation motion, while the PBr_W ones the weakest. It also shows that, at resonance, the foundation motion maximised, while the maximisation was more pronounced on the vertical component. The horizontal foundation component is much lower than the vertical motion for the FBr_2Ts and FBr_1Ts simulations. This is better shown in Figure 8.19 that plots the horizontal to vertical foundation motion ratios with frequency. Figure 8.19b, which is a zoom-in figure, shows that for the two experiments, the ratio is below unity for the entire frequency range, implying weaker horizontal than vertical foundation motion. It also shows that the ratios minimised at resonance, which corresponds to the rotational natural mode of oscillation of the model. The foundation rotation was more pronounced for the FBr_1Ts simulations as evidenced by the much lower ratios values than the ones produced by the FBr_2Ts simulations. Unlike the above simulations, the PBr_W ones produced ratio values that are highly dependent on the input frequency (Figure 8.19a). At some frequencies, the ratio is larger than unity, implying stronger horizontal than vertical foundation motion. In particular, the ratio maximised at 4Hz of applied frequency, indicating that this frequency is close to the swaying mode of oscillation of the SSI system.



(a) Vertical foundation motion (1.2z)

(b) Horizontal foundation motion (1.2n)

Figure 8.18: Comparison of the variation of foundation (a) vertical and (b) soil motions with applied frequency, that were produced by FBr_2Ts, FBr_1Ts and PBr_W simulations.



(a)

(b) zoom-in

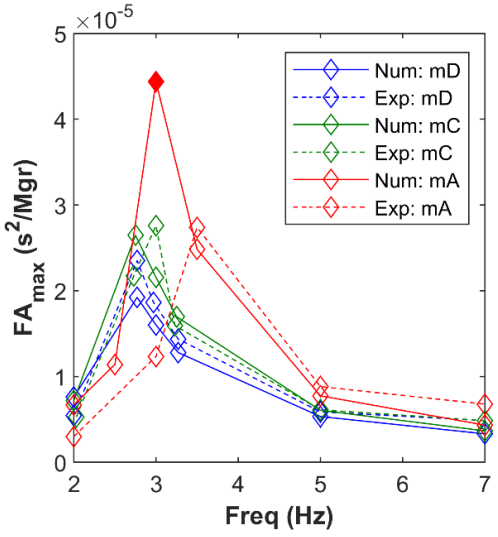
Figure 8.19: Variation of foundation transfer function (TF) ratio with applied frequencies. The TFs are computed as the foundation horizontal (1.2n) to vertical (1.2z) motion, which were produced by the FBr_2Ts, FBr_1Ts and PBr_W simulations.

8.3.4 Soil motion

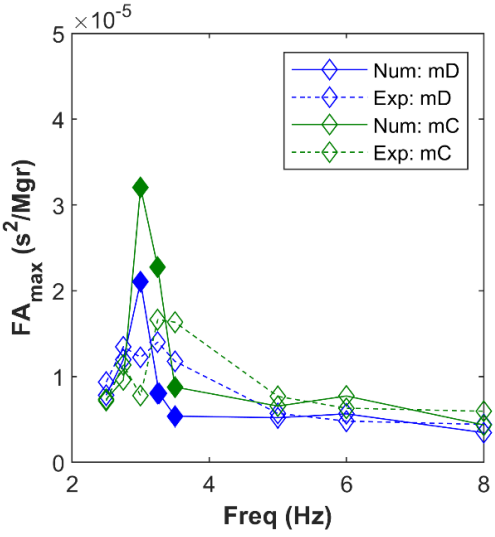
Figure 8.20 presents the variation of normalised vertical soil motion amplitude with applied frequencies, which interpreted from results of (a) FBr_2Ts, (b) FBr_1Ts and (c) PBr_W simulations. The motion amplitude is evaluated by the means of Fourier amplitude of the main peak of spectra, that were inferred from velocity time histories normalised by the amplitude of the input sinusoidal force. The time histories were computed/recorded at the position of 0.1 or 0.2 instruments, which were located 1.2m and 2.9m, respectively, North to the foundation edge (Figure 5.17). This figure compares numerical and experimental results, showing a relatively good agreement for the simulations of experiments with weak out-of-plane motion. These are the FBr_2Ts_5Hz, FBr_1Ts_5Hz and PBr_W experiments, while the numerical model cannot approach the soil motion for the remaining experiments.

The numerical results replicate qualitatively the experimental decrease of the normalised response with increasing magnitude of the excitation force for the FBr_2Ts and FBr_1Ts simulations (Figure 8.20a and b). This is a consequence of the stronger soil nonlinearity developed during stronger excitation, as it was earlier discussed in Section 8.3.2. For the FBr_1Ts experiment, the difference in soil motion between simulations of different magnitude of excitation force is also attributed to the interface nonlinearity. The stronger excitation promoted stronger foundation rocking and detachment from the soil beneath (Figure 8.17), which further decreased the soil motion. As already explained, interface nonlinearity did not exist in the FBr_2Ts and PBr_W simulations. The presence of an additional source of nonlinearity during the FBr_1Ts simulations provides justification for the increased dependency of the soil motion, resulting from these simulations, on the magnitude of the excitation force. In fact, the difference between the soil motions computed by the mC and mD set of analyses was larger for the FBr_1Ts simulations than the FBr_2Ts and PBr_W ones.

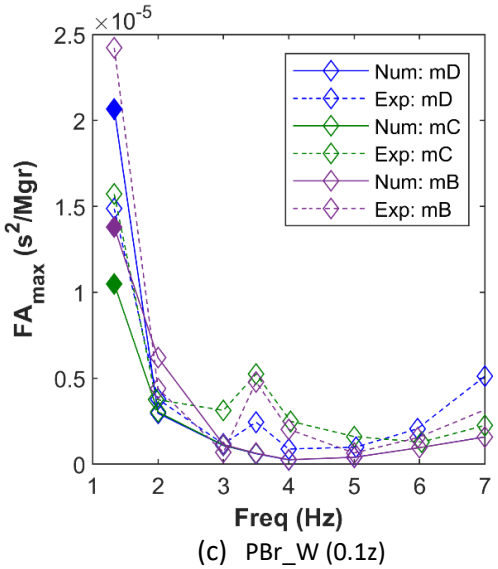
Figure 8.21 quantifies the difference in the soil motion amplitude that was computed by the mC and mD numerical simulations. The difference is calculated as $(FA_{mC}-FA_{mD})/FA_{mC}$, where FA are taken from Figure 8.20. This figure shows larger values for the FBr_1Ts simulations, demonstrating that the soil motions produced by these simulations were the most sensitive to the magnitude of the excitation force. The PBr_W simulations exhibited the least sensitivity to the excitation magnitude, as indicated by the almost zero difference shown in Figure 8.21. The latter observation implies very weak soil nonlinearity, which explains the very similar soil motion amplitude computed by the mA, mC and mD simulations shown in Figure 8.20c.



(a) FBr_2Ts (0.2z)



(b) FBr_1Ts (0.2z)



(c) PBr_W (0.1z)

Figure 8.20: Variation of normalised vertical soil motion, in Fourier amplitude units, with applied frequency, comparing numerical with experimental data. The caption of each figure reflects to the experiment and instruments of which data are used. Solid data points indicate simulations that exhibited resonant features.

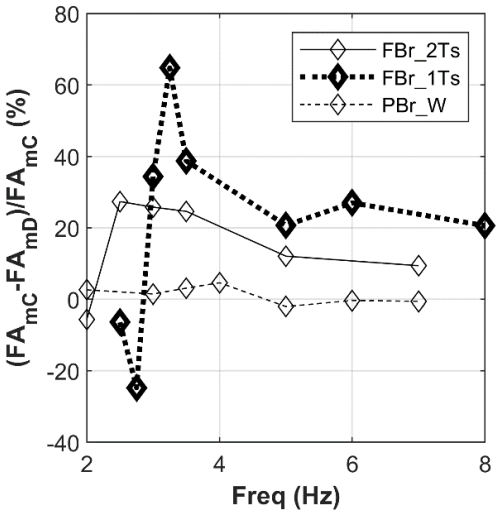
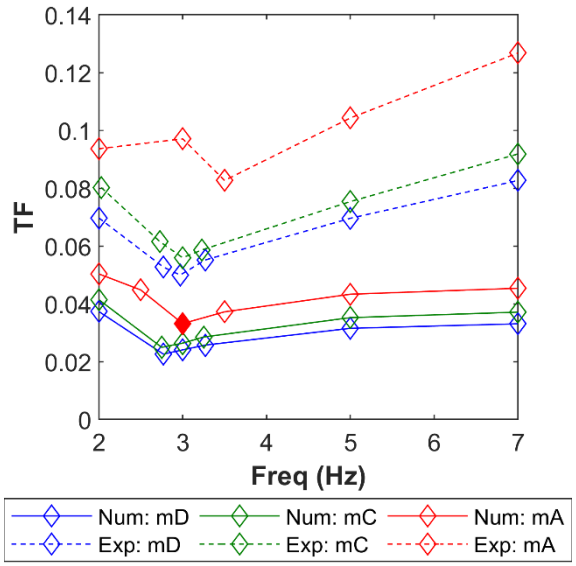


Figure 8.21: Difference of soil motion produced by the mC and mD simulations. The difference is computed in terms of Fourier amplitude, which are presented in Figure 8.20.

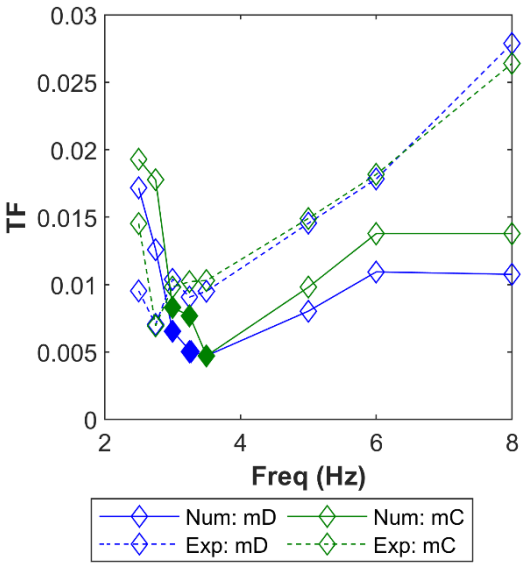
Considering the mD simulations, the maximum and minimum soil motion amplitudes (Figure 8.20) appear at the input frequencies at which the foundation motion maximised and minimised respectively (Figure 8.18). Similar to free vibration results discussed in Section 8.2.6, the importance of both soil and interface nonlinearities increases with foundation motion.

The relation between foundation and soil motion is better established through soil to foundation transfer function ratios. Figure 8.22 presents TF values computed as the ratio of Fourier amplitudes of soil motion to the amplitudes of the foundation motion. Fourier amplitudes correspond to the amplitude of the main peak of spectra that are inferred from foundation and soil velocities. Soil velocities were computed on the soil surface at the position of the 0.1 or 0.2 instruments (Figure 5.17), as reflected to the figure's captions. Foundation amplitudes were inferred from the motion at the position of 1.2 instrument, which was located at the edge of the foundation (Figure 5.16). Larger TF function values imply a foundation mode that promotes transmission of stronger motion to the soil. The variation of TFs with applied frequency is computed from numerical and strong motion data of (a) FBr_2Ts, (b) FBr_1Ts and (c) PBr_W experiments.

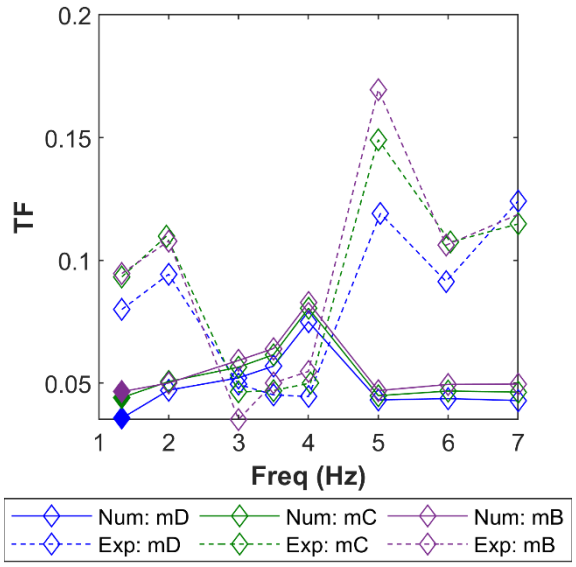
Figure 8.22 shows that the numerical foundation oscillation transmits lower motion to the soil than the experimental oscillation, for almost every applied frequency. Also, the figure demonstrates that, for all simulations, the variation of TFs with input frequency is very similar to the variation of the ratio of horizontal to vertical foundation motions, shown in Figure 8.19. Lower values of the latter ratio are associated with lower soil to foundation TF values, demonstrating that more pronounced foundation rocking results in lower transmission of waves to the soil. Larger horizontal to vertical foundation ratios indicate that the predominant foundation motion is the swaying mode, which was the case in the PBr_W simulation when the input frequency was 4Hz. For this simulation, the foundation motion ratio maximised (Figure 8.19), while the same is observed on the soil to foundation transfer function (Figure 8.22c). The above observations demonstrate that the amount of energy transmitted to the soil from foundation oscillation is dependent on the mode of foundation oscillation. As inferred from both forced and free vibration simulations (Section 8.2.6), the swaying mode of foundation oscillation transmits higher energy to the soil than the rotational mode.



(a) FBr_2Ts (0.2z/1.2z)



(b) FBr_1Ts (0.2z/1.2z)



(c) PBr_W (0.1z/1.2z)

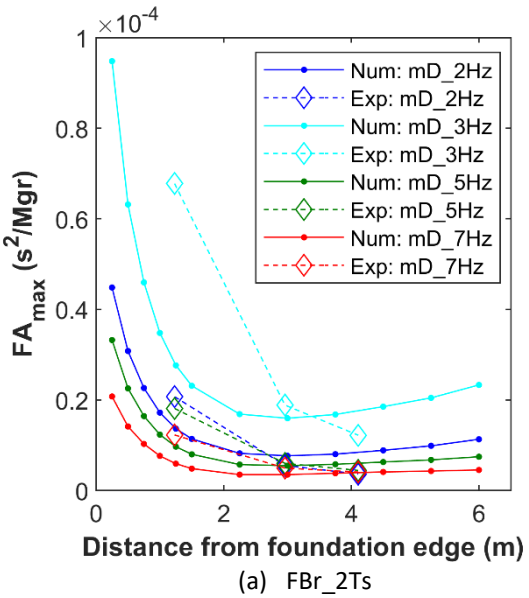
Figure 8.22: Variation of soil to foundation vertical motion transfer function ratios with applied frequency, comparing numerical with experimental data. The caption of each figure reflects to the experiment and instruments of which data are used. Solid data points indicate simulations that exhibited resonant features.

The discussed figures presented soil motion at a certain location on the soil surface, while the soil motion dissipation with distance from the foundation edge is following. Figures 8.23 to 8.26 present the variation of soil motion amplitude at different locations along a line on the soil surface that lies in the plane of symmetry. The line is placed North to the foundation, which in the numerical model coincides with the positive x-axis, with reference the coordinate system in Figure 7.3. The soil motion at each location is evaluated as a Fourier amplitude value (FA_{max}) that corresponds to the main peak of the Fourier spectrum of the corresponding velocity time history, which is normalised by the applied

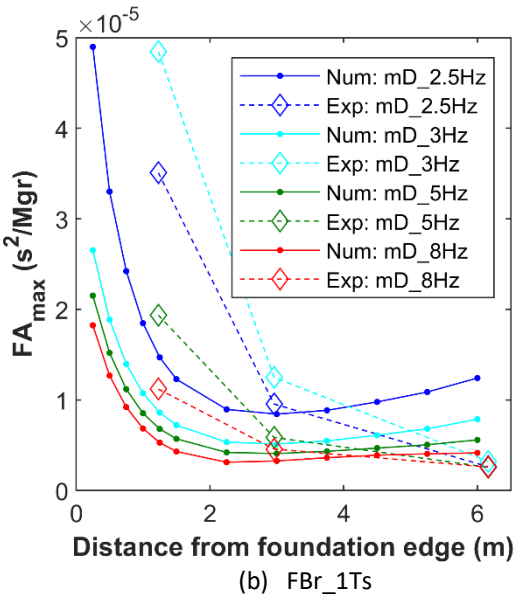
force. The employed normalised velocity time histories have a duration equal to 4 cycles, while each cycle consisted of 100 data points. As previously, the soil motion is also evaluated as a transfer function (TF) that is computed as the ratio of FA_{max} of soil motion to FA_{max} of foundation motion. The foundation motion is considered the source that transmitted waves to the soil medium. The normalisation of the soil motion to the foundation motion can indicate the capability of the vibrating foundation to transmit energy to the half-space.

Figure 8.23 presents the dissipation of vertical soil motion, in Fourier amplitude units, that is computed by (a) FBr_2Ts, (b) FBr_1Ts and (c) PBr_W simulations. The figure verifies the observation made in Section 8.2.6 that the soil motion is mostly dissipated within the vicinity of the foundation. It also shows that the models underpredict the vertical soil motions and the dissipation rate. Both numerical and experimental soil motions maximise at frequencies near the resonant ones, while they decrease for increasing frequencies. For larger frequencies, the force for which the soil motion is normalised is larger while the structural response weaker, which can justify the smaller normalised values.

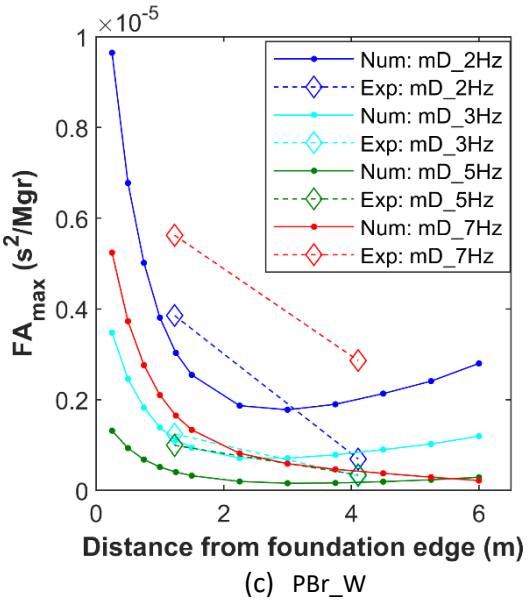
Figure 8.23 also shows that the normalised soil motion is larger for the FBr_2Ts simulations than the FBr_1Ts and PBr_W ones, despite that the largest foundation motion was produced by the FBr_1Ts simulations. The relation between the foundation and soil motion cannot be established through the above figures, the soil motions of which are normalised by the amplitude of the sinusoidal force. As previously mentioned, this relation can be investigated through soil to foundation motions transfer functions (TF). Assuming that the source is the foundation motion, any difference between TFs that are produced by analyses of different input frequency is attributed to nonlinearities. For the FBr_2Ts and PBr_W simulations, soil nonlinearity is the only nonlinear mechanism, while interface nonlinearity co-exists with soil nonlinearity for the case of FBr_1Ts simulations. TFs, also, depend on the horizontal to vertical foundation ratio ($TF_{1.2n/1.2z}$). Higher ratio implies stronger foundation horizontal motion, which is the motion component that transmits more energy to the soil and hence stronger soil motion. Therefore, it is expected that larger $TF_{1.2n/1.2z}$ values contributes to larger soil to foundation motions ratios.



(a) FBr_2Ts



(b) FBr_1Ts

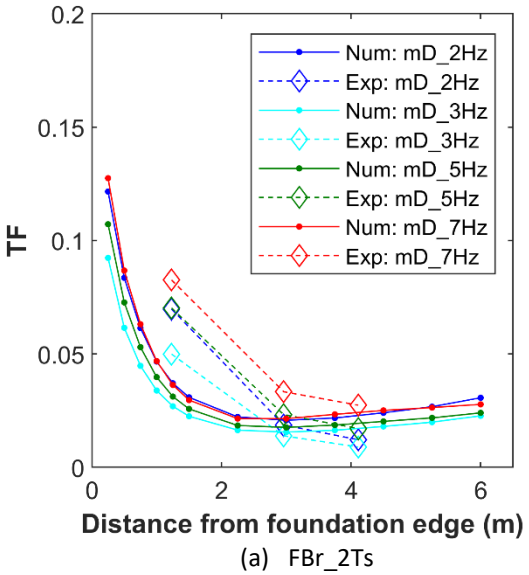


(c) PBr_W

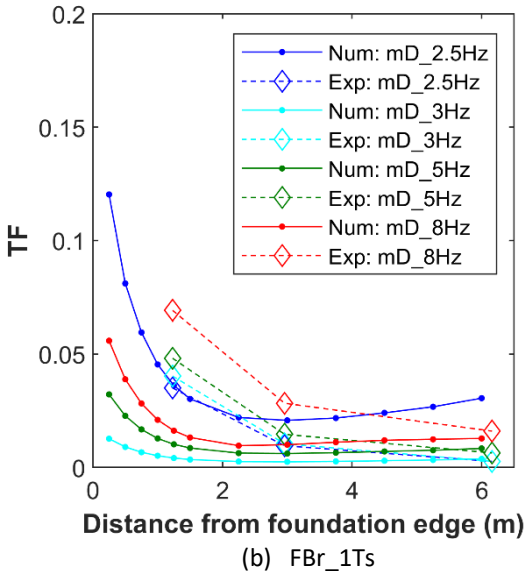
Figure 8.23: Vertical soil motion attenuation with distance, that is inferred from mD simulations and experiments. Soil motions are evaluated as Fourier amplitudes of the main peak of the corresponding spectra.

Figure 8.24 presents the variation of TF values with distance from the foundation edge, that were computed from the same simulations and experiments discussed earlier. It is observed that the TFs computed by numerical data are smaller than the ones inferred from the experimental data, which is an indication that the numerical foundation motion transfers less motion to the soil. This can be attributed to the fact that the modes of foundation oscillation predicted by the numerical model are different to the experimental. Figure 8.24 also shows that the lowest TF values are observed at applied frequencies which were near to the resonant ones. This stems from the fact that at these frequencies the soil nonlinearity maximised (Figure 8.16), while for the case of the FBr_1Ts simulations, the strongest interface nonlinearity, which promotes foundation rocking, was observed (Figure 8.17). The increase of material damping and reduction of soil stiffness decreased the soil motion, which is further decreased when foundation rocking was prominent. The impact of foundation rocking is also

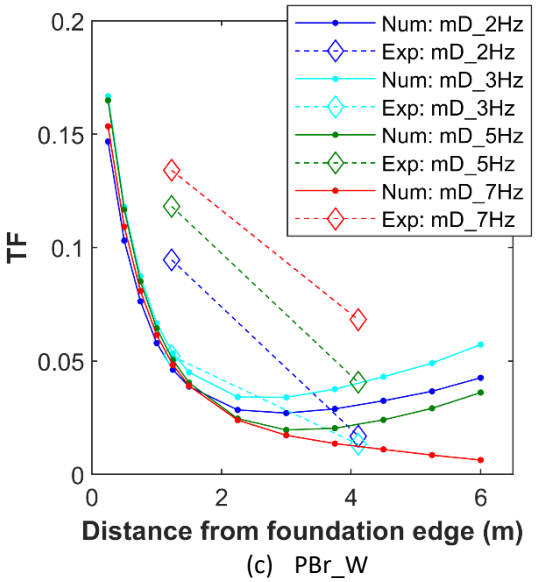
demonstrated by the fact that the lowest TF values, shown in Figure 8.24, and the lowest values of horizontal to vertical foundation motions ($TF_{1.2n/1.2z}$), shown in Figure 8.19, are observed at the same frequencies. This verifies the earlier claim that the weakest energy transmission to the soil took place when foundation rocking was the strongest.



(a) FBr_2Ts



(b) FBr_1Ts

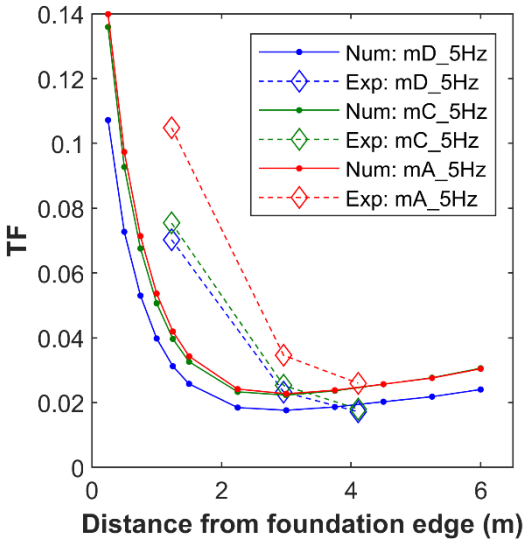


(c) PBr_W

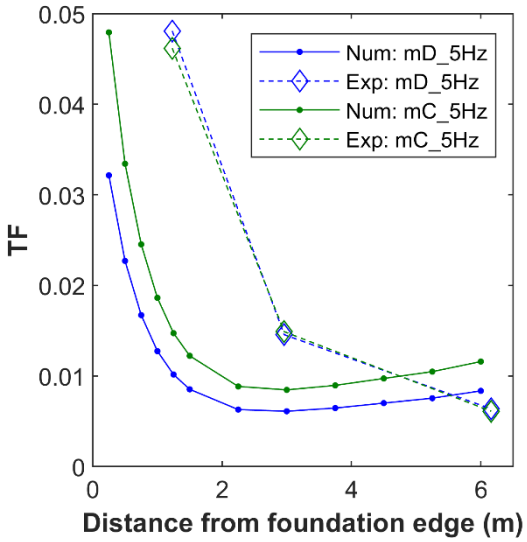
Figure 8.24: Variation of soil to foundation motions transfer function with distance from the foundation edge. Data are inferred from mD simulations and experiments.

Figure 8.25 investigates the impact of the level of excitation (i.e. mA, mB, mC and mD) on the variation of TF with distance. As discussed earlier, larger soil and interface nonlinearities as well as smaller $TF_{1.2n/1.2z}$ values were produced by simulations of which the input excitation was the largest (i.e. mD). This can justify the smaller TF values computed by mD simulations than simulations of weaker excitation (i.e. mC, mB, mA), observed in Figure 8.25. Figure 8.25c shows that the TFs computed from PBr_W simulations are almost independent of the magnitude of the excitation, which is a consequence of the weak soil nonlinearity. When soil nonlinearity was significant, as in the case for

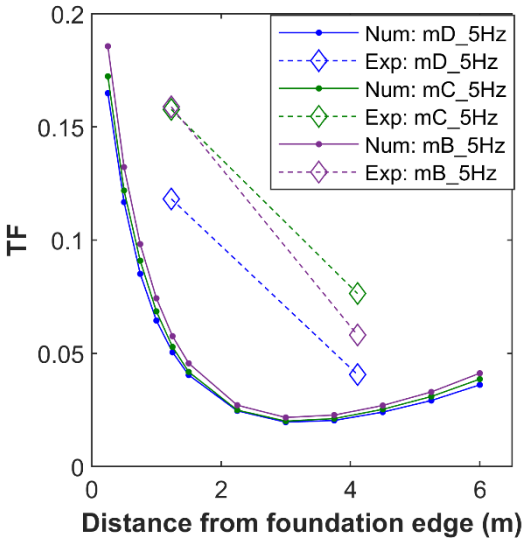
the FBr_2Ts simulations, the TFs computed by simulations of different excitation levels exhibit deviations (Figure 8.25a). These deviations were even more pronounced when interface nonlinearity became prominent, as observed in the FBr_1Ts simulations. This is evidenced by Figure 8.25b that illustrates that TFs inferred from the FBr_1Ts simulations were more affected by the level of excitation compared to the FBr_2Ts and PBr_W simulations.



(a) FBr_2Ts



(b) FBr_1Ts



(c) PBr_W

Figure 8.25: Impact of the vibrator force on the variation of soil to foundation motions transfer function with distance from the foundation edge. Data are inferred from simulations that imposed a 5Hz input excitation.

A better comparison between the soil motions produced by the FBr_2Ts, FBr_1Ts and PBr_W simulations is provided by Figure 8.26. This figure compares the soil motion dissipation with distance from the foundation edge, that was inferred from the above simulations assuming an excitation force of 5Hz frequency and magnitude according to the mD pair of vibrator's plates (Figure 5.12). The soil motions are evaluated as either maximum Fourier amplitudes of each soil motion (Figure 8.26a) or as soil to foundation motions TFs (Figure 8.26b). Figure 8.26a shows that the soil motion produced by

the PBr_W simulations was much weaker than the ones produced by the FBr_2Ts and FBr_1Ts simulations. However, the PBr_W simulations produced the largest TF values, demonstrating that, for equal foundation motions, the PBr_W simulations were able to transmit stronger motion to the soil than the FBr simulations. This is attributed to the higher level of nonlinearity and the stronger foundation rotation exhibited by the latter simulations. Foundation rotation produced by the FBr_1Ts simulations was the largest, and hence the foundation was able to transmit the smallest motion to the soil (i.e. smallest TFs).

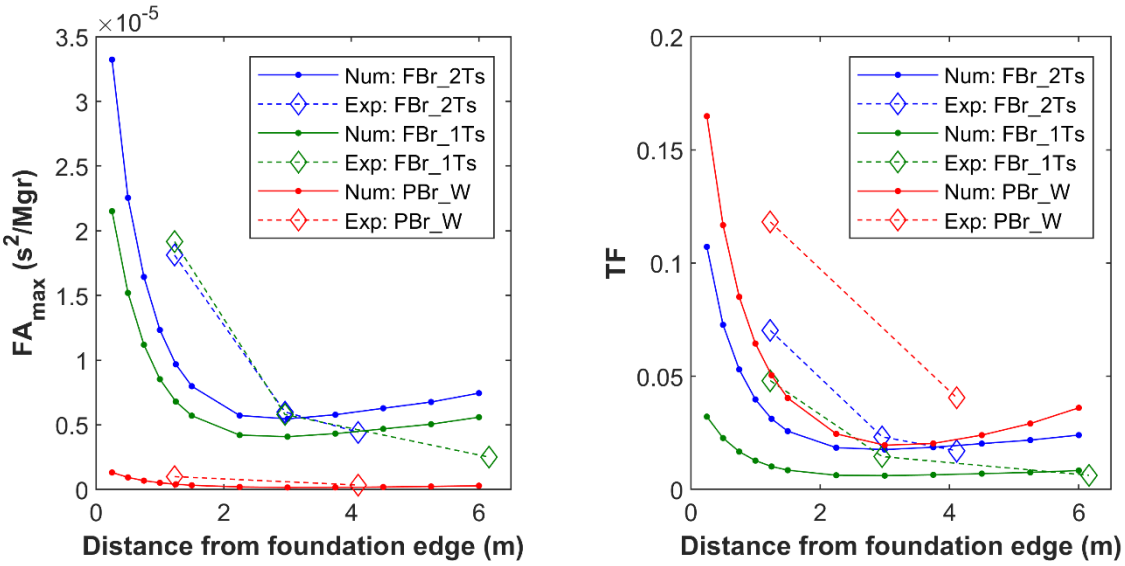


Figure 8.26: Comparison of soil motion attenuation between the FBr_2Ts, FBr_1Ts and PBr_W simulations. The soil motion is evaluated in terms of (a) maximum Fourier amplitudes and (b) soil to foundation motions transfer functions.

8.4 Summary

This chapter presented numerical results obtained from the model calibrated in Chapter 7. The results of both free and forced vibration simulations were compared to experimental data. The SSI system's natural frequency and its dependence on the magnitude of the excitation were sufficiently replicated by the models. The structural motion, including top slab and foundation motions, was also sufficiently reproduced, when the experimental structural motion perpendicular to the loading direction (out-of-plane motion) was weak. The numerical model, due to the adopted boundary conditions, could not produce structural motions that consist of swaying out-of-plane or torsional modes of oscillation. The incapability of the model to predict these oscillation modes can partly explain the difference between experimental and numerical soil motions, as soil motions are inherently associated with the foundation mode of oscillation. Despite this limitation associated with the adopted boundary conditions, qualitative findings were drawn from the presented predictive analyses.

Natural frequencies decreased with the magnitude of excitation force, as evidenced by both free and forced vibration data. The SSI natural frequencies were found to be much smaller than the fixed-base ones, with the exception of the PBr_W simulations. The period elongation mechanisms are soil compliance, interface gaps, soil and interface nonlinearities. For the free vibration tests, the impact of each mechanism was evaluated. The most important elongation mechanism was found to be the interface gaps, while soil compliance was similarly important. The impact of nonlinearities on period lengthening depended on the amplitude of the excitation force and the structural configuration. Stronger excitation led to stronger nonlinear phenomena and hence larger elongation. As interface nonlinearity increased, the elongation of the fundamental period became more pronounced. The most significant manifestation of interface nonlinearity, foundation detachment, was observed during the oscillation of the FBr_1Ts structural configuration, which exhibited the strongest period lengthening among all configurations analysed.

The same mechanisms (soil compliance, interface gaps, and nonlinearities) were also responsible for the variation of system's damping produced by models of different interface and soil conditions. It was shown that soil compliance can be a significant source of damping mechanism for stiff structures. Interface gaps and interface nonlinearity, though, decrease the damping that is produced by SSI systems, as they prohibit the transmission of energy to the half-space. Soil nonlinearity is an additional source of damping production, while it can become the dominant damping mechanism for strong excitations. Both soil and interface nonlinearities increased with the magnitude of the pull-out force, for the case of free vibration tests. However, forced vibration simulations showed that the level of nonlinearity was marginally affected by the level of excitation that was applied on the structure. Instead, it was significantly affected by the input frequency and the intensity of foundation motion, which was maximised at resonance. For this reason, the maximum soil nonlinearity and foundation detachment were observed at applied frequencies that coincided with the resonant ones, although the magnitude of input force was larger for larger applied frequencies.

The impact of soil nonlinearity on the overall response of the SSI system was shown to be controlled by the nonlinear behaviour of soil in the vicinity of the foundation. Within this area the most significant soil stiffness degradation and damping development took place, while these became much weaker at 1m distance or farther from the foundation edge. In the first meter from the foundation edge, the soil motion was found to be significantly dissipated, as a consequence of the observed strong soil nonlinearity.

Soil motion was also affected by the interface contact conditions and soil constitutive behaviour. The strongest soil motion was produced by models that assumed linear elastic soil and full contact conditions between the foundation and the soil beneath. Soil motion reduced when soil was

prescribed to behave nonlinearly, as damping development prohibits the development of strong soil motion. Soil motion was also found to be affected by interface gaps, which can either exist prior the application of the excitation load or are created as a consequence of foundation nonlinearity. Interface gaps promote two counteractive effects. Firstly, they increase the foundation motion which is expected to induce an amplified wavefield in the soil. Conversely, the existence of gaps decreases the contact interface allowing less energy to be transmitted from the structure to the soil. The latter consequence of interface gaps was prominent for the simulations of tests on the FBr_2Ts and FBr_1Ts structural configurations. Unlike these configurations, the PBr_W structure has, in relative terms, a very low structural stiffness compared with the stiffness of the soil-foundation system, when full bonding is assumed between the soil and foundation. This condition prevented the foundation to exhibit response and induce waves to the soil. The SSI response of this system was controlled by the deformability of the structure with minimal foundation motion. Interface gaps essentially reduced the stiffness of the soil-foundation system, allowing the foundation to participate in the motion, decreasing the flexural deformability of the PBr_W structure. The foundation motion increase outweighed the decrease of the interface contact area; hence, the overall impact of gaps formation increased the soil motion. It is therefore concluded that interface gaps can either increase or decrease the soil motion, depending on the relative stiffness between the structure and the soil-foundation system. It should be noted though, that the soil motion produced by the PBr_W simulations was very weak, as the SSI effects were weak. This makes the impact of interface gaps on the soil response insignificant, for the case of flexible SSI systems. It is safe to conclude that interface gaps decrease the soil motion at stiff systems, where the SSI effects are important.

According to the above conclusions, the existence of interface gaps can change the system's mode of oscillation, including the foundation mode of oscillation, relative to a system of which the foundation is fully bonded with the soil. The present study clearly establishes the dependency of the soil motion on the foundation motion amplitude and foundation mode of oscillation. As expected, soil motion amplitude increased with the intensity of the foundation motion. When, though, the soil motion was normalised by the foundation motion, which is considered the source of induced energy to the soil, the normalised motion was found to decrease with increasing excitation. This demonstrates that both soil and interface nonlinearities decreased the soil motion. Nonlinearities were the weakest for the PBr_W simulations, which produced the strongest normalised soil motion. The weakest normalised motion was produced by FBr_1Ts tests, during which the interface nonlinearity (foundation detachment) was the dominant nonlinear mechanism.

Soil and interface nonlinearities can also explain the difference in the soil response produced by identical simulations of different level of excitations. The analyses of stronger excitation produced

smaller normalised soil motions, which is a consequence of stronger nonlinearities. The soil motions produced by the FBr_1Ts simulations were shown to be the most sensitive to the intensity of excitation. This is also attributed to the high level of nonlinearities and especially the interface nonlinearity (foundation rocking). On the other hand, soil motions produced by PBr_W simulations were almost independent of the level of excitation, as nonlinearities were very weak.

The soil motion was also found to be associated with the foundation mode of oscillation, which, complying with the boundary conditions, could either be rotational or translational along the in-plane direction. In fact, the variation of soil motion normalised by the foundation motion was very similar to the ratio of horizontal to vertical foundation motions. Simulations with the highest ratio, indicating the greatest foundation translational motion, resulted in the most pronounced normalised soil motion. Similarly, the weakest normalised response was observed in simulations which produced the lowest foundation ratio, which indicates the strongest foundation rotation. This observation aligns with the ones made earlier that the existence of interface gaps decreases the soil motion and the system's damping. It is evident that the amount of energy transmitted to the soil from foundation oscillation is dependent on the mode of foundation oscillation. As inferred from both forced and free vibration simulations, the swaying mode of foundation transmits higher energy to the soil than the rotational mode. The latter conclusion agrees with Gazetas (1983), according to which foundation rotation produces less radiation damping than a corresponding swaying mode.

Chapter 9

Conclusions and Recommendations

9.1 Introduction

The aim of this research was to advance the current knowledge on Soil-Structure Interaction (SSI) effects and foundation rocking through a comprehensive investigation involving field experiments and three-dimensional (3D) numerical analyses. It provided insights into the impact of soil compliance, soil nonlinearity, interface nonlinearity and interface gaps on the response of a symmetric steel-frame structure that was founded on a surface foundation. The field experiments were carefully designed and carried out to promote the above aspects. They consisted of free and forced vibration tests with varying amplitudes and frequencies on the prototype structure of EUROPROTEAS, that features a removable cross-bracing system and adjustable superstructural mass.

The importance of SSI effects and foundation rocking was established in Chapter 2, which presented a literature review of these phenomena and the methods that are commonly used study the effects. This chapter also described the parameters that determine the importance of such phenomena, such as structural stiffness and mass. Chapter 3 presented a literature review of the existing real-scale experiments, demonstrating the benefits obtained from such tests, as well as the lack of experiments that focus on the behaviour of the soil-foundation interfaces. It also highlighted the very limited number studies that exploited real-scale experiments to calibrate numerical models, which are known to be a very rigorous way to study SSI effects.

Chapter 4 presented site response analyses that were carried out to investigate the local soil conditions at the site of the field SSI experiments. In Chapter 5, the SSI experiments were described in detail, with a thorough investigation of their reliability. The field data collected were comprehensively interpreted in Chapter 6, incorporating comparisons with findings sourced in the literature. Chapters 7 and 8 presented the numerical results of 3D analyses, showing good agreement with the field data.

The numerical study highlighted the importance of modelling both the soil constitutive behaviour and soil-foundation interface appropriately. It also proposed strategies to model the cyclic behaviour of soil and a novel approach to model interface gaps.

The results of both numerical and experimental studies were compared with each other as well as with findings from previous studies. This discussion includes the impact of structural stiffness and mass on the significance of SSI and foundation rocking effects, the relation between foundation mode of oscillation with radiation damping and the effects of nonlinear phenomena on the SSI response.

9.2 Free-field site response

Site response analyses, presented in Chapter 4, investigated the free-field seismic response of the soil stratigraphy at the EUROPROTEAS site. The analyses were conducted by employing both equivalent linear (EQL) and full nonlinear finite element (NLIN) approaches. The numerical models were calibrated against strong motion data recorded by a permanently installed downhole array of accelerometers during selected seismic events. The recorded earthquake events were of medium to weak intensities, hence, enabling the calibration of the model over the small strain range.

A procedure was proposed to back-calculate the shear wave velocity (V_s) profile of the site at very small strains. The procedure involved several iterations of EQL analyses. Each iteration simulated the bedrock at a different depth, starting from the shallowest and progressing to increasingly deeper depths. For each selected depth, recorded strong motion data were available, that were used as input motions at the base of the models. At the end of each step, the shear wave velocities of the modelled soil layers were calibrated. At the next step, the already calibrated layers were retained, while the V_s of newly added layers in the updated model are calibrated. The calibration procedure also involved calibration of the nonlinear behaviour of soil, including the stiffness degradation and damping ratio (G-γ-D) curves. While these curves were initially available from previous lab experiments, they required further refinement to reconcile the different conditions that existed between the lab and in-situ tests.

Following the model calibration, the calibrated V_s profile and cyclic nonlinear behaviour of soil layers were incorporated in the full nonlinear analyses. The results of EQL and NLIN analyses were very similar, verifying previous claims made in the literature that EQL method is applicable for small strain problems (e.g. Assimaki *et al.*, 2008; Kaklamanos *et al.*, 2015; Kim *et al.*, 2016; Foti *et al.*, 2019). Both types of analyses replicated the field data with sufficient veracity, validating the calibration of the model. While it may initially appear that relying on the back-calculation of the V_s profile to achieve agreement between numerical and field data could be seen as a potential limitation, the calibrated

model successfully replicated three additional independent events. This can be viewed as a verification of the model's capability, suggesting that it has the potential to accurately simulate events of similar intensity. Furthermore, it is worth noting that this limitation is partially mitigated by the fact that the back-calculated Vs profile closely aligns with profiles proposed by previous studies based on field tests.

EQL results were also used to investigate the impact of bedrock depth on the site response. It was observed that when the bedrock was set at depths shallower than the real bedrock depth, spurious peaks appeared in the acceleration response spectra of the surface motion. These peaks were found to be associated with the natural periods of the modelled soil column and hence were attributed to multiple reflections of waves on the surface and the rigid base. This observation justified the elimination of the spurious peaks when the bedrock was modelled at the real depth and the bedrock motion was used as input motion.

NLIN analyses and field data were used to identify the natural frequencies of the surface-to-bedrock soil column. This was achieved using transfer functions (TFs) that were computed as the ratio of the acceleration response spectrum of the surface motion to the spectrum of the bedrock motion. The study verified that certain natural periods corresponded to the first or higher modes of resonance of the surface-to-bedrock soil column. Also, it was shown that a natural period was associated with the resonance of the soil column from surface to 130m depth, which lies 70m above the bedrock. This observation aligns with previous studies (Baise and Glaser, 2000; Verdugo, 2002; Kokusho and Sato, 2008), that suggested that fundamental periods can be influenced by the resonance of soil layers above the bedrock.

9.3 Efficiency of the soil-structure interaction numerical model

The presented SSI numerical model simulated half of the geometry of the field experiments, exploiting the problem's inherent symmetry and neglecting geometric imperfections. This simplified assumption was deemed reasonable, as the model was calibrated against experiments where the primary motion occurred along the plane of load application (in-plane), while the motion perpendicular to that plane (out-of-plane) was weak. Special attention was given to calibrating soil's nonlinear behaviour and on the modelling of the soil-foundation interface. The calibration also involved adjusting of the parameters associated with the structural connections and structural damping. The model calibration benefitted from the several tests conducted on three different structural configurations, that were excited by various load amplitudes. The tests exhibited different levels of SSI effects, soil nonlinearity and foundation rotation, allowing the model calibration against various conditions.

A rigorous calibration procedure, that effectively exploits the advantages of the free and forced vibration tests, was proposed (see Section 7.8). Free vibration data were used to calibrate system's fundamental frequency and damping. Free vibration experiments that exhibited negligible SSI effects were used to calibrate the structural connections and damping, aiming to capture the natural frequency and motion amplitude of the assumed fixed-base system. The parameters of the adopted nonlinear soil constitutive model were calibrated against free vibration experiments of different excitation levels that exhibited strong SSI effects. These experiments induced strains in the soil within the very small and medium strain range, allowing the model calibration over this range. Finally, data from forced vibration experiments that exhibited strong foundation motions were used for the calibration of the interface model. As mentioned in Section 7.8.1, this type of test, particularly when prescribing experimentally output displacements at the top of the structure as the input excitation, can effectively isolate the impact of interface conditions, facilitating their calibration. The interface model was then refined against free vibration tests that mobilised the strongest foundation uplift, using the calibrated structural and soil properties.

It is acknowledged by the author that the choice to excite the structure by experimentally output displacements, for the case of forced vibration tests, is a potential limitation of the study. This is because the excitation itself is inherently influenced by the response of the SSI system. However, it is important to note that this approach was employed for calibration purposes in Chapter 7 only to facilitate the tuning of the interface conditions, while rigorous force-controlled analyses were later presented in Chapter 8. To mitigate the impact of the limitation of the calibration process, any conclusions drawn from displacement-controlled forced vibration analyses were verified through independent free vibration analyses and force-controlled forced vibration analyses.

The numerical results of the calibrated model show a very good agreement with the field data, when experiments with weak out-of-plane motions were simulated. The model reproduced well the natural frequency, motion amplitude, and their variations with the magnitude of excitation. It should be noted that while the structural motion was captured with high veracity, the soil motions were reproduced with lower accuracy due to potential experimental imperfections. Possible imperfection are the variable conditions around the soil instruments and the inherent sensitivity of the instruments themselves. Also, discrepancies can partly be attributed to the adopted boundary conditions. These restricted the out-of-plane motion of the structure and limited the radiation of waves within the half soil domain, rather than allowing for a spherical radiation pattern.

9.4 Soil constitutive model

The nonlinear soil behaviour was modelled using the Imperial College Generalised Small Strain Stiffness (IC.G3S) model (Taborda *et al.*, 2016). Such cyclic nonlinear models, which are typically used in numerical analysis to predict the hysteretic behaviour of soils, can simulate well either the stiffness degradation (G-γ) or the damping evolution (D-γ) with cyclic shear strain. When the calibration prioritises the G-γ curve, the damping is underestimated at low strains and highly overestimated at medium strains. Conversely, when the damping calibration is prioritised, the model underestimates the soil stiffness under cyclic conditions within the very small to small strain range. It also underestimates the stiffness under monotonic conditions for the entire small strain range. A parametric study was carried out to examine the impact of the calibration of the nonlinear model on the structural response when exhibiting different levels of motion intensity. The results below refer to SSI studies that developed very small to medium strains in the soil.

In SSI problems of low intensity motions that induce low soil levels of strains in the soil, the role of hysteretic damping is not significant, as it is considerably lower compared to the dominating radiation damping. Hence, in such problems, prioritising the model calibration against stiffness over damping would be preferred. However, this study showed that this approach can yield very unreliable results when medium strains develop in the soil, due to the crucial role of hysteretic damping for that strain range in the response. Specifically, it was found that if the calibration of stiffness is prioritised in medium strain problems, the motion will be strongly overdamped, as a result of damping overestimation at this strain range. Conversely, when the nonlinear model reproduces accurately the damping curve, the numerical results were found to be very reliable. The above observations imply that the calibration of the nonlinear model depends on the strain levels, and therefore not allowing a common calibration for all problems. Based on the findings of the present study, it is strongly suggested that the calibration should prioritise capturing the damping curve accurately. This approach allows for reliable predictions of the medium strain problems, while maintaining an acceptable accuracy for small strain problems. The stiffness underestimation, that results from this approach, can be compensated by prescribing an increased stiffness at very small strains (G_{max}). G_{max} should be a function of the mean effective stress (p') to enable an increased soil stiffness in the vicinity of the foundation, taking into account the influence of the structure's presence.

The imposition of a p' dependent G_{max} can mitigate the underestimation of the cyclic and monotonic stiffness degradation curves at small strains, but not the underestimation of the monotonic curve at larger strains. More specifically for the modelled experiments, during pull-out loading, which was applied monotonically, the strains induced in the soil beneath the foundation were up to 1%. For this

strain, the soil stiffness was significantly degraded leading in unreasonable large horizontal static displacements. These displacements were not recovered after the load removal. This behaviour was attributed to the notable difference between the monotonic and cyclic stiffness curves, which governed the loading and unloading behaviour, respectively. The significant difference of stiffness between the first loading and the subsequent unloading path resulted in an open stress-strain loop, which is manifested as structural unrecoverable displacements at the end of the oscillation.

The unrecoverable displacements were deemed unreasonably high, considering that they were not visually observed during the experiments, indicating their nonexistence These were found to be mitigated by imposing in the calibration of the G-γ-D curves a higher cut-off stiffness limit (G_{min}), beyond which shear stiffness does not degrade. The present study showed that a higher value of G_{min} can compensate the unreasonable strong degradation with increasing strains of the cyclic stiffness curve, that is predicted when the calibration prioritises the damping curve. Consequently, an appropriate value of G_{min} can result in smaller static horizontal displacements at the end of the pull-out loading, which can be recovered after unloading.

In addition to its influence on the stiffness curve, G_{min} also affects the damping curve. At the strain where G_{min} is mobilised, the damping curve begins to decline with increasing strains. While the imposition of a higher G_{min} value may initially appear as a limitation of the damping curve calibration, it did not significantly affect the presented numerical results. G_{min} was only mobilised during the monotonic loading, where damping does not exert, and at the first unloading cycle. Therefore, the study primarily benefitted only from the positive impact of using a higher G_{min} value. It should be noted that in larger strain problems, where G_{min} will be mobilised multiple times during the oscillation, the hysteretic damping will be underestimated and, hence, the motion will be overestimated. However, when G_{min} is mobilised, plasticity usually takes place and dominates the total material damping of soil, rendering the precise prediction of elastic hysteretic damping unnecessary.

9.5 Interface model

This study proposed an approach for modelling the soil-foundation interface aiming to:

(a) allow foundation detachment and sliding
(b) simulate initial interface gaps that can close and reopen during excitation or remained permanently opened
(c) manipulate the distribution of the static normal stresses at the interface between the soil and the foundation (e.g. uniform or parabolic distribution of interface stresses)

The calibration of the interface model involves considering several aspects, including:

(a) the constitutive behaviour of interface elements
(b) the modelling approach of gaps
(c) the initial gaps configuration
(d) the magnitude of initial gap
(e) the initial interface stresses under static conditions.

The proposed interface model incorporates zero thickness interface elements (Day and Potts, 1994), whose elastic deformations are controlled by the elastic normal (K_n) and shear (K_s) stiffness. Their plastic deformation, such as foundation uplift and sliding, is controlled by the plastic behaviour of the elements. In many of the presented analyses, the behaviour of the interface elements was associated with an elastoplastic Mohr-Coulomb failure surface, characterised by the angle of shearing resistance $\phi' = 30^{\mathrm{o}}$, cohesion $c' = 0$ and angle of dilation $\nu = 0^{\mathrm{o}}$. When the stress state reaches the yield surface, K_s switches to zero allowing sliding to occur, while K_n remains unchanged. On the other hand, if foundation rocking is prominent, the initially compressive interface normal stress will reduce in part of the foundation. When the normal stress of the interface elements exceeds the tensile strength, set as $c'/\tan\phi'$ (equal to zero in this case), those interface elements will open, allowing the foundation to rock and part of it to detach from the soil. As interface elements remain open, both shear and normal stiffness switch to zero, while the normal and shear stress remain at $c'/\tan\phi'$ and zero, respectively. At the same time, normal strains corresponding to the amount of interface opening are accumulated in the plastic hardening parameter, that represents the plastic part of normal strains (ε_{pl}) and the magnitude of the opened gap. When the loading conditions change in a way that forces the opening to reduce and eventually close, the plastic hardening parameter reduces and becomes zero upon full closure of the interface opening. At that stage, the normal and shear stress start to change again, and interface regains its elastic stiffness.

This study proposed a novel approach to model initial gaps at the soil-foundation interface prior to the application of the excitation, representing interface contact imperfections. The proposed approach initiates a gap by initiating the analysis with a non-zero value for the previously mentioned hardening parameter of the model. The approach consists of three main steps. In the first step, the non-contact areas and the magnitude of opening (*g*) are selected. The second step involves initiating gaps in the designated non-contact area for the analysis where only the static self-weight (StSW) is applied. At this stage, the gap magnitude is set larger than *g*, ensuring that the initially open gaps will not close due to the self-weight by the end of the StSW analysis. The target interface condition at the end of the StSW analysis is zero stresses at the interface elements that are intended to be initially open. In the final step of the process, in the analysis that follows the StSW analysis and where the excitation load is applied, the magnitude of the open integration points is re-defined to be equal to *g*.

The above approach achieves to initiate an analysis that intends to apply excitation loads on the structure with the desired interface stresses and gap magnitude. The gap magnitude, which is equivalent to ε_{pl}, is a parameter that was investigated. When a small ε_{pl} is assigned to a gap, the gap is able to close and re-open during the structural oscillation. In contrast, when the initial gap is of a larger magnitude, the gap remains open throughout the motion. In the case of permanently open gaps, the study showed that the gaps can also be simulated through low stiffness of elastic interface elements, which are more computationally efficient. In this study, the permanently open gaps were assigned to stiffness values of $K_s=K_n=1E2kN/m^2$, which are much lower than the stiffness of the initially close interface elements ($K_s=K_n=1E8kN/m^2$). For the case where an interface model intends to both simulate permanent gaps and allow for detachment and re-attachment successions of an interface area during the analysis, the present study proposed the use of a hybrid (HYBint) interface model. The HYBint uses low stiffness interface elements for the simulation of an interface area with permanent gaps and elastoplastic interface elements for the remaining interface area.

Additionally, the present study showed that foundation uplift can be dependent on the distribution of the effective normal stresses (σ'_n) that existed at the soil-foundation interface prior to the application of the excitation load. The σ'_n distribution can be manipulated by selecting appropriate values for K_s and K_n prior the application of self-weight (prior the StSW analysis). Large values of these properties essentially model a rigid foundation, resulting in accumulation of stresses below the foundation corners. On the contrary, lower interface stiffness can result to a more uniform static normal stress distribution. In the analyses conducted apart from the StSW analysis, K_n and K_s were assigned a very high value ($1E8kN/m^2$) to prohibit penetration of the foundation into the soil and restrict the development of large elastic shearing displacements, respectively. An exception to the above pertains to the interface stiffness of the permanently open interface elements, as already mentioned.

9.6 Practical applications of the proposed methods for interface modelling

In most real case projects, foundations are cast in-situ, providing good contact conditions and negligible gaps between the foundation and the soil. Nevertheless, the approach proposed by this study for the simulation of initial interface gaps can find application in practical problems where in-situ casting of foundations is not feasible and therefore interface gaps are likely to occur. One such problem is offshore foundation projects, where precast foundations are placed on inadequately prepared soil, necessitating the consideration of potential interface gaps during the design phase. Another potential application is the interaction between a railway track and the soil, where the

contact area between rail sleepers and subgrade constantly changes as trains pass. Additionally, during strong earthquake events, foundation motion can lead to the formation of interface gaps, which should be taken into account in analyses for future events. Similarly, the proposed procedure for manipulating the distribution of static normal stresses at the interface can find utility in projects where the stresses are anticipated for any reason to deviate from the norm.

9.7 Importance of soil-structure interaction effects and foundation rocking

Both experimental and numerical data were utilised to investigate the effects arising from soil-structure interaction and foundation rocking, commonly known as soil-foundation-structure (SFSI) effects. The primary focus was on examining the influence of these effects on period lengthening and damping increase observed in an SSI system, in relation with the equivalent fixed-base system. The effects were investigated on three different structural configurations with different structural stiffness and/or mass. These configurations are the fully braced configuration with two top slabs (FBr_2Ts), the fully braced with one top slab (FBr_1Ts) and the partly braced configuration with two top slabs (PBr).

In accordance with previous studies (e.g. Veletsos and Nair, 1975; Amorosi *et al.*, 2017), experimental and numerical investigations presented in this study have verified that the stiffer structure (FBr_2Ts) exhibited stronger SSI effects than the more flexible structure (PBr). For the same reason, the lighter structure (FBr_1Ts), which has the highest fixed-base frequency, exhibited stronger period lengthening than the identical but heavier structure (FBr_2Ts). The larger period lengthening of the lighter structure can also be attributed to larger developed foundation rocking. This was a consequence of the larger structural displacements, that are reasonably developed on the lighter structure for the case where the excitation force was applied on the structure (rather than at the bottom of the soil domain).

However, numerical results have demonstrated that structural mass exhibits different impact on the period lengthening and damping development. The relation between mass and damping depends on the interface conditions, such as the level of foundation rocking and uplift. The foundation motion and therefore the above relation depend on the magnitude of excitation force, while in numerical terms, they also depend on the adopted interface conditions, specifically whether gaps are modelled or not. Outcomes from the investigation with respect the interface conditions are summarised subsequently in Section 9.10.

For the flexible structure, i.e. the partly braced configuration, the foundation motion was very weak, while the overall structural response was predominantly governed by the structural bending deformation. The opposite observations were made for the structures that exhibited strong foundation rocking, such as the fully braced configurations. Experimental and numerical results have shown that the response of these structures was dominated by the rocking motion of the foundation, while its bending deformation was marginal. This observation aligns with previous numerical studies (e.g. Tabatabaiefar *et al.*, 2014; Gazetas, 2015; Zhang and Far, 2022a), which highlighted the dominance of foundation rocking in the response of slender structures specifically designed to facilitate this type of motion.

The significance of the SSI effects and foundation rocking varied with excitation levels, providing insights about the nonlinear behaviour of the SSI systems, including soil and interface nonlinearities.

9.8 Field evidence of nonlinear response

Experimental data showed that the structural response varied with the magnitude of the excitation force, due to nonlinearities. Specifically, both the observed natural frequencies and the magnitude of the excitation normalised by the applied forced decreased with increasing force. Notably, there was a 20% discrepancy observed in the frequencies of the swaying mode, inferred from the motions of the lowest and highest intensity. However, for the torsional resonant frequencies, a significantly lower deviation of only 5% was observed for the examined SSI system. This observation aligns with the conclusions of Pitilakis *et al.* (2014), who also demonstrated that SSI effects had a more pronounced influence on the swaying modes of the same SSI system than the torsional mode. Similarly, the damping of the system, computed using the free vibration data, was found to increase with the increase of excitation force, which is a consequence of stronger soil hysteretic damping.

Both natural frequencies and damping ratios of an SSI system, were found to vary with time during the free vibration response of the structure. The natural frequencies were the smallest and damping the largest at the initial cycles of the motion, while the former increased and the latter decreased for the subsequent cycles. When the motion is strongly dissipated, the natural frequency and damping ratio converged to the values that correspond to the ones of a linear elastic system. The above observation provides qualitative evidence that nonlinearity was more pronounced in the first cycles of the motion, due to stronger structural excitation.

9.9 Soil nonlinearity

Soil nonlinearity effects are associated with soil stiffness degradation and damping development with increasing strains. The former effect leads to a more flexible system, while the latter one increases system's damping for stronger structural oscillation, due to larger strains induced in the soil. These justify the observed smaller natural frequencies and normalised motion amplitudes exhibited by the SSI system that was subjected to stronger excitation.

It was indirectly inferred from field data and numerically verified that the highly nonlinear behaviour of the soil in the vicinity of the foundation dominated the total soil nonlinearity developed. The numerical results showed that, the stiffness degradation and damping ratio values developed in the soil below the foundation edge were found to be significant when the foundation motion was strong, due the accumulation of strains. These effects became much weaker at 1m lateral distance from the foundation edge, where soil motion was found to be strongly dissipated. The numerical investigation, also, demonstrated that a careful calibration of the uppermost 0.80m of soil was crucial for the estimation of the structural response. On the other hand, an assumption of linear elastic behaviour for the deeper soil layers was found to be sufficient, for the examined problems. It will not be sufficient though for problems where the input motion is applied as a seismic load at the bottom boundary of the soil domain, or where high strains are induced in the soil.

The above observations highlight the crucial role of this specific soil area in the response of a shallow or surface founded SSI system. This aligns with similar observations made by the lab study of Gazetas and Stokoe (1991) and the field study of Tileylioglu *et al.* (2011), who demonstrated the important role of the soil in this area for the estimation of both natural frequency and damping of an SSI system. Finally, the observed important role of the soil near the foundation underlined the necessity of incorporating an appropriate and well calibrated soil constitutive model for this soil area in the numerical studies.

9.10 Interface nonlinearity and gaps

Gaps at the interface between the foundation and the soil beneath were visually observed on site during the field experiments, and numerical analyses indicated the need to include them in the model. These gaps could either be permanently open or exhibit successive openings and closures. When only permanently open gaps were present during an analysis, the interface behaviour was linear. However, when successive detachments and reattachments of the surface foundation from the soil occurred, interface geometric nonlinearity arose.

The presence of interface gaps decreases the contact area between the foundation and adjacent soil. The expected consequence of this, as it was also verified by numerical analyses, is to make the SSI system more flexible. Interface gaps can change the system's mode of oscillation, promoting foundation rocking and decreasing the structural bending deformation. Gaps can also decrease the motion that is transferred from the structure to the soil, in relation to an SSI system that consists of foundation that is in full bond with the soil. From experimental and numerical investigations presented herein, this was manifested as smaller recorded soil motions and weaker radiation damping, which in-return decreased the damping of the overall SSI system. Gaps promoted the foundation's rotational mode of oscillation, which transmits lower motion to the soil than the translational mode (Gazetas, 1983, 1991), explaining the damping decrease. The impact of gaps is more pronounced when these are formed below the foundation edges, while it is negligible when gaps are formed below an inner area of the foundation.

Free vibration analyses showed that the presence of gaps significantly impacted the response of the stiffer structures, FBr_2Ts and FBr_1Ts, in the way described above. The response of these structures was dominated by the rocking foundation component, which was intensified by the existence of gaps. On the contrary, the response of the flexible structure examined, the PBr structure, was negligibly affected by the presence of gaps. This structure has a fixed-base natural frequency much lower than the one of the foundation-soil system, therefore, the response was dominated by the structural bending deformation with low contribution of the foundation motion. The incorporation of gaps decreased the difference between the above natural frequencies, slightly increasing the foundation response. This increased the radiation damping and hence the damping of the SSI system with interface gaps, in relation with the system without gaps. However, the damping increase was almost negligible and should not be interpreted as evidence that gaps can significantly increase the damping of an SSI system. Gaps essentially have negligible impact on systems that exhibit very weak SSI phenomena.

Experimental and numerical evidence, also, showed that the interface gaps influenced more the response of the lighter structure, FBr_1Ts, than the heavier structure with identical bracing system (FBr_2Ts). Experimental data have shown that the FBr_1Ts structure experienced longer period elongation than the FBr_2Ts one. However, period elongation was not accompanied by the larger damping, as it would have happened if the elongation was provoked by the stronger SSI effects due to soil compliance or by stronger soil nonlinearity. Therefore, it was concluded that stronger interface nonlinearity, in gap areas, took place during the experiments on the lighter structure. Numerical analyses have shown that permanent gaps affect in the same way the period elongation and damping of the FBr_1Ts and FBr_2Ts SSI systems, provided that interface nonlinearity was not allowed to take

place (i.e. elastic interface elements). However, when interface nonlinearity was allowed (i.e. use of elastoplastic interface elements), the lighter structure exhibited stronger period elongation and lower damping levels than the heavier one, due to stronger foundation rocking.

Unlike the simulation of the FBr_2Ts experiments, the simulation of the FBr_1Ts experiments required an interface model capable of incorporating interface nonlinearity. Such an interface model allows successions detachment and re-attachment of different foundation areas. It was found that the use of elastoplastic interface elements did not exhibit the ability to open any elements at any point during the analysis, unless the normal stress distribution resulting from static self-weight loads was adjusted. The interface stress distribution that corresponds to a rigid foundation, that is commonly predicted by FE software, leads to concertation of stresses at the corners of the interface contact area. These stresses were too high and could not be reduced to zero during the dynamic analysis, thereby preventing the initially close interface elements from opening.

For the reasons explained in Section 7.14, the distribution of the interface static normal stresses can be reasonable assumed as almost uniform. The investigation conducted within the calibration of the stress distribution illustrated the significant impact of the stress distribution on the SSI response of the lighter structure. The present study demonstrated that a smoother distribution facilitates the opening of initially closed interface elements, increasing the gap area and hence accentuating the gapping effects. The influence of the static stress distribution on the response becomes more prominent as the excitation magnitude increases, due to the increase of interface nonlinearity. Also, the impact is more noticeable on structures that tend to rotate around the foundation level, as observed in the case of the FBr_1Ts structure.

Lastly, this study explores the influence of gap magnitude when the gaps are defined using the corresponding hardening parameter of the plasticity model. The results revealed that even a very small initial opening can trigger subsequent opening and closure of interface elements and exhibit strong gapping effects on the response. This is associated with the zero normal stresses that exist below the initial gap areas prior to the excitation. While the stresses increase when a gap closes during an excitation, they remain sufficiently small to permit reopening. The numerical results from free vibration analyses revealed that the initially open interface elements exhibited succession of closure and re-opening for one to three cycles before they remained permanently open. It was observed that during the initial cycles of motion, the contact interface area was larger compared to subsequent cycles. Consequently, the SSI system responded to a higher frequency at the initial cycles than the following ones. At the time when the interface elements became permanently open, the interface behaviour became linear, while the nonlinearity of the response was controlled by the soil

nonlinearity. At this time, the natural frequency of oscillation started increasing with time, due to weakening of soil nonlinearity.

9.11 Period lengthening and damping development mechanisms

The study investigated various mechanisms contributing to period elongation of the examined SSI systems, including soil compliance, interface gaps, and soil and interface nonlinearities. The impact of each mechanism was evaluated through numerical simulations of free vibration tests. The results indicated that the most important elongation mechanism was the presence of interface gaps, followed by soil compliance. The effect of nonlinearities on period elongation increased for higher amplitudes of the excitation force. For low amplitudes, nonlinearities had a marginal effect on period elongation, while the effect was significant for higher amplitudes. Specifically, when the largest examined force was applied on the FBr_1Ts structure, the combination of soil and interface nonlinearities exhibited the highest degree of period elongation. As explained earlier, this can be attributed to the dominant effects of strong interface nonlinearity, which surpassed the effects of soil nonlinearity in the specific structural configuration.

The same mechanisms (soil compliance, interface gaps, and nonlinearities) also contributed to the variation of system's damping produced by models of different interface and soil conditions. It was observed that soil compliance can be a significant source of damping in stiff structures. Soil nonlinearity can also contribute to the damping development, while it can become the most pronounced source of damping when the foundation motion is prominent. On the other hand, for the same structures, interface gaps and interface nonlinearity decreased the overall damping of the SSI system by limiting the energy transmission to the half-space.

The increase of damping due to soil nonlinearity was more pronounced for larger pull-out forces, for the case of free vibration simulations. However, in forced vibration simulations, the level of nonlinearity and hence the associated damping were minimally affected by the excitation magnitude. Instead, they were predominantly influenced by the input frequency and the intensity of foundation motion, which reached its maximum at resonance. As a result, the highest levels of nonlinearity and its associate effects on damping were observed at frequencies that coincided with the resonant ones, even though the magnitude of the input force was larger for higher frequencies.

9.12 Soil motion

The soil motion was found to be associated with the foundation motion intensity and mode of oscillation. The numerical results indicated that when the rotational motion of the foundation was

prominent, the soil motion was weaker compared to cases where the translational foundation motion was more pronounced. This evidence aligns with findings of previous studies suggesting that the rotational foundation motion transmits less energy to the soil domain than the rotational one (Gazetas, 1983, 1991). It also agrees with the conclusion made earlier that interface gaps due to rocking can decrease the energy that is radiated to the soil domain.

Numerical results quantified the impact of the soil behaviour and interface conditions on the predicted soil motions. As expected, the strongest soil motion was predicted by linear elastic numerical analyses without interface gaps. Weaker soil motion was predicted when the soil was prescribed to behave in a nonlinear manner, due to the motion dissipation through hysteretic damping. Interface gaps and interface nonlinearity impact the soil motion with two counteractive effects. Firstly, they increase the motion of the foundation, leading to an expected amplification of the wavefield in the soil. On the other hand, they decrease the contact interface, resulting in a reduced transmission of energy from the structure to the soil. The latter impact of interface gaps was particularly prominent for the simulations of experiments on the fully braced structures, due to the rocking dominant mode of oscillation of these SSI systems. Unlike the fully braced ones, the partly braced structure has a fixed-base fundamental frequency much lower than the one of the soil-foundation system, when the foundation is assumed to be in full adherence with the soil below. This condition prevented the foundation to participate in the oscillation and induce waves to the soil. In this case, foundation gaps reduced the fundamental frequency of the soil-foundation system, which increased slightly foundation motion and allowed for more energy to be transmitted to the soil in relation to when interface gaps are not simulated. The effects of foundation motion increase on the soil motion outweighed the effects of the interface contact area decrease; hence, the overall impact of gaps formation increased the soil motion.

From the above discussion, the presence of interface gaps can either increase or decrease the soil motion. This depends on the relative difference between the fundamental frequency of the fixed-base structure with fundamental frequency of the soil-foundation system. It is important to note, however, due to the weak presence of SSI effects in the partly braced simulations, the predicted soil motion was very weak and the impact of gaps insignificant. Therefore, it is safe to conclude that interface gaps decrease the soil motion when the SSI effects are important, such as the case of a structure with high fixed-base fundamental frequency.

Soil and interface nonlinearities, which impacted the structural motion as described earlier, were also evidenced in both the experimental and numerical soil motions. As expected, the comparison of soil motions produced by experiments and analyses of different excitations revealed that the higher motion intensity resulted in higher soil motion. However, when normalising the soil motion by the

foundation motion to allow a comparison of motions that were produced by the same "input", it was observed that the experiments and analyses with stronger excitation exhibited weaker normalised soil motion. This is a consequence of stronger nonlinearities. The soil motions of the system with the lighter structure, FBr_1Ts, exhibited the highest sensitivity to the intensity of the excitation. This sensitivity can be attributed to the presence of significant nonlinearities, particularly the interface nonlinearity associated with foundation rocking, as explained earlier. In contrast, the soil motions resulting from the simulations on the more flexible structure, PBr, showed minimal dependence on the level of excitation, indicating weak nonlinearities.

Finally, this study investigated the variation of soil motion at different distance from the foundation, by comparing soil velocities computed or recorded at the ground surface. It was shown that the soil motion on the ground surface decayed exponentially with distance from the foundation edge. This observation complies with the outcome of Meek and Wolf (1993), who have shown that the energy of waves propagating in the 3D domain radiates proportionally to the square of distance from the source. In terms of absolute velocity units, radiation damping was more pronounced on experiments that transmitted more energy to the soil medium. This can be explained, firstly, by the larger energy loss due to radiation damping, and secondly, by the stronger hysteresis damping of soil due to nonlinearity. More energy is transmitted to the soil when the SSI effects and foundation motion were prominent during an experiment. For this reason, when the structure was fully braced, the motion decay with distance was more pronounced on the free vibration tests of larger pull-out force and forced vibration tests with an input frequency close to the resonant one.

9.13 Recommendations for future research

The recommendations for future research are divided into two parts. The first part proposes instrumentation and practices that, in the author's opinion, can advance the understanding of foundation rocking. The second part provides recommendations for numerical studies that aim to enhance the outcomes of the present study and further develop the proposed interface model. Essentially, some of the recommendations aim to tackle some of the limitations of the present study.

For future field experiments that will aim to study the dynamic SSI response and foundation rocking the following recommendations are made:

- Ensuring that the stiffness of structural connections is a known parameter. To facilitate numerical modelling, it is recommended to design the connections that are intended to carry moment in a way that allows them to be treated as rigid. This choice can also facilitate more reliable predictions of the fixed-base natural frequency of the system.

- Comparison can be made between experiments that use either a prefabricated foundation or an in-situ casted foundation.
- For the case of prefabricated foundations, it is recommended to document the deformed shape of the bottom of the foundation, with emphasis on capturing its vertical deflection.
- It would be interesting to examine the SSI response and foundation rocking performance of structures that are founded on prefabricated rigid foundations with varied shapes of their bottom side. The bottom shape depends on the casting process, such as the compliance of the formwork, and it can be either flat or parabolic of different levels of vertical deflections. This investigation can validate the claim made in the present thesis, that the deformed shape of the foundation can affect the foundation rocking in a significant way. To enhance the reliability of this potential future study, the investigation should focus on structural systems whose response is rocking dominated, such as a light structure that is subjected to lateral loading.
- It is strongly recommended for future field experiments to incorporate appropriate instrumentation (e.g. pressure cells) to allow monitoring of the stresses at the soil foundation interface. This can validate the numerical outcomes of the present study about the significant impact of the normal stress distribution of the interface on the rocking response of structures. It is advisable to use the same type of structure as mentioned in the previous suggestion for this investigation.
- Similarly, it would be extremely insightful, yet challenging, to monitor the interface contact conditions during the experiments. This can firstly provide an additional criterion for calibrating the numerical model. Also, it will provide quantitative measures of the soil-foundation system and its nonlinear variation with excitation loads.
- Future experiments that provide displacement data can be valuable for validating numerical models. Also, in the case of forced vibration tests, they can investigate the validity of the method proposed by the present study for extracting displacements from acceleration strong motion data.
- The above investigations refer primarily on rocking dominated systems. It is suggested to investigate experimentally the impact of SSI phenomena on systems whose response is strongly affected by foundation translation (e.g. short squatty structures).
- For future field tests, it is suggested to ensure that that both the monotonic and cyclic stiffness degradation and damping ratio curves are available for the soil layers in the vicinity of the foundation.

- For future field tests, it is suggested to ensure the availability of data to infer the stiffness of the superficial soil layer at very small strains, without and with the impact of the structural weight. This will enable the calibration of the parameters that constitute the relation between the mean effective stress with soil stiffness at this strain range.
- Finally, the experimental investigation of foundation embedment is also suggested.

Regarding future numerical studies on SSI related problems the following recommendations are made:

- Large strain analyses using the presented calibrated numerical model are suggested to be conducted. Such analyses can extend the model calibration for larger strains and investigate the use of plasticity models.
- Investigate the applicability of the proposed methods, such as the proposed interface model and the strategy for calibrating the cyclic nonlinear constitutive model for the soil, on larger strain problems.
- Large strain analyses will also enable the investigation of the interaction between foundation rocking and soil plasticity.
- For large strain numerical analyses, the adopted plasticity model for the soil should account for the hydromechanical behaviour of soil. Such analyses can be valuable in investigating the interaction of foundation rocking with excess pore water pressure generation.
- Using the calibrated model, parametric linear elastic analyses can be carried out to investigate the impact of the water table depth on the linear SSI response. Such analyses isolate the impact of the reflection of the compressional downward propagated waves on the water table back to the structure.
- The presented numerical models were verified against a rocking dominated system. The applicability of the interface model is recommended to be investigated for foundations of sliding-dominated SSI problems. If necessary, the shear strength constitutive behaviour of the interface should be calibrated.
- The performance of the proposed interface model is suggested to be examined for structures with more complex geometries, which may result to a significant torsional motion component.
- Using the proposed calibrated model with elastoplastic interface elements, the performance of embedded foundations can be evaluated. It is suggested that the same interface model is used both at the bottom and the side boundaries of the foundation.

- Using the calibrated model, the response of the SSI system under seismic motions can be investigated. Such analyses can provide insights about kinematic interaction effects on the examined structure, which were not of consideration of the present study. Note that seismic analyses will require a larger soil domain and nonlinear soil for the entire soil domain, which will significantly increase the computational time.
- Finally, using as benchmark the experimental data and the results from the calibrated numerical model, it is recommended to examine the extend of the applicability of the simplified methods that are used in the literature.

References

Abate, G., Gatto, M., Massimino, M.R. and Pitilakis, D. (2017) 'Large scale soil-foundation-structure model in Greece: Dynamic tests vs FEM simulation', in Proceedings of the 6th International Conference on Computational Methods in Structural Dynamics and Earthquake Engineering (COMPDYN 2015), pp. 1347–1359. Available at: https://doi.org/10.7712/120117.5497.16830.

Agalianos, A., Korre, E., Abdoun, T. and Anastasopoulos, I. (2023) 'Surface foundation subjected to strike-slip faulting on dense sand: centrifuge testing versus numerical analysis', Geotechnique, 73(2), pp. 165–182. Available at: https://doi.org/10.1680/jgeot.21.00083.

Amendola, C., de Silva, F., Vratsikidis, A., Pitilakis, D., Anastasiadis, A. and Silvestri, F. (2021) 'Foundation impedance functions from full-scale soil-structure interaction tests', Soil Dynamics and Earthquake Engineering, 141(August 2020). Available at: https://doi.org/10.1016/j.soildyn.2020.106523.

Amorosi, A., Boldini, D. and Lernia, A. (2016) 'Seismic ground response at Lotung: Hysteretic elasto-plastic-based 3D analyses', Soil Dynamics and Earthquake Engineering, 85, pp. 44–61. Available at: https://doi.org/10.1016/j.soildyn.2016.03.001.

Amorosi, A., Boldini, D. and di Lernia, A. (2017) 'Dynamic soil-structure interaction: A three-dimensional numerical approach and its application to the Lotung case study', Computers and Geotechnics, 90, pp. 34–54. Available at: https://doi.org/10.1016/j.compgeo.2017.05.016.

Amorosi, A., Boldini, D. and di Lernia, A. (2018) 'Dynamic soil-structure interaction: A three-dimensional numerical approach and its application to the Lotung case study', Computers and Geotechnics, 90(February), pp. 34–54. Available at: https://doi.org/10.1016/j.compgeo.2017.05.016.

Anastasopoulos, I., Gazetas, G., Loli, M., Apostolou, M. and Gerolymos, N. (2010) 'Soil failure can be used for seismic protection of structures', Bulletin of Earthquake Engineering, 8(2), pp. 309–326. Available at: https://doi.org/10.1007/s10518-009-9145-2.

Anastasopoulos, I., Gelagoti, F., Kourkoulis, R. and Gazetas, G. (2011) 'Simplified Constitutive Model for Simulation of Cyclic Response of Shallow Foundations: Validation against Laboratory Tests', Journal of Geotechnical and Geoenvironmental Engineering, 137(12), pp. 1154–1168. Available

at: https://doi.org/10.1061/(asce)gt.1943-5606.0000534.

Anastasopoulos, I. and Kontoroupi, T. (2014) 'Simplified approximate method for analysis of rocking systems accounting for soil inelasticity and foundation uplifting', Soil Dynamics and Earthquake Engineering, 56, pp. 28–43. Available at: https://doi.org/10.1016/j.soildyn.2013.10.001.

Anastasopoulos, I., Loli, M., Georgarakos, T. and Drosos, V. (2013) 'Shaking table testing of rocking-isolated bridge pier on sand', Journal of Earthquake Engineering, 17(1), pp. 1–32. Available at: https://doi.org/10.1080/13632469.2012.705225.

Anthi, M. (2021) Site response analysis for instrumented downhole seismic arrays. Imperial College London.

Assimaki, D., Li, W., Steidl, J. and Schmedes, J. (2008) 'Quantifying nonlinearity susceptibility via site-response modeling uncertainty at three sites in the Los Angeles basin', Bulletin of the Seismological Society of America, 98(5), pp. 2364–2390. Available at: https://doi.org/10.1785/0120080031.

Baise, L.G. (2000) PhD thesis: Investigations in Site Response from Ground Motion Observations in Vertical Arrays. University of California, Berkeley.

Baise, L.G. and Glaser, S.D. (2000) 'Consistency of ground-motion estimates made using system identification', Bulletin of the Seismological Society of America, 90(4), pp. 993–1009. Available at: https://doi.org/10.1785/0119980169.

Baise, L.G., Glaser, S.D. and Sugano, T. (2001) 'Consistency of dynamic site response at Port Island', Earthquake Engineering and Structural Dynamics, 30(6), pp. 803–818. Available at: https://doi.org/10.1002/eqe.38.

Barros, F.C.P. De and Luco, J.E. (1995) 'Hualien containment model', Soil Dynamics and Earthquake Engineering, 14(94), pp. 229–248.

Benz, T. (2007) Small-Strain Stiffness of Soils and its Numerical Consequences, Ph.D. Thesis. University of Stuttgart.

Bielak, J., Loukakis, K., Hisada, Y. and Yoshimura, C. (2003) 'Domain reduction method for three-dimensional earthquake modeling in localized regions, part I: Theory', Bulletin of the Seismological Society of America, 93(2), pp. 817–824. Available at: https://doi.org/10.1785/0120010251.

Bode, C., Hirschauer, R. and Savidis, S.A. (2002) 'Soil-structure interaction in the time domain using halfspace Green's functions', Soil Dynamics and Earthquake Engineering, 22(4), pp. 283–295.

Available at: https://doi.org/10.1016/S0267-7261(02)00020-9.

Boore, D.M. and Bommer, J.J. (2005) 'Processing of strong-motion accelerograms: Needs, options and consequences', Soil Dynamics and Earthquake Engineering, 25(2), pp. 93–115. Available at: https://doi.org/10.1016/j.soildyn.2004.10.007.

Borja, B.R.I. and Amies, A.P. (1994) 'MULTIAXIAL CYCLIC PLASTICITY MODEL FOR CLAY', Journal of Geotechnical Engineering, 120(6), pp. 1051–1070.

Borja, B.R.I., Chao, H., Montans, F.J. and Lin, C.-H. (1999a) 'NONLINEAR GROUND RESPONSE AT LOTUNG LSST SITE', JOURNAL OF GEOTECHNICAL AND GEOENVIRONMENTAL ENGINEERING, 125(3), pp. 187–197.

Borja, B.R.I., Chao, H., Montans, F.J. and Lin, C.-H. (1999b) 'SSI EFFECTS ON GROUND MOTION AT LOTUNG LSST SITE', JOURNAL OF GEOTECHNICAL AND GEOENVIRONMENTAL ENGINEERING, 125(9), pp. 760–770.

British Standards Institution (2004a) BS EN 1992-1-1:2004. Eurocode 2. Design of concrete structures. General rules and rules for buildings.

British Standards Institution (2004b) BS EN 1997-1:2004, Eurocode 7: Geotechnical design.

British Standards Institution (2004c) BS EN 1998-1:2004, Eurocode 8: Design of structures for earthquake resistance.

British Standards Institution (2005) BS EN 1993-1-1:2005, Eurocode 3. Design of steel structures. General rules and rules for buildings.

Butterfield, R. and Gottardi, G. (1994) 'A complete three-dimensional failure envelope for shallow footings on sand', Geotechnique, 44(1), pp. 181–184. Available at: https://doi.org/10.1680/geot.1994.44.1.181.

Cadet, H., Bard, P.Y., Duval, A.M. and Bertrand, E. (2012) 'Site effect assessment using KiK-net data: Part 2-site amplification prediction equation based on f0 and Vsz', Bulletin of Earthquake Engineering, 10(2), pp. 451–489. Available at: https://doi.org/10.1007/s10518-011-9298-7.

Cadet, H., Bard, P.Y. and Rodriguez-Marek, A. (2012) 'Site effect assessment using KiK-net data: Part 1. A simple correction procedure for surface/downhole spectral ratios', Bulletin of Earthquake Engineering, 10(2), pp. 421–448. Available at: https://doi.org/10.1007/s10518-011-9283-1.

Chao, H.Y. (1996) NONLINEAR DYNAMIC SOIL-STRUCTURE INTERACTION ANALYSIS AND APPLICATION TO LOTUNG PROBLEM, Arbor Ciencia Pensamiento Y Cultura. Available at: https://doi.org/10.16953/deusbed.74839.

Chávez-García, F.J. and Faccioli, E. (2000) 'Complex site effects and building codes: Making the leap', Journal of Seismology, 4(1), pp. 23–40. Available at: https://doi.org/10.1023/A:1009830201929.

Chávez-García, F.J., Manakou, M. V., Hollender, F. and Raptakis, D.G. (2017) 'Site effects using methods based on lateral homogeneity and laterally heterogeneous media: An impossible marriage?', Bulletin of Earthquake Engineering, pp. 1–28. Available at: https://doi.org/10.1007/s10518-017-0296-2.

Chávez-García, F.J., Raptakis, D., Makra, K. and Pitilakis, K. (1998) 'Site effects at Euroseistest-II. Results from 2D numerical modeling and comparison with observations', Soil Dynamics and Earthquake Engineering, 19(1), pp. 23–39. Available at: https://doi.org/10.1016/S0267-7261(99)00026-3.

Chopra, A. (2011) Dynamic of Structures Chopra, Pearson Education India.

Chung, J. and Hulbert, G.M. (1993) 'A time integration algorithm for structural dynamics with improved numerical dissipation: The generalized-α method', Journal of Applied Mechanics, 60, pp. 371–375. Available at: https://doi.org/10.1115/1.2900803.

Darendeli, M.B. (2001) Development of a new family of normalized modulus reduction and material damping curves. The University of Texas at Austin.

Day, R.A. and Potts, D.M. (1994) 'Zero thickness interface elements—numerical stability and application', International Journal for Numerical and Analytical Methods in Geomechanics, 18(10), pp. 689–708. Available at: https://doi.org/10.1002/nag.1610181003.

Day, S.M. (1977) Finite Element Analysis of Seismic Scattering Problems. University of California, San Diego.

Desai, C.S., Zaman, M.M., Lightner, J.G. and Siriwardane, H.J. (1984) 'THIN-LAYER ELEMENT FOR INTERFACES AND JOINTS', International Journal for Numerical and Analytical Methods in Geomechanics, 8, pp. 19–43.

Dikmen, S.U., Pinar, A. and Edincliler, A. (2016) 'Near-surface attenuation using traffic-induced seismic noise at a downhole array', Journal of Seismology, 20(1), pp. 375–384. Available at: https://doi.org/10.1007/s10950-015-9533-9.

Drosos, V., Georgarakos, T., Loli, M., Anastasopoulos, I., Zarzouras, O. and Gazetas, G. (2012) 'Soil-Foundation-Structure Interaction with Mobilization of Bearing Capacity: Experimental Study on Sand', Journal of Geotechnical and Geoenvironmental Engineering, 138(11), pp. 1369–1386. Available at: https://doi.org/10.1061/(asce)gt.1943-5606.0000705.

EAK2000 (2000) Greek Aseismic Code.

EKOS000 (2000) Greek Code for Reinforced Concrete.

Elgamal, A., Lai, T., Yang, Z. and He, L. (2001) 'Dynamics Soil Properties, Seismic Downhole Arrays and Applications in Practice', Proceedings of the 4th International Conference on Recent Advances in Geotechnical Earthquake Engineering and Soil Dynamics, 6. Available at: http://scholarsmine.mst.edu/icrageesdhttp://scholarsmine.mst.edu/icrageesd/04icrageesd/session13/6.

Elgamal, A., Zeghal, M., Parra, E. and Gunturi, R. (1996) 'Identification and modeling of earthquake ground response - I. Site amplification', Soil Dynamics and Earthquake Engineering, 15(8), pp. 449–522. Available at: https://doi.org/10.1016/S0267-7261(96)00022-X.

Elgamal, A., Zeghal, M., Tang, H.T. and Stepp, J.. C. (1995) 'Lotung Downhole Array I : Evaluation of site dynamic properties', Journal of Geoechnical Engineering, 121(4), pp. 350–362.

Elia, G., Rouainia, M., Karofyllakis, D. and Guzel, Y. (2017) 'Modelling the non-linear site response at the LSST down-hole accelerometer array in Lotung', Soil Dynamics and Earthquake Engineering, 102(September 2016), pp. 1–14. Available at: https://doi.org/10.1016/j.soildyn.2017.08.007.

Elsabee, F., Morray, J.P. and Roesset, J.M. (1997) Dynamic Behavior of Embedded Foundations, Massachusetts Institute of Technology, Department of Civil Engineering, Constructed Facilities Division.

Euroseistest Final Scientific Report (1995) 'Volvi-Thessaloniki a European test site for engineering seismology earthquake engineering and seismology' (Coordinator Pitilakis, K.), Pmject: EV5V - CT93 - 0281 (DIR 12 SOLS).

EUROSEISTEST Strong Motion Network (1993) Research Unit of Soil Dynamics and Geotechnical Earthquake Engineering, Aristotle University of Thessaloniki, International Federation of Digital Seismograph Networks. Available at: https://doi.org/https://doi.org/10.7914/SN/EG.

Fatahi, B. and Tabatabaiefar, S.H.R. (2014) 'Fully Nonlinear versus Equivalent Linear Computation Method for Seismic Analysis of Midrise Buildings on Soft Soils', International Journal of Geomechanics, 14(4), pp. 1–15. Available at: https://doi.org/10.1061/(asce)gm.1943-5622.0000354.

Foti, S., Passeri, F. and Rodriguez-Marek, A. (2019) 'Uncertainties and variabilities in seismic ground response analyses', in VII international conference on earthquake geotechnical engineering. Earthquake Geotechnical Engineering for Protection and Development of Environment and Constructions. Rome, pp. 153–172.

Gajan, S. and Kutter, B.L. (2008) 'Capacity, Settlement, and Energy Dissipation of Shallow Footings Subjected to Rocking', Journal of Geotechnical and Geoenvironmental Engineering, 134(8), pp. 1129–1141. Available at: https://doi.org/10.1061/(asce)1090-0241(2008)134:8(1129).

Gajan, S. and Kutter, B.L. (2009) 'Contact Interface Model for Shallow Foundations Subjected to Combined Cyclic Loading', Journal of Geotechnical and Geoenvironmental Engineering, 135(3), pp. 407–419. Available at: https://doi.org/10.1061/(asce)1090-0241(2009)135:3(407).

Gazetas, G. (1983) 'Analysis of machine foundation vibrations: State of the art', International Journal of Soil Dynamics and Earthquake Engineering, 2(1), pp. 2–42. Available at: https://doi.org/10.1016/0261-7277(83)90025-6.

Gazetas, G. (1991) 'Formulas and charts for impedances of surface and embedded foundations', Journal of Geotechnical Engineering, 117(9), pp. 1363–1381.

Gazetas, G. (2001) 'Soil-structure interaction on elastic and inelastic structures', in International Conferences on Recent Advances in Geotechnical Earthquake Engineering and Soil Dynamics.

Gazetas, G. (2015) '4th Ishihara lecture: Soil-foundation-structure systems beyond conventional seismic failure thresholds', Soil Dynamics and Earthquake Engineering, 68, pp. 23–39. Available at: https://doi.org/10.1016/j.soildyn.2014.09.012.

Gazetas, G., Anastasopoulos, I., Adamidis, O. and Kontoroupi, T. (2013) 'Nonlinear rocking stiffness of foundations', Soil Dynamics and Earthquake Engineering, 47, pp. 83–91. Available at: https://doi.org/10.1016/j.soildyn.2012.12.011.

Gazetas, G. and Stokoe, K. (1991) 'FREE VIBRATION OF EMBEDDED FOUNDATIONS: THEORY VERSUS EXPERIMENT', Journal of Geotechnical Engineering, 117(9), pp. 1382–1401.

Ghaboussi, J., Wilson, E.L. and Isenberg, J. (1973) 'FINITE ELEMENT FOR ROCK JOINTS AND INTERFACES', Journal of the Soil Mechanics and Foundations Division, 99(10), pp. 833–848.

Ghahari, S.F., Abazarsa, F., Ghannad, M.A. and Taciroglu, E. (2012) 'Response-only modal identification of structures using strongmotion data', Earthquake Engineering & Structural Dynamics, 42(8), pp. 1221–1242. Available at: https://doi.org/10.1002/eqe.

Ghahari, S.F., Ghannad, M.A. and Taciroglu, E. (2013) 'Blind identification of soil-structure systems', Soil Dynamics and Earthquake Engineering, 45, pp. 56–69. Available at: https://doi.org/10.1016/j.soildyn.2012.11.005.

Givens, M.J. (2013) Dynamic Soil-Structure Interaction of Instrumented Buildings and Test Structures. UNIVERSITY OF CALIFORNIA Los Angeles.

Givens, M.J., Mikami, A. and Kashima, T. (2012) 'Kinematic soil-structure interaction effects from building and free-field seismic arrays in Japan', in 9th International Conference on Urban Earthquake Engineering/ 4th Asia Conference on Earthquake Engineering. Available at: https://doi.org/10.1007/0-387-30842-3_18.

Givens, M.J., Mylonakis, G. and Stewart, J.P. (2016) 'Modular analytical solutions for foundation damping in soil-structure interaction applications', Earthquake Spectra, 32(3), pp. 1749–1768. Available at: https://doi.org/10.1193/071115EQS112M.

Glaser, S.D. and Baise, L.G. (2000) 'System identification estimation of soil properties at the Lotung site', Soil Dynamics and Earthquake Engineering, 19(7), pp. 521–531. Available at: https://doi.org/10.1016/S0267-7261(00)00026-9.

Goodman, R.E., Taylor, R.L. and Brekke, T.L. (1968) 'A MODEL FOR THE MECHANICS OF JOINTED ROCK', SOIL MECHANICS AND FOUNDATIONS DIVISION, 94(3), pp. 637–659.

Griffiths, D. V. (1985) 'Numerical modelling of interfaces using conventional finite elements', in 5th International conference on Numerical Methods in Geomechanics, pp. 837–844.

Groholski, D.R. and Hashash, Y.M.A. (2013) 'Development of an inverse analysis framework for extracting dynamic soil behavior and pore pressure response from downhole array measurements', International Journal for Numerical and Analytical Methods in Geomechanics, 32(March 2007), pp. 189–213. Available at: https://doi.org/10.1002/nag.

Groholski, D.R., Hashash, Y.M.A., Kim, B., Musgrove, M., Harmon, J. and Stewart, J.P. (2016) 'Simplified Model for Small-Strain Nonlinearity and Strength in 1D Seismic Site Response Analysis', Journal of Geotechnical and Geoenvironmental Engineering, 142(9), p. 04016042. Available at: https://doi.org/10.1061/(asce)gt.1943-5606.0001496.

Gudehus, G. and Nübel, K. (2004) 'Evolution of shear bands in sand', Geotechnique, 54(3), pp. 187–201. Available at: https://doi.org/10.1680/geot.2004.54.3.187.

Han, B. (2014) Hydro-mechanical coupling in numerical analysis of geotechnical structures under multi-directional seismic loading. Imperial College London.

Han, B., Yang, Z., Zdravkovic, L. and Kontoe, S. (2015) 'Non-linearity of gravelly soils under seismic compressional deformation based on KiK-net downhole array observations', Geotechnique Letters, 5(4), pp. 287–293. Available at: https://doi.org/10.1680/jgele.15.00130.

Han, Bo, Zdravkovic, L. and Kontoe, S. (2015) 'Stability investigation of the Generalised-α time integration method for dynamic coupled consolidation analysis', Computers and Geotechnics, 64, pp. 83–95. Available at: https://doi.org/10.1016/j.compgeo.2014.11.006.

Han, B., Zdravkovic, L. and Kontoe, S. (2018) 'Analytical and numerical investigation of site response due to vertical ground motion', Geotechnique, 68(6), pp. 467–480. Available at: https://doi.org/10.1680/jgeot.15.P.191.

Han, B., Zdravkovic, L., Kontoe, S. and Taborda, D.M.G. (2016) 'Numerical investigation of the response of the Yele rockfill dam during the 2008 Wenchuan earthquake', Soil Dynamics and Earthquake Engineering, 88, pp. 124–142. Available at: https://doi.org/10.1016/j.soildyn.2016.06.002.

Han, B., Zdravkovic, L., Kontoe, S. and Taborda, D.M.G. (2017) 'Numerical investigation of multi-directional site response based on KiK-net downhole array monitoring data', Computers and Geotechnics, 89, pp. 55–70. Available at: https://doi.org/10.1016/j.compgeo.2017.04.008.

Harichane, Z., Afra, H. and Elachachi, S.M. (2005) 'An identification procedure of soil profile characteristics from two free field acclerometer records', Soil Dynamics and Earthquake Engineering, 25(6), pp. 431–438. Available at: https://doi.org/10.1016/j.soildyn.2005.04.001.

Herrmann, L.R. (1979) 'FINITE ELEMENT ANALYSIS OF CONTACT PROBLEMS', JOURNAL OF THE ENGINEERING MECHANICS DIVISION, 104, pp. 1043–1057.

Huang, H.C., Shieh, C.S. and Chiu, H.C. (2001) 'Linear and nonlinear behaviors of soft soil layers using Lotung downhole array in Taiwan', Terrestrial, Atmospheric and Oceanic Sciences, 12(3), pp. 503–524.

Ishibashi, I. and Zhang, X. (1993) 'Unified dynamic shear moduli and damping ratios of sand and clay', Soils and foundations, 33(1), pp. 181–191.

Iwan, W.D., Moser, M.A. and Peng, C.-Y. (1985) 'SOME OBSERVATIONS ON STRONG-MOTION EARTHQUAKE MEASUREMENT USING A DIGITAL ACCELEROGRAPH', Bulletin of the Seismological Society of America, 75(5), pp. 1225–1246. Available at: https://doi.org/10.1785/BSSA0750051225.

Jardine, R.J., Potts, D.M., Burland, J.B. and Fourie, A.B. (1986) 'Studies of the influence of non-linear stress–strain characteristics in soil–structure interaction', Geotechnique, 36(3), pp. 377–396. Available at: https://doi.org/10.1680/geot.1986.36.3.377.

Jennings, P. and Bielak, J. (1973) 'Dynamics of building-soil interaction', Bulletin of the Seismological Society of America, 63(1), pp. 9–48.

Jones, J., Kalkan, E., Stephens, C. and Ng, P. (2017) 'PRISM software: Processing and review interface for strong-motion data', Seismological Research Letters, 88(3), pp. 851–866. Available at: https://doi.org/10.1785/0220160200.

Kaklamanos, J., Baise, L.G., Thompson, E.M. and Dorfmann, L. (2015) 'Comparison of 1D linear, equivalent-linear, and nonlinear site response models at six KiK-net validation sites', Soil Dynamics and Earthquake Engineering, 69, pp. 207–219. Available at: https://doi.org/10.1016/j.soildyn.2014.10.016.

Kawase, H. (2019) 'Site characterization of strong motion stations based on borehole and surface geophysical techniques', in VII international conference on earthquake geotechnical engineering. Earthquake Geotechnical Engineering for Protection and Development of Environment and Constructions. Rome, pp. 318–334.

Kellezi, L. (2000) 'Local transmitting boundaries for transient elastic analysis', Soil Dynamics and Earthquake Engineering, 19(7), pp. 533–547. Available at: https://doi.org/10.1016/S0267-7261(00)00029-4.

Kim, B., Hashash, Y.M.A., Stewart, J.P., Rathje, E.M., Harmon, J.A., Musgrove, M.I., Campbell, K.W. and Silva, W.J. (2016) 'Relative differences between nonlinear and equivalent-linear 1-D site response analyses', Earthquake Spectra, 32(3), pp. 1845–1865. Available at: https://doi.org/10.1193/051215EQS068M.

Kim, S. and Stewart, J.P. (2003) 'Kinematic Soil-Structure Interaction from Strong Motion Recordings', Journal of Geotechnical and Geoenvironmental Engineering, 129(4), pp. 323–335. Available at: https://doi.org/10.1061/(asce)1090-0241(2003)129:4(323).

Kokusho, T. (2004) 'Nonlinear site response and strain-dependent soil properties', Current Science, 87(10), pp. 1363–1369.

Kokusho, T. and Sato, K. (2008) 'Surface-to-base amplification evaluated from KiK-net vertical array strong motion records', Soil Dynamics and Earthquake Engineering, 28(9), pp. 707–716. Available at: https://doi.org/10.1016/j.soildyn.2007.10.016.

Kontoe, S. (2006) Developement of time integration schemes and advanced boundary conditions for dynamic geotechnical analysis. Imperial College London. Available at: http://ethos.bl.uk/OrderDetails.do?uin=uk.bl.ethos.435799.

Kontoe, S., Han, B., Zdravkovic, L. and Taborda, D.M.G. (2018) 'The Importance of Compressional Deformation in Three Dimensional Site Response Analysis', in 16th European Conference of Earthquake Engineering. Thessaloniki.

Kontoe, S., Zdravkovic, L. and Potts, D.M. (2008) 'An assessment of time integration schemes for dynamic geotechnical problems', Computers and Geotechnics, 35(2), pp. 253–264. Available at: https://doi.org/10.1016/j.compgeo.2007.05.001.

Kontoe, S., Zdravković, L. and Potts, D.M. (2008) 'The domain reduction method for dynamic coupled consolidation problems in geotechnical engineering', International Journal for Numerical and Analytical Methods in Geomechanics, 32(6), pp. 659–680. Available at: https://doi.org/10.1002/nag.

Kontoe, S., Zdravković, L. and Potts, D.M. (2009) 'An assessment of the domain reduction method as an advanced boundary condition and some pitfalls in the use of conventional absorbing boundaries', International Journal for Numerical and Analytical Methods in Geomechanics, 33(13), pp. 309–330. Available at: https://doi.org/10.1002/nag.

Kontoe, S., Zdravkovic, L., Potts, D.M. and Salandy, L. (2007) 'The use of absorbing boundaries in dynamic analyses of soil-structure interaction problems', 4th International Conference on Earthquake Engineering, Thessaloniki, Greece, (1231), pp. 1–10.

Korma, E. (2014) The influence of advanced features of cyclic soil response on wave propagation problems. Imperial College London.

Koronides, M. (2018) Site Response Analysis for an Instrumental Downhole Array. Imperial College London.

Kottke, A.R. and Rathje, E.M. (2009) 'Technical Manual for Strata'. Berkeley California: PACIFIC EARTHQUAKE ENGINEERING RESEARCH CENTER.

Kramer, S.L. (1996) Geotechnical earthquake engineering. Prentice Hall, New Jersey.

Kuhlemeyer, R.L. and Lysmer, J. (1973) 'FINITE ELEMENT METHOD ACCURACY FOR WAVE PROPAGATION PROBLEMS', Soil Mechanics & Foundations Div, 99(sm5), pp. 421–7.

Kwok, A.O.L., Stewart, J.P., Hashash, Y.M.A., Matasovic, N., Pyke, R., Wang, Z. and Yang, Z. (2007) 'Use of Exact Solutions of Wave Propagation Problems to Guide Implementation of Nonlinear Seismic Ground Response Analysis Procedures', Journal of Geotechnical and Geoenvironmental Engineering, 133(11), pp. 1385–1398. Available at: https://doi.org/10.1061/(asce)1090-0241(2007)133:11(1385).

López, A.R., Tsiampousi, A., Standing, J.R. and Potts, D.M. (2022) 'Numerical investigation of a segmental grey cast iron tunnel ring: validation with laboratory data and application to field conditions', Computers and Geotechnics, 141(May 2021). Available at: https://doi.org/10.1016/j.compgeo.2021.104427.

Luco, J.E. and Westmann, R.A. (1971) 'Dynamic response of circular footings', Journal of the Engineering Mechanics Division, 97(5), 1381-1395.

Luco, J.E. and Wong, H.L. (1992) 'Identification of soil properties from foundation impedance functions', Journal of Geotechnical Engineering, 118(5), pp. 780–795. Available at: https://doi.org/10.1061/(ASCE)0733-9410(1992)118:5(780).

Makra, K. and Chávez-García, F.J. (2016) 'Site effects in 3D basins using 1D and 2D models: an evaluation of the differences based on simulations of the seismic response of Euroseistest', Bulletin of Earthquake Engineering, 14(4), pp. 1177–1194. Available at: https://doi.org/10.1007/s10518-015-9862-7.

Makra, K., Chávez-García, F.J., Raptakis, D. and Pitilakis, K. (2005) 'Parametric analysis of the seismic response of a 2D sedimentary valley: Implications for code implementations of complex site effects', Soil Dynamics and Earthquake Engineering, 25(4), pp. 303–315. Available at: https://doi.org/10.1016/j.soildyn.2005.02.003.

Manakou, M. V., Raptakis, D.G., Chávez-García, F.J., Apostolidis, P.I. and Pitilakis, K.D. (2010) '3D soil structure of the Mygdonian basin for site response analysis', Soil Dynamics and Earthquake Engineering, 30(11), pp. 1198–1211. Available at: https://doi.org/10.1016/j.soildyn.2010.04.027.

Maravas, A., Mylonakis, G. and Karabalis, D.L. (2014) 'Simplified discrete systems for dynamic analysis of structures on footings and piles', Soil Dynamics and Earthquake Engineering, 61–62(December 2014), pp. 29–39. Available at: https://doi.org/10.1016/j.soildyn.2014.01.016.

Masing, G. (1926) 'Eigenspannungen und verfestigung beim messing', in 2nd international conference of applied mechanics, pp. 332–335.

Massimino, M.R., Abate, G., Grasso, S. and Pitilakis, D. (2019) 'Some aspects of DSSI in the dynamic response of fully-coupled soil-structure systems', Rivista Italiana di Geotecnica, (1), pp. 44–70. Available at: https://doi.org/10.19199/2019.1.0557-1405.044.

Maufroy, E., Chaljub, E., Hollender, F., Kristek, J., Moczo, P., Klin, P., Priolo, E., Iwaki, A., Iwata, T., Etienne, V., De Martin, F., Theodoulidis, N.P., Manakou, M., Guyonnet-Benaize, C., Pitilakis, K. and Bard, P.Y. (2015) 'Earthquake ground motion in the Mygdonian Basin, Greece: The E2VP verification and validation of 3D numerical simulation up to 4 Hz', Bulletin of the Seismological Society of America, 105(3), pp. 1398–1418. Available at: https://doi.org/10.1785/0120140228.

Measham, P.G., Taborda, D.M.G., Zdravkovic, L. and Potts, D.M. (2014) 'Numerical simulation of a deep excavation in London Clay', Numerical Methods in Geotechnical Engineering, pp. 771–776. Available at: https://doi.org/doi:10.1201/b17017-138.

Meek, J.W. and Wolf, J.P. (1993) 'Why cone models can represent the elastic half-space', Earthquake

Engineering & Structural Dynamics, 22(9), pp. 759–771. Available at: https://doi.org/10.1002/eqe.4290220903.

Mylonakis, G. and Gazetas, G. (2000) 'Seismic soil-structure interaction: Beneficial or detrimental?', Journal of Earthquake Engineering, 4(3), pp. 277–301. Available at: https://doi.org/10.1080/13632460009350372.

Mylonakis, G., Syngros, C., Gazetas, G. and Tazoh, T. (2006) 'The role of soil in the collapse of 18 piers of Hanshin expressway in the Kobe earthquake', Earthquake Engineering and Structural Dynamics, 35(5), pp. 547–575. Available at: https://doi.org/10.1002/eqe.543.

NERA (2014) Guidelines for optimal design of force vibration method.

Newmark, N.M. (1967) 'Problem in wave propagation in soil and rock', in Internatinal symposium on wave propagation and dynamic properties of earth materials. Albuquerque: University of New Mexico Press, pp. 7–26.

NIST (2012) Soil-Structure Interaction for Building Structures, International Journal for Research in Applied Science and Engineering Technology. Available at: https://doi.org/10.22214/ijraset.2021.37763.

Pais, A. and Kausel, E. (1988) 'Approximate formulas for dynamic stiffnesses of rigid foundations', Soil Dynamics and Earthquake Engineering, 7(4), pp. 213–227. Available at: https://doi.org/10.1016/S0267-7261(88)80005-8.

Pande, G.N. and Sharma, K.G. (1979) 'On joint/interface elements and associated problems of numerical ill-conditioning', International Journal for Numerical and Analytical Methods in Geomechanics, 3(3), pp. 293–300. Available at: https://doi.org/10.1002/nag.1610030308.

Papaspiliou, M., Kontoe, S. and Bommer, J.J. (2012) 'An exploration of incorporating site response into PSHA-Part I: Issues related to site response analysis methods', Soil Dynamics and Earthquake Engineering, 42, pp. 302–315. Available at: https://doi.org/10.1016/j.soildyn.2012.06.011.

Papazachos, B., Mountrakis, D., Psilovikos, A. and Leventakis, G. (1979) 'Surface fault traces and fault plane solutions of the May-June 1978 major shocks in the Thessaloniki area, Greece.', Tectonophysics, 53(3–4), pp. 171–183. Available at: https://doi.org/10.1016/0040-1951(79)90061-1.

Park, H.J. and Kim, D.S. (2013) 'Centrifuge modelling for evaluation of seismic behaviour of stone masonry structure', Soil Dynamics and Earthquake Engineering, 53, pp. 187–195. Available at: https://doi.org/10.1016/j.soildyn.2013.06.010.

Pelecanos, L. (2013) ‘Seismic Response and Analysis of Earth Dams’. Imperial College London.

Pelekis, I., McKenna, F., Madabhushi, G.S.P. and DeJong, M.J. (2021) ‘Finite element modeling of buildings with structural and foundation rocking on dry sand’, Earthquake Engineering and Structural Dynamics, 50(12), pp. 3093–3115. Available at: https://doi.org/10.1002/eqe.3501.

Phillips, C. and Hashash, Y.M.A. (2009) ‘Damping formulation for nonlinear 1D site response analyses’, Soil Dynamics and Earthquake Engineering, 29(7), pp. 1143–1158. Available at: https://doi.org/10.1016/j.soildyn.2009.01.004.

Pitilakis, D. et al. (2012) Report on field testing for assessing input motions and SSI, Seismic engineering research infrastructures for european synergies.

Pitilakis, D. and Clouteau, D. (2010) ‘Equivalent linear substructure approximation of soil-foundation-structure interaction: Model presentation and validation’, Bulletin of Earthquake Engineering, 8(2), pp. 257–282. Available at: https://doi.org/10.1007/s10518-009-9128-3.

Pitilakis, D., Dietz, M., Wood, D.M., Clouteau, D. and Modaressi, A. (2008) ‘Numerical simulation of dynamic soil-structure interaction in shaking table testing’, Soil Dynamics and Earthquake Engineering, 28(6), pp. 453–467. Available at: https://doi.org/10.1016/j.soildyn.2007.07.011.

Pitilakis, D., Lamprou, D., Manakou, M. and Rovithis, E. (2014) ‘System identification of soil-foundation structure systems by means of ambient noise records : the case of Europroteas model structure in Euroseistest’, Proceedings of the Second European Conference on Earthquake Engineering and Seismology (2ECEES), (August), pp. 1–11.

Pitilakis, D., Rovithis, E., Anastasiadis, A., Vratsikidis, A. and Manakou, M. (2018) ‘Field evidence of SSI from full-scale structure testing’, Soil Dynamics and Earthquake Engineering, 112(March), pp. 89–106. Available at: https://doi.org/10.1016/j.soildyn.2018.04.024.

Pitilakis, D., Rovithis, E., Massimino, M.R. and Gatto, M.P.A. (2015) ‘Numerical Simulation of Large-Scale Soil-Foundation-Structure Interaction Experiments In The EuroProteas Facility’, Proceedings of the 6th International Conference on Earthquake Geotechnical Engineering, (November). Available at: https://doi.org/10.13140/RG.2.2.20002.43203.

Pitilakis, D. and Vratsikidis, A. (2017) ‘Dynamic system properties from real-scale free- vibration soil-structure interaction experiments’, Proceedings of the 7th International Conference on Advances in Experimental Structural Engineering, pp. 283–293. Available at: https://doi.org/10.7414/7aese.T2.106.

Pitilakis, D. and Vratsikidis, A. (2018) ‘Damping Calculation From Free- and Forced-Vibration Field Experiments At the Large-Scale Structure of’, Proceedings of the 16th European Conference on

Earthquake Engineering, (June), pp. 1–13.

Pitilakis, K., Anastasiadis, A., Pitilakis, D. and Rovithis, E. (2013) 'Full-Scale Testing of a Model Structure in Euroseistest To Study Soil-Foundation-Structure Interaction', in 4th ECCOMAS Thematic Conference on Computational Methods in Structural Dynamics and Earthquake Engineering, pp. 1175–1188. Available at: https://doi.org/10.7712/120113.4585.c1546.

Pitilakis, K., Raptakis, D., Lontzetidis, K., Tika-Vassilikou, T. and Jongmans, D. (1999) 'Geotechnical and geophysical description of euro-seistest, using field, laboratory tests and moderate strong motion recordings', Journal of Earthquake Engineering, 3(3), pp. 381–409. Available at: https://doi.org/10.1080/13632469909350352.

Potts, D.M. and Zdravković, L. (1999) Finite element analysis in geotechnical engineering: theory. Thomas Telford, London.

Raptakis, D., Chávez-García, F.J., Makra, K. and Pitilakis, K. (2000) 'Site effects at Euroseistest-I. Determination of the valley structure and confrontation of observations with 1D analysis', Soil Dynamics and Earthquake Engineering, 19(1), pp. 1–22. Available at: https://doi.org/10.1016/S0267-7261(99)00025-1.

Raptakis, D. and Makra, K. (2015) 'Multiple estimates of soil structure at a vertical strong motion array: Understanding uncertainties from different shear wave velocity profiles', Engineering Geology, 192, pp. 1–18. Available at: https://doi.org/10.1016/j.enggeo.2015.03.016.

Raptakis, D.G., Manakou, M. V., Chávez-García, F.J., Makra, K.A. and Pitilakis, K.D. (2005) '3D configuration of Mygdonian basin and preliminary estimate of its site response', Soil Dynamics and Earthquake Engineering, 25(11), pp. 871–887. Available at: https://doi.org/10.1016/j.soildyn.2005.05.005.

Raychowdhury, P. and Hutchinson, T.C. (2009) 'Performance evaluation of a nonlinear Winkler-based shallow foundation model using centrifuge test results', EARTHQUAKE ENGINEERING AND STRUCTURAL DYNAMICS, (38), pp. 679–698. Available at: https://doi.org/10.1002/eqe.902.

Régnier, J. et al. (2016) 'International benchmark on numerical simulations for 1D, nonlinear site response (Prenolin): Verification phase based on canonical cases', Bulletin of the Seismological Society of America, 106(5), pp. 2112–2135. Available at: https://doi.org/10.1785/0120150284.

Régnier, J. et al. (2018) 'Prenolin: International benchmark on 1D nonlinear: Site-response analysis—validation phase exercise', Bulletin of the Seismological Society of America, 108(2), pp. 876–900. Available at: https://doi.org/10.1785/0120170210.

Régnier, J., Cadet, H. and Bard, P.-Y. (2017) 'IMPACT OF NON-LINEAR SOIL BEHAVIOR ON SITE

RESPONSE AMPLITUDE', in Proceedings of the 16th World Conference on Earthquake Engineering.

Régnier, J., Cadet, H., Bonilla, L.F., Bertrand, E. and Semblat, J.-F. (2013) 'Assessing nonlinear behavior of soils in seismic site response: Statistical analysis on KiK-net strong-motion data', Bulletin of the Seismological Society of America, 103(3), pp. 1750–1770. Available at: https://doi.org/10.1785/0120120240.

Roesset, J.M. (2013) 'Soil structure interaction the early stages', Journal of Applied Science and Engineering, 16(1), pp. 1–8.

Safak, E. (1991) 'Identification of linear structures using discrete-time filters', 117(10), pp. 3064–3085.

Sakellariadis, L., Anastasopoulos, I. and Gazetas, G. (2020) 'Fukae bridge collapse (Kobe 1995) revisited: New insights', Soils and Foundations, 60(6), pp. 1450–1467. Available at: https://doi.org/10.1016/j.sandf.2020.09.005.

Salonikos, T., Makarios, T., Sous, I., Lekidis, V. and Karakostas, C. (2005) 'DESIGN OF INSTRUMENTATION AND VIBRATION TESTING PROGRAMS OF STRUCTURES THROUGH ANALYTICAL INVESTIGATIONS', in Computational methods and experimental measurements XII. Malta, pp. 579–588.

Schanz, T., Vermeer, P.A. and Bonnier, P.G. (1999) 'The hardening soil model: formulation and verification', Beyond 2000 in computational geomechanics, 1, pp. 281–296.

Schnabel, P.B., Lysmer, J. and Seed, H.B. (1972) SHAKE: a computer program for earthquake response analyses of horizontally layered sites. California.

Seed, H.B. and Idriss, I.M. (1970) Soil Moduli and Damping Factors for Dynamic Analyses, Earthquake Engineering Research Center, EERC. California.

Seed, R.B., Dickenson, S.E. and Idriss, I. (1991) 'Principal Geotechnical aspects of the 1989 Loma Prieta earthquake', Soils and Foundations, 31(1), pp. 1–26.

Sharma, K. and Deng, L. (2020) 'Field testing of rocking foundations in cohesive soil: Cyclic performance and footing mechanical response', Canadian Geotechnical Journal, 57(6), pp. 828–839. Available at: https://doi.org/10.1139/cgj-2018-0734.

Shearer, P.M. and Orcutt, J.A. (1987) 'SURFACE AND NEAR-SURFACE EFFECTS ON SEISMIC WAVES - THEORY AND BOREHOLE SEISMOMETER RESULTS', Bulletin of Seismological Society of America, 77(4), pp. 1168–1196.

Star, L.M., Givens, M.J., Nigbor, R.L. and Stewart, J.P. (2015) 'Field-testing of structure on shallow foundation to evaluate soil-structure interaction effects', Earthquake Spectra, 31(4), pp. 2511–2534. Available at: https://doi.org/10.1193/052414EQS072.

Star, L.M., Tileylioglu, S., Givens, M.J., Mylonakis, G. and Stewart, J.P. (2019) 'Evaluation of soil-structure interaction effects from system identification of structures subject to forced vibration tests', Soil Dynamics and Earthquake Engineering, 116(September 2018), pp. 747–760. Available at: https://doi.org/10.1016/j.soildyn.2018.09.038.

Steidl, J.H., Tumarkin, A.G. and Archuleta, R.J. (1996) 'What Is a Reference Site?', Bulletin of the Seismological Society of America, 86(6), pp. 1733–1748.

Stewart, J.P. and Fenves, G.L. (1998) 'System identification for evaluating soil-structure interaction effects in buildings from strong motion recordings', Earthquake Engineering and Structural Dynamics, 27(8), pp. 869–885. Available at: https://doi.org/10.1002/(SICI)1096-9845(199808)27:8<869::AID-EQE762>3.0.CO;2-9.

Stewart, J.P., Fenves, G.L. and Seed, R.B. (1999a) 'SEISMIC SOIL-STRUCTURE INTERACTION IN BUILDINGS. I: ANALYTICAL METHODS', JOURNAL OF GEOTECHNICAL AND GEOENVIRONMENTAL ENGINEERING, 125(1), pp. 26–37.

Stewart, J.P., Fenves, G.L. and Seed, R.B. (1999b) 'SEISMIC SOIL-STRUCTURE INTERACTION IN BUILDINGS. II: EMPIRICAL FINDINGS', JOURNAL OF GEOTECHNICAL AND GEOENVIRONMENTAL ENGINEERING, 125(1), pp. 38–48.

Stewart, J.P., Kim, S., Bielak, J., Dobry, R. and Power, M.S. (2003) 'Revisions to Soil-Structure Interaction Procedures in NEHRP Design Provisions', Earthquake Spectra, 19(3), pp. 677–696. Available at: https://doi.org/10.1193/1.1596213.

Stewart, J.P., Seed, R.B. and Fenves, G.L. (1998) 'Empirical Evaluation of Inertial Soil-Structure Interaction Effects', Pacific Earthquake Engineering Research Center Research Reports, p. 233.

Tabatabaiefar, H.R., Fatahi, B., Ghabraie, K. and Zhou, W.H. (2015) 'Evaluation of numerical procedures to determine seismic response of structures under influence of soil-structure interaction', Structural Engineering and Mechanics, 56(1), pp. 27–47. Available at: https://doi.org/10.12989/sem.2015.56.1.027.

Tabatabaiefar, S., Fatahi, B. and Samali, B. (2014) 'Numerical and experimental investigations on seismic response of building frames under influence of soil-structure interaction', Advances in Structural Engineering, 17(1), pp. 109–130. Available at: https://doi.org/10.1260/1369-4332.17.1.109.

Taborda, D.M.G. (2011) Development of Constitutive Models for Application in Soil Dynamics. Imperial College London.

Taborda, D.M.G., Potts, D.M. and Zdravković, L. (2016) 'On the assessment of energy dissipated through hysteresis in finite element analysis', Computers and Geotechnics, 71, pp. 180–194. Available at: https://doi.org/10.1016/j.compgeo.2015.09.001.

Taborda, D.M.G. and Zdravkovic, L. (2012) 'Application of a Hill-Climbing technique to the formulation of a new cyclic nonlinear elastic constitutive model', Computers and Geotechnics, 43, pp. 80–91. Available at: https://doi.org/10.1016/j.compgeo.2012.02.001.

Tan, U., Veluvolu, K.C., Latt, W.T., Shee, C.Y., Riviere, C.N. and Ang, W.T. (2008) 'Estimating Displacement of Periodic Motion With Inertial Sensors', IEEE Sensors Journal, 8(8), pp. 1385–1388.

Tang, H.T., Tang, Y.K. and Stepp, J.C. (1990) 'Lotung large-scale seismic experiment and soil-structure interaction method validation', Nuclear Engineering and Design, 123(2–3), pp. 397–412. Available at: https://doi.org/10.1016/0029-5493(90)90260-5.

Tatsuoka, F., Presti, D. Lo and Kohata, Y. (1995) 'Deformation Characteristics of Soils and Soft Rocks under Monotonic and Cyclic Loads and Their Relationships', Third International Conference on Recent Advances in Geotechnical Earthquake Engineering & Soil Dynamics, II, pp. 851–879. Available at: https://scholarsmine.mst.edu/cgi/viewcontent.cgi?article=3258&context=icrageesd.

Teague, D.P., Cox, B.R. and Rathje, E.M. (2018) 'Measured vs. predicted site response at the Garner Valley Downhole Array considering shear wave velocity uncertainty from borehole and surface wave methods', Soil Dynamics and Earthquake Engineering, 113(June), pp. 339–355. Available at: https://doi.org/10.1016/j.soildyn.2018.05.031.

Thompson, E.M., Baise, L.G., Kayen, R.E. and Guzina, B.B. (2009) 'Impediments to predicting site response: Seismic property estimation and modeling simplifications', Bulletin of the Seismological Society of America, 99(5), pp. 2927–2949. Available at: https://doi.org/10.1785/0120080224.

Tileylioglu, S. (2008) Evaluation of Soil-Structure Interaction Effects from Field Performance Data. University of California, Los Angeles.

Tileylioglu, S., Nigbor, R.L. and Stewart, J.P. (2008) 'Determination of Soil-Structure Interaction Effects for a Model Test Structure Using Parametric System Identification Procedures', pp. 1–10. Available at: https://doi.org/10.1061/40975(318)123.

Tileylioglu, S., Stewart, J.P. and Nigbor, R.L. (2011) 'Dynamic Stiffness and Damping of a Shallow Foundation from Forced Vibration of a Field Test Structure', Journal of Geotechnical and Geoenvironmental Engineering, 137(4), pp. 344–353. Available at: https://doi.org/10.1061/(asce)gt.1943-5606.0000430.

Todorovska, M.I. (2002) 'FULL-SCALE EXPERIMENTAL STUDIES OF SOIL-STRUCTURE INTERACTION', ISET Journal of Earthquake Technology, 39(3), pp. 139–165.

Trifunac, M.D., Todorovska, M.I. and Hao, T.-Y. (2001) 'Full-scale experimental studies of soil-structure interaction - A review', in Proc. 2 U.S.-Japan Workshop on Soil-Structure Interaction, March 6-8, 2001, Tsukuba City, Japan.

Trifunac, M.D., Udwadia, F.E. and G., B.A. (1973) 'Analysis of errors in digitized strong-motion accelerograms', Bulletin of the Seismological Society of America, 63(I), pp. 157–187.

Tsai, C.-C. and Hashash, Y.M. (2009) 'Learning of Dynamic Soil Behavior from Downhole Arrays', Journal of Geotechnical and Geoenvironmental Engineering, 135(6), pp. 745–757. Available at: https://doi.org/10.1061/(asce)gt.1943-5606.0000050.

Tsai, C.C. and Hashash, Y.M.A. (2008) 'A novel framework integrating downhole array data and site response analysis to extract dynamic soil behavior', Soil Dynamics and Earthquake Engineering, 28(3), pp. 181–197. Available at: https://doi.org/10.1016/j.soildyn.2007.06.008.

Tsaparli, V., Kontoe, S., Taborda, D.M.G. and Potts, D.M. (2017) 'The importance of accurate time-integration in the numerical modelling of P-wave propagation', Computers and Geotechnics, 86, pp. 203–208. Available at: https://doi.org/10.1016/j.compgeo.2017.01.017.

Veletsos, A.S. and Meek, J.W. (1974) 'DYNAMIC BEHAVIOUR OF BUILDING FOUNDATION SYSTEM', Earthquake Engineering & Structural Dynamics, 3, pp. 121–138.

Veletsos, A.S. and Nair, V.V.D. (1975) 'Seismic interaction of structures on hysteretic foundations', Journal of the structural division, 101(1), pp. 109-129.

Veletsos, A.S. and Prasad, A.M. (1989) 'Seismic interaction of structures and soils : stochastic approach', Journal of Structural Engineering, 115(4), pp. 935–956.

Veletsos, A.S., Prasad, A.M. and Wu, W.H. (1997) 'Transfer functions for rigid rectangular foundations', Earthquake Engineering and Structural Dynamics, 26(1), pp. 5–17. Available at: https://doi.org/10.1002/(SICI)1096-9845(199701)26:1<5::AID-EQE619>3.0.CO;2-X.

Veletsos, A.S. and Verbic, B. (1973) 'Vibration of vicoelastic foundations', Earthquake Engineering & Structural Dynamics, 2, pp. 87–102.

Veletsos, A.S. and Wei, Y.T. (1971) 'Lateral and Rocking Vibration of Footings', Journal of Soil Mechanics and Foundation Division, 97(9), pp.1227-1248.

Verdugo, R. (2002) 'Amplification phenomena observed in downhole array records generated on a subductive environment', Physics of the Earth and Planetary Interiors, 175(1–2), pp. 63–77. Available at: https://doi.org/10.1016/j.pepi.2008.03.014.

Vratsikidis, A. and Pitilakis, D. (2018) 'Full-Scale Free- and Forced-Vibration Experiments At the Europroteas Ssi Facility : Experimental Data', Proceedings of the 16th European Conference on Earthquake Engineering, (June), pp. 1–12.

Vucetic, M. (1993) 'Cyclic threshold shear strains in soils', Journal of Geotechnical Engineering, 120(12), pp. 2208–2228.

Vucetic, M. and Dobry, R. (1991) 'Effect of soil plasticity on cyclic response', Journal of Geotechnical Engineering, 117(1), pp. 89–107.

Wen, K. -L, Beresnev, I.A. and Yeh, Y.T. (1995) 'Investigation of non-linear site amplification at two downhole strong ground motion arrays in Taiwan', Earthquake Engineering & Structural Dynamics, 24(3), pp. 313–324. Available at: https://doi.org/10.1002/eqe.4290240302.

Wolf, J.P. and Song, C. (2002) 'Some cornerstones of dynamic soil-structure interaction', Engineering Structures, 24(1), pp. 13–28. Available at: https://doi.org/10.1016/S0141-0296(01)00082-7.

Woodward, P.K. and Griffiths, D. V. (1996) 'Influence of Viscous Damping in the Dynamic Analysis of an Earth Dam Using Simple Constitutive Models', Computers and Geotechnics, 19(3), pp. 245–263. Available at: https://doi.org/10.1016/0266-352X(96)00002-X.

Yoshimura, C., Bielak, J., Hisada, Y. and Fernández, A. (2003) 'Domain reduction method for three-dimensional earthquake modeling in localized regions, part II: Verification and applications', Bulletin of the Seismological Society of America, 93(2), pp. 825–840. Available at: https://doi.org/10.1785/0120010252.

Zaman, M.M., Desai, C.S. and Drumm, E.C. (1984) 'INTERFACE MODEL FOR DYNAMIC SOIL-STRUCTURE INTERACTION', Journal of Geotechnical Engineering, 110(9), pp. 1257–1273. Available at: https://doi.org/10.1061/(ASCE)0733-9410(1987)113:5(537).

Zangeneh, A., Svedholm, C., Andersson, A., Pacoste, C. and Karoumi, R. (2018) 'Identification of soil-structure interaction effect in a portal frame railway bridge through full-scale dynamic testing', Engineering Structures, 159(December 2017), pp. 299–309. Available at: https://doi.org/10.1016/j.engstruct.2018.01.014.

Zeghal, M., Elgamal, A., Tang, H.T. and C., S.J. (1995) 'LOTUNG DOWNHOLE ARRAY. II: EVALUATION OF SOIL NONLINEAR PROPERTIES', Journal of geoechnical engineering, 121(4), pp. 363–378.

Zhang, X. and Far, H. (2022a) 'Effects of dynamic soil-structure interaction on seismic behaviour of high-rise buildings', Bulletin of Earthquake Engineering, 20(7), pp. 3443–3467. Available at: https://doi.org/10.1007/s10518-021-01176-z.

Zhang, X. and Far, H. (2022b) Seismic behaviour of high-rise frame-core tube structures considering dynamic soil–structure interaction, Bulletin of Earthquake Engineering. Springer Netherlands. Available at: https://doi.org/10.1007/s10518-022-01398-9.

Zienkiewicz, O.C., Bicanic, N. and Shen, F.Q. (1989) 'Earthquake Input Definition and the Trasmitting Boundary Conditions', in I.S. Doltsinis (ed.) Advances in Computational Nonlinear Mechanics, pp. 109–138. Available at: https://doi.org/10.1007/978-3-7091-2828-2_3.

Appendix A

Site response analyses input and results

Appendix A.1 Sample testing details in resonant column and cyclic triaxial apparatuses

Table A.1 presents details of samples that were tested in resonant column (RC) and cyclic triaxial (CTX) apparatuses. The first two columns present the soil formation classified by Euroseistest Final Scientific Report (1995) and the UCS description of layers from where samples were retrieved. The third column shows the site samples were taken from, with reference to Figure A.1 and the fourth column the name of the sample. The fifth column gives the depth limits of each sample, while the next column describes samples condition, either disturbed (D) or undisturbed (UN). The seventh column presents the in situ effective vertical stresses (σ'_{vo}). The last two columns present the mean effective stresses (p') that have been applied to the samples before applying torsion or shear.

Table A.1: Sample testing details in RC and CX apparatuses (Koronides, 2018).

Stratum	UCS	Site	Test no.	Depth (m)	Sample	In-situ σ'_{vo} (kPa)	p' (kPa) Applied for G_{max} determination	p' (kPa) Applied for G-γ-D curves determination
A	SM	S2	VOLVI-5	0.0-2.0	D	50	43, 103, 192, 296, 363	90-105 175-190 350-380
	SM	S2	VOLVI-6	0.0-2.0	D		40, 97, 179, 370	
	SM	S2	VOLVI-7	0.0-2.0	UN		40, 91, 178, 353	
	SM	S2	VOLVI-8	0.0-2.0	UN		47, 105, 190, 376	
	SM	S2	VOLVI-9	0.0-2.0	UN		52, 106, 186, 382	
B	CL-ML	S1	VOLVI-13	7.1-7.8	UN	102.5	53, 112, 200, 356	53, 112, 200, 356
C	CL-ML	S5	VOLVI-1	32.2-32.8	UN	435	67, 108, 194	193.9
	CL-ML	S12	VOLVI-2	7.0-7.5	UN	218	59, 106, 176, 390	106.5, 175.7, 387.9
	CI	S11	VOLVI-10	39.0-39.5	UN	732.5	48, 103, 142, 315	106, 180, 360
	CI	S10	VOLVI-12	13.6-14.0	UN		41, 100, 217, 355	200, 350
D	CH	S1	VOLVI-3	75.0-75.5	UN	782	58, 194, 390	195, 391
	CL	S1	VOLVI-11	55.6-56.0	UN	588	45, 115, 197, 374	195, 360

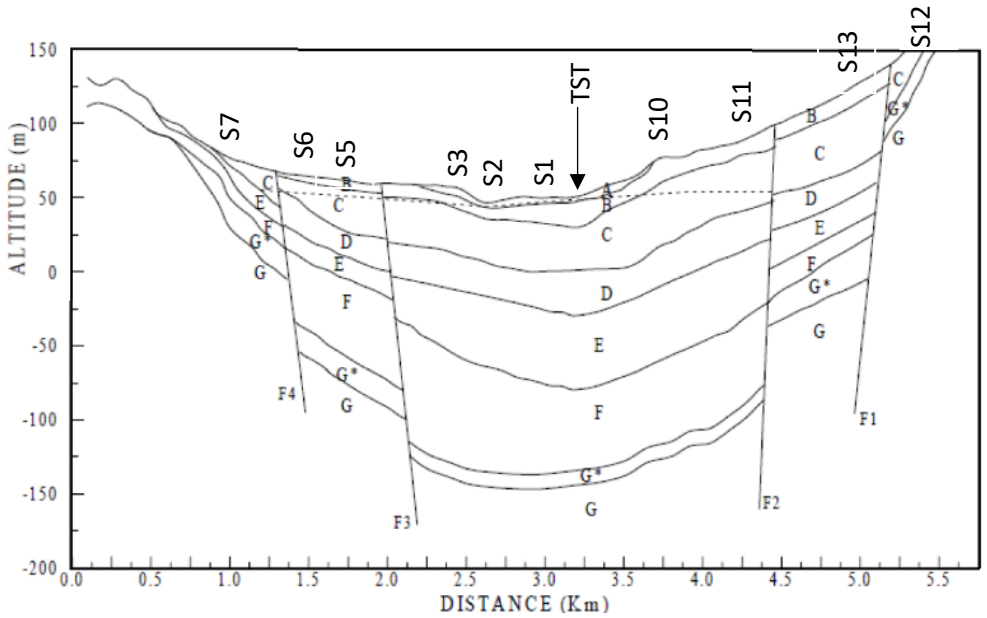


Figure A.1: Profitis-Stivos cross section illustrating the sites from where samples were retrieved, according to Table A.1 (Raptakis *et al.*, 2000)

Appendix A.2 Calibration of G-γ-D curves

Table A.2 presents the parameters input in the Darendeli (2001) equations, when assuming experimental conditions. The mean effective stress was estimated based on the pre-consolidation stage prior to the application of torque for RC tests, while the frequency (f) and number of cycles (N) were interactively calibrated. Additional parameters required calibration are the of ϕ_i's (ϕ_1-ϕ_6, ϕ_9-ϕ_{12}), the final parameters of which are shown in Table A.3. The remaining parameters of the Darendeli (2001) equations took the default values proposed by the referred author (Table A.4). Default values were used for layers that lack experimental data (i.e. layers 9-16). Following the calibration stage, the final G-γ-D curves were produced by incorporating the calibrated ϕ_i's and the in-situ conditions in the equations. The in-situ conditions are summarised in Table A.5.

Table A.2: Input parameters for Darendeli (2001) equations, when assuming experimental conditions.

Layer	p' (kPa)	f (Hz)	N
1	150	100	1000
2	40	50	1000
3	100	100	1000
4	200	100	1000
5	100	10	1000
6	360	1	1000
7	360	100	1000
8	391	100	10

Table A.3: Calibrated of ϕ_i's parameters of Darendeli (2001) equations.

Layer	ϕ_1	ϕ_2	ϕ_3	ϕ_4	ϕ_5	ϕ_6	ϕ_9	ϕ_{10}	ϕ_{11}	ϕ_{12}
1	0.0352	-5.8E-05	0.249	0.3483	0.919	0.8005	-0.372	0.233	0.748233	-0.0294
2	0.0352	0.00195	0.3246	0.3483	0.988	0.958	-0.2889	0.368	0.6329	-0.0057
3	0.043	0.000689	0.3246	0.3483	1	0.889	-0.2889	0.2919	0.73	-0.0057
4	0.0234	0.00101	0.3246	0.3483	0.919	0.8005	-0.2889	0.368	0.6329	-0.0057
5	0.0393	0.00101	0.3246	0.3483	0.919	0.8005	-0.2889	0.2919	0.804	-0.0057
6	0.0352	0.00101	0.3246	0.3483	0.988	0.8005	-0.2889	0.2919	0.6329	-0.0057
7	0.0352	0.00101	0.3246	0.3483	0.919	0.8005	-0.2889	0.2919	0.6329	-0.0057
8	0.0352	0.00209	0.3246	0.3483	0.988	0.8005	-0.2889	0.368	0.6329	-0.0057

Table A.4: Default ϕ_i's parameters of Darendeli (2001) equations.

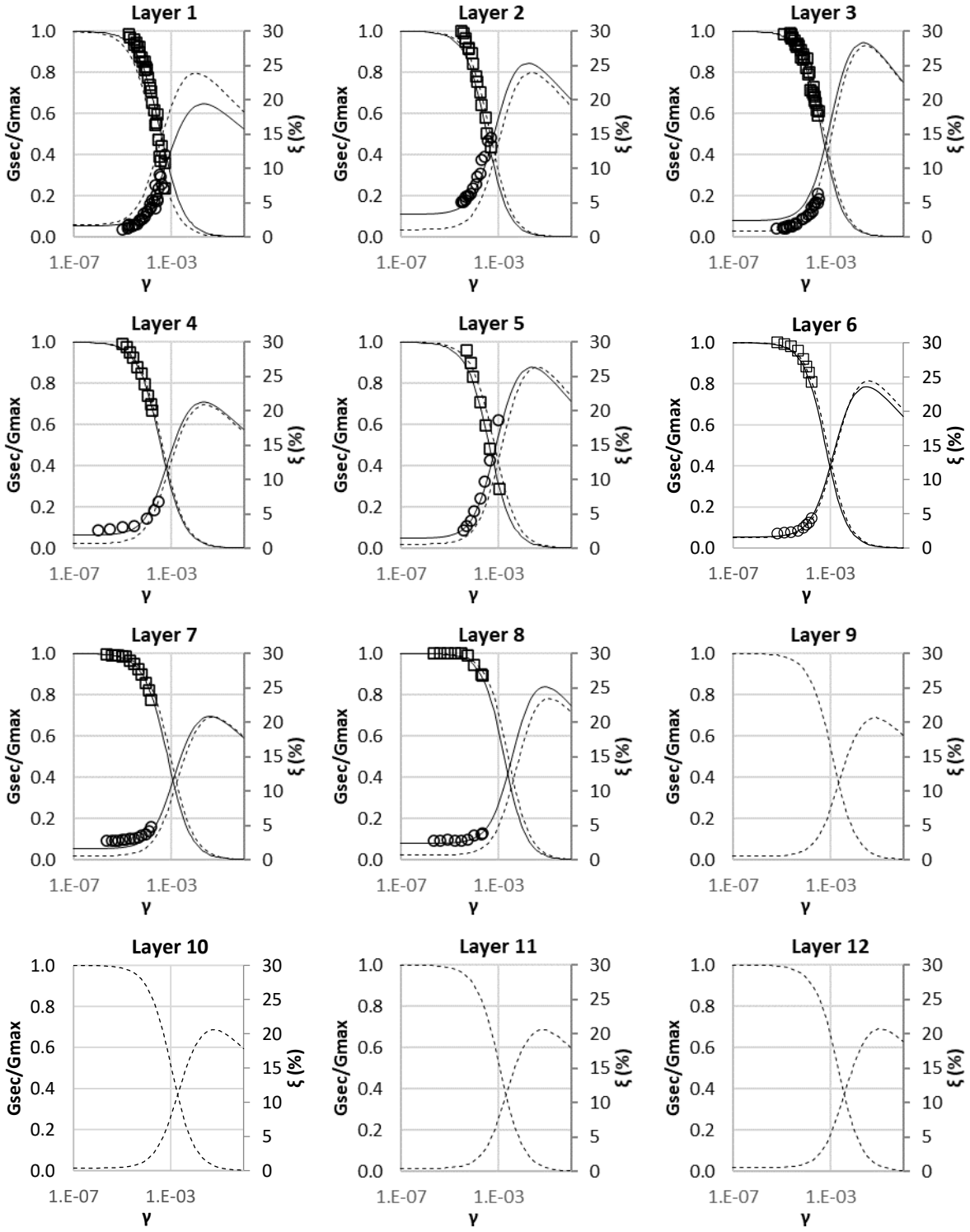
ϕ_1	0.0352	ϕ_7	0.0129	ϕ_{13}	-4.23
ϕ_2	0.00101	ϕ_8	-0.1069	ϕ_{14}	3.62
ϕ_3	0.3246	ϕ_9	-0.2889	ϕ_{15}	-5
ϕ_4	0.3483	ϕ_{10}	0.2919	ϕ_{16}	-0.25
ϕ_5	0.919	ϕ_{11}	0.6329	ϕ_{17}	5.62
ϕ_6	0.8005	ϕ_{12}	-0.0057	ϕ_{18}	2.78

Table A.5: Input for Darendeli (2001) equations assuming in-situ conditions.

Layer	p'(kPa)	PI (%)	$\phi'(^o)$	OCR	f (Hz) (in-situ)	N (in-situ)
1	19.3	10	32	1	1	10
2	98.4	7	20.6	1	1	10
3	184.1	7.5	30	1	1	10
4	291.7	7.5	28	1	1	10
5	408.2	5	30	1	1	10
6	616.2	5	28	1	1	10
7	805.2	12	30	1	1	10
8	1179.0	37	18	1	1	10
9	1416.9	15	29	1	1	10
10	1800.2	4	28	1	1	10
11	1882.6	8	30	1	1	10
12	2456.2	35	18	1	1	10
13	2281.3	4	28	1	1	10
14	2417.5	4	28	1	1	10
15	2404.3	8	32	1	1	10
16	2859.9	0	25	1	1	10

Appendix A.3 G-γ-D curves input in the EQL site response models

Figure A.2 presents the G-γ-D curves of each layer, computed using the calibrated parameters. The presented curves correspond to in-situ and experimental conditions, while they are compared against experimental data, where available. The in-situ curves are used as input in the EQL analyses.



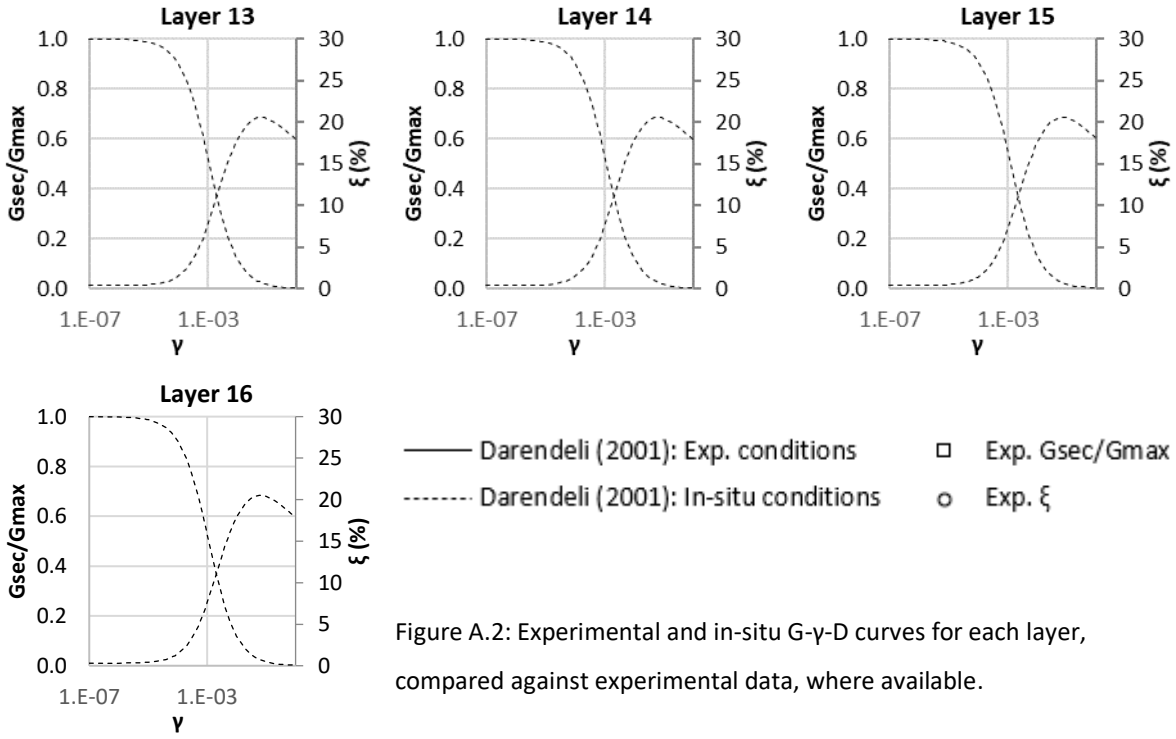


Figure A.2: Experimental and in-situ G-γ-D curves for each layer, compared against experimental data, where available.

Appendix A.4 Parameters and G-γ-D curves input in the Nonlinear site response analyses

The calibrated parameters of the nonlinear analyses for all layers are presented in Tables A.6 to A.21. Figure A.3 presents the resulting G-γ-D curves and their comparison with the reference (target) curves.

Table A.6: Layer 1: Calibrated parameters of the nonlinear model.

G_0 (MPa)	40.2	b_0	1.09	a_2	0.0	$d_{2,G}$	0.1942
m_G	0.0	a_0	1.194E-04	$d'_{1,G}$	105.0	$d_{3,G}$	5447.7
$R_{G,min}$	0.0	a_1	0.0	$d''_{1,G}$	0.0	$d_{4,G}$	0.839

Table A.7: Layer 2: Calibrated parameters of the nonlinear model.

G_0 (MPa)	77.6	b_0	1.1	a_2	0.0	$d_{2,G}$	0.2326
m_G	0.0	a_0	2.104E-04	$d'_{1,G}$	87.2	$d_{3,G}$	5548.2
$R_{G,min}$	0.0	a_1	0.0	$d''_{1,G}$	0.0	$d_{4,G}$	0.797

Table A.8: Layer 3: Calibrated parameters of the nonlinear model.

G_0 (MPa)	86.0	b_0	1.19	a_2	0.0	$d_{2,G}$	0.2162
m_G	0.0	a_0	2.0E-04	$d'_{1,G}$	66.3	$d_{3,G}$	8000.0
$R_{G,min}$	0.0	a_1	0.0	$d''_{1,G}$	0.0	$d_{4,G}$	0.77

Table A.9: Layer 4: Calibrated parameters of the nonlinear model.

G_0 (MPa)	182.7	b_0	1.07	a_2	0.0	$d_{2,G}$	0.1695
m_G	0.0	a_0	1.454E-4	$d'_{1,G}$	78.13	$d_{3,G}$	11006.0
$R_{G,min}$	0.0	a_1	0.0	$d''_{1,G}$	0.0	$d_{4,G}$	0.625

Table A.10: Layer 5: Calibrated parameters of the nonlinear model.

G_0 (MPa)	259.1	b_0	1.07	a_2	0.0	$d_{2,G}$	0.2234
m_G	0.0	a_0	2.299E-4	$d'_{1,G}$	60.0	$d_{3,G}$	30554.4
$R_{G,min}$	0.0	a_1	0.0	$d''_{1,G}$	0.0	$d_{4,G}$	0.75

Table A.11: Layer 6: Calibrated parameters of the nonlinear model.

G_0 (MPa)	259.1	b_0	1.17	a_2	0.0	$d_{2,G}$	0.215
m_G	0.0	a_0	2.386E-4	$d'_{1,G}$	71.1	$d_{3,G}$	2600.0
$R_{G,min}$	0.0	a_1	0.0	$d''_{1,G}$	0.0	$d_{4,G}$	0.6818

Table A.12: Layer 7: Calibrated parameters of the nonlinear model.

G_0 (MPa)	370.2	b_0	1.07	a_2	0.0	$d_{2,G}$	0.1919
m_G	0.0	a_0	3.0384E-4	$d'_{1,G}$	89.3	$d_{3,G}$	6000.0
$R_{G,min}$	0.0	a_1	0.0	$d''_{1,G}$	0.0	$d_{4,G}$	0.5769

Table A.13: Layer 8: Calibrated parameters of the nonlinear model.

G_0 (MPa)	370.2	b_0	1.18	a_2	0.0	$d_{2,G}$	0.1984
m_G	0.0	a_0	7.712E-4	$d'_{1,G}$	39.2	$d_{3,G}$	2000.0
$R_{G,min}$	0.0	a_1	0.0	$d''_{1,G}$	0.0	$d_{4,G}$	0.75

Table A.14: Layer 9: Calibrated parameters of the nonlinear model.

G_0 (MPa)	581.3	b_0	1.07	a_2	0.0	$d_{2,G}$	0.19
m_G	0.0	a_0	3.918E-4	$d'_{1,G}$	34.8	$d_{3,G}$	5000.0
$R_{G,min}$	0.0	a_1	0.0	$d''_{1,G}$	0.0	$d_{4,G}$	0.625

Table A.15: Layer 10: Calibrated parameters of the nonlinear model.

G_0 (MPa)	495.3	b_0	1.07	a_2	0.0	$d_{2,G}$	0.1935
m_G	0.0	a_0	3.319E-4	$d'_{1,G}$	87.9	$d_{3,G}$	5600.0
$R_{G,min}$	0.0	a_1	0.0	$d''_{1,G}$	0.0	$d_{4,G}$	0.577

Table A.16: Layer 11: Calibrated parameters of the nonlinear model.

G_0 (MPa)	791.9	b_0	1.18	a_2	0.0	$d_{2,G}$	0.1952
m_G	0.0	a_0	3.743E-4	$d'_{1,G}$	78.8	$d_{3,G}$	5000.0
$R_{G,min}$	0.0	a_1	0.0	$d''_{1,G}$	0.0	$d_{4,G}$	0.625

Table A.17: Layer 12: Calibrated parameters of the nonlinear model.

G_0 (MPa)	791.9	b_0	1.18	a_2	0.0	$d_{2,G}$	0.2
m_G	0.0	a_0	1.02E-3	$d'_{1,G}$	33.3	$d_{3,G}$	2000.0
$R_{G,min}$	0.0	a_1	0.0	$d''_{1,G}$	0.0	$d_{4,G}$	0.75

Table A.18: Layer 13: Calibrated parameters of the nonlinear model.

G_0 (MPa)	791.9	b_0	1.07	a_2	0.0	$d_{2,G}$	0.2
m_G	0.0	a_0	3.607E-4	$d'_{1,G}$	49.9	$d_{3,G}$	10000.0
$R_{G,min}$	0.0	a_1	0.0	$d''_{1,G}$	0.0	$d_{4,G}$	0.6818

Table A.19: Layer 14: Calibrated parameters of the nonlinear model.

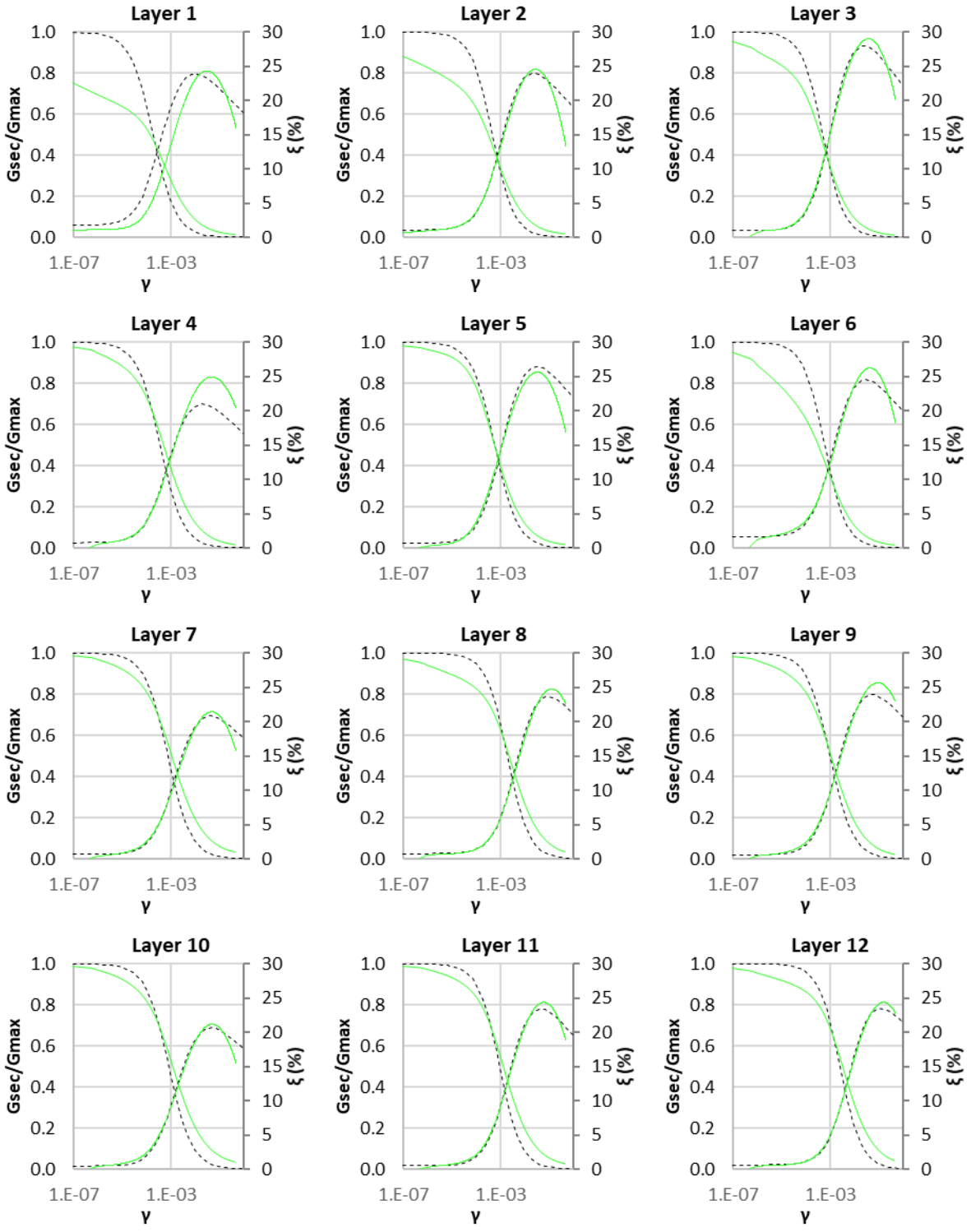
G_0 (MPa)	1077.9	b_0	1.07	a_2	0.0	$d_{2,G}$	0.1938
m_G	0.0	a_0	3.681E-4	$d'_{1,G}$	84.5	$d_{3,G}$	8000.0
$R_{G,min}$	0.0	a_1	0.0	$d''_{1,G}$	0.0	$d_{4,G}$	0.625

Table A.20: Layer 15: Calibrated parameters of the nonlinear model.

G_0 (MPa)	1077.9	b_0	1.07	a_2	0.0	$d_{2,G}$	0.1938
m_G	0.0	a_0	4.051E-4	$d'_{1,G}$	80.8	$d_{3,G}$	8000.0
$R_{G,min}$	0.0	a_1	0.0	$d''_{1,G}$	0.0	$d_{4,G}$	0.625

Table A.21: Layer 16: Calibrated parameters of the nonlinear model.

G_0 (MPa)	2499.5	b_0	1.07	a_2	0.0	$d_{2,G}$	0.1941
m_G	0.0	a_0	3.508E-4	$d'_{1,G}$	86.7	$d_{3,G}$	9000.0
$R_{G,min}$	0.0	a_1	0.0	$d''_{1,G}$	0.0	$d_{4,G}$	0.625



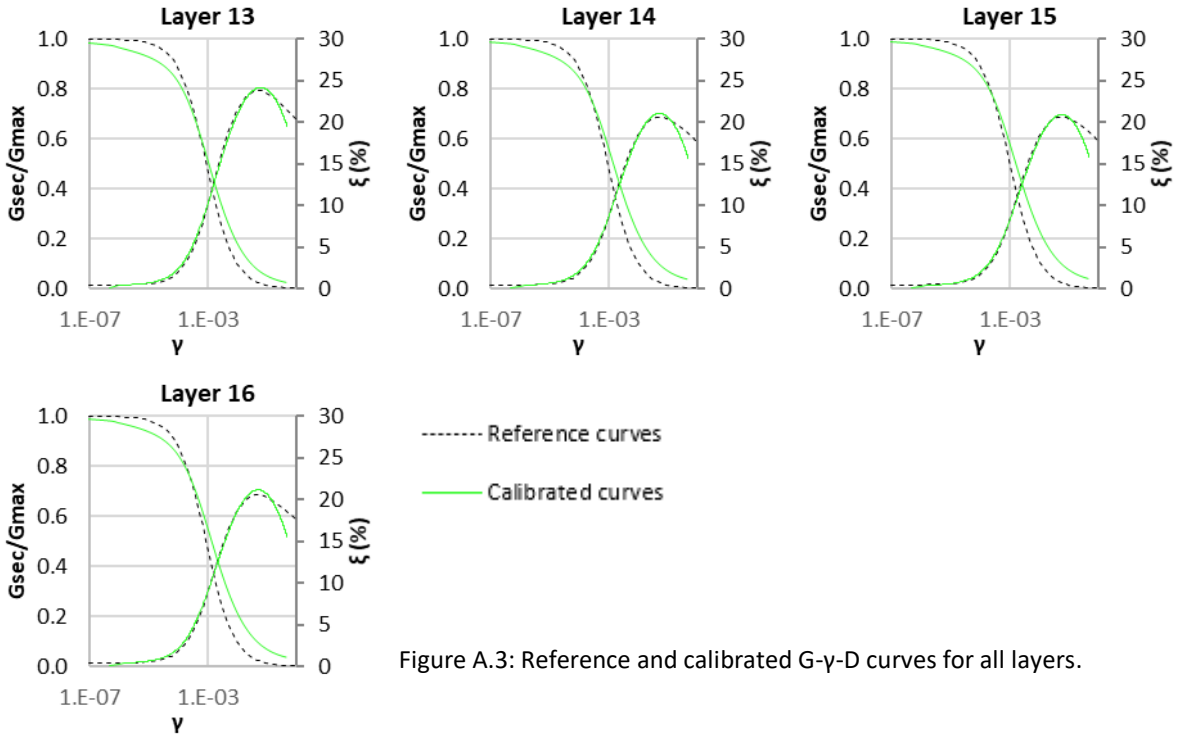


Figure A.3: Reference and calibrated G-γ-D curves for all layers.

Appendix A.5 EQL approach description

The equivalent linear analysis follows the steps (Kramer, 1996):

1) Input for each layers G-γ-D curves, elastic properties G_{max}, ξ_{min}, density and the thickness H.
2) Input the acceleration time history motion at bedrock level either as downhole ("within") or outcrop record.
3) Express the acceleration time history in the form of Fourier series, using Fourier Transforms
4) For each layer adopt the values of G and ξ of the first iteration: $G_1 = G_{max}$, $\xi_1 = \xi_{min}$.
5) Compute the transfer functions that relates the displacement/velocity/acceleration amplitude between two successive layers or between bedrock (input) and surface. Eq. 4.2 expresses the amplification of the above quantities from layer i to layer j.

$$F_{ij} = \frac{|u_i|}{|u_j|} = \frac{a_i(\omega) + b_i(\omega)}{a_j(\omega) + b_j(\omega)} \quad \text{A.1}$$

6) Multiply each term of input motion Fourier series by the appropriate transfer function to produce output motions at the surface at intermediate levels.
7) Apply inverse Fourier transform to express the output motions in the time domain.
8) Determine the maximum shear strain (γ_{max}) and then the effective one for each layer: $\gamma_{eff} = 0.6 \times \gamma_{max}$
9) Using the G-γ-D curves determine the G and ξ of the next iteration that correspond to γ_{eff}

10) Check convergence between two successive iterations for each layer: $\frac{G^{i-1}-G^{i}}{G^{i-1}}$ and $\frac{\xi^{i-1}-\xi^{i}}{\xi^{i-1}} <$ torelarce level (chosen 2%), where i is the current iteration.
11) If true, exit iteration process and the final stiffness and damping values are given by using G^{i} and ξ^{i}. If false, use the resulted G^{i} and ξ^{i} for a new iteration by returning to the step 5.

Appendix A.6 Imperial College Generalised Small Strain Stiffness (IC.G3S) Model

Detailed description of the IC.G3S model can be found in Taborda et al. (2016), while herein the equations and features of the model relevant to the current study are presented.

Stiffness at very small strains

The shear modulus at very small strains, G_{max}, as per Eq. A.2. It is a function of the current mean effective stress (p'), an m_G factor that controls the dependency of G_{max} on the mean effective stress p' and a shear stiffness G_0 that corresponds to a reference confining pressure p'_{ref}. G_{max} also depends on void ratio through the function f(e), which though is neglected in this study.

$$G_{max} = G_0 \cdot f(e) \cdot \left(\frac{p'}{p'_{ref}}\right)^{m_G} \quad \text{A.2}$$

Stiffness variation with deformation level

The tangential shear stiffness (G_{tan}) degrades with the accumulation deviatoric shear strain since the last reversal (E_d^*) as per Eq. A.3. The degradation is a function of a scaling factor n_G and $R_{G,min}$ that limits the degradation of shear stiffness. It is also a function of parameters *a* and *b* that incorporate the dependence of the degradation on the stress state (p') and the loading direction through the functions $i_a(\theta)$ and $i_b(\theta)$, as shown in Eqs. A.4 and A.5. Herein, both functions are set equal to unity to ignore the effect of loading direction. Parameters a_0, a_1 and a_2 incorporated in the calculation of *a* are calibrated to determine the horizontal position of the degradation curve, while b_0 parameter incorporated in the calculation of *b* is calibrated to determine the rate of degradation.

$$G_{tan} = G_{max} \cdot \left(R_{G,min} + \frac{(1 - R_{G,min})}{1 + \left(\frac{E_d^*}{n_G \cdot \alpha}\right)^b} \right) \geq G_{min} \quad \text{A.3}$$

$$\alpha = i_a(\theta) \cdot \left(\alpha_0 + \alpha_1 \cdot \left(\frac{p'}{p'_{ref}}\right)^{a_2} \right) \quad \text{A.4}$$

$$b = i_b(\theta) \cdot b_0 \quad \text{A.5}$$

The scaling factor n_G incorporated in Eq. A.3 for the calculation of G_{tan} degradation with E_d^* takes a value equal to 1 for monotonic loading, while it becomes strain dependent when a reversal is detected

according to Eq. A.6. The scaling factor is a function of a number of parameters ($d_{1,G}$, $d_{2,G}$, $d_{3,G}$, $d'_{1,G}$, $d''_{1,G}$) required calibration. $d_{1,G}$ parameter, computed as per Eq. A.7, expresses the impact of mean effective stress on the variation of damping ration with strain level.

$$n_G = (d_{1,G} + 2)^{E_d^{*\,d_{2,G}}} \cdot \left(\frac{(d_{3,G} + 1) \cdot E_d^*}{1 + (d_{3,G} + 1) \cdot E_d^*} \right)^{d_{4,G}} \quad \text{A.6}$$

where:

$$d_{1,G} = d'_{1,G} + d''_{1,G} \cdot \ln\left(\frac{p'}{p'_{ref}}\right) \quad \text{A.7}$$

Calculation of deformation level

The deviatoric strain (E_d) for a given strain state ε_i, is calculated as:

$$E_d(\varepsilon_i) = \frac{2}{\sqrt{6}} \sqrt{(\varepsilon_1 - \varepsilon_2)^2 + (\varepsilon_2 - \varepsilon_3)^2 + (\varepsilon_3 - \varepsilon_1)^2} \quad \text{A.8}$$

Reversal in deviatoric loading is detected when the following is satisfied:

$$E_d(\varepsilon_{i+1} - \varepsilon_{rev}) < E_d(\varepsilon_i - \varepsilon_{rev}) \quad \text{A.9}$$

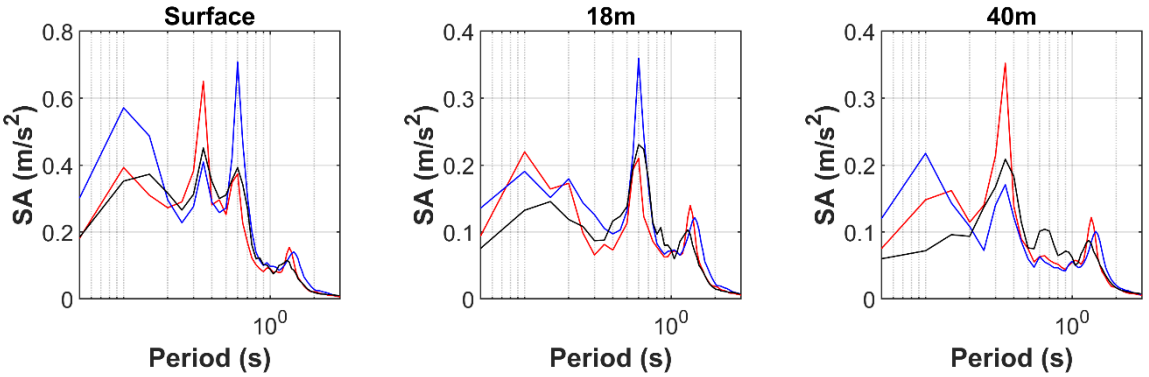
where, ε_{rev} is the strain state at the last known reversal.

E_d^*, which corresponds to the accumulation of deviatoric strain since the last reversal ($E_{d,r}$) is calculated as follows:

$$E_{d,i+1}^* = E_{d,i}^* + E_d(\varepsilon_{i+1} - \varepsilon_i) \quad \text{A.10}$$

Appendix A.7 Comparison between experimental and numerical data

The following figures compare strong motion data against EQL and NLIN data, resulted from numerical simulations of the 2006, 2013 and 2016 events, whose characteristics can be found in the Table 4.1. The comparison is made in terms of acceleration response spectra (ξ=5%).



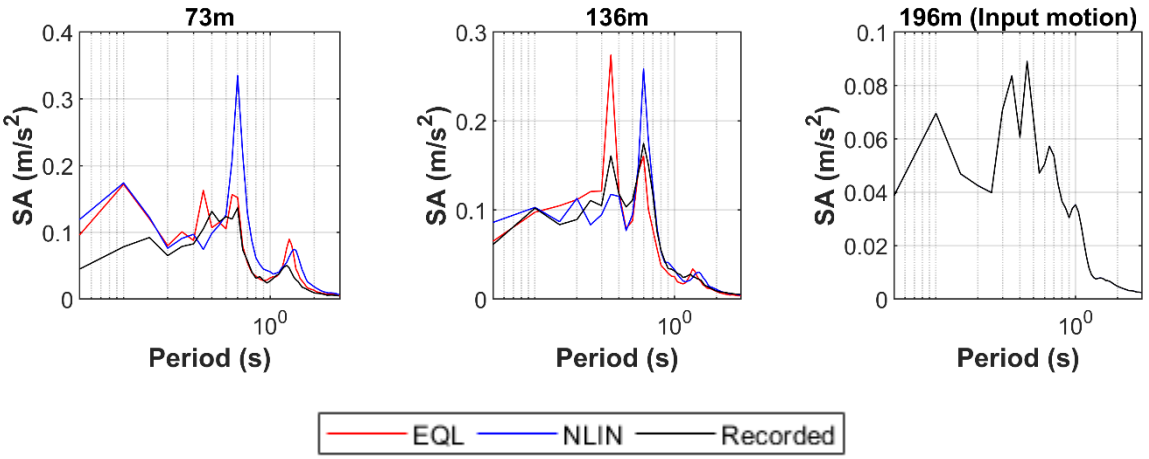
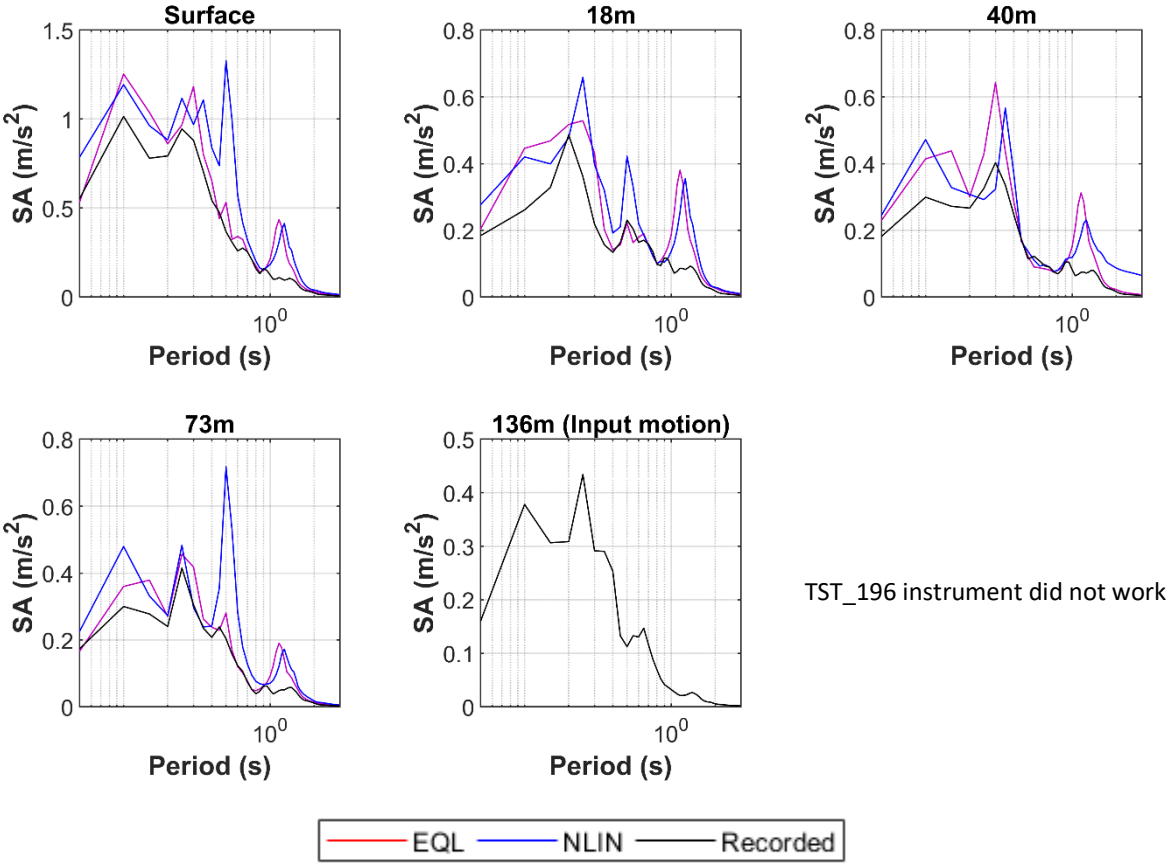


Figure A.4: Comparison of the recorded site response with results computed by EQL and NLIN analyses, that simulate the 2006 event. The results are presented in terms of acceleration response spectra at the locations where records are available.



TST_196 instrument did not work

Figure A.5: Comparison of the recorded site response with results computed by EQL and NLIN analyses, that simulate the 2013 event. The results are presented in terms of acceleration response spectra at the locations where records are available.

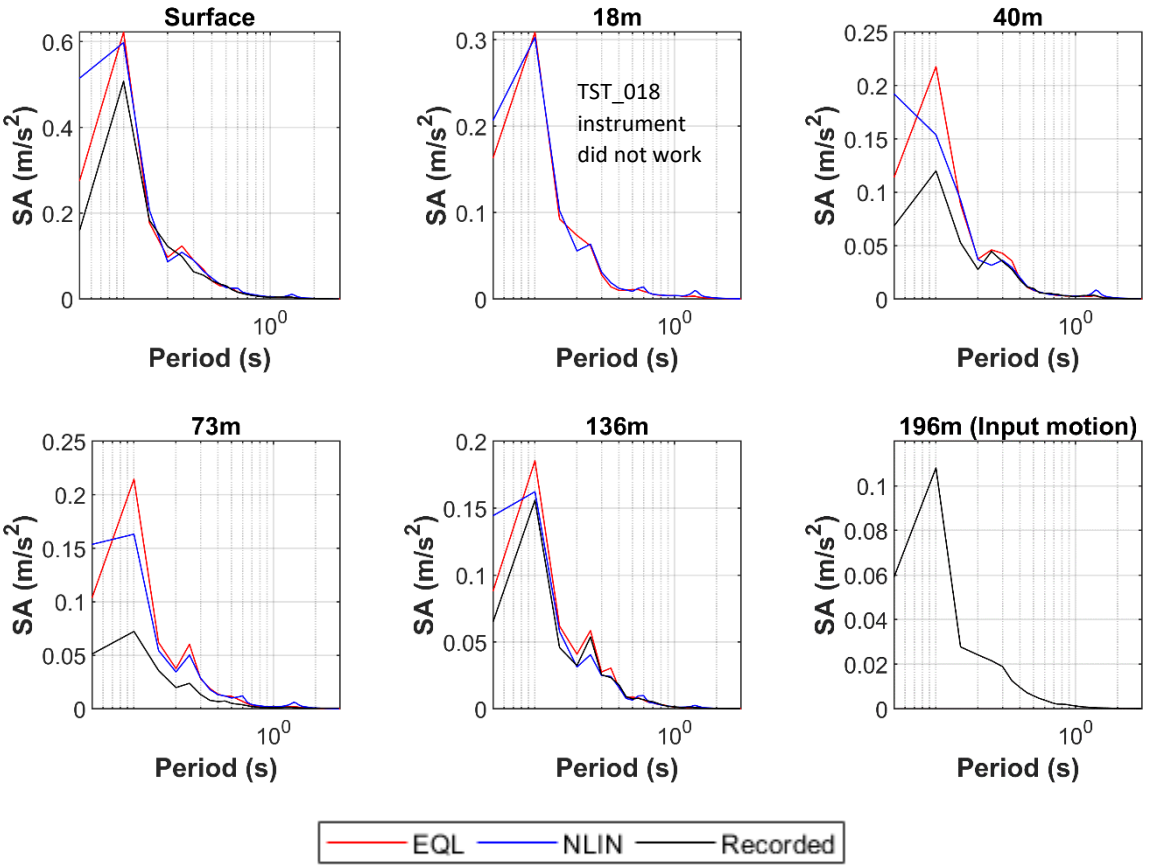


Figure A.6: Comparison of the recorded site response with results computed by EQL and NLIN analyses, that simulate the 2016 event. The results are presented in terms of acceleration response spectra at the locations where records are available.

Appendix B

Input excitation details

Appendix B.1 Forced vibration tests: applied frequencies

Tables B.1 to B.10 tabulate the applied frequencies for each mass combination (mA-mD) placed on the vibrator during the forced vibration tests. The local (or conventional time when the local one is omitted) time when each frequency was imposed is also stated, from which the time duration of each frequency can be inferred. Each frequency was kept constant for about 30 to 60 seconds, so that the steady state motion is achieved for each frequency.

Table B.1: Applied frequencies and for vibrator masses during exp1 (03/04/2019)

No	mA		mB		mC		mD	
	Local Time	F(Hz)	Local Time	F(Hz)	Local Time	F(Hz)	Local Time	F(Hz)
1	11:42	0.97	13:20	1.00	14:28	1.00	15:03	1.03
2	11:44	1.97	13:22	2.00	14:30	2.00	15:05	2.00
3	11:45	2.50	13:23	2.50	14:31	2.50	15:06	2.50
4	11:46	3.00	13:24	2.97	14:32	2.73	15:07	2.73
5	11:47	3.53	13:25	3.50	14:33	3.00	15:08	3.03
6	11:48	4.00	13:26	3.97	14:34	3.23	15:09	3.23
7	11:49	4.50	13:27	4.47	14:35	3.50	15:10	3.50
8	11:50	5.03	13:28	5.03	14:36	3.77	15:11	3.73
9	11:51	6.03	13:29	6.00	14:37	4.00	15:12	4.03
10	11:52	7.00	13:30	6.97	14:38	4.53	15:13	4.53
11	11:53	7.50	13:31	7.50	14:39	5.00	15:14	5.00
12	11:54	8.00	13:32	8.00	14:40	6.00	15:15	6.00
13	11:55	8.47	13:33	8.53	14:41	7.00	15:16	7.00
14	11:56	9.00	13:34	9.03	14:42	7.50	15:17	7.53
15	11:57	10.07	13:35	10.00	14:43	7.97	15:18	8.00
16	11:58	10.97	13:36	11.00				

Table B.2: Applied frequencies and for vibrator masses during exp2 (03/04/2019)

No	mA		mB		mC		mD	
	Local Time	F(Hz)	Local Time	F(Hz)	Local Time	F(Hz)	Local Time	F(Hz)
1	17:45	1.00	17:15	1.00	16:34	1.00	16:09	0.97
2	17:46	2.03	17:17	2.03	16:36	2.00	16:11	2.00
3	17:47	2.47	17:18	2.50	16:37	2.50	16:12	2.53
4	17:48	3.00	17:19	3.00	16:38	2.73	16:13	2.73
5	17:49	3.47	17:20	3.53	16:39	3.00	16:14	3.00
6	17:50	3.97	17:21	4.00	16:40	3.23	16:15	3.23
7	17:51	4.53	17:22	4.50	16:41	3.53	16:16	3.53
8	17:52	5.00	17:23	5.00	16:42	3.73	16:17	3.73
9	17:53	6.00	17:24	6.00	16:43	4.00	16:18	4.00
10	17:54	7.00	17:25	7.00	16:44	4.50	16:19	4.47
11	17:55	7.50	17:27	7.50	16:45	5.03	16:20	4.97
12	17:56	8.00	17:28	8.00	16:46	6.03	16:21	5.97
13	17:57	8.47	17:29	8.50	16:47	7.00	16:22	6.97
14	17:58	9.03	17:30	9.03	16:48	7.53	16:23	7.53
15	17:59	10.00	17:31	10.03	16:49	8.00	16:24	8.00
16			17:32	11.03				

Table B.3: Applied frequencies and for vibrator masses during exp5 (03/04/2019)

No	mass A		mB		mC		mD	
	Local Time	F(Hz)	Local Time	F(Hz)	Local Time	F(Hz)	Local Time	F(Hz)
1	14:29	1.00	15:00	1.00	15:26	1.00	15:47	1.00
2	14:31	2.00	15:02	2.00	15:28	2.03	15:48	2.00
3	14:32	2.50	15:03	2.50	15:29	2.53	15:49	2.50
4	14:33	3.00	15:04	3.00	15:30	2.73	15:50	2.77
5	14:34	3.50	15:05	3.53	15:31	3.00	15:51	2.97
6	14:35	4.00	15:06	4.00	15:32	3.23	15:52	3.27
7	14:36	4.53	15:07	4.53	15:33	3.53	15:53	3.53
8	14:37	5.00	15:08	5.03	15:34	3.77	15:54	3.77
9	14:38	6.00	15:09	6.00	15:35	4.00	15:55	4.00
10	14:39	7.03	15:10	7.00	15:36	4.50	15:56	4.50
11	14:40	7.50	15:11	7.50	15:37	5.00	15:57	5.00
12	14:41	8.00	15:12	8.00	15:38	6.00	15:58	6.00
13	14:42	8.53	15:13	8.50	15:39	7.00	15:59	7.00
14	14:43	9.03	15:14	9.00	15:40	7.50	16:00	7.50
15	14:44	10.03	15:15	10.00	15:41	8.00	16:01	8.00
16	14:45	11.00	15:16	11.00				

Table B.4: Applied frequencies and for vibrator masses during exp7 (04/04/2019)

No	mB		mC		mD	
	Local Time	F(Hz)	Local Time	F(Hz)	Local Time	F(Hz)
1	13:32	0.67	12:00	0.33	11:03	0.37
2	13:33:40	1.00	12:02	0.67	11:05	0.63
3	13:34:20	1.33	12:03	1.00	11:06	1.00
4	13:35:00	1.70	12:04	1.30	11:07	1.33
5	13:35:40	2.00	12:05	1.67	11:08	1.67
6	13:36:20	2.53	12:06	2.00	11:09	2.00
7	13:37:00	3.00	12:07	2.50	11:10	2.50
8	13:37:40	3.50	12:08	3.00	11:11	3.00
9	13:38:20	4.00	12:09	3.50	11:12	3.50
10	13:39:00	4.53	12:10	4.00	11:13	4.00
11	13:39:40	5.00	12:11	4.47	11:14	4.50
12	13:40:20	5.97	12:12	5.03	11:15	5.03
13	13:41:00	7.03	12:13	6.00	11:16	5.97
14			12:14	7.00	11:17	7.00

Table B.5: Applied frequencies and for vibrator masses during exp8 (04/04/2019)

No	mB		mC		mD	
	Local Time	F(Hz)	Local Time	F(Hz)	Local Time	F(Hz)
1	13:17:00	1.00	12:29	0.97	11:27	1.03
2	13:17:40	2.03	12:31	2.03	11:29	2.00
3	13:18:20	2.53	12:32	2.47	11:30	2.50
4	13:19:00	2.77	12:33	2.73	11:31	2.73
5	13:19:40	3.00	12:34	3.00	11:32	3.00
6	13:20:20	3.27	12:35	3.23	11:33	3.27
7	13:21:00	3.53	12:36	3.50	11:34	3.50
8	13:21:40	3.73	12:37	3.73	11:35	3.77
9	13:22:20	4.00	12:38	3.97	11:36	4.00
10	13:23:00	4.53	12:39	4.50	11:37	4.50
11	13:23:40	5.03	12:40	5.03	11:38	5.03
12	13:24:20	5.50	12:41	5.50	11:39	6.00
13	13:25:00	6.00	12:42	5.97	11:40	6.97
14	13:25:40	6.50	12:43	6.50	11:41	7.50
15	13:26:20	7.00	12:44	6.97	12:42	8.00
16	13:27:00	7.50	12:45	7.50		
17	13:27:40	8.00	12:46	8.00		

Table B.6: Applied frequencies and for vibrator masses during exp9 (04/04/2019)

No	mB		mC		mD	
	Local Time	F(Hz)	Local Time	F(Hz)	Local Time	F(Hz)
1	15:08:00	0.63	15:40	0.70	16:18	0.70
2	15:09:40	0.97	15:41:40	1.00	16:19:40	1.00
3	15:10:20	1.37	15:42:20	1.33	16:20:20	1.37
4	15:11:00	1.67	15:43:00	1.67	16:21:00	1.67
5	15:11:40	2.00	15:43:40	1.97	16:21:40	2.00
6	15:12:20	2.50	15:44:20	2.50	16:22:20	2.53
7	15:13:00	3.00	15:45:00	3.00	16:23:00	3.00
8	15:13:40	3.53	15:45:40	3.50	16:23:40	3.50
9	15:14:20	4.00	15:46:20	4.03	16:24:20	4.00
10	15:15:00	4.53	15:47:00	4.50	16:25:00	4.50
11	15:15:40	5.00	15:47:40	5.00	16:25:40	5.00
12	15:16:20	6.00	15:48:20	6.03	16:26:20	6.03
13	15:17:00	6.97	15:49:00	7.00	16:27:00	7.00

Table B.7: Applied frequencies and for vibrator masses during exp10 (04/04/2019)

No	mB		mC		mD	
	Local Time	F(Hz)	Local Time	F(Hz)	Local Time	F(Hz)
1	15:21:00	1.00	16:00:xx	1.00	16:31	1.00
2	15:22:40	2.00	16:01:40	2.00	16:32:40	2.00
3	15:23:20	2.53	16:02:20	2.50	16:33:20	2.50
4	15:24:00	2.73	16:03:00	2.70	16:34:00	2.77
5	15:24:40	3.00	16:03:40	3.00	16:34:40	3.03
6	15:25:20	3.27	16:04:20	3.27	16:35:20	3.23
7	15:26:00	3.50	16:05:00	3.50	16:36:00	3.50
8	15:26:40	3.77	16:05:40	3.77	16:36:40	3.77
9	15:27:20	4.00	16:06:20	4.00	16:37:20	4.03
10	15:28:00	4.50	16:07:00	4.47	16:38:00	4.47
11	15:28:40	5.00	16:07:40	5.03	16:38:40	5.03
12	15:29:20	5.50	16:08:20	5.50	16:39:20	5.53
13	15:30:00	6.03	16:09:00	6.00	16:40:00	6.00
14	15:30:40	6.53	16:09:40	6.50	16:40:40	7.00
15	15:31:20	7.03	16:10:20	7.00	16:41:20	7.50
16	15:32:00	7.50	16:11:00	7.57	16:42:00	8.00
17	15:32:40	7.97	16:11:40	8.00		

Table B.8: Applied frequencies and for vibrator masses during exp12 (05/04/2019)

No	mB		mC		mD	
	Local Time	F(Hz)	Local Time	F(Hz)	Local Time	F(Hz)
1	11:01:00	0.63	10:30:xx	0.67	10:00:xx	0.70
2	11:02:40	1.03	10:31:00	1.03	10:02:40	1.03
3	11:03:20	1.37	10:31:40	1.37	10:03:20	1.33
4	11:04:00	1.70	10:32:20	1.70	10:04:00	1.67
5	11:04:40	2.00	10:33:00	2.03	10:04:40	2.00
6	11:05:20	2.50	10:33:40	2.50	10:05:20	2.50
7	11:06:00	3.00	10:34:20	3.00	10:06:00	3.00
8	11:06:40	3.50	10:35:00	3.50	10:06:40	3.53
9	11:07:20	4.00	10:35:40	4.00	10:07:20	4.00
10	11:08:00	4.50	10:36:20	4.53	10:08:00	4.50
11	11:08:40	4.97	10:37:00	5.00	10:08:40	4.97
12	11:09:20	6.03	10:37:40	6.03	10:09:20	6.03
13	11:10:00	7.03	10:38:20	6.93	10:10:00	6.93

Table B.9: Applied frequencies and for vibrator masses during exp13 (04/04/2019)

No	mB		mC		mD	
	Local Time	F(Hz)	Local Time	F(Hz)	Local Time	F(Hz)
1	11:13:00	1.00	10:40:xx	0.97	10:12:xx	1.00
2	11:14:40	2.00	10:41:00	1.97	10:13:40	2.00
3	11:15:20	2.50	10:41:40	2.50	10:14:20	2.50
4	11:16:00	2.73	10:42:20	2.77	10:15:00	2.73
5	11:16:40	3.03	10:43:00	3.03	10:15:40	3.03
6	11:17:20	3.23	10:43:40	3.23	10:16:20	3.23
7	11:18:00	3.53	10:44:20	3.50	10:17:00	3.47
8	11:18:40	3.77	10:45:00	3.70	10:17:40	3.70
9	11:19:20	4.00	10:45:40	4.03	10:18:20	4.00
10	11:20:00	4.50	10:46:20	4.50	10:19:00	4.50
11	11:20:40	5.00	10:47:00	5.00	10:19:40	4.97
12	11:21:20	5.53	10:47:40	5.47	10:20:20	5.50
13	11:22:00	5.97	10:48:20	6.00	10:21:00	6.00
14	11:22:40	6.47	10:49:00	6.50	10:21:40	6.50
15	11:23:20	7.03	10:49:40	7.00	10:22:20	6.97
16	11:24:00	7.50	10:50:20	7.47	10:23:00	7.50
17	11:24:40	8.00	10:51:00	8.00	10:23:40	8.00

Table B.10: Applied frequencies and for vibrator masses during exp14 (17/10/2019)

No	mC		mD	
	Conventional Time	F(Hz)	Conventional Time	F(Hz)
1	00:00:00	1.00	00:10:00	1.00
2	00:00:30	2.00	00:10:30	2.00
3	00:01:00	2.50	00:11:00	2.50
4	00:01:30	2.75	00:11:30	2.75
5	00:02:00	3.00	00:12:00	3.00
6	00:02:30	3.25	00:12:30	3.25
7	00:03:00	3.50	00:13:00	3.50
8	00:03:30	3.75	00:13:30	3.75
9	00:04:00	4.00	00:14:00	4.00
10	00:04:30	4.50	00:14:30	4.50
11	00:05:00	5.00	00:15:00	5.00
12	00:05:30	6.00	00:15:30	6.00
13	00:06:00	7.00	00:16:00	7.00
14	00:06:30	7.50	00:16:30	7.50
15	00:07:00	8.00	00:17:00	8.00

Appendix B.2 Free vibration tests: applied pull-out forces

Tables B.11, B.12 and B.13 list the magnitudes pull-out forces applied during the FBr_2Ts$^{(3)}$, FBr_2Ts$^{(4)}$ and PBr_W$^{(11)}$ respectively. The tables also show the date and local time when the wire of the pull-out system was cut and the structure became free to oscillate.

Table B.11: Magnitudes of the pull-out forces applied during the FBr_2Ts$^{(3)}$ experiment (exp3, 03/04/2019)

No	Local Time	Applied Force (KN)
1	11:24:00	2.94
2	11:38:00	6.38
3	11:43:08	10.10
4	11:49:56	15.70

Table B.12: Magnitudes of the pull-out forces applied during the FBr_2Ts$^{(4)}$ experiment (exp4, 03/04/2019)

No	Local Time	Applied Force (KN)
1	12:55:13	1.96
2	13:00:56	2.40
3	13:06:42	5.03
4	13:13:25	9.64
5	13:18:15	12.53

Table B.13: Magnitudes of the pull-out forces applied during the PBr_W(11) experiment (exp11, 04/04/2019)

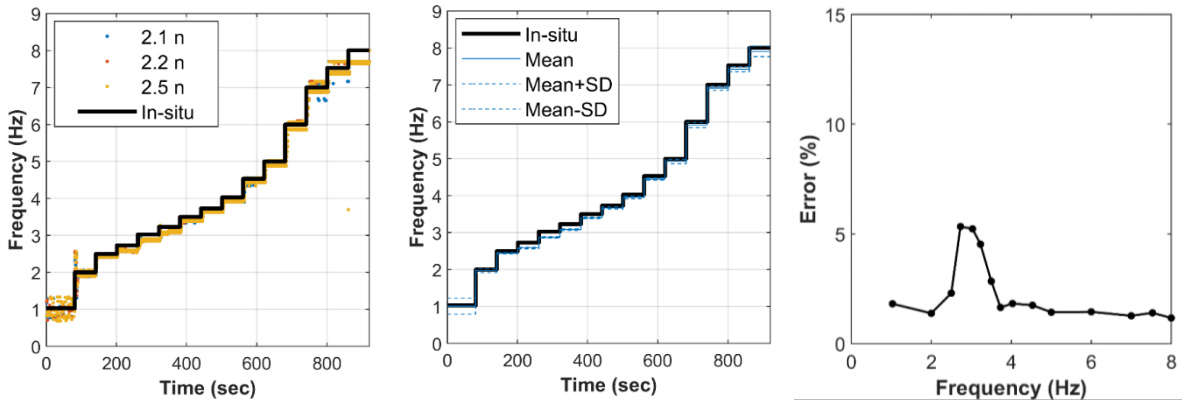
No	Local Time	Applied Force (KN)
1	12:55:13	1.96
2	13:00:56	2.40
3	13:06:42	5.03
4	13:13:25	9.64
5	13:18:15	12.53

Appendix C

Reliability of the experiments

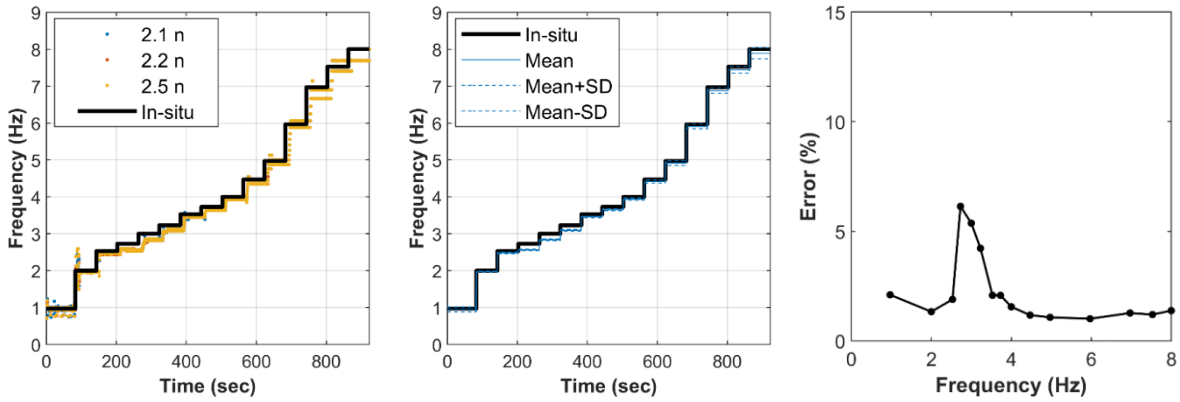
Appendix C.1 Vibrator reliability: Peak to Peak method

The following figures compare the frequency time history inferred from data of various experiments with the in-situ frequencies which were read out from the vibrator's speed drive during the experiment. The interpreted data were recorded by the top slab's instruments, 2.1n, 2.2n and 2.5n or 2.4n, when all four masses were placed on the vibrator (mD experiment). The mean values and the corresponding standard deviation of the calculated input frequencies are also plotted. Finally, the error that is calculated as $(F_{in\text{-}situ}\text{-}F_{mean}/F_{in\text{-}situ})*100$ is plotted for each applied frequency.



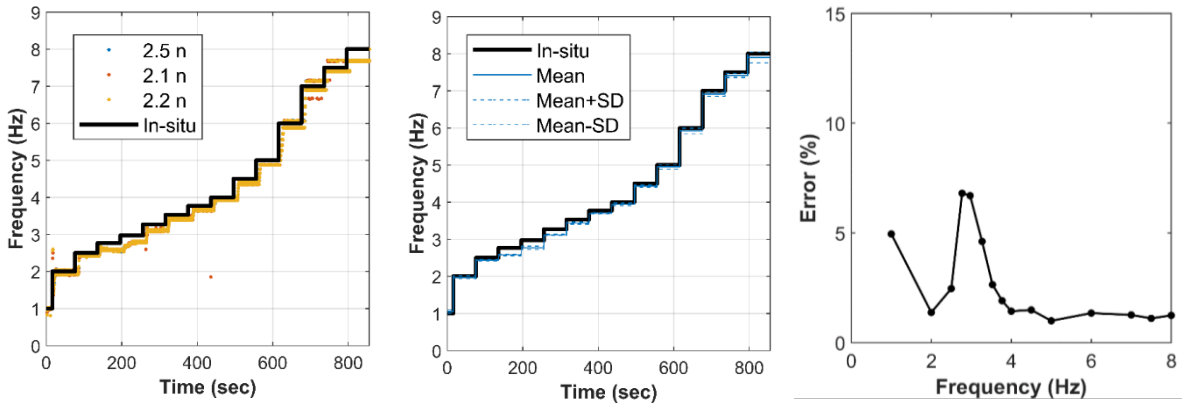
(a) (b) (c)

Figure C.1: Comparison between in-situ input frequency time history with (a) frequency time history inferred from top slab instruments and (b) mean frequency time history with the corresponding standard deviations. (c) error between the in-situ and estimated input frequencies. Data taken from the FBr_2Ts$^{(1)}$_mD experiment.



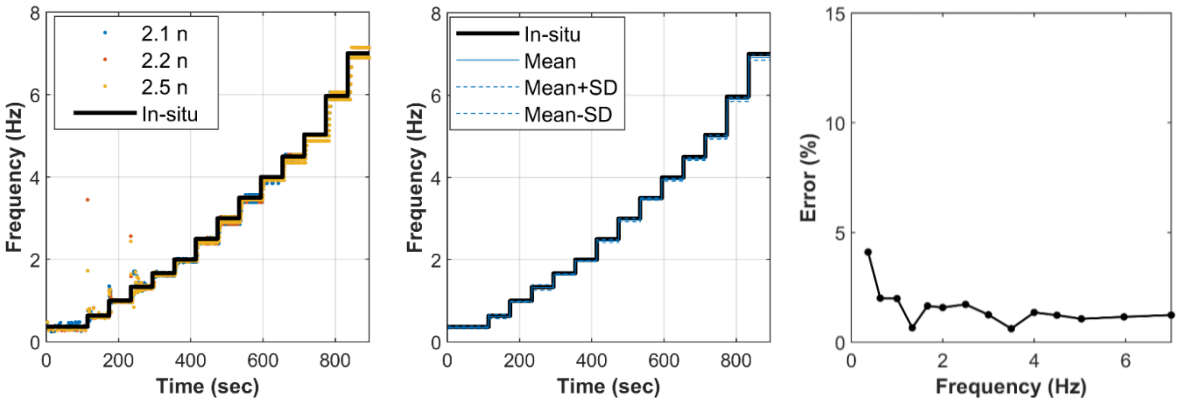
(a) (b) (c)

Figure C.2: Comparison between in-situ input frequency time history with (a) frequency time history inferred from top slab instruments and (b) mean frequency time history with the corresponding standard deviations. (c) error between the in-situ and estimated input frequencies. Data taken from the FBr_2Ts$^{(2)}$_mD experiment.



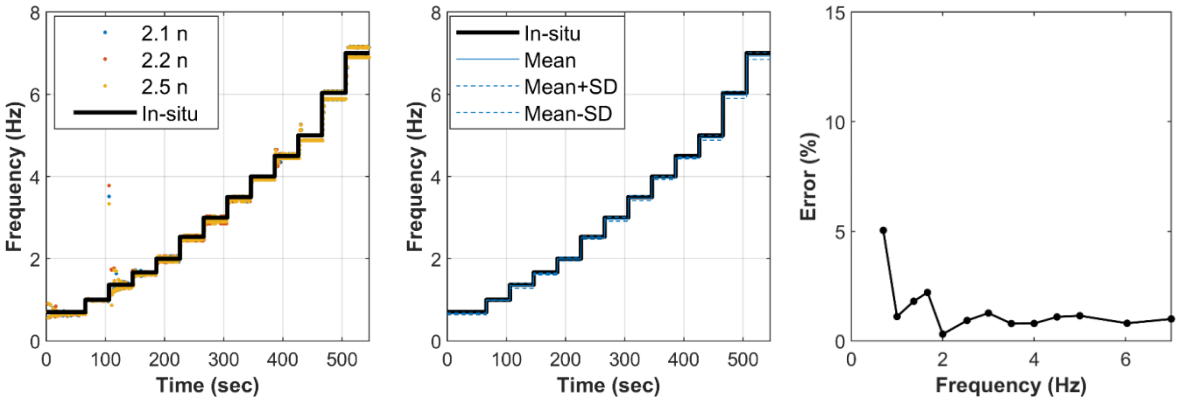
(a) (b) (c)

Figure C.3: Comparison between in-situ input frequency time history with (a) frequency time history inferred from top slab instruments and (b) mean frequency time history with the corresponding standard deviations. (c) error between the in-situ and estimated input frequencies. Data taken from the FBr_2Ts$^{(5)}$_mD experiment.



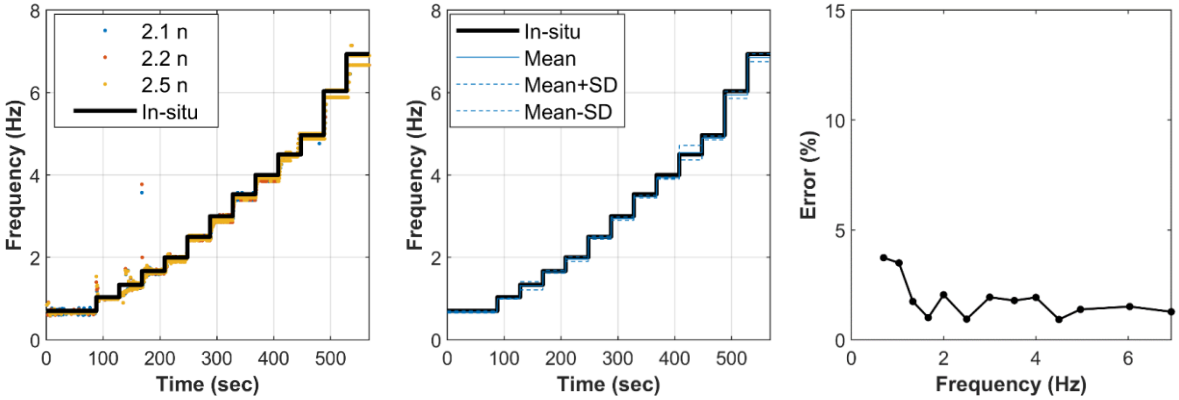
(a) (b) (c)

Figure C.4: Comparison between in-situ input frequency time history with (a) frequency time history inferred from top slab instruments and (b) mean frequency time history with the corresponding standard deviations. (c) error between the in-situ and estimated input frequencies. Data taken from the PBr_W$^{(7)}$_mD experiment.



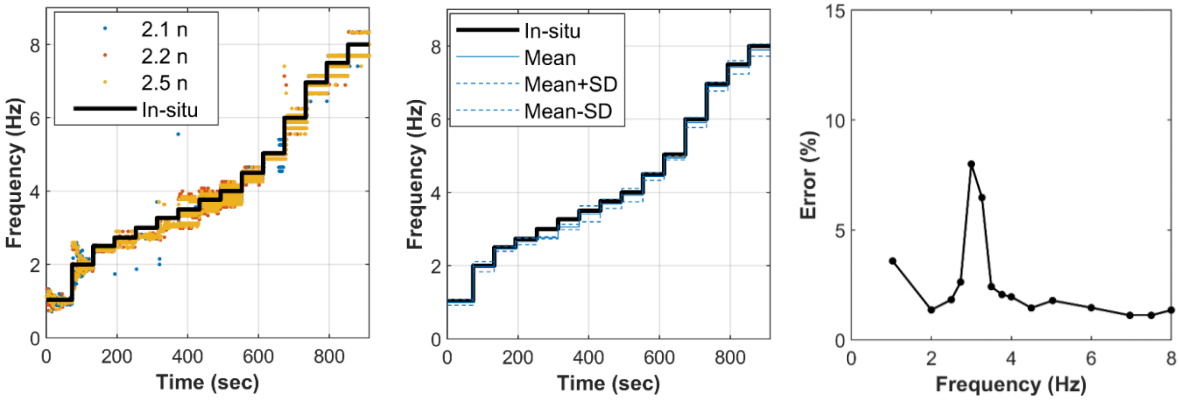
(a) (b) (c)

Figure C.5: Comparison between in-situ input frequency time history with (a) frequency time history inferred from top slab instruments and (b) mean frequency time history with the corresponding standard deviations. (c) error between the in-situ and estimated input frequencies. Data taken from the PBr_W$^{(9)}$_mD experiment.



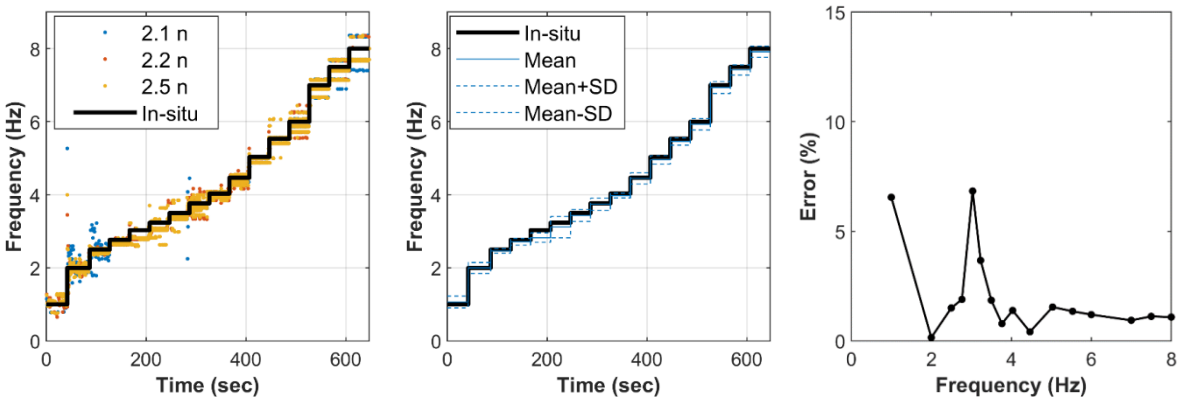
(a) (b) (c)

Figure C.6: Comparison between in-situ input frequency time history with (a) frequency time history inferred from top slab instruments and (b) mean frequency time history with the corresponding standard deviations. (c) error between the in-situ and estimated input frequencies. Data taken from the PBr_W$^{(12)}$_mD experiment.



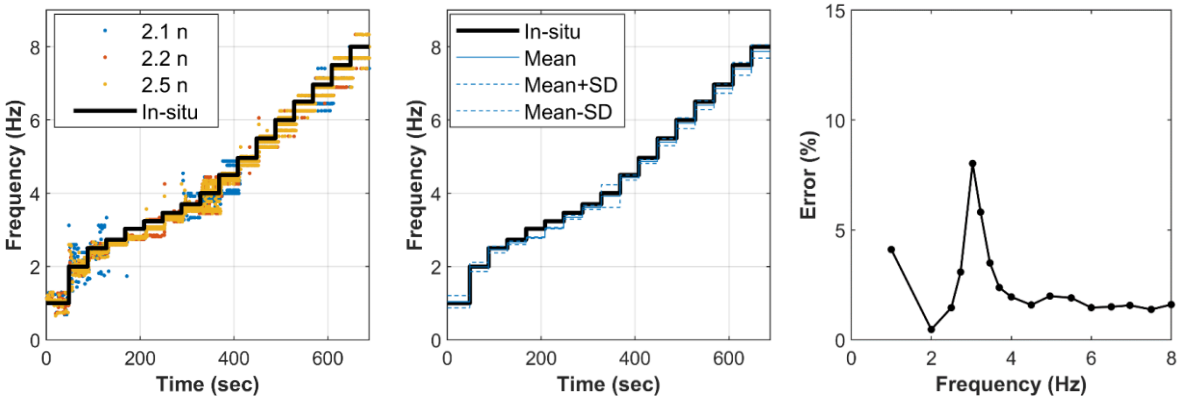
(a) (b) (c)

Figure C.7: Comparison between in-situ input frequency time history with (a) frequency time history inferred from top slab instruments and (b) mean frequency time history with the corresponding standard deviations. (c) error between the in-situ and estimated input frequencies. Data taken from the PBr_S$^{(8)}$_mD experiment.



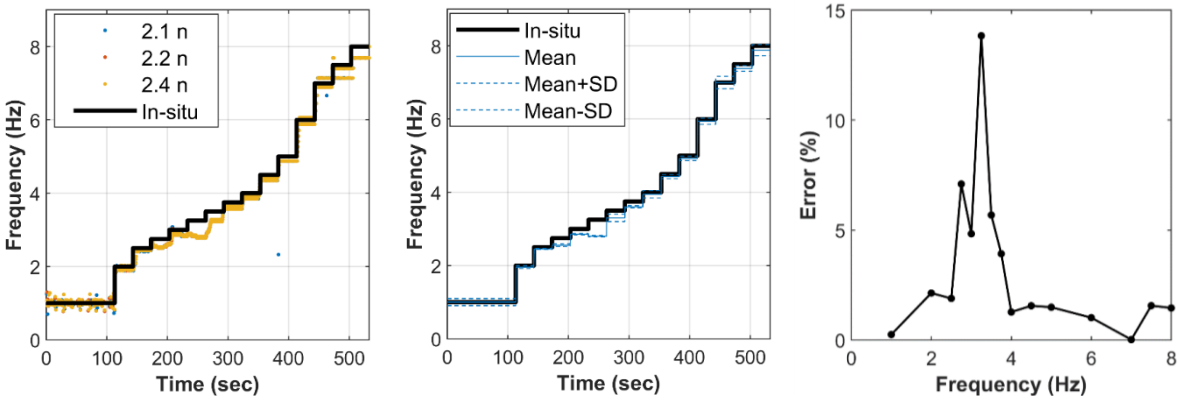
(a) (b) (c)

Figure C.8: Comparison between in-situ input frequency time history with (a) frequency time history inferred from top slab instruments and (b) mean frequency time history with the corresponding standard deviations. (c) error between the in-situ and estimated input frequencies. Data taken from the PBr_S$^{(10)}$_mD experiment.



(a) (b) (c)

Figure C.9: Comparison between in-situ input frequency time history with (a) frequency time history inferred from top slab instruments and (b) mean frequency time history with the corresponding standard deviations. (c) error between the in-situ and estimated input frequencies. Data taken from the PBr_S$^{(13)}$_mD experiment.

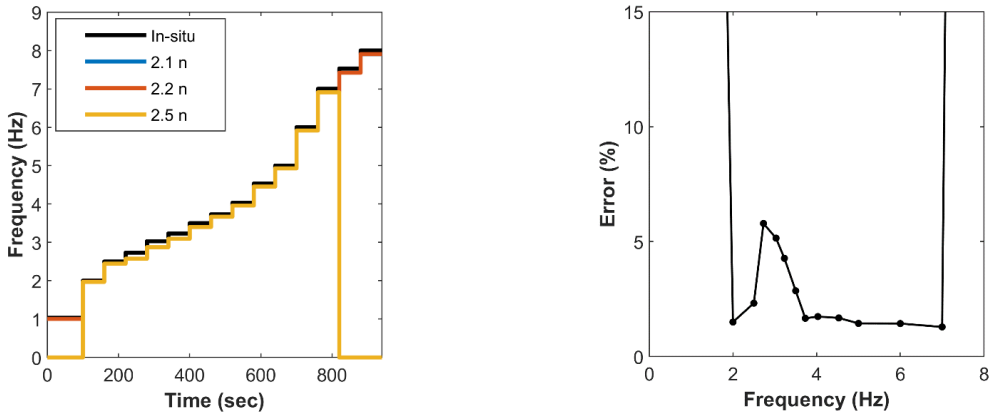


(a) (b) (c)

Figure C.10: Comparison between in-situ input frequency time history with (a) frequency time history inferred from top slab instruments and (b) mean frequency time history with the corresponding standard deviations. (c) error between the in-situ and estimated input frequencies. Data taken from the FBr_1TS$^{(14)}$_mD experiment.

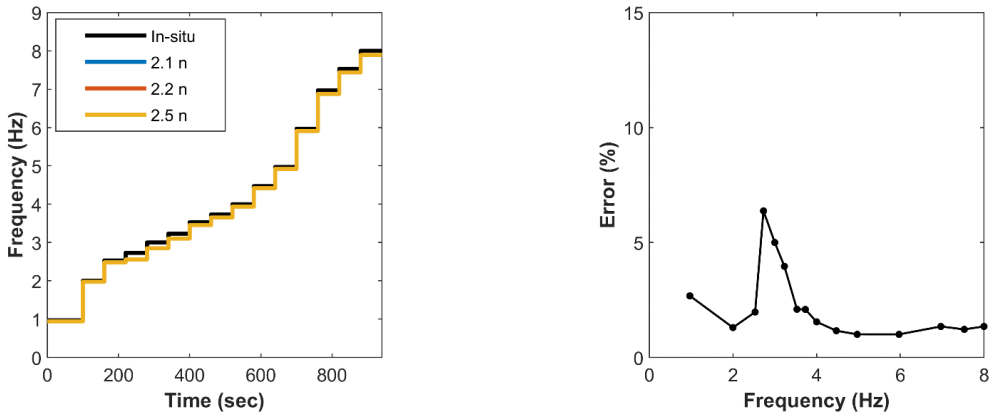
Appendix C.2 Vibrator reliability: Series of Fourier Spectra method

The following figures compare the frequency time history computed by employing the Series of Fourier Spectra (SoFS) method with the in-situ frequencies which were read out from the vibrator's speed drive during the experiments. The results were inferred from data that were recorded during different experiments when all four masses were placed on the vibrator. The data were recorded by the top slab's instruments, 2.1n, 2.2n and 2.5n or 2.4n. The error between each in-situ and calculated frequency exploiting the records of the 2.5n instrument, that is calculated as $(F_{in\text{-}situ}\text{-}F_{mean}/F_{in\text{-}situ})*100$, is also plotted.



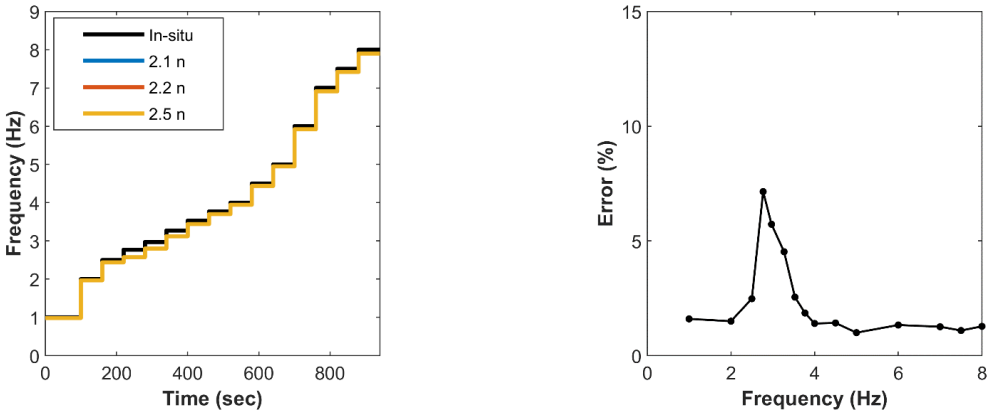
(a) (b)

Figure C.11: (a) Comparison between the frequency time history read out in-situ from the vibrator's speed drive with the one calculated by employing the SoFS method. (b) Error between in-situ frequencies and frequencies that were calculated by exploiting the 2.5n data. Data taken from the FBr_2Ts$^{(1)}$_mD experiment



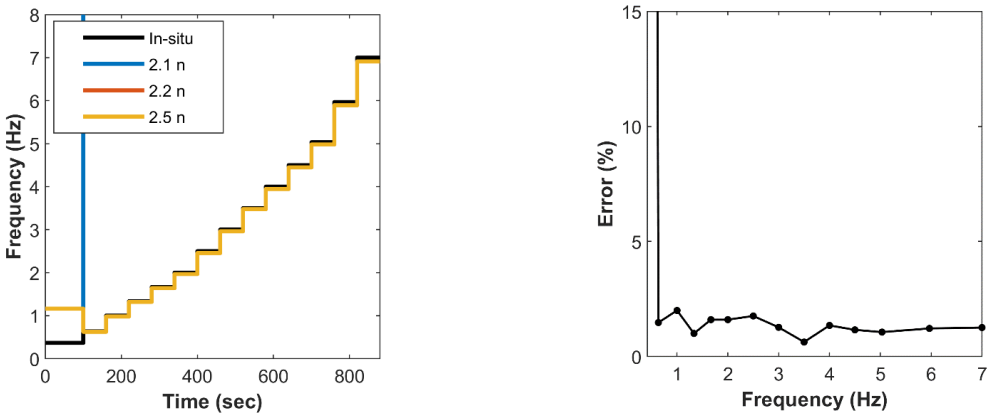
(a) (b)

Figure C.12: (a) Comparison between the frequency time history read out in-situ from the vibrator's speed drive with the one calculated by employing the SoFS method. (b) Error between in-situ frequencies and frequencies that were calculated by exploiting the 2.5n data. Data taken from the FBr_2Ts$^{(2)}$_mD experiment



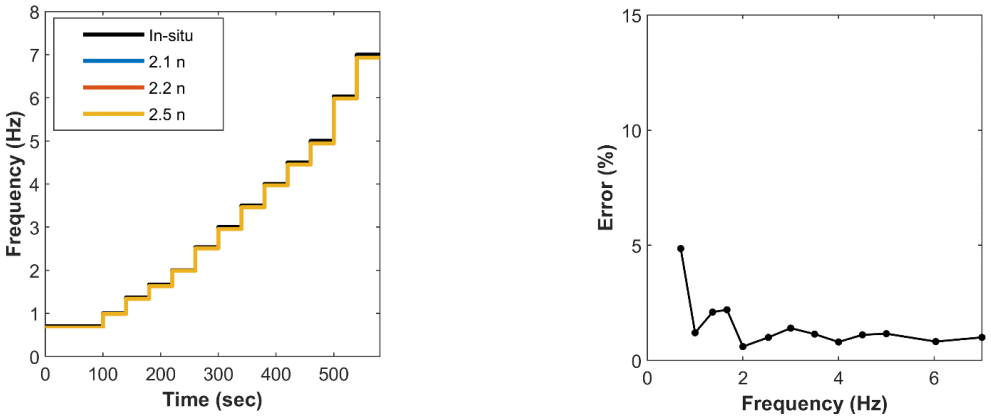
(a) (b)

Figure C.13: (a) Comparison between the frequency time history read out in-situ from the vibrator's speed drive with the one calculated by employing the SoFS method. (b) Error between in-situ frequencies and frequencies that were calculated by exploiting the 2.5n data. Data taken from the FBr_2Ts$^{(5)}$_mD experiment



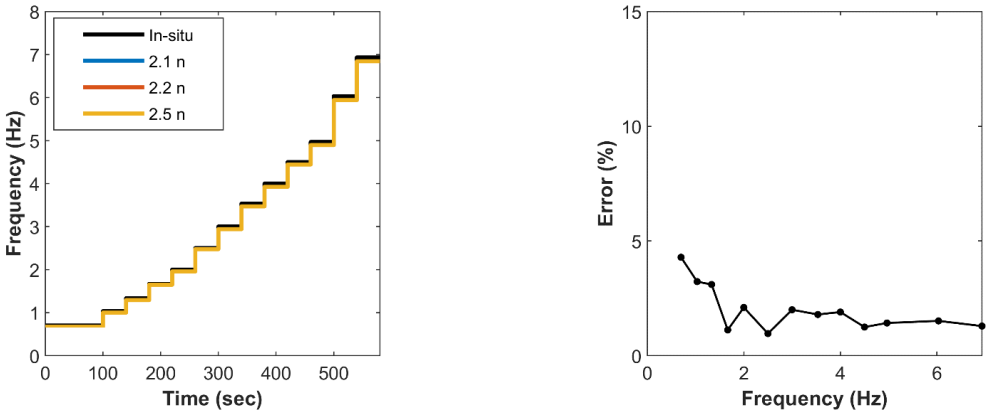
(a) (b)

Figure C.14: (a) Comparison between the frequency time history read out in-situ from the vibrator's speed drive with the one calculated by employing the SoFS method. (b) Error between in-situ frequencies and frequencies that were calculated by exploiting the 2.5n data. Data taken from the PBr_W$^{(7)}$_mD experiment



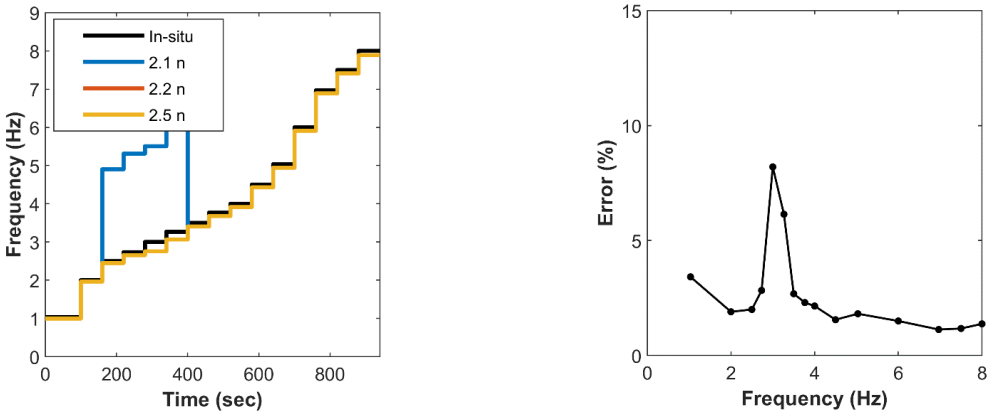
(a) (b)

Figure C.15: (a) Comparison between the frequency time history read out in-situ from the vibrator's speed drive with the one calculated by employing the SoFS method. (b) Error between in-situ frequencies and frequencies that were calculated by exploiting the 2.5n data. Data taken from the PBr_W$^{(9)}$_mD experiment



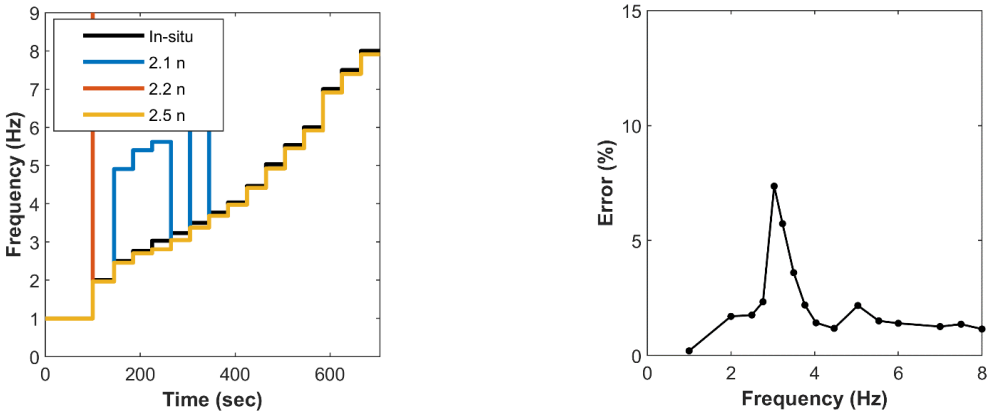
(a) (b)

Figure C.16: (a) Comparison between the frequency time history read out in-situ from the vibrator's speed drive with the one calculated by employing the SoFS method. (b) Error between in-situ frequencies and frequencies that were calculated by exploiting the 2.5n data. Data taken from the PBr_W$^{(12)}$_mD experiment



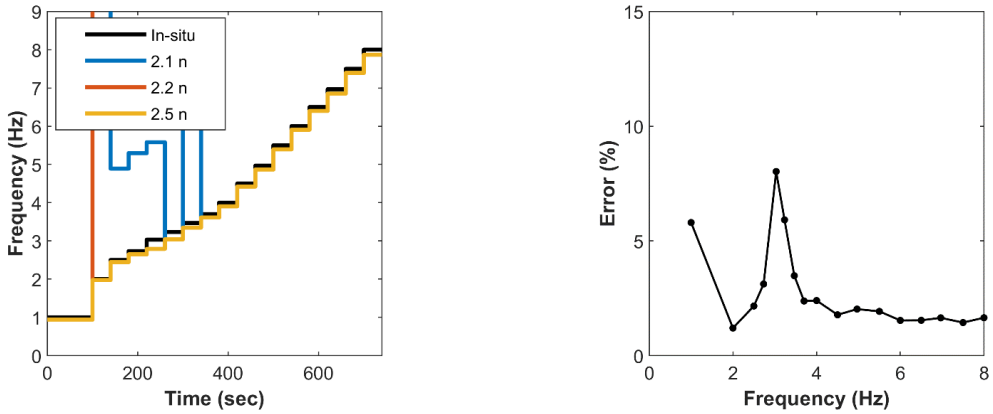
(a) (b)

Figure C.17: (a) Comparison between the frequency time history read out in-situ from the vibrator's speed drive with the one calculated by employing the SoFS method. (b) Error between in-situ frequencies and frequencies that were calculated by exploiting the 2.5n data. Data taken from the PBr_S$^{(8)}$_mD experiment



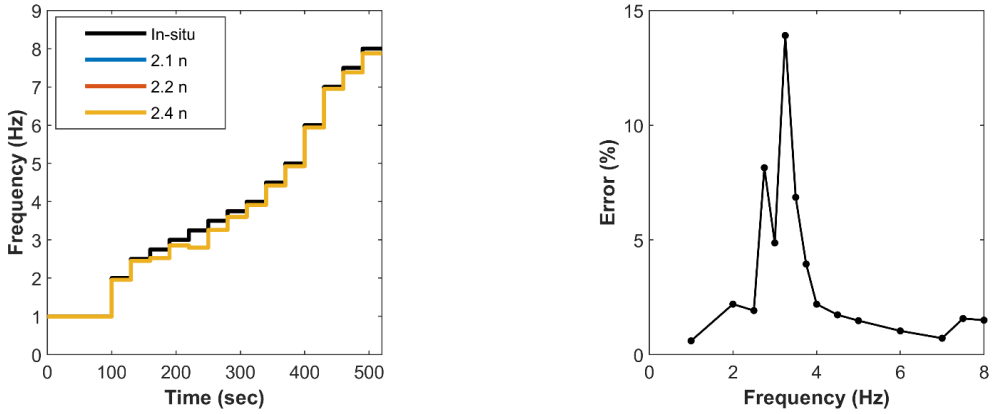
(a) (b)

Figure C.18: (a) Comparison between the frequency time history read out in-situ from the vibrator's speed drive with the one calculated by employing the SoFS method. (b) Error between in-situ frequencies and frequencies that were calculated by exploiting the 2.5n data. Data taken from the PBr_S$^{(10)}$_mD experiment



(a) (b)

Figure C.19: (a) Comparison between the frequency time history read out in-situ from the vibrator's speed drive with the one calculated by employing the SoFS method. (b) Error between in-situ frequencies and frequencies that were calculated by exploiting the 2.5n data. Data taken from the PBr_S$^{(13)}$_mD experiment



(a) (b)

Figure C.20: (a) Comparison between the frequency time history read out in-situ from the vibrator's speed drive with the one calculated by employing the SoFS method. (b) Error between in-situ frequencies and frequencies that were calculated by exploiting the 2.5n data. Data taken from the FBr_1Ts$^{(14)}$_mD experiment

Appendix C.3 Repeatability of data recorded during the Fully Braced 2-Top Slab experiments

The following figures compare the peak accelerations, recorded by various instruments for each applied frequency, during the Fully Braced 2-Top Slab experiments (FBr_2Ts). Three identical experiments (exp1, epx2 and exp3) are compared to each other. For each one, four different vibrator masses where used (mA, mB, mC and mD). Figures processed from data recorded by all structural

instruments available are presented. Also, all three North-South (n), East-West (e) and vertical (z) motion components are shown.

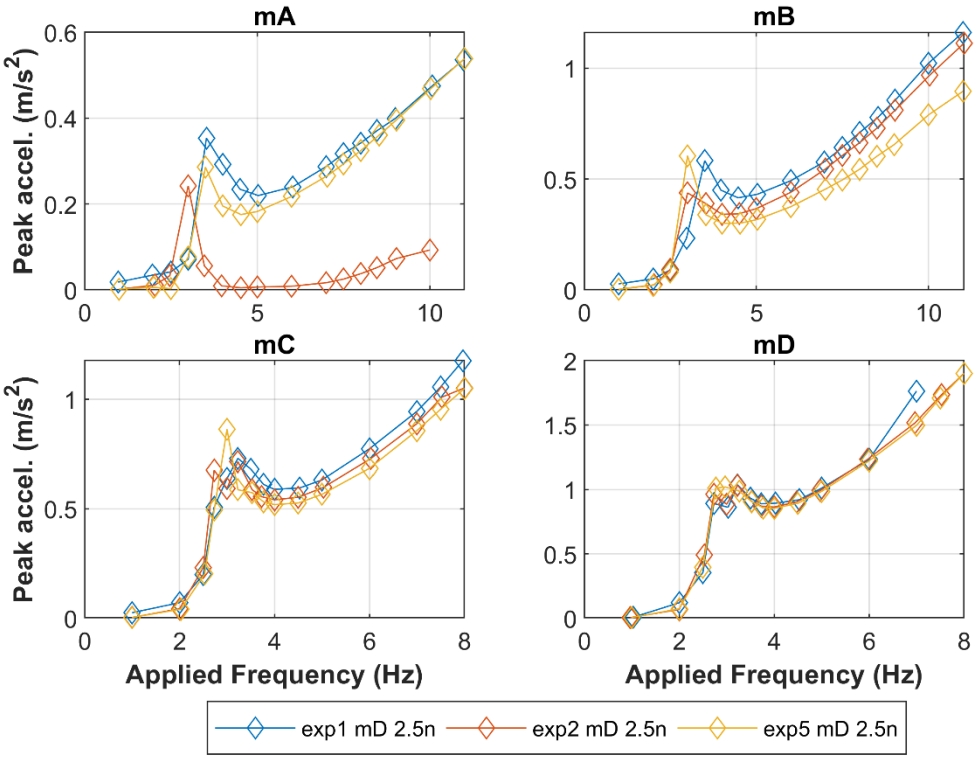


Figure C.21: Peak accelerations recorded along the North-South direction by the 2.5n instrument, at each applied frequency

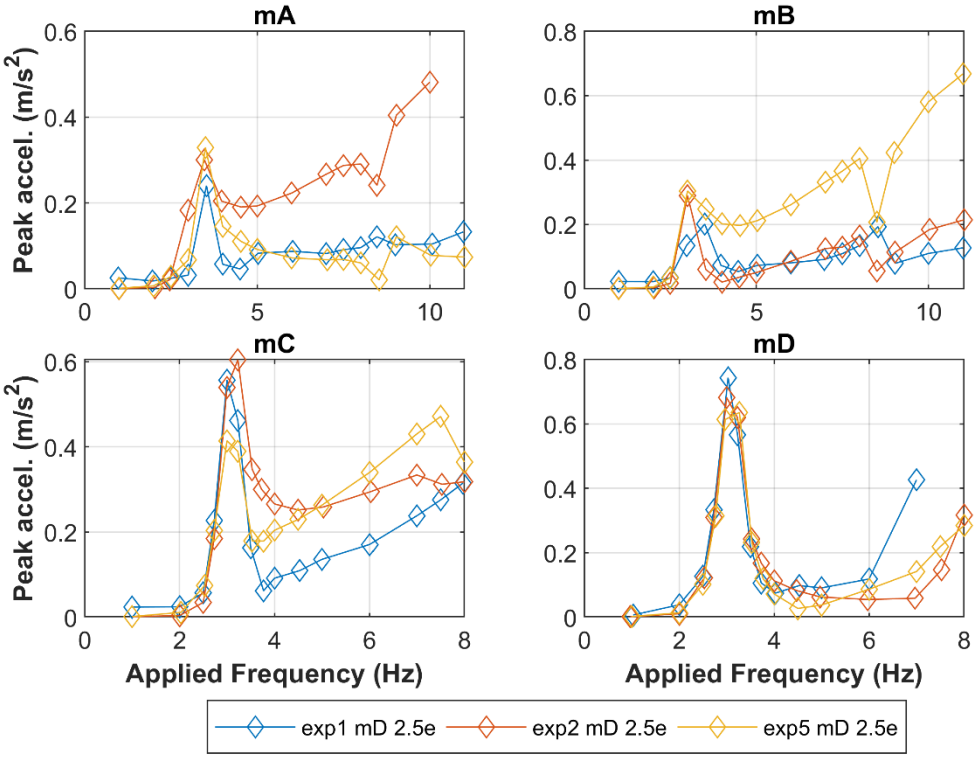


Figure C.22: Peak accelerations recorded along the North-South direction by the 2.5e instrument, at each applied frequency

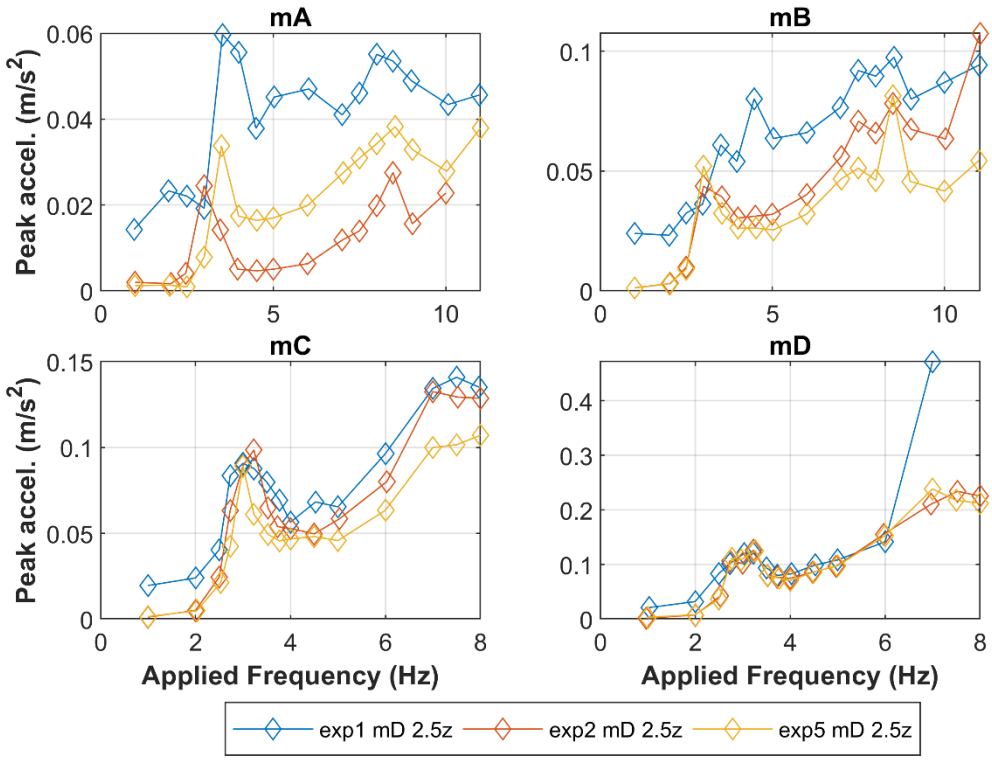


Figure C.23: Peak accelerations recorded along the North-South direction by the 2.5z instrument, at each applied frequency

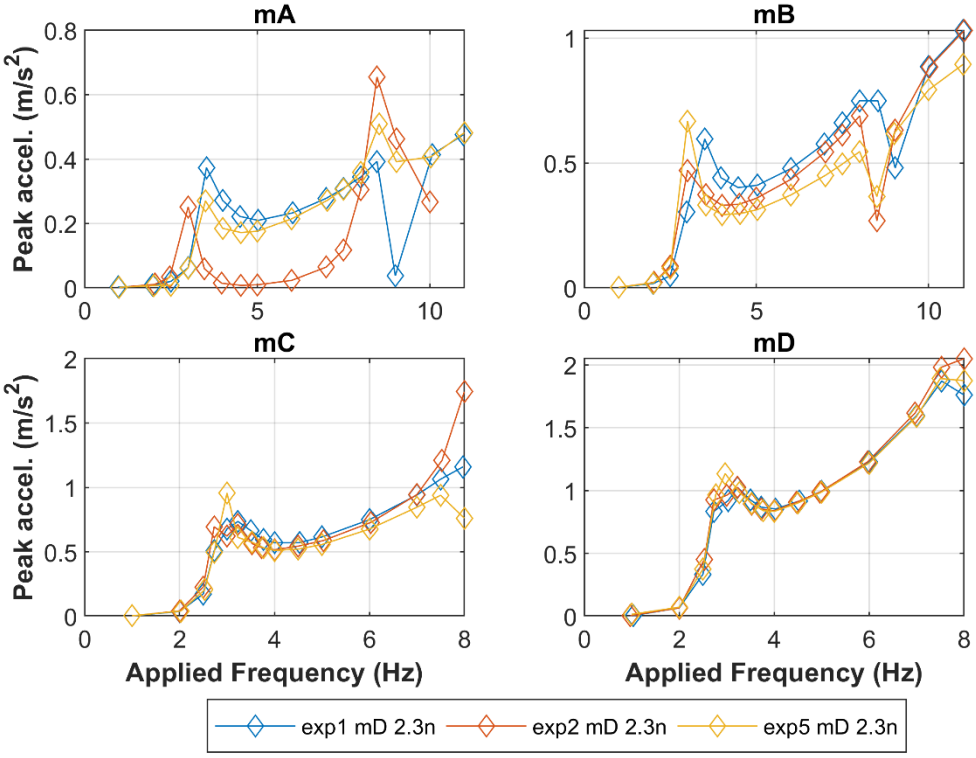


Figure C.24: Peak accelerations recorded along the North-South direction by the 2.3n instrument, at each applied frequency

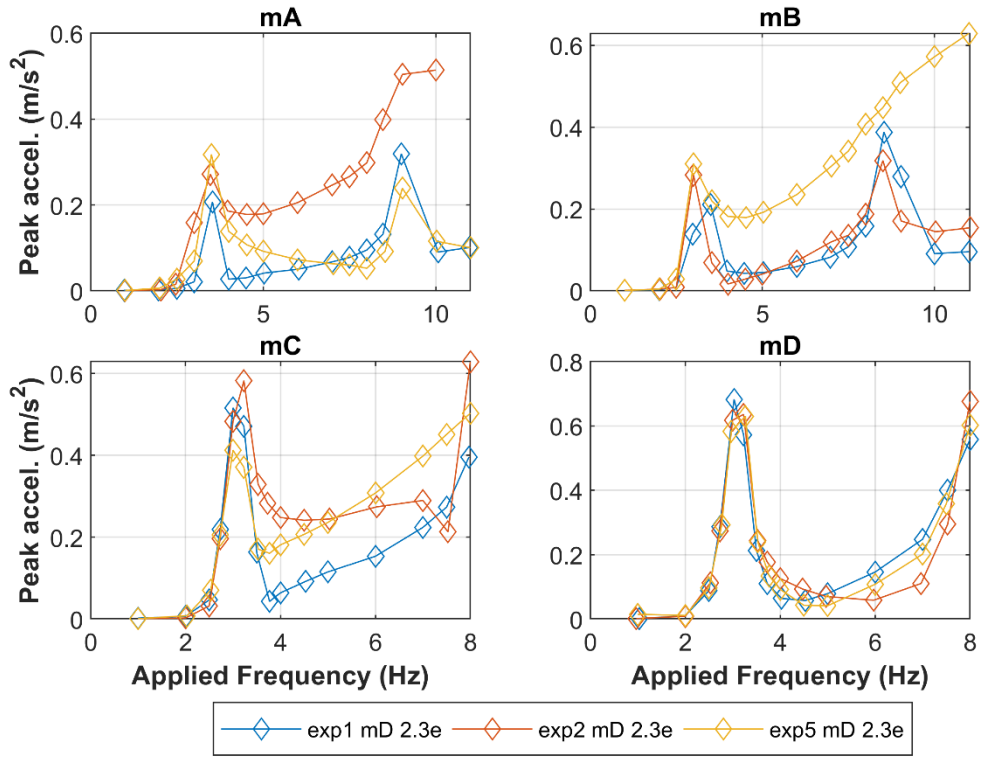


Figure C.25: Peak accelerations recorded along the North-South direction by the 2.3e instrument, at each applied frequency

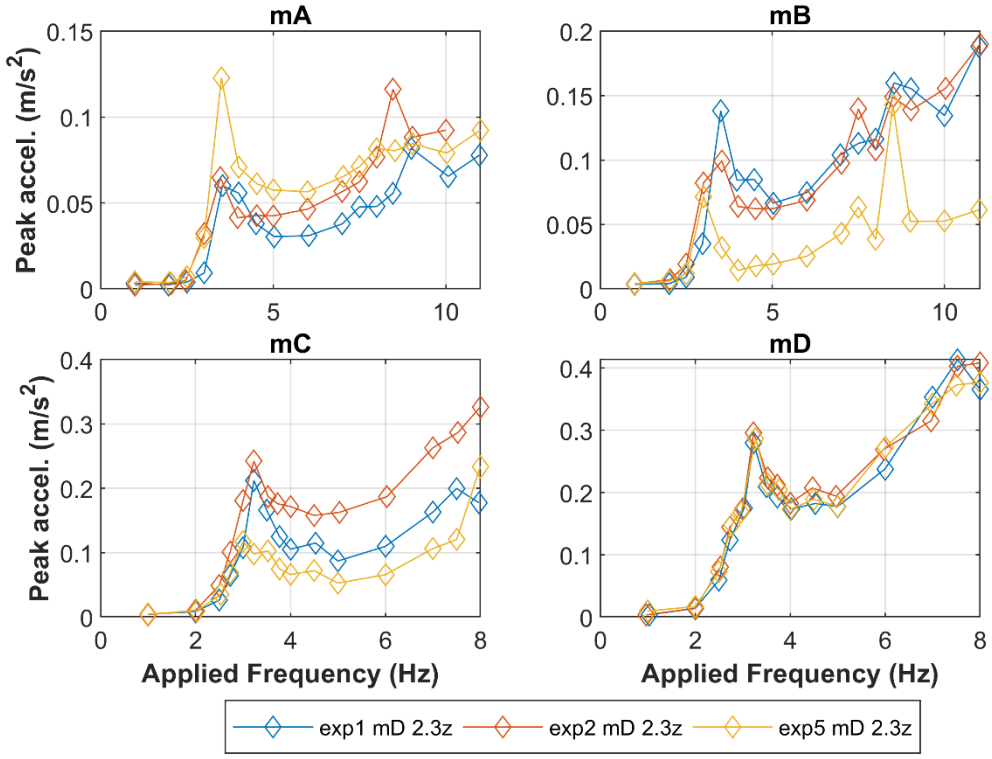


Figure C.26: Peak accelerations recorded along the North-South direction by the 2.3z instrument, at each applied frequency

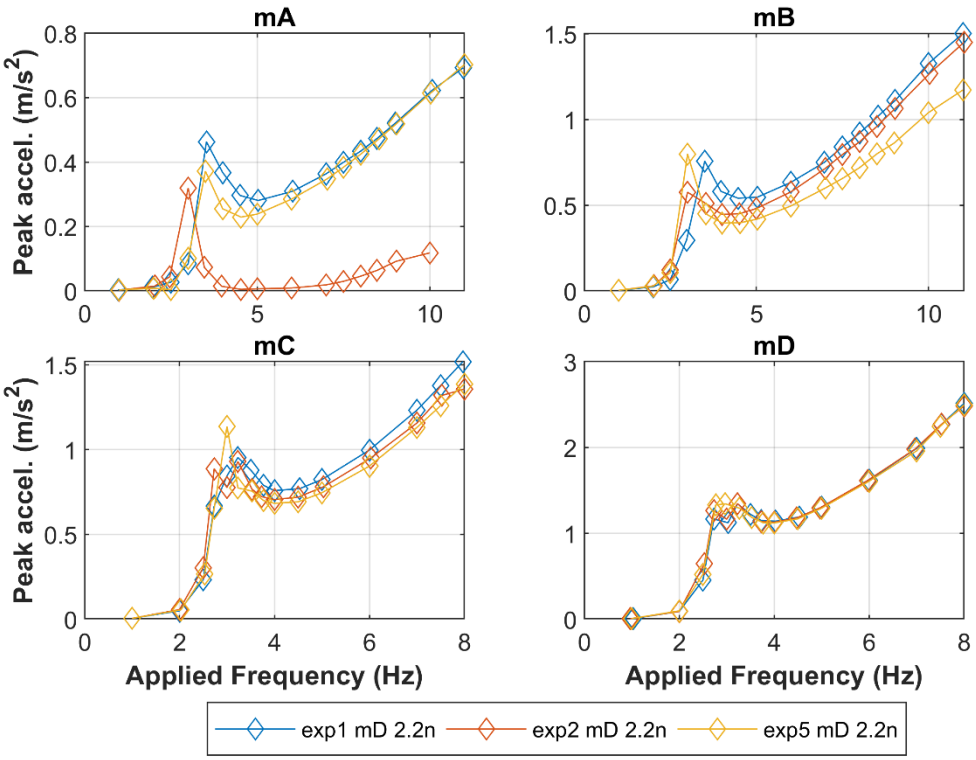


Figure C.27: Peak accelerations recorded along the North-South direction by the 2.2n instrument, at each applied frequency

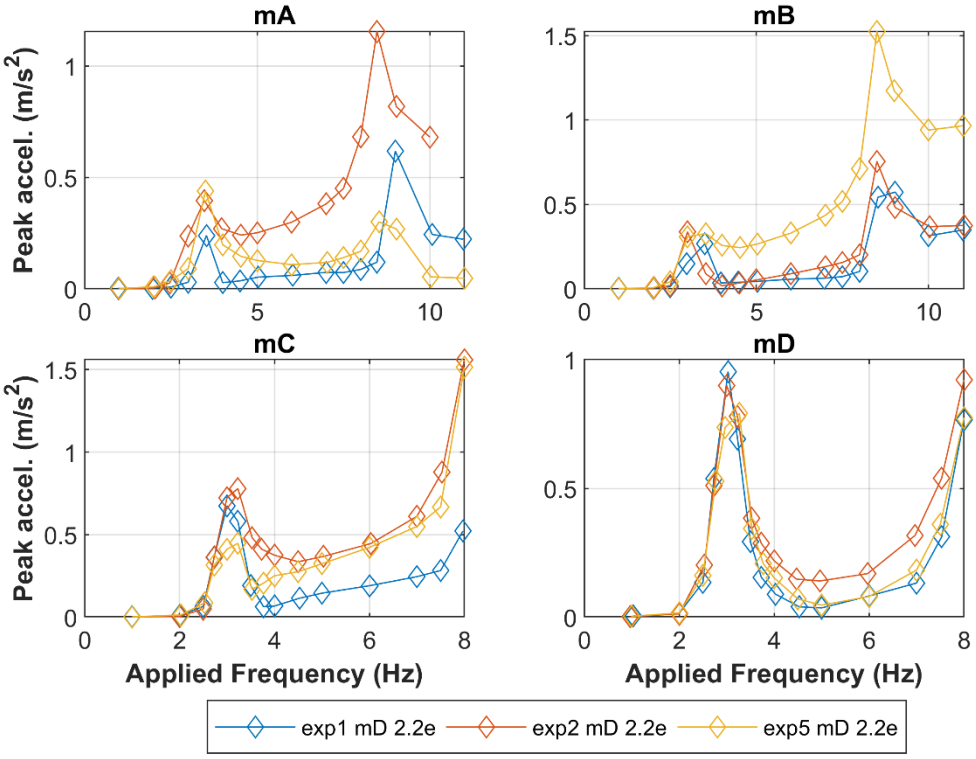


Figure C.28: Peak accelerations recorded along the North-South direction by the 2.2e instrument, at each applied frequency

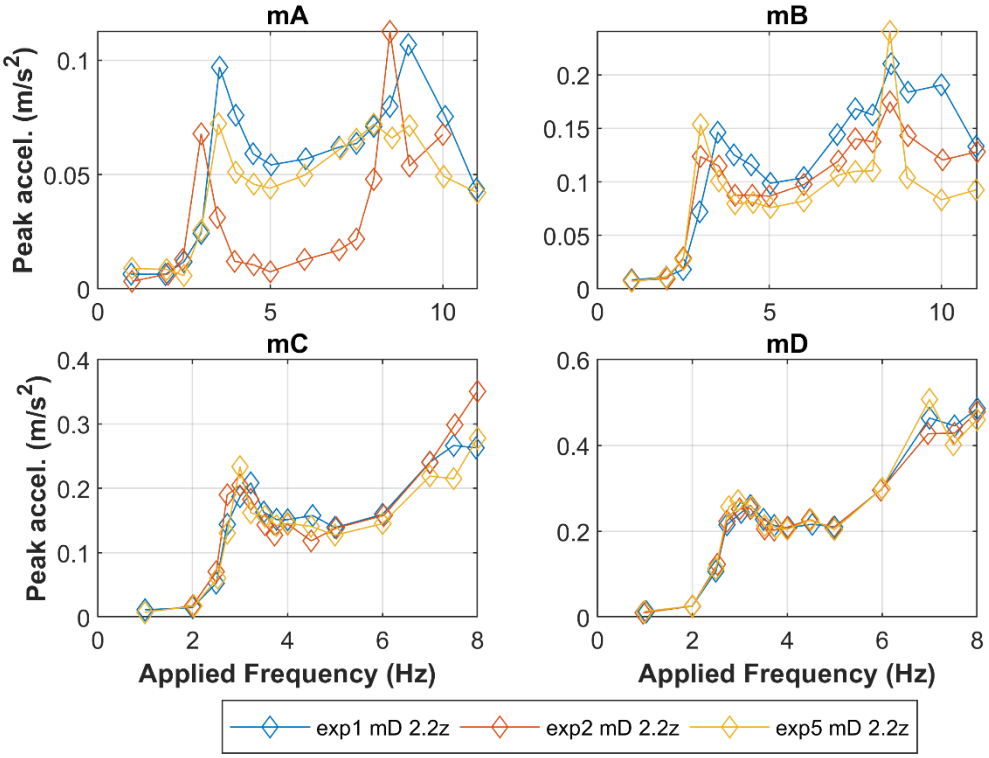


Figure C.29: Peak accelerations recorded along the North-South direction by the 2.2z instrument, at each applied frequency

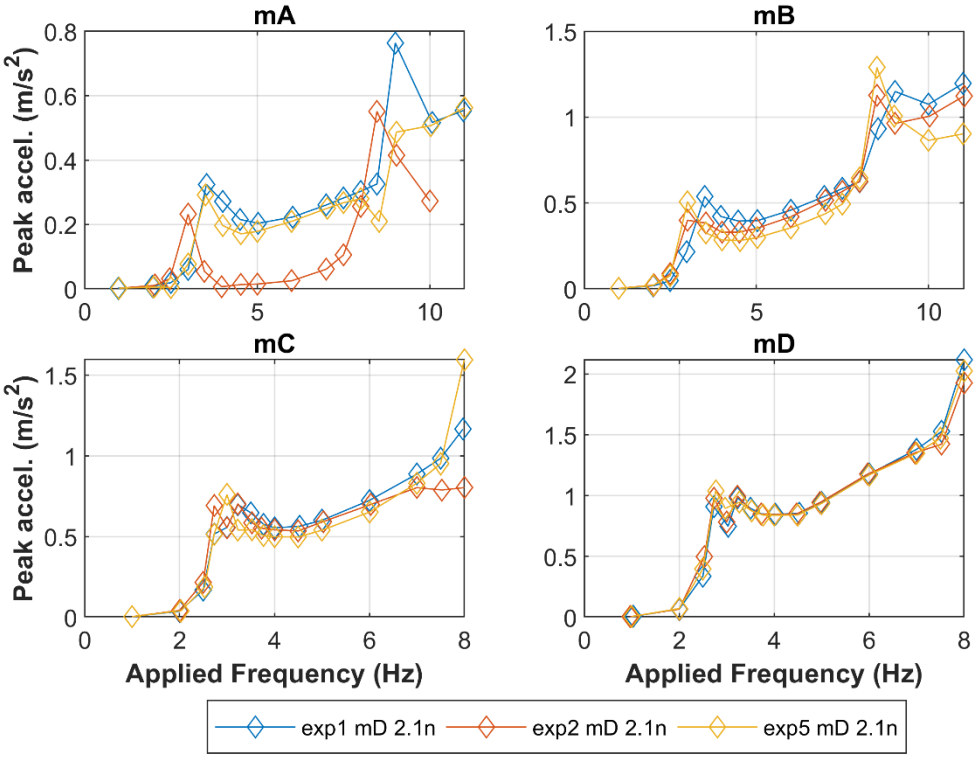


Figure C.30: Peak accelerations recorded along the North-South direction by the 2.1n instrument, at each applied frequency

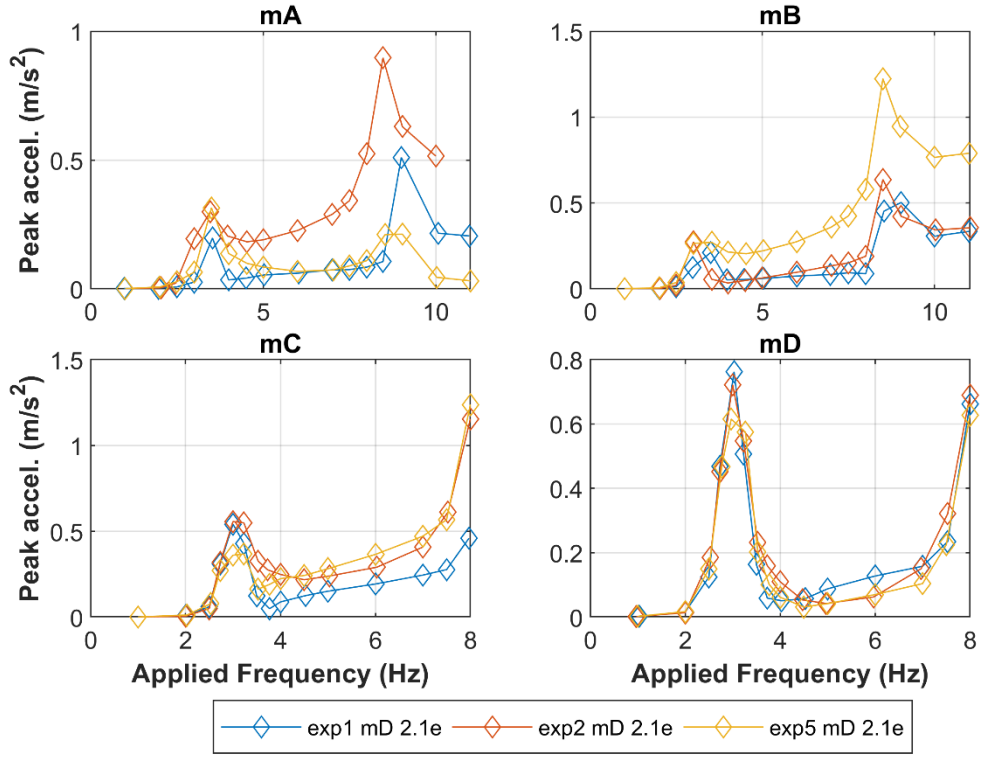


Figure C.31: Peak accelerations recorded along the North-South direction by the 2.1e instrument, at each applied frequency

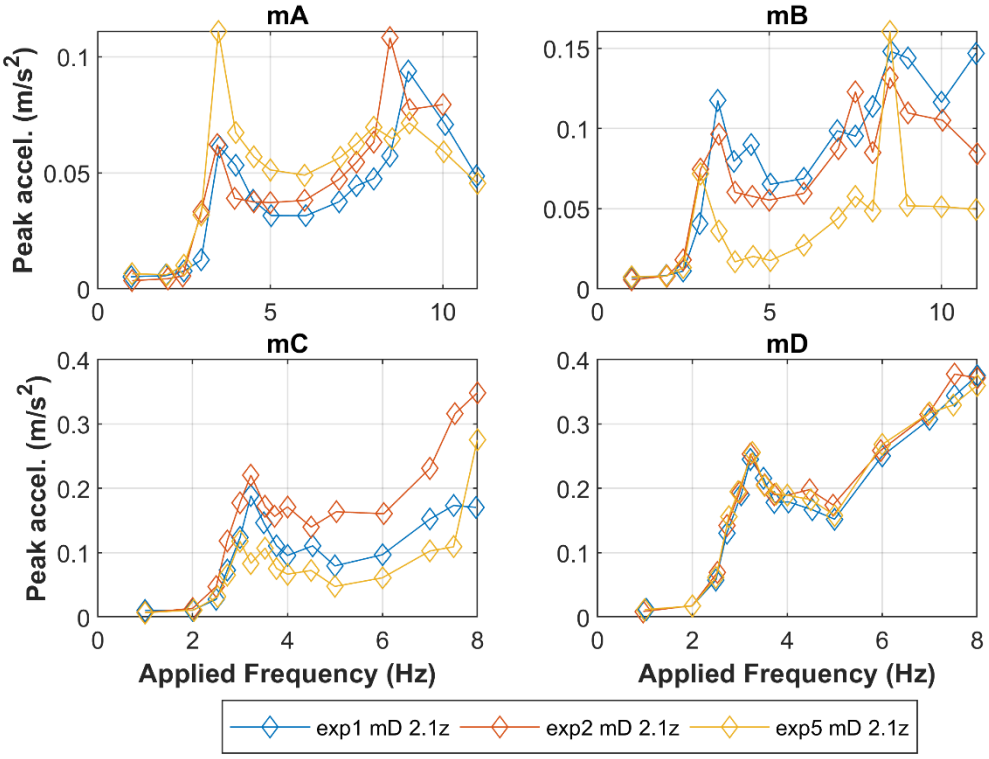


Figure C.32: Peak accelerations recorded along the North-South direction by the 2.1z instrument, at each applied frequency

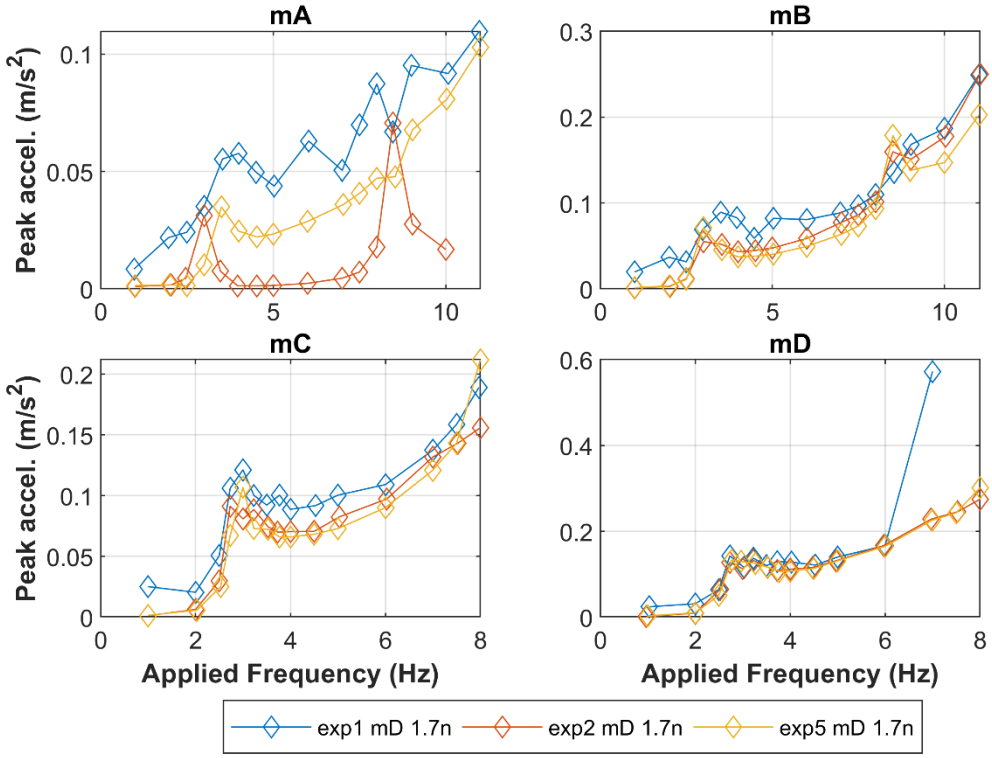


Figure C.33: Peak accelerations recorded along the North-South direction by the 1.7n instrument, at each applied frequency

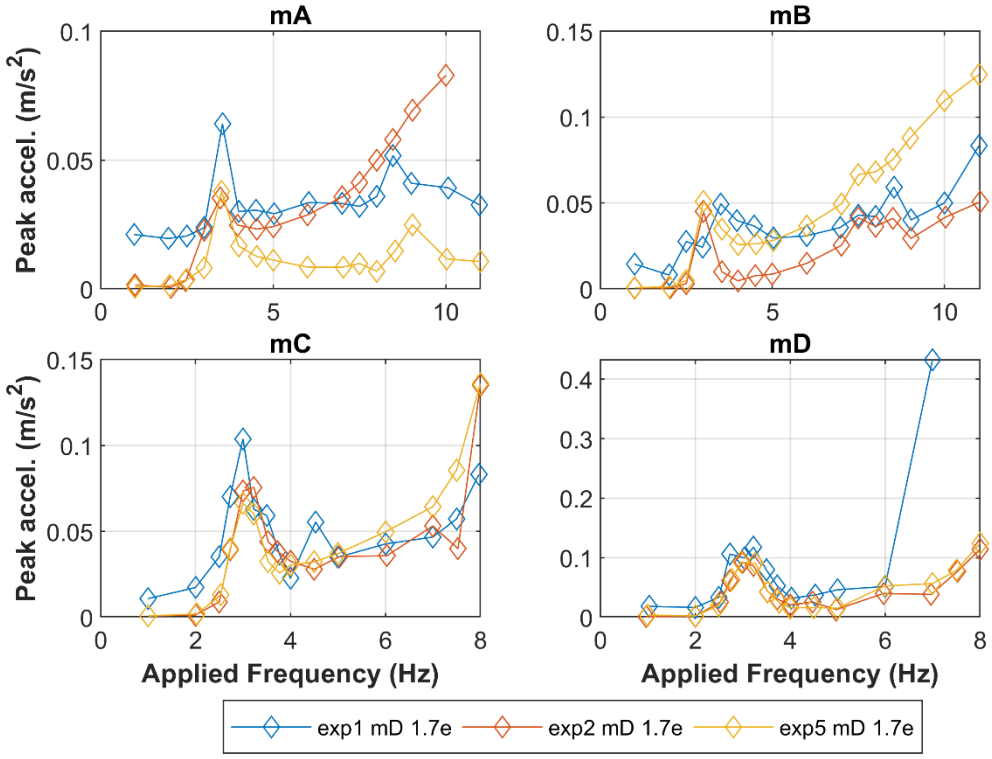


Figure C.34: Peak accelerations recorded along the North-South direction by the 1.7e instrument, at each applied frequency

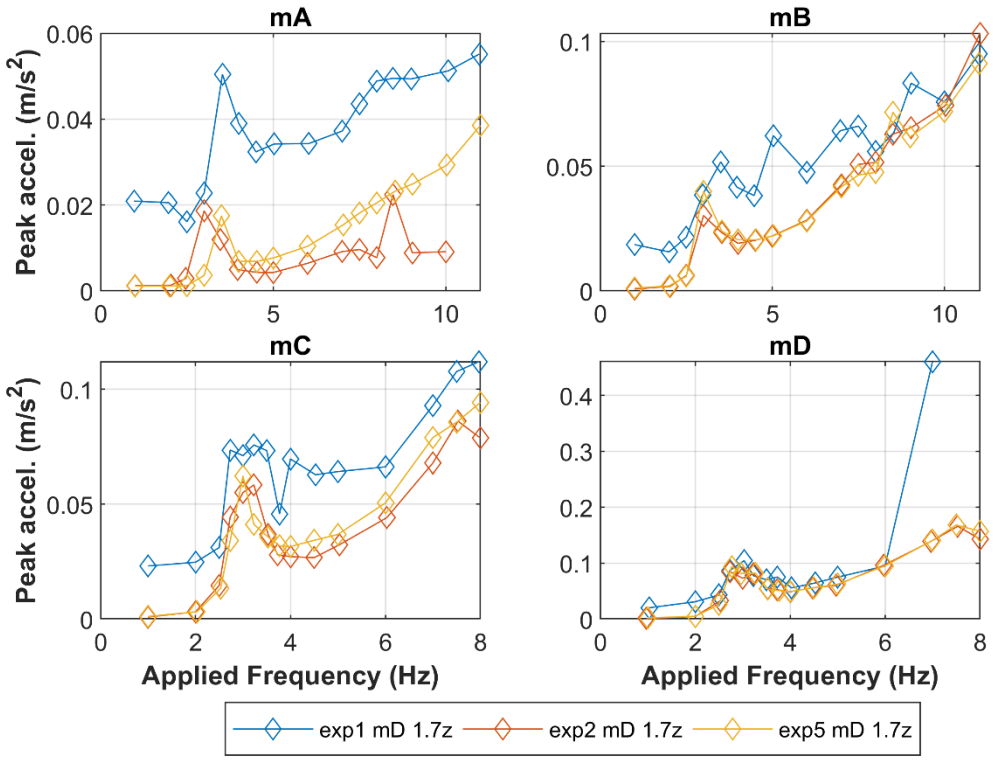


Figure C.35: Peak accelerations recorded along the North-South direction by the 1.7z instrument, at each applied frequency

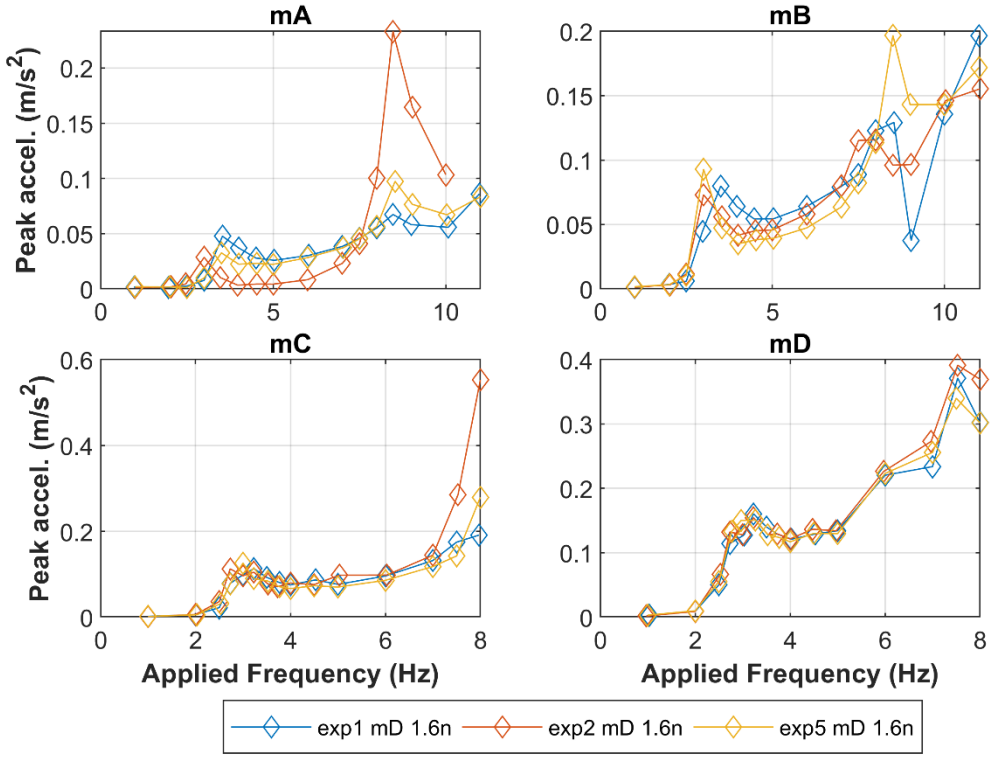


Figure C.36: Peak accelerations recorded along the North-South direction by the 1.6n instrument, at each applied frequency

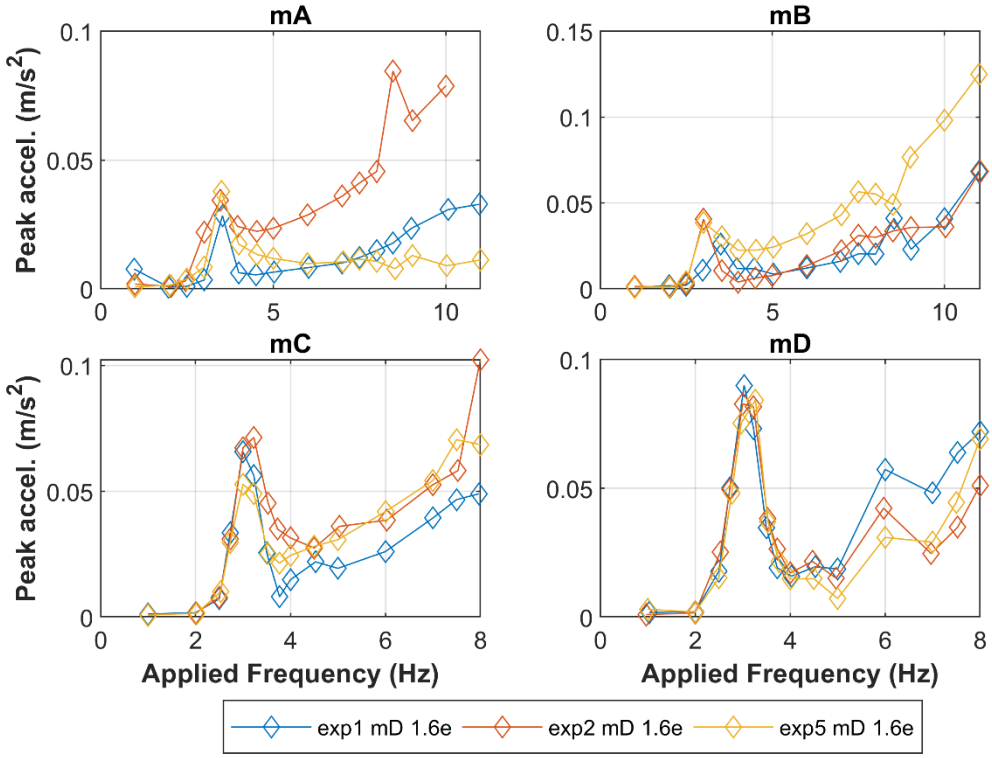


Figure C.37: Peak accelerations recorded along the North-South direction by the 1.6e instrument, at each applied frequency

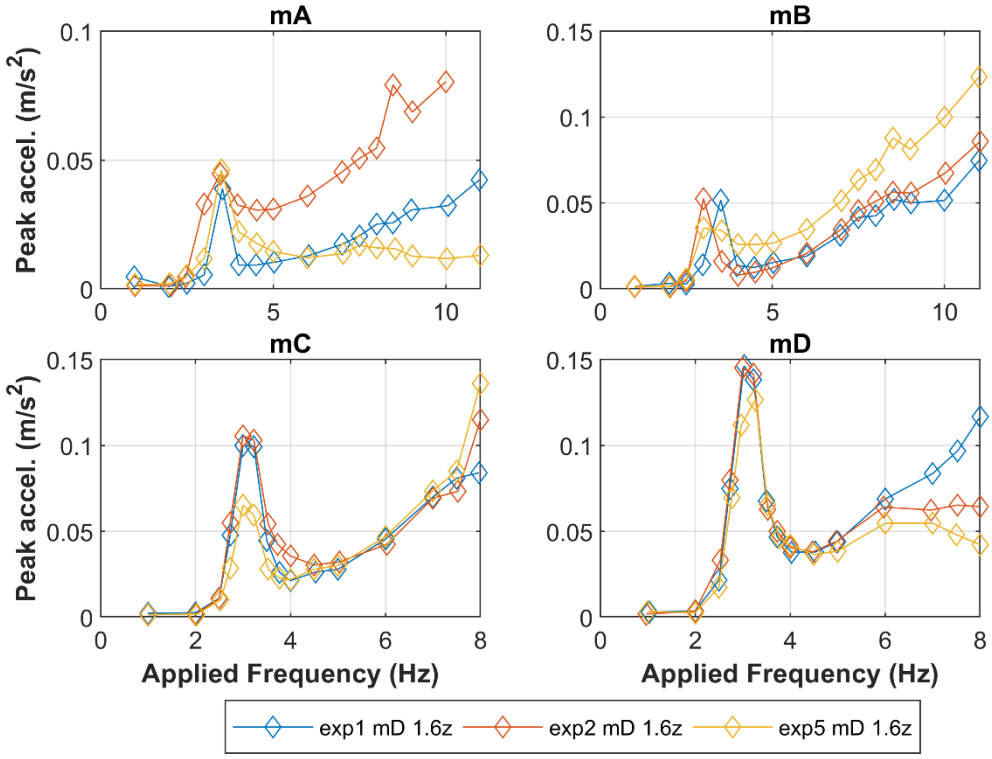


Figure C.38: Peak accelerations recorded along the North-South direction by the 1.6z instrument, at each applied frequency

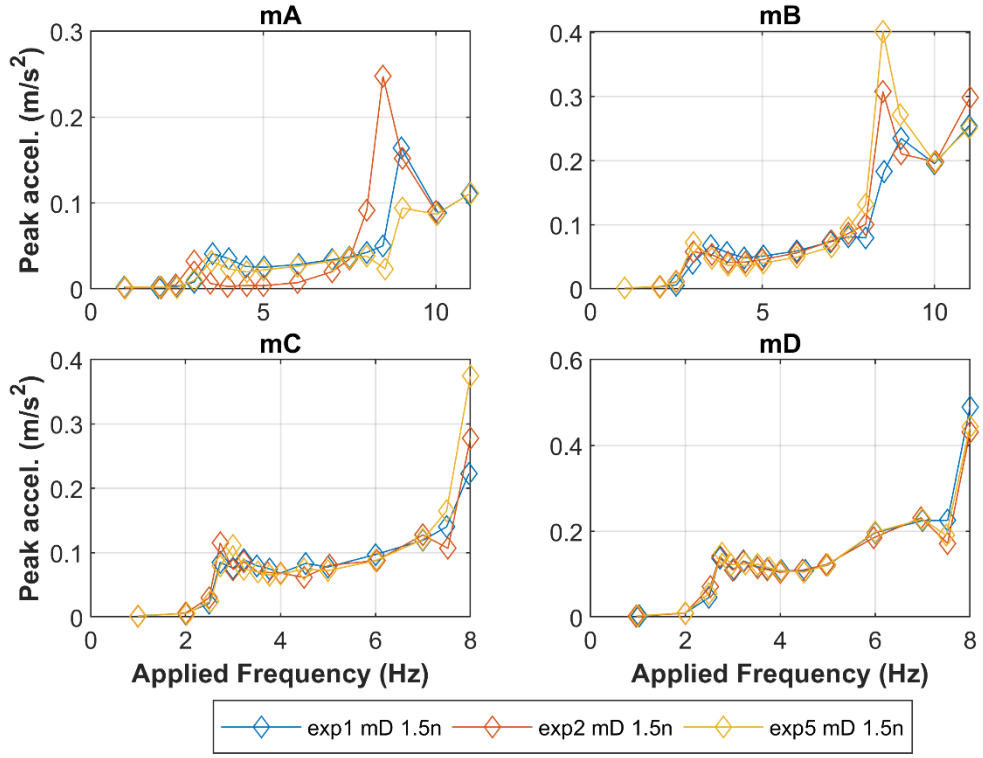


Figure C.39: Peak accelerations recorded along the North-South direction by the 1.5n instrument, at each applied frequency

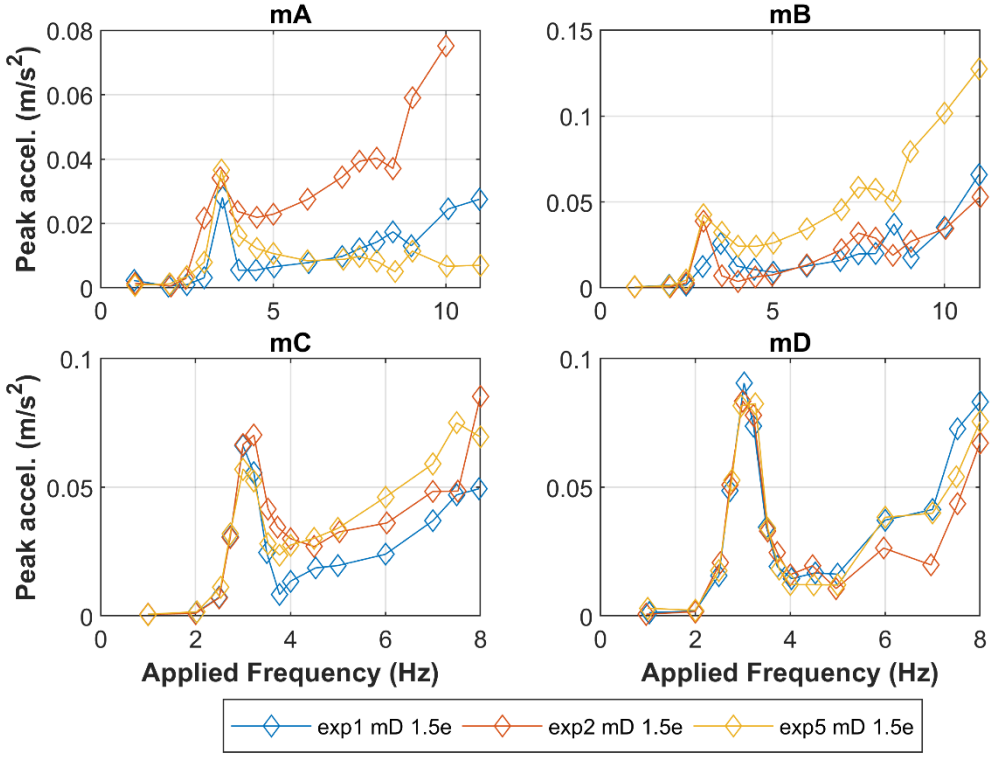


Figure C.40: Peak accelerations recorded along the North-South direction by the 1.5e instrument, at each applied frequency

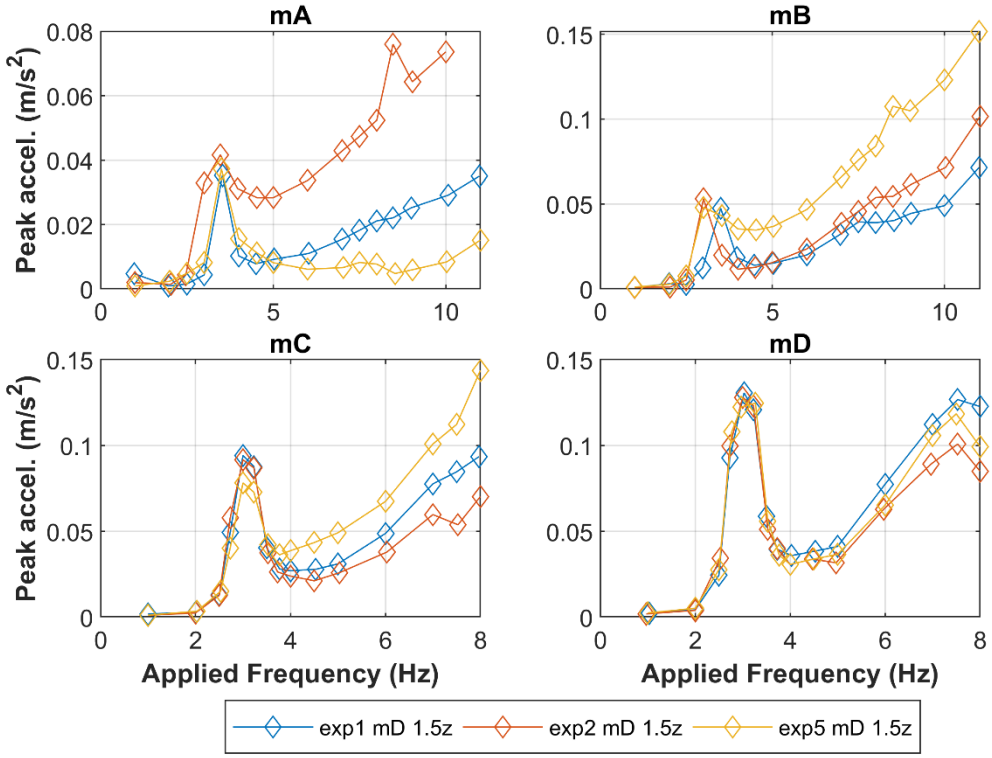


Figure C.41: Peak accelerations recorded along the North-South direction by the 1.5z instrument, at each applied frequency

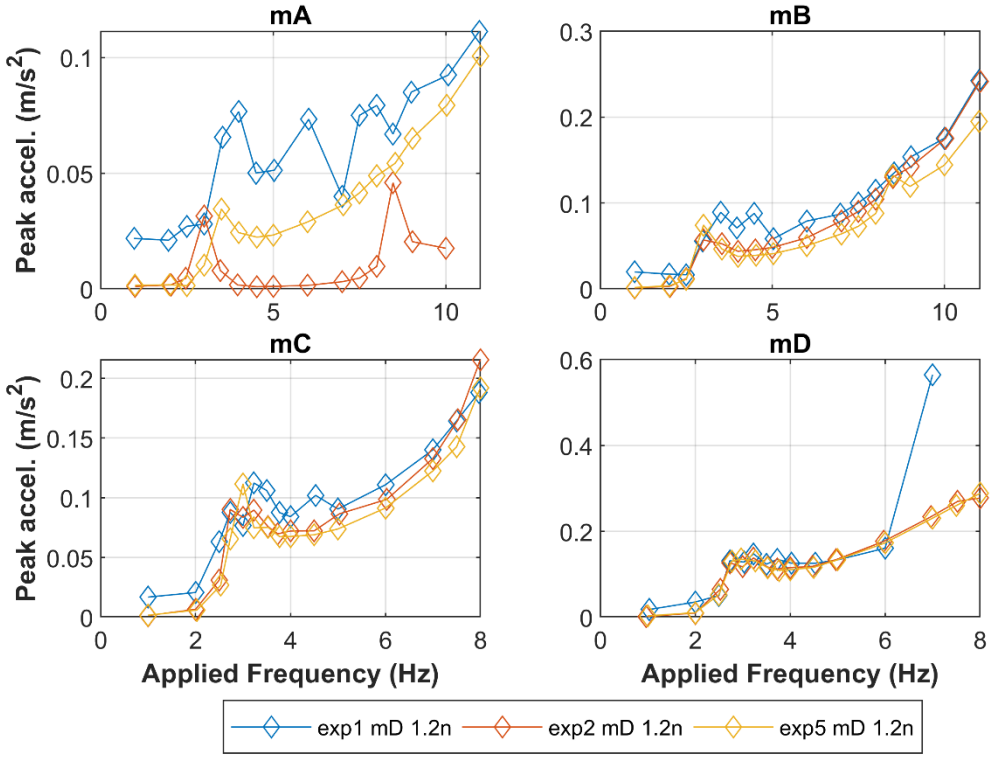


Figure C.42: Peak accelerations recorded along the North-South direction by the 1.2n instrument, at each applied frequency

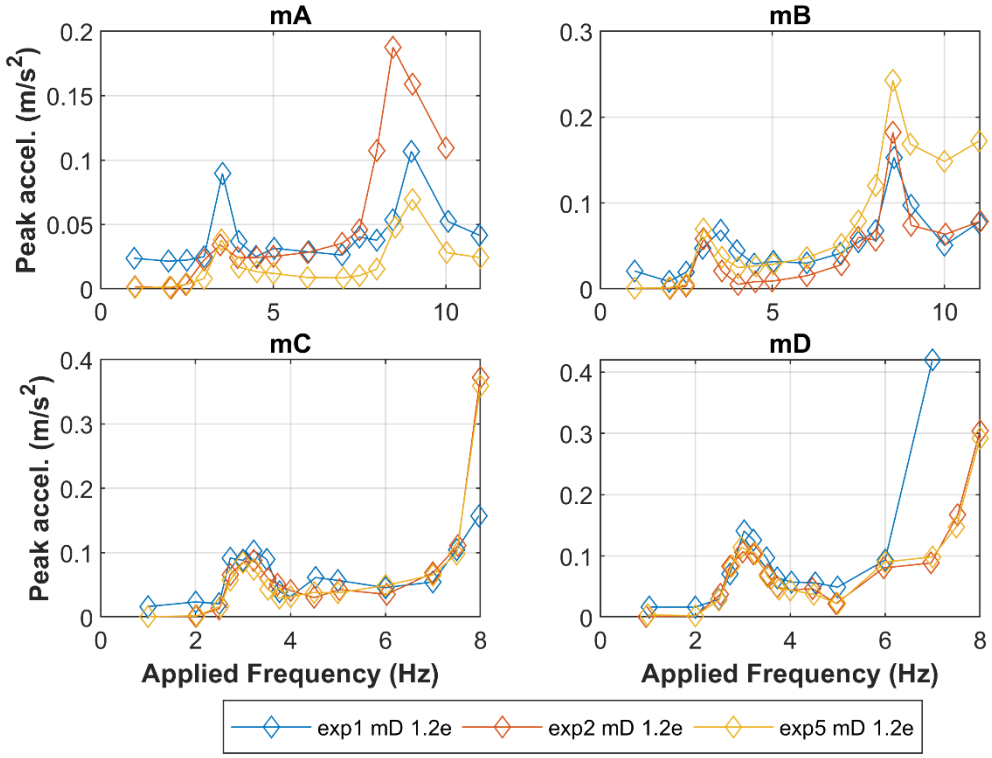


Figure C.43: Peak accelerations recorded along the North-South direction by the 1.2e instrument, at each applied frequency

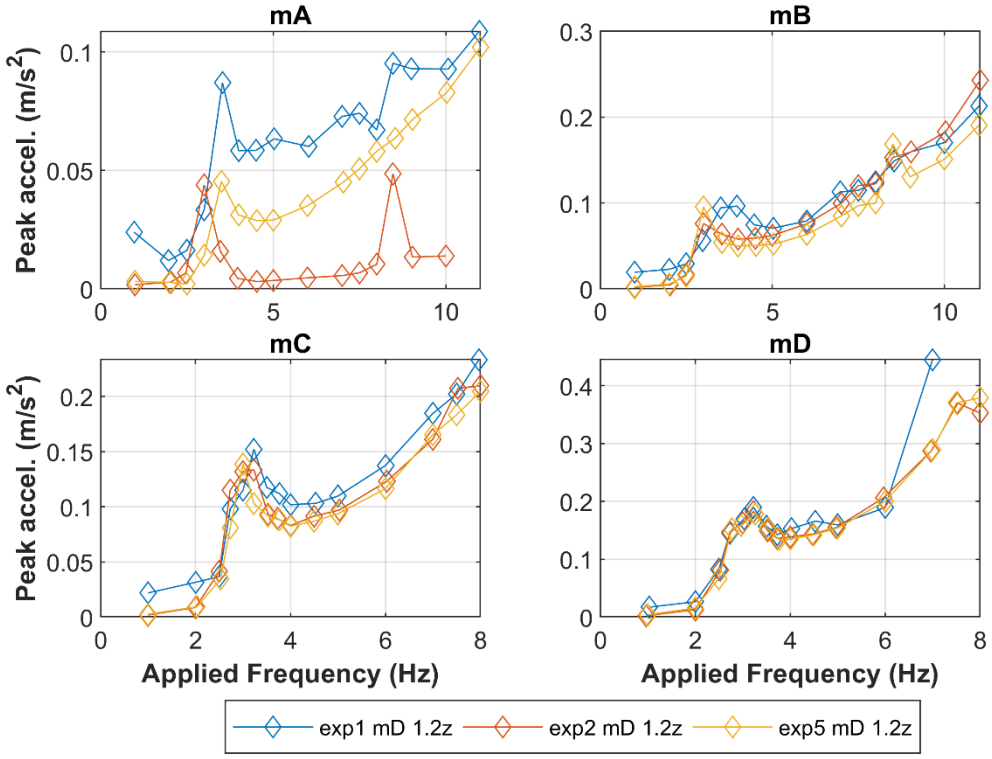


Figure C.44: Peak accelerations recorded along the North-South direction by the 1.2z instrument, at each applied frequency

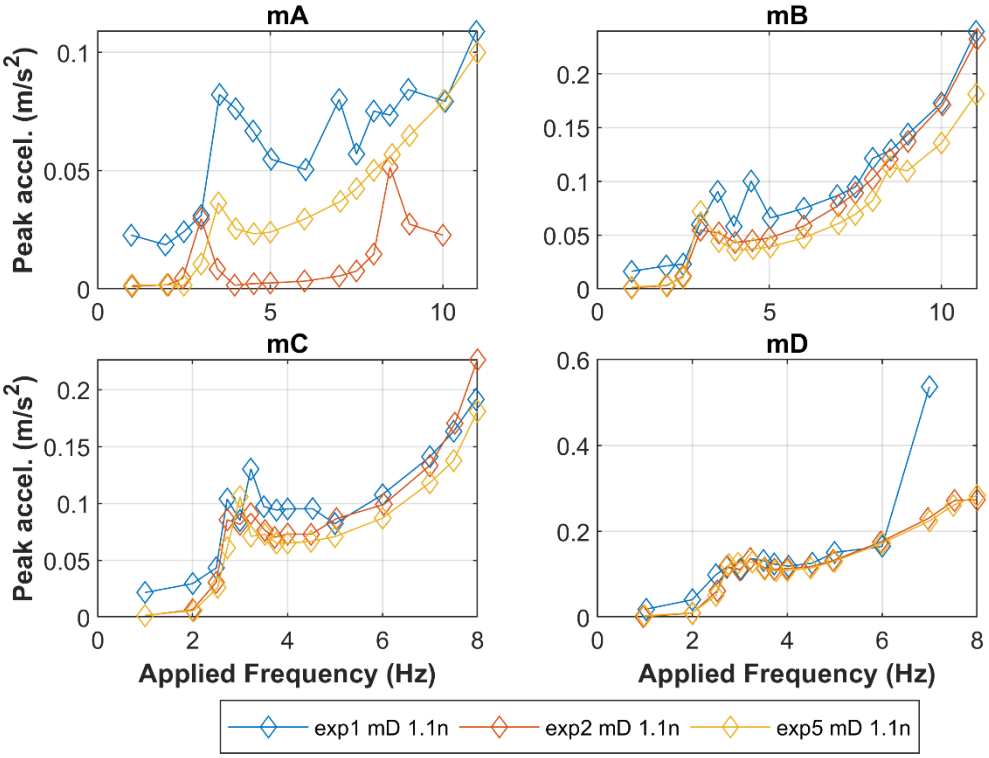


Figure C.45: Peak accelerations recorded along the North-South direction by the 1.1n instrument, at each applied frequency

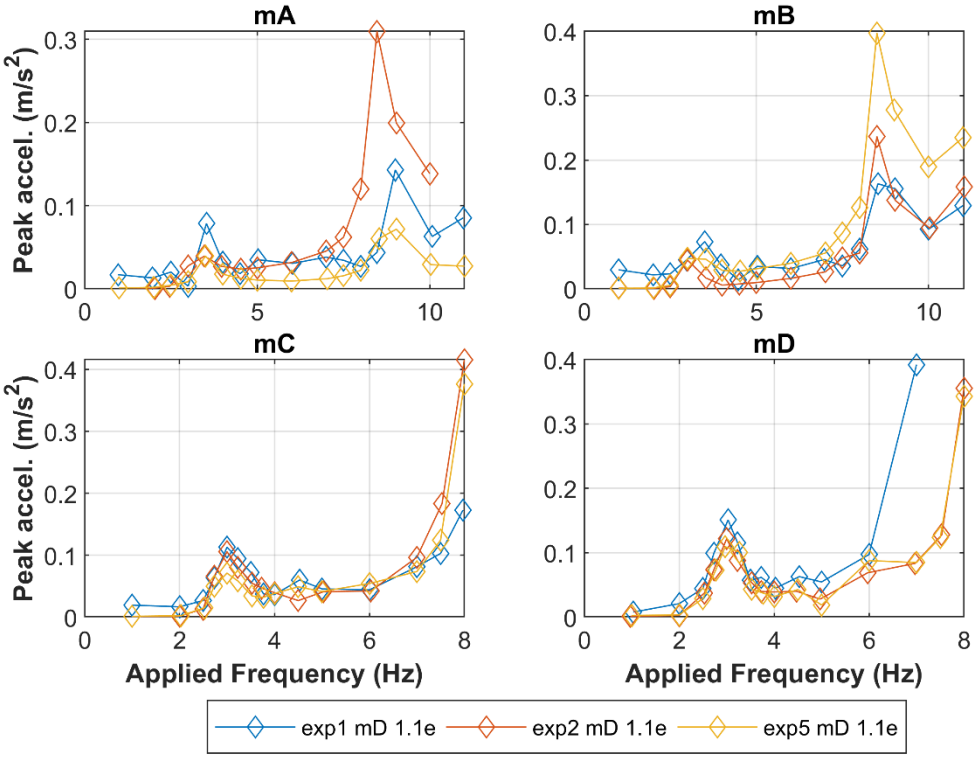


Figure C.46: Peak accelerations recorded along the North-South direction by the 1.1e instrument, at each applied frequency

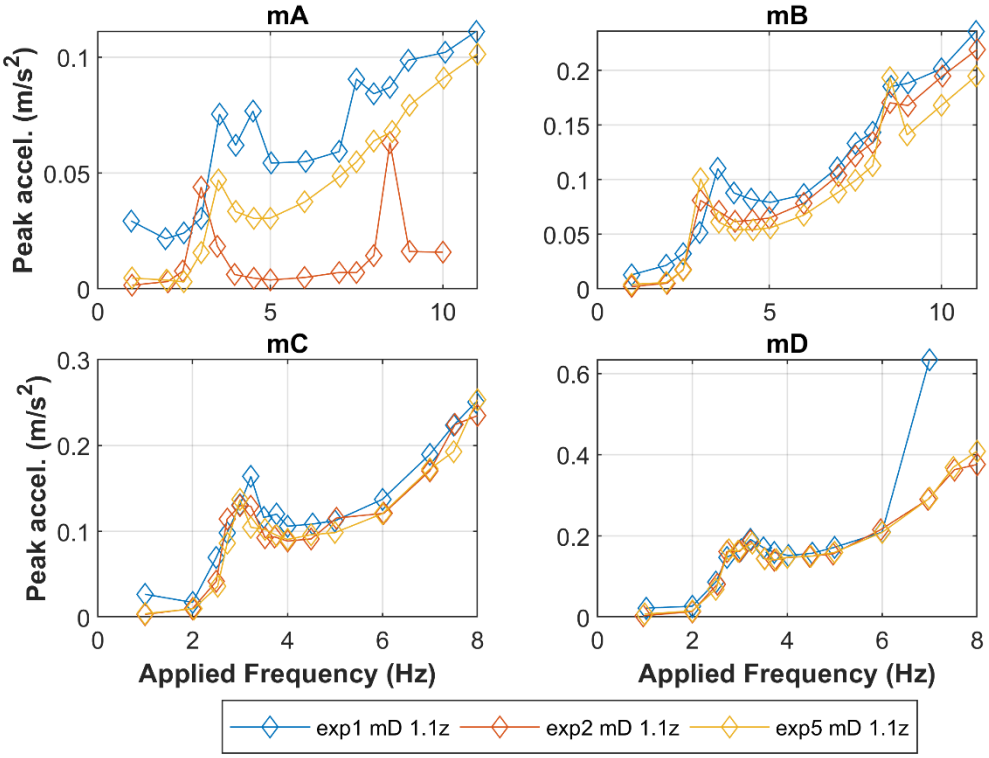


Figure C.47: Peak accelerations recorded along the North-South direction by the 1.1z instrument, at each applied frequency

Appendix C.4 Repeatability of data recorded during the experiments on the Partly Braced structure loaded along its Weak plane

The following figures compare the peak accelerations recorded by different instruments at each applied frequency, during the experiments on the Partly Braced structure which was loaded along its Weak plane (PBr_W) Three identical experiments (exp7, epx9 and exp12) are compared, while for each one, three different vibrator masses where used (mB, mC and mD). Figures processed from data recorded by all structural instruments are available are presented. Also, all three North-South (n), East-West (e) and vertical (z) motion components are shown.

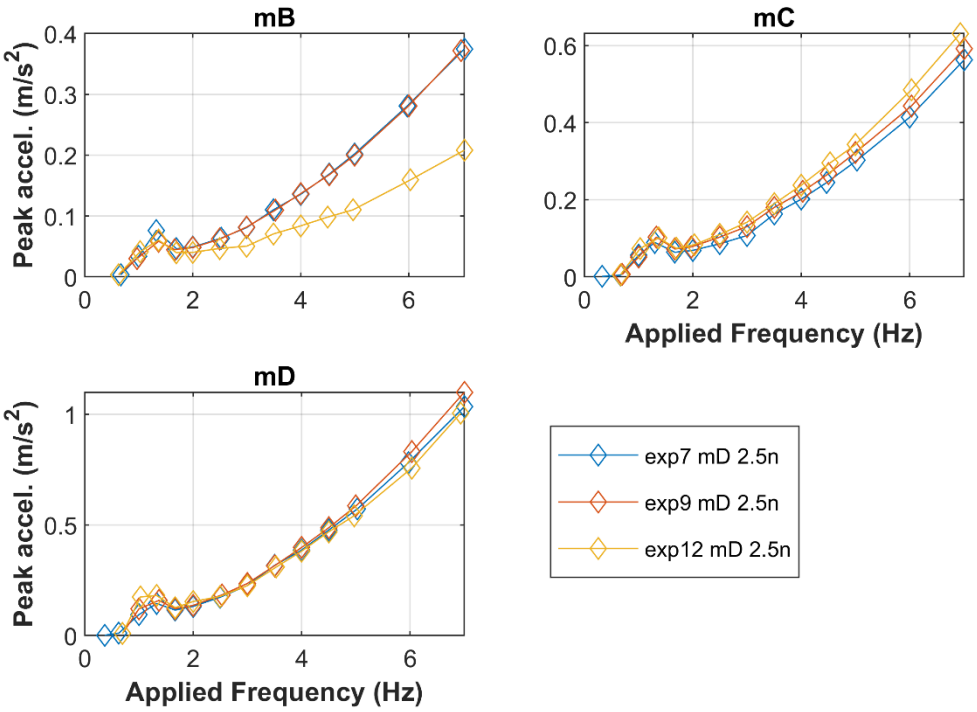


Figure C.48: Peak accelerations recorded along the North-South direction by the 2.5n instrument, at each applied frequency

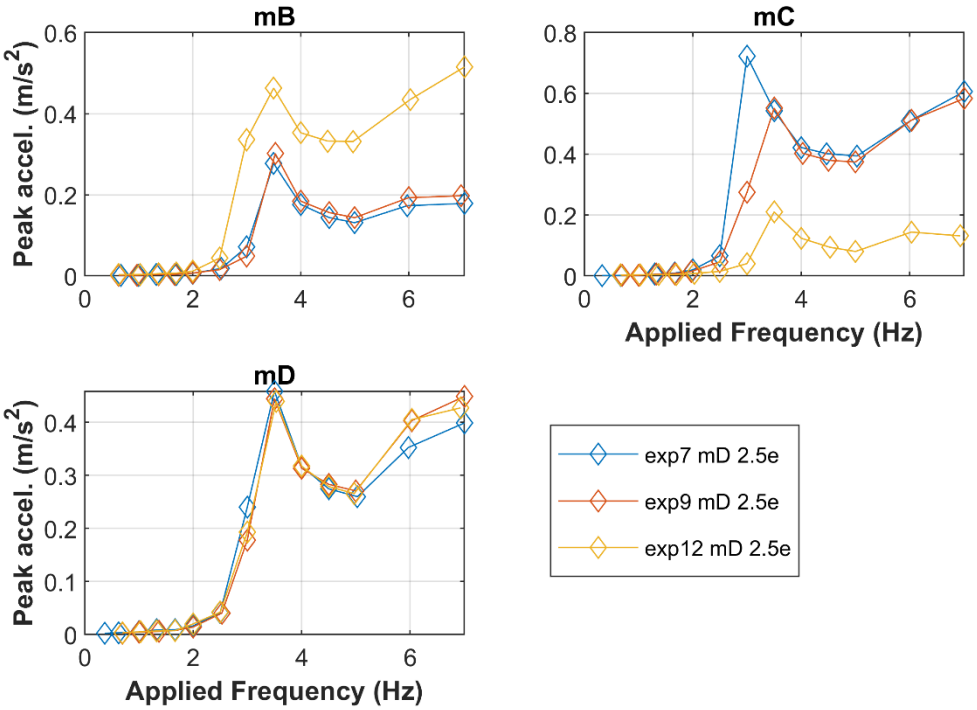


Figure C.49: Peak accelerations recorded along the North-South direction by the 2.5e instrument, at each applied frequency

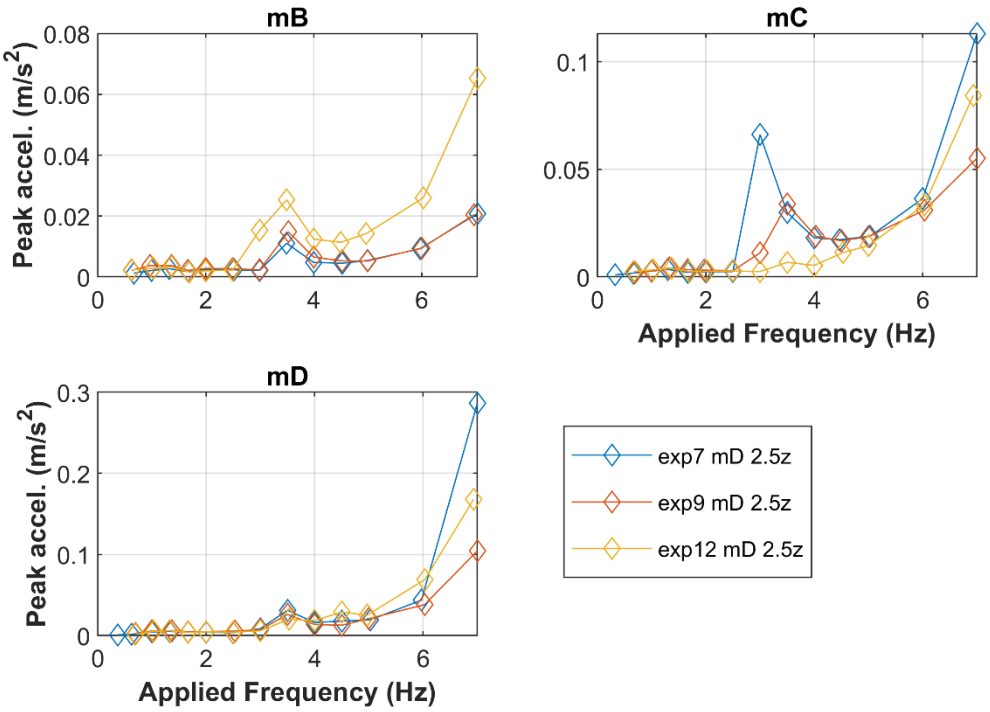


Figure C.50: Peak accelerations recorded along the North-South direction by the 2.5z instrument, at each applied frequency

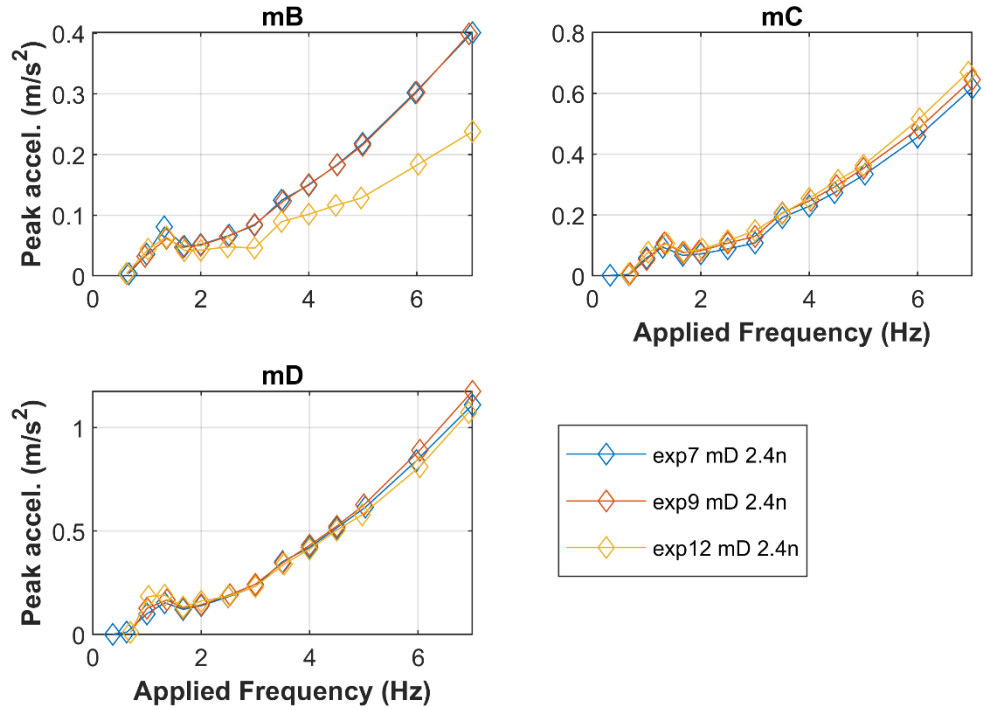


Figure C.51: Peak accelerations recorded along the North-South direction by the 2.4n instrument, at each applied frequency

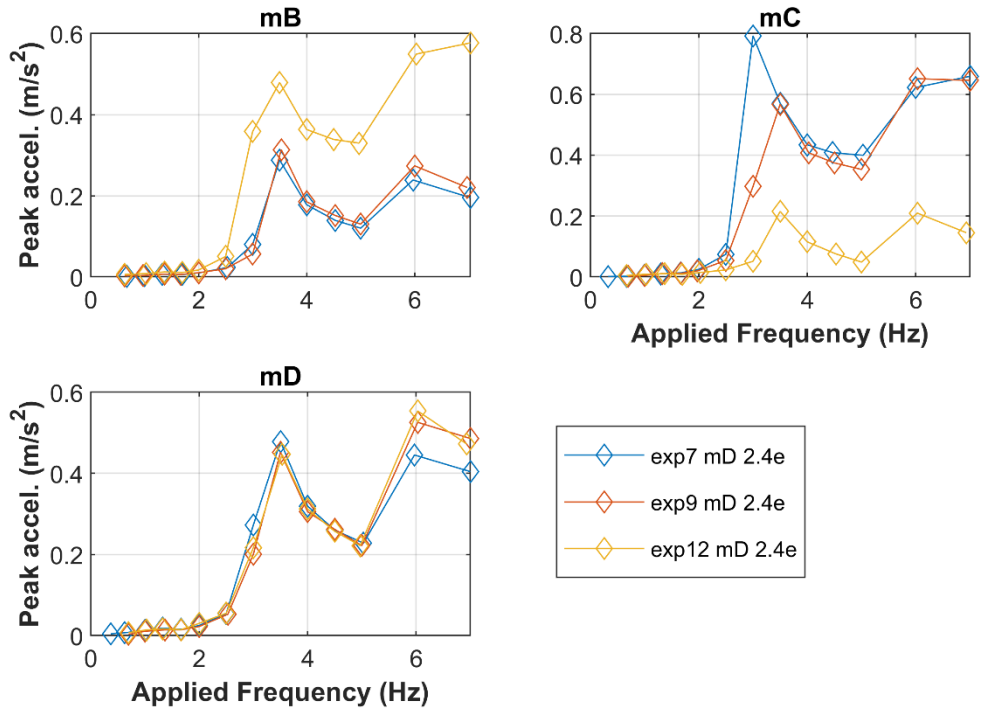


Figure C.52: Peak accelerations recorded along the North-South direction by the 2.4e instrument, at each applied frequency

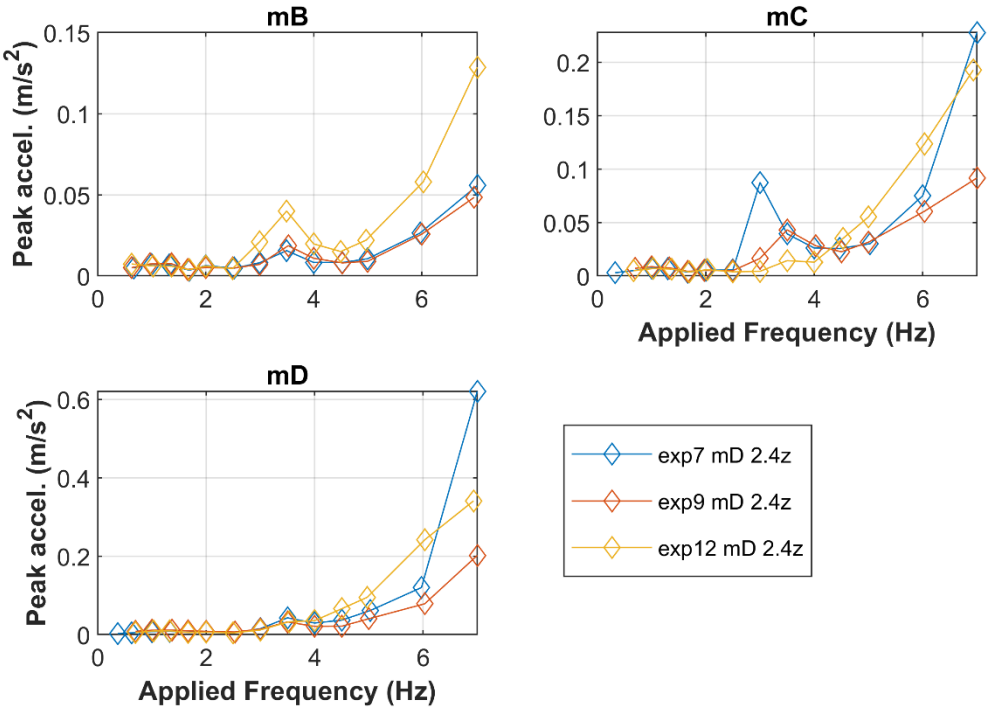


Figure C.53: Peak accelerations recorded along the North-South direction by the 2.4z instrument, at each applied frequency

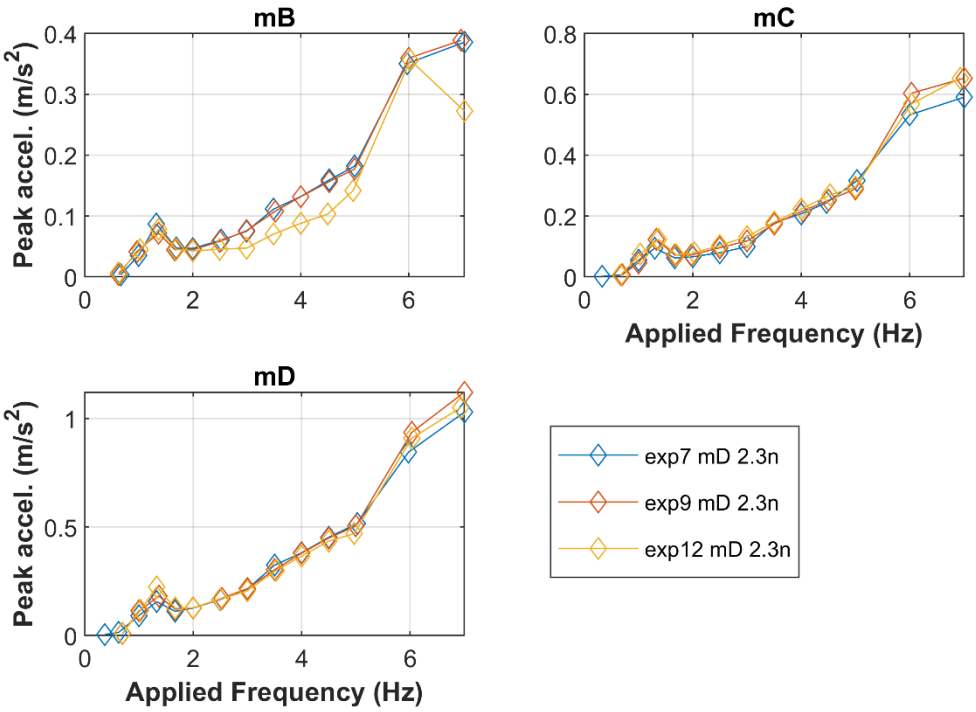


Figure C.54: Peak accelerations recorded along the North-South direction by the 2.3n instrument, at each applied frequency

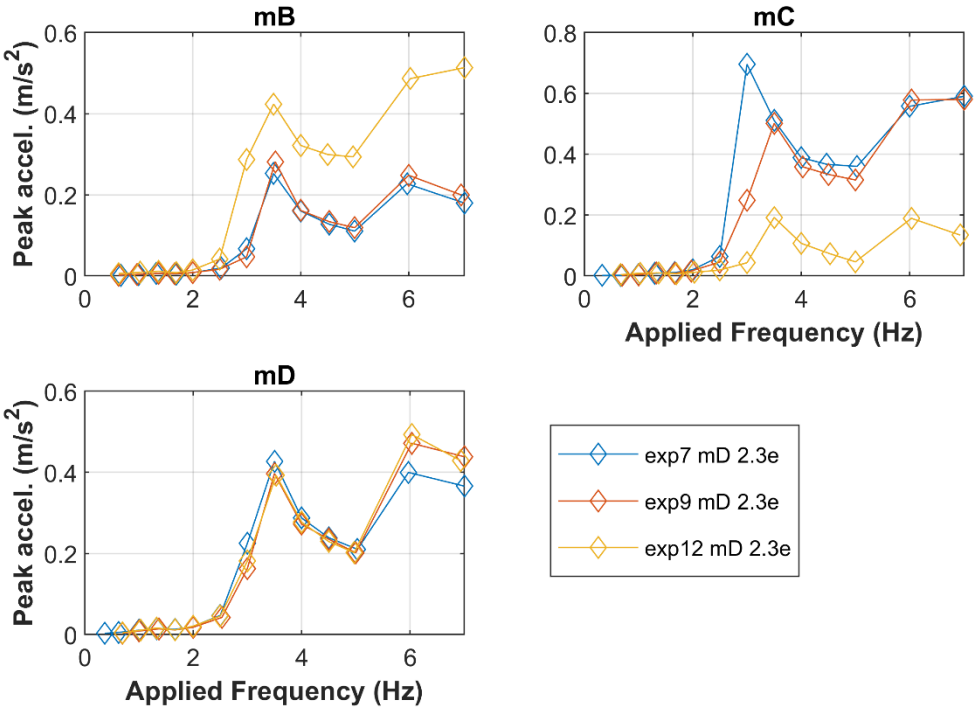


Figure C.55: Peak accelerations recorded along the North-South direction by the 2.3e instrument, at each applied frequency

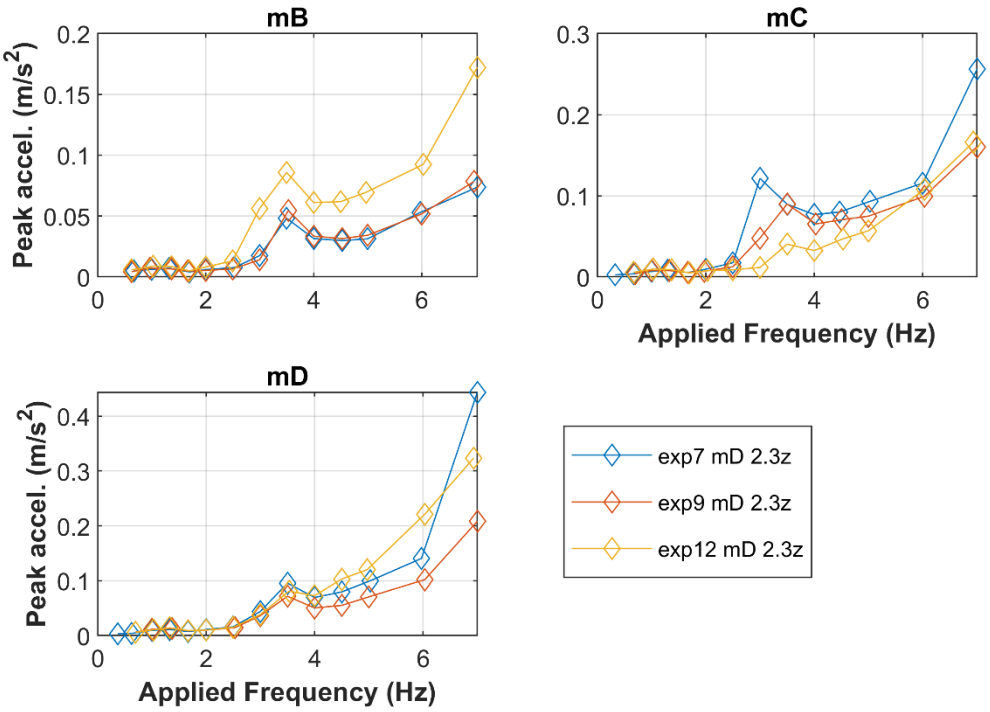


Figure C.56: Peak accelerations recorded along the North-South direction by the 2.3z instrument, at each applied frequency

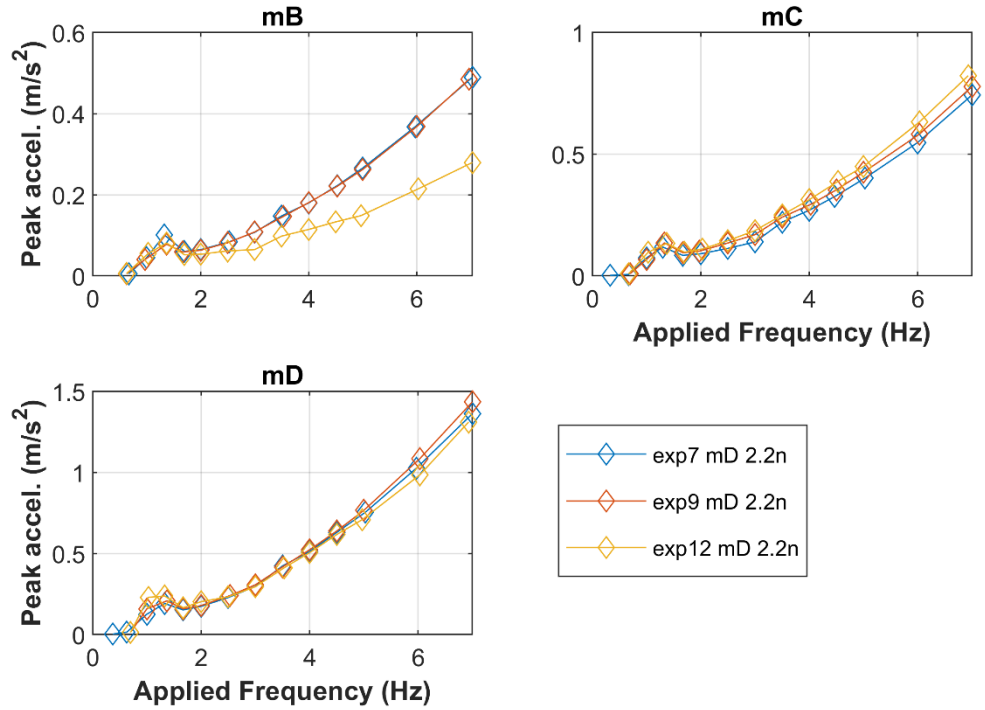


Figure C.57: Peak accelerations recorded along the North-South direction by the 2.2n instrument, at each applied frequency

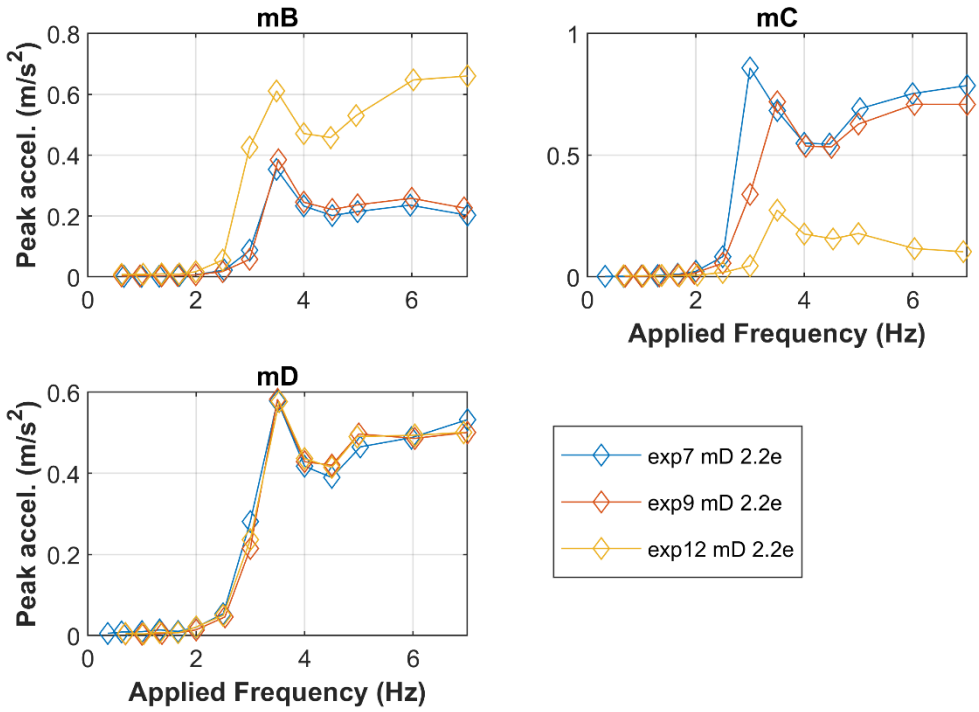


Figure C.58: Peak accelerations recorded along the North-South direction by the 2.2e instrument, at each applied frequency

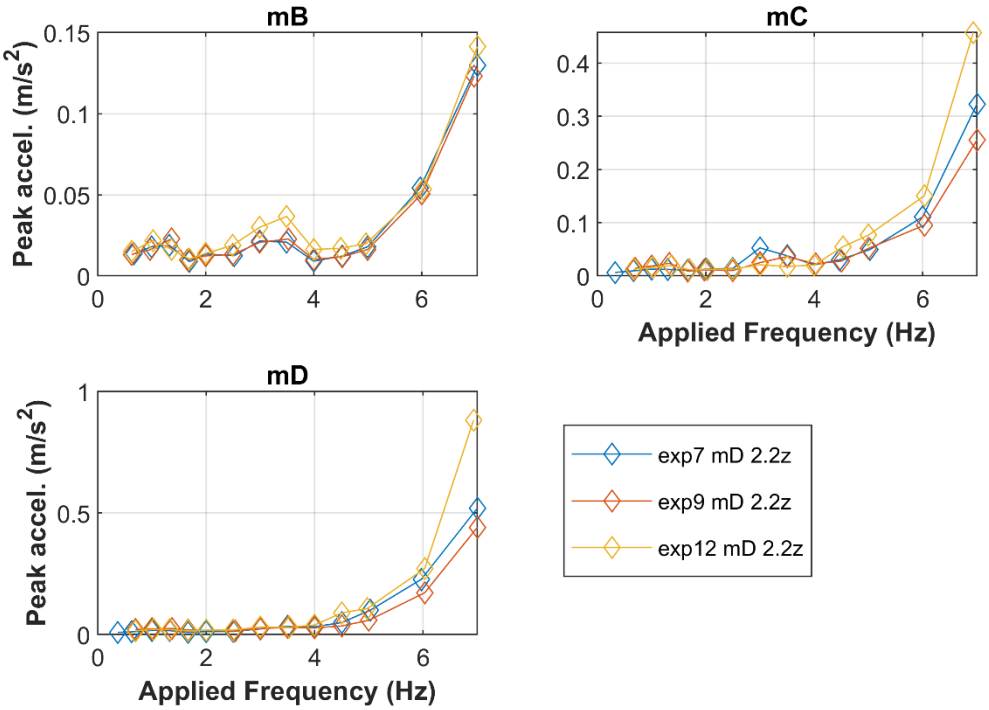


Figure C.59: Peak accelerations recorded along the North-South direction by the 2.2z instrument, at each applied frequency

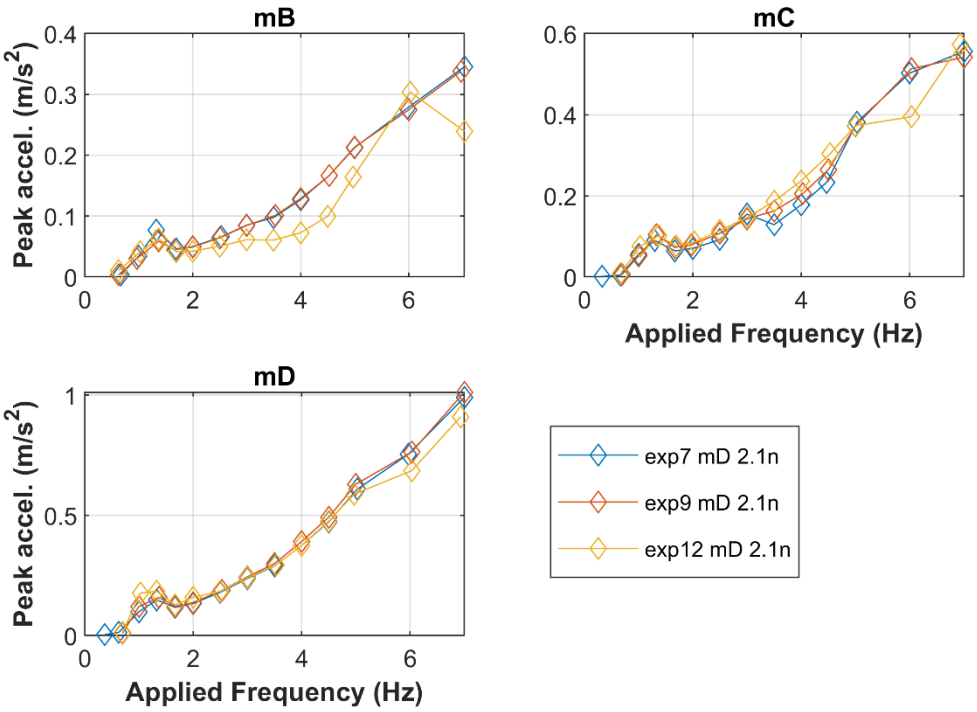


Figure C.60: Peak accelerations recorded along the North-South direction by the 2.1n instrument, at each applied frequency

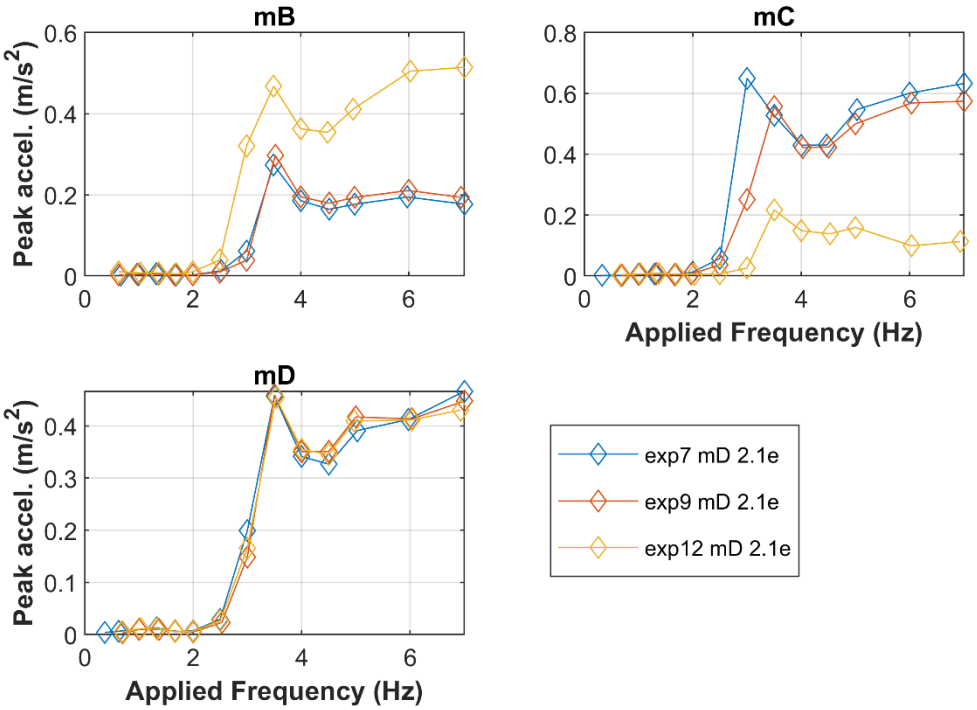


Figure C.61: Peak accelerations recorded along the North-South direction by the 2.1e instrument, at each applied frequency

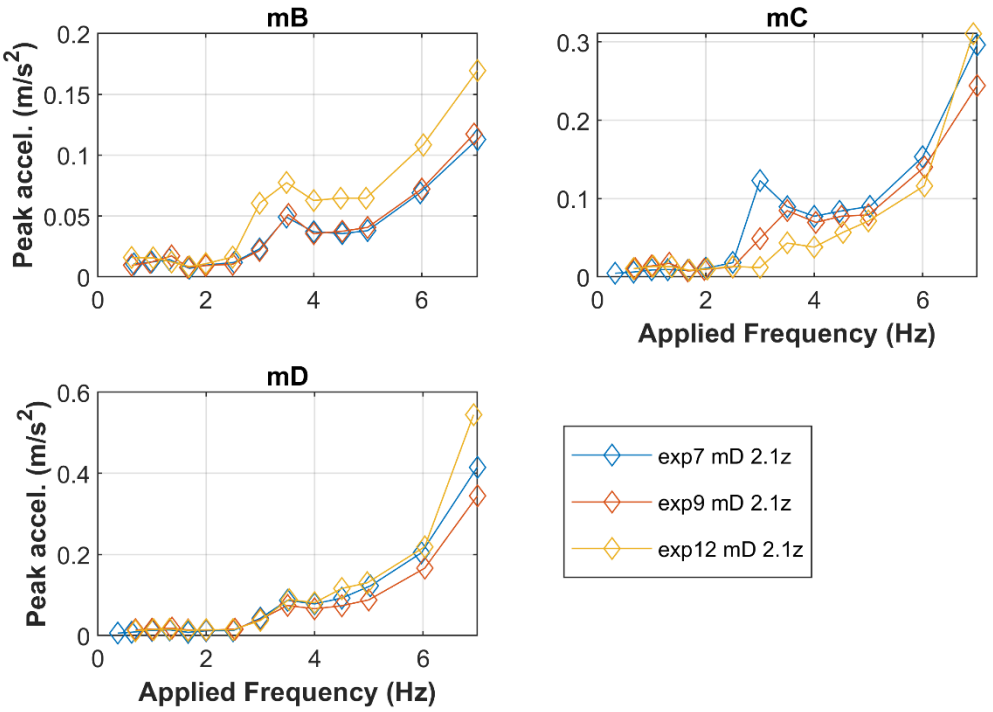


Figure C.62: Peak accelerations recorded along the North-South direction by the 2.1z instrument, at each applied frequency

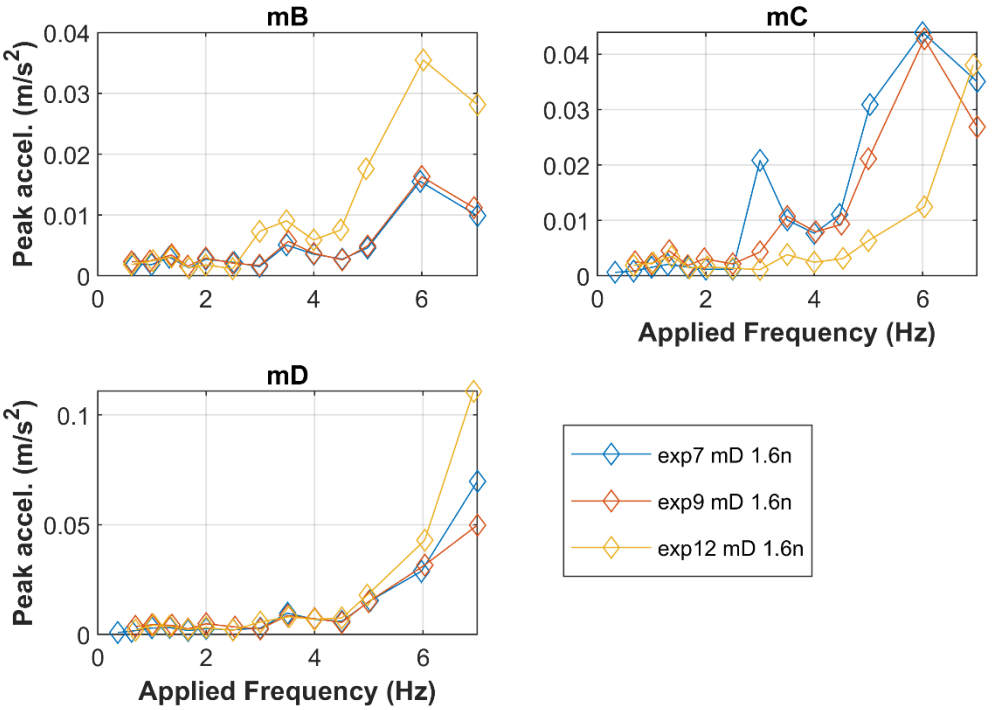


Figure C.63: Peak accelerations recorded along the North-South direction by the 1.6n instrument, at each applied frequency

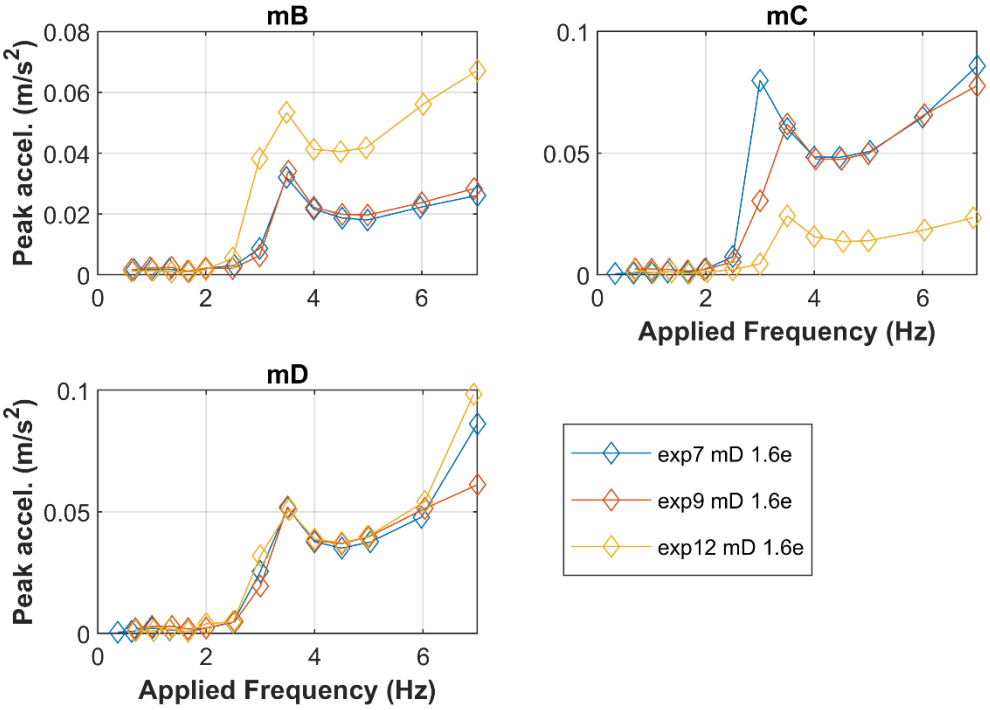


Figure C.64: Peak accelerations recorded along the North-South direction by the 1.6e instrument, at each applied frequency

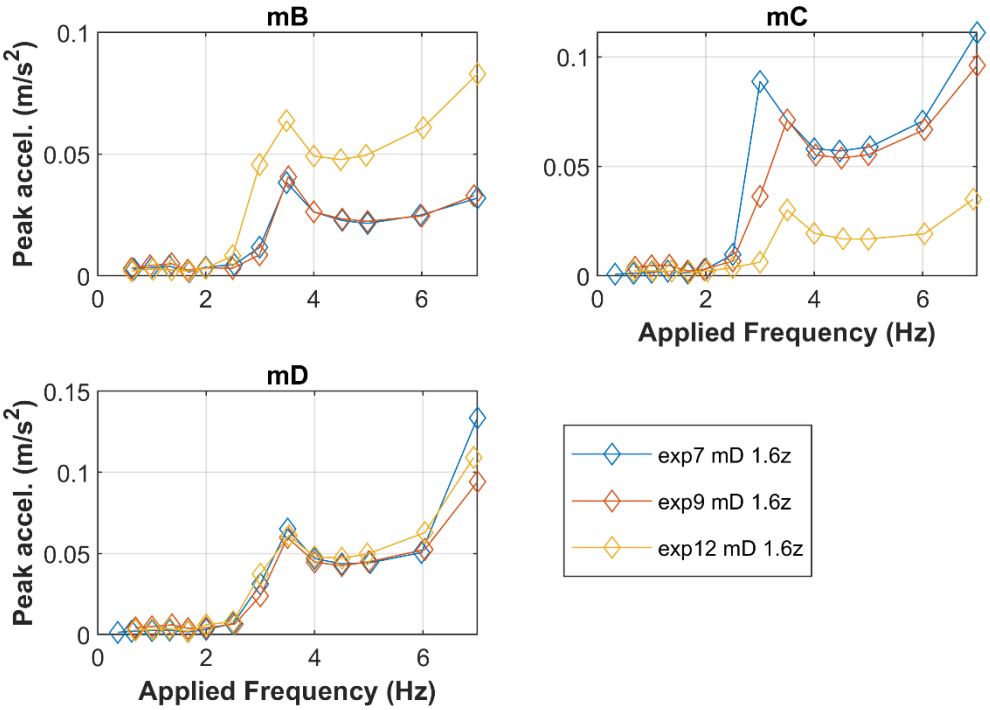


Figure C.65: Peak accelerations recorded along the North-South direction by the 1.6z instrument, at each applied frequency

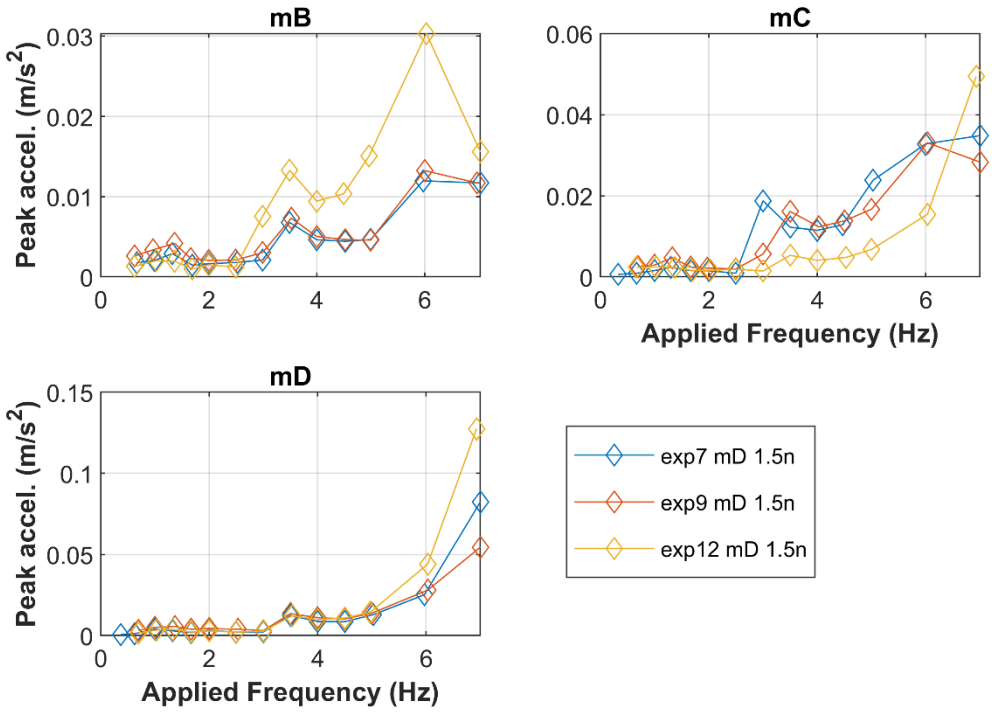


Figure C.66: Peak accelerations recorded along the North-South direction by the 1.5n instrument, at each applied frequency

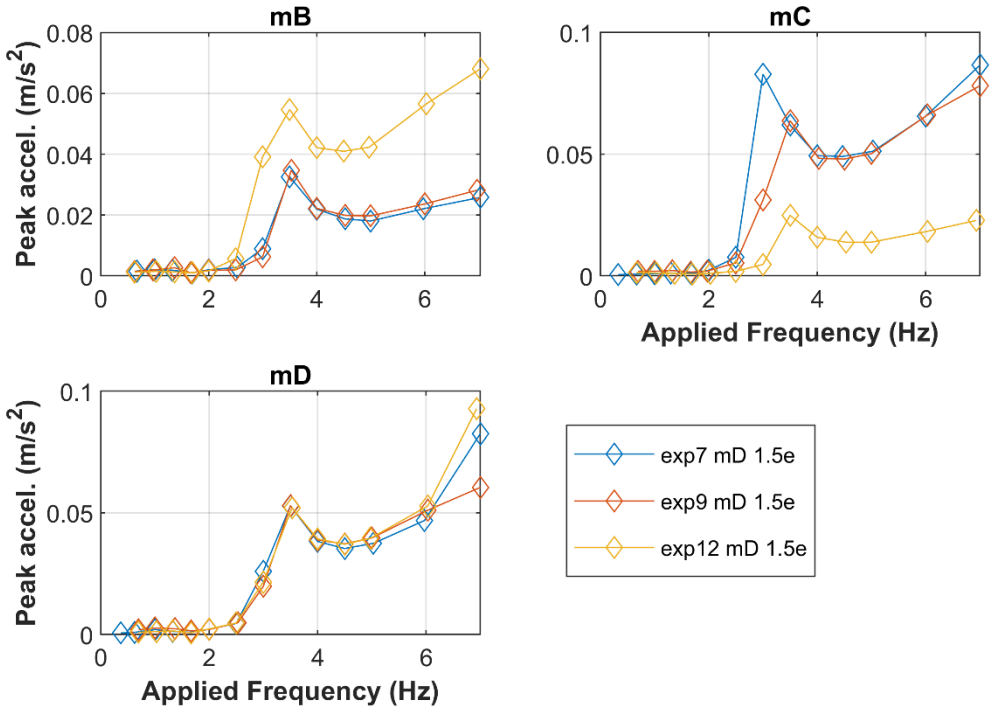


Figure C.67: Peak accelerations recorded along the North-South direction by the 1.5e instrument, at each applied frequency

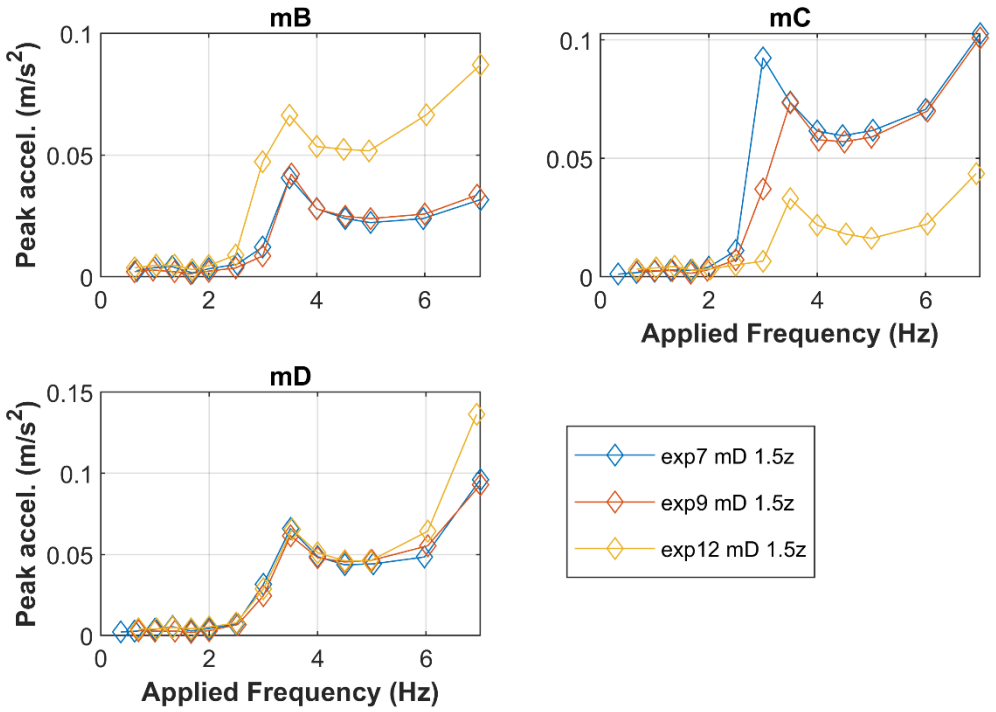


Figure C.68: Peak accelerations recorded along the North-South direction by the 1.5z instrument, at each applied frequency

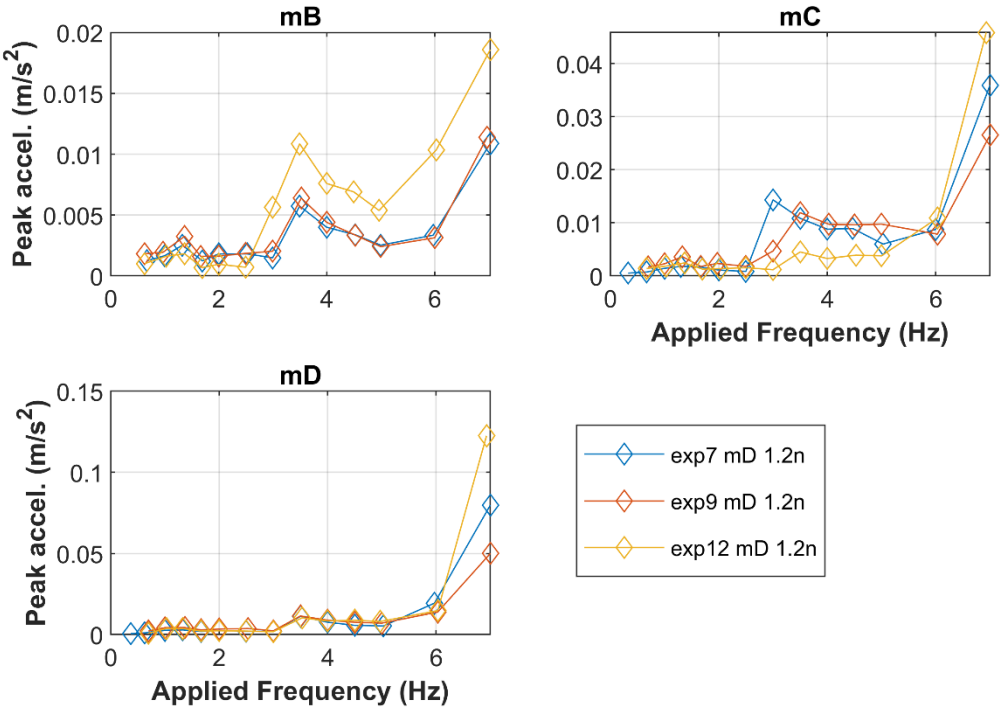


Figure C.69: Peak accelerations recorded along the North-South direction by the 1.2n instrument, at each applied frequency

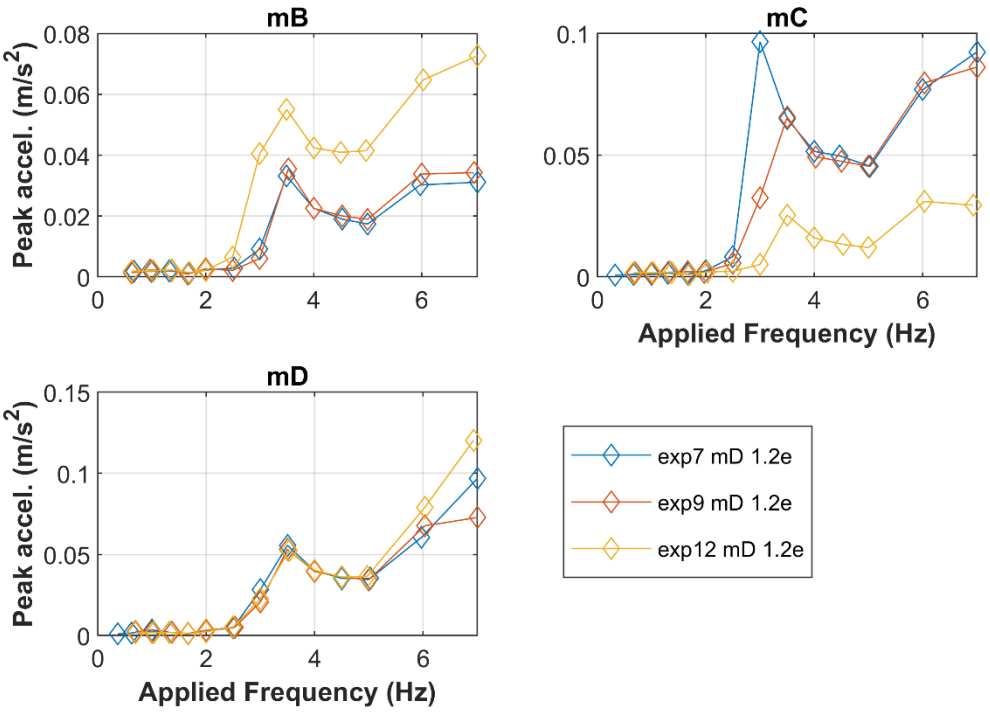


Figure C.70: Peak accelerations recorded along the North-South direction by the 1.2e instrument, at each applied frequency

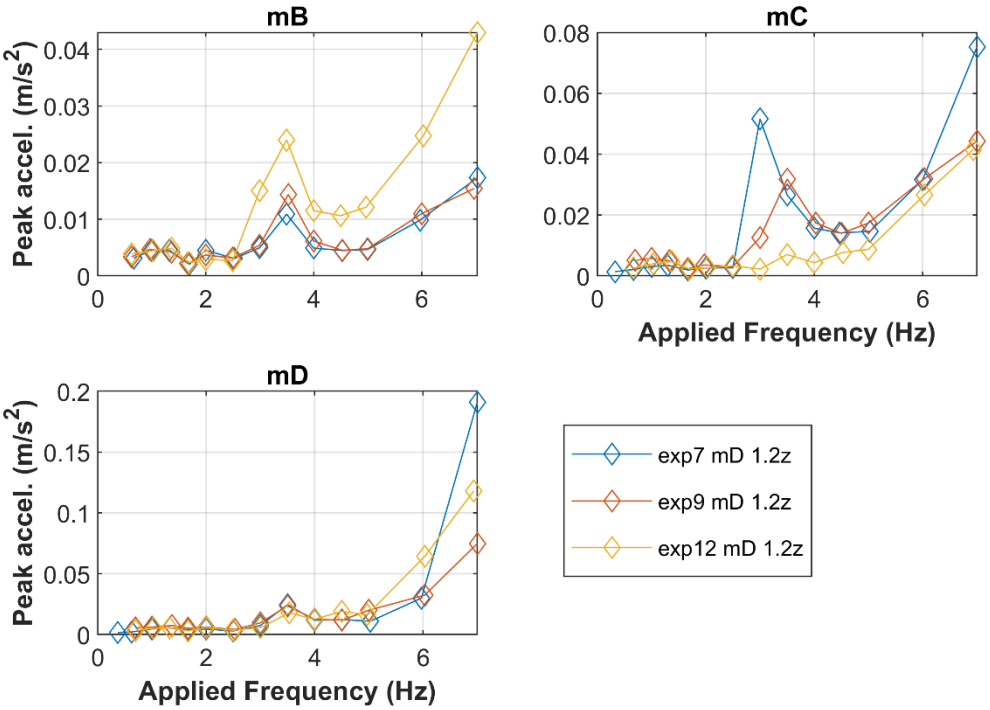


Figure C.71: Peak accelerations recorded along the North-South direction by the 1.2z instrument, at each applied frequency

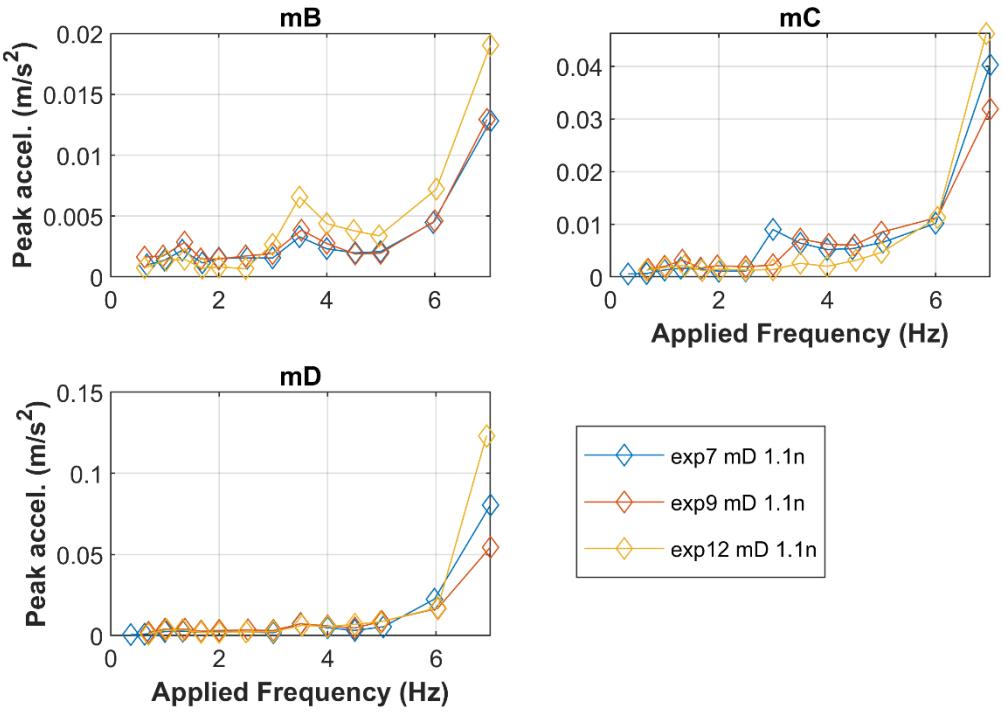


Figure C.72: Peak accelerations recorded along the North-South direction by the 1.1n instrument, at each applied frequency

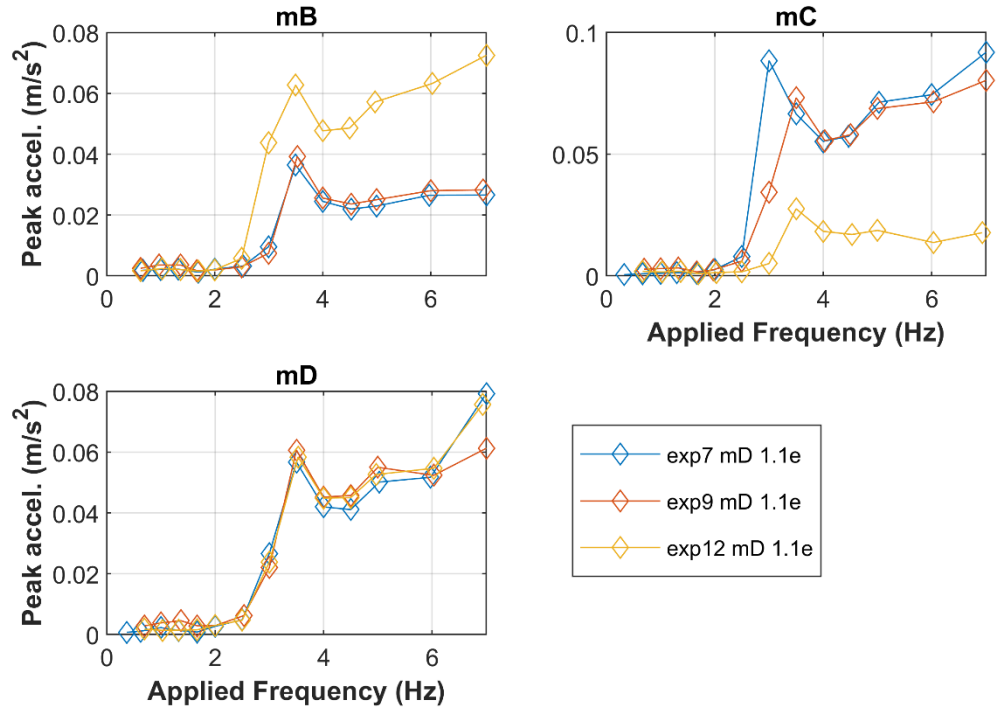


Figure C.73: Peak accelerations recorded along the North-South direction by the 1.1e instrument, at each applied frequency

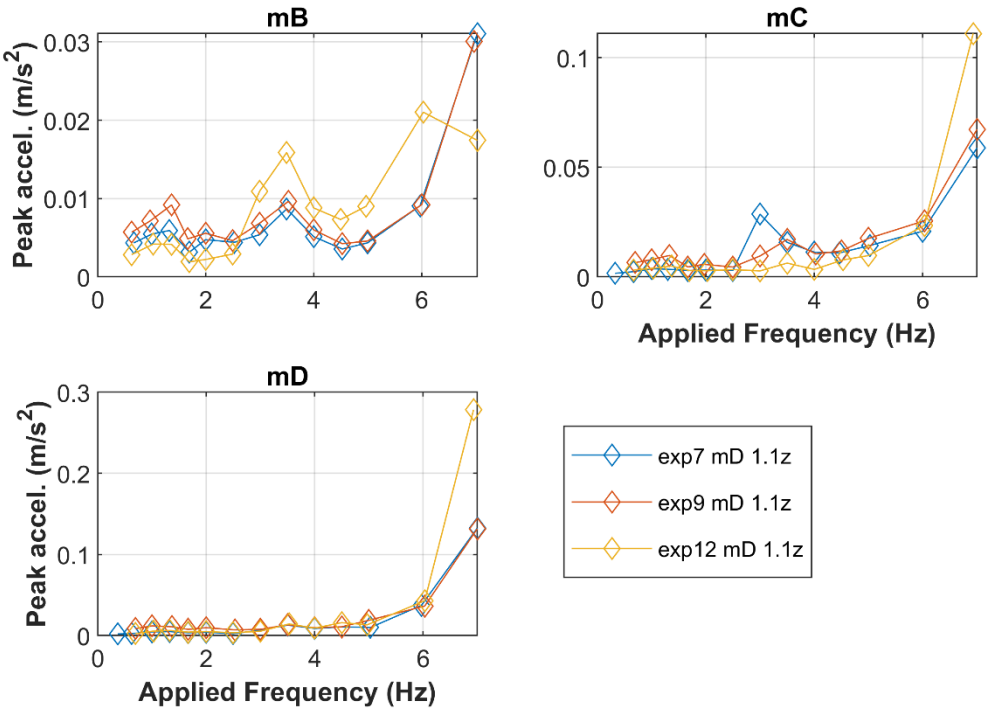


Figure C.74: Peak accelerations recorded along the North-South direction by the 1.1z instrument, at each applied frequency

Appendix C.5 Repeatability of data recorded during the experiments on the Partly Braced structure loaded along its Strong plane

The following figures compare the peak accelerations, recorded by different instruments at each applied frequency, during the experiments on the Partly Braced structure which was loaded along its Strong plane (PBr_S) Three identical experiments are compared (exp8, epx10 and exp13), while for each one, three different vibrator masses where used (mB, mC and mD). Figures processed from data recorded by all structural instruments are available are presented. Also, all three North-South (n), East-West (e) and vertical (z) motion components are shown.

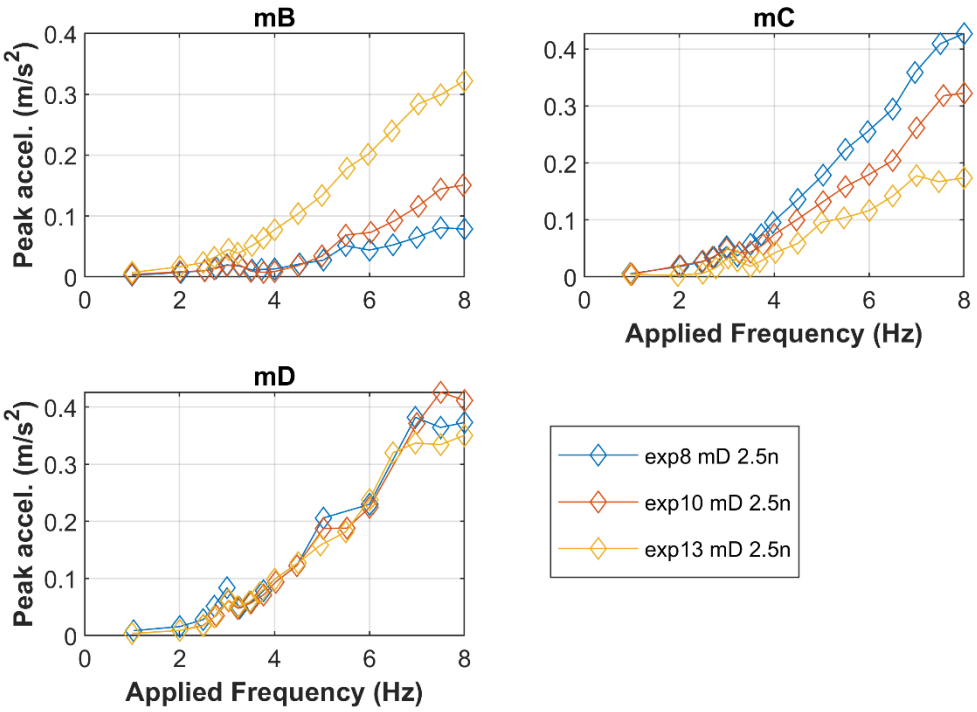


Figure C.75: Peak accelerations recorded along the North-South direction by the 2.5n instrument, at each applied frequency

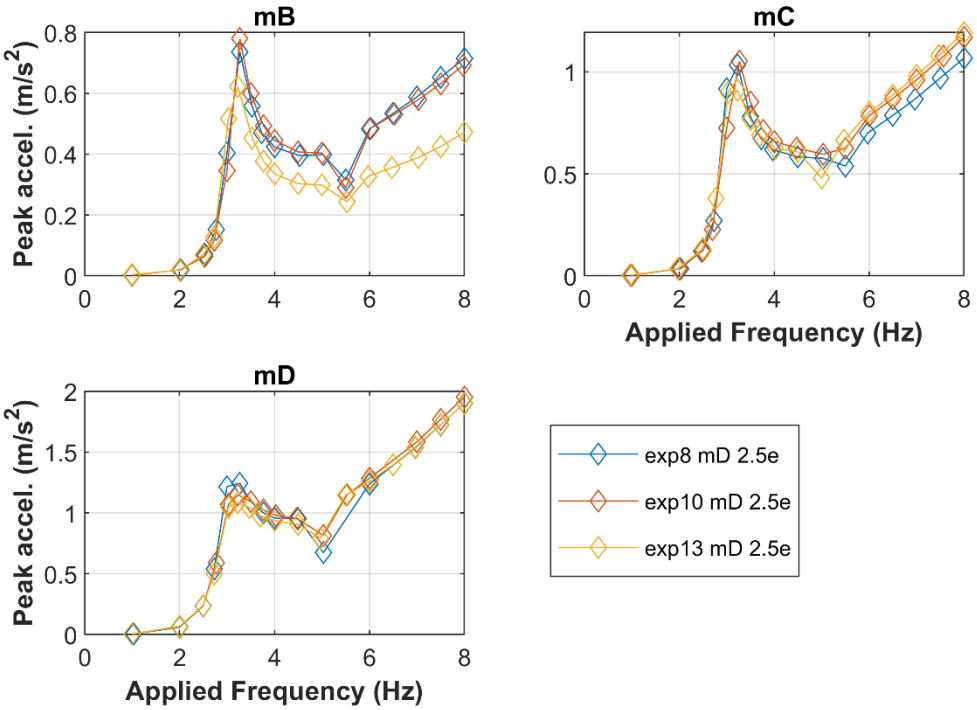


Figure C.76: Peak accelerations recorded along the North-South direction by the 2.5e instrument, at each applied frequency

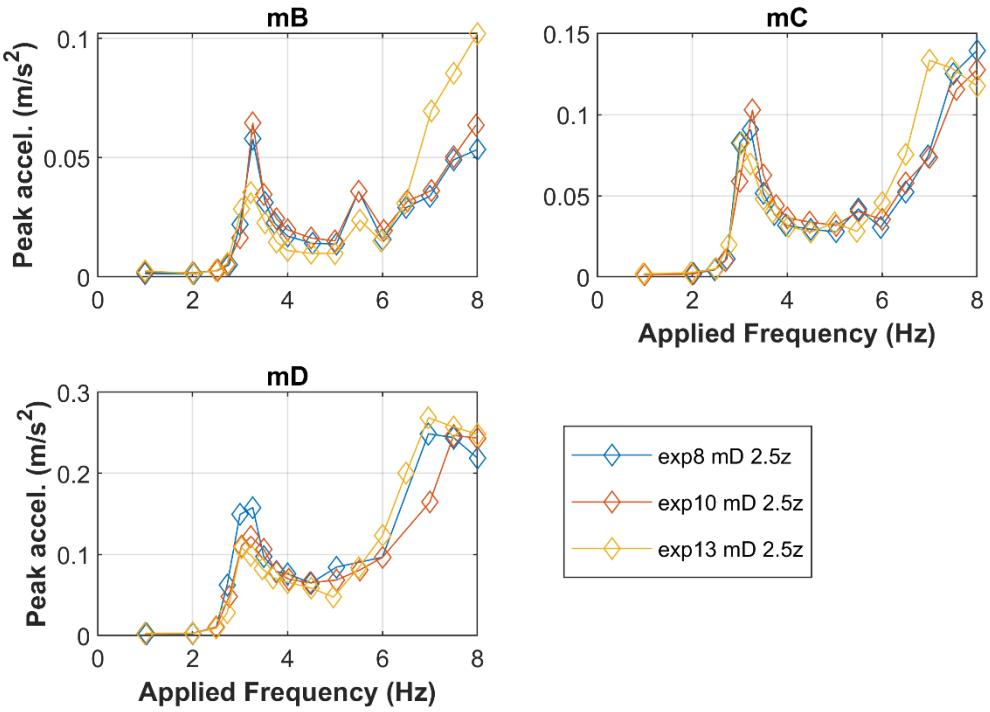


Figure C.77: Peak accelerations recorded along the North-South direction by the 2.5z instrument, at each applied frequency

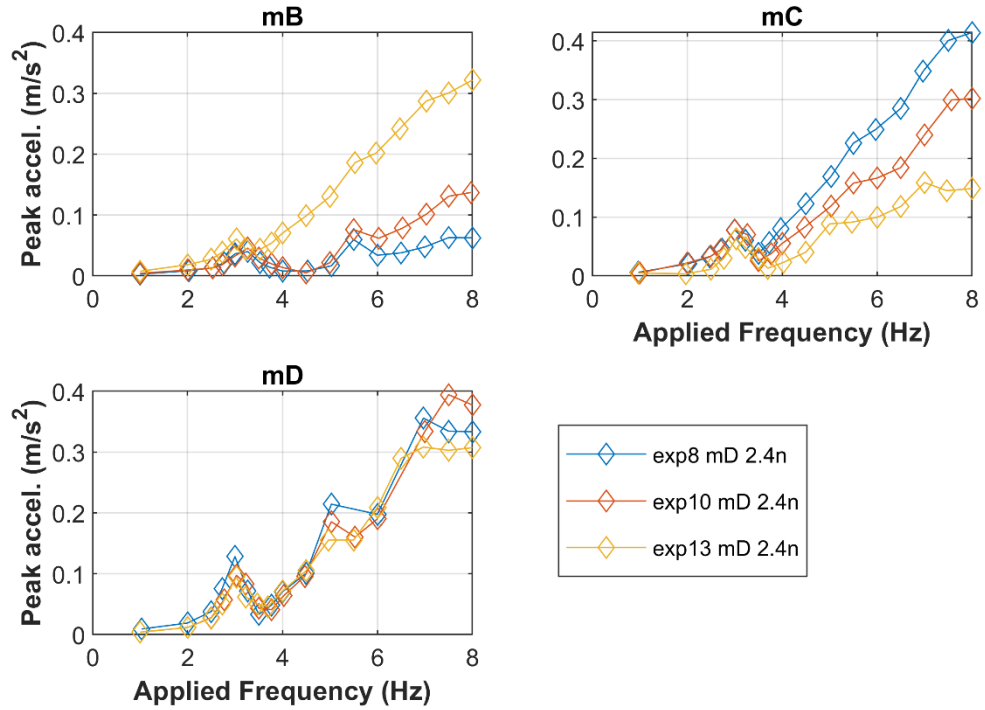


Figure C.78: Peak accelerations recorded along the North-South direction by the 2.4n instrument, at each applied frequency

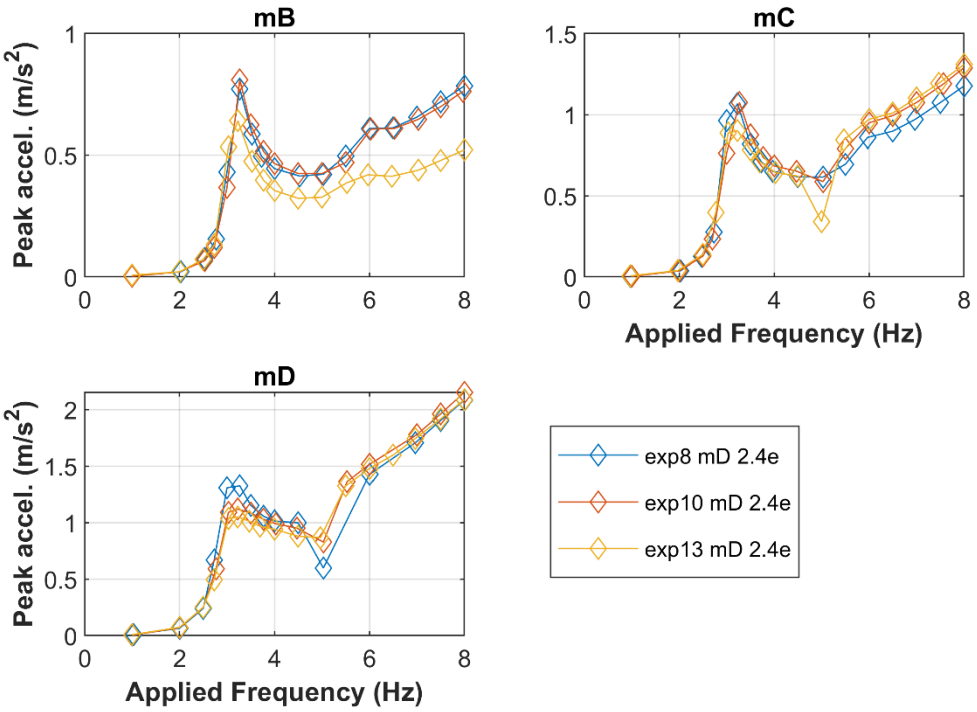


Figure C.79: Peak accelerations recorded along the North-South direction by the 2.4e instrument, at each applied frequency

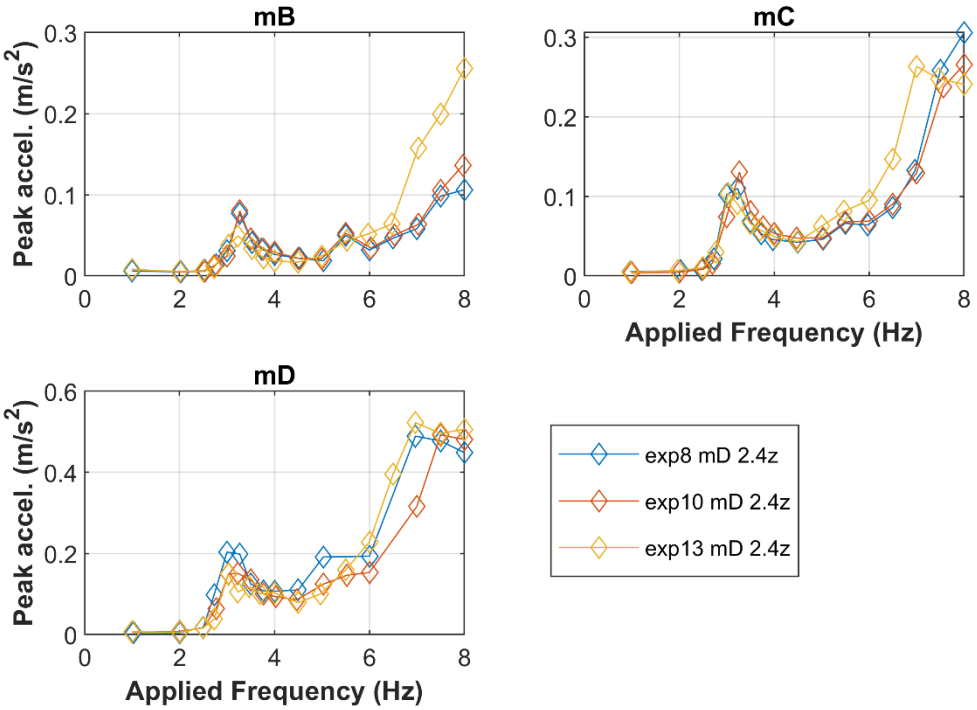


Figure C.80: Peak accelerations recorded along the North-South direction by the 2.4z instrument, at each applied frequency

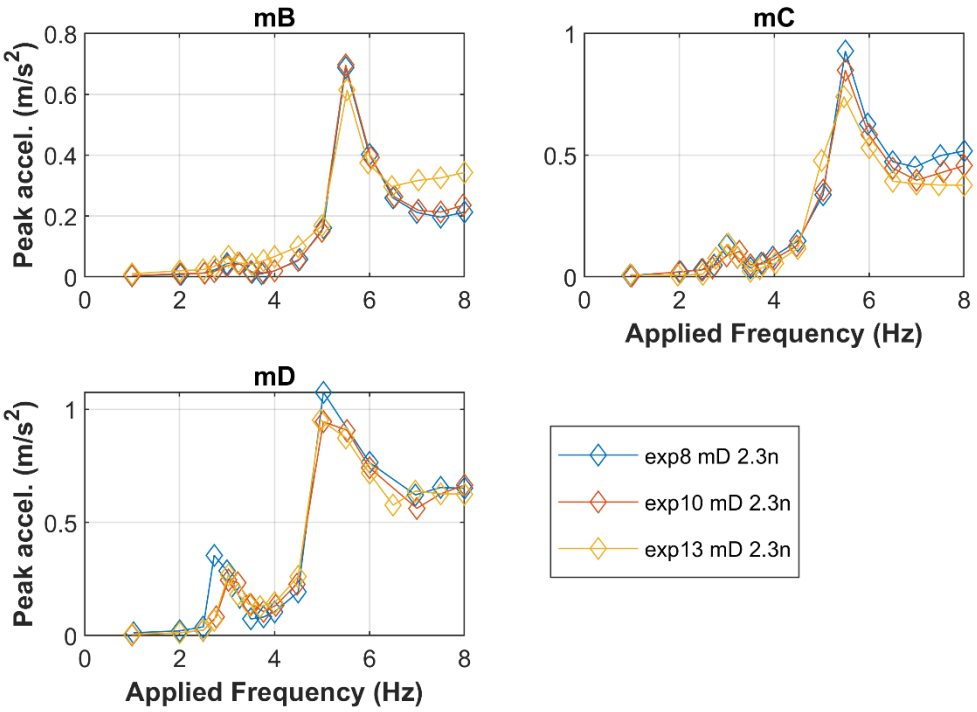


Figure C.81: Peak accelerations recorded along the North-South direction by the 2.3n instrument, at each applied frequency

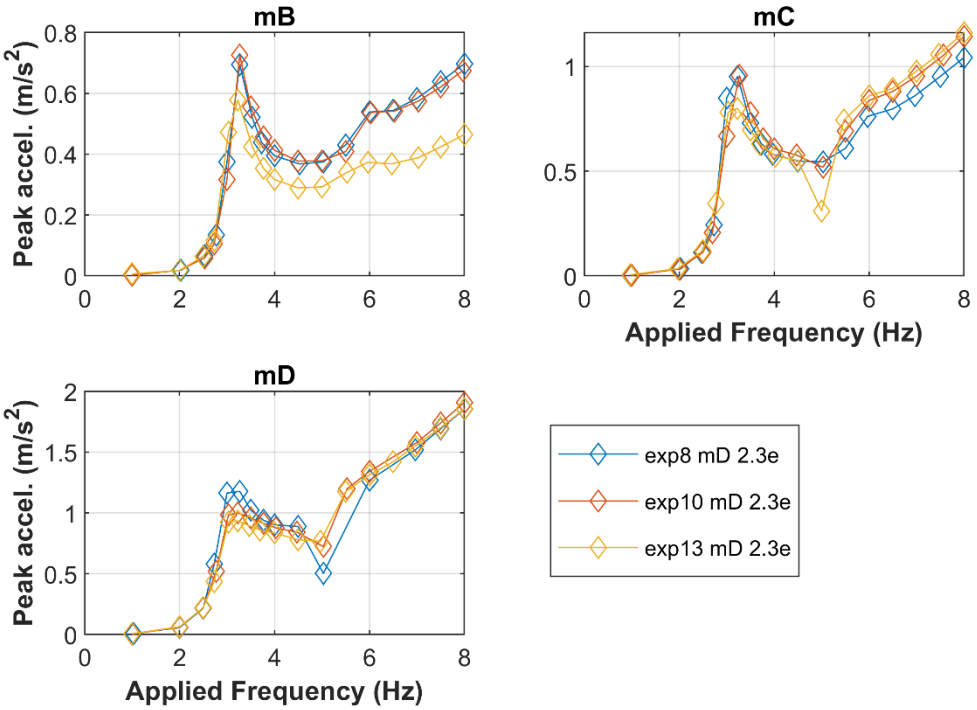


Figure C.82: Peak accelerations recorded along the North-South direction by the 2.3e instrument, at each applied frequency

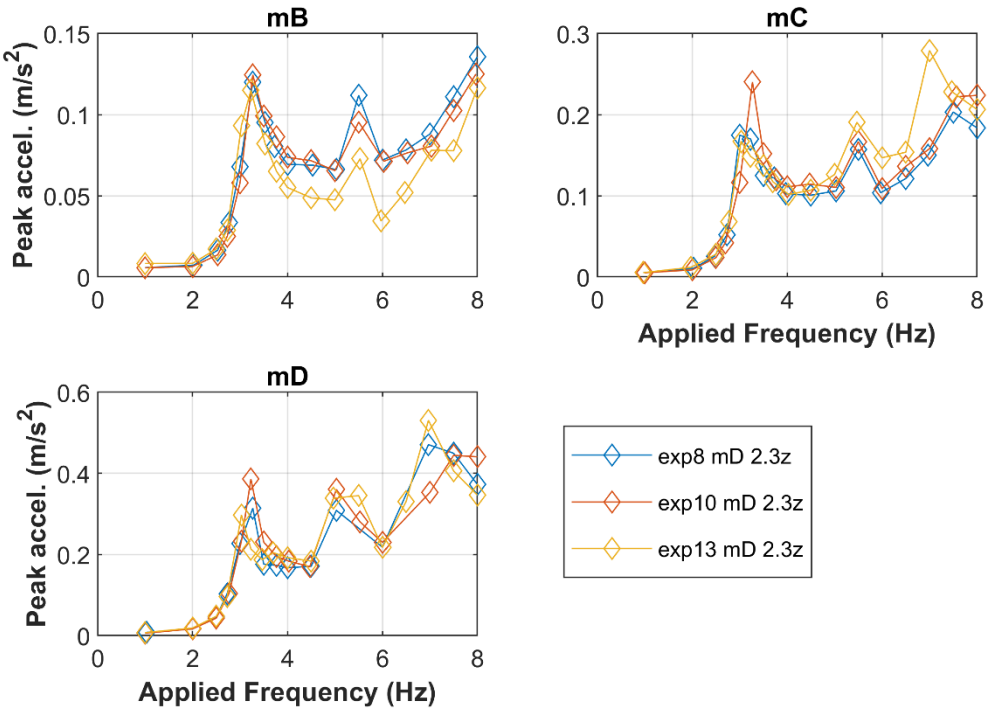


Figure C.83: Peak accelerations recorded along the North-South direction by the 2.3z instrument, at each applied frequency

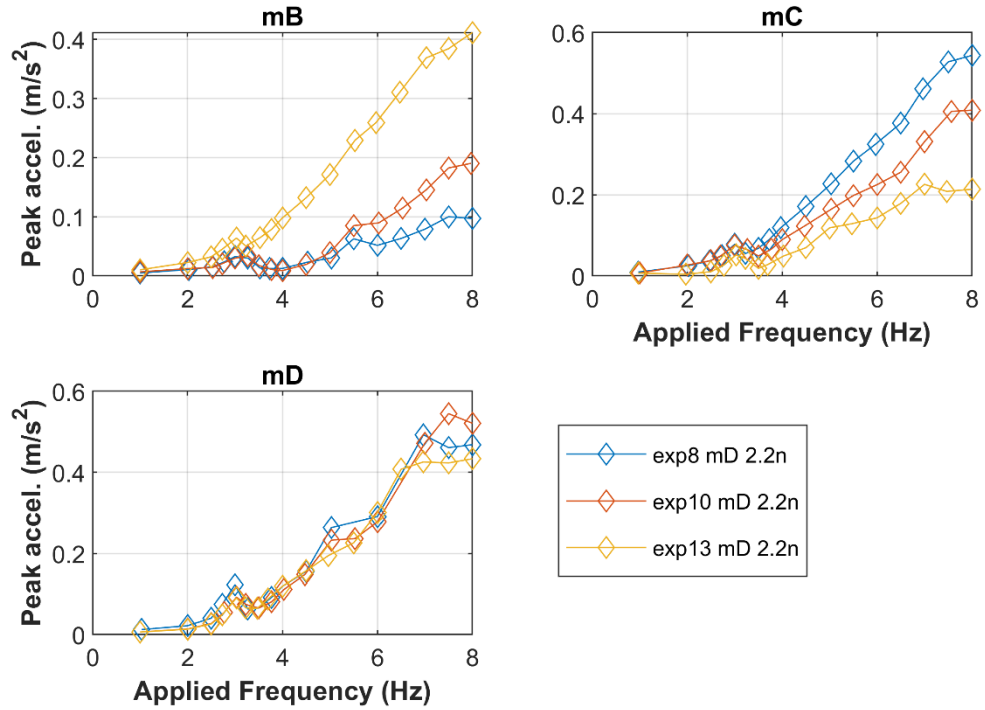


Figure C.84: Peak accelerations recorded along the North-South direction by the 2.2n instrument, at each applied frequency

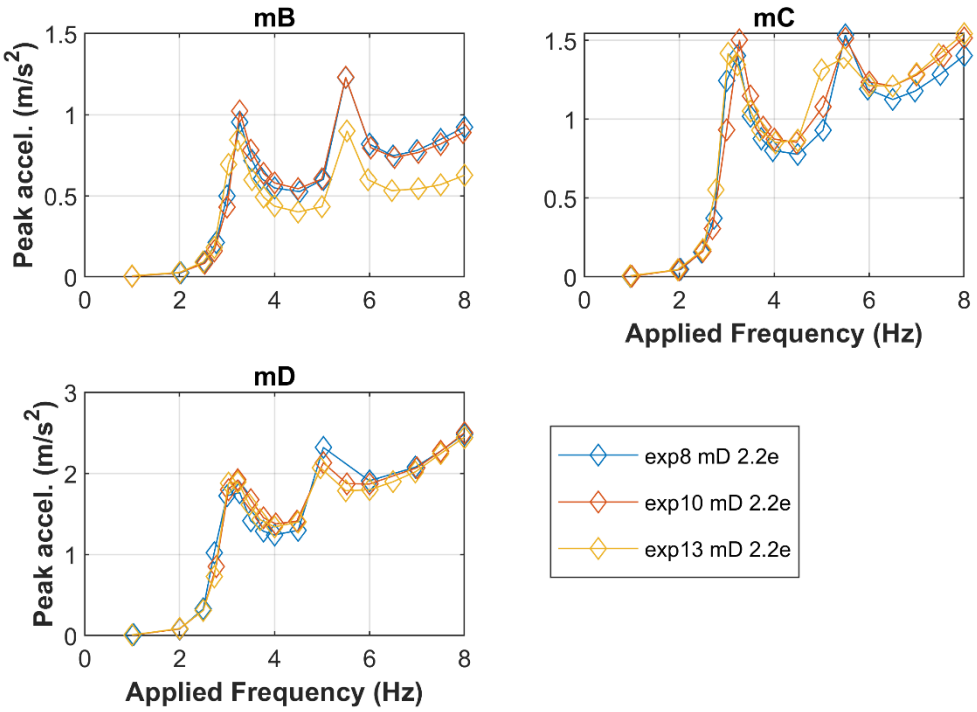


Figure C.85: Peak accelerations recorded along the North-South direction by the 2.2e instrument, at each applied frequency

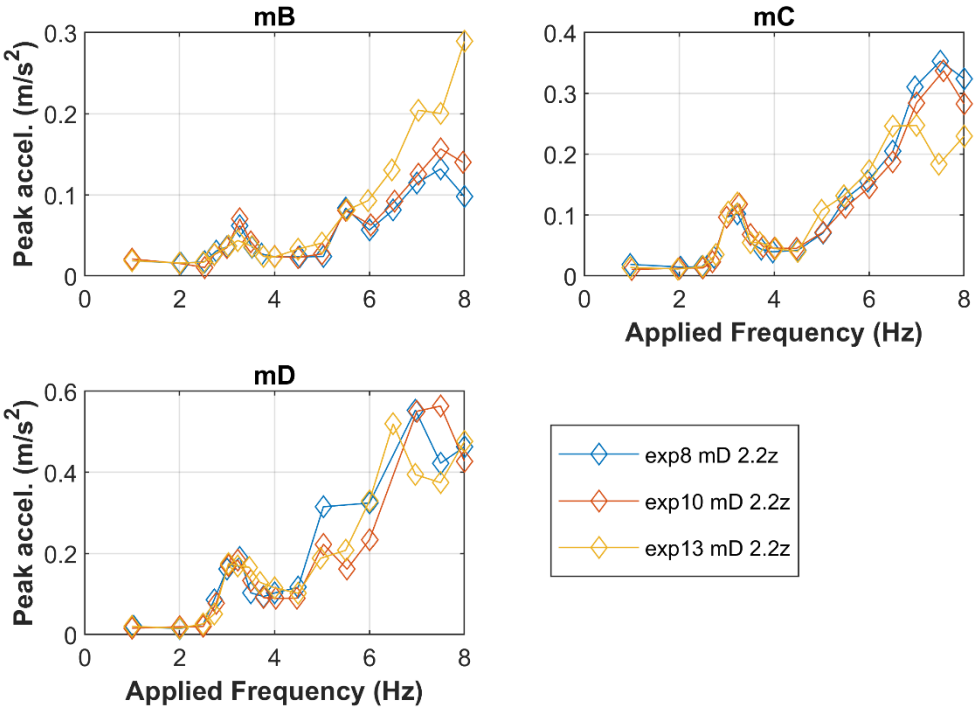


Figure C.86: Peak accelerations recorded along the North-South direction by the 2.2z instrument, at each applied frequency

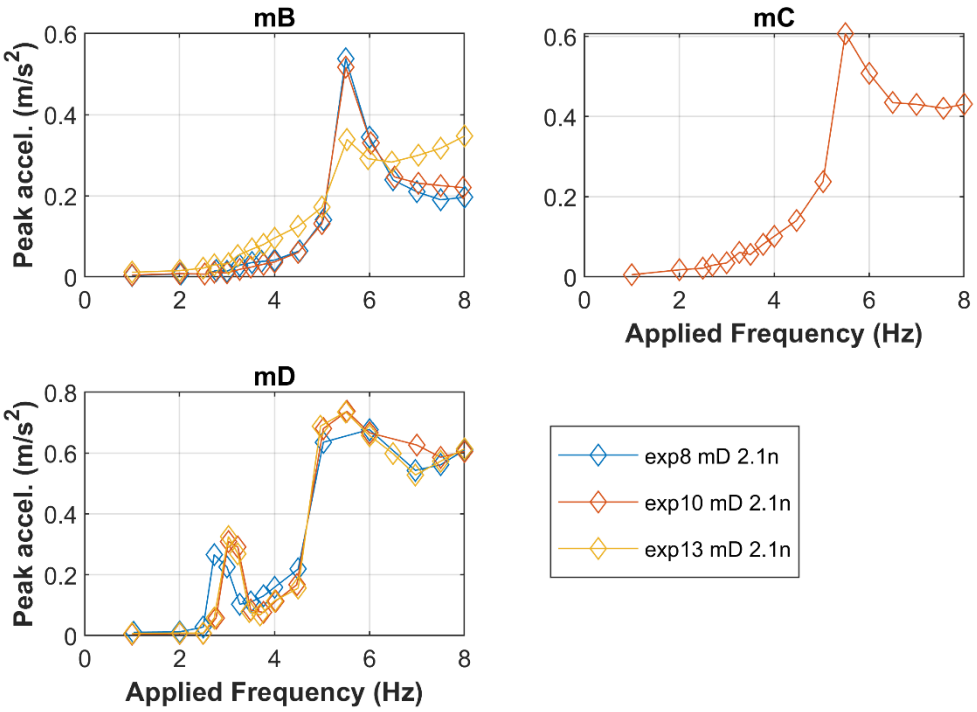


Figure C.87: Peak accelerations recorded along the North-South direction by the 2.1n instrument, at each applied frequency

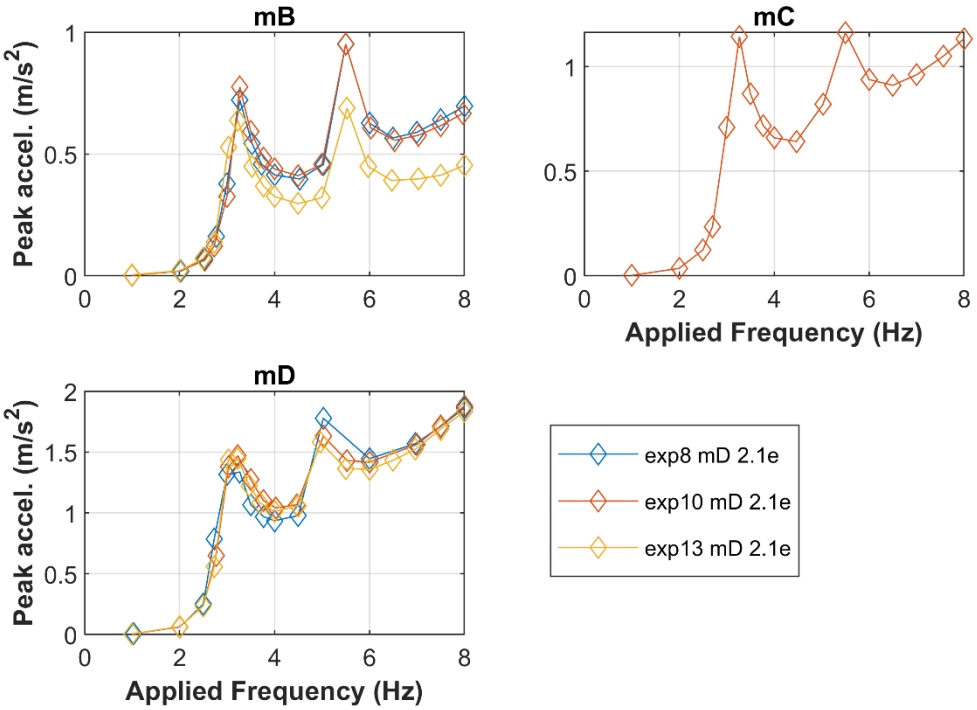


Figure C.88: Peak accelerations recorded along the North-South direction by the 2.1e instrument, at each applied frequency

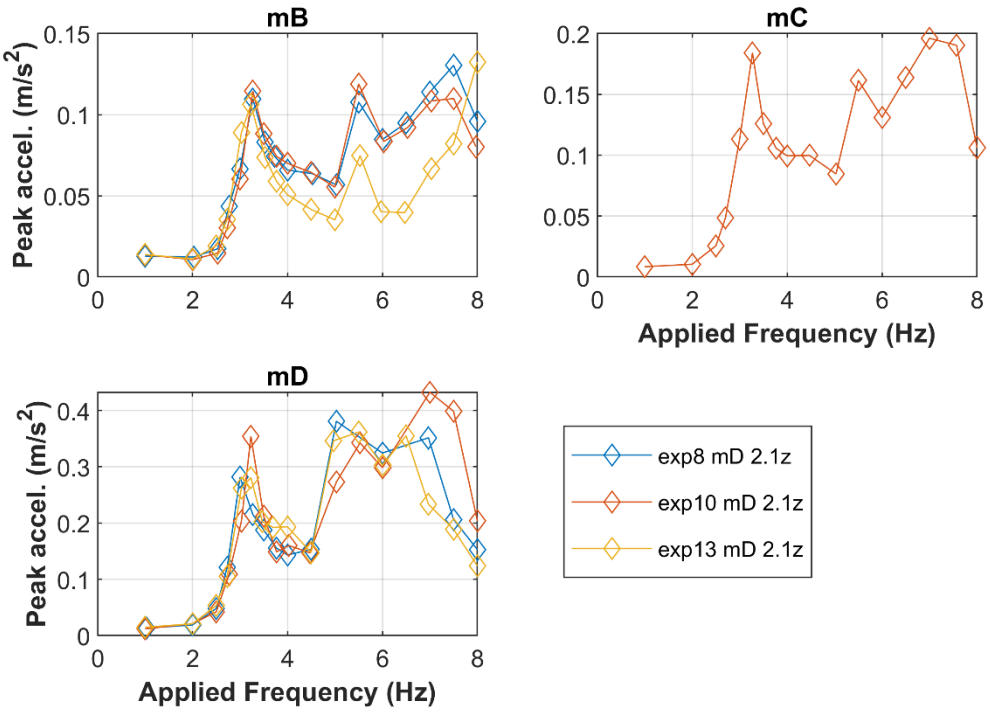


Figure C.89: Peak accelerations recorded along the North-South direction by the 2.1z instrument, at each applied frequency

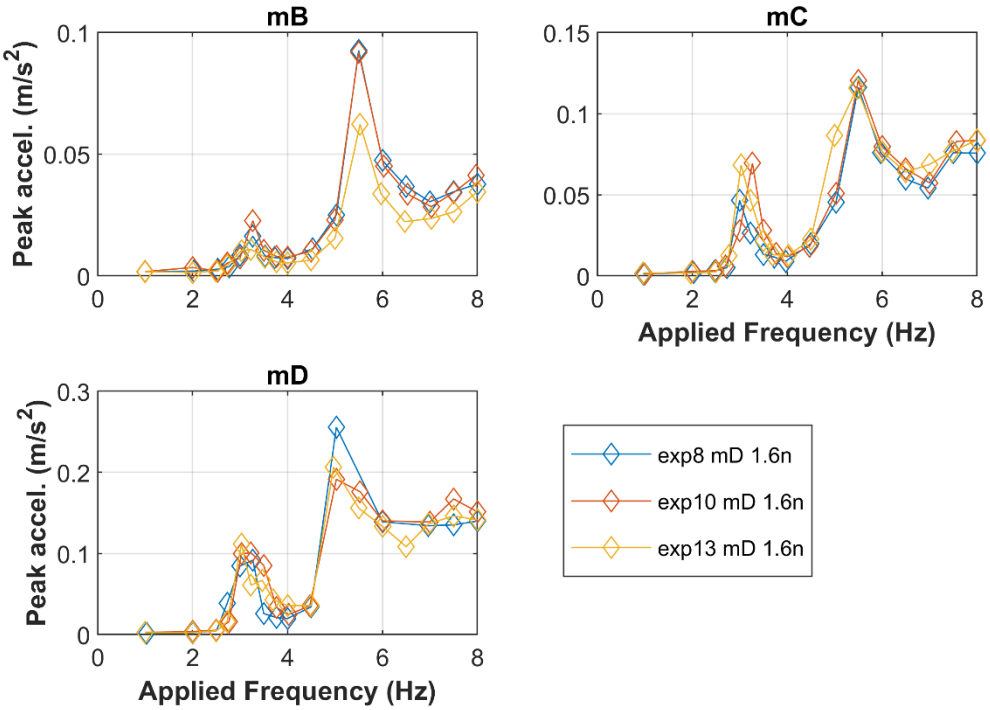


Figure C.90: Peak accelerations recorded along the North-South direction by the 1.6n instrument, at each applied frequency

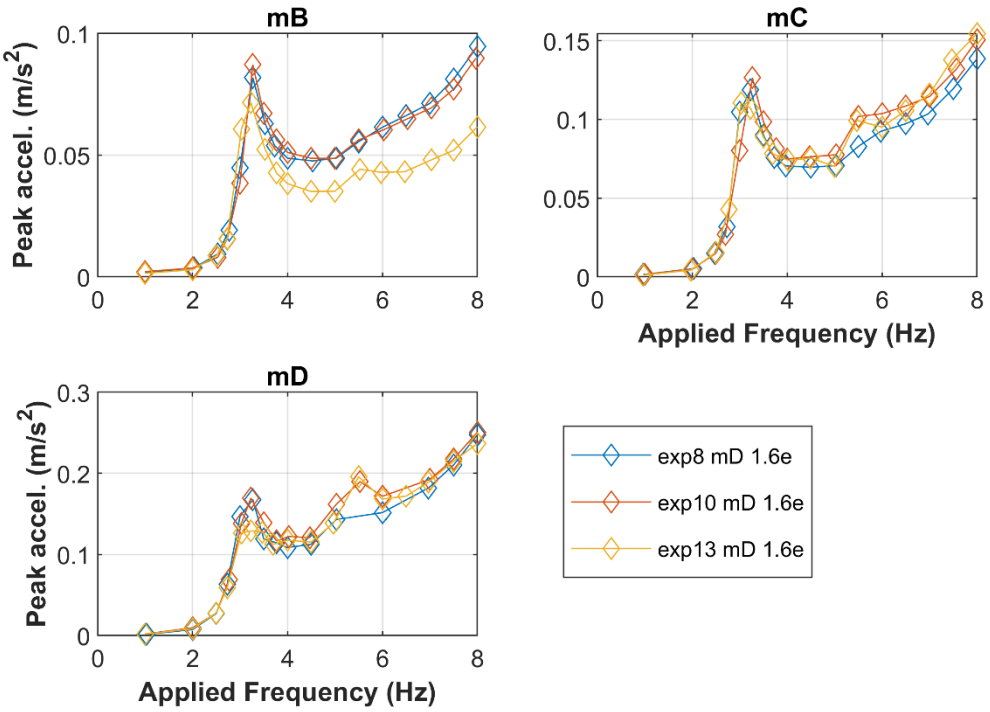


Figure C.91: Peak accelerations recorded along the North-South direction by the 1.6e instrument, at each applied frequency

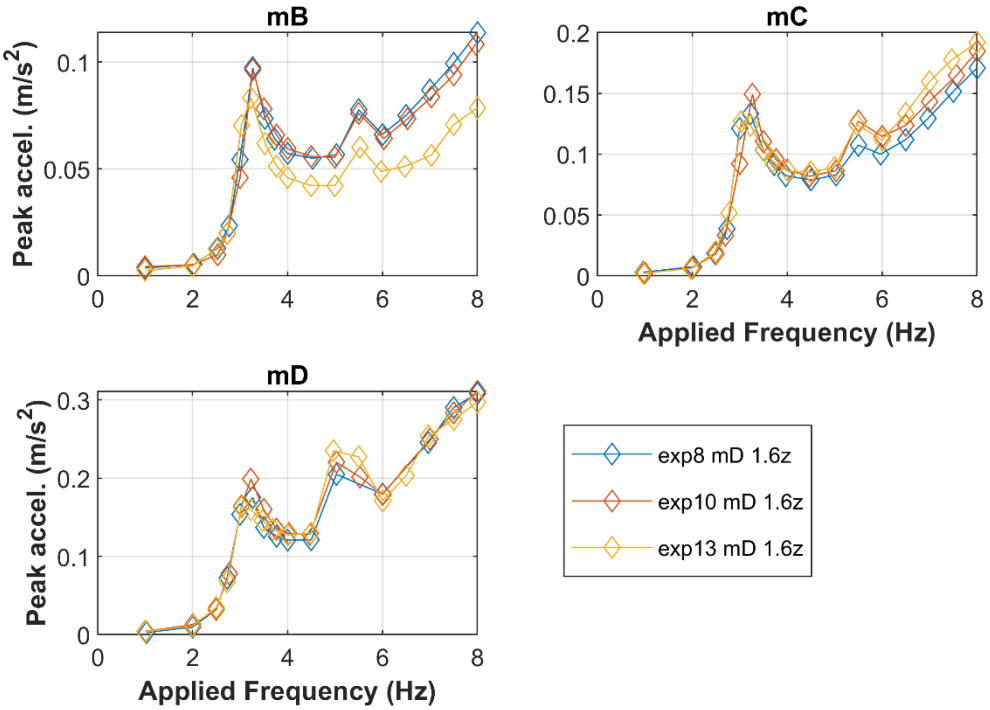


Figure C.92: Peak accelerations recorded along the North-South direction by the 1.6z instrument, at each applied frequency

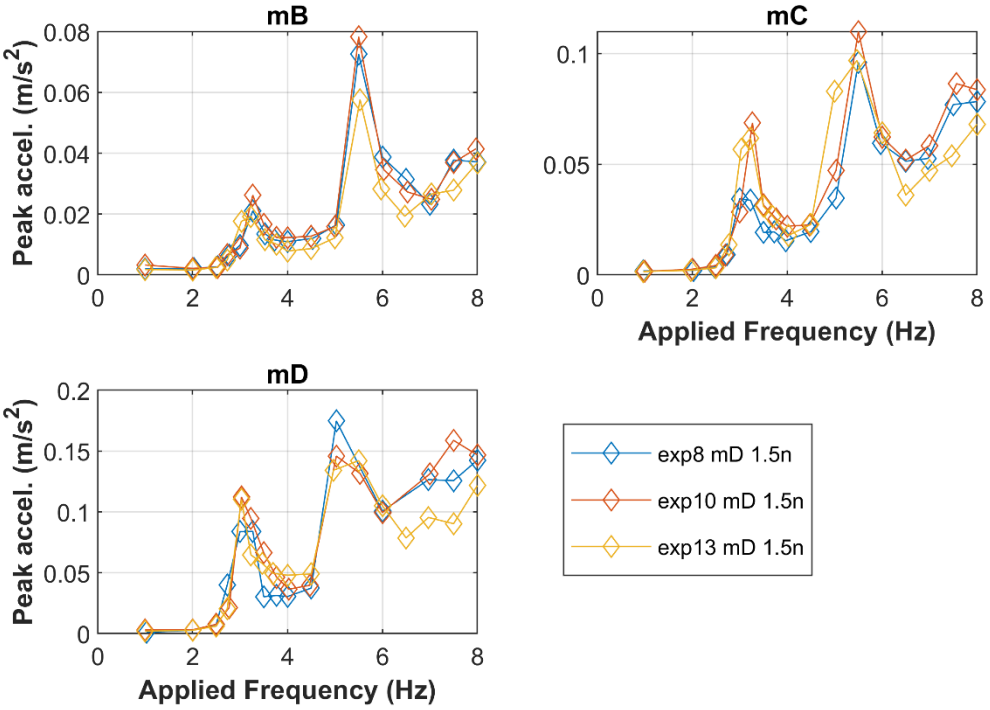


Figure C.93: Peak accelerations recorded along the North-South direction by the 1.5n instrument, at each applied frequency

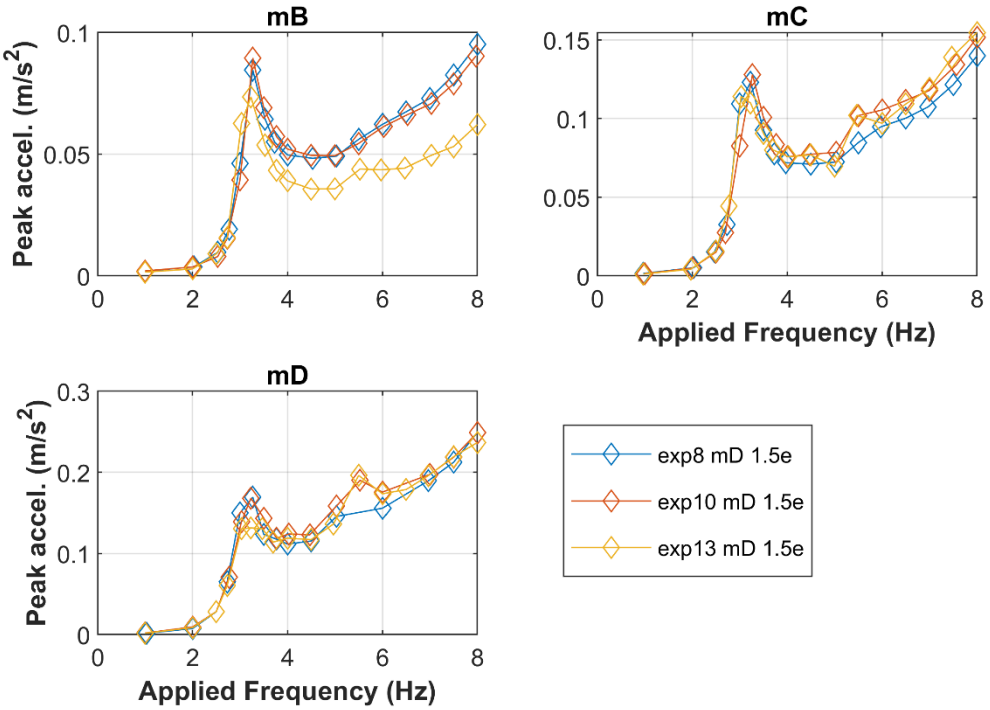


Figure C.94: Peak accelerations recorded along the North-South direction by the 1.5e instrument, at each applied frequency

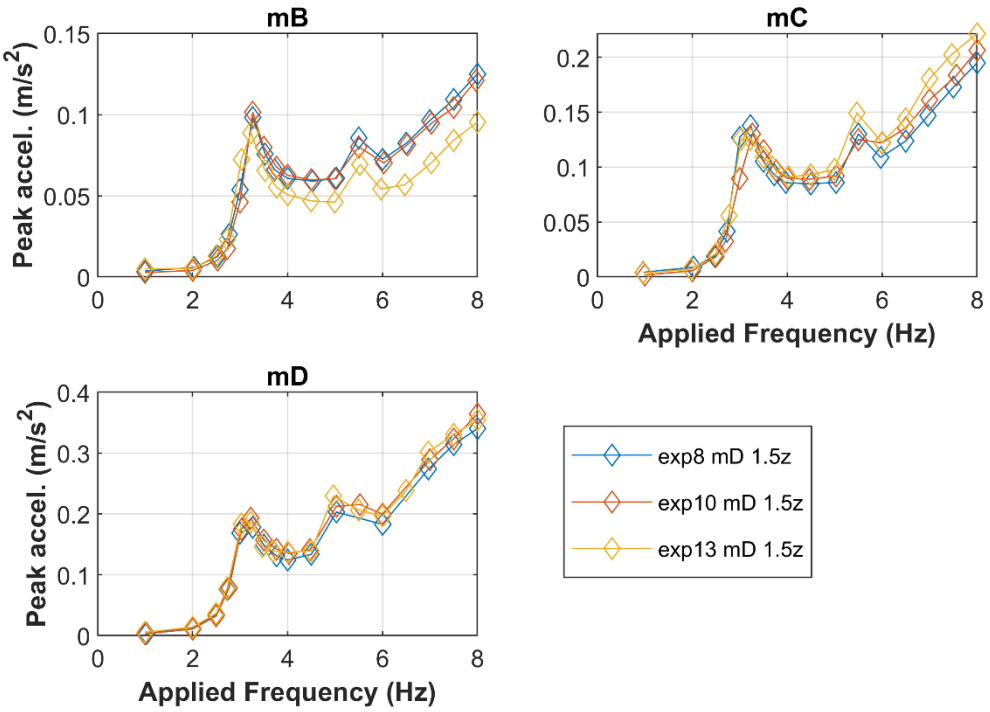


Figure C.95: Peak accelerations recorded along the North-South direction by the 1.5z instrument, at each applied frequency

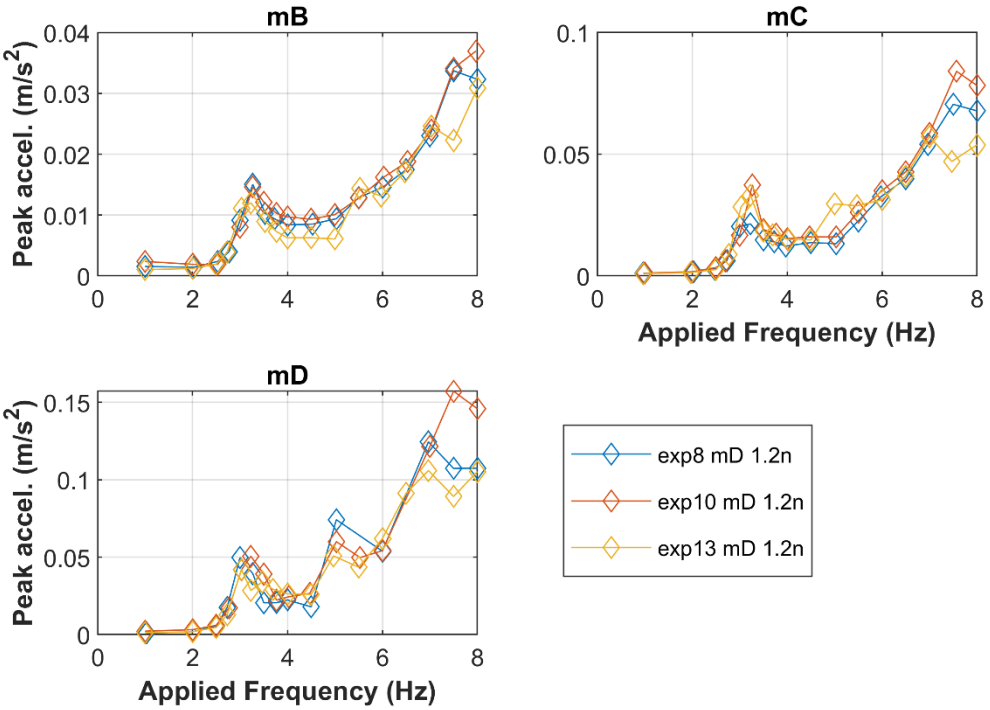


Figure C.96: Peak accelerations recorded along the North-South direction by the 1.2n instrument, at each applied frequency

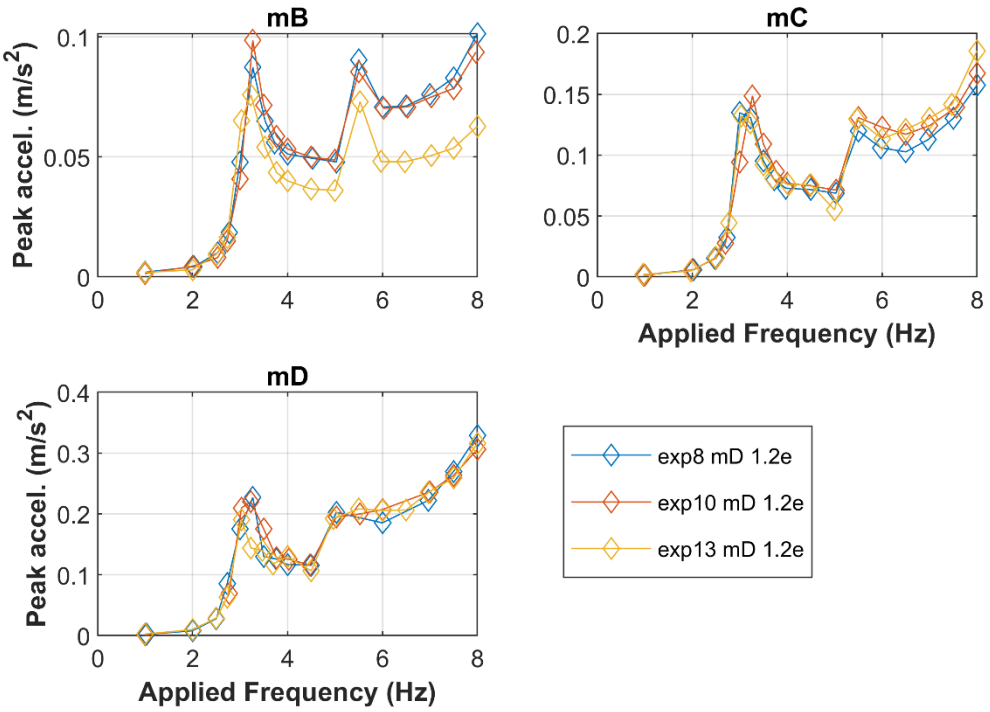


Figure C.97: Peak accelerations recorded along the North-South direction by the 1.2e instrument, at each applied frequency

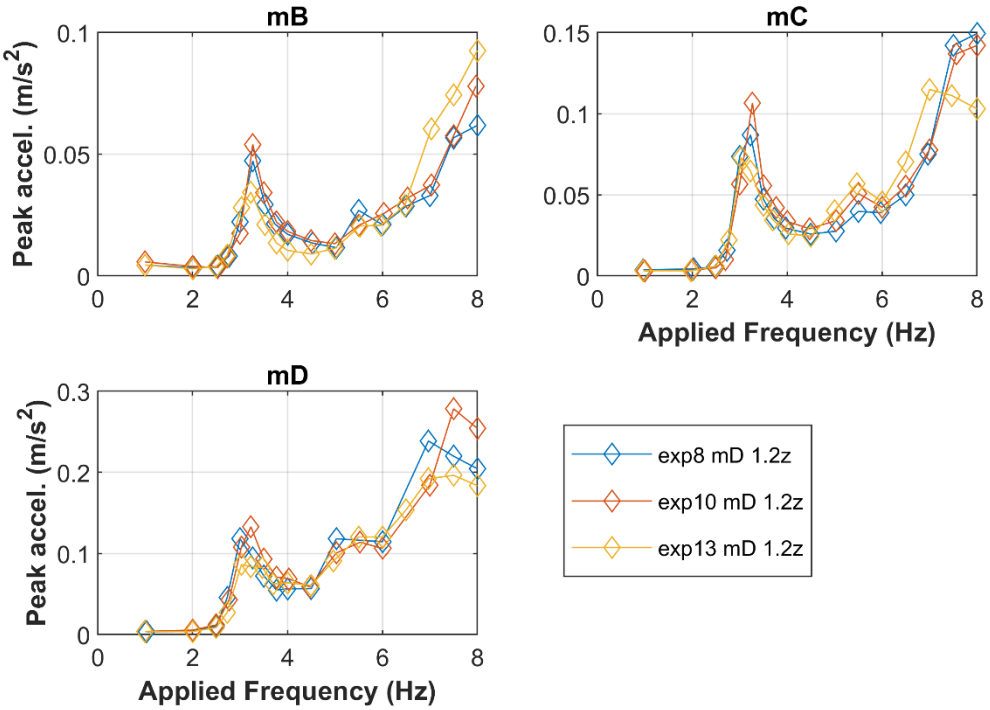


Figure C.98: Peak accelerations recorded along the North-South direction by the 1.2z instrument, at each applied frequency

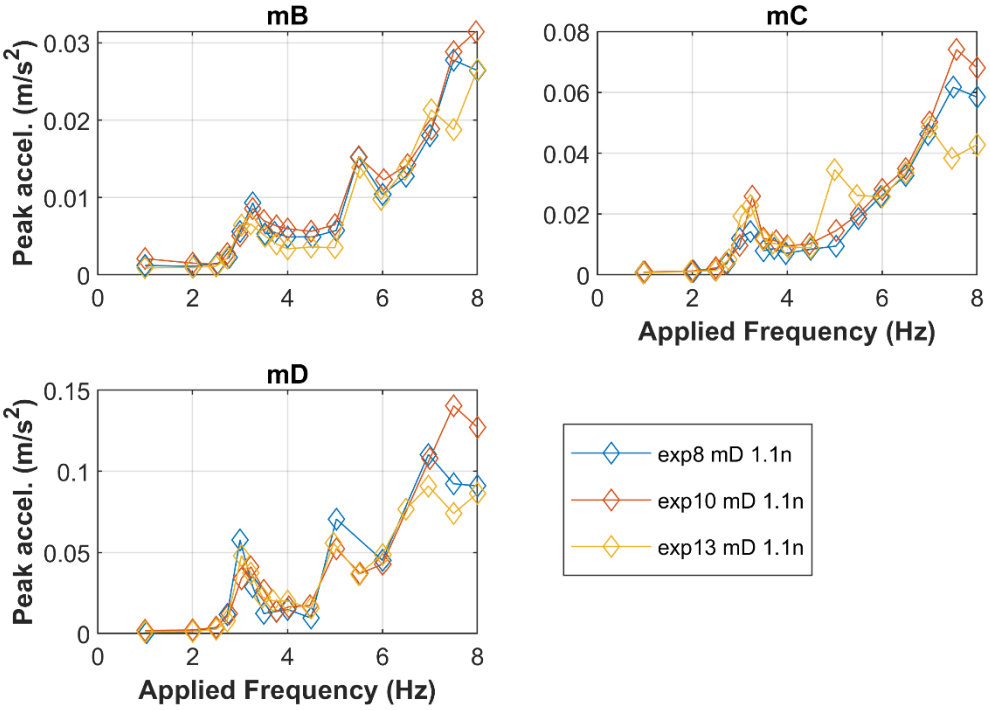


Figure C.99: Peak accelerations recorded along the North-South direction by the 1.1n instrument, at each applied frequency

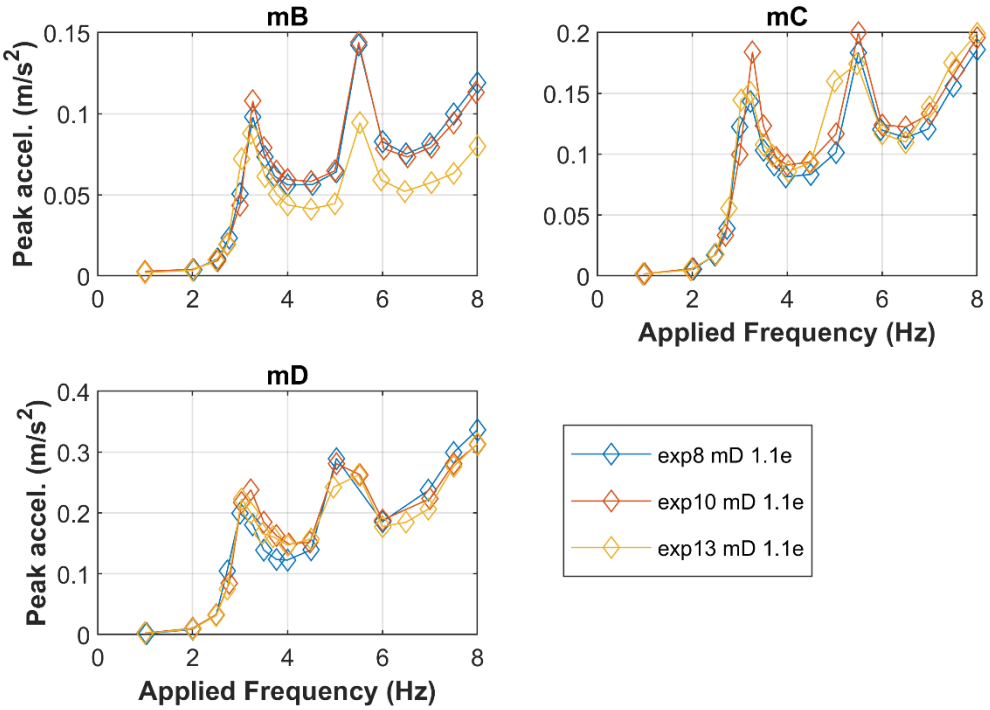


Figure C.100: Peak accelerations recorded along the North-South direction by the 1.1e instrument, at each applied frequency

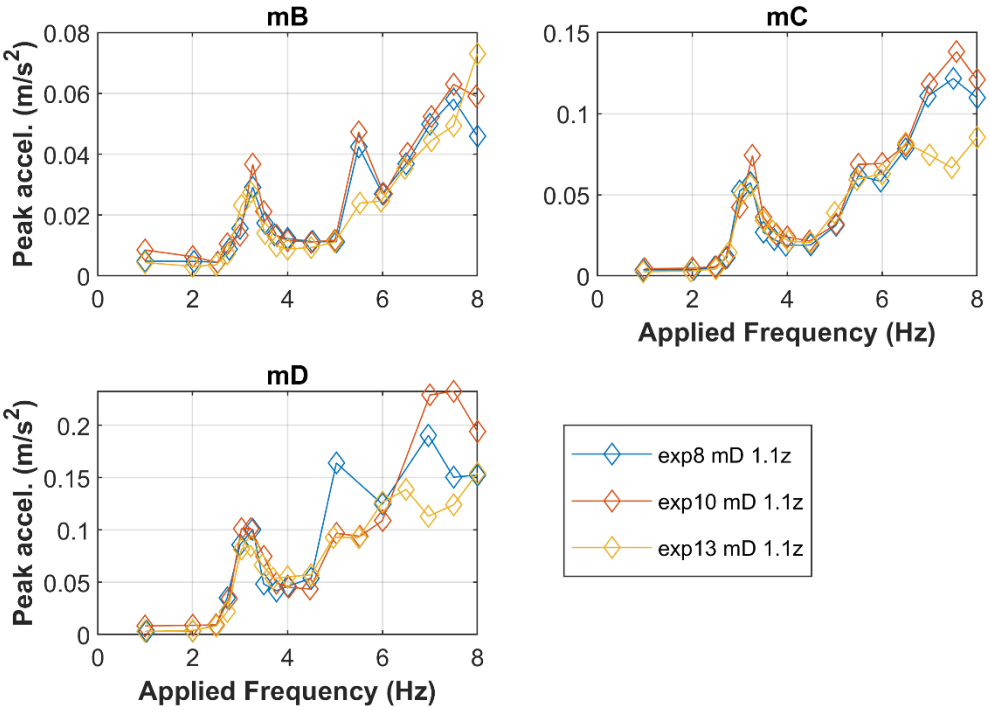


Figure C.101: Peak accelerations recorded along the North-South direction by the 1.1z instrument, at each applied frequency

Appendix C.6 Error between repeated top slab response of repeated experiments

The following figures illustrate the error that represent the divergence between outputs of identical experiments. The error is calculated according to Eq. 5.15, using the top slab accelerations recorded by the 2.5 instrument along the NS direction. Results from experiments on the FBr_2Ts, PBr_W and PBr_S structural configurations are presented. Error points larger than 50% are not shown in the figures.

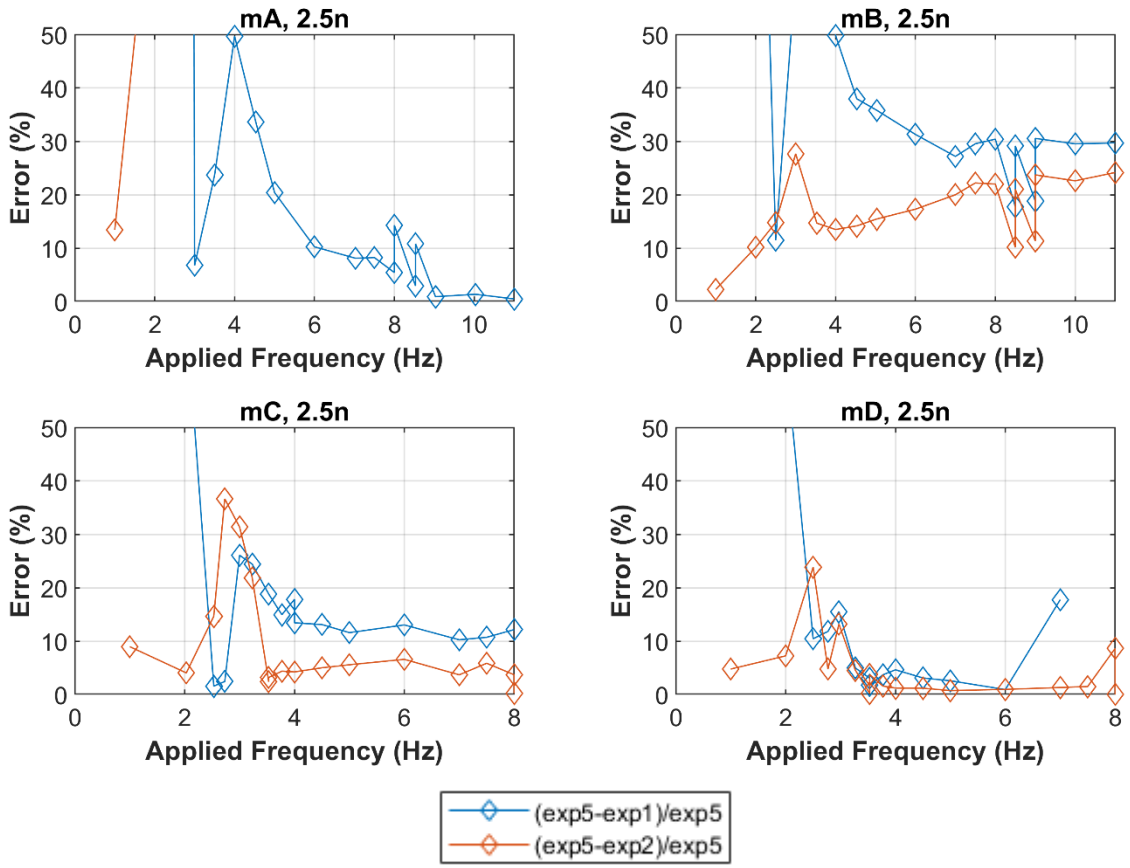


Figure C.102: Errors between forced vibration tests repeated on FBr_2Ts structure.

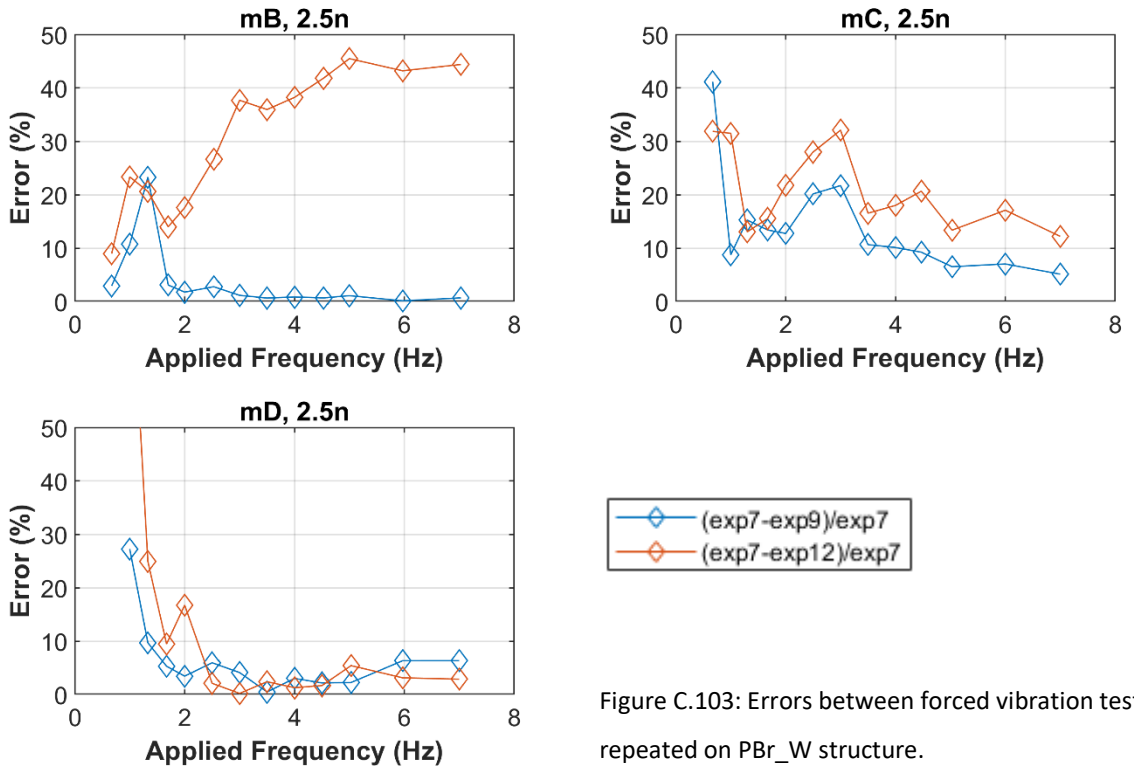


Figure C.103: Errors between forced vibration tests repeated on PBr_W structure.

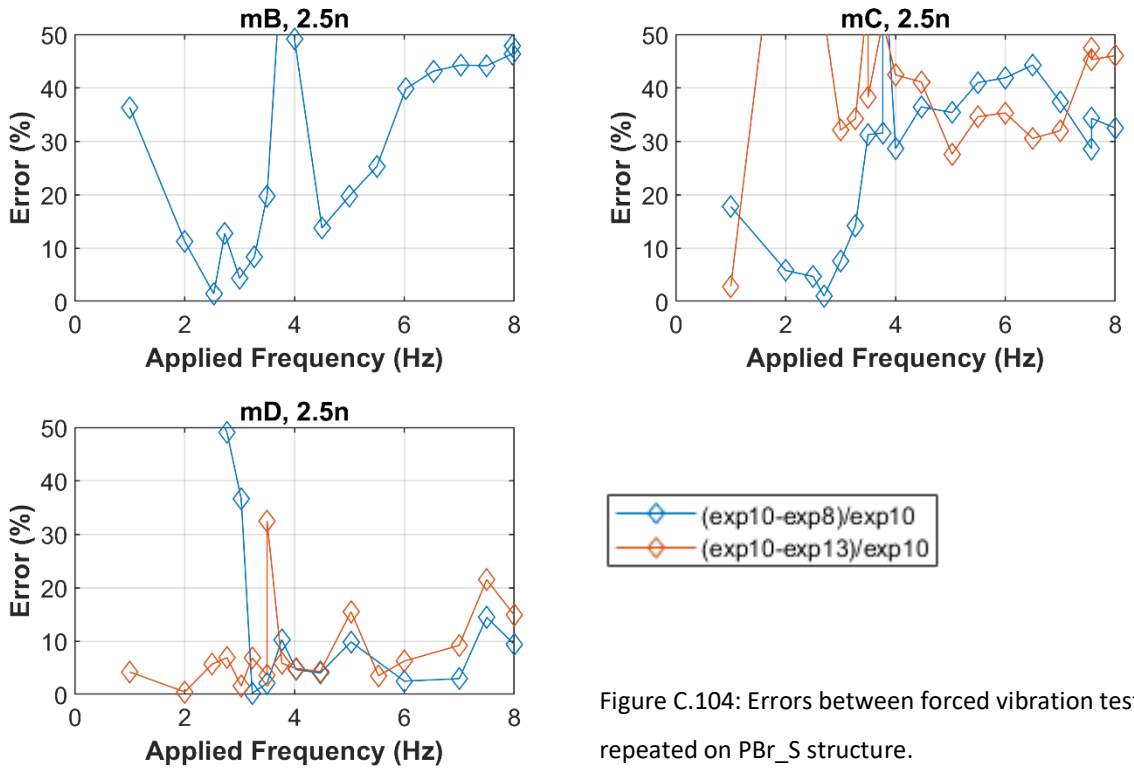


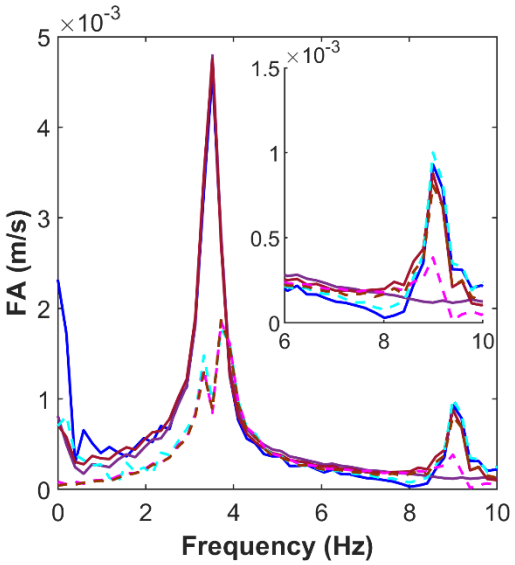
Figure C.104: Errors between forced vibration tests repeated on PBr_S structure.

Appendix D

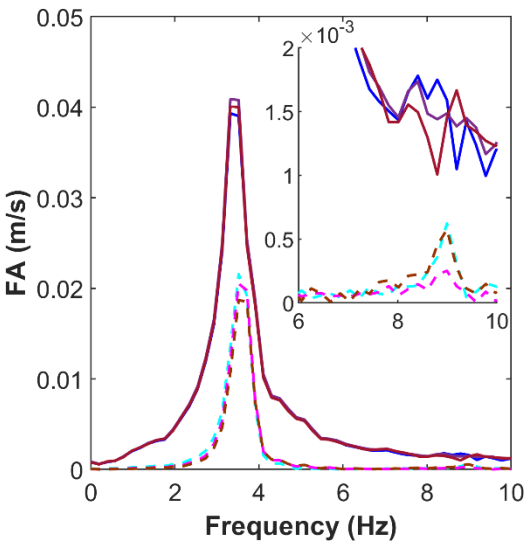
Free Vibration tests

Appendix D.1 Top slab Fourier spectra

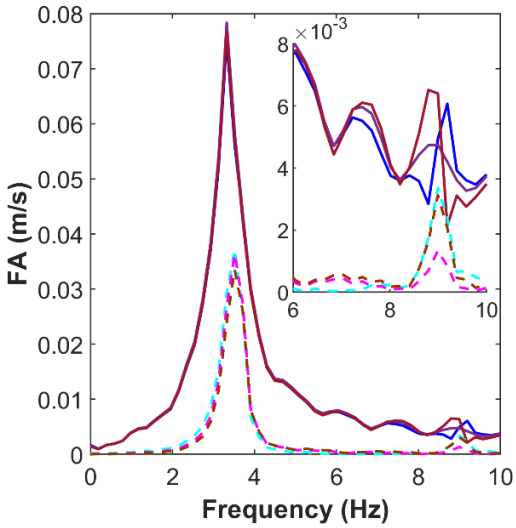
The following figures present the Fourier spectra inferred from free vibration data recorded on the top slab by various instruments. The Fourier spectra were computed by considering the first 3.5s and 29.5s of the motion after the load removal, for the FBr_2Ts and PBr_W experiments respectively. Exception are the Low Strain spectra which are computed by considering a part of the records that contains motion that is dissipated by 90% to 99%. This ensures the computation of the spectra at very low strains, and therefore minimising nonlinearities. The Low Strain spectra of the FBr_2Ts structure was calculated by taking into account the motion recorded, during the FBr_2Ts$^{(4)}$_2.40kN experiment, between 3s and 6.5s from the load removal. The Low Strain spectra of the PBr_W structure was calculated by taking into account the motion recorded, during the PBr_W$^{(11)}$_2.03kN experiment, between 29.5s and 59.5s from the load removal.



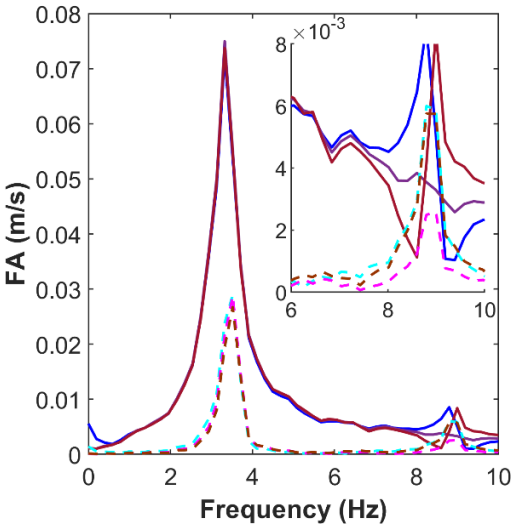
(a) FBr_2Ts Low Strain



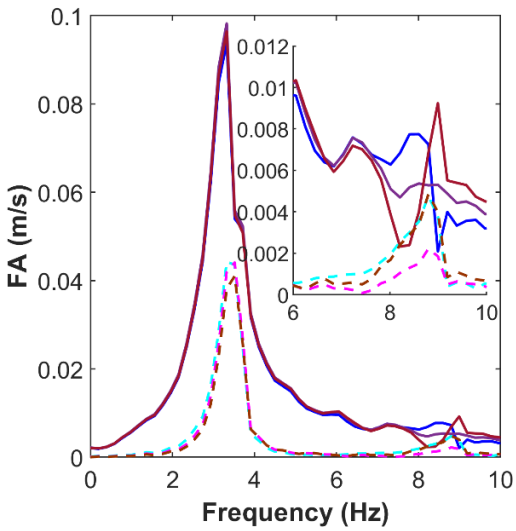
(b) FBr_2Ts$^{(4)}$_1.96kN



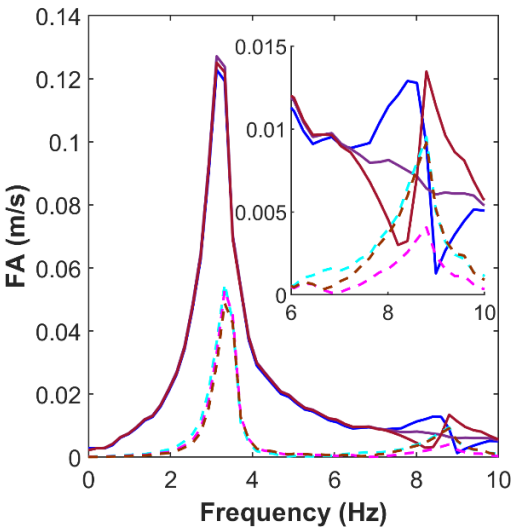
(c) FBr_2Ts$^{(4)}$_2.40kN



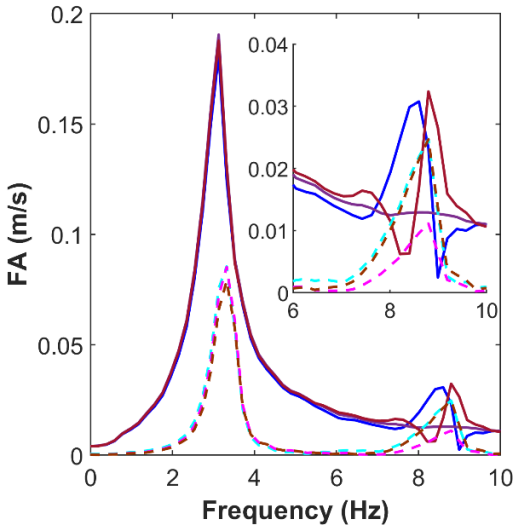
(d) FBr_2Ts$^{(3)}$_2.94kN



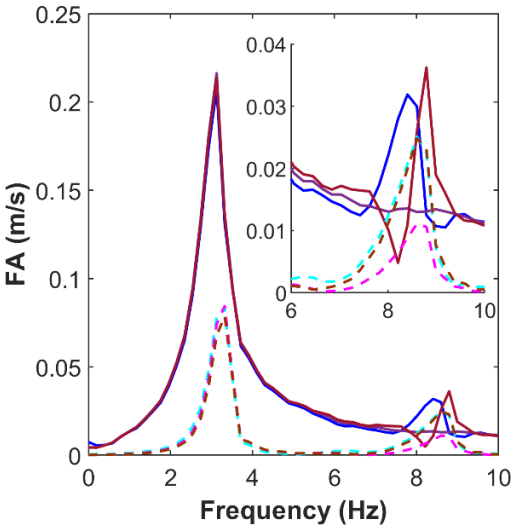
(e) FBr_2Ts$^{(4)}$_5.03kN



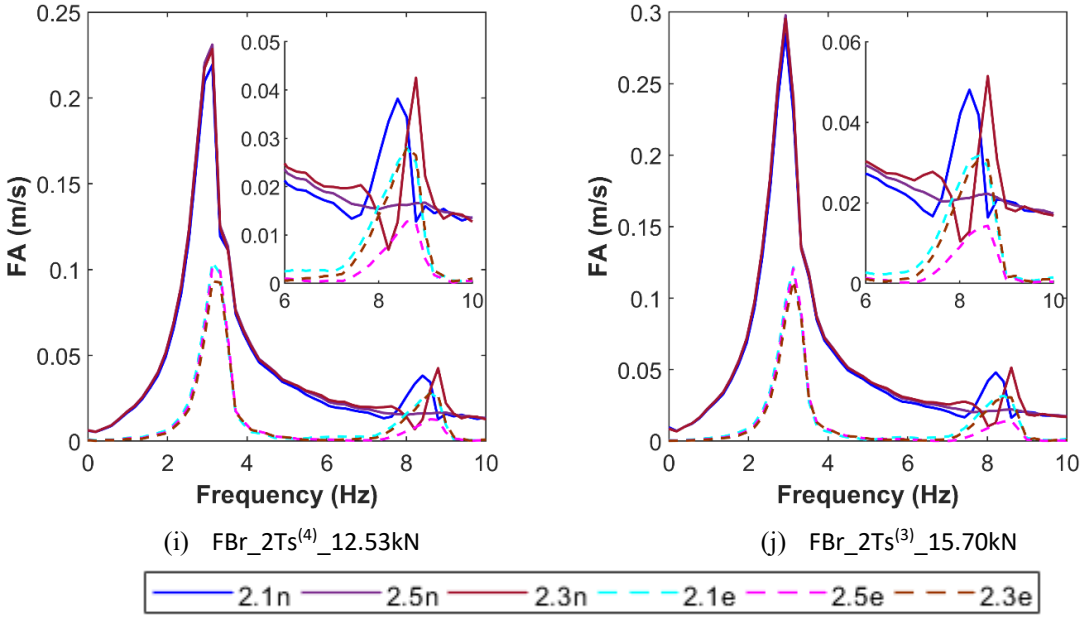
(f) FBr_2Ts$^{(3)}$_6.38kN



(g) FBr_2Ts$^{(4)}$_9.64kN

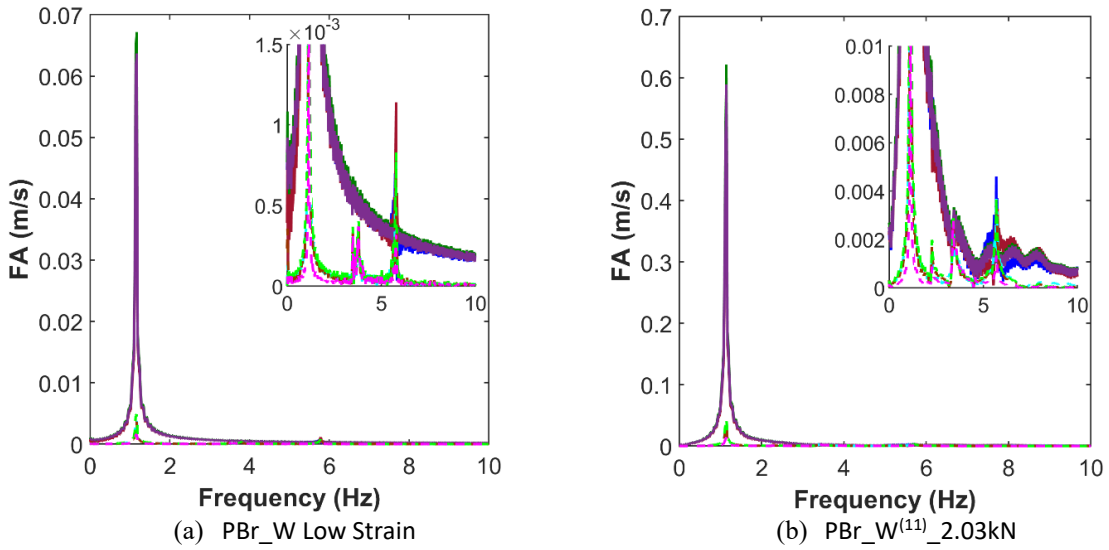


(h) FBr_2Ts$^{(3)}$_10.10kN

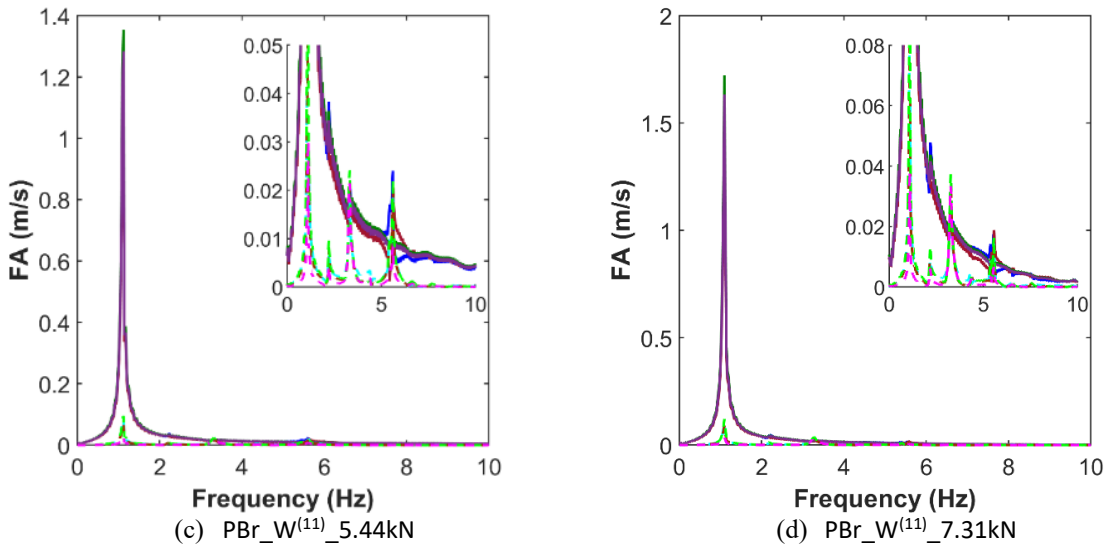


(i) FBr_2Ts$^{(4)}$_12.53kN (j) FBr_2Ts$^{(3)}$_15.70kN

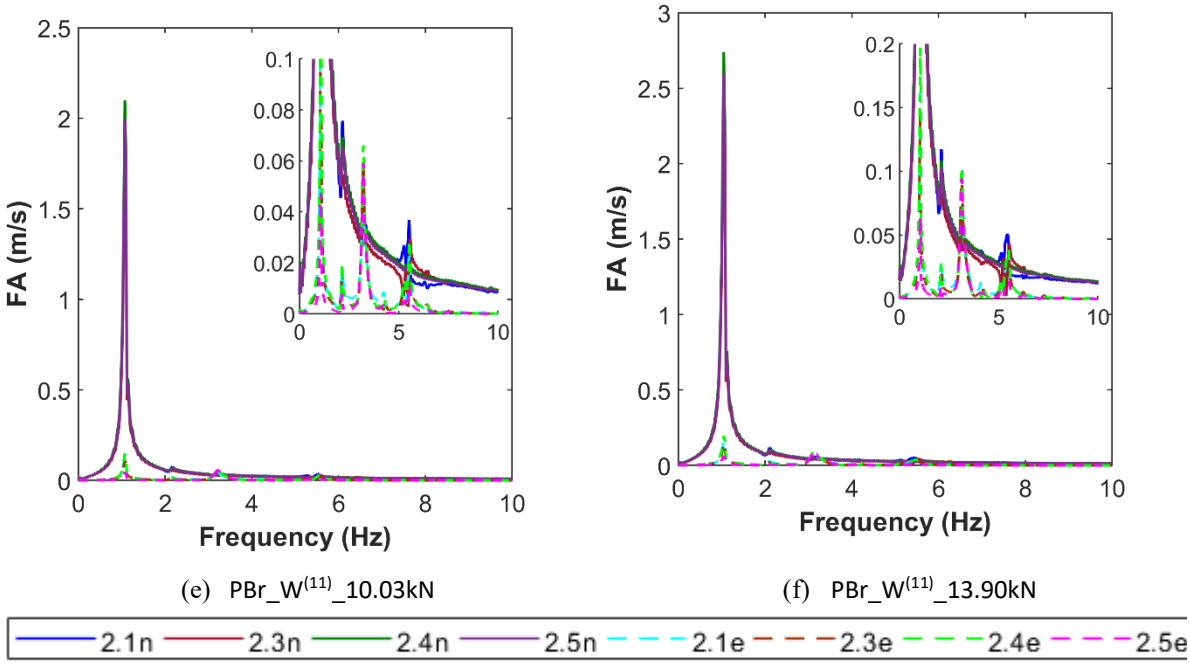
Figure D.1: Fourier spectra inferred from top slab accelerations recorded by different instruments during the free vibration experiments on the fully braced structure with 2 top slabs (FBr_2Ts).



(a) PBr_W Low Strain (b) PBr_W$^{(11)}$_2.03kN



(c) PBr_W$^{(11)}$_5.44kN (d) PBr_W$^{(11)}$_7.31kN



(e) PBr_W$^{(11)}$_10.03kN (f) PBr_W$^{(11)}$_13.90kN

Figure D.2: Fourier spectra inferred from top slab accelerations recorded by different instruments during the free vibration experiments on the partly braced structure with 2 top slabs loaded along its weak axis (PBr_W).

Appendix E

Forced Vibration tests

Appendix E.1 Evaluation of the response of the Fully Braced 2-Top Slab structure

The following figures evaluate the response of the top slab response of the Fully Braced 2-Top slab (FBr_2Ts) structure. The figures correspond to mA, mB, mC or mD experiments, with reference to the Section 5.3.1. Each figure evaluates the response in-terms of: (a) normalised accelerations, (b) Fourier Amplitude (FA) inferred from the normalised accelerations, (c) phase angle difference between two top slab instruments, and (d) snapshots of the displaced top slab during the natural frequencies identified by the (a) to (c) figures.

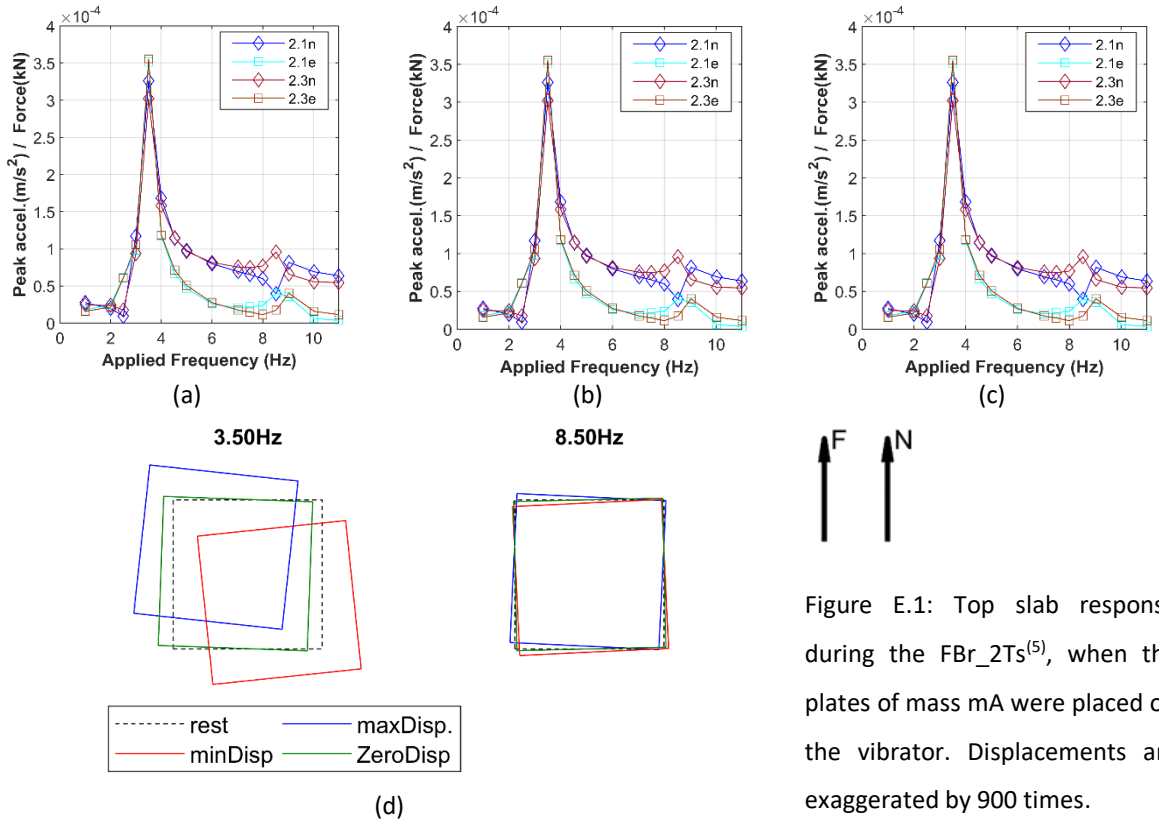
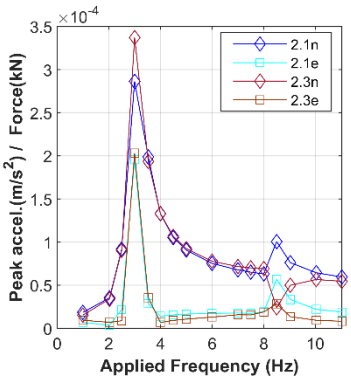
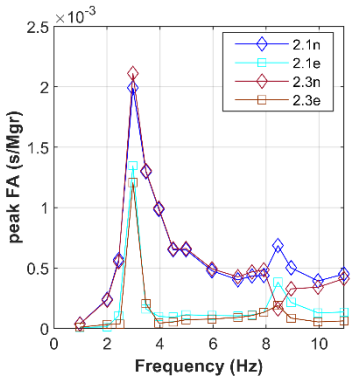


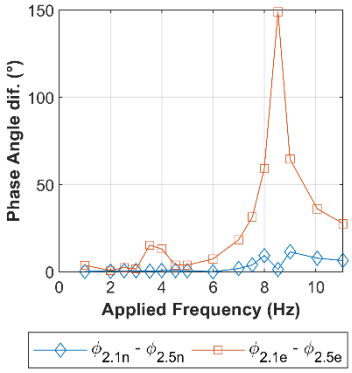
Figure E.1: Top slab response during the FBr_2Ts[(5)], when the plates of mass mA were placed on the vibrator. Displacements are exaggerated by 900 times.



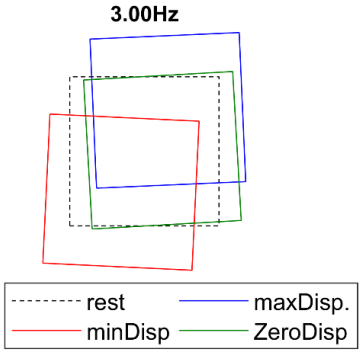
(a)



(b)



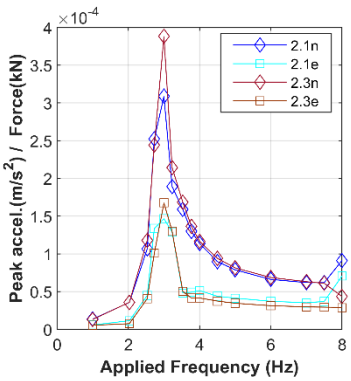
(c)



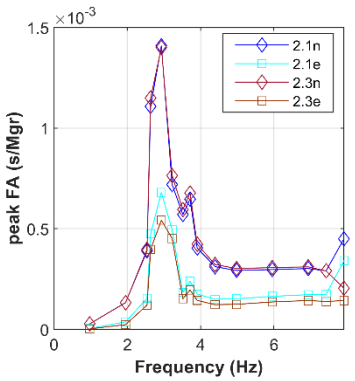
(d)



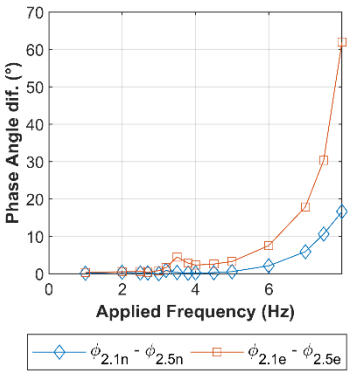
Figure E.2: Top slab response during the FBr_2Ts(2), when the plates of mass mB were placed on the vibrator. Displacements are exaggerated by 700 times.



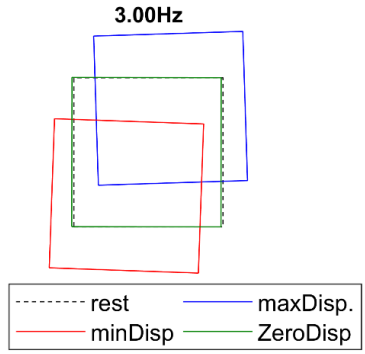
(a)



(b)



(c)



(d)



Figure E.3: Top slab response during the FBr_2Ts(5), when the plates of mass mC were placed on the vibrator. Displacements are exaggerated by 370 times.

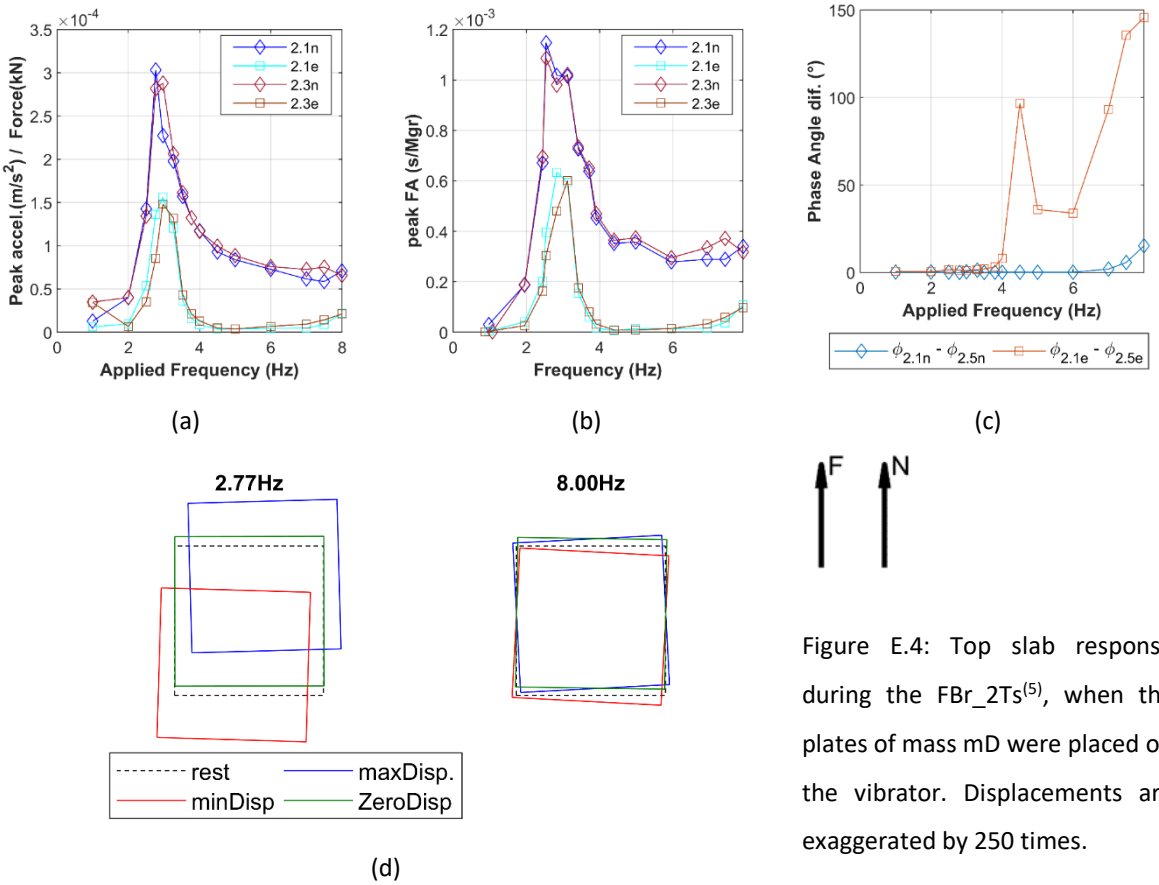
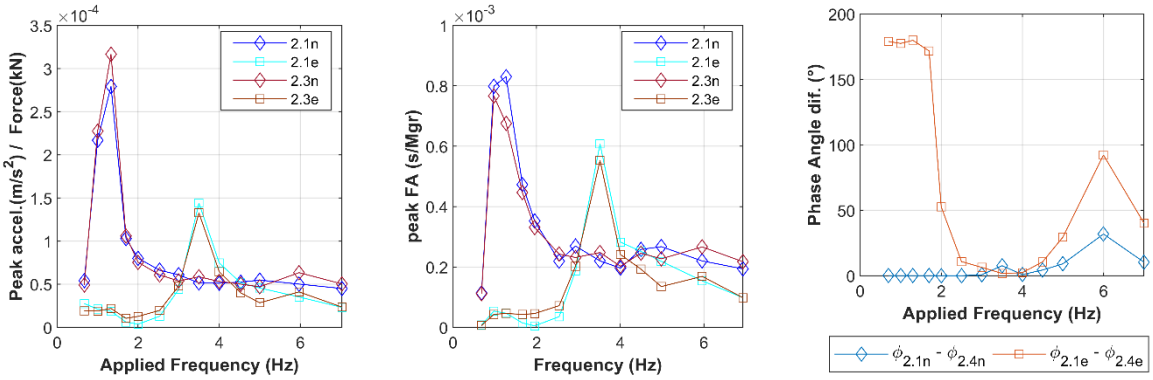


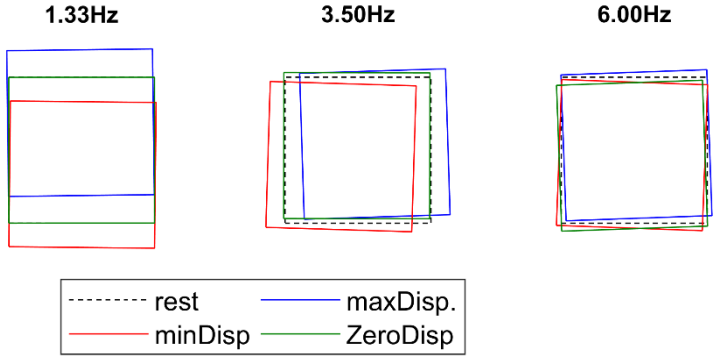
Figure E.4: Top slab response during the FBr_2Ts(5), when the plates of mass mD were placed on the vibrator. Displacements are exaggerated by 250 times.

Appendix E.2 Evaluation of the response of the Pully Braced structure loaded along its Weak plane

The following figures evaluate the response of the top slab response of the Partly Braced structure when it was loaded along its Weak plane (PBr_W). The figures correspond to the mB, mC or mD experiments, with reference to the Section 5.3.1. Each figure evaluates the response in-terms of: (a) normalised accelerations, (b) Fourier Amplitude (FA) inferred from the normalised accelerations, (c) phase angle difference between two top slab instruments, and (d) snapshots of the displaced top slab during the natural frequencies identified by the (a) to (c) figures.



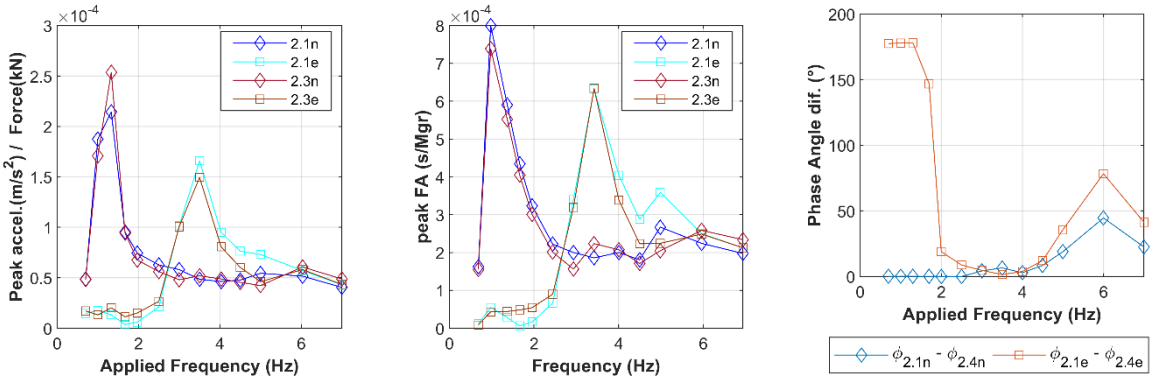
(a) (b) (c)



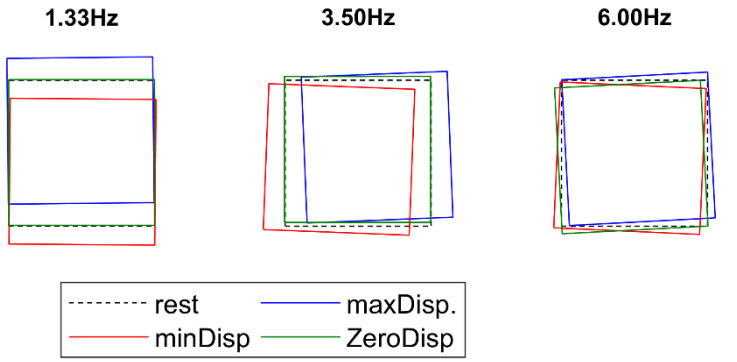
(d)



Figure E.5: Top slab response during the PBr_W(7), when the plates of mass mB were placed on the vibrator. Displacements are exaggerated by 540 times.



(a) (b) (c)



(d)



Figure E.6: Top slab response during the PBr_W(9), when the plates of mass mC were placed on the vibrator. Displacements are exaggerated by 300 times.

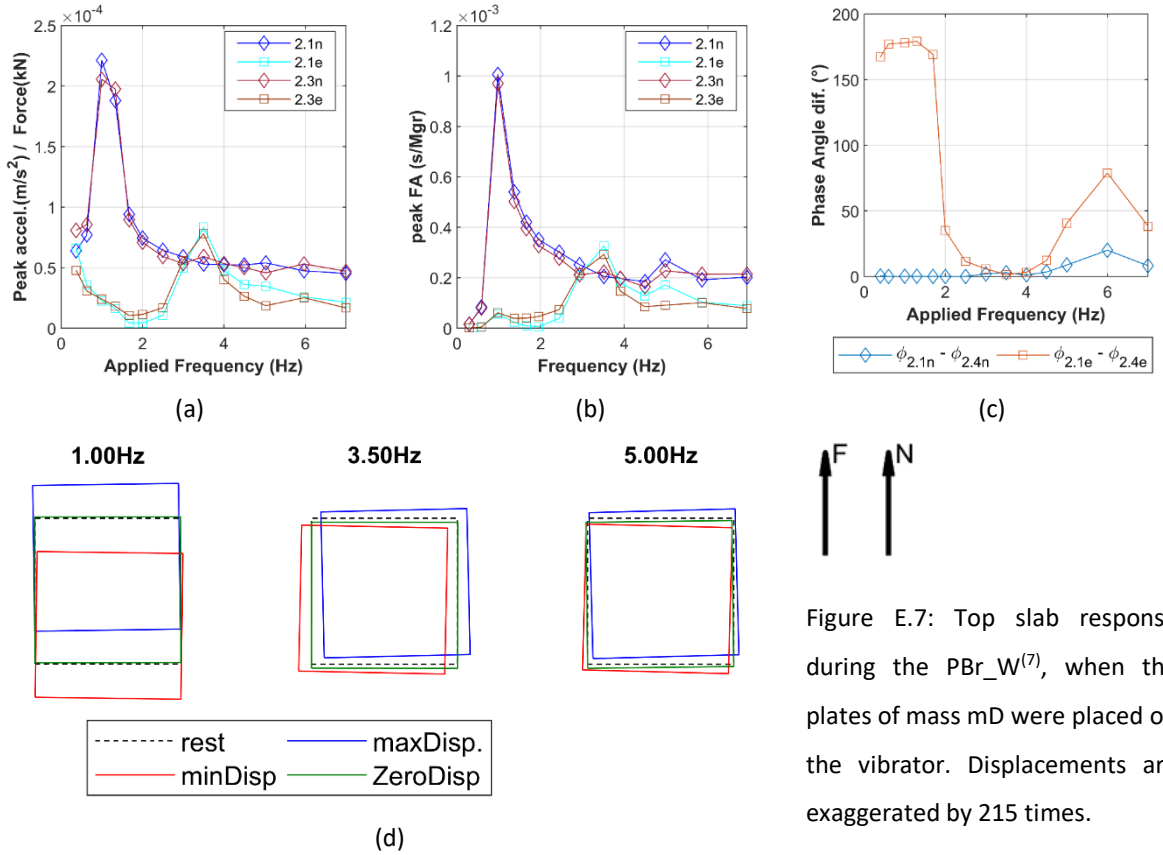


Figure E.7: Top slab response during the PBr_W(7), when the plates of mass mD were placed on the vibrator. Displacements are exaggerated by 215 times.

Appendix E.3 Evaluation of the response of the Pully Braced structure loaded along its Strong plane

The following figures evaluate the response of the top slab response of the Partly Braced structure when it was loaded along its Strong plane (PBr_S). The figures correspond to the mB, mC or mD experiments, with reference to the Section 5.3.1. Each figure evaluates the response in-terms of: (a) normalised accelerations, (b) Fourier Amplitude (FA) inferred from the normalised accelerations, (c) phase angle difference between two top slab instruments, and (d) snapshots of the displaced top slab during the natural frequencies identified by the (a) to (c) figures.

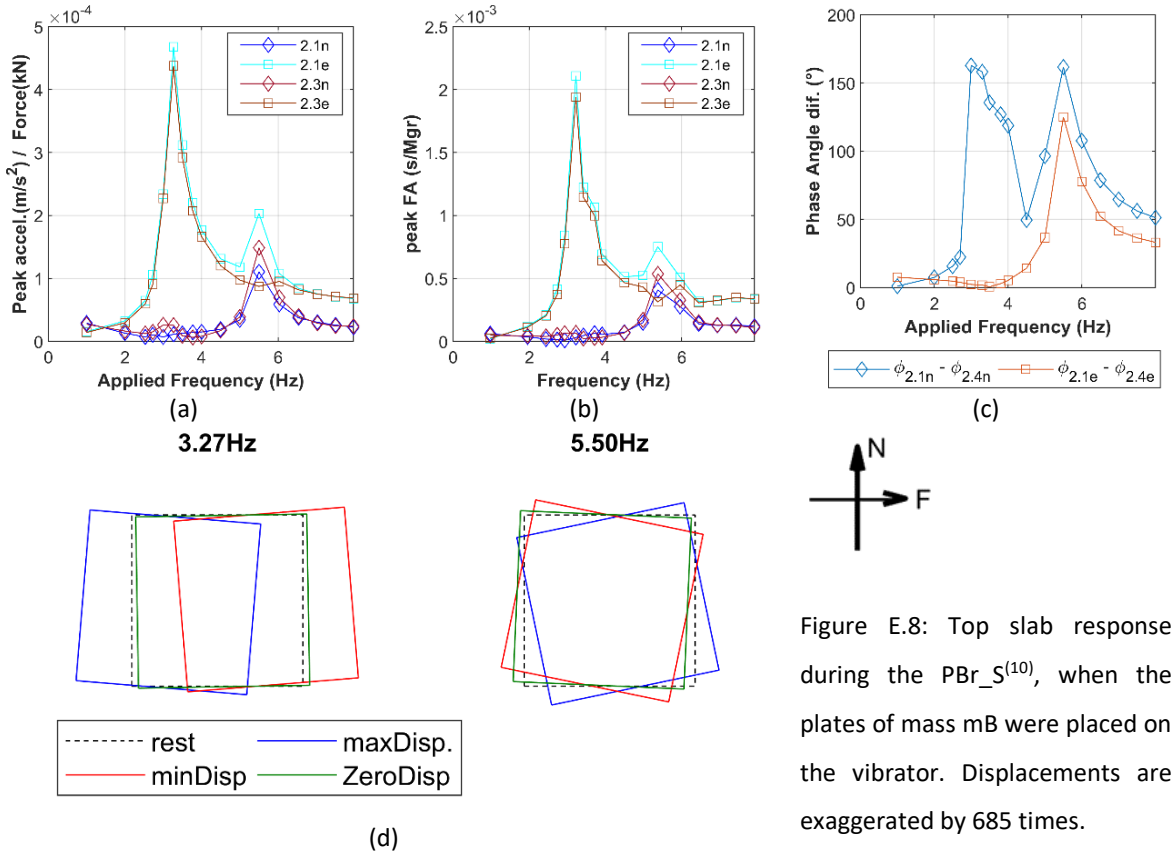


Figure E.8: Top slab response during the PBr_S$^{(10)}$, when the plates of mass mB were placed on the vibrator. Displacements are exaggerated by 685 times.

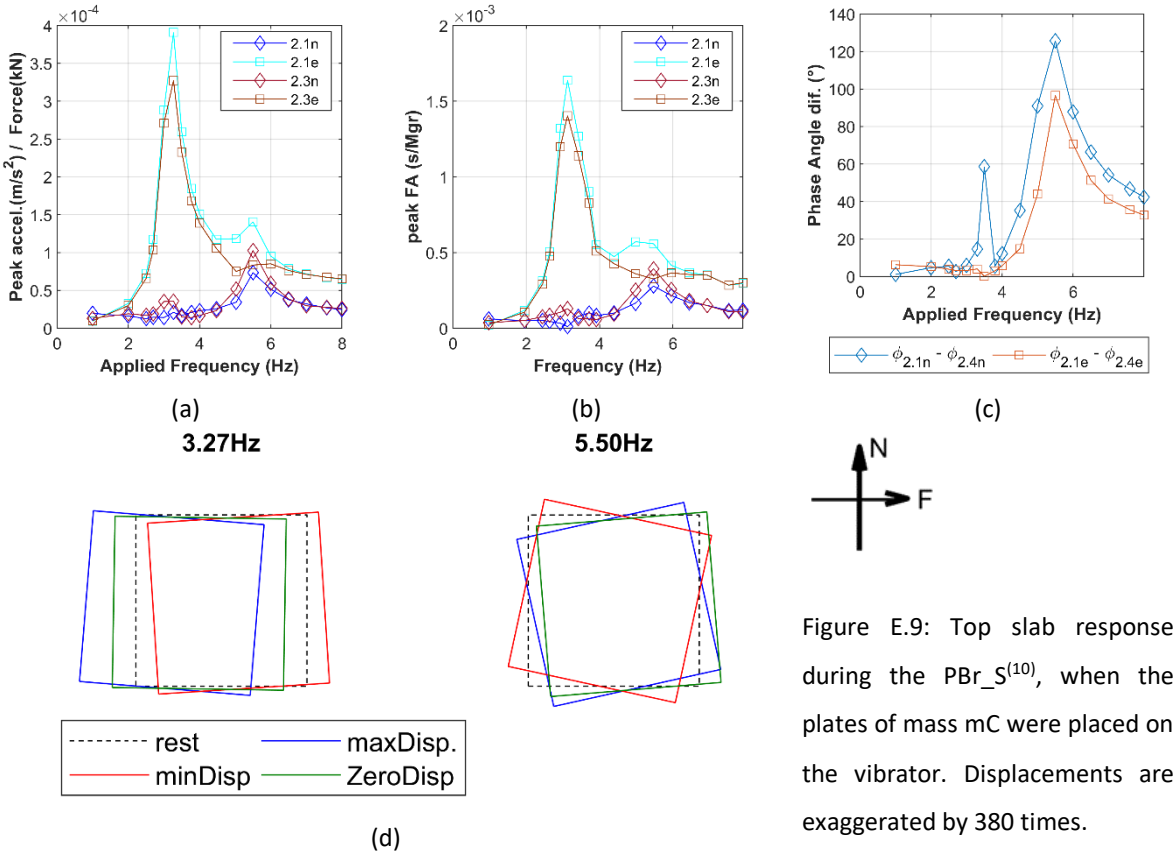


Figure E.9: Top slab response during the PBr_S$^{(10)}$, when the plates of mass mC were placed on the vibrator. Displacements are exaggerated by 380 times.

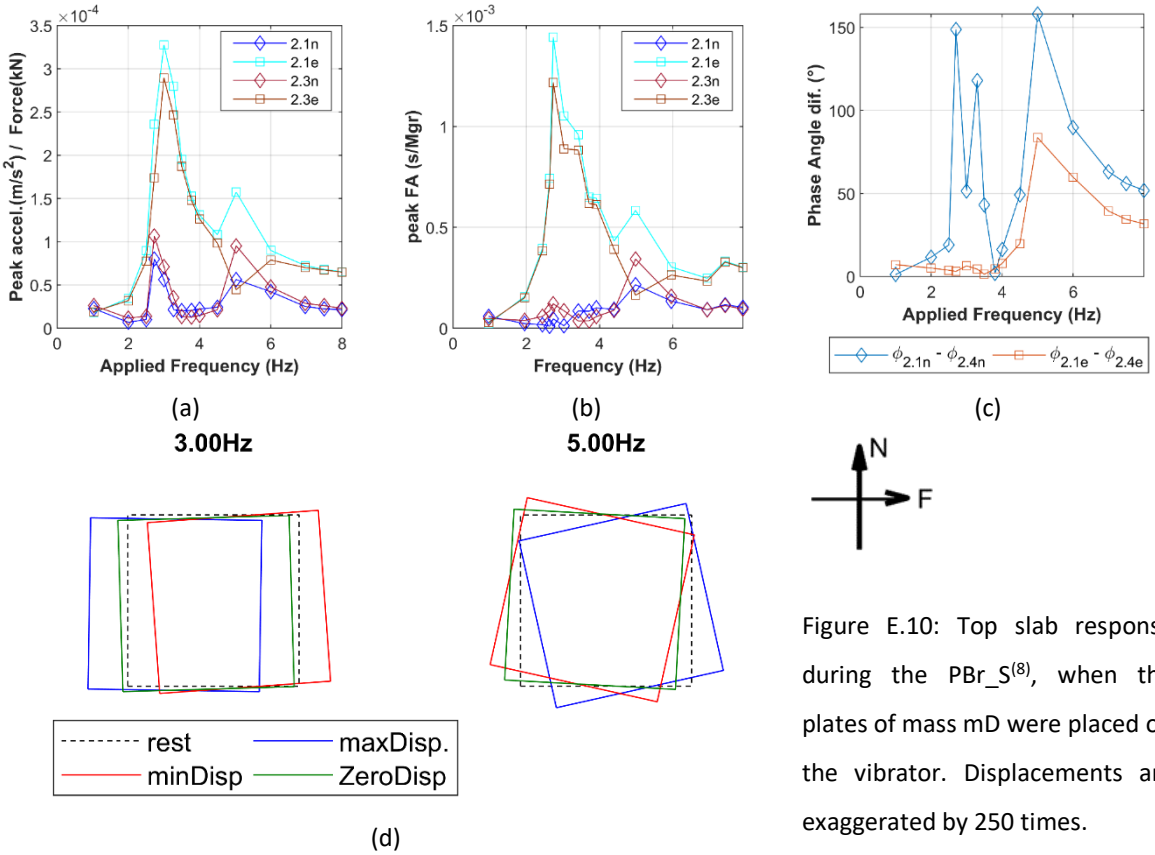
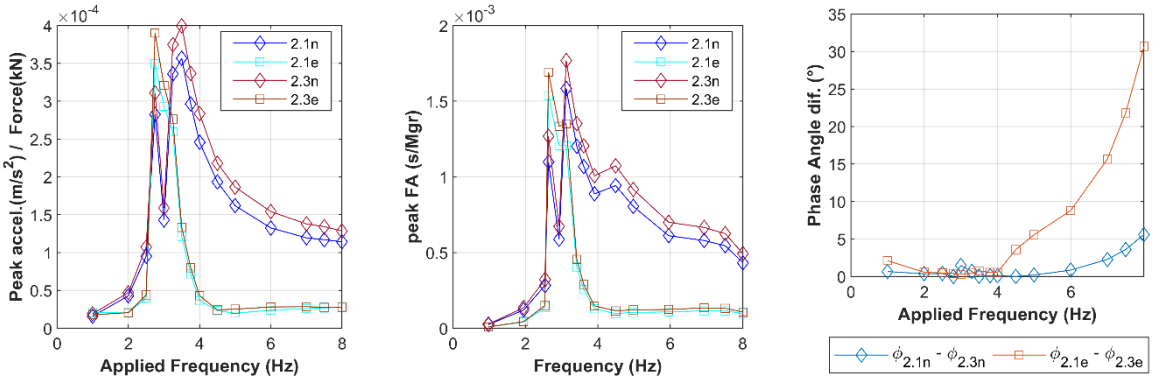


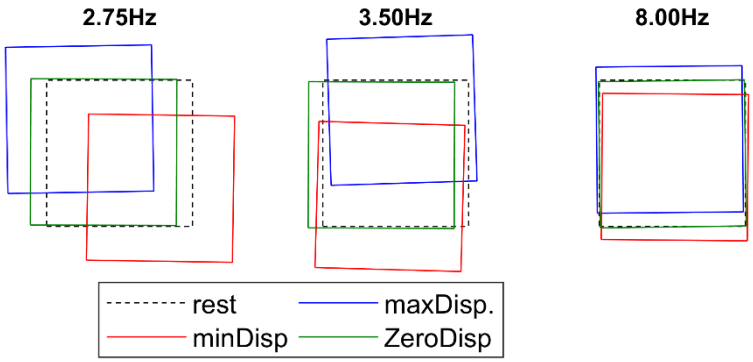
Figure E.10: Top slab response during the PBr_S[(8)], when the plates of mass mD were placed on the vibrator. Displacements are exaggerated by 250 times.

Appendix E.4 Evaluation of the response of the Fully Braced 1-Top slab structure

The following figures evaluate the response of the top slab response of the Fully Braced 1-Top slab structure (FBr_1Ts). The figures correspond to the mC or mD experiments, with reference to the Section 5.3.1. Each figure evaluates the response in-terms of: (a) normalised accelerations, (b) Fourier Amplitude (FA) inferred from the normalised accelerations, (c) phase angle difference between two top slab instruments, and (d) snapshots of the displaced top slab during the natural frequencies identified by the (a) to (c) figures.



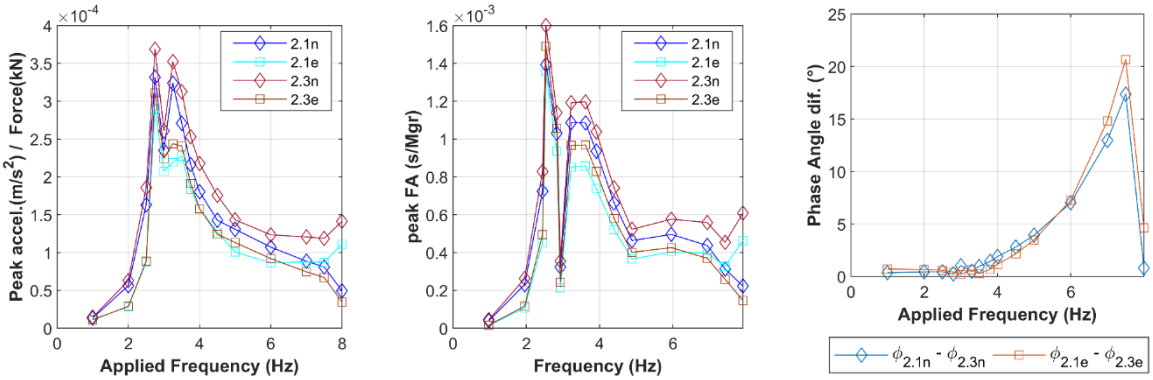
(a) (b) (c)



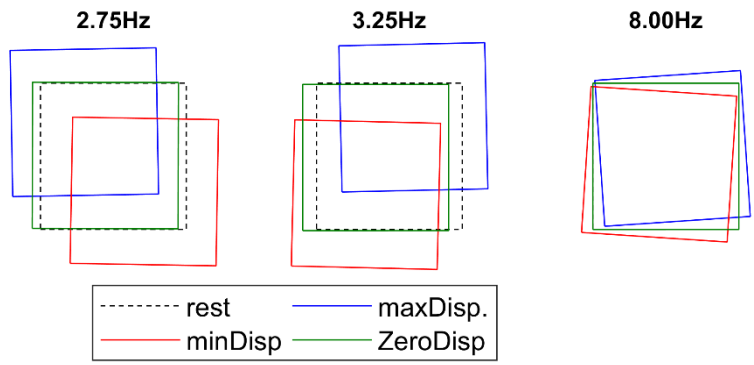
(d)



Figure E.11: Top slab response during the FBr_1Ts[14], when the plates of mass mC were placed on the vibrator. Displacements are exaggerated by 360 times.



(a) (b) (c)



(d)



Figure E.12: Top slab response during the FBr_1Ts[14], when the plates of mass mD were placed on the vibrator. Displacements are exaggerated by 170 times.

Appendix F

Numerical Model

Appendix F.1 Modelled forced vibration experiments

Table F.1 presents the modelled forced vibration experiments carried out on the fully braced 2-top slab (FBr_2Ts) structure, fully braced 1-top slab (FBr_1Ts) structure and partly braced structure loaded along its weak axis (PBr_W). The table specifies the mass of the plates that was adjusted on the vibrator and the frequency applied on the structure during the modelled experiments. The numerical results of the red color experiments, shown in the table, have been used in the model calibration process, as described in Section 7.8.

Table F.1: Modelled forced vibration experiments.

Exp. Name	Bracing system	Number of top slab masses.	Vibr. mass of plates	Frequency (Hz)
FBr_2Ts_mA	Fully braced	2	mA	2, 2.5, 3, 3.5, 5, 7
FBr_2Ts_mC	Fully braced	2	mC	2, 2.75, 3, 3.25, 5, 7
FBr_2Ts_mD	Fully braced	2	mD	2, 2.77, 3, 3.27, **5**, 7
FBr_1Ts_mC	Fully braced	1	mC	2.5, 2.75, 3, 3.25, 3.5, **5**, 6, 8
FBr_1Ts_mD	Fully braced	1	mD	2.5, 2.75, 3, 3.25, 3.5, 5, 6, 8
PBr_W_mB	Fully braced	2	mB	1.33, 2, 3, 3.5, 4, 5, 6, 7
PBr_W_mC	Partly braced	2	mC	1.33, 2, 3, 3.5, 4, 5, 6, 7
PBr_W_mD	Partly braced	2	mD	1.33, **2**, 3, 3.5, 4, 5, 6, 7

Appendix F.2 Modelled free vibration experiments

Table F.2 presents the modelled free vibration experiments carried out on the FBr_2Ts, FBr_1Ts and PBr_W structural configurations. Each table specifies the force applied on the structure during the modelled experiments. The numerical results of the red color experiments, shown in the table, have been used in the model calibration process, described as in Section 7.8. Also, the tables include some

free vibration finite element analyses that do not correspond to any physical experiment, which are denoted with the star-symbol (*).

Table F.2: Modelled free vibration experiments carried out on the fully braced 2-top slab structure.

Exp. Name	Bracing system	Number of top slab masses.	Force (kN)
FBr_2Ts	Fully braced	2	**2.94**, 6.38, 10.1, **15.7**
FBr_1Ts	Fully braced	1	2.94, 6.38, 10.1, **15.7**
PBr_W*	Fully braced	2	**2.03**, 5.44, 10.0, **13.9**

Appendix F.3 2D analyses: Model dimensions investigation

Kellezi (2000) and Kontoe (2006) suggest that the absorbing boundary should not be closer than 1.2 to 1.5 times the wavelength from the excitation source. The wavelength is calculated as the velocity over the frequency of the motion. Herein, the two are assumed to be equal to the shear wave velocity of the shallower layer (140m/s) and the input frequency (1-8Hz), respectively. The simulation with the smallest applied frequency, i.e. 2Hz, requires a soil domain of 170m wide and 85m depth. Such a mesh would be very computationally expensive, especially for the 3D numerical analyses. Therefore, it is imperative that the smallest mesh which produces acceptable boundary effects should be found and employed in all analyses.

An investigation about the boundary effects of different soil domain dimensions is presented by the means of 2D simulations. The simulated experiment is a forced vibration test when a vibratory force of 8Hz input frequency was applied on the fully braced 2-top slab structure. The meshes compared (M_0, M_1, M_2) are shown in Figure F.1. The soil domain of the M_0 mesh, which is used as a benchmark, has dimensions of 81m x 40m, the M_1 mesh has dimensions of 21m x 20.4m and the M_2 is of 15m wide and 6.2m deep. All elements incorporated in the numerical models were prescribed to behave linear elastically, which is a conservative assumption, as soil nonlinearity is expected to dimmish the boundary effects. The boundary conditions of the model can be found in Section 7.4, with the exception for the input excitation. The input excitation was applied as a force, instead of displacements, at the centre node of the top slab plane of symmetry. The input force was three times smaller than the actual force to account for the shrinkage of a three-dimensional problem to two dimensions. The factor of 3 compensates the fact that the mass of the 2D model is three times smaller than the one of the 3D problem. The discrepancy arises from the 2D model considering an out-of-plane dimension of 1m, in contrast to the original 3m dimension. Similarly, the properties of the steel columns and braces were adjusted so that the 2D elements have the same axial (EA) and bending (EI)

stiffness with the real problem. Table F.3 and Table F.4 show the elastic structural and soil properties input in the 2D problem. Finally, the normal and shear stiffness of the interface elements were assumed to be equal to 1E8kN/m^3, while a value equal to 1E2kN/m^3 was adopted for gap areas. As per 3D simulations, the presented 2D analyses incorporate gaps between the foundation and the soil. Gaps were formed below the two edges of the foundation with a length of two elements (0.50m) per edge.

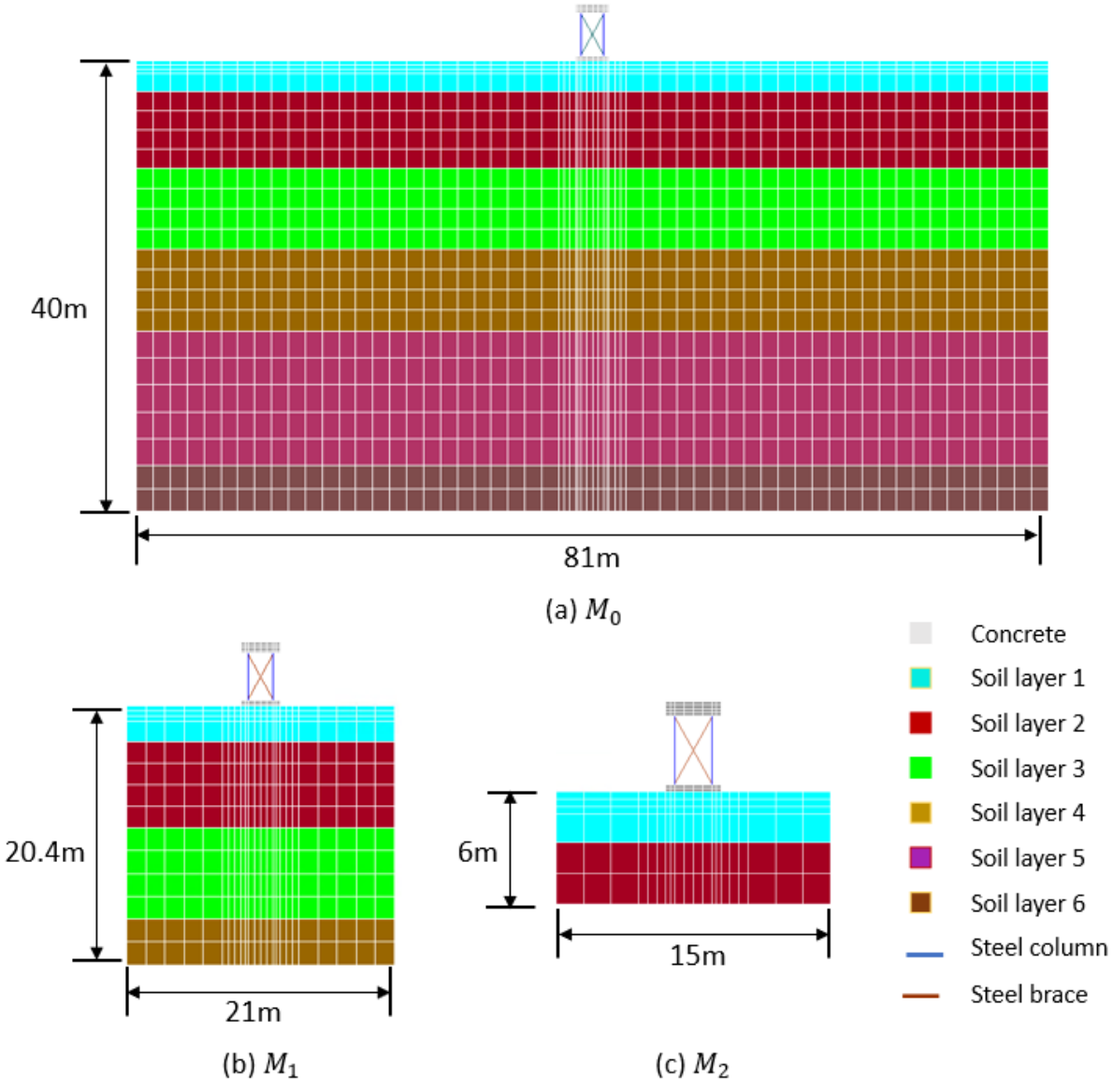


Figure F.1: Examined meshes with different soil domain dimensions

Table F.3: Elastic properties of the structural elements.

.	E (GPa)	ν	ρ (Mgr/m^3)	A (cm^2)	I (cm^4)	ξ (%)
Concrete	31	0.2	2.5	-	-	1
Braces	100	0.25	7.85	9.64	88.5	2
Columns	100	0.25	7.85	54.9	1770	2
Beam elements extended into the foundation	3	0.25	0.05	54.9	1770	-
Beam elements extended into the top slabs	200e4	0.25	0.05	54.9	1770	-

Table F.4: Elastic soil properties.

	E (MPa)	ν	ρ (Mgr/m^3)	ξ (%)
Layer 1	100	0.25	2.0	5%
Layer 2	186	0.2	2.1	5%
Layer 3	215	0.25	2.1	5%
Layer 4	547	0.25	2.1	5%
Layer 5	648	0.25	2.1	5%
Layer 6	648	0.25	2.1	5%

Figure F.2 presents the comparison of the SSI response computed by the analyses with different soil domain dimensions. It is shown that the horizontal and vertical accelerations computed on the top slab (2.5n, 2.5z) and foundation (1.1n, 1.1z) are the same for all three soil domain dimensions. The horizontal soil motion recorded on the soil surface at a distance of 1.5m from the foundation edge (0.1n) was slightly affected by the choice of dimensions. The impact of the dimensions is more pronounced for soil motion closer to the boundaries. Both the horizontal and vertical soil surface motion at the 0.2 node, which is located 3m from the foundation edge, have been impacted by boundary effects. Figure F.2 shows that the larger mesh (M_0) produced weaker soil motion, implying that the absorbing boundaries of the smaller mesh overdamp the motion. However, the difference between the largest (M_0) and the smallest (M_2) examined mesh was insignificant considering the uncertainties around the numerical problem. It is therefore concluded that the M_2 mesh with dimensions 15m x 6.2m is sufficient to predict the SSI response.

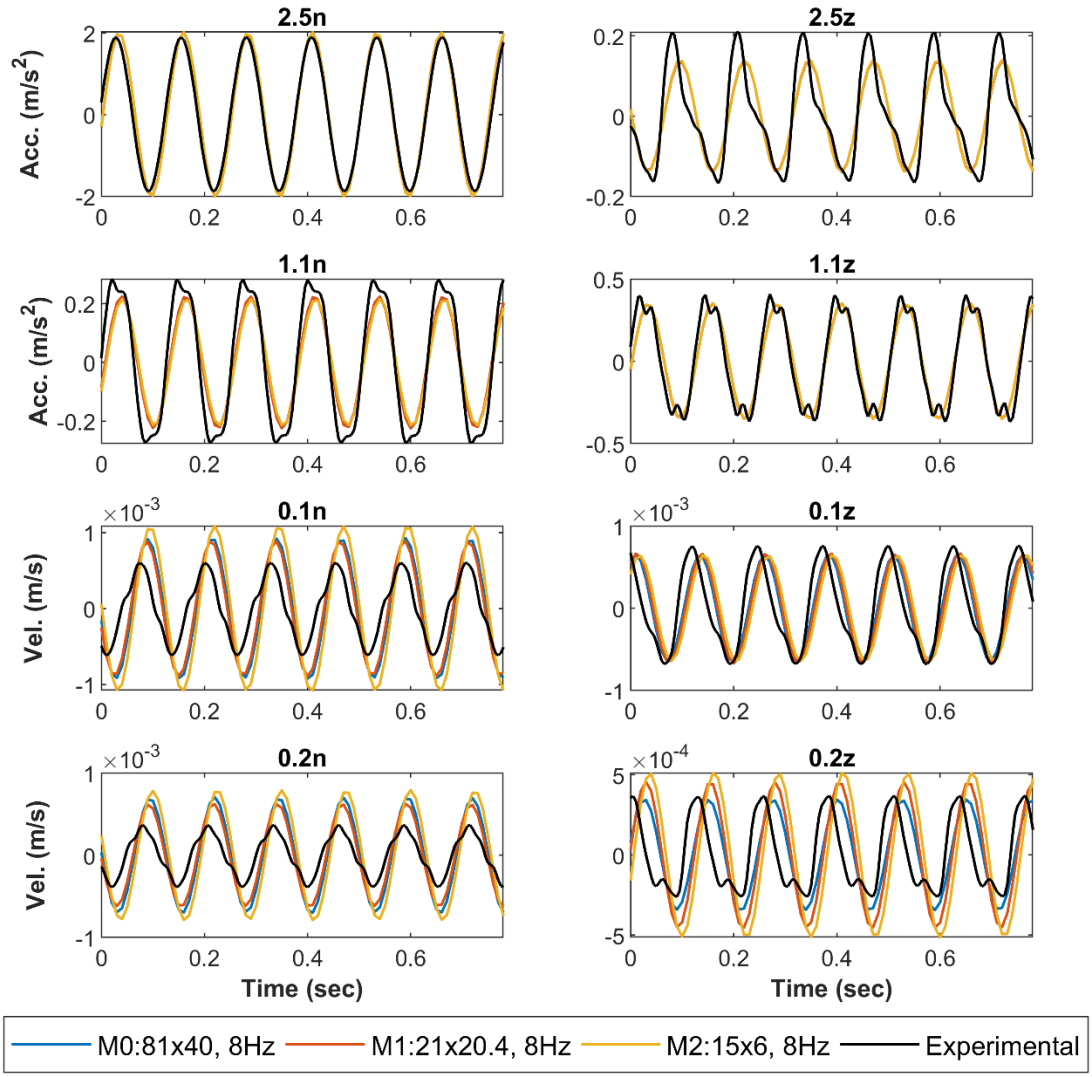


Figure F.2: Comparison of the SSI response computed by the analyses with different mesh. The horizontal (n) and vertical (z) response of the top slab (2.5), foundation (1.1) and soil (0.1, 0.2) are assessed, when the applied frequency was 8Hz.

Appendix F.4 Input parameters of the examined calibrations of the nonlinear model

Tables F.5 to F.11 present the input parameters of the examined calibrations of the nonlinear model (Calibr0, Calibr1, Calibr2, Calibe3, Calibr4, Calibr5 and Calibr6). The name convention is inferred from Taborda *et al*. (2016).

Table F.5: Input parameters of the calibration Calibr0.

G_0 (MPa)	88	b_0	1.09	a_2	0.0	$d_{2,G}$	0.1942
m_G	0.3	a_0	1.194E-04	$d'_{1,G}$	105.0	$d_{3,G}$	5447.7
$R_{G,min}$	0.0	a_1	0.0	$d''_{1,G}$	0.0	$d_{4,G}$	0.839

Table F.6: Input parameters of the calibration Calibr1.

G_0 (MPa)	88	b_0	1.4	a_2	0.0	$d_{2,G}$	0.1942
m_G	0.3	a_0	1.031E-04	$d'_{1,G}$	133.0	$d_{3,G}$	5447.7
$R_{G,min}$	0.0	a_1	0.0	$d''_{1,G}$	0.0	$d_{4,G}$	0.839

Table F.7: Input parameters of the calibration Calibr2.

G_0 (MPa)	88	b_0	1.1317	a_2	0.0	$d_{2,G}$	0.0
m_G	0.3	a_0	7.237E-05	$d'_{1,G}$	0.0	$d_{3,G}$	0.0
$R_{G,min}$	0.0	a_1	0.0	$d''_{1,G}$	0.0	$d_{4,G}$	0.0

Table F.8: Input parameters of the calibration Calibr3

G_0 (MPa)	88	b_0	0.792	a_2	0.0	$d_{2,G}$	0.04
m_G	0.3	a_0	2.7835E-05	$d'_{1,G}$	3.0	$d_{3,G}$	4000.0
$R_{G,min}$	0.0	a_1	0.0	$d''_{1,G}$	0.0	$d_{4,G}$	0.4

Table F.9: Input parameters of the calibration Calibr4

G_0 (MPa)	88	b_0	0.932	a_2	0.0	$d_{2,G}$	0.0
m_G	0.3	a_0	3.3402E-05	$d'_{1,G}$	4.0	$d_{3,G}$	3000.0
$R_{G,min}$	0.008	a_1	0.0	$d''_{1,G}$	0.0	$d_{4,G}$	0.8

Table F.10: Input parameters of the calibration Calibr5

G_0 (MPa)	88	b_0	1.1317	a_2	0.0	$d_{2,G}$	0.008
m_G	0.3	a_0	3.897E-05	$d'_{1,G}$	6.0	$d_{3,G}$	3000.0
$R_{G,min}$	0.02	a_1	0.0	$d''_{1,G}$	0.0	$d_{4,G}$	0.8

Table F.11: Input parameters of the calibration Calibr6

G_0 (MPa)	88	b_0	0.932	a_2	0.0	$d_{2,G}$	0.001
m_G	0.3	a_0	3.619E-05	$d'_{1,G}$	3.6	$d_{3,G}$	3000.0
$R_{G,min}$	0.008	a_1	0.0	$d''_{1,G}$	0.0	$d_{4,G}$	0.7

Appendix F.5 Boundary effects using the final calibration

The boundary effects on the structural and soil motion predicted by the calibrated numerical model are investigated. The investigation is carried out by comparing results from analyses that use the adopted mesh with soil domain dimensions of 15 x 7.5 x 6m (M15x7.5x6) and a larger mesh with

dimensions of 39 x 19.5 x 20.4m (M39x19.5x20.4). The latter model is assumed to have negligible boundary effects and hence it is considered the benchmark.

Free Vibration

The free vibration response of the SSI systems is evaluated through Fourier spectra that were inferred from numerical and experimental time series. Figures F.3 and F.4 show that the small soil domain produced negligibly small boundary effects on the top slab (2.5) and foundation (1.1) free vibration response of the FBr_2Ts and PBr_W structures. Boundary effects are pronounced, though, on the soil response as illustrated by Figures F.5 and F.6, that present the Fourier spectra of soil motions produced by the FBr_2Ts and PBr_W simulations. The figures show that the smaller soil domain overamplified the soil motion. For locations near the foundation and far from the lateral boundaries of the mesh (i.e. 0.1), the motion amplification was pronounced for the horizontal motion component, while it was negligible for the vertical component. Boundary effects were more significant for soil motions near the boundaries (i.e. 0.2, 0.41), where both horizontal and vertical motion components were affected.

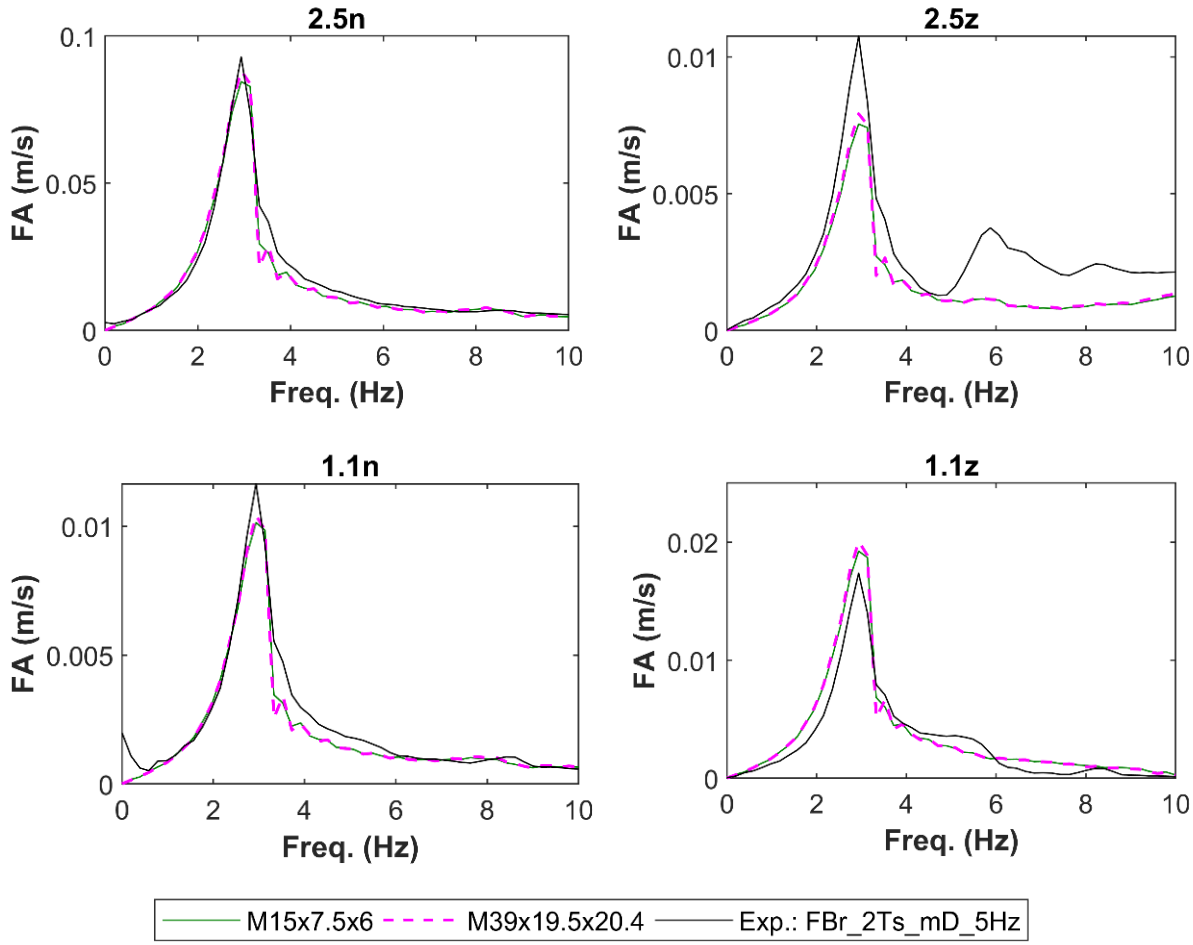


Figure F.3: Boundary effects on the structural response predicted by the FBr_2Ts_15.70kN free vibration simulation.

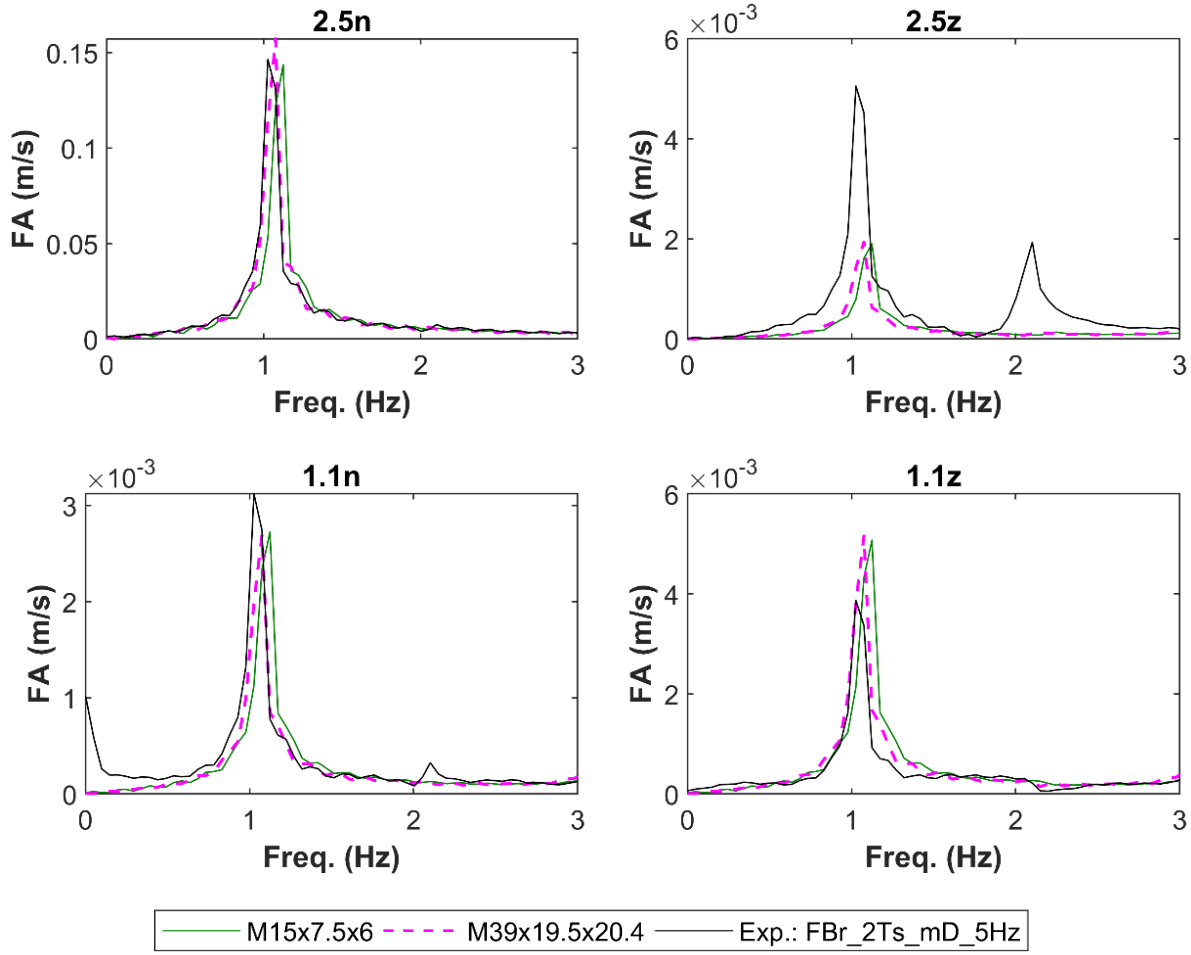


Figure F.4: Boundary effects on the structural response predicted by the PBr_W_13.90kN free vibration simulation.

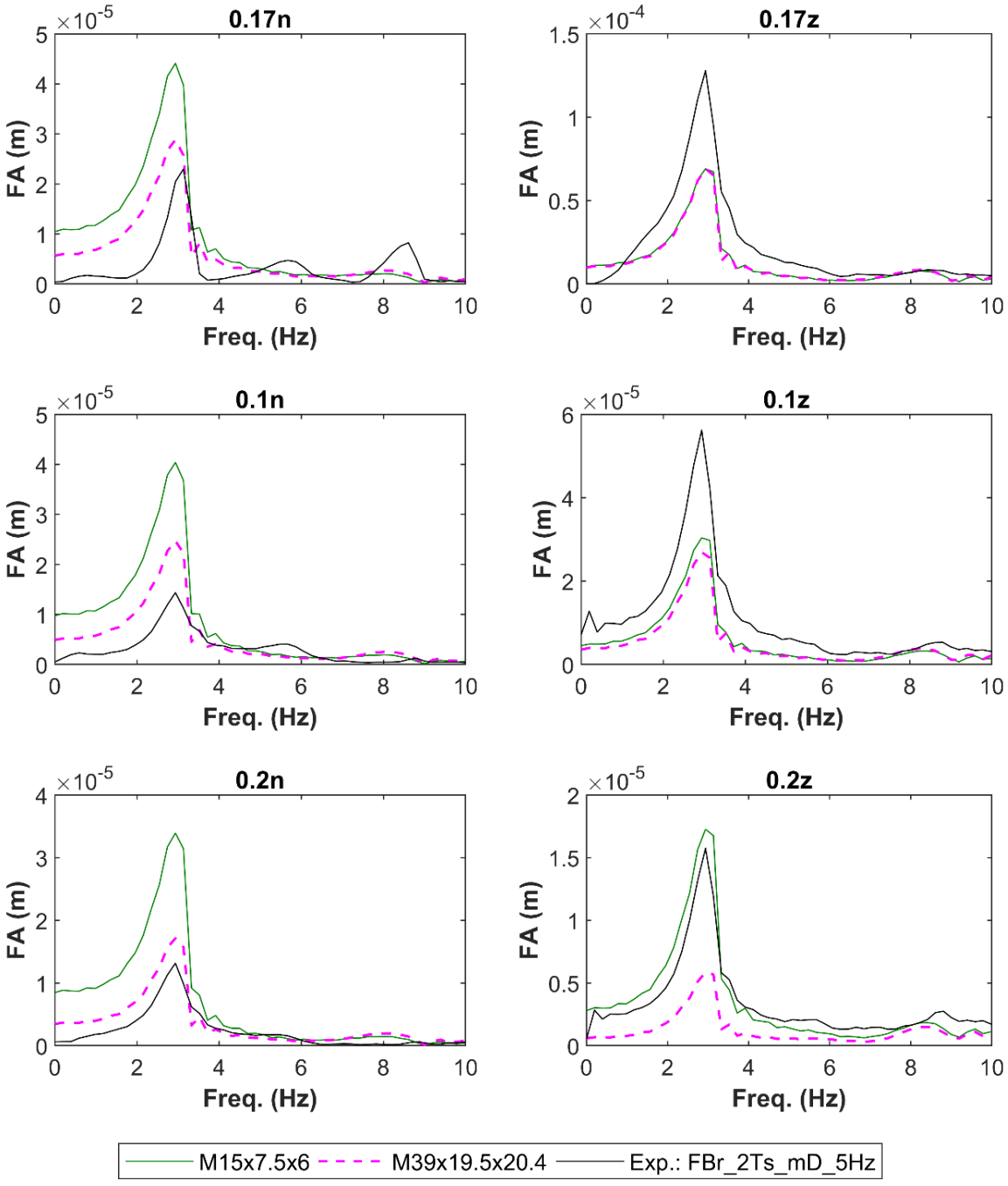


Figure F.5: Boundary effects on the soil response at different locations predicted by the FBr_2Ts_15.70kN free vibration simulation.

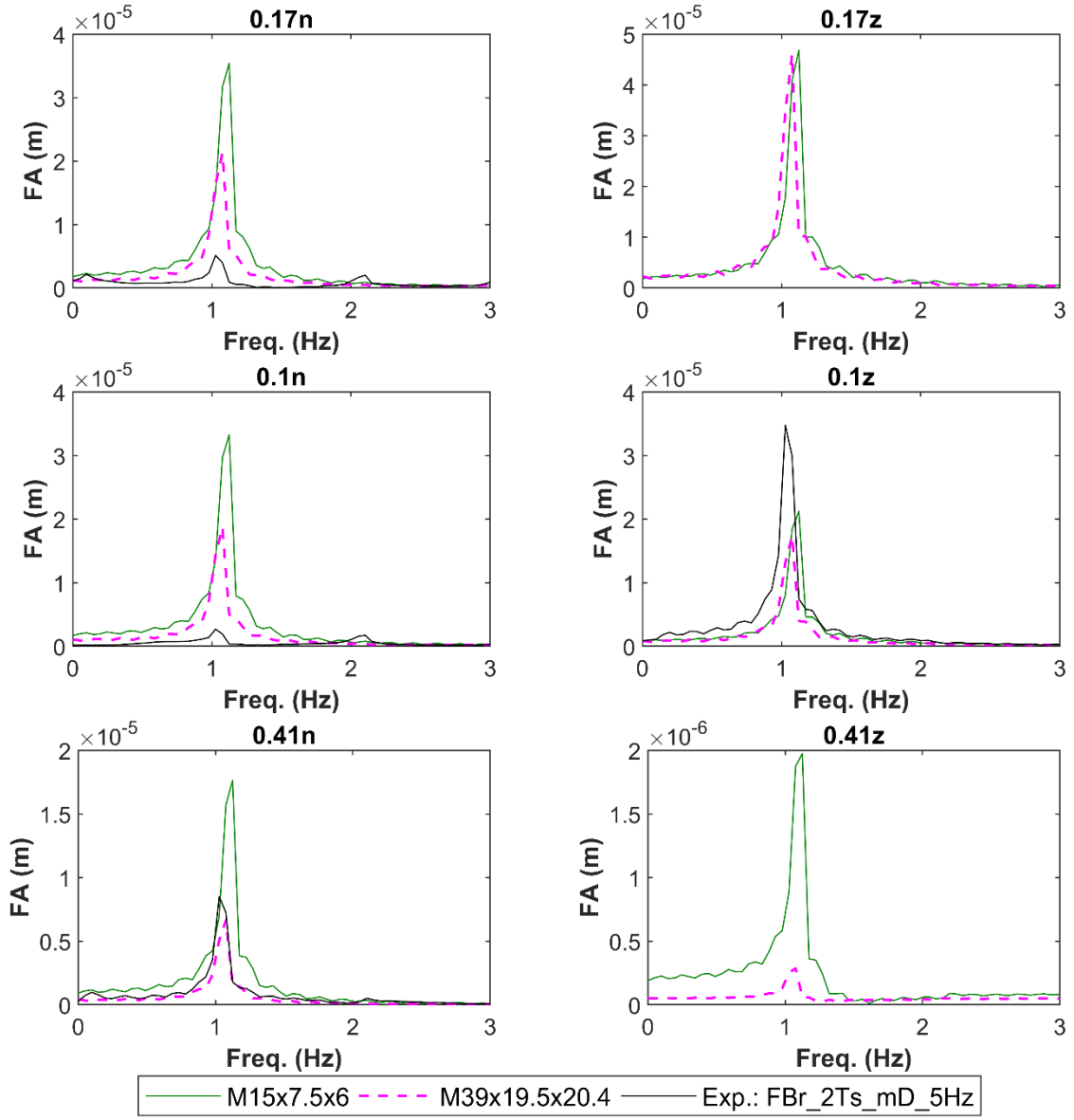


Figure F.6: Boundary effects on the soil response at different locations predicted by the PBr_W_13.90kN free vibration simulation

Forced Vibration

The forced vibration response is evaluated through both time histories and the corresponding Fourier spectra. Figures F.7, F.8 and F.9 present the top slab (2.5) and foundation (1.1) response predicted by the two models that simulate the FBr_2Ts, FBr_1Ts and PBr_W experiments. The figures demonstrate that the structural forced vibration response is marginally affected by the boundary conditions of the model with smaller soil domain dimensions. Unlike structural motion, soil motion was found to me more sensitive to soil domain dimensions. This is illustrated by Figures F.10, F.11 and F.12, that present the soil motions predicted by the same simulations. Similar to free vibration simulations, the horizontal soil motion component is more sensitive to boundary effects. The impact of the boundary

effects on the soil motion increases at locations closer to the boundaries of the domain (i.e. 0.2, 0.41), where both horizontal and vertical components are significantly impacted.

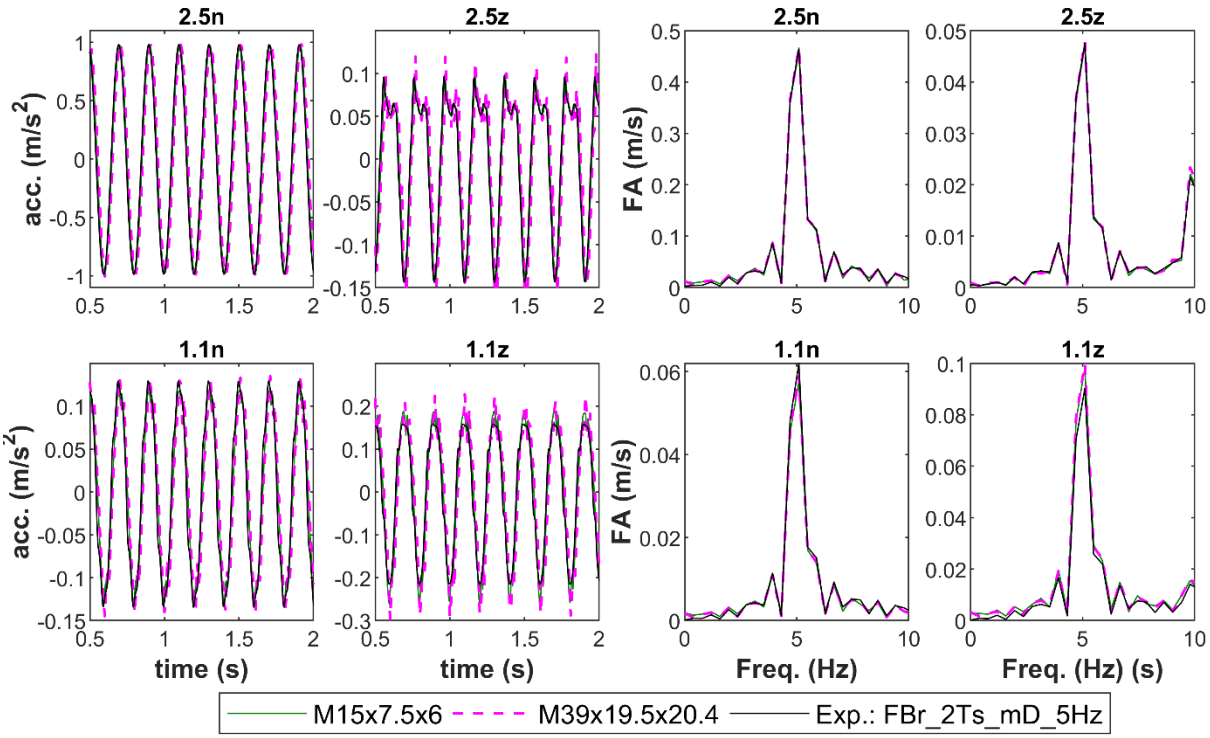


Figure F.7: Boundary effects on the structural response predicted by the FBr_2Ts_mD_5Hz forced vibration simulation.

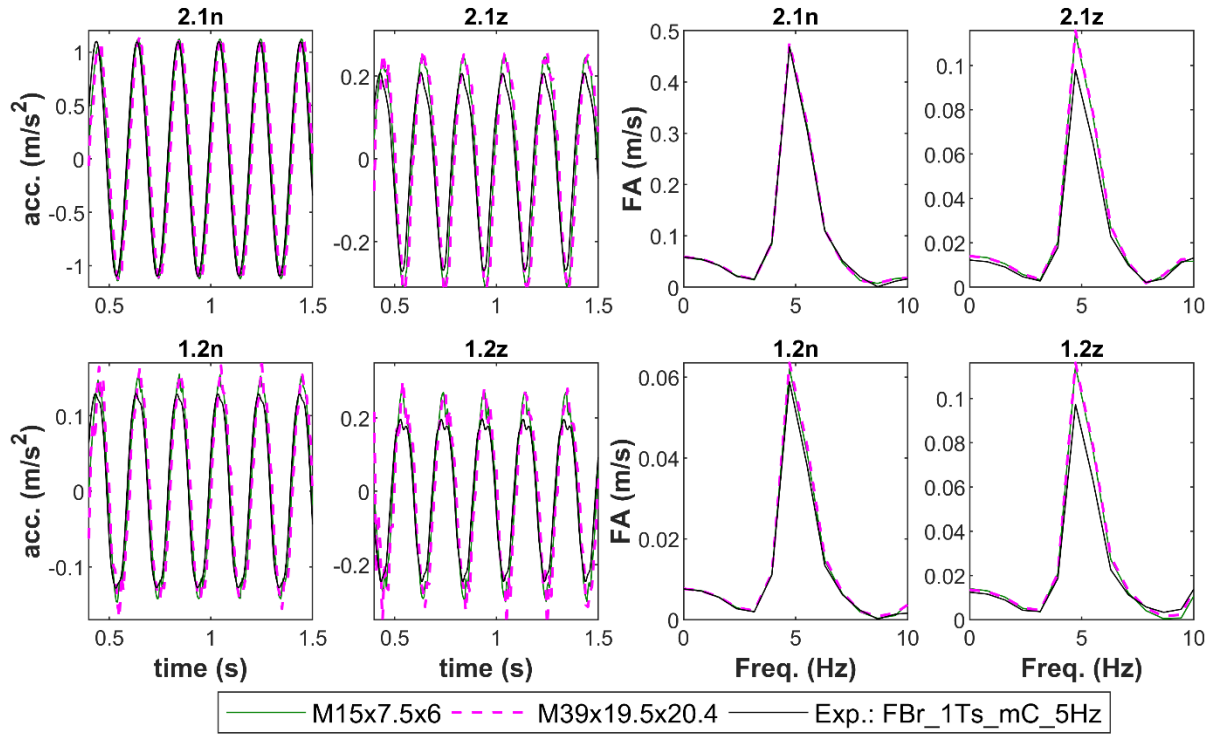


Figure F.8: Boundary effects on the structural response predicted by the FBr_1Ts_mC_5Hz forced vibration simulation.

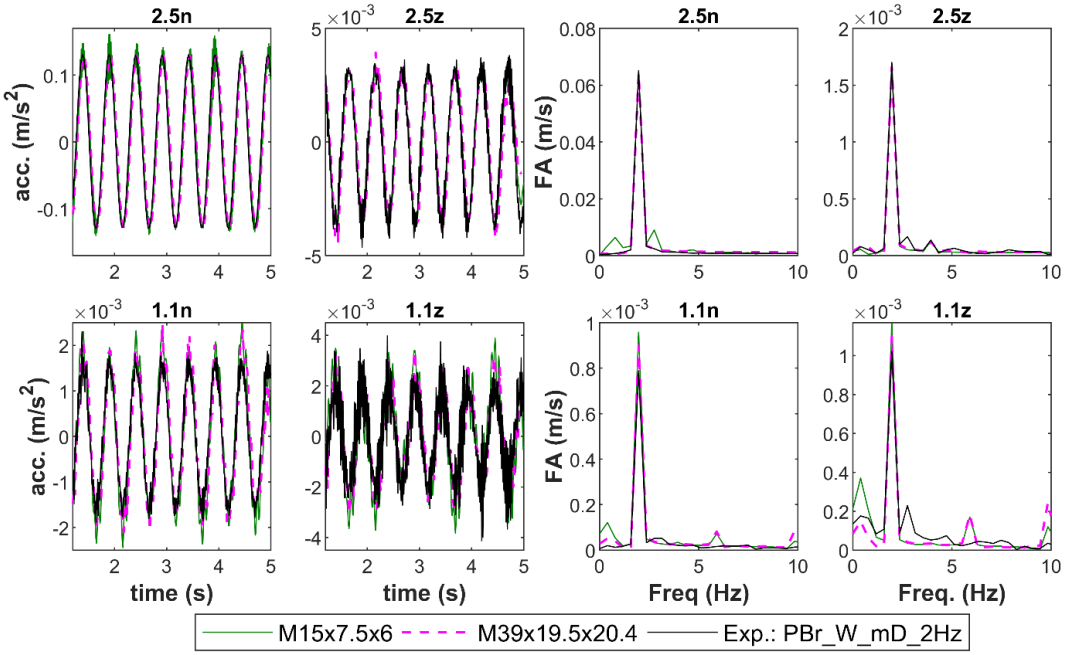


Figure F.9: Boundary effects on the structural response predicted by the PBr_W_mD_2Hz forced vibration simulation.

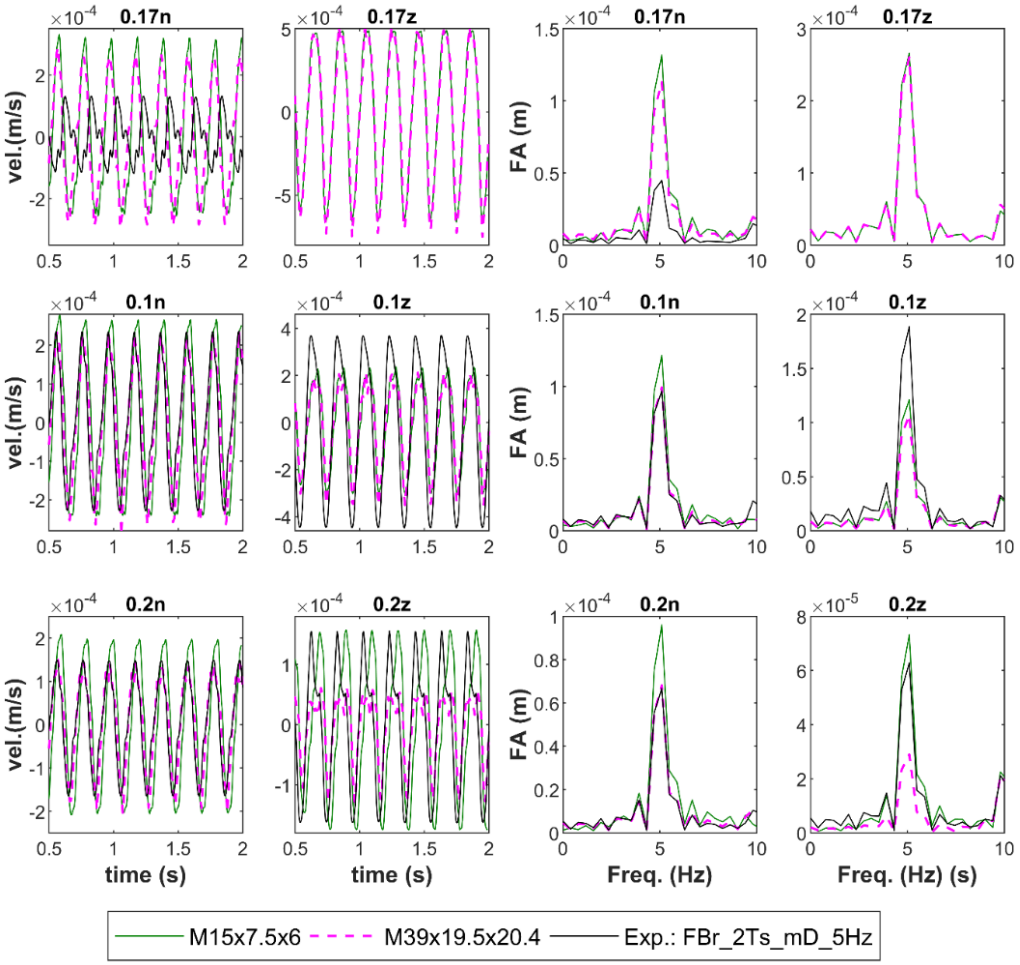


Figure F.10: Boundary effects on the soil response at different locations predicted by the FBr_2Ts_mD_5Hz forced vibration simulation.

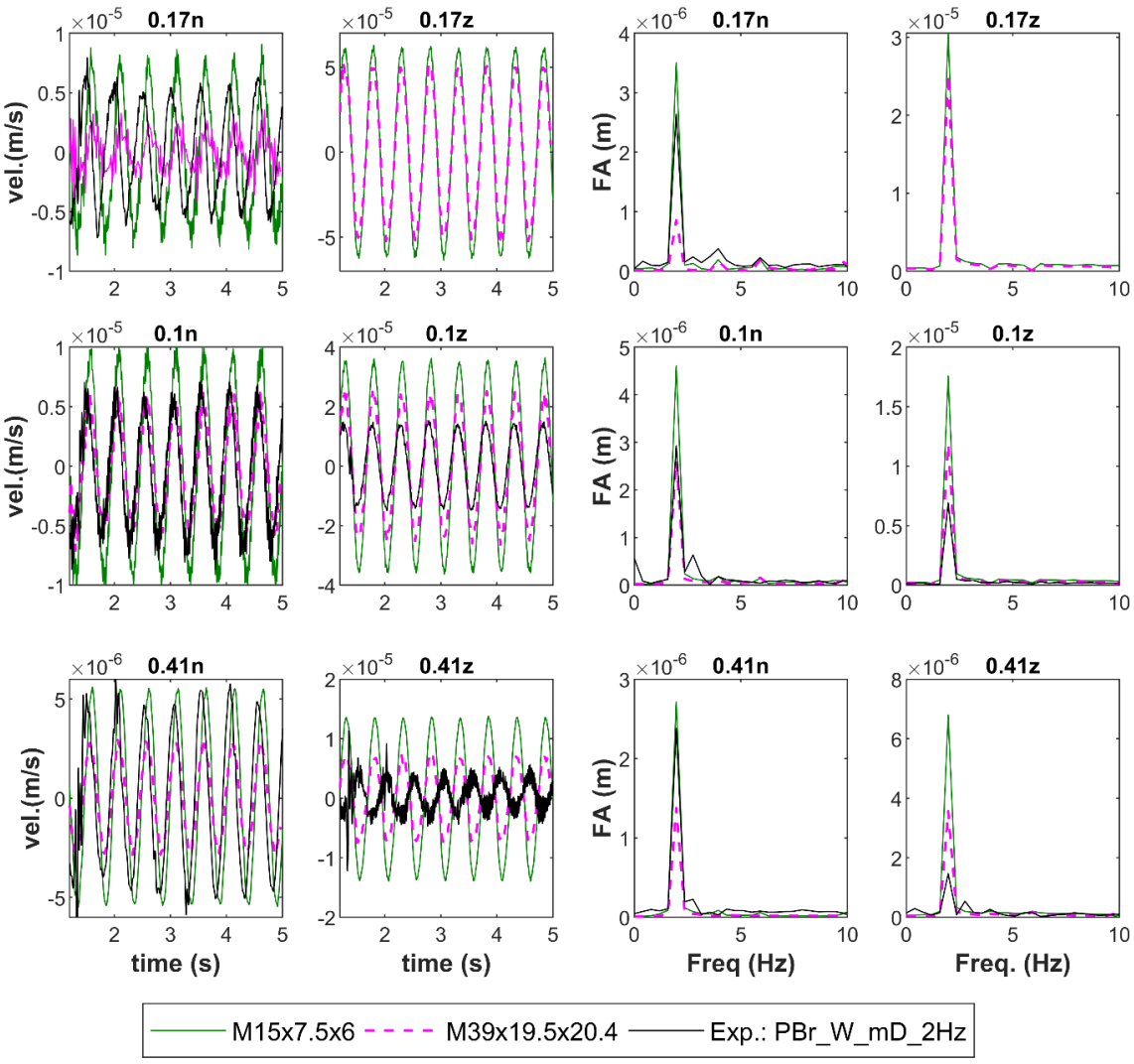


Figure F.11: Boundary effects on the soil response at different locations predicted by the PBr_W_mD_2Hz forced vibration simulation.

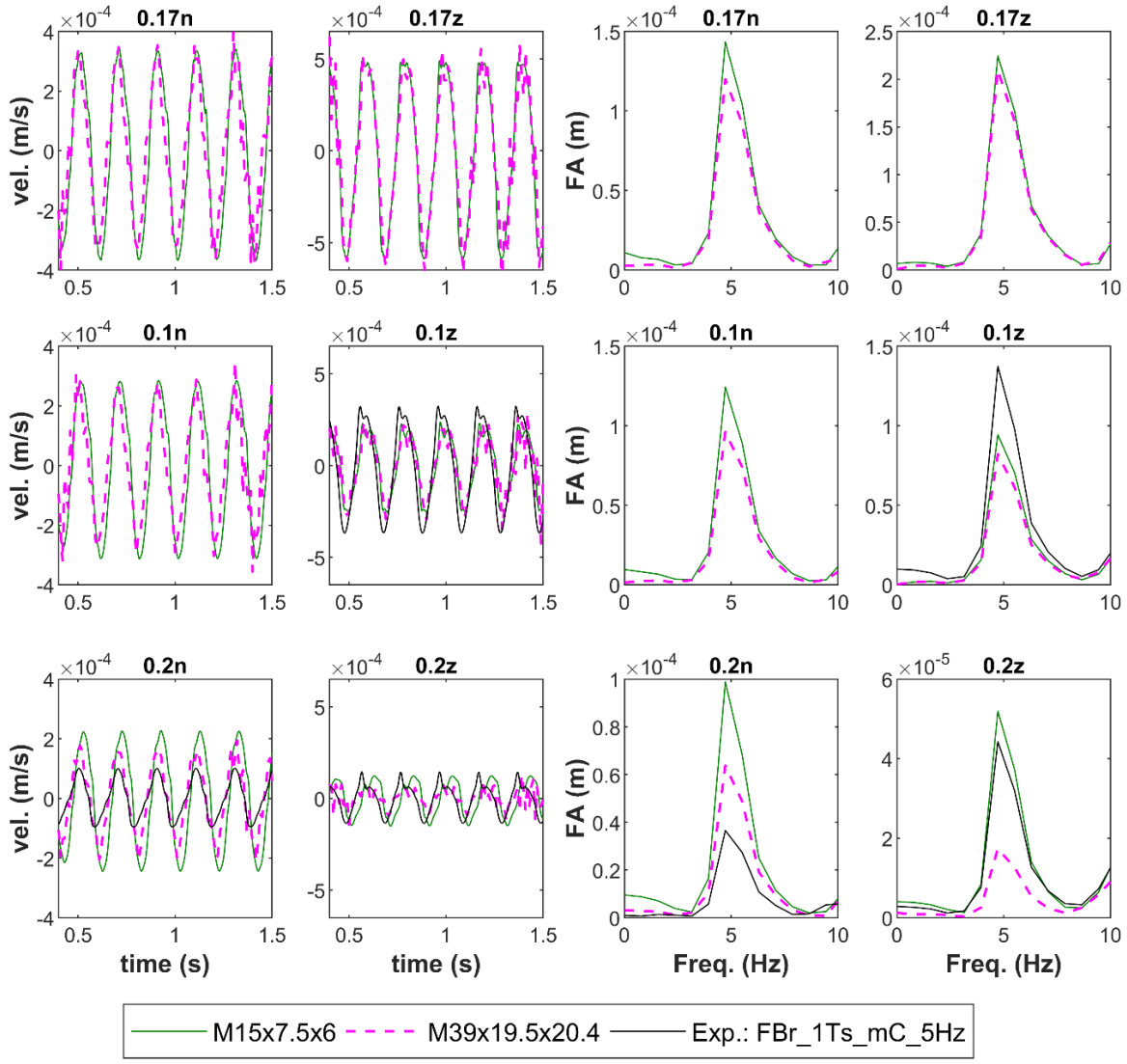


Figure F.12: Boundary effects on the soil response at different locations predicted by the FBr_1Ts_mC_5Hz forced vibration simulation.

Appendix G

Predictive Results

Appendix G.1 Free Vibration: Soil motion

Figures G.1 to G.4 present the variation of (a, b) vertical and (c, d) horizontal soil motion components with distance from the foundation edge. The results are presented in terms of Fourier amplitude (FA) of the main peak of spectra, that are inferred from numerical and experimental velocity time histories. The results are computed from NLINs_HYBint_StSW3_GC2 analyses, that simulate FBr_2Ts and PBr_W free vibration tests. Figures G.1 and G.2 present soil motions of the FBr_2Ts simulations, that are extracted from the soil surface along lines that extend North and East to the foundation, respectively. Similarly, Figures G.3 and G.4 present results from the PBr_W simulations, that are taken from nodes which lie on the same lines. For simplicity, the two lines are referred to as *North line* and *East line*. The North line lies in the plane of symmetry and coincides with the positive x axis, with reference the coordinate system in Figure 7.3. The East line is perpendicular to the plane of symmetry and coincides with the negative y axis.

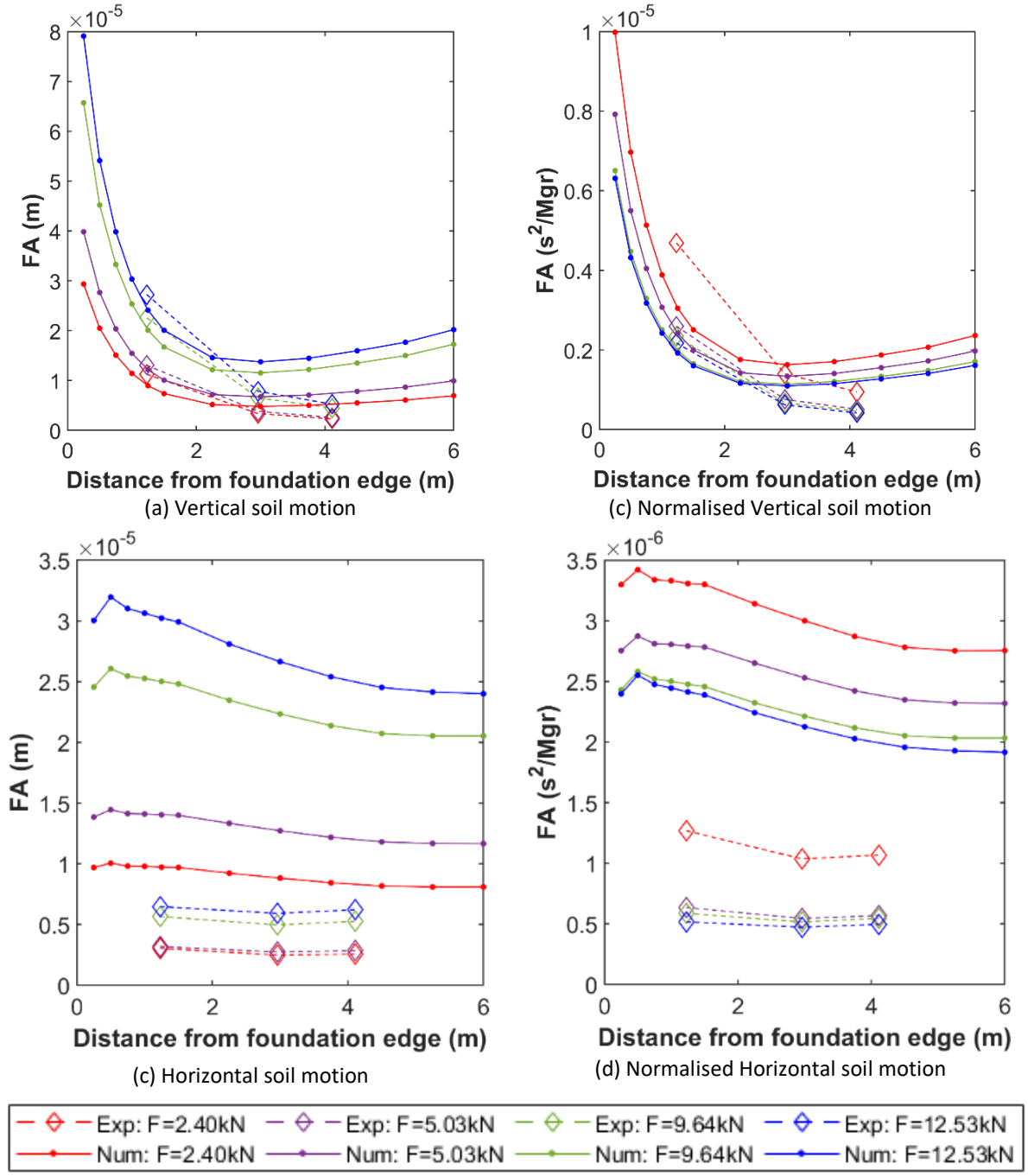


Figure G.1: Variation of (a, b) vertical and (c, d) horizontal soil motion components with distance from the foundation edge, as computed by FBr_2Ts simulations. The results are obtained from nodes and instrument of the North line.

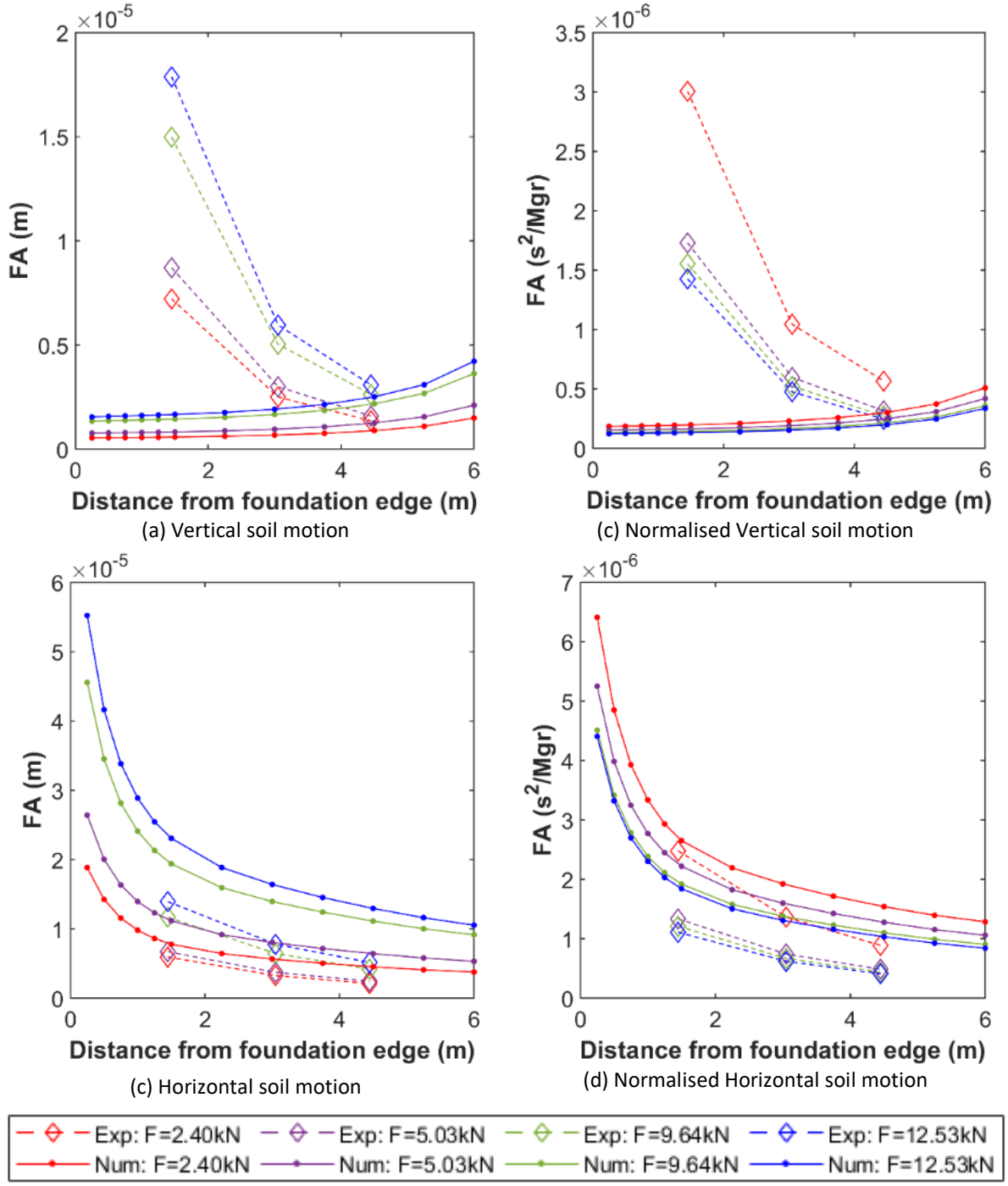


Figure G.2: Variation of (a, b) vertical and (c, d) horizontal soil motion components with distance from the foundation edge, as computed by FBr_2Ts simulations. The results are obtained from nodes and instrument of the East line.

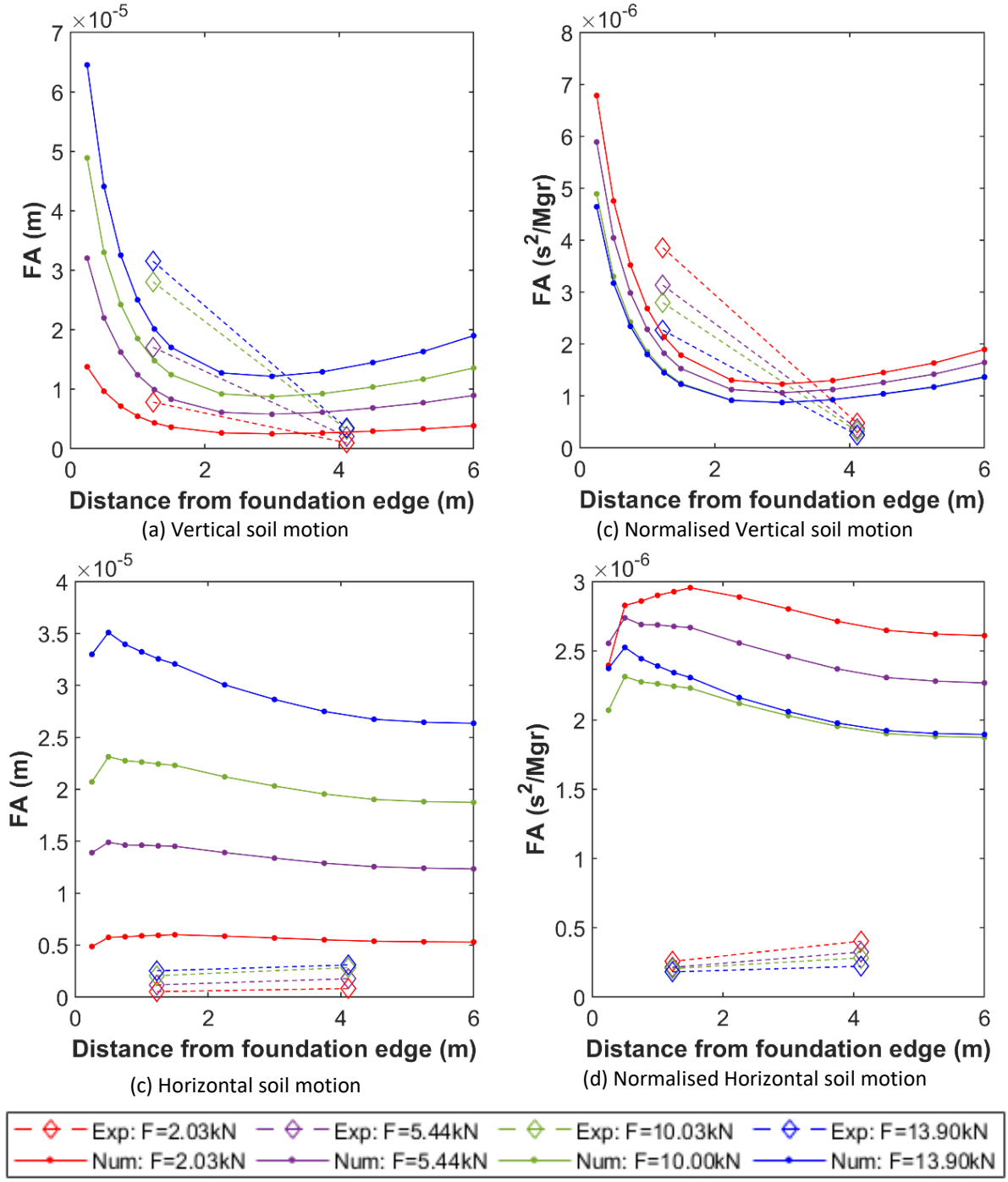


Figure G.3: Variation of (a, b) vertical and (c, d) horizontal soil motion components with distance from the foundation edge, as computed by PBr_W simulations. The results are obtained from nodes and instrument of the North line.

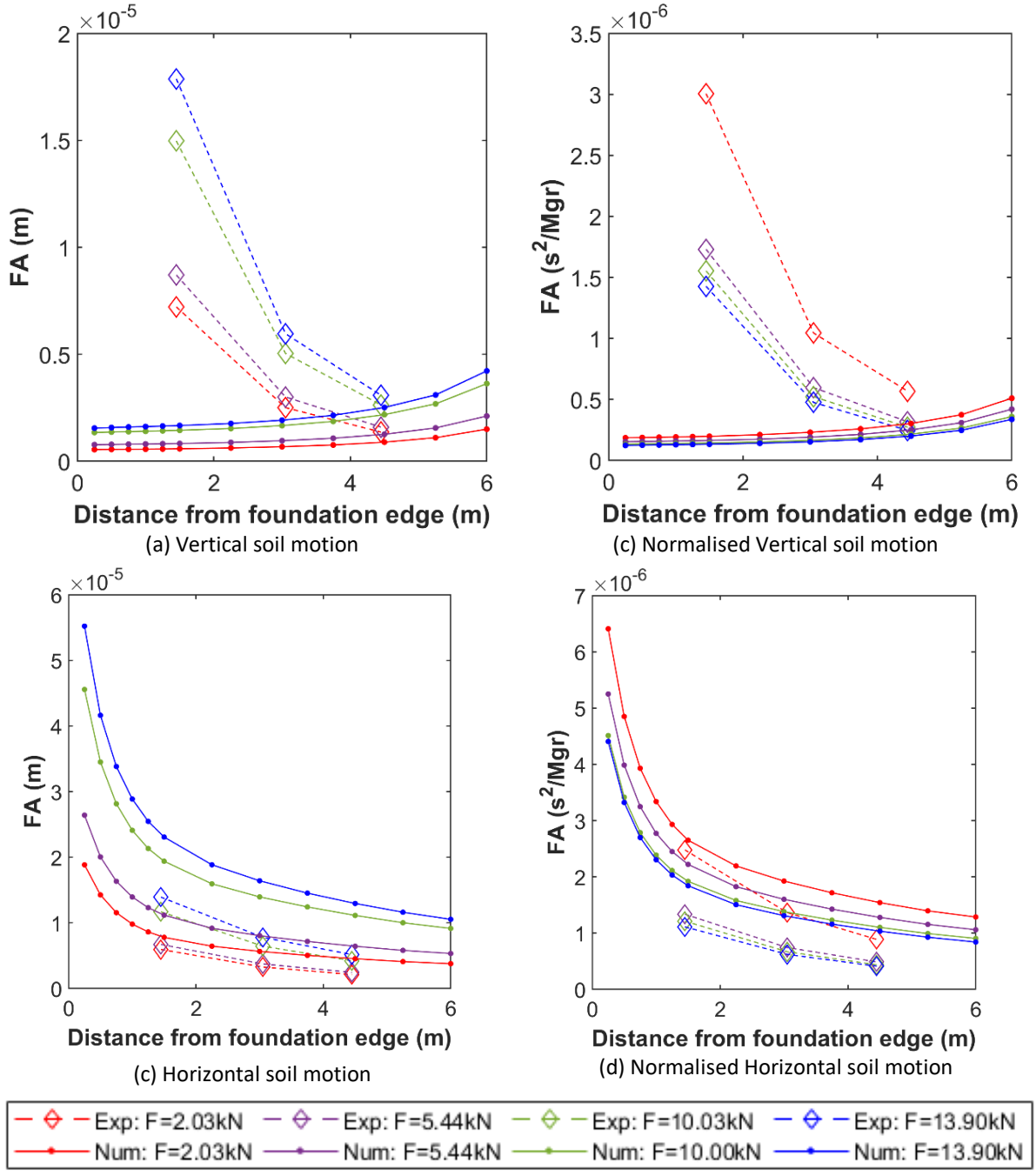


Figure G.4: Variation of (a, b) vertical and (c, d) horizontal soil motion components with distance from the foundation edge, as computed by PBr_W simulations. The results are obtained from nodes and instrument of the East line.